CYC2022

23rd International Conference on Cyclotrons and their Applications

December 5-9, 2022 • Beijing, China

Honorary Chairman: Professor Mingwu Fan (HUST) & Professor Xiaogang Xue (CIAE)

Hosted by China Institute of Atomic Energy & Huazhong University of Science and Technology

China Institute of Atomic Energy

PROCEEDINGS

The Scientific Themes

1. Cyclotron and Technology
2. Theory, Models and Simulations
3. Operation and Upgrades
4. Cyclotron Applications
5. Cyclotron in Medicine
6. FFAG and new projects
7. Session for young scientists

International Organizing Committee

Yuri Bylinski (TRIUMF, CA)
Lowry Conradie (Emeritus TLABS, ZA)
Andrea Denker (HZB, DE)
Mitsuhiro Fukuda (RCNP, JP)
Ralf Gebel (FZJ, DE)
Alexander Gerbershagen (PARTREC, NL)
Boris Gikal (JINR, RU)
Pauli Heikkinen (JYFL, FI)
Yves Jongen (IBA, BE)
Donald May (TAMU, US)
Yoshiharu Mori (RRI, JP)
Koji Noda (NIRS, JP)
Hiroki Okuno (RIKEN, JP)
Nancy Postiau (UCL, BE)
Danilo Rifuggiato (INFN, IT)
Alain Savalle (GANIL, FR)
Hermann Schweickert (ZAG, DE)
Mike Seidel (PSI, CH)
Susan Smith (STFC, UK)
Andreas Stolz (MSU, US)
Damon Todd (LBNL, US)
Wenlong Zhan (IMP, CN)
Tianjue Zhang (**Chairman**) (CIAE, CN)
HongWei Zhao (IMP, CN)

Scientific Programme Committee Chair: Shizhong An, CIAE, CN
Scientific Programme Committee Co-chair: Daniela Kiselev, PSI, CH
Local Organizing Committee Chair: Yuntao Liu, CIAE, CN

E-mail: cyclotron-2022@ciae.ac.cn
Website: https://www.cyc2022.cn/event/1/

Foreword

The 23rd International Conference on Cyclotrons and their Applications (CYC2022) took place from December 5 to 9 in Beijing, P. R. China. It was hosted by China Institute of Atomic Energy (CIAE) and Huazhong University of Science and Technology (HUST). Due to COVID-19, it is the first time in history that the Cyclotron Conference was held in the form of virtual conference.

The mission of the conference is to highlight the achievements and new trends of the development of international cyclotron community in recent years. Due to the boom of the development of cyclotron in the field of nuclear medicine and biological effect "Cyclotron in Medicine" has been included as one of the application sessions of CYC2022. This is to encourage participation from hospitals and relevant agencies, and to promote mutual understanding and potential joint innovations in cyclotron and medicine.

Lowry Conradie, IOC and SPC Chair of CYC2019, pointed out that the declining trend of student participation needs additional attention. This conference provided ample opportunities for young students to participate, study, present and share ideas. Finally, 38 students from 5 countries registered for free and got involved in all the academic activities of CYC2022.

Although we faced a difficult situation due to COVID-19 for international communication, more than 260 delegates including 237 registered delegates attended CYC2022 virtual conference for sharing information, finding mutual interests and forming collaborations. The quantity and quality of submitted papers kept almost the same level as before with the great joint efforts of all authors and editors. I hope that in the near future face-to-face academic communication will be again possible, keeping alive the cyclotron community, generating new ideas for cyclotron research and applications, and ultimately resulting in meaningful benefits for the society.

Finally, I would like to thank all participants for attending the conference. Their impressive scientific contributions made this conference such a success. At the same time, the diligent contribution of all the IOC, SPC and LOC members also deserves our sincere gratitude and respect.

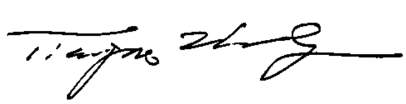

Tianjue Zhang
IOC Chair of CYC2022

International Organizing Committee (IOC)

Yuri Bylinski		TRIUMF, CA
Lowry Conradie		Emeritus iThemba Labs, ZA
Andrea Denker		HZB, DE
Mitsuhiro Fukuda		RCNP, JP
Ralf Gebel		FZJ, DE
Alexander Gerbershagen		PARTREC, NL
Boris Gikal		JINR, RU
Pauli Heikkinen		JYFL, FI
Yves Jongen		IBA, BE
Donald May		TAMU, US
Yoshiharu Mori		RRI, JP
Koji Noda		NIRS, JP
Hiroki Okuno		RIKEN, JP
Nancy Postiau		UCL, BE
Danilo Rifuggiato		INFN, IT
Alain Savalle		GANIL, FR
Hermann Schweickert		ZAG, DE
Mike Seidel		PSI, CH
Susan Smith		STFC, UK
Andreas Stolz		MSU, US
Damon Todd		LBNL, US
Wenlong Zhan		IMP, CN
Tianjue Zhang	**IOC & Conference Chair**	CIAE, CN
HongWei Zhao		IMP, CN

Scientific Program Committee (SPC)

Shizhong An	**SPC Chair**	CIAE, CN
Lowry Conradie		Emeritus iThemba LABS, ZA
Andrea Denker		HZB, DE
Santo Gammino		INFN, IT
Yoshihiro Ishi		RRI, JP
Ivan Ivanenko		JINR, RU
Daniela Kiselev	**SPC Co-Chair**	PSI, CH
Wiel Kleeven		IBA, BE
Hiroki Okuno		RIKEN, JP
Thomas Planche		TRIUMF, CA
Liangting Sun		IMP, CN
Daniel Winklehner		MIT, US

Local Organizing Committee (LOC)

Jingyu Di	**Chair Support**	CIAE, CN
Jianhua Feng	**PCO Manager**	PCO, CN
Mingzhi Hu	**SPMS IT Support**	CIAE, CN
Xianlu Jia	**Conference Coordinator**	CIAE, CN
Pengzhan Li	**Industrial Exhibition Manager**	CIAE, CN
Yuntao Liu	**LOC Chair**	CIAE, CN
Bin Qin	**Communications**	HUST, CN
Qiqi Song	**SPMS IT Support**	CIAE, CN
Ping Tan	**Communications**	HUST, CN
Zhiguo Yin	**SPMS Admin & Conference Secretary**	CIAE, CN

JACoW Editorial Team

Jan Chrin		PSI, CH
Aoxuan Ding		CIAE, CN
Pengzhan Li	**Editor-in-Chief**	CIAE, CN
Michaela Marx	**Slides Editor**	DESY, DE
Joele Mira		iThemba Labs, ZA
Volker RW Schaa	**Technical Editor**	GSI, DE

In Memoriam:
Dr. Gerardo Dutto

By Tianjue Zhang, Beijing, 9 December 2022

At the age of 81 Gerardo Dutto, the former Head of the TRIUMF Cyclotron Division, passed away in Nanaimo, Canada on February 13, 2020. Over the years Gerardo made many contributions to the development of cyclotron technology at TRIUMF and around the world, and also to the good relations and collaborations between TRIUMF and other Institutes including China Institute of Atomic Energy (CIAE) all over the world.

Gerardo Dutto was born on August 8, 1938 in Berlin, Germany. He received his doctorate in physics in 1971 from the University of Rome La Sapienza. Soon after Gerardo arrived at TRIUMF, he first worked on the Centre Region Cyclotron, a 3 MeV full-sized prototype of the main cyclotron center region. His beam dynamics support and other innovations improved the cyclotron's beam-current performance by a factor of three over the original 100 μA design specification. After that, Gerardo became part of the 500 MeV cyclotron commissioning team. Over the next few years, he headed the task force which worked on increasing the cyclotron beam current to its design level of 100 microamps, where he initiated many upgrades required to obtain the requisite licensing. These upgrades improve reproducibility and eliminate problems found with beam intensity limitations in the Centre Region.

Gerardo became the TRIUMF Cyclotron Division Head in 1981, a position he maintained until his retirement in 2003. Under his leadership, the cyclotron team demonstrated that 420 μA was possible, quadruple the initial 100 μA design goal. Perhaps even more impressive was Gerardo's commitment to cyclotron reliability. Now 46 years after first acceleration, the cyclotron has consistently achieved >90% availability, in large part due to the culture and expertise that Gerardo cultivated. During his final years at TRIUMF, Gerardo was involved in beam intensity stability developments for the multiple extracted beams, which was particularly important for ISAC to maximize production since the targets were being run near their limits.

Gerardo was a 'people' person with an amazing ability to bring people together. This ability extended far beyond the TRIUMF offices and included many memorable social gatherings. His global reach extended beyond well-known major labs in the USA and Europe to China. He developed meaningful and productive bridges with China during last 30 years.

Around 2000, CIAE started to design a 100 MeV compact cyclotron CYCIAE-100. This is the first time we have developed such a high intensity compact cyclotron with energy up to 100 MeV. Since then, Dr. Gerardo Dutto had visited CIAE in person year by year to introduce his experience to CIAE's cyclotron team and supervised our young researchers for the cyclotron development. And according to the needs of the design and construction, he also timely recommended and helped to invite the cyclotron experts from TRIUMF, PSI, INFN and GANIL etc. to visit Beijing and have cooperative research. More importantly, he helped us to organize two technical meetings of cyclotron experts in Tokyo in 2004 and Sicily in 2007 to discuss problems in the design and construction of CYCIAE-100. Our cyclotron successfully extracted the first proton beam in 2014 and achieved 520 μA on the beam dump in 2018, which is inseparable from his original help.

He also comprehensively promoted the technical collaboration between TRIUMF and CIAE for more than 15 years. The collaboration for the past years has proved to be very productive in many aspects, especially in the field of Accelerator Science and Technology. The mutual exchange of personnel within the framework of the collaboration has taken place. According to available statistics, the visitors including: Gerardo Dutto, Igor Sekachev, Ken Fong, George Mackenzie, Mike Craddock, Qiwen Zheng, Shuyao Fang, Tom Kuo, Dick Yuan, Paul Schmor, Alan Shotter, Bruce Milton, Yi-Nong Rao, Yuri Bylinski, Robert Laxdal, Michael Laverty, Richard Baartman, Nigel Lockyer, Jonathan Bagger, etc. from TRIUMF and, Tianjue Zhang, Chengjie Chu, Hongjuan Yao, Yinlong Lv, Bin Ji, Sumin Wei, Zhenguo Li, Jiansheng Xing, GaofengPan, Fang Yan, Zhiguo Yin, Xianlu Jia, Yanyun Ma, Xiaoliang Fu, Baoqun Cui, Weiping Liu, etc. from CIAE.

Dr. Garardo Dutto was awarded "Friendship Award" in 2015, which is the upmost prize set by Chinese government for foreign experts who has made great contribution during Chinese cause of modernization and reform and opening up. This is the most top Chinese national-level prize for foreign experts for their contributions of the country. The premier and vice premier of the State Council presented at this awarding ceremony and exchanged ideas with the awarded scientists, every year. However, Dr. Dutto was absent at this awarding ceremony at the Great Hall of the People in October 2015 for his health reason.

Consul General of P. R. China in Vancouver Madame Liu Fei awarded the prize on behalf of Chinese government to Dr. Dutto and his family in the Coast Bastion Hotel in Nanaimo, on April 20, 2016. I, on behalf of CIAE and Prof. Bagger, on behalf of TRIUMF attended the event and share a pleasant reward for our continuing cooperation in the past years.

Here that: feel good when somebody miss you, feel better when somebody loves you, but feel best when somebody never forgets you. We mourn and miss Dr. Dutto. He may be out of our sight, but not out of our mind; He may be out of our reach, but not out of our heart. At this moment, and forever, let's remember Dr. Gerardo Dutto's contribution to the cyclotron Community.

Contents

ISBN: 978-3-95450-212-7 ISSN: 2673-5482 doi:10.18429/JACoW-CYCLOTRONS2022-MOAI01

STATUS OF THE HIAF ACCELERATOR FACILITY IN CHINA*

J. C. Yang†, L. T. Sun, Y. J. Yuan and HIAF project team, IMP CAS, Lanzhou, China

Abstract

The High Intensity heavy-ion Accelerator Facility (HIAF) is under constructed at IMP in China. The HIAF main feature is to provide high intensity heavy ion beam pulse as well as high intensity CW beam. A rapid acceleration in the booster synchrotron ring (BRing) with the ramping rate of 12 T/s is used. The challenges related to the injector systems, RF cavities, power supplies, vacuum system are reported in this paper. The status of the HIAF project construction is presented.

INTRODUCTION

The High Intensity heavy-ion Accelerator Facility (HIAF) is a new accelerator under construction at the Institute of Modern Physics (IMP) in China [1]. It is designed to provide intense primary heavy ion beams for nuclear and atomic physics. The facility mainly consists of a superconducting electron-cyclotron-resonance (SECR) ion source, a continuous wave (CW) superconducting ion linac (iLinac), a booster synchrotron (BRing) and a high precision spectrometer ring (SRing). A fragment separator (HFRS) is also used as a beam line to connect BRing and SRing. Six experimental terminals will be built at HIAF. The layout of the HIAF accelerator is shown in Fig. 1. The main parameters are listed in Table 1.

The construction of the HIAF project was started in December 23rd, 2018. Up to now, roughly 50% of civil construction is finished, as shown in Fig. 2. The first component of SECR is planned to installed in the tunnel in 2023. The first accelerated beam at BRing is expected in the middle of 2025. Day-one experiment is scheduled by the end of 2025. A brief time schedule of HIAF construction is shown in Fig. 3.

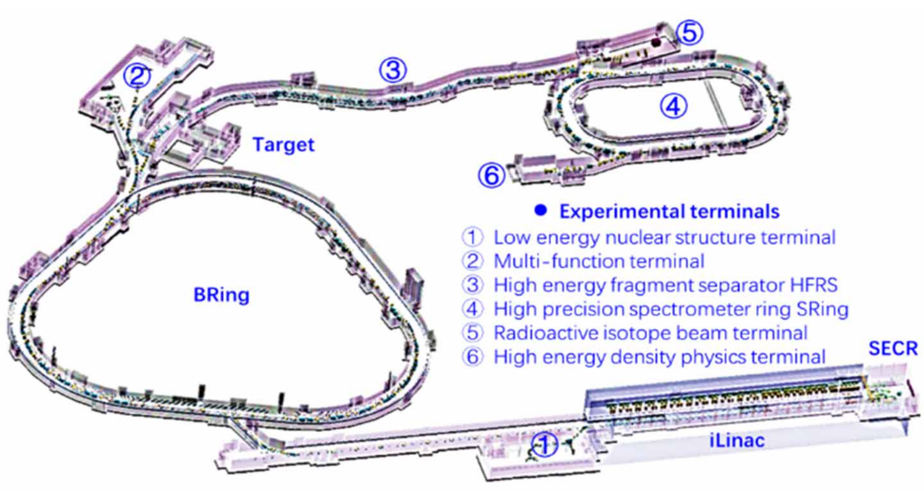

Figure 1: Layout of the HIAF project.

Figure 2: Civil construction of the HIAF project.

* Work supported by the National Development and Reform Commission, China

† yangjch@impcas.ac.cn.

ISBN: 978-3-95450-212-7 ISSN: 2673-5482 doi:10.18429/JACoW-CYCLOTRONS2022-MOAI01

Table 1: Main Parameters of the HIAF Accelerators

	SECR	iLinac	BRing	HFRS	SRing
Length / circumference (m)	---	114	569	192	277
Final energy of U (MeV/u)	0.014 (U^{35+})	17 (U^{35+})	835 (U^{35+})	800 (U^{92+})	800 (U^{92+})
Max. magnetic rigidity (Tm)	---	---	34	25	15
Max. beam intensity of U	50 pμA (U^{35+})	28 pμA (U^{35+})	10^{11}ppp (U^{35+})		10^{10}ppp (U^{92+})
Operation mode	DC	CW or pulse	fast ramping (12T/s, 3Hz)	Momentum-resolution 1100	DC or deceleration
Emittance or Acceptance (H/V, π·mm·mrad, dp/p)		5 / 5	200/100, 0.5%	±30mrad(H)/±15 mrad(V), ±2%	40/40, 1.5%, normal mode

Currently, most of the prototypes related to the HIAF technical challenges have being manufactured or tested. In this paper, the status and perspectives of the HIAF project are presented. The developments and test results of hardware are reported.

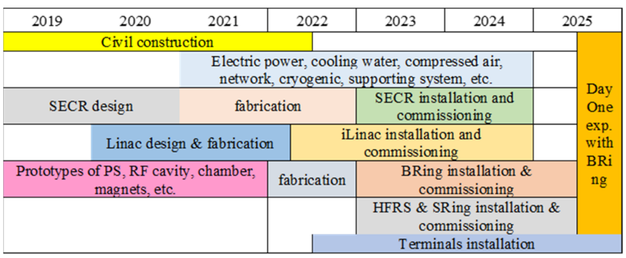

Figure 3: time schedule of the HIAF construction.

ION SOURCE

Pulsed 50 pμA (1 ms) U^{35+} ion beam from SECR is required in the HIAF project, which is 5 times higher than the present records of the 3rd generation ECR ion source. It can only be met by sources operating at higher magnetic field and microwave frequency. SECR incorporates with a Nb_3Sn high field superconducting magnet and a quasi-optical 45 GHz gyrotron microwave system, as shown in Fig. 4. The main parameters are listed in Table 2. The biggest challenge lies in the design and fabrication of the Nb_3Sn magnet. A promising cold mass design has been completed by a collaboration with LBNL. Up to now, a 1/2 cold-mass prototypes related to critical technologies have be fabricated and tested. The full-sized cold-mass completion is scheduled in 2023 [2].

Table2: Typical Parameters of SECR

Specs.	Unit	SECR
Frequency	GHz	45
RF power	kW	20
Chamber ID	Mm	>Φ140
Mirror fields	T	≥6.4/3.2
B_{rad}	T	≥3.2
B_{max} in conductor	T	11.8
Magnet coils	---	Nb_3Sn
Cooling capacity at 4.2 K	W	>10

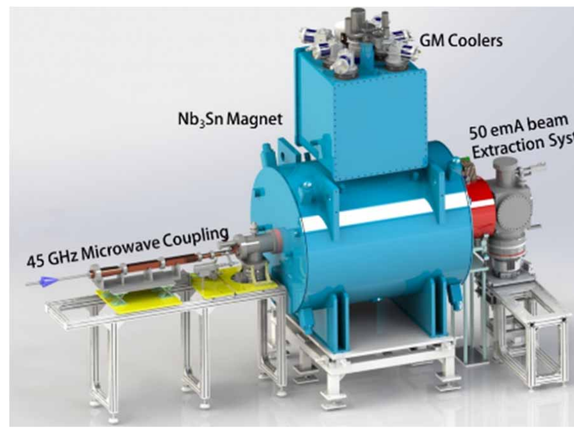

Figure 4: the 4th generation ion source SECR

The microwave power transmission coupling and ECR heating are critical issues. Based on the present ion source SECRAL-2 at IMP, a study with a 45 GHz gyrotron microwave system by GYCOM Ltd was reported [3]. The transmission lines combined quasi-optical mirror and wave guide mode converter are manufactured. The 45 GHz microwave power at TE01 mode has been fed into SECRAL-2 and got the first stable 45 GHz ECR plasma and Xenon beam.

LINAC INJECTOR

The iLinac is used as the injector of BRing and the main accelerator for the low energy nuclear structure terminal. That's why a CW superconducting linac is proposed in HIAF. Two types of accelerating structures in 17 cryomodules are used to achieve the energy of 17 MeV/u for U^{35+} ion beam. The first 6 cryomodules with QWR007 cavities is used to accelerate U^{35+} ions to 5.4 MeV/u. The rest cryomodules are installed with HWR015 cavities. These cavities will be made based on the experience of the CiADS project. A layout of iLinac is shown in Fig. 5. The physics design has been finished.

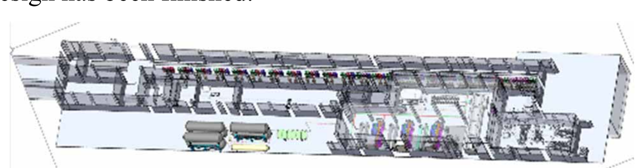

Figure 5: 3-D view of iLinac. SECR locates on left side.

ISBN: 978-3-95450-212-7 ISSN: 2673-5482 doi:10.18429/JACoW-CYCLOTRONS2022-MOAI01

BOOSTER SYNCHROTRON

BRing is the key component of the HIAF project. It is designed with a maximum magnetic rigidity of 34 Tm, which is intended for the storage of U^{35+} ions to an intensity of 2×10^{11} particles with the energy of 835 MeV/u. The BRing lattice and its beta function and dispersion function are shown in Fig. 6. The ionization of residual gas particles is the main concern with respect to potential beam loss. Therefore, the lattice design is to localize the beam loss at certain positions to install collimators. It has a three-fold symmetry lattice with DBA (double bend achromat) structure. BRing offers a transverse acceptance of 200 / 100 π·mm·mrad to overcome space charge limits of high intensity beams. It is operated below the transition energy to avoid beam loss by transition-energy crossing [4].

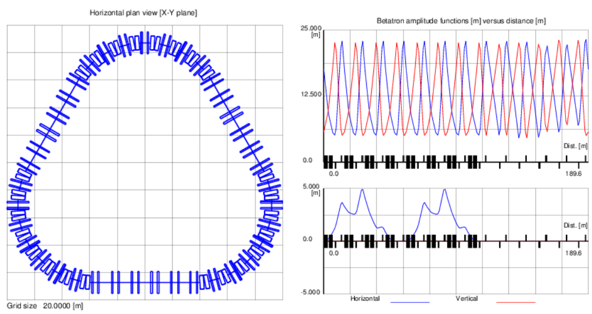

Figure 6: BRing lattice structure and its beta function and dispersion function.

Beam stacking with the electron cooling method is not possible for fast ramping synchrotrons. To obtain a high average beam intensity and avoid space charge limits, transverse phase space painting (4-D) is implemented for beam accumulation and a rapid ramping cycle is used to reduce the integral ionization cross section. Related prototypes as tilted electrostatic septum, thin-wall vacuum chamber, fast-cycling power supply and magnetic alloy (MA) acceleration cavities are developed for BRing.

Transverse Phase Space Painting Injection

In the 4-D painting injection scheme, the closed orbit is moved with the horizontal and vertical injection bumps as functions of time. Unlike the injection using charge exchange implemented in proton machine (SNS, J-PARC), a tilted corner septum is used for both transverse phase spaces simultaneous injection in BRing. Low-loss and low phase space dilution are basic requirements. Injection begins with both horizontal and vertical bump close to the centroid of injection beam, and then gradually move away from it. Both the horizontal and vertical emittances are painted from small to large [5]. Figure 7 shows the particle invariant distribution at the end of injection and its evolution up to 1000 turns. The simulation is performed with U^{35+} ions at the injection energy of 17 MeV/u. The total emittance and momentum spread of iLinac beam are 5 π·mm·mrad and ±0.2%, respectively. Space charge effect is included in the simulation. Due to a small gap between the closed orbit and the injection point, the injection efficiency is low at the beginning. A "hollow" beam in horizontal and vertical phase space is obtained after the injection. However, such a beam profile is susceptible to transverse coupling due to space charge forces in simulation. Finally, the particle emittance reaches a Gaussian-like distribution in both phase spaces.

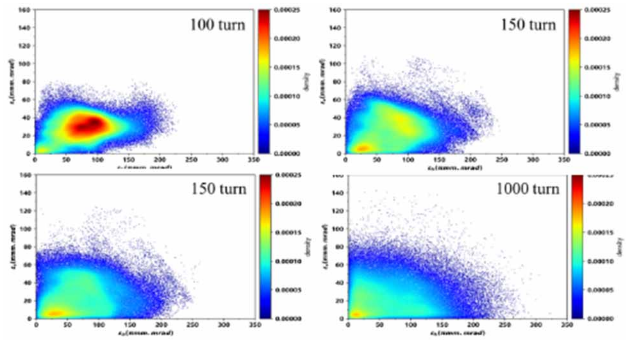

Figure 7: particle invariant distribution after 4-D painting injection.

Fast Ramping

Since the cross sections of ionization are decreasing significantly with ion energies, the integral cross section can be kept very small with a fast ramping rate. Rapid accelerating was proposed and tested at SIS18 in 2005, shown an optimistic result for minimum beam loss and dynamic vacuum effect. In BRing, a ramping rate of 12T/s is needed for optimising the space charge limits and collimators. Therefore, a dipole power supply with a rate of 38 kA/s and maximum current of 4 kA is desired. One power supply can be used for 4 dipoles connected in series and 12 groups are needed in BRing. A full-energy storage technology is developed to reduce its power consumption. The analytic modelling optimal control with kinetic inductance fine turning method is used in the control system, to improve the precision of current ramping. A prototype was already tested at IMP. The maximum current of 5.1 kA was obtained for a solenoid load with the ramping rate of 40 kA/s, as shown in Fig. 8. The output current average tracking error is around 5×10^{-4}, which meets the requirements of BRing.

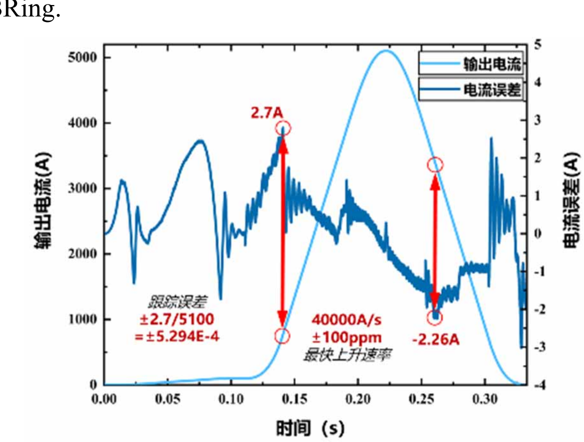

Figure 8: current curve of fast ramping power supply.

ISBN: 978-3-95450-212-7 ISSN: 2673-5482 doi:10.18429/JACoW-CYCLOTRONS2022-MOAI01

High accelerating voltage up to 240 kV is used in the fast ramping of BRing, which will be provided by new MA acceleration cavities. The quality factor (*Q value*) is set at 0.45 to cover a wide frequency range of 0.3 to 2 MHz. A typical acceleration process is shown in Fig. 9. There are four stages. The first capture stage is used to capture the coasting beam after 4-D multi-turn painting injection. Usually two or even more bunches are obtained in the first capture stage, since a high harmonic should be used at such low injection energies. At the acceleration stage, the maximum ramping rate is 12 T/s, corresponding to the maximum RF voltage of 240 kV. At the de-bunching stage, the RF voltage decreases to zero rapidly, a coasting beam is obtained again in BRing. Two extraction schemes are designed in BRing. The slow extraction mode starts at the end of de-bunching. In the fast extraction mode, additional second capture stage is needed, to make only one bunch in BRing. the extraction starts at the end of the second capture stage.

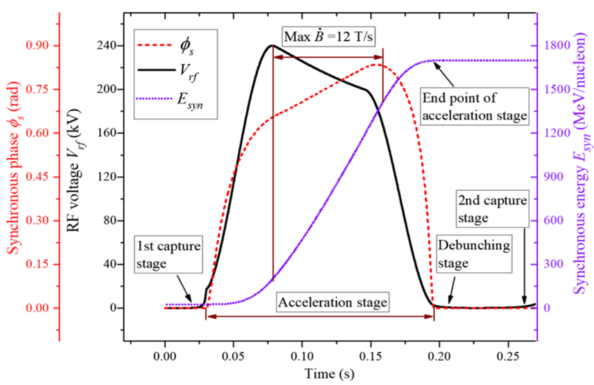

Figure 9: Corner septum cross section and its field map.

The fast ramping of the magnets induces eddy currents in the vacuum chamber wall, which could make a distortion of magnetic field. Thin-wall vacuum chamber is a good solution to reduce the eddy current effect. A stainless steel with the thickness of 0.3 mm is used for the BRing vacuum chamber. To withstand the atmospheric pressure, the thin wall vacuum chamber is supported by titanium alloy (TC4) rings inside. Compared to the similar chamber with reinforced ribs, the gap size of the dipole decreases significantly. A prototype of the TC4 rings has been tested, as shown in Fig. 10.

Figure 10: the TC4 rings inside of the chamber.

Fast and Slow Extraction System

To meet the requirements of multi-purpose experiments, fast and slow extraction systems sharing the same extraction channel have been designed in BRing. Fast extraction system is used to provide single-short bunched beam, and it comprises seven kicker cells, three orbit bumpers and four magnetic septa. The phase advance be-tween the first three kicker cells and magnetic septa is optimized to 3π/2, and that of the rest four kicker cells is near to π/2. Together with three orbit bumpers increasing a local bump amplitude of 20 mm, a total horizontal kick angle about 6.42 mrad can be provided by the kicker cells, and it can create a separation about 40 mm in front of the first magnetic septum. The fast extraction beam envelopes are shown in Fig. 11. The zone in green is the acceptance, and the one in cyan and yellow are the circulating and extracted beams with $\varepsilon_{x,total}$= 24 π·mm·mrad and $\delta p/p = \pm 0.2\%$ respectively. The slow extraction is applied for acquiring quasi-continuous beam by third-order resonance and RF-knockout scheme, and it consists of three 1.5 m-long successive electrostatic septa and two kinds of different functional orbit bump magnets. One is four horizontal correctors for raising a height of 10 mm at the entrance of first electrostatic septum to save effective aperture of the elements in the BRing. The other one is the three orbit bumpers also used in fast extraction to reduce the deflection voltage of the electro-static septa. Consequently, a field up to 90 kV/cm with electrode spacing of 15 mm can realize identical entrance position of extracted $^{238}U^{35+}$ with the energy of 835 MeV/u beam at the first magnetic septum.

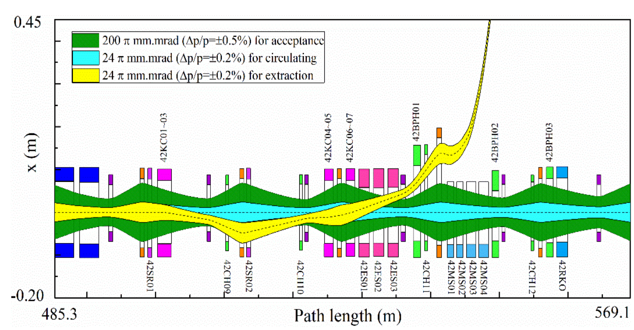

Figure 11: The fast extraction beam envelopes.

SPECTROMETER RING

SRing is designed as a multi-function experimental storage ring, which can be operated in three modes. Firstly, it will be used as an isochronous mass spectrometer (IMS mode) with two TOF detectors for short-lived neutron-rich nuclei. Secondly, it is used to collect and cool long-lived rare isotopes for nuclear experiments, or accumulate and extract highly-charged stable ions for high energy density physics (normal mode). Thirdly, it can be used to store H-like, He-like or other special charge state ions for internal target experiments (target mode). Ions can be decelerated to tens MeV in this mode. Details are available in [6].

ISBN: 978-3-95450-212-7 ISSN: 2673-5482 doi:10.18429/JACoW-CYCLOTRONS2022-MOAI01

FRAGMENT SEPARATOR

The High energy Fragment Separator (HFRS) is an in-flight separator at relativistic energy. The schematic layout is shown in Fig. 12. A primary beam from BRing hits the target at PF0. The rare isotopes produced by projectile fragmentation or fission will be collected and purified by the HFRS with the Bρ-ΔE-Bρ method. The magnetic rigidity up to 25 Tm can be operated in HFRS. The large acceptance including the angular acceptances ±30 mrad (H) / ±15 mrad (V) and the momentum acceptance ±2% provides a high collecting efficiency. A two-stage structure is used in HFRS design. The pre-separator is used to dump the primary beams and undesired fragments. The main separator is used to identify the rare isotopes. Details of the HFRS design can be found in [9].

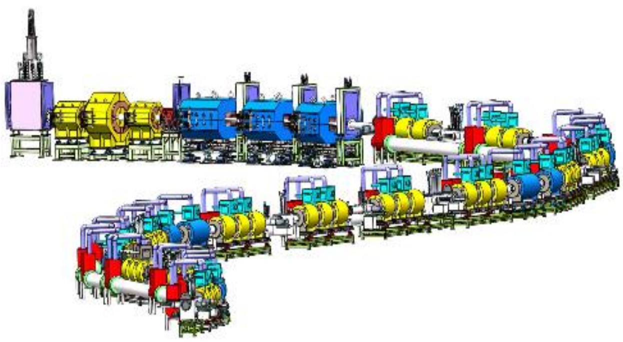

Figure 12: 3-D view of HFRS beam line.

CONCLUSION

The HIAF project is large scale heavy ion accelerator project under-construction in China. There are several challenges related to the ion source, the linac, the RF cavities, the power supplies, the vacuum system and so on. In the past few years, the HIAF project team have completed the development of several prototypes and obtained test results successfully. The HIAF construction will benefit from those progresses. The systematic commissioning of the accelerator complex is planned in 2025.

ACKNOWLEDGEMENTS

We thank all the colleagues working on the HIAF project for their valuable contributions on this article.

REFERENCES

[1] J. C. Yang, J. W. Xia, G. Q. Xiao, *et. al.*, "High Intensity heavy ion Accelerator Facility (HIAF) in China", *Nucl. Instrum. Methods Phys. Res. Sect. B*, vol. 317, part B, pp. 263-265, Dec. 2013. doi:10.1016/j.nimb.2013.08.046

[2] Liangting Sun, Wang Lu, Enming Mei, et.al., "Superconducting Magnets for High Performance ECR Ion Sources," in *IEEE Transactions on Applied Superconductivity*, vol. 28, no. 3, pp. 1-6, Apr. 2018. doi:10.1109/TASC.2018.2791943

[3] J. W. Guo, L. Sun, X. J. Niu, *et. al.*, "45 GHz microwave power transmission and coupling scheme study with superconducting ECR ion source at IMP", in *AIP Conference Proceedings*, vol. 2011, p. 090001, Sep. 2018. doi:10.1063/1.5053382

[4] Peng Li, Y. J. Yuan, J. C. Yang, *et. al.*, "The collimation system design for the Booster Ring in the HIAF project", *Nucl. Instrum. Methods Phys. Res. Sect. A*, vol. 920, pp. 14-21, Mar. 2019. doi:10.1016/j.nima.2018.12.064

[5] C. R. Prior, G. H. Rees, "Multiturn injection and lattice design for HIDIF", *Nucl. Instrum. Methods Phys. Res. Sect. A*, vol. 415, no. 1-2, pp. 357-362, Sep. 1998. doi:10.1016/S0168-9002(98)00406-0

[6] B. Wu, J. C. Yang, J. W. Xia, *et. al.*, "The design of the Spectrometer Ring at the HIAF", *Nucl. Instrum. Methods Phys. Res. Sect. A*, vol. 881, pp. 27-35, Feb. 2018. doi:10.1016/j.nima.2017.08.017

[7] L. J. Mao, J. Li, H. J. Lu, *et. al.*, "The Electron Cooling System for the HIAF Project in China", in *Proc. COOL'19*, Novosibirsk, Russia, Sep. 2019, pp. 14-17. doi:10.18429/JACoW-COOL2019-MOZ01

[8] V. B. Reva, E. Behtenev, V. Bocharov, V. Bubley, *et. al.*, "Commission of Electron Cooler EC-300 for HIRFL-CSR", in *Proc. EPAC'04*, Lucerne, Switzerland, Jul. 2004, paper TUPLT120, pp. 1419-1421.

[9] L. N. Sheng, X. H. Zhang, J. Q. Zhang, *et. al.*, "Ion-optical design of High energy FRagment Separator (HFRS) at HIAF", *Nucl. Instrum. Methods Phys. Res. Sect. B*, vol. 469, pp. 1-9, Apr. 2020. doi:10.1016/j.nimb.2020.02.026

23rd Int. Conf. Cyclotrons Appl. CYCLOTRONS2022, Beijing, China JACoW Publishing
ISBN: 978-3-95450-212-7 ISSN: 2673-5482 doi:10.18429/JACoW-CYCLOTRONS2022-MOAI02

UPGRADE AND CURRENT STATUS OF HIGH-FREQUENCY SYSTEMS FOR RIKEN RING CYCLOTRON

K. Yamada*, RIKEN Nishina Center, Wako, Japan

Abstract

The high-frequency systems for the RIKEN Ring Cyclotron (RRC) were upgraded to increase the acceleration voltage at 18.25-MHz operation by remodeling its cavity resonators and rf controllers. After the upgrade, the maximum gap voltage at 18.25 MHz improved from about 80 kV to more than 150 kV. The beam intensity of ^{238}U for the RI Beam Factory was increased up to 117 pnA in 2020 by overcoming the beam intensity limitation of the RRC due to the space charge effect. This article presents the details of the upgrade as well as the current status of the high-frequency systems for the RRC.

INTRODUCTION

RI Beam Factory

The Radioactive Isotope Beam Factory (RIBF) [1, 2] at the RIKEN Nishina Center started operation in 2006 in order to pursue heavy-ion beam science through basic and applied research, such as determining the origin of the elements, establishing new nuclear models, synthesizing new elements and isotopes, researching nuclear transmutation, and supporting industrial applications including biological breeding and producing useful RIs. The RIBF has four separate-sector cyclotrons: the RIKEN ring cyclotron (RRC [3], K = 540 MeV), the fixed-frequency ring cyclotron (fRC [4–6], K = 700 MeV), the intermediate-stage ring cyclotron (IRC [7], K = 980 MeV), and the world's first superconducting ring cyclotron (SRC [8], K = 2600 MeV). The RIBF can provide the world's most intense RI beams for all masses by accelerating heavy-ion beams up to 70% of light speed in cw mode, using a cascade of the four ring cyclotrons combined with different types of injectors: a variable-frequency heavy-ion linac (RILAC [9, 10]), a fixed-frequency heavy-ion linac (RILAC2 [11, 12]), and a K70-MeV AVF cyclotron (AVF [13]).

Uranium is one of the most important beams in the RIBF because it can produce many rare isotopes via the in-flight fission of uranium ions by a superconducting in-flight fragment separator, BigRIPS [14]. As shown in Fig. 1, the uranium ions are produced with a powerful 28-GHz superconducting ECR ion source [15, 16] at the charge state of 35+ and accelerated through the RILAC2 and RRC up to 11 MeV/u. After changing their charge state to 64+ by a helium gas stripper [17], they are further accelerated in the fRC and converted to 86+ by a graphite sheet stripper [18]. Finally, they are boosted up to 345 MeV/u by the IRC and SRC, and directed to the BigRIPS.

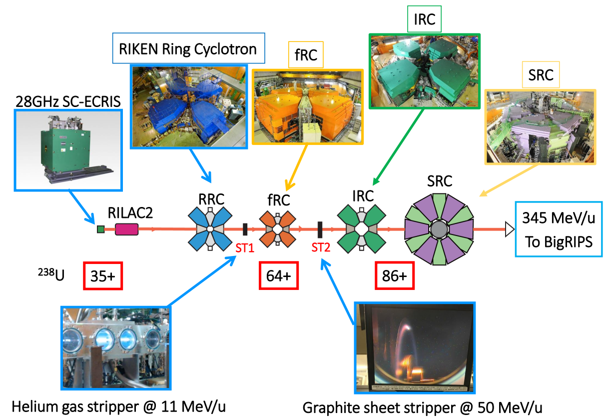

Figure 1: Schematic of uranium acceleration at the RIBF.

This article describes in detail the modification of the high-frequency systems for the RRC.

Overview of RRC

The RRC is a four-sector normal-conducting isochronous ring cyclotron that has been in operation for over 35 years. The RRC can accelerate light ions up to 135 MeV/u and is also frequently used to provide the intermediate-energy beams. Figure 2 indicates the equipment layout of the RRC. The RRC has an injection radius of 89.3 cm and an extraction radius of 356 cm, giving a large velocity gain of 4. Each radial sector has a sector angle of 50 degrees and is equipped with 26 trim coils. Beams are injected and extracted by one electrostatic deflector and two magnetic channels and bending magnets, respectively. The specifications of the RRC are summarized in Table. 1.

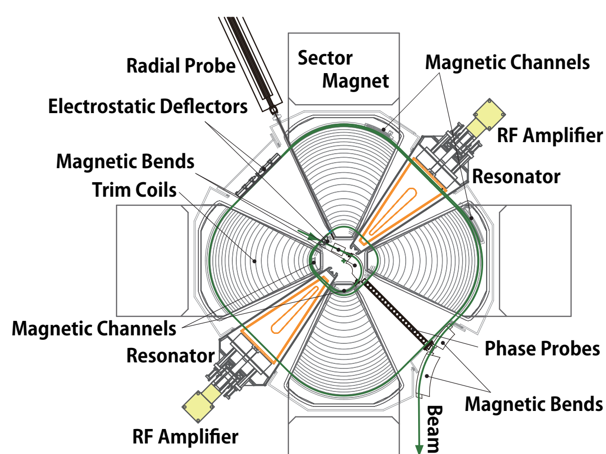

Figure 2: Equipment layout of the RRC.

* nari-yamada@riken.jp

ISBN: 978-3-95450-212-7 ISSN: 2673-5482 doi:10.18429/JACoW-CYCLOTRONS2022-MOAI02

Table 1: Specifications of the RRC

Parameter	Value
K-value	540 MeV
Sectors	4
Sector angle	50°
Pole gap	80 mm
Maximum field	1.6 T
Trim coils	26
Velocity gain	4.0
Mean injection radius	89 cm
Mean extraction radius	356 cm
Acceleration cavities	2
Frequency range	18–42 MHz
Harmonics	5, 9, etc.

The RRC has two variable-frequency acceleration cavities and does not use a flat-top system. The acceleration cavities of the RRC [19] are based on a half-wavelength resonator, which has two gaps between the dee electrode and the outer wall. The dee angle is 23.5 degrees, the acceleration gap length is 100 mm, and the outer dimensions of the cavity are 2.1 m(H)×3.5 m(W)×1.6 m(D). As shown in Fig. 3, the variable frequency devices of the RRC use a unique mechanism called a movable-box-type. The movable box is not in contact with the stem, only with the outer wall. The frequency can be varied using not only a change in the inductance but also the capacitance when the movable-box approaches the dee electrode. This mechanism makes it possible to vary the frequency from about 20 to 45 MHz with a size less than one-third that of a movable-short-type cavity. However, the dee voltage is frequency dependent due to the large shunt-impedance variation. The rf amplifier of the RRC is a three-stage configuration using tetrodes and has a maximum rf output of around 150 kW. The rf system has a voltage stability of less than 0.1% and a phase stability of less than 0.1 degree. We are currently using low-level circuits with analog feedback.

UPGRADE OF HIGH-FREQUENCY SYSTEM FOR RRC

Objective of the Upgrade

As a result of many improvements [20] since the beginning of the operation of the RIBF in 2007, the beam intensity was steadily increased to nearly 1 pμA, the target value of the RIBF project, for various ion beams. However, the intensity of the uranium beam had reached a peak at about 70 pnA at the exit of the SRC in 2017, in contrast to other ion beams. The transmission efficiency of the RIBF was also increased over the years, but the beam loss at the RRC extraction on the electrostatic deflection channel (EDC) was close to reaching its limit of about 300 W. As the beam intensity supplied from upstream increased, the beam quality deteriorated due to space-charge effects in the RRC [21], resulting in increased beam loss at the RRC extraction. This was a major cause limiting the uranium beam intensity of the RIBF.

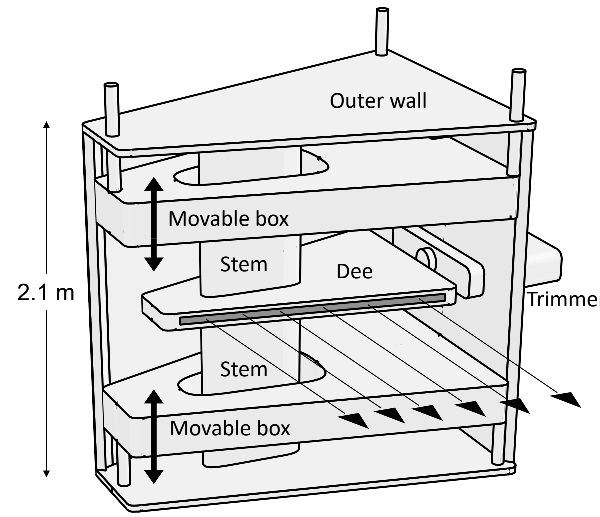

Figure 3: Schematic drawing of the movable-box-type cavity resonator for the RRC. An rf power coupler is concentric with a fine-tuner (trimmer).

The underlying cause of this increased beam loss was the inability to obtain enough turn separation due to the insufficient acceleration voltage of the RRC. During the acceleration of very heavy ions including uranium, the rf system of RRC have to operate at 18.25 MHz. However, a gap voltage of only 85 kV could be generated at this frequency because the operation frequency of 18.25 MHz was actually out of the design specifications. For example, applying the RRC parameters to the equation reported by Baartman [22], the limit current for the uranium beam acceleration of the RRC with an rf voltage of 85 kV was derived to be 2.3 pμA. This value was close to the beam current in the RRC at that time.

The upper panel of Fig. 4 shows the calculation model with the original cavity operated at about 18.25 MHz. The gap length between the dee electrode and the movable box had to be set very small, about 20 mm beyond the design range. As a result, the maximum voltage had been limited to 85 kV, because of the frequent rf discharge caused by this small gap. The actual parallel shunt impedance was also very low, less than 40 kΩ, and the large rf input power caused a severe shock during discharge. Therefore, we decided to modify the cavity resonators to increase the acceleration voltage of the RRC.

Design and Modification of RF Components

To increase the acceleration voltage of the RRC, the gap between the dee electrode and the movable box had to be widened. As shown in the lower panel of Fig. 4, a new slanted stem structure was adopted to shift the resonance frequency range to the lower side by increasing the inductance of the resonator. The increased inductance reduced the capacitance for the same frequency, so the gap length could be almost doubled at 18.25 MHz as shown in Fig. 4. At the same time, the shunt impedance was more than doubled and thus the required rf power was significantly reduced. This modification was expected to increase the voltage at 18.25 MHz by a factor of 1.5 or more.

ISBN: 978-3-95450-212-7 ISSN: 2673-5482 doi:10.18429/JACoW-CYCLOTRONS2022-MOAI02

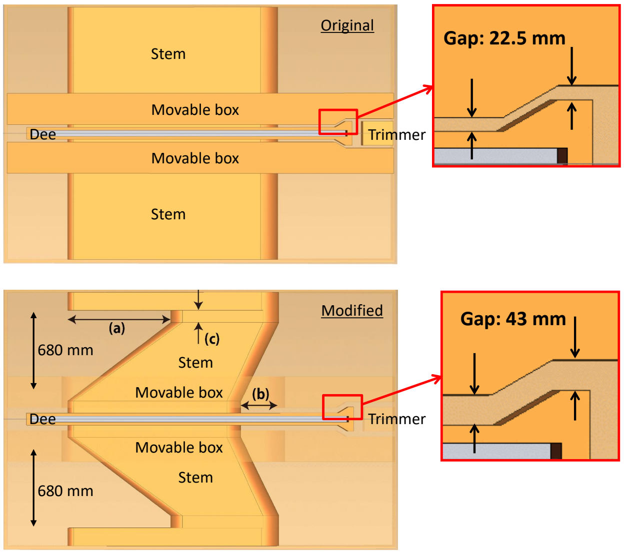

Figure 4: Calculation models of the original cavity (upper panel) and the modified cavity (lower panel).

For this modification, we decided to replace only the internal conductors, the stem and dee, and to not change other components such as the outer wall and movable box. 3D electromagnetic calculations were performed using the CST Studio Suite [23] to find the optimal geometry of the inner conductor. As shown in the lower panel of Fig. 4, the three dimensions (a), (b), and (c) were used as parameters to determine well-balanced dimensions to ensure the required frequency range was obtained while widening the gap as much as possible and increasing the shunt impedance. The calculated design parameters are summarized in Table 2 as well as the original cavity values. Since frequencies above 39 MHz are not used today, the maximum resonant frequency was designed to be less than 39 MHz. The mounting parts were made to have identical dimensions for compatibility. The distribution of heat generation obtained from the electromagnetic calculation was also used for the cooling design.

The radial voltage distribution at the acceleration gap was also taken into account with regard to maintaining the bunch compression effect by the high-frequency magnetic field [24]. Since there is no flat-top cavity in the RRC and the phase acceptance is small, acceleration with compression of the bunch is advantageous for beam extraction. From this point of view, the voltage distribution should be such that the voltage increases toward the outer circumference without any mid-range sagging, and such a distribution was obtained in the original cavity. Noted that the voltage distribution of the RRC is gentle at the low-frequency side, which affects the high-frequency side. In the calculation, dimension (b) works to compensate for the mid-range sag. The mid-range sag was not completely eliminated, but it was kept to a level that did not affect the beam acceleration.

Figure 5 shows pictures during the modification work of the RRC cavity. As shown in panel (a), the new dee electrode and stem were fabricated as four sets of half-units using

Table 2: Calculation results for the original cavity and the modified cavity. The definition of shunt impedance is $R = V_{\mathrm{gap}}^2/2P$ here

	Original Cavity	Modified Cavity
Frequency range	20–45 MHz	16–38.8 MHz
Stroke of MBOX	680 mm each	680 mm each
Shunt impedance	61–594 kΩ	78–451 kΩ
Shunt impedance (around 18.25 MHz)	~48 kΩ	~99 kΩ
Quality factor Q_0 (around 18.25 MHz)	8865	11160
Gap length (b/w dee and MBOX)	22.5 mm	43 mm
Maximum voltage (around 18.25 MHz)	~85 kV	>120 kV

oxygen-free copper. The modification work was performed from February to March 2018, and the interior of the cavity after completion of the modification is shown in panel (d) of Fig. 5.

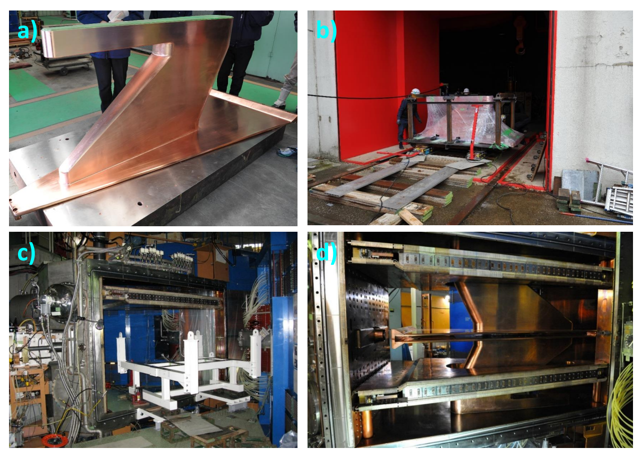

Figure 5: Photographs of the modification work, showing a new half-unit of the stem and dee electrode (a), delivery of fabrication parts (b), replacement of cavity contents (c), and completed assembly (d).

The aging rf control system and tetrode grid power supplies for the RRC were also updated before and after the cavity upgrade. The rf controller, which was implemented with hardware relay logic, was replaced by a programmable logic controller (PLC) based system. All the driving motors and motor drivers for the cavity resonators were also replaced, with only the analog low-level circuits retained. All the components are now controlled directly from the PLC, and remote operation has been moved to an Ethernet base. This renewal resulted in a faster recovery time in a trip event, less damage to the amplifiers, and improved resolution of rf voltage and phase set points. The aging grid power supplies, in use for more than 30 years, were renewed because they were beyond repair and had been unstable in re-

ISBN: 978-3-95450-212-7 ISSN: 2673-5482 doi:10.18429/JACoW-CYCLOTRONS2022-MOAI02

cent years. Since they are placed in a radiation environment, they were manufactured using a standard logic IC without using a micro-controller.

UPGRADE RESULTS AND CURRENT STATUS

After the modification, the frequency response was measured with a network analyzer in April 2018. For each movable-box position, the resonant frequency corresponding to each trimmer position is plotted in Fig. 6. Each point represents the result of a measurement and the curves indicate the calculation results for four movable-box positions. As shown in Fig. 6, the frequency response is almost exactly as expected from the calculations. No detrimental resonance peaks were observed up to 200 MHz for each operating frequency. The quality factor was also measured with a network analyzer for each frequency. The internal quality factor of each frequency is almost 80% of the calculation. This is due

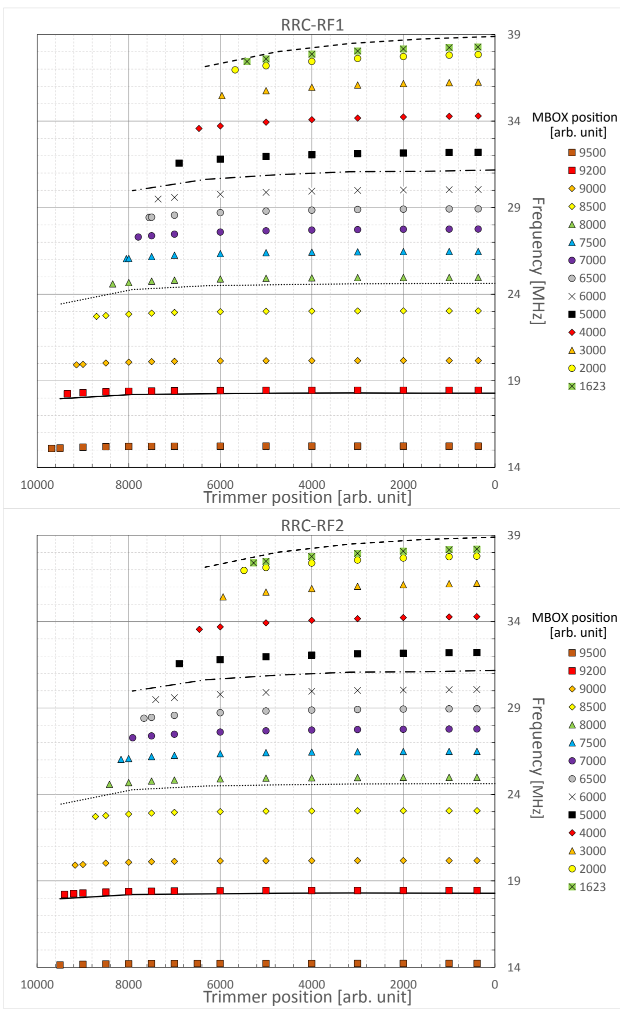

MBOX position: —— 13 mm (gap 43 mm) ······· 100 mm
-·- 300 mm --- 680 mm

Figure 6: Resonant frequencies measured with a network analyzer for two cavities. The markers are changed according to the movable-box position.

to the many contact points of the sliding parts, however it is consistent with the value assumed in advance based on past experience.

Immediately after the low power test, we started applying high power at 32.6 MHz for conditioning. In a few hours, the voltage was up to the specified voltage of 220 kV for 32.6-MHz operation, and a week later in May 2018, the beam supply to the experiment was resumed. In the 18.25-MHz operation, the voltage was increased step by step. The maximum acceleration voltage of 160 kV was achieved at 18.25 MHz in 2020 by increasing the anode voltage of the final stage tetrode from 10 kV to 12 kV. The shunt impedance at 18.25 MHz was also more than double the previous value based on the relationship between voltage and power. Thus, it is now possible to operate the cavity at a voltage about twice as high as before at 18.25 MHz.

Figure 7 shows the radial beam pattern of the uranium accelerated in 2017 and 2020. The left side is injection and the right side is extraction. The operating voltage in 2017 was 85 kV and in 2020 it was 140 kV. As can be seen in Fig. 7, the effect of the voltage enhancement is remarkable, and the turn separation of the RRC has been significantly improved even with uranium acceleration. This increased turn separation has reduced the beam loss on the RRC EDC by a factor of three. Thus, there is now a margin for beam intensity that can be accelerated by the RRC.

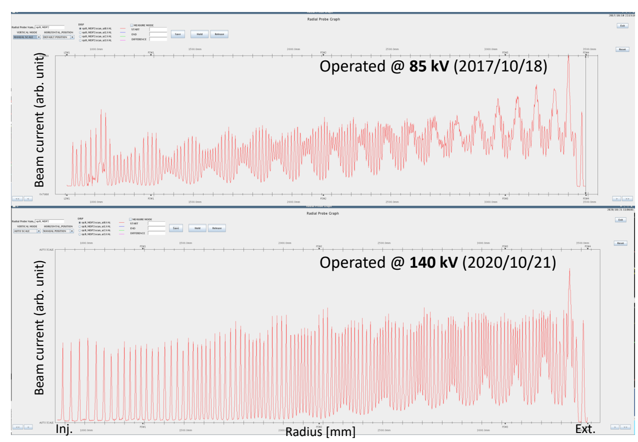

Figure 7: Radial beam pattern in the RRC for the uranium beam acceleration before (upper panel) and after modification (lower panel).

In addition, the cavity modifications significantly reduced rf discharges and resulting trips as expected. The upper panel of Fig. 8 shows the number of rf discharges-per-day and rf trips-per-day during uranium acceleration in 2017, before the cavity modification. We suffered from rf discharges about 20 to 60 times per day at around 85 kV. On the other hand, after the modification, the number of discharges has been greatly reduced to only a few times per day in spite of the higher voltage, and tripping almost never occurs, as shown in the lower panel of Fig. 8. This dramatic reduction in rf discharges also contributes to improving the beam availability of the RIBF and now exceeds 90%.

ISBN: 978-3-95450-212-7 ISSN: 2673-5482 doi:10.18429/JACoW-CYCLOTRONS2022-MOAI02

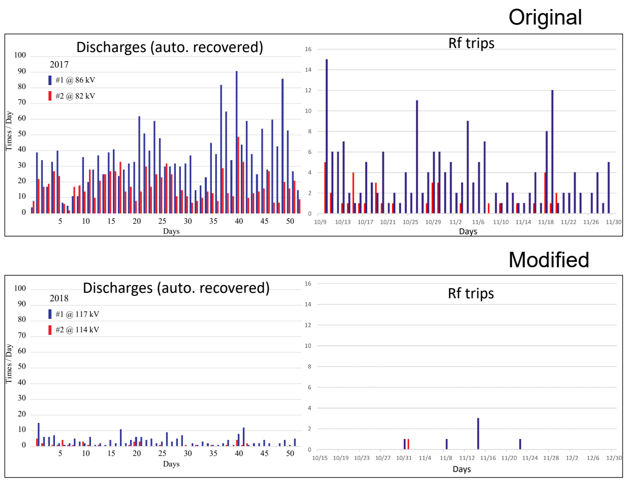

Figure 8: Comparison of rf discharges and trips during uranium acceleration. Upper panel indicates the numbers per day in 2017 and lower panel indicates those in 2018.

Figure 9 shows the evolution of the maximum beam intensity at the exit of the SRC from 2007 to summer 2022. After the upgrade of the RRC high-frequency systems, the uranium beam current achieved 117 pnA at the end of 2020, which corresponds to almost 10 kW. The beam power of other ions in the medium-mass regions now approaches 20 kW.

The modification of the RRC cavity resonator has improved the transmission efficiency of RRC to about 90%. This efficiency value of 90% excludes components that cannot be accelerated by the RRC in principle. This is because the upstream RILAC2 is operated at twice the frequency of the RRC, 36.5 MHz, and thus some of the beam components are injected in the deceleration phase of the RRC.

Recently, we have clearly seen a phenomenon in which the beam transmission efficiency decreases due to the influence of fluctuations in the receiving voltage. This occurs when the receiving voltage drops, but the cause is still unclear as it seems to have a compound cause. It has been found that the rf voltage of the RRC fluctuates very slightly despite the feedback. This may be due to an unstabilized filament current and anode voltage. At present, the rf voltage is fine-tuned manually by the operator when the receiving voltage fluctuates. We are planning to introduce a new digital low-level circuit in the RRC next year to further increase stability. Prior to this, a similar circuit was introduced into the injector RFQ, and it is clear that the new circuit has greatly improved stability. If this does not improve the situation, we will consider updating the filament power supplies.

ACKNOWLEDGEMENTS

The author is grateful to Dr. O. Kamigaito, Dr. N. Fukunishi, Dr. N. Sakamoto, Dr. K. Ozeki, and Dr. K. Suda for technical advice on this work. I would like to express my gratitude to the operators from SHI Accelerator Service Ltd. for their hard work preparing for the upgrade. I would like to thank Sumitomo Heavy Industries, Ltd. for their efforts in modifying the cavity.

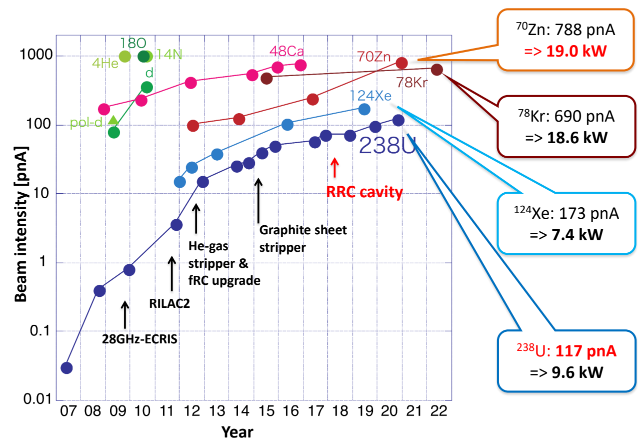

Figure 9: Evolution of the maximum beam intensity at the exit of the SRC up to summer 2022. The major R&D works for increasing the uranium beam are also indicated.

REFERENCES

[1] Y. Yano, "The RIKEN RI Beam Factory Project: A status report", *Nucl. Instr. Meth. B*, vol. 261, pp. 1009–1013, 2007. doi:10.1016/j.nimb.2007.04.174

[2] H. Okuno *et al.*, "Progress of RIBF accelerators", *Prog. Theor. Exp. Phys.*, vol. 2012, p. 03C002, 2012. doi:10.1093/ptep/pts046

[3] Y. Yano, "Recent achievements at the RIKEN Ring Cyclotron", in *Proc. 13th Int. Conf. on Cyclotrons and their Applications (Cyclotrons'92)*, Vancouver, Canada, Jul. 1992, pp. 102–105.

[4] N. Inabe *et al.*, "Fixed-frequency ring cyclotron (fRC) in RIBF", in *Proc. 17th Int. Conf. on Cyclotrons and their Applications (Cyclotrons'04)*, Tokyo, Japan, Oct. 2004, pp. 200–202.

[5] T. Mitsumoto *et al.*, "Construction of the fRC sector magnet for RIKEN RI Beam Factory", in *Proc. 17th Int. Conf. on Cyclotrons and their Applications (Cyclotrons'04)*, Tokyo, Japan, Oct. 2004, pp. 384–386.

[6] N. Fukunishi *et al.*, "Acceleration of intense heavy ion beams in RIBF cascaded cyclotrons", in *Proc. 20th Int. Conf. on Cyclotrons and their Applications (Cyclotrons'13)*, Vancouver, Canada, Sep. 2013, pp. 1–6.

[7] J. Ohnishi *et al.*, "Construction status of the RIKEN intermediate-stage ring cyclotron (IRC)", in *Proc. 17th Int. Conf. on Cyclotrons and their Applications (Cyclotrons'04)*, Tokyo, Japan, Oct. 2004, pp. 197–199.

[8] H. Okuno *et al.*, "The superconducting ring cyclotron in RIKEN", *IEEE Trans. Appl. Supercond.*, vol. 17, pp. 1063–1068, 2007. doi:10.1109/TASC.2007.899864

[9] M. Odera *et al.*, "Variable frequency heavy-ion linac, RILAC", *Nucl. Instr. Meth. A*, vol. 227, pp. 187–195, 1984. doi:10.1016/0168-9002(84)90121-9

[10] O. Kamigaito *et al.*, "Construction of a booster linac for the RIKEN heavy-ion linac", *Rev. Sci. Instr.*, vol. 76, p. 013306, 2005. doi:10.1063/1.1834708

[11] K. Yamada *et al.*, "Beam commissioning and operation of new linac injector for RIKEN RI Beam Factory", in *Proc. 3rd Int. Particle Accelerator Conf. (IPAC'12)*, New Orleans, USA, May 2012, pp. 1071-1073.

[12] K. Suda *et al.*, "Design and construction of drift tube linac cavities for RIKEN RI Beam Factory", *Nucl. Instr. Meth. A*, vol. 722, pp. 55–64, 2013. doi:10.1016/j.nima.2013.04.007

[13] A. Goto *et al.*, "Injector AVF cyclotron at RIKEN", in *Proc. 12th Int. Conf. on Cyclotrons and their Applications (Cyclotrons1989)*, Berlin, Germany, May 1989, pp. 51–54.

[14] T. Kubo, "In-flight RI beam separator BigRIPS at RIKEN and elsewhere in Japan", *Nucl. Instr. Meth. B*, vol. 204, pp. 97–113, 2003. doi:10.1016/S0168-583X(02)01896-7

[15] T. Nakagawa *et al.*, "First results from the new RIKEN superconducting electron cyclotron resonance ion source (invited)", *Rev. Sci. Instr.*, vol. 81, p. 02A320, 2010. doi:10.1063/1.3259232

[16] Y. Higurashi *et al.*, "Recent development of RIKEN 28 GHz superconducting electron cyclotron resonance ion source", *Rev. Sci. Instr.*, vol. 85, pp. 02A953, 2014. doi:10.1063/1.4848976

[17] H. Imao, "Development of gas stripper at RIBF", in *Proc. 9th Int. Particle Accelerator Conf. (IPAC'18)*, Vancouver, Canada, Apr.-May 2018, pp. 41–46. doi:10.18429/JACoW-IPAC2018-MOZGBE1

[18] H. Hasebe *et al.*, "Development of a high-density highly oriented graphite stripper", *EPJ Web of Conf.*, vol. 229, p. 01004, 2020. doi:10.1051/epjconf/202022901004

[19] T. Fujisawa *et al.*, "The radiofrequency system of the RIKEN Ring Cyclotron", *Nucl. Instr. Meth. A*, vol. 292, pp. 1–11, 1990. doi:10.1016/0168-9002(90)91728-T

[20] O. Kamigaito *et al.*, "Recent progress in RIKEN RI Beam Factory", in *Proc. 22nd Int. Conf. on Cyclotrons and their Applications (Cyclotrons'19)*, Cape Town, South Africa, Sep. 2019, pp. 12–16. doi:10.18429/JACoW-Cyclotrons2019-MOB01

[21] H. Okuno *et al.*, "Operational experience and upgrade plans of the RIBF accelerator complex", in *Proc. 21st Int. Conf. on Cyclotrons and their Applications (Cyclotrons'16)*, Zurich, Switzerland, Sep. 2016, pp. 1–6. doi:10.18429/JACoW-Cyclotrons2016-MOA01

[22] R. Baartman, "Space charge limit in separated turn cyclotrons", in *Proc. 20th Int. Conf. on Cyclotrons and their Applications (Cyclotrons'13)*, Vancouver, Canada, Sep. 2013, pp. 305–309.

[23] CST Studio Suite, https://www.3ds.com/products-services/simulia/products/cst-studio-suite/

[24] W. Joho, "Application of the phase compression – phase expansion effect for isochronous storage rings", *Particle Accelerators*, vol. 6, pp. 41–52, 1974.

ISBN: 978-3-95450-212-7 ISSN: 2673-5482 doi:10.18429/JACoW-CYCLOTRONS2022-MOA001

STATUS OF THE IsoDAR HIGH-CURRENT H_2^+ CYCLOTRON (HCHC-XX) DEVELOPMENT

Loyd Waites, Jose Alonso, Janet Conrad, Daniel Winklehner
Massachusetts Institute of Technology, Cambridge, MA, USA

Abstract

The potential existence of exotic neutrinos beyond the three standard model neutrinos is an important open question in particle physics. IsoDAR is a cyclotron-driven, pure electron-antineutrino source with a well-understood energy spectrum. High statistics of anti-electron neutrinos can be produced by IsoDAR, which, when coupled with an inverse beta decay detector such as the LSC at Yemilab, is capable of addressing observed anomalies attributed to sterile neutrinos at the 5 sigma level using electron-flavor disappearance. To achieve this high significance, the IsoDAR cyclotron must produce 10 mA of protons at 60 MeV. This is an order of magnitude more current than any commercially available cyclotron has produced. To achieve this, IsoDAR takes advantage of several innovations in accelerator physics, including the use of H_2^+ and RFQ direct injection, paving the way as a new high power accelerator technology. These high currents also allow for new experiments in dark matter, as well as high production rates of rare isotopes such as ^{225}Ac and ^{68}Ge.

INTRODUCTION

The design of the IsoDAR experiment is set to produce a high flux of anti-electron neutrinos using a compact system that will be in close proximity to a kiloton scale, underground neutrino detector, see Figure 1.

Leading exclusions of sterile neutrinos could be provided by this experiment over five years, in which the IsoDAR experiment could provide a five-sigma exclusion over several anomalies [1]. However, two conditions must be met:

1. The accelerator must be sufficiently compact to be constructed underground in close proximity to the detector, preventing the use of a separated sector cyclotron [2].
2. The accelerator must provide 10 mA of protons at 60 MeV.

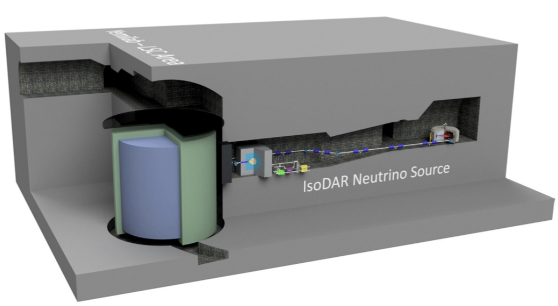

Figure 1: Diagram showing the layout of the IsoDAR experiment. The experiment uses an H_2^+ ion source, which is directly injected into a cyclotron, which accelerates the H_2^+ up to 60 MeV. The H_2^+ is stripped into protons before colliding with the a beryllium target, producing neutrons. The neutrons are absorbed by a highly pure ^{7}Li sleeve, which then undergoes beta decay, and produces anti-electron neutrinos. These neutrinos can then be detected by the nearby detector via inverse beta decay (IBD).

The use of H_2^+ can be used to alleviate space charge in the beam. This is critical for maintaining beam quality in low energy, high intensity regions. Another is the use of a Radio Frequency Quadrupole (RFQ) direct injection system that bunches the beam and leads to higher transmission through the system.

However, high power cyclotrons have applications beyond the particle physics scope. The most common use of cyclotrons is to produce medical isotopes. Rare isotopes are often prohibitively expensive to produce, limiting treatment options for those who require them. The IsoDAR cyclotron can address the bottlenecks of this industry, and help produce large yields of currently rare medical isotopes.

PATH TO HIGHER CURRENTS

Use of H_2^+

The Coulomb repulsion between ions within a beam can lead to emittance and beam size growth. This is particularly important in low energy regions. Most modern cyclotrons accelerate H^- ions, which allows convenient extraction using a stripping foil. However, there are significant advantages to accelerating and extracting H_2^+. This allows twice as many protons to be accelerated with limited space charge effects. The H_2^+ is later run through a stripping foil, which removes the molecular electrons and leaves protons, effectively doubling the beam current.

RFQ Direct Injection

Following the production of H_2^+ is extraction system with four electrodes which is designed to steer and shape the beam in order to properly match the desired input parameters of the RFQ and maximize end-to-end transmission.

The beam is injected as direct current (DC), however as it traverses the RFQ the beam is bunched by the shaped electrodes and RF acceleration. While the beam is only accelerated from 15 keV to 60 keV, the primary purpose of the RFQ is to act as a beam buncher. The RFQ converts the DC beam into a 32.8 MHz beam to match the frequency of the cyclotron. Transmission from ion source to the end of the RFQ has been calculated to be >90% [1].

ISBN: 978-3-95450-212-7 ISSN: 2673-5482 doi:10.18429/JACoW-CYCLOTRONS2022-MOA001

The high bunching efficiency of the RFQ allows for higher phase acceptance by the cyclotron. Because the beam is properly bunched, a higher fraction of the beam is put within the phase acceptance window of the cyclotron, allowing for a higher fraction of the beam to be accelerated, and preventing loses early on. Being as efficient as possible with the beam is important to limit space charge in low energy regions, as well as reducing the strain on our filament driven ion source.

The use of an RFQ direct injection system also leads to a far more compact system than a traditional LEBT design. This allows for easier installation in compact regions such as an underground mine.

Use of Machine Learning for RFQ Optimization

An RFQ design can be represented as a point in a very large parameter space who's dimensions include factors such as vane voltage, cell number, cell size, and input beam parameters. This is difficult to design by hand due to the size of the parameterspace. To accelerate this process (*audible groan), we used machine learning techniques to create surrogate beam dynamics models for the RFQ, which could then be coupled with an optimizer. We used for this for two scenarios:

1. Optimize the beam input from the tetrode extraction system into a fixed RFQ.
2. Optimize the full RFQ design.

We modeled the beam inputs with only the Twiss parameters of the beam to fully describe its profile. To model the full RFQ design we required 14 input parameters. This requires a much larger dataset to train the machine learning algorithms, but covers a much larger space.

We generated a training dataset using RFQGen [3].The inputs are parameterized, then used to generate this data are used for the inputs for the surrogate model. Due to the nature of pretrained ML models, theses could now rapidly simulate the beam dynamics through the specified RFQ. The RFQ design can then be optimized by tuning these input parameters in order to match the desired beam dynamics through the RFQ.

Surrogate models were generated using a Polynomial Chaos Expansion (PCE) using the the UQ tool kit made by sandia labs [4] and a Deep Neural Network (DNN) which was produced using tensorflow [5]. To mimic a similar neural network architecture used in accelerators found in Ref. [6], we used a neural network with structure 14-10-20-20-14 and use an Adam optimizer with a learning rate of .001.

We were then able to use these surrogate models to alter the design of the RFQ and tetrode extraction system. We were able to optimize the designs based on the output beam dynamics of the RFQ, for which we then used a bayesian optimizer [7]. The optimizer would return the best design inputs to the surrogate model, which then described an optimium design. For a more detailed look at this process, see Ref. [8].

MEDICAL ISOTOPE PRODUCTION

PET scans and alpha therapies have gained a lot of attention due to their ability to potentially transform cancer treatment and diagnostics. However, these treatments are still prohibitively expensive for many of those who require them. This expense is partially driven by the high cost of production for these radio-isotopes.

To produce more of these isotopes the problem is simple in concept: more protons on target, at higher energies. This unfortunately does not fully reflect reality. Higher protons on target means higher power, which in turn leads to thermal constraints in the target. To keep the target from being damaged or destroyed, these thermal constraints need to be well managed and understood.

The IsoDAR cyclotron would have record setting power and protons on target. Compared to comercial devices, seen in Table 1, the IsoDAR cyclotron would have a higher power by an order of magnitude.

Table 1: Comparison of commercial cyclotrons from IBA with the IsoDAR cyclotron, from Ref. [9].

Parameter	**IsoDAR**	**IBA C30**
Energy (MeV/nucleon)	60	30
Proton Current (mA))	10	1.2
Beam Power (kW)	600	36
Outer Diameter (m)	6.2	3

This higher power clearly leads to more protons on target. However, this high power also exceeds any thermal constraints of the target. However, because IsoDAR extracts H_2^+, it is possible to easily split the beam to defuse this power. Using a system including a double focusing dipole magnet and stripping foil, it is possible to break the beam up into several lower power, controlled parts, as seen in Figure 2. This would provide a perfect testbed for the research and development of high power targets, as this system would provide variable power to multiple stations that could be used to produce isotopes, develop and test new targets, or run new experiments. Not only this, but the power could be adjusted in a modular and continous way.

This would provide multiple targets with acceptable levels of power, while also utilizing the full potential of the IsoDAR cyclotron.

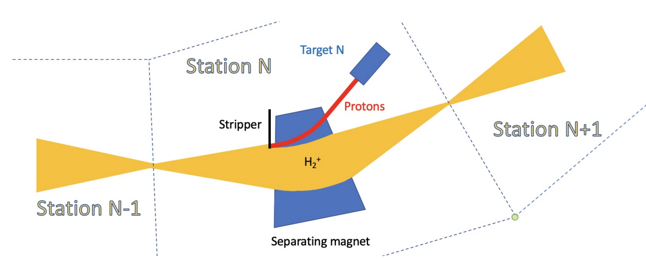

Figure 2: Diagram showing the H_2^+ beam from the IsoDAR cyclotron iteratively being broken up across several (n) stations. Taken from Ref. [10]

ISBN: 978-3-95450-212-7 ISSN: 2673-5482 doi:10.18429/JACoW-CYCLOTRONS2022-MOA001

CONCLUSION

While originally intended for an ambitious particle physics experiment, the IsoDAR cyclotron is capable of also making changes in the medical isotope field. We have taken advantage of several new developments and technologies in order to design a higher power, compact cyclotron. Our of H_2^+ mitigates space charge as well as allows it to be a testbed for target research. Our use of an RFQ-direct injection system also provided an example of using machine learning in accelerators. Coupling these technologies will help pave the way for new developments in multiple fields.

REFERENCES

[1] D. Winklehner *et al.*, "High intensity cyclotrons for neutrino physics", *Nucl. Instrum. Methods Phys. Res., Sect. A*, vol. 907, pp. 231–243, 2018. doi:10.1016/j.nima.2018.07.036

[2] A. Kolano *et al.*, "Intensity limits of the PSI Injector II cyclotron", *Nucl. Instrum. Methods Phys. Res., Sect. A*, vol. 885, pp. 54–59, 2018. doi:10.1016/j.nima.2017.12.045

[3] K.R. Crandall, T.P. Wangler, L.M. Young, *et al.*, "RFQ Design Codes", Los Alamos National Laboratory, NM, USA, Rep. LA-UR-96-1836, Dec. 2005.

[4] B.J. Debusschere, H.N. Najm, P.P. Pébay, O.M. Knio, R.G. Ghanem, and O.P. Le Maître, "Numerical challenges in the use of polynomial chaos representations for stochastic processes", *SIAM J. Sci. Comput.*, vol. 26 pp. 598–719, 2004. doi:10.1137/S1064827503427741

[5] M. Abadi *et al.*, "Tensorflow: A system for large-scale machine learning", in *Proc. 12th USENIX Symp. on Operating Systems Design and Implementation (OSDI'16)*, Savannah, GA, USA, Nov. 2016, pp. 265–283. doi:10.48550/arXiv.1605.08695

[6] A. Edelen, N. Neveu, M. Frey, Y. Huber, C. Mayes, and A. Adelmann, "Machine learning for orders of magnitude speedup in multiobjective optimization of particle accelerator systems", *Phys. Rev. Accel. Beams*, vol. 23, no. 4, p. 044601, 2020. doi:10.1103/PhysRevAccelBeams.23.044601

[7] F. Noguiera, "Bayesian Optimization open source constrained global optimization tool for Python", 2014. https://github.com/fmfn/BayesianOptimization

[8] D. Koser, L. Waites, D. Winklehner, M. Frey, A. Adelmann, and J. Conrad, "Input Beam Matching and Beam Dynamics Design Optimization of the IsoDAR RFQ using Statistical and Machine Learning Techniques", *arXiv*, Dec. 2021. doi:10.48550/arXiv.2112.02579.

[9] L.H. Waites, J.R. Alonso, R. Barlow, and J.M. Conrad, "What is the potential impact of the IsoDAR cyclotron on radioisotope production: a review", *EJNMMI Radiopharm. Chem.*, vol. 5, no. 6, 2020. doi:10.1186/s41181-020-0090-3

[10] J.R. Alonso, R. Barlow, J.M. Conrad, and L.H. Waites, "Medical isotope production with the IsoDAR cyclotron", *Nat. Rev. Phys.*, vol. 1, no. 9, pp. 533–535, 2019. doi:10.1038/s42254-019-0095-6

ISBN: 978-3-95450-212-7 ISSN: 2673-5482 doi:10.18429/JACoW-CYCLOTRONS2022-MOA002

THE COMMISSIONING OF A 230 MeV SUPERCONDUCTING CYCLOTRON CYCIAE-230*

Chuan Wang†, Zhiguo Yin, Tianjue Zhang, Wei Fu, Hongji Zhou, Xueer Mu, Bin Ji, Xianlu Jia, Jiansheng Xing, Pengfei Zhu, Jie Liu, Zhengwei Liu, Hongru Cai, Jingyuan Liu, Lipeng Wen, Xia Zheng, Luyu Ji, Xiaofeng Zhu, Fei Wang, Junyi Wei, Shilun Pei, Guofang Song, Suping Zhang, Yunsheng Jia, Dezhi Zhang, Tianyi Jiang, Aolai He, Qiqi Song, Ping Liu, Mingzhi Hu, and the Cyclotron Team at CIAE, China Institute of Atomic Energy, Beijing, P. R. China

Abstract

There are very strong demands for proton accelerators in medium energy range in recent years due to the fast growth of proton therapy and the space science in China. For the applications of proton therapy and proton irradiation, the energy range of proton beam is usually from 200 MeV to 250 MeV, or even higher for astronavigation. An R&D project for constructing a 230 MeV superconducting cyclotron (CYCIAE-230) has been initiated at China Institute of Atomic Energy (CIAE) since Jan 2015. In July of 2016, after the funding was approved by China National Nuclear Corporation (CNNC), the construction project was fully launched. In Dec 2019, the superconducting main magnet and the RF system were transferred to the newly built commissioning site. Then, the RF commissioning, ion source and central region test were performed even during the pandemic in early 2020. In September 2020, after finishing the commissioning tests of all subsystems, the beam was reached the extraction channel but with very low efficiency. Since then, with more efforts on beam diagnostics, the fine tuning of the beam phase and the adjusting of the superconducting coil have been proven to be useful to get higher beam extraction efficiency ~55%. In this paper, the commissioning of the key components, including the main magnet, SC coils, internal ion source and central region, extraction system, etc, as well as the commissioning progress of the machine CYCIAE-230 will be presented.

INTRODUCTION

To meet the requirements of proton beam in the energy range of 200 MeV to 250 MeV for the uses of proton therapy and space science research in China, a superconducting cyclotron CYCIAE-230 was designed in CIAE. The overall parameters are listed in Table 1. And the layout of the very compact CYCIAE-230 superconducting cyclotron is shown in Fig. 1 [1].

Table 1: The Overall Parameters of CYCIAE-230

Beam	
Beam current from ion source	>10 μA
Ion source type	Cold PIG
Extracted beam energy	≥230 MeV
Extracted beam current	a few hundreds of nA
Magnet	
Pole structure	Spiral
Pole radius	85 cm
Weight	~ 80 ton
Hill gap	5.0 cm
Central field	2.3 T
Coils	
Coil type	NbTi wire
Current density	≤50 A/mm^2
Ampere-Turn Number	~600000 A.T×2
RF Cavity	
Number of cavities	4
RF frequency	~71.1 MHz
Harmonic Mode	2
Cavity Voltage	80 kV～110 kV
RF Amp. output Power	200 kW (max)
Extraction	
Method	Resonance crossing & processional motion
Elements for extraction	2 electrostatic deflectors and 6 magnetic channels
Deflector voltage	< 100 kV/cm
Deflector gap	5–7 mm

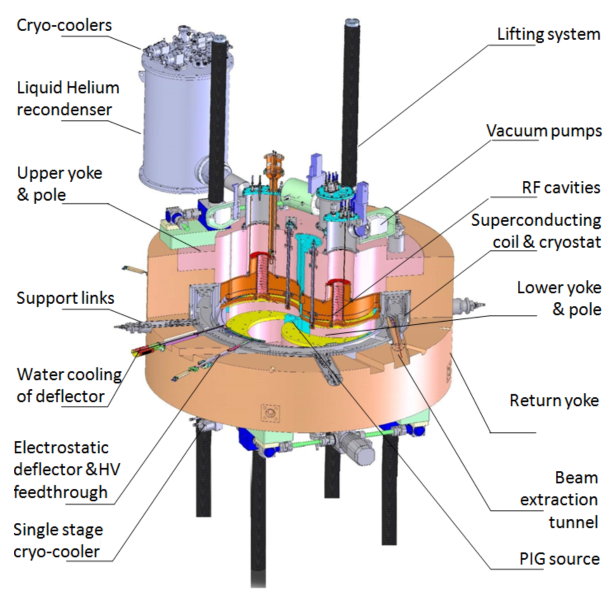

Figure 1: The layout of CYCIAE-230.

* Work supported by National Natural Science Foundation of China under Grants 11475269, 11375274; † cwang@ciae.ac.cn.

ISBN: 978-3-95450-212-7 ISSN: 2673-5482 doi:10.18429/JACoW-CYCLOTRONS2022-MOA002

COMMISSIONING OF SUBSYSTEMS

As the commissioning cite could not be in use before the end of 2019, the field mapping and shimming of the superconducting main magnet was performed in a different cite. The main magnet along with other subsystems of the cyclotron were then transferred to the commissioning cite.

Superconducting Main Magnet

As the requirements on the compactness, low cost and long-term operation stability for proton therapy, the warm iron with superconducting coil was adopted for the main magnet design of CYCIAE-230.

Enlightened by the superconducting coil technologies popular in the superconducting MRIs, the liquid helium zero-boiling cooling combined with GM coolers and the high copper/Sc ratio monolith or wire-in-channel NbTi wires, were used for CYCIAE-230 project. The R&D of the superconducting coil is successful for the team at CIAE as it is the first time for the team to deal with the superconducting magnet technology. Since the first cooling down and current excitation of the superconducting main magnet of CYCIAE-230 in 2018, it was only one time that helium leakage was encountered during last 5 years' operation, and it was due to both the failure of the power supply and the malfunction of the topology of the energy release module. The superconducting main magnet itself is very stable.

A search-coil based mapping system, consisting of a nuclear magnetic resonance (NMR) probe to precisely measure the field at the cyclotron centre and a moving search coil to obtain the field differences, was developed to satisfy the isochronous field accuracy requirements of 5×10^{-5}, as is shown in Fig. 2 [2].

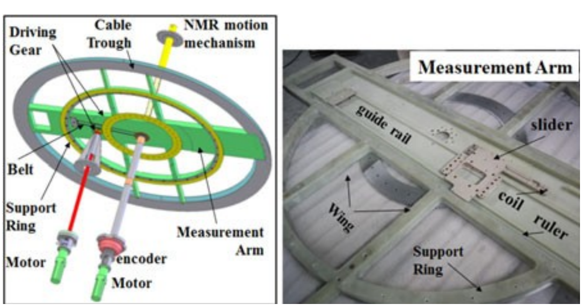

Figure 2: Layout of search-coil based mapping system.

After 5 times' shimming, the good isochronism has been achieved, and the integrated phase slip is within ±25°, as is shown in Fig. 3.

The first harmonic field is reduced to within 5Gs by slightly adjusting the radial support links of the superconducting coil, as is shown in Fig. 4.

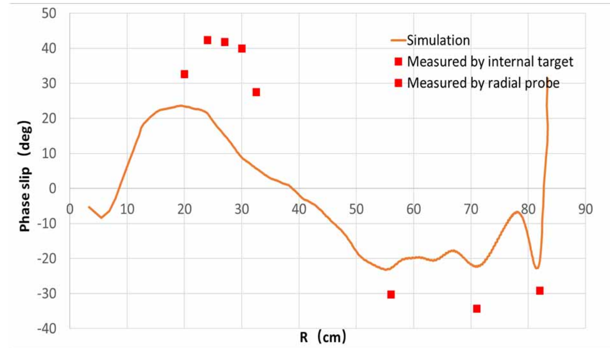

Figure 3: Integrated phase slip (solid line: SEO simulation with field mapping data; square dot: beam measurement using Smith-Garren method [3, 4]).

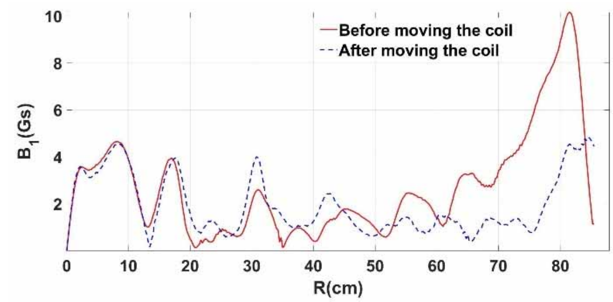

Figure 4: Shimming of the first harmonic field.

RF System

The RF system of CYCIAE-230 is quite unique. It contains four cavities working in push-pull mode to provide higher energy gain per turn, just like RF system design of other cyclotrons. However, each opposing pairs of cavities are mechanically connected in/underneath the central region and the coupled four Dees are driven by two separated power supplies through two independent RF couplers located in two valleys of the cyclotron [5]. The voltage and the phase of the Dees are controlled by one set of LLRF controller, as is shown in Fig. 5.

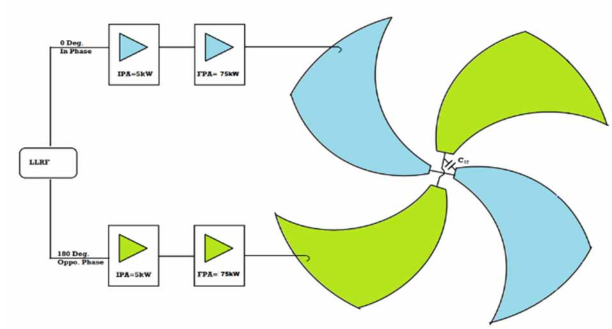

Figure 5: Layout of the RF system of CYCIAE-230.

The installation of RF cavities, coaxial line and RF amplifiers was finished in early 2020, as is shown in Fig. 6.

And both the frequency and Q value are within designed tolerance.

ISBN: 978-3-95450-212-7 ISSN: 2673-5482 doi:10.18429/JACoW-CYCLOTRONS2022-MOA002

Figure 6: Installation of RF cavities (upper left), coaxial lines (upper right) and RF amplifiers (lower).

Ion Source and Central Region

The ion source is a cold cathode PIG source. The beam trajectories in central region under different RF phase and the layout of the elements of central region are shown in Fig. 7. The central region consists of 4 electrodes, a fixed phase slit and a collimator.

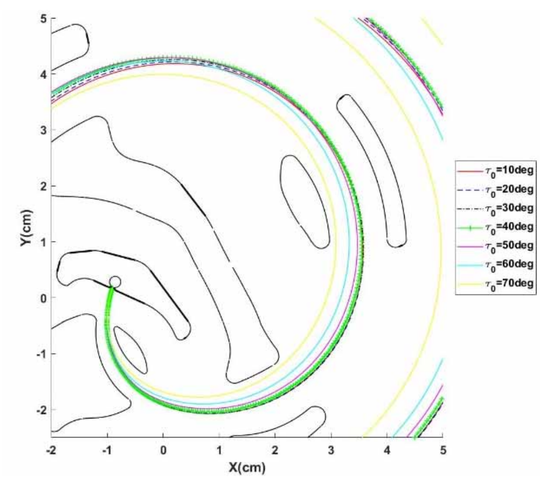

Figure 7: Beam trajectory at different RF phase in the central region.

By using an internal probe, the beam intensity in central region without any phase cut-off or collimation was measured and it is over 300 µA, which is more than adequate. The vertical centering of beam in the central region was verified by using copper films, phase slit or collimator, as is shown in Fig. 8.

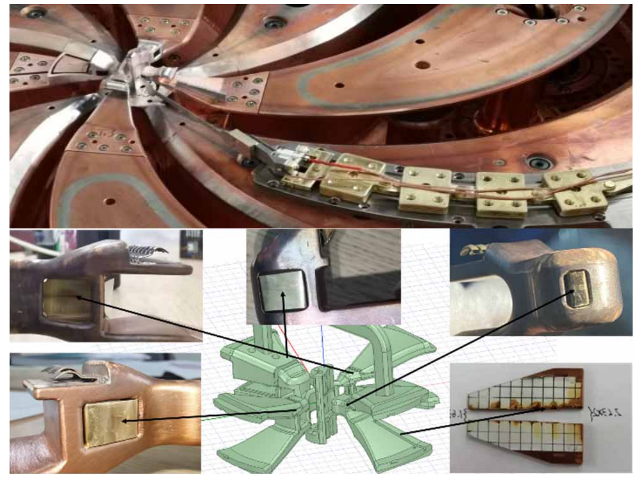

Figure 8: Beam measurement using internal probe (upper); vertical centering verification in the central region (lower).

Extraction System

The extraction system contains two electrostatic deflectors (ESD1 and ESD2) and multiple magnetic channels (MCs). The ESDs are each with 5~7 mm gap and operation voltages less than 70 kV. The MCs consist of multiple focusing and compensating iron bars with field gradient of ~3 kGauss/cm. A set of trim rods in extraction region is used to provide additional first harmonic field to generate processional motion and further enlarge the turn separation. Beam tracking at the extraction region shows that ~80% beam could be extracted and the most of the beam are lost on the deflectors. However, due to the compactness of the structure, the beam trajectory in extraction region is close to either ESDs, MCs or RF structure, as is shown in Fig. 9.

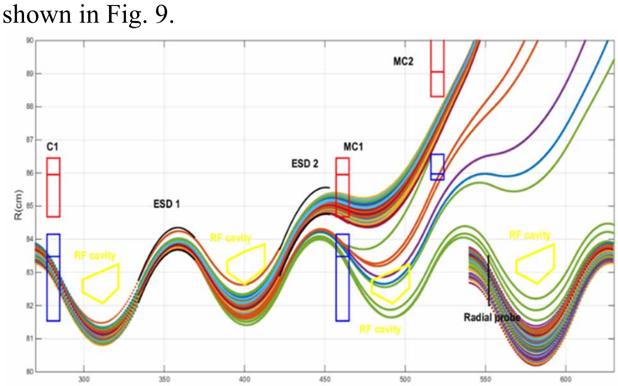

Figure 9: Calculated beam trajectories in extraction region.

Although the required the voltage for ESDs is not critical for high voltage (HV) engineering, many sparks in the ESDs were still encountered until a modification on HV feedthrough and a surface anodic oxidation on electrodes were applied. And now the operational HV of the ESDs could be achieved within 30 minutes without many sparks.

ISBN: 978-3-95450-212-7 ISSN: 2673-5482 doi:10.18429/JACoW-CYCLOTRONS2022-MOA002

BEAM COMMISSIONING

Compared to the experiences of beam commissioning of other cyclotrons at CIAE, the commissioning of CYCIAE-230 is more difficult. Due to the compact structure, the high and coupled magnetic-electromagnetic-electrostatic field, the beam diagnostics becomes difficult. And the use of the superconducting coil may introduce extra beam positioning error.

The commissioning process of CYCIAE-230 is also a process of inventing new beam diagnostics, which will be illustrated as follows.

Radial Centering

The beam is designed to be centered in central region, however, due to misalignment of the ion source, unexpected first harmonic field etc., beam off-centering is observed. A set of central region trim rods is used to generate a certain pattern of first harmonic field to suppress the beam off-centering, as is shown in Fig. 10.

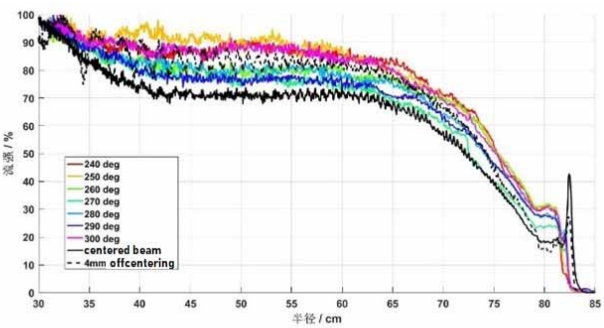

Figure 10: The comparison of simulated centered beam and measured beam in radial probe with different phase of first harmonic field in central region.

By using central region trim rods and with the signal from radial probe, beam centering could be achieved. Also, with the beam intensity signals from radial probe, the isochronous measurements were performed by using Smith Garron method [3, 4], as is shown in square dots in Fig. 3. The integrated phase slip is slightly larger than simulation using field mapping data.

Vertical Centering and SC Coil Alignments

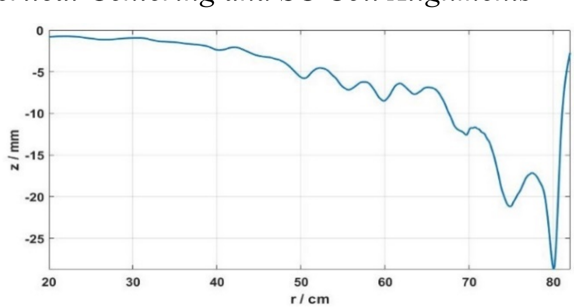

Figure 11: The change of vertical position of reference particle at different radius, when superconducting coil shifts 1 mm in vertical direction.

One of the major differences between superconducting and normal conducting cyclotrons is that the ratio of magnetic field generated by coil over the total magnetic field is much larger in superconducting cyclotron thus the coil position is very sensitive to the position of beam. According to our simulation, 1 mm coil shift in vertical direction equals to ~30 mm beam shift (as seen Fig. 11).

By using radial probe with 3 fingers, and adjusting the position of superconducting coil accordingly, the beam achieves vertical centering, as is shown in Fig. 12.

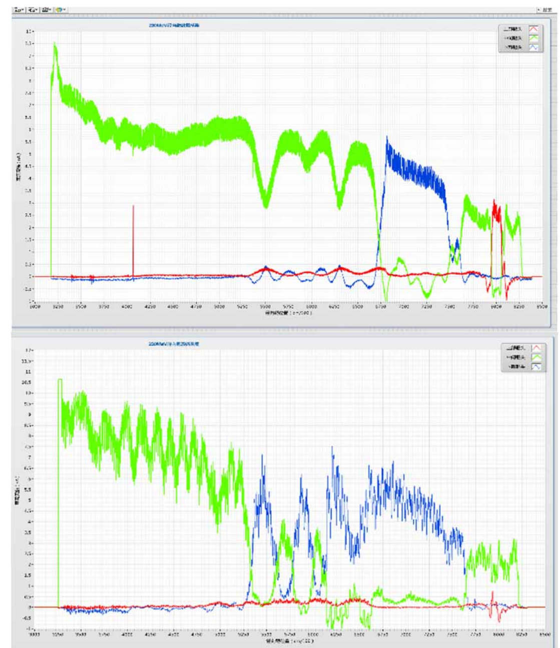

Figure 12: Radial probe signal before and after adjusting the position of superconducting coil. (green: middle finger; red: upper finger; blue: lower finger)

Beam Extraction Tests

The beam must pass the ESDs, MCs and the tailboard of the RF cavities before extraction with the tolerance of ~2 mm, where high magnetic field, electromagnetic field and electrostatic field are coupled. Special efforts have been made to develop reliable diagnostics to give more information on beam position, intensity etc., as is shown in Fig. 13.

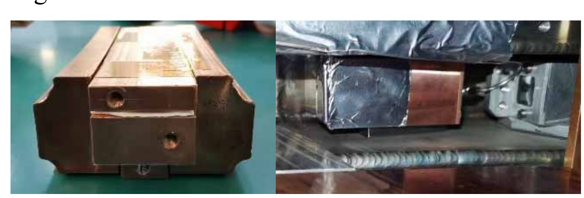

Figure 13: Probe with radial fingers used for the commissioning of ESDs (left) and self-shielded probe for the commissioning of MCs(right).

After ~700 turns, the extracted beam has been measured at the end of the extraction port with a LIBERA current meter, as is shown in Fig. 14.

ISBN: 978-3-95450-212-7 ISSN: 2673-5482 doi:10.18429/JACoW-CYCLOTRONS2022-MOA002

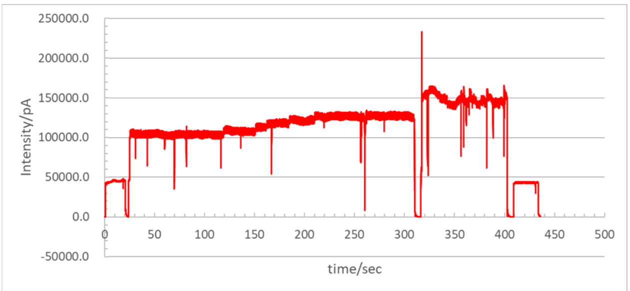

Figure 14: The beam on the copper target is over 150 nA with the energy of 241.6 MeV ~ 242.7 MeV (the energy is estimated by extraction simulation).

CONCLUSION

The commissioning progress of the machine CYCIAE-230 is presented and over 150 nA beam is obtained. However, the extraction efficiency is 55% at lower beam intensity (~10 nA) and will drop to ~40% at higher intensity. More efforts will be made to increase the extraction efficiency to further increase the beam intensity.

REFERENCES

[1] T. Zhang *et al.*, "Developments for 230MeV superconducting cyclotrons for proton therapy and proton irradiation", *Nucl. Instrum. Methods*, vol. 406, pp. 244-249, 2017. doi:10.1016/j.nimb.2016.11.010

[2] M. Li *et al.*, "Field Mapping System Design for the Superconducting Cyclotron CYCIAE-230", IEEE Trans. Appl. Supercond., vol. 28, no. 3, pp. 1-4, April 2018. doi:10.1109/TASC.2018.2789447

[3] A. Garren *et al.,* "Diagnosis and Correction of Beam Behaviour in an Isochronous Cyclotron", in *Proc. Cyclotrons'63,* CERN, Geneva, Switzerland, Apr. 1963, pp. 18-23, paper CYC63A03.

[4] C. Baumgarten *et al.,* "Isochronism of the ACCEL 250MeV medical proton cyclotron", *Nucl. Instrum. Methods*, vol. 570, pp. 10-14, 2007. doi:10.1016/j.nima.2006.09.112

[5] Z. Yin *et al.,* "Design of RF system for CYCIAE-230 superconducting cyclotron", *Nucl. Instrum. Methods*, vol. 854, pp. 25-30, 2017. doi:10.1016/j.nima.2017.02.051

ISBN: 978-3-95450-212-7 ISSN: 2673-5482 doi:10.18429/JACoW-CYCLOTRONS2022-MOBI01

SUMMARY OF THE SNOWMASS'21 WORKSHOP ON HIGH POWER CYCLOTRONS AND FFAS

D. Winklehner*, J.R. Alonso[1], Massachusetts Institute of Technology, Cambridge, MA, USA
A. Adelmann[2], M. Haj Tahar[3], Paul Scherrer Institut, Villigen, Switzerland
L. Calabretta, INFN - Laboratori Nazionali de Legnaro, Legnaro, Italy
H. Okuno, RIKEN, Japan
T. Planche, TRIUMF, Vancouver, Canada
[1]also at Lawrence Berkeley National Laboratory, Berkeley, CA, USA
[2]also at ETHZ, Zürich, Switzerland
[3]also at TRANSMUTEX, Geneva, Switzerland

Abstract

In this talk, we summarize the presentations and findings of the "Workshop on High Power Cyclotrons and FFAs" that we held online in September 2021. The workshop was held as part of the 2021 Snowmass Community Exercise – in which the US particle physics community came together in a year-long effort to provide suggestions for a long-term strategy for the field – and the "Accelerators for Neutrinos" subpanel thereof. Topics that were discussed during our high-power cyclotron workshop were the application of cyclotrons in particle physics, specifically neutrino physics, and as drivers for muon production. Furthermore, as these same accelerators have important applications in the fields of isotope production and possibly in energy research, we have included those topics as well. Finally, we took a look at Fixed Field Alternating Gradient accelerators (FFAs) and their potential to become high-intensity machines.

INTRODUCTION

We report the state of the field of "High-Power Cyclotrons and FFAs" (Fixed Field alternating-gradient Accelerators) as discussed by international experts during a three-day workshop of the same name [1]. The workshop was held online Sep 7 to Sep 9, 2021 with 50 registered participants, as part of the US Snowmass'2021 community exercise; specifically, the Accelerator Frontier (AF) and the subpanel Accelerators for Neutrinos (AF02). This conference proceeding is a concise summary of the workshop reports available on the ArXiv [2] and in Ref. [3].

The workshop charge was to take stock of the world inventory of high-power cyclotrons and FFAs, to asses available beam currents and beam powers, and to investigate limitations. Furthermore, to evaluate the role of cyclotrons in particle physics, directly used or as injectors to other machines. Finally, to discuss novel concepts to push the power, and provide recommendations to the particle physics and accelerator physics communities.

The program of talks is listed on the Indico website [1], and slides are available by navigating to "Timetable" then "Detailed view." References to all individual presentations are also given in the bibliography of the workshop reports.

The workshop was coarsely organized in three topical areas (one per day): 1. State-of-the-Art and Limitations; 2. Applications of high-power cyclotrons and FFAs; 3. Novel Concepts and Computation. In this manuscript, we follow the same structure.

STATE-OF-THE-ART AND LIMITATIONS

State-of-the-Art

The classical cyclotron was invented and developed for research in nuclear physics. The first major evolution of this type of accelerator was the introduction of the azimuthally varying field (AVF) cyclotron, otherwise known as the isochronous cyclotron [4]. The development of computers and superconductivity produced a further broad band of cyclotrons of different types tuned for different researches in the field of nuclear physics but also for a wide range of applications. The golden age of the cyclotron was the period from 1960 to 1990 when many cyclotron projects were studied, financed and built. Some examples are LBNL [5–7], DUBNA [8–10], GANIL [11], MSU [12, 13], iThemba Labs [14], RCNP [15], and RIKEN [16], just to remember the largest and most famous laboratories. They were often equipped with more than one cyclotron, aimed mainly at research in the field of nuclear physics and in the projects of synthesis of Super Heavy Elements [17, 18]. A special mention goes to the two large cyclotrons of PSI (Switzerland) [19] and TRIUMF (Canada) [20], laboratories which delivered the first beam in 1974 and 1975 respectively. These two machines deliver proton beams with a maximum energy of 590 MeV and 520 MeV, respectively, and were built to feed the so-called Meson Factories. Despite the fact that the initial design beam currents were only 100 µA and 50 µA, respectively, today they have significantly exceeded their initial target. In particular, the PSI machine is able to supply proton beams with currents up to 2.4 mA and probably even more in the future. A survey of the RIKEN laboratory illustrates the flexibility of cyclotrons operated in cascade, up to 4 cyclotrons including the largest superconducting cyclotron [18]. Moreover, a talk presented by Jongwon Kim (IBS, South Korea) [21, 22] describes how a new generation

* winklehn@mit.edu

ISBN: 978-3-95450-212-7 ISSN: 2673-5482 doi:10.18429/JACoW-CYCLOTRONS2022-MOBI01

of commercial cyclotrons, the IBA Cyclone-70 [23], can be used to drive an ISOL facility. The latter aims at producing radioactive isotopes and perform experiments at the extreme limits of nuclear physics.

Comparing the three types of fixed field accelerators, we find that the average beam current from isochronous cyclotrons is typically two orders of magnitude higher than synchrocyclotrons, while FFAs (fixed field alternating gradient accelerators), despite their potential for applications beyond the GeV-level, have yet to demonstrate their capability for higher currents.

Limitations

The technical limits are mainly due to the original design of these machines. They could probably be overcome thanks to new technology and to new mechanical design options. The experiences gained along these long years of operation offer us valuable insights to apply to the problem of upgrading. It is quite evident that the amount of knowledge gained in these years allows starting new projects to achieve higher energy and higher current. The goal of 1 GeV and 10 mA for a proton beam delivered by a cyclotron seems feasible today, both using conventional technology, or also using superconducting technology to reduce the footprint of the machine (example the superconducting ring cyclotron K2500 of RIKEN). A problem that must be optimized is related to the reliability and to the maintenance of these new machine. This is a serious problem for accelerator proposed to drive sub critical reactor, so-called ADS. For cyclotrons used in the field of nuclear or particle science this is not a real limit. As pointed out in the talk by Grillenberger, technical problems like deflector failures and their replacement and the reliability of the RF cavities have to be minimized. For example, some of these problems could be mitigated using robots to replace people in the maintenance operations of the critical components like electrostatic deflectors. Of course, this implies that cyclotron components must be properly designed to allow robot maintenance. The introduction of robot or automatic maintenance will allow to operate the cyclotron also with larger amount of beam losses due to the higher accelerated current. Also, the problem to build safer RF cavities avoiding the multipactoring effect need to be optimized. Careful study of the cavity shapes and using local magnetic field to freeze the multipactoring effect could be an alternative solution to be investigated. The problem of the limit of the beam acceptance present in the compact cyclotron could be again upgraded using special ferromagnetic materials as Vanadium Permendur that allow to achieve higher magnetic field respect to the classical iron pole and then higher vertical focusing became feasible. Despite all the technical problems of cyclotrons they are up to now the only "cheaper" solution to achieve 10 MW proton beam at 1 GeV. Indeed, the FFAs while achieving energies higher than 1 GeV, have not yet a viable solution to achieve the high-power regime. Moreover, the machine protection system must be improved not only to protect the infrastructure from serious damage, but also to understand the source of the failure and to allow restarting the accelerator in a short time. Probably this goal can be accomplished using the new tool of machine learning.

The useful information collected by the operations of cyclotrons in the research centers developed worldwide have been received by commercial companies that are today able to supply high-current and reliable machine as the one bought by IBS, to drive their Rare Isotope Science Project. Commercial companies can sell cyclotrons delivering more than 700 µA of proton beam and new frontiers could be overcome soon.

The goal to achieve a proton beam with 5 mA at 800-1000 MeV using a cyclotron accelerator is realistic. However, the critical item to investigate is the best cyclotron configuration to achieve beam currents higher than 10 mA.

APPLICATIONS OF HIGH-POWER CYCLOTRONS AND FFAS

Isotope Production

Cyclotron beams [24], mainly protons, irradiate targets external to the cyclotron, reactions are characterized as A(p,X)B, where target species A is irradiated with protons, resulting in product B and emitting X particles and/or γs. Using particle beams has the advantage that B is usually a different atomic species than A, so chemical separation of the product from the target can be done yielding "carrier free" sources [25]. This allows much higher concentration of the activity in clinical use. It is usually not possible to do this with reactor-produced sources.

Medical isotopes are either "diagnostic" (for imaging of selected areas of the body) or "therapeutic" (for causing radiation damage to localized regions) [26]. A recent development has been identification of "theranostic" pairs [27], with matched isotopes of similar chemical properties, one diagnostic and one therapeutic.

Isotope production is one of the main applications of cyclotrons nowadays. Examples presented at this workshop were: RIKEN outside Tokyo, Japan, whose broadly-based research programs with beams from protons to uranium cover not only isotopes but many areas of nuclear research; TRIUMF, Canada's premier accelerator center with world-leading programs in many fields, particularly beam-based applications in nuclear physics and the life-sciences [28]; And the cyclotron center at the University of Alabama at Birmingham, a mainstream university-based facility dedicated to production and distribution of established radioisotopes, and to development of new radioisotopes and pharmaceuticals for nuclear medicine [29].

Particle Physics

The cyclotron with its capability to produce high currents of cw proton (and other ion) beams with moderate facility footprint has seen renewed interest in particle physics. Here we highlight two experiments planning to use a cyclotron driver: the highly anticipated particle physics experiments

ISBN: 978-3-95450-212-7 ISSN: 2673-5482 doi:10.18429/JACoW-CYCLOTRONS2022-MOBI01

IsoDAR and Mu3e as presented at the workshop by J.B. Spitz [30] and F. Meier Aeschbacher [31], respectively.

If the IsoDAR design proves successful, a 60 MeV/amu compact cyclotron will accelerate 5 mA of H_2^+ ions that are stripped of the electron to form a 10 mA proton beam directly after extraction. The IsoDAR cyclotron will utilize direct axial injection using an RFQ embedded in the cyclotron yoke and a beam physics effect in space-charge dominated cyclotrons beams called *vortex motion*. IsoDAR's main goal is to provide a definitive search for sterile neutrinos, but it has many other interesting beyond-standard-model search capabilities. The main physics cases are presented in detail in Ref. [32] and recent accelerator design considerations in Refs. [33–35]. IsoDAR has preliminary approval to run at the Yemilab Center for Underground Physics, using the 2.3 kt LSC [36] as its detector.

The Mu3e experiment aims to observe the lepton flavor changing process $\mu^+ \rightarrow e^+e^-e^+$ and to exclude a branching fraction of $> 10^{-16}$ at 90 % confidence level [37]. The main backgrounds are the standard Michel decay and the radiative SM decay. The experiment requires very high rates of muons. Muons for Mu3e will be produced at PSI's *Swiss Muon Source*, which is driven by the High Intensity Proton Accelerator (HIPA) facility. Protons at HIPA are accelerated using the 590 MeV separated-sector cyclotron [19], fed by Injector II.

Other ideas to use $O(10\text{ mA})$ cyclotrons in modern particle physics experiments are: 1. @60 MeV: Cross Section Measurements with a ^{8}Li-based $\bar{\nu}_e$ flux. As discussed in Ref. [38], new facilities built with an IsoDAR target/sleeve configuration will permit measurement of the antineutrino cross sections for neutrino coherent scattering for nuclei (CEνENS); 2. @15 MeV: Neutrino flux measurements. ν_e (as versus $\bar{\nu}_e$) fluxes can be produced up to 3.75 MeV by targeting 15 MeV protons on ^{27}Al to produce ^{27}Si. This was proposed in Ref. [39] for an accelerator-based study of the vacuum-matter transition region relevant for solar neutrino experiments using a radiochemical detector located 10 m from the target; 3. Monoenergetic Photons for BSM Searches (energy to be optimized): For a future experiment, the beam energy can be chosen and the target/sleeve material selected for the purpose of producing specific monoenergetic photon peaks of interest use in searches for new physics that couples to photons, such as axion-like and Z′ particles; 4. Detector design, calibration, and testing in high-neutron-flux environments.

Accelerator-Driven Sub-critical Reactor

The Accelerator Driven Sub-critical Reactor (ADSR) is a hybrid system coupling a particle accelerator to a sub-critical reactor core: the accelerator produces the high power beam which strikes a heavy metal target, in solid or liquid state. The spallation target will thus emit neutrons among other particles in the forward direction of the beam. Such neutrons are fed into the sub-critical reactor core to induce further fission reactions. Owing to the sub-critical state of the reactor, ADSR is considered as inherently safe and shutting down the reactor can be achieved by switching off the high power beam. Two important use cases are the incineration of nuclear waste in dedicated systems with a large fraction of Minor Actinides (Np, Am, Cm,...); And Thorium-fuel cycles where producing the fissile ^{233}U from Thorium requires the intermediate ^{233}Pa ($t_{1/2}$ = 27 days).

The main challenges for the use of cyclotrons as drivers for ADSR are that 1. no existing machine currently accelerates multi-mA beams to 1 Gev energies; and 2. ADSR requires very high reliability and cannot tolerate frequent trips, which cyclotrons are prone to. Nevertheless, conceptual designs exist, e.g., the DAEδALUS [40], AIMA [41], and TAMU [42] designs.

NOVEL CONCEPTS AND COMPUTATION

Novel Concepts

We discussed novel concepts to realize high-power cyclotrons and FFAs. The main challenges are (1) increased space charge and (2) high beam losses. Space-charge leads to beam growth, tune depression, and difficulties keeping the beam focused, which leads to more beam losses and also potentially poor beam quality. The concepts discussed here covered injection, acceleration Specifically, several new ideas for spiral inflectors were presented (transverse gradient electrostatic inflectors [43], active magentic inflectors [44, 45], and cylindrically symmetric passive inflectors [46]), and a concept for embedding an RFQ directly into the cyclotron yoke for bunching and pre-acceleration [34, 35]. Another concept was to use vortex motion as a means to reduce interturn particle halo and improve extraction efficiency [35]. We also heard about concepts for self-extraction from a cyclotron [47, 48], single-stage high-energy cyclotrons [41], and multi-port injection. For FFAs the concept of vertical excursion was discussed [49, 50]. In the interest of space, we refer the reader to the given references.

Computation

In the final session of the workshop, we heard about new mathods and algorithms in computational accelerator physics. C. Rogers was talking about the use of a map approach for tracking in FFAs, P. Calvo gave an account of the Development of the simulation code OPAL and T. Planche described the TRIUMF Simulation Tools Status & Future. A thorough review of available numerical codes can also be found in the article of Smirnov [51]. The consensus was that, particularly to reproduce space-charge effects accurately and on the order of 10^{-4} in terms of relative particle loss, computationally costly particle-in-cell codes give the highest accuracy. While codes like OPAL [52] are constantly being further developed to become more efficient, include more of the pertinent physics, and run on the highest performing clusters, new technologies like machine learning (e.g., surrogate modeling) should be embraced and included.

ISBN: 978-3-95450-212-7 ISSN: 2673-5482 doi:10.18429/JACoW-CYCLOTRONS2022-MOBI01

CONCLUSION

Findings

We found that there have been several breakthroughs in the past years to further increase the available beam currents (and thus total delivered power) that make continuous wave (cw) isochronous cyclotrons the accelerator of choice for many high power applications at energies up to 1 GeV. Key innovations are: Improved injection (through RFQ direct injection, transverse gradient inflectors, and magnetic inflectors), improved acceleration (utilizing *vortex motion*, single-stage high energy designs, vertical excursion FFAs), and improved extraction (through new stripping schemes and by *self-extracting*, using built-in magnetic channels). The use of H_2^+ as accelerated ion instead of protons or H^- has also received much attention lately. Here, stripping the electron during extraction or directly after doubles the electrical beam current mitigating some of the space charge issues with high current beams in the accelerator.

There are now several projects designing new powerful cyclotrons for particle physics, medicine, and accelerator driven systems (ADS) for energy research. These are cost-effective devices with small facility footprint, thus following the mantra *better, smaller, cheaper*. Among them, the IsoDAR compact cyclotron promises a 10 mA cw proton beam at 60 MeV/amu, improving by x4 over PSI injector 2 and by x10 over commercial cyclotrons for isotope production. A design for a 2 mA superconducting cyclotron is underway at TRIUMF, further reducing the footprint. Several designs (AIMA, DAEδALUS, TAMU) are being developed for ADS and particle phyiscs (CP-violation in the neutrino sector).

Finally, we found that the field of computational (accelerator) physics has made great strides and high fidelity simulations have become a necessity to understand and design accelerators with high space charge. High performance- and exascale computing will be needed in order to accurately simulate many-particle interactions (e.g., space-charge and halo-formation), and beam-environment interactions (e.g., residual gas, wakefields). As in other fields, Machine Learning can play a big role by providing new tools to understand and predict complex behavior, and significantly reduce simulation execution time, enabling virtual particle accelerators and faster and better optimization.

Recommendations

We, the community of particle physicists, particle accelerator physicists, and funding agencies, should:

1. Recognize the important role cyclotrons are playing in Nuclear- and Particle Physics;
2. Encourage development of this type of accelerator, as an investment with high potential benefits for Particle Physics, as well as outstanding societal value;
3. Recognize and encourage the high benefit of collaboration with the cyclotron industry.
4. Recognize the opportunities the Exascale computing era will provide and adjust development of beam dynamics simulation tools accordingly.
5. Aim for a close connection of traditional beam dynamics models with (1) machine learning (surrogate models) and (2) feedback (measurements) from the accelerator, as they will pave the way to an intelligent accelerator control and on-line optimisation framework.

ACKNOWLEDGEMENTS

We would like to sincerely thank all participants of the Snowmass'21 Workshop on High-Power Cyclotrons/FFAs (listed in Refs. [1, 2]) for the interesting discussions. We are particularly thankful to the presenters (in order of appearance during the workshop): Jongwon Kim, Joachim Grillenberger, Christian Baumgarten, Hiromitsu Haba, Suzanne Lapi, Thomas Ruth, Joshua Spitz, Frank Meier Aeschbacher, Francois Meot, Roger Barlow, Jean-Baptiste Lagrange, Grazia D'Agostino, Loyd Waites, Hugo Barnard, Lige Zhang, Chris Rogers, and Pedro Calvo.

REFERENCES

[1] *Snowmass'21 Workshop on High-Power Cyclotrons/FFAs*, `https://indico.mit.edu/e/cyclotrons`, 2021.

[2] D. Winklehner *et al.*, *Report of the Snowmass'21 Workshop on High-Power Cyclotrons and FFAs*, arXiv:2203.07919 [physics], 2022. `doi:10.48550/arXiv.2203.07919`

[3] D. Winklehner *et al.*, "High-power Fixed-Field Accelerators," *Journal of Instrumentation*, vol. 18, no. 05, T05008, 2023, Publisher: IOP Publishing. `https://dx.doi.org/10.1088/1748-0221/18/05/T05008`

[4] F. A. Heyn and K. K. Tat, "Operation of a radial sector fixed-frequency proton cyclotron," *Review of Scientific Instruments*, vol. 29, no. 7, pp. 662–662, 1958, Publisher: American Institute of Physics. `doi:10.1063/1.1716293`

[5] E. Gardner and C. M. G. Lattes, "Production of mesons by the 184-inch berkeley cyclotron," *Science*, vol. 107, no. 2776, pp. 270–271, 1948. `doi:10.1126/science.107.2776.270`

[6] J. Burfening, E. Gardner, and C. M. G. Lattes, "Positive mesons produced by the 184-inch berkeley cyclotron," *Physical Review*, vol. 75, no. 3, pp. 382–387, 1949. `doi:10.1103/PhysRev.75.382`

[7] E. L. Kelly, "General description and operating characteristics of the berkeley 88-inch cyclotron," *Nuclear Instruments and Methods*, vol. 18-19, pp. 33–40, 1962. `doi:10.1016/S0029-554X(62)80006-8`

[8] G. Gul'bekyan *et al.*, "New development at the JINR heavy ion cyclotron facility," in *Proceedings of the 13th International Conference on Cyclotrons and their Applications*, 1992, p. 11.

[9] B. Gikal, G. Gul'bekyan, and V. Kutner, "Recent developments at dubna u400 and u400m cyclotrons," in *Proceedings of the 15th International Conference on Cyclotrons and their Applications*, 1998, p. 5.

ISBN: 978-3-95450-212-7 ISSN: 2673-5482 doi:10.18429/JACoW-CYCLOTRONS2022-MOBI01

[10] B. N. Gikal *et al.*, "IC-100 accelerator complex for scientific and applied research," *Physics of Particles and Nuclei Letters*, vol. 5, no. 1, pp. 33–48, 2008. https://doi.org/10.1134/S1547477108010068

[11] J. Fermé, M. Gouttefangeas, and T. G. Group, "Status report on GANIL," in *Proceedings of the 9th International Conference on Cyclotrons and their Applications*, 1981, p. 9.

[12] H. G. Blosser, "The michigan state university superconducting cyclotron program," *IEEE Transactions on Nuclear Science*, vol. 26, no. 2, pp. 2040–2047, 1979. doi:10.1109/TNS.1979.4329804

[13] F. Resmini, G. Bellomo, E. Fabrici, H. G. Blosser, and D. Johnson, "Design characteristics of the k=800 superconducting cyclotron at m.s.u.," *IEEE Transactions on Nuclear Science*, vol. 26, no. 2, pp. 2078–2085, 1979. doi:10.1109/TNS.1979.4329811

[14] A. H. Botha *et al.*, "Operation and development of the NAC accelerator facilities," in *Proceedings of the 12th International Conference on Cyclotrons and their Applications*, 1989, p. 4.

[15] H. Ikegami, "The RCNP ring cyclotron facilities," in *Proceedings of the 12th International Conference on Cyclotrons and their Applications*, 1989. https://accelconf.web.cern.ch/c89/papers/b-03.pdf

[16] Y. Yano, "Status report on RIKEN ring cyclotron," in *Proceedings of the 12th International Conference on Cyclotrons and their Applications*, 1989, p. 4.

[17] S. Dmitriev *et al.*, "SHE factory: Cyclotron facility for super heavy elements research," *Proceedings of the 22nd International Conference on Cyclotrons and their Applications*, vol. Cyclotrons2019, in collab. with C. Lowry (Ed.), D. V. Garrett (Ed.) John, and S. RW (Ed.) Volker, 5 pages, 2.555 MB, 2020. http://jacow.org/cyclotrons2019/doi/JACoW-Cyclotrons2019-THC01.html

[18] Y. Yano, A. Goto, M. Kase, and T. Katayama, "RI beam factory project at RIKEN," in *Proceedings of the 16th International Conference on Cyclotrons and their Applications*, 2001, p. 6.

[19] J. Grillenberger, C. Baumgarten, and M. Seidel, "The High Intensity Proton Accelerator Facility," *SciPost Phys. Proc.*, vol. 002, p. 2, 5 2021. doi:10.21468/SciPostPhysProc.5.002

[20] G.C. Ball, G. Hackman, and R. Krücken, "The TRIUMF-ISAC facility: Two decades of discovery with rare isotope beams," *Physica Scripta*, vol. 91, no. 9, p. 093 002, 2016. https://doi.org/10.1088/0031-8949/91/9/093002

[21] J. Kim, "A 70 MeV cyclotron facility of IBS for ISOL and other uses," en, in *Presentations at the Snowmass'21 Workshop on High-Power Cyclotrons/FFAs*, 2021. https://indico.mit.edu/event/150

[22] J. Kim, "Construction of a 70 MeV proton cyclotron facility of IBS for multidisciplinary utilization," en, *Journal of the Korean Physical Society*, 2022. https://doi.org/10.1007/s40042-022-00415-z

[23] *Cyclone 70 (IBA – Ion Beam Applications S.A.)* http://www.iba-cyclotron-solutions.com/products-cyclo/cyclone-70, 2013.

[24] P. Schmor, "Review of cyclotrons used in the production of radio-isotopes for biomedical applications," in *Proceedings of the 19th International Conference on Cyclotrons and their Applications*, 2011, p. 6.

[25] J. De Goeij and M. Bonardi, "How do we define the concepts specific activity, radioactive concentration, carrier, carrier-free and no-carrier-added?" *Journal of radioanalytical and nuclear chemistry*, vol. 263, no. 1, pp. 13–18, 2005.

[26] J. J. P. de Lima, "Radioisotopes in medicine," *European journal of physics*, vol. 19, no. 6, p. 485, 1998.

[27] P. Zarrintaj, F. Mostafapoor, P. B. Milan, and M. R. Saeb, "Theranostic platforms proposed for cancerous stem cells: A review," *Current stem cell research & therapy*, vol. 14, no. 2, pp. 137–145, 2019.

[28] J. Dilling and O. Kester, "Fifty years of triumf: Canada's particle accelerator laboratory," *Nuclear Physics News*, vol. 29, no. 4, pp. 21–25, 2019.

[29] *Lapi research group at the university of alabama at birmingham*, 2022. http://www.lapilab.com/

[30] J. Spitz, "An application of high power cyclotrons in physics: IsoDAR," en, in *Presentations at the Snowmass'21 Workshop on High-Power Cyclotrons/FFAs*, 2021. https://indico.mit.edu/event/150/contributions/337/attachments/152/284/snowmass%5C_cyclotrons%5C_spitz.pdf

[31] F. Meier Aeschbacher, "The search for μ→eee and what it may need beyond Mu3e phase II," en, in *Presentations at the Snowmass'21 Workshop on High-Power Cyclotrons/FFAs*, 2021. https://indico.mit.edu/event/150/contributions/338/attachments/151/283/praesMu3eSnowmass210908.pdf

[32] J. Alonso *et al.*, "Neutrino physics opportunities with the IsoDAR source at Yemilab," *Physical Review D*, vol. 105, no. 5, p. 052 009, 2022, Publisher: American Physical Society. doi:10.1103/PhysRevD.105.052009

[33] D. Winklehner, R. Hamm, J. Alonso, J. M. Conrad, and S. Axani, "Preliminary design of a RFQ direct injection scheme for the IsoDAR high intensity H2+ cyclotron," *Review of Scientific Instruments*, vol. 87, no. 2, 02B929, 2015, Publisher: American Institute of Physics. doi:10.1063/1.4935753

[34] D. Winklehner *et al.*, "High intensity cyclotrons for neutrino physics," *Nuclear Instruments and Methods in Physics Research Section A: Accelerators, Spectrometers, Detectors and Associated Equipment*, vol. 907, pp. 231–243, 2018.

[35] D. Winklehner *et al.*, "Order-of-magnitude beam current improvement in compact cyclotrons," *New Journal of Physics*, vol. 24, no. 2, p. 023 038, 2022. doi:10.1088/1367-2630/ac5001

[36] S.-H. Seo, "Neutrino telescope at yemilab, korea," *arXiv:1903.05368 [astro-ph, physics:hep-ex, physics:physics]*, 2019.

[37] K. Arndt *et al.*, "Technical design of the phase i mu3e experiment," *Nuclear Instruments and Methods in Physics Research Section A: Accelerators, Spectrometers, Detectors and Associated Equipment*, vol. 1014, p. 165 679, 2021. doi:10.1016/j.nima.2021.165679

ISBN: 978-3-95450-212-7 ISSN: 2673-5482 doi:10.18429/JACoW-CYCLOTRONS2022-MOBI01

[38] O. Tomalak, P. Machado, V. Pandey, and R. Plestid, "Flavor-dependent radiative corrections in coherent elastic neutrino-nucleus scattering," *JHEP*, vol. 02, p. 097, 2021. doi:10.1007/JHEP02(2021)097

[39] J. W. Shin, M.-K. Cheoun, T.-S. Park, and T. Kajino, "New neutrino source for the study of solar neutrino physics in the vacuum-matter transition region," *Phys. Rev. C*, vol. 94, no. 4, p. 045 804, 2016. doi:10.1103/PhysRevC.94.045804

[40] M. Abs *et al.*, "Multimegawatt DAEδALUS Cyclotrons for Neutrino Physics," *arXiv preprint arXiv:1207.4895*, 2012.

[41] P. Mandrillon and M. Conjat, "Single Stage Cyclotron for an ADS Demonstrator," in *Proc. of International Conference on Cyclotrons and Their Applications (Cyclotrons'16), Zurich, Switzerland, September 11-16, 2016*, Zurich, Switzerland, 2017, pp. 387–393. doi:10.18429/JACoW-Cyclotrons2016-FRA01

[42] S. Assadi *et al.*, "Strong-focusing Cyclotron - High-current Applications," *Conf. Proc. C*, vol. 1205201, pp. 436–438, 2012.

[43] A. H. Barnard *et al.*, "Longitudinal and vertical focusing with a field gradient spiral inflector," en, *Physical Review Accelerators and Beams*, vol. 24, no. 2, p. 023 501, 2021. doi:10.1103/PhysRevAccelBeams.24.023501

[44] D. Campo *et al.*, "High power cyclotrons for neutrino experiments," in *5th Int. Particle Accelerator Conf.(IPAC'14), Dresden, Germany, June 15-20, 2014*, JACOW Publishing, Geneva, Switzerland, 2014, pp. 788–790.

[45] L. Calabretta, D. Rifuggiato, and M. Maggiore, "Review of high power cyclotrons and their applications," *Proceedings of the 22nd International Conference on Cyclotrons and their Applications*, vol. Cyclotrons2019, in collab. with C. Lowry (Ed.), D. V. Garrett (Ed.) John, and S. RW (Ed.) Volker, 5 pages, 1.062 MB, 2020. doi:10.18429/JACOW-CYCLOTRONS2019-THB01

[46] L. Zhang, Y.-N. Rao, T. Planche, R. Baartman, and Y. Bylinski, "Feasibility study for the cylindrically symmetric magnetic inflector," en, in *Presentations at the Snowmass'21 Workshop on High-Power Cyclotrons/FFAs*, 2021.

[47] . G. D'Agostino *et al.*, "InnovaTron: An innovative industrial high-intensity cyclotron for production of 99m Tc and other frontier medical radioisotopes," *Proc. IPAC'21, Campinas, SP, Brazil, May 2021*, vol. TUPAB188, p. 1841, 2019.

[48] . W. Kleeven *et al.*, "The IBA self-extracting cyclotron project," *Proc. Nukleonika*, vol. 48, S59, 2003.

[49] S. Brooks, "Vertical orbit excursion fixed field alternating gradient accelerators," *Physical Review Special Topics - Accelerators and Beams*, vol. 16, no. 8, p. 084 001, 2013, Publisher: American Physical Society. doi:10.1103/PhysRevSTAB.16.084001

[50] S. Machida, D. J. Kelliher, J.-B. Lagrange, and C. T. Rogers, "Optics design of vertical excursion fixed-field alternating gradient accelerators," *Physical Review Accelerators and Beams*, vol. 24, no. 2, p. 021 601, 2021, Publisher: American Physical Society. doi:10.1103/PhysRevAccelBeams.24.021601

[51] V. Smirnov, "Computer codes for beam dynamics analysis of cyclotronlike accelerators," *Phys. Rev. Accel. Beams*, vol. 20, p. 124 801, 12 2017. doi:10.1103/PhysRevAccelBeams.20.124801

[52] A. Adelmann *et al.*, "OPAL a Versatile Tool for Charged Particle Accelerator Simulations," *arXiv:1905.06654 [physics]*, 2019, arXiv: 1905.06654. http://arxiv.org/abs/1905.06654

ISBN: 978-3-95450-212-7 ISSN: 2673-5482 doi:10.18429/JACoW-CYCLOTRONS2022-MOBI02

STATUS OF SPES CYCLOTRON AT LABORATORI NAZIONALI OF LEGNARO

M. Maggiore, P. Antonini, L. Pranovi, A. Ruzzon
Laboratori Nazionali of Legnaro-INFN, Padua, Italy

Abstract

The SPES cyclotron at Laboratori Nazionali of Legnaro (LNL) was installed and commissioned in 2017 and the accelerator was operational until March 2021. The shutdown was foreseen in order to permit the completion of the SPES facility, while the resume of activities is expected in 2023. The status of the SPES cyclotron and related high intensity beamlines will be presented as well as the last performance achieved in terms of accelerated current up to 1 MeV. Moreover, the program of upgrade of the ancillary systems shall be discussed.

STATUS OF SPES PROJECT

The SPES project [1] is developing in the international framework of the new facilities producing exotic beams for astrophysics research, fundamental interactions, and applications for society, including in medicine.

The project was divided into four phases aiming to provide a multipurpose facility whose accelerator complex is shown in Fig. 1:

- α-phase: construction of main building and installation and commissioning of the high intensity accelerator delivering the high-power proton beams.
- β-phase: installation and commissioning of Radioactive Ion Beams (RIB) facility. It consists of ISOL targets, low energy beam transport lines, beam cooling device and High-Resolution Mass Separator (HRMS), charge breeding system (ADIGE), new RFQ injector and re-acceleration by actual superconducting Linac ALPI.
- γ-phase: installation and commissioning of equipment and laboratories for production and R&D of radioisotopes for medical applications.
- δ-phase: realization of experimental hall to produce neutron beams by interaction of high intensity protons with heavy and light targets.

Once the alpha-phase was completed in 2017, the SPES project has entered in 2018 in the crucial beta-phase of installation of target and low energy beamlines. Moreover, at the same time, the completion of the related infrastructures is carrying on in order to provide a full power facility plant including the implementation of the HVAC upgrades.

Without a doubt. the emergency due to the Covid-19 pandemic had strongly impacted with the progress of the scheduled works. Moreover, the international situation worsening since beginning of 2022 has further delayed the planning, but nevertheless, very important progresses were done in the last three years.

The ISOL target station was installed in 2021, including the first section of the beam transport line downstream the source: i.e., the Wien filter beam selector and first electrostatic quadrupole. The High Voltage platform providing 40 kV voltage for the ion source is under commissioning. The main electrostatic lenses and the recombination magnets of the first leg of low energy beamline were also installed in 2022.

The beam cooler device which is necessary to improve the quality of beams produced by the plasma source, it was completed from the Laboratoire de Physique Curpusculaire (LPC) of Caen (France) and the beam commissioning is ongoing in the French laboratory. The installation in the SPES facility is foreseen in late 2023.

The final design of the High-Resolution Mass Spectrometer was accomplished out and the tender for the supply of the resistive magnets and the electrostatic lenses was awarded to the Elytt Energy company [2] in 2022. The delivery is expected by the end of 2024.

The charge breeder device is installed and the ion source for stable beams has been commissioned in 2022. The High Voltage platform has been finished while the installation of the Medium Resolution Mass Spectrometer is under completion.

The post acceleration section is progressing very well, as the new resistive RFQ injector is finalizing, and the first module was mounted at LNL. The upgrade of superconducting Linac ALPI has been carried out and the first accelerating beams started in December this year.

During the 2023, the resume of cyclotron operation is expected to allow the commissioning of new high intensity proton beamlines. In 2024, the first exotic beam produced by the small size ISOL target, hit by few hundred watts of primary beam, should be available for the low energy experiments in the dedicated area of SPES facility (see Fig.1).

SPES CYCLOTRON STATUS

The SPES Cyclotron is a four sectors compact cyclotron supplied by Best Theratronics [3], capable to accelerate H^- ions up to the maximum energy of 70 MeV. The protons are extracted by the stripping of the H- ions passing thru a thin graphite foil where the two electrons were stopped.

The proton beams are available in the energy range within 30-70 MeV and with an average current varying from few tens of nA up to the nominal value of 750 µA.

The vacuum system is equipped with four cryogenic pumps CTI-10 of Brooks Company installed into the two valleys, providing a vacuum level of 3×10^{-6} Pa. A scroll pump allows to get the primary vacuum level of 1.5 Pa.

ISBN: 978-3-95450-212-7 ISSN: 2673-5482 doi:10.18429/JACoW-CYCLOTRONS2022-MOBI02

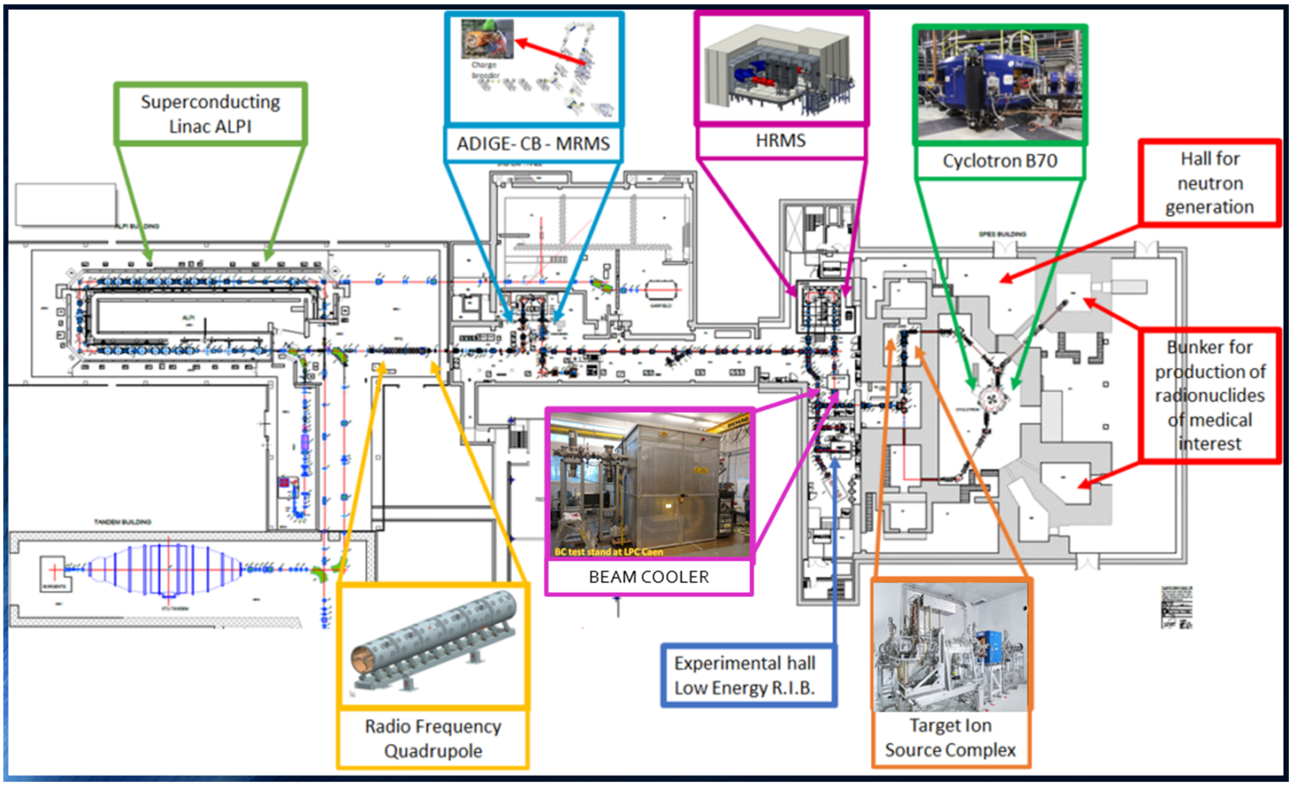

Figure 1: Layout of SPES facility complex at Laboratori Nazionali of Legnaro, Italy.

The RF system consists of 2 delta-type cavities (half-wave) placed in the valleys, providing up to 70 kV of accelerating voltage. The devices operate in 4^{th} harmonic mode at the frequency of 56 MHz. To optimize the performance of the whole system, the cavities are fed by two separated amplifiers (dual stage, tetrode based) able to provide up to 55 kW RF power each.

The injection of the beam is axial and a multicusp H^- ion source (IS) is placed underneath the cyclotron in the pit. A beam stop is placed downstream the IS for current measurement. The injection line is composed by two magnetic solenoids for focusing the beam in series with two quadrupoles needed to provide the matching with the inflector entrance.

The central region has been designed in order to maximize the phase acceptance up to the value of 50 RF deg. It allows to have margin for optimizing the injected current. A beam stop is placed into the cyclotron intercepting the accelerated particles once they have made few turns (1 MeV energy). It permits to setup the best conditions of the injected beam before the full acceleration and extraction.

The extraction mechanism allows changing the stripper foil without breaking the vacuum in the main chamber. The device has been designed in order to hold up to 20 stripper foils quickly movables and easy to re-charge entirely.

Two main extraction lines come from the Cyclotron. Each line ends in a switching magnet (10 tons) bending the beam along three potential lines to be used exclusively.

Each beamline is equipped with a cryogenic pump CTI-8 type and with the necessary beam diagnostics device. A fast gate valve is installed along each beamline line arm, in order to prevent any damage coming from potential vacuum breaks at the target stations. Table 1 summarizes the performance.

Table 1: Cyclotron Parameters

Parameter	Value/Description
Cyclotron type	Compact, resistive magnet
Sectors number	4 straight sectors
Accelerated particle	H^- (protons extracted)
Beam energy range	35÷70 MeV
Beam current range	50 nA÷750 µA
Magnetic field at center	1 tesla
Peak magnetic field	1.6 tesla
Pole radius	135 cm
Weight	~200 tons
RF system	2 delta-type cavities λ/2
RF frequency	56 MHz, harmonic=4
Extraction system	Stripping process
Injection system	Axial from external IS
Ion Source (IS)	Volumetric multi-cusp
Nominal intensity IS	6÷10 mA
Voltage IS	40 KV

During the three-year period 2020-2022, the cyclotron systems have been upgraded. In the following we reported the main interventions we carried out.

ISBN: 978-3-95450-212-7 ISSN: 2673-5482 doi:10.18429/JACoW-CYCLOTRONS2022-MOBI02

Electrical Systems

During the 2021 year, the electrical systems to support the components of the beamlines LARAMED and ISOL2 were completed. The wiring of both DC cables and signals from the power supply room to the magnets and ancillary devices was carried out. The new cabinets were placed in the dedicated room and the power supplies have been mounted inside these. The old main electrical board was replaced with a new one by increasing the number of available slots for future upgrade of the facility (see Fig. 2).

Figure 2: On right side, the picture shows the new main local electrical board dedicated to supply the cyclotron's components. On the right side the new cabinet with the power supplies of LARMAED beamlines magnet.

Water Cooling System

In 2018 it was decided to replace the actual single cooling system supplied by Best Theratronics which provides the water for the cyclotron and related subsystems with a new one. The latter consists into five independent skids and related distribution circuits which supply respectively.

- Cyclotron and injection line systems.
- Beamline devices branching off from exit port 1.
- Beamline devices branching off from exit port 2.
- Activated devices (Faraday cups, collimators, baffles).
- Radio Frequency and vacuum systems: power amplifiers and cryo-compressors.

The new configuration will allow to improve the maintenance activity by separating the management of potential activated components from the 'cold' ones. Moreover, the upgraded system will increase the reliability of the facility during the beam operation.

During the 2021 year the old skid was dismantled, and the new five devices have been positioned in the final destination inside the technological room of SPES building. The design of the ultimate distribution of the water lines connecting the skids to the apparata was carried out in 2022. In 2023 we expect to dismantle the old system then replace it with the new lines.

New Server for Control System

Due to the obsolescence of the hardware dedicated to the cyclotron control system, two new DELL workstations were setup up and a new DELL server has replaced the original HP machine. A dedicated QNAP NAS quad-core provides comprehensive backup and data storage instead of actual HDD device with limited performances.

The system has been designed to be expandable based on future needs of beamlines deployment and accelerator system upgrades.

Diagnostics

During the commissioning of high intensity beam, we observed the anomalous activation of the beampipe in correspondence of a doublet quadrupole magnets, where in effect we expect the beam size should increase. Evidently, the hot spot was caused by a beam loss due to a wrong setup of magnetic lenses setting. To prevent this kind of problems, we decided to adopt a system of beam loss monitoring able to detect the neutron contribution caused by the interaction of protons with material of the beam pipe.

The detectors will be connected to the cyclotron Machine Protection system to interlock the accelerator once a certain threshold of produced neutrons is exceeded.

Moreover, the devices will be placed in well known points where the beam size reaches the maximum envelope, i.e. in the middle of the two quadrupole magnet lenses.

Preliminary test on commercial devices were carried out at LNL, in particular we employed the system offered by Instrumentation Technologies, Libera [4] which is based on scintillators integrated on a photomultiplier, flash ADC and data acquisition [5].

BEAM OPERATION

Once all the system are restored, we proceeded to run the beam. As first step, we planned to inject the beam and accelerate it up to 1 MeV.

In order to avoid that accelerated particles overcome the 1 MeV energy, the movable diagnostic pop-up probe which is installed inside the cyclotron, has been blocked in the lifted position. In such configuration, the injected beam carries out few turns, then it is stopped on the copper made dump (see Fig. 3).

Several setting in terms of extracted current beam from the ion source have been tested and the efficiency of the injection transmission has been verified to achieve the value of 13%, which corresponds to 47 deg of phase acceptance of the cyclotron central region.

Finally, we accomplished out a test aimed to establish the upper limit of injected current achievable into the cyclotron. The maximum value of current injected up to 1 MeV energy was 956 µA.

Table 2 shows the readback current values of diagnostics along the injection lines.during the test.

ISBN: 978-3-95450-212-7 ISSN: 2673-5482 doi:10.18429/JACoW-CYCLOTRONS2022-MOBI02

Figure. 3. The picture shows the pop-up probe mechanism installed into the valley of the cyclotron.

Table 2: Current Readback

Parameter	**Current** [µA]
BS Beamstop	7597.23
IFCOL	45.03
PP Pop-Up	956.20

The *BS Beamstop* is the current extracted from the ion source; the *IFCOL* is the current lost on the collimator placed upstream the inflector entrance; *PP Pop-Up* is the current of beam intercepted by the 1 MeV probe.

The second important test was carried on in order to check the maximum current delivered with a good stability versus time. As shown in the Fig. 4, the ion source set was tuned until a stable current value of 930 µA was measured on the pop-up probe.

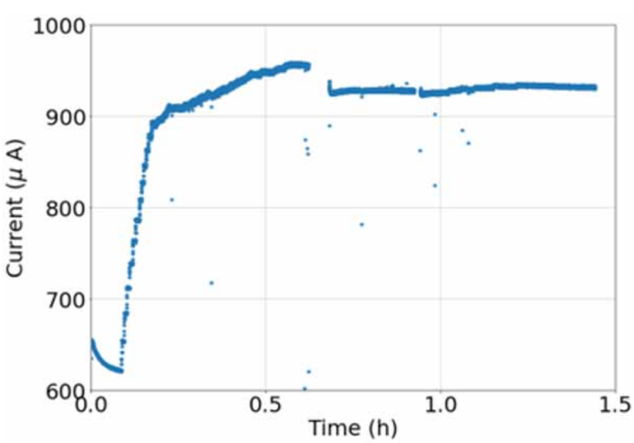

Figure 4. The plot shows the trend of the beam current readback at 1 MeV versus the time.

CONCLUSION

The status of SPES cyclotron and related subsystem was presented. The SPES facility during last three years is growing considerably. Many infrastructures and plants have been accomplished out as well the accelerator systems, i.e., ISOL target station, charge breeder device, etc.

The cyclotron was operational for limited time also due to the Covid-19 pandemic break. Anyway, in June 2020 the beam test demonstrated once again the good performance of the accelerator in terms of high injected current (950 uA) up to 1 MeV energy.

In March 2021, the cyclotron was again turned off to allow the installation of SPES equipment and proceed with the completion of the facility (new safety system, plants upgrading, civil works, compliance with fire brigade directives). Meanwhile the major upgrades of cyclotron systems are still proceeding.

The restart of operations is expected by the end of 2023 with the goal to deliver the first proton beam to ISOL target so that SPES project begins.

REFERENCES

[1] F. Gramegna *et al.*, "The SPES exotic beam ISOL facility", *Il Nuovo Cimento C*, vol. 41, no. 5, article no. 195 (7 pages), 2018. doi:10.1393/NCC/I2018-18195-3

[2] Elytt Energy, http://www.elytt.com

[3] Best Theratronics, http://www.theratronics.ca

[4] Instrumentation Technologies, Libera, http://www.i-tech.si

[5] M. L.Allegrini, LNL Annual Report 2021, Italy, 2012, pp. 34-52.

ISBN: 978-3-95450-212-7 ISSN: 2673-5482 doi:10.18429/JACoW-CYCLOTRONS2022-MOBO01

HIGH INTENSITY CYCLOTRONS FOR PRODUCTION OF MEDICAL RADIOISOTOPES

E. van der Kraaij†, J. M. Geets, W. Kleeven, J. Mandrillon, N. Mine, V. Nuttens, P. Verbruggen
Ion Beam Applications, Louvain-la-Neuve, Belgium

Abstract

At the previous cyclotron conference an overview of the cyclotrons for radioisotopes production was shown. Here, we will focus on the development of IBA's accelerators in the recent three years. Notably the Cyclone® 70, the Cyclone® 30XP and the Cyclone® KIUBE have made progress. The expertise gained with the development of these machines has led IBA to develop a completely new cyclotron for 30 MeV protons, the Cyclone® IKON. As its first construction is ongoing, details on the design of this accelerator will be presented.

ONGOING COMMISSIONINGS

Two major projects are ongoing for the older generation cyclotrons: a Cyclone® 70 at IBS in Korea, and a Cyclone® 30XP at the INM in Germany [1].

Cyclone® 70

In 2019 a contract was signed between IBA and IBS for the installation of a 70 MeV cyclotron with beam lines leading to two separate target vaults [2]. After a design phase fitting the system in the already existing building, the installation was performed in 2021.

For this installation, IBA developed a beam profile monitor using a wire scanner. In Fig. 1, results from the tuning at 70 MeV are shown with the donut-shape requested by the customer. As of November 2022, only 12 months after the start of the rigging, the commissioning was finished with a beam of 715 µA on target.

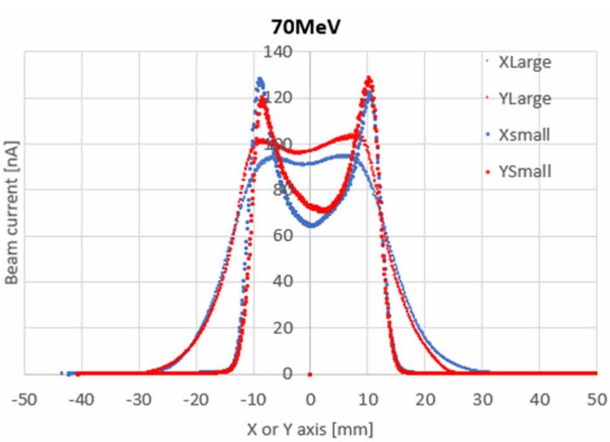

Figure 1: Beam current measured along the X and Y axis, using either a large or a small beam spot, with wobbler.

† erik.vanderkraaij@iba-group.com

Cyclone® 30XP

The Cyclone® 30XP is a multi-particle cyclotron that IBA is to install at the Forschungszentrum Jülich in Germany. The installation had been on hold for several years, but recently the commissioning could finally start.

Table 1: Properties of the Multi-particle Cyclone® 30XP

Particle	Energy	Beam Intensity	Extraction Method
Proton	15 ~ 30 MeV	300 eµA	Stripping
Deuteron	8 ~ 15 MeV	50 eµA	Stripping
Alpha	30 MeV	50 eµA	Electrostatic deflection

In Table 1, an overview is given of the different particle beams that can be extracted. For the proton and deuteron beams, stripping extraction is used. The latest results of the commissioning, only recently obtained, confirm that also the third particle type can be extracted: a stable alpha beam of 20 eµA has been measured on target, with an efficiency of the deflector of 75%. Higher beam intensities are expected soon.

CYCLONE® IKON

With the expertise gained on IBA's Cyclone® KIUBE [3, 4], the new Cyclone® IKON was designed, see Fig. 2. Compared to the previous 30 MeV cyclotron, it is more compact, more efficient and delivers better performance.

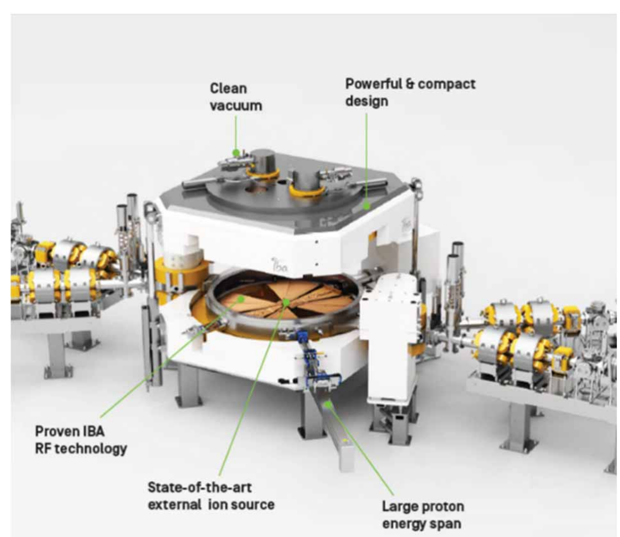

Figure 2: Image of the Cyclone® IKON with dual extraction, switching magnets and the start of four beam lines. A third target can be mounted on each switching magnet.

ISBN: 978-3-95450-212-7 ISSN: 2673-5482 doi:10.18429/JACoW-CYCLOTRONS2022-MOBO01

Table 2: Parameters of the New 30 MeV Cyclotron Design Compared with its Predecessor

Parameters	Cyclone® 30P	Cyclone® IKON
Pole gap	30 mm	30 mm
Valley depth	550 mm	159 mm
Cyclotron height	1550 mm	920 mm
Diameter (width)	2700 mm	2145 mm
Ampere-turns	42.7×10^3 A	35.9×10^3 A
Iron mass	43 T	23 T
Coil mass	1440 kg	1125 kg
RF frequency	62 MHz	75 MHz
Energy	15 ~ 30 MeV	13 ~ 30 MeV
Extr. current	0.5 ~ 1.2 mA	1.2 mA

In Table 2, the parameters of the old and new accelerator are listed. As can be seen, its height has significantly been reduced, mainly by lowering the valley depth. Consuming less Ampere-turns, the machine can extract a larger span of energies, with 1.2 mA of 30 down to 13 MeV.

The injection line, seen in Fig. 3, is similar to that of the injection line designed for a previous upgrade of the Cyclone® 30HC [1]. One difference is that the Glaser has its own yoke, as it is now outside of the cyclotron's yoke. A D-pace DC Volume-Cusp source is used, designed for 15 mA of H^- beam at 30 keV [5].

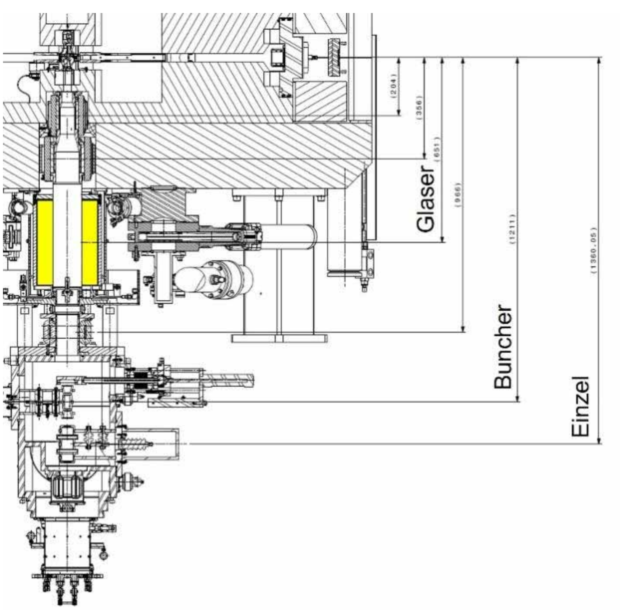

Figure 3: Injection line of the Cyclone® IKON.

Magnetic field optimizations were computed in Simulia OPERA [6], whereas beam tracking was performed with AOC [7]. Using these tools, an inflector has been designed and the dee tips were optimized for good orbit centring, phase acceptance and electric focusing, see Fig. 4, for an injected beam of 40 keV.

As its baby brother, the Cyclone® KIUBE, the Cyclone® IKON comes with pole inserts in the centre of the poles, that can be removed during the magnetic mapping process and easily milled to obtain an isochronous magnetic field [8]. In Fig. 5 the inserts can be seen, mounted in the poles.

Figure 4: View of the inflector and dee tips.

Figure 5: View of the inserts mounted in the poles, assembled with the dees.

The position of the switching magnets has been optimized to minimize the cut-out in the return yoke, while taking into account the properties of the beam as extracted from 13 to 30 MeV, as seen in Fig. 6. The result is a clocking of the external squared yoke by 20° compared to the symmetry axes of the poles.

According to the calculated beam transport from the switching magnet through the beamlines (with one permanent magnet focussing element, plus two quadrupole doublets), a minimal transmission of 94% at 13 MeV is expected, and 99% at 30 MeV.

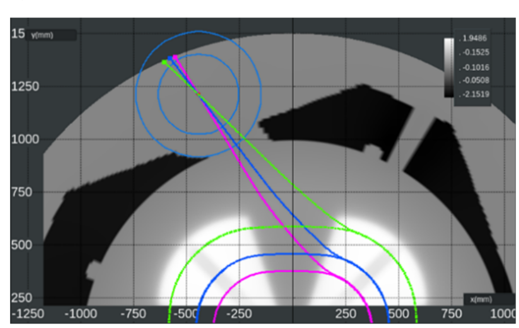

Figure 6: Return yoke has been rotated compared to the poles, to optimize the extraction.

ISBN: 978-3-95450-212-7 ISSN: 2673-5482 doi:10.18429/JACoW-CYCLOTRONS2022-MOBO01

The magnetic field is shaped by machining the pole inserts according to field map results, all while taking into account external magnetic elements such as the hydraulic jacks, switching magnets, etc. The deformations of the magnet yoke due to atmospheric pressure and magnetic force are also considered. In Fig. 7, the integrated phase shift as a function of the radius is shown with less than ± 10° of excursion.

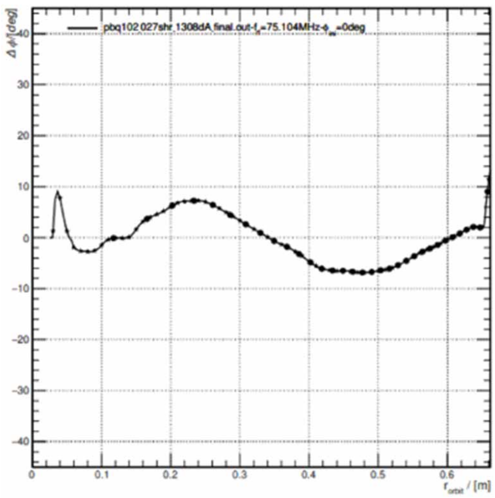

Figure 7: Integrated phase shift. Stars indicate the integer values of the average closed equilibrium orbit radii every 1 cm. Bullets correspond to integer values of the kinetic energy every 1 MeV.

In Fig. 8 the operation curve is shown. The resonance line that may deteriorate the beam emittance is the Walkinshaw resonance ($\nu_r - 2\nu_z = 0$). This resonance is crossed before an orbit radius of 25 cm, where large turn separation per MeV is found, see the bullets separation in Fig. 8. Fast crossing of the resonance condition is expected which will not deteriorate the beam emittance. Also, the crossing of the Walkinshaw resonance was avoided at energies close to extraction during the pole inserts correction.

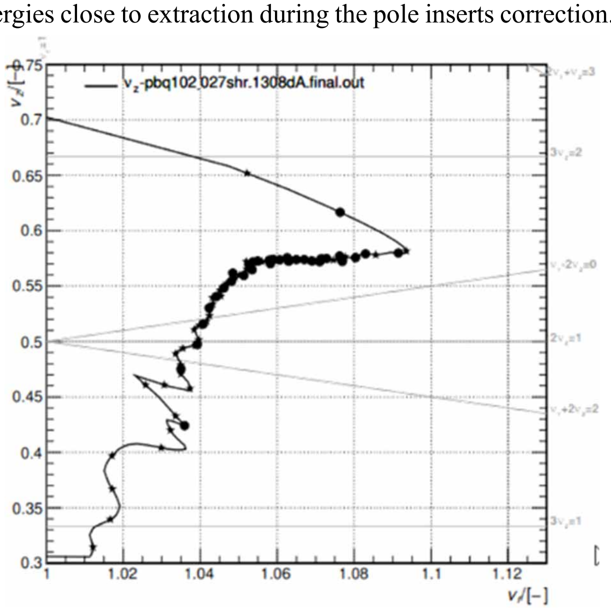

Figure 8: Operation point curve.

SPACE CHARGE CALCULATIONS

In AOC, there is the option to include the calculations of the space charge (SC) effects. For this, the particle-to-particle method is used for the calculation of the self-field of a bunch. It is assumed that the bunch is in free space, i.e. there are no electromagnetic boundary conditions, and the self-field acting on one particle is obtained as the sum of contributions of all other particles in the bunch. This slows down the calculation for large number of particles N, as computing time scales with N_2. However, for the injection and central region calculations, ~ 10000 particles can be enough, which keeps the needed CPU time reasonable.

The main advantage of the chosen method is that one can immediately include the SC option together with the existing 3D features of the E- and B-fields, simplifying tracking through regions such as that of a spiral inflector.

Transport Results Compared to AOC

In the Transport code, there is also the option to include space charge effects [9-11]. In Fig. 9, upper plot, the beam envelop can be seen as calculated by Transport for the Cyclone® IKON injection line, with and without space charge effects for a 15 mA beam. In the lower plot the same is given for the calculations with AOC.

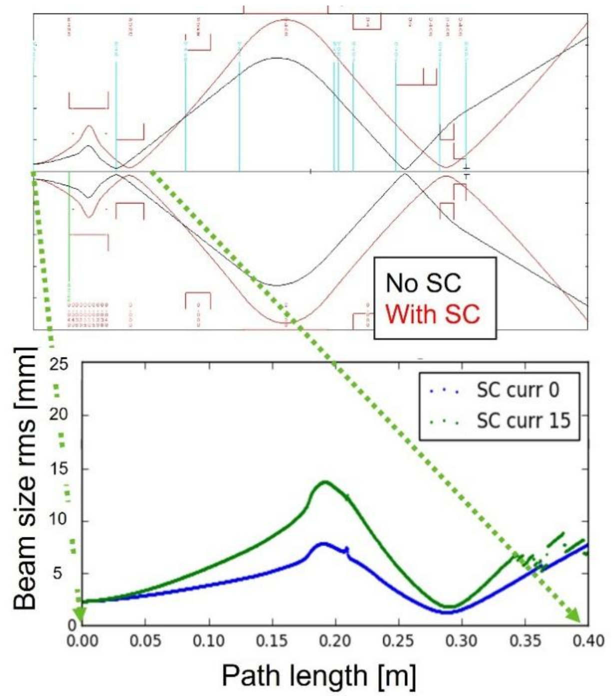

Figure 9: Beam envelope (2σ) calculations in Transport (up) and in AOC (down). In the upper plot the full injection line length is displayed, whereas in the lower plot only the first 40 cm is shown. The Einzel lens is located at ~ 20 cm and focuses the beam.

Including the SC effects, the transverse beam size increases in AOC by the same amount as in Transport. However, in Transport we notice a longitudinal shift of the waist of ~ 50 mm just after the Einzel lens, whereas it is not more than 5 mm in AOC, see also Table 3.

Table 3: Distance from the source to the waist after the Einzel lens, calculated with transport and AOC, with and without the SC effects of a 15 mA beam.

Code	No SC	15 mA SC
Transport	300 mm	350 mm
AOC	285 mm	290 mm

The difference in results between the two programs comes from the fact that in Transport the beam is always assumed to be of a gaussian distribution. In AOC however, each particle is tracked individually and the dense distribution in the waist changes the transverse distribution: even though the beam starts gaussian at the source, the gaussian distribution is lost, as the halo is more populated.

Longitudinal Properties

In AOC, the particles extracted from the source come one by one. Thus, at the start of the calculations, there is only one particle, then two, etc. The first particle sees only particles behind it, and the last particle sees only others in front of it. Longitudinally, the SC effects thus create a debunching force, which is non-existent in a real DC beam.

To see this effect, we populate the beam in the simulation with 3 bunches, that is a uniform distribution of particles longitudinally, over a distance of 3× the $\beta\lambda$, which is equal to 37 mm. With the buncher set to its theoretical value of 563 V, to obtain the smallest bunches possible at the median plane, the distances between the bunches can be measured at the inflector: the results show that, with the SC effects of a 1 mA beam, the distance between bunches is ~ 36 mm, as expected from the $\beta\lambda$, but with the SC effects of a 5 mA beam the distance increases to 45 mm.

CONCLUSION

At IBA, the high intensity cyclotrons for the production of medical radioisotopes continue to evolve. The last two cyclotrons of the "previous" generation, the Cyclone® 70 and the Cyclone® 30XP, have been commissioned at the customer's sites. From the knowledge acquired with the Cyclone® KIUBE, a new 30 MeV proton cyclotron has been launched, the Cyclone® IKON. We presented the design of the new machine. It has been produced and isochronized in factory, and its installation is ongoing at the first customer's site.

With increasing requested beam intensities, as well as cyclotron compactness, the space charge effects in the beams become more and more relevant for the design and performances of high intensity cyclotrons. We have presented the start of a study on the space charge effects in the injection line of the Cyclone® IKON, using AOC. Benchmarking the results against those of Transport, some different results are observed. At the same time, a longitudinal defocussing effect is introduced in the particle-by-particle tracking in AOC, which is non-existent in a real DC bunch. Further studies will be needed to resolve this issue.

REFERENCES

[1] W. J. G. M. Kleeven *et al.*, "Recent development and progress of IBA cyclotrons", *Nucl. Instrum. Methods Phys. Res., Sect. B*, vol. 269, no. 24, pp. 2857-2862, Dec. 2011. doi:10.1016/j.nimb.2011.04.031

[2] J. Kim, "Construction of a 70 MeV proton cyclotron facility of IBS for multidisciplinary utilization", *J. Korean Phys. Soc.*, vol. 80, pp. 551-557, Jan. 2022. doi:10.1007/s40042-022-00415-z

[3] B. Nactergal *et al.*, "Development of the Cyclone® KIUBE: a compact, high performance and self-shielded cyclotron for radioisotope production", in *Proc. Cyclotrons'16*, Zurich, Switzerland, Sep. 2016, pp. 238-240. doi:10.18429/JACoW-Cyclotrons2016-TUD03

[4] S. Zaremba *et al.*, "Magnet design of the new IBA cyclotron for PET radio-isotope production", in *Proc. Cyclotrons'16*, Zurich, Switzerland, Sep. 2016, pp. 170-172. doi:10.18429/JACoW-Cyclotrons2016-TUP04

[5] D-Pace, https://d-pace.com/images/products/Ion%20Sources/ISV.F-040/spec/2120061_D%20-%20Filament-Powered%20Turnkey%20Negative%20Ion%20Source%20System.pdf

[6] Simulia Opera, https://www.3ds.com/products-services/simulia/products/opera/

[7] W. J. G. M. Kleeven *et al.*, "AOC, a beam dynamics design code for medical and industrial accelerators at IBA", in *Proc. IPAC'16*, Busan, Korea, May 2016, pp. 1902-1904. doi:10.18429/JACoW-IPAC2016-TUPOY002

[8] M. Abs, S. Zaremba, "Pole insert for cyclotron", European Patent EP3244707, May 13, 2016.

[9] F. J. Sacherer and T. R. Sherwood, "Space-charge modifications for transport", CERN, Geneva, Switzerland, Rep. CERN-MPS-SI/Note-LIN/71-7, May 1971.

[10] F. J. Sacherer, "RMS envelope equations with space charge", June 1971, *IEEE Trans. Nucl. Sci.*, vol. 18, no. 3, pp. 1105-1107. doi:10.1109/TNS.1971.4326293

[11] F. J. Sacherer and T. R. Sherwood, "The effect of space charge in beam transport lines", *IEEE Trans. Nucl. Sci.*, vol. 18, no. 3, pp. 1066-1067, June 1971. doi:10.1109/TNS.1971.4326279

ISBN: 978-3-95450-212-7 ISSN: 2673-5482 doi:10.18429/JACoW-CYCLOTRONS2022-MOBO02

IMPACT: A SUBSTANTIAL UPGRADE TO THE HIPA INFRASTRUCTURE AT PSI

D. Kiselev†, R. Eichler, M. Haj Tahar*, M. Hartmann[1], K. Kirch[2], A. Knecht, A. Koschik, D. Laube, N. P. van der Meulen, T. Rauber, D. Reggiani, R. Schibli, J. Snuverink, U. Wellenkamp, H. Zhang
Paul Scherrer Institut, 5232 Villigen PSI, Switzerland
[1]also at École Polytechnique Fédérale de Lausanne (EPFL), Lausanne, Switzerland
[2]also at ETH Zürich, Institute for Particle Physics and Astrophysics, 8093 Zürich, Switzerland

Abstract

The High Intensity Proton Accelerator (HIPA) complex at the Paul Scherrer Institute (PSI), Switzerland, delivers a 590 MeV CW (50.6 MHz) proton beam with currents up to 2.4 mA (1.4 MW) to several user facilities and experimental stations. In addition to the two spallation targets for thermal/cold neutrons (SINQ) and ultracold neutrons (UCN), the beam feeds two meson production targets, Target M and Target E, serving particle physics experiments and materials research via seven secondary beam lines.

IMPACT (Isotope and Muon Production with Advanced Cyclotron and Target technologies) aims to expand the infrastructure at HIPA in two ways: by HIMB (High-Intensity Muon Beams), increasing the surface muon rate by a factor 100, and TATTOOS (Targeted Alpha Tumour Therapy and Other Oncological Solutions), producing promising radionuclides for diagnosis and therapy of cancer in doses sufficient for clinical studies. HIMB and TATTOOS are located close to each other. HIMB has to fit into the existing main proton beam line towards Target E and SINQ, while TATTOOS will occupy an area in a new, adjacent building using 100 µA, 590 MeV protons split from the main beam. TATTOOS will be a perfect complement to the existing radionuclide production using 72 MeV, adding a smorgasbord of nuclides at a large scale for potential medical purposes. At HIMB, the current Target M will be replaced by a four-fold thicker Target H consisting of a graphite wheel optimized for surface muon production. In addition, both muon beam lines feature optimized transmission from target to experiment. Due to the thicker Target H, the proton beam line has to be tuned to reduce the losses to an acceptable level and to maximize the transmission at the same time.

Installation towards the implementation of IMPACT is foreseen from 2027.

MOTIVATION

At the High Intensity Proton Accelerator (HIPA) [1], protons are accelerated using two cyclotrons, namely, Injector II to 72 MeV followed by the Ring cyclotron to 590 MeV. Up to 2.4 mA current is possible and has been demonstrated in routine operation. The 72 MeV beam also feeds the Isotope Production target station (IP2). The beam from the Ring cyclotron serves four target stations, two spallation targets (UCN for ultracold neutrons and SINQ for cold and thermal neutrons) and two meson production targets called Target M and Target E [2]. Before the beam reaches SINQ, it passes through Target M and Target E, whereas the full beam is kicked to UCN every five minutes for a few seconds.

IMPACT will add a new target station (TATTOOS) adjacent to UCN, providing innovative and otherwise not accessible radionuclides for research in nuclear medicine, and to replace the Target M station (built in 1985) with a new Target H(IMB) to increase the surface muon rate to 10^{10} µ/s. Figure 1 shows the close location of HIMB in the so-called experimental hall and TATTOOS in a new building.

The IMPACT collaboration at PSI consists of more than 100 people in 35 working groups. At the beginning of 2022, the Conceptual Design Report (CDR) [3] was submitted to support the project proposal for the Swiss Roadmap for Research Infrastructure, a joint application of PSI, University of Zurich (UZH) and University hospital Zurich (USZ). IMPACT was well received and reviewers gave the highest scientific evaluation in 2022.

In this paper, the purpose and concepts for HIMB and TATTOOS are described with focus on beam transport.

HIMB

The present Target M station consists of an effective 5 mm thick graphite target-wheel with two beam lines called PiM1 and PiM3 for secondary particles, both aligned in a forward direction. As a consequence, these beam lines are optimized for particles of higher momentum, originally pions of momenta larger than 100 MeV/c. The beam lines are used for different purposes: PiM1 for particle physics and PiM3 for material physics. While PiM3 already uses surface muons exclusively with the µSR technique, particle physics experiments aim for large rates of surface muons as well. A two orders of magnitude larger surface muon rate will boost the attractiveness for users as well as the competiveness of future experiments, both in the hunt for forbidden muon decay channels as stress test of the standard model and for the investigation of magnetic properties deeper below the surface.

To optimize the future target station H and its two beam lines for surface muons, the new concept comprises several improvements: Two large capture solenoids, one at each side of the target, with inner diameters of up to 500 mm are placed in a close distance of 250 mm to the interception of beam and target, perpendicular to the proton beam to guide a large fraction of the muons from the target to the second-

† Daniela.Kiselev@psi.ch
* now at Transmutex, Geneva, Switzerland

ISBN: 978-3-95450-212-7 ISSN: 2673-5482 doi:10.18429/JACoW-CYCLOTRONS2022-MOBO02

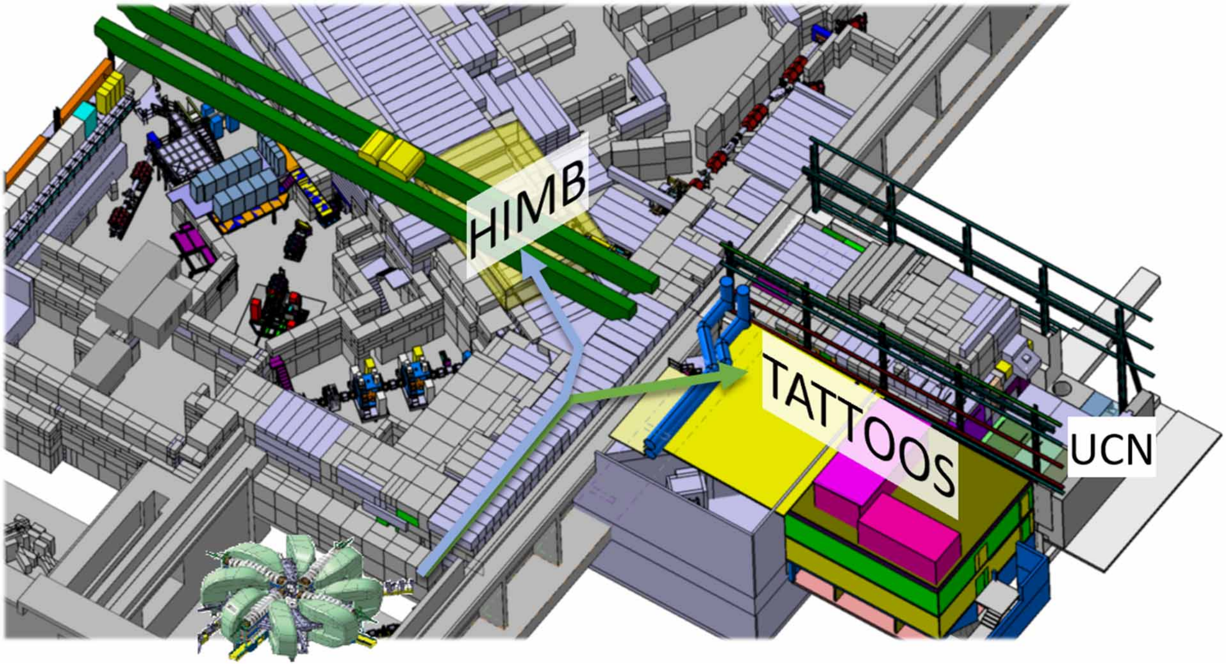

Figure 1: This CAD model shows the location of the target station H(IMB) under the yellow concrete bars with the secondary beam line MuH2 on the left. In close proximity, TATTOOS, adjacent to UCN, is located in a new building. Courtesy of M. Kalt, PSI.

ary beam lines (Fig. 2). The solenoidal beam lines are optimized for large transmission of surface muons. More information about the beam line design for the new MuH2 and MuH3 experimental areas can be found in [4]. For the capture solenoid a graded-field design is favoured with approximately 0.45 T in its centre. The graphite target itself is optimized for the production of surface muons by using a so-called slanted target design. The proton beam passes through the target rim of the rotating wheel at a small angle. The target rim is extended in the beam direction, significantly increasing the muon production surface. This type of target was already successfully tested in the target E station, increasing surface muon rates by up to 50% [5]. In addition, the effective target H thickness is increased from 5 to 20 mm compared to target M, leading to larger beam spread and, consequently, thicker shielding. It also requires a new collimator system and careful beam transport studies up to the SINQ target to match the beam profile for safe operation. Further, the fringing field at the target, due to the capture solenoids, has to be taken into account and corrected for.

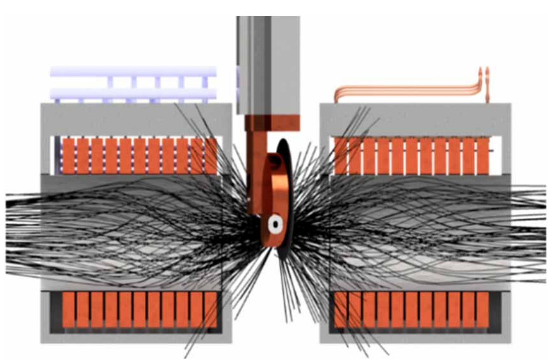

Figure 2: On both sides of Target H the capture magnets with particle trajectories from simulation are shown.

The complete beam line from the Ring cyclotron to the SINQ target was modelled by building Geometry Description Markup Language (GDML) files [6] and partly importing CAD models for important components, such as collimators and targets. Before the beam optics for the new Target H was optimized for small losses, the simulation software BDSIM [7] was benchmarked against the current optics using various techniques [8]. For example, very good agreement was obtained between the simulated losses on the collimators and the measured temperature increase of the cooling water. It was recognized that the losses do not scale linearly with the current. This was traced back to the dependence of the beam size with current, which was finally determined and confirmed by measurements with a profile monitor located just after the Ring cyclotron. Using this beam size–current dependence, the beam envelope obtained by BDSIM with the current 5-mm Target M could be well matched to the beam profile measurements from the Ring to the SINQ target.

For the proposed 20 mm Target H, a collimator system was designed, minimizing losses and maximizing transmission up to the SINQ target. The quadrupoles after Target H had to be tuned to larger focussing to accommodate the larger beam spread. The simulations with BDSIM revealed that the energy spread after Target E is twice as large with the 20-mm Target H compared to the 5-mm Target M. Therefore the losses in the AHL dipole, which bends the beam down on its way to SINQ, are higher compared to the present situation. With the optimized optics a transmission of 67 % can be kept compared to the current 70 %. Replacing the present collimator system KHE2/3 after Target E

ISBN: 978-3-95450-212-7 ISSN: 2673-5482 doi:10.18429/JACoW-CYCLOTRONS2022-MOBO02

with an existing new design for 3 mA beam [2], the transmission could be increased back to 70 % while keeping the required beam profile for SINQ.

TATTOOS

Several radionuclides are already produced at PSI for research towards cancer therapy and diagnostics, using the 72 MeV proton beam at the IP2 station [9] or thermal neutrons at the irradiation station close to the SINQ target [10]. Particularly interesting are the radioisotopes belonging to the same element, which can be used for therapy as well as diagnostics (theragnostics). This approach allows better and personalized therapy planning for cancer. Promising radioisotopes in this regard are those of terbium, with ^{155}Tb and ^{161}Tb, already produced at IP2 and SINQ, respectively. The aim of TATTOOS is to extend the list of radionuclides for theragnostics to the region of neutron-deficient isotopes such as ^{152}Tb and ^{149}Tb, the latter a promising agent for α-particle therapy [11]. In Phase 1, TATTOOS will focus its production on these nuclides using a tantalum (Ta) target; later, targets containing uranium or thorium are planned.

For the efficient production of sufficient quantities at PSI a 100 µA proton beam at 590 MeV on target, containing effectively 10 cm Ta, is proposed. This beam has to be split from the main beam. Due to space limitations, the first part of the UCN beam line will also be used for TATTOOS. Therefore, TATTOOS cannot be operated whenever a beam pulse is being delivered to UCN. This quasi-parallel operation mode results in 15 % loss of beam time, which is anticipated as acceptable. To switch from TATTOOS to UCN operation the splitter needs to be retracted from the beam, while a dipole magnet changes its polarity to bend the beam from the TATTOOS to the UCN branch of the beam line.

The splitter, already installed in the late 1990s for proton therapy, was developed and tested for 20 µA [12]. It consists of 175 stripes, 2 mm wide with a thickness of 50 µm. A high voltage is applied at two cathodes to achieve a deflection of 6 mrad. The current of the colliding protons is measured on the first three stripes and restricted to 1 µA for safe operation. This limit was deduced from comparison of simulation and operation of the splitter used for 72 MeV beam. To split a large fraction of the beam and, at the same time, respect the current limit, the beam optics was broadened in the horizontal direction in a recent beam study under the condition that beam operation up to SINQ as well as UCN kicks were still feasible. Since the TATTOOS beam line does not yet exist, as part of a demonstration, 80 µA of the beam could be successfully split with these optics onto the UCN target. However, the beam losses after the splitter were increased with respect to the operation without splitter, which was expected. Further studies and measures to reduce losses are needed as this part of the beam line is maintained hands-on.

To better distribute the heat on the target more uniformly, the beam will be wobbled in two dimensions. Further, the beam profile will be broadened to about 60 mm diameter for an optimal distribution on the target. The produced isotopes diffusing out of the hot target are preselected by Resonance Ionization Laser Ion Source (RILIS) [13, 14]. Another selection occurs on the way from the target to the three shielded cells by mass separation (ISOL technique). Finally, the desired nuclide is chemically purified and isolated from potential isobars in the shielded cells. The radionuclides shall be used for preclinical as well as clinical studies. The radiopharmaceutical manufacture needed for clinical applications are done in GMP (Good Manufacturing Practice) laboratories.

The free space between the experimental hall, where the Ring cyclotron, the two meson production targets and later Target H are located (Fig. 1), and the UCN office/laboratory building is only 14 m by 16 m. This is quite small for the shielded target station, the three shielded cells for chemistry separation, an extra one for target exchange, the access lock for personnel and material, as required for an area handling α-emitting nuclides as well as the needed infrastructure for operation. Therefore the UCN office/laboratory building will be rebuilt and extended to the experimental hall. Part of the space of the former office building will be used by TATTOOS in addition. However, it requires the relocation and rebuilding of infrastructure to free the space for the new building.

SCHEDULE

The installation of HIMB is planned for 2027, with first beam after the regular winter-spring shutdown of HIPA in 2028. Since Target Station M of the main beam line to SINQ has to be removed and rebuilt, there will be no operation of HIPA in 2027. In the same year, the building for TATTOOS will be constructed and finished in 2028, such that the TATTOOS facility can be installed in 2029 with first beam after the regular HIPA shutdown in 2030. This schedule avoids the installation of two target facilities in parallel, with the advantage that more PSI resources and more storage space are available at a given time. In addition, the building construction will not be particularly constrained by the operation of HIPA and UCN. A lot of preparation work will be carried out before the start of the installations in 2027.

CONCLUSION

IMPACT covers a broad field of applications, particle and solid state physics as well as life sciences. Realization of the two target stations for HIMB and TATTOOS is planned from 2027, for completion in 2030. The conceptual design presented in the CDR was refined in 2022. The feasibility to operate a four-fold thicker target at the location of the target M station was shown, a prerequisite for the realization of HIMB. Further, good progress was made in simulation as well as beam studies to demonstrate that the fraction of the beam, almost the full current proposed for TATTOOS, could be peeled off from the main beam using the existing splitter.

ISBN: 978-3-95450-212-7 ISSN: 2673-5482 doi:10.18429/JACoW-CYCLOTRONS2022-MOBO02

ACKNOWLEDGEMENT

The authors thank all who are contributing to or supporting IMPACT. The great strides made would not have been possible without the ambition, dedication and expert knowledge of many people. For the support on the splitter operation, the authors thank Dietmar Goetz, his team and the Controls experts.

The authors are greatly appreciative for the financial and general support of the PSI directorate and the NUM, GFA, NES and BIO divisions, as well as the strong support from the service groups in the LOG division.

REFERENCES

[1] J. Grillenberger, C. Baumgarten, and M. Seidel "The High Intensity Proton Accelerator Facility", *SciPost Phys. Proc.*, vol. 5, p. 002, 2021. doi:10.21468/SciPostPhysProc.5.002

[2] D. Kiselev *et al.* "The Meson Production Targets in the high energy beamline of HIPA at PSI", *SciPost Phys. Proc.*, vol. 5, p. 003, 2021. doi:10.21468/SciPostPhysProc.5.003.

[3] R. Eichler, D. Kiselev, A. Knecht, A. Koschik, N. van der Meulen, R. Scheibl, *et al.* (Editors), "IMPACT: Conceptual Design Report", Jan. 2022, https://www.dora.lib4ri.ch/psi/islandora/object/psi:41209

[4] G. Dal Maso *et al.*, "Future facilities at PSI, the High-Intensity Muon Beams (HIMB) project" in *Proc. 8th Int. Symp. on Symmetries in Subatomic Phys. (SSP'22)*, Vienna, Austria, Aug.-Sept. 2022, to be published.

[5] D. Kiselev *et al.*, "Progress and challenges of the PSI meson targets and relevant systems", in *Proc. 3rd J-PARC Symp. (J-PARC'19)*, *JPS Conf. Proc.,* vol. 33, p. 011102, 2021. doi:10.7566/JPSCP.33.011102

[6] GDML description website, 2022, https://gdml.web.cern.ch/GDML/.

[7] L. Nevay *et al.*, "BDSIM: An accelerator tracking code with particle–matter interactions", *Comput. Phys. Commun.*. vol. 252, p. 107200, 2020. doi:10.1016/j.cpc.2020.107200

[8] M. Haj Tahar, D. Kiselev, A. Knecht, D. Laube, D. Reggiani, and J. Snuverink, "Probing the losses for a high power beam", *Nucl. Instrum. Methods Phys. Res. Sect. A*, vol. 1046, p. 167638, 2023. doi:10.1016/j.nima.2022.167638

[9] N. P. van der Meulen *et al.*, "The use of PSI's IP2 beam line towards exotic radionuclide development and its application towards proof-of-principle preclinical and clinical studies", in *Proc. Cyclotrons2019*, Cape Town South Africa, Sep. 2019, pp. 132-135. doi:10.18429/JACoW-Cyclotrons2019-TUA03

[10] N. Gracheva *et al.*, "Production and characterization of no-carrier-added ^{161}Tb as an alternative to the clinically-applied ^{177}Lu for radionuclide therapy", *EJNMMI Radiopharm. Chem.*, vol. 4, article 12, 2019. doi:10.1186/s41181-019-0063-6

[11] C. Umbricht *et al*., "Alpha-PET for Prostate Cancer: Pre-clinical investigation of ^{149}Tb-PSMA-617", *Sci. Rep.,* vol. 9, p. 17800, 2019. doi:10.1038/s41598-019-54150-w.

[12] M. Olivo, E. Mariani, and D. Rossetti, "An electrostatic beam splitter for the PSI 590 MeV - 1MW proton beam line", in *Proc. 6th European Particle Accelerator Conf. (EPAC'98)*, Stockholm, Sweden, Jun. 1998, pp. 2129-2131.

[13] R. Li, M. Mostamand, J. Romans, B. B. Reich, and J. Lassen, "Recent RILIS developments at the TRIUMF offline laser ion source test stand", *Hyperfine Interact.,* vol. 241, p. 22, 2020. doi:10.1007/s10751-020-1694-4

[14] S. Rothe *at al.*, Laser ion beam production at CERN-ISOLDE: new features – more possibilities", *Nucl. Instrum. Methods Phys. Res. Sect. B,* vol. 376, pp. 91–96, 2016. doi:10.1016/j.nimb.2016.02.024

ISBN: 978-3-95450-212-7 ISSN: 2673-5482 doi:10.18429/JACoW-CYCLOTRONS2022-MOBO03

PROTON IRRADIATION SITE FOR HIGH-UNIFORMITY RADIATION HARDNESS TESTS OF SILICON DETECTORS AT THE BONN ISOCHRONOUS CYCLOTRON

D. Sauerland*, R. Beck, P. D. Eversheim
Helmholtz-Institut f. Strahlen- u. Kernphysik, Bonn, Germany
J. Dingfelder, P. Wolf, Silizium Labor Bonn, Physikalisches Institut, Bonn, Germany

Abstract

The Bonn Isochronous Cyclotron provides proton, deuteron, alpha particle and other light ion beams, having a charge-to-mass ratio $Q/A \geq 1/2$, with kinetic energies in the range of 7 to 14 MeV per nucleon.

At the irradiation site, a 14 MeV proton beam with a diameter of a few mm is used to irradiate detectors, so-called devices under test (DUTs), housed in a thermally-insulated and gas-cooled box. To ensure homogeneous damage application, the DUT is moved through the beam in a row-wise scan pattern with constant velocity and a row separation, smaller than the beam diameter. During irradiation, beam parameters are continuously measured non-destructively using a calibrated, secondary electron emission-based beam monitor, installed at the exit to the site. This allows a beam-driven irradiation scheme, enabling the setup to autonomously react to changing beam conditions, resulting in highly-uniform proton fluence distributions with relative uncertainties of typically 2%.

In this work, the accelerator facility is introduced, the proton irradiation site with focus on its beam diagnostics is presented in detail and resulting fluence distributions are shown.

BONN ISOCHRONOUS CYCLOTRON

The accelerator facility of the Bonn Isochronous Cyclotron is shown in Fig. 1. Here, proton, deuteron, alpha and other light ion beams with kinetic energies of 7 to 14 MeV/A and currents of $\lesssim 1\,\mu$A, are provided to five experimental sites.

The ion beam is generated by two external electron cyclotron resonance sources: One source (two-stage, 5 GHz) located beside, the other (single-stage, 2.5 GHz, polarized beam) situated underneath the cyclotron. Here, the generated beam with a kinetic energy of 2 to 8 keV is guided through a low-energy beamline below the cyclotron and then is injected vertically into its magnetic center using an electrostatic hyperboloid inflector.

The Bonn Isochronous Cyclotron [1] is an isochronous, three-sector, azimuthally varying field cyclotron. Its main parameters are shown in Table 1. The cyclotron shows a 120°-symmetry in its azimuthal magnetic field pattern due to its magnet yoke being separated into three hill-and-valley sectors with 0° spiral angle. In each valley, a broadband

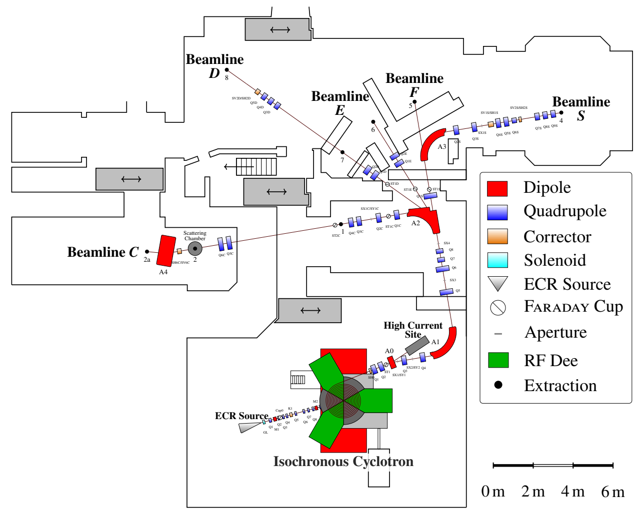

Figure 1: Overview of the accelerator facility.

Table 1: Parameters of the Bonn Isochronous Cyclotron

available ions	p, d, α, …, $^{16}O^{6+}$
energy ($h = 3$, $Q/A \geq \frac{1}{2}$)	7 to 14 MeV/A
beam current (ext.)	$\lesssim 1\,\mu$A
injection / extraction radius	38 mm / 910 mm
number of revolutions	approx. 120
hill sectors	3 × 40°, 0° spiral angle
hill / valley field strength	1.9 / 0.7 T (max.)
flutter factor	0.62
dees	3 × 40°, 40 kV (max.)
cyclotron harmonic h	3, 9
RF frequency ν_{RF}	20.1 to 28.5 MHz
hor. / vert. emittance	16 / 22 mm mrad
relative energy spread	4×10^{-3}

dual-gap dee is located, providing an acceleration voltage of up to 40 kV.

Due to its symmetry, the cyclotron typically operates at the third cyclotron harmonic $h = 3$, where the RF frequency ν_{RF} equals three times the ions' cyclotron frequency ν_0, but also an operation at $h = 9$ is possible for heavier ions with $Q/A \leq 1/3$. The RF frequency range of 20.1 to 28.5 MHz and the maximum average magnetic flux density $\langle B \rangle_{max}$ of approx. 1.4 T define the cyclotron's mass-to-charge acceptance, as shown in Fig. 2.

* sauerland@hiskp.uni-bonn.de

ISBN: 978-3-95450-212-7 ISSN: 2673-5482 doi:10.18429/JACoW-CYCLOTRONS2022-MOB003

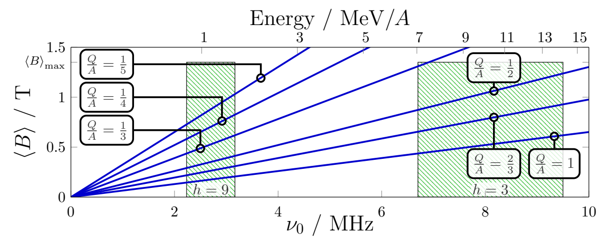

Figure 2: Parameter space of possible cyclotron operation (green) with average magnetic flux density $\langle B \rangle$ and ν_0.

After approx. 120 revolutions, the beam is extracted to a field-compensated channel in a single-turn extraction, using an electrostatic septum. The extracted beam can either be guided to the high current site, used to produce induced radioactivity in target material, or it is transported to the experimental sites via the high-energy beamline, featuring a versatile double mono or achromator system [2].

IRRADIATION SITE

In the *C* beamline, at extraction 2a (comp. Fig. 1), a new site for proton irradiation of silicon (pixel) detectors has been installed [3], enabling the application of highly-uniform damage profiles. The site is shown in Fig. 3. A calibrated beam monitor is used for non-destructive, continuous beam diagnostics, which is situated directly upstream of the beam exit window. The experimental setup is positioned on an optical breadboard in front of the window, mounted on a rail system with a supporting structure made of aluminum profiles. The rail system allows to retract the setup along the beam axis, enabling the positioning of a Faraday cup (FC) for e.g. beam monitor calibration (see Fig. 3, top right) in front of the exit window, using a vertical linear stage. A *Chromox* scintillation screen, installed on top of the FC enables visual beam diagnostic. The site is complemented by a 19″ rack for installation of the readout electronics as well as other devices and provides external interfaces to the irradiation site.

Beam Monitor

The custom-made beam monitor, comprising a secondary electron monitor (SEM) module and a beam loss monitor (BLM) module, is shown in Fig. 4.

In the SEM module, the surface emission of low-energy secondary electrons (SE), upon impact of fast ions into matter, is used to measure the beam current and relative position. Here, the beam propagates through two 5 µm-thick, carbon-coated[1] Al foil pairs, which are segmented vertically (SEM R & L) and horizontally (SEM U & D). Removing emitted SE from the electrically-isolated SEM-foils, results in a current signal proportional to the incident ion beam current and kinetic energy. Therefore, pull electrodes are located in close proximity to each SEM-foil's surface, consisting of

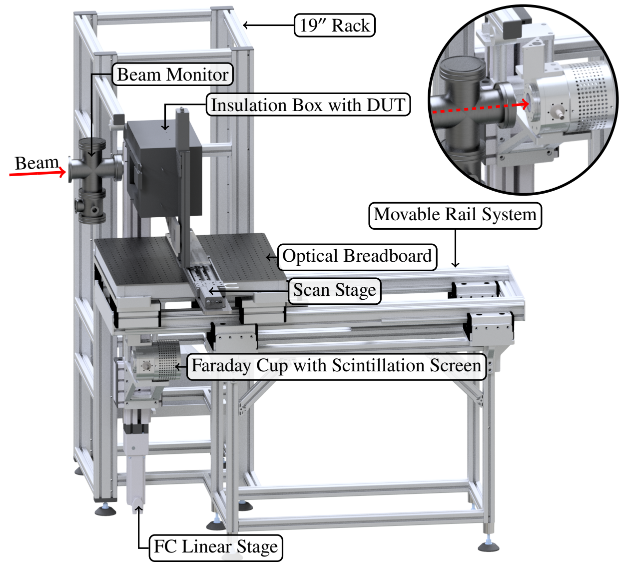

Figure 3: CAD render of the irradiation site. In the top right, beam monitor and Faraday cup are aligned for calibration.

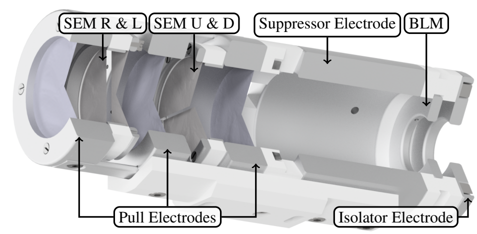

Figure 4: CAD render of a sectional view of the beam monitor with SEM (left) and BLM module (right).

three 5 µm-thick Al foils, biased with +100 V. After calibrating the SE to the ion beam current using the FC, the sum of all foil signals allows online measurement of the beam current whereas the foil-segmentation enables to determine the relative beam position.

The BLM module consist of a 3 mm-thick Al iris with a 20 mm diameter, mimicking the dimensions of the exit window, as well as two suppressor electrodes positioned in front of and behind the iris. Upon ion impact on the BLM iris, a current is flowing, indicating beam-truncation at the exit window. To prevent charge-loss due to SE emission, the suppressor electrodes are biased with −100 V.

Using the information provided by the BLM as well as the calibrated SEM, the beam monitor enables to determine the beam current which is extracted to the irradiation site. The beam monitor is designed utilizing the `Electrostatic` and `Particle in Cell (PIC) Solver` of `CST Studio Suite` to maximize the SE collection from the SEM-foils. A scenario with a 13.6 MeV proton beam is shown in Fig. 5. Here, SE trajectories are simulated, based on the potential of the electrodes and the SE-generated space charge. The SE yield (SEY) due to proton impact is calculated on basis of measurements of [4]. According to [5], the downstream SEY is approx. twice as large as upstream, for high-energy protons. The SE emission energy probability density func-

[1] To anticipate surface carbonization in vacuum with time, ≈ 70 nm layer thickness

23rd Int. Conf. Cyclotrons Appl. CYCLOTRONS2022, Beijing, China JACoW Publishing
ISBN: 978-3-95450-212-7 ISSN: 2673-5482 doi:10.18429/JACoW-CYCLOTRONS2022-MOB003

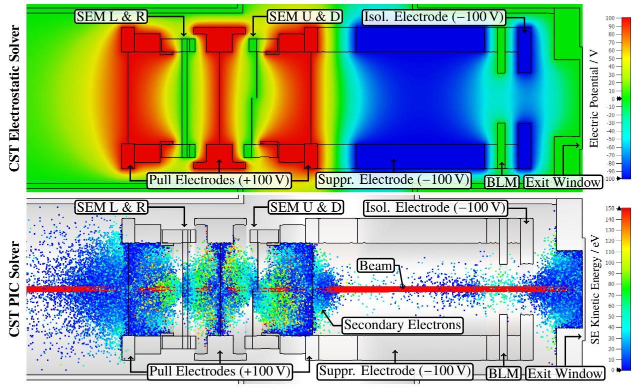

Figure 5: CST simulations: Electric potential of the beam monitor (top). Spatial distribution of SE for a proton beam current of 1 µA in its equilibrium state (bottom).

tion is a gamma distribution with an estimated mean energy of 15 eV, based on measurements of [6]. For this scenario, the resulting SE collection efficiency for both SEM-foils is (99.11 ± 0.19) % (upstream) and (99.77 ± 0.04) % (downstream).

Faraday Cup

The in-house developed Faraday cup, used for calibration of the beam monitor, is shown in Fig. 6.

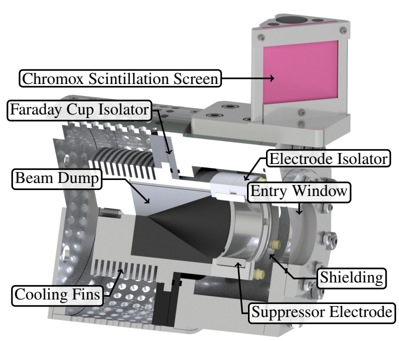

Figure 6: CAD render of a sectional view of the Faraday cup.

When positioned in front of the exit window, the beam enters the FC's vacuum system through a 30 µm thick AlMg3 entry window and impinges on the graphite beam dump after passing through a cylindrical suppressor electrode ring. The beam dump has an inverted cone-shape, preventing the majority of SE to escape, as their emission angle in reference to the surface normal is a cosine probability distribution with its maximum at an angle parallel to surface normal. For SE with unfavorable emission angles, the suppressor electrodes potential barrier, biased with typ. −100 V, repels them back into the cup (see Fig. 7 (left)).

The Faraday cup's inner geometry is designed to prevent an escape of the majority of emitted SE out of the cup also using CST. With identical SEY and SE emission energy probability density function as in the beam monitor simulations, the SE distribution in its equilibrium state is shown in Fig. 7

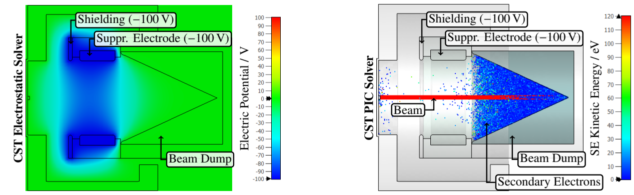

Figure 7: CST simulations: Electric potential of the Faraday cup (left). Spatial distribution of SE for a proton beam current of 1 µA in its equilibrium state (right).

(right) for an impinging 13.6 MeV proton beam with a current of 1 µA. In this scenario, the relative SE escape ratio of the FC is 7.6×10^{-5}.

Calibration

In the top-right of Fig. 3, the configuration of the site for beam monitor calibration is depicted. The beam traverses the beam monitor and is subsequently extracted into the FC. The sum of the SEM module foil currents I_Σ is calibrated against the beam current I_{beam} measured in the FC. The calibration factor is defined as $\lambda = \beta / 5\,\text{V}$ with $\beta = I_{\text{beam}} / I_\Sigma$ and can be obtained by varying the incident beam current as shown in Fig. 8. This allows to determine the beam current I_{beam} online, as a function of the SEM module signals and data acquisition parameters. λ is proportional to the SEY for 100 % SE collection efficiency in the beam monitor and thus depends on the ion species, used for the irradiation, and its kinetic energy.

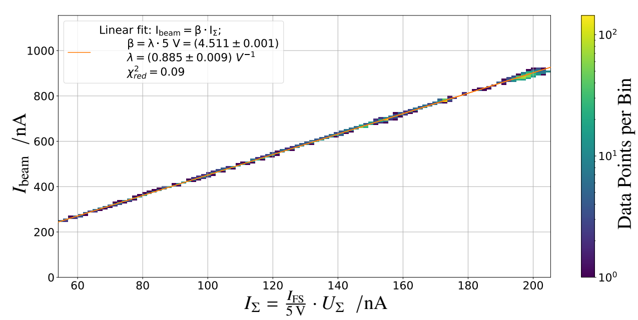

Figure 8: Calibration of the beam monitor using the FC.

DUT IRRADIATION

A 14 MeV proton beam is used to irradiate DUTs, housed in a thermally-insulated cooling box (comp. Fig. 3). The box fits DUTs with a maximum size of $19 \times 11\,\text{cm}^2$ and is attached to a scan stage, which has a range of 30 cm × 30 cm. Typically, DUTs are mounted behind a customized, 6 mm-thick Al shielding, exposing only the DUT to the beam. A scintillation screen on the shielding allows for an optical, beam-based alignment of the setup. To prevent annealing during irradiation, a temperature of < −20 °C is maintained at the DUT by guiding cool nitrogen gas onto the irradiated area. To ensure uniform irradiation profiles, the scan stage is used to move the DUT on a row-based grid through the beam (see Fig. 9).

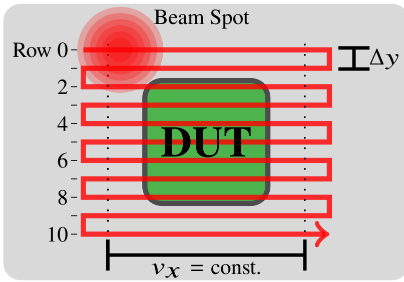

Figure 9: Relative movement of the beam along the scan pattern over the DUT (green) and the shielding (gray).

DAQ and Control

A custom-made analog readout board is used to convert the current signals from the beam monitor and the FC to voltages according to $U_{\mathrm{out}} = 5\,\mathrm{V}/I_{\mathrm{FS}} \cdot I_{\mathrm{in}}$. To resolve different magnitudes of currents, the board features several gain settings, corresponding to full-scale currents I_{FS} between 50 nA to 100 µA. In addition to the conversion, the ±5 V-normalized analog sum of the SEM foil signals U_{Σ} is generated, serving as the calibration signal.

Typically, one or more *Raspberry Pi* single-board computers are used as servers to interface the setup and collect irradiation-relevant data. Through these servers, the *Python* package `irrad_control` [7] provides full setup control, data acquisition and analysis. The software features online data visualization and interpretation with graphical user interface, allowing a beam-driven irradiation procedure as well as post-irradiation corrections, resulting in highly-uniform damage distributions.

Beam-Driven Irradiation Procedure

To ensure a uniform particle fluence distribution, an area larger than the DUT is defined and divided into a row-based grid (see Fig. 9). In this scan pattern, the DUT is repeatedly moved along the rows through the beam, with the turning points located off the DUT on an Al shielding. A constant scan velocity v_x and a row separation Δy smaller than the beam diameter allow to unfold the beam's transversal charge distribution homogeneously onto the DUT area. Online measurement of the beam parameters enables a beam-driven procedure: beam characteristics (e.g. current, position and stability) are probed against predefined requirements at the turning points, before scanning a row. Consequently, the scan parameters are adapted or the procedure is paused off DUT until conditions suffice. This autonomous procedure results in highly-uniform fluence distributions.

Fluence Distribution and Error Estimation

Extensive data acquisition of the setup components during irradiation enables to generate particle fluence distributions across the scan area. A typical fluence distribution is shown in Fig. 10. In the central region, containing the DUT, the fluence is applied homogeneously. In contrast, the turning point regions, located at the opposite ends of the area, are exposed to a higher fluence due to the turning itself as well as irradiation pauses, initiated by the beam-driven irradiation procedure. The variance of the proton fluence within the homogeneous region is insignificant with respect to its relative uncertainty of typically 2%. It is composed of the individual error on the beam monitor calibration and the readout board accuracy.

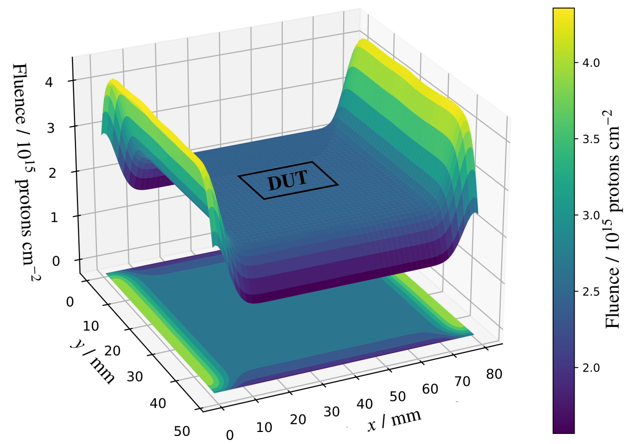

Figure 10: Typical fluence distribution on the scan area for a DUT aim fluence of $2.5 \cdot 10^{15}$ protons cm^{-2}.

REFERENCES

[1] "The AEG isochronous cyclotron at the University of Bonn", *IEEE Trans. Nucl. Sci.*, vol. 13, no. 4, pp. 435–436, 1966. doi:10.1109/TNS.1966.4324267

[2] F. Hinterberger *et al.*, "The beam handling system at the Bonn isochronous cyclotron", *Nucl. Instrum. Methods*, vol. 130, pp. 335–346, 1975. doi:10.1016/0029-554X(75)90033-6

[3] D. Sauerland *et al.*, "Proton irradiation site for Si-detectors at the Bonn Isochronous Cyclotron", in *Proc. IPAC'22*, Bangkok, Thailand, Jun. 2022, pp. 130–132. doi:10.18429/JACoW-IPAC2022-MOPOST030

[4] H. P. Beck and R. Langkau, "Die Sekundärelektronen-Ausbeute verschiedener Materialien bei Beschuß mit leichten Ionen hoher Energie", *Zeitung für Naturforschung A*, vol. 30, no. 8, pp. 981-985, 1975. doi:10.1515/zna-1975-0810

[5] E. F. Da Silveira and J. M. F. Jeronymo, "Secondary electron emission from the entrance and exit surfaces of thin aluminium foils under fast light ion bombardment", *Nucl. Instrum. Methods Phys. Res. Sect. B*, vol. 24-25, part 1, pp. 534–537, 1987. doi:10.1016/0168-583X(87)90702-6

[6] H. Rothard, K. O. Groeneveld, and J. Kemmler, "Kinetic Electron Emission from Ion Penetration of Thin Foils in Relation to the Pre-Equilibrium of Charge Distributions", *Particle Induced Electron Emission II*, Springer Verlag, 1992.

[7] P. Wolf, "irrad_control: Control, DAQ and Analysis Software for the Irradiation Site at the Bonn Cyclotron", https://github.com/Cyclotron-Bonn/irrad_control

ISBN: 978-3-95450-212-7 ISSN: 2673-5482 doi:10.18429/JACoW-CYCLOTRONS2022-MOBO04

EXPERIMENTAL STUDY ON PROTON IRRADIATION EFFECT OF GALLIUM NITRIDE HIGH ELECTRON MOBILITY TRANSISTOR

Zheng Zhang, Gang Guo*, Cuicui Liu, Qiming Chen
Department of Nuclear Physics, China Institute of Atomic Energy, Beijing 102413, China

Abstract

As a third-generation power semiconductor device, gallium nitride (GaN) high electron mobility transistor (HEMT) has a broad application prospects in the aerospace field. However, when a spacecraft is performing a flight mission, the GaN HEMT will inevitably be affected by the irradiation of high-energy charged particles from the space environment, most of which are protons. Therefore, it is of great significance to understand the effect of proton irradiation on GaN HEMT performance for its future development in the space field. In this paper, the proton radiation effect of GaN HEMT is studied by means of a medium energy proton irradiation platform. After proton irradiation, the threshold voltage of the GaN HEMT decreases, and the lower the incident proton energy, the more obvious the threshold decreases. The output characteristics curve, off-state leak current and gate forward leakage current of the GaN HEMT all increase after proton irradiation. After annealing at room temperature for 10 days, the electrical parameters of the GaN HEMT changed by proton irradiation are restored to the corresponding values before the proton irradiation. These changes indicate that medium energy proton irradiation with a fluence of 10^{12} p/cm^2 can improve the GaN HEMT performance, and the related reasons are discussed in detail.

INTRODUCTION

As an important third-generation semiconductor material, gallium nitride (GaN) has the advantages of high breakdown electric field, high electron saturation speed, high operating temperature and strong radiation resistance, and has broad application prospects in the aerospace field in the future [1, 2]. GaN HEMT is an important member of GaN-based electronic devices, and has super advantages in high frequency, high power, high temperature and high voltage applications. Therefore, GaN HEMT is widely considered to play an important role in spacecraft power supply and RF communication and other important fields in the future. However, GaN HEMT will inevitably be affected by the space radiation environment when the spacecraft performs relevant space flight missions [3–5]. Due to the wide band gap of GaN, GaN-based electronic devices should have an excellent radiation resistance in theory. Unfortunately, the radiation resistance of GaN HEMT is often affected by the preparation process and device structure, so the current radiation resistance of GaN HEMT still fails to reach the expected target.

* ggg@ciae.ac.cn

Due to proton accounts for more than 85% and 90% of galactic cosmic rays and solar cosmic rays [6], respectively, the research work related to proton radiation effect of GaN HEMT has been widely concerned. White et al. found that GaN HEMT performance did not change significantly when proton fluence is lower than 10^{14} p/cm^2, the degradation of GaN HEMT is enhanced by the proton fluence when the proton fluence was greater than 10^{15} p/cm^2 [7]. Kim et al. found that when the proton fluence is 10^{15} p/cm^2, the degradation caused by low-energy proton is more serious than that caused by high-energy proton [8], the off-state stress creates more irradiated defects in GaN HEMT, while annealing can remove the stress-generated defects [9]. Greenlee et al. found that proton irradiation broadened the heterojunction interface in GaN HEMT, and then decreased the carrier density and mobility simultaneously [10]. Zheng et al. first observed changes in defects at the AlGaN/GaN heterojunction interface in GaN HEMTs after proton irradiation [11]. CareyIV et al. found that increasing the Al concentration can effectively weaken the effect of proton irradiation on GaN HEMT performance [12].

Previous researches on proton radiation effects of GaN HEMT are based on proton irradiation experiments with energy less than 10 MeV, and all the studies show that proton irradiation degrades the device performance. At present, the research work related to the radiation effect of medium-energy proton on GaN HEMT is rarely reported. Therefore, the proton radiation effect of GaN HEMT has been studied systematically through the medium energy proton irradiation platform in this paper. Different from previous research results, our research show that the electrical performance of the GaN HEMT is improved after medium-energy proton irradiation with fluence of 10^{12} p/cm^2. The deep physical mechanism of improving GaN HEMT performance by medium-energy proton irradiation is discussed in detail in this work.

EXPERIMENTAL DETAILS

In this experiment, eight qualified enhanced GaN HEMTs from the same batch produced by China Xinguan Semiconductor Co., LTD were randomly selected, and the official model of the GaN HEMTs is XG65T125PS1B. The proton irradiation experiment of the GaN HEMT was carried out in the medium-energy proton irradiation platform of China institute of atomic energy (CIAE), as shown in Fig. 1. The proton beam induced by the 100 MeV high-current proton cyclotron (CYCIAE-100) passes through different energy drop plates, and the proton energy decreases to 30 MeV, 40 MeV, 60 MeV and 90 MeV, respectively. During irradi-

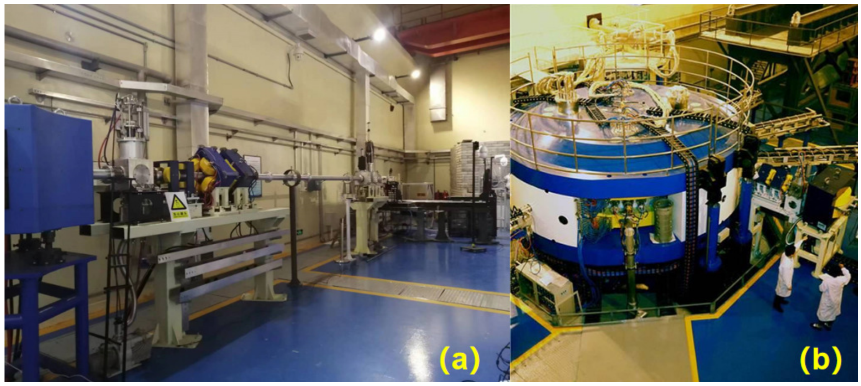

Figure 1: Schematic of the medium-energy proton irradiation platform (a) of the CYCIAE-100 high current proton cyclotron(b).

ation, the proton fluence rate was set to 10^8 p/cm^2 s, and the total fluence to the GaN HEMT was 10^{12} p/cm^2, all electrodes of the GaN HEMT were suspended. In order to ensure the accuracy of the experimental data, two devices A and B are used for the irradiation experiment of the same energy proton. The electrical parameters of GaN HEMT were measured at room temperature immediately after proton irradiation using the test system shown in Fig. 2. After annealing at room temperature for 10 days, the electrical parameters of the GaN HEMT were measured again by this system.

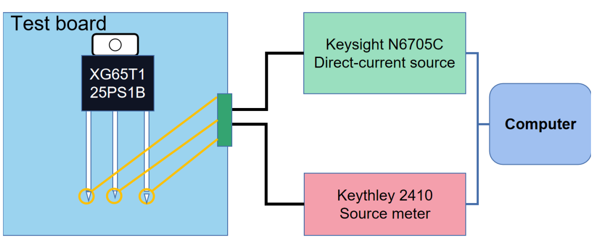

Figure 2: Electrical parameter test system of the GaN HEMT before and after proton irradiation.

RESULTS AND DISCUSSION

Gate-source threshold voltage is the turning on voltage of the enhanced GaN HEMT, the typical gate-source threshold voltage of the GaN HEMT according to the manual is 1.84 V. Figure 3 shows the change of gate-source threshold voltage of GaN HEMTs after proton irradiation with different energy, and the dash line in the figure represents the typical gate-source threshold voltage of the GaN HEMTs. In general, the threshold voltage of GaN HEMT decreases after proton irradiation. The higher the proton energy, the less the GaN HEMTs gate-source threshold voltage decreases. The experiments of Abbate et al. also showed that the gate-source threshold voltage of GaN HEMT decreased by 1 V after being irradiated with 3 MeV proton at an fluence of 4×10^{14} p/cm^2 [13]. The results of Kim et al. showed that the degradation of GaN HEMT electrical properties caused by low-energy proton irradiation was more serious than that caused by high-energy proton irradiation [9]. The results show that the electrical properties of GaN HEMTs used in this paper show the same degradation trend as that of the GaN HEMTs produced by foreign manufacturers after proton irradiation. Therefore, the research results of this work are reliable. In this experiment, the reduction of the gate-source threshold voltage is relatively lower compared with other experiments due to the use of high energy and low fluence of protons for irradiation.

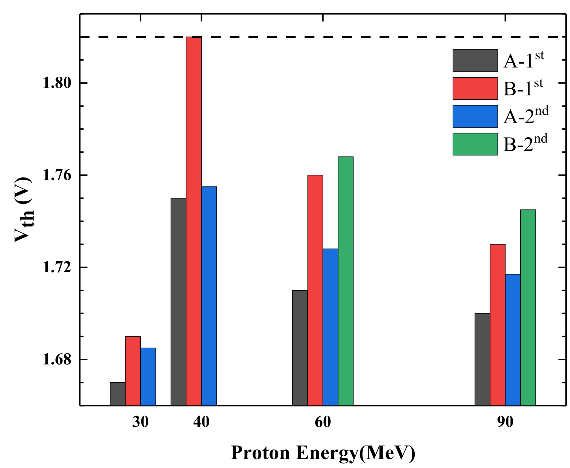

Figure 3: Gate-source threshold voltage of the GaN HEMT after proton irradiation with different energy.

At the same time, it is noted that the change trend of the gate-source threshold voltage caused by proton irradiation of 40 MeV is different from the results obtained after proton irradiation of other energies, this is because the 40 MeV proton irradiation experiment is carried out with other user experiments to save time. During the 40 MeV proton irradiation experiment, the GaN HEMTs are placed near the edge of the proton beam spot, and the total fluence of proton irradiation to the GaN HEMTs may be less than 10^{12} p/cm^2. Therefore, the gate-source threshold voltage reduction of the GaN HEMTs caused by proton irradiation with 40 MeV is lower than that caused by proton irradiation with other energy.

ISBN: 978-3-95450-212-7 ISSN: 2673-5482 doi:10.18429/JACoW-CYCLOTRONS2022-MOBO04

The gate-source threshold voltage of the GaN HEMT can be expressed by the following formula:

$$V_{th}(x) = \phi(x) - \Delta E_C(x) - \frac{qN_d d_d^2}{2\varepsilon(x)} - \frac{\sigma(x)}{\varepsilon(x)} \quad (1)$$

where, $\phi(x)$ is the height of the Schottky barrier, $\Delta E_C(x)$ is the conduction band discontinuity, $\sigma(x)$ is the polarization charge concentration, N_d, d and $\varepsilon(x)$ are the doping concentration, thickness and dielectric constant of AlGaN layer, respectively. Among these parameters, $\phi(x)$, N_d and $\sigma(x)$ are the main parameters affected by proton irradiation. The hole generated by ionization is captured by the vacancy defect generated by proton irradiation and becomes a fixed positive charge, and the electric field generated by it will enhance the discontinuity of the conduction band, increase the 2DEG carriers, and then make the gate-source threshold voltage drift negatively.

The output characteristic of the GaN HEMT is defined as a function of the current between the drain and source poles and their voltages when different voltages are applied to the gate. Figure 4 shows the output characteristic curve of GaN HEMTs before and after proton irradiation. Since the output characteristic curves of the GaN HEMTs in groups A and B are consistent, only the output characteristic curve of the GaN HEMTs in group A is shown here. As can be seen from the figure, the output characteristic curve of the GaN HEMTs increased after proton irradiation compared with that before irradiation, indicating that the saturation current of the GaN HEMTs increased. The larger the V_{GS}, the more obvious the increase of the GaN HEMT output characteristic curve after proton irradiation. The GaN HEMTs output characteristic curve recovered to the corresponding value before proton irradiation after 10 days annealing at room temperature, and the GaN HEMTs output curve after 40 MeV proton irradiation is the most close to the corresponding value before proton irradiation, because the proton fluence in 40 MeV proton experiment may be lower than 10^{12} p/cm^2.

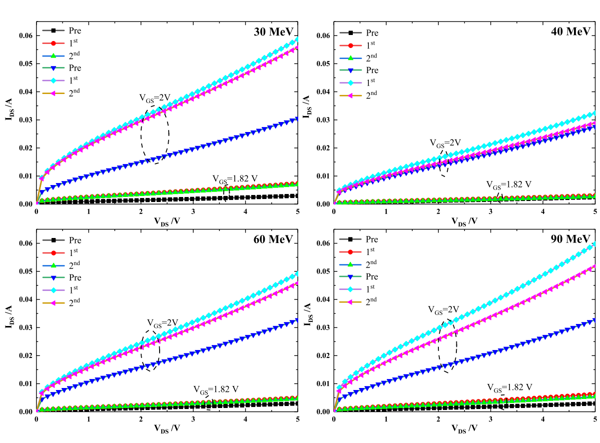

Figure 4: Output characteristic curves of the GaN HEMT before and after proton irradiation with different energy.

For GaN HEMT, the current expression at position x of the 2DEG channel is as follows:

$$I = qn_s(x)Wv(x) \quad (2)$$

$$v(x) = \begin{cases} \mu E, & E < E_C \\ v_s, & E \geq E_C \end{cases} \quad (3)$$

$$n_s = \frac{\varepsilon(n)}{qd}\left[V_{gs} - V_{th} - \frac{E_F}{q}\right] \quad (4)$$

where, $n_s(x)$ is the carrier concentration in 2DEG, W is the gate width, $v(x)$ is the carrier migration velocity at channel position x, μ is the carrier mobility, V_s is the saturation velocity of the carrier, d is the distance between the gates, V_{th} the the gate-source threshold voltage, ε is the dielectric constant of AlGaN, E_F is the Fermi level of the two-dimensional well, and n is the mole fraction of Al in AlGaN. Related studies have shown that displacement defects caused by proton irradiation will change the mobility of carriers. According to the above formula, the increase of carrier mobility will increase the output characteristics of the GaN HEMT. Due to irradiation defects, proton irradiation will reduce the gate-source threshold voltage of the GaN HEMT, increase the carrier concentration, and then increase the output characteristic.

Figure 5 shows the off-state leakage current of the GaN HEMTs before and after proton irradiation. It can be seen from the figure that after proton irradiation, the off-state leakage current of the GaN HEMTs has a significant increase compared with that before proton irradiation, especially when the V_{DS} is ≤250 V. The carriers concentration at the AlGaN/GaN interface in the GaN HEMTs after proton irradiation depends on the competition between carrier removal due to Ga vacancies and carrier increase due to the total ionizing dose effect. When the irradiated proton energy is low and the fluence is high, the displacement damage of the GaN HEMTs is dominant, and the carrier concentration in 2DEG decreases, which makes the off-state leakage current of the GaN HEMT decrease. When the proton energy is high and the fluence is low, the total ionizing dose effect is more significant, resulting in the increase of the off-state leakage current. The 40 MeV proton irradiation experiment shows that the off-state leakage current of the GaN HEMT decreases after proton irradiation, indicating that the proton fluence is less than 10^{12} p/cm^2 at this time.

Figure 6 shows the change of static forward gate current of the GaN HEMT when the gate voltage is equal to 20 V after proton irradiation with different energy, where the positive value represents the increase of static forward gate current and the negative value represents the decrease of static forward gate leakage current. The first test shows that proton irradiation increases the static forward gate current of the GaN HEMT, which is consistent with the change trend of the off-state leakage current. After annealing at room temperature for 10 days, the second test found that the static forward gate current of the GaN HEMT decreased and is smaller than that before proton irradiation. Wang et al. also observed similar changes in neutron irradiation experiments

ISBN: 978-3-95450-212-7 ISSN: 2673-5482 doi:10.18429/JACoW-CYCLOTRONS2022-MOB004

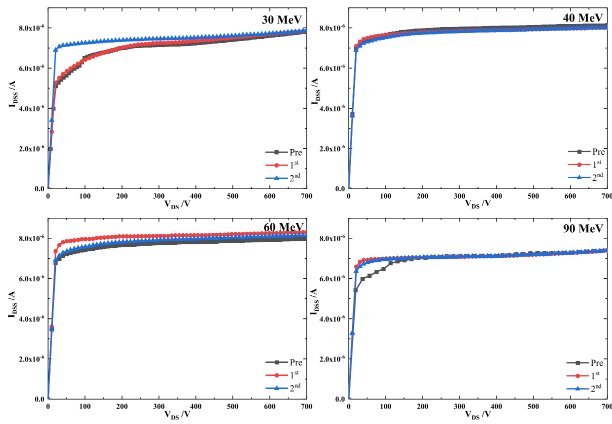

Figure 5: The off state leakage current of the GaN HEMT before and after proton irradiation.

on GaN HEMT [14], the static forward gate current of the GaN HEMT increased after neutron irradiation, and the static forward gate current of the GaN HEMT recovered to the same value as that before irradiation after 24 hours annealing at room temperature.

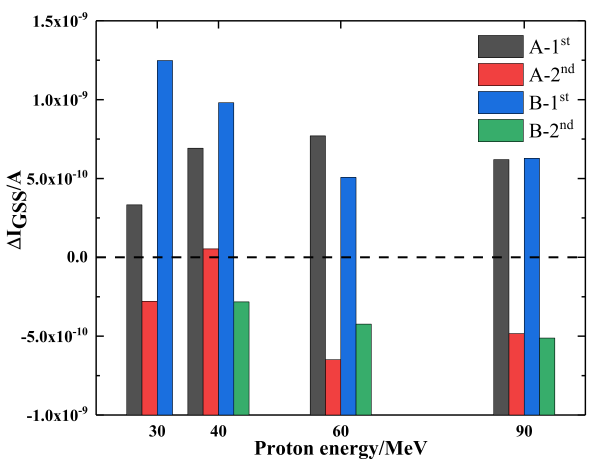

Figure 6: Static forward gate current of the GaN HEMT after proton irradiation with different energy.

The density of interface states at the Schottky junction in the gate decreased by proton irradiation, and the energy level of the Schottky contact interface defect expanded to the shallow energy level. Previous studies have found that the interface states density of AlGaN/GaN channel region increases slightly. The decrease of interface state density will lead to the decrease of the number of channels through which the auxiliary electron tunneling through the barrier, which will reduce the static forward gate leakage and improve the static forward gate leakage characteristics of the GaN HEMT. At the same time, proton irradiation will continuously shallower the interface energy level, which will theoretically lead to the increase of static forward gate leakage.

CONCLUSION

In this work, the proton radiation effect of GaN HEMT was studied in detail by medium-energy proton irradiation experiment. The experimental results show that the gate-source threshold voltage of the GaN HEMT decreases after proton irradiation, and the output characteristics, off-state leakage current and static forward gate current increase. After annealing at room temperature for 10 days, these electrical parameters of the GaN HEMTbecome close to their pre-irradiation values. On the whole, the electrical properties of the GaN HEMT are improved by proton irradiation under the experimental conditions in this paper. The reasons for the improvement of the electrical properties of the GaN HEMT by medium-energy proton irradiation were preliminarily discussed in this paper, but the involved physical mechanism needs to be further studied.

REFERENCES

[1] Y. Wu *et al.*, “Very high breakdown voltage and large transconductance realized on GaN heterojunction field effect transistors”, *Appl. Phys. Lett.*, vol. 69, no. 10, pp. 1438–1440, 1996. doi:10.1063/1.117607

[2] M. A. Khan *et al.*, “GaN based heterostructure for high power devices”, *Solid State Electron.*, vol. 41, no. 10, pp. 1555–1559, 1997. doi:10.1016/S0038-1101(97)00104-4

[3] Z. Lin *et al.*, “Effect of heavy ion irradiation on the interface traps of AlGaN/GaN high electron mobility transistors”, *Chin. Phys. B*, vol. 31, no. 3, p. 31, 2022. doi:10.1088/1674-1056/ac11e4

[4] S. J. Pearton, F. Ren, E. Patrick, M. E. Law, and A. Y. Polyakov, “Review–ionizing radiation damage effects on GaN devices”, *ECS J. Solid State Sci. Technol.*, vol. 5, no. 2, p. Q35, 2022. doi:10.1149/2.0251602jss

[5] H. Sasakia *et al.*, “Ultra-high voltage electron microscopy investigation of irradiation induced displacement defects on AlGaN/GaN HEMTs”, *Microelectron. Reliab.*, vol. 81, pp. 312–319, 2018. doi:10.1016/j.microrel.2017.10.005

[6] B. He, C. He, S. Shen, and M. Chenyuan, “Geant4 simulation of proton displacement damage in GaN”, *Atomic Energy Sci. Technol.*, vol. 51, no. 3, pp. 543–548, 2017. doi:10.7538/yzk.2017.51.03.0543

[7] B. White *et al.*, “Electrical, spectral, and chemical properties of 1.8 MeV proton irradiated AlGaN/GaN HEMT structures as a function of proton fluence”, *IEEE Trans. Nucl. Sci.*, vol. 50, no. 6, pp. 1934–1941, 2003. doi:10.1109/TNS.2003.821827

[8] H. Y. Kim, C. Lo, L. Liu, F. Ren, J. Kim, and S. Pearton, “Proton-irradiated InAlN/GaN high electron mobility transistors at 5, 10, and 15 MeV energies”, *Appl. Phys. Lett.*, vol. 100, no. 1, p. 012107, 2012. doi:10.1063/1.3673906

[9] B. J. Kim, S. Ahn, F. Ren, S. J. Pearton, G. Yang, and J. Kim, “Effects of proton irradiation and thermal annealing on off-state step-stressed AlGaN/GaN high electron mobility transistors”, *J. Vac. Sci. Technol. B*, vol. 34, no. 4, p. 041231, 2016. doi:10.1116/1.4959028

ISBN: 978-3-95450-212-7 ISSN: 2673-5482 doi:10.18429/JACoW-CYCLOTRONS2022-MOBO04

[10] J. D. Greenlee *et al.*, "Degradation mechanisms of 2 MeV proton irradiated AlGaN/GaN HEMTs", *Appl. Phys. Lett.*, vol. 107, no. 8, p. 083504, 2015. doi:0.1063/1.4929583

[11] X. Zheng *et al.*, "Characterization of bulk traps and interface states in AlGaN/GaN heterostructure under proton irradiation", *Appl. Phys. Lett.*, vol. 112, no. 23, p. 233504, 2018. doi:10.1063/1.5024645

[12] P. H. Carey, F. Ren, J. Bae, J. Kim, and S. J. Pearton, "Proton irradiation of high aluminum content AlGaN polarization doped field effect transistors", *ECS J. Solid State Sci. and Technol.*, vol. 9, no. 2, p. 025003, 2020. doi:10.1149/2162-8777/ab71f0

[13] C. Abbate *et al.*, "Developments on DC/DC converters for the LHC experiment upgrades", *J. Instrum.*, vol. 9, no. 2, p. C02017, 2014. doi:10.1088/1748-0221/9/02/C02017

[14] Y. Wang, Y. Luo, K. Zhang, and W. Yuanming, "Experimental study of neutron irradiation effects on GaN HEMT devices", *Research & Progress of SSE*, vol. 31, no. 6, pp. 540–544, 2011.

23rd Int. Conf. Cyclotrons Appl. CYCLOTRONS2022, Beijing, China JACoW Publishing
ISBN: 978-3-95450-212-7 ISSN: 2673-5482 doi:10.18429/JACoW-CYCLOTRONS2022-MOPO001

A REAL-TIME CONTROLLER FOR RAPID ENERGY DEGRADING OF THE CYCIAE-230 CYCLOTRON BEAM PRODUCTION SYSTEM*

Qiqi Song, Aolai He, Zhiguo Yin†, Tianyi Jiang, Hongru Cai, Bohan Zhao, Yang Wang, Qiankun Guo, Tianjue Zhang, China Institute of Atomic Energy, Beijing, China

Abstract

The energy selection system (ESS) plays an important role in a proton therapy system. Usually, it consists of an energy degrader, a set of achromatic bending magnets, an envelope collimator, and a momentum-selecting slit. In CIAE, a dedicated beam transportation line, including these essential elements, for the CYCIAE-230 superconducting cyclotron has been designed and manufactured for study purposes. To reduce the layer switching time, e.g. typically within 50 milliseconds, this ESS system takes advantage of VME-based real-time controller design. On one side, this controller uses S-curve to direct drive the step motors of various actuators, this is done by an off-the-shelf embedded controller. On the other hand, it uses Data Distribution Service (DDS) communication protocol to directly tap into the nozzle control system network. In such a manner, the energy requirement can be efficiently handled and the controller is also responsible for the current regulation for the 46 magnets. The design of this high-efficiency controller will be reported in this paper, both from hardware and software aspects. Preliminary test results will also be evaluated and analysed to direct further improvement of the system.

INTRODUCTION

The rate of human suffering from tumours has been increasing in recent years [1], and proton therapy is one of the effective means to treat tumours. "Bragg peaks" occur during the energy release of proton rays, and the excellent dose distribution of this Bragg peak drives the energy of the proton beam to be released concentrated at cancer cells, so the location of the proton beam energy release is directly related to the proton beam energy, and the proton beam energy is adjusted to achieve radiotherapy at different depths in the tissue to kill cancer cells [2, 3]. In cyclotron-based proton therapy facilities, the energy variation of the proton beam is carried out by controlling the thickness of the degrader [4]. Currently, well-established degrader materials use graphite, boron carbide [5], and beryllium [6]. The CYCIAE-230 is designed to achieve beam energy control mainly by controlling the graphite degrader of the double-wedge shape. The energy selection system (ESS) usually consists of an energy degrader, a set of achromatic bending magnets, an envelope collimator, and a momentum-selecting slit. In CIAE, a dedicated beam transportation line, including these essential elements, for the CYCIAE-230 superconducting cyclotron has been designed and manufactured for study purposes.

* Work supported by Zhiguo Yin
† zhiguoyin@ciae.ac.cn

OVERVIEW OF THE REAL-TIME CONTROL SYSTEM

The real-time control system (Fig. 1) is divided into a hardware part and a software part. The hardware part includes the VxWorks-based VME bus controller, while the software part is developed based on Qt and communicates between devices via the DDS middleware protocol. This real time controller is highly reliable and real time, and is able to quickly control the devices on the ESS section to adjust them to the appropriate values, it is capable of controlling the beam energy from 70 MeV to 240 MeV. The control effect of the controller is mainly reflected in: adjusting the degrader to the corresponding thickness to control the beam energy; adjusting the envelope collimator and the energy-selective slit to the corresponding position for suppressing the growth of beam emissivity; and indicating the achromatic bending magnets to the corresponding value to control the trajectory of the beam motion.

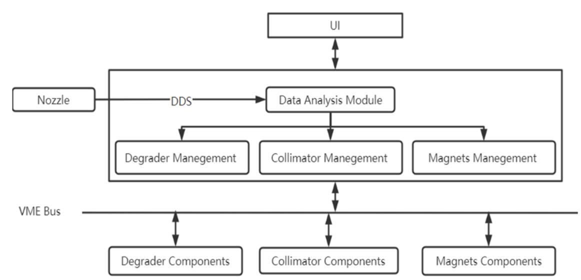

Figure 1: Architecture of the real-time control system.

Table 1: Performance Comparison of Existing Energy Degraders

Manufacturer	Energy range	Material	Shape	Energy switching time
IBA	70~230 MeV	C	Spiral type	≈ 500ms
Varian	70~250 MeV	C	Triangular wedge	≈ 150ms
Pronova	70~230 MeV	Be	Double-wedge wing type	≈ 500ms

Compared with the existing well-known degraders, as in Table 1, the real-time control system is able to receive energy information and issue commands to adjust the degrader to the corresponding energy position within 50 ms.

ISBN: 978-3-95450-212-7 ISSN: 2673-5482 doi:10.18429/JACoW-CYCLOTRONS2022-MOPO001

HARDWARE COMPONENTS OF THE REAL-TIME CONTROLLER

The hardware part (Fig. 2) uses the MVME6100 VME single board computer as, which provides the VxWorks board support package. The stepper motor control is implemented by a MAXv motion controller, which can control up to 8 axes of the stepper system.

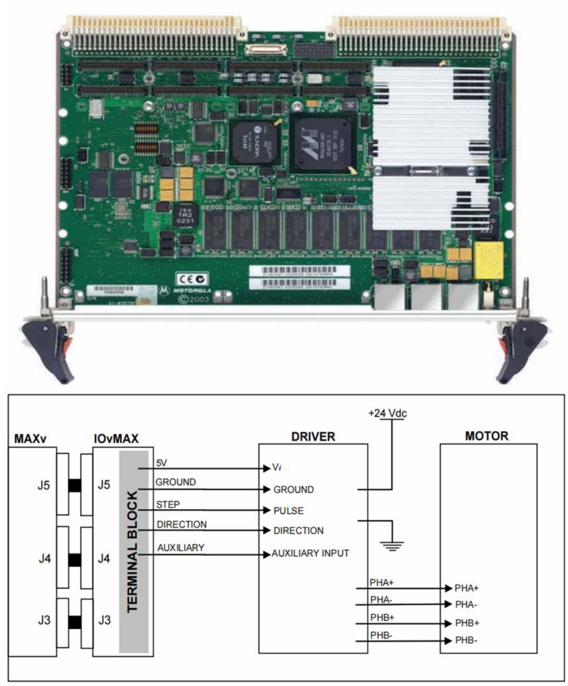

Figure 2: Hardware components for real-time controller, a) system board MVME6100, b) wiring diagram of MAXv controller via the IOvMAX interface module.

On the MVME6100, data is exchanged with each module through the VME backplane bus to control each processing module and display the signal processing results. The MVME6100 module runs under the embedded real-time operating system VxWorks. The MVME6100 provides a network interface that enables the system to communicate with the controllers of the achromatic bending magnets through this network interface, instructing them to adjust the current and PID to the appropriate values.

Self-developed signal transmission combinations (Fig. 3) are used to isolate motion controllers, reduce neutron interference near the beam line, and improve the reliability of data transmission.

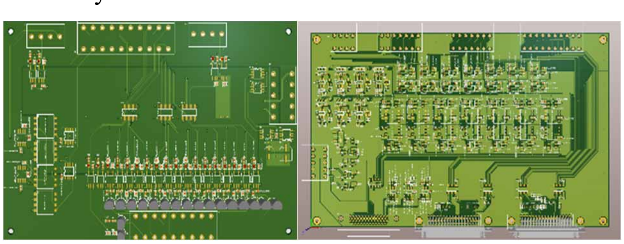

Figure 3: Signal transmission combinations, a) motor signal board, b) position signal board.

SOFTWARE OF THE REAL-TIME CONTROLLER

Software Architecture

The software of this real-time controller is deployed in the VxWorks real-time control system and is divided into three parts: DDS communication, real-time task calling, and data processing. The software system uses DDS communication as the main task and designs a unique subtask scheduling sequence based on the characteristics of the VxWorks operating system, which includes the control of different devices under the ESS as several different subtasks.

Database Preparation

The main function of the energy degrader is to realize the energy drop using the Bethe-Bloch formula shown in Eq. (1):

$$-\left(\frac{dE}{dx}\right) = 4\pi N_a r_e^2 m_e c^2 z^2 \cdot \left(\frac{Z}{A}\right)\left(\frac{1}{\beta^2}\right)\left[\ln\left(\frac{2m_e c^2\gamma^2\beta^2}{I}\right) - \beta^2 - \frac{\delta}{2}\right] \quad (1)$$

where E denotes the particle energy, $x = X \cdot \rho$ is the thickness of the medium, r_e is the classical electron radius, m_e is the electronrest mass, c is the speed of light, z is the amount of particle variation, $\frac{Z}{A}$ is the specific charge of the energy-reducing material, β, γ is the relativistic factor, I is the ionization potential, and $\frac{\delta}{2}$ denotes the density effect.

In addition to the energy loss, the proton beam passing through the degrader target material also collides with atomic nuclei, resulting in multiple Coulomb scattering effects and causing an increase in the beam geometric emittance. The emissivity of the beam passing through the degrader is shown in Eq. (2):

$$\varepsilon_1 = \varepsilon_0 + \langle\theta_x^2\rangle \sum_i \beta_i \quad (2)$$

where ε_0 and ε_1 are the beam emissivity before and after the beam passes through the degrader, respectively, and $\langle\theta_x^2\rangle$ is the mean square value of the emissivity growth versus the multiple scattering angle after the beam passes through the degrader; β is the TWISS parameter characterizing the size of the beam envelope.

According to the range of the beam in every 2 mm of water, this project has been converted to obtain the range of the beam in graphite as the thickness of the energy-reducing material corresponding to each energy layer. CYCIAE-230 calculates the thickness of the degraded material at the specified arrival beam energy by SRIM and stores it in the database.

The energy range of proton therapy is 70 MeV to 240 MeV, which is a wide energy range and a set of PID parameters is difficult to adapt to all the full energy range. For the three deflection magnets of CYCIAE-230, three different sets of PID parameters are used in the beam

ISBN: 978-3-95450-212-7 ISSN: 2673-5482 doi:10.18429/JACoW-CYCLOTRONS2022-MOPO001

energy range between 240 MeV and 145 MeV, 145 MeV and 110 MeV, 110 MeV and 70 MeV, separately. The controller passes the corresponding PID parameters for different energy bands to the magnet controller by calling the SQL database.

Communication Advantage

In order to receive energy information from the nozzle in real time, the controller communicates with the nozzle via the Data Distribution Services (DDS) bus. As a subscriber of information, this real-time controller can quickly acquire data and process it while the nozzle is releasing energy information (Fig. 4), which has the advantage of reducing the communication time between systems.

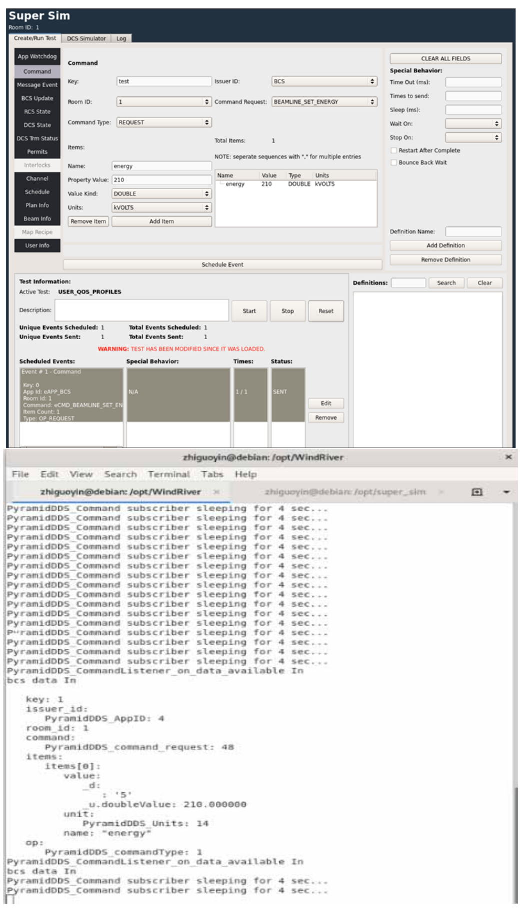

Figure 4: Controller communicates with Nozzle via DDS, a) the nozzle simulator sends energy messages, b) The controller receives beam energy information.

Open-loop control of the magnet power supply is achieved by real-time monitoring of the current, voltage, and component status of the 43 magnet power supplies (see Fig. 5).

The real-time controller interacts with the achromatic bending magnet powers based on the UDP protocol. This communication method is simple and fast, and its communication time is in the nanosecond range.

Figure 5: Open-loop control of ESS magnet power supply

S-Curve Algorithm of Motion Controller

The control of the stepper motor is realized by the motion controller, which uses an S-curve algorithm to regulate the speed of the stepper motor. Since the torque of the stepper motor may not be able to drive the load, this can result in the stepper motor not turning as many degrees as the number of degrees corresponding to the input pulse.

The graphite degrader used in CYCIAE-230 requires a certain thickness for the wedge structure to meet the energy reducing conditions, so the unavoidable problem is that the stepper motor needs to drive a large mass of degrader material.

By setting the optimal parameters of the S-Curve algorithm (Fig. 6) in the software system of the real-time controller, the stepper motor is able to adjust its speed to the specified value in a smooth and fast manner, thus avoiding the motor "out-of-step" phenomenon and reducing the negative effects of possible damage to the stepper motor due to the high inertia of the controlled device.

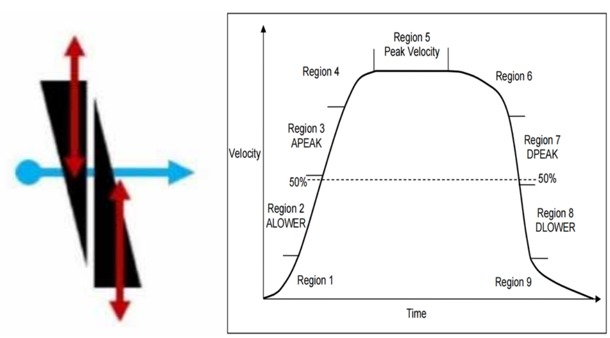

Figure 6: Motion design by S-curve algorithm, a) the graphite degrader, b) S-Curve algorithm.

TEST RESULTS AND FUTURE WORK

CYCIAE-230 has now completed the equipment installation and commissioning of the ESS section: including the energy degrader installation, the envelope collimator installation, the achromatic bending magnet power performance test, and the real-time controller performance test.

The results of the current tests show that the real-time controller receives energy from the nozzle at each level of energy switching, and is able to control the energy degrader, a set of achromatic bending magnets, the envelope collimator, and the momentum-selecting slit to move or adjust these devices to a specified position or value within 50 ms (Fig. 7).

ISBN: 978-3-95450-212-7 ISSN: 2673-5482 doi:10.18429/JACoW-CYCLOTRONS2022-MOPO001

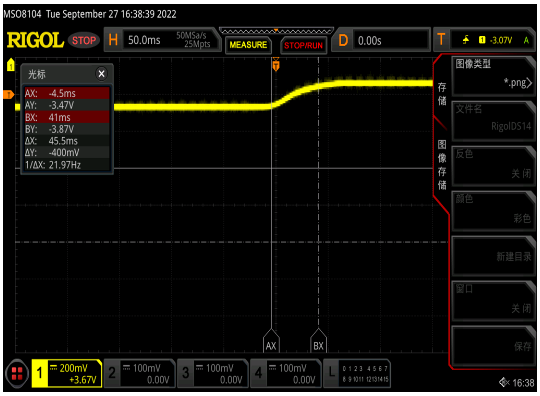

Figure 7: Energy degrader response time.

With the detection results of the position information returned at the device, the accuracy is up to 0.1%.

In 2023, the energy selection system will be tested under real beam conditions, and the reliability of the real-time controller will be further determined by combining numerical analysis of the magnetic properties with a more accurate determination of the actual response time in the real-time controller.

REFERENCES

[1] F. Bray *et al.*, "Global cancer statistics 2018: GLOBOCAN estimates of incidence and mortality worldwide for 36 cancers in 185 countries," *CA Cancer J. Clin.*, vol. 70, no. 4, p. 313, Nov. 2018. doi:10.3322/caac.21492

[2] T. Zhang *et al.*, "Developments for 230 MeV Superconducting Cyclotrons for Proton Therapy and Proton Irradiation," *Nucl. Instrum. Methods Phys. Res. Sect. B*, vol. 406, part A, pp. 244-249, Sept. 2017. doi:10.1016/j-nimb.2016.11.010

[3] R. R. Wilson, "Radiological use of fast protons," *Radiology*, vol. 47, no. 5, p. 487, Nov. 1946. doi:10.1148/47.5.487

[4] V. Rizzoglio *et al.*, "On the accuracy of Monte Carlo based beam dynamics models for the degrader in proton therapy facilities," *Nucl. Instrum. Methods Phys. Res. Sect. A*, vol. 898, pp. 1-10, Aug. 2018. doi:10.1016/j.nima.2018.04.057

[5] C. M. Charlie Ma, T. Lomax, *Proton and Carbon Ion Therapy*, CRC Press, Taylor & Francis Group, 2013.

[6] V. A. Anferov, "Energy degrader optimization for medical beam lines," *Nucl. Instrum. Methods Phys. Res. Sect. A*, vol. 496, no. 1, pp. 222-227, Jan. 2003. doi:10.1016/S0168-9002(02)01625-X

ISBN: 978-3-95450-212-7 ISSN: 2673-5482 doi:10.18429/JACoW-CYCLOTRONS2022-MOPO003

SAWTOOTH WAVE BUNCHER UPGRADE FOR SFC CYCLOTRON *

R. F. Zhang†, X. W. Wang, Z. Xu, X. M. Su, Institute of Modern Physcis, CAS, Lanzhou, China

Abstract

To increase extracted beam intensity, the SFC cyclotron requires that the sawtooth wave buncher on its injection line provide the effective voltage up to 2.5kV and cover a wide frequency range of six times. We develope a multi-harmonic synthesis method by combining a broadband amplifier and impedance transformer, which provide a high-voltage single-gap buncher at limited space and cost. With this method, the maximum voltage of the new buncher exceeds 2.5kV and the beam intensity increases by a factor of 6.7.

INTRODUCTION

The Heavy Ion Research Facility in Lanzhou (HIRFL) is the largest heavy ion accelerator complex in China, which consists of two electron cyclotron resonant (ECR) ion sources, sector focused cyclotron (SFC), separated sector cyclotron (SSC), cooling storage ring ring (CSR), radioactive beam line and experimental terminal [1]. The injector SFC cyclotron is a 1.7 meters sector-focused cyclotron with the K value of 69. It is equipped with two exteranl ECR ion sources named LECR3 and SECRAL-II respectively [2]. The layout of SFC injection system is shown in Fig. 1. A linear buncher B02 was installed in the vertical beam line section underneath the cyclotron center area, about 2.3 meters upstream the inflector. As the only buncher used in the

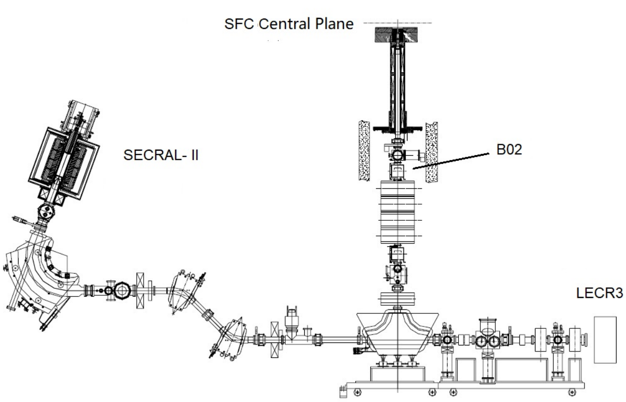

Figure 1: Layout of SFC axial injection system.

axial injection system, the B02 in principle improves the injection efficiency of the SFC and increases the extracted beam intensity compared with the case without it. However, from the operation in the past few years, there are still 3 aspects need to be improved: (1) intense beams with high and intermediate charge states from ECR ion sources requires high bunching voltage to compensate space charge effect; (2) there is no half-frequency mode which can increase longitudinal matching efficiency between SFC and SSC in cascade with SSC [3]; (3) equipment faults of B02 due to aging components have reduced the beam supply time of SFC [4].

PHYSICAL REQUIREMENTS

In this chapter theoretical description of axial velocity modulation of continuous DC ion beam is given as well as the special physical requirements. The overall specification of buncer is shown in Table 1.

SFC is a multi-particle and variable energy accelerator, and the design specifications of the buncher should adapt to its transformation range. The voltage amplitude of the buncher can be expressed as [5]

$$V_b = (\beta\lambda/L)(\eta)V_{inj} , \tag{1}$$

where L is the bunching distance, η is the effective duty cycle, and V_{inj} is the injection voltage. In our case the maximum ECR extraction voltage is 25 kV. The distance from the buncher to the inflector is 2.3 meters and $\beta\lambda$ is 16 mm when operating in the first harmonic mode with the maximum frequency of 16 MHz. These parameters give us an estimation of 1200 V for the saw-tooth voltage.

Due to mismatching of the SFC's extraction radius (R=0.75 meters) with the SSC's injection radius (R=1.0 meters), when SFC works at the mode h=1 and SSC at h=2, the longitudinal match efficiency between the two cyclotrons is only 50% in theory [3]. To regain the lost beam, a additional half-frequency bunching mode is required. In this mode, the buncher operates at half-frequency of SFC RF frequency with the double bunching voltage squeezing the original two packets into the one that can be accepted by the RF of SSC. Therefore, the buncher working frequency range is changed from 5.5-16.0 MHz to 2.75-8.0 MHz with the Maximum bunching voltage increasing from 1.27 kV to 2.54 kV.

Table 1: Design Parameters of Buncher

Parameter	Value
Input Frequency	5.5~16.0MHz
Input Level	7dBm
Work Frequency	5.5MHz~16.0MHz
Work Frequency∗	2.75MHz~8.0MHz
Voltage	≤1.27kV
Voltage∗	≤2.54kV
Amplitude Stability	≤1%
Phase Stability	≤1°

* Work supported by the HIRFL operation and maintenance project [grant number Y9HIRLL100]
† zhangruifeng@impcas.ac.cn

ISBN: 978-3-95450-212-7 ISSN: 2673-5482 doi:10.18429/JACoW-CYCLOTRONS2022-MOPO003

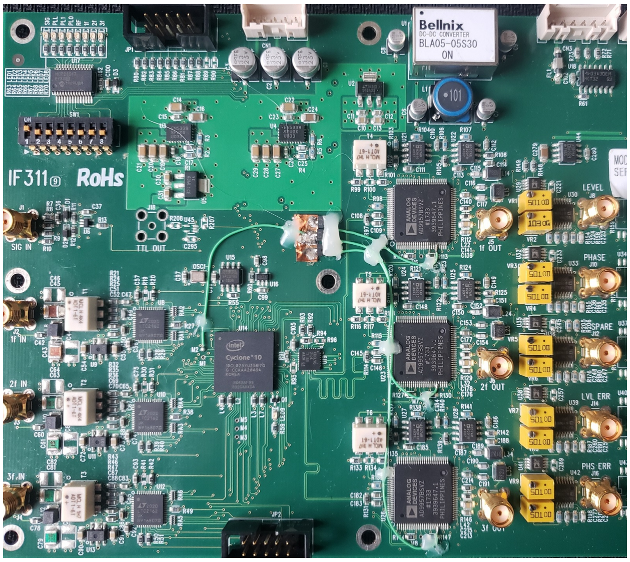

Figure 2: Sawtooth wave synthesis.

RF DESIGN OF THE NEW BUNCHER

Based on different specifications of operating frequency and bunching voltage, the sawtooth buncher is realized with different methods at different facilities. These include: (1) resonator-based multi-harmonics buncher developed at ATLAS or FRIB [6]; (2) high voltage direct forming method used at HIRFL or SPIRAL [3, 7]; (3) double drift system proposed by Goldstein and Laisne [8]; (4) low-level multi-harmonic synthesis and wide frequency band amplifier used in RIKEN.

Considering the limiation in space, the broad frequency band and high bunching voltage, and the maintainance, the present system is designed to be modular, which includes a sawtooth wave generator, wide-band amplifier and power supply, electrode, and impedance transformer.

Sawtooth Wave Generator

The sawtooth wave generator is designed to generate low-level sawtooth waves by combining fundamental wave, 2nd harmonic, and 3rd harmonic. The voltage signal composed of three harmonics is given by

$$V(t) = V_0[sin(\omega t) - 1/3sin(2\omega t) + 1/9sin(3\omega t)], \quad (2)$$

where V_0 is the fundamental wave voltage, $V(t)$ is the total voltage, and ω is the frequency of fundamental wave. As described in Fig. 2, the fundamental wave is generated by Quadrature Digital Up Converters (QDUC) chip, Analog Devices AD9957, which functions as a universal IQ modulator and agile upconverter. The AD9957 integrates a high-speed, direct digital synthesizer (DDS), a high performance, high speed 14 bit digital to analog converter (DAC), clock multiplier circuitry, and digital filters onto a single chip. In order to optimize the waveform generation both the amplitude and phase of the fundamental wave are precisely regulated with a feedback loop. RF pick-up signals from the electrode are

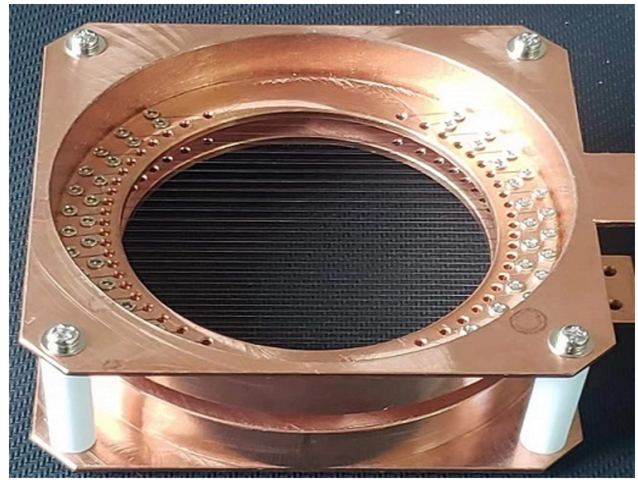

Figure 3: Electrode.

Figure 4: Transmission line transformer.

filtered by the corresponding bandpass filter and conditioned, then sampled by 16-bit ADC. Digital signal processing of the sampled RF signals is implemented in FPGA. IQ demodulator, cordic, and PID controller module were implemented with Verilog code. The 2nd and 3rd harmonics are generated and regulated in the same way.

Electrode and Impedance Matching Unit

Figure 3 shows a improved grid with parallel wires made of 0.1 mm wire spaced 3 mm apart. The grid is aligned with a similar grid 6 mm away. Compared with the existing B02 grid, the improved grid increases the transmissivity by 10%.

The impedance transformer is used to match the capacitive load of the electrode with the 50 Ω output impedance of the power amplifier. Considering the frequency range of 2.75-48 MHz, a 1:9 transmission line transformer is used to convert 50 Ω to 450 Ω load (Fig. 4). As a result, the required maximum output power is reduced to one-ninth and the 2500 W broadband RF amplifier meets the requirements.

RF Broadband Amplifier

The broadband RF amplifier amplifies the sawtooth wave that combines the fundamental wave, 2nd harmonic, and

ISBN: 978-3-95450-212-7 ISSN: 2673-5482 doi:10.18429/JACoW-CYCLOTRONS2022-MOPO003

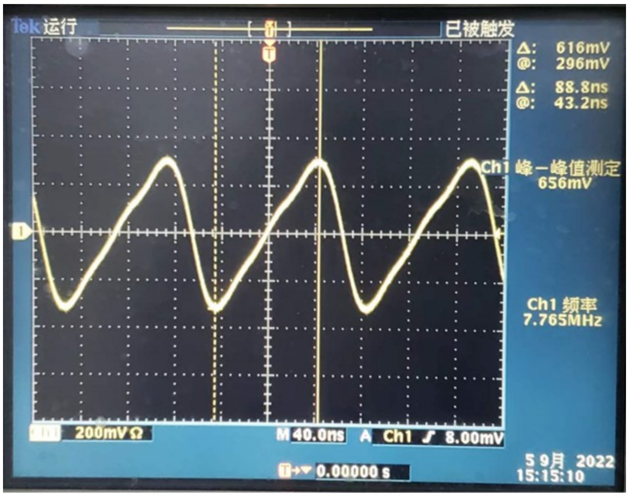

Figure 5: Sawtooth wave pickup

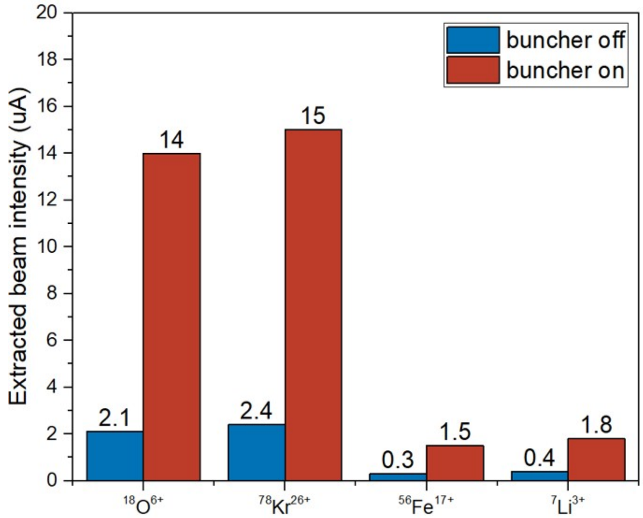

Figure 6: Beam test results

3rd harmonic. It consists of one power supply unit and two amplification units. The maximum input is 4dBm, the output power is 2500W for the fundamental wave, 250W for the 2nd harmonic and 25W for the 3rd harmonic, and -20dB for the harmonic suppression.

PERFORMANCE AND BEAM TEST

The new buncher has been installed online since September 2022. Several beam experiments have been carried out. The system has turned out to be reliable in operation and very useful in increasing the intensity level of the beam. In Fig.6 we have collected preliminary results for some heavy ion beams. As seen the gains in the beam intensity ranges from 4.5 up to 6.7. Next step, the detailed beam tests will be carried out, especially the half frequency mode which designed to improve SSC beam intensity.

CONCLUSION

A compact high voltage and broadband sawtooth wave buncher has been developed for the SFC cyclotron. The buncher is capable of being operated at full-frequency mode and half-frequency mode with the frequency ranging from 2.75 MHz to 8.0 MHz and 5.5 MHz to 16.0 MHz, and providing the effective voltage up to 1.27 kV and 2.54 kV respectively. Laboratory and online beam tests show that a 4.5 to 6.7 times gain in the beam intensity can be achieved with this method. The online test also verify the reliability and stability of the newly-designed system.

ACKNOWLEDGEMENTS

The authors would like to thank the collegues of the radio-frequency group of the Institute of Modern Physics, CAS, for their constructive suggestions and support. This work is supported by the HIRFL operation and maintenance project [grant number Y9HIRLL100].

REFERENCES

[1] J. W. Xia, W. L. Zhan, B. W. Wei, Y. J. Yuan, H. W. Zhao, J. C. Yang, Heavy Ions Research Facility in Lanzhou (HIRFL), Chinese Science Bulletin, 61 (2016) 467 - 477.

[2] H. W. Zhao, L. T. Sun, H. Y. Zhao, etal, An Advanced Superconducting ECR Ion Source SECRAL at IMP: Fisrt Results and Operation at 18 GHz, in. Proc. 18th International conference on Cyclotrons and their Applications, Caen, France, 2007, p271.

[3] J. Y. Tang, J. Z. Jiang, A. M. Shi, Z. K. Yin, Y. F. Wang, Linear bunchers and half-frequency bunching method, Nuclear Instruments and Methods in Physics Research A, 455(2000) 533 - 538.

[4] W. Q. Yang, L. T. Sun, J. C. Yang, L. J. Mao, J. W. Xia, Operation Status and Upgrading of Cyclotrons in Lanzhou, 22nd International conference on Cyclotrons and their Applications, Cape Town, South Africa, 2019.

[5] J. Y. Tang, J. Z. Jiang, A. M. Shi, etal, Linear Bunchers on the SFC Axial Injection Line, Nuclear Techniquew , 23(2000) 475 - 478.

[8] S. V. Kutsaev, A. Yu. Smirnov, R. Agustsson, D. Chao, S. Lynam, Four-harmonic Buncher for Radioactive and Stable Beams Switching at the ATLAS Facility, Nuclear Inst. and Methods in Physics Research, A, 905 (2018) 149–159.

[9] A. Chabert, Ch. Ricaud, L. Boy, B. Monsanglant, etal, The Linear Buncher of SPIRAL Beam Test of a Prototype, Nuclear Inst. and Methods in Physics Research, A, 423 (1999) 7–15.

[8] C. Goldstein, A. Laisn, Third Harmonic Simulated Buncher, Nuclear Instruments and Methods, 61 (1968) 221-225.

ISBN: 978-3-95450-212-7 ISSN: 2673-5482 doi:10.18429/JACoW-CYCLOTRONS2022-MOPO004

BEAM DUMP DEVELOPMENT FOR HIGH POWER PROTON AND ELECTRON BEAM

Jingyuan Liu†, Tianjue Zhang, Guofang Song, Lei Wang, Zhiguo Yin, Shilun Pei, Suping Zhang, Gaofeng Pan, Sumin Wei, Yang Wang, Xiaofeng Zhu, Hongru Cai, Mingzhi Hu
China Institute of Atomic Energy, Beijing, China

Abstract

The high-intensity 100 MeV proton cyclotron CYCIAE-100 had provided 52 kW beam to the beam dump in 2018, is planning to be upgraded at China Institute of Atomic Energy (CIAE). It is designed to provide a 75-100 MeV, 1 mA proton beam. A new beam dump for higher beam power have been developed since 2020. At the same time, a 1:4 scale, RF cavity with Q value up to 42000, is constructed for the engineering feasibility verification of a 2 GeV/6 MW CW FFAG, which is also being considered as a main accelerating cavity of a 100 kW electron accelerator. The electron beam will be rotated and accelerated 7 times by the gradient dipoles and the high Q cavity. The beam dump is designed to also use for the 100 kW electron beam. With the same-level beam power of the two accelerators above the content, a beam dump for absorbing two kinds of particle beams according to the characteristics of the modification was designed. The energy deposition of 100 MeV proton beam and 5 MeV electron beam in the beam dump was investigated by the Monte-Carlo simulation program FLUKA. The beam dump cooling structure was optimizing by ICEM-CFD and fluent, so that the water temperature was controlled less than 100 °C, and the maximum temperature on the beam dump is less than 450 °C. The beam dump is designed as a cube (450 mm * 200 mm * 200 mm) with two 2.5° V-type copper pentagon and two flat parts. All the details about the simulation of energy deposition, thermal distribution and structure design will be presented in the paper.

INTRODUCTION

The high-intensity 100 MeV proton cyclotron CYCIAE-100 had provided 52 kW beam in 2018, is planning to be upgraded to provide the beam power reached 75-100 kW proton beam [1, 2]. A 1:4 scale, RF cavity is constructed for the engineering feasibility verification of a 2 GeV/6 MW CW FFAG, which is also being considered as a main accelerating cavity of a 100 kW electron accelerator [3]. The beam dump is the major part for absorbing high-energy particle beam at the end of accelerator. With high power density and small cross-section, if the heat flux is not reduced and the heat is not taken away in time, the vacuum will be destroyed, and even affect the normal operation of accelerator.

STRUCTURAL DESIGN

The beam dump, shown in Fig. 1, is located in a vacuum box at the end of the beam line designed, as a cube (450 mm * 200 mm * 200 mm). the beam dump consists of two 2.5° V-type pentagon and two flat parts fabricated from copper. Two fluid regions are distributed symmetrically as S-channels. The fluid regions are almost parallel to the 2.5° V-surface, and the distance from the V-surface is about 20~25 mm. The gap of channel is optimized to 3 mm and with 3 fins, the thickness is 1.5 mm, to enhance convective heat transfer. The purpose of the two side plates is to block the few edge beam particles that might be present.

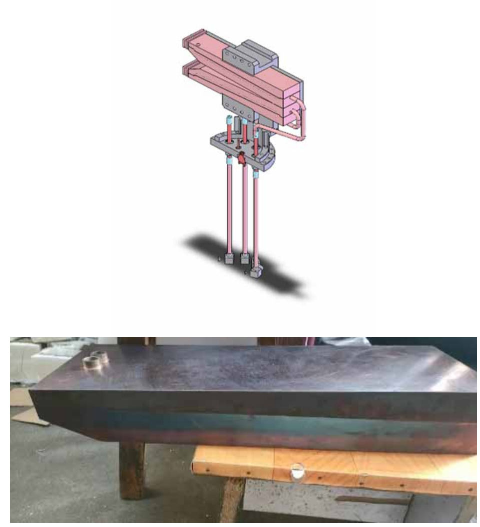

Figure 1: Three-dimensional drawing of the beam dump and the 2.5° V-type copper pentagon target in processing.

CALCULATION ABOUT THE BEAM ENERGY DISTRIBUTION

In order to obtain more accurate temperature distribution, the input condition of the V-type pentagon in the depth of direction is result of heat source probability density calculated by FLUKA, and the energy of the beam and copper has a Gaussian distribution. Figure 2 shows the energy probability of the proton/electron-copper interaction in the depth direction. The energy deposit increases with incidence depth, and the relation is not linear. For easy to calculation, the relationship between the energy deposit and incidence depth is assumed to be energy probability density.

ISBN: 978-3-95450-212-7 ISSN: 2673-5482 doi:10.18429/JACoW-CYCLOTRONS2022-MOPO004

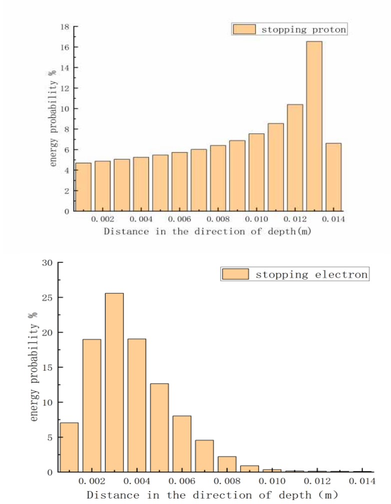

Figure 2: Energy probability in the beam dump of (a) 100 MeV proton, (b) 5 MeV electron.

MESH AND THERMAL ANALYSIS

Figure 3 shows the 2.5° V-type pentagon target divided into five areas to optimize calculate the temperature distribution with ICEM. To adapt probability density of proton and electron particles, two energy distribution regions are separated as 2.5° inclined plane and 30° inclined plane according to proton range. When the beam dump intercepts electrons, the energy probability density at the distribution regions beyond the depth of 10 mm is assumed to be 0. Two fluid regions are separated as Tube A and Tube B to improve the speed of calculation. Hexa-mesh is used in the above four regions. The last area called heat transfer region is meshing with Tetra-mesh. Those five grids are merged into one grid [4]. Table 1 shows the mesh information of different regions.

The beam dump should be designed to prevent the temperature from exceeding the boiling point, otherwise bubbles forming in the overheated area will isolate the water and copper, causing the temperature to get out of control and damaging the beam dump from the inside face. In addition, the maximum temperature of the beam dump should not exceed the melting point of the material to prevent damage the dump from the outside face. Cooling water is entered into beam dump from the trumpet, taking away 50 kW from one V-type target.

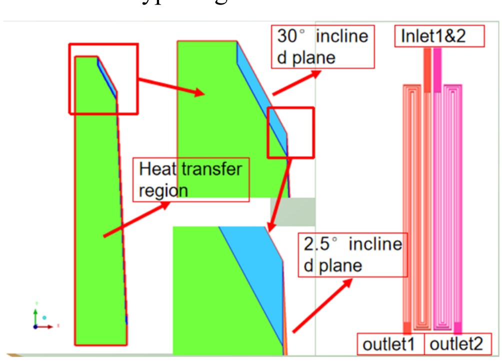

Figure 3: Divided Regions of the V-Type Pentagon.

Table 1: Mesh Information

Region	Element Types	Total Elements
2.5° inclined plane	Hexa-mesh	70 thousand
30° inclined plane	Hexa-mesh	16 thousand
Tube A	Hexa-mesh	27 thousand
Tube B	Hexa-mesh	27 thousand
Heat transfer region	Tetra-mesh	600 thousand

The fluid mechanics software fluent was used to simulate the temperature distribution. The viscous model was adopted k-ε model. The flow rate of cooling water was 1 kg/s and the corresponding inlet pressure was about 0.07 MPa. After entering the fin area, the cross section of fluid decreases and the flow velocity increases. The flow velocity distribution and heat transfer coefficient of cooling water is shown in the Fig. 4. The average velocity in the fin gap area is about 1.9 times of where without fins at the inlet and outlet, the highest velocity occurs at the end of the U-tube with the smallest turning radius in the fin gap. The distribution of convective heat transfer coefficient is same as that of velocity.

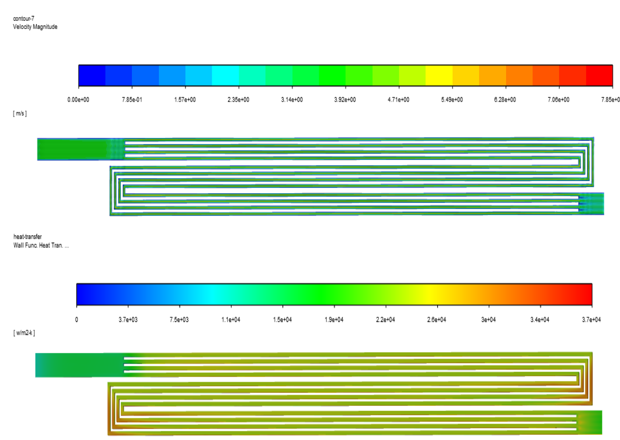
Figure 4: Distribution of Velocity and Convective Heat Transfer Coefficient.

Assuming the beam size is 9 mm, assembled symmetrically along the central plane of the beam, each V-type target absorbs half of the beam, which is 50 kW. Flow rate is 1 kg/s and the temperature of inlet water is about 27 ℃. Figure 5 shows the curves of the peak temperature on the target and the surface of the cooling channel at different y director. As y director increasing, the temperature on the target and on the surface of channel rises to the maximum temperature at 0.05 m, the position where the Angle of the target is 2.6°, then the temperature gradually decreases from 0.05 m to 0.3 mm. and rises again to the peak temperature at 0.33 m, the Angle of the target becomes 30°, then the temperature drops rapidly.

ISBN: 978-3-95450-212-7 ISSN: 2673-5482 doi:10.18429/JACoW-CYCLOTRONS2022-MOPO004

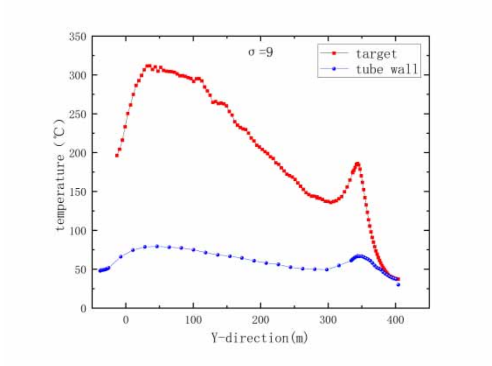

Figure 5: Curves of Peak Temperature.

Figures 6 and 7 show the temperature distribution, under four conditions, which are formed by the combination of two kinds of particles (100 MeV proton and 5 MeV electron) and two kinds of depth direction energy distributions (average density and probability density). For the condition of V-type target stopping 100MeV proton with energy distribution as probability density. The highest temperature is about 357 ℃ (Th) at the 2.5° inclined plane, the peak temperatures is about 190 ℃ (Tp1) at the 30° inclined plane, and about 80 ℃ (Tp2) at the surface of the cooling channel. The results of other conditions are shown in Table 2, it shows that the temperature on the target is much lower than the melting point of copper and the fluid wall temperature does not exceed the boiling point of water. A phenomenon is that the temperature on the target calculated using the energy distribution of probability density is lower than the average density, and the energy distribution has little effect on the temperature of surface channel.

Table 2: Maximum Temperature in the Crucial Area

Particle	**Energy Distribution**	T_h	T_{p1}	T_{p2}
proton	probability density	357	190	80
proton	average density	374	264	82
electron	probability density	373	334	84
electron	average density	396	316	85

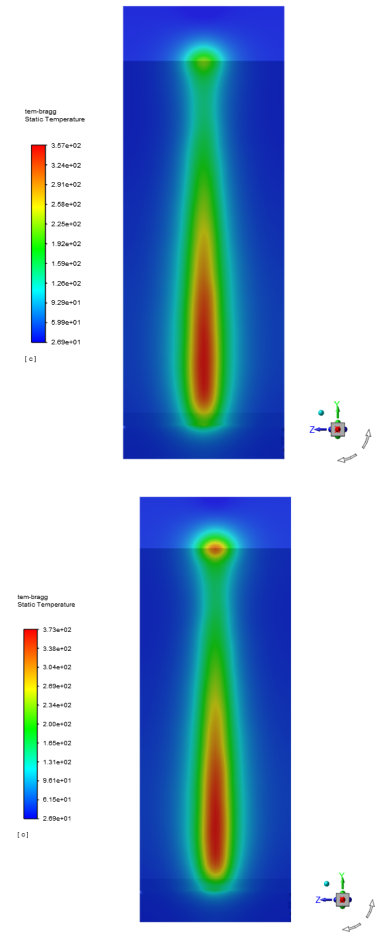

Figure 6: Temperature distribution of calculation energy probability density in depth direction by FLUKA, (a) target stopping 100 MeV proton, (b) target stopping 5 MeV electron.

Figure 8-a shows the curves of the maximum temperature by different flow rate at beam size 9 mm, when the beam flow rate is reduced to 30 L/min (0.5 kg/s), the wall temperature exceeds 100 ℃. Figure 8-b shows the curves of the maximum temperature by different beam size at flow rate 1 kg/s, when the beam size is less than 6 mm and the wall temperature exceeds 100 ℃. The beam dump should be avoided from operating under these critical conditions.

ISBN: 978-3-95450-212-7 ISSN: 2673-5482 doi:10.18429/JACoW-CYCLOTRONS2022-MOPO004

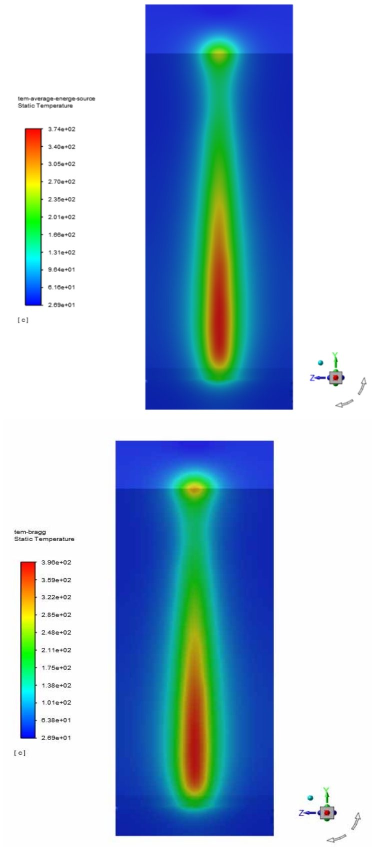

Figure 7: Temperature distribution of average density in depth direction, (a) target stopping 100 MeV proton, (b) target stopping 5 MeV electron.

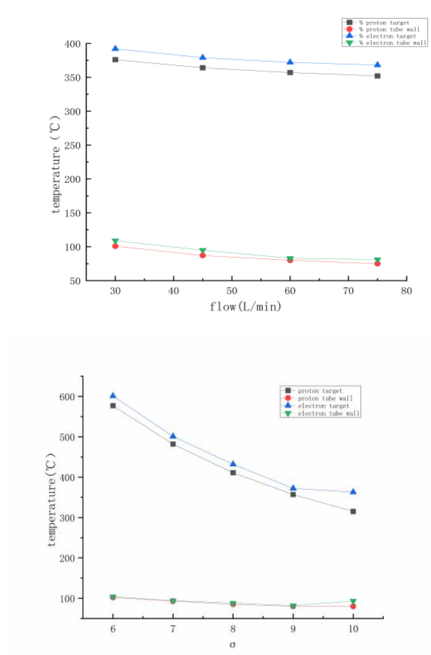

Figure 8: Curves of the Maximum Temperature, (a) different flow rate at beam size 9 mm, (a) different beam size at flow rate 1 kg/s.

The temperature almost has similar distribution, except for the condition where the electron beam size reaches 10 mm, which shows in Fig. 9. In this condition, the temperature distribution of the electron and proton target changes greatly, and the highest temperature of the electron appears in the region between 30° and 2.6°, that is, y = 0.33 m.

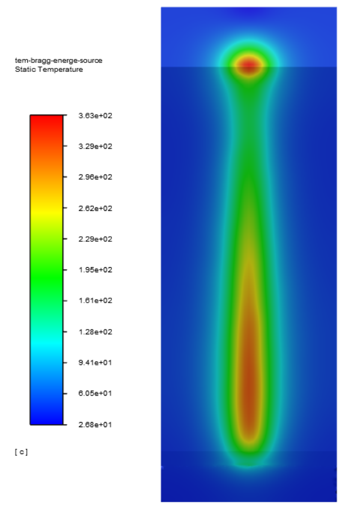

Figure 9: Temperature Distribution of the Electron Beam Size is 10 mm.

CONCLUSION

The design of a beam dump for 100 kW proton beam and 100 kW electron beam is described in this paper. The probability density of particle energy deposition in the depth direction was calculated by FLUKA, which is used as the input condition to calculate the temperature distribution of the beam dump. The cooling structure of the beam dump is optimized. The flow and beam size were used as variables to study the working conditions of the beam dump under different working conditions. The beam dump is currently being manufactured, the installation and test will be carried out in the near future.

REFERENCES

[1] T. Zhang *et al.*, "Isotope production by the high current proton beam of CYCIAE-100," *Nucl. Instrum. Methods Phys. Res. Sec. B*, vol. 463, pp. 119-122, Jan. 2020. doi:10.1016/j.nimb.2019.07.001

[2] T. Zhang *et al.*, "52 kW CW proton beam production by CYCIAE-100 and general design of high average power circular accelerator," *Nucl. Instrum. Methods Phys. Res. Sect. B*, vol. 468, pp. 60-64, Jan. 2020. doi:10.1016/j.nimb.2020.02.025

[3] T. Zhang *et al.*, "Coupling design of combined function bending magnet and high current electron beam for 100 kW irradiation accelerator," *IEEE J. Appl. Supercond.*, vol. 32, no. 6, pp. 1-5, Sep. 2022. doi:10.1109/TASC.2022.3150255

[4] Ansys Inc. Fluent user's guide, http://www.ansys.com

ISBN: 978-3-95450-212-7 ISSN: 2673-5482 doi:10.18429/JACoW-CYCLOTRONS2022-MOPO005

IMPEDANCE CHARACTERISTIC ANALYSIS AND MATCHING NETWORK DESIGN FOR A 100 mA H⁻ ION SOURCE

Aoxuan Ding†, Zhujie Nong, Pengzhan Li, Xianlu Jia, Tianjue Zhang, He Zhang, Xia Zheng, Jingfeng Wang, Gaofeng Pan, Hongru Cai
China Institute of Atomic Energy, Beijing, China

Abstract

China Institute of Atomic Energy (CIAE) has developed a series of multi-cusp H^- ion sources (IS) with DC beam intensity ranging from 3 to 18 mA for high intensity proton cyclotron uses such as cyclotron PET application, neutron source and boron neutron capture therapy (BNCT) facilities. Based on the previous experiences, a new project of radio frequency (RF) antenna driving ion source has been launched for pulse accelerator research. This new ion source is expected to provide over 100 mA peak intensity H^- beams of 60 keV and a longer maintenance interval than conventional filament-driving ion sources above. Impedance matching is indispensable for efficient RF power coupling in the whole working process of the ion source for high-intensity H^- beam extraction. In this paper, impedance characteristic of the IS antenna with various plasma loading is analysed. Eight typical matching topologies are discussed on their electrical requirements. A type-L and a type-γ network are finally selected for the 2 MHz and 13.56 MHz chains respectively. This design may provide a better compromise between the matching performance and the cost of implementation for a wide dynamic loading range. Design of the network is evaluated on the power delivering efficiency in each of the two RF chains and isolation between one and the other. The IS structure and near-future work plan are also presented.

INTRODUCTION

A high-intensity H^- ion source driven by internal RF antenna is under development at CIAE. Design of this new ion source is based on a high-compatibility test-bench which shares similar plasma discharging chamber, magnet layout and extraction system with the conventional filament-driving ion sources [1]. An internal enamel-coated solenoid antenna of 2.5 turns would be applied for the new IS in replacement of the filament, expecting for a longer life-time (> 50 hours) immersed in large-volume plasma. This overall design is shown in Fig. 1.

To obtain a peak intensity over 100 mA, an 80 kW 2 MHz solid-state amplifier (SSA) is adopted in generating large-volume RF coupled hydrogen plasma. And in each pulse interval, from every falling-edge to the following rising-edge, the plasma would be kept *simmering* by a CW 500 W 13.56 MHz amplifier module, aiming to reduce the probability of large-volume plasma generation failure. This module would be set ON at the very beginning for plasma ignition and throughout the whole working process of the ion source. Shifting of the plasma discharging state follows the rule that shown in Fig. 2.

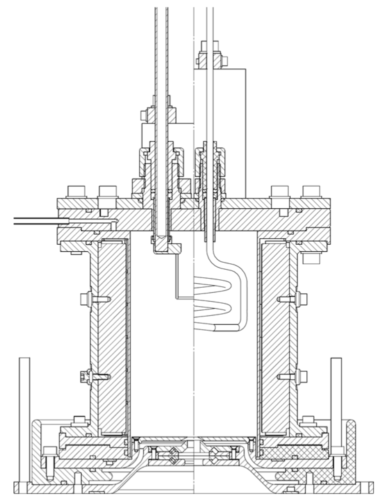

Figure 1: CIAE high-compatibility multi-cusp ion source test-bench. Left: filament driving design. Right: antenna driving design.

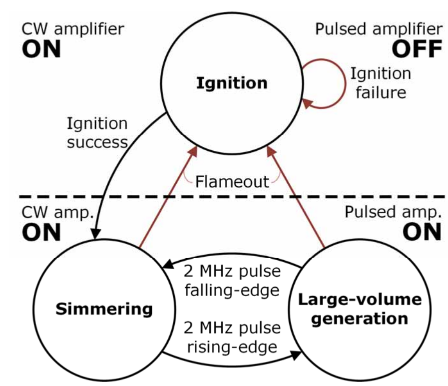

Figure 2: Plasma working states flow.

As the impedance of IS antenna varies dramatically from one discharging state to another, matching networks for the 2 MHz and the 13.56 MHz chains should be designed separately. Each of the networks demands a rather large adjustable matching range to cover most of possible antenna impedances with corresponding plasma loads. Efficient RF power delivery from the 50 Ω transmission-line system to the antenna could be attained only via careful designs of these matching networks, based on the reliable estimates of the IS antenna impedance characteristic. This paper is analysing the equivalent resistance and inductance of the antenna with different plasma loads, comparing basic matching network topologies, presenting and evaluating the design for the new 100 mA ion source.

† ding_aoxuan@outlook.com

ISBN: 978-3-95450-212-7 ISSN: 2673-5482 doi:10.18429/JACoW-CYCLOTRONS2022-MOPO005

IMPEDANCE CHARACTERISTIC OF THE ION SOURCE ANTENNA

In the newly developing 100 mA ion source, hydrogen plasma would be produced by inductive discharging, in which an axial alternating magnetic field would be generated by the RF current through the ion source solenoid antenna. This time-domain sinusoidal magnetic field would further induce a vortex electric field which accelerates the electrons in the discharging chamber and makes the ionization occur. The transformer theory of plasma discharging [2] views the antenna and inductive coupled plasma (ICP) load as the primary and secondary side of a transformer. In this case, the equivalent resistance and inductance of the IS antenna will increase and decrease respectively as hydrogen plasma raises. However, these two values may display the opposite trends when much larger RF power is applied to the plasma load [3-7].

In our design of the ion source, the resistance and inductance of the unloaded 2.5-turn antenna prototype are estimated as 0.013 mΩ and 0.313 µH respectively. While for the large-volume plasma generation state and the plasma simmering state, the values may be decided as 1.2 Ω with 0.8 µH and 0.4 Ω with 2 µH. Matching range for each of the two RF chains is always of demand due to the unpredictability of the impedance. Therefore, impedance coverages of 0.5~2 Ω with 0.2~2 µH and of 0.03~5.56 Ω with nearly any µH levels are separately set for the 2 MHz pulsed chain and the 13.56 MHz CW one. Frames of matching network would be then discussed and compared in the context of these two RF chains on their electrical requirements.

MATCHING NETWORK TOPOLOGIES

In order to minimize the cost and power consumption of the matching network for each chain, dual-capacitor topologies, in type-L or in type-γ form, as the simplest ones, have been taken into account for RF power coupling. For the high-voltage extraction of H^- beam, electrical isolation of the ion source from the grounded solid-state amplifiers is to be established by transformers. Thus, addition of one such component in the networks is also considered.

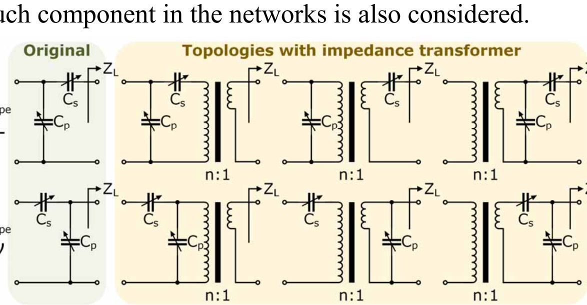

Figure 3: Dual-capacitor type-L and -γ matching networks with or without an impedance transformer. C_s stands for the series capacitor and C_p stands for the shunt one.

The only eight two-port matching network topologies that can be obtained by two capacitors with or without a transformer, as shown in Fig. 3, are evaluated on their requirements of capacitance and RF voltage and current endurance in each of the two chains. Analysis of the impedance matching equation for each network topology in either 2 MHz or 13.56 MHz chain yields the shunt and series capacitance requirement when the assumed equivalent impedance of RF antenna perfectly matched to the 50 Ω system. Corresponding RMS voltage and current are also calculated to evaluate such electrical endurance demands.

Addition of an inductor in series with the IS antenna is found of help to extend the matching coverage, reaching some of the small values that the equivalent inductance of the antenna and plasma load may occur. Analysis of the eight matching topologies with proper additional series inductances for the 2 MHz and 13.56 MHz chains has yield their dominant advantage and disadvantage to be chosen for the network, listed in Table 1, from either comparation of every matching equation or observation of the contours of needed capacitances and of voltage and current endurance requirements, shown later in Fig. 5 and 6.

Table 1: Advantage and Disadvantage of the 8 Matching Network Topologies in the 2 MHz and 13.56 MHz Chains

Topology	Advantage	Disadvantage
80 kW 2 MHz Chain		
Type-L, original	Original	Very large C_s and C_p (tens nF)
Type-L + Trans. on load side	Lower C_s and C_p	Unbearable RF voltage on C_s
Type-L + Trans. inserted	Well balanced	
Type-L + Trans. on source side	Lower C_s	Very large C_p (tens of nF)
Type-γ, original	Much lower C_s and lower C_p	Tuning difficulty
Type-γ + Trans. on load/source side or inserted	Much lower C_s and C_p	Tuning difficulty and unbearable voltage on C_s
500 W 13.56 MHz Chain		
Type-L, original or + Trans. on load/source side or inserted	Small or very small C_s; smaller C_p for ones with a transformer	Unbearable voltage on C_s
Type-γ + Trans. on load side or inserted	Smaller C_s and C_p	Unbearable voltage on C_s and C_p
Type-γ + Trans. on source side	Well balanced	Patience needed when tuning

A type-L matching network with one 3:1 transformer inserted between the capacitors is finally chosen for the 80 kW 2 MHz chain. And a type-γ one with one 3:1 transformer on the source side is selected for the 500 W 13.56 MHz chain.

ISBN: 978-3-95450-212-7 ISSN: 2673-5482 doi:10.18429/JACoW-CYCLOTRONS2022-MOPO005

DESIGN AND EVALUATION OF THE MATCHING NETWORK

Design of the entire matching network is shown in Fig. 4, in which three ports can be seen totally:

- Port 1 – Pulsed 80 kW 2 MHz input, 50 Ω.
- Port 2 – Ion source antenna, impedance unknown.
- Port 3 – CW 500 W 13.56 MHz input, 50 Ω.

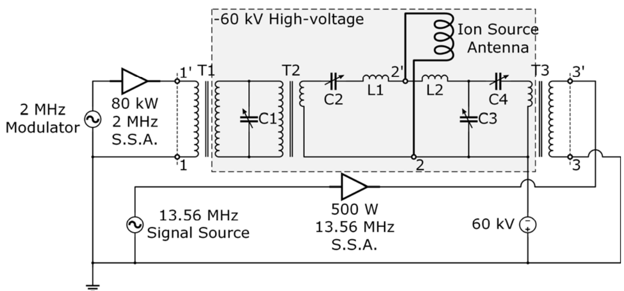

Figure 4: Design of the matching structure.

Matching capacitances for the 80 kW 2 MHz chain and corresponding electrical endurance requirements of this structure can be draw into contours as in Fig. 5. One may directly read out needed parameters of each element in this matching network for every specific antenna impedance range. Similar analysis for the 500 W 13.56 MHz chain yields the results presented in Fig. 6. Less than six adjustable vacuum capacitor of 1500 pF and 2 smaller (< 100 pF) ones are expected for the matching box's implementation.

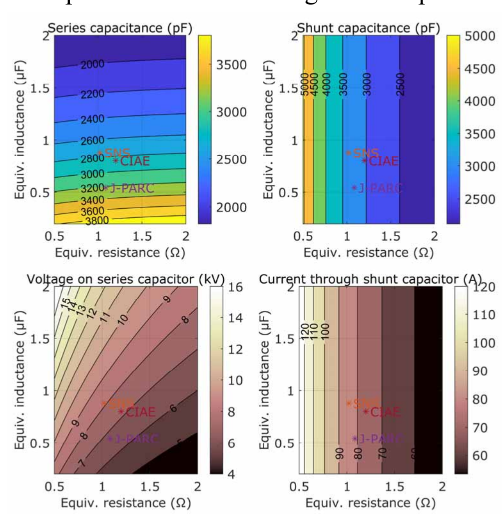

Figure 5: Electrical requirement contours of the series and shunt capacitors in the type-L matching network with 3:1 transformer for the 80 kW 2 MHz chain. Impedances of projects marked by coloured stars.

Evaluation of the RF power deliver efficiency in each plasma discharging states and the power isolation, especially from port 1 to 3 is given out by simulation based on LTspice XVII. The S21, S23 and S31 curves for this 3-port network are shown in Fig. 7, which strongly support the feasibility of each of the RF chains and the sufficient isolation between one and the other.

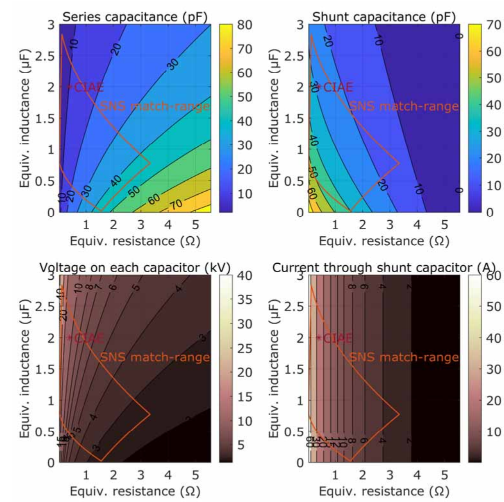

Figure 6: Electrical requirement contours for the type-γ network for the 500 W 13.56 MHz chain.

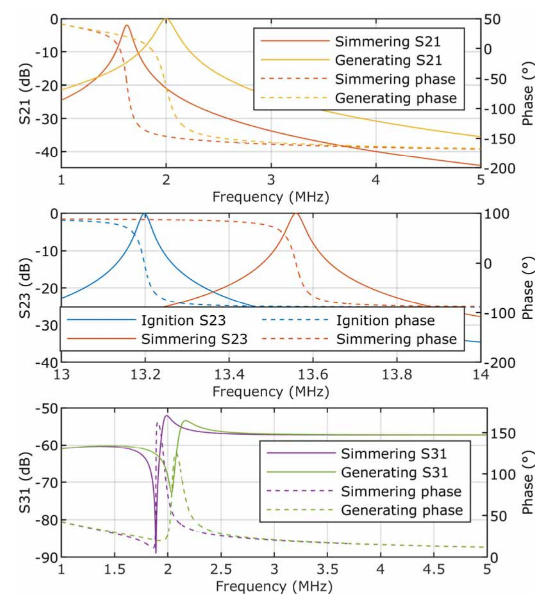

Figure 7: S21, S23 and S31 of the matching network

Moreover, analysis of the S-parameters indicates that when shifting from the plasma simmering state to the large-volume generation state, or from the cold ignition state to the simmering state, RF power delivering efficiency may decline dramatically if the frequency is kept constant. Therefore, a slight increase of the driving frequency may be of help in changing from one plasma working state to another.

CONCLUSION

In the project of a RF-driving 100 mA H^- ion source, a dual-channel impedance matching network is designed to realize a matching coverage of large impedance range. Evaluations show that such a structure provides a balance between its matching performance and the cost of implementation. Simulation proves the network's feasibility, and indicates that proper modulation helps to improve the generating efficiency of RF driven hydrogen plasma.

ISBN: 978-3-95450-212-7 ISSN: 2673-5482 doi:10.18429/JACoW-CYCLOTRONS2022-MOPO005

Mechanical and water-cooling connections between the IS antenna and matching box should be taken into careful account for safety purpose. Remote controlled motors are planned to be installed to adjust the matching box for the ease of impedance matching.

REFERENCES

[1] X. L. Jia, T. J. Zhang, X. Zheng, and J. C. Qin, "Development of a compact filament-discharge multi-cusp H^- ion source", *Rev. Sci. Instrum.*, vol. 83, no. 2, p. 02A730, Feb. 2012. doi:10.1063/1.3680265

[2] R. B. Piejak, V. A. Godyak, and B. M. Alexandrovich, "A simple analysis of an inductive RF discharge", *Plasma Sources Sci. Technol.*, vol. 1, no. 3, pp. 179-186, Jul. 1992. doi:10.1088/0963-0252/1/3/006

[3] M. M. Paoluzzi, M. Haase, J. Marques Balula, and D. Nisbet, "CERN LINAC4 H^- Source and SPL plasma generator RF systems, RF power coupling and impedance measurements", *AIP Conf. Proc.*, vol. 1390, pp. 265-271, Sep. 2011. doi:10.1063/1.3637396

[4] A. Ueno, Y. Namekawa, K. Ohkoshi, K. Ikegami, and H. Oguri, "Impedance measurement of an antenna with hydrogen plasma driven by 13.56 MHz RF for J-PARC H^- ion source", *AIP Conf. Proc.*, vol. 1390, pp. 292-299, Sep. 2011. doi:10.1063/1.3637399

[5] A. Ueno *et al.*, "Perfectly matched pulsed 2 MHz RF network and CW 30 MHz RF matching network for the J-PARC RF-driven H^- ion source", *AIP Conf. Proc.*, vol. 1515, pp. 409-416, Feb. 2013. doi:10.1063/1.4792810

[6] B. X. Han *et al.*, "Characterization of the CW starter plasma RF matching network for operating the SNS H^- ion source with lower H_2 flows", *Rev. Sci. Instrum.*, vol. 87, no. 2, p. 02B143, Dec. 2015. doi:10.1063/1.4937772

[7] W. D. Chen *et al.*, "Operation of RF-driven negative hydrogen ion source in China Spallation Neutron Source", *Rev. Sci. Instrum.*, vol. 90, no. 11, p. 113320, Nov. 2019 doi:10.1063/1.5128553

23rd Int. Conf. Cyclotrons Appl. CYCLOTRONS2022, Beijing, China JACoW Publishing
ISBN: 978-3-95450-212-7 ISSN: 2673-5482 doi:10.18429/JACoW-CYCLOTRONS2022-MOPO006

DEVELOPMENT OF HIGH TEMPERATURE SUPERCONDUCTING ECR ION SOURCE USING REBCO COILS

T. H. Chong*, M. Fukuda, T. Hara, H. Kanda, M. Kittaka, S. Matsui, S. Nagaya, K. Takeda, Y. Yasuda, T. Yorita, H. Zhao, Research Center for Nuclear Physics, Osaka University, Osaka, Japan
A. Ishiyama, Waseda University, Tokyo, Japan
S. Noguchi, Hokkaido University, Sapporo, Japan
H. Ueda, Okayama University, Okayama, Janpan
S. Fukui, Niigata University, Niigata, Japan
T. Hirayama, Y. Matsubara, U. Mikami, N. Takahashi, J. Yoshida
Sumitomo Heavy Industries Ltd., Kanagawa, Japan
T. Watanabe, Chubu Electric Power Co., Inc., Aichi, Japan

Abstract

A High Temperature Superconducting ECR ion source (HTS-ECR) using REBCO coils is under development in Research Center for Nuclear Physics (RCNP), Osaka University. REBCO tapes are the second-generation high temperature superconductor, which maintains a high critical current even being placed in a strong external magnetic field. Using this REBCO coils as electromagnets, the HTS-ECR was designed to operate at microwave frequencies of 2.45 GHz and 10 GHz, for the purpose of propducing high intensity proton, deuteron and helium beams. In this work, the low-temperature perfromance test results of the REBCO coils will be presented. The coil system and plasma chamber designed for the HTS-ECR will also be discussed. Results yielded in this research will also be made the best use of the development of a skeleton cyclotron, a compact air-core cyclotron which is under development in RCNP, Osaka University.

REBCO COILS IN HTS-ECR

Electromagnet using REBCO Tape

REBCO ($REBa_2Cu_3O_{7-x}$, RE=rare earth) is a second generation high temperature superconducting material, which has critical temperature T_c higher than 90K. It also remain high critical current dendity even being placed in a strong external magnetic field. Under 20 T of external perpendicular magnetic field component, REBCO's critical current density remain larger than 400 A/mm^2 [1].

For its capability to carry high current under strong external magnetic field, REBCO tape is a promising material to construct iron-less electromagnet for cyclotron and ion source. An iron-less electromagnet, which has no hysteresis property, will permit quick adjustment on the magnetic field configuration according to the objective of the operation. An High Temperature Superconducting ECR ion source (HTS-ECR), which use only REBCO coils to induce magnetic field, is under development at Research Center for Nuclear Physics (RCNP), Osaka University. Results yielded in this research will also be made the best use of the development of a skeleton cyclotron [2]. a compact air-core cyclotron which is also under development in RCNP.

HTS-ECR

HTS-ECR has 4 circular REBCO solenoids and 6 racetrack sextupole coils to induce axial magnetic mirror field and sextupole field respectively. Figure 1 shows the coil assembel of HTS-ECR. Starting from the injection end, solenoid coils are called M1, PC and M2 solenoids, which has 106 turns two double pancakes, 103 turns double pancake and 68 turns double pancake configuration respectively.

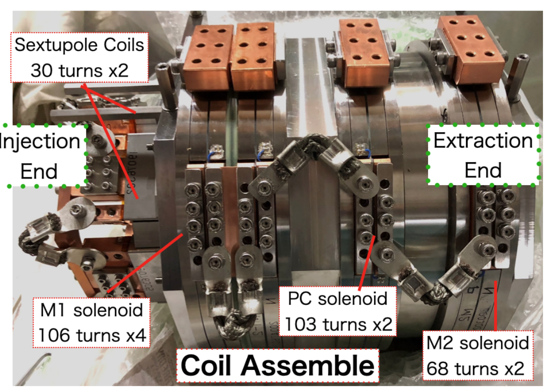

Figure 1: Coil assemble of HTS-ECR.

Specifications of HTS-ECR is shown in Table 1. HTS-ECR will provide high intensity proton, deuteron and He^{2+} to applications like RI production, BNCT and Targeted Alpha-particle Therapy. Although REBCO has critical temperature higher than 90K, HTS-ECR are designed to operate in 20~30 K, with large thermal margin to pursue stable operation. Also, in order to examine the adjustability of magnetic field configuration induced by REBCO coils, HTS-ECR are designed to operate at frequency of 2.45 GHz and 10 GHz.

LOW TEMPERATURE PERFORMANCE TEST ON REBCO COIL ASSEMBLE

The REBCO coils' capabilities of inducing magnetic field with high stability and reproducibilty in seperate operation

* oscar@rcnp.osaka-u.ac.jp

ISBN: 978-3-95450-212-7 ISSN: 2673-5482 doi:10.18429/JACoW-CYCLOTRONS2022-MOPO006

Table 1: HTS-ECR Specifications

Paramter	Value
Particle Type	p^+, d^+ and He^2+
Cooling System	GM cryocooler
Operation Temperature	20 ~ 30 K
Extraction Vlotage	50 kV
Operation Frequency	2.45 GHz and 10 GHz

are reported in previous work [3]. However, external magnetic field tends to limit the critical current density and stability of superconducting coils. Therefore, low temperature performance test on the coil assemble are carried out. In this case, REBCO coils are subjected to the magnetic field produced by each other.

In the low temperature performance test, the coil assemble is putted into liquid Nitrogen (77K). 3 solenoid coils are arranged to be in one series, and 6 sextupole coils another series. Currents are applied to the solenoid and sextupole coil series independently, while voltage of coils were measured by digital multimeters(KEITHLEY, DMM6500). The test result of M2 solenoid and sextupole coil No.1~3 are shown in Figs. 2 and 3.

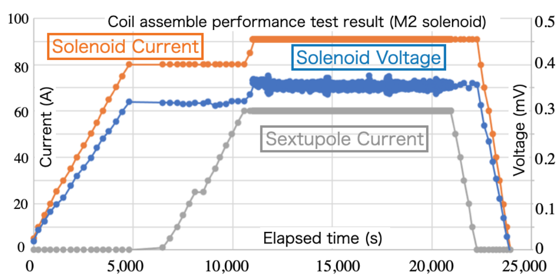

Figure 2: Voltage of M2 solenoid during 77 K coil assemble performance test.

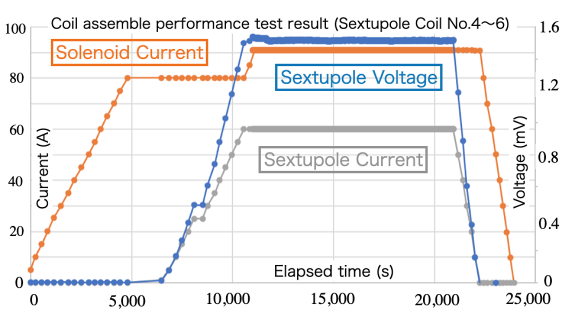

Figure 3: Voltage between sextupole No. 1~3 during 77 K coil assemble performance test.

In Fig. 2 and 3, applied current in solenoids was first increased from 0 A to 80 A, then current in sextupoles was increased from 0 A to 60 A, and current in solenoids was finally increased from 80 A to 90 A. Voltage of M2 solenoid increased proportional only to the current in the solenoids series,and sextupole coils voltage increased proportional only to the sextupole current. This result implys that the voltage increases is due to the normal conducting part in the coil assemble, and there was no normal conducting state transition in the whole process. There was no degeneration on the coil properties due to the external magnetic field.

Voltage in both coils remain the same at elapsed time from 11,000 s to 22,000 s, implying that both coils have good stability under external magnetic field. Similar results are also obtained from the other coils. Since the performance test lasted for 7 hours, the coil assemble proved its capability of hours long operation as an electromagnet.

MAGNETIC FIELD CONFIGURATION DESIGN

Magnetic Field Configuration of HTS-ECR

Magnetic field required for high-performance ion source are designed, and it will be provided by the REBCO coil assemble. Figure 4 shows the designed magnetic field configuration of HTS-ECR for 10 GHz and 2.45 GHz operation.

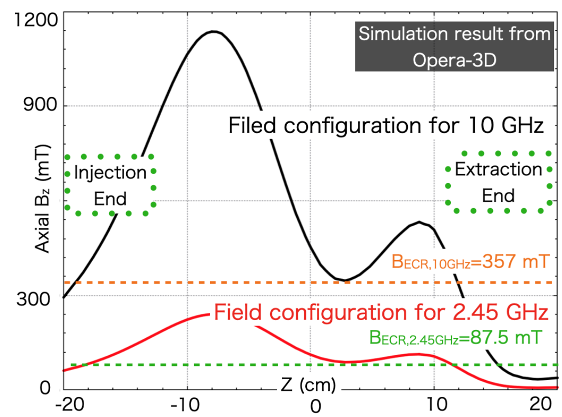

Figure 4: Magnetic field configuration of HTS-ECR.

Figure 4 shows the calculated axial magnetic field on the center of the coil assemble. Mirror field will be used in both 2.45 GHz and 10 GHz operation. In order to provied this configuration, for 10 GHz operation, currents in M1, PC, M2 and sextupole coils are 500 A, -580 A, 500 A and 250 A respectively. For 2.45 operation, it is 101 A, -66.6 A, 103 A and 250 A.

Design Concept

There are two objective in the magnetic field design in Fig. 4. It is to avoid the microwave cut-off, and to maximize the electron energy gain from ECR effect.

Avoiding R-wave Cut-off Inside a magnetized plasma, microwave can be interpreted by four principle waves, which are R-wave, L-wave, O-wave and X-wave [4]. Only R-wave corresponds to the ECR effect, and it is critical to let R-wave propogate to the resonance zone. However, R-wave is cuted-off when the below creterion is met, and the ion source performance will be limited.

$$\omega = (\omega_{ce} + \sqrt{\omega_{ce}^2 + 4\omega_{pe}^2}/2) \quad (1)$$

In Eq. (1), ω is the angular frequency of the input microwave, ω_{pe} the plasma frequency, and $\omega_{ce} = qB/m$ the electron cyclotron frequency. In order to avoid R-wave cut-off, $\omega_{ce} > \omega$ must be satisfied everywhere inside the plasma chamber except for the resonance zone. Since ω_{ce} is proportional to magnetic field magnitude B and ω is proportional to the resonance field B_{ECR}, the criterion to avoid R-wave cut-off can be written as $B > B_{ECR}$. For this reason, magnetic field in Fig. 4 has magnetic field magnitude larger than the resonance field everywhere in the plasma chamber, in order to avoid R-wave cut-off and to maximize the ion source perfromance.

Maximizing Electron Energy Gain Inside an ECR ion source, electrons gain energy at the resonance zone, where $B = B_{ECR}$. The energy gain is proportional to the square of the electric field magnitude, and the reverse of the gradient of the magnetic field. It can be writted as Eq. (2) [4].

$$W \propto E^2/(\Delta B/\Delta z) \quad (2)$$

In Eq. (2),W is the electron energy gain, E the electric field magnitude, and $(\Delta B/\Delta z)$ the gradient of the magnetic field. By putting the resonance zone at the bottom of the mirro field, as we do in Fig. 4, the gradient of magnetic field $\Delta B/\Delta z$ is almost zero. Therefore electron energy gain will be maximized.

PLASMA CHAMBER DESIGN

Chamber Dimension

A plasma chamber that can be used for both 10 GHz and 2.45 GHz operation is designed. In order to obtain large electromagnetic field magnitude, a standing wave is required inside a plasma chamber. The criterion of constructing a stangind wave inside a cylindrical chamber is shown below.

$$f_{mnp} = \frac{c_0}{2\pi}\sqrt{\left(\frac{j'_{mn}}{r}\right)^2 + \left(\frac{p\pi}{d}\right)^2} \quad (3)$$

where f_{mnp} is the frequency of the input microwave, r is the radius of the chamber, d is the length of the chamber, j'_{mn} is the zeroes of the derivatives of Bessel function. m, n, p is the index to distinguish the mode of the standing wave. When Eq. (3) is satisfied, a large magnitude of electromagnetic field can be obtained.

In order to change the operation mode between 10 GHz and 2.45 GHz without changing the plasma chamber, we decided to desgin a plasma chamber that create standind wave in both operation frequency. Through numerical analysis on Eq. (3), the required radius and length of a chamber is obtained. The result of the numerical analysis is shown in Fig. 5.

In Fig. 5, lines with different color represent dimensions of chamber that satisfy the standing wave criterion Eq. (3) with different operation frequency. The overlaps of two lines represent dimensions that are able to create standing wave in both 10 GHz and 2.45 GHz. Therefore, according to the result in Fig. 5, the plasma chamber of HTS-ECR is decided to be 38 mm in radius, 184.5 mm in length.

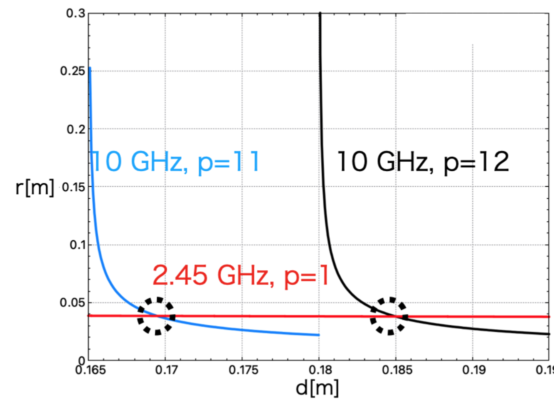

Figure 5: Numerical analysis result of Eq. (3). The overlaps of two lines imply a chamber dimension that can create standing wave in both 10 GHz and 2.45 GHz operation.

Energy Gain inside the Designed Plasma Chamber

By using simulation software Ansys-HFSS, electromagnetic field that can be created inside the designed chamber are calculated. The results are shown in Figs. 6 and 7.

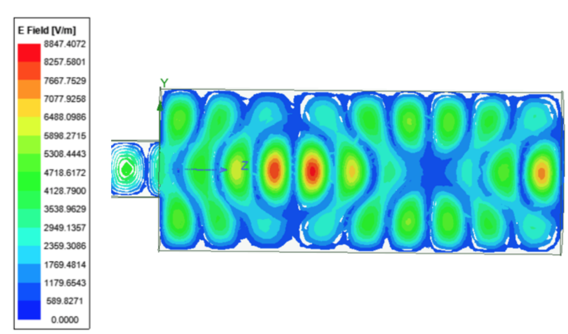

Figure 6: Magnitude of electric field that can be created inside the designed chmaber in 10 GHz operation, with 1 W input.

According to Cannobio's Theory [5], the maximum energy that electrons can gain can be written as below.

$$W_{max} = 1.5 \times 10^9 \left(\frac{E(\mathrm{Vcm}^{-1}}{\omega}\right) \quad (4)$$

According to Eq. (4), with 18 W microwave input, the designed plasma chamber can provide electron with maximum energy of 12 keV for 10 GHz and 30 keV for 2.45 GHz operation. Since ionization energy of proton and He^{2+} is 14 eV and 54 eV, it is expected that the designed chamber can provide sufficiently strong electric field for effective ionization.

ISBN: 978-3-95450-212-7 ISSN: 2673-5482 doi:10.18429/JACoW-CYCLOTRONS2022-MOPO006

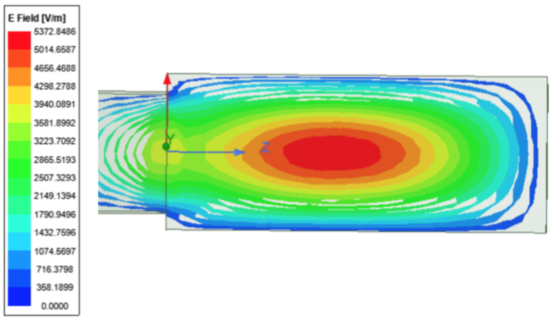

Figure 7: Magnitude of electric field that can be created inside the designed chmaber in 2.45 GHz operation, with 1 W input.

CONCLUSION

An high temperature superconducting coil assemble for an ECR ion source is constructed. The magnetic field configuration and plasma chamber for the ECR ion soruce is also designed.

The coil assemble is made by iron-less REBCO solenoid and sextupole coils. It showed high stability in the 77 K performance test, and the capability of operating for 7 hours without degeneration occuring on the coil property. The magnetic field configuration is designed based on the mode theory of magnetized plasma, to avoid R-wave cut-off and maximize the electron energy gain. A plasma chamber that can be used in both 2.45 GHz and 10 GHz operation is also designed. The electromagetic field that can be constructed inside the chamber is sufficient for effective ionization.

As future work, performance test on the magnetic field inducing ability of the coil assemble will be done. Also, performance test at the operation temperature, 30 K, is also necessary. The cryostat for 30 K operation is under development, and is expected to be completed in the next year.

REFERENCES

[1] National High Magnetic Field Laboratory, *Engineering Critical Current Density vs. Applied Field for Superconductors Available in Long Lengths*, 2018. `https://nationalmaglab.org/magnet-development/applied-superconductivity-center/plots/critical-current`

[2] H. W. Koay, M. Fukuda, H. Kanda, and T. Yorita, “Beam dynamics and characterization of a new high-intensity compact air-core high temperature superconducting skeleton cyclotron (HTS-SC)”, *Results Phys.*, vol. 33, p. 105090, 2022. `doi:10.1016/j.rinp.2021.105090`

[3] T. H. Chong *et al.*, “Development of ECR ion source with high-temperature superconducting REBCO coils”, *J. Phys.: Conf. Ser.*, vol. 2244, p. 012108, 2022. `doi:10.1088/1742-6596/2244/1/012108`

[4] M.A. Liberman and A. J. Lichtenberg, *Principles of Plasma Discharges and Materials Processing*, Wiley Interscience, 2005.

[5] R. Geller, *Electron Cyclotron Resonance Ion Sources and ECR Plasmas*, Institute of Physics, Bristol, 1996.

ISBN: 978-3-95450-212-7 ISSN: 2673-5482 doi:10.18429/JACoW-CYCLOTRONS2022-MOPO007

THE DESIGN AND COMMISSION OF VACUUM SYSTEM FOR CYCIAE-230 SUPERCONDUCTING CYCLOTRON

Suping Zhang†, Gaofeng Pan, Xiaofeng Zhu, Hongrui Cai, Jingyuan Liu, Zhiguo Yin, Bin Ji, Chuan Wang, Hongji Zhou, Wei Fu, Tianjue Zhang
China Institute of Atomic Energy, Beijing, China

Abstract

In this paper, the design, installation and commission of CYCIAE-230 superconducting cyclotron vacuum system are described. 8 sets of high compression ratio TMPs, which shielded by magnet material are used in combination with oil mechanical vacuum backing pumps and dry mechanical vacuum pumps. Another set of high compression ratio TMP is used to increase the central region degree. The pressure in the particle acceleration chamber is better than 2×10^{-6} mbar in 48 hours.

INTRODUCTION

CYCIAE-230, a superconducting cyclotron aims for proton therapy, is under design and construction at China Institute of Atomic Energy [1-3]. Vacuum system of CYCIAE-230 are studied for years. There are three technical difficulties of the CYCIAE-230 vacuum system, one is that 8 magnetic poles, 8 high frequency resonators, and 2 sets of striper targets and 2 sets of radial targets are installed in the accelerator vacuum chamber, which resulting in technical difficulties in many types of materials and large gases loads. Another is that CYCIAE-230 does not have a separate valley area for pumping, and can only be shared with RF vacuum vessel for exhaust. It means The more complex the high-frequency structure, the smaller conductance to pump. Third is that the residual magnetic field near the accelerator magnet is about 2000 Gs to 3000 Gs [4]. Many equipment, for example, molecular pumps, vacuum valves and other components will be damaged in such large residual magnetic fields. Therefore, these components need to be shielded from magnetic fields. To solve the above 3 technical problems of superconducting cyclotron CYCIAE-230 vacuum system, 8 sets of TMPs with magnet shields are installed on the valley of magnet poles, which also used as RF cavity [5], 1 set of TMP with magnet shields is installed on the central magnet pole to increase the vacuum degree of central region. The vacuum in the particle acceleration chamber is better than 5.6×10^{-7} mbar in 48 hours without ion source. The detail design and commission of CYCIAE-230 vacuum system will be presented.

CHALLENGES FOR VACUUM SYSTEM OF CYCIAE-230

Design of the vacuum system of CYCIAE-230 has gone through several listed and unlisted challenges:

- Shared with RF used the same cavity for exhaust.
- The strong residual magnetic for TMPs
- Inner Ion source.
- Thousands of internal welds in vacuum chamber

Meanwhile, technical requirements shall be met as the followings:

- Static pressure better than 2×10^{-6} mbar
- Dynamic pressure better than 5×10^{-5} mbar
- Clean, oil-free vacuum system
- Overall leakage rate less than 2×10^{-11} mbar·l/s

ACCELERATOR GAS LOAD IN ACCELERATION CHAMBER

The accelerator components in the superconducting cyclotron chamber include magnetic poles, high-frequency cavity, cryostat inner surface etc. The materials are accelerator iron, oxygen-free copper, stainless steel etc. The total volume is 10 m^3, and the outgassing area is about 200 m^2. CYCIAE-230 superconducting cyclotron is symmetric separated into two parts. The two halves and other seals on magnet yoke are sealed from the atmosphere using Viton O-rings with a hardness of 70 Shore, which cause more gas loading arising. The designing gas load of the ion source is less than 1 cm^3/min H_2. All sources of gas, such as the ion source gas inlet, leaks, permeation through gaskets and gas desorption is 210 mbar·l/s [6]. 2 sets of slim striper targets and 1 set of radial probes are also equipped with vacuum connector as shown in Figs. 1 and 2. The designation of vacuum devices and the cross-section of the inlet pipes have been dictated by their structure.

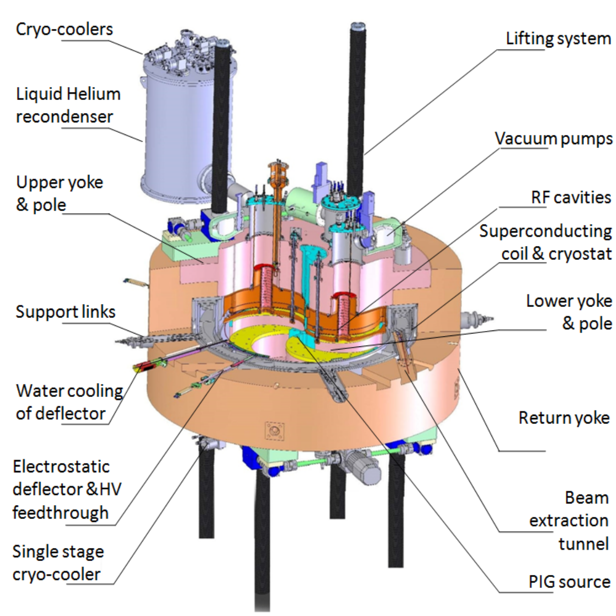

Figure 1: CYCIAE-230 cyclotron.

† 107824284@qq.com

23rd Int. Conf. Cyclotrons Appl. CYCLOTRONS2022, Beijing, China JACoW Publishing
ISBN: 978-3-95450-212-7 ISSN: 2673-5482 doi:10.18429/JACoW-CYCLOTRONS2022-MOPO007

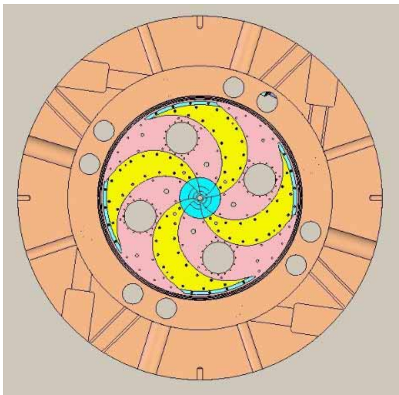

Figure 2: The median of CYCIAE-230 cyclotron.

VACUUM SYSTEM DESIGN

Considering a leakage of 10 mbar·l/s and the permeation through gaskets are the most relevant gas sources for the final pressure, effective pumping speed of 2000 l/s is needed for the final pressure 2×10^{-6} mbar. The conductance of the RF cavity the valley area is limited to only 1170 l/s, and the valley in which feed-in component stays, the conductance only is 540 l/s, the conductance of stem for the central region only 40l l/s, therefore the required pumping speed of 5000 l/s is calculated from the specified final pressure of 2×10^{-6} mbar. The total installed pumping speed of 5000 l/s could be distributed optimally in the whole cyclotron with nine TMPs. 8 sets of TMPs with magnet shields are installed on the valley of magnet poles, which also used as RF cavity, 1 set of TMP with magnet shields is installed on the central magnet pole to increase the vacuum degree of central region. 3 sets of slim striper targets and 1 set of radial probes are also equipped with vacuum connector. The differential exhaust vacuum vessel is used to reduce the difference between the pressure in the target rod and the pressure in the accelerator chamber. 1 set of TMP with magnet shields and the cross-section pipe have been installed near the support of magnet yoke as shown in Fig. 3.

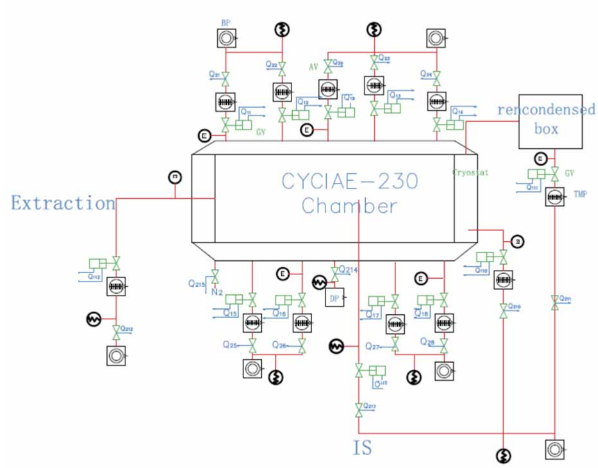

Figure 3: Schematic chart of CYCIAE-230.

Sets of TMPs installed on the cryostat always are used for insulation vacuum of the cyclotron magnet superconducting coils. The vacuum system diagram and the photo of the vacuum are shown as Figs. 3 and 4.

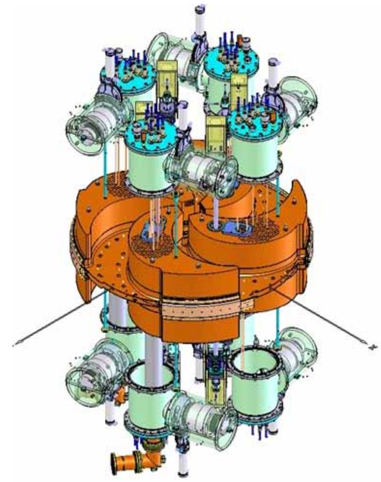

Figure 4: Nine TMPs used for CYCIAE-230 accelerator chamber.

COMMISSION OF CYCIAE-230 VACUUM SYSTEM

All the parts of CYCIAE-230 superconducting cyclotron and vacuum system are tested while processing, ensuring that the leak rate of vacuum components and seals meet the design requirements. With this well-established concept, a rapid whole set leakage detect commissioning in one day is guaranteed.

Figure 5: Leakage detecting.

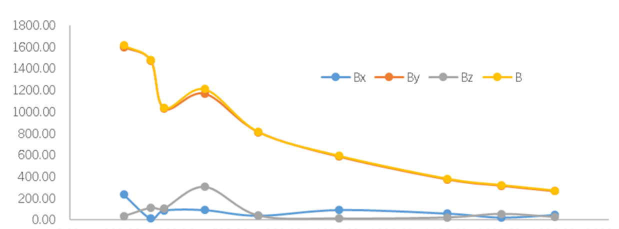

Figure 6: Residual magnetic of CYCIAE-230.

23rd Int. Conf. Cyclotrons Appl. CYCLOTRONS2022, Beijing, China JACoW Publishing
ISBN: 978-3-95450-212-7 ISSN: 2673-5482 doi:10.18429/JACoW-CYCLOTRONS2022-MOPO007

Residual magnetic around CYCIAE-230 has been measured. Figure 6 shows that there is more than 1000 Gauss inevitably residual magnetic at the TMP installation ports [4], where the magnetic flux density reaches which is 20 times larger than the turbo pump's safe operation limit. This may further cause the malfunction of the turbo pumps. Shielding for TMPs are used as shown in Fig. 7 in order to guarantee secure operation.

Figure 7: Shield for TMPs.

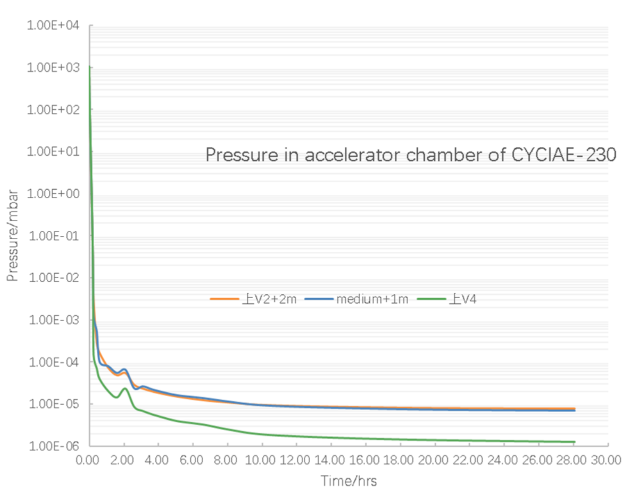

Figure 8: Pressure in accelerator chamber.

The Pressure in accelerator chamber shown in Fig 8, recorded on Mar 17th, 2020, shows that all requirements for the vacuum system have been achieved. The orange line in Fig. 7 means the measure gauge is 2 m from the flange. The blue line means the gauge is 1 m from the flange and the green one the measure gauge is fixed on the flange. So the further distance the worse pressure. Figure 9 shows pressure in accelerator chamber changes with RF power conditioning. Figure 10 shows dynamic pressure in CYCIAE-230 accelerator chamber changes with ion source and beam current recorded on May 19th, 2020.

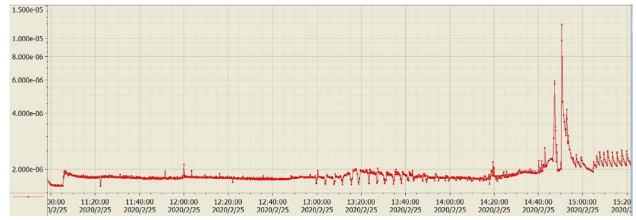

Figure 9: Pressure in accelerator chamber changes with RF power conditioning.

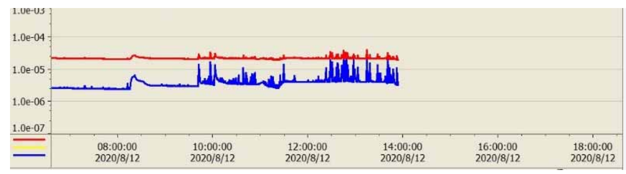

Figure 10: Dynamic pressure of CYCIAE-230 accelerator chamber.

After design, development and commission, CYCIAE-230 vacuum system has been successfully developed, static pressure is better than 5.6×10^{-7} mbar, and the dynamic pressure is better than 5×10^{-6} mbar, which is better than the design. And it has been in stable operation for more than two years.

CONCLUSION

The challenges for the vacuum system of CYCIAE-230 are as follows: the first one is that the exhaust system and the strong RF system share same magnet valley area; Second strong residual magnetic has to be considered in the design, magnetic field shielding is designed to protect the vacuum equipment; 1 SCCM gas load for inner ion source also is the challenge for CYCIAE-230 vacuum system. 8 sets of TMPs (1600 l/s) with magnet shields are installed on the valley of magnet poles, which also used as RF cavity, 1 set of TMP (200 l/s) with magnet shields is installed on the central magnet pole to increase the pressure of central region. After design, development and commission, we have got 5.6×10^{-7} mbar and 5×10^{-6} mbar separately for static pressure and dynamic pressure. And it has been in stable operation for more than two years.

REFERENCES

[1] T. J. Zhang *et al.*, "Design and construction of the main magnet for a 230 MeV superconducting cyclotron", *IEEE Trans. Appl. Supercond.*, vol. 28, no. 3, pp. 1-5, Apr. 2018. doi:10.1109/TASC.2017.2777469

[2] C. Wang *et al.*, "Superconducting coil system R&D for a 230 MeV superconducting cyclotron", *IEEE Trans. Appl. Supercond.*, vol. 28, no. 2, pp. 1-4, Apr. 2018. doi:10.1109/TASC.2017.2778706

[3] T. J. Zhang *et al.*, "Developments for 230 MeV superconducting cyclotrons for proton therapy and proton irradiation", *Nucl. Instrum. Methods Phys. Res. Sect. B*, vol. 406, no. 1, pp. 244-249, Sep. 2017. doi:10.1016/j.nimb.2016.11.010

[4] X. F. Zhu, S. P. Zhang, L. L. Guan, G. F. Pan, S. L. Wang, T. J. Zhang, "Design and research of a magnetic shield for turbo-molecular pump under strong stray magnetic field", *Chinese J. Vac. Sci. Technol.*, vol. 41, no. 212, pp. 1130-1135, 2021. doi:10.13922/j.cnki.cjvst.202106012

[5] Z. G. Yin, B. Ji, X. L. Fu, X. L. Cao, Z. L. Zhao, T. J. Zhang, "Design of RF system for CYCIAE-230 superconducting cyclotron", *Nucl. Instrum. Methods Phys. Res. A*, vol. 854, pp. 25-30, May 2017. doi:10.1016/j.nima.2017.02.051

[6] G. F. Pan *et al.*, "Development of vacuum system for 100 MeV high intensity proton cyclotron", *Atomic Energy Science and Technology*, 2018, vol. 52, no. 11: pp. 2084-2088. doi:10.7538/yzk.2018.youxian.0415

ISBN: 978-3-95450-212-7 ISSN: 2673-5482 doi:10.18429/JACoW-CYCLOTRONS2022-MOPO008

PLC BASED VACUUM CONTROL AND INTERLOCK SYSTEM OF THE CYCIAE-230 SUPERCONDUCTING CYCLOTRON BEAM LINE

Mingzhi Hu†, Xiaofeng Zhu, Jingyuan Liu, Hongru Cai, Zhiguo Yin, Tianjue Zhang, Ping Liu, Yang Wang, Bohan Zhao, Shangmeng Jiang, Aolai He, Qiqi Song, Fangdi Yang, Tianyi Jiang
China Institute of Atomic Energy, Beijing, China

Abstract

In the CYCIAE-230 superconducting cyclotron beam line, a vacuum system capable of providing a pressure of about 5E-4 Pa is required for particle beam transport. In order to provide adequate interlocking to safeguard the vacuum environment and ensure the regular transmission of particles within the beam line, a vacuum control system based on programmable logic controller (PLC) has been developed and integrated into the accelerator monitoring system. The PLC not only interfaces with the quick-acting relay based on interlocking signals but also interfaces with the equipment based on Profibus communication to monitor and control various parameters in the vacuum system, such as pump speed, vacuum pressure reading, valve status, water cooling status, etc. This work presents the structure and interface logic necessary for communication with a series of valves, vacuum gauges, and molecular pump controllers. Also presented is an interface approach between vacuum control and the rest of the accelerator control system.

INTRODUCTION

The CYCIAE-230 superconducting cyclotron leads out a proton beam with high energy and low current intensity, which is transmitted to the irradiation terminal through the beam line system. Figure 1 shows the complete layout [1].

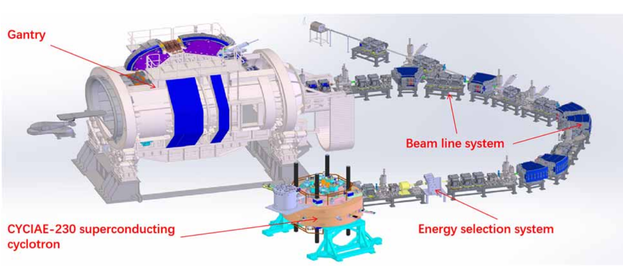

Figure 1: Layout of CYCIAE-230 and beam line.

Among them, the beam line control system is an essential part of proton therapy and is responsible for transmitting the proton beam with the energy needed for the therapy from the superconducting cyclotron to the therapeutic equipment. The general control equipment of the beam line includes: molecular pump power supply, mechanical pump, vacuum gauge, vacuum valve, water-cooled flowmeter, faraday cage, fluorescent target, etc. In this beam line control system, vacuum control and interlocking system is essential.

SYSTEM REQUIREMENT

The pneumatic system can control the opening and closing of the valves and correspondingly assist in the realization of the vacuum environment of the beamline. The water cooling system mainly ensures that the equipment, including molecular pumps, magnets, etc., works regularly at the appropriate temperature. In order to ensure the normal transmission of particles in the beamline, the vacuum system needs to provide a vacuum environment with a pressure of about 5E-4 Pa.

According to the design principle of obtaining an oil-free vacuum as much as possible and the requirement of vacuum degree, a molecular pump with a pumping speed of more than 300 L/s is selected as the vacuum obtaining equipment on the beam line, and a mechanical pump is equipped as the backing pump. Before starting the molecular pump, it is necessary to start the mechanical pump for vacuum pre-extraction, and the molecular pump can only be started when the vacuum is better than 1E-2 Pa. Figure 2 shows the layout of the beamline vacuum system.

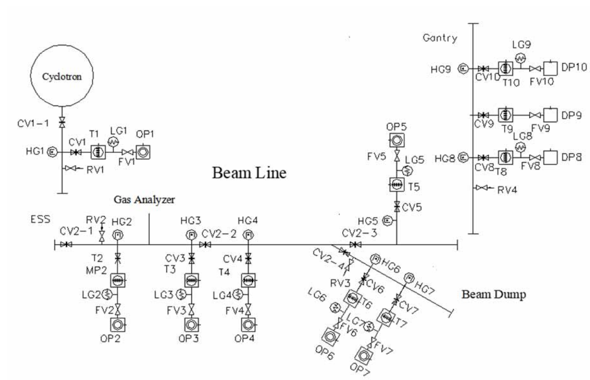

Figure 2: Layout of beam line vacuum system.

For machine protection and personal safety, it is necessary to design and add an interlocking system [2]. The vacuum interlock system will protect the vacuum gate valve to prevent it from accidentally closing during operation. At the same time, the interlocking system will also protect faraday cages, molecular pumps, magnets, and additional devices by monitoring temperature signals. If necessary, the beam line's vacuum interlocking system will notify the beam interlocking system to request that the beam be stopped to prevent additional operation [3].

† 2261398922@qq.com

ISBN: 978-3-95450-212-7 ISSN: 2673-5482 doi:10.18429/JACoW-CYCLOTRONS2022-MOPO008

CONTROL SYSTEM

The PLC was used to develop the vacuum control and interlocking system for the beamline. The programmable logic controller (PLC) is chosen because it is more suitable for this task, especially because it can provide simple and economical solutions for logic control, process automation, and condition monitoring. At the same time, the familiar Siemens PLC is preferred for control. In addition, its standardized hardware and software components make it easy to assemble and program. Rapid controls for vacuum interlocks and machine safety are written in ladder logic for simplicity and speed [4].

In our controller, the Siemens series CPU 1516-3 is used, which is primarily used to realize equipment interlocking and running sequence control. Other modules used are the Siemens series distributed IO slave station IM155-6, the analog input module, and the digital input and output module. With the TIA system setup, the analog input module can choose an input range of 0~10 V voltage and 0~20 mA current. Figure 3 shows a ladder diagram of the vacuum degree calibration from the analog input module, which converts the voltages into digital vacuum values.

Figure 3: Ladder diagram of voltage to digital vacuum value.

For the control of the mechanical pumps, the main controller keeps the output at 24 volts, drives the contact wire package to close, and controls the remote control of the mechanical pump to open. The main controller outputs 0 volts, drives the contact to disconnect the wire package, and controls the mechanical pump to shut off.

For the control of the molecular pumps, the TC353 molecular pump controller is used in this beamline. Connect to the PLC via PROFIBUS, create the corresponding GSD file, and import it into Snep7 for configuration. The address of the corresponding molecular pump can be set through the dip switches on TC353. The molecular pump is then controlled remotely by TIA. Figure 4 shows the wiring diagram of the Siemens DP connector. Figure 5 shows the ladder diagram of the molecular pump control. Table 1 lists the definition of I/O data.

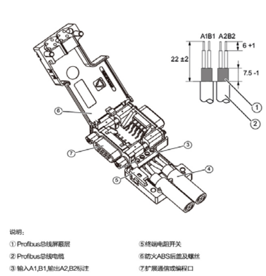

Figure 4: The wiring diagram of the Siemens DP connector.

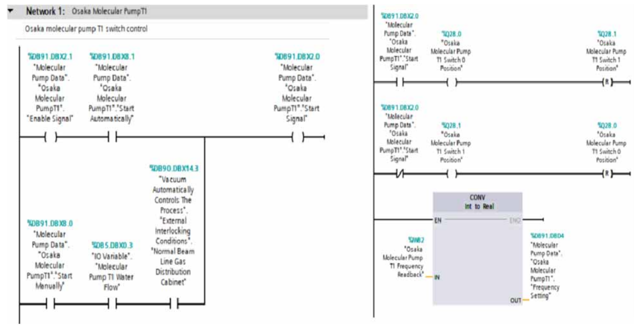

Figure 5: The ladder diagram of molecular pump control.

Table 1: I/O Data Definition

Name	Address	Length	Meaning
Status Byte		Byte Input	Length of data received in each communication
SDR	QB0	Byte Output	Control the start and stop of the equipment; when the output is 1, start the equipment; When it is 2, stop the equipment.
RSS	ID1	Byte Input	Status Word
RRS	PIW256-257	Word Input	Output frequency (rotational speed)

Due to the cost, stability, reliability, and ease of maintenance, the vacuum control and interlock system for this beamline was designed based on data communication between the CPU and distributed IO slave stations. The basic protocol for data transactions is called the Modbus protocol. It uses a query-response loop between the master and slave devices. The fundamental function codes are read from or written to a single or multiple register [5]. The protocol used on Ethernet is called Modbus TCP/IP. It basically inserts a Modbus frame into a TCP frame and sends it as a message. Packaging information can be found in the Modbus/TCP specification manual.

The basic control logic of the vacuum control and interlocking system is as follows: under the condition of ensuring the normal water-cooling and pneumatic state of the equipment, first close the vent valve, then close the gate valve of the beam line, and divide the beam line into four sections to extract vacuum. The mechanical pump and front valve are turned on for pre-pumping, and the molecular pump is turned on when 1E-2 Pa is reached for high vacuum pumping. Observe the number on the vacuum gauge, and when each section reaches the high vacuum state, open the gate valve of the beamline and complete the vacuum extraction. Figure 6 shows the block diagram of this control system.

ISBN: 978-3-95450-212-7 ISSN: 2673-5482 doi:10.18429/JACoW-CYCLOTRONS2022-MOPO008

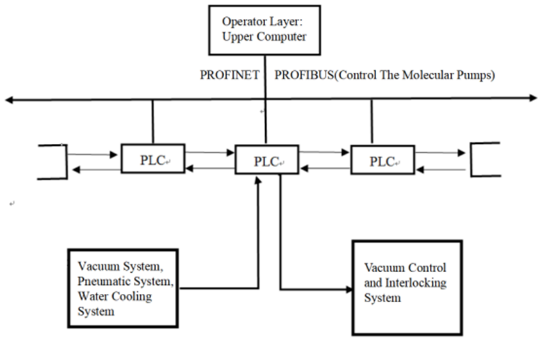

Figure 6: Control system block diagram.

This beam line water flow monitoring interlock system is monitored by piston pointer flow switches. This piston pointer type flow switch is equipped with a spring-supported piston. Based on the principle of magnetic induction, when the flow reaches a preset value, the mechanical structure triggers a magnetic switch to emit a switching signal for the on-off detection of the flow. Based on this working principle, the water flow signal can be converted into a digital signal, and the digital input signal module can be directly used to collect the water flow signal.

The main function of the PLC program is to call each functional module according to the actual work flow of the bench equipment. Figure 7 shows a flowchart of the PLC program.

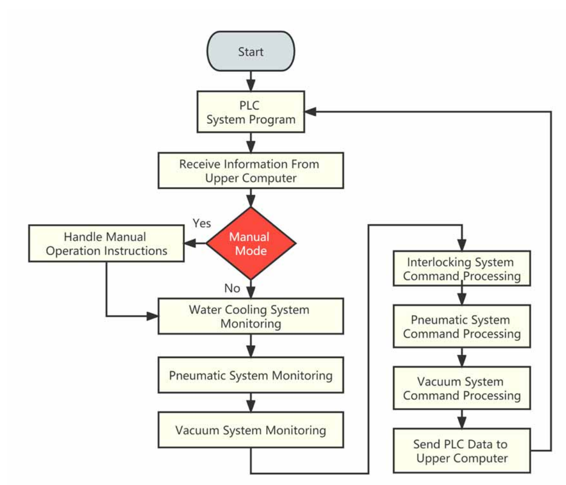

Figure 7: The flow chart of the PLC program.

The realization of the human-machine interface is based on the design pattern of the producer and consumer, and it is also designed for the CYCIAE-230 beam line control program.

Figure 8 shows the human-machine interface of the PLC based vacuum control and interlock system for the beamline. Figure 9 shows the interface of the vacuum gauge controller of the vacuum system, from which the vacuum state of this beamline can be seen. Among them, the input and output variables of digital quantities are mainly in a set state through a set cycle period. And the timer compares the timing delay of the operation code for each step with the condition of the next operation.

Figure 8: Human Machine Interface (HMI).

Figure 9: The interface of the vacuum gauge controller.

CONCLUSIONS

The vacuum control and interlock system of the beam line based on PLC has been successfully applied to the beam line of the CYCIAE-230 superconducting cyclotron and tested. The system can successfully operate valves, mechanical pumps, and molecular pumps and monitor the status of related equipment. Some vacuum interlocking operations are also being verified. At present, the beam line control system based on PLC is being further developed, which will make the beam line-related functions, including the beam diagnosis control system, more perfect and allow it to better adjust the proton beam from the accelerator to the treatment end.

REFERENCES

[1] M. Yin *et al.*, "Mechanical Design of Beam Lines for a 230 MeV SC Cyclotron at CIAE," in *Proc. Cyclotrons'19*, Cape Town, South Africa, Sep. 2019, pp. 42-44. doi:10.18429/JACoW-CYCLOTRONS2019-MOP008

[2] H. S. Kim *et al.*, "PLC Control System for Vacuum and 20 kW RF Amplifier", in *Proc. Cyclotrons'16*, Zurich, Switzerland, Sep. 2016, pp. 215-217. doi:10.18429/JACoW-Cyclotrons2016-TUP22

[3] M. Zaera-Sanz *et al.*, "Methodology, Design and Physical Deployment of Highly Dependable PLC Based Interlock Systems for ESS," in *Proc. IPAC'17*, Copenhagen, Denmark, May 2017, pp. 1887-1889. doi:10.18429/JACoW-IPAC2017-TUPIK083

[4] C. E. Peters *et al.*, "PLC Based Vacuum Controller Upgrade and Integration at the Argonne Tandem Linear Accelerator System," in *Proc. ICALEPCS'17*, Barcelona, Spain, Oct. 2017, pp. 724-727. doi:10.18429/JACoW-ICALEPCS2017-TUPHA131

[5] S. Ramamoorthy *et al.*, "NSLS Control Monitor and Its Upgrade", in *Proc. PAC'93*, Washington D.C., USA, Mar. 1993, pp. 1849-1852.

ISBN: 978-3-95450-212-7 ISSN: 2673-5482 doi:10.18429/JACoW-CYCLOTRONS2022-MOPO009

STUDY ON THE EXTRACTION OF A COMPACT CYCLOTRON FOR BNCT

Luyu Ji†, Shizhong An, Tianjian Bian, Fengping Guan, Sumin Wei, Jiansheng Xing, Huaidong Xie
China Institute of Atomic Energy, Beijing, China

Abstract

An 18 MeV, 1 mA H^- compact cyclotron is under design at China Institute of Atomic Energy (CIAE). The proton beam bombards a beryllium target, producing high-flux neutron beam for Boron Neutron Capture Therapy (BNCT). Stripping extraction is adopted in this cyclotron. The position of the stripping point affects the trajectory and beam quality of the extracted beam. In this paper, we use orbit-tracking method to simulate the beam trajectory and emittance with different positions and tilt angles of stripping foil, and adopt the extraction point whose radius is 53.6 cm, azimuth is 57° and the tilt angle of the stripping foil is 15°.

INTRODUCTION

BNCT is one of the most advanced cancer treatment technologies in the world because of its advantages of less toxic and relatively low cost [1]. Because the neutron beam of the accelerator has the characteristics of adjustable energy, and the accelerator also has the safety advantage that the reactor does not have, the accelerator-based BNCT (AB-BNCT) has been paid more and more attention by all countries [2].

CIAE has been developing clinical cyclotron since 2010. In 2012, PET cyclotron CYCIAE-14 was successfully developed, which can provide 14 MeV, 200 μA proton beam [3]. The 14 MeV, 1 mA BNCT high-intensity proton cyclotron developed by CIAE was installed in Sept. 2020, and in Jan. 2022, the extracted beam current reached 1 mA. At present, neutron target experiment and accelerator stability test are under way. In order to improve the neutron flux and product medical isotopes, we plan to develop a new cyclotron, increasing the extraction energy to 18 MeV.

THE POSITION OF THE STRIPPING FOIL

External H^- ion source and stripping extraction are adopted in this cyclotron. The 35 keV H^- beam is produced by a multi-cusp ion source [4] and vertically injected into the cyclotron by an electrostatic inflector. Accelerated over 100 turns, H^- beam is stripped by a carbon foil then extracted to the beam line. When accelerated to 18 MeV, the beam can be extracted at this energy by a stripping foil at any azimuth. However, considering the construction cost and compatibility with other systems, the following restrictions are proposed for the position of stripping foil:

(1) The stripping probe is installed on the magnet pole.
(2) The extracted beam passes through the valley of yoke.
(3) The extracted beam doesn't pass through the RF cavities.

The two RF cavities are installed in the valley at 0° and 180°, so the beam can be extracted in the valley at 90° and 270°. Due to the symmetry of the cyclotron, the extraction designs of the two valleys are the same. Here, the extraction design at 90° valley is taken as an example.

By orbit-tracking program, the reference particle is tracked from 1 MeV to the extraction region. The orbits after extraction are shown in Fig. 1. Compared with the radius of stripping foil, the azimuth has a greater impact on the trajectory. The azimuth should be within 52°-60° to make the beam pass through the valley of yoke.

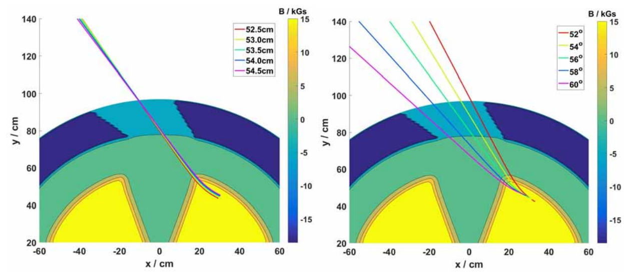

Figure 1: Extracted beam trajectory with different radii (left) and azimuths (right) of the stripping foil.

MULTI-PARTICLE SIMULATION FOR STRIPPING EXTRACTION

Distribution on the Stripping Foil

In the physical design of extraction, the emittance and beam envelope of the extracted beam are expected to be as small as possible, which is beneficial to reduce beam loss and provide higher quality beam. The multi-particle tracking method is used to simulate the emittance, beam envelope and other parameters of the extracted beam to optimize the position of stripping foil.

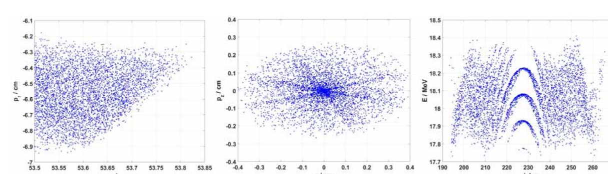

Figure 2: The particle distribution on the stripping foil in radial (left), axial (middle) and longitudinal (right) phase space.

Particles are tracked from 1 MeV. According to the acceptance of this cyclotron, initial horizontal acceptance is 4 π-mm-mrad and phase width is 60°. The result is shown in Fig. 2. τ is the RF time:

†luyu_ji@163.com.

ISBN: 978-3-95450-212-7 ISSN: 2673-5482 doi:10.18429/JACoW-CYCLOTRONS2022-MOPO009

$$V = V_0 \sin \tau \tag{1}$$

We define a momentum unit:

$$\text{Momentum unit} = m_0 c / a \tag{2}$$
$$a = c/\omega_0 \tag{3}$$

where m_0 is the rest mass, ω_0 is the orbital frequency, and a is the cyclotron radius. Thus, all momenta have length units. The beam size on the stripping foil 3.2 mm × 8.0 mm, the size of stripping foil should be greater than it. Because of the serious overlap of neighbour bunches in extraction region, the multiple turns extraction is obvious in the vertical phase space distribution. The rms energy spread is 0.064 MeV.

Distribution at the Entrance of the Beam Line

One of the purposes of the extraction design is to make the beam have a good distribution when entering the beam line, which is beneficial to the beam line design. At the same time, the distribution the entrance of the beam line is obtained as the initial condition of the beam line design. The cyclotron radius is 96.5 cm, and we set the radius of 97.0 cm as the entrance of the beam line. Particles are tracked from the stripping to the entrance of the beam line. The result with the natural coordinate system is shown in Fig. 3. The symbols *x'* and *y'* are the relative rates at which the particle is moving away from the horizontal and vertical axes. The red ellipses are fitted phase ellipses. Because particles are not accelerated after being stripped, the longitudinal distribution is similar to that on the stripping foil.

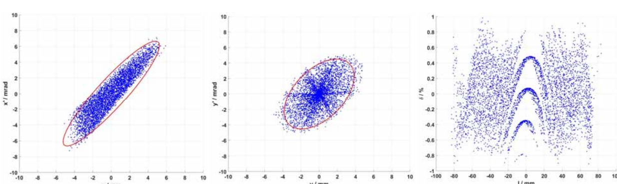

Figure 3: The particle distribution at the entrance of the beam line in horizontal (left), vertical (middle) and longitudinal (right) phase space.

BEAM FOCUSING AT EXTRACTION

As shown in Fig. 1, beam trajectories at the stripping foil with different azimuths are quite different. The radial tune ν_r and the vertical tune ν_z are calculated by Eq. (4) and (5).

$$\nu_r^2 = 1 - n \tag{4}$$
$$\nu_z^2 = n \tag{5}$$

where n is the field index:

$$n = -\frac{r}{B}\frac{dB}{dr} \tag{6}$$

If the stripping point is close to the centre of the magnetic pole, the field index will decrease. Therefore, the closer the stripped foil is to the inside of the magnetic pole, the stronger the radial focusing is, and the weaker the axial focusing is. The simulation results are shown in Fig. 4.

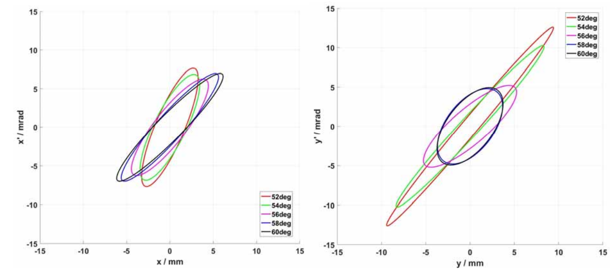

Figure 4: The horizontal (left) and vertical (right) distributions with different azimuths of the stripping foil at the entrance of the beam line.

According to the extraction study on the cyclotron CYCIAE-100, if there is an angle α between the stripping foil and the normal direction of the beam, x' and y' will increase [5]:

$$\begin{cases} \Delta x' = \frac{2\tan\alpha}{\rho}x - \frac{2n\tan\alpha}{\rho^2}x^2 - \frac{2\tan\alpha}{\rho}x\delta \\ \Delta y' = -\frac{2n\tan\alpha}{\rho^2}xy + \frac{2n\tan\alpha}{\rho^2}xy\delta \end{cases} \tag{7}$$

where ρ is the bending radius of the particle. Ignoring higher terms, Eq. (7) can be written as:

$$\begin{cases} \Delta x' = \frac{2\tan\alpha}{\rho}x \\ \Delta y' = 0 \end{cases} \tag{8}$$

Therefore, the tilt angle of stripping affects the horizontal focusing, which is similar to the inlet and outlet angles of dipoles. The simulation results in Fig. 5 are consistent with the theoretical analysis.

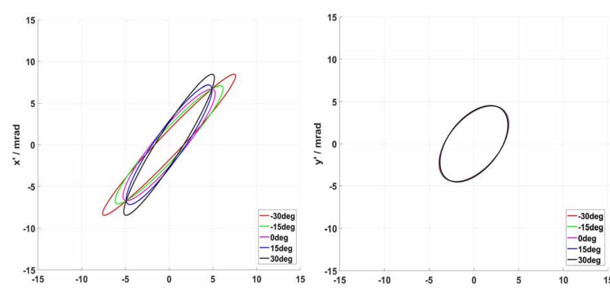

Figure 5: The horizontal (left) and vertical (right) distributions with different tilt angles of the stripping foil at the entrance of the beam line.

In conclusion, there are two methods to adjust the focusing at extraction. The azimuth of stripping foil affects both horizontal and vertical focusing, and the tilt angle only affects horizontal focusing. Therefore, we first choose an appropriate azimuth to obtain good vertical focusing. Then adjust the tilt for better horizontal focusing. The azimuth of 57° and the tilt angle of 15° are adopted, and the beam parameters are shown in Table 1.

ISBN: 978-3-95450-212-7 ISSN: 2673-5482 doi:10.18429/JACoW-CYCLOTRONS2022-MOPO009

Table 1: The Extracted Beam Parameters at the Entrance of the Beam Line ($\sqrt{6}$×rms value)

Parameters	Value
ε_x/π-mm-mrad	13.49
x/mm	4.81
x'/mrad	7.04
α_x	-2.30
β_x/mm·mrad^{-1}	1.71
γ_x/mm^{-1}·mrad	3.68
ε_y/π-mm-mrad	15.00
y/mm	3.82
y'/mrad	4.52
α_x	-0.57
β_y/mm·mrad^{-1}	0.97
γ_y/mm^{-1}·mrad	1.36
l/mm	99.99
δ/%	0.87

THICKNESS OF THE STRIPPING FOIL

The stripping foil with a certain thickness is required for high stripping efficiency. However, a thick foil will increase the energy loss of the beam on the foil, leading to the decline of the lifetime of the carbon foil. Therefore, it is necessary to select the thinnest carbon foil while ensuring sufficient stripping efficiency.

$$\frac{dF_j}{d\pi} = \sum_i \left(F_i\sigma_{ij} - F_j\sigma_{ji}\right) \tag{9}$$

The fraction of ions F_j can be calculated by Eq. (9). Where i and j are charge states, σ_{ij} is the charge exchange cross-section of ions from charge state i to j, and π is the foil thickness. Compared with the electron loss process, the electron capture process is negligible. Therefore, the solution of Eq. (9) is written as:

$$\begin{cases} F_{-1} = e^{-(\sigma_{-10}+\sigma_{-11})\pi} \\ F_0 = \frac{\sigma_{-10}}{\sigma_{-10}+\sigma_{-11}-\sigma_{01}}\left[e^{-\sigma_{01}\pi} - e^{-(\sigma_{-10}+\sigma_{-11})\pi}\right] \\ F_1 = 1 - F_{-1} - F_0 \end{cases} \tag{10}$$

The reaction cross sections of different energies have the relation:

$$\sigma \propto 1/\beta^2$$

where β is the relativistic factor. We adopt the cross-sections measured at 800 MeV [6] and estimate those at 18 MeV. Calculated fractions are depicted in Fig. 6. The carbon foil with a thickness 1.36×10^{18} cm^{-2} (27 μg·cm^{-2}) has a stripping efficiency of 99.9%.

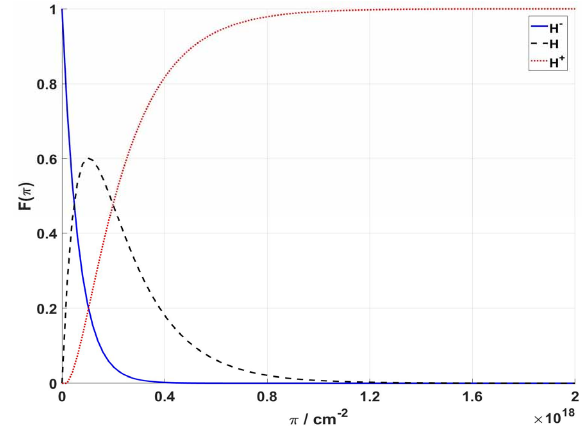

Figure 6: Fractions of hydrogen beam with different thickness of the carbon foil.

CONCLUSION

Orbit-tracking method is used to simulate the extraction of the 18 MeV BNCT cyclotron. The initial normalized emittance of 4 π-mm-mrad is used in the simulation. The azimuth and tilt angle of the stripping foil affect the beam focusing at extraction. The azimuth of 57° and the tilt angle of 15° are adopted. At the entrance of the beam line, the horizontal half size is 4.81 mm and the vertical half size is 3.82 mm.

REFERENCES

[1] M. A. Dymova *et al.*, "Boron neutron capture therapy: Current status and future perspectives," *Cancer Communications*, vol. 40, no. 9, pp. 406-421, Aug. 2020. doi:10.1002/cac2.12089

[2] S. Kawabata *et al.*, "Survival benefit from boron neutron capture therapy for the newly diagnosed glioblastoma patients," *Appl. Radiat. Isot.*, vol. 67, no. 7-8, pp. S15-S18, Jul. 2009. doi:10.1016/j.apradiso.2009.03.015

[3] T. Zhang et al., "Overall design of CYCIAE-14, a 14 MeV PET cyclotron," *Nucl. Instrum. Methods Phys. Res. Sect. B*, vol. 269, no. 24, pp. 2950-2954, Dec. 2011. doi:10.1016/j.nimb.2011.04.049

[4] X. L. Jia *et al.*, "Ion source and injection line for high intensity medical cyclotron," *Rev. Sci. Instrum.*, 2014, vol. 85, no. 2, p. 02C102, Feb. 2014. doi:10.1063/1.4829739

[5] S. M. Wei *et al.*, "Envelope Control of the Extracted Beam from Compact Cyclotron", in *Proc. SAP'17*, Jishou, China, Aug. 2017, pp. 31-33. doi:10.18429/JACoW-SAP2017-MOPH03

[6] M. S. Gulley *et al.*, "Measurement of H$^-$, H^0, and H$^+$ yields produced by foil stripping of 800-MeV H− ions," *Phys. Rev. A*, vol. 53, no. 5, p. 3201, May 1996. doi:10.1013/PhysRevA.53.3201

ISBN: 978-3-95450-212-7 ISSN: 2673-5482 doi:10.18429/JACoW-CYCLOTRONS2022-MOPO011

DESIGN AND OPERATION OF THE NEW FAST BEAM CHOPPER BETWEEN TANDETRON AND CYCLOTRON

T. Fanselow†, J. Bundesmann, A. Dittwald, A. Denker[1], U. Hiller
Helmholtz-Zentrum Berlin GmbH für Materialen und Energie (HZB), Berlin, Germany
[1]also at Berliner Hochschule für Technik, Berlin, Germany

Abstract

In collaboration with Charite - Universitätsmedizin Berlin, patients with ocular melanomas are treated with protons at Helmholtz Zentrum Berlin. Accompanying research includes beam delivery for Flash irradiation, thus it became necessary to set up a fast and reliable beam Chopper. The new beam Chopper can deliver much shorter pulses than needed for Flash irradiation, minimum pulse widths down to 70 ns at 1 kV amplitude can be delivered. A short description of the design and installation process, which occurred in 2020, and the experiences of the first 2 years of operation with the new fast beam Chopper system is presented.

INTRODUCTION

At the cyclotron of the Helmholtz Zentrum Berlin two injectors can be used for tumor therapy and experiments. A 6 MV Van-de-Graaff injector and a 2 MV Tandetron (Fig. 1). Due to its stability and reliability, the Tandetron is mainly used for tumor therapy and Flash experiments [1]. For rapid beam on/off switching in Flash experiments, a mechanical scissor-like beam stop has been used in Tandetron operation to date. Due to the sluggish mechanics, the beam stop requires 40 ms to fully open and 47 ms to fully close. Since Flash experiments require beam pulses between 1-100 ms, the mechanical beam stop can only be used to a limited extent. Due to this limitation, it was necessary to build a fast beam Chopper that can realize minimum pulse widths of 1 ms. For this purpose, 1 m beamline is available directly behind the Tandetron. The deflection of the beam is to be done via two deflection plates. The setup of the new Chopper is to be done via an existing CAMAC power supply controller, whereas the Beam control runs via the FPGA and LabVIEW of the flash control.

DESIGN OF THE NEW FAST BEAM CHOPPER

An existing 94 cm long vacuum chamber with deflector plates was selected for the fast on/off switching of the beam. The available area directly behind the tandetron is 1m long and has so far only been used for steerer tests. For the complete setup of the Chopper, in addition to the vacuum chamber with the deflection plates, a fast semiconductor switch, processing and control electronics including power supply, a HV power supply for the deflection plates and a cooling system are required.

† timo.fanselow@helmholtz-berlin.de

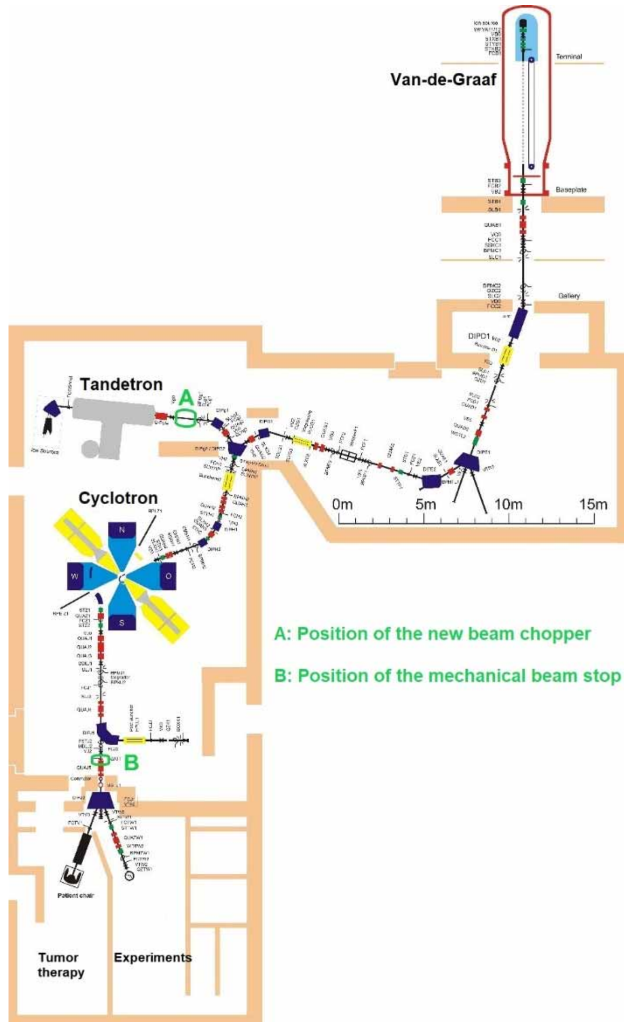

Figure 1: Layout of the accelerator complex including the location of the mechanical beam stop and the new Fast Beam Chopper.

VACUUM CHAMBER AND DEFLECTION PLATES

The existing vacuum chamber with deflection plates is 94 cm long and has 2 DN 160 CF flanges at the inlet and outlet. Another DN 200 CF flange is provided for an ion getter pump. Furthermore, there are two flanges for the HV voltage feed-through of the deflection plates as well as 4 adjusting screws for the adjustment of the plate distance. The already existing 4 cm wide deflection plates were reworked and shortened to 90 cm to avoid interference at the input and output of the Chopper. The two deflection plates made of V4A steel were then aligned with the beam axis and adjusted to 2 cm spacing (Fig. 2).

ISBN: 978-3-95450-212-7 ISSN: 2673-5482 doi:10.18429/JACoW-CYCLOTRONS2022-MOPO011

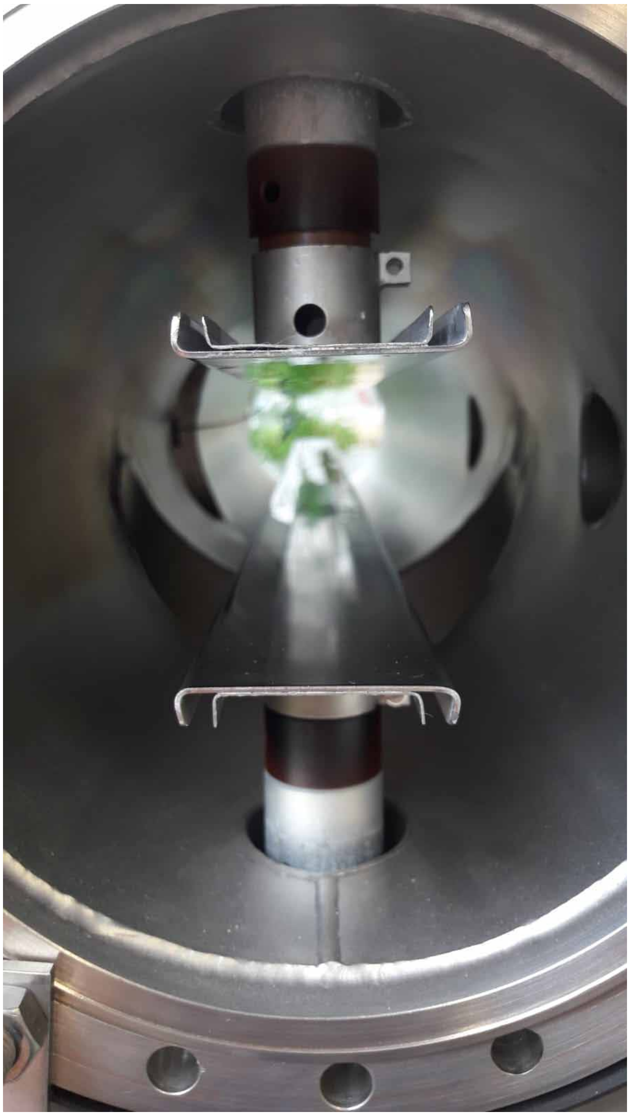

Figure 2: Deflection plates.

Figure 3: Vacuum chamber with the frame made of Item profiles.

Furthermore, the vacuum feedthroughs of the plate connections were renewed and provided with new seals. For the installation in the Beamline behind the Tandetron, a frame made of Item profiles was built that accommodates the vacuum chamber itself as well as the 19-inch electronic crates units and the ion getter pump (Fig. 3).

FAST SWITCHING HALF BRIDGE MOSFET MODULE

A half-bridge Mosfet module from the Behlke company was used for fast switching on and off of the deflector plate. The Fast Square Wave Pulser FSWP 41-03 from Behlke is designed for operating voltages up to 4 kV and can handle a peak current of 30 A. The maximum switching frequency is 3 MHz with sufficient cooling and power losses up to 1500 W can be dissipated. Depending on the capacity of the connected load, a pulse rise and fall time of 8 ns can be achieved with a minimum pulse duration of 50 ns. For the Chopper the FSWP Mosfet module with direct liquid cooling was chosen to allow higher switching frequencies than needed for the flash measurements. For this a liquid cooling including heat exchanger had to be provided. For the operation of the FSWP Mosfet module, two supply voltages of 15 V 1.5 A and 120 V 1 A are required in addition to the HV voltage to be switched (Fig. 4).

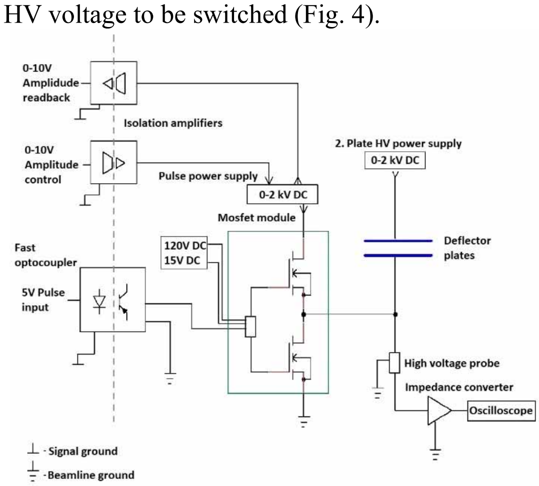

Figure 4: Operating principle of the fast Chopper.

ISBN: 978-3-95450-212-7 ISSN: 2673-5482 doi:10.18429/JACoW-CYCLOTRONS2022-MOPO011

The FSWP Mosfet module is controlled by a 5 V TTL signal with an input impedance of 100 Ohm. For the galvanic decoupling between Chopper and control two isolation amplifiers and fast optocouplers were used.

PROCESSING AND CONTROL ELECTRONICS

The pulse electronics mainly consists of 4 segments the power supply, the control electronics, the pulse processing and the FSWP Mosfet module itself (Fig. 5). The power supply section provides the 15 V and 120 V for the FSWP Mosfet module, further 15 V for the isolation amplifiers and 24 V for the control electronics. For the control electronics a Siemens LOGO PLC is used, which handles the sequence control of the Chopper including the connection to the CAMAC Power Supply Controller and the FUG MCP 2800-2000 Power Supply. In addition, the control electronics is responsible for monitoring error conditions of the FSWP Mosfet module, the power supply and the flow meter. Pulse processing provides galvanic isolation between the Chopper and the control system. Fast optocouplers for the pulse signals and isolation amplifiers for the analog amplitude setting and readback are used.

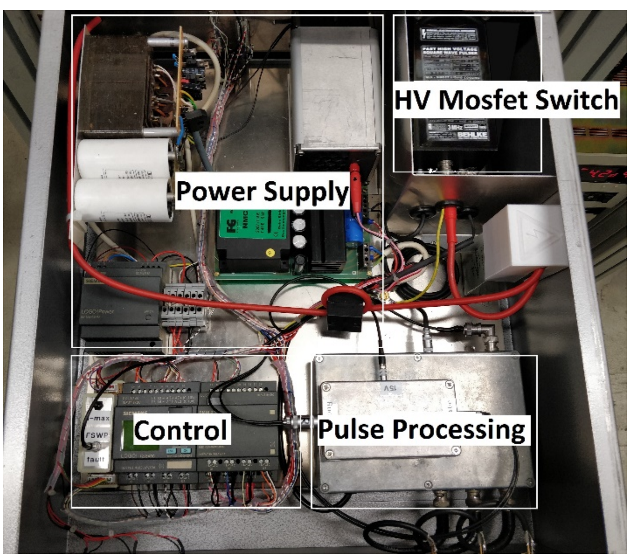

Figure 5: Processing and control electronics crate.

HV POWER SUPPLIES

For each of the two deflection plates, an HV power supply is required which is controlled by a CAMAC power supply controller. For the fixed voltage supply required to deflect the beam, an HMI N102N power supply unit with 0-5 kV 0.2 mA housed in the NIM frame is used. The voltage of the other deflector plate required to deflecting in the beam again is supplied by a FUG MCP 2800-2000 0-2kV 1.2 A, this voltage being switched via the FSWP Mosfet module (Fig. 6).

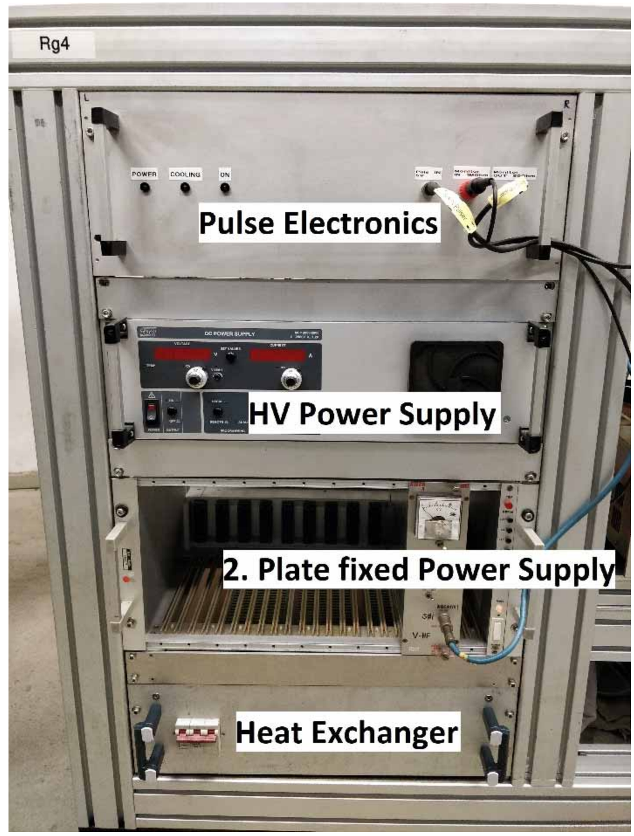

Figure 6: Chopper crates.

COOLING

For the direct liquid cooling of the FSWP Mosfet module the non-conductive HT135 PFPE Cooling Fluid from Galden is used. To remove the heat, the cooling fluid is pumped through a Behlke HE-10 heat exchanger using an EHEIM universal 600 pump, with counter-cooling provided by an external cooling compressor. Both the temperature and the flow rate of the cooling fluid are monitored and lead to the shutdown of the FSWP Mosfet module in the event of a fault. The temperature monitoring is done directly in the FSWP Mosfet module itself. For flow monitoring a UCC DFC.9000 flow meter is used which is evaluated by the control electronics. The waste heat generated in the Pulse Electronics Crate is dissipated directly to the outside via an 80 x 80 mm fan.

INSTALLATION

The preparations for the installation started already at the beginning of 2020 and included the ordering of the required components, the reworking of the vacuum chamber including leakage test, the construction of the Item frame, the Processing and the Control electronics. In addition, the CAMAC connection to the control system and the mains voltage line with 3x400 V 16A were installed. The actual installation took place in summer 2020 and had to be done between 2 beam time blocks within 3 weeks. After ventilating the vacuum section behind the tandetron, the relevant beamline was removed and the Item frame including the Chopper vacuum chamber was installed. The vacuum

ISBN: 978-3-95450-212-7 ISSN: 2673-5482 doi:10.18429/JACoW-CYCLOTRONS2022-MOPO011

chamber including deflector plates was measured optically on the beam axis using theodolites and reference points. The beamline section was then evacuated and baked out again, and finally a leak test and residual gas analysis were performed using a mass spectrometer. Initial functional testing included manual application of static voltages of 0-2 kV to both deflection plates and subsequent commissioning of the control electronics and remote operation via the CAMAC Power Supply Controller.

Figure 7: Beamline behind the Tandetron before installation of the Chopper.

Figure 8: Beamline behind the Tandetron after installation of the Chopper.

EXPERIENCES OF THE FIRST 2 YEARS

The first test with the beam showed that amplitudes between 0.7 kV-1 kV are sufficient for a complete deflection of the 3.6 MeV proton beam. In the first flash measurements pulse widths of 1ms could be achieved without any problems with a rise and fall time of only 18 ns. Subsequent measurements with continuous pulses showed that from a frequency of 2.5 MHz strong reflections occur at the pulsed deflection plate. Therefore, frequencies above 2.4 MHz should be avoided for stable operation. The minimum pulse width to be achieved is 70 ns, whereby the pulse shape is determined to a large extent by the rise and fall time. When performing Flash measurements, much more precise rise and fall times of the beam were found. Together with the possible shorter pulse times, a more precise Flash irradiation is now possible. Problems were encountered with static charging of the deflector plates during the beamtime with the Chopper turned off, which damaged one FSWP mosfet module and broke several suppressor diodes. After switching off the Chopper, both deflection plates are now manually grounded to prevent static charging. Furthermore, a leak in the cooling system caused the Chopper to fail during test measurements.

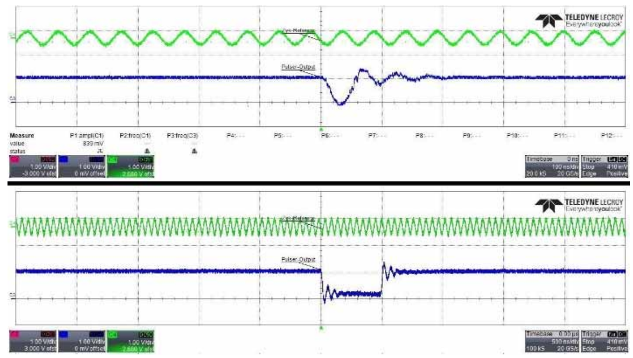

Figure 9: Above in blue is a 70 ns pulse and below in blue is a 500 ns pulse. The green signal is in both cases the cyclotron frequency of 19.3178 MHz.

CONCLUSION

The beamline area behind the Tandetron provided enough space for the mechanical setup of the Chopper. The flat beam profile at this location allows a small plate spacing of only 20 mm and thus a deflection amplitude of less than 1 kV. The achievable pulse frequencies and pulse widths are far better than required for Flash irradiations. For experiments, pulses synchronized to the cyclotron frequency with repetition rates up to 2.4 MHz and minimum pulse widths of 70 ns can be achieved with the DC beam of the Tandetron.

OUTLOOK

Work is being done on automated grounding of the deflector plates when the Chopper is switched off. In addition, a solution is being worked on to detect leaks in the cooling system earlier. Due to the supply difficulties of spare parts as a result of the Covid 19 pandemic, timely procurement of spare parts is necessary.

REFERENCES

[1] G. Kourkafas *et al.*, "Expanding proton FLASH capabilities to kGy/s within ms for clinical applications at HZB", presented at the Flash Radiotherapy and Particle Therapy Conf. (FRPT'22), Barcelona, Spain, Nov. 2022. doi:10.14293/S2199-1006.1.SOR-.PPRDNQW.v1

ISBN: 978-3-95450-212-7 ISSN: 2673-5482 doi:10.18429/JACoW-CYCLOTRONS2022-MOPO012

AN EMBEDDED BEAM DIAGNOSTIC ELECTRONICS FOR 230 MeV SUPERCONDUCTING CYCLOTRON RADIAL PROBE AND SCANNING WIRES

Tianyi Jiang, Zhiguo Yin†, Yang Wang, Qiqi Song, Xueer Mu, Ping Liu, Tianjue Zhang
China Institute of Atomic Energy, Beijing, China

Abstract

For the 230 MeV superconducting cyclotron, once again, the differential radial probe has been proven to be crucial for the beam commission procedure. It can provide various information about the particles inside the cyclotron, such as the vertical position, the relative intensity as well as the oscillation frequency and radius, etc. In practice, however, the electronics system suffered from the leaking alternating RF field as well as the static magnetic field. Besides the EM shielding, an absorptive high-frequency filter has been included as the first element of the readout electronics. A high dynamic range readout electronic unit has been included to adapt to the fluctuation of the beam in the hole commissioning phase. The electronics box is designed as a network-attached embedded device so that it can be powered by a POE switch and transmits measurement results via MODBUS protocol. A dedicated digital signal processor and calibration units are also included, together with the ADCs, to facilitate the daily calibration process. The same electronics are used for the beamline wire scan system to determine the position of the beam, with a small improvement at a lower range. The design of this multi-purpose beam diagnostics electronics will be reviewed in this paper, together with several measurement results.

INTRODUCTION

The China Institute of Atomic Energy (CIAE) is developing a 230 MeV superconducting cyclotron, a commercial prototype that can be used for proton therapy, which is designed to induce energy of 230 MeV and beam current over 300 nA [1, 2]. During the beam commission procedure, the radial probe can measure beam parameters from a radius of 300 mm to 850 mm inside the cyclotron. It can provide the intensity and the alignment information of the beam. The material of the head of the radial probe is tungsten, the beam will deposit on the head, so it's an interception measurement method. The drive unit of the radial probe is mounted on a stand and the rod drives the head, which is fixed to the drive unit. The drive unit drives the head in a reciprocating motion inside the cyclotron and a potentiometer determines the position of the head movement [3, 4]. Scanning wires is a non-intercepting beam diagnostic method used to measure beam position on the beamline [5]. The probe head used by CIAE is a double-wire structure with an angle of 90°. The material of the measuring strip is a copper alloy with a width of 5 mm and a thickness of 0.1 mm.

Since the beam current may work in the case of low intensity and high intensity, CIAE designed a beam diagnostic electronics system. The existing diagnostic electronics for 230 MeV superconducting cyclotron radial probe and scanning wires can measure currents from 1 pA to 10 mA range. However, its measurements are not continuous, and the readout electronic unit is based on a trans-impedance amplifier that requires manual switching of the different feedback resistors depending on the signal being measured. The data processing module of the existing wire scan system is based on PLC, and the sampling rate (2 Hz) of the system is also low.

DESIGN OVERVIEW

The new embedded electronics under development will eventually replace the existing boards used for the initial phase of the 230 MeV superconducting cyclotron project. The new electronics allow for continuous, high dynamic range measurements with higher sampling rates than previous designs.

The new electronics box is designed as a network-attached embedded device so that it can be powered by a POE switch and transmits measurement results via MODBUS protocol. To reduce electromagnetic interference, an absorptive high-frequency filter (RLC filter) has been included as the first block of the readout electronics. The core part of the electronics is the high dynamic range readout electronics unit. The board has 3 I/V conversion channels, each including a wide dynamic range I/V converter and a weak signal I/V converter. The 4 channels (3 I/V conversion channels and a position signal channel) are digitized using AD7665 16-bit ADCs, and then further processed on the DSP, Butterworth filter is applied to process the raw data. Embedded SRAM is used for the temporary storage of measurement data, while a calibration unit facilitates the daily calibration process. Triaxial connectors are used to transmit beam current signals to adapt to weak signal detection. A protection circuit (gas discharge tube and JFET) is set before the readout electronics unit to prevent accidental damage.

† zhiguoyin@ciae.ac.cn

ISBN: 978-3-95450-212-7 ISSN: 2673-5482 doi:10.18429/JACoW-CYCLOTRONS2022-MOP0012

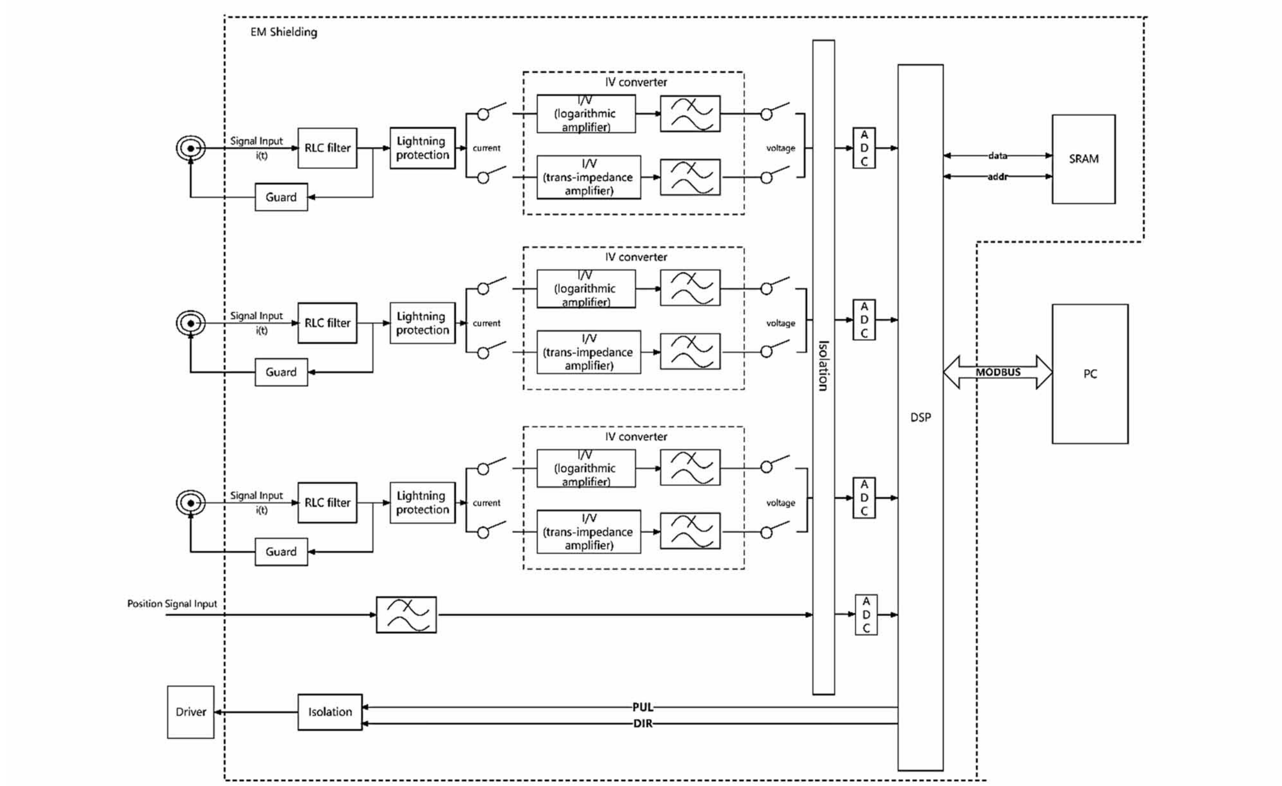

Figure 1: Design of the beam diagnostic electronics.

READOUT ELECTRONICS FOR HIGH DYNAMIC RANGE CURRENTS

The Basic Principle of I/V Converters

The principle of the wide dynamic range I/V converter is based on logarithmic amplifiers. In the linear domain, a high dynamic range signal will generally cause the existing ADCs to fail to work properly, logarithmic amplifiers can effectively solve this problem. The basic schematic of the logarithmic amplifier is shown in Fig. 2, using the logarithmic relationship between the emitter voltage and the collector current of a transistor [6].

$$V_O = -\frac{kT}{q}\ln\left(\frac{I_{in}}{I_s}\right), \quad (1)$$

where k is the Bolzmann's constant ($1.38 \times 10^{-23} J/K$), T the temperature in K, q the electronic charge ($1.6 \times 10^{-19} C$), and I_s a reference current depending on the temperature (Eq. (1)).

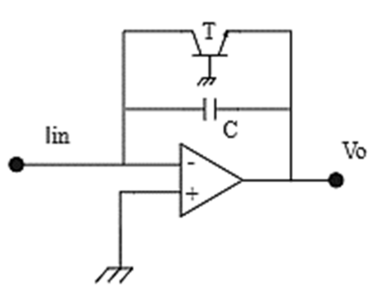

Figure 2: Basic schematic of the logarithmic amplifier.

Using the logarithmic property, when the input signal is weak, the input and output are approximately linear and the system is highly sensitive; when the input signal increases, the input signal varies over a wide range while the output signal varies less.

The principle of the weak signal I/V converter is based on a trans-impedance amplifier (see Fig. 3).

$$V_O = -I_{in} \times R, \quad (2)$$

where R is a high-resistance resistor and the input impedance of the op-amp is much higher than R [7] (Eq. (2)). I/V conversion sensitivity increases as the value of the resistor R increases.

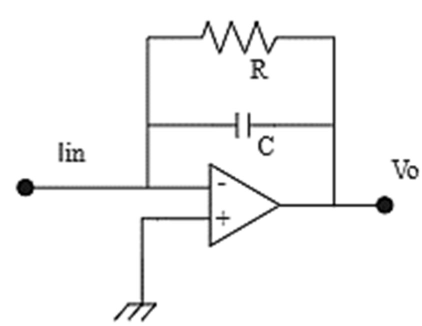

Figure 3: Basic schematic of the trans-impedance amplifier.

Design of I/V Converters

The high dynamic range readout electronic unit contains the I/V converters for 3 channels, using relays to select different I/V converters. The wide dynamic range I/V

ISBN: 978-3-95450-212-7 ISSN: 2673-5482 doi:10.18429/JACoW-CYCLOTRONS2022-MOPO012

converter uses commercially available logarithmic amplifiers AD8304 and this module allows current from 100 pA to 5 mA to be measured. Low input bias current ($\leq 20fA$) amplifier ADA4530-1 used in the weak signal I/V converter. The module can measure currents from 100 fA to 60 pA when the feedback resistance is taken to be 100 GΩ.

The I/V converter is followed by a low-pass filter with a cut-off frequency of 16 kHz which, in addition to filtering, provides further gain to the I/V converter output signal. For improved measurement accuracy, a metallic enclosure shields the electronics from external electromagnetic interference. Triaxial Cables are used to transmit beam current signals, besides that the electrical ground of the readout electronic unit (I/V converter, filter) and the data processing module (DSP, ADCs, SRAM) are separated to avoid ground loop problems. The offset and gain of each I/V channel will be manually calibrated separately.

Figure 4: The beam diagnostic electronics for 230 MeV superconducting cyclotron radial probe and scanning wires.

Experimental Results

Using the DC precision current source (Keithley 6220) to simulate the measurement signal. The results of the wide dynamic range I/V converter are shown in Fig. 5. The figure shows input currents from 0.1 nA to 5 mA, corresponding to output voltages from 0.5 V to 5 V. It can be seen that the input current is logarithmically related to the output voltage, and the I/V converter sensitivity is high when the input current is weak.

The feedback resistance of the weak signal I/V converter is 100 GΩ and a measured conversion sensitivity of 10^{11} V/A.

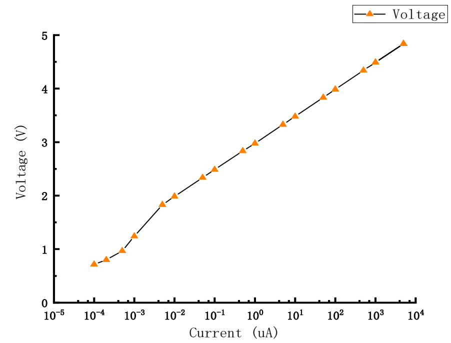

Figure 5: The results of the wide dynamic range I/V converter.

CONCLUSION

The new embedded electronics contain both logarithmic amplifiers and trans-impedance amplifiers as I/V converters for high dynamic range signal measurements, enabling continuous measurement of currents from 100 pA to 5 mA and transimpedance amplifiers with a sensitivity of 10^{11} V/A. The electronics are designed to reduce external electromagnetic interference through electrical isolation and shielding enclosures. Embedded ADCs, SRAM and a DSP effectively increase the sampling rate. The design is suitable for the radial probe and the wire scan systems.

REFERENCES

[1] T. J. Zhang *et al.*, “The cyclotron development activities at CIAE”. *Nucl. Instrum. Methods Phys. Res. Sect. B*, vol. 269, no. 24, pp. 2863-2870, Dec. 2011. doi:10.1016/j.nimb.2011.04.047

[2] T. J. Zhang *et al.*, “Research progress in high intensity cyclotron technology,” *Chinese Science Bulletin*, vol. 54, no 21, pp. 3931-3939, Nov. 2009. doi:10.1007/s11434-009-0503-x

[3] L. P. Wen *et al.*, “Radial probe installation and experiment for the CRM cyclotron,” Annual Report of China Institute of Atomic Energy, pp. 62-63, 2009.

[4] X. Zheng *et al.*, “Design and research of beam measuring device for 230 MeV superconducting cyclotron,” *Vacuum*, vol. 58, no. 4, pp. 54-57, 2021. doi:10.13385/j.cnki.vacuum.2021.04.10

[5] R. Dölling *et al.*, “Profile measurement of scanning proton beam for LiSoR using carbon fibre harps,” *AIP Conf. Proc.*, vol. 648, pp. 361, Nov. 2002. doi:10.1063/1.1524421

[6] P. A. Duperrex *et al.*, “Latest diagnostic electronics development for the PROSCAN proton accelerator,” *AIP Pub. Conf. Proc.*, vol. 732, pp. 268-275, Nov. 2004. doi:10.1063/1.1831157

[7] L. Q. Wei *et al.*, “An I-V converter in picoampere current measurement,” *Instrum. Anal. Monitoring*, pp. 28-31, no. 3, 2010.

ISBN: 978-3-95450-212-7 ISSN: 2673-5482 doi:10.18429/JACoW-CYCLOTRONS2022-MOPO013

EXPERIMENTAL STUDY OF BEAM ENERGY CONTROL AT THE TIARA AVF CYCLOTRON

N. Miyawaki†, S. Watanabe, H. Kashiwagi, N. S Ishioka, S. Kurashima
Takasaki Advanced Radiation Research Institute, National Institutes for Quantum Science and Technology, Takasaki, Gunma, Japan
Mitsuhiro Fukuda[1], [1]Research Center for Nuclear Physics, Osaka University, Ibaraki, Osaka, Japan

Abstract

The TIARA AVF cyclotron provides a helium (He) beam for producing ^{211}At, as one of its many beam applications. The generation rate of ^{211}At increases with the energy of the He beam. However, contamination of ^{210}Po produced by the radioactive decay of ^{210}At, which is generated by energy above 29 MeV, must be prevented for medical applications. Therefore, the energy of the He beam must be precisely measured and controlled. A time-of-flight beam energy monitor was installed in the direct beamline from the cyclotron to measure the beam energy in real-time. The cyclotron magnetic field and accelerating voltage, which are two potential causes of the beam energy change, were arbitrarily adjusted within a range of around 1%. With this control, the generation rate of ^{211}At and ^{210}At was investigated as the beam energy was varied. The results showed that the cyclotron parameters were easily controlled to the optimum beam energy that increased generation rate of ^{211}At and did not produce ^{210}At.

INTRODUCTION

The azimuthally varying field (AVF) cyclotron with a K number of 110 MeV in an ion beam irradiation facility, Takasaki Ion Accelerators for Advanced Radiation Application (TIARA) provides various ion beams from 10 MeV H^+ to 490 MeV Os^{30+} for experiments in the field of materials and biotechnology research, etc. [1]. To produce RI, light ion beams such as proton and helium (He) are mainly used. Recently, ^{211}At (half-life, 7.2 h) is produced for alpha nuclear medicine therapy research using the He beam accelerated by the TIARA AVF cyclotron. The production of ^{211}At uses the nuclear reaction of ^{209}Bi (α, 2n) ^{211}At. The ^{211}At yield in this nuclear reaction increases up to about 30 MeV in the injection energy of the He beam into the Bi target [2]. On the other hand, the nuclear reaction of ^{209}Bi (α, 3n) ^{210}At produces ^{210}At (half-life, 8.1 h) when the injection energy of the He beam into Bi surpasses 29 MeV. ^{210}At is chemically inseparable from ^{211}At, and radioactive decay produces ^{210}Po (half-life, 138 d), which is highly toxic [3]. Given that ^{210}Po has a longer half-life than that of ^{211}At, this poses the problem of being left as an impurity, such as in the case of drugs manufactured for clinical use. Therefore, for the mass production of ^{211}At, it is necessary to increase the intensity of the injection beam and precisely control the beam energy near the upper limit, wherein ^{210}At is not generated.

A precise bending magnet with beam slits installed in front of and behind it can be used to quantify the energy of the beam accelerated by the TIARA AVF cyclotron. However, this method cannot supply the beam to the RI production equipment installed in the beamline located straight from the cyclotron. Moreover, it was difficult to pass the beam through the slits before and after the magnets in a short time when parameters such as the magnetic field were changed in the cyclotron to fine-tune the beam energy. Therefore, a beam energy and position monitor (BEPM) system [4] was installed on this linear beamline to allow real-time measurements without blocking the beam. A BEPM can measure changes in beam energy due to changes in the cyclotron parameters in real-time. The generation rate of impurity-free ^{211}At can be maximized by controlling the He beam energy near the upper limit, where no ^{210}At is produced, based on the beam energy measurement using the BEPM. Therefore, the beam energy was measured using the BEPM to investigate the relationship between the cyclotron parameters and the beam energy and the variation of the beam energy from experiment to experiment.

In this study, we give an overview of the BEPM and the measurement results of the beam energy for each experiment and describe the beam-energy change measurement results using the Dee voltage and magnetic field used to tune the cyclotron. Additionally, the generation rate results from the measurement of ^{211}At obtained by irradiating the Bi target with the beam energy changed by the cyclotron tuning are described.

BEAM ENERGY MEASUREMENTS

Measurement Method

As shown in Fig. 1, RI production for the TIARA cyclotron is performed in the RI production equipment located at the end of the linear beamline from the cyclotron exit.

A precision-bending magnet (TAM) installed in this beamline deflects the beam to supply other experimental ports and measures the beam energy. However, when the beam energy to be supplied to the RI production system is measured using the TAM, irradiation for RI production cannot be performed for about 1 h because of the excitation and demagnetization of the TAM, beam energy measurement, and further beam transport adjustments. Therefore, a BEPM system was introduced to obtain the beam energy in real-time by measuring the time-of-flight of the beam bunch passing through the two pickup electrodes.

† miyawaki.nobumasa@qst.go.jp

ISBN: 978-3-95450-212-7 ISSN: 2673-5482 doi:10.18429/JACoW-CYCLOTRONS2022-MOPO013

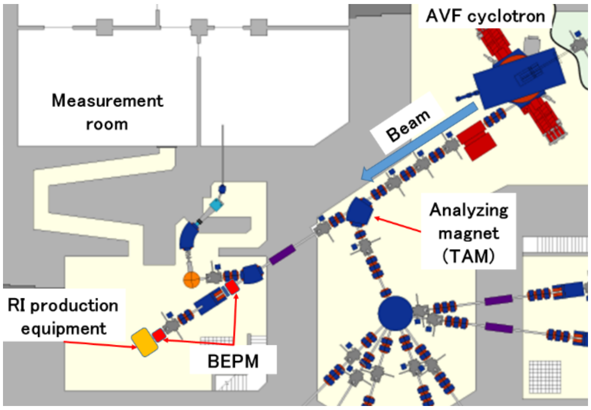

Figure 1: Schematic layout of the TIARA AVF cyclotron and beam transport line for RI production. BEPM electrodes are installed at two locations in the beamline. For applications other than RI production, the beam is deflected by the TAM.

The BEPM pickup electrodes shown in Fig. 2 were installed at two locations in the beamline from the cyclotron to the RI production system. To measure the beam position, the pickup electrodes are divided into four sections. A total of eight signals from the pickup electrodes are each amplified by an amplifier and then transmitted by coaxial cable. In the measurement room, the upstream and downstream signals are switched by switch modules (PXI-2599: NI) and signal processing is performed to digitize them with a digitizer (PXIe-5160: NI). These signal processes are integrated and processed by the LabVIEW development system program installed on the PC, and the respective measurement results are stored. Based on the difference between the voltages measured at the top and bottom of the electrode and the left and right electrodes, the beam position is calculated as the distance from the center. Additionally, the beam energy is calculated from the time difference between the averaged signals of the upstream and downstream pickup electrodes.

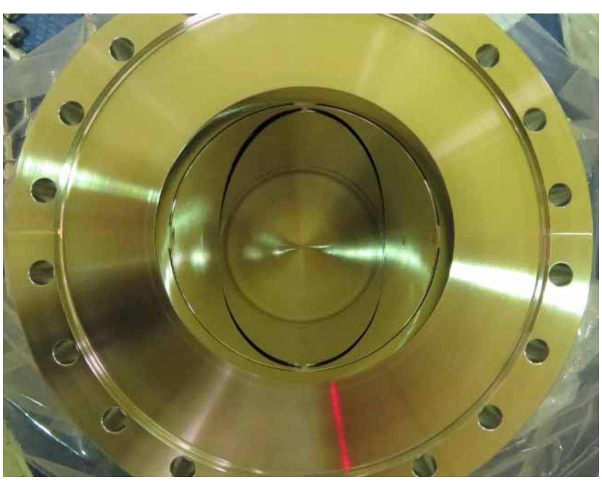

Figure 2: Photograph of the BEPM pickup electrode. The pickup electrodes are divided into four sections: upper, lower, left, and right.

Beam Energy Measurements for Each Experiment

In the production of ^{211}At at the RI production equipment of the TIARA the target Bi plate is fixed to an aluminium (Al) holder. The Al holder used to fix the target is cooled by water and the Bi plate is cooled by the He gas, given that the melting point of Bi is as low as 271.5 °C [5]. A 100 µm thick titanium (Ti) plate is installed to separate the helium gas for cooling from the vacuum in the beamline. The He beam is accelerated to about 50 MeV by the cyclotron, considering the energy lost by passing through the Ti plate and the helium gas. In addition, an Al plate about 0.39 mm thick is inserted in front of the Bi plate to adjust the energy of the He beam on the Bi plate to about 29 MeV. We measured the energy of the 50 MeV He beam using BEPM and TAM for each experiment. The results are shown in Fig. 3.

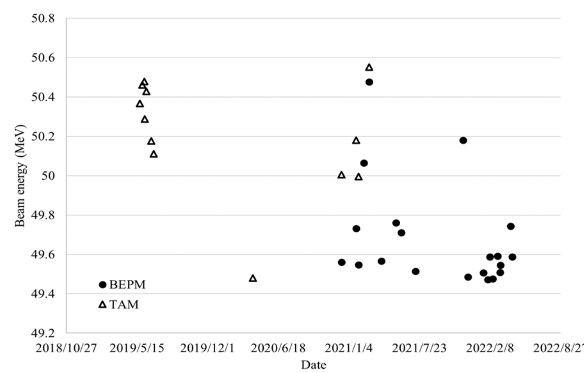

Figure 3: Distribution of the measured beam energy by the BEPM and the TAM for each experiment.

Both measurement methods show that the energy of the He beam often varies daily around 50 MeV. Energy measurement using TAM cannot be performed every time because of the time required for excitation, demagnetization, and adjustment. Therefore, there were few opportunities to measure beam energy with both measurement methods on the same day. When both methods were used on the same day, the results of energy measurements using the TAM were always higher than those using the BEPM, but the magnitude of the measured energy change was the same. This is because the angle of the injection beam into the TAM cannot be restricted, and the beam with an angle of injection into the TAM was deflected. Therefore, the energy measurement using TAM has the disadvantage of being time consuming and lacking in accuracy. On the other hand, the BEPM, which can monitor the beam energy in real-time, showed that the beam energy fluctuation during the same day after the adjustment at the start of the cyclotron operation was less than about 0.1%. Therefore, slight differences in the magnetic field, etc. at the start-up of the cyclotron for each experiment and the accompanying adjustment caused changes in the beam energy. As a result of investigating the adjusted cyclotron parameters for the cause of this energy change, it was found that there is a difference between the acceleration voltage and the

ISBN: 978-3-95450-212-7 ISSN: 2673-5482 doi:10.18429/JACoW-CYCLOTRONS2022-MOP0013

excitation current of the harmonic coils. Therefore, we controlled the change in beam energy caused by these parameters and measured the beam energy using the BEPM.

BEAM ENERGY CONTROL WITH CYCLOTRON PARAMETERS

Dee Voltage

When the Dee voltage is increased, the beam orbit in the cyclotron moves outward as the energy gain increases. In this case, if the beam can pass through the deflector electrodes or other extraction equipment, the beam with increased energy can be extracted. Figure 4 shows the measured beam energy and relative position at the upstream BEPM for each Dee voltage.

The positive relative position of the beam at the BEPM is to the right of the beam's direction of travel, while the negative direction is to the left. Given that the beam orbit in the TIARA AVF cyclotron rotates clockwise as viewed from above, if the energy of the accelerated beam is lower than expected, the rotation radius of the beam is reduced and the deflected beam to the right is extracted from the cyclotron. Conversely, if the beam energy is higher, the deflected beam to the left is extracted from the cyclotron. The energy of the extracted beam increased by 0.15 keV and the relative position of the beam changed by 15 mm in the negative direction by increasing the Dee voltage from 31 kV to 32.5 kV. The range of change in the Dee voltage is limited by the acceptance of the beam by the extraction device, and large changes in the Dee voltage cause the beam to collide with the extraction device, resulting in a loss. This requires additional orbit correction by steering magnets or other means to irradiate the target. Therefore, although the Dee voltage can vary the beam energy, it is difficult to produce a large difference in beam energy by the Dee voltage alone because of the large changes in beam intensity and orbit.

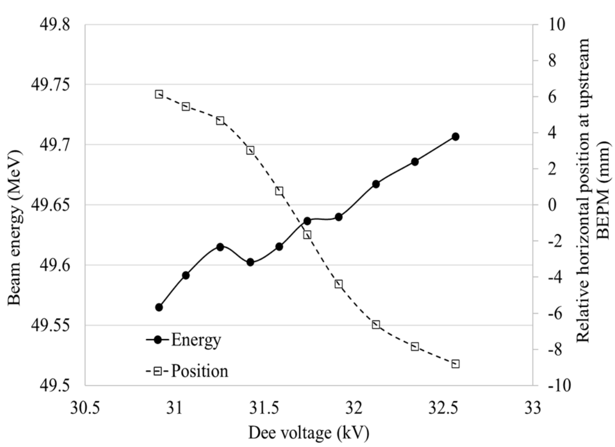

Figure 4: Correlations between the Dee voltage and relative horizontal position of the beam and between the Dee voltage and beam energy. The left and right vertical axes show the beam energy and relative horizontal beam position as line and dashed line graphs, respectively.

Harmonic Coils in the Central and Extraction Regions

In the center and extraction regions, two pairs of coils, known as harmonic coils, are installed in the valley sections of the upper and lower magnetic poles and are excited with opposite polarity to one another. The harmonic coils in the central region (CR) are mainly used for centering the injected ion orbit. The harmonic coils in the extraction region (ER) are used for modifying the beam orbit, such as enlarging the turn separation for beam extraction. The change in beam energy concerning the excitation current of one set of harmonic coils in the CR and the ER was measured using the BEPM. The beam energy changes with the excitation current of the harmonic coils, as shown in Fig. 5. The beam energy change by the harmonic coils in the CR and the ER was about 0.4 MeV and 0.7 MeV, respectively. The width of the change in the excitation current of the harmonic coils in the ER was narrower and more sensitive than those in the CR. Furthermore, the extracted beam current decreased rapidly with changes in the excitation current of the harmonic coils in the ER. On the contrary, the extracted beam current was almost unaffected by changes in the excitation current of the harmonic coils in the CR. Therefore, the beam energy can be controlled by using the harmonic coils in the ER for coarse adjustment and the harmonic coils in the CR, wherein the beam current fluctuation is small, for fine adjustment.

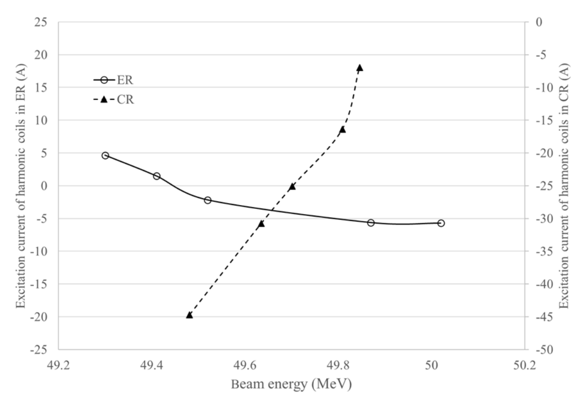

Figure 5: Relations between the beam energy and excitation currents of the harmonic coils in the extraction region (ER) and the central region (CR). The left and right vertical axes show the excitation currents of the harmonic coils in the ER and the CR as line and dashed line graphs, respectively.

GENERATION RATE OF ASTATINE BY BEAM ENERGY CONTROL

To confirm the change in beam energy by adjusting the cyclotron parameters, the production rates of ^{211}At and ^{210}At were measured by irradiating the Bi target with the He beam of different energies. The Dee voltage and the excitation current of one set of harmonic coils in the CR were used as parameters for the energy change of the He beam. Figure 6 shows the results of nuclide identification and quantitative analysis of irradiated Bi using a Ge

ISBN: 978-3-95450-212-7 ISSN: 2673-5482 doi:10.18429/JACoW-CYCLOTRONS2022-MOPO013

semiconductor detector. The energy of the He beam is reduced to nearly 29 MeV between the BEPM and the Bi target by the 0.1 mm Ti foil, He gas layer of 1.2 kgf/cm^2, and 0.39 mm Al foil. The results show that the generation rate of ^{211}At increases as the energy of the He beam is increased by adjusting the parameters of the cyclotron. ^{210}At was measured above about 49.7 MeV of the He beam energy, and its generation rate increased with energy. Therefore, we found that the optimum beam energy to produce ^{211}At in our irradiation equipment is about 49.6 MeV.

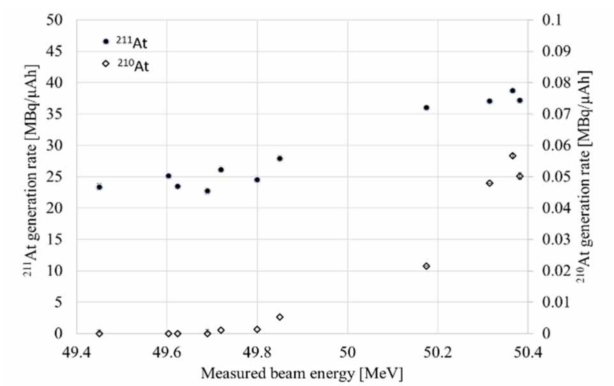

Figure 6: Relations between the beam energy and measured generation rates of ^{211}At and ^{210}At. The left and right vertical axes show the generation rates of ^{211}At and ^{210}At, respectively.

CONCLUSION

The TIARA AVF cyclotron allows precise control of the beam's energy by changing the Dee voltage and the excitation current of the harmonic coil. Changes in the beam energy due to these parameters can be measured in real-time using the BEPM. The change in beam energy with the Dee voltage ranged up to 0.3 MeV but was accompanied by a decrease in the extracted beam current and a change in the beam orbit. The beam energy could be changed by the excitation current of the harmonic coil in the ER in the range of about 0.7 MeV. However, the adjustable range of the excitation current was narrow, and the extracted beam current was reduced significantly.

The beam energy can be changed by the excitation current of the harmonic coil in the CR in the range of 0.4 MeV, and the change in the extracted beam current is small. The optimum beam energy for ^{211}At production in the current RI production system is 49.6 MeV, based on the relationship between the He beam energy and the production rates of ^{211}At and ^{210}At by the Dee voltage and the excitation current of the harmonic coil in the CR. In this study, using excitation current of one set of the harmonic coil in the CR was optimal for controlling the beam energy. We plan to search for the optimal parameters with less variation in the extracted beam current and beam position and a wider range of beam energy changes because they are the effects of limited parameters.

ACKNOWLEDGEMENTS

This work was supported by the JSPS KAKENHI Grant Numbers JP 20K08014.

REFERENCES

[1] S. Kurashima *et al.*, “Irradiation Facilities of the Takasaki Advanced Radiation Research Institute”, *Quantum Beam Sci.*, vol. 1, no. 2, pp. 1-19, Mar. 2017. doi:10.3390/qubs1010002

[2] K. Gagnon *et al.*, “Design and evaluation of an external high-current target for production of ^{211}At”, *J. Label Compd. Radiopharm*, vol. 55, no. 12, pp. 436-440, Oct. 2012. doi:10.1002/jlcr.2968

[3] A. Alfarano *et al.*, “Thick target yield measurement of ^{211}At through the nuclear reaction 209Bi(α,2n)”, *J. Phys.: Conf. Ser.*, vol. 41, pp. 115-122, 2006. doi:10.1088/1742-6596/41/1/009

[4] T. Watanabe *et al.*, “Development of beam energy and position monitor system at RIBF”, in *Proc. 14th Annu. Meeting Part. Accel. Soc. Jpn.*, Sapporo, Japan, Aug. 2017, https://www.pasj.jp/web_publish/pasj2017/proceedings/PDF/WEP0/WEP091.pdf.

[5] S. Watanabe *et al.*, “Evaluation of the cooling effect by He Gas for the production of ^{211}At with a Bi plate”, in *QST Takasaki Annual Rep.*, p. 105, 2019. https://www.qst.go.jp/uploaded/attachment/21756.pdf

ISBN: 978-3-95450-212-7 ISSN: 2673-5482 doi:10.18429/JACoW-CYCLOTRONS2022-MOPO014

DESIGN STUDIES OF THE CYLINDRICALLY SYMMETRIC MAGNETIC INFLECTOR

Lige Zhang*, Yi-Nong Rao, Rick Baartman, Yuri Bylinski, Thomas Planche
TRIUMF, Vancouver, BC, Canada

Abstract

The magnetic inflector is a promising alternative to achieve axial beam injection in a cyclotron with high beam energy. To demonstrate the technology, we use the TR100, a conceptual H2+ cyclotron, as a testbench to study the inflection conditions and optics of the passive magnetic inflector with a cylindrically symmetric structure. A mirror-like field with optimized mirror length and ratio provides a well-focused beam arriving at the median plane. The required magnetic field is produced by shimming a center plug in the injection hole. The space charge effect is also discussed with the simulation of a high-intensity injection beam.

INTRODUCTION

The spiral inflector steers the beam from the bore in the main magnet into the median plane to achieve the axial injection with an external ion source. In a conventional electrostatic inflector, the injection beam energy is limited by the breakdown voltage on the electrodes. While the injection intensity is also limited by the small aperture in the electrostatic inflector. Magnetic inflector is promising to overcome these disadvantages.

Recently, There are two types of magnetic inflector. One is the passive type which uses the iron in the injection hole to produce the required magnetic field. [1] The other is the active one which uses a permanent magnet array. [2] The passive type is more robust because there is no concern about the degaussing of the permanent magnet under the high beam loss in the injection hole. But it is only a concept, that has no existing design. To demonstrate the technology, we designed a magnetic inflector model for the conceptual H2+ cyclotron, TR100 [3]. The inflection conditions and focal properties of the passive magnetic inflector are studied using the particle tracking method. The preliminary simulation considering space charge is also discussed.

REFERENCE ORBIT

Motion Equations

In a cylindrically symmetric magnet. The magnetic vector potential A only consists of the azimuthal component A_θ. A_θ is the function of r and z. Thus, the hamiltonian is independent from θ, which is written as:

$$H = \sqrt{P_r^2 c^2 + P_z^2 c^2 + c^4 m_0^2 + \frac{c^2\,(P_\theta - qr\,\mathrm{A}_\theta\,(r,z))^2}{r^2}} \tag{1}$$

where the canonical momenta are:

$$\begin{aligned} P_r &= p_r \\ P_\theta &= \gamma m_0 \theta' r^2 + qrA_\theta\,. \\ P_z &= p_z \end{aligned} \tag{2}$$

We can easily find that the canonical momentum in the azimuthal direction is a constant. Defining a potential function U with the constant azimuthal momenta and the magnetic vector potential as:

$$U = \frac{(P_\theta - qr\,\mathrm{A}_\theta\,(r,z))^2}{2\gamma m_0 r^2} \tag{3}$$

the motion equation, essentially as obtained by Glaser [4], could be written in the following form:

$$\begin{aligned} P_r' &= \frac{\partial U}{\partial r} \\ P_\theta' &= 0 \quad . \\ P_z' &= \frac{\partial U}{\partial z} \end{aligned} \tag{4}$$

Substituting Eq. (2) into Eq. (4), the motion equation is written as:

$$\begin{aligned} \theta' &= \theta_0' r_0^2/r^2 + \frac{q}{\gamma m_0 r^2}(r_0\,\mathrm{A}_{\theta 0} - r\,\mathrm{A}_\theta) \\ \gamma m_0 r'' &- \frac{\partial U}{\partial r} = 0 \\ \gamma m_0 z'' &- \frac{\partial U}{\partial z} = 0 \end{aligned} \tag{5}$$

Because U is independent of θ and time t, the motion on the r-z plane is conservative. To find a proper reference orbit, we only need to solve the 2-D motion equation on the r-z plane.

Numerical Solution for a Mirror-like Magnetic Vector potential

The magnetic mirror is a component that is used to confine the charged particles. The particles inside a magnetic mirror are bounced back before the mirror point, in this paper we use a similar field to inflect the beam. The vector potential used to define the axial symmetric magnetic field in a mirror field is given as:

$$A_\theta = \frac{A_1 \beta r}{2} - A_2 I_1(\beta r)\cos\beta z \tag{6}$$

where π/β is the mirror length, $\beta(A_1 + A_2)/(A_1 - A_2)$ is the mirror ratio.

* lzhang@triumf.ca

ISBN: 978-3-95450-212-7 ISSN: 2673-5482 doi:10.18429/JACoW-CYCLOTRONS2022-MOPO014

The given magnetic field satisfies Laplace's equation, which ensures the curl of the magnetic field is zero. The linear approximation of the vector potential is given as:

$$A_{theta} = \frac{\beta r}{2}(A_1 - A_2 \cos \beta z)\,. \tag{7}$$

We use the TR100 main magnet model as a test bench to study the injection. The magnetic field in the central region is 2 T. The designed injection energy is around 35 keV. Figure 1(a) shows the conceptual model. By tracking the particle reversely from the median plane to the injection point with different Pitch angles, the different reference orbits are shown in Fig. 1 (b). Without breaking the median plane symmetry, the particle starting with 0 pitch angles on the median plane could not travel up to the injection point, which means we still need an electrostatic deflector on the median plane to fully steer the beam into the median plane. The single B_r bump field near the median plane could reduce the pitch angle by about 20° from the injection point to the median plane.

The final pitch angle on the median plane is around 20°, which only needs around 5 times less electrical field to fully steer the beam onto the median plane compared with a similar size inflector.

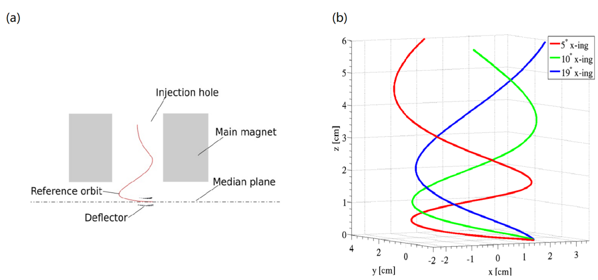

Figure 1: Reference orbit in the injection hole.

BEAM OPTICS

Coordinates Transformation

In this paper, we use the coordinate (α, β, γ) in the optical coordinate system, which moves along the reference orbit as shown in Fig. 2 [5]. The γ direction is the same as the velocity of the reference particle. The β direction is perpendicular to the γ direction and parallel to the median plane. At the same time, the cross product of the unit vector of the γ direction and β direction should have a positive projection on z-axis. The α direction is defined by the cross product of the unit vector of the γ direction and β direction.

The position vector $\vec{c}$ of the point on the reference orbit in cartesian is written as:

$$\vec{c} = (x_c(s), y_c(s), z_c(s)) \tag{8}$$

where s, the distance along the reference orbit, is the independent variable. The base vector $\vec{e} = (\vec{e_\alpha}, \vec{e_\beta}, \vec{e_\gamma})$ of the moving optical coordinate on the reference orbit is written as:

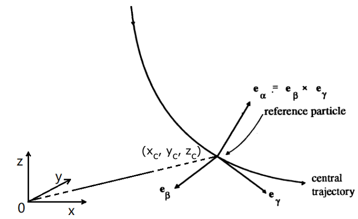

Figure 2: The moving optical coordinate system.

$$\begin{aligned} \vec{e_\alpha} &= (x_\alpha(s), y_\alpha(s), z_\alpha(s)) \\ \vec{e_\beta} &= (x_\beta(s), y_\beta(s), z_\beta(s)) \\ \vec{e_\gamma} &= (x_\gamma(s), y_\gamma(s), z_\gamma(s))\ . \end{aligned} \tag{9}$$

The transformation from cartesian coordinates (x, y, z) to the moving coordinates (α, β, γ) is written as:

$$\begin{aligned} x &= x_c(s) + \alpha x_\alpha(s) + \beta x_\beta(s) + \gamma x_\gamma(s) \\ y &= y_c(s) + \alpha y_\alpha(s) + \beta y_\beta(s) + \gamma y_\gamma(s) \\ z &= z_c(s) + \alpha z_\alpha(s) + \beta z_\beta(s) + \gamma z_\gamma(s)\ . \end{aligned} \tag{10}$$

Thus, the transformation matrix from the moving coordinates to the cartesian coordinates is:

$$\mathrm{M} = \begin{bmatrix} x_\alpha(s) & x_\beta(s) & x_\gamma(s) \\ y_\alpha(s) & y_\beta(s) & y_\gamma(s) \\ z_\alpha(s) & z_\beta(s) & z_\gamma(s) \end{bmatrix}\ . \tag{11}$$

The inverse transformation matrix $\mathrm{M}' = \mathrm{M}^T$, as the $(e_\alpha, e_\beta, e_\gamma)$ are orthogonal bases. Choosing a possible generating function that is consistent with Eq. (10).

$$\begin{aligned} G = &-P_x[x_c(s) + \alpha x_\alpha(s) + \beta y_\alpha(s) + \gamma z_\alpha(s)] \\ &- P_y[y_c(s) + \alpha x_\beta(s) + \beta y_\beta(s) + \gamma z_\beta(s)] \\ &- P_z[z_c(s) + \alpha x_\gamma(s) + \beta y_\gamma(s) + \gamma z_\gamma(s)]\ . \end{aligned} \tag{12}$$

The new canonical momenta is derived from the given generating function:

$$\begin{aligned} P_\alpha &= -\frac{\partial G}{\partial \alpha} = P_x x_\alpha(s) + P_y x_\beta(s) + P_z x_\gamma(s) \\ P_\beta &= -\frac{\partial G}{\partial \beta} = P_x y_\alpha(s) + P_y y_\beta(s) + P_z y_\gamma(s) \\ P_\gamma &= -\frac{\partial G}{\partial \gamma} = P_x z_\alpha(s) + P_y z_\beta(s) + P_z z_\gamma(s)\ . \end{aligned} \tag{13}$$

The canonical momenta under the cartesian coordinate system is given by:

$$\begin{aligned} P_x &= m_0 v_x + qA_x = m_0 v_0 x' + qA_x \\ P_y &= m_0 v_y + qA_y = m_0 v_0 y' + qA_y \\ P_z &= m_0 v_z + qA_z = m_0 v_0 z' + qA_z \end{aligned} \tag{14}$$

ISBN: 978-3-95450-212-7 ISSN: 2673-5482 doi:10.18429/JACoW-CYCLOTRONS2022-MOPO014

where the prime denotes differentiation with respect to s, v_0 is the velocity. Substitute Eq. (14) into Eq. (13), the new canonical momenta is written as

$$\begin{bmatrix} P_\alpha \\ P_\beta \\ P_\gamma \end{bmatrix} = m_0 v_0 \mathrm{M}^T \begin{bmatrix} x' \\ y' \\ z' \end{bmatrix} + q\mathrm{M}^T \begin{bmatrix} A_x \\ A_y \\ A_z \end{bmatrix}. \qquad (15)$$

Substituting the coordinates on the reference orbit into Eq. (15), the canonical momenta on the reference trajectory is:

$$\begin{bmatrix} P_{\alpha 0} \\ P_{\beta 0} \\ P_{\gamma 0} \end{bmatrix} = m_0 v_0 \mathrm{M}^T \begin{bmatrix} x'_c \\ y'_c \\ z'_c \end{bmatrix} + q\mathrm{M}^T \begin{bmatrix} A_{x0} \\ A_{y0} \\ A_{z0} \end{bmatrix}. \qquad (16)$$

To make the canonical variable small quantities, we subtract Eq. (16) from Eq. (15). Thus, the generating function becomes:

$$\begin{aligned} G = &-P_x[x_c(s) + \alpha x_\alpha(s) + \beta y_\alpha(s) + \gamma z_\alpha(s)] \\ &- P_y[y_c(s) + \alpha x_\beta(s) + \beta y_\beta(s) + \gamma z_\beta(s)] \\ &- P_z[z_c(s) + \alpha x_\gamma(s) + \beta y_\gamma(s) + \gamma z_\gamma(s)] \\ &+ \alpha P_{\alpha 0} + \beta P_{\beta 0} + \gamma P_{\gamma 0} \end{aligned}. \qquad (17)$$

The new momenta is given by:

$$\begin{bmatrix} P_\alpha \\ P_\beta \\ P_\gamma \end{bmatrix} = m_0 v_0 \mathrm{M}^T \begin{bmatrix} x' - x'_c \\ y' - y'_c \\ z' - z'_c \end{bmatrix} + q\mathrm{M}^T \begin{bmatrix} A_x - A_{x0} \\ A_y - A_{y0} \\ A_z - A_{z0} \end{bmatrix}. \qquad (18)$$

Using Eq. (10) and Eq. (18) expand the transform matrix M into a 6 × 6 matrix the transformation from (x, P_x, y, P_y, z, P_z) to $(\alpha, P_\alpha, \beta, P_\beta, \gamma, P_\gamma)$ is given by:

$$\begin{bmatrix} \alpha \\ P_\alpha \\ \beta \\ P_\beta \\ \gamma \\ P_\gamma \end{bmatrix} = \mathrm{M}^T \begin{bmatrix} x - x_c \\ m_0 v_0 (x' - x'_c) \\ y - y_c \\ m_0 v_0 (y' - y'_c) \\ z - z_c \\ m_0 v_0 (z' - z'_c) \end{bmatrix} + q\mathrm{M}^T \begin{bmatrix} 0 \\ A_x - A_{x0} \\ 0 \\ A_y - A_{y0} \\ 0 \\ A_z - A_{z0} \end{bmatrix}. \qquad (19)$$

Transfer Matrix

In order to calculate the transfer matrix, we need to run 6 particles with orthogonal initial coordinates and momenta in the magnetic inflector. After transforming the coordinates at the end of the orbit into the moving coordinates system with the unit (mm, mrad, mm, mrad, mm, mrad), the transfer matrix is calculated as:

$$\mathrm{R} = \begin{bmatrix} 1.99 & 0.15 & -1.68 & -0.02 & 0.38 & 0.13 \\ -5.02 & 0.19 & -0.23 & -0.18 & 3.87 & 0.21 \\ 0.58 & 0.02 & 0.84 & 0.03 & -0.55 & -0.01 \\ -13.80 & -0.37 & -8.08 & 0.39 & 1.94 & -0.64 \\ -0.03 & 0.04 & -0.30 & 0.02 & 0.61 & 0.10 \\ 5.32 & 0.22 & -12.48 & 0.27 & -5.43 & 0.86 \end{bmatrix} \qquad (20)$$

Testing the symplectic of the transfer matrix,

$$\mathrm{R^T J R - J} = \begin{bmatrix} 0 & -0.004 & -0.026 & 0.036 & 0.008 & -0.008 \\ 0.004 & 0 & -0.015 & 0.001 & -0.003 & -0.000 \\ 0.026 & 0.015 & 0 & -0.002 & 0.001 & 0.004 \\ -0.036 & -0.001 & 0.002 & 0 & 0.001 & -0.001 \\ -0.008 & 0.003 & -0.001 & -0.001 & 0 & -0.001 \\ 0.008 & 0.000 & -0.004 & 0.001 & 0.001 & 0 \end{bmatrix} \qquad (21)$$

where J is given as:

$$\mathrm{J} = \begin{bmatrix} 0 & 1 & 0 & 0 & 0 & 0 \\ -1 & 0 & 0 & 0 & 0 & 0 \\ 0 & 0 & 0 & 1 & 0 & 0 \\ 0 & 0 & -1 & 0 & 0 & 0 \\ 0 & 0 & 0 & 0 & 0 & 1 \\ 0 & 0 & 0 & 0 & -1 & 0 \end{bmatrix}. \qquad (22)$$

The symplectic error is between 10^{-3} and 10^{-2}, which may be resulted from the non-linear of the motion and the noise when tracking the particles numerically.

Beam Envelopes

The beam envelope is studied in the $\alpha - \beta - \gamma$ moving frame. In previous study [6], we found that a proper beam focusing in both directions could be achieved by adjusting the mirror length and the mirror ratio. In this paper, an optimal magnetic inflector field with mirror length of 10 cm and mirror ratio of 2 is produced by carefully shimming the iron in the injection hole. The envelop and 3D trajectory in the designed magnetic inflector is shown in Fig. 5 (a).

MAGNET DESIGN

A 2D model is used to calculate the magnetic field in the injection hole. The sector structure is modelled by introducing the pseudo material which uses a lumped factor k to calculate the B-H curve, different k means different width ratios of the sectors. for a 4-sector magnet with a sector width of 45 degrees, k is 0.5. For the yoke, k is 1, thus the B-H curve is that of the real steel. Figure 3 shows the structure of the central plug that we used to optimize the mirror field in the injection hole. Figure 4 shows the magnetic field of the optimal magnet model.

HIGH INTENSITY SIMULATION

Figure 5 shows the Comsol simulation of the beam injection with considering space charge.

ISBN: 978-3-95450-212-7 ISSN: 2673-5482 doi:10.18429/JACoW-CYCLOTRONS2022-MOPO014

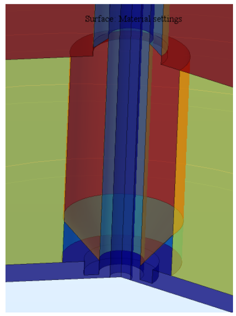
Figure 3: Steel plug in the injection hole. Blue colored material is the vacuum, green is the sector poles and red is the steel structure in the injection hole.

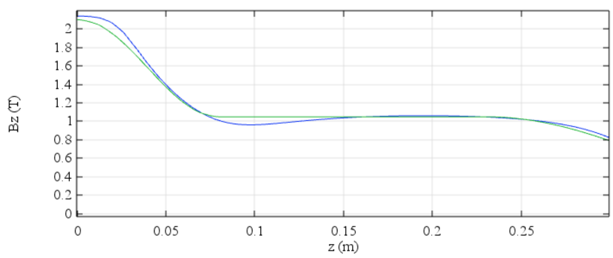

Figure 4: On-axis magnetic field in the injection hole after optimizing the shape of the center plug. The green line is the theoretic mirror field that could properly focus the beam in the inflector. Blue line is the on-axis magnetic field produced by the designed main magnet with a properly shimmed central plug.

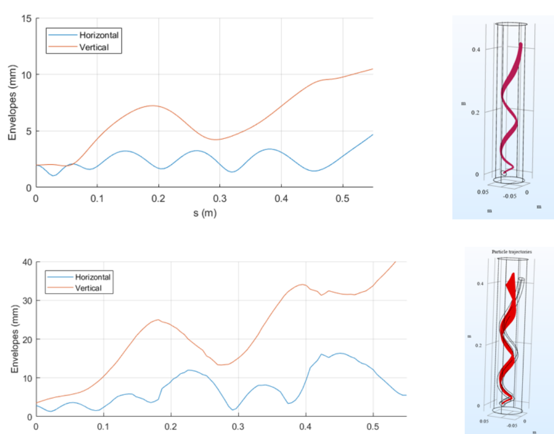

Figure 5: Envelope simulation considering space charge. The upper plots show the simulation a 1 nA injection beam. The lower one shows that of the 10 mA injection beam. The frame of a spiral pipe in the lower 3D beam plot shows the reference beam path without considering the space charge effect. Obviously, the reference orbit is changed by the space charge. A further design study of a shielding structure is needed to remove the repulsive force from different turns.

CONCLUSION

To maintain the median plane symmetry of the magnet, an electrostatic deflector should be placed at the end of the magnetic inflector, which will finally deflect the beam into the median plane with 0 vertical momenta. The required electric field strength in the electrostatic deflector is much lower than that in a conventional inflector. The envelope study suggests that the beam could be focused both horizontally and vertically in the moving frame under the optimized mirror ratio and mirror length. A steel plug in the center region is designed to produce the required field in the injection hole. A preliminary simulation of the high-intensity DC beam injection is simulated using Comsol, the reference orbit is changed by the space charge. Thus, a further design study of a shielding structure should be pursued.

ACKNOWLEDGEMENTS

This work was funded by TRIUMF which receives federal funding via a contribution agreement with the National Research Council of Canada.

REFERENCES

[1] W. Kleeven, “Injection and extraction for cyclotrons”, CERN Accelerator School, 2003.

[2] D. Winklehner *et al.*, “High power cyclotrons for neutrino experiments”, in *Proc. 5th Int. Particle Accelerator Conf.(IPAC'14)*, Dresden, Germany, Jun. 2014, pp. 788-–790.

[3] Y.-N. Rao, R. Baartman, Y. Bylinskii, T. Planche, and L. Zhang, ”Conceptual design of TR100+: an innovative superconducting cyclotron for commercial isotopes production”, in *Proc. 22nd Int. Conf. on Cyclotrons and their Applications (Cyclotrons'19)*, Cape Town, South Africa, Sep. 2019, pp. 298–301. doi:10.18429/JACoW-CYCLOTRONS2019-THB03

[4] W. Glaser, *Grundlagen der Elektronenoptik*, Springer-Verlag, 2013.

[5] R. Baartman and W. Kleeven, “A canonical treatment of the spiral inflector for cyclotrons”, *Part. Accel.*, vol. 41, pp. 41–53, 1993.

[6] D. Winklehner *et al.*, “Report of the Snowmass'21 Workshop on High-Power Cyclotrons and FFAs”, Mar 2022. doi:10.48550/ARXIV.2203.07919

ISBN: 978-3-95450-212-7 ISSN: 2673-5482 doi:10.18429/JACoW-CYCLOTRONS2022-MOPO015

TRIUMF LLRF CONTROL SYSTEM UPGRADE

Xiaoliang Fu*, Ken Fong, Qiwen Zheng, Thomas Au, TRIUMF, Vancouver, Canada

Abstract

The LLRF system for Transfer line from Drift Tube LINAC(DTL) to Superconducting Linac (SCB) (DSB) was an analog-digital hybrid system running at 35.36MHz. The system controls the amplitude/phase and tuning for a buncher cavity on the beamline. During the 2022 October shutdown, the system is upgraded to a new fully-digital LLRF system. The new digital LLRF system is based on TRIUMF's universal LLRF hardware with a new firmware. Instead of using a VXI mainframe, the new system adopts a NIM bin and uses USB communication with the local control PC. The amplitude/phase regulation is implemented in the FPGA firmware, and the tuning loop is implemented in the PC software, but driven by the FPGA. The Debian 11 linux OS is running on ARM CPU, and the new digital LLRF system works as a standard window HID device. The linux OS allows the firmware be updated in-situ using Ethernet communication. The detailed design is described in this paper.

INTRODUCTION

The previous LLRF system for DSB was an analog-digital hybrid system based on VXI mainframe that controls the amplitude/phase and tuning of the cavity. The LLRF system works at 35.36MHz, and this frequency is generated from the harmonics of the 5.89MHz main reference source. The tuning loop was implemented with phase comparison method, then upgraded with the sliding mode control. The RF part of the system works great for years. However, the motor control function of the tuning loop has minor problem related to the limit switch. Meanwhile, the VXI mainframe is obsolete and hard to buy for the future system. To fix the motor problem, a new digital LLRF system is designed to replace the existing system. The new system is based on ZYNQ FPGA and installed in the NIM bin crate instead of VXI mainframe. The daughter board is TRIUMF's universal LLRF hardware [1], and the mother board is equipped with RF signal conditioning circuit. The local control PC communicates with the LLRF system through USB and Ethernet. The new system adopts 35.36MHz reference signal and the output of the system is phase-locked to it. There are two outputs provided by the new system: one is for driving the amplifier chain and the other one is used as the reference for Isotope Separator and Accelerator(ISAC) II. The hardware of the new digital LLRF system is shown in Fig. 1.

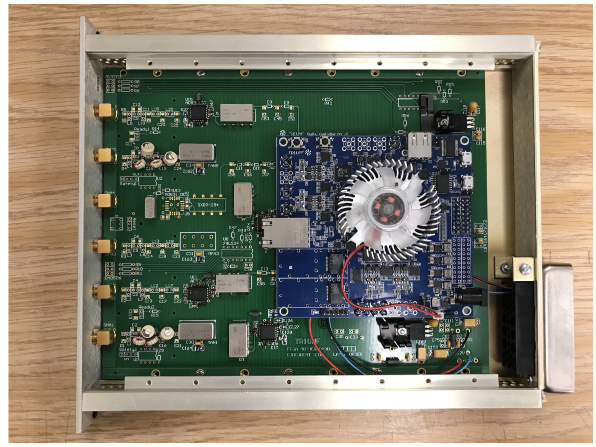

Figure 1: Picture of Digital LLRF system for DSB.

SYSTEM DESIGN

The system requires amplitude/phase control, tuning(step motor) control, and the global phase control. The 35.36MHz signal is used as the reference input. There are one cavity pickup signal and two output signals in the system. The system works in generator driven mode. From the previous experience of TRIUMF's digital LLRF system [1, 2], the new system for DSB is designed as below in Fig. 2.

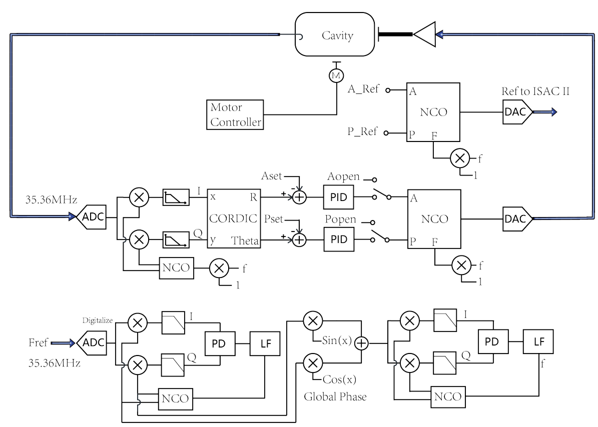

Figure 2: Digital LLRF system design for DSB.

Phase-locked Loop and Global Phase Shifter

The new digital LLRF system works in driven mode and the phase of the output signal is not phase-locked to the reference signal. To resolve this issue, a digital phase-locked loop is introduced to the system. The digital phase-locked loop is based on a Costas loop which is widely used in communication systems. The first Costas loop is used to lock the frequency of the NCO to the 35.36MHz reference signal. After the first digital phase-locked loop, a global phase shifter is used to shift the phase of the reference signal, then the phase-shifted signal is used as the reference of the second phase-locked loop. The output of the second phase-locked loop is used as the basic frequency correction value for the system. Then, the two outputs of the system can be locked to the phase-shifted reference signal by adjusting

* xfu@triumf.ca

ISBN: 978-3-95450-212-7 ISSN: 2673-5482 doi:10.18429/JACoW-CYCLOTRONS2022-MOPO015

the frequency tuning words of the NCOs. Assume that the reference signal is [3]:

$$x(t) = A\cos(\omega_c t) \tag{1}$$

And the output of the local NCO is:

$$\begin{cases} I_0 &= \cos(\omega_0 t + \phi(t)) \\ Q_0 &= \sin(\omega_0 t + \phi(t)) \end{cases} \tag{2}$$

The results of the quadrature multiplier after the low-pass filter is:

$$\begin{cases} I_o = A/2 \cdot \cos[(\omega_c - \omega_0)t - \phi(t)] \\ Q_o = A/2 \cdot \sin[(\omega_c - \omega_0)t - \phi(t)] \end{cases} \tag{3}$$

After the phase detector, which is also a multiplier, the result is:

$$P_e(t) = A/8\sin(2(\omega_c - \omega_0)t - 2\phi(t)) \tag{4}$$

If we define:

$$\Delta\theta(t) = (\omega_c - \omega_0)t - \phi(t) \tag{5}$$

Then Eq. (4) can be written as:

$$P_e(t) = A/8\sin(2\Delta\theta(t)) \tag{6}$$

Based on Eq. (6), $P_e(t)$ is a function of $2\Delta\theta(t)$. Therefore, the frequency of the local NCO is controlled by the frequency and phase error between the reference signal and the local NCO. While in phase lock mode, $\omega_c = \omega_0$, the phase error and frequency error between the two signals are zero.

After the first phase-locked loop, an I/Q phase shifter is used to phase-shift the output of the NCO of the first phase-locked loop. The phase-shifted signal is used as the input of the second phase-locked loop. Thus, the global phase can be changed easily by the ARM CPU. Further more, the frequency of the output signal may be an integral multiple of the frequency of the reference signal, and the ratio is also controlled by the ARM CPU.

Amplitude and Phase Control

For a single frequency system, assume the the cavity pick up signal is [1, 2, 4, 5]:

$$u_0(t) = A_0[1 + f(t)]\cos[\omega t + \phi'(t)] \tag{7}$$

where $f(t)$ is the amplitude modulation signal of the cavity. The output signal of tuning NCO is:

$$\begin{cases} I = \cos(\omega_1 t) \\ Q = \sin(\omega_1 t) \end{cases} \tag{8}$$

After the low pass filters, the mixing results of cavity signal and NCO signal are:

$$\begin{cases} I_2 = A_0[1 + f(t)]/2 \cdot \cos[(\omega - \omega_1)t + \phi'(t)] \\ Q_2 = A_0[1 + f(t)]/2 \cdot \sin[(\omega - \omega_1)t + \phi'(t)] \end{cases} \tag{9}$$

The amplitude can be calculated by:

$$U_2(t) = \sqrt{I_2^2(t) + Q_2^2(t)} = \frac{A_{0[1+f(t)]}}{2} \tag{10}$$

The phase of the cavity pickup signal is:

$$\Delta\theta = \phi'(t) = \arctan\frac{Q_2}{I_2} \tag{11}$$

Eq. (11) indicates that the phase error is independent from amplitude, frequency, and their modulation. Therefore, the phase control won't be effect by the phase-locked loop. After the amplitude error and phase error is obtained from the demodulator, a close loop amplitude and phase control is achieved by the PID controller. Since the NCO IP core doesn't have the amplitude modulation, the amplitude modulation is done by the multiplier whose inputs are the output of the amplitude PID controller and the NCO.

Tuning Loop

The step motor controller is implemented in the FPGA and controlled by the ARM CPU. The ARM CPU can control the frequency, duty factor, and the operation mode of the motor controller. To work with different kinds of motor drivers, the polarities of the limit pins and enable pins can be programmed as well. An up/down counter is also included in the design to count the pulse number of each direction and the summation can be read by the CPU, as shown in Fig. 3. This summation can be used as the backup value of the motor position if the potentiometer is not available. There are three kinds of operation modes in the motor controller: manual control mode, single side hold mode, and auto reverse mode. In the manual mode, the controller ignore the limit signal and do what the users want. In the single side hold mode, if the motor hits the limit, the motor can't move towards this direction anymore, but it can still move towards the opposite direction. In the auto reverse mode, if the motor hits the limit switch, the motor will automatically switch to the other direction and keep moving. The LLRF system adopts the single side hold mode. Since the system has only one pickup signal from the cavity, the traditional phase comparison tuning method is not a good option for this system. The local control PC reads the phase of the LLRF output and the phase of the cavity pickup signal and then controls the motor through the motor controller. To achieve the best tuning condition, an open loop calibration has to be done before the system runs in closed loop mode. The user must run the system in open loop mode, and then manually tune the system. When the system is in perfect tuning condition, the user has to drag the sliding bar on the GUI to set the phase compensation value, shown in Fig. 4. This phase compensation value is the phase delay of the whole amplifier chain. Then the PC software can calculate the detuning angle correctly and maintain the tuning condition. When the phase delay of the amplifier is changed due to temperature changing or power level changing, the phase compensation value has to be changed as well.

ISBN: 978-3-95450-212-7 ISSN: 2673-5482 doi:10.18429/JACoW-CYCLOTRONS2022-MOPO015

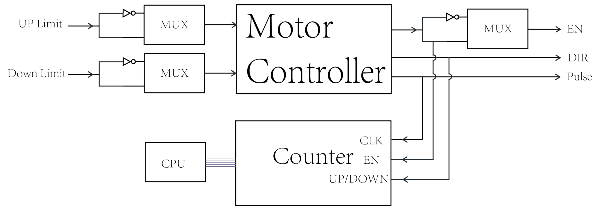

Figure 3: Motor controller for DSB LLRF system.

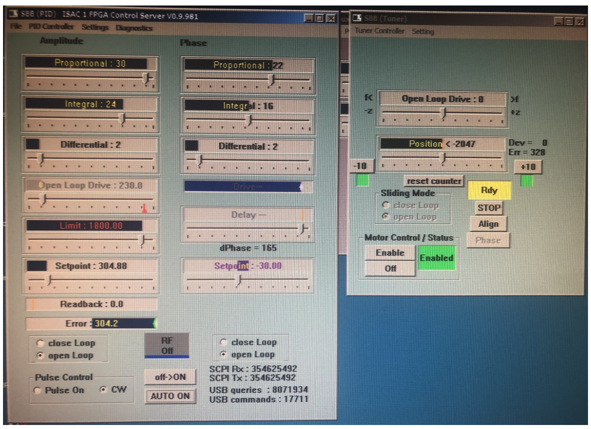

Figure 4: Local PC GUI for DSB LLRF system.

Linux OS and LLRF Apps

The hardware system is equipped with large DDR3 RAM, Ethernet, and USB. In the previous TRIUMF LLRF system, the system is running with standalone code. Although the standalone code works well, it's hard to maintain and it's not user friendly since the programmer has to know all the details about the hardware system. A better solution is to use embedded Linux OS to manage all the hardware resources. The digital LLRF system adopts the Debian 11 as the Linux file system. The source code of Debian 11 is compiled and customized for the LLRF system. Python3 is chosen as the default Python environment. GCC is also available for users to compile source code locally. By default the user for the system is llrf and the root user is not enabled for ssh connections. Every operation is able to be done by the llrf account. The ARM CPU controls the FPGA hardware by reading and writing through the AXI-GPIOs. The Linux char device drivers are developed for the AXI-GPIOs. The device drivers are compiled into the Linux kernel and loaded when the OS is booting. The traditional read and write functions are not working well with Python code because of the buffer mechanism in Python. The ioctl driver is used for AXI-GPIOs writing and reading. Since the device driver is also very closed to the hardware level, it is not very convenient to call the device driver directly. A Python library is used to wrap the details of the hardware to make the system more user friendly. This Python library is called `pyllrf`, and by default it is installed in the system. Users can control the LLRF system without knowing anything about the FPGA firmware with the help from `pyllrf`. The hardware system can be initialized with four lines of Python code.

With the help from Python, the Jupyter notebook is also available. The new digital LLRF system runs a Jupyter notebook server by default and users can access to it through the internet. The port of jupyter notebook is set to 8888 by default. To access the jupyter notebook, users need to know the ip address of the LLRF system. With any web broswer, users can control LLRF system with python code. The popular Python libraries such as Numpy, scipy, pandas, matplotlib, and skit-learn are also avalible for the users. Jupyter bootebook also makes it possible to upload files to the filesystem and copy them to the FAT partition and upgrade the FPGA hardware design online without power off the system. The Linux HID device driver is implemented with the HID gadget feature of Linux kernel. Then in the Python code, the HID device information can be decided dynamically when the system is booting. The digital LLRF system is configured as an USB compliant device. When the system is plugged into a windows PC, the PC will automatically load the HID device driver and recognize the system as an USB HID device and an USB serial port. The system adopts 48 bytes length customized HID commands. The first two bytes of the commands determine the channel of the system to access, and the third byte determines if this a write or read operation. The rest bytes are for the parameters. The read/write command can read/write multiple parameters with one command to speed up the reading/writing. The local PC can control everything of the system through the HID commands.

Startup Procedure

The system startup procedure is controlled by the local PC. The local PC accepts remote control commands from the control room through EPICS. After receiving the auto-on command, the system will start to work in pulse mode. The tuner will be moved to the open loop set-point. If the amplitude read back is bigger than the threshold, the local PC will switch the system into CW mode and close the tuning loop. Then the system enters the power ramping state to raise the power level. In the end, the amplitude and phase control loop will be closed and the startup procedure is done.

TEST AND TUNE

The new digital system for DSB is installed on the control station and tested online. First of all, the motor controller is tested with the tuner. With the new system, the tuner will stop when hitting the limit switch, and then the limit indicator will be turned on on the local control GUI. The tuner can be moved out of the limit position by the GUI to the other direction. After the motor function test, the RF part is tested. The auto-on function works well and the system can finish the startup procedure in less than 2 minutes. The first test achieved 5kW power on the amplifier and the system is stable for one night. The next day, 10kW RF power was achieved on the amplifier and the system is still stable. However, the ISAC II LLRF system couldn't work well with the new reference signal from the new digital

ISBN: 978-3-95450-212-7 ISSN: 2673-5482 doi:10.18429/JACoW-CYCLOTRONS2022-MOPO015

LLRf system. The phase noise of the reference signal is measured and the result shows that there is a phase noise peak at 1.2kHz. Although this phase noise is out of the cavity bandwidth and it's under -70dBm, somehow it causes the ISAC II LLRF system to be unstable and the self-excited loop can't be locked.

The phase noise of the previous reference signal is quite clean and the new reference signal has a noise peak at 1.2kHz. This is the only difference between the two reference signals. In order to offer a better performance reference signal, the parameters of the digital PLL is tuned to reduce the phase noise in the low frequency range. After the proper adjustment, the phase noise is measured again, and the result is shown in Fig. 5. The green line in Fig. 5 is the phase noise of the reference signal and the blue line is the phase noise of the LLRF output after the parameter tuning. The test result shows that the phase noise peak at 1.2kHz is removed. With the tuned reference signal, ISAC II LLRF system can work properly, and the self-excited loop can be locked without any problem.

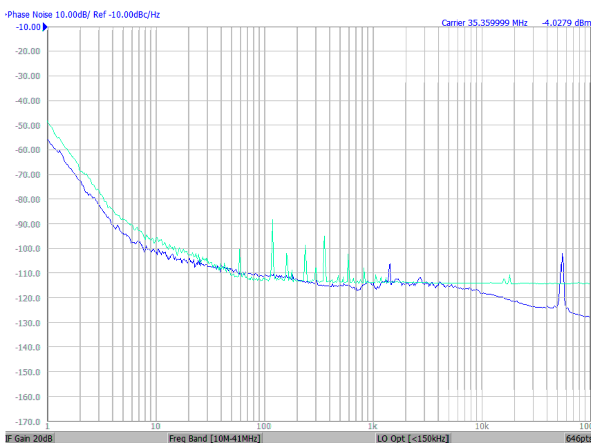

Figure 5: Phase noise of LLRF after tuning.

CONCLUSION

An NIM bin based digital LLRF system is developed for TRIUMF DSB project. The hardware is based on TRIUMF's universal LLRF hardware and the software adopts Debian 11 as the Linux operating system. The communication between LLRF system and the local control PC is based on USB. A customized USB HID command set is designed for TRIUMF's new digital LLRF systems. A python library is written to control all the hardware of the system and communicate with the PC through USB HID commands. The online test shows that the requirement of the low-level RF control system has been satisfied.The new digital system is installed on the DSB system and the previous LLRf system is replaced cucessfuly.

REFERENCES

[1] Xiaoliang Fu, Ken Fong, Zhiguo Yin, Qiwen Zheng, Thomas Au, "A digital phase-locked loop based LLRF system", *Nucl. Instrum. Methods Sect. A,* vol. 962, p. 163688, 2020. 10.1016/j.nima.2020.163688

[2] Xiaoliang Fu, Thomas Au, Ken Fong, Qiwen Zheng, "Saw-tooth generation and regulation with a simple FPGA for TRIUMF'S ARIEL prebuncher", in *Proc. 10th Int. Particle Accelerator Conf. (IPAC'19)*, Melbourne, Australia, May 2019, pp. 2801–2803. doi:10.18429/JACoW-IPAC2019-WEPRB004

[3] Yong Du, "Digital filters based on MATLAB and FPGA", Publishing house of Electronics Industry, Beijing, 2014, pp. 320–334.

[4] Xiaoliang Fu, Zhiguo Yin, Ken Fong, *et al.*, "LLRF controller for high current cyclotron based BNCT system", *IEEE Trans. Nucl. Sci.*, vol. 68, no.10, pp. 2452–2458, 2021. doi:10.1109/TNS.2021.3097702

[5] Xiaoliang Fu, Zhiguo Yin, Ken Fong, *et al.*. "Design and implementation of general hardware and firmware for cyclotron low level radio frequency system", *At. Energy Sci. Tech.*, vol. 55, pp. 1886–1892, 2021.

ISBN: 978-3-95450-212-7 ISSN: 2673-5482 doi:10.18429/JACoW-CYCLOTRONS2022-MOPO016

CONTROL OF CYCLOTRON VERTICAL DEFLECTOR FOR PROTON THERAPY

F. Yang[1], Z. Yin[1†], X. Mu[1], T. Zhang[1], T. Jiang[1], X. Fu[2], Y. Wang[1]
[1]China Institute of Atomic Energy, Beijing, China
[2]Canada's National Laboratory for Particle and Nuclear Physics (TRIUMF), Vancouver, Canada

Abstract

China Institute of Atomic Energy (CIAE) has designed a superconducting cyclotron CYCIAE-230 to enhance the domestic development of proton therapy. A research program on the beamline and experimental stations for the proton therapy and the space science was launched by China National Nuclear Corporation (CNNC). The modern therapy methodology often requires rapid beam modulation on both the beam energy and the intensity. In this scenario, a vertical deflector is designed and installed in the cyclotron's central region. Applying a high-voltage electric field between the two plates can quickly adjust the intensity of the low-energy beam. Nevertheless, the voltage applied is nonlinear to the beam intensity. According to this requirement, a homemade controller for the vertical deflector is designed. Since the beam loss caused by the energy degrader is also nonlinear, this controller can compensate for the beam loss caused by energy modulation. To realize real-time control, the controller combines Field Programmable Gate Array (FPGA) and Digital Signal Process (DSP) as its control scheme design. Carried out by the DSP by interpolating the lookup table data, a feed-forward regulation is also designed to take care of the nonlinear compensation for the beam loss on the energy degrader. In the meantime, an ionized chamber provides feedback readings of the intensity just before the nozzle. A PID algorithm is also included by using FPGA, to archive the feedback control of the vertical deflector.

INTRODUCTION

Compact superconducting (SC) cyclotrons have the advantage of small size, cost effectiveness, high extraction efficiency and beam stability, which are very suitable for medical applications. A 230 MeV superconducting cyclotron is designed by China Institute of Atomic Energy (CIAE) to provide fix energy beam of 246 MeV with an intensity of about 300 nA for proton therapy [1, 2]. There are several items in the cyclotron that are related to the output beam current. For instance, the arc power of the internal ion source, the phase selecting system, the Dee voltage, and extracting high voltage (HV). Nonetheless, the arc power of the ion source and phase selecting system are not fast enough. The Dee voltage and extracting HV are too complicated to have fast modulation. Therefore, a fast beam modulation technique is urgently needed to speed up the beam intensity modulation in order to shorten the treatment time.

The upstream part of the beamline includes an energy degrader, which aims to adapt the beam energy to different treatment requirements, is adjusted by the Treatment Control System (TCS). The drawback of the energy degrader is that it modulates the current nonlinearly when changing beam energy. Due to the nonlinear nature of this energy change means, the beam transmission rate before and after the energy degrader will change drastically as the final energy changes.

Therefore, a vertical high voltage deflection system is installed in the central area of the cyclotron, which can modulate the beam in an independent manner and limit the loss of the beam at lower energy. Although this vertical high voltage deflection system is also nonlinear, the designed vertical deflector controller will solve this problem. It will compensate the beam lost on the degrader and the system. In the meantime, it will achieve fast switching of the beam within 100 µs and stable control of the beam to realize the new intensity modulated proton therapy (IMPT) and a new generation of time-driven intensity modulation continuous line scan technology to shorten patient treatment time. Last but not the least, it can provide redundant beam cut-offs for medical safety interlocks for proton therapy, safeguarding patient safety during the proton therapy.

OPERATING PRINCIPLES

This vertical high voltage deflection system comprises a pair of vertical deflector plates and a passive collimator. The plates are connected to a power supply outside of the cyclotron. It can actively provide initial power for low-energy beam. The vertical oscillation generated by the magnetic field will enhance the vertical off-axis motion, and the downstream collimator will eventually intercept these particles. The structure of the vertical deflector plate in the central area of the superconducting cyclotron and the principle of particles passing through the vertical deflector plate and collimator to regulate the beam intensity are shown in Figs. 1 and 2. The simulation assumes that the electric field in the vertical deflector plate is constant and acts in the 2nd to 4th turns of the particle trajectory to apply axial momentum to the particles. In contrast, the axial collimator acts in the 2nd to 5th turns, and the particles with

† zhiguoyin@ciae.ac.cn

ISBN: 978-3-95450-212-7 ISSN: 2673-5482 doi:10.18429/JACoW-CYCLOTRONS2022-MOPO016

larger axial bias are lost in the axial collimator to regulate the beam intensity.

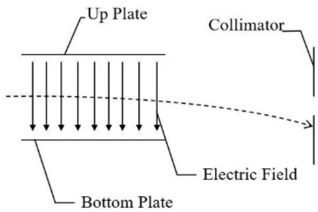

Figure 1: The deflector and collimator.

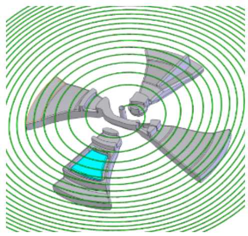

Figure 2: Vertical deflector beam modulation schematic.

As illustrated in Fig. 3, the hardware of the vertical deflector system consists of three parts. The first part is a wide bandwidth, high-voltage power amplifier, a commercial product widely used in precise high voltage control applications. An analog 0-10 V voltage from the controller commands the power amplifier to provide a high voltage of 0-2 kV. The second one is a homemade controller, the vertical deflector controller, which is the most complicated device in the vertical deflector system; hence the operating principle will be discussed in detail and reported below. The last one is a 2 kV power supply that provides the amplifier power. The controller receives four signals from the outside, namely: arc power, potentiometer signal, SMA interface signal and beam set signal, which is an analog 0-10 V voltage.

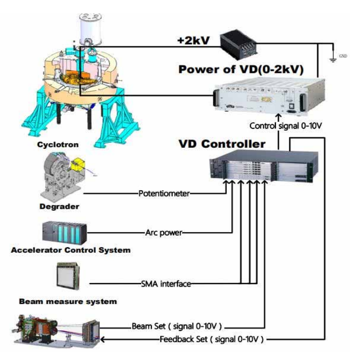

Figure 3: Vertical deflector system hardware.

HARDWARE

The vertical deflector controller board is based on the compact PCI architecture. Consisting of a pair of front and rear boards, this design allows for greater solution flexibility and versatility. The two front and single rear boards are connected by an FPGA Mezzanine Card (FMC) board. Since the design uses industry-standard interfaces, this complete digital board can also be reused in other designs. For example, beam diagnostics, etc. This makes the set of boards a digital development platform, providing greater efficiency in hardware and firmware development. In the application of rapid beam intensity control, look-up tables, PID algorithms and CPCI communication interfaces are implemented using digital resources such as DSP and FPGA on the motherboard.

According to the design requirements, the hardware architecture of the CPCI board is chosen to combine the FPGA of XC7A100T-2FGG484 under the ARTIX-7 series of Xilinx and the DSP of MC56F83789VLL, providing 4-channel ADC and 4-channel DAC; using Modbus TCP as the main serial communication interface; using RS232 as the test port for hardware function testing; 1GB DDR3 is used as the system memory; most of the FPGA's IOs are led out as backup IOs, with about 30 digital IOs; a clock input/output interface is provided for the system to accept sampling clocks from external sources or for cascading between multiple boards. The design block diagram of the whole set of boards is shown in Fig. 4.

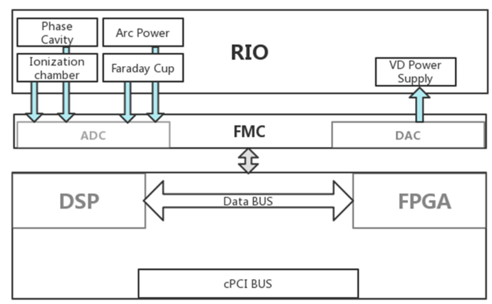

Figure 4: Block diagram of daughter-mother board circuit.

In Fig. 5, it shows a physical view of the motherboard. The motherboard mainly completes the implementation of the control algorithm and the CPCI communication with the upper computer, and the main chips are FPGA and DSP. The FPGA implements the PID control algorithm, ADC/DAC driver and CPCI communication, while the DSP implements the lookup table algorithm and Modbus TCP communication.

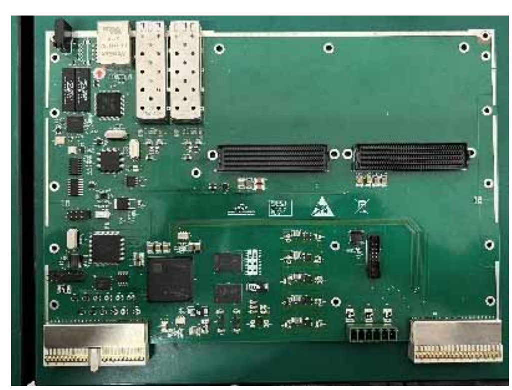

Figure 5: the vertical deflector controller mother board.

In Fig. 6, the daughter board is developed according to the operating principles of the vertical deflector system. According to functional requirements, the daughter board is equipped with 6-channel ADC and 1-channel DAC to the

ISBN: 978-3-95450-212-7 ISSN: 2673-5482 doi:10.18429/JACoW-CYCLOTRONS2022-MOPO016

HV power supply. The daughter board's core function is to provide the necessary signal conditioning for the beam measurements and digitalization for the motherboard. The PID feedback of FPGA uses 3 ADC channels, and the look-up table of DSP uses three analog conversion channels.

As the main function board, the daughter board will input the signals obtained after photoelectric isolation into each function module, such as the detector module will convert the obtained power signal to the output voltage; the IV conversion module will convert the current signal to get the voltage signal, and the current signal has eight gear switching ranges; the ionization chamber module will convert the current signal to voltage signal; finally, the required four values of beam intensity, degrade beam transmission rate, Dee voltage beam transmission rate and vertical deflector voltage are obtained, so that four look-up tables can be established and processed by DSP to realize the look-up table algorithm.

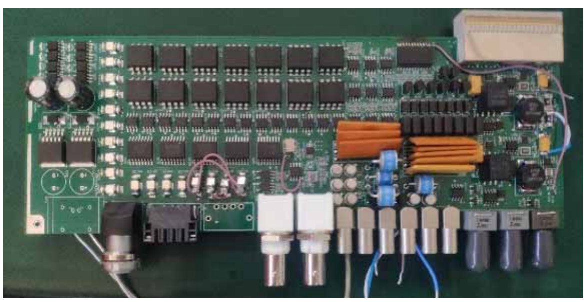

Figure 6: the vertical deflector controller daughter board.

In Fig. 7, The FMC board that connects the two boards is shown in the picture. The FMC board implements digital-to-analog and analog-to-digital conversion. ADC converts the current and voltage values of the daughter board to get the corresponding Dee voltage and other corresponding values, which are output to DSP to build a lookup table and calculated in DSP to get the corresponding values of arc power and other corresponding values to output to FPGA. This board is mainly for some fast digital-to-analog/analog-to-digital conversion calculations.

Figure 7: FMC board.

SOFTWARE

The software of the vertical deflector system involves embedded system development and host system interface development. Further, to meet the timing requirements of the dose delivery system, the algorithms of the vertical deflector system are implemented in dedicated hardware, e.g. the DSP and the FPGA. Related Single-Board Computer (SBC) runs the real-time operating system, VxWorks 6.9. The SBC is responsible for none time-critical tasks, such as communication with the Graphical User Interface (GUI). There is no operating system for the development of embedded software on DSP and FPGA.

In the DSP, a set of C codes is developed to achieve the feedforward control functions using a two-dimensional look-up table. As presented in Fig. 8, a higher voltage on the plates will yield a lower beam transfer ratio at certain beam energy. Under the same high voltage on the deflection plate, the lower the beam energy, the lower the beam transmission rate.

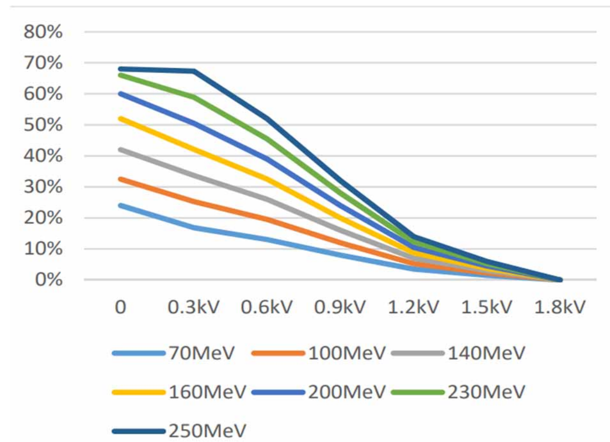

Figure 8: The corresponding relationship between vertical deflector voltage and beam current at the different energy.

The main system utilized for the software part is VxWorks. VxWorks operating system is an embedded real-time operating system (RTOS) designed and developed by WindRiver, Inc. in 1983 and is a key component of the embedded development environment. With good sustainability, high performance kernel and a user-friendly development environment, it occupies a place in the field of embedded real-time operating systems. It is widely used in communication, military, aviation, aerospace and other areas with high precision technology and high real-time requirements, such as satellite communication, military exercises, ballistic guidance, aircraft navigation, etc., with its good reliability and excellent real-time performance. The operation page of the VxWorks system is shown in Fig. 9.

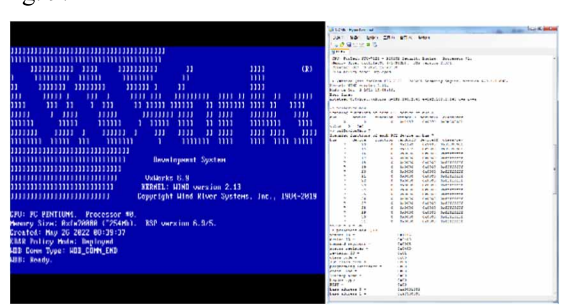

Figure 9: VxWorks system operation page diagram.

ISBN: 978-3-95450-212-7 ISSN: 2673-5482 doi:10.18429/JACoW-CYCLOTRONS2022-MOPO016

CONCLUSION

The existing research work on the vertical deflector controller has more research results, and the technology is more mature, which has a more significant reference value for how to accurately and quickly control the beam intensity, and has greatly improved the system response speed and beam intensity adjustment accuracy.

The development of the vertical deflector controller is a key technology for the development of localized proton therapy devices, which will provide a technical guarantee for the localized proton therapy device to catch up with the latest generation of continuous line scan therapy technology and FLASH therapy.

REFERENCES

[1] T. Zhang *et al.*, “Investigation and quantitative simulation of beam physics for 230 MeV SC cyclotron under construction at CIAE,” *Nucl. Instrum. Methods Phys. Res. Sect. B*, vol. 468, pp. 8-13, Apr. 2020. doi:10.1016/j.nimb.2020.02.008

[2] T. Zhang *et al.*, “Developments for 230 MeV superconducting cyclotrons for proton therapy and proton irradiation,” *Nucl. Instrum. Methods Phys. Res. Sect. B*, vol. 406, pp. 244- 249, Sep. 2017. doi:10.1016/j.nimb.2016.11.010

[3] T. Stephani *et al.*, “Automated Operation and Optimization of the VARIAN 250 MeV Superconducting Compact Proton Cyclotron,” in *Proc. Cyclotrons'10*, Lanzhou, China, Sep. 2010, paper MOPCP021, pp. 93-95.

[4] S. Psoroulas *et al.*, “Challenges in Fast Beam Current Control Inside the Cyclotron for Fast Beam Delivery in Proton Therapy,” in *Proc. Cyclotrons'16*, Zurich, Switzerland, Sep. 2016, pp. 126-129. doi:10.18429/JACoW-Cyclotrons2016-TUA02

[5] J. M. Schippers, “Fast Scanning Techniques for Cancer Therapy with Hadrons - a Domain of Cyclotrons,” in *Proc. Cyclotrons'10*, Lanzhou, China, Sep. 2010, paper FRM1CIO04, pp. 410-415.

ISBN: 978-3-95450-212-7 ISSN: 2673-5482 doi:10.18429/JACoW-CYCLOTRONS2022-MOPO017

RF CAVITY RESONANT CONTROL USING MINIMAL SEEKING SLIDING MODE CONTROLLER

K. Fong, R. Leewe, T. Au, X. Fu, Q.W. Zheng, TRIUMF, Vancouver, BC, Canada

Abstract

Accelerating RF normal conducting cavities having Quality Factors of over 10^3. These cavities must be constantly tuned to maintain resonance for maximum power efficiency. Traditional tuning method uses 'phase comparison method' by monitoring the phase shift across the input and output of the cavity. This method suffers from phase drift due to diurnal temperature variations. Since 2017, TRIUMF ISAC-1 cavities are tuned using minimal seeking sliding mode controllers, which eliminate effects drift due to temperature changes. As with all extremum seeking algorithm, chattering is present in the system, especially near the end-stage. This paper also includes a new chattering suppression method known as 'surface skipping', which is slated to be installed in ISAC-1 LLRF upgrade in 2023.

INTRODUCTION

In a RF cavity, with $\Delta\omega = \omega - \omega_c$, with ω as the operating frequency, τ the time constant of the cavity and ω_c its resonant frequency, the steady state complex cavity voltage V is given by [1]

$$V \cong \frac{\Gamma + 1}{1 + (\Delta\omega\tau)^2}(1 + j\Delta\omega\tau)v_F \qquad (1)$$

where Γ is the reflection coefficient, is the result of impedance matching. Using Kirchhoff's voltage law

$$v_F + v_R = V \qquad (2)$$

The reflected voltage v_R is [1]

$$v_r \cong v_f \frac{\Gamma + j\Delta\omega\tau}{1 - j\Delta\omega\tau} \qquad (3)$$

The reflected power P_R in relation to the forward power P_F is

$$P_R \cong P_F \frac{\Gamma^2 + (\Delta\omega\tau)^2}{1 + (\Delta\omega\tau)^2} \qquad (4)$$

and

$$\frac{dP_R}{d(\Delta\omega)} = P_F(1 - \Gamma^2)\tau^2\Delta\omega \qquad (5)$$

Minimum P_R occurs when

$$\frac{dP_R}{d(\Delta\omega)} = P_F(1 - \Gamma^2)\tau^2\Delta\omega = 0 \qquad (6)$$

or $\Delta\omega = 0$.

From Eq. (1), the phase angle between V and v_F is

$$\phi = \tan^{-1}\Delta\omega\tau \qquad (7)$$

At $\Delta\omega = 0$, the RF cavity in will be operating most efficiently. Most cavity do this by applying Eq. (6), monitoring the monotonic ϕ and move the tuner such that $\phi = 0$. However, ϕ cannot be measured in-situ, as there must be some lengths of cables from the input pickup and the output pickup. The lengths of these cables must be carefully matched to prevent phase drift due to diurnal temperature changes. In TRIUMF's ISAC-1, ϕ is measured from the output of the LLRF to the feedback input of the LLRF. This makes the phase measurement even more prone to error due to the rf amplifier chains inherent phase shift dependency on power and temperature. To avoid phase measurement, tuning algorithm in ISAC-1 cavities try to minimize the reflected power P_R instead. From Eq. (4), minimizing v_R or P_R will result in $\Delta\omega \to 0$ and therefore maximizing V. However, as can be seen from Eq. (4) and Fig. 1, P_R is neither linear nor monotonic. This leads us to minimum reflecting power seeking algorithm. There are several minimum seeking algorithms, all of them involve perturbing the system to detect the correct slope to minimization. In gradient estimation minimum seeking algorithm, $\frac{dP_R}{dt}$ is calculated to obtain the direction of travel for the tuner. However, numerical differentiation enhances high frequency noise. The sliding mode extremum seeking algorithm, P_R is used instead to suppress the noise generated by slope detection.

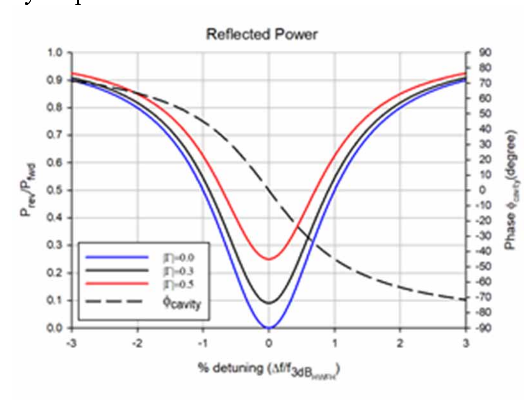

Figure 1. Reflected power vs tuning.

SLIDING MODE EXTREMUM SEEKING ALGORITHM

The original sliding mode equation is given as [2-4]

$$\frac{d\theta}{dt} = k_0 \operatorname{sgn}\left[\sin\left(\frac{\pi s}{\varepsilon}\right)\right]F(\theta) \qquad (8)$$

ISBN: 978-3-95450-212-7 ISSN: 2673-5482 doi:10.18429/JACoW-CYCLOTRONS2022-MOPO017

with $s(t) = F(\theta) + \rho t$ (9)

A block diagram of a minimum seeking sliding mode controller is shown in Fig. 2.

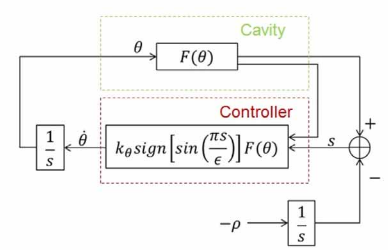

Figure 2. Block diagram of sliding mode controller.

The function to be minimized is $F(\theta) \equiv P_R$, the reflected power, whereas θ is the distance to minimum. ρ, ε and k_0 are tuneable parameters to be optimized for speed of convergence and stability. The sliding mode surfaces are where $s = \varepsilon n$, where $n = 0, \pm 1, \pm 2, \cdots$. For this reason, ε is the separation between the sliding mode surface. As soon as s crosses over one of these surfaces, the movement of the tuner $\frac{d\theta}{dt}$ is reversed. Differentiating Eq. (9) we get

$$\frac{ds}{dt} = \frac{dP_R}{d(\Delta\omega)} \frac{d(\Delta\omega)}{dt} + \rho \tag{10}$$

and using Eq. (5),

$$\frac{ds}{dt} = P_F\left(1 - \Gamma^2\right)\tau^2 \frac{1}{2}\left(\frac{d(\Delta\omega)^2}{dt}\right) + \rho \tag{11}$$

Since P_F, $\left(1-\Gamma^2\right)$, τ and ρ are always positive, $\frac{ds}{dt}$ is smaller when $\left(\frac{d(\Delta\omega)^2}{dt}\right)$ is negative, i.e. $|\Delta\omega| \to 0$.

When $\frac{ds}{dt}$ is small, s remains longer in the same region bounded by two switching surface. Computationally, one can get rid of the sine and sign function in Eq. (8) and simplified and codified as:

```
if ((s %2) >=0 && (s %2)<1) tuner in;
else                         tuner out;
```

The movement is illustrated in Fig. 3 as plots of P_R vs time steps. The green line illustrates idealistic case of the rate of movement completely matches with the decrease in P_R, i.e. $\frac{dP_R}{dt} = -\rho$. The red and blue lines represent more realistic cases when $\frac{dP_R}{dt} \neq -\rho$. When P_R changes slowly compared to ρt the convergence is represent in the blue line, while the red line is when P_R changes rapidly. It shows that in both cases, when P_R is decreasing, the controller stays within this direction longer. However, each time s crosses over a sliding mode surface, the tuner reverses direction, resulting in a sharp increase or decrease in s, causing shorter time in the wrong direction. When P_R reaches the minimum at t=9, the tuner moves back and forth around the minimum point. This end-point chattering can be easily removed by stopping the tuner when P_R falls below a threshold.

SYSTEM PERFORMANCE

In 2016, the resonant controls of ISAC-1's DTL4 and DTL5 were retrofitted with sliding mode controller, and their long-term performances were measured. Fig. 4 shows the performance of the DTL5's sliding mode tuner controller over a period of 4 days in summer of 2016. The purple line is the ambient temperature, clearly showing a diurnal temperature variation of ~10ºC. The red line is the forward power P_F and the purple line is the motor position θ. It is clear from the figure the motor position tracked with the ambient temperature. Within the same time period, there was a setpoint changes as indicated by the jump in P_F as indicated by the red line, which is tracked by the tuner position as well.

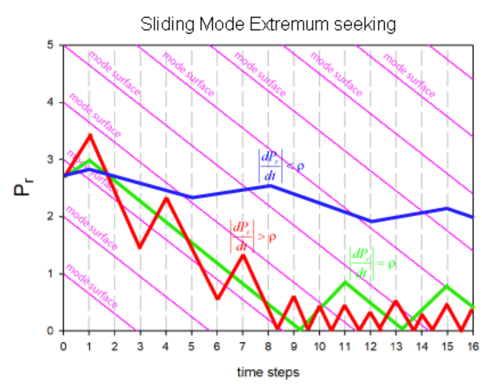

Figure 3. Sliding function dependence on mode surface.

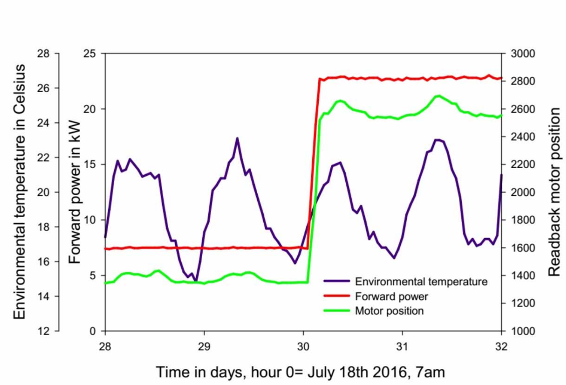

Figure 4. Long term performance of DTL5 in 4 days.

ISBN: 978-3-95450-212-7 ISSN: 2673-5482 doi:10.18429/JACoW-CYCLOTRONS2022-MOPO017

DECHATTERING

As with all extremum seeking algorithm, chattering is present in the system [5-6]. In Fig. 3, the direction of the tuner can switch rapidly, causing a lot of chatter but little overall movement. For example, when the switching function s is close to zero, i.e., from Eqs. (8) and (9)

$$s = P_R + \rho t \approx> 0 \ , \ \frac{dP_R}{dt} + \rho \approx< 0 \ \text{and} \ \frac{dP_R}{dt} < 0 \ ,$$

s will drift slowly toward the switch surface $s = 0$. But as soon as $s < 0$, the tuner moves in an opposite direction, causing $\frac{dP_R}{dt} > 0$ and s will arise sharply and back to $s > 0$ and therefore $\frac{dP_R}{dt} < 0$. This process repeats for a while resulting in chatter as illustrated as in both the red and blue curves in Fig. 3. To prevent this from happening, we can add $t \rightarrow t + \Delta t$ to increase s when $s < 0.1$, as well as at other surface boundaries. We call this "switching surface skipping", as it behaves very much like a stone skipping on the surface of water. The following code does this function to every switching function:

```
if (s>-0.1 && s<0) gtime -=  5*Δt;
if (s<0.1 && s>0)  gtime +=  5*Δt;
if (s>0.9)    gtime -=  5*Δt;
if (s<-0.9)    gtime +=  5*Δt;
```

which will set back the value of s to about $0.5 \cdot \Delta t$ as before to eliminate the chatters. This skipping is illustrated in Fig. 5 in a plot of the sliding function vs time. Since skipping changes the values of s but not P_R, the vertical axis is now plotted in s instead of P_R. The blue line is when there is no dechattering and the red line is when dechattering is applied. when the sliding functions get close to a sliding surface, "skipping" cause them to go back to the centre between the two mode surfaces. Since P_R keeps decreasing, P_R would have reached zero at $t \approx 5$ and the controller would enter end-point detection. Figure 6 shows the improvement in convergence when "switching surface skipping" is used as well as end-point detection. In this figure, the blue lines show the movement of a normal sliding mode movement, while the red line show that when the skipping is introduced to make it stay within the same region to prevent a reversal of direction. This also result in a faster convergence as the tuner does not spend time switching direction.

END POINT DETECION

When the minimum is reached, any minimum seeking algorithm will move back and forth around the minimum point and results in further chattering and mechanical wear. To prevent this from happening an endpoint detection must be used, pausing when minimum has been reached. Because the minimum is not necessary equals to zero due to mismatch, so using P_R below a set value is not a good criterion. Instead, the timed average of P_R is used, i.e.,

$$\left\langle \left| \frac{dP_R}{dt} \right| \right\rangle <\approx \varepsilon$$

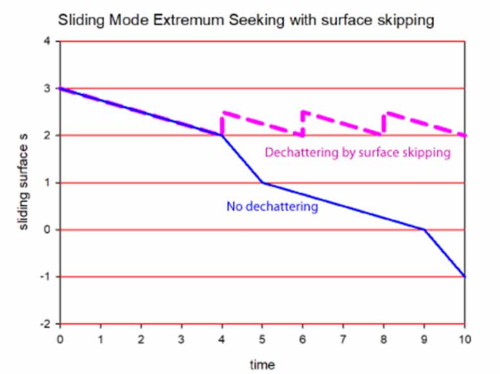

Figure 5. Comparison of sliding mode with and without surface skipping dechattering.

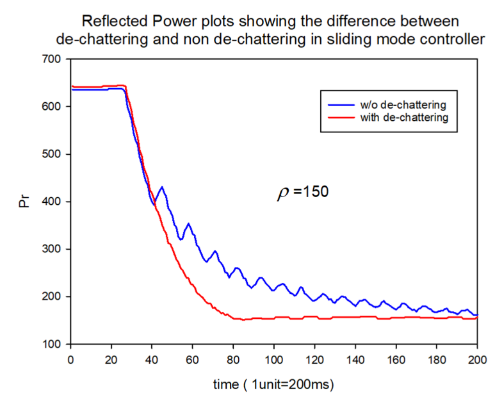

Figure 6. Comparison of reflected power with and without surface skipping dechattering.

to indicate that the end point has been reached. A moving average of 40 samples are used for the averaging, while the differentiation is obtained from coefficients of a Savitzky-Golay filter. The results are shown in Fig. 7, using a $|\Gamma| = 0.3$, where at time=150 the minimum is achieved at about $P_r = 140$. The system continues to switch directions until $\left\langle \left| \frac{d\,P_R}{dt} \right| \right\rangle$ becomes small enough to put the system into hibernation. As can be seen from Fig. 8, there still remains a large amount of chatters before the system finally goes into hibernation. But however this is a small amplitude tuner drive, and the effect on the reflected power is quite small. Nevertheless, in an effort to reduce this chatter, ρ is reduced by a factor of $\frac{1}{2}$ when the reflected power P_R has been reduced to below a pre-set amount closed to

ISBN: 978-3-95450-212-7 ISSN: 2673-5482 doi:10.18429/JACoW-CYCLOTRONS2022-MOPO017

the minimum. But since we cannot reduce ρ without affecting s in Eq. (8), we reduce Δt instead. This is illustrated in Fig. 10. The effect of the reducing of ρ occurs at $t \cong 30$, at which $P_R = 250$. As can be seen in the plot this reduction resulted in a much gentler slope in s. This significantly reduces the amount of chatter and therefore $\left\langle \left| \frac{d\,P_R}{dt} \right| \right\rangle$, allowing the system to go into hibernation much sooner. Furthermore, when the reflected power is below a threshold and $\left\langle \left| \frac{d\,P_R}{dt} \right| \right\rangle > 0$, indicating the power starts to rise again, the system immediately goes into hibernation. These are summarized in the following snippets to reduce Δt. The first part is called "ρ reduction",

```
if ( reversePower < 1.25*slidingMode.dead-band) dtx = 0.5*deltaTime;
if ( reversePower < 1.00*slidingMode.dead-band) dtx = 0.25*deltaTime;
```

and to go into hibernation using the "end detection" :

```
if (fabs(devAvg.val.avg) < 0.5 && rever-sePower < 1.5*slidingMode.deadband) {…}
if (devAvg.val.avg < 1.0 && reversePower < slidingMode.deadband) {…}
if (SGAvgRev.val.der>0 && reversePower < slidingMode.deadband) {…}
```

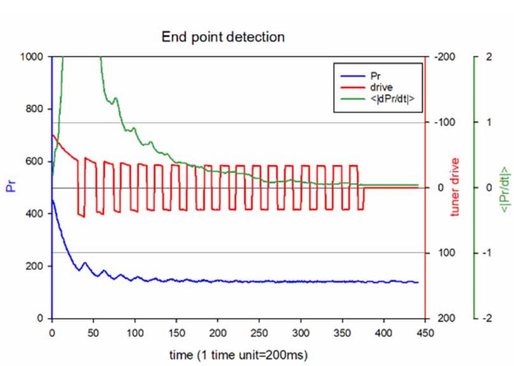

Figure 7. End point (Minimum Reflected power) detection.

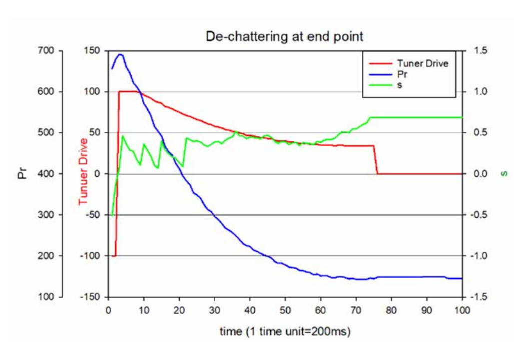

Figure 8. Dechattering at end point by reducing Δt.

However, when the reflected power drops below 250, ρ falls on the correct range and the power reduction is smooth and has a lot less chatter. Conversely for the dechattered case at the mid range the switching is protected by the halo and avoids chattering. However, at $P_R < 300$ the ρ-reduction kicks in and since the original ρ is already too low, the reduced ρ increases the chatter until the "end detection" algorithm kicks in and stop the movement.

CONCLUSION

The position preset, phase alignment and sliding mode controllers will be used in the new ISAC-1 resonance control. Based on each system's strength and weakness, they will be used at different stages of powering up. The position preset mode is used during the initial stage of powering up, when the RF is not yet established and is still in pulse mode. When the RF level reaches a preset value, and switching from pulse to CW is successful, the control enters into phase alignment mode. At this stage the RF will continue to be ramping up. When phase alignment is completed the control will switch to sliding mode. Using a combination of these three modes, the system will benefit from fast ramp-up and resilient to diurnal temperature variations.

REFERENCES

[1] K. Fong, "Beam loading equations", TRIUMF, Vancouver, BC, Canada, Design Note: TRI-DN-13-22, 2013.

[2] R. Leewe, M. Noallem, and K. Fong, "System modeling and control of resonance frequency frequency for an RF cavity using reflected power measurements", in *Proc. 2014 IEEE/ASME Int. Conf. Adv. Intell. Mechantronics*, Besacon, France, Jul. 2014, pp. 703-708. doi:10.1109/AIM.2014.6878161

[3] R. Leewe, "RF Cavity Tuning Based on Reflected Power Measurements", Ph.D. Thesis, Simon Fraser University, Vancouver, BC, Canada, 2017.

[4] R. Leewe, Z. Shahriari, and K.Fong, "Novel Scheme to Tune RF Cavities using Reflected Power", in *Proc. 28th Linear Accelerator Conf. (LINAC'16)*, East Lansing, MI, USA, Sep. 2016, pp. 757-759. doi:10.18429/JACoW-LINAC2016-THOP06

[5] J. Gulder and V. I. Utkin, "The chattering problem in sliding mode systems", in *Proc. 14th Int. Symp. of Mathematical Theory of Networks and Systems"*, Perpignan, France, Jun. 2000. A.E. Jai and M. Fliess, Eds. Université de Perpignan.

[6] H. Lee and V. I. Utkin, "Chattering suppression methods in sliding mode systems", *Annual Reviews in Control*, vol. 32, no 2, pp.179-188, 2007.

ISBN: 978-3-95450-212-7 ISSN: 2673-5482 doi:10.18429/JACoW-CYCLOTRONS2022-MOPO018

THE MAGNETIC FIELD DESIGN OF A 16 MeV VARIABLE ENERGY CYCLOTRON

Z. Wu, K. Z. Ding, J. Zhou
Institute of Plasma Physics, Chinese Academy of Sciences, Hefei, China
S. W. Xu, Hefei CAS Ion Medical and Technical Devices Co., Ltd., Hefei, China

Abstract

The development of a 16 MeV H^- cyclotron is in progress at CIM company (Hefei, China). Such machine is designed for radio-isotope production which is used for nuclear medicine. Beam extraction is ensured by means of stripper foils located at different radii to achieve variable extraction energy between 10 and 16 MeV. In this paper, the main magnet design was demonstrated in detail. An AVF magnet with four radial sectors was adopt to get strong axial focusing. The hill angular widths and hill gaps with radius were designed to meet the isochronous magnetic field. The tunes were optimized to avoid dangerous resonance. The result of magnet design was verified by beam dynamics simulations. After the presentation of the magnet design, some results on stripping extraction were also discussed. TOSCA (OPERA-3D) was used to perform 3D magnetic field simulation. An efficient beam simulation code developed by MATLAB was used to do beam dynamics simulations.

INTRODUCTION

In recent years, the Institute of Plasma Physics of the Chinese Academy of Sciences (ASIPP) and Hefei CAS Ion Medical and Technical Devices Co., Ltd. (CIM) are jointly developing a 10~16 MeV variable energy proton cyclotron, which can be used to produce medical radioisotopes.

Medical radioisotopes, such as ^{18}F and ^{11}C, are in great demand in China. Chinese government issued the Medium and Long term Development Plan for Medical Isotopes (2021-2035) in 2021, vigorously encouraging the application and innovation of nuclear medicine technology. The low energy (10-20 MeV) proton cyclotron has become the main equipment for isotope preparation with its advantages of small size and low cost [1].

ASIPP and CIM have rich experience in the manufacture and commissioning of cyclotrons. The cyclotrons such as SC200 [2] and CIM14-A developed have successfully extracted the beam. In order to further enrich the company's accelerator product series and meet the growing demand for radioisotopes, ASIPP and CIM decided to develop a proton cyclotron with a maximum extraction energy of 16 MeV and a maximum extraction current of 100 µA. Because the extraction method is stripping extraction, the extraction energy can be adjusted from 10 to 16 MeV to produce as many kinds of radioisotopes as possible. The cyclotron accelerates H^- ions. H^- ions whirl in the magnetic field at a frequency of 23.45 MHz. After passing through the stripping foil at the extraction radius (29.9~37.1 cm), two electrons are stripped off and become protons. The magnetic field design and beam dynamics simulation are described below.

MAGNET DESIGN

The cyclotron magnet system is shown in Fig. 1. It is composed of a conventional conductor coil, an iron yoke and 4 pairs of radial sectors. The magnet system is square in shape, 185 cm in side length, 92 cm in height, and 19.7 tons in total weight. It conforms to the characteristics of compactness and flexibility of medical cyclotron, and can be installed in the built hospital. The radius of the magnetic pole is 44.8 cm, which is a flat magnetic pole, and the gap between the magnetic poles is 4.1 cm. The hill-valley modulated magnetic field formed by 4 pairs of magnetic poles can provide axial focusing force for the beam. By shimming the width of the magnetic pole, the isochronism of the magnetic field can be optimized, the phase slip of the beam can be reduced, and the acceleration efficiency can be improved. The central field is designed to be about 1.54 T, which can be realized by conventional conductor coil, and the current density of the main coil is 250 A/cm^2. The main parameters of the magnet system are shown in Table 1.

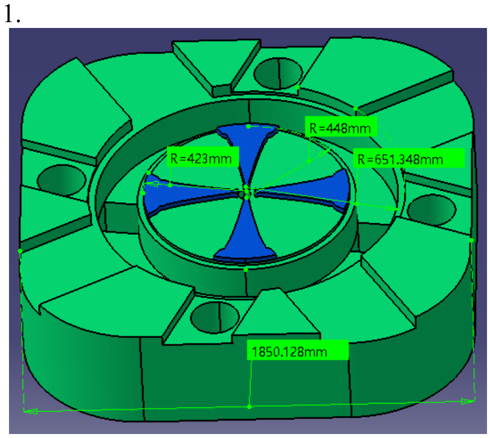

Figure 1: Magnet model of cyclotron.

Table 1: Preliminary Magnet System Parameters

Parameter [unit]	Value
Pole radius [cm]	44.8
Diameter of iron yoke [cm]	185
Hill gap [cm]	4.1
Valley gap [cm]	8.7
Main coil current density [A/cm2]	250
Magnet Height [cm]	92
Magnet weight [t]	19.7

23rd Int. Conf. Cyclotrons Appl. CYCLOTRONS2022, Beijing, China JACoW Publishing
ISBN: 978-3-95450-212-7 ISSN: 2673-5482 doi:10.18429/JACoW-CYCLOTRONS2022-MOPO018

ANALYSIS OF MAGNETIC FIELD

Through several rounds of iterative optimization of parameters such as main coil current, resonance orbital frequency and magnetic pole width, we finally obtained the physical design magnetic field that meets the requirements of isochronism. The axial magnetic field distribution in the middle plane is shown in Fig. 2. The deviation between the average field and the theoretical isochronous field is within ± 10 G, and the phase slip can be controlled within ± 20 °, as shown in Fig. 3. As shown in Fig. 4, the working diagram of the magnetic field can be seen that the axial working point Qz is greater than 0.05, which can provide sufficient magnetic focusing force and does not cross the dangerous resonance line. Since the 1/4 model is used to calculate the magnetic field, the 1st~3rd harmonic amplitude of magnetic field is less than 0.1 G, and the symmetry is perfect.

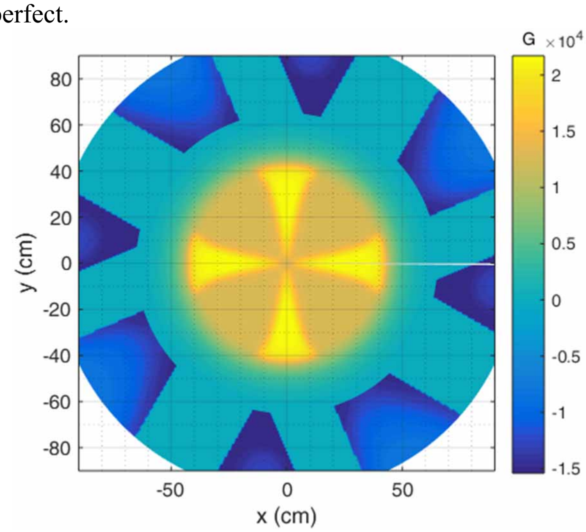

Figure 2: Axial magnetic field distribution in the middle plane.

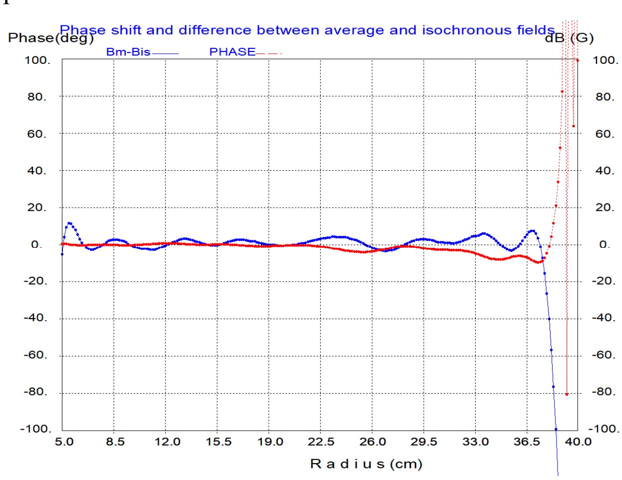

Figure 3: The deviation of the average field from the isochronous field and the slip phase.

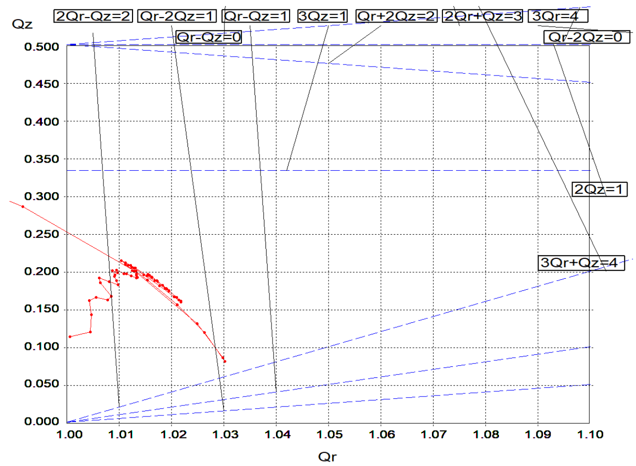

Figure 4: Working diagram and resonance line crossing.

BEAM DYNAMICS SIMULATION

In order to calculate the beam trajectory, we developed a beam dynamics simulation code based on MATLAB. The differential equation of motion of particles in the electromagnetic field can be derived from the momentum theorem. As shown in equation (1~3), it is a set of second-order ordinary differential equations with time t as the independent variable. Where, ε stands for electric field, B stands for magnetic field. The fourth order Runge-Kutta (RK4) algorithm is used to solve the differential equation, and the third order Lagrange interpolation is used to obtain the electromagnetic field data of any point, which can make the calculation efficiency and accuracy of the software reach a perfect balance. As shown in Fig. 5, the extraction trajectory of different energy particles calculated by the beam dynamics simulation code shows that the cyclotron can successfully achieve the extraction of 10~16 MeV variable energy beam, with the corresponding extraction radius of 29.9~37.1 cm.

$$\frac{dv_x}{dt}\cdot\frac{m}{q}+\frac{\varepsilon_x v_x+\varepsilon_y v_y+\varepsilon_z v_z}{c^2}\cdot v_x=v_yB_z-v_zB_y+\varepsilon_x \quad (1)$$

$$\frac{dv_y}{dt}\cdot\frac{m}{q}+\frac{\varepsilon_x v_x+\varepsilon_y v_y+\varepsilon_z v_z}{c^2}\cdot v_y=v_zB_x-v_xB_z+\varepsilon_y \quad (2)$$

$$\frac{dv_z}{dt}\cdot\frac{m}{q}+\frac{\varepsilon_x v_x+\varepsilon_y v_y+\varepsilon_z v_z}{c^2}\cdot v_z=v_xB_y-v_yB_x+\varepsilon_z \quad (3)$$

where:
v: speed of particle;
t: time;
m: mass of particle;
q: charge of particle;
ε: electric field intensity;
c: speed of light;
B: Magnetic induction intensity.

ISBN: 978-3-95450-212-7 ISSN: 2673-5482 doi:10.18429/JACoW-CYCLOTRONS2022-MOP0018

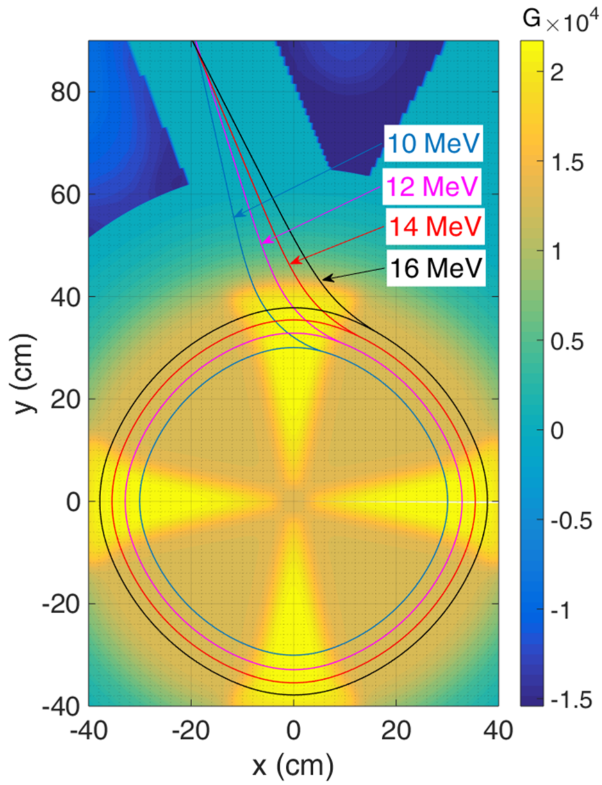

Figure 5: Extraction trajectories of particles with different energies.

CONCLUSION

The magnet of a 10~16 MeV variable energy cyclotron is designed at ASIPP and CIM, which has 4 pairs of radial sectors. The central field is designed to be about 1.54 T. The deviation between average and isochronous field is optimized to be less than 10 G. The working diagram is good as well. No dangerous resonance line is crossed. Beam dynamics simulations show that particles with energy of 10~16 MeV can be extracted at extraction radius of 29.9~37.1 cm.

REFERENCES

[1] T. J. Zhang *et al.*, "Overall design of CYCIAE-14, a 14 MeV PET cyclotron", *Nucl. Instrum. Methods Sect. B*, vol. 269, no. 24, pp. 2950-2954, Dec. 2011. doi:10.1016/j.nimb.2011.04

[2] K. Z. Ding *et al.*, "Study of the Beam Extraction from Superconducting Cyclotron SC200", in *Proc. 21st Int. Conf. on Cyclotrons and their Applications (Cyclotrons'16)*, Zurich, Switzerland, Sep. 2016, pp. 87-90. doi:10.18429/JACoW-Cyclotrons2016-MOP14

ISBN: 978-3-95450-212-7 ISSN: 2673-5482 doi:10.18429/JACoW-CYCLOTRONS2022-MOPO019

OPTIMIZATION OF RAPID MAGNETIC FIELD CONTROL OF THE CYCIAE-230 CYCLOTRON BEAMLINE MAGNETS

Aolai He, Zhiguo Yin, Qiqi Song, Tianjue Zhang, Peng Huang, Hongru Cai, Yang Wang, Bohan Zhao, Qiankun Guo, China Institute of Atomic Energy, Beijing, China

Abstract

The magnetic field precise and rapid control of the beamline magnets is essential to the Energy Selection System (ESS) for the proton therapy facility. During the scanning of proton beam for therapy, the field of each beamline magnet should be precisely controlled within the set time, layer upon layer. The position of beam spot to the nozzle should undoubtedly be stable and unchanged during the process. In practice, however, due to the wide energy range of proton therapy (70 ~ 230 MeV), the dynamic response of the beamline magnets usually shows nonlinear performances at a different energy, e.g., the magnetic field may cause a significant overshoot for some specific beam energy if one ignores the nonlinear effect. More challenge is that the magnetic field drops too slowly between the energy steps, which compromises the overall performance of rapid intensity modulated scanning therapy. A dynamic PID parameter optimization method is reported in this paper to address this issue. According to the transfer function of each magnet, the entire energy range is divided into several steps. Then, the experiments are carried out to find the most suitable PID parameters for each energy step. Finally, the "beam energy − excitation current − PID parameters" lookup table (LUT) is generated and stored in the beamline control system BCS for automation. During the treatment, using the LUT allows the energy setting for beamline magnets to be adjusted automatically with the most appropriate PID parameter, guaranteeing the overall performance of rapid scanning therapy. The experimental results show the overall response time of all the beamline magnets reduced from several hundred milliseconds to less than 65 ms, which meets the design requirement of less than 80 ms.

INTRODUCTION

CIAE is developing a proton therapy facility base on a superconducting cyclotron. The beamline is one of the important components of the therapy facility, which guarantees the proton track can be fixed from the cyclotron to the nozzle [1, 2]. When adjusting the treatment layer, the dynamic response of beamline magnets should be as fast as possible, reasons as follows: Firstly, it can reduce the treatment interval time between different layers and improve the efficiency of the therapy. Secondly, it minimizes the damage to the patient's healthy tissue. Thirdly, a long energy switching process will undoubtedly increase the cyclotron operation time when treating a patient. The total time loss added up by every treatment layer will be considerable. So, it will lead to a significant increase in total energy consumption. At present, the total energy selection time of proton therapy centers worldwide is mostly on the order of several hundred milliseconds scale. For example, the time for IBA in Belgium is 500 ms and the time for PSI in Swiss and Varian in America can be 150 ms. The energy selection time of the HUST-PTF proton therapy system at Huazhong University of Science and Technology is 144 ms, and its magnetic field dynamic response time is 105 ms [3].

The total energy selection time of CYCIAE-230 developed by CIAE is less than 80 ms. To guarantee the faster speed of magnetic field response, this paper presents a dynamic PID parameter optimization method.

MAGNET POWER SUPPLY CONTROL

The discrete PID algorithm is used for the magnet power supply. Figure 1 shows the control block diagram. The control loop adopts a double closed-loop control structure of output current outer loop and load voltage inner loop. The output current feedback value is obtained by DCCT. The load voltage control loop can solve the voltage disturbance in the main circuit of the power supply more quickly, and increase the stability of the system. In contrast, if there is only a single current control loop, the voltage disturbance needs to be reflected as output current fluctuation, then compensated. This process has hysteresis, and voltage disturbance cannot be eliminated essentially either.

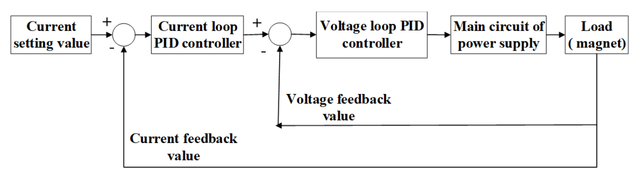

Figure 1: Control block diagram of magnet power supply.

OPTIMIZATION OF RAPID MAGNETIC FIELD CONTROL

Two Main Difficulty of Accelerating the Dynamic Response of Magnetic Field

The energy range of proton therapy is wide, which is 70 ~ 230 MeV. This leads to one set of PID parameters not being adapted to all the energy steps. The reasons are mainly divided into two aspects: the nonlinear variation of the magnetic field and the influence of hysteresis.

The Influence of Nonlinear Magnetic Field Variation The SRIM software was used to approximate the energy required for the beam to hit the body at various thicknesses. As the interval between each treatment layer is 2 mm in this project, the proton range interval is set as 2 mm in the calculation. Figure 2 shows the calculation results. It can be seen that the relationship between energy and range is not linear. To increase the same range, the energy variation (dE) is 1.89 MeV for 70 MeV and 0.81 MeV for 230 MeV. The difference can be 2.33 times.

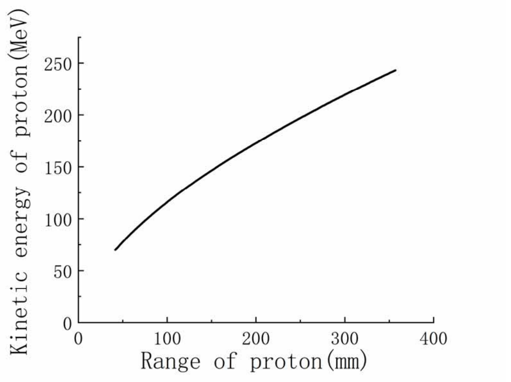

Figure 2: Proton range versus energy diagram.

According to the magnetic stiffness formula, the required field and excitation current of the bending magnet at each energy is calculated. The magnetic stiffness formula is as follows.

$$B = \frac{\sqrt{E^2 - E_r^2}}{300\rho} \tag{1}$$

where B is the magnetic induction intensity of the bending field, and the unit is T; ρ is the radius of curvature of the beam bending orbit; E is the proton's total energy and E_r = 938 MeV is the rest energy of the proton. By bringing in the energy data obtained by SRIM, the required magnetic induction intensity at each energy can be obtained. Derivation of Eq. (1) gives:

$$\frac{dB}{dE} = \frac{1}{300\rho}\sqrt{1 + \frac{E_r^2}{E^2 - E_r^2}} \tag{2}$$

where one can see that the smaller the energy is, the greater the magnetic field variation (dB) will be.

Table 1 shows the dE, dB, and the excitation current variation (dI) of the 60° deflection magnet. It can be seen that dB for 70 MeV extraction is 121.03 G while it is 30.99 G for 230 MeV. The difference can be 3.5 times.

Table 1: Comparison of dE, dB, and dI in different energy steps of 60° bending magnet

Energy segments	**dE**	**dB**	**dI**
~ 230 MeV	0.81 MeV	30.99 G	1.2319 A
~ 145 MeV	1.12 MeV	50.93 G	1.8627 A
~ 70 MeV	1.89 MeV	121.03 G	4.2335 A

In PID control, the steady-state error is controlled by the integral link, therefore the greater the dB, the stronger the integral effect. In the low energy segments, e.g., 70 MeV, due to a large amount of magnetic field change, the integration effect is very powerful, so it is very easy to cause an overshoot in response. In contrast, smaller dB makes a weaker integral effect, which results in a slow descent response when the beam energy is around 230 MeV. Figure 3 shows the different responses for 70 MeV and 230 MeV with the same PID parameters. Both of them take more than 80 ms.

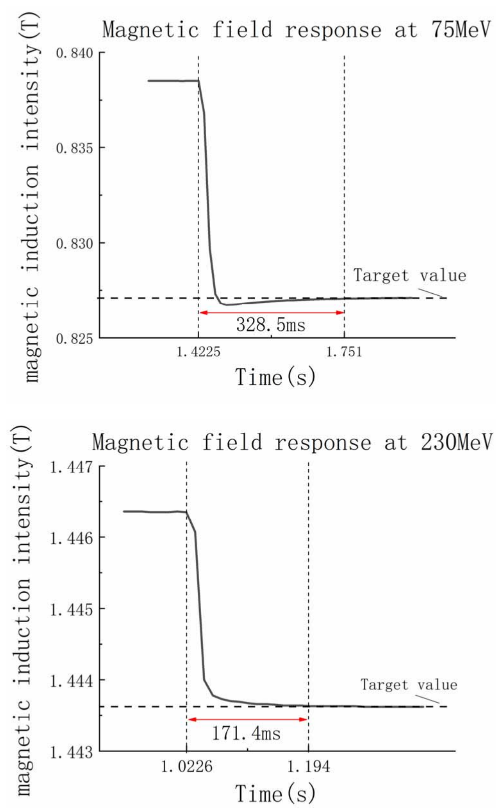

Figure 3: Under the same PID parameters, the responses at 70 MeV (top) and at 230 MeV (bottom) are apparently different.

The Influence of Hysteresis on Magnetic Field Response Hysteresis refers to the hysteresis loop relationship between magnetic induction intensity (B) and magnetic field intensity (H) when the magnetic state of ferromagnetic materials changes. The stronger the magnetic field, the more obvious the hysteresis effect. The formula of magnetic field intensity (H) and excitation current (I) is as follows:

$$I = \oint \vec{H} \cdot \vec{dl} = 2\pi r H \tag{3}$$

There is a linear relationship between H and I, so in the process of energy reduction, when the magnetic field is stronger, e.g., at 230 MeV, the hysteresis of B relative to I is more obvious. Figure 4 shows a comparison of responses with or without hysteresis. The error caused by hysteresis also needs to be eliminated by the integral link of PID control. Therefore, a larger integration factor is needed in higher energy segments.

ISBN: 978-3-95450-212-7 ISSN: 2673-5482 doi:10.18429/JACoW-CYCLOTRONS2022-MOPO019

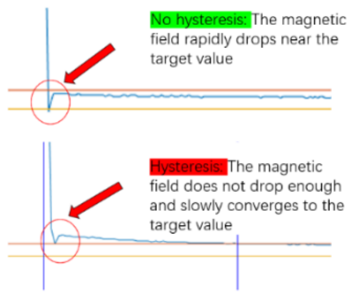

Figure 4: Comparison of response with/without hysteresis.

In summary, the field dynamic response usually shows nonlinear performances at different energy steps due to the two main difficulties. Therefore, facing a load of such characteristics, an optimal control method with dynamic PID parameters is proposed in this paper to speed up the magnetic field dynamic response.

Optimal Control Method for Dynamic PID Parameters

Firstly, a large number of magnetic field response data in different beam energies are obtained through vast experiments. Based on this, the energy range of 70 ~ 230 MeV can be divided into several segments. Each energy segment uses one set of PID parameters appropriate for the segment. This guarantees that the magnetic field at each energy converges quickly to the target value.

Secondly, the magnetic field dynamic response at 230 MeV is prioritized to regulate. At this time, since the field variation is small and the hysteresis is obvious, it is advisable to use a larger scale factor (K_P) and integration factor (K_I) to make the field value converge to the target value quickly. This group of PID parameters is suitable for the high-energy segment.

Thirdly, experiments with lower energy are gradually performed until a significant overshoot of the dynamic process occurs. This means that this set of parameters is no longer appropriate for this beam energy segment, and is definitely not suited for beam energies smaller than this. The PID parameters need to be set again to obtain a better dynamic response for this segment. Then, record this set of parameters and their appropriate energy segment. Repeat the above process until the parameterization of the entire energy range is completed.

Finally, a "beam energy − excitation current − PID parameter" LUT can be made based on the above results and stored in the BCS controller.

For the three kinds of bending magnets in CYCIAE-230, the first set of PID parameters with a larger integration factor (K_I) is used in the beam energy range of 230 ~ 145 MeV. Using the second set of PID parameters in the range of 145 ~ 110 MeV, the K_I is reduced. And the third set of PID parameters matches the range of 110 ~ 70 MeV, the K_I is further reduced to prevent overshoot, while the scaling factor (K_P) is appropriately increased.

The "beam energy − excitation current − PID parameter" LUT is made and stored in the controller of BCS, which is automatically called during the dynamic process of energy reduction, as illustrated in Fig. 5. The left side indicates the stepdown of the magnetic field with the beam energy during the treatment process, layer upon layer; the right side indicates the automatic modification of suitable PID parameters for different energy segments.

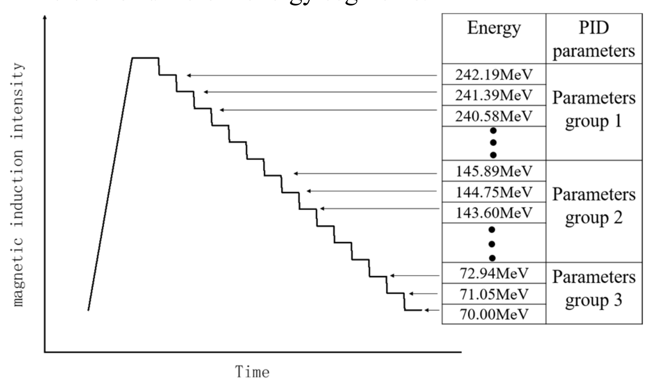

Figure 5: Logic schematic.

TEST RESULTS

Tests were performed on the CYCIAE-230 proton therapy system beamline. Figure 6 illustrates the comparison of the magnetic field response before and after optimization, using a 60° magnet as an example. All the magnetic induction intensity values (B) have been normalized to fit in the same graph. After optimization, the dynamic responses of each energy segment are matched to the best PID parameters, so the responses could end within 80 ms, with the shortest time being only 32.5 ms. In Fig. 6, the red curve represents the response in the 230 ~ 145 MeV segment before optimization. It can be seen that it has a lower descending slope and takes 120.47 ms. In contrast, the black curve shows the optimized response in this segment, with the time reduced to 63.3 ms. The field drop rate increased to 1.9 times the original. The green curve represents the response in the 110 ~ 70 MeV segment before optimization, which shows the drop overshoot and response time up to 273.5 ms. In contrast, the blue curve indicates the optimized response of this energy segment. The time is reduced to 50.67 ms and the response speed is increased to 5.4 times the original.

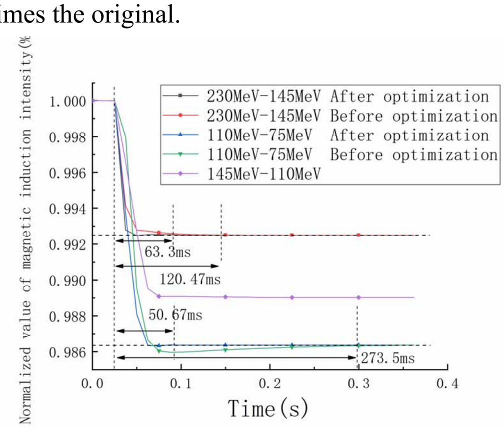

Figure 6: Comparison of field response before and after optimization.

ISBN: 978-3-95450-212-7 ISSN: 2673-5482 doi:10.18429/JACoW-CYCLOTRONS2022-MOPO019

For other types of magnets, the energy range of 30° and 75° bending magnets is also divided into three segments. Figure 7 shows the normalized dynamic response data in different segments, represented by different colour curves. The response speed of the 30° bending magnet in the 110 ~ 70 MeV segment is the slowest one (purple triangle curve), and the time is 65 ms, within 80 ms.

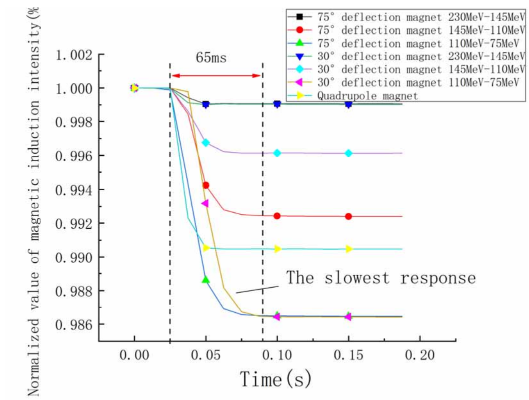

Figure 7: Comparison of other magnets in different energy segments.

CONCLUSION

To achieve the field precise and rapid control of the beamline magnets within the set time, an optimal control method of dynamic PID parameters is proposed in this paper. Large quantities of experiments are carried out to find the most suitable PID parameters for every energy step and LUT is used to adjust parameters automatically. Test results show that the field response time has been shortened from hundreds of milliseconds to 65 ms, which meets the design requirements of less than 80 ms. This work has been applied to the ESS of CYCIAE-230 in CIAE and provides a new idea for solving the problem of slow field dynamic response of large magnets.

REFERENCES

[1] T. J. Zhang *et al.*, "Developments for 230 MeV Superconducting Cyclotrons for Proton Therapy and Proton Irradiation", *Nucl. Instrum. Methods Phys. Res., Sect. B*, vol. 406, Part A, pp. 244-249, Sept. 2017. doi:10.1016/j.nimb.2016.11.010

[2] A. Degiovanni and U. Amaldi, "History of hadron therapy accelerators", *Physica Med.*, vol. 31, no. 4, pp. 322-332, June 2015. doi:10.1016/j.ejmp.2015.03.002

[3] P. L. Li *et al.*, "Design of HUST-PTF beamline control system for fast energy changing", *Nucl. Eng. Technol.*, vol. 54, no. 8, pp. 2852-2858, Aug. 2022. doi:10.1016/j.net.2022.02.023

ISBN: 978-3-95450-212-7 ISSN: 2673-5482 doi:10.18429/JACoW-CYCLOTRONS2022-TUAI01

CYCLOTRON BEAM EXTRACTION BY ACCELERATION

C. Baumgarten*, Paul Scherrer Institut, 5232 Villigen PSI, Switzerland

Abstract

One of the decisive issues in the design of a new cyclotron is the choice of the beam extraction method. Typical methods are extraction by electrostatic extractors and by stripping. The former method requires DC high voltage electrodes which are notorious for high-voltage breakdowns. The latter method requires beams of atomic or molecular ions which are notorious for rest-gas- and Lorentz-stripping. We discuss the conditions to be met such that a charged particle beam will leave the magnetic field of an isochronous cyclotron purely by fast acceleration.

INTRODUCTION

One of the first decisions to be made in the conceptual design phase of a new cyclotron regards the method of beam extraction. The most frequently used methods are extraction by electrostatic septum extractors or by stripper foils. The latter requires the use of projectiles which are not fully stripped yet, i.e., for instance H^- or H_2^+ instead of bare protons (H^+). But stripping of H^- or H_2^+ is also known due to scattering of the projectiles with rest gas or by strong fields (i.e., Lorentz stripping). In order to avoid internal loss of particles and the ambient activation due to these losses, the field must be limited to rather low values (especially in case of H^-), and/or an excellent vacuum pressure is obligatory, typically 10^{-7} bar and below.

The use of electrostatic extractors (EEs) has the disadvantage that such devices are notorious for high-voltage breakdowns. Experience at PSI has shown that EEs are also sensitive to contamination by dust and dirt and to rf-power leaking off the accelerating structures.

So-called "self-extracting" cyclotrons have been suggested and built before [1], but the conditions to be met by such cyclotrons have, to the author's knowledge, never been fully clarified.

Here we investigate the question whether cyclotrons can be designed such that the beam leaves the cyclotron purely by fast acceleration. In order to answer this question we will first review the reasons why the beam does (usually) not leave the field of isochronous cyclotrons simply by acceleration.

THE SMOOTH ACCELERATION APPROXIMATION

For this purpose we use a simplified cyclotron model, i.e., we will ignore the requirement to use azimuthally varying fields (AVF) to obtain vertical stability. In cases where one is interested exclusively in the radial motion, this approximation is adequate since the AVF has only a weak influence on the radial tune.

* christian.baumgarten@psi.ch

Hence we assume rotational symmetry, that is, the field is a function of radius only $B = B(R)$. As well known, the field is isochronous for

$$B_{iso}(R) = B_0\,\gamma \tag{1}$$

where $\gamma = (1-\beta^2)^{-1}$ is the relativistic factor. Since the orbit length per revolution is $s = 2\pi\sqrt{R^2 + (\frac{dR}{d\theta})^2}$ and since $\frac{dR}{d\theta} \ll R$ usually holds, the velocity is in good approximation given by $v = \omega_{rev}\,R$ and hence we define the radial function

$$\gamma_R = \frac{1}{\sqrt{1 - R^2/a^2}} \tag{2}$$

with the so-called "cyclotron radius" $a = c/\omega_{rev}$. However any real world machine has a finite radius $R < a$ and is isochronous only up to the fringe field. A simple and reasonably realistic model of the fringe field is given by an Enge-type function [2, 3]

$$f(R) = (1 + \exp\left((R - R_h)/g\right))^{-1} \tag{3}$$

where R_h is the radius for $f = 1/2$ and g is a parameter which is approximately half of the pole gap. The magnetic field is then assumed to be

$$B(R) = B_{iso}\,f(R) = B_0\,\gamma_R\,f(R)\,. \tag{4}$$

When the beam enters the fringe field, the bunches will necessarily get out of sync with the accelerating rf voltage. The revolution frequency ω_{rev} is

$$\omega_{rev} = \frac{q}{m\,\gamma}\,B = \frac{q}{m\,\gamma}\,B_0\,\gamma_R\,f = \omega_0\,\frac{\gamma_R}{\gamma}\,f\,. \tag{5}$$

The velocity then is $v = \omega_{rev}\,R$ and the relativistic γ-factor

$$\gamma = 1/\sqrt{1 - \omega_{rev}^2\,R^2/c^2} = 1/\sqrt{1 - (\gamma_R^2 - 1)\,f^2/\gamma^2}\,. \tag{6}$$

Solving for γ gives

$$\gamma = \sqrt{1 + (\gamma_R^2 - 1)\,f^2}\,. \tag{7}$$

THE BENDING LIMIT

Any finite magnetic field has a bending limit, which can be obtained from

$$p = q\,R\,B(R)\,. \tag{8}$$

The momentum is maximal when $\frac{dp}{dR} = 0$ with

$$\frac{dp}{dR} = q\,B\,(1 + k) \tag{9}$$

where the field index k is defined by

$$k = \frac{R}{B}\,\frac{dB}{dR}\,. \tag{10}$$

ISBN: 978-3-95450-212-7 ISSN: 2673-5482 doi:10.18429/JACoW-CYCLOTRONS2022-TUAI01

Hence the bending limit is reached for $k = -1$. Inserting $B(R)$ from Eq. (4) gives

$$k = \gamma_R^2 - 1 - (1-f)\,\frac{R}{g} \tag{11}$$

so that the ultimate extraction point is characterized by

$$f = 1 - \gamma_R^2\,\frac{g}{R}\,. \tag{12}$$

Since γ_R is of order $O(1)$, and since the half-gap g holds usually $g \ll R$, the value of f at extraction is still close to one, and $1 - f$ is small.

THE PHASE SHIFT BY THE FRINGE FIELD

Usually the rf frequency is an integer multiple N_h (called *harmonic number*) of the orbital frequency ω_0: $\omega_{rf} = N_h\,\omega_0$. The phase shift per turn $\frac{d\phi}{dn}$ is given by

$$\frac{d\phi}{dn} = T_{rev}\,(\omega_{rf} - N_h\,\omega_{rev}) = 2\,\pi\,N_h\,(\frac{\omega_0}{\omega_{rev}} - 1)\,. \tag{13}$$

The phase shift per radius can therefore be written as

$$\frac{d\phi}{dR} = \frac{d\phi}{dn}/\frac{dR}{dn}\,. \tag{14}$$

The phase shift hence strongly depends on the radius gain per turn, which is known to be directly proportional to the energy gain per turn dE/dn:

$$\frac{dR}{dn} = \frac{dE}{dn}\,\frac{R\,\gamma}{E\,(\gamma+1)\,(1+k)}\,. \tag{15}$$

Most cyclotrons have an energy gain which is too small to prevent the phase from approaching 90° in the fringe field and from being decelerated back to the center. On the other hand, *if* the rf voltage of the accelerating structures ("Dees" or cavities) is high enough to approach the bending limit, then the beam will leave the magnetic field.

It follows, after some algebra [1], that

$$\frac{d\phi}{dR} = \frac{2\,\pi\,N_h\,m\,c^2}{dE/dn}\,(1 - \frac{\gamma_R\,f}{\gamma})\,(1+k)\,\gamma_R\,f\,\frac{R}{a^2}\,. \tag{16}$$

By the use of

$$\frac{df}{dR} = -\frac{1}{g}\,f\,(1-f) \tag{17}$$

one can change the independent variable from R to f so that

$$\frac{d\phi}{df} = -\frac{2\,\pi\,N_h\,m\,c^2}{dE/dn}\,(1 - \frac{\gamma_R\,f}{\gamma})\,(\frac{g\,\gamma_R^2}{1-f} - R)\,\gamma_R\,\frac{R}{a^2}\,. \tag{18}$$

In the region of interest, i.e., the fringe field region, the value of $1 - f$ changes rapidly over short distances, while the (relative) change of R and γ_R is small. Hence one can obtain a reasonable approximation of the term $(1 - \frac{\gamma_R\,f}{\gamma})$ by a first order Taylor series in f, located at $f = 1$, assuming that R and γ_R are constant:

$$(1 - \frac{\gamma_R\,f}{\sqrt{1 + (\gamma_R^2 - 1)\,f^2}}) = \frac{1-f}{\gamma_R^2} + \ldots \tag{19}$$

With this approximation one obtains

$$\frac{d\phi}{df} \approx -\frac{2\,\pi\,N_h\,m\,c^2}{dE/dn\,\gamma_R}\,(g\,\gamma_R^2 - R\,(1-f))\,\frac{R}{a^2}\,. \tag{20}$$

With the energy gain given by

$$E = q\,V_{rf}\,\cos(\phi) \tag{21}$$

it follows that

$$d\sin(\phi) \approx -\frac{2\,\pi\,N_h\,m\,c^2}{q\,V_{rf}\,\gamma_R}\,(g\,\gamma_R^2 - R\,(1-f))\,\frac{R}{a^2}\,df\,. \tag{22}$$

the integration, again assuming that R and γ_R are approximately constant, from $f = 1$ to the extraction point (Eq. (12)) then gives

$$\sin(\phi_f) - \sin(\phi_i) = \frac{\pi\,N_h\,m\,c^2\,g^2\,\gamma_R\,(\gamma_R^2 - 1)}{q\,V_{rf}\,R^2}\,. \tag{23}$$

Finally we may approximate $\gamma_R \approx \gamma$ so that our main result becomes

$$\sin(\phi_f) - \sin(\phi_i) = \frac{\pi\,N_h\,E\,\gamma\,(\gamma+1)}{q\,V_{rf}}\,\frac{g^2}{R^2}\,. \tag{24}$$

If the initial phase ϕ_i is zero, and the final phase is supposed to be below 90°, $\sin(\phi_f) \le 1$ then

$$\frac{\pi\,N_h\,E\,\gamma\,(\gamma+1)}{q\,V_{rf}}\,\frac{g^2}{R^2} \le 1 \tag{25}$$

and hence

$$\frac{q\,V_{rf}}{E} \ge \pi\,N_h\,\gamma\,(\gamma+1)\,\frac{g^2}{R^2}\,. \tag{26}$$

EXAMPLES

COMET

The first example we consider is PSI's 250 MeV proton therapy cyclotron "COMET" [5, 6], which has a harmonic number $N_h = 2$, an extraction radius of $R = 810$ mm and a half-gap of about 22 mm. Inserting these numbers into Eq. (26) yields a minimal accelerating voltage of ≈ 3.25 MV per turn. The real voltage is about 380 kV, i.e., about an order of magnitude to low. Escape extraction would therefore be within reach, if the gap would be reduced by a factor of about 3, which is about 7 mm.

[1] More details are given in Ref. [4].

ISBN: 978-3-95450-212-7 ISSN: 2673-5482 doi:10.18429/JACoW-CYCLOTRONS2022-TUAI01

Ring Cyclotron

The second example is the PSI's 590 MeV Ring cyclotron, an 8-sector machine with an extraction radius of 4.5 m, operated with $N_h = 6$. The gap has an elliptic shape, but at extraction it has almost the same gap as COMET, i.e., $g = 20$ mm. According to Eq. (26) the minimal voltage required for escape extraction is then $V_{rf} \geq 940$ kV. Since the average energy gain per turn of the PSI Ring is about 2.8 MeV, this machine already fullfills the condition for escape extraction.

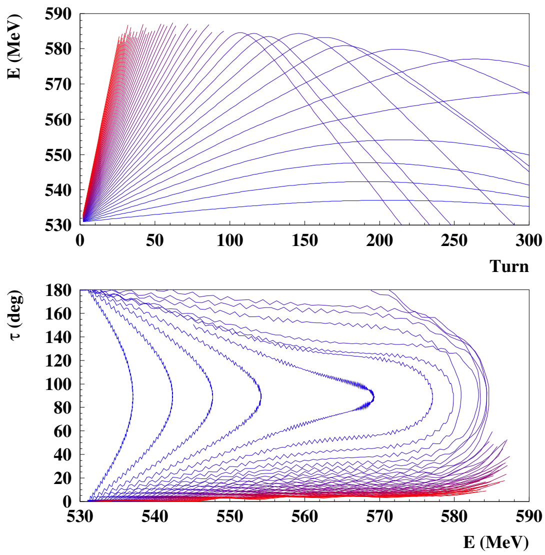

Figure 1: Top: Energy vs. turn-number for particles starting with phase $\phi_i = 0$ for various values of V_{rf} (increasing from blue to red). Bottom: Phase $\phi(E)$ for the same conditions.

Figure 1 shows some results of tracking calculations for the PSI Ring machine for various rf voltages, from zero (blue) to the actual voltage (red), without electrostatic extractor. The calculation start with initial phase $\phi_i = 0$ before extraction (at $E = 530$ MeV). For about 90 turns and less, i.e., for a voltage V_{rf} of more than (590 MeV – 560 MeV)/90 = 670 kV/turn, the beam does not reach 90° before extraction. As the red lines in Fig. 1 show, the change in phase due to the fringe field is very small and can almost be neglected.

However, even though the protons will definitely leave the field without electrostatic extractor, the strong negative gradient of the fringe field severely defocuses the beam. Without any measures - like for instance a magnetic gradient corrector - the protons would leave the field almost without preferred direction. Figure 2 shows that the final direction of a family of tracks with very similar starting conditions as some central orbit is almost arbitrary. Therefore extraction by acceleration (or "self-extraction"), requires a method to keep the beam radially compact. The simplest method to introduce a "gradient corrector" is the installation of a passive magnetic channel, i.e., of iron bars or stripes in the pole gap of the sector magnets which are magnetized by the main field itself. As orbit tracking calculations showed, the extraction is so fast that the field gradient is negative

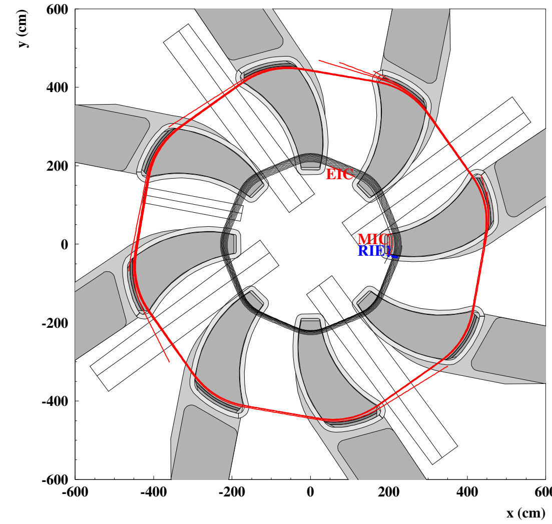

Figure 2: Top view the PSI Ring cyclotron (sector shapes and positions of the cavities) with a family of median plane orbits. The first few turns are indicated in black and the last turns in red.

only in the very last sector so that a gradient correction of the last sector should be sufficient to keep the beam radially compact (see Fig. 3). As shown in Fig. 4, this chosen family

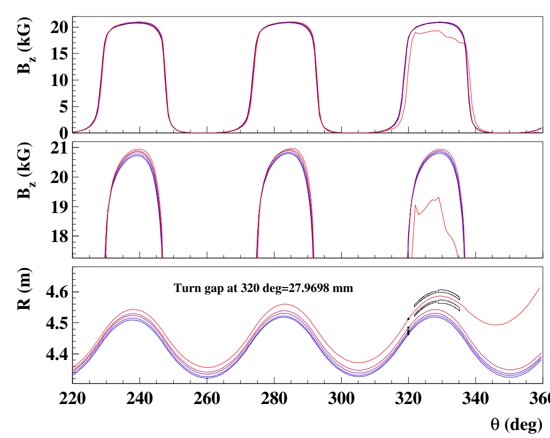

Figure 3: Top: Magnetic field along the last five turns (blue to red) in the Ring cyclotron with a magnetic gradient corrector installed on the last sector before extraction. Middle: Same plot with different scale. The last turn (red) "sees" the highest field up to the last sector. Bottom: Radius versus angle of the last five turns and the last sectors before extraction. The location of the main iron strips of the gradient corrector is indicated in black.

of tracks remains close together. An answer to the question whether this method could be used in the PSI Ring cyclotron with the required extraction efficiency of 99.99 %, requires further detailed studies. Nonetheless, the results show, as we believe, that extraction without electrostatic extractors

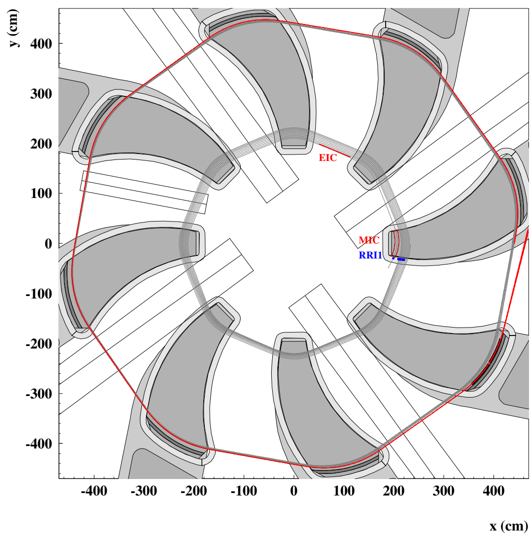

Figure 4: Median plane of the PSI Ring cyclotron with a family of median plane orbits. The first few turns are indicated in black and the last turns in red. The last sector (at $\theta \approx 315°$) before extraction is equipped with a passive magnetic channel.

is possible, specifically in cyclotrons with a small ratio g/R and a high energy gain per turn.

DREAM MACHINES

Both conditions, i.e., high radius and high energy gain per turn, are met in so-called "Dream machines" [7, 8], high current proton drivers for energies ≥ 800 MeV, which could be used for the transmutation of nuclear waste or for spallation neutron sources. The incredible increase of the beam current of the PSI Ring cyclotron from the originally specified 100 µA to 2.4 mA confirmed Joho's N^3-law [9], which states that the maximum beam current, assuming constant losses, increases with the third power of the energy gain per turn - or with the third power of the inverse turn number N^{-3}, respectively. Due to this law Dream machines require a large energy gain per turn.

The energy efficiency η_{acc}, one of the most important figures of this type of machines, is given by [10, 11]:

$$\eta_{acc} = \frac{P_{beam}}{P_{ohmic} + P_{beam}/\eta_{rf} + P_{aux}} \tag{27}$$

where $P_{ohmic} = N_{cav}\, V_{cav}^2/(2\, R_{cav})$ is the total ohmic loss in the walls of the cavities. Hence the ohmic loss increases linear with the number of cavities but quadratic with the voltage of the individual cavities. From the point of view of energy efficiency and reliability, dream machines have a large number of cavities, which naturally leads to a large number of sectors and a large radius. According to our result, these requirements reduce the phase shift caused by the lack of isochronism in the fringe field region and therefore facilitate extraction by acceleration.

ACCURACY

With respect to the accuracy of Eq. (26) one can distinguish two sources of uncertainty, firstly the error due to the use of the sectorless smooth acceleration approximation and secondly the error due to the approximations which have been used to derive Eq. (26). The former uncertainty can not be avoided and the latter depends on the accuracy of the fringe field model and the accuracy of the main parameter g.

The accuracy of Eq. (26) depends of the validity of it's main assumption, namely that the simplest Enge function with a single parameter g, which is proportional to the gap size, provides a reasonable description of the fringe field. As

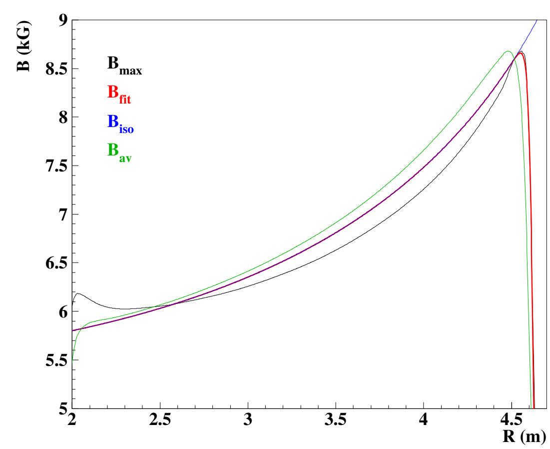

Figure 5: Fringe field of the PSI Ring cyclotron: Azimuthal average (green) vs. maximum field (black) and fit with Enge function to maximum field (red). The isochrounous field $B_{iso} = B_0\,\gamma_R$ is shown is blue.

shown in Fig. 5, the exact shape of the fringe field - and the parameter g - in a real cyclotron might depends significantly on the method of evaluation. Due to the azimuthal scalloping of the orbit, the azimuthal average of the magnetic field is usually less steep than the maximum field, taken as a function of radius. The attempt to obtain g from a fit to the average field therefore provides a too large value and a fit to the maximum field a slightly to low g.

CONCLUSION

We calculated an approximation for the integral phase shift of a cyclotron beam passing the simplest Enge-type fringe field. The result indicates that electrostatic extractors, though certainly helpful, are not intrinsically required for the beam extraction from high power cyclotrons of the kind of the PSI Ring cyclotron. Due to the high energy gain per turn, the beam leaves the magnetic field in any case. In order to extract a well-focused beam, measures to correct the gradient of the magnetic fringe field are required. However, even with electrostatic extractors, the gradient field of PSI Ring cyclotron requires an additional focusing magnet as

ISBN: 978-3-95450-212-7 ISSN: 2673-5482 doi:10.18429/JACoW-CYCLOTRONS2022-TUAI01

part of extraction system [12, 13], so that the total number of extraction elements would not increase.

An extrapolation of the design principles of dream machines appears to facilitate extraction by acceleration in high power proton drivers. The possibility to avoid electrostatic elements in this kind of machines sheds new light on the possibility to use highly energy-efficient cyclotrons as drivers for accelerator driven systems.

REFERENCES

[1] W. Kleeven *et al.*, "The self-extracting cyclotron", in *Proc. 16th Int. Conf. on Cyclotrons and their Applications (Cyclotrons'01)*, East Lansing, MI, USA, May 2001, pp. 69–73.

[2] H. A. Enge, "Effect of extended fringing fields on ion-focusing properties of deflecting magnets", *Rev. Sci. Instrum.*, vol. 35, no. 3, pp. 278–287, 1964. doi:10.1063/1.1718806

[3] H. A. Enge, "Deflecting Magnets", in *Focusing of Charged Particles Vol. 2*, Albert Septier, Ed. Academic Press, 1967, pp. 203–263.

[4] C. Baumgarten, "Cyclotron Beam Extraction by Acceleration", in *ICFA Newsletter No. 84*, to be published. Preprint: doi:10.48550/arXiv.2205.04124

[5] M. Schillo *et al.*, "Compact superconducting 250 MeV proton cyclotron for the PSI PROSCAN proton therapy project", *AIP Conference Proceedings*, vol. 600, no. 1, 2001, pp. 37–39.

[6] A. E. Geisler *et al.*,"Commissioning of the ACCEL 250 MeV proton cyclotron", in *Proc. 18th Int. Conf. on Cyclotrons and Their Applications (Cyclotrons'07)*, Giardini-Naxos, Italy, Oct. 2007, pp. 9–14.

[7] Th. Stammbach, "High intensity problems, revisited or cyclotron operation beyond limits", in *Proc. 15th Int. Conf. on Cyclotrons and their Applications (Cyclotrons'98)*, Caen, France, Jun. 1998, pp. 369–376.

[8] T. Zhang *et al.*, "Conceptual design of an 800 MeV high power proton driver", *Nucl. Instrum. Methods Phys. Res. Sect. B*, vol. 269, no. 24, pp. 2964–2967, 2011. doi:10.1016/j.nimb.2011.04.053

[9] W. Joho, "High intensity problems in Cyclotrons", in *Proc. 9th Int. Conf. on Cyclotrons and their Applications (Cyclotrons'81)*, Caen, France, Sep. 1981, pp. 337–347.

[10] J. K. Grillenberger, M. Seidel, S.-H. Kim, M. Yoshii, and V. P. Yakovlev, "The energy efficiency of high intensity proton driver concepts", in *Proc. 8th Int. Particle Accelerator Conf. (IPAC'17)*, Copenhagen, Denmark, May 2017, pp. 4842–4847. doi:10.18429/JACoW-IPAC2017-FRXCB1

[11] J. Grillenberger, C. Baumgarten, and M. Seidel, "The high intensity proton accelerator facility", *SciPost Phys. Proc.*, article no. 2 (18 pages), 2021. doi:10.21468/SciPostPhysProc.5.002

[12] U. Schryber *et al.*, "High power operation of the PSI-accelerators, in *Proc. 14th Int. Conf. on Cyclotrons and their Applications (Cyclotrons'95)*, Cape Town, South Africa, Oct. 1995, pp. 32–38.

[13] M. Olivo. "The electrostatic channel for the S.I.N. 590 MeV ring cyclotron" , in *Proc. 7th Int. Conf. on Cyclotrons and their applications (Cyclotrons'75)*, Zurich, Switzerland, Aug. 1975, pp. 292–296.

ISBN: 978-3-95450-212-7 ISSN: 2673-5482 doi:10.18429/JACoW-CYCLOTRONS2022-TUA001

HISTORY AND PROSPECTIVES OF GANIL

A. Savalle, O. Kamalou, on behalf of the GANIL Collaboration
GANIL, Grand Accélérateur National d'Ions Lourds, CEA-DSM/CNRS-IN2P3, France

Abstract

The first beam of the GANIL facility (Grand Accélérateur National d'Ions Lourds) at Caen was ejected from the second separated sector cyclotron forty years ago (November 19th, 1982). Since then, several evolutions occurred. In 2001, the first exotic beam, produced by the Isotope Separation On-Line method at the SPIRAL1 facility, was delivered to physics. The GANIL team realized an upgrade of this facility in order to extend the range of post-accelerated radioactive ions in years 2013-2017, with first radioactive beams delivered in 2018. In 2019, GANIL became also a LINAC facility, with the first beam accelerated in the SPIRAL2 facility. The DESIR facility is aimed at using beams from SPIRAL2 and from SPIRAL1 facility, motivating a major renovation plan of the cyclotron facility. Parts of ancient and recent history of GANIL will be presented as well as its future.

FROM THE BEGINNING FORTY YEARS AGO TO UPGRADE OF SPIRAL1

November 19th, 1982, 12h30 am, the first beam was seen on the profiler located at the output of the second separated sector cyclotron at GANIL (Fig. 1) 5 nA were ejected from 150 nA injected ($^{40}Ar^{16+}$), starting from 200 nA $^{40}Ar^{4+}$ ejected of SSC1.

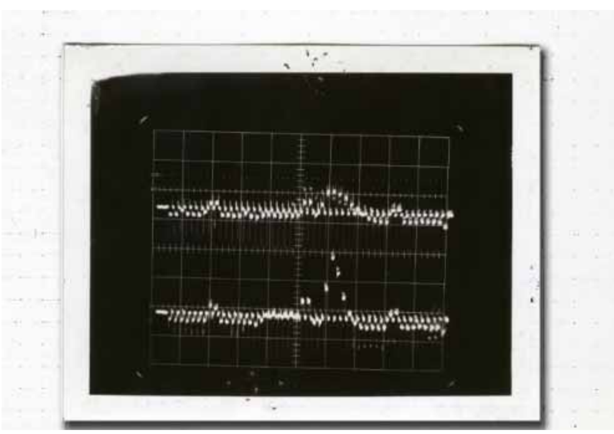

Figure 1: 1st beam profile, SSC2 ejection.

GANIL construction was decided in 1975. The design included two compact cyclotrons as injectors, one for SSC1 and for SSC2. In the final design, the two injectors may inject the beam into SSC1, and also SSC2 (the two SSCs were identical). There is one rebuncher between the injectors and SSC1, one stripper between SSC1 and SSC2, one low energy spectrometer and a high-energy one, called "Alpha" spectrometer due to its shape. The beam is distributed to experimental areas through a "fishbone" (Fig. 2).

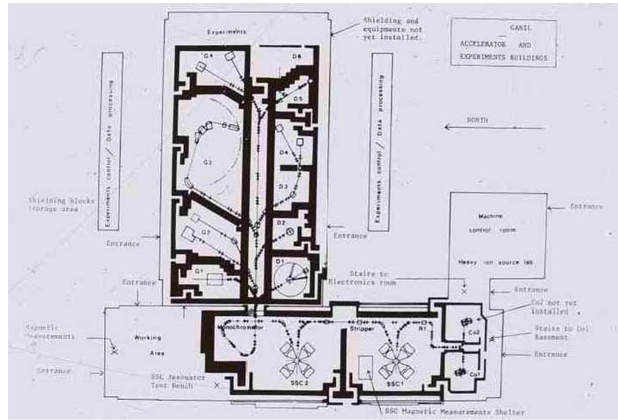

Figure 2: Design of GANIL.

The facility was built in the years 1978 – 1982. In 1983, the first experimental took place in January. That year, Ne, Ar, Kr, and O were accelerated. The O was accelerated at the maximal energy, 95 MeV/nucleon, but the energy was low for heavier beams (45 MeV/A for Kr beam).

Figure 3 shows an RF cavity ready for installation into the SSC.

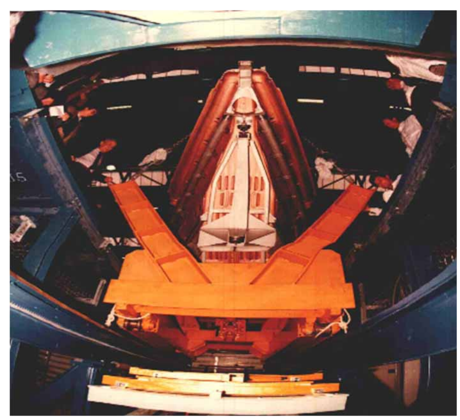

Figure 3: RF cavity installation.

In 1989, the OAE project was achieved [1], increasing the maximal energy for heavy beams. The key point was the stripping efficiency, increased with a higher SSC1 ejection energy (operation of SSC1 with harmonic 5 instead of 7, and new injection radius in SSC2 – 1,2 m instead of 0,825).

Increasing SSC1 energy was facilitated by the new sources, ECR technology replacing the PIG sources, inside the cyclotrons, in 1985. In 1992, the C01 ECR source was installed in a 100 kV platform and a new injection beam line was built, leading to better intensities and higher transmission (up to 65%). However, there were discharges in the accelerator tube and in 2004, we added a solenoid and a dipole inside the platform to have a pre-selection and limit the intensity in the tube.

23rd Int. Conf. Cyclotrons Appl. CYCLOTRONS2022, Beijing, China JACoW Publishing
ISBN: 978-3-95450-212-7 ISSN: 2673-5482 doi:10.18429/JACoW-CYCLOTRONS2022-TUA001

With high energies and intensity, we could get radioactive beams. The firsts were produced in flight in SISSI [2]. The target was cooled, rotated and designed for 1 KW deposited power (Fig. 4). A first superconducting solenoid gave a beam size of 0.2 mm radius, a second gave an angular acceptance of 80 mrad.

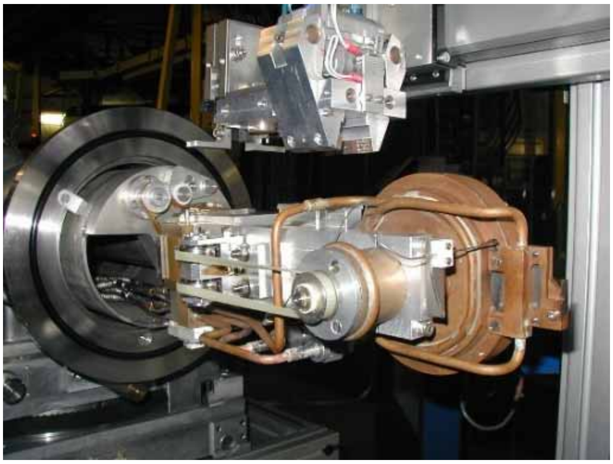

Figure 4 : SISSI target.

The THI project [3] increased the beam intensity in the years 95 – 2001, up to 5 kW. This was realized with beam loss monitors, a new rebuncher, a new septum for SSC2 deflector, and many hours of beam tests.

In parallel, it was the building and commissioning of SPIRAL1 [4], which consists in a **Isotope Separation On-Line method :** the beam is stopped in a carbon target, to produce secondary elements which diffuse in the target, are ionized in an ion source and transported to a new cyclotron to be post-accelerated. The cyclotron energy is 1.2 to 25 MeV/A using harmonics 2 to 6. In the original project there were two caves for the Target-Ion Sources (Fig. 5).

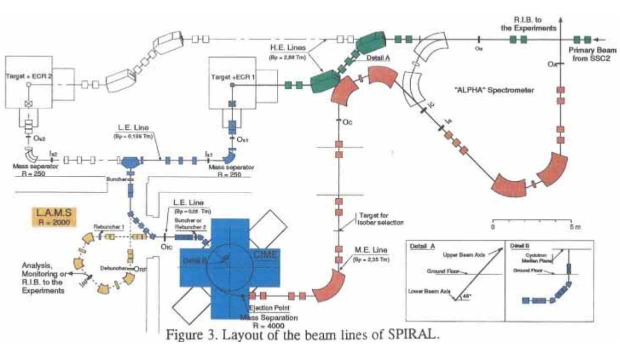

Figure 5: 1st design of SPIRAL1.

Three modifications were made to extend the use of GANIL beams: Medium Energy Exit (SME in French) in 1989, Low-energy irradiation south of injectors (IRRSUD) in 2002, and LIRAT which use the low energy beam of SPIRAL1 in 2005. LIRAT consists in a beam line, an RFQ-cooler and a trap in a platform to study the radioactive beam properties.

In recent years SPIRAL1 was upgraded. It is now possible to use different targets (and no more carbon only), different ion sources in particular FEBIAD source which is non selective and produces many elements, but is a 1+ source so that a Phoenix charge breeder is needed (Fig. 6). However, we use also N+ ECR sources, and in that case the beam must pass through the charge breeder.

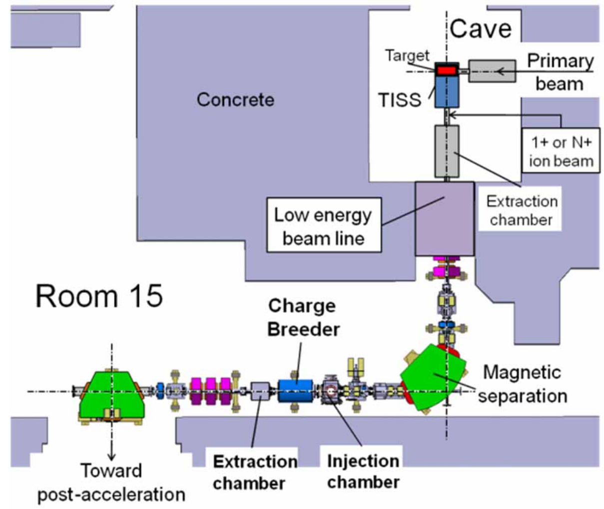

Figure 6: Schematic of the SPIRAL1 upgrade.

The integration of charge breeder and beam line modification was achieved between 2013 and 2016. In 2017, the charge breeder and beam line commissioning was started. The whole system was validated (performance, beam optics) by the end of 2017 [5]. First radioactive beams (^{17}F, ^{38}K) were delivered in 2018-2019. The mass resolution of CIME cyclotron allows us to purify the beam in many cases for light element (A<20). For heavier masses, stripping foils are generally used.

SPIRAL2 AND DESIR

From 2005 to 2019, GANIL was more concerned by the SPIRAL2 project than extending the cyclotron facility (Fig. 7). The original project included post-accelerations of fission products in CIME; only the LINAC part with 2 experimental rooms are built today. In 2019, GANIL became also a LINAC facility, with the first beam accelerated in the SPIRAL2 facility.

The DESIR (Decay, Excitation, Storage of Radioactive Ions) facility is aimed at using radioactive beams from SPIRAL2 and from SPIRAL1 facility (Fig. 8). The French Safety authority has now authorized its construction, which should begin in June 2023.

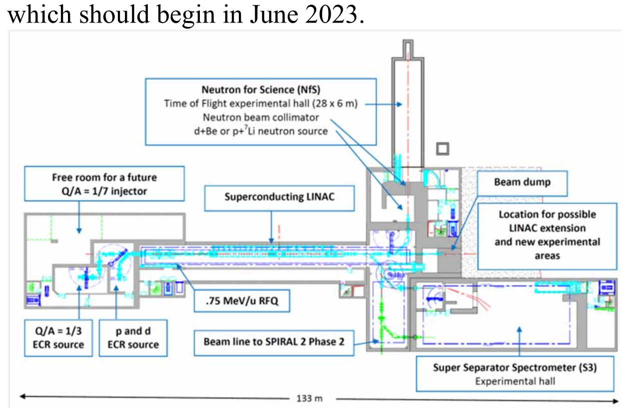

Figure 7: Layout of SPIRAL2.

ISBN: 978-3-95450-212-7 ISSN: 2673-5482 doi:10.18429/JACoW-CYCLOTRONS2022-TUA001

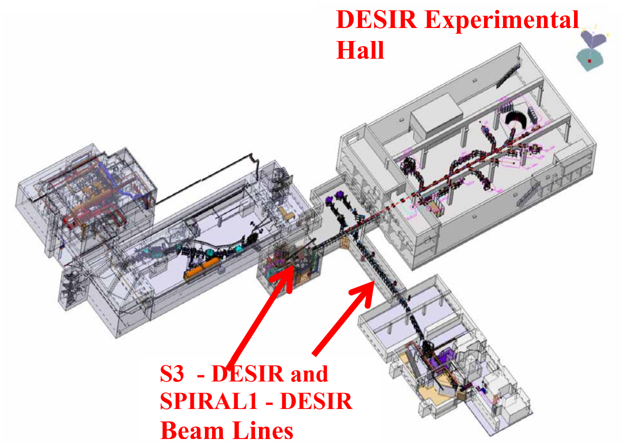

Figure 8: DESIR facility.

GANIL OPERATION STATUS

From the beginning, the time available for physics with cyclotrons was increasing until 2005, where we had a peak (more than 4000 hours physics time). Since then, the total operation time and the physics time are decreasing. Since 2019 yet, LINAC operation (2800 hours in 2021) is to be added to cyclotron operation (Fig. 9).

In the last 3 years we have an increase of the gap between the 2 curves. Indeed, we have a rise of the failure rate these last years, mainly due to water leak inside the machine, and particularly on the RF cooling circuits.

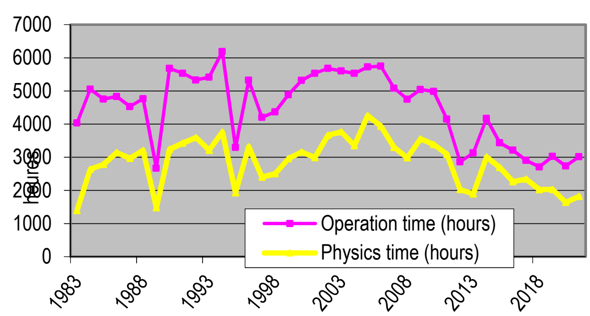

Figure 9: Beam time available for physics since 1983.

FUTURE OF THE CYCLOTRONS

There is still more demand at the PAC – Physics Advisory committee - than time available for cyclotrons. Demand include use of SSC2 beams in LISE spectrometer (fragmentation), fusion reactions with SSC1 beams, post-accelerated new SPIRAL1 beams, industrial beams, and, in next future, studies of SPIRAL1 beams in DESIR. Thus, we estimate that the cyclotrons will be used 20 years more. This motivates to continue developments for radioactive beams at SPIRAL1. The FEBIAD ion source, which at the beginning failed after a few days, has now been finalized. This source has first been used in alkali mode, with first post-accelerated beams K ones. The source team has now tested the FEBIAD with several primary beams, 80 different isotopes were produced [6]. The booster is to be upgraded to be used in double-frequency mode, one at 14 GHz with a klystron and one at 18 GHz with a travelling-wave tube amplifier. This mode will improve the charge states efficiency. There is also a motivation for a major renovation plan of the cyclotron facility. This is the CYREN (Cyclotron Renovation) project. The objective is to operate the facility 20 years more.

The main subject is the RF cavities with the water leaks concern. In the reference scenario a cavity will be constructed, will replace a SSC1 one, and the old one stored as a spare. The cost for a 1st cavity is estimated to 6 M€, and the delay 2 years plus the RF tests. There are difficulties with the storage and handling conditions (40 years ago, a storage area was present, now replaced by SPIRAL1 building extension. The girders were not present). In the "high scenario", the four RF cavities of the two SSCs will be replaced. Other major topics are power supplies, cooling systems and remote control.

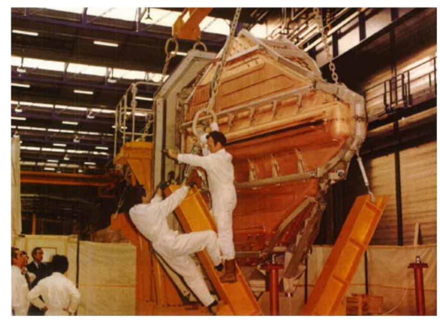

Figure 10: An RF cavity.

CONCLUSION

After forty years, GANIL cyclotrons are still demanded and it should be true for 20 years, including use of new SPIRAL1 beams in DESIR facility. SPIRAL1 development concerns Target Ion Source, charge breeder, and acceleration at low energy (1.2 MeV/A in harmonics 6). A large renovation plan of the cyclotrons is to be launched (5 to 8 years and 16 to 32 M€ depending on the scenario).

REFERENCES

[1] J. Fermé, "Project OAE at GANIL - A project for increasing the heavy ion energies", in *Proc. 11th Int. Cyclotron Conf. and their Applications (Cyclotrons'86)*, Tokyo, Japan, Oct. 1986, pp. 24-30.

[2] A. Savalle *et al.*, "The SISSI facility at GANIL", in *Proc. 5th European Particle Accelerator Conf. (EPAC'96)*, Sitges, Spain, Jun. 1996, paper MOP050G, pp.2403-2405.

[3] E. Baron *et al.*, "High intensity heavy ion beams for Exotic Nuclei Production at GANIL", in *Proc. 16th Int. Conf. on Cyclotrons and their Applications (Cyclotrons'01)*, East Lansing, MI, USA, May 2001, pp. 431-433.

[4] M. Lieuvin *et al.*, "High intensity heavy ion beams for Exotic Nuclei Production at GANIL", in *Proc. 16th Int. Conf. on Cyclotrons and their Applications (Cyclotrons'01)*, East Lansing, MI, USA, May 2001, pp. 59-63.

[5] A. K. Orduz *et al.*, "SPIRAL2 final commissioning results", in *Proc. 31st Linear Accelerator Conf. (LINAC'22)*, Liverpool, UK, Aug.-Sep. 2022, pp. 314-318. doi:10.18429/JACoW-LINAC2022-TU2AA02

[6] P. Chauveau *et al.,* presented at the 19th Int. Conf. on Electromagnetic Isotope Separation and Related Topics (EMIS'22), Daejon, South Korea, Oct. 2022.

ISBN: 978-3-95450-212-7 ISSN: 2673-5482 doi:10.18429/JACoW-CYCLOTRONS2022-TUA004

DESIGN OF A MULTI-HARMONIC BUNCHER FOR TRIUMF 500 MeV CYCLOTRON

S. Saminathan*, R. Baartman, Y. Bylinskii, M. Ilagan, P. Jung, O. Law, R. E. Laxdal, M. Marchetto, T. Planche, V. Zvyagintsev
TRIUMF, Vancouver, Canada

Abstract

The TRIUMF 500 MeV cyclotron injection system consists of a 40 m long beamline to transport the 300 keV H^- ion beams into the cyclotron. Part of the original beamline, the vertical injection section, was replaced in 2011, while the remaining horizontal injection section is currently being redesigned for replacement. As part of the horizontal injection beamline upgrade, the present buncher system will be replaced with a new one. The current buncher configuration consists of two double gap bunchers: the first buncher operates at the cyclotron RF frequency (23.06 MHz) while the second operates at the second harmonic frequency (46.12 MHz). The proposed new buncher is based on a two-electrode multi-harmonic system, which will be operated by up to three harmonics. The beam dynamics studies have been performed, including the space-charge effects using the particle-in-cell code WARP. Simulation results of longitudinal beam dynamics are presented for transporting beam intensity up to 1 mA.

INTRODUCTION

The demand for the total extracted beam from the TRIUMF 500 MeV cyclotron is increasing with the addition of the new rare isotope beam facility ARIEL [1]. In order to meet the increased total output from the cyclotron, the injection intensity and beam brightness also needed to be improved. The injection beam upgrade program has started in order to meet the increased total output by improving the injection intensity of high-brightness beams. The vertical injection beamline was upgraded in 2011 as the initial phase [2]. The second phase of the upgrade program consists of upgrading the horizontal injection beamline [3] and adding a new ion source injection terminal (I2) [4]. The new buncher is part of the ongoing upgrade of the horizontal injection beamline. The basic parameters through the injection beamline is presented in Table 1.

Currently, two double gap bunchers are being used in the injection beamline [5]. The first buncher is located 21 m downstream from the injection point in the horizontal injection beamline, while the second buncher is located 4.54 m downstream from the first buncher. The first buncher operates at the cyclotron RF frequency of 23.06 MHz, while the second buncher operates at the second harmonic of 46.12 MHz. Using the current buncher system, the total extracted current from the cyclotron is approximately 0.28 mA, with an injection current of 0.4 mA. As part of the upgrade of the horizontal injection beamline, the current buncher system will be replaced with a new multi-harmonic buncher.

* suresh@triumf.ca

Table 1: Basic Beam Specifications

Parameter	Value
Beam species	H^-
Beam energy	300 keV
Maximum beam intensity	1 mA
Maximum emittance ($4\epsilon_{RMS}$) at 300 keV	12.0 µm
Beam duty cycle	0.1% – 99%
Bunching frequency	23.06 MHz

MULTI-HARMONIC BUNCHER

The concept of a multi-harmonic buncher has been widely used elsewhere in an ion bunching system by combining the fundamental RF wave with its various higher harmonics to obtain a nearly sawtooth-like waveform [6–8]. In our case, a two-electrode three-gap multi-harmonic buncher system has been designed with a 1.27 cm cm aperture radius and a 0.5 cm gap between the electrodes. The layout of the buncher system is shown in Fig. 1. The center distance between the first and second RF gap is 16.765 cm and 8.383 cm for the second and third RF gap, respectively. The first (23.06 MHz) and third harmonics (69.18 MHz) are applied to the first electrode, while the second electrode is applied with the second harmonics (46.12 MHz). The electrostatic modeling of the buncher has been done with the code COMSOL [9]. Figure 2 shows the calculated electrostatic field along the

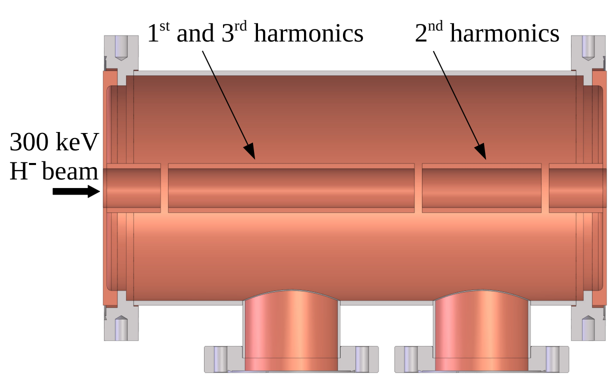

Figure 1: A cross section view of the new multi-harmonic buncher. Note that the RF resonators are not included in this figure.

ISBN: 978-3-95450-212-7 ISSN: 2673-5482 doi:10.18429/JACoW-CYCLOTRONS2022-TUA004

axis of the buncher with an applied potential of 1 V. The particle-in-cell code WARP3D [10] was used in an earlier work to simulate the longitudinal beam dynamics for the existing buncher system in the injection beamline [11]. In this work, the WARP3D code has also been chosen to study the performance of the multi-harmonic buncher.

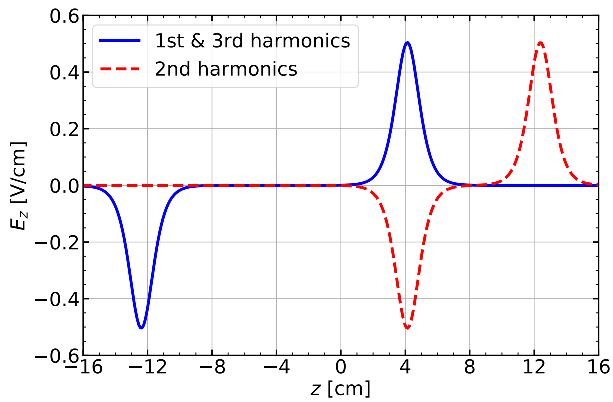

Figure 2: Calculated electrostatic field (E_z) along the axis of the buncher with an applied potential of 1 V.

Beamdynamics Simulations

The calculated electrostatic field along the axis of the multi-harmonic buncher is shown in Fig. 2 and the calculated field map is imported into the particle tracking code WARP3D. The buncher is used to create a more focused beam of ions by modulating the beam with the first three harmonics of 23.06 MHz. The buncher is installed at a distance of 20 m from the injection point, which is one meter closer than the existing buncher system. In order to keep the simulation model simple, 20 lattice periods have been assumed between the multi-harmonic buncher and the injection point at the cyclotron. The length of one lattice period is 1 m with a phase-advance of 45°, and each lattice consists of two electrostatic quadrupoles. Space-charge effects from the neighboring bunchers are included in the simulations by using periodic boundary conditions along the beam direction.

The TRIUMF cyclotron's longitudinal acceptance is determined by the spiral inflector's dispersion, the RF dee voltage, and space charge [12]. To simplify comparisons, the buncher performance is evaluated using a rectangular window in phase space, with 50° phase acceptance and 1 % in $\Delta p/p$. The multi-harmonic buncher is compared to the existing buncher using simulations with an initial beam intensity of 0.650 mA. The results of the simulations show that the performance of the multi-harmonic buncher is comparable to the existing buncher, with approximately 56 % of the particles within the desired phase acceptance and momentum spread. Figure 3 (left) shows the calculated longitudinal phase-space for the existing buncher, and Fig. 3 (right) shows the calculated longitudinal phase-space for the new multi-harmonic buncher at the injection point.

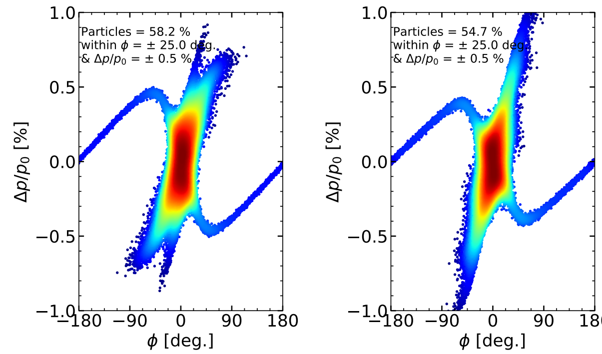

Figure 3: Calculated longitudinal phase-space of the 300 keV H^- beam at the cyclotron injection for the existing two double gap buncher(left) and for the multi-harmonic buncher configuration (right) with an initial beam intensity of 0.650 mA and $\varepsilon_{4\mathrm{rms}} = 8\,\mu\mathrm{m}$.

In order to improve the bunching efficiency in the case of higher beam intensity, particularly above 0.5 mA, the buncher needs to be located closer to the injection point. As moving the position of the buncher along the beamline is impractical for various beam intensities, an additional first harmonic buncher (re-buncher) 13.5 m away from the multi-harmonic buncher has been included as a re-buncher in the simulation for beam intensities higher than 0.5 mA. The calculations show that adding a re-buncher 13.5 m away from the multi-harmonic buncher improves the bunching efficiency for beam intensities higher than 0.5 mA. As an example, Fig. 4 shows the calculated longitudinal phase-space with an initial beam intensity of 1 mA. The bunching efficiency of this system is about 67 % (within $\phi = \pm 25°$ and $\Delta p/p = \pm 0.5\%$) at a 1 mA injection line current, which could support up to 0.67 mA of extracted current from the cyclotron. Figure 5 shows the calculated transverse phase-space in the horizontal (x) and vertical (y) planes at the location of the injection point. Figure 6 shows the calculated

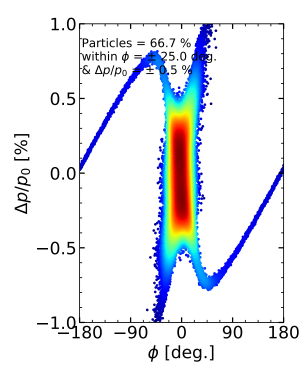

Figure 4: Calculated longitudinal phase-space of the 300 keV H^- beam at the cyclotron injection for the multi-harmonic buncher along with a re-buncher with an initial beam intensity of 1 mA and $\varepsilon_{4\mathrm{rms}} = 8\,\mu\mathrm{m}$. About 67 % particles are within the phase acceptance of ±25° and momentum spread ($\Delta p/p$) of ±0.5%.

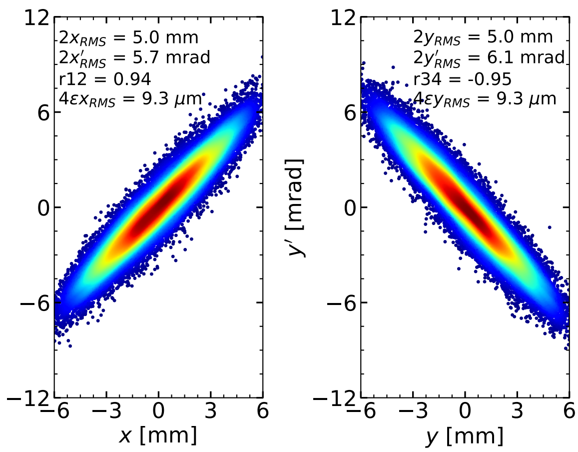

Figure 5: Calculated transverse phase-space of the 300 keV H^- beam at the cyclotron injection for the multi-harmonic buncher along with a re-buncher with an initial beam intensity of 1 mA and $\varepsilon_{4\mathrm{rms}}$ = 8 µm.

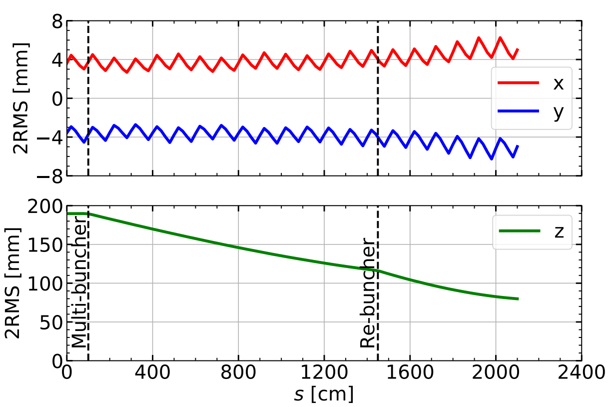

Figure 6: Calculated beam envelope (2RMS, positive for x, negative for y, longitudinal for z) for a 1 mA of 300 keV H^- beam transport through 21 periodical lattice along with the multi-harmonic buncher and a re-buncher with $\varepsilon_{4\mathrm{rms}}$ = 8 µm.

transverse (top) and longitudinal (bottom) beam envelope through these lattice periods, including the space-charge effects, with an initial beam intensity of 1 mA.

SUMMARY AND OUTLOOK

A new multi-harmonic buncher system has been designed that will be operated up to three harmonics. A particle-in-cell code was used to study the longitudinal beam dynamics for the new buncher system, including the space-charge effects. The new bunching system will be a combination of a multi-harmonic buncher and a first harmonic re-buncher for transporting beam injection beamline intensities higher than 0.500 mA. Simulation results of longitudinal beam dynamics are presented for transporting beam intensities up to 1 mA. In the near future, the new multi-harmonic buncher system will be installed and commissioned for use in the new horizontal injection beamline of the 500 MeV cyclotron at TRIUMF.

REFERENCES

[1] L. Merminga *et al.*, "ARIEL: TRIUMF'S advanced rare isotope laboratory", in *Proc. 2nd Int. Particle Accelerator Conf. (IPAC'11)*, San Sebastian, Spain, Sep. 2011, paper WEOBA01, pp. 1917–1919, https://accelconf.web.cern.ch/ipac2011/papers/weoba01.pdf

[2] R. Baartman, "Optics design of the ISIS vertical section replacement", TRIUMF, Vancouver, BC, Canada, Internal Note TRI-DN-09-11, document-22849.

[3] M. Marchetto and S. Saminathan, "Replacement of the ISIS horizontal injection beamline", TRIUMF, Vancouver, BC, Canada, Internal Note TRI-DN-22-05, document-218327.

[4] S. Saminathan, "Beam transport for the new ion source injection terminal I2", TRIUMF, Vancouver, BC, Canada, Internal Note TRI-DN-21-16, document-213184.

[5] R. Baartman, G. Dutto, and P. W. Schmor, "The TRIUMF high efficiency beam bunching system", in *Proc. 10th Int. Cyclotron Conf. and their Applications (Cyclotrons'84)*, East Lansing, MI, USA, Apr.-May 1984, paper B39, pp. 158–160, https://accelconf.web.cern.ch/c84/papers/b39.pdf

[6] F. J. Lynch, R. N. Lewis, L. M. Bollinger, W. Henning, and O. D. Despe. "Beam buncher for heavy ions", *Nucl. Instrum. Methods*, vol. 159, nos. 2-3, pp. 245–263, 1979. doi:10.1016/0029-554X(79)90651-7

[7] P. N. Ostroumov *et al.*, "Beam test of a grid-less multi-harmonic buncher", in *Proc. 22nd Particle Accelerator Conf. (PAC'07)*, Albuquerque, NM, USA, Jun. 2007, paper WEPMN091, pp. 2242–2244, https://accelconf.web.cern.ch/p07/PAPERS/WEPMN091.PDF

[8] J. Labrador, M. A. Carrera, J. DueÃ±as, A. Garbayo, I. Martel, and A. Villari, "Design of a multi-harmonic buncher for LINCE", in *Proc. 5th Int. Particle Accelerator Conf. (IPAC'14)*, Dresden, Germany, Jun. 2014, pp. 508–510. doi:10.18429/JACoW-IPAC2014-MOPME059

[9] COSMOL, https://www.comsol.com/comsol-multiphysics

[10] A. Friedman *et al.*, "Computational methods in the Warp code framework for kinetic simulations of particle beams and plasmas", *IEEE Trans, Plasma Sci,*, vol. 42, no. 5, pp. 1321–1334, May 2014. doi:10.1109/PLASMA.2013.6633427

[11] P. M. Jung, T. Planche, and R. Baartman, "Hybrid macroparticle algorithm for modeling space charge", *Phys. Rev. Accel. Beams*, vol. 25, no. 8, p. 084602, Aug. 2022. doi:10.1103/PhysRevAccelBeams.25.084602

[12] T. Planche, R. Baartman, H.W. Koay, Y.-N. Rao, and L.G. Zhang, "Intensity limit in compact H^- and H_2^+ cyclotrons", in *ICFA Beam Dynamics Newsletter #84 - Dynamics of high power and high energy cyclotrons*, to be published in *J. Instrum.*

ISBN: 978-3-95450-212-7 ISSN: 2673-5482 doi:10.18429/JACoW-CYCLOTRONS2022-TUBO01

MEASUREMENT OF DETECTOR RESPONSE FUNCTIONS FOR FAST NEUTRON SPECTROSCOPY WITH ORGANIC SCINTILLATORS

T. Hutton*, Z. Ndabeni, K. Maibane, E. Jarvie, A. Buffler
Metrological and Applied Sciences University Research Unit,
Department of Physics, University of Cape Town, Cape Town, South Africa

Abstract

Spectrum unfolding decouples spectroscopic measurements of neutron fields from accelerator facilities by making use of a well-characterised detector response matrix. Measurements of detector response matrices, derived from time-of-flight, were made at the fast neutron facility at iThemba LABS, South Africa, with neutrons with energies between 10 - 65 MeV for: a traditional BC-501A organic liquid scintillator detector with photomultiplier tube and analogue pulse processing and acquisition; and a modern system comprised of an EJ-276 plastic scintillator, silicon photomultiplier and digital pulse processing and acquisition. The detector response matrices were validated by unfolding neutron energy spectra from measured light output spectra, and compared to the associated energy spectra derived from time-of-flight. Both detector systems demonstrated good agreement between the energy spectra derived from time-of-flight, which is promising for fast neutron spectroscopy with organic scintillators in environments outside of the laboratory.

CONTEXT

Fast neutron fields with energies up to several GeV are a concern for aviation, manned space missions, workplace exposure and radiation therapy [1–3], and are often poorly understood due to a lack of appropriate measurement devices and reference facilities. In aviation environments the interaction of cosmic rays in the atmosphere and aircraft material produces a shower of secondary radiation with complex composition and energy distribution. At an altitude of 11 km fast neutrons contribute up to 40% of the equivalent dose [4], with peaks in the energy spectrum around 1 MeV and 100 MeV [5], and during unpredictable, short-lived space weather events, the flux of cosmic rays, and secondary neutrons, increases dramatically [6]. Fast neutron interactions with biological or electronic matter cause indirect damage through the production of ionising reaction products, which results in an increased risk to both people and electronic systems [7, 8] and requires continuous monitoring to properly assess, and regulate, the radiation exposure of aircrew. The recent developments of solid (plastic) scintillators capable of pulse shape discrimination (PSD), low-voltage silicon photomultipliers (SiPMs) and digital data acquisition, coupled with spectrum unfolding now offers a viable solution to the development of a compact fast neutron spectrometer, which is suitable for use in a range of applications, including dosimetry in aircraft. We present the measurement and validation of detector response functions for fast neutrons (10 – 65 MeV) with a traditional liquid scintillator and NIM-electronics based system, and a compact detector system utilising modern acquisition technologies.

MEASUREMENTS

Measurements were made at the iThemba LABS (iTL) fast neutron facility [9, 10], where ns-pulsed fast neutron beams are produced in the energy range of 30 - 200 MeV using proton beams from the k = 200 cyclotron. The time spread of a proton bunch is approximately 1 ns, and a beam pulse selector is used to increase the time between bunches up to 360 ns. Neutrons were produced using a beam of 66 MeV protons incident on an 8.0 mm thick ^{nat}Li target. The neutron energy spectrum is comprised of a forward-biased mono-energetic peak from the ^{7}Li(p, n)^{7}Be reaction, which proceeds only by the transition to the ground state and the first excited state of ^{7}Be, with all higher levels being unstable [11], and a nearly isotropic, lower energy continuum that extends up to the primary peak [12]. Neutron beams are produced at 0° and 16° relative to the incident proton beam using a 2.0 m thick steel collimator (5.0 x 5.0 cm^2 apertures).

In time-of-flight spectroscopy [13], a ns-pulsed beam of ions are incident on a neutron producing target, and the time of arrival T of those neutrons reaching a detector is measured for a known distance d. The neutron energy E_n can then be determined from:

$$E_n = mc^2 \left[\frac{1}{\sqrt{1-(d/cT)^2}} - 1 \right] \quad (1)$$

where m is the rest-mass of a neutron, and c is the speed of light.

Measurements were made with a ⌀ 5.1 cm x 10.2 cm BC-501A organic liquid scintillation detector at 0° and at d = 8.0 m from the ^{nat}Li target, and data were acquired in coincidence in list-mode for time-of-flight (T), pulse shape (S) and pulse height (L) parameters using a NIM-based acquisition system (Fig. 1). The pulse shape parameter S is determined by the zero-crossover method and is implemented with a FAST ComTec 2160A module [14] on the fast anode output. Neutron only events are separated from gamma ray events as indicated by the dashed line in the L-S histogram in Fig. 2. The pulse height parameter L is calibrated with known gamma ray sources to produce a MeV electron-equivalent (MeV$_{ee}$) scale. The time-of-flight parameter T was calibrated by inserting several delays of known length

* tanya.hutton@uct.ac.za

ISBN: 978-3-95450-212-7 ISSN: 2673-5482 doi:10.18429/JACoW-CYCLOTRONS2022-TUBO01

between the start and stop of the time-to-amplitude converter (TAC) shown in Fig. 1, and by the time of arrival of the gamma ray flash produced at the target.

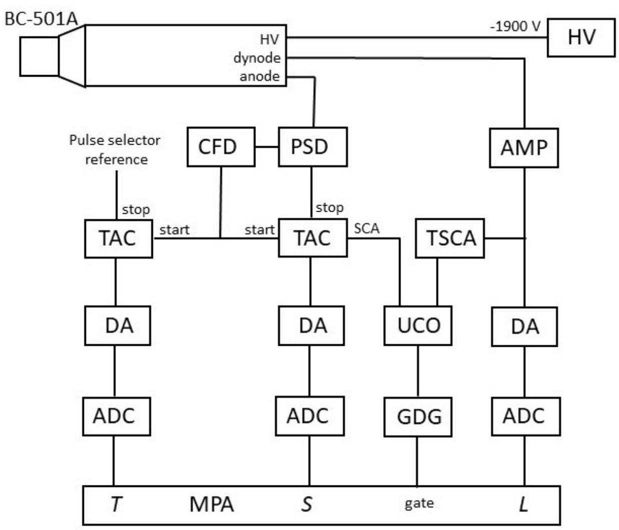

Figure 1: Schematic of NIM-based pulse processing for a BC-501A detector to record time-of-flight (T), pulse shape (S) and pulse height (L) parameters in coincidence with.

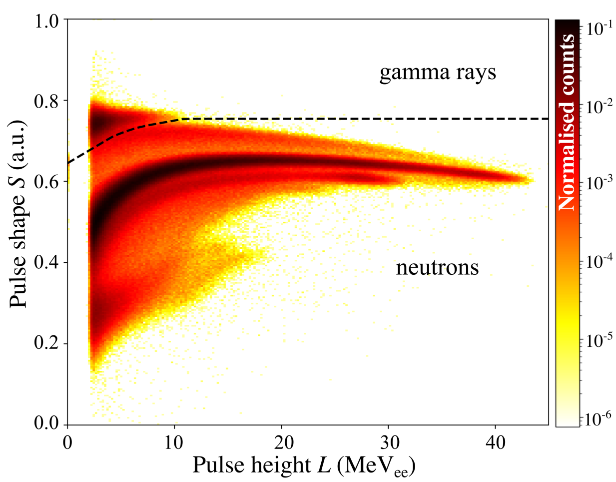

Figure 2: Distribution of events as a function of pulse height parameter L and pulse shape parameter S measured with a BC-501A detector at 8.0 m and 0° for a 66 MeV proton beam on an 8.0 mm ^{nat}Li target.

The compact spectrometer shown is shown in Fig. 3, which comprised of a 6 x 6 x 120 mm^3 EJ-276 [15] scintillator optically coupled to a MicroFC-60035 [16] silicon photomultiplier (SiPM). Full waveform data were acquired in list mode using a CAEN DT5730 [17] digitizer and QtDAQ [18] software for offline processing. Figure 4 shows the L-S histogram measured for the compact detector at 16° and 8.0 m from the ^{nat}Li target. The light output parameter L was determined from the integral of the SiPM pulse and calibrated with a series of known gamma ray sources, and the shape parameter S was calculated according to the charge comparison method of pulse shape discrimination (PSD) [19]. Neutron events were separated as indicated by the dashed line. The time-of-flight parameter T was determined from the time difference between the detected event and the reference pulse associated with the proton beam, where both waveforms were acquired in coincidence and a software implemented digital constant fraction discriminator [11] was used to determine the time associated with the reference pulse and radiation induced event.

Figure 3: The compact spectrometer comprised of an EJ-276 scintillator optically coupled to a silicon photomultiplier, with an aluminium and 3D printed casing.

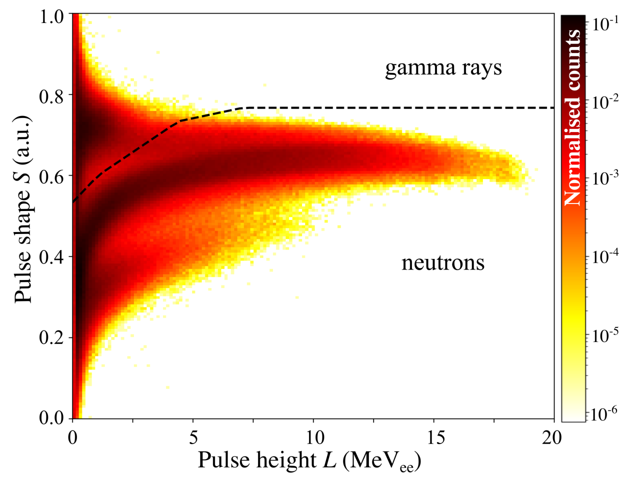

Figure 4: Distribution of events as a function of pulse height parameter L and pulse shape parameter S measured with an EJ-276 detector at 8.0 m and 16° for a 66 MeV proton beam on an 8.0 mm ^{nat}Li target.

RESULTS AND ANALYSIS

Time-of-flight

Figure 5 shows the time-of-flight spectra measured at d = 8.0 m for a 66 MeV proton beam irradiating an 8.0 mm ^{nat}Li target. Measurements were made with the BC-501A and EJ-276 detector systems at 0° and 16° respectively. For each detector system the gamma ray contributions were excluded via PSD (Fig. 2, 4), and Eq. (1) was used to derive the neutron energy spectra, which are shown in Fig. 6. The measurement at 0° shows an enhancement at 63.2 ± 0.3 MeV associated with the forward-biased ^{7}Li(p, n)^{7}Be reaction

ISBN: 978-3-95450-212-7 ISSN: 2673-5482 doi:10.18429/JACoW-CYCLOTRONS2022-TUBO01

relative to the measurement at 16°, and the lower energy continuum has a similar shape at both measurement angles.

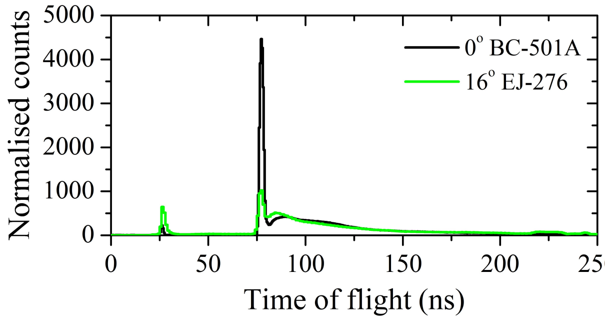

Figure 5: Time-of-flight spectra measured at 8.0 m with a BC-501A detector at 0° and EJ-276 detector at 16° for a 66 MeV proton beam on an 8.0 mm ^{nat}Li target.

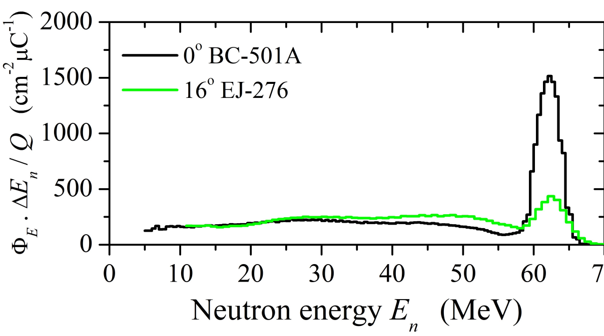

Figure 6: Neutron energy spectra derived by time-of-flight measured at 8.0 m with a BC-501A detector at 0° and EJ-276 detector at 16° for a 66 MeV proton beam on an 8.0 mm ^{nat}Li target.

Spectrum Unfolding

In spectrum unfolding, the neutron energy spectrum is deconvolved from the measured neutron light output spectrum using a known detector response matrix coupled with an unfolding algorithm, and can be used in situations where time-of-flight is unavailable. For organic scintillators, the detector response matrix is comprised of a series of normalised light output spectra for mono-energetic neutrons incident on the detector, which can reliably be simulated for neutron energies below 20 MeV [20]. At higher energies the range of the recoil particles and the increase in available n-C reaction channels results in unreliable response functions derived from calculation [21]. As the quality of the unfolded neutron energy spectrum is entirely dependent on the quality of the detector response functions, these must be measured above 20 MeV.

A detector response matrix was obtained for each detector by selecting energies, derived from time-of-flight, between 10 - 65 MeV in steps of 0.5 MeV (BC-501A) or 3.0 MeV (EJ-276), and calculating the L spectrum associated with that range. As the measured statistics were better for the BC-501A system due to a larger detection volume, a finer binning structure could be obtained both in L and E. The individual light output spectra were normalised to unity and a selection of these are shown in Fig. 7.

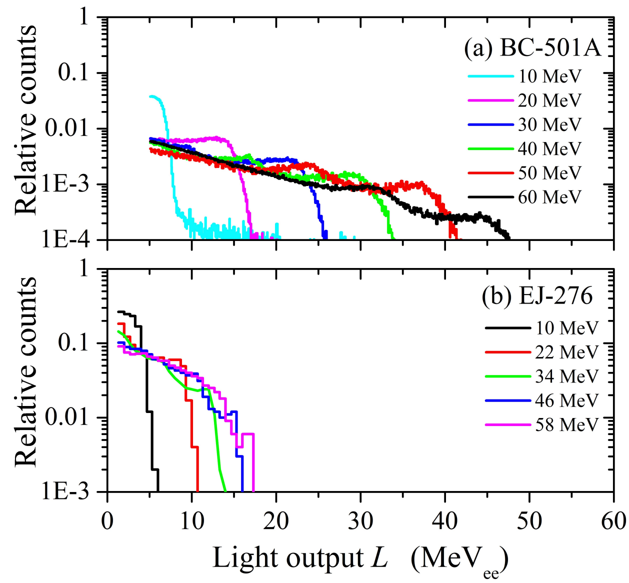

Figure 7: A selection of measured neutron response functions between 10 – 65 MeV for the (a) BC-501A and (b) EJ-276 detector systems.

A superior L resolution is observed in the response functions measured with the BC-501A detector, which is most noticeable in the high-L region associated with the proton recoil edge, and is attributed to the larger light collection area of the detector.

The measured detector response matrices were then used to unfold the neutron light output spectra measured for 66 MeV protons incident on an 8.0 mm ^{nat}Li target at 0° for the BC-501A detector, and 16° for the EJ-276 detector. Figure 8 shows the measured L spectra for the two detector systems alongside the refolded spectra obtained using MAXED [22] with a flat default spectrum and a target χ^2 of 1.0. The solution energy spectra are shown in Fig. 9. For the reference detector system, the energy spectra derived from time-of-flight and unfolding are in good agreement, both in the peak energy (63.0 ± 0.6 MeV) and the overall shape of the continuum. For the compact detector system, the peak energy is well matched within uncertainties (62.5 ± 0.9 MeV), but there are some inconsistencies observed between 30 - 50 MeV, which suggests that the response functions in this region are not sufficiently unique and is attributed to poorer light collection characteristics.

CONCLUSION

Detector response functions were measured at the iThemba LABS fast neutron facility using time-of-flight spectroscopy for neutrons with energies between 10 - 65 MeV for a traditional BC-501A and compact EJ-276 detector systems. Energy spectra were unfolded using MAXED

ISBN: 978-3-95450-212-7 ISSN: 2673-5482 doi:10.18429/JACoW-CYCLOTRONS2022-TUBO01

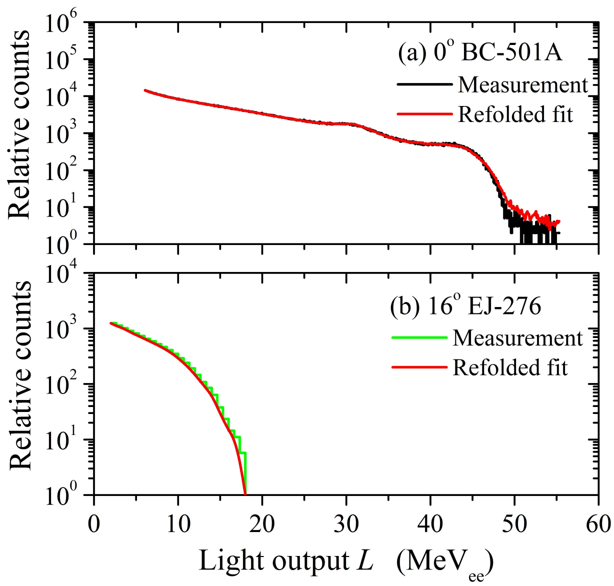

Figure 8: Measured and refolded L spectra for neutrons at 8.0 m with a (a) BC-501A detector at 0° and (b) EJ-276 detector at 16° for a 66 MeV proton beam on an 8.0 mm ^{nat}Li target

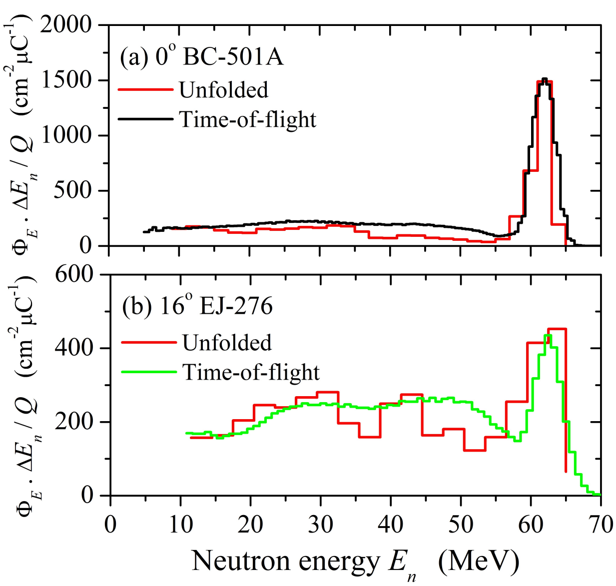

Figure 9: Neutron energy spectra unfolded with MAXED for the BC-501A and EJ-276 detectors and compared the time-of-flight derived energy spectra.

and were comparable to those measured by time-of-flight, which is promising for fast neutron spectroscopy with organic scintillators outside of the traditional laboratory environment. The quality of the energy spectrum unfolded using the compact detector response matrix was limited by low measurement statistics, and a poor L resolution. A significant improvement in L resolution is expected with the addition of a second SiPM to double the light collection area[ref], and further measurements are planned for energies up to 200 MeV to improve the statistics of the response functions and extend the range of applications. The compact detector system developed as part of this work forms one of the key work packages associated with the South African Space Neutron Initiative (SASNI)[1] and will be used for spectral measurements of cosmic ray induced neutrons at aviation altitudes.

ACKNOWLEDGEMENTS

This work was partially funded by the National Research Foundation (NRF), grant number 138069.

REFERENCES

[1] P. Grieder, *Cosmic Rays at Earth: Researcher's Reference Manual and Data Book*, Elsevier, 2001.

[2] J. M. Clem *et al.*, *Rad. Prot. Dos.*, vol. 110, nos. 1-4, p. 423, 2004.

[3] M. Bagshaw and P. Illig, *Travel Medicine*, 4th Ed., Elsevier, 2019.

[4] C. J. Guembou Shouop *et al.*, *Eur. Phys. J. Plus*, vol. 135, p. 438, 2020.

[5] P. Goldhagen *et al.*, *Rad. Prot. Dos.*, vol. 110, p. 387, 2004.

[6] P. Beck, "Aircraft Crew Radiation Exposure in Aviation Altitudes During Quiet and Solar Storm Periods", in *Space Weather*, Ed. J. Lilensten, Springer, 2007.

[7] A. J. Sigurdson and E. Ron, *Cancer Invest.*, vol. 22, no. 5, p. 743, 2004.

[8] B. Todd and S. Uznanski, Proc. CAS-CERN Accelerator School, CERN, Geneva, Switzerland, Rep. CERN-2015-003, p. 245, 2015.

[9] M. Mosconi *et al.*, *Rad. Meas.*, vol. 45, no. 10, p. 1342, 2010.

[10] N. B. Ndlovu *et al.*, "Upgrade of the iThemba LABS neutron beam vault to a metrology facility", in *Proc. 22nd Int. Conf. on Cyclotrons and their Applications (Cyclotrons'19)*, Cape Town, South Africa, Sep. 2019, pp. 181–184. doi:10.18429/JACoW-CYCLOTRONS2019-TUP012

[11] A. C. Comrie *et al.*, *Nuc. Instrum. Meth. A*, vol. 227, p. 43, 2015.

[12] A. Buffler *et al.*, "Modern Neutron Detection", *Proc. Technical Meeting*, Int. Atomic Energy Agency, Vienna, Austria, IAEA-TECDOC-1935, p. 209, 2020, https://www.iaea.org/publications/14690/modern-neutron-detection

[13] J. Copley and J. Udovic, *J. Res. Natl. Inst. Stand. Technol.*, vol. 98, no. 1, p. 71, 1993.

[14] FAST ComTec, Model 2160A Pulse Shape Discriminator, https://www.fastcomtec.com/fileadmin/fwww/datashee/nim/2160a.pdf, accessed 21 Dec. 2022.

[15] Eljen Technology. EJ-276 plastic scintillator, https://eljentechnology.com/products/plastic-scintillators/ej-276, accessed 21 Dec. 2022.

[1] SASNI is comprised of members from the Department of Physics, University of Cape Town, South African National Space Agency (SANSA) and iThemba LABS fast neutron and radiation biophysics divisions.

ISBN: 978-3-95450-212-7 ISSN: 2673-5482 doi:10.18429/JACoW-CYCLOTRONS2022-TUBO01

[16] SensL, C-series silicon photomultiplier, https://www.onsemi.com/, accessed 21 Dec. 2022.

[17] CAEN, DT5730 digitizer, https://www.caen.it/products/dt5730/, accessed 21 Dec. 2022.

[18] A. Comrie, QtDAQ, https://github.com/veggiesaurus/qtdaq, accessed 21 Dec. 2022.

[19] C. Sole *et al.*, *IEEE Trans. Nucl. Sci.*, vol. 69, p. 1780, 2022.

[20] NRESP-3, Organic Scintillation Detector Response to Monoenergetic Fast Neutron, 26. Oct. 1985, available online: http://www.nea.fr/abs/html/nea-0700.html

[21] A. Buffler *et al.*, *IEEE Trans. Nucl. Sci.*, vol. 62, p. 1422, 2015.

[22] M. Reginatto, *Nucl. Instrum. Meth. A*, vol. 476, p. 242, 2002.

ISBN: 978-3-95450-212-7 ISSN: 2673-5482 doi:10.18429/JACoW-CYCLOTRONS2022-TUB002

REAL TIME DETERMINATIONS OF THE RANGE AND BRAGG PEAK OF PROTONS WITH A DEPTH PROFILE CAMERA AT HZB

A. Dittwald†, J. Bundesmann, A. Denker[1], S. Dillenardt[1], T. Fanselow, G. Kourkafas
Helmholtz-Zentrum Berlin für Materialien und Energie (HZB), Berlin, Germany
[1]also at Berliner Hochschule für Technik, Berlin, Germany

Abstract

The cyclotron at HZB provides a 68 MeV proton beam for therapy as well as for experiments. By using a novel camera setup, the range of the proton beam is measured optically. The setup consists of a phantom with a luminescent layer inside and a CMOS camera. By measuring the emission of the luminescent layer, the Bragg peak and the range of the proton beam can be visualized for different energies. In contrast to a water phantom, the camera system offers much shorter measurement times. A dedicated LabVIEW code provides various evaluation possibilities: the Bragg curve and the lateral beam profile are generated and displayed. The system is sensitive to energy differences of less than 400 keV. The results were obtained with a beam intensity of less than 10 pA/cm^2 homogenous proton beam in front of the degrader. The measurement is done in real time and provides live feedback on changes such as beam energy and beam size. The results of the camera are presented and compared to water phantom measurement.

MATERIALS AND METHODS

Cyclotron at HZB and Water Phantom

The HZB cyclotron provides protons for the eye tumor therapy since 1998. More than 4400 patients from all over the world have been treated here [1]. There are two injectors and a cyclotron as main accelerator which provides a 68 MeV proton beam for eye tumor therapy and for experiments. The facility is under continuous development for therapy.

A water phantom is normally used to determine the Bragg curve of the proton beam. To measure a complete Bragg curve with an energy of 68 MeV for the therapy, the measurement takes 5 minutes for a resolution of 0.1 mm [2]. A finer resolution with the water phantom is possible but means a much longer measuring time. For experiments where the Bragg curve is essential, the same water phantom has been used so far for calibration. This means for experiments with different energies a very long preparation time is needed. Even with smallest changes, the measurement of the Bragg curve must be repeated. Therefore, a measurement system had to be developed which reduces the preparation time and allows a real-time evaluation of the Bragg curve of the proton beam.

There are also other systems with different phantoms like liquid scintillators [3] or plate phantom systems [4]. Most of them need longer measuring time, have rather coarse resolutions and no real-time evaluation. Another system is a multi-leaf faraday cup [5]. This system can quickly evaluate a Bragg curve but is heavy and very expensive in commercial form.

Camera System

The camera system has a patent pending. It consists of a phantom, a luminescent layer (interaction layer), a housing and a camera shown in Fig. 1. The phantom is the main point of the system. It consists of two plastic blocks. The dimension of the phantom is matched to the maximum available energy of the proton beam. Between the blocks of the phantom is diagonal the luminescent layer (e.g., Gd_2O_2S) or interaction layer placed.

For the interaction layer, a material is used which exploits the effect of fluorescence. The proton beam is decelerated in the phantom. Depending on the position of the proton beam, it collides with the luminescent layer and the light intensity is equivalent to the energy loss.

Centered on the phantom is the camera. It is a FLIR camera with a CMOS sensor. The camera is equipped with a lens that focuses the detected signals of the luminescent layer. The captured image of the Bragg curve is readout by a LabVIEW (NI, Austin, USA) code. The entire setup is located in a housing sealed by light. A crosshair at the entrance of the beam in the system allows a fast optical alignment. The total size is as small as 35 cm x 20 cm x 20 cm and it's very light with only 1.5 kg. Due to the compactness of the system, it is easily transportable and can be used at different target stations. The system is easy and inexpensive to realize in contrast to conventional water phantoms.

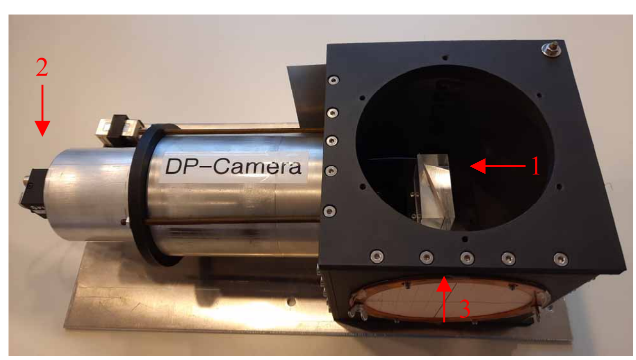

Figure 1: View inside the camera system. 1- shows the phantom block with the luminescent layer inside. 2 - position of the camera. 3 – beam direction.

LabVIEW Code

A LabVIEW code is used to evaluate and visualize the data from the camera system. Different aperture sizes can

† alina.dittwald@helmholtz-berlin.de

ISBN: 978-3-95450-212-7 ISSN: 2673-5482 doi:10.18429/JACoW-CYCLOTRONS2022-TUB002

be used to define the beam spot size of the scattered proton beam (Fig. 2).

On the left side of the LabVIEW graphical interface is the live image in monochrome intensity displayed. The exposure time can be set from 1 - 2000 ms so the image is not overexposed. On the image a "ROI area" (region of interest) can be chosen. It is selectable in a rectangular size (green box) and can be marked freely on the image. This “ROI area” is displayed on the right side in a color-coded intensity. The violet parts show pixel with low intensities, and the red parts shows pixel with high intensities.

From this color-coded image both the distal and lateral profile of the beam can be generated at different positions on the image. The position can be chosen freely, and the profile histograms are plotted below the colour image. The white line shows the Bragg curve which is generated in the phantom. The red line shows a lateral beam profile and can be selected at any position on the phantom. It is live feedback of two important beam parameters.

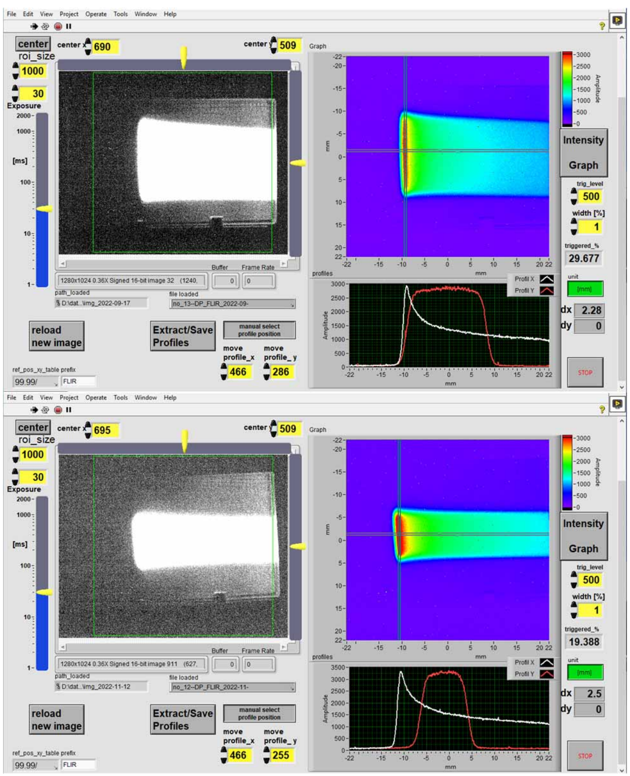

Figure 2: Two LabVIEW visualizations with different apertures. Upper image with a 20 mm x 20 mm aperture. Lower image with a 10 mm x 10 mm aperture.

By the function “extract/save profiles” a data file of the profiles is generated. It can be used for other programs for evaluating.

Measurements

Different Energies The measurement plotted in Fig. 3 shows different proton beam energies from 68 MeV down to 16 MeV. The nominal energy was 68.5 MeV. The proton beam was slowed down by using different absorber plates of aluminium. The first energy without absorber plates is 67.7 MeV where is to account the exit foil, the scattering foil and the air gap between the exit foil and the camera. The lower energies in Fig. 3 which were achieved with the absorber plates are calculated with SRIM [6].

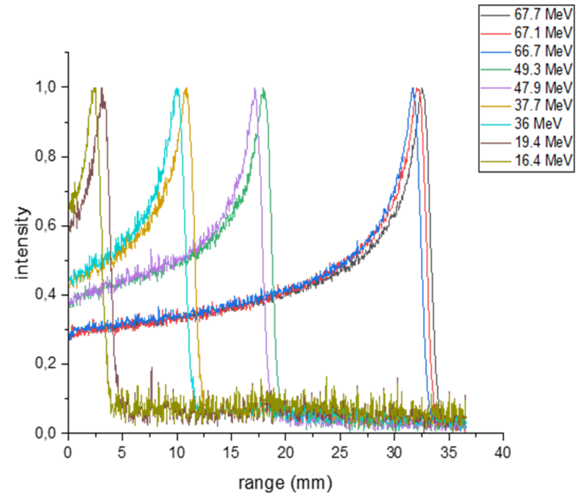

Figure 3: Measurement with depth profile camera for different proton beam energies of 16 MeV to 68 MeV.

The different energies are directly visible with the Bragg curve. Even small steps of 400 keV are visible. The system shows good results.

Table 1: Measured and Theoretical Values of Different Energies

Energy [MeV]	Camera Range [mm]	PSTAR Range [mm]
67.1	32.96	32.61
66.7	32.46	32.20
19.4	3.86	3.45
16.4	3.02	2.57

The measured range with the camera system were compared with the theoretic ranges of PSTAR at different energies [7]. All measured ranges are taken at 80% of the Bragg-peak. The values are larger at lower energies (Table 1). For higher energies is a difference of 1% and for lower energies is the difference more than 10%. For low energies a correction factor must be defined to reduce the strong difference between the measured and theoretic ranges. An adjustment of the phantom could be a benefit.

Camera System vs Water Phantom The measurement plotted in Fig. 4 shows the camera system compared to a water phantom. All measured ranges with the camera system are converted to water ranges for comparability. The solid line with the noisiness shows the measurement with the camera system. The dashed line shows the measurement with the water phantom. The measurements range from 68 MeV down to 18 MeV.

23rd Int. Conf. Cyclotrons Appl. CYCLOTRONS2022, Beijing, China JACoW Publishing
ISBN: 978-3-95450-212-7 ISSN: 2673-5482 doi:10.18429/JACoW-CYCLOTRONS2022-TUB002

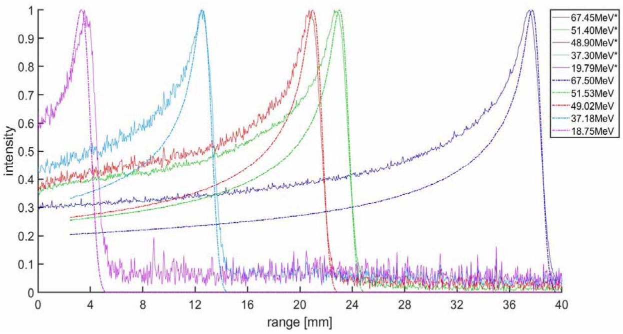

Figure 4: Measurements for different ranges with the camera system compared to a water phantom. Solid line shows camera measurement. Dashed line shows water phantom measurement.

In direct comparison the Bragg curves of both systems are very similar. The noise of the camera system graphs can be reduced. For this measurement the scattering system from the eye tumor therapy was used. This scattering system is more than 5 meters away from the camera system. With the scattering system close to the camera system (1 meter), the influence of the beam scattering system should be reduced. Other factors are:

- uncertainties for phantom and absorber materials of interaction layers
- geometry of camera lenses
- warming of the camera chip by longer power-on time

Minimum Energy Resolution The camera system should have a single pixel resolution of 40 keV for a 68 MeV proton beam. The measurement is shown in Fig. 5 and thin aluminium foils were used with 20 µm to 150 µm to try if this minimum resolution is possible.

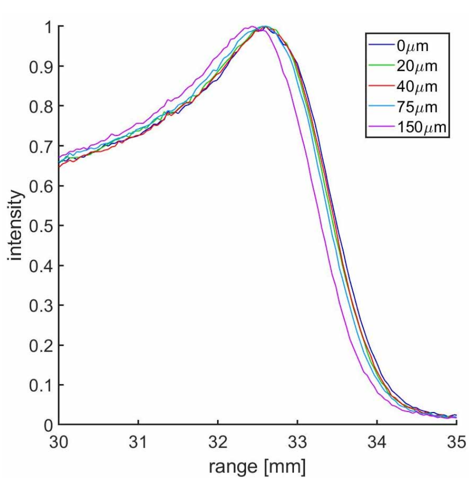

Figure 5: Measurement with camera system for minimum energy resolution of a 68 MeV proton beam with thin aluminium foils of 20 µm up to 150 µm.

An optically evaluation of the minimum resolution is difficult. This is especially the case for the very thin foils of 20 µm and 40 µm. For the foil with 75 µm thickness is a difference in the graph visible. It is clearer with the profile data from the LabVIEW visualization (Table 2).

The measured ranges show small differences. The measured values are bigger than the expected values.

Table 2: Energy Resolutions for Different Foils and the Measured Ranges

Foil Thickness [µm]	Measured Range [mm]	Calculated Energy [MeV]
0	33.20	67.90
20	33.16	67.84
40	33.13	67.81
75	33.08	67.75
150	32.96	67.61

For the camera system an energy loss of 100 keV is easily measurable with 68 MeV proton beam parameters.

Different Ion Species For this measurement is a 90 MeV helium beam ($^{4}He^{2+}$) chosen. Figure 6 shows the measured Bragg curve. For this measurement the scattering system near to the camera system is used. Less noise was observed.

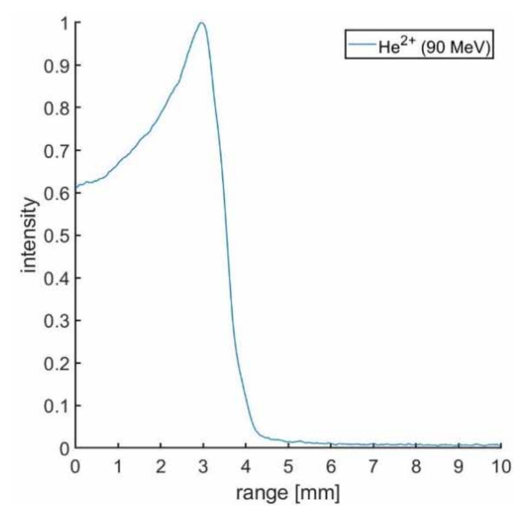

Figure 6: Measurement with the camera system of a 90 MeV helium beam.

For the ion a calculated and a measured energy is available (Table 3). The calculated energy is the nominal energy from the accelerator taking into account the exit foil at the target station and the air pass between the exit foil and the camera system.

The energy values show a good agreement. Between the calculated energy and measured energy, the difference is less than 2%.

Table 3: Ion Energy Difference from Calculated and Measured Energies

Ion	Nominal Energy [MeV]	Calculate Energy [MeV]	Measured Energy [MeV]
$^{4}He^{2+}$	90	78.48	76.02

ISBN: 978-3-95450-212-7 ISSN: 2673-5482 doi:10.18429/JACoW-CYCLOTRONS2022-TUB002

This shows that the camera system can also detect and evaluate different ions with very good results. The camera system has to be matched for other ions with different ranges.

CONCLUSION

The camera system is an inexpensive and lightweight invention. With only a few components excellent results are shown. The camera system works for different ions and energies. A minimal energy resolution of 100 keV is shown for a 68 MeV proton beam. There is a very good agreement in comparison with a water phantom with only small differences in the measurements.

A system upgrade with different phantom materials, luminescent layer, camera and camera lens could give more opportunities. The noise can be further reduced, and beams with higher and lower intensities can be used. A correction factor for low energies can give a better agreement to theoretically values.

REFERENCES

[1] A. Denker *et al.*, "Status of the HZB cyclotron", presented at the 23rd Int. Conf. on Cyclotrons and their Applications (Cyclotron'2022), Beijing, China, Dec. 2022, paper WEAO4, this conference.

[2] G. Kourkafas *et al.*, "FLASH proton irradiation setup with a modular wheel for a single mouse eye", *Med. Phys.*, vol. 48, no. 4, pp. 1839-1845, Apr. 2021. doi:10.1002/mp.14730

[3] D. G. Robertson, "Volumetric scintillation dosimetry for scanned proton beams", Ph.D. thesis, Faculty of the University of Texas Graduate School of Biomedical Sciences at Houston, Houston, USA, 2014.

[4] L. Keller *et al.*, "A scintillator-based range telescope for particle therapy", *Phys. Med. Biol.*, vol. 65, no. 16, p. 165001. Aug. 2020. doi:10.1088/1361-6560/ab9415

[5] S. Seidel, J. Bundesmann, T. Damerow, A. Denker, C. S. G. Kunert, and A. Weber, "A multi-leaf faraday cup especially for proton therapy of ocular tumors", in *Proc. Cyclotrons'16*, Zurich, Switzerland, Sep. 2016, pp. 118-120. doi:10.18429/JACoW-Cyclotrons2016-MOE02

[6] SRIM, http://www.srim.org/

[7] PSTAR, https://physics.nist.gov/PhysRefData/Star/Text/PSTAR.html

23rd Int. Conf. Cyclotrons Appl. CYCLOTRONS2022, Beijing, China JACoW Publishing
ISBN: 978-3-95450-212-7 ISSN: 2673-5482 doi:10.18429/JACoW-CYCLOTRONS2022-TUB003

APPLICATION PROGRESS OF CYCIAE-100 HIGH CURRENT PROTON CYCLOTRON*

L. Cao†, X. L. Jia, Z. W. Liu, G. F. Song, T. J. Zhang
China Institute of Atomic Energy, Beijing, China

Abstract

A new RIB facility, Beijing radioactive ion-beam facility (BRIF) had been constructed at CIAE. A 100 MeV H$^-$ cyclotron (CYCIAE-100) is selected as the driving accelerator which can provide a 70–100 MeV, 10 pA–520 µA proton beam for basic and applied research in the field of nuclear science and technology. The application of this facility has promoted the development of frontier scientific research in China, such as radioactive nuclear beam physics, nuclear data, neutron physics and space radiation effects. Recently, quasi-monoenergetic neutron source above 20 MeV and the white light neutron source with the best time resolution were completed, which had filled the gap in the measurement of neutron data in the range of energy of 100 MeV in China. In this paper, the main milestones in the use and development of CYCIAE-100 high current proton cyclotron are reviewed, the scientific applications based on platform are described, and the important topics in proton applications based on intermediate energy are discussed, including space radiation hardening, neutron standard radiation field and biological radiation damage mechanism.

INTRODUCTION

BRIF was started at CIAE in 2004. The project outline is shown in Fig. 1. It consists of a 100 MeV cyclotron, an isotope separator online system (ISOL), modification of the existing tandem, a superconducting Linac booster (SCL), various experimental terminals, and an isotope production station [1].

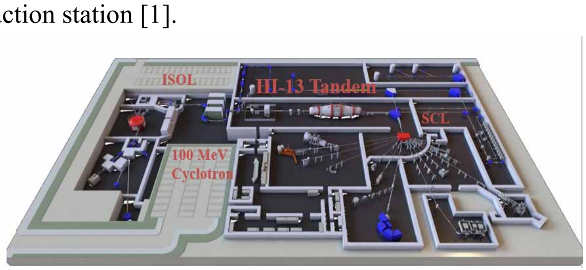

Figure 1: Layout of BRIF.

On July 4th 2014, first 100 MeV/20 µA proton beam shot on the target from CYCIAE-100, and the achievement was awarded as Top10 scientific achievements of 2014 in China. Figure 2 illustrates the main parts of the cyclotron. It is connected with five beamlines as follows:

- Northward can supply beam to ISOL beamline and isotope target terminal.
- Southward can supply beams to three beam lines that are White light neutron target line (15 m neutron tube and 30 m neutron tube), single event effect test bench and quasi-monoenergetic neutron source terminal.

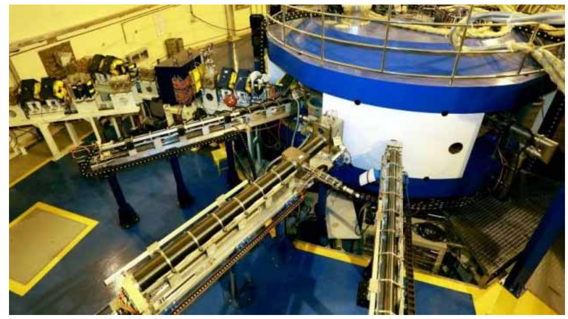

Figure 2: The CYCIAE-100 cyclotron.

APPLICATION ON CYCIAE-100

Up to Dec 2022, CYCIAE-100 has produced over 5000 hours beam time for users. Users are from different area institutes for nuclear physics, medical schools and institutes for electronic and space technology universities. The Usage of Cyclotron in our lab mainly focused on nuclear physics research, nuclear reaction, nuclear data, radiation effect Research proton-neutron SEE, radiation hardness, medical and other applications including medical isotope production and proton therapy.

Nuclear Reaction

Innovative achievements in radioactive nuclear beam physics had been carried out. The highest quality Na-20 radioactive beam is produced by using high resolution ISOL device in 2015, and the strange decay mode of β-γ-α of ^{20}Na is discovered for the first time in the world which brought China's nuclear astrophysics, radioactive nuclear beam physics and other scientific research into the international forefront. The ^{20}Na energy spectrum diagram is shown in Fig. 3.

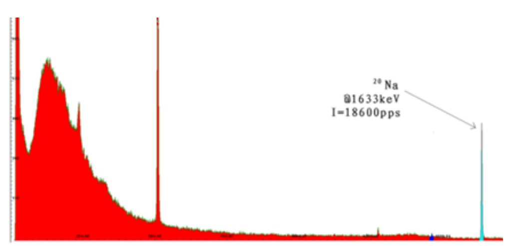

Figure 3: ^{20}Na energy spectrum diagram.

Nuclear Data

Quasi-monoenergetic neutron source above 20 MeV and the white light neutron source with the best time resolution were completed. In order to take the calibration of high energy neutron that is a bottleneck restricting space neutron

* Work supported by NNSF of China under Grant No.11375273.
† caolei@ciae.ac.cn

ISBN: 978-3-95450-212-7 ISSN: 2673-5482 doi:10.18429/JACoW-CYCLOTRONS2022-TUB003

detection, the quasi-monoenergetic neutron reference radiation field in the energy region above 20 MeV is established that is shown in Fig. 4. The quasi-monoenergetic neutron target consists of three beryllium targets with thickness of 0.4 mm, 0.5 mm and 0.6 mm and one fluorescent target. China is the second country in the world with neutron reference radiation field and calibration ability in the energy region above 20 MeV.

Figure 4: Quasi-monoenergetic neutron source.

Also, white light spectrum neutron nuclear data Measurement platform is constructed by proton bombardment of tungsten target to produce neutrons. The collimator is set in the neutron pipe. The co-axiality error between neutron collimation hole and neutron beam pipe is less than 0.10 mm. The collimator is composed of 35 cm copper at the front end and 65 cm iron at the rear segment. Four kinds of collimating aperture choices of 30 mm, 60 mm, 100 mm and complete shielding are selected. Measurement of spectrum are done by double liquid scintillation neutron time-of-flight method. The results show neutron energy range is 3-100 MeV. When the proton current is 1 μA, the measured neutron Fluence in the energy region of 3-100 MeV is about 3.28×10^4 $cm^{-2}s^{-1}$.

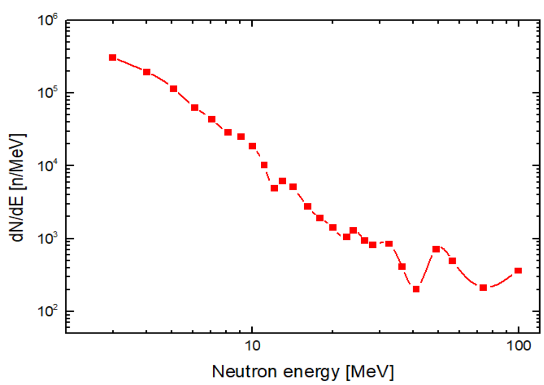

Figure 5: 3-100 MeV neutron energy spectrum diagram.

The first neutron single event effect (SEE) experiment was carried out using neutron beam line. Three kinds of SRAM devices with different characteristic sizes were tested by single event reversal (SEU). The chip shows malfunction to some extent Respectively.

Radiation Effect

Nowadays, cell density of devices in the circuit continues to increase, the range of radiation of a single particle can cover multiple devices. Furthermore, the charge collection effect is caused by multiple nodes in the circuit, and the displacement effect is produced in the circuit. A new proton single event effect line is reconstrued. Figure 6 illustrates the components of this line. The proton single event effect irradiation device is mainly composed of five systems: beam lowering system, beam scattering system, energy degrader system, beam diagnosis system and sample platform.

The cyclotron is a strong current accelerator, which generally provides an initial current of the order of μA, while the single particle effect experiment generally requires a weak beam of nano-Ampere level, so it is necessary to reduce the proton beam intensity. Therefore, the effect of beam reduction can be achieved by using a quadrupole lens to disperse the beam in the X and Y directions, and then intercept a small part of the beam in the centre through the slit.

The original beam spot provided by the accelerator is generally small, while the single particle effect experiment generally needs a uniform large beam spot to cover the whole electronic chip, so it is necessary to enlarge the beam spot size.

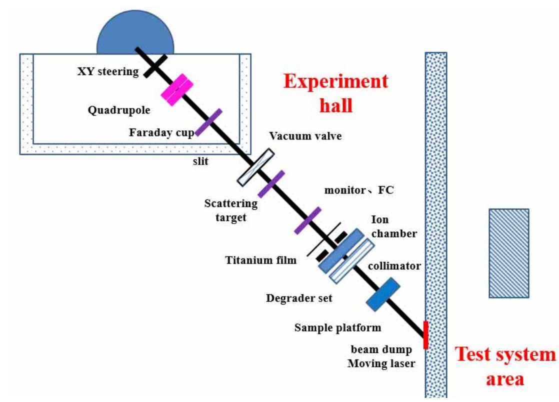

Figure 6: Proton single event effect line diagram.

Therefore, by using the method of beam expansion by double scattering targets, the proton beam forms a Gaussian distribution after passing through the first scattering target, and then passes through the second scattering target, because the heavy nuclear material in the center has stronger scattering ability and has a stronger weakening effect on the beam current. after a certain flight distance, a large area uniform beam spot can be obtained in the sample plane.

Accelerators can only provide proton beams with initial energy of 75-100 MeV, while single-particle effect experiments generally need proton beams with a wide energy range to measure a more complete cross-section curve, so it is necessary to reduce proton energy. Therefore, by placing a group of energy-reducing sheets with accurately calculated thickness on the beam line, the fast switching of proton beams in a certain energy range can be realized by the combination of multiple energy-reducing sheets.

In order to carry out the single particle effect experiment, it is necessary to measure the beam parameters such as proton irradiation Fluence and uniformity. The proton beam flux is measured by on-line monitoring of transmission ionization chamber, plastic scintillator detector or Faraday

ISBN: 978-3-95450-212-7 ISSN: 2673-5482 doi:10.18429/JACoW-CYCLOTRONS2022-TUB003

cup. The plastic scintillator detector is used at low injection rate and the Faraday cup is used at high injection rate.

With the SEE platform, CIAE jointly carried out the first experiment on the proton single event effect. Fill the gap in the anti-radiation experiment of intermediate energy protons in China. Then, experimental verification of key technologies of LHC/ATLAS single crystal diamond detector was done. In order to verify resistance to proton irradiation, test comparation of protons and heavy ions radiation damage mechanism of 0.18 μm CMOS devices were carried out. Results show no obvious SEL and SEFL occurred when the total dose of 5E^{10} in turn reached.

Medical and other Applications

In the face of complex space radiation environment, Proton radiation has an important effect on the life and health of astronauts of space mission. The batch of important data of intestinal microflora of mice irradiated by intermediate energy proton were successfully obtained and confirmed for the first time that proton irradiation had an effect on intestinal microflora in mice. The findings enhance the health protection ability of astronauts, which will provide a solid scientific and theoretical support for the smooth promotion of China's deep space exploration.

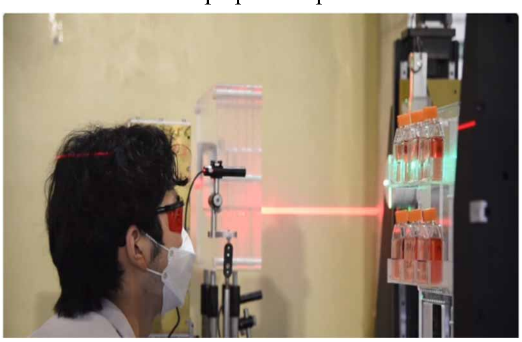

Figure 7: Experiment samples.

Additional, sensitivity of nasopharyngeal carcinoma and glioma to proton irradiation is determined. A375 cancer cells were irradiated by proton to study the changes of cell survival rate, cell cycle change, apoptosis and DNA damage with dose.

Radiotherapy, a common method for the treatment of cancer. FLASH imaging is delivered at an ultra-high dose rate (> 40 Gy/s), meanwhile reducing the normal tissue toxicity. On the N3 line of CYCIAE-100, three-dimensional water phantom PTW, Bragg peak ionization chamber, reference ionization chamber and finger ionization chamber were used for dose measurement [2, 3]. The ultra-high dose rate of 40.76 Gy/s (204.9 for 5 second) is obtained in this test, which can be used in the study of proton FLASH as shown in Fig. 8.

Figure 8: Proton FLASH set.

In radioactive isotope development study, medium energy proton can be used to radiated kinds of target materials for rare isotope. Through the design and research of isotope solid target system, a high-power solid target radionuclide experimental device has been successfully developed, and core technologies have been mastered. The first-time test of Ac-225 with 100 MeV cyclotron has been completed. ^{221}Fr characteristic ray proved the existence of mother nuclide of ^{225}Ac shown in Fig. 9. It has laid a solid foundation for the research of other nuclides related to the production of accelerators.

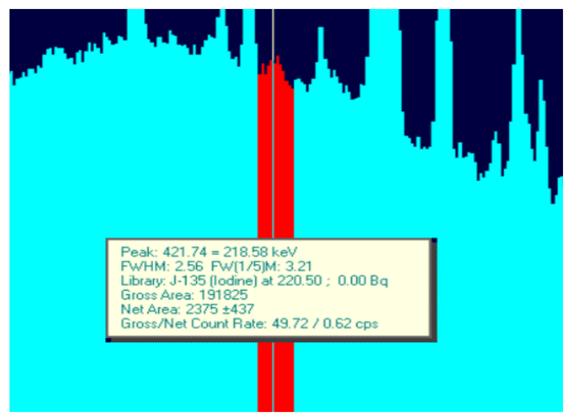

Figure 9: ^{225}Ac-^{221}Fr: characteristic ray.

CONCLUSION

CYCIAE-100 facility as the core of BRIF, is playing more and more important role in the nuclear data, radiation effect, agriculture, medical and isotope production area. We will continue to improve the performance and efficiency of the accelerator, complete the upgrading of aging devices, and maintain the stability of the beam.

In the future, it is planned to continue to expand the facility capacity, and give full play to the potential of large scientific devices in the application of accelerator neutron sources and nuclear waste transmutation (ADS), and make vital contributions to the promotion of the country's nuclear scientific and technological strength.

ACKNOWLEDGEMENTS

The authors would like to thank related institutes and colleagues in the development and study process. This work is supported by the National Natural Science Foundation of China under Grant No.11375273.

ISBN: 978-3-95450-212-7 ISSN: 2673-5482 doi:10.18429/JACoW-CYCLOTRONS2022-TUB003

REFERENCES

[1] T. Zhang *et al.*, “Design & construction status of CYCIAE-100, a 100 MeV H$^-$ cyclotron for RIB production”, *Nucl. Instrum. Methods in Phys. Res. Sect. B*, vol. 266, pp. 4117-4122, May 2008. doi:10.1016/j.nimb.2008.05.021

[2] L. Cao *et al*., “The design of scanning control system for proton therapy at CIAE”, in Proc. 7th Int. Beam Instrumentation Conf. (IBIC’2018), Shanghai, China, Sep. 2018, pp. 319-321. doi:10.18429/JACoW-IBIC2018-TUPC10

[3] Z. W. Zhang *et al.*, “The Control System Dedicated for Beam Line of Proton Radiography on 100 MeV Cyclotron CYCIAE-100”, in *Proc. Cyclotrons'16*, Zurich, Switzerland, Sep. 2016, pp. 202-204. doi:10.18429/JACoW-Cyclotrons2016-TUP15

ISBN: 978-3-95450-212-7 ISSN: 2673-5482 doi:10.18429/JACoW-CYCLOTRONS2022-TUB004

EVALUATION OF PLC-BASED ETHERNET/IP COMMUNICATION FOR UPGRADE OF ELECTROMAGNET POWER SUPPLY CONTROL AT RIBF

A. Uchiyama†, K. Kumagai, M. Komiyama, N. Fukunishi, RIKEN Nishina Center, Wako, Japan

Abstract

In the Radioactive Isotope Beam Factory (RIBF), a front-end controller consisting of a computer automated measurement and control (CAMAC)-based system and I/O devices are utilized for the power supplies of many electromagnets upstream from the RIKEN RING Cyclotron. The CPU installed in the system is an x86-based CAMAC crate controller known as "CC/NET". An experimental physics and industrial control system (EPICS) input/output controller (IOC) running embedded Linux is used to remotely control the electromagnet power supplies. However, these CAMAC-based systems are outdated and require replacement. The FA-M3 programmable logic controller (PLC) is an alternative candidate device that can be incorporated into the magnet power supply. However, a high-reliability network between the EPICS IOC and the device is required compared to a conventional socket connection via Ethernet. Therefore, we evaluated a system that uses EtherNet/IP to communicate between these devices and the EPICS IOC. The EtherNet/IP system is based on the TCP/IP protocol, which is widely used for field bus communications via Ethernet. An advantage of using EtherNet/IP is that it enables cost-effective reliable communication despite the use of TCP/IP. It is possible to improve the reliability of the interlock output even when using conventional TCP/IP-based network.

INTRODUCTION

RIKEN had the former accelerator facility, RARF (RIKEN Accelerator Research Facility), consisting of the RIKEN Ring Cyclotron (RRC), and RIKEN Linear Accelerator (RILAC) as an injector since 1986 [1]. Three new cyclotrons, the FRC, IRC, and SRC, were constructed downstream of the RRC in the new Radioactive Isotope Beam Factory (RIBF) project, and beam commissioning of the new cyclotrons was completed in the 2006 fiscal year [2]. RIBF is currently a heavy-ion accelerator facility with five cyclotrons and three injectors [3]. Furthermore, the original RARF power supplies are still in use while beam-tuning the electromagnets upstream of RRC because RIBF is an upgrade of project RARF. Thus, outdated I/O modules and communication boards used to control electromagnet power supplies are still in use.

Figure 1 shows a block diagram of the control system at the time of RARF. Furthermore, electromagnet power supply control in RARF is a computer-automated measurement and control (CAMAC) system. The system consists of a communication interface module (CIM), which is a communication module attached to the CAMAC crate, and a device interface module (DIM)[4], which is an I/O built into the electromagnet power supply and is connected via an optical fiber to enable serial communication. CAMAC was initially controlled by the MELCOM 350-60/500, a minicomputer manufactured by Mitsubishi Electric Corp [5]. The minicomputer was replaced in 2001 by a VME CPU board with a VxWorks OS to operate via the Experimental Physics and Industrial Control System (EPICS) [6]. To stabilize the control system, a CPU board running EPICS was replaced in 2004 with an x86 CAMAC crate controller, CC/NET manufactured by Toyo Tecnica [7]. This system is unique because it is an embedded system that runs EPICS on Debian 3.0, a Linux operating system for CC/NET. Figure 2 shows the CAMAC-based system for the electromagnet power supply that is currently in operation.

The VME CPU board has been replaced with CC/NET as the CAMAC-based controller of the electromagnet power supply systems, but CIM/DIM system have already been used for more than 30 years since the beginning of RARF operations and have become obsolete. For example, poor CIM/DIM communication causes a bottleneck in some cases during operation; hence, these CIM/DIM systems must be urgently replaced. The FA-M3 programmable logic controller (PLC) manufactured by Yokogawa Electric Corporation was chosen as a potential replacement for the DIM built inside the power supply chassis while considering replacing the outdated CIM/DIM system. Figure 3 shows the DIM functional part currently under development. The FA-M3 PLC is a candidate device for the function corresponding to the DIM, we designed the communication between the controllers corresponding to the CIM, and the EPICS implementation method.

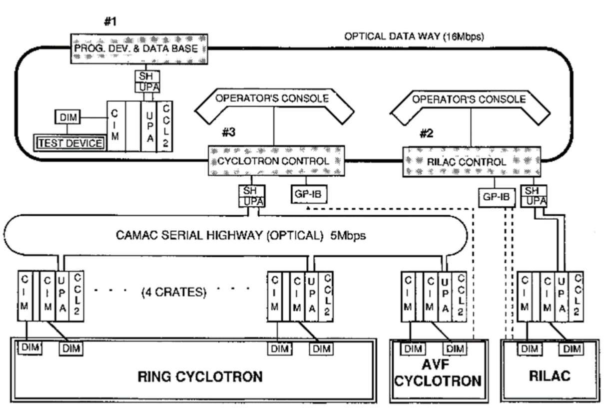

Figure 1: Block diagram of RARF control system (the original figure is Fig. 2 in reference 5).

† a-uchi@riken.jp

ISBN: 978-3-95450-212-7 ISSN: 2673-5482 doi:10.18429/JACoW-CYCLOTRONS2022-TUB004

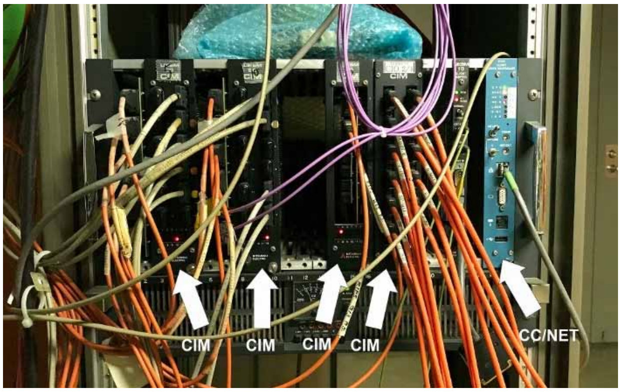

Figure 2: CC/NET, CAMAC-based controller with CIMs installed for communication to DIM.

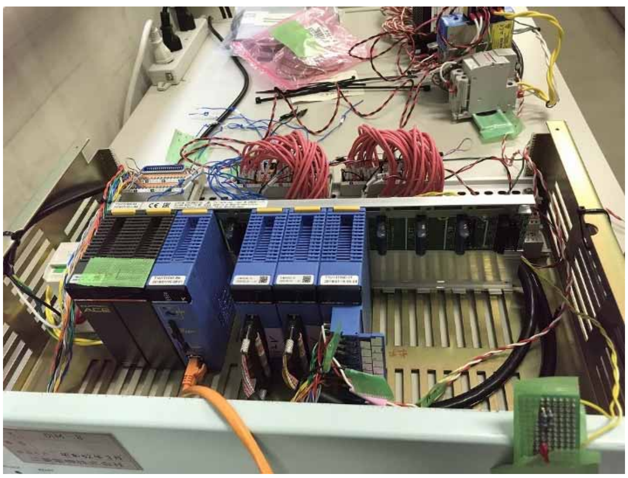

Figure 3: Photograph of DIM functional part by FA-M3 currently under development.

DEVICE INTERFACE LAYER OVER TCP/IP

When developing the DIM compatibility function with the FA-M3 PLC, the sequence CPU module (F3SP71/F3SP76 [8]) is equipped with standard Ethernet port and its EPICS device support software using NetDev [9] is already provided. Hence, it is possible to develop low-cost control systems with EPICS. In this case, TCP/IP is used for communication between the EPICS Input/Output Controller (IOC) and devices, which is the device interface layer. TCP/IP-based devices are helpful for reducing development cost, and various types of TCP/IP-based devices are utilized for the RIBF control system; they are operated remotely via the EPICS channel access (CA) protocol. However, TCP/IP-based devices occasionally do not reconnect to the EPICS IOC after a power failure or unintended device restart, which causes operational concerns. The RIBF control system frequently restores the connection by restarting the EPICS IOC process, even though it is preferable if the reconnection is reliably established after restoration.

For example, the EPICS IOC start-up script can output a message informing the user of the EPICS IOC's disconnection from the device. However, such features are just for developers, not a mechanism to alert accelerator operators as an EPICS CA client. In addition, the EPICS management system [10] can monitor the TCP/IP-based device status using ping and port scans. However, it cannot be decided to the socket connection status between the EPICS IOC and TCP/IP-based devices because it bases an alive monitoring by an external program.

FIELD NETWORK COMMUNICATION

The RIBF control network is usually placed in the power supply and accelerator rooms, so TCP/IP-based devices' advantage is that they require minimal Ethernet cable installation. Conversely, they are unreliable owing to their low real-time performance, slow I/O communication, and reconnection problems in RIBF control systems. On the other hand, development of a new proprietary dedicated protocol, such as NIO [11], used in the RIBF control system, would be too expensive. Therefore, we considered Ethernet-based field networks (EtherCAT, FL-net, EtherNet/IP), which are general-purpose protocols and standard FA-M3 modules, for the interface between the FA-M3 PLC-based DIM (included in the electromagnetic power supply) and the EPICS IOC. FL-net and EtherCAT, further require a dedicated network and cannot be mixed with the control network, reducing convenience. As a result, we evaluated EtherNet/IP.

EtherNet/IP

EtherNet/IP is a network widely used in Ethernet industrial fields [12]. There are various industrial devices that use it, and it is managed as an open standard by the Open DeviceNet Vendor Association (ODVA). EtherNet/IP is compatible with conventional Ethernet, and shares the same physical layer, such as the frame structure, connectors, cables, and is also compatible with TCP/IP. Furthermore, it utilizes a Common Industrial Protocol (CIP) in the application layer. Thus, the main features allow general-purpose network switches with other TCP/IP protocols, low-cost wiring, and relatively high real-time performance. Additionally, an Allen-Bradley Control-Logix PLC and the EtherNet/IP were used by the Spallation Neutron Source (SNS) to build a subsystem as an illustration of how they could be used in an accelerator control system [13]. Furthermore, SOLARIS Synchrotron has used PLCs in a TANGO-based control system to implement machine protection and personal safety systems. PLC nodes communicate via EtherNet/IP [14].

SYSTEM DESIGN

An EtherNet/IP-based system generally consists of a scanner and adapter. The scanner is on the EPICS IOC side of the system designed for electromagnetic power supply control, and the adapter is the DIM integrated into the electromagnetic power supply. The network segments are point-to-point connections in star topology designed for installation in an existing RIBF control network.

The scanner consists of FA-M3 series PLCs, and the dedicated module F3LN01-0N [15] realizes inter-PLC communication via EtherNet/IP with the DIM functional part.

ISBN: 978-3-95450-212-7 ISSN: 2673-5482 doi:10.18429/JACoW-CYCLOTRONS2022-TUB004

The sequence CPU F3SP76 was installed in the first slot to of the proposed system to realize the interlock function of the beam interlock system (BIS) [16] for machine protection. In the second slot, a Linux CPU, F3RP71-1R [17], is installed in the second slot to implement the CA protocol for interfacing high-level applications, resulting in a multi-CPU configuration. The link register (W register) is used to exchange I/O between the FA-M3 PLC, adapter, and scanner. As a result, developers use the FA-M3 PLC system's standard development method because it is cost-effective and only requires the link register, regardless the EtherNet/IP protocol.

EPICS INTERFACE

This system realizes the EPICS IOC using the F3RP71-1R installed in the second slot of the scanner. The DIM installed in the electromagnet power supply becomes an adapter(s) and exchanges data with the node that becomes the scanner via Ethernet/IP using the link register. However, the link register in a multi-CPU environment does not support by the EPICS device support for F3RP61/71 [18]. As a result, the link register is sent and received by F3SP76, the sequence CPU installed in the first slot, and the use of shared memory realizes the interface with the EPICS IOC installed in F3RP71-1R. Figure 4 shows the system chart of the pro-posed EPICS-based system. At this point, the internal register of the sequence CPU enters the connection status of the adapter and scanner, while it is available to activate an interlock output and alerting the operator of a disconnection

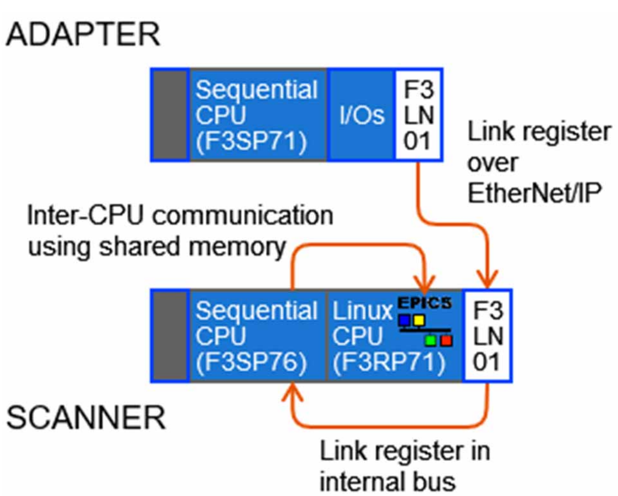

Figure 4: System chart of the proposed EPICS-based system. Data is exchanged between PLCs using link registers on EtherNet/IP. Data is exchanged from the sequential CPU to the Linux CPU using shared memory.

IMPLEMENTATION TEST

We tested the response using a configuration of one Ethernet/IP scanner and one adapter connected in one 1Gbps switching hub. Figure 5 shows the response test environment. Table 1 lists the settings of the adapter used to connect the scanner. The scanner's sequence CPU was used to generate a 10 Hz internal signal for the test, which was trigger output to the scanner and adapter simultaneously. The time difference was calculated based on the EtherNet/IP communication. As a result, the difference in the average response time was approximately 2.3 ms. This result is comparable to the performance of a previous application with a minimum number of nodes connected to the FL-net [16]. In addition, while the transmission time of FL-net becomes proportionally slower as the number of connected nodes increases, the transmission time of EtherNet/IP related to the switch latency [19]. As a result, unlike the FL-net, the response time is not expected to slow in proportion to the number of adapters.

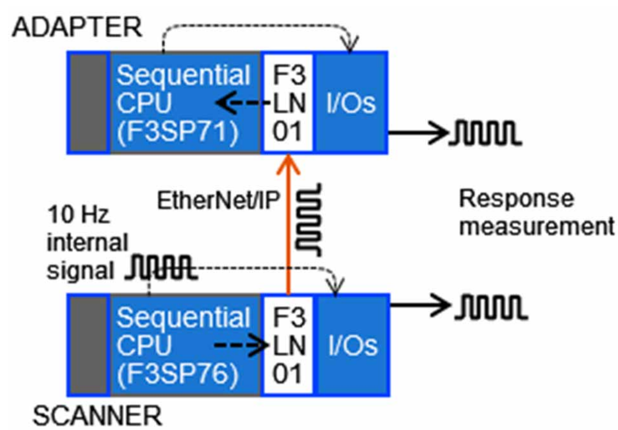

Figure 5: System chart of the response test environment. It generates an internal signal, triggered and compared with its node and via EtherNet/IP.

Table 1: Adapter Connection Setting for Implementation Test

Communication type	Symbolic Segment
Trigger	Cyclic
Requested Packet Interval (RPI)	1 ms
Connection type	Point-to-point
Data size	100 bytes

Because EtherNet/IP is a field network with soft real-time, the real-time performance could be a bottleneck. Furthermore, we measured jitter to calculate the arrival time of signals caused by EtherNet/IP to the equipment varied in the implementation test. Figure 6 shows the test environment for the jitter measurement. The scanner, adapter, and switching hub had the same configuration as the response measurements. In this test, a function generator generated a 100 Hz external signal and input it to the scanner. Additionally, the sequence CPU of the scanner triggered the input signal and output to both the scanner and adapter simultaneously to measure jitter. As a result, the jitter of the scanner output was 1.08 ms, and the jitter of the adapter output was 1.8 ms. Therefore, the jitter was approximately 0.7 ms larger via EtherNet/IP. The Ethernet/IP of the requested packet interval was set to 1 ms, and the timing of that communication and the scans of both sequence CPUs caused a slight increase in the jitter. Based on these

ISBN: 978-3-95450-212-7 ISSN: 2673-5482 doi:10.18429/JACoW-CYCLOTRONS2022-TUB004

responses and jitter results, field communication using EtherNet/IP can be used not only for electromagnet power control, but also for outputting slower interlocks with reaction times of a few milliseconds [20].

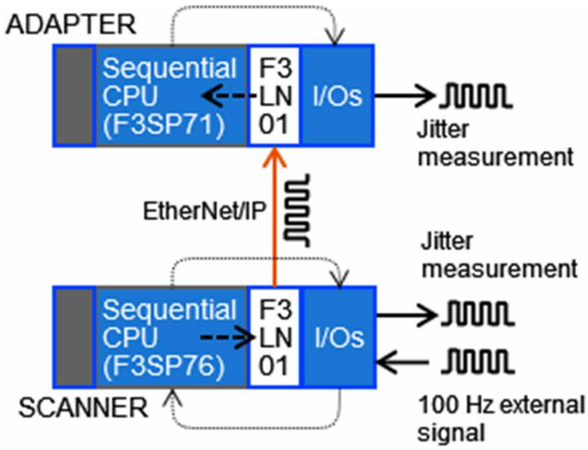

Figure 6: System chart of the jitter test environment. The scanner inputs an external signal of 100 Hz and compares it with the output of its node and output via EtherNet/IP.

CONCLUSION

In this study, we studied the EPICS IOC and device interface layer, which is a network between devices, to upgrade the outdated electromagnet power supply control in the RIBF control system. The part corresponding to the DIM built into the electromagnetic power supply is under development in FA-M3 as a candidate. Therefore, we evaluated EtherNet/IP for interfacing with the DIM and EPICS. The data received over EtherNet/IP by the sequence CPU installed in the first slot were passed to the Linux CPU with EPICS installed in the second slot via shared memory. Hence, a dedicated network is unnecessary as a field network. Thus, a conventional network system can be used without modification. The performance is sufficient, and the system is efficient and convenient. In the future, we plan to test the operation of the electromagnetic power supply by connecting it to the DIM under development. The requested packet interval was set to 1 ms, which is the fastest F3LN01-0N in the implementation test. However, only five adapters are available to be used per scanner in this situation. In the actual implementation, when the interlock output is not required for the BIS, setting the interval to 10 ms allows one scanner to hold approximately 30 adapters.

REFERENCES

[1] Y. Yano, "Status report on RIKEN Ring Cyclotron", in *Proc. 12th Int. Conf. on Cyclotrons and their Applications (Cyclotrons'89)*, Berlin, Germany, May 1989, paper A-04, pp. 13-16.

[2] N. Fukunishi *et al.*, "Present Performance and Commissioning Details of RIBF Accelerator Complex", in *Proc. 18th Int. Conf. on Cyclotrons and Their Applications,* Giardini Naxos, Italy, Oct. 2007, pp. 21-23.

[3] O. Kamigaito *et al.*, "Recent Progress in RIKEN RI Beam Factory", in *Proc Cyclotrons'19*, Cape Town, South Africa, Sept. 2019, pp. 12-16. doi:10.18429/JACoW-Cyclotrons2019-MOB01

[4] K. Shimizu, "New general purpose interfacing modules for an accelerator control system", *Nucl. Instrum. Methods Phys. Res. A,* vol. 236, issue 1, May 1985, pp. 109-116. https://doi.org/10.1016/0168-9002(85)90134-2

[5] T. Wada *et al.*, "Control System of RIKEN Heavy Ion Accelerator Complex", *Jpn. J. Appl. Phys.*, vol. 30, no. 11A, Nov. 1991, pp. 2947-2955.

[6] M. Kobayashi-Komiyama *et al.*, "New Control System for the RIKEN Ring Cyclotron Using EPICS", *RIKEN Accel. Prog. Rep.*, vol. 34, 2001, pp. 318-319.

[7] M. Komiyama *et al.*, "Control System for the RIKEN Accelerator Research Facility and RI-Beam Factory", in *Proc. Cyclotron'04,* Tokyo, Japan, Oct. 2004, paper 19P32, pp. 478-480.

[8] https://www.yokogawa.co.jp/solutions/products-and-services/control/control-devices/programmable-logic-controller/plc-sequence-cpu-f3spxx/

[9] https://github.com/shuei/netDev

[10] A. Uchiyama *et al.*, "EPICS PV Management and Method for RIBF Control System", in *Proc. ICALEPCS'15,* Melbourne, Australia, Oct. 2015, pp. 769- 771. doi:10.18429/JACoW-ICALEPCS2015-WEPGF032

[11] T. Tanabe *et al.*, "Current Status of the Control System Development at RIKEN RI-Beam Factory", in *Proc. ICALEPCS'03*, Gyeongju, Korea, Oct. 2003, paper TH613, pp. 597-599.

[12] http://odvatagjapan.iinaa.net/index.html

[13] K. U. Kasemir *et al.*, "Interfacing the Controllogix PLC over EtherNet/IP", in *Proc. ICALEPCS'01,* San Jose, California, USA, Nov. 2001, paper THDT002, pp. 481-483.

[14] P. P. Goryl *et al.*, "TANGO Based Control System at SOLARIS Synchrotron", in *Proc. IPAC'16,* Busan, Korea, May 2016, pp. 4101-4103. doi:10.18429/JACoW-IPAC2016-THPOY008

[15] https://library.yokogawa.com/document/download/AxkHnJ89/0000092698/5/JA/

[16] M. Komiyama *et al.*, "Recent Update of the RIKEN RI Beam Factory Control System", in *Proc. ICALEPCS'17,* Barcelona, Spain, Oct. 2017, pp. 427-430. doi:10.18429/JACoW-ICALEPCS2017-TUPHA028

[17] https://www.yokogawa.co.jp/solutions/products-and-services/control/control-de vices/real-time-os-controller/rtos-cpu/rtos-linux-cpu/

[18] https://github.com/EPICS-F3RP61/epics-f3rp61

[19] Xuepei Wu, Lihua Xie, "Performance evaluation of industrial Ethernet protocols for networked control application", *Control Eng. Pract.*, vol. 84, March 2019, pp. 208-217. doi:10.1016/j.conengprac.2018.11.022

[20] R. Schmidt *et al.*, "Machine Protection and Interlock Systems for Large Research Instruments", in *Proc. ICALEPCS'15*, Melbourne, Australia, Oct. 2015, pp. 537-542. doi:10.18429/JACoW-ICALEPCS2015-TUC3I01

23rd Int. Conf. Cyclotrons Appl. CYCLOTRONS2022, Beijing, China JACoW Publishing
ISBN: 978-3-95450-212-7 ISSN: 2673-5482 doi:10.18429/JACoW-CYCLOTRONS2022-WEAI01

SELF-CONSISTENT SIMULATION OF AN INTERNAL ION SOURCE PLASMA MENISCUS AND ITS EXTRACTED SPACE CHARGE DOMINATED BEAM IN THE CYCLOTRON CENTRAL REGION *

G. D'Agostino†, Istituto Nazionale di Fisica Nucleare-Laboratori Nazionali del Sud, Catania, Italy
W. Kleeven, Ion Beam Applications (IBA), Louvain-la-Neuve, Belgium
†also at Ion Beam Applications (IBA), Louvain-la-Neuve, Belgium

Abstract

Central region design simulations for cyclotrons with internal ion source are often complicated by the fact that the initial particle phase space distribution is not well known. Especially for high-intensity cyclotrons, one would like to have a quantitative self-consistent approach for a more accurate simulation of the beam extracted from the ion source and its acceleration in the first accelerating gaps under space charge conditions. This paper proposes some new ideas and methods for this problem. The simulation approach has been developed at IBA for the high-intensity compact self-extracting cyclotron in the EU-H2020-MSCA InnovaTron project. Detailed results of simulations on plasma meniscus and space charge dominated beam extracted from it and accelerated in the cyclotron centre are shown in the paper.

INTRODUCTION

At IBA a high-intensity compact self-extracting cyclotron, called InnovaTron, is being studied. The machine is a promising tool for large-scale production of medical radioisotopes. Self-extraction allows spontaneous beam extraction. It is based on a very steep fall-off of the magnetic field near the outer pole radius [1]. First harmonic coils increase the turn-separation at extraction. A 14 MeV proton cyclotron build by IBA in 2000 provided the proof-of-principle for this extraction method (extracted beam currents up to 2 mA) [2]. However, rather poor beam quality was observed and the extraction efficiency was limited to about 80% at low intensities. Increase of the dee-voltage ripple resulting from the noisy PIG-source and beam-loading led to an extraction efficiency of about 70%-75% at higher intensities. Main goals set for the project are: i) improvement and optimization of the magnet, extraction elements and central region, ii) space charge simulations, iii) improvement of turn-separation at extraction. Proton currents up to 5 mA are aimed for.

Here, we discuss detailed results obtained for central region studies including space charge in beam dynamics simulations. Space charge plays an important role already during the process of bunch formation in the first gap. It also induces a vortex motion during beam acceleration and an increase of energy spread in the bunch [3]. Simulation results obtained for magnet optimization and a new IBA tool for automated optimization of cyclotron settings are also discussed.

* Work supported by the European Union's Horizon 2020 research and innovation programme under the Marie Skłodowska-Curie grant agreement No 886190.
† grazia.dagostino@lns.infn.it

MAGNET OPTIMIZATION

Figure 1 shows the main features of the prototype. The pole gap has a quasi-elliptical shape, allowing for the steep fall-off of the magnetic field (Fig. 1 (a)) by the machining of a groove on the long pole (on which the beam is extracted) at a radius where the gap is small (Fig. 1 (b)). Figure 1 (c) shows one of the harmonic coils. A gradient corrector is used for radial and vertical focusing of the extracted beam. Parts of the beam that are not properly extracted are intercepted by a beam separator shown in Fig. 1 (d). The extraction path in the machine is shown in Fig. 1 (e). More details are in [2].

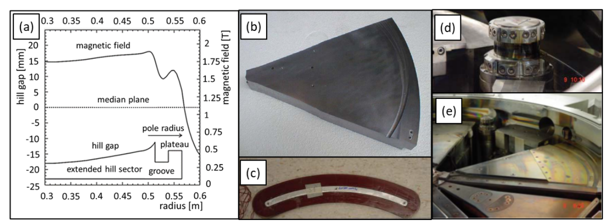

Figure 1: The prototype of the self-extracting cyclotron.

The following improvements have been implemented as compared to the prototype: i) the magnet (and also the accelerating structure) has perfect 2-fold symmetry. This allows irradiation of two targets stations at opposite exit ports and to place two internal ion sources. The latter will increase cyclotron reliability and uptime; ii) the groove in the extraction path is replaced by a "plateau" (Fig. 2 (a)). This reduces the strong sextupole component in the extraction path and improves the extracted beam quality. Figure 2 (b) shows the magnetic field along a line that bisects the long and short poles as shown in Fig. 2 (a); iii) the pole gaps still have a quasi-elliptical shape, decreasing towards larger radii, but the iso-gap contours follow equilibrium orbits. This enables a steeper transition from the internal stable orbit towards the non-stable extracted orbit; iv) an improved gradient corrector has been designed for radial focusing of the extracted beam (Fig. 2 (c,d)).

Figure 2 (e) is a view on the lower half of the magnet developed in Opera3D and shows the harmonic coils (in red), the gradient correctors (in green) and the beam separators (in yellow). The dees (in light blue) are also shown. A beam simulation of the last 5 turns superimposed on the FEM model is shown in Fig. 2 (f). Automatic and parametrized FEM models have been developed for the magnet but also for the central region. More details are given in [4].

23rd Int. Conf. Cyclotrons Appl. CYCLOTRONS2022, Beijing, China JACoW Publishing
ISBN: 978-3-95450-212-7 ISSN: 2673-5482 doi:10.18429/JACoW-CYCLOTRONS2022-WEAI01

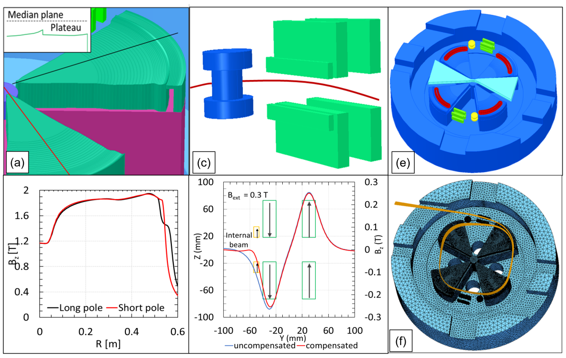

Figure 2: InnovaTron improved magnet design.

CENTRAL REGION STUDIES

We do an effort for a self-consistent simulation of the space charge dominated beam in the central region. This method consists of three steps. In the first step, the SCALA space charge solver of Opera3D is used to find the plasma meniscus of the ion source. In the second step, the same central region model is solved again, but now with the TOSCA electrostatic solver of Opera3D. Here the meniscus surface is put at ground potential. This provides the 3D electric field map everywhere in the central region, including the source-puller gap. In the third step, the beam extracted from the meniscus is simulated in the 3D field map using the self-consistent in-house space-charge code AOC [5]. This code has been extended to also simulate the bunch formation process in the first gap. More details can be found in [6].

SCALA Simulations

The plasma-free boundary module of SCALA calculates the plasma meniscus and the extracted beam phase space and current density on the meniscus in a DC electric field. SCALA does not solve the plasma itself: the meniscus surface is determined by the Child-Langmuir condition where the external electric field on the surface is cancelled by the space charge electric field. The surface is found in an iterative process. The electric field in a cyclotron central region is not DC but RF. The RF frequency, however, is so high that it will be impossible for the plasma meniscus to follow it, in its motion. The maximum velocity of a material wave is roughly equal to the speed of sound in the material which, for a plasma, will be close to the Bohm-velocity $v_B = \sqrt{kT_e/m_p}$, where T_e is the plasma electron temperature and m_p is the proton mass. Assuming $kT_e \approx 10$ eV we find that the meniscus could move only about 0.1 mm in a quarter of the wave period at 70 MHz. So, it seems that the meniscus will move only weakly in the RF electric field; we therefore make the assumption that the meniscus shape and position can be found by solving the problem for the rms-value of the gap-voltage. It is clear that this is a strong assumption and an important simplification which we can, at this point, not further validate.

For the solution of the SCALA problem we only need to model the local geometry of the source-puller gap. Our

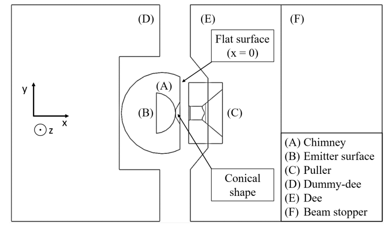

Figure 3: Top view of the SCALA source-puller model.

example is shown in Fig. 3. In this geometry the puller (C) and the dee (E) are placed at high (negative) potential and the chimney (A) and the dummy-dee (D) are at ground potential. The ion source full slit aperture in our example is $\Delta y \times \Delta z = 1 \times 8$ mm^2. SCALA launches beamlets from the (flat) emitter surface (B), which move to the right towards the ion source slit. At this position, space charge builds up which limits the flow of extracted particles. Besides the geometry, the two important parameters in the simulation are i) the dee-voltage V_{dee} and ii) the emitter current density J_{emit}. Two additional but less critical parameters are iii) the electron temperature T_e and iv) the meniscus voltage V_m. Figure 4 shows examples of four different cases: a) (V_{dee}=42.1 kV, J_{emit}=0.4 A/cm^2), b) V_{dee}=9.5 kV, J_{emit}=0.4 A/cm^2), c) (V_{dee}=38.9 kV, J_{emit}=0.2 A/cm^2) and d) (V_{dee}=38.9 kV, J_{emit}=2 A/cm^2). The first column in the figure is a vertical section through the chimney and shows the position and shape of the meniscus (only the upper half is shown). The middle column shows the vertical beam profile (seen from the $-y$ direction) and the right column shows the horizontal beam profile (seen from the $+z$ direction). The extracted DC currents for the four cases are 100 mA (a), 36.7 mA (b), 67.4 mA (c) and 222 mA (d).

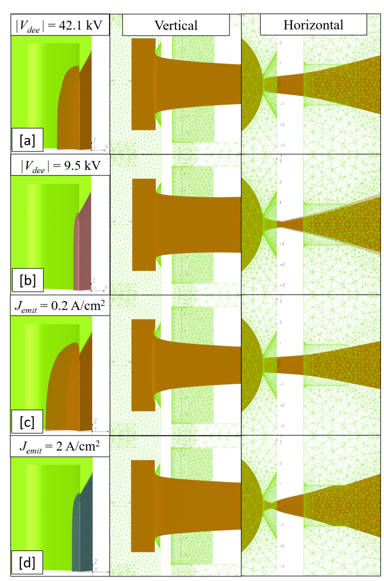

Figure 4: Examples of meniscus shape and beam projections.

A close inspection shows that the extracted current is (almost perfectly) proportional to the surface of the meniscus times the emitter current density. The beamlets cross the

ISBN: 978-3-95450-212-7 ISSN: 2673-5482 doi:10.18429/JACoW-CYCLOTRONS2022-WEAI01

meniscus (almost perfectly) perpendicularly and the flow is (almost perfectly) laminar. It is seen that higher V_{dee} pushes the meniscus to the left and higher J_{emit} pushes the meniscus to the right. Horizontally the beam is strongly converging, with an (over-) focus close to the slit and vertically the beam is weakly converging. This relates directly to the slit dimensions which make that the meniscus is strongly curved in the xy-plane and much more flat in the xz-plane.

Figure 5 shows the extracted current and meniscus position as a function of the four parameters V_{dee}, J_{emit}, T_e and V_m. The position is the distance between the extreme meniscus x-coordinate and the intersection between x-axis and plasma chamber cylinder.

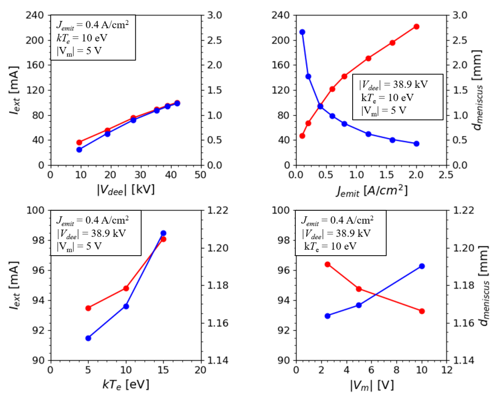

Figure 5: DC extracted current (red) and meniscus position (blue) as function of the four main parameters.

TOSCA Simulations

We extract from the beamlets calculated by SCALA (those who are extracted from the ion source) the particle position coordinates, the velocity components and the beamlet current at the meniscus intersection. These data are used to fit the meniscus x-coordinate, the transverse divergencies (y', z') and the beamlet currents as a function of y and z. The latter two are considered as independent variables. We use a double polynomial fit up to order 7 (the sum of the y and z exponents) and take into account the symmetry: x is even in y and z; y' is odd in y and even in z; z' is even in y and odd in z. This allows to represent the surface of the meniscus as a wire-edge structure with a triangular mesh. This surface is included in the TOSCA model of the central region, where it is put at ground potential (see Fig. 6). With this, one can simulate precisely the value and shape of the 3D electric field in the source-puller gap. The representation also allows to create a file with particle starting conditions for tracking, when y and z are generated randomly and the other variables (x, y', z') are calculated from the fits.

Figure 7 shows projections of the fitted phase space on the planes xy, xz, yy', zz'. Three cases are shown: V_{dee}=38.9 kV, J_{emit}=0.4 A/cm^2 (green), V_{dee}=18.8 kV, J_{emit}=0.4 A/cm^2 (blue), V_{dee}=38.9 kV, J_{emit}=2 A/cm^2 (red).

Figure 8 shows in (a) the TOSCA electric field in the source-puller gap for three different cases. One case is for

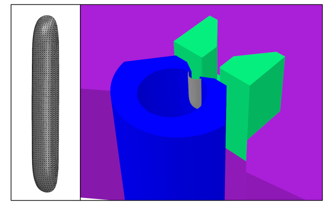

Figure 6: Modeling of the plasma meniscus in TOSCA.

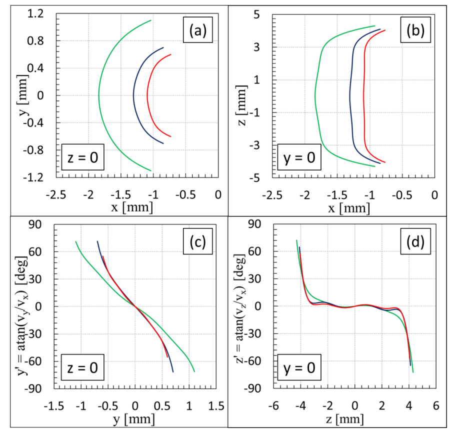

Figure 7: Fitted phase space projections.

the chimney with the conical shape as shown in Fig. 3; for the other two cases, this cone is not present. The meniscus was calculated at V_{dee}=35.3 kV for the first case (blue curve) and 18.8 kV for the other two cases. For all three cases, the electric field drops quickly in the space in between the meniscus and the chimney slit ($x < x_{slit}$) . As a consequence, the particles must leave early from the meniscus surface in order to be able to cross the gap. This is illustrated in figures (b-d). They show the particle energy gain as a function of time for different starting RF phases ranging from -180° (the moment of zero dee-voltage) up to -130° in steps of 5° (with V_{dee}=55 kV). Later starting phases are not properly accelerated by the central region. The worst case is (b) where the energy gain is the lowest and the energy spread is the largest. For this case, the electric field near the meniscus is the lowest and the particles are lost after a few turns in the central region. For cases (c) and (d) the electric field near the meniscus is higher and a phase range of about 40° can be accepted and accelerated. Case (c) is the best as it has good energy gain and the smallest energy spread.

Space Charge in AOC

In the default use of AOC, the full 6D phase space of the initial particles in the bunch must be specified. Recently, a new option has been added in AOC for simulating the formation of the bunch extracted from the ion source meniscus. In this case, the particle properties on the meniscus must be defined and also the number of time-steps that are needed to complete the bunch formation. The bunch will be sliced according to the number of time-steps. For each new step, the bunch is re-defined by adding the additional slice and

ISBN: 978-3-95450-212-7 ISSN: 2673-5482 doi:10.18429/JACoW-CYCLOTRONS2022-WEAI01

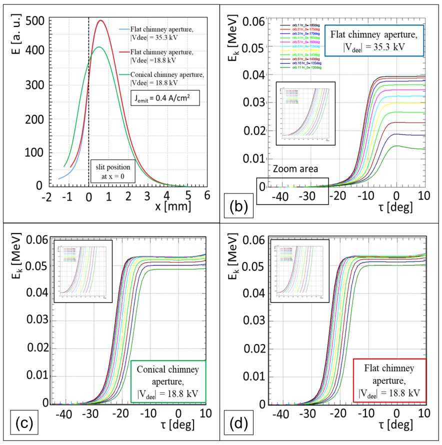

Figure 8: Electric field and energy gain in the first gap.

then advanced using the iterative process. After completing the formation of the bunch, it is continued in the usual way.

FULL BEAM TRACKING

We track a full beam through the central region shown in Fig. 9. The position and orientation of the ion source and the first few accelerating gaps in this central region are optimized in order to obtain good beam centering and good vertical electric focusing. Some additional tools have been made in AOC that allow to slightly rotate/translate the central region geometry without the need to each time solve its 3D FEM model. The collimators (shown in blue) are optimized to limit the accelerated RF phase range to about 40° and by so to remove particles that would otherwise be lost at higher energies. Note that the beam shown in Fig. 9 only includes the "successful" particles. The starting beam, obtained from a SCALA simulation (J_{emit}=0.4 A/cm^2 and V_{dee}=18.8 kV) and representing a starting average current of 100 mA on the meniscus, is sampled with 100000 particles in a RF phase range between -180° and 0°.

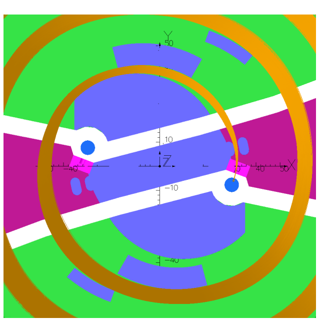

Figure 9: The 2-fold rotational symmetric central region.

Figure 10 shows transmission (a), centering (b), vertical beam size (c) and vertical emittance (d) of the accelerated beam during the first 25 turns. In the representation shown, the particles are binned according to their RF starting phase on the meniscus in four groups of each 10° wide. Only particles in the phase range between -180° and -140° are accepted. The particles must leave early from the meniscus as explained before. Figure 10 (a) shows that there are high losses in the first 2 turns. This is not only due to the unfavorable transit time but also to the strong over-focusing action in the horizontal plane at the ion source exit (see Fig. 4). Only about 1.7% of the particles is accepted, corresponding to an average beam current of 1.7 mA. The losses are distributed as follows: about 88.7% on the chimney+puller+puller collimators, about 5.8% in the phase selecting collimators and about 3.9% vertically on the dees and dummy-dees. Beyond the second turn all beam properties stabilize.

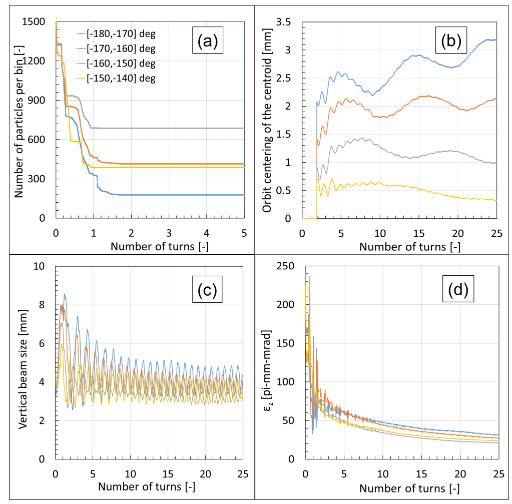

Figure 10: Beam rms properties, binned according to RF starting phase: (a) transmission, (b) beam centroid off-centering, (c) vertical beam size (2σ value), (d) normalized vertical emittance (2σ value).

Figure 11 (a) shows the shape of the accelerated bunches by their projection on the xy-plane, followed during 25 turns at moments when the RF phase equals zero. In another (earlier) simulation, we started a bunch just beyond the source-puller gap with an average beam current of 5 mA, horizontal and vertical emittances of about 20 π mm-mrad (1σ) and a total bunch length of about 3 mm (corresponding to 30° RF phase width). The shape of the bunches for this case is shown (for the first 20 turns) in Figure 11 (b). Here we observe the appearance of circular bunches (with a tail however) which probably is due to the well-known vortex motion [3], turned on by high space charge forces.

Optimization of Cyclotron Settings

Extracted beam optimization is a difficult and tedious process as it depends on multiple parameters (for example harmonic coil settings, dee-voltage, collimator geometry, etc.) and requires full beam tracking (if possible with space charge) from the ion source up to the cyclotron exit. In order to facilitate this process an optimization program (`project_optimizer`) was written. This program uses standard optimization routines to optimize a task (project). The task is defined by a user-defined script which is executed by the program in an iterative process. It reads new values of independent variables as suggested by the program,

ISBN: 978-3-95450-212-7 ISSN: 2673-5482 doi:10.18429/JACoW-CYCLOTRONS2022-WEAI01

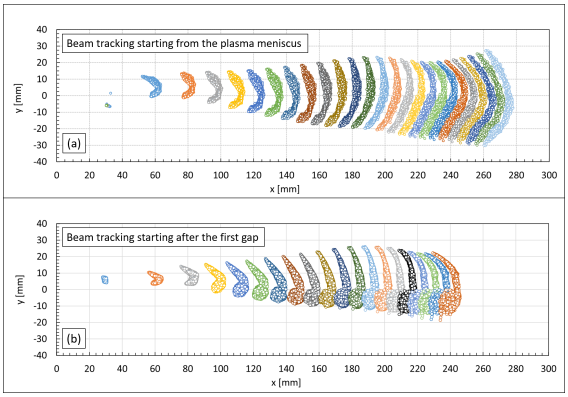

Figure 11: XY projection of accelerated bunches started (a) on the ion source meniscus and (b) after the first gap.

executes the task and writes its results (new values of the objectives) to a file. The program then resumes and compares the results of the script with the (user defined) objectives in order to calculate the fitting error and suggest new values for the variables. This process is repeated until the fitting error is smaller than a given tolerance. In the present study, the script reads all AOC input data and adjusts input field maps as needed. Then, it runs AOC and post-processes its results to extract the objective values. Three standard multiple dimension optimization routines have been implemented (Downhill Simplex Method, Direction SET Powell Method and Simulated Annealing Method).

Extraction efficiency [%] 1° exit port	Dee voltage 55.17 KV	Harmonic coils currents on the long poles					
		-0.35	-0.3	-0.25	-0.2	-0.15	-0.1
Harmonic coils current on the short poles	-0.35	59.2	63.1	68.5	76.0	78.7	78.4
	-0.3	59.8	67.0	78.4	82.1	82.2	81.1
	-0.25	60.9	77.2	87.7	87.9	84.9	84.3
	-0.2	81.8	89.6	89.4	89.2	83.7	69.0
	-0.15	91.3	87.3	82.2	68.5	52.3	45.7
	-0.1	76.9	66.3	65.0	72.5	67.6	12.6

Figure 12: Optimization of extraction efficiency.

The process has been tested (without space charge) for a beam of 2000 particles, tracked from the ion source position up to extraction. The starting conditions at the ion source were taken as: E=100 eV, ϵ_x=125 π mm-mrad, ϵ_z=500 π mm-mrad, slit aperture $w \times h = 1 \times 4$ mm^2 and starting RF phases $-145° < \Phi < -115°$. The settings of the two pairs of harmonic coils were optimized by `project_optimizer` to obtain maximum extraction efficiency on the first exit port. We found an extraction efficiency of 91% with 7.7% losses on the first beam seperator and 1.3% extracted towards the second exit port. Figure 12 illustrates the process of optimization of extraction efficiency as function of harmonic coil settings. Note that this case was still done "by hand".

Figure 13 shows the extracted phase space just beyond the beam separator. At this point we find (1σ) emittances and energy spread of: ϵ_x=104 π mm-mrad, ϵ_z=1.25 π mm-mrad, $\Delta E/E$=0.44%. As can be seen, there is a large X vs Z asymmetry and the vertical emittance is nicely linear. For the self-extracting cyclotron, good turn separation helps to obtain high extraction efficiency. Turn-separation may be reduced or lost if the RF dee-voltage is rippled. At high beam intensities this may happen due to beam loading of the RF cavity, if the injected beam intensity is noisy. Internal ion sources indeed are rather noisy. Figure 13 (c,d) shows the extraction efficiency and the beam energy spread as a function of a simulated dee-voltage ripple. It is seen that the RF control system should keep this ripple as low as possible.

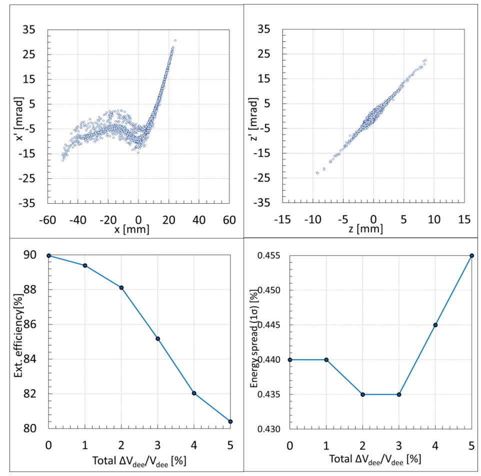

Figure 13: Extracted emittances and dependence of extraction efficiency and energy spread on dee-voltage ripple.

CONCLUSION

We developed new tools i) for the study of space charge beams extracted from the plasma meniscus and bunch formation in the source-puller gap and ii) for automated optimization of cyclotron settings aiming at highest extraction efficiency. Studies are planned to see if the turn-separation at extraction can be further improved.

REFERENCES

[1] W. Kleeven, "Isochronous cyclotron and method of extraction of charged particles from such cyclotron", Patent No.: US 6,683,426 B1, 27 January 2004.

[2] W. Kleeven *et al.*, "The IBA self-extracting cyclotron project", in *Proc. Nukleonika*, vol. 48, supplement 2, pp. S59-S67, 2003.

[3] W Kleeven, "Some examples of recent progress of beam-dynamics studies for cyclotrons", in *Proc. Cyclotrons'16*, Zurich, Switzerland, Sep. 2016, pp. 244–250. doi:10.18429/JACoW-Cyclotrons2016-WEA01

[4] G. D'Agostino *et al.*, "InnovaTron: an innovative high-Intensity industrial cyclotron for production of Tc-99m and other frontier medical radioisotopes", in *Proc. IPAC'21*, Campinas, SP, Brazil, May 2021, pp. 1841–1844. doi:10.18429/JACoW-IPAC2021-TUPAB188

[5] W. Kleeven *et al.*, "AOC, A beam dynamics design code for medical and industrial accelerators at IBA", in *Proc. IPAC'16*, Busan, Korea, May 2016, pp. 1902-1904. doi:10.18429/JACoW-IPAC2016-TUPOY002

[6] G. D'Agostino and W. Kleeven, "Beam dynamics and space charge studies for the InnovaTron cyclotron", *ICFA Newsletter #84 on Dynamics of High Power and High Energy Cyclotrons*, Ed. Rick Baartman, to be published in *J. Instrum.*

ISBN: 978-3-95450-212-7 ISSN: 2673-5482 doi:10.18429/JACoW-CYCLOTRONS2022-WEAI02

UPGRADE OF THE RCNP AVF CYCLOTRON*

M. Fukuda†, T. Yorita, H. Kanda, Y. Yasuda, K. Hatanaka, T. Saito, H. Tamura, S. Morinobu, K. Nagayama, H. Yoshida, S. Ano, D. Tomono, H. Kamano, T. Aoi, T. Shima, E. Ideguchi, S. Ota, N. Kobayashi, T. Furuno, S. Imajo, M. Murata, Y. Yamamoto, T. Suzuki, Y. Kon, Y. Morita, K. Takeda, T. Hara, T. H. Chong, H. Zhao, M. Kittaka, S. Matsui
RCNP, Osaka University, Ibaraki, Japan
M. Nakao, GHMC, Gunma University, Maebashi, Japan
Design and Manufacture Teams, Sumitomo Heavy Industries, Ltd., Niihama, Japan

Abstract

The upgrade program of the K140 AVF cyclotron at Research Center for Nuclear Physics (RCNP), Osaka University, was started in 2019 to provide not only intense light ion beams for production of short-lived radioisotopes (RIs), neutrons and muons but also high-quality intense beams for precision experiments in nuclear physics. Most of equipment besides the main coil, pole and yoke of the cyclotron magnet was replaced by new one. Especially the RF, injection and extraction systems were fully modified to increase a beam current. A new coaxial-type resonator was designed to cover a frequency range from 17 to 37 MHz for acceleration of staple particles using acceleration harmonic mode of 2 and 6. The acceleration voltage of ion sources was increased from 15 kV to 50 kV to enhance the beam intensity and to reduce the beam emittance for injecting a high-quality intense ion beam into the cyclotron. The central region of the cyclotron was fully redesigned to improve beam transmission from the LEBT system. Beam commissioning was started from May 2022, and a 28.5 MeV $^{4}He^{2+}$ beam was supplied to produce a short-lived RI of ^{211}At used for the targeted alpha-particle therapy. A 65 MeV proton beam was successfully injected into the K400 ring cyclotron to provide a 392 MeV proton beam for production of a white neutron flux and a muon beam. Several ion beams have been already used for academic research and industrial applications.

INTRODUCTION

RCNP was founded in 1971 as Domestic Joint Usage Center for nuclear physics research in Japan. Construction of the RCNP AVF cyclotron with K-number of 140 MeV was completed in 1973, and nuclear physics experiments started from 1976 [1]. The accelerator facility was fully opened to nuclear physics community globally. The cyclotron cascade project was started in 1987 and construction of the K400 ring cyclotron was completed in 1991 [2]. The AVF cyclotron was mainly used as an injector for the ring cyclotron. Partial upgrade of the two cyclotrons and beam lines was conducted in 2005 [3] and 2014. The bird-eye view of the cyclotron facility is shown in Fig. 1.

In recent years, the strong demand for increasing beam intensity was growing for production of short-lived RIs such as ^{211}At and secondarily produced particles such as neutrons and muons. In addition, intense halo-free high-quality light ion beams are required for very precise nuclear experiments with energy resolution less than 0.01 %. On the other hand, the number of troubles with the AVF cyclotron was increasing and the condition of the AVF cyclotron has deteriorated gradually. We decided the full-scale upgrading of the AVF cyclotron for improvement of beam performance and operation reliability.

Renovation and reinforcement of the RCNP accelerator facility was started in 2019. After completing the renewal of the building and facilities, the most of the AVF cyclotron components except for the main magnet were removed in 2020, and reinstallation of new components was completed in March 2021. Adjustment of the new components was conducted in 2021, and beam commissioning was started in March 2022. Trial beam utilization has been carried out occasionally in parallel with beam commissioning.

AIM OF THE UPGRADE

When the AVF cyclotron is operated in the standalone mode, lower energy proton and helium ion beams are mainly provided for RI production. We have two experiment rooms exclusively used for RI production in the AVF cyclotron building. In one of the experiment rooms, ^{211}At is frequently produced and provided for non-clinical research on targeted alpha-particle therapy. In November 2021, investigator-initiated clinical trial for practical treatment was started at Osaka University Hospital. We will need to supply ^{211}At of the order of more than several hundred MBq for the clinical trials in 2023. In addition, we have another beam line for production of short-lived RIs. In recent years, there is a growing need for supplying short-lived RIs for academic use, especially for the research on diagnosis and therapy in nuclear medicine. In Japan, the short-lived RI supply platform was organized in 2016 in cooperation among RCNP, Osaka University, RIKEN RIBF, CYRIC and ELPH, Tohoku University, QST NIRS and TIARA to support basic and applied research using RIs in a variety of academic fields. The ^{211}At with a half-life of 7.2 hours, is one of the major short-lived RIs which are provided from the short-lived RI supply platform. One of the main purposes of the AVF cyclotron upgrade was increase of the light ion beam intensity to more than 100 μA.

A 392 MeV proton beam is used to produce secondary particles such as neutrons and muons. Especially the neutrons, obtained at an emitted angle of 30 degrees from a tungsten target, have almost the same energy distribution as terrestrial neutrons. The so-called white neutrons are very useful for accelerated-simulation experiments of soft-errors occurred in semi-conductor devices resulting from

ISBN: 978-3-95450-212-7 ISSN: 2673-5482 doi:10.18429/JACoW-CYCLOTRONS2022-WEAI02

the terrestrial neutrons. Muons, produced by irradiating a graphite target with the 392 MeV proton beam, are provided especially for non-destructive element analysis and μ–SR analysis. The maximum proton beam current was limited to 1.1 μA due to the regulation of radiation shielding performance of the RCNP accelerator facility so far. Objective of the upgrade program was to increase the beam intensity of the 392 MeV proton up to more than 10 μA.

A high-quality light ion beam with the energy spread of $\Delta E/E = 10^{-4}$ is available for very precise nuclear physics experiments using an ultra-high-resolution spectrograph called Grand-RAIDEN. Increase of the high-quality beam will give advantage to high efficiency of data acquisition in the precise nuclear physics experiments. In addition, intense heavy ion beams accelerated by the AVF cyclotron is required for increase of secondarily produced unstable nuclei beam intensity used for high-spin-state nuclear physics experiments.

Figure 1: The bird-eye view of the cyclotron facility.

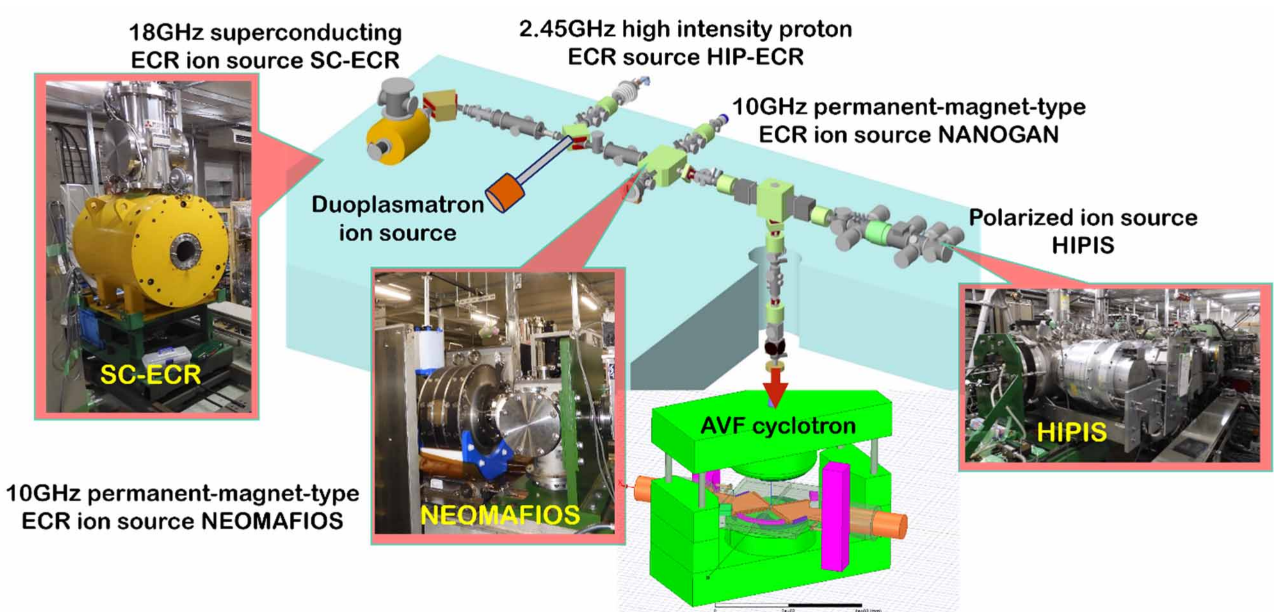

Figure 2: Layout of six ion sources and the LEBT system.

ISBN: 978-3-95450-212-7 ISSN: 2673-5482 doi:10.18429/JACoW-CYCLOTRONS2022-WEAI02

MODIFICATIONS OF ION SOURCE AND LEBT SYSTEMS

Ion Sources

Before the AVF cyclotron upgrade, light ions such as protons, deuterons, $^{3}He^{2+}$, $^{4}He^{2+}$ were produced mainly by a 10 GHz permanent-magnet type ECR ion source called NEOMAFIOS. Polarized proton and deuteron beams were provided by a polarized ion source with 2.45 GHz ionizer called HIPIS. Heavy ions were mainly produced by an 18 GHz superconducting ECR ion source called SC-ECR. For increase of the light ion beam intensity, a 2.45 GHz ECR proton source called HIP-ECR was developed, and another 10 GHz permanent-magnet type ECR ion source called NANOGAN and a duoplasmatron ion source were introduced in the LEBT system. A layout of the ion sources and the LEBT system is shown in Fig. 2.The extraction voltage of the ion sources was set at 10 or 15 kV to inject the ions efficiently into the former AVF cyclotron. The ion acceleration system of the six ion sources has been modified to increase the maximum voltage to 50 kV to improve the beam current and emittance.

Configuration of LEBT magnets and beam diagnostics stations was maintained since the space for LEBT components was limited. All of power supplies of magnets were replaced by new ones to increase the magnetic field of the LEBT magnets for the maximum acceleration voltage of 50 kV. The LEBT optics for each ion source was redesigned to optimize the beam injection into the central region of the upgraded AVF cyclotron for the ion energy higher than before.

Beam Buncher

Two types of bunchers with single-gap electrodes were installed in the axial injection beam line. A beam buncher of harmonic-voltage superimposing type is located just at the entrance of the upper yoke of the AVF cyclotron magnet. A saw-tooth-like voltage waveform is generated by mixing the second and third harmonic voltages with the fundamental one. The other beam buncher of charge-and-discharge type is located at the exit of the vertical bending magnet. Both beam bunchers are operated in sub-harmonic bunching mode using a half frequency of the fundamental one for the RF system of the AVF cyclotron. Originally the fundamental frequency range of both beam bunchers was from 5.5 to 20 MHz, covering the original fundamental frequency range of the former AVF cyclotron. The sub-harmonic bunching is needed to keep a period of beam bunches unchanged, because the ring cyclotron can be operated using the same parameters as before.

SPECIFICATIONS OF THE UPGRADED AVF CYCLOTRON

Design Principle

The upgraded AVF cyclotron is shown in Fig. 3. Main parameters of the upgraded AVF cyclotron are listed in Table 1. The maximum acceleration energy is the same as the original one since the yoke, pole, spiral sector, and main coil of the cyclotron magnet were reused. Sixteen pairs of trim coils and two sets of valley coils in the central and extraction regions were renewed due to deterioration of hollow conductors. Two Dee electrodes with an opening angle of 87 degrees were installed to increase the energy gain per turn to enlarge the turn separation before extraction. The fundamental RF frequencies are doubled, ranging from 17 to 37 MHz to accelerate most of light ions in the second harmonic mode to improve extraction efficiency.

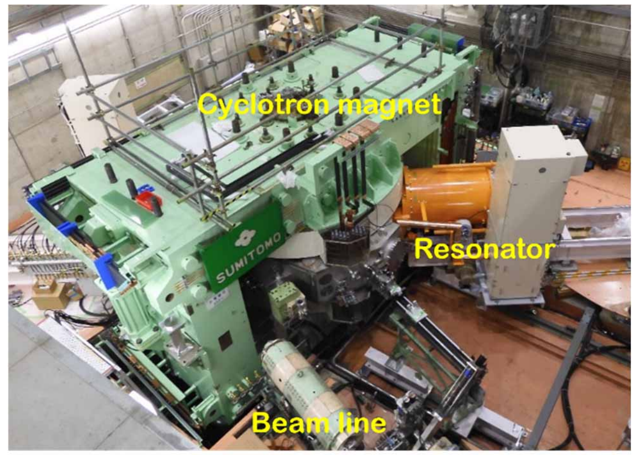

Figure 3: Photo of the RCNP AVF cyclotron.

Table 1: AVF Cyclotron Main Parameters

Parameter	New	Previous
K-value	140 MeV	140 MeV
Extraction radius	1 m	1 m
Max. $B_{extraction}$	1.65 T	1.65 T
Resonator and Dee electrodes	Double	Single
Opening angle of Dee	87 degrees	180 degrees
RF frequency	17 to 37 MHz	6 to 18 MHz
Harmonics	1, 2, 3, 6	1, 3
Max. V_{Dee}	60 kV	60 kV

A layout of the AVF cyclotron components is shown in Fig. 4. There was a severe geometrical condition that the position of the main magnet and the beam line were previously fixed and the space in the cyclotron vault was limited. That's why this layout was a unique solution to satisfy the difficult condition. First, we determined the resonator position considering the maintenance space of the cavities. Second, the deflector and field gradient corrector positions were fixed concerning the beam trajectory matching with the existing beam line. There were no room for putting other devices such as beam probes and phase slits, vacuum pumps.

ISBN: 978-3-95450-212-7 ISSN: 2673-5482 doi:10.18429/JACoW-CYCLOTRONS2022-WEAI02

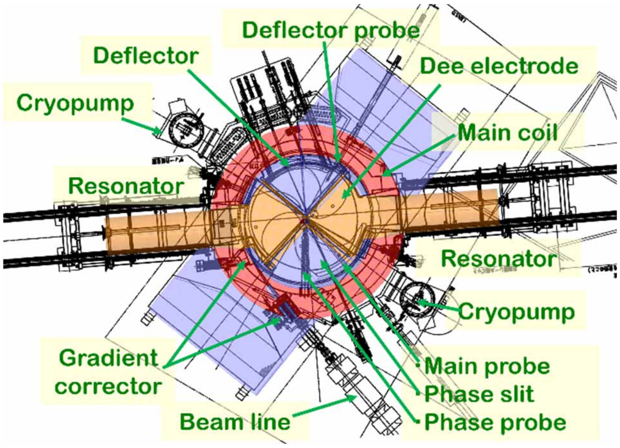

Figure 4: Layout of the cyclotron components.

Operation diagrams of the upgraded AVF cyclotron is shown in Figs. 5 and 6 as a function of a particle frequency and energy per nucleon, respectively. Most of high energy particles are accelerated in the harmonic mode of 2. Lower energy ion beams are provided by accelerating in the harmonic mode of 3 or 6. Especially, a 28.5 MeV $^{4}He^{2+}$ ion beam for ^{211}At production is accelerated using the harmonic mode of 6 to enlarge the energy gain per turn and to improve the beam extraction efficiency.

RF System

There was a severe restriction on the design of the new resonant cavity due to a vertical space between upper and lower main coils. When the resonant frequency is increasing, the short-plate position should be changed toward the center of the cyclotron. However, the effective vertical gap between the upper and lower main coils was 730 mm, which was obviously smaller than the reasonable diameter of the short plate and the outer tube. This meant that the short plate could not be placed at a position where a distance from the center of the cyclotron was less than 1800 mm. On the other hand, the fundamental frequency range of 17 to 37 MHz was required to accelerate most of light ions in the harmonic mode of 2. Thus, we optimized the size of inner and outer tubes, the gap between a Dee electrode and an earth plate, the neck width of the Dee electrode to fulfil the requirement. Finally, the diameter of the inner and outer tubes was determined to be 700 mm and 1000 mm, respectively.

A tetrode, EIMAC 4CW100,000E, was used for the final amplifier of the RF system. The output RF power from the final amplifier was transferred through a 50 W coaxial tube and fed into the cavity by a capacitive coupler. The resonator and the final amplifier are shown in Fig. 7. Main components in the vacuum chamber of the AVF cyclotron are shown in Fig. 8. An electrostatic deflector is placed in between the Dee electrodes. We have two gradient correctors for focusing a beam before extraction.

During the commissioning of the RF system, we had serious troubles with a final amplifier system. We observed large parasite components at a plate pick up, which were generated by the magnetic flux surrounding the amplifier tube. We placed many ferrite plates around the amplifier to absorb the parasite magnetic flux components. The variable capacitor located between the final amplifier and the coaxial power feeder, was damaged by sparking due to harmonic components with high amplitude, which might be generated by the RF power reflected from the capacitive coupler. We installed a corona ring outside of the capacitor to avoid the sparking damage on the capacitor. In addition, the length of the coaxial power feeder tube was configured to be changeable in accordance with the resonant frequency to decrease amplitude of the harmonic voltages. After making the improvements, the output power of the final amplifier became stable.

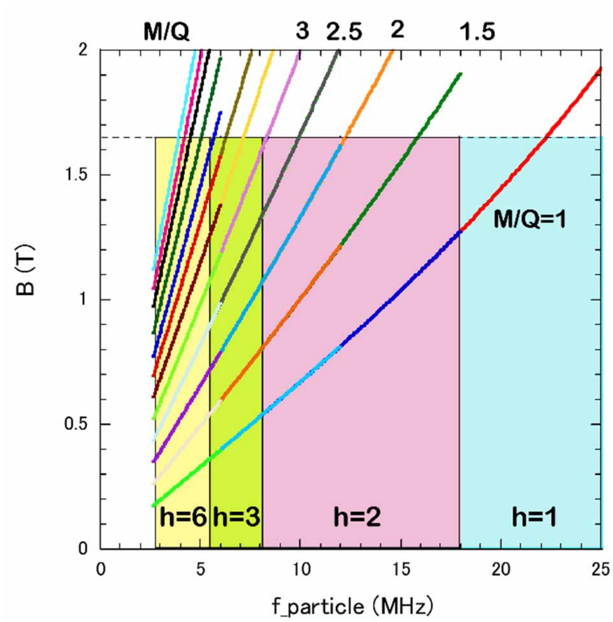

Figure 5: Operation diagram of the upgraded AVF cyclotron as a function of the particle frequency.

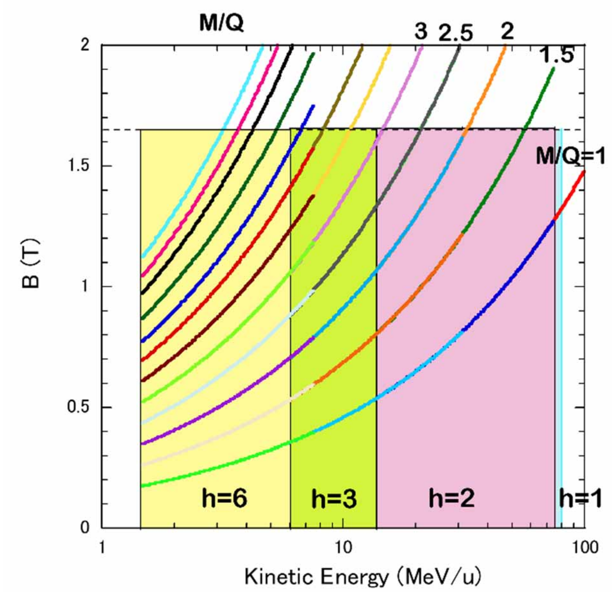

Figure 6: Operation diagram of the upgraded AVF cyclotron as a function of the particle energy.

ISBN: 978-3-95450-212-7 ISSN: 2673-5482 doi:10.18429/JACoW-CYCLOTRONS2022-WEAI02

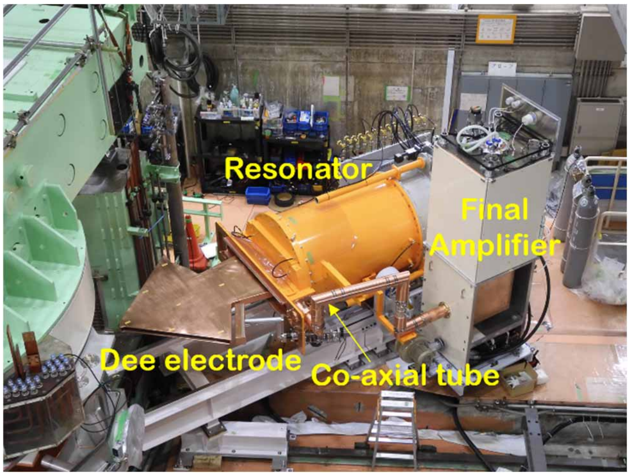

Figure 7: Dee electrode, resonator, power feeder and final amplifier.

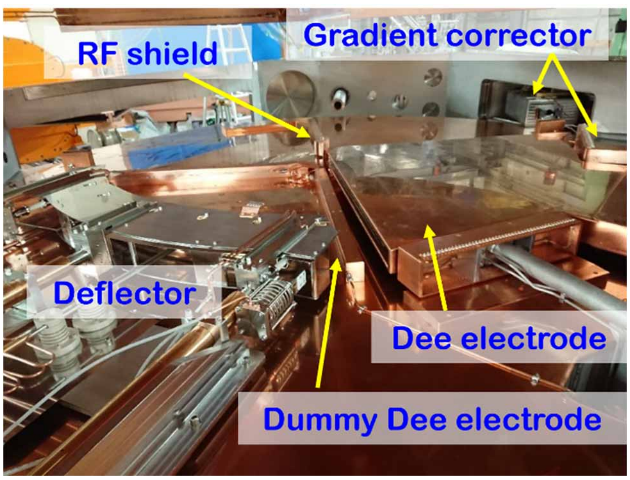

Figure 8: Main components in the vacuum chamber of the AVF cyclotron.

We had other RF troubles with inside of the vacuum chamber. A part of RF power was transmitted to the space between the dummy Dee electrodes, because the radial length of the dummy dee electrodes was not enough long to suppress the RF leakage. Beam probes and phase slits suffered from the large RF leakage noise. Therefore, we decided to install additional RF shield copper walls at the outside of the dummy Dee electrodes in the larger radius region. After this improvement, the RF leakage seemed to be reduced so much.

Central Region

Single particle trajectories for each acceleration harmonics of 1, 2, 3, 6 are shown in Fig. 9. First, we tried to design an inflector electrode for each harmonic mode to inject particles to the same Dee electrode. However, the performance of the phase defining by a phase slit was insufficient for the harmonic number of 3 and 6. Thus we decided that the inflector electrode for h = 3 and 6 was rotated by 180 degrees and inject the beam to another Dee electrode. Two configurations of the inflector electrode placed inside of an RF shield cover are shown in Fig. 9.

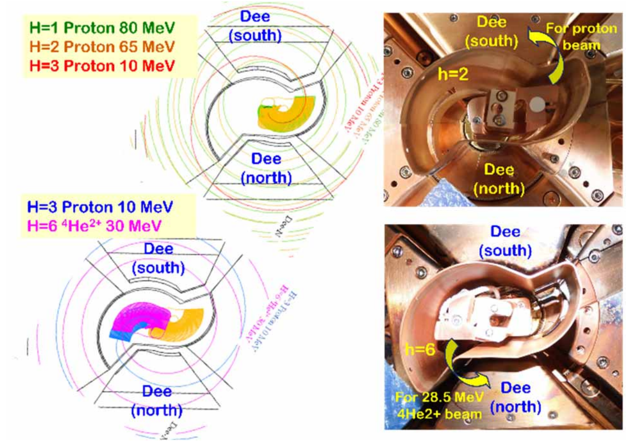

Figure 9: Single particle trajectories designed for each acceleration harmonic mode are shown in the left figure. Actual inflector electrodes for h = 2 and 6 are shown on upper right and lower right parts, respectively.

Extraction System

The maximum deflector voltage is 60 kV. The position and gap of the entrance and exit of the deflector electrode can be changed to optimize the extracted beam trajectories. The first gradient corrector placed downstream of the north Dee electrode is a half quadrupole type with active coils. The second gradient corrector of a quadrupole type with active coils is located at the exit of the vacuum chamber.

BEAM COMMISSIONING

We obtained permission for acceleration from Government on March 16th, 2022. We started beam commissioning from the end of March and the injected beam was successfully observed in the central region of the AVF cyclotron soon. In the beginning of April, the beam reached the entrance of the deflector, and the first extracted beam was observed on April 21st, 2022. In the beginning of May, we passed at the radiation facility inspection using a 65 MeV proton beam. After that, we started regular beam commissioning [4]. Occasionally, we provided a 28.5 MeV $^4He^{2+}$ beam for ^{211}At production, and 65 and 392 MeV proton beams for commissioning of the nuclear physics experiment equipment and for semiconductor soft-error analysis using secondarily produced neutrons.

REFERENCES

[1] M. Kondo *et al.*, "AVF Cyclotron", RCNP Annual Report, 1976, pp. 1-75.

[2] I. Miura *et al.*, "Commissioning of the RCNP ring cyclotron", in *Proc. 13th Int. Conf. on Cyclotrons and their Applications*, Vancouver, BC, Canada, Jul. 1992, pp. 3-10.

[3] K. Hatanaka *et al.*, "Development of the RCNP cyclotron cascade", in *Proc. 18th Int. Conf. on Cyclotrons and their Applications*, Giardini Naxos, Italy, Oct. 2007, pp. 125-127.

[4] M. Fukuda *et al.*, "Beam commissioning of the RCNP AVF cyclotron", in *Proc. 19th Annual Meeting of Particle Accelerator Society of Japan*, online, Japan, Oct. 18-21, 2022, pp. 166-169.

ISBN: 978-3-95450-212-7 ISSN: 2673-5482 doi:10.18429/JACoW-CYCLOTRONS2022-WEA001

OPAL SIMULATION ON THE BEAM TRANSMISSION IN THE CENTRAL REGION OF THE MEDICAL CYCLOTRON COMET AT PAUL SCHERRER INSTITUTE

H. Zhang†, Ch. Baumgarten, P. Frey, M. Hartmann, R. Kan, M. Kostezer, A. Mülhaupt, M. Schippers, A. Schmidt, J. Snuverink, Paul Scherrer Institut, 5232 Villigen PSI, Switzerland

Abstract

The use of the medical cyclotron COMET for FLASH proton therapy requires a high beam transmission from the ion source through the central region apertures. This paper first presents a model of the COMET cyclotron featuring a rotatable ion source, a movable puller, and an adjustable first fixed slit (FFS), implemented with the OPAL framework. The electromagnetic field is individually created to match each specific configuration. The beam optics parameters, especially beam position and beam size upon approaching and after passing FFS, have been studied in detail. The OPAL simulations demonstrate that an optimal configuration of the ion source, the puller and the FFS is key to achieve a high beam transmission. An experimental test gave a 2.8 times higher intensity within COMET cyclotron with the modifications derived on the basis of the simulations: a 0.57 mm shift of puller and a 5.6° rotation of ion source. The simulations indicate that, with these modifications, the beam can still be centered and accelerated to the extraction energy of 250 MeV. Next step is to investigate the influence of such modifications upon the acceleration and the extraction, again with an iterative approach combining simulations and experiments.

INTRODUCTION

The compact superconducting cyclotron COMET delivers a 250 MeV beam for proton therapy at PSI [1-2]. The central region of the cyclotron, consisting of the ion source, the puller and the first fixed slit (FFS) as shown in Fig. 1, has been under investigation and development throughout the stages of design, commissioning, and routine operation [3-7]. It was recently reported that the beam transmission from the ion source passing through the FFS could be increased up to 60% after a puller shift of 0.56 mm towards the centre [8]. A high FFS transmission is an important step towards extracting beam of high intensity desirable for FLASH proton therapy as well as for patient treatment in a shorter treatment time in order to mitigate problems of organ motion during the treatment. Simulation may lead to a quantitative understanding on the factors correlated with FFS transmission, and to explore improvement potential. OPAL, a parallel open source tool developed at PSI for charged-particle optics in accelerators and beam lines [9], is suited not only for high intensity machines like PSI Ring Cyclotron operating up to 2.4 mA, but also for the medical cyclotron COMET extracting a beam well below 1 µA [6].

† hui.zhang@psi.ch

OPAL SIMULATION

Model of Central Region of COMET Cyclotron

As shown in Fig. 1, three key components in the central region, namely the chimney of the ion source, the puller, and the FFS, are approximated with multiple rectangular pieces, the only form to specify a collimator inside a cyclotron for OPAL simulation. In OPAL input, the chimney may be rotated around its axis, and the puller may be shifted towards the centre. We considered rotation angles θ in the order of a few degrees and displacements s in the sub-millimetre range. Furthermore, the position of the FFS may be shifted while its aperture may be varied. In practice, it is rather cumbersome to adjust the position of the real FFS. However, an FFS with an aperture of 0.16 mm, 0.18 mm, or 0.2 mm, has been applied for routine patient treatment. An FFS of 0.2 mm aperture is mostly used for both simulation and operation. In OPAL the model of COMET cyclotron is a mirror image of the real machine.

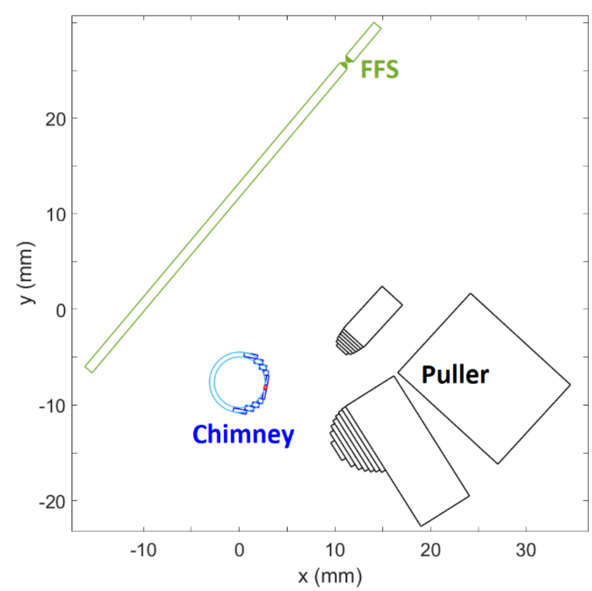

Figure 1: OPAL model for central region of COMET.

Field Maps for Particle Tracking

OPAL features particle tracking through multiple field maps, 2D and 3D, electric and magnetic, static and time varying, separated and overlapped, which is essential for the simulation of the central region of COMET cyclotron. Figure 2 shows the static magnetic field map in the median plane, while Fig. 3 shows the magnitude of the E component of the RF field in the median plane.

ISBN: 978-3-95450-212-7 ISSN: 2673-5482 doi:10.18429/JACoW-CYCLOTRONS2022-WEA001

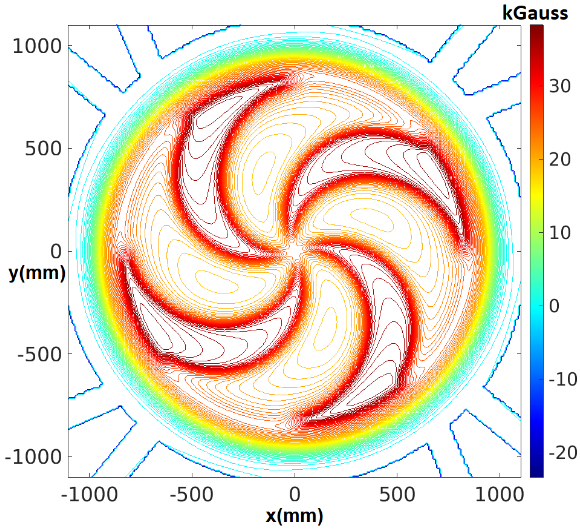

Figure 2: Map of static magnetic field in median plane.

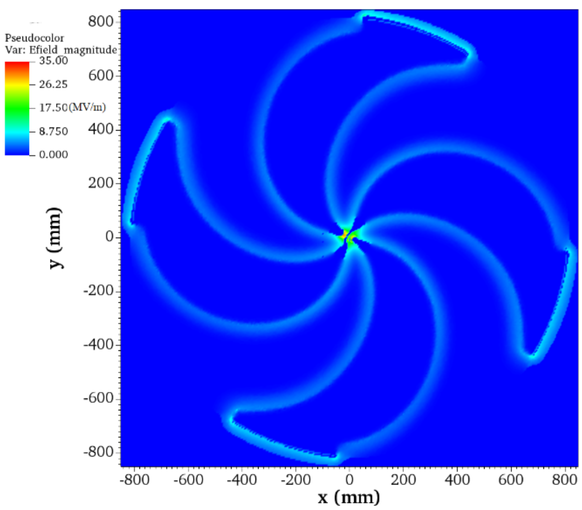

Figure 3: Map of E-magnitude of RF field.

Start Position for Particle Tracking

The so-called reference particle starts from the centre of a zero potential surface at the chimney opening, which is determined with the finite element (FE) method applying the program ANSYS. The peak voltage V_0 of the puller is approximately 80 kV [10], and the voltage V of the puller varies with the time t according to

$$V = -V_0 cos(\omega t + \phi_0), \quad (1)$$

where $\omega = 2\pi f$ and f = 72.61 MHz for OPAL simulation.

The zero potential surface and the electrostatic field in the central region is individually calculated for a specific configuration defined by the parameters (θ, s, ϕ_0). V = $-80\cos(\phi_0)$ kV is applied at the puller which is the most central part of Dee 1, as well as on Dee 3 which is opposite to Dee 1. V = $+80\cos(\phi_0)$ kV is applied on Dee 2 and Dee 4 which are at 180° RF-phase with respect to Dee 1 and Dee 3. The FFS lies entirely within Dee 2 having little influence on the field calculation. ϕ_0 is the initial RF phase when the tracking starts at t = 0, and must be in the range between -90° and 0°, so that the protons can be pulled out of the chimney and be further accelerated to the FFS.

Figure 4 shows zero potential lines in the median plane corresponding to ϕ_0 = -80°, -60°, -40°, -20° and 0° for the original configuration. Figure 5 shows the E-field map between the chimney and the puller in the median plane for the configuration of 5.6° chimney rotation and 0.57 mm puller shift.

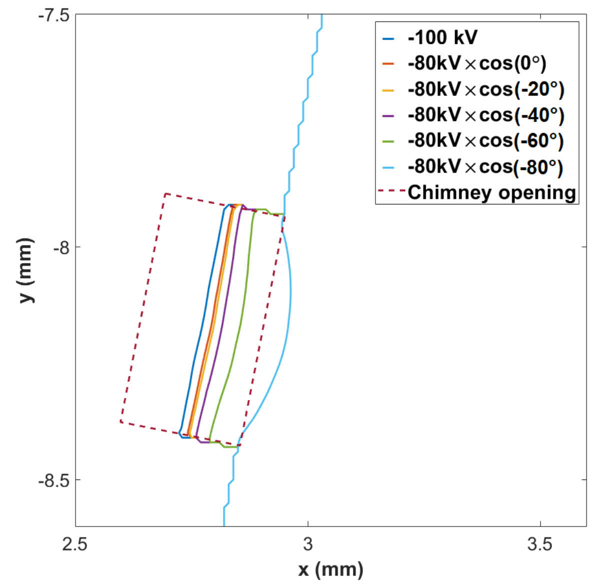

Figure 4: Zero potential lines in chimney opening for different puller voltages (i.e. RF phases).

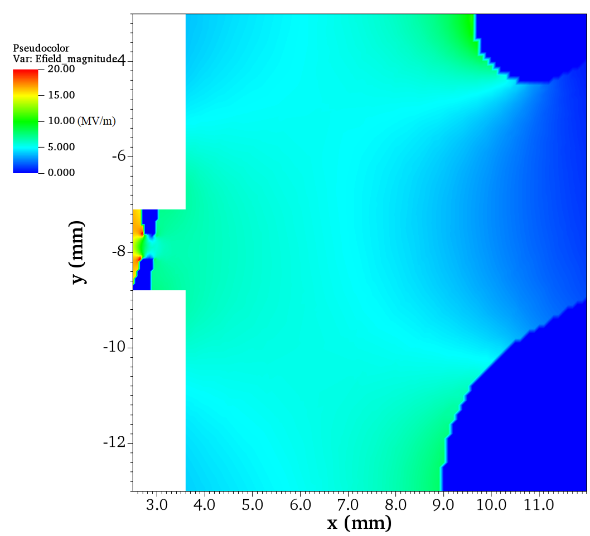

Figure 5: Map of E field in the median plane between chimney (left) and puller (right), (θ, s, ϕ_0. V_0) = (5.6°, 0.57 mm, -60°, 80 kV).

Initial Conditions for Particle Tracking

The initial energy and the initial momentum of the reference particle is set to 1 eV and 43319 eV/c, respectively [4]. The opening of the chimney is 0.5 mm wide (horizontal direction x) and 3 mm high (vertical direction z). 10000 protons are generated from a Gaussian distribution with σ_x = 0.083 mm, σ_y = 0, σ_z = 0.5 mm, and $\sigma_{px} = \sigma_{py} = \sigma_{pz}$ = 30631 eV/c. y is basically the longitudinal direction and parallel to the direction of the reference particle at t = 0.

ISBN: 978-3-95450-212-7 ISSN: 2673-5482 doi:10.18429/JACoW-CYCLOTRONS2022-WEA001

Beam upon Reaching FFS

Beam position and shape upon reaching the FFS are dependent on θ, s, ϕ_0 and V_0. Figure 6 shows the particle distribution on the front surface of the FFS plate for ϕ_0 from −85° to −25° in 5° step, while (θ, s) = (0, 0). A photo of the FFS with irradiation trace is inserted on the top left corner of the figure.

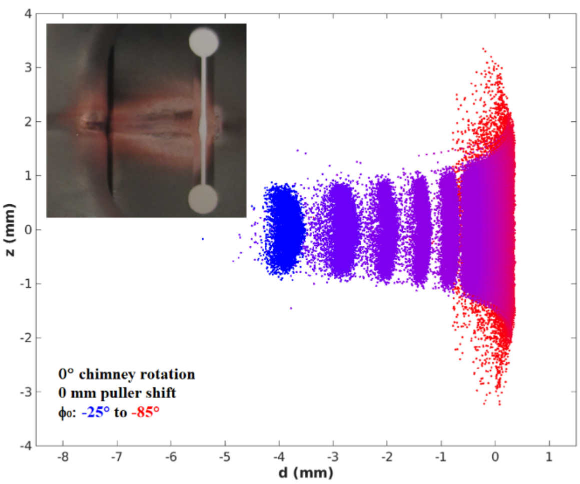

Figure 6: Proton distribution on the front of FFS.

In order to quantify the beam position and size upon reaching the FFS, an axis is defined by the intersection of the FFS front surface and the median plane. The axis points outwards and the origin is the projection of the centre of the FFS aperture on the axis. The average position d measured on the axis and its RMS σ_d can be derived for chosen ϕ_0 and V_0. In Fig. 7, d and σ_d are plotted against ϕ_0 for two configurations (θ, s) = (0, 0) and (θ, s) = (5.6°, 0.57 mm), while V_0 = 79.6 kV. The FFS of 0.2 mm aperture is at its original position, and marked by two dashed green lines on the plot.

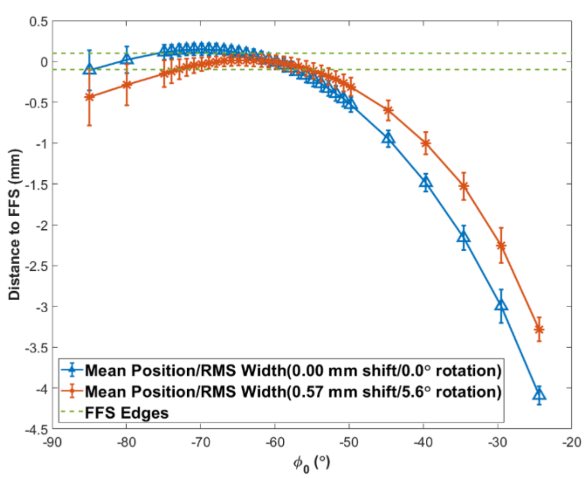

Figure 7: Beam position and size upon reaching FFS.

Transmission Passing FFS

For chosen (θ, s, ϕ_0, V_0), the number of protons passing through the FFS can be readily derived from particle tracking. In Fig. 8 this is plotted against ϕ_0 for (θ, s) = (0, 0) and (5.6°, 0.57 mm), while V_0 = 79.6 kV and a FFS of 0.2 mm aperture is at its original position. The total FFS transmission may be calculated by an integration over ϕ_0, equivalent to an integration over time. The ratio of the integrated FFS transmissions for the above two configurations is around 1.72.

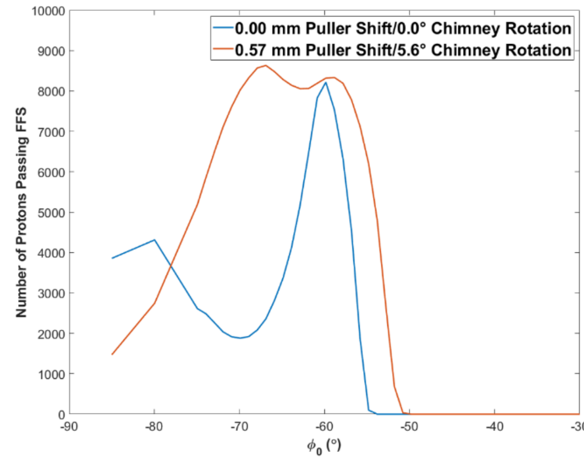

Figure 8: Protons passing FFS with respect to ϕ_0.

The integrated FFS transmission from OPAL simulation may be plotted against V_0, as shown in Fig. 9 for (θ, s) = (0, 0) and (5.6°, 0.57 mm), respectively. In general, the integrated FFS transmission is practically zero if V_0 is so low that the proton is not sufficiently accelerated to reach the FFS aperture. When V_0 increases, the FFS transmission increases and peaks at a certain value V_0. However, the FFS transmission starts to decrease when V_0 is increased further, as the protons are accelerated to a radius higher than the FFS aperture.

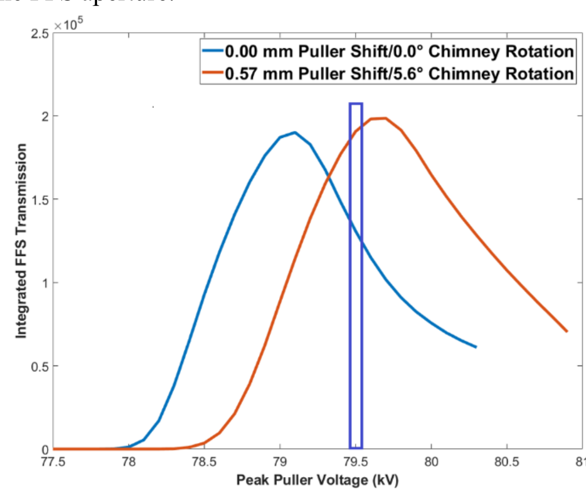

Figure 9: Integrated FFS transmission with respect to V_0.

EXPERIMENT

In order to catch the proton beam passing the FFS, the radial probe is moved to the inner most position, that is 310 mm to the machine centre [1, 7], and the beam path between the FFS and the radial probe is completely cleared out. With a FFS of 0.16 mm aperture a beam current of 368 nA was detected with the radial probe. Then the puller was shifted 0.57 mm towards the centre and the chimney was rotated 5.6° clockwise (anticlockwise in simulation).

This modification was performed in parallel with the installation of a new FFS of 0.2 mm aperture as required by the following patient treatment. Subsequently 1310 nA were collected at the radial probe, while the arc current and voltage of the cold cathode ion source were kept unchanged [7]. This corresponds to improvement of the FFS transmission by a factor of 2.8.

Furthermore, the beam current on the radial probe was measured as a function of the RF voltage after reducing the arc current from 80 mA to 50 mA. Figure 10 shows the plot of the beam current RMJ:IST1:2 in nano-Ampere against CMJLL:SOLA:2 in Volt, which is the average of voltages on pickups inside the Dees, and is 8.4 V during normal operation. A comparison between the measurement and the simulation suggests that CMJLL:SOLA:2 = 8.4 V corresponds to a voltage V_0 around 79.6 kV [7]. This is in good agreement with the X-ray spectral measurement [10].

Figure 10 shows that the FFS transmission is almost at the peak when the Dees are running at the operation point, which implicates that the new configuration is almost optimal for the FFS transmission.

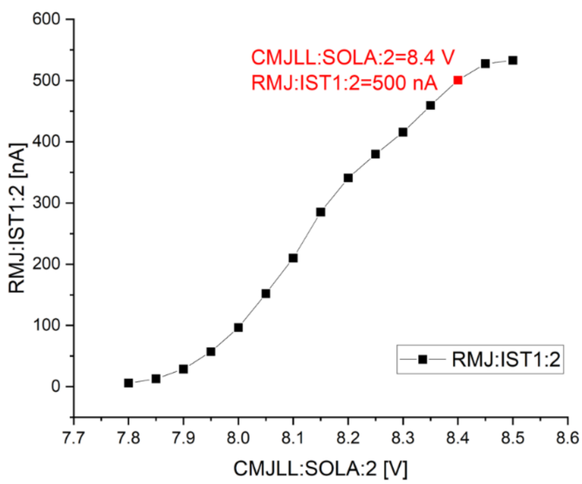

Figure 10: Beam intensity collected by the radial probe against the average of voltages on pickups in the Dees.

DISCUSSION AND CONCLUSION

It is a simplification to assume a constant V_0 over the puller. Nevertheless, it is a normally used and accepted method to investigate the central region of a cyclotron with an electrostatic approach [3-4]. There also seems to be evidence that the plasma boundary bulges out of the chimney aperture when a negative electrostatic voltage on the puller is approaching zero [3]. Therefore we not only take the zero potential surface as the plasma boundary, but further assume the oscillation of the plasma boundary with RF frequency.

It might be reasonable to assume that the reference particle starts from the centre of the zero potential surface, that its initial direction is perpendicular to the zero potential surface, and that the initial energy is around 1 eV. Nevertheless, the initial distribution is likely not Gaussian. Moreover, the proton beam current is likely not constant but rather dependent on many factors like the puller voltage [3].

In spite of the uncertainties of the initial conditions for particle tracking, the OPAL simulation still delivered results that were comparable with experimental observations. The beam distribution from particle tracking agrees well with the image of irradiation trace on the front surface of the FFS. Both simulation and measurement demonstrate that the FFS transmission may be significantly improved by a 5.6° chimney rotation combined with a 0.57 mm puller shift.

Our results show that the reference orbit can still be centred with this modification of the central region. The configuration may be further optimized to achieve even higher FFS transmission. In future work we will verify whether the beam of higher intensity inside the cyclotron can be extracted out of the cyclotron with sufficiently high efficiency, again with an iterative approach combining simulations and experiments.

ACKNOWLEDGEMENTS

The authors would like to thank Dr. O. Boldt from Varian Medical Systems for communicating their results and experience, L. Stingelin for providing the RF map, and M. Schneider for support on the experiment with RF.

REFERENCES

[1] A. E. Geisler *et al.*, “Commissioning of the ACCEL 250 MeV proton cyclotron”, in *Proc. Cyclotrons’07*, Giardini Naxos, Italy, Oct. 2007, pp. 9-14.

[2] J. M. Schippers *et al.*, “The SC cyclotron and beam lines of PSI’s new proton therapy facility PROSCAN”, *Nucl. Instrum. Methods Phys. Res. Sect. B,* vol. 261, pp. 773-776, 2007. doi:10.1016/j.nimb.2007.04.052

[3] J. R. Schubert, “Extending the feasibility boundary of the isochronous cyclotron”, Ph.D. thesis, Michigan State University, East Lansing, USA, 1997.

[4] Ch. Baumgarten *et al.*, “A beam profile measurement in the ACCEL 250 MeV medical proton cyclotron”, *Nucl. Instrum. Methods Phys. Res. Sect. A*, vol. 569, pp. 706-712, 2006. doi:10.1016/j.nima.2006.09.077

[5] J. M. Schippers *et al.*, “Beam intensity stability of a 250 MeV SC cyclotron equipped with an internal cold-cathode ion source”, in *Proc. Cyclotrons’07*, Giardini Naxos, Italy, Oct. 2007, pp. 300-302.

[6] H. Zhang *et al.*, “OPAL simulation for PSI medical cyclotron COMET”, presented at the 38th European Cyclotron Progress Meeting (ECPM’12), Paul Scherrer Institut, Villigen, Switzerland, May 2012, unpublished.

[7] M. Hartmann, “Beam dynamics in the central region of the COMET cyclotron”, Master thesis, EPFL, Lausanne, Switzerland, 2020.

[8] O. Boldt, Varian Medical Systems Particle Therapy GmbH, private communication, Feb. 2020.

[9] A. Adelmann *et al.*, “The OPAL Framework (Object Oriented Parallel Accelerator Library) Version 2.4.0 User’s Reference Manual”, Oct. 2021. https://gitlab.psi.ch/OPAL/src/-/wikis/home

[10] J. H. Timmer *et al.*, “Dee voltage calibration for the ACCEL proton therapy cyclotron”, in *Proc. ICAP’06*, Chamonix, France, Oct. 2006, pp. 102-105.

ISBN: 978-3-95450-212-7 ISSN: 2673-5482 doi:10.18429/JACoW-CYCLOTRONS2022-WEA002

SIMULATION AND ANALYSIS OF HIMM-IC BEAM DYNAMICS WITH OPAL*

G. L. Dou†[1,2], B. Wang[1], X. Chen[1,2], Q. G. Yao[1], X. W. Wang[1], L. Yang[1], C. C. Li[1], L. T. Sun[1,2], H. W. Zhao[1,2]
[1]Institute of Modern Physics, Chinese Academy of Sciences, Lanzhou, China
[2]School of Nuclear Science and Technology, Univ. of Chinese Academy of Sciences, Beijing, China

Abstract

Since 2020, HIMM (Heavy ion medical machine) facilities in both Wuwei and Lanzhou cities have been installed and put into clinical application or commissioning experiments. As an injector cyclotron (IC), HIMM-IC can provide 6.8 MeV/10eμA $^{12}C^{5+}$ beam for the synchrotron. Nevertheless, in terms of better beam quality and operation efficiency, HIMM-IC design still has a lot of room for improvement. We used OPAL (Object oriented Parallel Accelerator Library) simulation program to complete the 3D multi-particle dynamics simulation of HIMM-IC including the space charge effect. And the results show that it is in good agreement with the actual experimental measurements.

INTRODUCTION

China's carbon ion therapy facility, also named HIMM, is a cancer treatment facility designed by the Institute of Modern Physics of the Chinese Academy of Sciences. It has two ECR ion sources and uses an axial injection to deliver $^{12}C^{5+}$ into HIMM-IC (see Fig. 1), which can accelerate the beam to about 7 MeV/u. The main accelerator HIMMSYN (HIMM Synchrotron) accelerates the beam further to 120-400 MeV/u. Its maximum particle number at the terminal is about 1.2×10^9 ppp. Through the HEBT line, the beam will be delivered to 5 fixed treatment terminals in 4 treatment rooms. As the injector cyclotron of the HIMM, HIMM-IC is a compact isochronous cyclotron. The overall diameter is only 2.92 m. The magnetic field is composed of a whole magnet without any trimming coils. It can provide 7 MeV/u, 10 eμA $^{12}C^{5+}$. The other basic parameters are shown in the Table 1 [1, 2].

Table 1: HIMM-IC Basic Parameter

Parameter	Value
Central magnetic fields	1.212 T
Injection radius	2.7 cm
Injection Energy	111.6 keV
RF frequency	31.02 MHz
Harmonic number	4
Extraction radius	75 cm

According to the operation of HIMM-IC (taking the Wuwei heavy ion therapy facility as an example) [3], the ECR ion source provides 82.5 eμA $^{12}C^{5+}$, and the extraction beam intensity of HIMM-IC is up to 11.06 eμA, with an overall transmission efficiency of about 13.75%. Considering the strict safety operation standard of the medical facility, we stop to overhaul (including check and clean inflector and RF cavities) every two years and clean the inflector once a year. In long-term stable operation, HIMM-IC can extract about 5.5 eμA $^{12}C^{5+}$ with the injection beam intensity of about 50 eμA provided by the ECR ion source and the total transmission efficiency is more than 10%. Although the operating status meets the need of clinical treatment, there is still a lot of room to upgrade it for better performance.

Figure 1: HIMM-IC.

During the design phase, we used the cyclotron dynamics simulation software – SNOP to model and simulate the HIMM–IC and obtained a better coincidence between the two by comparing with experimental measurements. Therefore, we use a new cyclotron dynamic simulation software, OPAL [3, 4], to re-model and simulate the HIMM-IC with 3D beam dynamics including space charge effects.

To overcome the operation problems of the low beam intensity and quality and to prepare for the further upgrade, the following approaches are considered in this work:

- Generation of the three-dimensional electric and two-dimensional magnetic field map.
- Analysis of the performance of the cyclotron units: CR (Central Region), Acceleration and Extraction. The other units (like LEBT) are not discussed in this work because they are not suitable for simulation using OPAL.
- Estimation of the overall cyclotron transmission (extraction to injection beam intensity ratio) and output beam parameters (emittance, energy spread, time pulse, and dispersion).

* Work supported by Technology development programme 22ZY2QA003.
†email address: douguoliang@impcas.ac.cn

ISBN: 978-3-95450-212-7 ISSN: 2673-5482 doi:10.18429/JACoW-CYCLOTRONS2022-WEA002

The aim of the simulation was to increase the cyclotron transmission and output beam quality by improving the matching at the injection, optimizing the acceleration regime parameters, and increasing focusing at the extraction.

The 2D (two dimensional) magnetic fields used in the beam dynamics simulation were from the measurements of the manufactured magnets. The measurement of the magnetic field, including manufacturing errors, has a better reliability than the modelled field used in the design phase, and can reflect more realistically the magnetic field that governs the beam in the cyclotron. Since there were no data on the physically measured RF cavities after manufacturing, the three-dimensional electric fields we used were extracted from the CST software.

For the analysis of the beam dynamics, a detailed computer model of the HIMM-IC was built including the central region, acceleration and extraction, based on the real structure of the HIMM-IC, including some variations in manufacturing and installation.

ISOCHRONOUS ANALYSIS OF MAGNETIC FIELDS

Static Equilibrium Orbit Calculation

The analysis of the isochronous magnetic field is the first step in the design and simulation of the cyclotron. SEO (Static Equilibrium Orbit) is obtained from the tunes calculation module of OPAL-cycl, as shown in Fig. 2.

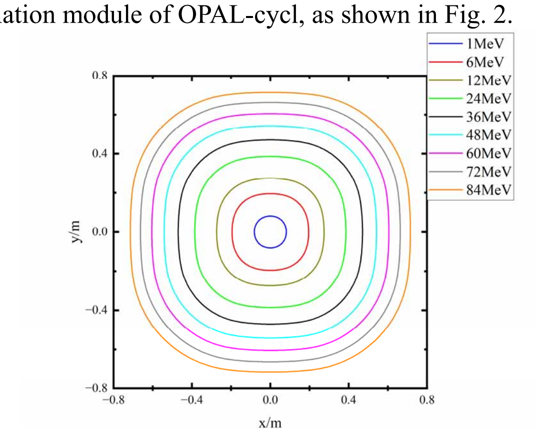

Figure 2: Static Equilibrium Orbit.

In addition, the RF phase shift error (see Fig. 3) for various energies according to the output results, which represents the size of the phase shift due to the error between the measured magnetic field and the theoretical isochronous field. We define the frequency shift error as:

$$\Omega(E) = \frac{\omega_0}{\omega} - 1. \tag{1}$$

$$\omega_0 = \frac{2\pi f_{RF}}{h}. \tag{2}$$

where ω_0 is the particle cyclotron frequency at the theoretical isochronous field, determined by f_{RF} and the harmonic number h. From this, the relationship between phase shift and energy can be obtained as:

$$sin(\varphi(E)) = sin(\varphi_i) + \frac{\pi h}{2Vq}\int \Omega(E)dE. \tag{3}$$

where V is the voltage of RF cavity.

From the calculation of the RF phase shift at various energies, we obtain the results as shown in Fig. 3, which shows that the overall frequency shift has a small error. When the integral calculation is performed according to the above equation, we can obtain a total phase shift of 13° throughout the acceleration process.

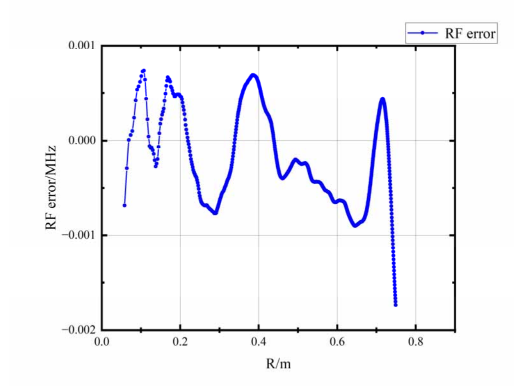

Figure 3: RF phase shift error.

Betatron Tunes

The analysis of the isochronous magnetic field is the first step in the design and simulation of the cyclotron. We have calculated the radial and axial focusing frequencies of the HIMM-IC in the measured magnetic field according to the tunes calculation module of OPAL-cycl, and the energy step is taken as 0.1 MeV. According to the calculation and analysis of the tunes in the whole range from the injection to the extraction energy(see Fig. 4), we can see that the HIMM-IC does not have the problems of dangerous resonances in both radial and axial directions, and the axial focusing frequency is kept above 0.4 in the most of the energy range, which basically satisfies the focusing of the beam transversely to avoid the deterioration of the beam transverse quality due to various resonances.

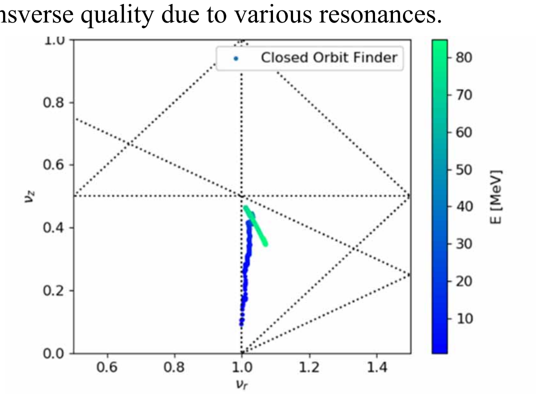

Figure 4: Tune diagram.

Therefore, from the above rechecked calculations of the isochronous magnetic field of HIMM-IC, we can see that the measured magnetic field ensures good results in both SEO calculations and tunes calculations, satisfying the focusing and isochronous requirements for the stable operation of the cyclotron with basically no obvious problems.

SIMULATION OF ACCELERATION

In the particle tracking simulation stage, we set the initial injection point of the particle at the exit position of the inflector cylinder. According to the 3D modelling and particle tracking simulation of the inflector in other software, and the installation mode of the inflector, we obtained the information of the initial particle injection point as follows: R=37.5 mm, φ=140 deg, E_k=112.2 keV, P_r=0.101 rad [2]. We modelled and analysed the beam status evolution during the whole acceleration region from the injection to the extraction energy, using the single and multi-particle modes of OPAL. The modelling and beam simulation of the elements of the extraction system are not completed and will not be reported in this paper.

Single Particle Simulation

In the single-particle mode, we obtained a stable AEO (Accelerated equilibrium orbit) using a 3D electric field, a 2D magnetic field and a known initial injection point, by scanning the initial phase of the electric field within 2π as shown in Fig. 5.

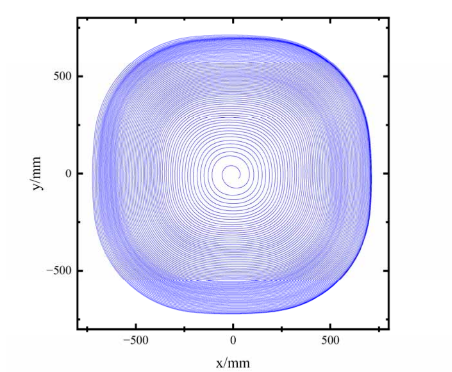

Figure 5: Accelerated equilibrium orbit.

According to the analysis of the results, HIMM-IC could accelerate $^{12}C^{5+}$ from 0.1122 MeV to 84.917 MeV in 77 turns and obtain a variation of the turn separation at an azimuth of 45 deg. The last turn separation could reach 5mm, and the energy gain per turn is about 1.2 MeV (see Fig. 6).

Multi-Particle Simulation

The initial information of the beam corresponding to the exit of the reflector was generated according to the primary settings in the single-particle model in Table 2.

Table 2: Initial Beam Parameters

Parameters	Value
Beam Intensity	20 μA
Horizontal Geometry emittance(4σ)	50 mm·mrad
Vertical Geometry emittance(4σ)	50 mm·mrad
Energy spread	±0.5%
Phase spread	±10°
Number of macro particles	10^4

In the transverse direction, we pay attention to the beam size, emittance and other parameters that show the beam quality. From the simulation results (see Fig. 7), we can see that the beam size oscillates throughout the acceleration but the overall is under control, and the RMS beam size at the extraction energy point is 3.91 mm in horizontal and 1.58 mm in vertical. Considering the comparison with the turn separation, there is an overlap between the inner and outer turns of the beam at large radius, which causes the problem of increasing the emittance of the beam. In the horizontal direction, the RMS geometry emittance of the beam reaches its maximum in the low-energy region (~15 MeV) and then gradually decreases, and a similar situation occurs in the vertical direction. The emittance at the extraction point is 22.27 pi·mm·mrad in horizontal and 2.77 pi·mm·mrad in vertical, which is in good agreement with the simulation results of SNOP in the design phase [5]. In the longitudinal direction, we pay attention to the variation of energy dispersion and momentum dispersion of the beam. From the simulation results, the energy dispersion is about 0.3 MeV, and the momentum dispersion is about 0.34% (see Fig. 8), which meet the requirements of HIMMSYN for beam injection. In addition, the beam acceleration efficiency from the injection point to the extraction is about 99.07% (see Fig. 9), which is in a good agreement with the operational measurement results [6].

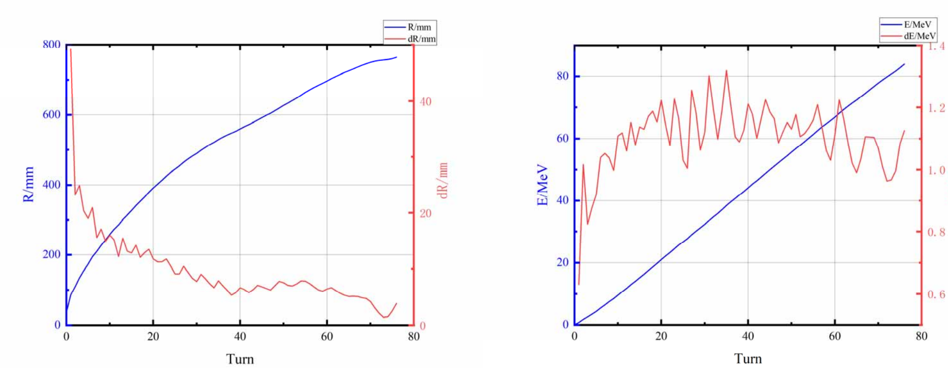

Figure 6: Turn separation(left) and Energy gain(right). The last turn separation could reach 5mm, and the energy gain per turn is about 1.2 MeV.

ISBN: 978-3-95450-212-7 ISSN: 2673-5482 doi:10.18429/JACoW-CYCLOTRONS2022-WEA002

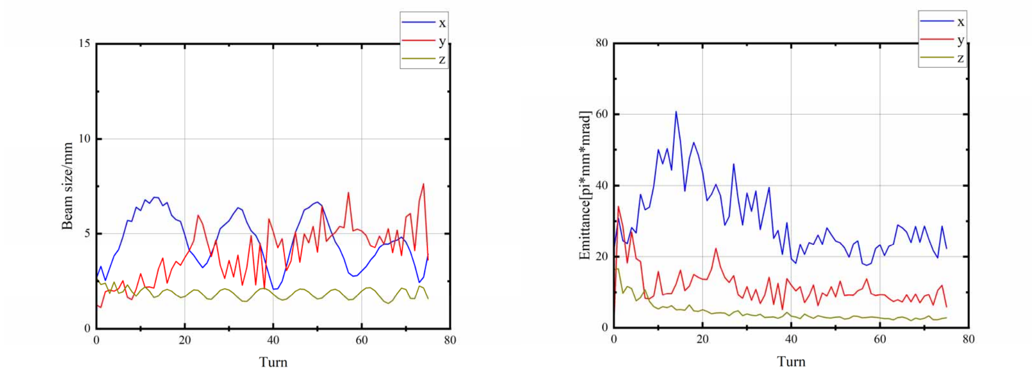

Figure 7: RMS Beam size(left) and RMS Geometry Emittance(right). The RMS beam size of last turn in x, y and z is 3.91555, 3.60329 and 1.58493mm; The RMS geometry emittance of last turn in x, y and z is 22.27046, 5.83704 and 2.77792 pi•mm•mrad.

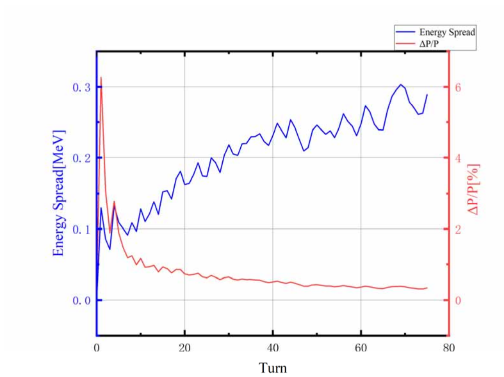

Figure 8: Energy spread and momentum dispersion.

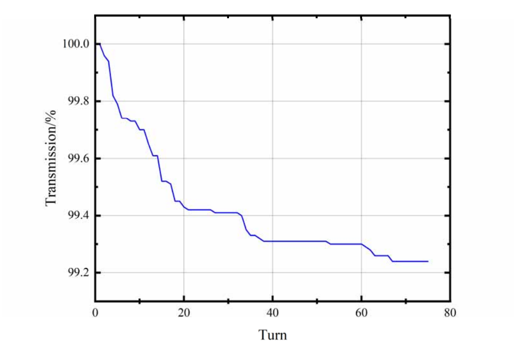

Figure 9: Transmission.

In general, the OPAL simulation results agree well with the SNOP design results in the transverse directions and the operation measurements in the longitudinal direction. The increased transverse emittances and small turn separation of the beam in the cyclotron during acceleration is a critical issue that affects the extracted beam intensity (or efficiency) and quality in the extraction system.

CONCLUSION AND OUTLOOK

According to the simulation results of OPAL, the real magnetic field of HIMM-IC is good in isochronism and focusing. In the acceleration region, the transverse emittances of OPAL and SNOP are in good agreement, and the transmission efficiency is in good agreement with the experimental measurements. Moreover, we have confirmed the issues of transverse emittances and small turn separation in large radial. Although the simulation of the extraction system has not been completed yet, it can be seen from the results of the beam analysis in the acceleration region that this is a major reason for the low extraction intensity and poor beam quality, which needs obvious improvement and optimization to refine the cyclotron extraction so as to extract more intense beam with good quality for the synchrotron injection.

As a continuous work of this study, the simulation of the extraction system needs to be fully implemented to help us find the main reasons for the low efficiency and intensity of the extracted ion beam from the cyclotron. In addition, we also want to use OPAL to complete a “end to end” beam dynamics simulation of the cyclotron, and therefore the cyclotron injection parts should be included in the simulation in the future.

REFERENCES

[1] B. Wang *et al.*, “Design and construction progress of a 7 MeV/u cyclotron”, in *Proc. 19th Int. Conf. on Cyclotrons and their Applications (Cyclotrons’10)*, Lanzhou, Sep.2010, China, TUA2CCO03, pp. 317-320.

[2] H. F. Hao, “Design and development of a 7 MeV/u heavy ion cyclotron”, Lanzhou, China: Ph.D. thesis, 2014.

[3] OPAL, `https://gitlab.psi.ch/OPAL/src/-/wikis/home/`

[4] A. Adelmann *et al.*, “OPAL a versatile tool for charged particle accelerator simulations”, *arXiv e-prints*, May. 2019. `doi:10.48550/arXiv.1905.06654`

[5] B. Wang *et al.,* “Computer design of a compact cyclotron”, *Physics of Particles and Nuclei Letters*, vol. 9, no. 3, pp. 288–298, 2012. `doi:10.1134/S1547477112030053`

[6] Lanzhou Ion Therapy Co., Ltd, “Operation of HIMM-IC in Wuwei”, unpublished.

ISBN: 978-3-95450-212-7 ISSN: 2673-5482 doi:10.18429/JACoW-CYCLOTRONS2022-WEA003

DEVELOPMENT OF THE CYCLONE®KEY: HOW INTEROPERABILITY LEADS TO COMPACTNESS*

V. E. Nuttens†, M. Abs, J. Caulier, Q. Flandroy, W. Kleeven, E. Kral, J. Mandrillon, O. Michaux, N. Mine, E. Van der Kraaij, Ion Beam Applications, Louvain-la-Neuve, Belgium

Abstract

In 2020, IBA has started the design, construction, tests and industrialization of a new proton cyclotron for the low energy range, the Cyclone® KEY, for PET isotope production (^{18}F, ^{13}N, ^{11}C) for neurology, cardiology or oncology imaging. It is a compact and fully automated isochronous cyclotron accelerating H^- up to 9,2 MeV. Based on the successful design history and return of experience of the Cyclone® KIUBE, the Cyclone® KEY design has been focused on compactness (self-shielding enabled), cost effectiveness and ease of installation, operation, and maintenance. The innovative design consists in the interoperability of the different subsystems: the magnet, the RF system, the vacuum system, the ion source, the stripping extraction, and target changer (with up to three targets). First beam tests results will also be presented.

THE CYCLONE®KEY

The Cyclone® KEY (Fig. 1) is the little brother of the Cyclone® KIUBE [1, 2]. Aiming at the low energy radioisotope production market, it has been designed to be simple to install and operate. Its compact design enables self-shielding operation with the possibility of low activation concrete [3]. All the different subsystems of the cyclotron have been nested in each other to optimize the compactness of the machine. The main parameters of the cyclotron are summarized in Table 1.

Table 1: Cyclone® KEY Design Parameters

Parameter	Value
Accelerated ions	H^-
Ion source	Internal PIG
Number of sectors	4
RF frequency	41MHz
RF mode	2
Dee angle	40°
Dee voltage	32kV
Extraction	Stripper (1+5 spares)
Extracted energy	9.2MeV
Cyclotron footprint (L×W×H)	1.5m×1.4m×1.35m

Figure 1: The Cyclone® KEY.

Magnet Design

The magnet inherited the vertical median plane of the Cyclone® 3d [4], which avoids the cost of a yoke lifting system. The magnetic structure, see Fig. 2, takes benefit from the successful design of the Cyclone® KIUBE [2]:

- Vertical gap between pole is 24mm to optimize the coil power consumption.
- The square shape to optimize the presence of iron only where it is needed, i.e. behind the poles.
- Symmetrical yoke penetrations for RF coupler (left), RF tuner and coil connections (right), ion source (bottom) and target (top).
- Pole inserts, in the centre of the pole, milled during magnetic mapping to obtain the isochronous magnetic field.
- The vacuum chamber sits on the sector behind the poles.

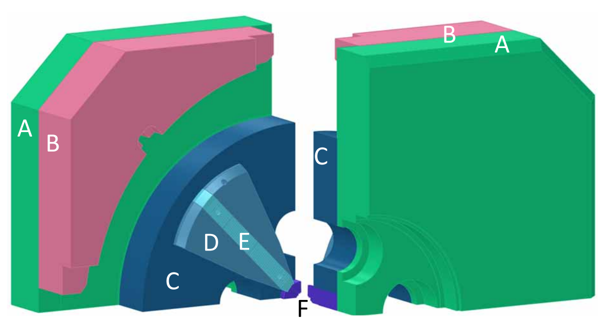

Figure 2: Magnetic circuit, including (A) the return yoke, (B) lateral return yoke, (C) sector, (D) the pole, (E) the pole insert and (F) the central plug.

* Work supported by Pole Mecatech/Biowin/SPW RW - convention 8150: CardiAmmonia.
† vincent.nuttens@iba-group.com

ISBN: 978-3-95450-212-7 ISSN: 2673-5482 doi:10.18429/JACoW-CYCLOTRONS2022-WEA003

Each half of the magnet is milled from a single iron plate which, thanks to precision milling, enables a very low level of harmonic imperfection and better vacuum performances. The valleys are drilled for the vacuum and the RF system at the same time. All magnetic field optimization were computed in Simulia OPERA [5].

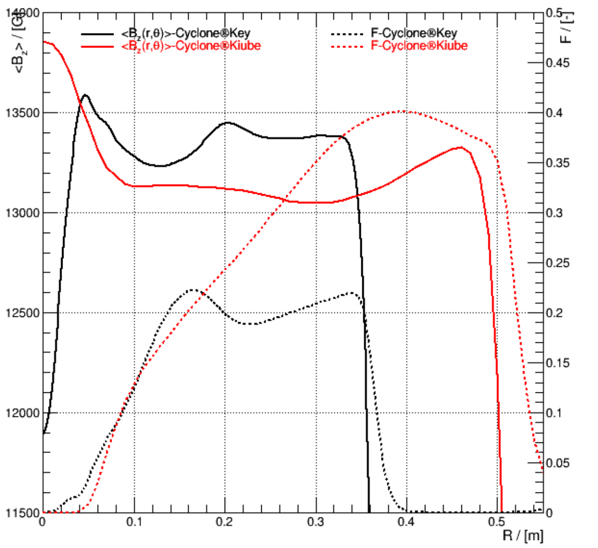

Figure 3: Average magnetic field and flutter in the Cyclone® KEY and in the Cyclone® KIUBE.

Ion Source and Central Region

The Cyclone® KEY uses the powerful PIG internal ion source of the Cyclone® KIUBE. The vertical gap between the central plug was then constraint to the ion source height. As shown by Fig. 3, the average magnetic field in the centre is quite small compared to the Cyclone® KIUBE. This is mainly due to the smaller gap in the valley which prevents the flux from going into the central plug. To still provide sufficient magnetic field in the centre for the particle to stay isochronous, two iron extensions have been added on the central plug (Fig. 4), but sufficiently far from the ion source to avoid any plasma column deformation. The dee tip geometry has been optimized by beam tracking in AOC [6] to provide good orbit centring, phase acceptance and electric focusing.

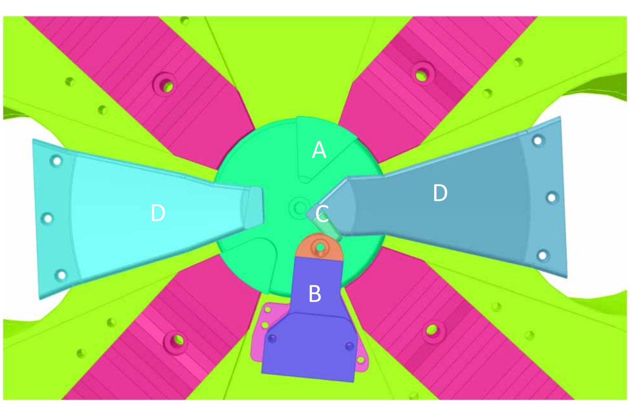

Figure 4: Central region: (A) central plug with iron extensions, (B) Ion source, (C) puller and (D) dee tips.

RF System

The RF system has a perfect cyclotron median plane symmetry and was modelled in Simulia CST studio Suite (Fig. 5) [7]. Such a configuration ensures a better stability in the operation of the cyclotron. Indeed, no RF current is flowing in the iron poles, which are more stable in temperature. No liners are therefore needed on the pole. No voltage occurs neither between the upper and the lower pole, improving the stripper reliability. The geometry and penetration in the iron were optimized for the cavity to resonate at 41 MHz with an effective voltage in the accelerating gap of 32 kV.

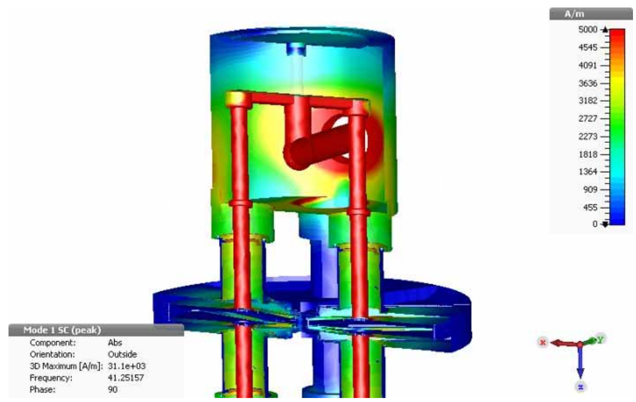

Figure 5: Surface current distribution in the RF cavity.

Vacuum System

Since the beginning of the project, the constraint was to combine the RF system with the vacuum box. The turbomolecular vacuum pump (Pfeiffer HiPace® 2300) is directly connected to the RF cavity which also serves as vacuum chamber that interconnects the four holes in the valley allowing to pump inside the cyclotron. Such configuration also allows for the connection of one or two pumps, depending on the customer's beam requirements. The vacuum system has been modelled in 3D using Molflow+ (Fig. 6) [8]: H_2 gas was emitted from the slit of the ion source. The hole's dimensions in the valleys were optimized for vacuum conductance, RF power and magnetic field. Pressures measured in the model and during beam test were in good agreement.

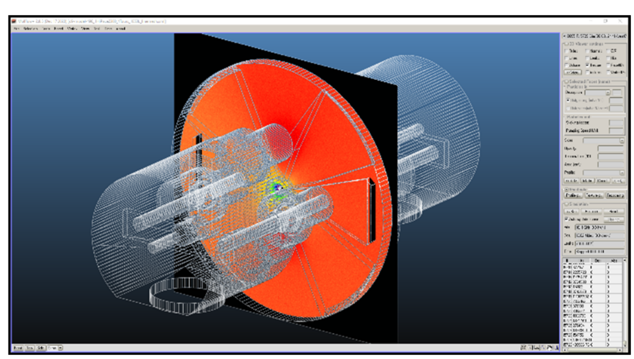

Figure 6: Vacuum model in Molflow+.

ISBN: 978-3-95450-212-7 ISSN: 2673-5482 doi:10.18429/JACoW-CYCLOTRONS2022-WEA003

Extraction System and Target Changer

Stripping extraction is the method of choice for such cyclotron. Given the reduced size of the machine, a single exit is only possible, but the return yoke penetrations have been made such that there is sufficient space for a target changer with up to three different targets. A stripper carousel with up to six strippers also allows for improved redundancy and reduced number of cyclotron openings. A rotating pop-up probe and beam collimators (left and right before vacuum chamber) measurements are available as diagnostic tools (Fig. 7). All the mechanical design could fit into the coil gap to limit the impact on the magnet and the self-shielding dimensions. Tracking of the ion beam from the ion source up to the target was performed with AOC [6]. The 1σ beam size at the target level is expected to be around $\sigma_x = 2.1$ mm and $\sigma_y = 1.7$ mm in the target, with an energy of 9.2±0.15 MeV.

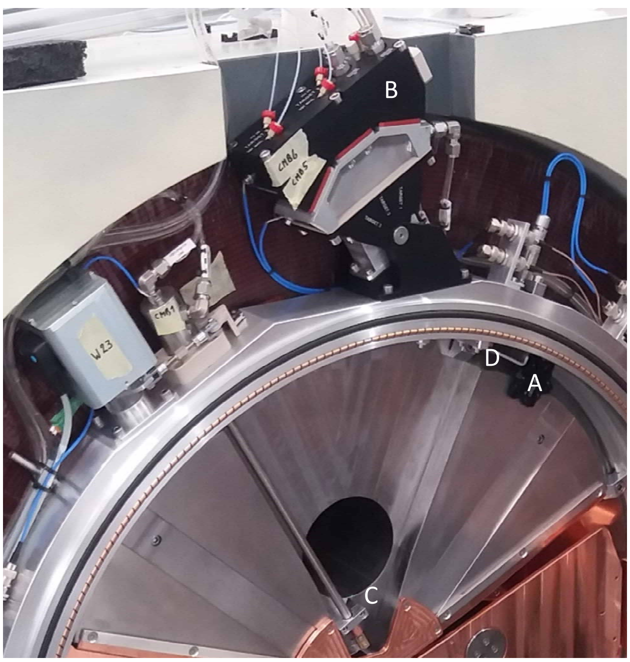

Figure 7: Extraction system and diagnostics: (A) Stripper carousel, (B) target changer, (C) pop-up probe and (D) left/right collimators through the vacuum chamber.

TEST RESULTS

The first machine was completely produced, mapped and first beam test campaign was conducted. Mapping results prove that the harmonic content is very low (<5Gs) and perfectly isochronous (only a few degrees of integrated phase slip). Beam tests with H^+ instead of H^- also confirmed the good isochronism of the machine.

High intensity beam tests with a two turbo molecular pumps configuration demonstrated a constant current of 100 µA on the stripper for 2 hours. The vacuum pressure was also excellent (base: 5.3E-7 mbar, source ON: 1.2E-5 mbar). Beam transmission between pop-up probe and stripper varies between 60-67% depending on the source gas quantity and source current (but still 100 µA on stripper).

CONCLUSION

Following the success of the Cyclone® KIUBE, we have designed, developed, produced, and tested a new powerful cyclotron for the low energy range, the Cyclone® KEY. All the subsystems' imbrications allow for a compact, powerful, and simple operation. The detailed simulation of the different subsystems allows us to have a well born machine. First beam tests have shown promising results and we are waiting for the radioisotope production test at full beam current at customer's site to prove the radioisotope production performances of the machine.

ACKNOWLEDGEMENTS

This work was supported by the Pole MecaTech and Biowin of the SPW RW - convention 8150: CardiAmmonia.

REFERENCES

[1] B. Nactergal *et al.*, "Development of the Cyclone® KIUBE: a compact, high performance and self-shielded cyclotron for radioisotope production", in *Proc. Cyclotrons'16*, Zurich, Switzerland, Sep. 2016, pp. 238-240. doi:10.18429/JACoW-Cyclotrons2016-TUD03

[2] S. Zaremba *et al.*, "Magnet design of the new IBA cyclotron for PET radio-isotope production", in *Proc. Cyclotrons'16*, Zurich, Switzerland, Sep. 2016, pp. 170-172. doi:10.18429/JACoW-Cyclotrons2016-TUP04

[3] E. Ramoisiaux *et al.*, "Self-consistent numerical evaluation of concrete shielding activation for proton therapy systems", in *Eur. Phys. J. Plus,* vol 137, no. 889, Aug. 2022. doi:10.1140/epjp/s13360-022-02960-9

[4] J. G. M. Kleeven *et al.*, "Upgrade of the IBA Cyclone 3D cyclotron", in *Proc. Cyclotrons'10*, Lanzhou, China, Sep. 2010, paper MOPCP074, pp. 197-199.

[5] Simulia Opera, https://www.3ds.com/products-services/simulia/products/opera/.

[6] W. Kleeven *et al.*, "AOC, a beam dynamics design code for medical and industrial accelerators at IBA", in *Proc. IPAC'16*, Busan, Korea, May 2016, pp. 1902-1904. doi:10.18429/JACoW-IPAC2016-TUPOY002

[7] Simulia CST Studio Suite, https://www.3ds.com/products-services/simulia/products/cst-studio-suite/.

[8] R. Kersevan and M. Ady, "Recent developments of monte-carlo codes Molflow+ and Synrad+", in *Proc. IPAC'19*, Melbourne, Australia, May 2019, pp. 1327-1330. doi:10.18429/JACoW-IPAC2019-TUPMP037

ISBN: 978-3-95450-212-7 ISSN: 2673-5482 doi:10.18429/JACoW-CYCLOTRONS2022-WEA004

STATUS OF THE HZB CYCLOTRON

A. Denker†,1, J. Bundesmann, T. Damerow, A. Dittwald, T. Fanselow, D. Hildebrand, U. Hiller, G. Kourkafas, S. Ozierenski, J. Röhrich, D. Rössink[1], C. Zimmer
Helmholtz-Zentrum Berlin für Materialien und Energie, Berlin, Germany
[1]also at Berliner Hochschule für Technik, Berlin, Germany
D. Cordini, J. Heufelder, S. Seidel, R. Stark, A. Weber
Charité – Universitätsmedizin Berlin, Berlin, Germany

Abstract

For more than 20 years eye tumours are treated in collaboration between the Helmholtz-Zentrum Berlin (HZB) the Charité – Universitätsmedizin Berlin (Charité).

The close co-operation between Charité and HZB permits joint interdisciplinary research. Irradiations with either a sharp, well focused or a broad beam, either in vacuum or in air are possible. In the past few years, we concentrated on beam delivery for FLASH experiments and the related dosimetry. For example, intraocular lenses have been irradiated under normal and FLASH conditions to investigate possible changes in the translucence. Furthermore, radiation hardness tests on solar cells for space have been performed.

A modernization project has been started in order to secure a long term and sustainable operation of our accelerator complex for therapy and research.

The accelerator operation for therapy as well as ongoing experiments and results will be presented.

ACCELERATOR OPERATION

A layout of the facility can be found in Ref. [1]. Either the 2 MV Tandetron or the 6 MV Van-de-Graaff serves as injector into the k=130 cyclotron of HZB. Overall, accelerator operation went quite well in the past years (see Fig. 1). Only in 2015 and in 2021 the downtime was above 5%.

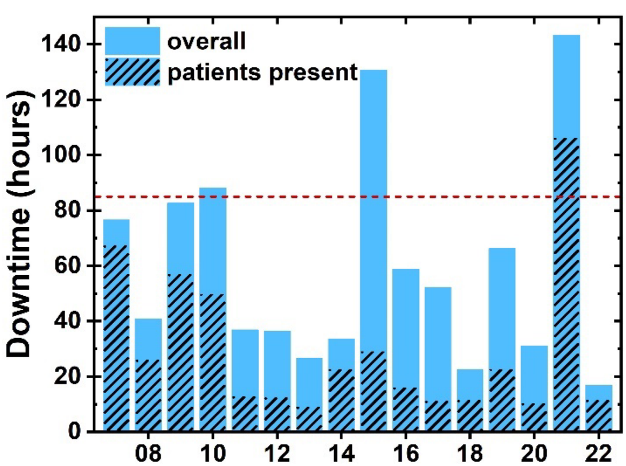

Figure 1: Downtime in hours for the past years. With exception of 2015 and 2021, the relative downtime was below 5%.

In 2021, a water leak in the extraction magnet required an opening of the cyclotron. For this reason, the scheduled therapy week had to be suspended. This explains the large duration of downtime with patients present, as the postponement is counted as downtime.

Fortunately, a new coil for the extraction according to the original plans had already been acquired. Hence, a rapid 1:1 exchange was possible. In the extraction magnet resides also a correction coil (see Fig. 2), which has never been used in the past. After the exchange of the coil, we failed to extract the beam. Only after connecting and using the correction coil the beam could be extracted with the usual transmission. As the magnet has adjust pins and the extraction coil fits snugly in the magnet, it is most probably the vacuum chamber which is now on a slightly different position.

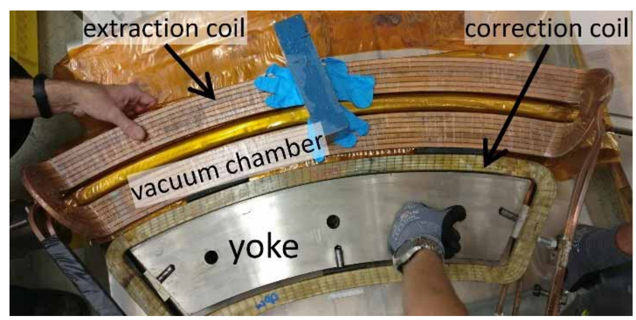

Figure 2: The extraction magnet with extraction and correction coil. On the yoke, the adjust pins are visible.

BEAM UTILIZATION

Roughly 83% of the beam time is used for therapy, the other 17% for experiments. Experiments comprise accelerator research and development (9%) [2, 3] as well as medical physics and dosimetry, (4%) e.g. [4, 5]. The distinction between the two topics is sometimes difficult. The final 4% of the beamtime is used for radiation hardness testing by external users, e.g. [6, 7].

Beam Delivery for FLASH Irradiations

The definition of FLASH irradiation is the delivery of the dose in a time of less than 1 s with a dose rate above 40 Gy/s [8]. The idea is to maintain tumour control and minimize side effects. The high dose rates pose challenges both for dosimetry in terms of linearity and saturation effects, and for reliable beam delivery in terms of beam stability and providing the same dose from shot to shot.

† denker@helmholtz-berlin.de

ISBN: 978-3-95450-212-7 ISSN: 2673-5482 doi:10.18429/JACoW-CYCLOTRONS2022-WEA004

The short irradiation times led to a closer look on the switching times: The Faraday cups with a stroke of 50 mm are too slow for this purpose, as they operate within 0.1 s. The special mechanical, scissor-like beam shutter used for therapy (BSATT) is faster, with an opening time of ~ 10 ms and a closing time of ~ 5 ms. This is more than sufficient for our conventional irradiation times of 30 s to 60 s. However, in order to provide a homogenous field this limited the achievable FLASH times to 200 ms.

Furthermore, the delays between beam demand and full intensity as well as stop command and zero beam have to be considered (see Fig. 3). The real irradiation starts with a delay time of t_1, then there is the time t_2 while the shutter opens, after t_3 the request to stop the beam occurs, however, there is the delay time t_4 until the shutter starts moving and closes within time t_5. The area under the curve corresponds to the applied dose. The dose applied within time t_4 and t_5 is called excess dose, because it arrives after the stop signal has been triggered.

In order to provide a dose controlled irradiation instead of setting a fixed time, a LabVIEW code and a FPGA was programmed. The FPGA board processes the signals of the Faraday cup and two ionization chambers. The FPGA board controls the Faraday Cup, the fast beam stopper and the electric beam deflector.

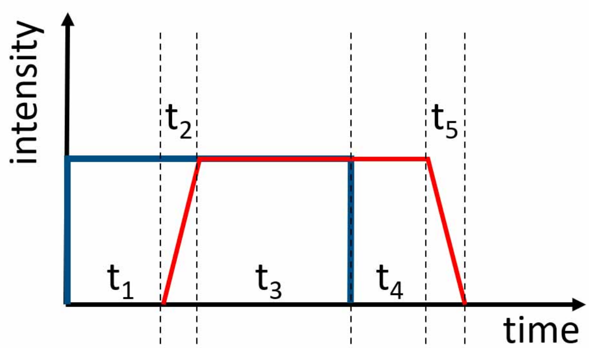

Figure 3: the blue line depicts the ideal FLASH irradiation, the red curve the reality. The different times to be considered are the delay between beam request (t=0) and start of opening of the beam shutters (t_1), opening time (t_2), time between request to interrupt the beam until (t_3) start of closing (t_4), closing of the shutter (t_5).

In the so-called calibration mode, the irradiation time is fixed, and the dose is measured via a Markus chamber (PTW Freiberg) and entered manually. The code correlates the sum of the counts of the ionisation chambers to the measured dose and integrates the counts after the stop-signal was triggered (excess counts). This defines the switch-off strategy: in “dose mode” the stop-signal is given for the corresponding dose minus expected excess counts.

After the calibration several trial runs are performed to verify the set-up for the day and to determine the dose fluctuation from shot to shot. This takes only a few minutes. In the conventional irradiation mode applying 15 Gy with 0.25 Gy/s and 60 s total irradiation time, statistically no fluctuations were observed. In FLASH mode with a dose rate of 75 Gy/s after 30 trial runs a mean dose of 14.9 Gy with a standard deviation of 0.6% was determined. Thus, since then FLASH irradiations with a very high dose accuracy are now possible.

Irradiation of Mice Eyes under Conventional and FLASH Conditions

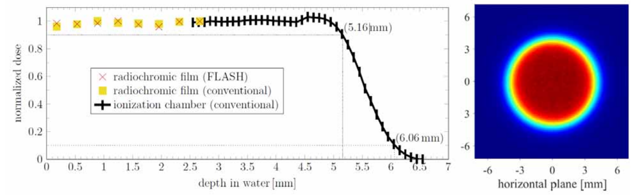

Figure 4: The field size for the irradiation of single mouse eyes. Left: Spread out Bragg Peak with a range of 5.2 mm and a distal fall-off of 0.9 mm, measured with ionisation chamber and radiochromic film. Right: Lateral beam distribution measured with a camera, showing a field size of 6.3 mm and a penumbra of 1.7 mm.

Mice eyes are small, thus providing challenges for the beam delivery. The FLASH irradiations for mice eyes should provide the same irradiation field as in the conventional irradiation in order to irradiate a **single** eye, thus leaving the other one for comparison purposes: a range of 5.2 mm in water with a 0.9 mm distal fall-off as well as a lateral field size of 6.3 mm with a lateral penumbra of 1.7 mm (see Fig. 4). Distal fall-off and penumbra are both from 90% to 10% of the isodose. This was achieved by aluminium for beam scattering and range shifting and a brass collimator. The desired full spread-out Bragg Peak was achieved by a modulator wheel providing 960 spread-out Bragg Peaks per second [9]. Figure 5 shows the experimental set-up.

FLASH irradiations with an extended Bragg Peak and a good confinement to the target volume are now feasible, the final data evaluation is still on-going [10].

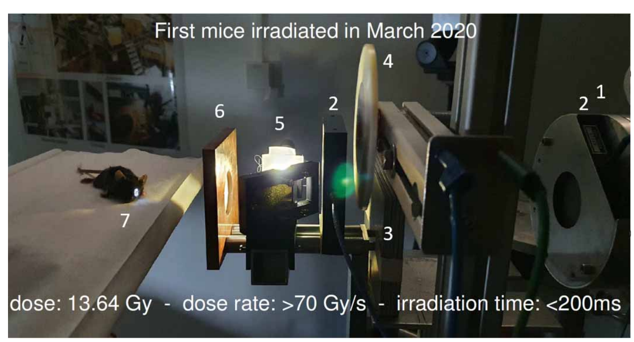

Figure 5: The set-up for the Flash irradiation of single mouse eyes: 1 vacuum window, 2 monitor chambers (7861, PTW-Freiburg, Germany), 3 combined degrader and scattering system (16 mm Al), 4 3D printed modulator wheel (periods: 48; rotation speed: 20 Hz), 5 light field system (LED lamp and mirror foil (25 µm Kapton), 6 collimator (brass; Ø5.5 mm), 7 anesthetized mouse with light field for positioning.

ISBN: 978-3-95450-212-7 ISSN: 2673-5482 doi:10.18429/JACoW-CYCLOTRONS2022-WEA004

Further Developments of FLASH Irradiations

At the moment the best irradiation time and the best dose rate are unknown. There is some evidence, that the times should be shorter than 100 ms [11]. Then the mechanical shutter is too slow and has to be replaced by an electrical deflector. Until recently, only for the Van-de-Graaff injector such a deflector was available, not for the Tandetron, the standard injector for proton therapy. Such a deflector has been developed and is now available [12]. Furthermore, a transmission ionisation chamber with a linear dose response up to 400 Gy/s has been developed [13].

The next steps of further development of the experimental set-up are the replacement of the low-efficient single scattering beam shaping system by a double scattering system and the replacement of a rotating modulator wheel by ridge filters. In the near future, FLASH irradiations of sarcoma and uveal melanoma organoids will be performed.

Determination for Appropriate Material for Intraocular Lenses in Ocular Proton Therapy

Intraocular lenses from various manufacturers have been irradiated with protons under conventional and FLASH mode in order to investigate changes in the material. The lenses were mounted in the water phantom just behind the entrance window with a Markus chamber for absolute dosimetry (see Fig. 6). The irradiation field size was identical for both modes. In conventional mode 60 Gy were applied with a dose rate of 0.2 Gy/s, while in FLASH mode the same dose was applied with a dose rate of 70 Gy/s.

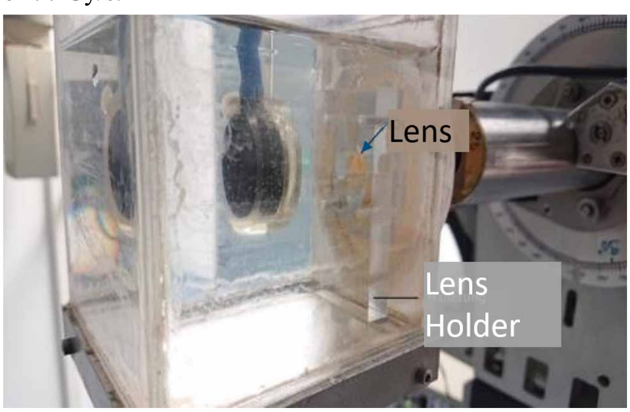

Figure 6: The lens is mounted inside the water phantom right behind the entrance window with a Markus chamber behind for dosimetry. The proton beam is coming from the right.

Lenses from different manufacturers with different dioptres (D) have been irradiated:

- Bausch+Lomb “enVista” +10.0 D Modell MX60 with UV absorber
- Bausch+Lomb “Akreos” +11.5 D with UV absorber
- Bausch+Lomb “Softport” +17 D
- Zeiss “CT Lucia 201P” + 19.5
- Zeiss “CT Asphina 509 MP” +21 D

Before and after the irradiation the transmission of the lenses was measured for light ranging from 200 nm to 900 nm. One example is given in Fig. 7. Only slight, but non-relevant changes in the transmission before and after the irradiation could be observed, the edges and peaks in transmission were at the same wavelength. The result was the same for conventional and FLASH irradiation, meaning that the dose rate is irrelevant. Only after an irradiation with ^{60}Co γ-rays with a dose 20000 Gy, a typical sterilisation dose, changes in transmission were observed.

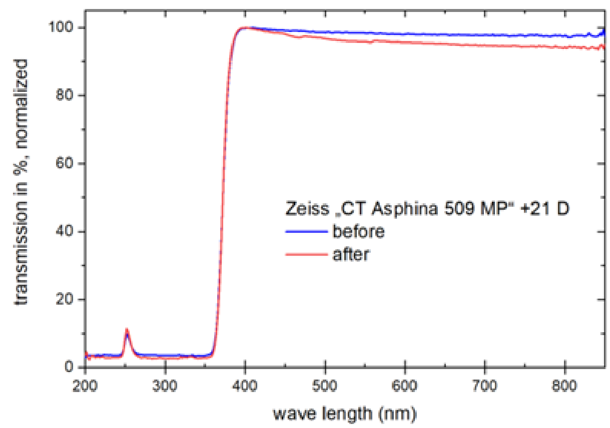

Figure 7: Normalised transmission curves for the Zeiss CT Asphina 509 MP +21D lens before and after the irradiation. Only slight changes are visible.

CONCLUSION

Over the past years the cyclotron operation went quite smooth, with just one major event leading to the postponement of a therapy week. Having the spare part, the extraction coil, already in house, helped tremendously. In total, more than 4400 patients have been treated and, in spite of Covid-19, patient numbers were high.

Beam delivery for FLASH irradiations has been developed, allowing now dose controlled FLASH irradiations. For this purpose, the different times playing a role in the process have been investigated and are now handled via a FPGA board together with a LabVIEW code.

We have developed an irradiation set-up which allows the irradiation of single mouse eyes, thus leaving the other eye for comparison. This set-up operates under conventional as well as under FLASH conditions.

Intraocular lenses have been irradiated under normal and FLASH conditions. No significant changes in transmission could be observed.

In near future irradiations of sarcoma and uveal melanoma organoids are scheduled.

Furthermore, experiments for dosimetry and improved beam delivery, especially for FLASH conditions will be performed as well as irradiations of electronic devices and solar cells for radiation hardness tests.

ISBN: 978-3-95450-212-7 ISSN: 2673-5482 doi:10.18429/JACoW-CYCLOTRONS2022-WEAO04

REFERENCES

[1] J. Bundesmann *et al.,* "Beam properties at the experimental target station of the proton therapy in Berlin", in *Proc. 22nd Int. Conf. on Cyclotrons and their Applications (CYC2019)*, Cape Town, South Africa, Sep. 2019, pp. 199-201. doi:10.18429/JACoW-Cyclotrons2019-TUP020

[2] G. Kourkafas *et al.,* "Acceleration and measurement of alpha particles and hydrogen molecular ions with the HZB cyclotron", in *Proc. 12th Int. Particle Accelerator Conference (IPAC 2021)*, Campinas, SP, Brazil, May 2021, pp. 1264-1266. doi:10.18429/JACoW-IPAC2021-MOPAB

[3] J. Bundesmann *et al.,* "Upgrading the beam diagnostic of the HZB-cyclotron from an analogue to a new digital platform", presented at the 23rd Int. Conf. on Cyclotrons and their Applications (Cyclotrons'22), Beijing, China, Dec. 2022, paper WEPO011, this conference.

[4] A. Dittwald, *et al.,* "Real time determination of the range and Bragg peak of protons with a depth profile camera at HZB", presented at the 23rd Int. Conf. on Cyclotrons and their Applications (Cyclotrons'22), Beijing, China, Dec. 2022, paper TUBO2, this conference.

[5] J. Wulff *et al.,* "Technical Note: Impact of proton beam properties for uveal melanoma", *Med. Phys.,* vol. 59, pp. 3481-3488. doi:10.1002/mp.15573

[6] F. Lang *et al.,* "Proton radiation hardness of Perovkite tandem photovoltaics", *Joule,* vol. 4, pp. 1054-1069. doi:10.1016/j.joule.2020.03.006

[7] S. Barthelmes *et al.,* "MMX Rover locomotion subsystem – development and testing towards the flight model", in *Proc. IEEE Conf. on Aerospace (AERO'22),* Big Sky, USA, Mar. 2022, pp. 1-13. doi:10.1109/AERO53065.2022.9843723

[8] B. Lin *et al.,* "FLASH radiotherapy: history and future", *Front. Oncol.,* vol 11, May 2021, pp. 1-7. doi:10.3389/fonc.2021.644400

[9] G. Kourkafas *et al.,* "FLASH proton irradiation setup with a modulator wheel for a single mouse eye", *Med. Phys.,* vol 48, Apr. 2021, pp. 1839-1845. doi:10.1002/mp.14730

[10] G. Kourkafas *et al.,* "Early normal tissue reactions after FLASH proton beam exposure of mice eye: preliminary results from in-vivo investigation using optical coherence tomography", presented at the 2nd Flash Radiotherapy and Particle Therapy Conference (FRPT'222), Barcelona, Spain, Nov. 2022.

[11] S. Boucher *et al.,* "Transformative technology for FLASH radiation therapy: a Snowmass 2021 white paper", Mar. 2022. doi:10.48550/arXiv.2203.11047

[12] T. Fanselow *et al.,* "Design and operation of the new fast beam chopper between tandetron and cyclotron", presented at the 23rd Int. Conf. on Cyclotrons and their Applications (Cyclotrons'22), Beijing, China, paper MOPO011, Dec. 2022, this conference.

[13] S. Gerke *et al.,* "Entwicklung einer Dosismonitorkammer für Flash-Bestrahlungen mit Protonen", Master's thesis, Fachbereich 2, Beuth Hochschule für Technik Berlin, Berlin, Germany, 2021.

ISBN: 978-3-95450-212-7 ISSN: 2673-5482 doi:10.18429/JACoW-CYCLOTRONS2022-WEA005

INVESTIGATION OF LONG RADIAL PROBE ACTIVATION IN THE PSI MAIN RING CYCLOTRON

M. I. Besana*, E. Hohmann, M. Sapinski, J. Snuverink, D. Werthmüller
Paul Scherrer Institut, 5232 Villigen PSI, Switzerland

Abstract

During an inspection of a new Long Radial Probe, inserted into the Ring cyclotron only a month earlier, an activation hot spot has been identified. The nature of this hot spot has been investigated by performing measurements of the residual activation using shielded Al_2O_3:C dosimeters, 5 mm in diameter, and a portable gamma spectrometer. Monte Carlo simulations of the probe activation with various proton energies have been performed. Results show that most of the activation comes from relatively fast decaying radionuclides and therefore the residual dose drops sufficiently during the shutdown to allow for maintenance and upgrade works. Comparing the abundances of various radionuclides estimated from measured gamma spectra with simulations at various proton energies we conclude that the most probable loss mechanism is scattering of the protons on the upstream collimator.

INTRODUCTION

The Long Radial Probe (RRL) is a device installed in the PSI's Ring cyclotron. It measures transverse beam position and profile of all orbits by measuring the effects of interaction of the beam with a thin, moving target (carbon fibre). The measured radius extends between 2080 and 4500 mm [1].

A picture of the probe moved out of the cyclotron during the gamma spectroscopy measurement is shown in Fig. 1. The cyclotron chamber is behind the large vacuum valve on the right side of the plot. The RRL structure, here in a service box with side flanges open, is normally manually inserted into the cyclotron before the start of the beam operation.

After 19 days of being inserted into the cyclotron the RRL had to be serviced. A routine activation measurement revealed presence of a hot spot with 1 mSv/h. Red star marks the location of this hot spot. Additional measurements performed using small Al_2O_3:C chips exposed directly to activated structure and shielded from other directions revealed that the hot spot is on the upper structure of the RRL.

MONTE CARLO SIMULATIONS

The established method for the activation calculations at PSI is the coupling of Monte Carlo simulations with the general purpose radiation transport code MCNP [2] and the nuclide inventory code FISPACT [3].

The object under study is modeled in the MCNP 6.2 geometry and it is divided in smaller cells to estimate the activation as a function of the position. Particles are transported from the loss points to the regions of interest with MCNP. The flux of neutrons up to 20 MeV and the production rates of radionuclides are calculated in each cell of the geometry. The coupling script [4] is then used to prepare the input files for the FISPACT code, which include MCNP results and the irradiation history. The nuclide inventory of each cell at any time step is finally calculated.

The RRL device is modeled as two blocks of an aluminium-magnesium alloy called EN-AW-508, with dimensions of 1 m in the radial direction (x), 0.5 cm in the vertical direction (y) and 11.75 cm along the beam direction (z) (see Fig. 2). The distance between the two blocks in the vertical plane is 4 cm. The upper part, where higher activation has been measured, is divided in 12 cells. Cells 100-105 are between y=2 cm and y=2.2 cm, while cells 110-115 are between y=2.2 cm and y=2.5 cm. The lower part is not segmented and it is called cell 200.

Since the beam losses at the location of the RRL device are not known, some assumptions have been made for the simulations. The proton beam is moving along the z direction and it is impacting on the device front face. It is uniformly distributed over 1 m in x and between 2.0 cm and 2.2 cm in y. Twelve simulations have been performed considering the following beam energies (in MeV): 10, 20, 40, 60, 80, 100, 140, 200, 300, 400, 500, and 590.

The spectrum of the produced neutrons and the rates of residual nuclei have been calculated for each cell and used as input for the FISPACT calculations. The considered operation history is summarized in the Table 1. A constant lost current of 1 nA has been assumed for both irradiation periods. The end of the first cooling time corresponds to the moment when the hot spot was identified, while the end of the third cooling time corresponds to the time of the gamma spectra measurement.

Table 1: Part of the beam exposition history relevant for this activation study.

	Dates (2022)	Length
1st irradiation	Apr., 27th - May, 16th	19 days
1st cooling	May, 16th ev. - May, 18th	36 hours
2nd cooling	May, 18th - May, 19th	29 hours
2nd irradiation	May, 19th - June, 13th	25 days
3rd cooling	June, 14th	12 hours

For each cell, the nuclide inventory at each time step is calculated, as well as the residual dose that would be generated at 1 m by 1 g of material. The highest dose rates are always observed in cell 100.

* Ilaria.Besana@psi.ch

ISBN: 978-3-95450-212-7 ISSN: 2673-5482 doi:10.18429/JACoW-CYCLOTRONS2022-WEA005

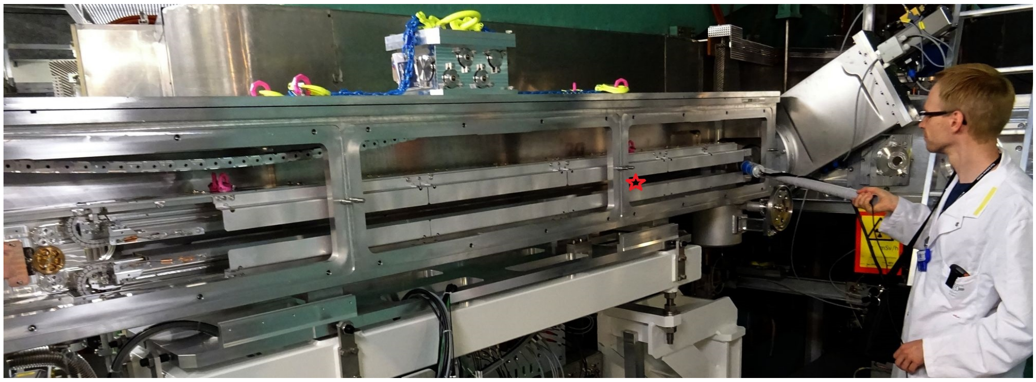

Figure 1: Gamma spectroscopy measurement of the RRL moved out of the cyclotron.

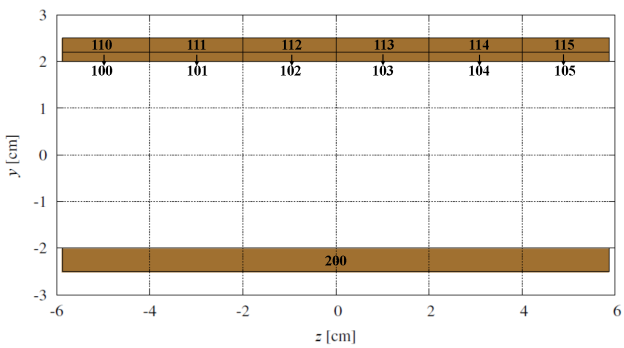

Figure 2: RRL device geometry in MCNP. The numbers in the figure correspond to the cell numbers.

For beam energies above 60 MeV, the dominant contribution comes from the decay of sodium isotopes (Na-22 and Na-24).

To calculate the residual dose to be compared with the measurements, the spectra of the gammas emitted by the radioactive nuclides and their normalisation are extracted from the output of FISPACT for each cell. The sum of the gamma spectra is used as source term for a second calculation in MCNP [5]. The expected dose map has been calculated for all proton beam energies. An example is shown in Fig. 3.

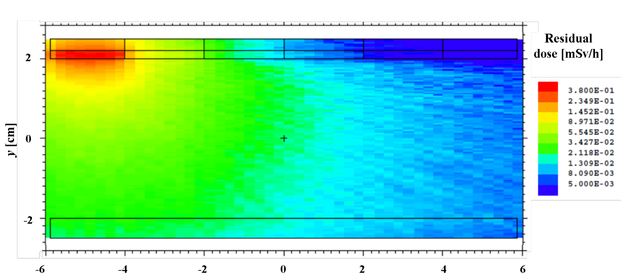

Figure 3: Residual dose map [mSv/h] at the time of the first measurement in the z-y plane, for 80 MeV proton beam and 1 nA lost current.

GAMMA SPECTROSCOPY

Several measurements of the gamma-ray energy spectrum were performed along the inner structure of the RRL (see Fig. 1). Monte Carlo simulations of the used detector were carried out in order to obtain the gamma energy distributions of various radionuclides. The sum of these distributions have then been fitted to the measured spectra to estimate the individual contributions of each of the involved nuclides.

The main region of interest is located at an orbit radius of about 230 cm, where gamma dose rate measurements revealed a radiation hot spot (see Fig. 1). A $LaBr_3$-based hand-held scintillator detector (model B-RAD by ELSE Nuclear [6]) was used to measure gamma spectra up to an energy of 2 MeV with a resolution of 3.3% (FWHM) at 662 keV. The black line in Fig. 4 shows the obtained spectrum at the location of the major hot spot.

Using the FISPACT calculations for proton energies between 20 and 200 MeV, a list of key nuclides is identified, which contribute ≥95% to the total nuclide activity for a given proton energy. Monte Carlo simulations of the B-RAD detector are carried out to obtain the individual energy distributions of these nuclides in the detector. For this purpose, a simplistic detector model (cylindrical $LaBr_3$ crystal in aluminium housing according to the B-RAD geometry) located in front of a $5 \times 5 \times 14\ \mathrm{cm}^3$ aluminium block at a distance of 1.5 cm is built using the Geant4 framework [7–9]. Radioactive decays of the key nuclides are generated homogeneously distributed within the aluminium block. The total energy deposition in the $LaBr_3$ crystal is registered and subsequently folded with the known detector resolution.

Given the energy-dependent spectra $s_i(E_\gamma)$ for each nuclide i from the Geant4 simulation, the ansatz

$$S(E_\gamma) = \sum_{\text{Nuclide } i} c_i \cdot s'_i(E_\gamma) \tag{1}$$

with properly normalized spectra $s'_i(E_\gamma)$ of nuclide i is fitted to the measured energy distribution in the range $E_\gamma = [270, 1900]$ keV using a χ^2 minimization (ROOT MINUIT package [10]) to extract the nuclide contribution coefficients c_i. Some nuclides in the previously built list of key nuclides do not show any sensitivity in the fit ($c_i \approx 0$) and are

ISBN: 978-3-95450-212-7 ISSN: 2673-5482 doi:10.18429/JACoW-CYCLOTRONS2022-WEA005

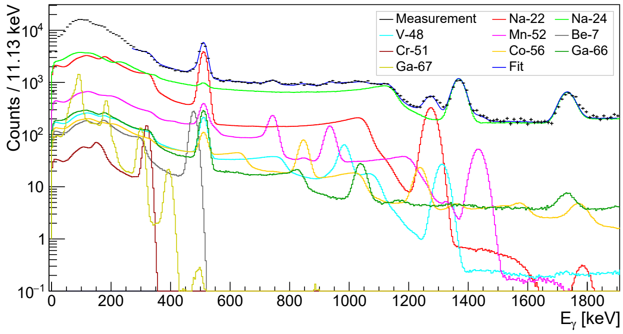

Figure 4: Measured gamma-ray energy spectrum (black points) compared to the fitted sum of simulated nuclide contributions $S(E_\gamma)$ (blue curve) and individual contributions of key nuclides.

therefore removed from the list. Figure 4 shows the measured distribution along with the fitted sum and individual nuclide contributions. The relative contributions r_i are then calculated as

$$r_i = \int_{E_0}^{E_1} c_i \cdot s_i'(E_\gamma)\, dE_\gamma \Bigg/ \int_{E_0}^{E_1} S(E_\gamma)\, dE_\gamma \qquad (2)$$

with $E_0 = 270$ keV and $E_1 = 1900$ keV. The numerical values of r_i can be found in Table 2.

Table 2: Relative contributions r_i of key nuclides obtained from the fit of the measured gamma spectrum and from the Monte Carlo simulation (cell 100) of a 80 MeV proton beam.

Nuclide	r_i^{Fit} [%]	$r_i^{\mathrm{MC}}(80)$ [%]
Na-22	24.6 ± 0.9	30.1
Na-24	60.0 ± 1.1	58.5
V-48	2.6 ± 0.7	3.8
Mn-52	6.9 ± 0.5	5.5
Be-7	0.9 ± 0.1	0.1
Cr-51	0.3 ± 0.1	0.6
Co-56	2.3 ± 0.5	1.0
Ga-66	2.2 ± 1.0	0.2
Ga-67	0.3 ± 0.1	0.1

COMPARISON OF SIMULATED AND MEASURED NUCLIDE CONTRIBUTIONS

In order to identify the energy of the impacting protons, the relative nuclide contributions from the fit r_i^{Fit} are compared to the values $r_i^{\mathrm{MC}}(E_p)$ estimated by Monte Carlo simulations with proton energy E_p by calculating

$$\chi^2(E_p) = \sum_{\text{Nuclide } i} \left(\frac{r_i^{\mathrm{Fit}} - r_i^{\mathrm{MC}}(E_p)}{\Delta r_i^{\mathrm{Fit}}} \right)^2 \qquad (3)$$

with uncertainties $\Delta r_i^{\mathrm{Fit}}$ originating from the spectrum fit of the key nuclides. Figure 5 shows the E_p-dependence of

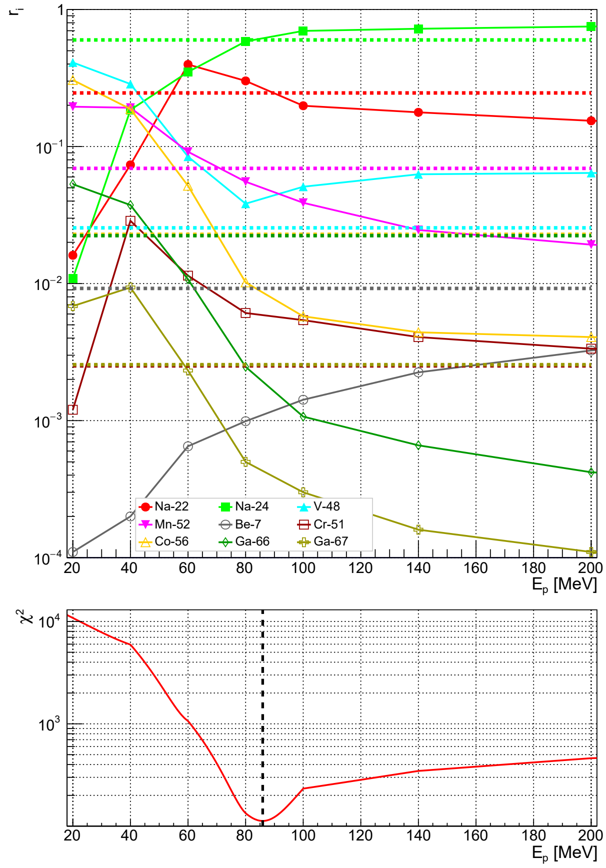

Figure 5: Top: relative nuclide contributions r_i of key nuclides obtained from measurement fit (horizontal dotted lines) and Monte Carlo simulations (solid curves) as a function of the proton energy E_p. Bottom: E_p-dependence of χ^2 with minimum at $E_p \approx 86$ MeV.

r_i^{MC} and χ^2. The latter has a minimum at $E_p \approx 86$ MeV indicating that the best agreement between measurement and Monte Carlo simulation is found at this energy.

CONCLUSIONS

A comprehensive study of the activation of the Long Radial Probe structure revealed that the observed hot spot is most likely due to protons scattered on the upstream collimator, as the best agreement between the measured and simulated gamma spectrum was found for a proton energy of $E_p \approx 86$ MeV, whereas the primary beam energy at this location is in the range of 150–180 MeV. The main radionuclide responsible for the activation is Na-24, which has a short decay time, therefore no significant buildup of the activation is expected. Nevertheless during the upcoming winter shutdown the probe will be motorized, so it will not remain inserted into the cyclotron when it is not in use.

ACKNOWLEDGEMENTS

The authors would like to thank S. Lindner, M. Rohrer, M. Hauenstein, E. Yukihara, L. Bossin, R. Dölling and the PSI operator team.

ISBN: 978-3-95450-212-7 ISSN: 2673-5482 doi:10.18429/JACoW-CYCLOTRONS2022-WEA005

REFERENCES

[1] M. Sapinski, R. Doelling, and M. Rohrer, "Commissioning of the renewed radial probe in PSI's ring cyclotron", in *Proc. 11th Int. Beam Instrum. Conf. (IBIC'22)*, Kraków, Poland, Sep. 2022, pp. 76–79. doi:10.18429/JACoW-IBIC2022-MOP19

[2] C. J. Werner *et al.*, "MCNP6.2 Release Notes", Los Alamos National Laboratory, USA, Rep. LA-UR-18-20808, 2018.

[3] R. Forrest, "FISPACT-2007: User Manual", Technical Rep. UKAEA FUS 534, EURATOM/UKAEA, 2007.

[4] F. X. Gallmeier *et al.*, "An environment using nuclear inventory codes in combination with the radiation transport code MCNPX for accelerator activation problems", in *Proc. 8th Int. Topical Meeting on Nuclear Applications and Utilization of Accelerators (AccApp'07)*, Pocatello, ID, USA, Jul.-Aug. 2007, pp. 207-211.

[5] M. Wohlmuther and F. X. Gallmeier, "User Guide for Gamma Source Perl Script 2.0", Paul Scherrer Institut, Villigen, Switzerland, Rep. TM-85-13-05.

[6] B-RAD, ELSE Nuclear, http://www.elsenuclear.com/en/b-rad

[7] S. Agostinelli *et al.*, "Geant4—a simulation toolkit", *Nucl. Instrum. Methods Phys. Res. Sect. A*, vol. 506, pp. 250–303, 2003. doi:10.1016/S0168-9002(03)01368-8

[8] J. Allison *et al.*, "Geant4 developments and applications", *IEEE Trans. Nucl. Sci.*, vol. 53, pp. 270-278, 2006. doi:10.1109/TNS.2006.869826

[9] J. Allison *et al.*, "Recent developments in Geant4", *Nucl. Instrum. Methods Phys. Res. Sect. A*, vol. 835 pp. 186–225, 2016. doi:10.1016/j.nima.2016.06.125

[10] R. Brun and F. Rademakers, "ROOT — An object oriented data analysis framework", *Nucl. Instrum. Methods Phys. Res. Sect. A*, vol. 389, pp. 81–86, 1997. doi:10.1016/S0168-9002(97)00048-X

ISBN: 978-3-95450-212-7 ISSN: 2673-5482 doi:10.18429/JACoW-CYCLOTRONS2022-WEA006

DEVELOPMENT OF HEAVY ION RADIOTHERAPY FACILITIES IN CHINA*

Jian Shi†, Qiang Li, Lizhen Ma, Jiawen Xia, Guoqing Xiao, Jiangcheng Yang, Wen-Long Zhan
Institute of Modern Physics, Chinese Academy of Sciences, Lanzhou, China

Abstract

In China, there are currently 2 carbon facilities in operation, Shanghai proton/heavy ion center and Wuwei heavy ion therapy center, 8 facilities are under construction. This paper will introduce the development of heavy ion radiotherapy facilities in China.

INTRODUCTION

Currently, there are about 19 million cancer cases arise every year and 10 million cases dead from cancer every year globally; these numbers will increase to 29.5 million and 16.4 million at 2040 according to the prediction of IARC (The International Agency for Research on Cancer), with an annual increase rate of 2.4% and 2.6% respectively. In China, whose population is about 20% of the world, there are 4.5 million new cases and 3 million cases dead from cancer every year, which will increase to about 6.7 million and 5.1 million at 2040, with an annual increase rate of 2.2% and 2.9%. Heavy (Carbon) ion radiotherapy offers superior dose conformity in the treatment of deep-seated tumors compared with conventional X-ray therapy due to its Bragg-peak feature of energy deposition, the higher RBE (Relative Biological Effectiveness) and lower OER (Oxygen Enhancement Ratio).

Shanghai Proton Heavy Ion Hospital purchased a heavy ion facility from Siemens in 2008 and began operation in 2015. At present, more than 1000 patients receive treatment every year. Wuwei Heavy Ion Center purchased HIMM (Heavy Ion Medical Machine) facility, which is designed and produced by IMP (Institute of Modern Physics). The construction of the facility was completed in 2019 and was put into operation in 2020. Affected by COVID-19, the number of patients treated in the first year was only 200, but the number of patients treated is increasing every year.

STATUS OF HEAVY ION RADIOTHERAPY FACILITIES IN CHINA

In China, there are 2 heavy ion facilities in operation. They are Shanghai proton and heavy ion center and Wuwei Heavy ion therapy center. There are also 8 facilities under construction, which are Lanzhou Heavy ion therapy hospital, Xuzhou heavy ion center (Hitachi), Mazu Health center, Hubei general hospital, Zhejiang cancer hospital, Jiangsu cancer hospital, The First Bethune hospital of Jilin University, Heyou international hospital (Hitachi). All the heavy ion facilities that are under construction list above are produced by IMP except Xuzhou and Heyou hospital.

HIMM FACILITY DEVELOPED BY IMP

Heavy ion medical machine (HIMM) was constructed on the basis and with the experience gained from the Heavy Ion Research Facility in Lanzhou-Cooler Storage Ring (HIRFL-CSR) project [1]. The facility consists of an electron cyclotron resonance (ECR) ion source, a cyclotron injector, a compact synchrotron ring, and 5 treating terminals [2]. The C^{5+} beam generated by the ECR ion source is accelerated by the cyclotron to 6.2 MeV/u and then injected into the synchrotron using the CEI (charge exchange injection) method [3]. The injected beam is accelerated from 6.2 MeV/u to an extraction energy ranging from 120 to 400 MeV/u.

Figure 1 shows an aerial view of the HIMM. The facility consists of four treatment rooms, A, B, C, and D. Five fixed irradiation ports are installed in the rooms: horizontal, horizontal plus vertical, vertical, and 45° irradiation ports. Active scanning is conducted in Room A, while passive scanning is adopted in the other rooms. The maximum irradiation field at the tumor is $200 \times 200\ \mathrm{mm}^2$ for all the irradiation ports.

Unlike other cancer therapy machines, the HIMM synchrotron uses a cyclotron as the injector. The beam intensity of the cyclotron injector is approximately 10 μA, and the emittance of the beam is approximately $25\,\pi \cdot \mathrm{mm} \cdot \mathrm{rad}$ ($\pm 3\sigma$). Compared to the linear injector, the beam intensity is much weaker and the beam emittance is much larger. To store enough particles in the ring, the CEI method is adopted. This method overcomes the limitations set by Liouville's theorem so that beams can be injected at the point of phase space already occupied by previously injected beam. Therefore, an intense beam can be accumulated in the ring without increasing the beam emittance too much. In addition, the injected beam can be painted in the horizontal phase space by changing the local closed orbit during injection to reduce the probability the particles hit the stripping foil, thus increasing the injection efficiency. This scheme has been proved to be very efficient in the CSRm for light-heavy ions.

The beam orbit and envelopes during injection are shown in Fig. 2. Four bump magnets (Bpi1-Bpi4 in Fig. 1) are used to sweep the closed orbit of the circulating beam. Special vacuum chambers with large aperture are used at magnets located in the injection section. C^{5+} beam with an energy of 7 MeV/u from the cyclotron injector are injected into the synchrotron at a small angle (1.85°) and then reach the stripping foil, by which they are stripped to C^{6+}. The stripping

* Work supported by Talent Fundation of Lanzhou 2019-RC-4.
† shijian@impcas.ac.cn

ISBN: 978-3-95450-212-7 ISSN: 2673-5482 doi:10.18429/JACoW-CYCLOTRONS2022-WEA006

Figure 1: Aerial view of the HIMM

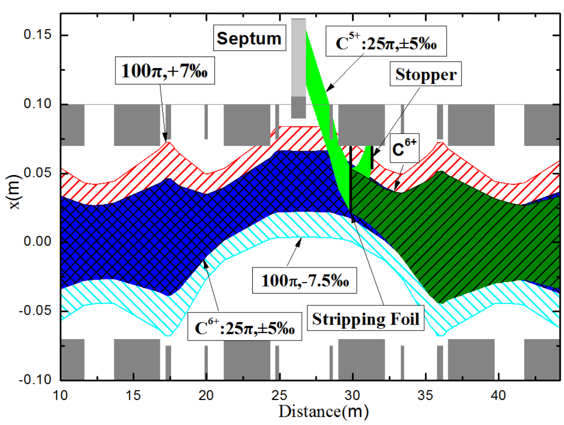

Figure 2: The beam orbit and envelop during injection

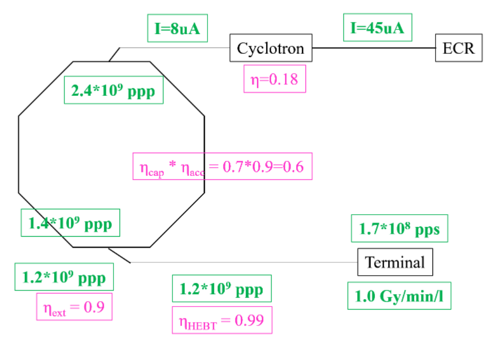

Figure 3: The beam intensity in the whole facility

foil is located 0.84 m away from the entrance of the main dipole with a thickness of 20 µg/cm^2.

The RF-KO (radio frequency knockout) [4] method is widely used for third-order resonant extraction because it has many advantages over other methods, such as a fast response to beam-on/off signal, the production of static target beam spots during extraction, the ability to easily control the spill intensity and the ability to keep the lattice of the synchrotron constant.

The beam commissioning is finished in 2018 [5] and the the beam intensity of the whole facility is shown in Fig. 3.

Besides the part of the accelerator, the typical equipment in the treatment room is shown in Fig. 4 as an example. There are 2 nozzles in this room, one is horizontal, another is vertical. The robot coach, CT (Computed Tomography), and DR (Digital Radiography) are the standard configuration in the treatment room. The TPS (Treatment Planning System), which is based on Simplified Monte Carlo algorithm, is configured. The features such as optimization engine based on GPU (Graphics Processing Unit), supporting multiple biophysical models and multiple particle types, dose comparison among multiple radiation treatment devices (X ray, proton, helium, carbon, and so on) are included.

Figure 4: A typical treatment room

ISBN: 978-3-95450-212-7 ISSN: 2673-5482 doi:10.18429/JACoW-CYCLOTRONS2022-WEA006

REFERENCES

[1] J.W.Xia, W.L.Zhan, B.W.Wei, *et al.*, "The heavy ion cooler-storage-ring project (HIRFL-CSR) at Lanzhou", *Nucl. Instrum. Methods A*, vol. 488, pp. 11-25, 2002. doi:10.1016/S0168-9002(02)00475-8

[2] J.C.Yang, J.Shi, W. P. Chai, J. W. Xia, Y. J. Yuan, and Y. Li, "Design of a compact structure cancer therapy synchrotron", *Nucl. Instrum. Methods A*, vol. 756, pp. 19-22, 2014. doi:10.1016/j.nima.2014.04.050

[3] W.P.Chai, J.C.Yang, *et al.*, "Stripping accumulation and optimization of HIMM synchrotron", *Nucl. Instrum. Methods A*, vol. 763, pp. 272-–277, 2014. doi:10.1016/j.nima.2014.05.117

[4] K. Noda, T. Furukawa, S. Shibuya, *et al.*, "Advanced RF-KO slow-extraction method for the reduction of spill ripple", *Nucl. Instrum. Methods A*, vol. 492, pp. 253–263, 2002. doi:10.1016/S0168-9002(02)01319-0

[5] J. Shi, J. C. Yang, J. W. Xia, R. S. Mao, and L. R. Zhou, "Heavy ion medical machine (HIMM) slow extraction commissioning", *Nucl. Instrum. Methods A*, vol. 918, pp. 76–81, 2019. doi:10.1016/j.nima.2018.11.014

ISBN: 978-3-95450-212-7 ISSN: 2673-5482 doi:10.18429/JACoW-CYCLOTRONS2022-WEBI01

AN OVERVIEW OF THE SOUTH AFRICAN ISOTOPE FACILITY (SAIF) PROJECT

I. L. Strydom, iThemba LABS, Somerset-West, South Africa

Abstract

The South African Isotope Facility (SAIF) is a new radioisotope production facility currently under construction at iThemba LABS in Cape Town and scheduled for completion in 2023.

A commercial 70 MeV proton cyclotron from IBA with a number of beam lines equipped with isotope production stations, have been installed in retrofitted concrete vaults. The facility is supported by new infrastructure and services which are being commissioned. The completion of SAIF will greatly increase the radioisotope production capability of iThemba LABS, and enable the existing Separated Sector Cyclotron (SSC) to be dedicated to nuclear research activities.

An overview of the SAIF project from the inception phase through to the construction phase is provided here, discussing all related workstreams and progress made to date. A more detailed discussion of some specific systems is given, including the design of the isotope production stations, target handling system, and a new radioactive waste management facility.

INTRODUCTION

iThemba LABS is a national facility of the National Research Foundation (NRF) in South Africa, an entity of the Department of Science and Innovation. The mandate of iThemba LABS is to operate a number of cyclotrons for purposes of conducting research in subatomic physics, producing medical radioisotopes and performing patient treatment using proton and neutron beam therapeutic protocols.

The available beam time of the facility was historically divided more-or-less equally between the above-mentioned operational mandates since its commissioning in the early 1980's. However, in recent years the ageing facility for patient treatment was no longer compatible with modern neutron/proton treatment protocols and the patient treatment service was subsequently discontinued a few years ago. Since then, the allocation of available beam time gradually became more weighted towards medical radioisotope production due to growing demand for radioisotope products from the public and private health sectors. Today, iThemba LABS is a key producer and supplier of medical radioisotopes which are distributed throughout South Africa and globally into ~60 countries. As a result of this demand growth for radioisotopes, more than 50% of beam time is currently utilised for radioisotope production.

The demand for increased beam time for subatomic physics research at iThemba LABS as well as the necessity to continue to serve the health sector both locally and globally are the main driving factors for phase 1 of the South African Isotope Facility (SAIF) project which was conceived several years ago and which started officially in 2019 when the first budget for the SAIF project was approved. The SAIF project involves the installation of a new 70 MeV cyclotron into the decommissioned patient therapy vaults at iThemba LABS and which will be dedicated to radioisotope production. This will in turn release the existing Separated Sector Cyclotron (SSC) complex to be fully dedicated to the subatomic and nuclear physics research programmes of the international scientific user base of iThemba LABS (Fig. 1).

EXISTING ACCELERATOR FACILITIES AT iThemba LABS

A number of existing accelerator facilities are currently in operation at iThemba LABS. The main facility is located at Faure near Cape Town, South Africa where the following accelerators are installed:

General Layout

- 200 MeV Separated Sector Cyclotron
- 8 MeV Solid Pole injector Cyclotron (SPC1) with internal PIG ion source for proton beams
- 8 MeV Solid Pole injector Cyclotron (SPC2) with a number of external ion sources for both light and heavy ion production
- A number of experimental beam lines dedicated to neutron production, gamma ray arrays (ALBA and Aphrodite facilities) and radiation biophysics
- K600 magnetic spectrometer for light ions
- 11 MeV self-shielded cyclotron for F-18 production
- Hotlab and cleanroom complex for chemical extraction and production of radiochemical and radiopharmaceutical products under cGMP conditions
- 3MV Tandetron accelerator and beam lines for materials research using Ion Beam Analysis (IBA) and microprobe analysis.

Additionally, a 6 MV tandem accelerator is in operation in Johannesburg, South Africa. This facility is dedicated to materials research using IBA, microprobe analysis as well as Accelerator Mass Spectrometry (AMS).

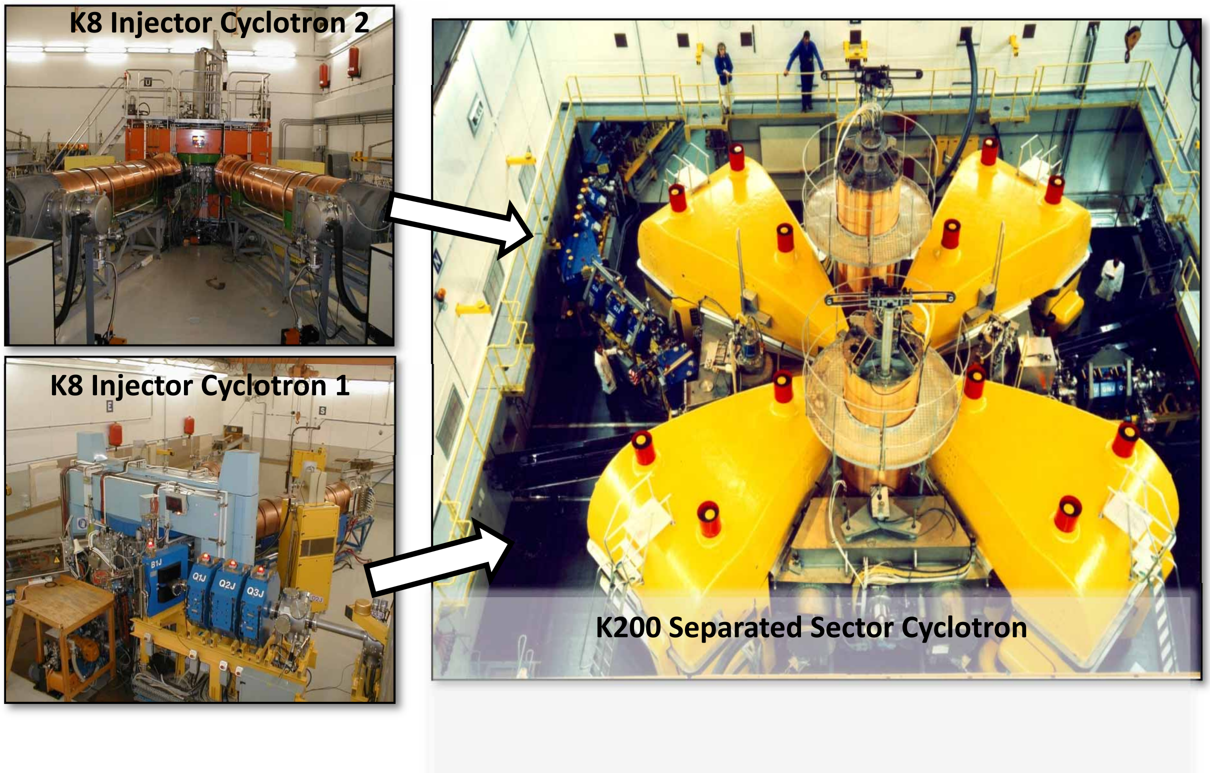

Figure 1: Photograph of the 200 MeV Separated Sector Cyclotron (SSC) and SPC1/SPC2 injector cyclotrons in Cape Town.

MOTIVATION FOR SOUTH AFRICAN ISOTOPE FACILITY (SAIF) PROJECT

The oversubscription of beam time on the existing SSC complex and the increasing interest for research with unstable isotopes led to the concept of establishing the South African Isotope Facility (SAIF) which involves in its first phase the procurement and installation of a new 70 MeV cyclotron, four beam transport lines and target stations to be dedicated to radioisotope production. Once fully commissioned, this will release approximately 50% of SSC beam time currently allocated for radioisotope production to be used for subatomic and nuclear physics research programmes of the international scientific user base of iThemba LABS.

The SAIF facility was conceptualised to be housed in the three vaults of the decommissioned patient treatment facility, where the cyclotron would be installed in the centre vault with beam transport lines leading into two adjoining target vaults on either side which will house the four target stations.

The re-purposing of the existing vaults previously used for the patient therapy programme would realise significant cost savings for the SAIF project, but also introduced some spatial constraints for the installation of equipment and radiation shielding requirements which had to be met. The general layout of the SAIF facility is shown in Fig. 2.

The first budget allocation for the SAIF project was approved in 2018 when the project formally launched. The execution of the project was planned with five major workstreams:

- 70 MeV cyclotron and beamline procurement
- Additional beamline equipment development and manufacturing
- New target stations manufacturing
- New building construction for utility services and radioactive waste disposal
- Regulatory licensing

CURRENT STATUS OF THE PROJECT

The SAIF project is currently in the construction phase with equipment procurement taking place in parallel. The status of the various workstreams is further described in detail below.

Procurement of 70 MeV Cyclotron

Following a competitive bidding process, IBA Radiopharma Solutions in Belgium was appointed to manufacture and supply a commercially available Cyclone 70P cyclotron with four beam transport lines for the SAIF facility. The C70 cyclotron can supply variable energy proton beams with energy from 30 – 70 MeV and up to 750 µA beam intensity. It has the capability to extract two beams simultaneously from two extraction ports with up to 375 µA intensity each.

A multicusp ion source can provide 10 mA of H- current for injection into the cyclotron.

ISBN: 978-3-95450-212-7 ISSN: 2673-5482 doi:10.18429/JACoW-CYCLOTRONS2022-WEBI01

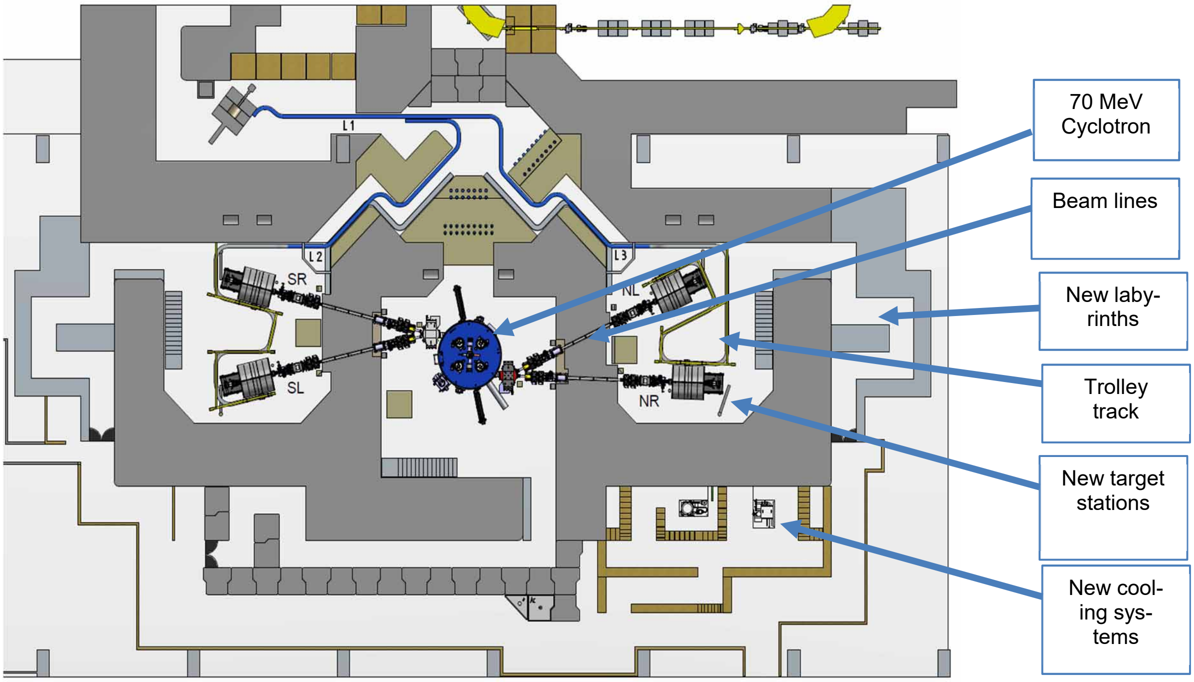

Figure 2: General layout of the SAIF facility in the three existing vaults.

The cyclotron is equipped with a 1.6 T four-sector magnet, a directly coupled RF system with 2 dees operating in the 4th harmonic mode. The four beam transport lines are fully equipped with beam diagnostics, Faraday cups and neutron shutters to isolate the cyclotron vault from the two target vaults. The C70 cyclotron successfully passed factory acceptance testing in Belgium in July 2021 and was delivered to South Africa in December 2021.

The C70 cyclotron was finally installed in the centre vault in April 2022 (Fig. 3). Due to space constraints imposed by the use of existing concrete vaults for the new facility, special logistical arrangements had to be made to install the heavy cyclotron parts inside the vaults. The vault walls extend 10m above ground level inside an existing building. In addition, the capacity of the overhead crane inside the building was insufficient to lift the heavy cyclotron parts, being the two magnet yokes weighing ~ 60 ton each.

A special temporary gantry therefore had to be constructed on the vault walls to lift the two magnet yokes over the 7 m high wall and to install them in the designated position inside the vault, as shown in Fig. 4. In addition to the beam transport line equipment supplied by IBA Radiopharma Solutions, iThemba LABS is also implementing a beam sweeper/steerer facility designed to sweep the proton beam in a circular pattern over the target surface (Fig. 5). This is required to assist with dissipation of up to 26 kW of heat from the target capsule with diameter of 54 mm.

Additional Beamline Equipment Development and Manufacturing

The beam sweeping is achieved by constructing a sweeper magnet with two H-type dipole magnets operating with 90 degrees phase difference which is placed directly in front of the target system at the end of the beam transport lines. The sweeper magnet makes use of a ceramic beam pipe inside the magnet in order to minimise the generation of Eddy currents and subsequent power losses and heat generation.

New Target Station Manufacturing

The target system is based on an in-house development of a target station design that has been in use in the existing radioisotope facility for some 25 years. The target station provides for placement of the target capsule in front of the beam using a pneumatically controlled robot arm, retrieval of the target holder at the completion of bombardment and placement of the target holder on a trolley system to transfer the target from the target station to the radiochemical process facility some 120m distant from the target vaults.

The target station furthermore provides local radiation shielding inside the target vault by using a combination of shielding elements manufactured from steel, lead and borated wax. The target station is designed with a motorised mechanism to open and close the shielding elements to allow for placement and retrieval of the target holder with the robotic arm.

The target station provides pressurised water cooling to the target capsule through a pusher arm mechanism as well as helium cooling to a vacuum window which separates the beam line vacuum from atmosphere in front of the target capsule (Fig. 6).

New Building Construction for Utility Services and Waste Disposal

Construction works are currently underway on various infrastructure modifications and additions required for the SAIF project. These include the following:

- Construction of new plant rooms for a main water-cooling system and electrical distribution (including rotary UPS systems);
- Structural modifications to the existing vaults to accommodate the new C70 cyclotron and beam transport lines, as well as to provide new entry labyrinths for radiation shielding;
- Construction of new facilities to house the various electronics, power supplies, cooling systems and control room for the C70 cyclotron;
- Construction of a new building to house the radioactive waste processing and storage facility;
- Manufacturing of the new target cooling systems;
- Installation of new ventilation systems required to maintain the specified air changes and air pressure cascades of the cyclotron and target vaults;
- Installation of the supervisory control systems for vault clearance and safety interlocking.

The structural modifications to the cyclotron and target vaults were informed by the radiation shielding requirements as dictated by the facility licencing conditions. The radiation levels inside and outside the vault areas were simulated by using the FLUKA simulation software under worst-case conditions for dose conversion factors (FLUKA option EWT74) based on data sets from ICRP74.

Figure 3: The C70 cyclotron installed in its final position.

Figure 4: Rigging of the magnet yokes into the centre vault.

ISBN: 978-3-95450-212-7 ISSN: 2673-5482 doi:10.18429/JACoW-CYCLOTRONS2022-WEBI01

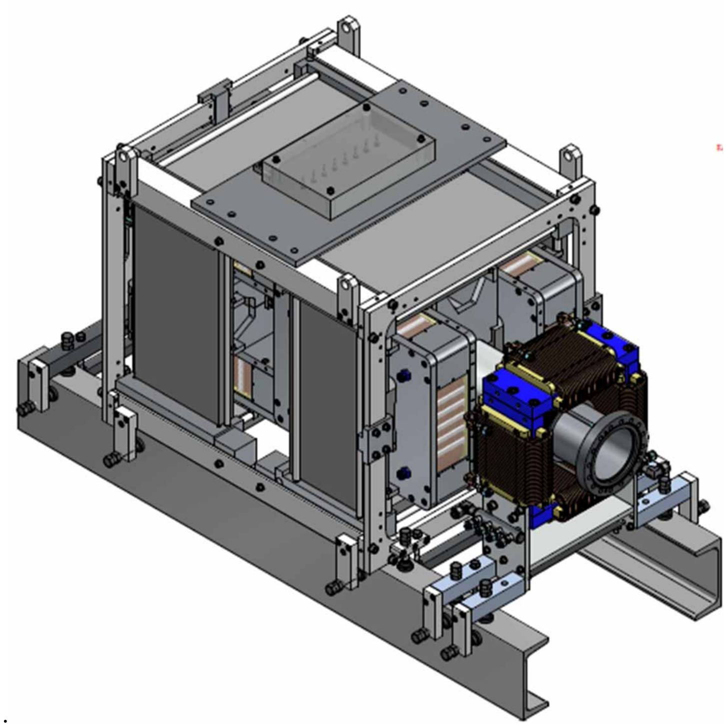

Figure 5: The beam sweeper magnet.

Figure 6: The SAIF target station showing the pneumatically controlled pusher arm and robot arm mechanisms.

Regulatory Licensing

An important aspect of the SAIF project is to obtain the necessary regulatory licenses for the new facility. In this respect, a license to import the cyclotron and beam transport line equipment was granted by the regulatory authority (Department of Health) on 8 Oct. 2019. This follows a process of basic design with safety assessment, submission of plans and designs as well as decommissioning strategies and construction reports.

Subsequently, a license to install the cyclotron and beam transport line equipment was granted on 18 Nov 2020.

Application for a license to operate the C70 cyclotron will be launched when the facility is ready for cold commissioning, when further safety case documentation will be submitted for approval.

ISBN: 978-3-95450-212-7 ISSN: 2673-5482 doi:10.18429/JACoW-CYCLOTRONS2022-WEBI01

SUMMARY

Construction and equipment installation on the South African Isotope Facility (SAIF) project are in progress. An overview of the status of the SAIF facility is provided, where progress with the installation of a new 70 MeV cyclotron and beam transport lines, manufacturing of the target stations and additional beam line equipment, and construction of buildings for utility services is reported.

Completion of the project is scheduled for early 2023 when first beam will be extracted from the cyclotron. Final site acceptance testing of the C70 cyclotron is planned for April 2023 after which production of radioisotopes can commence.

ACKNOWLEDGEMENTS

The following institutions are acknowledged:

- National Research Foundation (South Africa)
- IBA Radiopharma Solutions (Belgium)

REFERENCES

[1] G. F. Steyn *et al.*, “Development of new target stations for the South African Isotope Facility”, *J. Instruments*, vol. 2, no. 4, p. 29, 2018. doi:10.3390/instruments2040029

ISBN: 978-3-95450-212-7 ISSN: 2673-5482 doi:10.18429/JACoW-CYCLOTRONS2022-WEBI02

COMPACT ACCELERATOR BASED EPITHERMAL NEUTRON SOURCE AND ITS APPLICATION FOR CANCER THERAPY

N. Hu[†,1,2], T. Aihara[1], K. Akita[1], R. Kakino[1]. K. Nihei[1], K. Ono[1], H. Tanaka[2]
[1]Osaka Medical and Pharmaceutical University, Takatsuki-shi, Japan
[2]Kyoto University Institute for Integrated Radiation and Nuclear Science, Sennan-gun, Japan

Abstract

The world's first accelerator based epithermal neutron source for clinical boron neutron capture therapy (BNCT) was designed, developed, and commissioned between 2008 and 2010 by Sumitomo Heavy Industries in collaboration with Kyoto University at the Kyoto University Institute for Integrated Radiation and Nuclear Science. The Osaka Medical and Pharmaceutical University, Kansai BNCT Medical Center installed the same equipment in 2016. On March 11, 2020, the Japanese Ministry of Health, Labor, and Welfare approved the system as a novel medical device for the manufacture and sale of an accelerator BNCT system (NeuCure® System) and the dose calculation software (NeuCure® Dose Engine). On June 1st, 2020, the national health insurance system approved the reimbursement of these products for unresectable, locally advanced, and recurrent carcinoma of the head and neck. Commissioning tests were performed to evaluate the system before clinical use. Neutron and gamma ray distribution inside a water phantom was experimentally measured and compared with Monte Carlo simulation results. The peak thermal neutron flux inside a water phantom for a 12 cm diameter circular collimator was 1.4×10^9 n·cm^{-2}·s^{-1}. The experimental values closely matched the Monte Carlo simulation results.

INTRODUCTION

BNCT is a form of particle therapy that selectively targets cancer cells by producing high-LET particles by the nuclear reaction between a thermal neutron and a ^{10}B atom. Up until 2012, all clinical BNCT were performed using neutrons generated from a nuclear reactor. Nowadays, neutrons generated from an accelerator is increasing and more hospital-based BNCT centers are opening, worldwide [1, 2]. The NeuCure® BNCT system was installed at the Kansai BNCT Medical Center in the Osaka Medical and Pharmaceutical University, shown in Fig. 1. This is the first facility in the world to provide BNCT at a university hospital that is covered by insurance. The system installed at the Kansai BNCT Medical Center is the same type as the one installed at the Kyoto University Institute for Integrated Radiation and Nuclear Science [3, 4].

The accelerator system is a cyclotron and accelerates a proton up to an energy of approximately 30 MeV. Fast neutrons are generated when the accelerated proton strikes the beryllium target traverse through a beam shaping assembly (BSA) to reduce the energy of the neutron down to the epithermal energy range, which has been shown to be an effective energy for deep-seated tumours [5]. This paper describes the beam characterisation tests performed at the Kansai BNCT Medical center as part of the clinical commissioning of the system.

Figure 1. Image of the NeuCure® BNCT system at the Kansai BNCT Medical Center.

MATERIAL AND METHODS

NeuCure® BNCT System: Beam Characteristics

Cyclotron-based Epithermal Neutron Source Beam Model The simulation of the neutron and gamma ray distribution was performed using a general-purpose Monte Carlo particle transport simulation code system (Particle and Heavy Ion Transport code System: PHITS version 3.24 [6]). The parameters were evaluated inside a water phantom for a 12 cm diameter circular collimator. The neutron energy range was defined as 0-5×10^{-2} eV (thermal), 5×10^{-2} eV-10 keV (epithermal), and 10 keV-30 MeV (fast). Detail on the beam modelling and source information can be found elsewhere [7].

Neutron Flux Determination A common method for measuring the neutron spectrum is metal activation, with gold and indium being frequently used for the measurement of thermal and fast neutrons, respectively. An acrylic phantom filled with distilled water was used. A 10 cm long gold wire (diameter of 0.25 mm with a 99.95% purity, The Nilaco Corporation) was placed along the central axis and off-axis at a depth of 2 cm inside the water phantom. As gold reacts to both thermal and epithermal neutrons, measurements were performed with and without a cadmium cover to shield the thermal neutrons. A total of 0.3 C for the gold wire and 0.6 C for the gold wire with cadmium cover was delivered. After irradiation, the gold wire was

† naonori.ko@ompu.ac.jp

ISBN: 978-3-95450-212-7 ISSN: 2673-5482 doi:10.18429/JACoW-CYCLOTRONS2022-WEBI02

cut into small pieces (approximately 5 mm in length) and the gamma rays emitted from the activated gold was measured using a germanium detector.

The reaction rate per unit charge of the gold sample was calculated using the expression below.

$$R = \frac{\lambda N}{\epsilon\gamma e^{-\lambda T_c}(1-e^{-\lambda T_m})\sum_{i=1}^{n}\left(\frac{Q_i}{\Delta t}(1-e^{-\lambda\Delta t})e^{-\lambda(n-i)\Delta t}\right)},$$

where ϵ is the detection efficiency of the detector of the gamma rays emitted from ^{198}Au, γ is the gamma ray emission rate from ^{198}Au decay, λ is the decay constant of ^{198}Au, Tc is the time from the irradiation to the start of the measurement, Tm is the measurement time, N is the peak count due to the detector measured gamma rays emitted from ^{198}Au and Q_i is the electric charge irradiated on the target at each interval, Δt.

Indium foil with a 99.99% purity and dimensions of 3 mm in diameter by 0.1 mm thickness was used to measure the fast neutrons. The (n, n') process excites the ^{115}In resulting in ^{115m}In, which decays to the ground state by emitting a 340 keV gamma ray. As indium also reacts to thermal neutrons, the indium foils were covered in cadmium to shield the low energy neutrons.

Gamma Ray Dose Rate Determination Thermoluminescence dosimeters (TLD) were used for the measurement of the gamma ray dose rate. A special-ordered BeO powder TLD enclosed in a quartz glass capsule was used to reduce the thermal neutron sensitivity. TLDs were placed along the central axis and off-axis at a depth of 2 cm inside the water phantom. Measurements were performed with the 12 cm diameter circular collimator.

RESULTS AND DISCUSSIONS

The central axis and off-axis thermal neutron distribution inside the water phantom are shown in Figs. 2 and 3, respectively. The simulation results closely matched the experimentally determined values. For the 12 cm diameter circular collimator, the peak of the thermal neutron flux inside the water phantom occurred at a depth of around 2 cm with a value of 1.4×10^9 n·cm^{-2}·s^{-1}. With this level of neutron flux, the irradiation time can be kept within 1 hour [8].

The central axis fast neutron distribution measured with indium is shown in Fig. 4. The gamma ray dose rate along the central axis and off-axis is shown in Figs. 5 and 6, respectively. The distribution closely resembled the thermal neutron distribution, which indicated most gamma rays detected inside the water phantom was due to the ^{1}H(n,γ)^{2}H reaction.

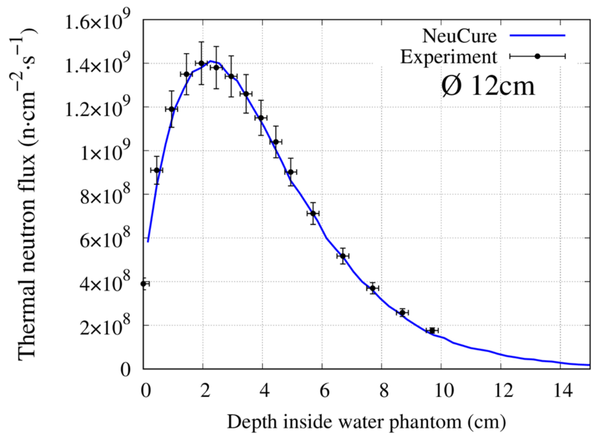

Figure 2. Thermal neutron distribution inside the water phantom along the beam central axis for the 12 cm diameter collimator.

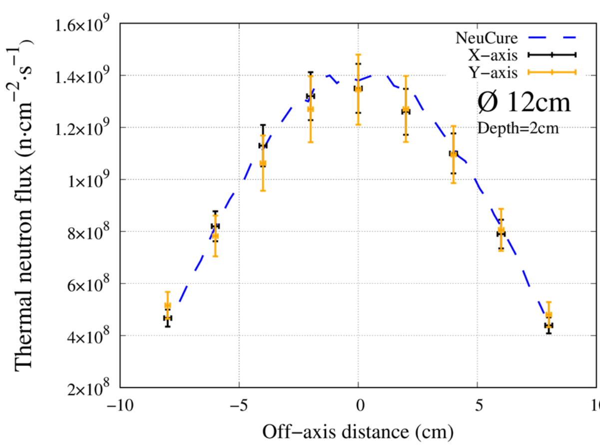

Figure 3. Off-axis thermal neutron distribution inside the water phantom at a depth of 2 cm for the 12 cm diameter collimator.

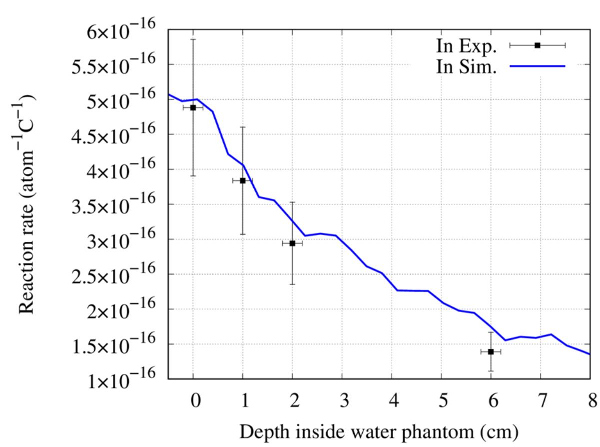

Figure 4. Fast neutron distribution along the beam central axis for the 15 cm diameter collimator.

ISBN: 978-3-95450-212-7 ISSN: 2673-5482 doi:10.18429/JACoW-CYCLOTRONS2022-WEBI02

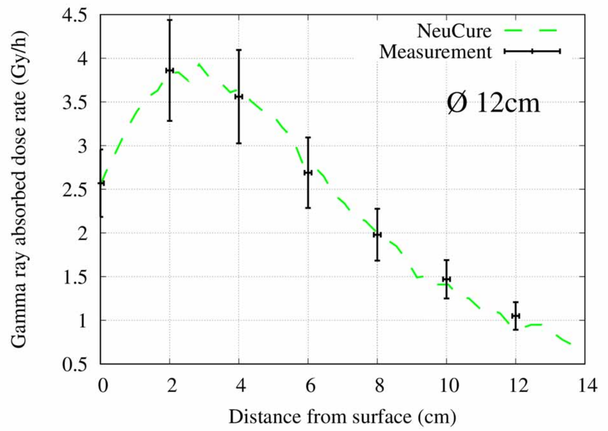

Figure 5. Gamma ray dose rate distribution along the beam central axis for the 12 cm diameter collimator.

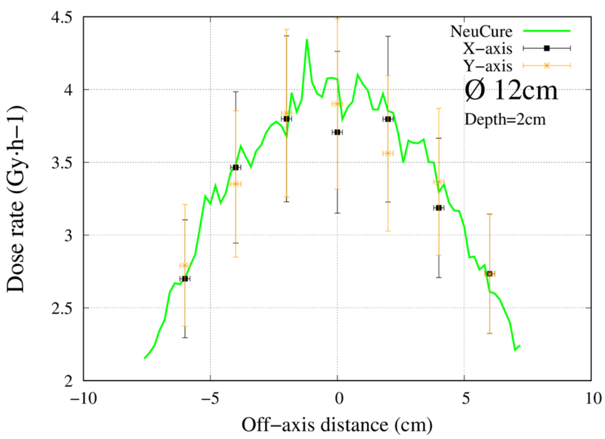

Figure 6. Off-axis gamma ray dose rate at a depth of 2 cm inside the water phantom for the 12 cm diameter collimator.

CONCLUSION

The world's first clinical accelerator based epithermal neutron source developed by Sumitomo Heavy Industries was installed at the Kansai BNCT Medical Center and performance tests were undertaken to verify the system before clinical use. The neutron and gamma ray distribution inside a water phantom was verified by experimental measurements and Monte Carlo simulations. The peak thermal neutron flux inside the water phantom for the 12 cm diameter circular collimator was measured to be 1.4×10^{9} $n{\cdot}cm^{-2}{\cdot}s^{-1}$. Using this accelerator system, patients can receive insurance covered BNCT in Japan for head and neck cancer.

ACKNOWLEDGEMENT

The authors would like to thank Sumitomo Heavy Industries Ltd., for their assistance in the beam modelling process.

REFERENCES

[1] A. J. Kreiner, J. Bergueiro, D. Cartelli, *et al.,* "Present status of Accerelerator-Based BNCT", *Reports Pract. Oncol. Radiother.,* vol. 21, pp. 95–101, 2016. doi:10.1016/j.rpor.2014.11.004

[2] Y. Kiyanagi, Y. Sakurai, H. Kumada, and H. Tanaka, "Status of accelerator-based BNCT projects worldwide", *AIP Conf. Proc.*, vol. 2160, p. 050012, 2019. doi:10.1063/1.5127704

[3] H. Tanaka, Y. Sakurai, M. Suzuki, *et al.,* "Experimental verification of beam characteristics for cyclotron-based epithermal neutron source (C-BENS)", *App.l Radiat. Isot*., vol. 69, pp.1642-1645, 2011. doi:10.1016/j.apradiso.2011.03.020

[4] T. Mitsumoto, S. Yajima, H. Tsutsui, *et al.,* "Cyclotron-based neutron source for BNCT", *AIP Conf. Proc*., vol. 1525, pp. 319–322, 2013. doi:10.1063/1.4802341

[5] J. C. Yanch, X. L. Zhou, and G. Brownell, "A Monte Carlo investigation of the dosimetric properties of monoenergetic neutron beams for neutron capture therapy", *Radiat Res*. vol. 126, pp. 1–20, 1991. doi:10.2307/3578165

[6] T. Sato, Y. Iwamoto, S. Hashimoto, *et al.,* "Features of Particle and Heavy Ion Transport code System (PHITS) version 3.02", *J. Nucl. Sci. Technol*., vol. 55. pp. 684–690, 2018. doi:10.1080/00223131.2017.1419890

[7] N. Hu, H. Tanaka, R. Kakino, *et al.,* "Evaluation of a treatment planning system developed for clinical boron neutron capture therapy and validation against an independent Monte Carlo dose calculation system", *Radiat. Oncol.,* vol. 16, pp. 1–13, 2021. doi:10.1186/s13014-021-01968-2

[8] International Atomic Energy Agency. *Current Status of Neutron Capture Therapy*, Vienna: IAEA-TECDOC-1223, 2001. https://www-pub.iaea.org/MTCD/Publications/PDF/te_1223_prn.pdf

ISBN: 978-3-95450-212-7 ISSN: 2673-5482 doi:10.18429/JACoW-CYCLOTRONS2022-WEBO01

BENCH TO BEDSIDE: TRANSLATIONAL NUCLEAR MEDICINE RESEARCH AND CLINICAL THERANOSTICS IN PUMCH

Li Huo†, Peking Union Medical College Hospital, Beijing, China

Abstract

Peking Union Medical College Hospital (PUMCH) was founded in 1921. In 1958, PUMCH established the first nuclear medicine (NM) department in the country which eventually became the most comprehensive unit of nuclear medicine in China. The department has topped the ranking in "China's Hospital Rankings" for consecutively 7 years and has done great efforts in translational research of nuclear medicine and molecular imaging. By now, over 10 isotopes and 100 radiopharmaceuticals are employed to support routine clinical work and more than 50 research projects as well, involving theranostic and preclinical exploration. These research achievements were highly glorified in the top international conferences and journals. The department not only keeps up with the advanced medical technologies in the world but also indulges in promoting novel technology applications in domestic hospitals. After a 60 years journey, the department of nuclear medicine in PUMCH with her superior capability will continuously lead NM exploration and development in China. The department will begin another new and prosperous journey in the new era.

INTRODUCTION OF PUMCH AND NUCLEAR MEDICINE DEPARTMENT

PUMCH is renowned both at home and abroad for its comprehensive disciplines, high technical capabilities, outstanding specialties, and integrated disciplinary strengths. Undergirded by a commitment to professional ethics and a rigorous academic attitude, each department indulges in providing the best possible medical service and being a hospital and department that is nothing less than the best in China and internationally renowned. Depending on the constant efforts of generations, PUMCH has been leading the advances of modern medical sciences in China, standing Top 1 every year from 2009 to 2022 in the Chinese best hospitals ranking.

PUMCH established the nuclear medicine department in 1958, which was also the first one in the mainland of China. Now, the department is the most comprehensive unit of nuclear medicine in China. It consists of 7 PET and 10 SPECT scanners for imaging diagnosis, 1 ward with 10 beds for nuclide therapy, radioimmunoassay lab, and radiochemistry labs. Each year, more than 30 thousand patients received NM service and 100 thousand samples were tested in our department. More than 10 isotopes and 90 radiopharmaceuticals are employed to support clinical work and nearly 50 research projects as well. As shown in Fig. 1, over 60 members now work and study every day in the department. Our department eventually made the history of nuclear medicine science in the country and takes the leading place in medical care, teaching, and scientific research in nuclear medicine. We have gained nuclear medicine top 1 for consecutively 7 years since NM was recruited in "China's Hospital Rankings" in 2014.

Figure 1: Faculties and staffs of the PUMCH nuclear medicine department in 2021.

TRANSLATIONAL RESEARCH IN NUCLEAR MEDICINE DEPARTMENT

The UM department also attempts to do great efforts in translational research of nuclear medicine. For example, we attempted to use ^{188}Re, ^{89}Zr, ^{64}Cu, and ^{86}Y labeling novel precursors and endothelial progenitor cells for preclinical theranostic research [1-3], see Fig. 2 to 4. These

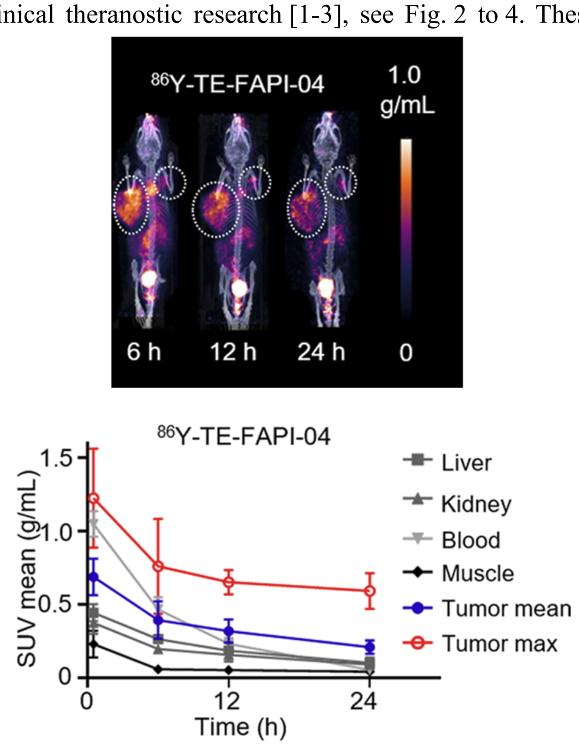

Figure 2: PET/CT MIP images and time activity curve of ^{86}Y-TE-FAPI-04 for late-time-point cancer diagnosis [1].

† huoli@pumch.cn

ISBN: 978-3-95450-212-7 ISSN: 2673-5482 doi:10.18429/JACoW-CYCLOTRONS2022-WEB001

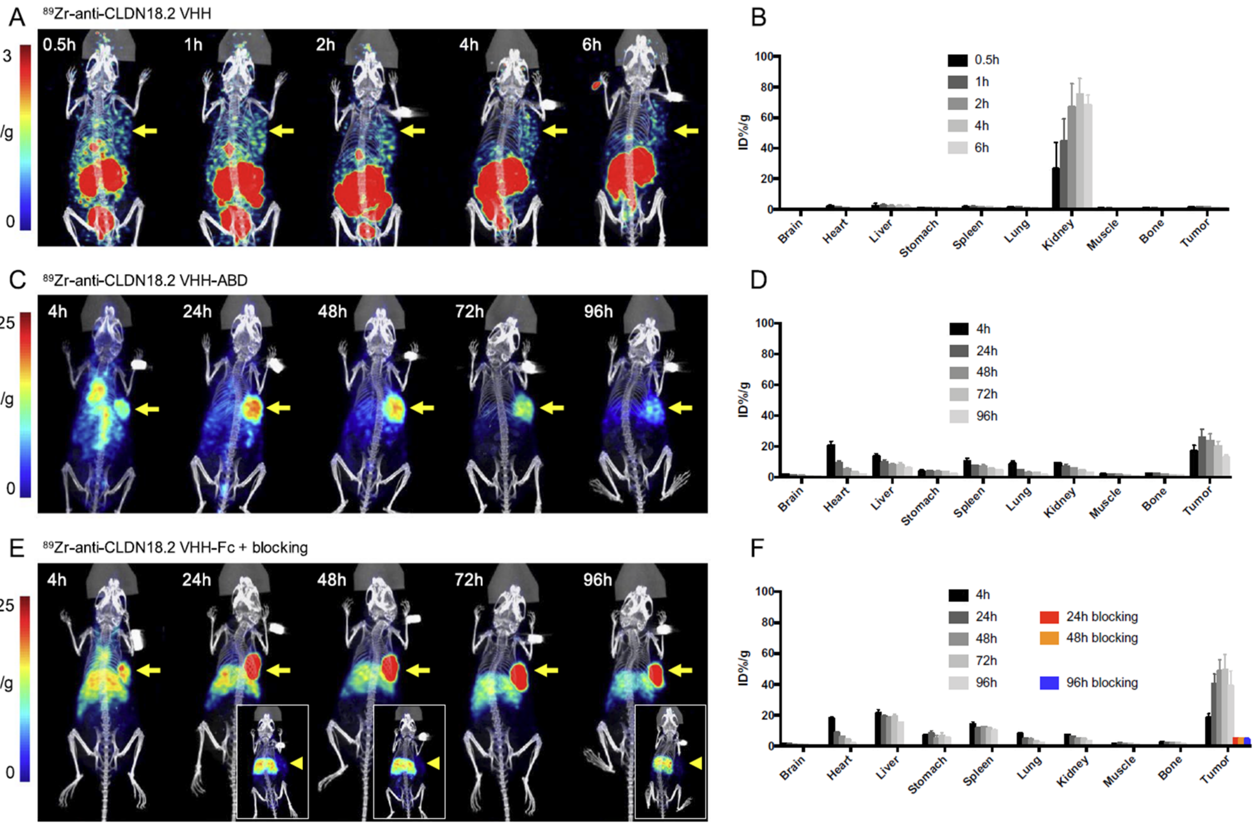

Figure 3: ^{89}Zr- anti-CLDN18.2 for evaluating CLDN18.2 expression in gastric cancer [2].

preclinical research achievements were highly glorified in the top international conferences and journals. However, the advantages of these glories are present only in so far as they have been proven to be valuable approaches to diagnosing and treating diseases. Therefore, translational medicine research must be done with these preclinical results.

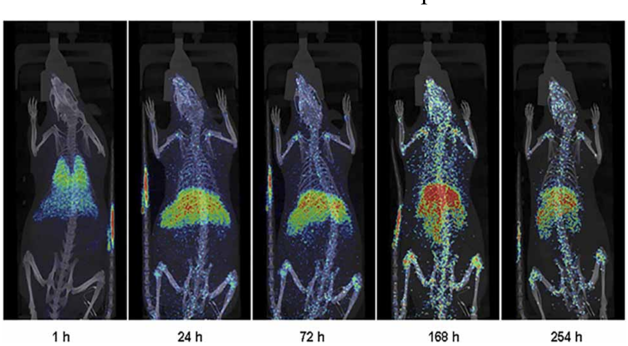

Figure 4: Whole-body microPET/CT MIPs of ^{89}Zr-oxine EPCs in health rats [3].

The conventional translational research in our department is following international advances timely and effective. For example, about 40 years of serial translational research on somatostatin receptors. From technetium to Gallium labeling, from imaging to therapy, from agonist to antagonist, we followed the international steps in this area. Some research was published in the Journal of Nuclear Medicine, and some even as a featured article and cover image [4-5]. These confirm authoritatively the quality and innovation of our research work.

APPLICATION OF TRANSLATIONAL RESEARCH IN CLINIC

In addition to conventional translational research, we indulge in giving hand to clinicians when they meet difficult cases in PUMCH. As the best hospital in China, The PUMCH has always played a leading role in the diagnosis and treatment of complex, severe, and rare diseases. For example, ^{18}F-MFBG illustrates more sensitivity and specificity than ^{123}I-MIBG in diagnosing primary pheochromocytoma and metastasis [6-7]. ^{177}Lu TATE is used for the patient with advanced and cureless GEP NET [8-9], as shown in Fig. 5. The largest sample size cohort study on

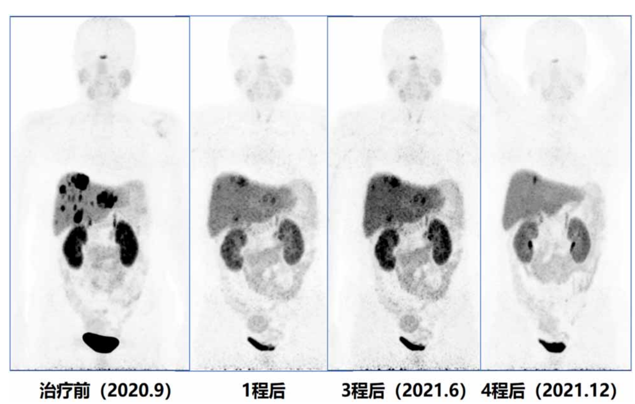

Figure 5: ^{177}Lu TATE for patient with advanced GEP NET within the 4 cycles of treatment. Left to right: before treatment, and after 1 course, and 3 and 4 courses of treatment.

insulinoma detection and localization with GLP-1 receptor imaging was conducted in our department [10], see Fig. 6. Aldosterone-producing adenoma diagnosis with CXCR4 receptor imaging could help clinicians [11-13]. We also made a lot of effort in establishing and popularizing PYP imaging for ATTR-CM in China, as well as exploring the frontiers in myocardium amyloydosis, such as improving ATTRm diagnosis sensitivity and AL-CM risk assessment [14-15].

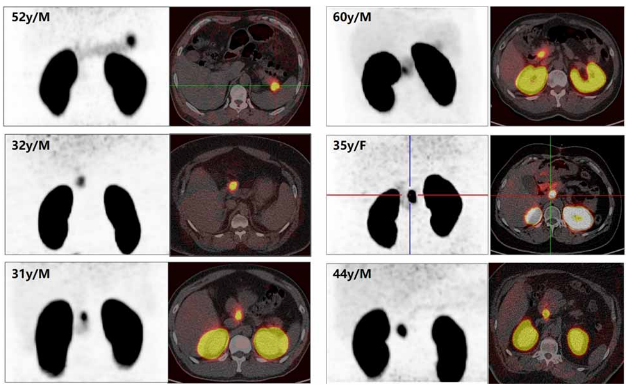

Figure 6: ^{68}Ga-NOTA-Exendin-4 for detecting localized insulinoma.

Now, we set up a translational medicine corporation platform with the clinical departments in PUMCH. We also establish close collaboration with universities, institutions, companies, and the government to support NM translational research in PUMCH, such as nuclide production, radiopharmaceuticals, image data analysis, and quality control. All these platforms lay a foundation for comprehensive clinical resources, and technical advantages result in innovation for translational nuclear medicine in our department. This is the entire research journey of a self-dependent theranostic tracer. In order to deal with the difficulties we meet in renal cell carcinoma treatment, we focus on the CAIX target. Synthesized tracer and labeled. After preclinical research work, including cells and animals, we began the clinical trial. By now, the results are very promising.

CONCLUSION

From bench to bedside, the NM department shows great advantages in translational medicine research and effective outcomes. PUMCH nuclear medicine department will still strive forward to in-depth studies for further exploration and improvement.

REFERENCES

[1] J. Ding, M. Xu, J. Chen, P. Zhang, L. Huo, Z. Kong, and Z. Liu, "^{86}Y-labeled albumin-binding fibroblast activation protein inhibitor for late-time-point cancer diagnosis", *Mol. Pharmaceutics*, vol. 19, no. 9, pp. 3429-3438, Sep. 2022. doi:10.1021/acs.molpharmaceut.2c00579

[2] G. Hu, W. Zhu, Y. Liu, Y. Wang, Z. Zhang, S. Zhu, W. Duan, P. Zhou, C. Fu, F. Li, and L. Huo, "Development and comparison of three ^{89}Zr-labeled anti-CLDN18.2 antibodies to noninvasively evaluate CLDN18.2 expression in gastric cancer: a preclinical study", *Eur. J. Nucl. Med. Mol. Imaging*, vol. 49, no. 8, pp. 2634-2644, July 2022. doi:10.1007/s00259-022-05739-3

[3] Y. Liu, X. Zhao, J. Ding, Y. Xing, M. Zhou, X. Wang, W. Zhu, L. Huo, and J. Yang, "Evidence of accumulated endothelial progenitor cells in the lungs of rats with pulmonary arterial hypertension by ^{89}Zr-oxine PET imaging", *Mol. Ther. Methods Clin. Dev.*, vol. 17, pp. 1108-1117, June 2020. doi:10.1016/j.omtm.2020.04.021

[4] W. Zhu, Y. Cheng, R. Jia, H. Zhao, C. Bai, J. Xu, S. Yao, and L. Huo, "A prospective, randomized, double-blind study to evaluate the safety, biodistribution, and dosimetry of ^{68}Ga-NODAGA-LM3 and ^{68}Ga-DOTA-LM3 in patients with well-differentiated neuroendocrine tumors", *J. Nucl. Med.*, vol. 62, no. 10, pp. 1398-1405, Oct. 2021. doi:10.2967/jnumed.120.253096

[5] W. Zhu, Y. Cheng, X. Wang. S. Yao, C. Bai, H. Zhao, R. Jia, J. Xu, and L. Huo, "Head-to-head comparison of ^{68}Ga-DOTA-JR11 and ^{68}Ga-DOTATATE PET/CT in patients with metastatic, well-differentiated neuroendocrine tumors: a prospective study", *J. Nucl. Med.*, vol. 61, no. 6, pp. 897-903, June 2020. doi:10.2967/jnumed.119.235093

[6] P. Wang, T. Li, Z. Liu, M. Jin, Y. Su, J. Zhang, H. Jing, H. Zhuang, and F. Li, "[^{18}F] MFBG PET/CT outperforming [^{123}I] MIBG SPECT/CT in the evaluation of neuroblastoma", *Eur. J. Nucl. Med. Mol. Imaging*, May 2023. doi:10.1007/s00259-023-06221-4

[7] P. Wang, T. Li, Y. Cui, H. Zhuang, F. Li, A. Tong, and H. Jing, "^{18}F-MFBG PET/CT is an effective alternative of ^{68}Ga-DOTATATE PET/CT in the evaluation of metastatic pheochromocytoma and paraganglioma", *Clin. Nucl. Med.*, vol. 48, no. 1, pp. 43-48, Jan. 2023. doi:10.1097/RLU.0000000000004447

[8] Y. Jiang, Q. Liu, G. Wang, H. Sui, R. Wang, J. Wang, J. Zhang, Z. Zhu, and X. Chen, "Safety and efficacy of peptide receptor radionuclide therapy with ^{177}Lu-DOTA-EB-TATE in patients with metastatic neuroendocrine tumors", *Theranostics*, vol. 12, issue 15, pp. 6437-6445, Sep. 2022. doi:10.7150/thno.77219

[9] Q. Liu, J. Zang, H. Sui, J. Ren, H. Guo, H. Wang, R. Wang, O. Jacobson, J. Zhang, Y. Cheng, Z. Zhu, and X. Chen, "Peptide receptor radionuclide therapy of late-stage neuroendocrine tumor patients with multiple cycles of ^{177}Lu-DOTA-EB-TATE", *J. Nucl. Med.*, vol. 62, no. 3, pp. 386-392, Mar. 2021. doi:10.2967/jnumed.120.248658

[10] Y. Luo, Q. Pan, S. Yao, M. Yu, W. Wu, H. Xue, D. O. Kiesewetter, Z. Zhu, F. Li, Y. Zhao, and X. Chen, "Glucagon-like peptide-1 receptor PET/CT with ^{68}Ga-NOTA-Exendin-4 for detecting localized insulinoma: a prospective cohort study", *J. Nucl. Med.*, vol. 57, no. 5, pp. 715-720, May 2016. doi:10.2967/jnumed.115.167445

[11] J. Ding, A. Tong, Y. Zhang, J. Wen, H. Zhang, M. Hacker, L. Huo, and X. Li, "Functional characterization of adrenocortical masses in nononcologic patients using ^{68}Ga-pentixafor", *J. Nucl. Med.*, vol. 63, no. 3, pp. 368-375, Mar. 2022. doi:10.2967/jnumed.121.261964

[12] J. Ding, Y. Zhang, J. Wen, H. Zhang, H. Wang, Y. Luo, Q. Pan, W. Zhu, X. Wang, S. Yao, M. Kreissl, M. Hacker, A. Tong, L. Huo, and X. Li, "Imaging CXCR4 expression in patients with suspected primary hyperaldosteronism", *Eur. J. Nucl. Med. Mol. Imaging*, vol. 47, pp. 2656-2665, Oct. 2020. doi:10.1007/s00259-020-04722-0

[13] J. Ding, A. Tong, M. Hacker, M. Feng, L. Huo, and X. Li, "Usefulness of ^{68}Ga-Pentixafor PET/CT on diagnosis and management of cushing syndrome", *Clin. Nucl. Med.*, vol. 47, no. 8, pp. 669-676, Aug. 2022. doi:10.1097/RLU.0000000000004244

[14] X. Wang, Y. Guo, Y. Gao, C. Ren, Z. Huang, B. Liu, X. Li, L. Chang, K. Shen, H. Ding, H. Zhang, Z. Tian, M. Hacker, S. Zhang, Y. Wang, J. Li, X. Li, and L. Huo, "Feasibility of ^{68}Ga-labeled fibroblast activation protein inhibitor PET/CT in light-chain cardiac amyloidosis", *JACC Cardiovasc Imaging,* vol. 15, no. 11, pp. 1960-1970, Nov. 2022. doi:10.1016/j.jcmg.2022.06.004

[15] X. Wang, Y. Wang, J. Li, L. Huo, and S. Zhang, "Noninvasive detection of cardiac amyloid with ^{11}C-Pittsburgh compound B PET/CT and ^{99m}Tc-PYP scintigraphy", *Clin. Nucl. Med.,* vol. 46, no. 9, pp. 776-778, Sep. 2021. doi:10.1097/RLU.0000000000003665

ISBN: 978-3-95450-212-7 ISSN: 2673-5482 doi:10.18429/JACoW-CYCLOTRONS2022-WEB003

POSITRON EMITTERS PRODUCED FROM NATURALLY OCCURRING TARGETS

T. W. Leadbeater†, A. Buffler, T. Hutton, M. van Heerden, Metrological and Applied Sciences University Research Unit, Department of Physics, University of Cape Town, South Africa

Abstract

Short lived positron emitters are used as flow following tracer particles in the study of dynamic processes within physics and engineering applications. For full representation of the materials of interest, tracer particles must be activated with proton rich radionuclides utilising reactions on their naturally abundant isotopic content. Cyclotron accelerated alpha particle beams incident upon (^{16}O) oxygen rich targets have been investigated in producing the positron emitter ^{18}F within naturally occurring materials.

Simulations and numeric calculations of the beam conditions are used to maximise the activation yield and minimise heat load by carefully placing the Bragg peak in relation to the water-cooled target. Corresponding to the target thickness, the 100 MeV extraction energy is degraded to match a broad resonance in ^{18}F production around 35 MeV, while maintaining energy above the 18 MeV threshold. Beam currents below 1 microamp resulted in typical ^{18}F yields of 1 - 2 mCi within spherical SiO_2 targets of diameters 1 - 10 mm, ideal for envisaged application studies.

INTRODUCTION

Positron emitting species are used in the non-invasive investigation and radiological imaging of dynamic physical and engineering systems, and those of industrial interest. Materials representation is critical in these applications, requiring the positron emitting species to be produced within naturally occurring materials as it is infeasible to use isotopically enriched targets for this purpose. Production of the medically significant positron emitting radioisotopes uses a range of different target systems and natural or isotopically enriched targets. The focus of this article is on ^{18}F production with naturally occurring solid targets. Production of ^{18}F and other isotopes within the context of this work are summarised in Table 1.

The predominant production of ^{18}F (110 minute half-life) results in free $^{18}F^-$ ions in aqueous solution (the use of gaseous targets is excluded in this discussion), with the majority of conventional global production prepared by irradiating ^{18}O-water targets. The resultant solution can be processed chemically, leading to the vector molecules of diagnostic imaging (including for example 18-fluorodeoxyglucose (^{18}FDG)), or other materials used as radiological tracers. Similarly, ^{68}Ge offers a convenient radiochemical synthesis route, being produced from a solid target loaded onto a SnO_2 based separation column. The long lived (271 day half-life) ^{68}Ge decays via electron capture to the short lived ^{68}Ga (68 minute half-life) which collects as free $^{68}Ga^{3+}$ ions in liquid form within the column. In the cases of both $^{18}F^-$ and $^{68}Ge^{3+}$, the ions can be extracted, concentrated, and processed radiochemically to produce tracer substances and radiopharmaceuticals as required by the imaging application in question. These techniques have been utilised in imaging physical and industrial systems with success, however they suffer from questionable species representation and often cannot survive the harsh conditions (e.g., temperatures, pressures, and chemical environment) they are subjected to in such devices.

Table 1: Reactions and Targets (adapted from Ref. [1])

Reaction	Target	State, % abundance	Energy range [MeV]
$^{18}O(p, n)^{18}F$	$H_2{}^{18}O$, $^{18}O_2$	Liquid, 0.2	18 – 4
$^{16}O(^3He, p)^{18}F$	$^{nat}H_2O$	Liquid, 99.7	15 – 1
$^{16}O(^3He, n)^{18}Ne \rightarrow {}^{18}F$			40 – 15
$^{16}O(\alpha, np)^{18}F$	$^{nat}H_2O$,	Liquid /	40 – 20
$^{16}O(\alpha, 2n)^{18}Ne \rightarrow {}^{18}F$	$^{nat}SiO_2$	Solid, 99.7	
$^{16}O(\alpha, d)^{18}F$			
$^{40}Ca(\alpha, p)^{43}Sc$	^{nat}Ca	Solid, 96.9	~ 50
$^{40}Ca(\alpha, n)43Ti \rightarrow 43Sc$			
$^{nat}Ga(p, xn)^{68}Ge$	^{nat}Ge	Solid, 60.1	< 66

Ideally, for applications in industrial systems, tracer materials produced from the bulk materials of interest are required, such that the imaging or other measurement is truly non-invasive. To this end, the production of ^{18}F in naturally occurring solid targets has been utilised. At the University of Birmingham, UK, the ^3He reactions are utilised, with ^3He beam of 35 MeV energy and ~ 5 µA beam current. Under these conditions the Birmingham MC40 cyclotron can produce up to 1.5 GBq / 40 mCi of ^{18}F activity in 3 ml of ($^{nat}H_2O$) water for radiochemical tracer production, and similar activity on solid targets containing sufficient oxides [1]. The $^{18}O(p, n)^{18}F$ reaction is used when preparing ^{18}F in solution to be processed chemically.

The University of Cape Town has established a positron imaging facility used for the study of physical, engineering, and industrial applications on the National Research Foundation (NRF) accelerator facility iThemba LABS (iThemba Laboratory for Accelerator Based Sciences) [2]. The primary tracer isotope used has been ^{68}Ga, produced from commercial $^{68}Ge/^{68}Ga$ radioisotope generators manufactured by iThemba LABS. The ^{68}Ge is extracted and radiochemically treated to produce a wide range of representative tracer materials, often starting from an ion-exchange resin polymer core and modifying the density and surface properties to match those characteristics required by the application and research questions [3]. Recently, ^{18}F has been extracted from commercial medical supplies of

† Tom.Leadbeater@uct.ac.za

ISBN: 978-3-95450-212-7 ISSN: 2673-5482 doi:10.18429/JACoW-CYCLOTRONS2022-WEB003

^{18}FDG and used successfully in radiochemically labelling the surface of solid materials for similar applications [4].

For the direct activation of solid materials of industrial interest, we turn to the alpha particle induced reactions on oxide bearing targets utilising the available beams accelerated at iThemba LABS. Fig. 1 shows the cross-sections for the different reaction channels between alpha particles and oxygen-16 up to 100 MeV beam energy. The ^{18}F producing reactions are highlighted in red, having a threshold at 18 MeV and a broad resonance peaking at around 0.1 barn at 35 MeV. The competing reactions consist mostly elastic and inelastic scattering, and capture reactions leading to short lived (< 2.5 minute half-lives) or stable end products.

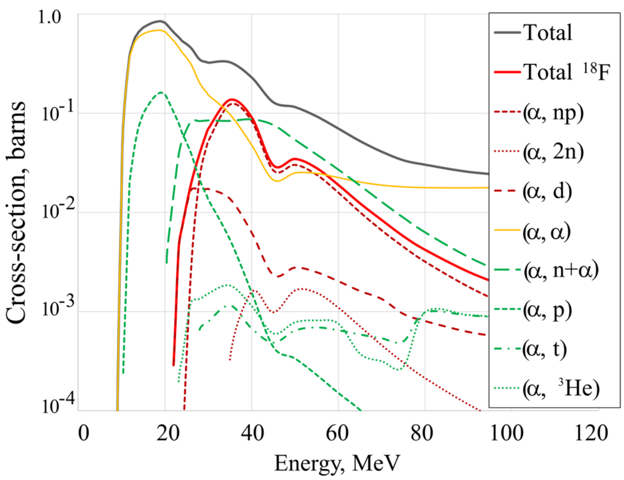

Figure 1: Interaction cross-sections for ^{16}O(α, x) [5].

BEAMLINE CONSIDERATIONS

For irradiation, helium ions are produced in the ECR ion source and accelerated to 8 MeV using the solid pole injector cyclotron. The beam is then injected into the $k = 200$ Separated Sector Cyclotron (SSC) of iThemba LABS and accelerated to 100 MeV. Following extraction of the beam from the SSC, it is directed through a set of beam delivery lines using a $k = 100$ switching magnet and delivered to horizontal target station 1. The target system consists of a target holder designed to hold the target capsule in the irradiation position and to provide cooling in the form of water circulation. The target capsule contains the material to be irradiated, in this case in the form of SiO_2 based glass beads of diameters ranging from 1 – 10 mm. The target capsule, mounted in the holder, and target holder are manipulated robotically to place them inside target station 1, which provides the interface between the beam delivery line vacuum and water-cooled environment of the target volume. In passing from the beamline vacuum to the target material the beam traverses structural materials in the form of entrance/exit windows and the cooling layers. The beam exits the vacuum through two 25 µm Havar foils (ICRU-470 / UNS R30004) separated by a 10 mm helium gas flow maintained at 1.2 bar pressure. A 4.0 mm air gap separates the final Havar exit window and a 0.5 mm thick aluminium layer serving as the entrance window to target station 1. Inside the target station a circulating water flow at 10 bar pressure and 30 l/min flow rate cools the target holder, capsule and aluminium beam stop positioned behind the target capsule. In this work a perforated target capsule was used, allowing the flow of cooling water into the capsule, and immersing the target spheres. The direct contact of coolant with the target serves two purposes: to increase efficiency of heat removal from the material, and to agitate and/or rotate the targets increasing the effective irradiation area. A schematic of the layers the beam passes through in reaching the beam stop is shown in Fig. 2.

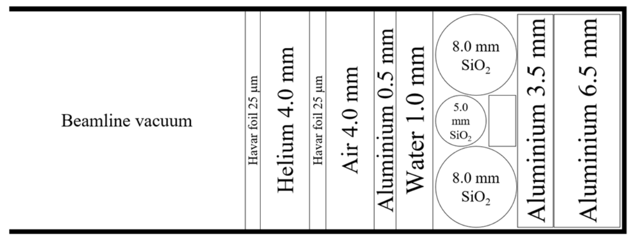

Figure 2: Target stack and material layers.

Numerical modelling for the target stack described above has been used to calculate the residual energy and energy deposition curves shown in Fig. 3. The perforated target capsule has not been included, assuming that the beam passes unhindered through this layer apart from the occupying water. The model proceeds by calculating successive energy loss per 10 µm linear path length through the given material for the current energy of the beam at that position. The beam energy is calculated using a linear interpolation between entries in the stopping power tables taken from the NIST stopping power and range tables for helium ions [6].

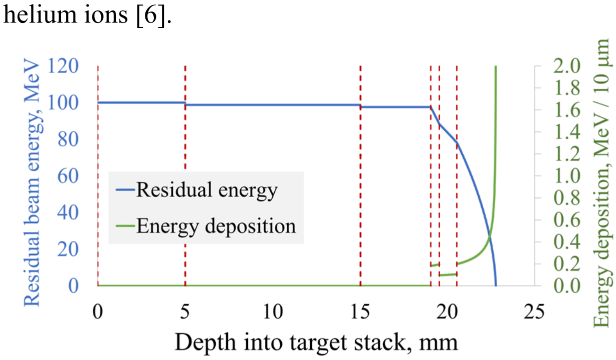

Figure 3: Energy and energy loss per 10 µm linear depth.

The numerical modelling is consistent with a Monte Carlo approach constructed using SRIM/TRIM. Fig. 3 shows the residual energy (MeV) (blue curve) defined as the beam energy remaining after traversing the given thickness of material in the target stack, where zero is defined as the edge of the beamline vacuum and the initial energy is 100 MeV. The energy deposition per unit 10 µm linear path length is shown on the same horizonal scale (green curve), illustrating the layers where energy deposition is enhanced due to materials differences (density and proton number) between layers, the Bragg peak near the end of the particle range is clearly visible. The boundaries between target stack layers are shown in red.

ISBN: 978-3-95450-212-7 ISSN: 2673-5482 doi:10.18429/JACoW-CYCLOTRONS2022-WEB003

TARGET CONSIDERATIONS

It is useful to consider the energy and energy loss in more detail within the SiO_2 target material, for the beam having already traversed the dead layers of the target stack. These data are presented in Fig. 4, where the depth is now measured relative to the front surface of the target and the residual beam energy entering the target is approximately 80 MeV from a 100 MeV extraction. Under these conditions the maximum linear penetration depth of the beam into the target is around 2.3 mm. In Fig. 4 the energy loss curve is shown as a proxy to heat deposition by the beam, with the majority of heating occurring within the Bragg peak at the end of the trajectory. The expected ^{18}F yield is shown as the red curve, calculated by convolving the microscopic cross sections for production in Fig. 1 with the beam energy at the given depth within the target. The yield is given in arbitrary units, where calibration to absolute units depends on target density and beam conditions and is left as further work. The grey shaded region illustrates the region where the majority of activation is produced (the resonance peak shown by the dotted line), with the beam energy dropping below the threshold limit for production (dotted line) after penetrating 2 mm into the target. The yellow shaded region therefore shows the region within the target where the beam serves solely to heat the target without producing useful activation species (and area under the green and red curves serves as proxy to target activation and heating respectively).

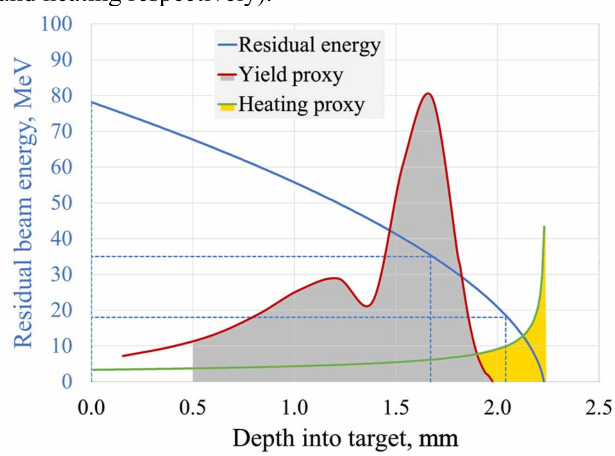

Figure 4: Energy, energy loss, and expected ^{18}F yield per 10 μm linear depth into the target material only.

An optimisation approach can be considered, where the activation curve (grey) is placed within the target material and the heating curve (yellow) is placed outside of the target and in the cooling water or aluminium beamstop. The optimisation is achieved by altering the beam energy to match the dimensions of the target for the specific activation. In practice the beam energy delivered by the SSC remains at the 100 MeV maximum that can be delivered to the target station (limited by the $k = 100$ switching magnet), and is degraded by placing aluminium absorbers of different thicknesses within the target stack upstream of the target capsule. Fig. 5 illustrates the calculated optimisation for the range of alpha particle energies possible from the SSC (200 MeV – 75 MeV) where the lower energy is that which barely penetrates into the target layer when using the current target stack. The 100 MeV beam (red curve) produces useful activation yield up to 2 mm depth, limiting the maximum diameter of the target to this value when keeping the heating outside of the target. The optimal beam energy when leaving the target is around 20 MeV to maximise yield and minimise heating. To optimally activate larger targets higher incident beam energy or a redesigned target stack would be required.

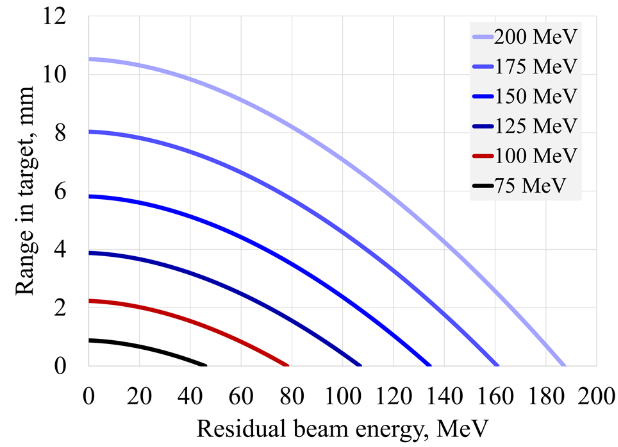

Figure 5: Range into target for incident beam energy.

The linear position along the target stack where the maximum ^{18}F yield is expected to be produced (blue points), and the maximum thickness of target where the heat deposition curve is placed outside of the target material (green) for the range of initial beam energy considered is shown in Fig. 6.

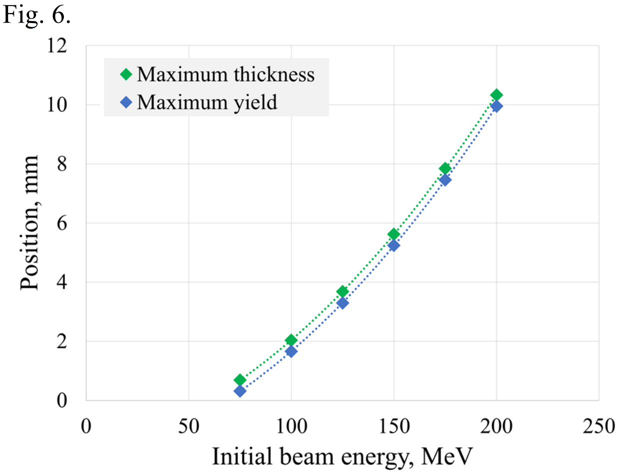

Figure 6: Range into target for incident beam energy.

The zero position is taken as the front face of the SiO_2 target material, and quadratic fits are shown to guide the eye. It is clear from these data that the maximum thickness of target increases with increasing beam energy, and that the region of maximum activation occurs close to the back surface of the target, it is therefore advantageous to enable rotation of the target within the beam to distribute the production yield while maintaining the heat load outside of the material.

ISBN: 978-3-95450-212-7 ISSN: 2673-5482 doi:10.18429/JACoW-CYCLOTRONS2022-WEB003

In practice it is possible to activate larger targets to a surface layer, with the beam fully stopping within the target provided that it can survive the beam heating. The circulating cooling water has the advantage of agitating the target spheres and seems to provide rotation, enabling isotropic beam entry relative to the target centre, thus distributing activation yield and heat load through the target. For the larger spheres the heat load limits the beam current that can be delivered without damaging the materials. A simple reaction rate activation model has been used to estimate the expected ^{18}F yield, using the parameters as delivered experimentally [7]. An average microscopic production cross-section for total ^{18}F production of 12 mb and beam current of 0.8 μA incident for 2 hours is considered. The target density is 2.5 g cm^{-3}, and thickness 0.1 cm. For our beam and target conditions the expected yield is then around 2 mCi. A more advanced model building on the energy loss calculations outlined above is left for future work. Experimental campaigns using the target stack as described above, with initial beam energy of 100 MeV and target spheres of diameters ranging from 1 – 10 mm resulted in a total of 24 samples with activities in the 1 – 2 mCi range. Isotopic characterisation measurements confirmed the yield at end of beam to be predominantly ^{18}F (> 95%) produced by the reactions as described. The experimental results are broadly consistent with the expectations from the modelling. Contaminant positron and gamma emitting species were observed at the percent level, with their origins traced to alpha particle and fast neutron (spallation) interactions with trace amounts of other naturally occurring materials present in the target [7]. The positron emitter ^{43}Sc was observed at around 5% yield, produced from ^{40}Ca offering a potential isotope for future work.

Potential applications are targeted towards production of tracer particles used for the study of physical flows and engineering systems using positron emission particle tracking (PEPT). It is desirable for the tracer particle materials to accurately reflect the motion and behaviour of the inactive bulk particles forming the system under study. For most applications, and specifically those of industrial interest, solids of naturally occurring isotopic content are required. For full representation of the materials of interest, tracer particles must therefore be activated with proton rich radionuclides utilising reactions on their naturally abundant isotopic content. Typical PEPT studies are used to measure dynamic and kinematic properties of the tracer particle, which is mixed within the bulk material of the system under study. A single tracer particle may therefore represent the behaviour of many millions and/or many tons of bulk material, with local bulk densities, residence times, and velocity flow fields being of particular interest [8, 9].

CONCLUSION

A target holding system has been modified to enable SiO_2 glass spheres of diameters 1 – 10 mm to be irradiated with up to 100 MeV alpha particles using the horizontal target station 1 and separated sector cyclotron of iThemba LABS. The $^{16}O(\alpha, x)^{18}F$ reactions have been explored to produce the positron emitter ^{18}F within these naturally isotopically occurring solid materials. Simulations and numerical calculations of the beam conditions have been used to maximise the activation yield and minimise heat load by carefully placing the Bragg peak in relation to the water-cooled target. In correspondence to the target thickness, the 100 MeV extraction energy is degraded to match a broad resonance in ^{18}F production around 35 MeV, while maintaining energy above the 18 MeV threshold. Beam currents below 1 microamp resulted in activities between 1 - 2 mCi, with around 95% of the yield attributed to ^{18}F. The activated samples have applications in the technique of positron emission particle tracking, where short lived positron emitters are used as flow following tracer particles. As the tracer is designed to be representative of the bulk materials in question, the positron emitting species must be produced from the naturally occurring isotopic content of the particles, motivating this application.

REFERENCES

[1] D. J. Parker, "Positron emission particle tracking and its application to granular media", *Rev. Sci. Instrum.*, vol. 88, p. 051803, 2017. doi: 10.1063/1.4983046

[2] A. Buffler *et al.*, "PEPT Cape Town: a new positron emission particle tracking facility at iThemba LABS", IAEA, Nuclear Research Applications and Utilization of Accelerators, Proceedings series (International Atomic Energy Agency. CD-ROM) CN-173, IAEA, Vienna, 2010.

[3] M. van Heerden, A. Buffler, K. Cole, and T. Leadbeater, "Density-modified tracers for positron emission particle tracking", *J. Phys.: Conf. Ser.,* to be published.

[4] A. Camroodien, M. van Heerden, S. Nair, and T. Leadbeater, "Radiochemistry for Positron Emission Particle Tracking (PEPT)", in *Proc. South African Institute of Physics (SAIP'21)*, Potchefstroom, South Africa, Jul. 2021, pp. 542 – 547. ISBN: 978-0-620-97693-0

[5] A. J. Koning, D. Rochman, J. Sublet, *et al.*, "TENDL: complete nuclear data library for innovative nuclear science and technology", *Nucl. Data Sheets*, vol. 155, pp. 1-55, 2019. doi:10.1016/j.nds.2019.01.002

[6] M. J. Berger, M. Inokuti, *et al.*,, "Stopping Powers for Protons and Alpha Particles", International Commission on Radiation Units and Measurements (Bethesda Maryland), ICRU Report 49, January 1, 1993.

[7] T. Leadbeater, A. Buffler, M. van Heerden, A. Camroodien, and D. Steyn, "Development of tracer particles for positron emission particle tracking (PEPT)", *Nucl. Sci. Eng.*, to be published.

[8] T. W. Leadbeater, D.J. Parker, and J. Gargiuli, "Positron imaging systems for studying particulate, granular and multiphase flows", *Particuoloy*, vol. 10, no.2, pp. 146-153, 2012. doi:10.1016/j.partic.2011.09.006

[9] T. Leadbeater, J.P.K. Seville, and D.J. Parker, "On trajectory and velocity measurements in fluidized beds using positron emission particle tracking (PEPT)", *Can. J. Chem. Eng.*, vol. 101, no. 1, pp. 269-282, 2022. doi:10.1002/cjce.24622

ISBN: 978-3-95450-212-7 ISSN: 2673-5482 doi:10.18429/JACoW-CYCLOTRONS2022-WEBO04

COMMISSIONING OF THE SUMITOMO SUPERCONDUCTING AVF CYCLOTRON SC230

Y. Ebara†, H. Tsutsui, S. Nakajima, J. Yoshida, T. Tsurudome, T. Miyashita, Y. Kumata
Sumitomo Heavy Industries, Ltd., Tokyo, Japan

Abstract

A 230-MeV superconducting azimuthally varying field (AVF) cyclotron SC230 was developed by Sumitomo Heavy Industries, Ltd. This is the world's smallest isochronous cyclotron for proton therapy, and its weight is 65 tons, which is 0.3 times that of our previous cyclotron model. The size is reduced by generating high magnetic fields using NbTi superconducting coils cooled without cryogen. In addition, this cyclotron features the maximum beam current >1 μA and low power consumption <200 kW. The beam-commissioning test was started at the end of 2020. The first extracted beam was observed in July 2021. Subsequently, and the basic performance of the beam was measured. The processes and results of the beam commissioning are reported.

INTRODUCTION

Proton therapy was proposed in 1946 and first used to treat patients in 1954 [1, 2]. No incision is required, and the characteristic depth dose distribution with a Bragg peak minimizes damage to normal cells. Afterward, patients can receive outpatient treatment while continuing their daily lives, contributing to the maintenance of their quality of life (QOL). Therefore, proton therapy is becoming more prevalent in cancer treatment, and the number of proton therapy facilities is increasing. More than 100 facilities are in operation worldwide [3], and further growth is expected in the future. However, the large device size limits its use in hospitals. Therefore, miniaturization of the device size is one of the issues in proton therapy. Manufacturers have been promoting the development of miniaturization of equipment, and in recent years, the miniaturization of the accelerator, which is one of the primary mechanisms, has been conducted with superconducting coils. Commercial superconducting accelerators for proton therapy were developed by Varian, Mevion, and IBA [4-6].

Miniaturization of accelerators with superconducting coils has the following merits:

- Reduction of building cost
- Shorter delivery times
- Lower operating costs
- Reduced daily downtime

Downsizing is expected to lower the building cost by reducing the construction site area and lowering load-bearing requirements. Moreover, because the large assembly can be transported as it is, disassembly and reassembly times are reduced, and delivery times are shortened. Furthermore, with superconducting coils, the power consumption of coils and running costs can be reduced. In addition, as the power consumption of coils can be reduced, continuous energization at night is possible, which eliminates the daily coil excitation and demagnetization time in hospitals and contributes to the reduction of downtime. Hospitals benefit from a variety of services. Many superconducting accelerators for proton therapy are being designed and developed to provide such benefits.

Sumitomo Heavy Industries developed the superconducting cyclotron SC230. The weight of the yoke is 65 tons, equivalent to 3/10 times that of the conventional model [7]. Additionally, it is not only compact but also consumes low energy and offers a high beam current. Energy saving is not only a countermeasure against recent issues, such as unstable energy supply and global warming but it is also expected to reduce operating costs. The power consumption is ≤200 kW, equivalent to 3/5 times that of conventional models. Its high-current beam contributes to shortening the treatment time. The maximum beam current of the cyclotron is ≥1 μA, which is 3.3 times that of the conventional machine, which is the maximum for proton therapy accelerators. It reduces patient burden, increases patient throughput, and allows for more patients to be treated. In the future, it can be applied to treatment methods that require high-current beams, such as FLASH treatment and the breath-hold irradiation method.

The basic design of the cyclotron was reported in 2013 [8]. The design and fabrication of each component including the superconducting magnet have been completed thus far, and the mapping and formation of the magnetic field have been completed [9-13]. A new test site was established in 2020. The cyclotron was relocated to this site and conditioned. Commissioning tests started at the end of the same year and the beam was extracted in July 2021. Additionally, the extracted beams met the performance requirements, and the development of SC230 was completed. Here, we report on the commissioning.

SC AVF CYCLOTRON SC230

The developed superconducting AVF cyclotron SC230 for proton beams is a four-spiral sector-type AVF cyclotron. Figure 1 shows an image of the external appearance of the cyclotron. The main specifications for its components are presented in Table 1.

It produces a fixed-energy proton beam required for proton therapy. The cyclotron was miniaturized by using a superconducting magnet to generate a high magnetic field of 3–5 T. The average magnetic field was approximately 3.9 T at the extraction radius of 0.6 m.

† yuta.ebara@shi-g.com

ISBN: 978-3-95450-212-7 ISSN: 2673-5482 doi:10.18429/JACoW-CYCLOTRONS2022-WEB004

Figure 1: Sumitomo superconducting AVF cyclotron SC230.

Table 1: Main Specifications of SC230

Parameter	Specification
Accelerator type	AVF cyclotron
Number, shape of sector	Four, spiral
Particle species	Proton
Beam energy	233–238 MeV (Fixed)
Maximum beam current	≥1000 nA
Beam structure	CW
Extraction diameter	0.6 m
Yoke size	Diameter: 2.8 m Height: 1.7 m
Yoke weight	65 t
RF frequency	95.3 MHz (h = 2)
Dee voltage	50 kV (Inside) 75 kV (Outside)
Number of dees	2
RF power	<70 kW
Total power consumption	<200 kW

Two upper and lower NbTi superconducting coils were used as magnetomotive force sources. The superconducting coils were installed inside a cryostat for vacuum insulation and cooled below 5 K by a conduction cooling method using four cryocoolers. With the conduction cooling method, the coils have improved maintainability. They were accessible from outside the cyclotron, and maintenance was allowed while keeping the coil cool. The operation of the cryocoolers is simple, with a simple button operation. Furthermore, since it is cryogen-free and does not use liquid helium, it does not emit helium even during quenching that can occur during a long-term power outage. Furthermore, it is an effective countermeasure against the instability of helium supply, which has become an issue in recent years. Its cooling time is 14 days. With a damper protection, quench recovery time is 17 hours [11].

When an AVF cyclotron is miniaturized by a high magnetic field, flutter becomes smaller because it is inversely proportional to the square of the average magnetic field. Therefore, to prevent beam divergence, the gap between the magnetic poles should be shortened to increase the difference between the hill and valley magnetic fields, thereby suppressing flutter reduction. Additionally, countermeasures should be obtained such as a large spiral angle, which increases the complexity of the magnetic field distribution. In SC230, to realize a compact AVF cyclotron, a magnetic pole gap is ±10 mm in a wide area, and ±6 mm at the nearest point, and a maximum spiral angle of approximately 70 degrees. The magnetic pole shape required complex and high dimensional accuracy, and the magnetic pole was manufactured by precision machining on the order of 0.01 mm. In addition, mapping and adjustment were performed to produce the average magnetic field at 50 ppm or less. Finally, it was confirmed that the isochronous magnetic field satisfying the requirements was formed.

The power consumption of the coils was low owing to their conductivity; therefore, RF power consumption was dominant in this cyclotron and must be kept low. To reduce the RF power consumption, the number of dees was two, which is minimum for commercial use, and the applied dee voltages were designed to be 50 kV on the inside and 75 kV on the outside. The total power consumption was below 200 kW owing to the small number of dees and the low dee voltage. However, the energy saving dees reduce not only its power consumption but also the energy gain per turn. Small turn separation reduces the beam extraction efficiency. Therefore, the precessional extraction method, which increases the turn separation by resonance, was adopted.

The maximum beam current was 1 μA, which is the highest among commercial accelerators for proton therapy. Because it is an AVF cyclotron, it had achieved a large beam current that could be regarded as continuous. In addition, the beam current upper limit in the conventional machine was set such that the electrostatic deflector (ESD), which was one of the extraction components, would not be damaged by beam loss. In SC230, the beam loss in the ESD was reduced to realize a large current beam. The turn separation increased, and the passage efficiency of the ESD improved by adopting the precessional extraction method described above. The $\nu_r = 1$ resonance was used for the method. The first harmonic component of the axial magnetic field B_{Z_1} should be precisely adjusted. B_{Z_1} was almost zeroed by the vertical coil position adjustment in advance [12]. In the commissioning, B_{Z_1} was adjusted by the horizontal coil position adjustment, and extraction harmonic coils (EHCs). The EHCs, which are facing two sets, can increase the B_{z1} to 8×10^{-4} T around the beam-extraction radius. In addition, owing to the feature of the narrow pole gap, the fringe field was attenuated with a high gradient in the extraction region, which contributed to efficient beam extraction.

Table 2: Design Specifications of the Components

Parameter	Specification
Ion source type	Hot cathode-type PIG ion source
Cryostat outer diameter	1.74 m
Cryostat height	0.64 m
Number of coils	2
Superconducting wire	Monolith NbTi/Cu
Coil current	442 A (488 A Max.)
Maximum stored energy	5.3 MJ
Coil temperature	<5 K
Cooling method	Conduction-cooling
Cryocoolers	4K-GM cryocoolers
Number of cryocoolers	4
Cooling time	14 days
Quench recovery time	17 hours
Coil supports	4 (vertical) 4 (horizontal)
Vacuum pumps	Two cryocoolers, dry pump
Operable vacuum	$< 1 \times 10^{-2}$ Pa
Extraction method	Precessional extraction
Extraction components	EHCs, ESD, MC1, MC2

COMMISSIONING

Parameters were adjusted along the beam flow from the ion source to the extraction components. Regions from the center to the exterior were named the central, isochronous, and extraction regions.

In the central region, the parameters of the ion source were adjusted primarily. The source was a Penning ionization gauge ion source using a hot cathode, and its electrical parameters were adjusted. The position and angle was adjusted from outside the cyclotron to maximize the beam current.

In the isochronous region, the isochronous field was formed by mapping and adjustment performed in advance. No adjustment mechanism was available. During commissioning, the beam was confirmed to pass through the isochronous region without any parameter adjustment. The formation of a distinct isochronous field was observed.

In the extraction region, parameters such as the central harmonic coils (CHCs), EHCs, ESD, and the position of the main coil were adjusted. The current of CHCs was tuned to adjust the orbital center. Additionally, to obtain an appropriate B_{Z_1} for precessional extraction, the horizontal-coil position and the currents of the EHCs were adjusted for coarse and fine adjustments of B_{Z_1}. The normalized beam current for each combination of EHCs-current values is shown in Fig. 2.

The ESD voltage adjusted the final extraction trajectory. After passing through the ESD, the beam passed through two passive magnetic channels and exited the cyclotron through a beam port located through the cryostat and yoke. Beam extraction was confirmed by observing using films.

The normalized beam current at each ESD voltage is shown in Fig. 3. Furthermore, the parameters were set to maximize the extracted beam current.

A beam extracted from the cyclotron was stopped by a damper after passing through two bending and two focusing magnets. An ion chamber was installed in front of the damper, and the beam current was measured. In addition, a measurement area was set up between the ion chamber and the damper, and key beam performances, including beam profile and energy, were measured using a beam profiler and a range measurement module. The SC230 supports fast scanning with 0.1 second energy switching and scan speeds of up to 100 m/s. Therefore, in addition to the maximum beam current, the current and position must be highly stable. Table 3 shows the required main beam specifications. During the commissioning, the maximum beam current was confirmed to exceed 1 μA, and the beam extraction efficiency was confirmed to be 67 %, which satisfy the specifications. In addition, current and position stabilities were measured, and the beam met all specifications.

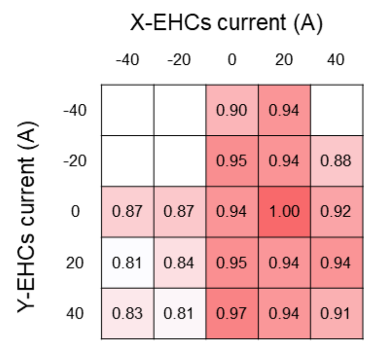

Figure 2: Normalized beam current for each combination of extraction harmonic coils (EHCs)-current values. The x and y directions are perpendicular to each other, and the relationship between the current and the first harmonic component of the axial magnetic field B_{Z_1} on MP is 7.6×10^{-6} T/A. The extraction beam current peaked under the conditions of the current set (0 A, 20 A), i.e., when B_{Z_1} of 1.5×10^{-4} T was generated in the x direction.

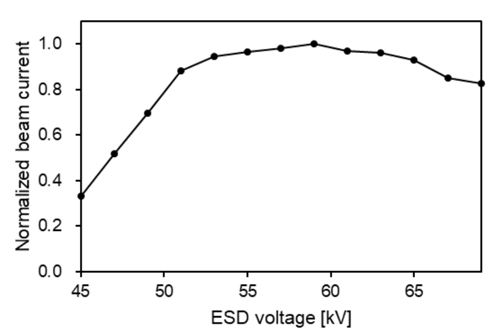

Figure 3: Normalized beam current at each electrostatic deflector (ESD) voltage. A broad distribution over 10 kV was confirmed. Finally, the voltage was set to 55 kV, a relatively low voltage within the flat peak area.

ISBN: 978-3-95450-212-7 ISSN: 2673-5482 doi:10.18429/JACoW-CYCLOTRONS2022-WEBO04

Table 3: Main Beam Specifications of SC230

Parameter	Value
Energy reproducibility	<0.2 MeV
Extraction efficiency	≥60 %
Minimum controllable beam current	<1 nA
Ripple current	≤2 % (1σ)
Beam current stability	≤1 % (1σ) for 2 min.
Beam responsivity	≤50 μsec
Beam position stability	<0.1 mm for 2 min.
RMS emittance	<2.2 μm (x), 1.4 μm (y)

Details of the commissioning and test results and the performance of the superconducting magnet were reported in Refs. [14, 15].

CONCLUSION

The world's smallest superconducting AVF cyclotron for proton therapy was developed. Challenging designs were adopted for each mechanism, including the complex yet precise magnetic-pole shape and energy saving dees. Each component adopting a design was realized through precise fabrication, assembly, and adjustment.

Transfer to the new test site and the assembly of the components were completed. The commissioning test was initiated in 2020. During the commissioning, the parameters were adjusted, and the results confirmed that the accelerated beam was extracted from the cyclotron through the central, isochronous, and extraction regions. The maximum extracted beam current was >1 μA, and the extraction efficiency was 67 %. In addition, all necessary specifications for proton therapy were satisfied. Through these tests, we observed that the performance requirements were reached. The development was completed in 2021.

The SC230 is compact and energy saving. Furthermore, its high beam current will improve patient throughput and enables treatment of more patients. In addition, the high-current beams should contribute to the expansion of treatment methods such as FLASH treatment and breath-hold irradiation. This cyclotron is expected to be installed in several hospitals and contribute to many treatments.

ACKNOWLEDGEMENTS

The commissioning was extensively supported by several engineers. We especially thank Dr. K. Taki, Mr. S. Hara, Dr. S. Nomura, Mr. K. Suga, Mr. H. Oda, and Mr. S. Fujita for their assistance with equipment adjustment and measurement.

REFERENCES

[1] R. R. Wilson, "Radiological use of fast protons", *Radiology* vol. 47, no. 5, pp 487-491, 1946. doi:10.1148/47.5.487

[2] C. A. Tobias *et al.*, "Pituitary irradiation with high-energy proton beams a preliminary report", *Cancer Research*, vol. 18, no. 2, pp. 121-134, 1958.

[3] Particle Therapy Co-operative Group (PTCOG), "Particle therapy facilities in clinical operation", https://www.ptcog.ch/index.php/facilities-in-operation

[4] H. U. Klein, A. Geisler, A. Hobl, D. Krischel, H. Röcken, and J. H. Timme, "Design, manufacturing and commissioning of compact superconducting 250 MeV cyclotrons for proton therapy: A short report from the field", *IEEE/CSC & ESAS Eur. Supercond. News Forum (SNF),* issue no. 2, paper ST7 (6 pages), Oct. 2007.

[5] Mevion Medical Systems Proton Therapy; https://www.mevion.com

[6] S. Henrotin *et al.*, "Commissioning and testing of the first IBA S2C2", in *Proc. 21th Int. Conf. on Cyclotrons and their Applications (Cyclotrons'16)*, Zurich, Switzerland, Sep. 2016, pp. 178-180. doi:10.18429/JACoW-Cyclotrons2016-TUP07

[7] A. Goto, T. Tachikawa, Y. Jongen, and M. Schillo, "8.12 - Cyclotrons", *Compr. Biomed. Phys.*, vol. 8, pp. 179-195, 2014. doi:10.1016/B978-0-444-53632-7.00612-2

[8] H. Tsutsui *et al.*, "Design study of a superconducting AVF cyclotron for proton therapy", in *Proc. 20th Int. Conf. on Cyclotrons and their Applications (Cyclotrons'13)*, Vancouver, Canada, Sep. 2013, paper MO3PB02, pp. 102-104.

[9] H. Tsutsui *et al.*, "Status of Sumitomo's superconducting isochronous cyclotron development for proton therapy", in *Proc. 13th Int. Topcial Meeting on Nuclear Applications of Accelerators (AccApp '17)*, Quebec, Canada, Jul.-Aug., 2017, pp. 412-419.

[10] H. Tsutsui *et al.*, "Current Status of Sumitomo's Superconducting Cyclotron Development for Proton Therapy", in *Proc. 22nd Int. Conf. on Cyclotrons and their Applications (Cyclotrons'19)*, Cape Town, South Africa, Sep. 2019, pp. 340-343. doi:10.18429/JACoW-CYCLOTRONS2019-FRA02

[11] J. Yoshida *et al.*, "Excitation test of superconducting magnet in 230-MeV isochronous cyclotron for proton therapy," *IEEE Trans. Appl. Supercond.,* vol. 30, no. 4, article no. 4400205 (5 pages), 2020. doi:10.1109/TASC.2019.2962675

[12] Y. Ebara *et al.*, "Field mapping system and field adjustment for a 230-MeV proton cyclotron" *Nucl. Instrum. Methods Phys. Res. Sect. A*, vol. 953, article no. 163355, 2022. doi:10.1016/j.nima.2019.163186

[13] N. Kamiguchi *et al.*, "Development of a center region for new Sumitomo cyclotron," Cyclotrons (2019)

[14] Y. Ebara *et al.*, "First beam extraction from a superconducting azimuthally varying field cyclotron for proton", submitted for publication.

[15] Y. Ebara *et al.*, "Performance of cryogen-free superconducting magnet in isochronous cyclotron for proton therapy", submitted for publication.

ISBN: 978-3-95450-212-7 ISSN: 2673-5482 doi:10.18429/JACoW-CYCLOTRONS2022-WEB005

UPGRADE OF A CLINICAL FACILITY TO ACHIEVE A HIGH TRANSMISSION AND GANTRY ANGLE-INDEPENDENT FLASH TUNE*

Isabella Colizzi[†,1], Vivek Maradia[1], Rene Kuenzi, Alexander Gabard, Christian Baumgarten, Damien Charles Weber[2,3], Antony John Lomax[1], David Meer, Serena Psoroulas
Paul Scherrer Institut, 5232 Villigen PSI, Switzerland
[1]also at ETH Zurich, Switzerland
[2] also at University Hospital Zurich, Switzerland
[3]also at Department of Radiation Oncology, Inselspital, Bern University Hospital, Switzerland

Abstract

In proton therapy, FLASH-RT, irradiation at ultra-high dose rates (>40 Gy/s) that can minimize radiation-induced harm to healthy tissue without reducing its ability to treat tumors, is a topic of great interest. However, in cyclotron-based proton therapy facilities, losses caused by the energy degradation process reduce the transmission to less than 1% for low energies, making it difficult to achieve high dose rates over the clinical range (70-230 MeV).

We will demonstrate how an already existing clinical beamline can be converted into a FLASH beamline by mainly beam optic changes. To achieve maximum transmission, we have developed a new optics that transports the undegraded 250 MeV beam from the cyclotron to the isocenter. However, this has a slightly asymmetric emittance in the transverse planes, leading to gantry angle-dependent beam characteristics at the patient.

Particle transport has been simulated with MINT (in-house matrix multiplication transport program with Monte Carlo simulations for scattering effects) and benchmarked with beam profile measurements. We used the optimization criteria for sigma matrix matching to achieve gantry angle-independent optics.

Simulations and beam profile measurements showed a good agreement**,** and with FLASH optics, we experimentally achieved 90% transmission at the patient, translating to a maximum current of 720 nA (>9000 Gy/s on-axis). Further, we demonstrate that using the matrix matching optimization criteria together with fine tuning of the magnets, we could achieve gantry angle-independent beam profiles at the patient location.

In conclusion, we have shown how an already existing cyclotron-based proton gantry can be adapted to achieve ultra-high dose rates at 250 MeV, enabling investigations of FLASH radiotherapy with protons, with the drawback of downstream energy modulation, if required. Since most of the modifications are performed on the beam optics, it is completely transparent to clinical operations, making the method transferable to other facilities.

* Work supported by SNF (Grant No. 200822) and PSI's CROSS funding scheme
† isabella.colizzi@psi.ch

INTRODUCTION

The delivery of ultra-high dose rates (>40 Gy/s), also known as FLASH radiotherapy, has proven in preclinical investigation to allow tumour control while minimizing damage to surrounding healthy tissues [1]. In 2014, the effect was demonstrated on mice with a 4.5 MeV electron beam [2] and in 2018, the first human patient was successfully treated with electron-FLASH radiotherapy at the Lausanne University Hospital (CHUV, Switzerland) [3]. After that, many biological cell experiments and even a few clinical trials started to investigate the parameters that triggers the FLASH effect. Nowadays, the effect has been confirmed by different institutes and for different beam modalities (electrons, photons, proton and heavy ions [4]) and organs [5].

Some proton centres around the world have begun to look at whether it's possible to use current treatment equipment to achieve FLASH dose rates. The FLASH dose rate requirements can theoretically be met by cyclotron-based facilities, at least for high energies [6]. However, there is no conclusive proof that dose rates greater than 40 Gy/s cause the FLASH effect since this limit was derived in a limited number of experiments and tissues. Therefore, flexibility is required.

In this study we report how the clinical Gantry 2 [7] at the Paul Scherrer Institute could be adapted to achieve ultra-high dose rates at 250 MeV, without affecting clinical operations. The aim of this update is to enable clinical investigation of conformal FLASH radiotherapy using protons in scanning mode, hence a symmetric and gantry-angle independent beam is required.

METHODS AND MATERIALS

PSI Beamline and Gantry 2

In the PSI proton therapy center the proton beam is generated by the COMET cyclotron (Fig. 1). The extracted beam has an energy of 250 MeV and up to 800 nA intensity. For treatment, energies in the range 70-230 MeV are required and the energy modulation is done by mean of a degrader placed right after the cyclotron. We lose more than 99% of the particle for low energies due to the collimators following the degrader and the energy selection slits, resulting in a transmission of less than 1% at the isocenter [8, 9]. Consequently, in order to obtain ultra-high

ISBN: 978-3-95450-212-7 ISSN: 2673-5482 doi:10.18429/JACoW-CYCLOTRONS2022-WEB005

dose rates, we optimized the transport of the undegraded 250 MeV proton beam to the treatment room with the least amount of losses. However, PSI Gantry 2 dipole magnets [10] were designed to transport only energies up to 230 MeV and therefore an investigation of the flexibility of the power supplies as well as the magnet cooling system had to be conducted.

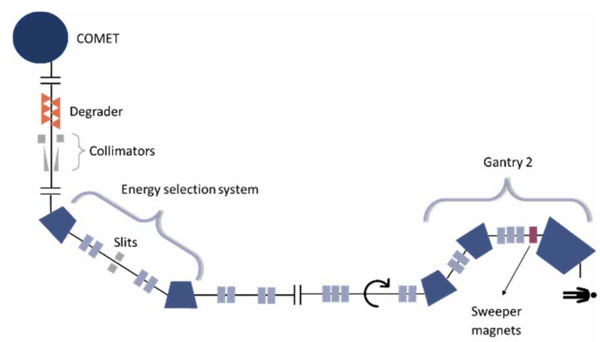

Figure 1: Schematic of the PSI beamline from the cyclotron (COMET) to Gantry 2. The light blue rectangles represent the quadrupoles, the blue trapezoid the dipoles.

Beam Transport

The particle transport was simulated with MINT [11], an in-house developed matrix multiplication program with Monte Carlo calculations of scattering effects, which occurs due to permanent monitors or foils placed along the beamline. The following criteria were used in the optimization of the beamline:

- Beam size smaller than magnets and collimators aperture.
- Three imaging point (after the energy selection system, at the coupling point between the beamline and the gantry and at the isocentre).

The isocenter beam parameters were optimized to account for the slightly asymmetric emittance in the transverse planes of the undegraded beam (6.1π mm mrad in y and 3.7π mm mrad in x, 1σ emittance), which might result in undesired gantry angle-dependent beam characteristics at the patient. We utilized the matrix matching approach [12] to achieve an angle independent and symmetric beam, which requires:

- Symmetric beam size at the gantry entrance.
- Beam waist at the gantry entrance.
- Diagonal transfer matrix from the gantry entrance to the isocentre.

Measurement

The beam profiles were measured with strip chamber monitors [13, 14] distributed along the beamline. The precision of the measured beam profile reduces for low current due to sensitivity and small beam sizes due to the strip resolution. The transmission at the treatment room was calculated with the ratio between the current monitor after the cyclotron and the two transmission monitors (plane parallel ionisation chambers) in the nozzle [15].

The beam size at the isocentre was measured with a scintillating foil connected to a charge coupled device (CCD) camera. The (pixel) resolution of the camera was 0.3 mm.

RESULTS

Hardware Adaptation for 250 MeV

The needed coil current of the gantry magnets at 250 MeV was determined by extrapolating the measured current from 70 to 230 MeV while accounting for saturation effects observable at high energies. We parametrize the hysteresis curve using a linear function for low current (energies) and a quadratic function for higher current (energies). Due to the limited amount of data, the parametrization of the saturation zone was sensitive to uncertainty. In Fig. 2 we show in red the maximum current that we could achieve with the previous power supply configuration (500 A) and in green the required current (518 A). The dashed lines represent the current with 10% and 25% error in the parametrization of the quadratic function. After ulterior measurements, we found the required current to be 515 A, which agrees with less than 1% with our extrapolation. The specifications were translated in a new configuration of the power supplies which was tested and implemented without affecting clinical operation. In particular, no adaptation to magnets operation conditions (such as cooling water flow etc.) was needed.

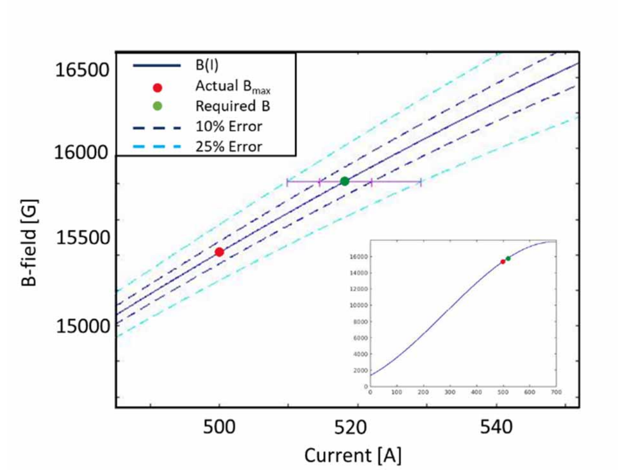

Figure 2: The interpolated hysteresis curve of the largest dipole magnet in the gantry is plotted for positive current in the smaller plot. The red point shows the actual maximum current achievable and the green the requirement for 250 MeV. In the larger plot we zoom in the region of interest, and we show with dashed lines 10% and 25% error in the parametrisation.

FLASH Optimized Beam Transport

Figure 3 shows a comparison between the simulated (and hand-tuned) particle transport and the measured beam profile at different position in the beamline. Hand-tuning was necessary for different reasons, for gantry misalignment due to the weight of the magnet when we change the gantry angle and, as will be discussed later, to produce a circular beam at the isocentre.

23rd Int. Conf. Cyclotrons Appl. CYCLOTRONS2022, Beijing, China JACoW Publishing
ISBN: 978-3-95450-212-7 ISSN: 2673-5482 doi:10.18429/JACoW-CYCLOTRONS2022-WEB005

The mean deviation lies around 12%, in particular, only 10% in the beamline and 17% in the gantry region. From the degrader until the gantry entry, the disagreement in x and y is nearly same (less than 1% difference). The agreement is however satisfactory for our purpose.

It is important to mention that the simulation's starting assumption of the phase space is an important factor in determining whether measurements and simulations match. By changing the initial parameters, the beam size at the monitor's position will vary even if the overall beam envelope (shape) stays constant.

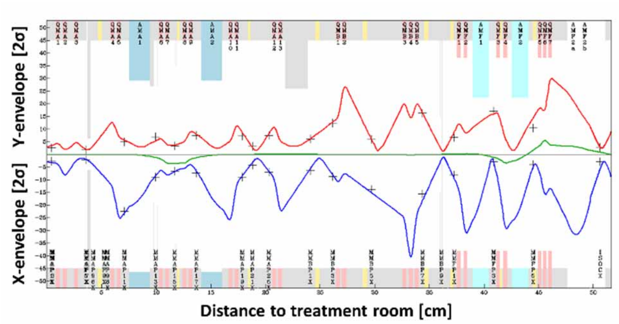

Figure 3: Comparison between the simulated particle transport (full red and blue line) and the measured beam profile (red dots). The lower half of figure shows beam envelope in X-plane (2σ) and the upper half shows envelope in Y-plane (2σ). The dispersion (mm per mil dp/p) is represented with the green line. The beamline and gantry quadrupoles are indicated in red and the diploes in blue.

We experimentally achieved a transmission of 90% from cyclotron to isocenter that can be translated to a maximum current of 720 nA (>9000 Gy/s peak dose rate on-axis, since the dose distribution in a proton beam is not uniform, we mention the dose on-axis defined as the dose on the proton beam's center axis), thus enabling investigations of FLASH radiotherapy with protons.

Beam Characteristics at the Isocentre

To demonstrate the independence of the tune on the gantry angle, we measured the beam size at different gantry positions, and we plot in Fig. 4 the results. The beam size variation is overall smaller than 10%. On average the beam size is 1.36 +/- 0.02 mm in y and 1.37 +/- 0.02 mm in x.

This result was obtained in two steps. Firstly, we optimised the magnetic settings using matrix matching optimization constraints in MINT. Secondly, fine-tuning the gantry's quadrupoles was the required step to experimentally achieve a symmetric and angle independent beam size at the isocentre.

We provide in Fig. 5 a spot map measurement for a scanning pattern of 16 cm x 12 cm. In the plane orthogonal to the bending plane (x) of the magnet we see a significant distortion and non-parallelism at the corner of the scanning area. However, in the central region, which is important for our purposes, we measured a regular grid with a round beam.

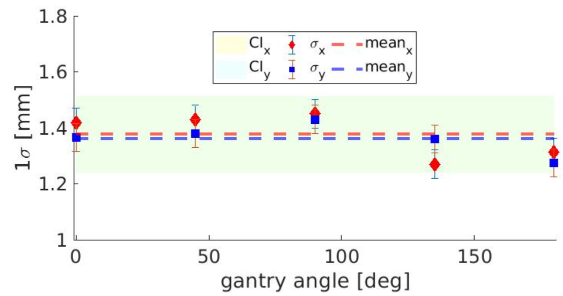

Figure 4: Measured beam size (1σ) as a function of the gantry angle. The dashed line is the mean value of the beam size in x (red) and y (blue). The orange and light blue band indicate 10% variation of the beam size.

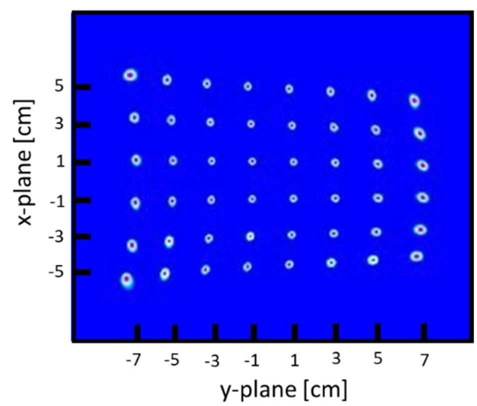

Figure 5: Measured spot map at the isocentre.

DISCUSSION

In this work, we demonstrate that we could upgrade PSI Gantry 2 to transport 250 MeV and achieve UHDR at the patient position. Even though the gantry was designed to transport proton beams with a maximum energy of 230 MeV, the flexibility of the design enables us to extend the power supply limits and transport 250 MeV without affecting clinical operations.

We simulate the particle transport in MINT, and we benchmarked the simulations with profile measurements. We achieved an overall agreement, and the small discrepancies can be explained by different reasons. Firstly, the initial beam size definition may not be accurate. It has been calculated a posteriori comparing profile measurements performed over months with simulations with varying initial beam parameters (beam size and divergence). Further, since we were operating at very low current (0.2 nA), due to radiation protection requirements, we observed deformation of the beam in y due to the vertical deflector in the cyclotron used to reduce the beam current. Since simulation tools assume a Gaussian beam, this could explain the minor deviation in the y-envelope in the first monitors. Additionally, the profile monitors along the beamline do not work optimally at low current and for very narrow beams with a width comparable to or smaller than the strip pitch, the width is usually overestimated. This would explain why there is a slight discrepancy when the beam size is very small. The inaccuracy of the simulation's definition of the

ISBN: 978-3-95450-212-7 ISSN: 2673-5482 doi:10.18429/JACoW-CYCLOTRONS2022-WEBO05

gantry magnets' effective length in particular may be used to explain the discrepancy in the gantry. Lastly, missing second order terms might be in general a cause of discrepancy.

However, the simulations in MINT provided us a beneficial guide for beam line tuning, offering an important qualitative description of our beam transport.

We show that we could achieve a symmetric and gantry angle independent beam size at the patient position. The observed small discrepancy (<10%) is however negligible if we consider scattering in the patient. We noticed, according to a simple estimation of the multi-coulomb-scattering (using the Lynch and Dahl constants [16]), that the scattering in air and in the nozzle has a non-negligible contribution (30% of the beam size) in achieving a symmetric beam at the isocentre. However, a more detailed analysis is outside the scope of this study.

In the corner of the scanning region, the measured spot map reveals a non-parallel pattern and distortion. This can be explained by the final bending magnets' effective field edge curvature at the exit edge, which is bigger than 0.4 m-1 for 250 MeV [17], as well as by the large gap. However, FLASH clinical trials are usually conducted on small animals with small tumour sizes and since the tumour is usually located in the centre of scanning map, this distortion will affect only marginally the experiments.

We experimentally achieved a transmission of 90% meaning >9000 Gy/s peak dose rate on-axis, thus achieving the dose rate requirements for FLASH radiotherapy. Nevertheless, since there is no absolute evidence of the required parameters to achieve the FLASH effect, developing a versatile irradiation facility able to work under different dose rate conditions is crucial. Furthermore, with the objective of translating FLASH radiotherapy into the clinic, we will investigate FLASH proton beam scanning techniques rather than the transmission approach often utilized in clinical studies. For this, we must minimize the time necessary to change energies, for example, by modulating the beam with devices such as ridge filters [18] to increase the Bragg peak width from a few millimeters to a few centimeters.

CONCLUSION AND OUTLOOK

We have demonstrated how a cyclotron-based proton gantry can be modified to achieve ultra-high dose rates at 250 MeV and have achieved the desired beam quality (symmetric and small beam size at the isocenter, angle independent beam size) to enable investigations of FLASH radiotherapy using protons in pencil beam scanning mode. Since most of the modifications are performed on the beam optics, the method transferable to other facilities, too.

Further investigation of energy modulation techniques and monitoring systems for ultra-high dose rate will be the main topic of future studies.

In conclusion, PSI Gantry 2, an operating clinical gantry, will provide a unique setting for researching FLASH-PT and demonstrating FLASH's adaptability in the clinic.

ACKNOWLEDGEMENTS

We would like to thank Roland Deckardt and all involved people of the PSI magnetic and power supply group for the power supply upgrade of the Gantry 2 magnets. Further, we thank Zema Chowdhuri, Michele Tongo, Robert Schäfer, Benno Rohrer, and Martina Bochsler for their support during the measurements.

REFERENCES

[1] M.-C. Vozenin, J. Bourhis, and M. Durante, "Towards clinical translation of FLASH radiotherapy'', *Nat. Rev. Clin. Oncol.,* pp. 1-13, 2022. doi:10.1103/PhysRevLett.114.050511

[2] V. Favaudon *et al.,* "Ultrahigh dose-rate FLASH irradiation increases the differential response between normal and tumor tissue in mice'', *Sci. Transl. Med.,* vol. 6, no. 245, p. 245ra93, 2014. doi:10.1126/scitranslmed.3008973

[3] J. Bourhis *et al.,* "Treatment of a first patient with FLASH-radiotherapy", *Radiother. Oncol.,* vol. 139, pp. 18-22, 2019. doi:10.1016/j.radonc.2019.06.019

[4] U. A. Weber, E. Scifoni, and M. Durante, "FLASH radiotherapy with carbon ion beams", *Med. Phys.*, vol. 49, no. 3, pp. 1974-1992, 2022. doi:10.1002/mp.15135

[5] T. T. Böhlen *et al.,* "Normal tissue sparing by FLASH as a function of single-fraction dose: a quantitative analysis", *Int. J. Radiat. Oncol. Biol. Phys.*, vol. 114, no.5, pp. 1032-1044, 2022. doi:10.1016/j.ijrobp.2022.05.038

[6] S. Jolly, H. Owen, M. Schippers, and C. Welsch, "Technical challenges for FLASH proton therapy", *Physica Med.,* vol. 78, pp. 71-82, 2020. doi:10.1016/j.ejmp.2020.08.005

[7] E. Pedroni *et al.*, "The PSI Gantry 2: a second generation proton scanning gantry", *Zeitschrift für Medizinische Physik* vol. 14, no. 1, pp. 25-34, 2004. doi:10.1078/0939-3889-00194

[8] V. Maradia, D. Meer, D. C. Weber, A. J. Lomax, J. M. Schippers, and S. Psoroulas, "Application of a scattering foil to increase beam transmission for cyclotron based proton therapy facilities'', *Front. Phys.*, article no. 10:919787, 2022. doi:10.3389/fphy.2022.919787

[9] V. Maradia, D. Meer, D. C. Weber, A. J. Lomax, J. M. Schippers, and S. Psoroulas, "A new emittance selection system to maximize beam transmission for low-energy beams in cyclotron-based proton therapy facilities with gantry*", Med. Phys.,* vol. 48, no. 12, pp. 7613-7622, 2021. doi:10.1002/mp.15278

[10] M. Negrazus, A. Gabard, D. George, and V. Vrankovic, "The fast ramped bending magnets for the gantry 2 at PSI*", IEEE Trans. Appl. Supercond.,* vol. 18, no. 2, pp. 896-898, 2008. doi:10.1109/TASC.2008.920627

[11] C. Baumgarten, "MinT: A fast lightweight envelope/monte-carlo beam optics code for the proton beamlines of the Paul Scherrer Institute", arXiv article no. arXiv:2202.07245, Feb. 2022. doi:10.48550/arXiv.2202.07245

[12] M. Benedikt and C. Carli, "Matching to gantries for medical synchrotrons", in *Proc. 1997 Particle Accelerator Conf. (IPAC'97),* vol. 2, pp. 1379-1381. doi:10.1109/PAC.1997.750699

[13] R. Dölling, "Ionisation chambers and secondary emission monitors at the PROSCAN beam lines", *AIP Conf. Proceedings,* vol. 868, p. 262, 2006. doi:10.1063/1.2401414

[14] R. Dölling, "Profile, current, and halo monitors of the PROSCAN beam lines", *AIP Conf. Proceedings*, vol. 732, p. 244, 2004. doi: 10.1063/1.1831154

[15] S. Lin, T. Boehringer, A. Coray, M. Grossman, and E. Pedroni, "More than 10 years experience of beam monitoring with the Gantry 1 spot scanning proton therapy facility at PSI", *Med. Phys.,* vol. 36, no. 11, pp. 5331-5340, 2009. doi:10.1118/1.3244034

[16] S. Safai, T. Bortfeld, and M. Engelsman, "Comparison between the lateral penumbra of a collimated double-scattered beam and uncollimated scanning beam in proton radiotherapy", *Phys. Med. Biol.,* vol. 53, no. 6, p. 1729, 2008. doi:10.1109/TASC.2008.920627

[17] E. Pedroni, D. Meer, C. Bula, S. Safai, and S. Zenklusen, "Pencil beam characteristics of the next-generation proton scanning gantry of PSI: design issues and initial commissioning results", *Eur. Phys. J. Plus,* vol. 126, no. 7, pp. 1-27, 2011. doi:10.1140/epjp/i2011-11066-0

[18] V. Maradia *et al.*, "Universal and dynamic ridge filter for pencil beam scanning particle therapy: a novel concept for ultra-fast treatment delivery", *Phys. Med. Biol.,* vol. 67, no. 22, p. 225005, 2022. doi:10.1088/1361-6560/ac9d1f

ISBN: 978-3-95450-212-7 ISSN: 2673-5482 doi:10.18429/JACoW-CYCLOTRONS2022-WEBO06

ACCELERATOR AND DETECTOR DEVELOPMENTS FOR THE PRODUCTION OF THERANOSTIC RADIOISOTOPES WITH SOLID TARGETS AT THE BERN MEDICAL CYCLOTRON

A. Gottstein[1,†], P. Casolaro[1], G. Dellepiane[1], I. Mateu[1], P. Scampoli[1,2], S. Braccini[1]
[1] Albert Einstein Center for Fundamental Physics (AEC), Laboratory for High Energy Physics (LHEP), University of Bern, Bern, Switzerland
[2] Department of Physics "Ettore Pancini", University of Napoli Federico II, Complesso Universitario di Monte S. Angelo, Napoli, Italy

Abstract

Theranostics in nuclear medicine is realized by using two different radionuclides to label the same radiopharmaceutical, one for diagnosis via PET or SPECT (positron or gamma emitter, respectively) and one for targeted radioligand therapy (alpha, beta minus, Auger emitter). To assure the same chemistry and metabolic behaviour in the human body, the best option is to employ two radioisotopes of the same element, the so called theranostic pair. In view of clinical trials and routine applications, the production and supply of novel radioisotopes for theranostics in adequate quality and quantity is essential and represents nowadays a scientific and technical challenge. The most promising methodology relies on hospital-based 15-25 MeV compact medical cyclotrons equipped with solid target stations. Being designed for the production of ^{18}F by means of liquid targets, innovative solutions are needed. Therefore, a research program is ongoing at the Bern medical cyclotron, a facility equipped with a Solid Target Station and a 6.5 m Beam Transfer Line ending in a separate bunker. To irradiate isotope-enriched materials in form of compressed powder pellets (6 mm diameter), a novel target coin was conceived and realized together with methods to assess the beam energy and the production cross sections. To optimize the irradiation procedure, a novel ultra-compact Active Focusing System based on a specific magnetic device and a two-dimensional beam monitoring detector was conceived, constructed and tested. Several solutions for the beam detector were developed and others are under study. The system allows to control on-line the size and position of the beam and to correct its characteristics by steering and focusing it in order to keep it on target. Results on accelerator and detector developments together with achievements in the production of radionuclides for theranostics (^{43}Sc, ^{44}Sc, ^{47}Sc, ^{61}Cu, ^{64}Cu, ^{67}Cu, ^{68}Ga, ^{165}Er, ^{165}Tm, ^{167}Tm and ^{155}Tb) are presented.

INTRODUCTION

To enhance the availability of novel medical radioisotopes that can be used as theranostic pairs is crucial for the advancement of nuclear medicine. Theranostic pairs consist of two complementary radionuclides; a β^+ or γ emitting radionuclide is used for diagnosis via PET or SPECT imaging respectively, while the other radionuclide undertakes the radioimmuno-therapeutic task of emitting β^-, Auger, or α particles. These radionuclides must have similar or identical chemical properties, as in the case of isotopes of the same element. They can be used to label the same biomolecules, which are then injected into the patient's body and undergo the same metabolic processes. This allows for the treatment of the disease while simultaneously assessing uptake and monitoring the progress of the therapy through medical imaging. Examples of promising theranostic pairs include ^{43,44}Sc/^{47}Sc and ^{61,64}Cu/^{67}Cu, which are bound to proteins and peptides.

The availability of these radionuclides is a limiting factor in the development of theranostics in nuclear medicine. One solution is to utilize compact medical cyclotrons for the radionuclides' production, as they are commonly installed at medical institutions. Medical cyclotrons produce proton beams of low energy (15-20 MeV) and relatively high intensity (>100 μA). They are primarily used to produce ^{18}F - the most common PET radioisotope - through irradiation of liquid targets. However, to produce radiometals, rare and expensive isotope-enriched materials must be bombarded, which are often only available in powder form. To obtain high yields, solid target stations represent the best solution. These solid target stations, however, are rare and are typically designed to irradiate target 'disks' on which the enriched material is electroplated, a method not suitable for the production of various radiometals. Therefore, new irradiation instruments and methods must be developed to bombard compressed materials in powder form and in small dimensions of 6 mm diameter and smaller.

At the Bern University Hospital's cyclotron laboratory, research programs are ongoing to address these challenges and develop new solutions. The facility is equipped with an IBA Cyclone 18/18 medical cyclotron (18 MeV proton beams, maximum extracted current of 150 μA, 8 output ports). Six outports are used for routine production of ^{18}F at night, while the other two are used for multidisciplinary research during the day. One of the research outports is equipped with a 6.5 m long Beam Transport Line leading to a second bunker with separate access, which facilitates daily research. This is uncommon for a hospital-based facility but has been essential to achieve the results reported in this paper. The second research outport is equipped with a commercial IBA Nirta Solid Target Station (STS). This STS was customized by our group and upgraded to optimize

† alexander.gottstein@lhep.unibe.ch

ISBN: 978-3-95450-212-7 ISSN: 2673-5482 doi:10.18429/JACoW-CYCLOTRONS2022-WEB006

usability and efficiency, and is also part of several ongoing research projects, as also reported in this paper.

SOLID TARGET STUDIES

Target Coin

To irradiate solid targets for research on theranostic pairs of radionuclides we use an IBA Nirta STS. It is a commercial product that has been designed for the irradiation of disk shaped targets of 24 mm diameter and 2 mm thickness. Since several radiometals of theranostic interest are obtained from the irradiation of pellets of compressed powder (e. g. $CaCO_3$ or CaO irradiation for the production of scandium isotopes), our group conceived and produced a particular 'coin' target disk [1]. The coin is composed of two halves made from high purity aluminium and held together by permanent SmCo magnets that are arranged around the the disk's edges. Its size is of the same dimension as the intended STS targets. At the coin's centre a special cavity is placed, which leaves space for the containment of compressed powder pellets. Both, to bring the target coin into the STS before the irradiation and to bring it out again after an irradiation, respective remotely controllable systems have been installed. Coins can be loaded into the STS from outside the cyclotron's bunker with a custom system called *Hyperloop* [2]. To off load the coin safely after an irradiation, the STS is equipped with a commercially available pneumatic Solid Target Transfer System (STTS) by TEMA Sinergie.

Cross Section Measurements

To perform cross section measurements on the beam transfer line (BTL) a specific target station has been designed [4]. With the aid of these solid target irradiation set-ups several cross section measurements have been performed on isotopes of radiometals relevant for theranostics. A list of measured cross sections is shown in Table 1 (table taken from [3]). Additionally, studies have been performed for the isotopes ^{47}Sc [5] and ^{67}Cu [6], and are ongoing for ^{43}Sc and ^{167}Tm.

CURRENT HARDWARE DEVELOPMENTS

Our existing infrastructure at the Bern medical cyclotron, i.e. the STS and the BTL beam line are part of a constant improvement process where new devices and methods are tested with the aim of optimizing the production of radioisotopes. The latest projects are shortly described in the following section:

Automatic Focusing System

A device which is in advanced progress is the so-called Automatic Focusing System (AFS) [7, 8]. It's main goal is to enhance the production of non-conventional medical radioisotopes using solid targets. The first prototype of the AFS has been installed and tested on the BTL. It's integral part is an algorithm that calculates the optimal control currents of a Mini-PET beam line's quadrupole focusing magnets, provided by the Canadian company D-Pace, by means of real time beam shape measurements it obtains from a 2D beam monitoring device, such as the Pi2 detector or a two-dimensional UniBEaM detector [9]. The algorithm is capable of optimising the beam focus for a requested target geometry and, furthermore, it can also restore beam focus on target in the case of occurring perturbations. With irradiations performed at the BTL it could be shown that the yield of ^{66,67}Ga isotopes could be improved by a factor 20 with the usage of the AFS. After successful tests on the BTL, the AFS has also been installed on the STS outport, as shown in Fig. 1. This installation needs to undergo some optimisations, though, as in comparison to the BTL installation the proton beam's drift space is reduced and the algorithm needs to be updated. Furthermore, it is planned to replace the currently installed UniBEaM detector as the beam monitoring feedback device. The main reason for this is that the UniBEaM's beam detecting optical fibres are potentially unsuitable for high dose irradiations as they could melt under currents larger than 20 µA. Potential candidates that could serve as beam monitoring devices are e.g. the Pi2 detector or an apparatus called *Collar*, both of which are currently

Table 1: Main achievements in non-standard radioisotope production obtained with the STS at the Bern medical cyclotron. The integrated current corresponds to the amount of protons hitting the target material. The table is taken from [3].

Isotope	Reaction	Target	Mass [mg]	Charge [µAh]	Y [GBq/µAh]
^{44}Sc	(p, n)	^{enr44}CaO pellet	30	27	0.6
^{47}Sc	(p, α)	$^{enr50}TiO_2$ pellet	35	3.9e-3	0.001
^{61}Cu	(p, α)	^{enr64}Zn pellet	40	2.7e-4	0.14
^{64}Cu	(p, n)	^{enr64}Ni deposition	63	160	0.13
	(p, α)	^{enr67}ZnO pellet	59	2.7e-4	0.02
^{67}Cu	(p, α)	^{enr70}ZnO pellet	34	1.7e-3	0.001
^{68}Ga	(p, n)	^{enr68}Zn pellet	40	0.24	4.5
^{155}Tb	(p, n)	$^{enr155}Gd_2O_3$ pellet	40	1.1e-3	0.004
	(p, 2n)	$^{enr156}Gd_2O_3$ pellet	40	1.1e-3	0.01
^{165}Er	(p, n)	^{nat}Ho metal disk	160	1.7	0.07
^{165}Tm	(p, 2n)	$^{enr166}Er_2O_3$	59	1.1	0.02
^{167}Tm	(p, n)	$^{enr167}Er_2O_3$	41	0.01	0.003

ISBN: 978-3-95450-212-7 ISSN: 2673-5482 doi:10.18429/JACoW-CYCLOTRONS2022-WEB006

being developed by our group and are outlined in following sections in this paper.

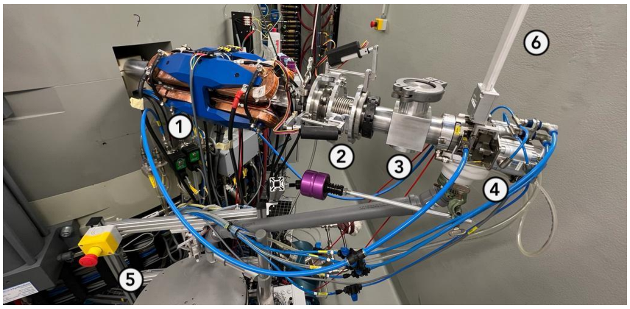

Figure 1: STS with AFS installed on the Bern medical cyclotron. 1: Mini-PET beam line, 2: Bellow++, 3: Space for beam monitoring device, 4: target holder, 5: Solid target transfer system (STTS), 6: Hyperloop target loading system.

Beam Monitoring

The UniBEaM beam monitor detector is a device developed by our group and commercialised by D-Pace. It is our go-to device for beam monitoring. Besides the UniBEaM detector also other instruments are being tested or under development:

Pi2 Detector The Pi2 detector is a beam monitoring device which is based on a coated thin aluminium foil. A picture of the detector installed on the BTL is shown in Fig. 2. The foil's P47 coating scintillates visible light when irradiated, which is then observed with a camera to evaluate the transverse position, shape, and the intensity of the beam by means of the analyzed camera output. A pneumatic system allows for the coated aluminium foil to be inserted into and removed from the proton beam, such that the beam is only minimally intrusive to the proton beam. The development of the device is in its final stages and the corresponding paper is in preparation.

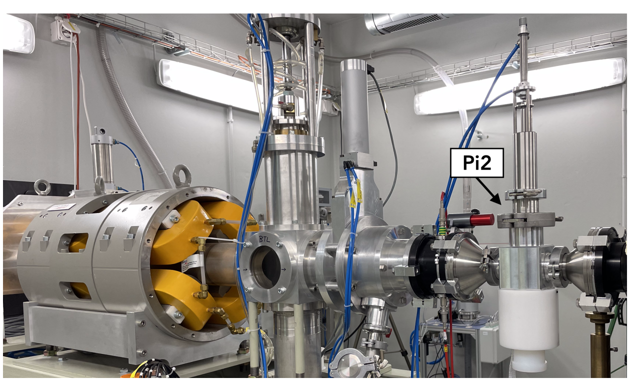

Figure 2: The Pi2 beam monitoring device installed on the BTL beam line during an irradiation.

Collar In a collaboration with TRIUMF [10] and D-Pace the development of a novel, totally non-beam invasive device called Collar is ongoing. On the basis of doped silica fibres responding to secondary radiation emitted from a respective target, the device can potentially help to give information about beam orientation and beam focusing without directly interacting with the proton beam itself, since the fibres are only mounted on the outside of the respective target and not in the actual beamline.

FURTHER MEASUREMENTS AND IMPROVEMENTS

Beam Energy Measurement

When irradiating solid targets, besides knowing the shape, direction and intensity of the proton beam, it also very important to know the exact proton energy. To accurately measure this quantity, our group made use of a technique using the well known ^{nat}Ti(p,X)^{48}V monitor reaction. Stacks of thin titanium layers are separated by an energy absorbing Nb-layer and placed in a special target coin. The number of layers per stack as well as the thickness of the layers is configured in a way, such that the layers are irradiated at energies where the monitor reaction's cross section gradient is the steepest. Additionally to the current on target, each layer's activity is then measured by gamma spectroscopy and compared to theoretical activities that are calculated for several initial beam energies. Using a least square fit, the proton beam's energy is then determined within uncertainties. The method has been tested and implemented for the BTL and a beam energy of 18.28 ± 0.05 MeV has been measured [11]. Beam energy measurements for the STS are in progress and a publication is soon to be released.

Bellow++

The STS has been very recently upgraded with an additional tool which will help in the optimisation of the beam steering and focusing, and enhance the usability of the target station. Regular maintenance works on the cyclotron's hardware can lead to changes to the extracted proton beam's geometry. Since the STS only has a limited drift space, there are limits set with regard to focusing and steering capabilities of the Mini-PET beam line. To change the absolute position of the target, a remotely controllable bellow has been installed on the beam line, as can be seen in Fig. 1. Two linear motors can move the target with respect to the outport independently in horizontal and vertical direction. A range of motion of ±5 mm in both directions is enough to compensate for the potentially occurring deviations in the beam's extraction geometry. The device is being tested and the controlling software is under development.

CONCLUSION

The Bern cyclotron laboratory is currently conducting a research program focused on the production of nonconventional radioisotopes. Besides studies on the production of novel radioisotopes for theranostic applications the program involves the development and testing of novel instruments for beam monitoring and methods based on advancements in accelerator and detector physics. The successful results

ISBN: 978-3-95450-212-7 ISSN: 2673-5482 doi:10.18429/JACoW-CYCLOTRONS2022-WEB006

obtained so far represent a significant advancement towards the goal of establishing efficient and reliable radioisotope supply using compact medical cyclotrons for theranostic applications in nuclear medicine.

ACKNOWLEDGEMENTS

We acknowledge the contributions from LHEP engineering and technical staff to various projects of us. We would like to thank to TRIUMF, D-Pace and Samuel Usherovich for the fruitful collaboration on the Collar project. This research was partially supported by the Swiss National Science Foundation (SNSF). Grants: 200021_175749 and CRSII5_180352

REFERENCES

[1] S. Braccini, C. Belver-Aguilar, T. Carzaniga, G. Dellepiane, P. Haeffner, and P. Scampoli, "Novel Irradiation Methods for Theranostic Radioisotope Production With Solid Targets at the Bern Medical Cyclotron", in *Proc. Cyclotrons'19*, Cape Town, South Africa, 2020, pp. 127–131. doi:10.18429/JACoW-Cyclotrons2019-TUA02

[2] G. Dellepiane *et al.*, "New methods for theranostic radioisotope production with solid targets at the Bern medical cyclotron", *EPJ Web of Conferences*, vol. 261, p. 05 006, 2022. doi:10.1051/epjconf/202226105006

[3] G. Dellepiane *et al.*, "Research on theranostic radioisotope production at the Bern medical cyclotron", *Il Nuovo Cimento C*, vol. 44, pp. 1–4, 2021. doi:10.1393/ncc/i2021-21130-6

[4] T. S. Carzaniga *et al.*, "Measurement of ^{43}Sc and ^{44}Sc production cross-section with an 18 MeV medical PET cyclotron", *Appl. Radiat. Isot.*, vol. 129, pp. 96–102, 2017. doi:10.1016/j.apradiso.2017.08.013

[5] G. Dellepiane, P. Casolaro, I. Mateu, P. Scampoli, N. Voeten, and S. Braccini, "^{47}Sc and ^{46}Sc cross-section measurement for an optimized ^{47}Sc production with an 18 MeV medical PET cyclotron", *Appl. Radiat. Isot.*, vol. 189, p. 110 428, 2022. doi:10.1016/j.apradiso.2022.110428

[6] G. Dellepiane, P. Casolaro, A. Gottstein, I. Mateu, P. Scampoli, and S. Braccini, "Optimised Production of ^{67}Cu Based on Cross-Section Measurements of ^{67}Cu and ^{64}Cu Using an 18 MeV Medical Cyclotron", *Social Sci. Res. Network*, 2022. doi:10.2139/ssrn.4305864

[7] P. D. Häffner, C. Belver-Aguilar, P. Casolaro, G. Dellepiane, P. Scampoli, and S. Braccini, "An Active Irradiation System with Automatic Beam Positioning and Focusing for a Medical Cyclotron", *Appl. Sci.*, vol. 11, p. 2452, 2021. doi:10.3390/app11062452

[8] P. Casolaro *et al.*, "An Automatic Focalization System for Enhanced Radioisotope Production with Solid Targets", in *Proc. IBIC'21*, Pohang, Rep. of Korea, 2021, pp. 150–153. doi:10.18429/JACoW-IBIC2021-MOPP38

[9] S. Braccini *et al.*, "A beam monitor detector based on doped silica and optical fibres", *J. Instrum.*, vol. 7, 0T02001, 2012. doi:10.1088/1748-0221/7/02/T02001

[10] S. Usherovich, C. Penner, G. Hodgson, E. Thoeng, M. Dehnel, and C. Hoehr, "Optical fibre array detector to monitor irradiations for medical radioisotope production", *J. Phys.: Conf. Ser.*, vol. 2374, p. 012 182, 2022. doi:10.1088/1742-6596/2374/1/012182

[11] E. Zyaee, "A Novel Method to Measure the Energy of Accelerated Protons based on the Irradiation of Stacked Titanium Foils - Master Thesis", University of Bern - Laboratory for High Energy Physics (LHEP), 2021.

ISBN: 978-3-95450-212-7 ISSN: 2673-5482 doi:10.18429/JACoW-CYCLOTRONS2022-WEPO001

FIELD MATCHING OF F-D-F, GAP SHAPING MAGNETS FOR A 2 GeV CW FFA*

Wei Fu†, Tianjue Zhang, Chuan Wang, Tianjian Bian, Hongji Zhou, Xiaofeng Zhu, Suping Zhang
China Institute of Atomic Energy, P.O. Box 275(3), Beijing, China

Abstract

Fixed Field Alternating Gradient Accelerators have been developed for decades. A continuous wave (CW) 2 GeV FFA which aims at high-power proton beam applications is under developing in China Institute of Atomic Energy (CIAE). To avoid dangerous resonance lines and manipulate the tune diagram flexibly, 3rd order magnetic field is applied along the radius and 10-fold symmetrical F-D-F scheme has been proved to be feasible. In this paper, Integral Equation Method (IEM) is introduced and shown more efficient than adjusting the variable gap manually, saving time for magnet design. First of all, the radial mean field is set as a main design goal and the ΔH at different radii is solved by linear equations based on IEM. The isochronism is done when the mean field is well matched with the design value, whereas some precise corrections are needed for the oscillating frequency ν_r and ν_z, such as fringe field effects and multipole components near the end of pole face. The tune shift caused by fringe field is also included in this paper. Fringe field is more crucial for HTS magnets especially, since the leaked field of superconducting coil is ~1 kGs. Considering that, we apply an angular matching method to compensate the tune shift by fringe field.

INTRODUCTION

Continuous wave (CW) FFA which combines the characteristics of both cyclotrons and synchrotrons is a potential solution to provide MW proton beams for many important applications, such as accelerator driven subcritical system (ADS), neutron sources and neutrino factory [1]. CIAE launched the researches on CW FFAs in 2013 and proposed an energy efficient FFA design in 2019 [2]. High temperature superconducting (HTS) magnets and high-Q value RF cavities are adopted in the overall design of 2 GeV CW FFA, for a higher energy efficiency and less operating cost. Different types of magnets are presented for both scaling and non-scaling FFA, such as room temperature magnets [3], superferric magnets [4] (superconducting coils with warm iron) and iron-free superconducting magnets [5]. Gap shaping iron with HTS coils is applied in consideration of engineering convenience and operating cost. The 10-fold symmetrical F-D-F lattice design for the main machine is completed, which leads to next stage of magnet design. HTS magnets for FFA application are researched for serval years and some experimental coils are wound to support engineering feasibility [6]. In practice, field matching is not crucial issue in FFA design. But for our non-scaling 2 GeV FFA, which introduces third order field in wide range along radius, it is important to match the second and third order field to ensure isochronism and tune.

Moreover, fringing fields of entrance and exit side can affect the working diagram and result in tune shift, which requires prudent evaluation and compensation [3, 7], even if we match the mean field almost perfectly. This problem is more prominent in superconducting magnets and need to be well considered. Above all, the basic design of F-D-F lattice is introduced. The F-D-F lattice and static equilibrium orbits are shown in Fig. 1, in which red blocks represent focusing magnets and yellow block for defocusing magnet.

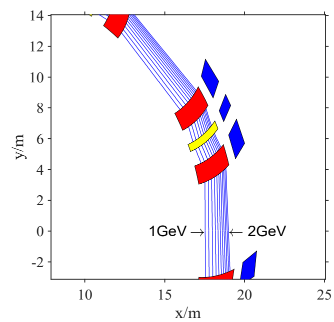

Figure 1: Layout of F-D-F magnets and static equilibrium orbits (1 GeV to 2 GeV).

Basic parameters of focusing and defocusing magnets are listed in Table 1.

Table 1: Parameters of Focusing and Defocusing Magnet

Item	Focusing magnet	Defocusing magnet
Pole length / m	2.1	2.1
Field range / T	1.57~2.66	-2.31~-1.15
Angular width / deg	4	1.6
Spiral angle / deg	0~36	0~36

ANALYTICAL MODEL

Approximation of Saturated Iron Blocks

In scaling FFAs, the magnetic field distribution is clear and defined using the Eq. (1) below:

$$B(r) = B_0\left(\frac{r}{r_0}\right)^k . \quad (1)$$

Therefore, the gap shape is expressed by:

$$g(r) = g_0\left(\frac{r}{r_0}\right)^k , \quad (2)$$

* Work supported by the National Natural Science Foundation of China under Grant 12135020 and the basic research fund from the Ministry of Finance of China under Grant BRF201901.
† fuwei@ciae.ac.cn.

ISBN: 978-3-95450-212-7 ISSN: 2673-5482 doi:10.18429/JACoW-CYCLOTRONS2022-WEPO001

simply. For CIAE 2 GeV FFA machine, though the peak field is described by 3rd order polynomial, the gap shape could be obtained in a similar way. However, magnetic field distribution of gap size which is attained Eq. (2) is far from accurate gap size due to complicated magnetization. Analogous to the shimming process of traditional cyclotrons, magnetic field of iron blocks which are located in different radius can be calculated using finite element method (FEM). In superferric magnets, due to the utilization of superconducting coils with higher current for excitation, some simplifications could be reasonable in calculating the field. In detail, the field in iron poles are close to saturation, which could be verified by FEM later. The state of iron magnetization can be regarded as saturated and the numerical calculation of small iron blocks with a cutting height of ΔH can be performed using the IEM. The field of saturated iron blocks is obtained by Eq. (3):

$$\boldsymbol{H_m} = \frac{1}{4\pi}\oint(\boldsymbol{M_s}\cdot\boldsymbol{n})\frac{(\boldsymbol{r}-\boldsymbol{r_i}')}{|\boldsymbol{r}-\boldsymbol{r_i}'|^3}\mathrm{d}s, \tag{3}$$

where $\boldsymbol{M_s}$ is the magnetization and $\boldsymbol{n}$ is the normal vector. The integration is implemented in both upper and lower surfaces of iron block as illustrated in Fig. 2.

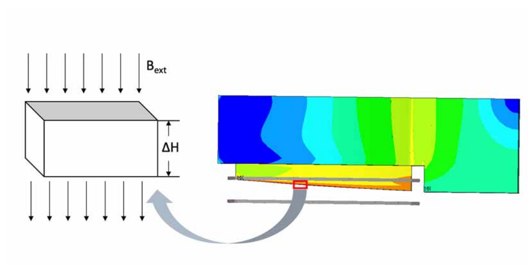

Figure 2: Schematic diagram of saturated iron blocks.

In view of this, IEM is more efficient than FEM to obtained the field caused by iron blocks. For simplicity, we assume that the magnetic field contribution from iron at different radius can be combined and the amplitude of field bump is linear to the height of iron block. The difference between the magnetic field required by the theoretical design and the magnetic field calculated by FEM can be expressed as ΔB in Eq. (4).

$$\Delta B(r) = \sum_{i=0}^{n}\alpha_i \Delta B_i(r) \tag{4}$$

To verify this approximation of saturation, two cases for uniform gap 0.1 m and 0.05 m are calculated. Comparisons between IEM and FEM calculated fields at different location of spiral magnet are shown in Fig. 3(a) and 3(b), while ΔH of each case is 10 mm. The amplitude of IEM result is different from FEM, which indicates that the saturated field is mutative with gap size. Adjustment coefficients of a series of gap sizes could be useful for more accurate calculation.

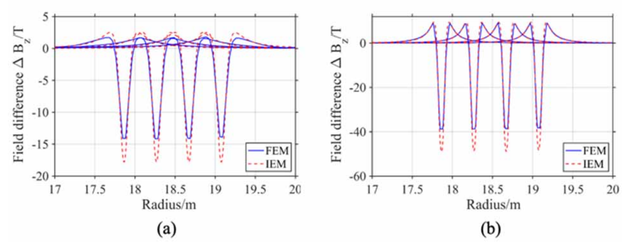

Figure 3: Comparison between IEM and FEM, two cases (a) gap = 0.1 m, (b) gap = 0.05 m.

Construction of Linear Equations System

The linear assumption metioned above is only valid within a certain range of adjustment. If the range of the adjustment needs to be limited, linear programming (LP) method could be used to solve this prolem. In other words, Eq. (4) could be transformed into following minimum optimization problem, shown in Eq. (5):

$$\min \lambda \\ \begin{cases} M\cdot\alpha - \lambda \le 0 \\ -(M\cdot\alpha+\lambda) \le 0\,, \\ \alpha_l \le \alpha_i \le \alpha_u \end{cases} \tag{5}$$

where M is the coefficient matrix quantifies magnetic field caused by unit iron block, α_l and α_u are the upper and lower limits of the adjustment coefficient. The optimized goal λ stands for the maximum of field deviation. When the solution of this LP problem is found, optimal gap shape is obtained at the same time.

Fringe Field of Spiral Edges

Many analytical models have been proposed for fringe field of magnets. For convenience and conciseness, theoretical fields of F-D-F magnets adopts Enge function to model the fringe field. However, opposite field occurs near the edge of HTS magnet which makes it inaccurate using Enge function. Researchers have found that the variable gap is conflict with tuning of fringe field in scaling FFAs [3]. In our CW machine, mean field is set as matching goal to construct isochronous field primarily. For fringe field correction, the difference of flutter plays an important role in tune shift and high order contribution to vertical oscillation frequency is eliminated. Since the mean field has been well-matched with theoretical field distribution, only the $\langle B^2\rangle$ items should be considered, which can be separated in Eq. (6) below.

$$\langle B^2\rangle = \langle (B_f+B_d)^2\rangle \approx \langle B_f^2\rangle + \langle B_d^2\rangle, \tag{6}$$

where B_f is the field of two focusing magnet, B_d is the field of one defocusing magnet. Consistent with the traditional effective length adjustment method, one can obtain an adjustment amount for the pole face length based on the flutter matching. The quantity of adjustment can be expressed as Eq. (7):

$$\Delta l = l' - l = l_d\sqrt{\frac{\int f_1^2(s)\mathrm{d}s}{\int g^2(s)\mathrm{d}s}} - l, \tag{7}$$

ISBN: 978-3-95450-212-7 ISSN: 2673-5482 doi:10.18429/JACoW-CYCLOTRONS2022-WEPO001

where f and g are the normalized distribution function of focusing and defocusing magnet. Since function of distribution would change with pole length, correction process is carried out iteratively.

FIELD MATCHING RESULTS

Mean Field Matching in Radial direction

According to this IEM-based method, magnetic field differences between the FEM model and theoretical calculation are shown in Fig. 4, which illustrates that the relative error of the mean field can be minimized to 2%.

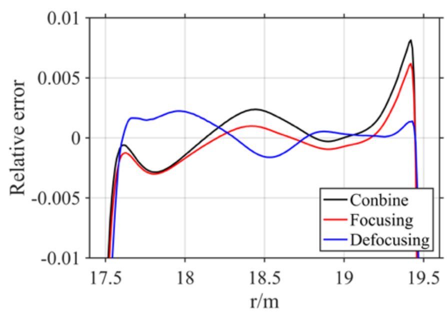

Figure 4: Radial mean magnetic field relative error.

Isochronism

Static beam dynamic of single particle is carried out to verify the FEM model. Differential and integral phase slip with FEM field is shown in Fig. 5 below, which indicates that average fields of FEM calculated field and theoretical design is matched well.

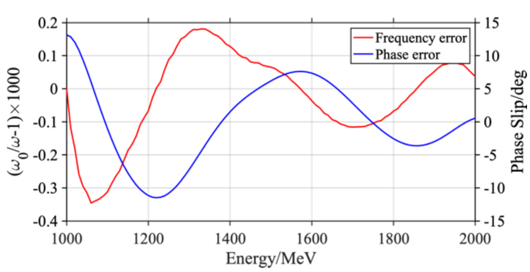

Figure 5: Differential and integral phase slip with FEM field.

Tune Diagram and Stable Regions

The tune diagram calculated by different FEM models is shown in the Fig. 6 below. The axial oscillation frequency is much higher than the design without any correction and the reason is the fringe field of the opposite direction. If we adopt the effective length correction mentioned in analytical equation, the working path is closer to the design result. Furthermore, the gap between design and FEM results can be narrowed with fringe field correction using Eq. (7). By adjusting the angular width, the change of flutter with the radius can be corrected, so that the axial working point calculated by finite element can be adjusted to the vicinity of the theoretically designed axial working point, which proves that the method is feasible.

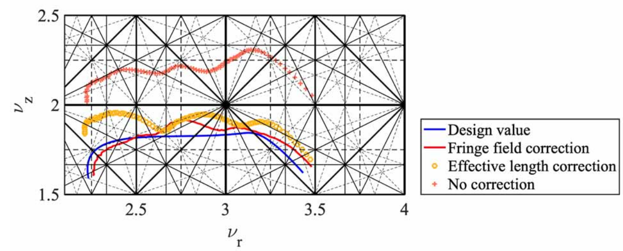

Figure 6: Tune diagram correction process.

Stable region for particle motion is also calculated based on FEM field. It can be seen from Fig. 7, that the dynamic aperture obtained by FEM calculation is not much different from the theoretical magnetic field for the resonance line of $3\nu_r = 10$; but for the high-order resonance $4\nu_r = 10$, the aperture obtained by finite element calculation is much smaller than theoretical value. The numerical error in the modelling and calculation process of the FEM magnetic field is the main reason, which leads to the local drastic change of the high-order driving term.

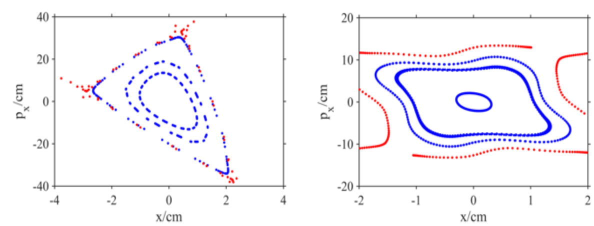

Figure 7: Stable phase region calculated with FEM field, $3\nu_r = 10$ (left), $4\nu_r = 10$ (right).

CONCLUSION

In this paper, a method for matching field distribution between FEM model and theoretical design is introduced. There are some problems coming with high field and compact scheme of magnet, such as fringe field and high order components. Two main problems have been solved, which are high order field matching and tune shift correction caused by fringe field. Particularly, the field matching result demonstrates relative error between design and FEM model is 2%, which guarantees the isochronism of whole machine. Based on this method, the gap between magnetic engineering and physical design is narrowed.

REFERENCES

[1] C. Johnstone *et al.*, "Advances in nonlinear non-scaling FFAGs," *Int. J. Modern Phys. A*, vol. 26, no. 10-11, pp. 1690-1712, Apr. 2011. doi:10.1142/S0217751X11053110

[2] T. J. Zhang *et al.*, "A New Solution for Cost Effective, High Average Power (2 GeV, 6 MW) Proton Accelerator and its R&D Activities", in *Proc. Cyclotrons'19*, Cape Town, South Africa, Sep. 2019, pp. 334-339. doi:10.18429/JACoW-CYCLOTRONS2019-FRA01

[3] T. Planche *et al.*, "Design of a prototype gap shaping spiral dipole for a variable energy proton therapy FFAG," *Nucl. Instrum. Methods Phys. Res. Sect. A*, vol. 604, no. 3, pp. 435-442, 2009. doi:10.1016/j-nima.2009.02.026

[4] B. Qin *et al.*, "Compact superferric FFAG accelerators for medium energy hadron applications," *Nucl. Instrum. Methods Phys. Res. Sect. A*, vol. 648, no. 1, pp. 28-34, Aug. 2011. doi: 10.1016/j.nima.2011.05.035

[5] T. Obana *et al.*, "Magnetic field design of a superconducting magnet for a FFAG accelerator," *IEEE Trans. Appl. Supercond.*, vol. 15, no. 2, pp. 1185-1188, Jun. 2005. doi:101109/TASC.2005.849528

[6] N. Amemiya *et al.*, "Research and development of fundamental technologies for accelerator magnets using high Tc superconductors," *Physica C Supercond. Appl.*, vol. 482, no. 1, pp. 74-79, Nov. 2012. doi:10.1016/j.physc.2012.05.017

[7] J. Fourrier *et al.*, "Spiral FFAG lattice design tools. Application to 6-D tracking in a proton-therapy class lattice," *Nucl. Instrum. Methods Phys. Res. Sect. A.*, vol. 589, no. 2, pp. 133-142, May 2008. doi:10.1016/j-nima.2008.01.082

ISBN: 978-3-95450-212-7 ISSN: 2673-5482 doi:10.18429/JACoW-CYCLOTRONS2022-WEPO002

A COMPARSION STUDY OF THE DESIGNING MODELS OF RANGE MODULATOR BY USING FLUKA SIMULATION CODES*

Yue Wang, Li Sui†, Yihao Gong, Jiancheng Liu, Qiaojuan Wang
China Institute of Atomic Energy, Beijing, China
National Innovation Center of Radiation Application, Beijing, China

Abstract

In this study, we investigated the optimization of the range modulator. Range modulator used in proton radiotherapy is expected to be accurate enough to achieve spread-out Bragg peak (SOBP). Based on the theory of Thomas Bortfeld, four different range modulator models were designed and compared using FLUKA simulation codes. The four models were: uneven ridge filter, smooth ridge filter, uneven range modulator wheel, and smooth range modulator wheel. Using 100 MeV and 230 MeV proton beams, the dose spatial distribution of the four models were calculated when the SOBP sections were 3, 5, 10, and 20 cm. The results showed that in ideal motion condition, the four models all showed the ideal range modulation effect. The best average value of the difference was less than 2%, while the worst one was still less than 5%. The evenness of the smooth models is improved compared with the uneven models. The smooth ridge filter model performed best. Based on this model, we tried to realize the movement of the SOBP region by adding a binary shielding layer. The results showed that the SOBP region can move in a small range at the expense of acceptable accuracy error. This study provides a design reference for the range modulator in proton therapy, and provides a new technical scheme to fill the target area for precise therapy.

INTRODUCTION

Radiation therapy is one of the three most effective treatments for cancer, the other two being chemotherapy and surgical resection. Radiation therapy refers to the use of radiation to irradiate the tumor area, and the relative biological effect of the radiation to damage the DNA of malignant tumor cells, so as to achieve the purpose of killing or reducing cancer cells.

Charged particle therapy (CPT), including proton and heavy ion therapy, is currently the advanced direction of radiotherapy. The advantage of CPT is that the concentrated dose distribution pattern of charged particles makes it possible to artificially and accurately control the dose distribution in the target area, thereby achieving higher tumor control probability and lower normal tissue complication probability. The unique Bragg peak dose distribution pattern of protons and heavy ions makes the advantages of CPT possible [1]. Taking protons as an example, single-energy protons have a low dose before the human body, slowly increase the dose after entering the human body, climb rapidly to the terminal peak, and finally decline rapidly, achieving a high concentration of doses, of which the highest point of the dose is called Bragg peak [2], see Fig. 1. In actual use, Bragg peak needs to include the lesion to ensure an even and flat dose distribution in the target area. The Bragg peak of a single-energy proton ray is extremely narrow, generally between a few millimeters and one centimeter. It is impossible to encompass the lesion completely, so the Bragg peak needs to be widened. The most basic broadening way is to use particle beams of different energies to irradiate together, and superimpose them according to different weights to form a relatively gentle flat area in the target area [3]. In actual use, only one single energy particle beam can be provided at one time, so the device that can convert a single energy particle beam into a multi-energy particle beam with a specified weight ratio is needed, which is called range modulator. The range modulator to achieve SOBP is an extremely important part of the treatment head system of CPT equipment.

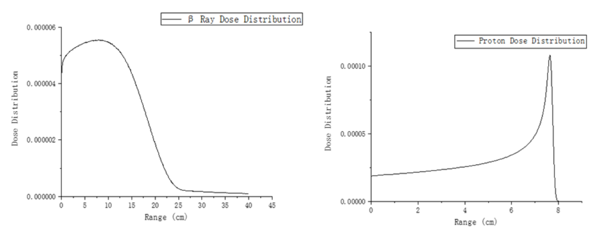

Figure 1: The dose distribution of β-ray and proton.

The Bragg peak of the single energy particle beam is broadened to a flat dose distribution region by the modulator's geometry and relative motion. Because the parameters of the range modulator vary with different width and depth of certain SOBP, it is necessary to customize the range modulator according to the patient's situation in actual use, so it is of great significance to study the design process and optimization of the range modulator.

SIMULATION METHOD

Since experimental opportunities are precious, it is necessary to conduct simulation studies of range modulators prior to experiments.

Monte Carlo Simulation Codes

In this study, FLUKA was selected as the Monte Carlo (MC) simulation software. FLUKA is a universal MC particle transport simulation software that runs on Linux. Through continuous updates, FLKUA now supports the transport process and measurement simulation of about 60 kinds of particles including photons, electrons, protons, and various heavy ions in magnetic field, electric field, and thermal field, and supports users to program the particle

* Work supported by CIAE Youth Fund YC202212000201
† lisui@ciae.ac.cn

ISBN: 978-3-95450-212-7 ISSN: 2673-5482 doi:10.18429/JACoW-CYCLOTRONS2022-WEPO002

distribution and motion in the transport process through the FORTRAN interface to realize complex processes. Through custom program compilation, FLUKA allows users to perform partial or global spatial calculations during particle transport. FLUKA itself is difficult to build complex geometric structures, and users can build complex geometry through CG tool kits or SimpleGeo.

Typical Range Modulator Models

The existing commonly used range modulators are divided into range modulator wheels (RMW) and ridge filters (RF). Through periodic movement, the fixed particle beam passes through the shielding layer of different thickness. The particle energy is the smallest when passing through the thickest area, while the particle energy is the largest when passing through the smallest thickness area. The area of different thicknesses and the particle movement speed are adjusted to achieve the distribution of scanning time in line with the weight ratio, thereby realizing the SOBP of the single-energy particle beam.

The common design method of the range modulator wheel is to divide the entire circumferential area into several equal pieces, each piece is divided according to the center angle of the multi-energy particle beam weight, and each small piece divided has a different specific material thickness (Fig. 2). RMW rotates at a uniform speed under the irradiation of the particle beam, and the size of the center angle determines the residence time of the particle beam in this area, and the corresponding material thickness determines the energy of the outgoing particle beam, so that the dose average is achieved on the time scale [4].

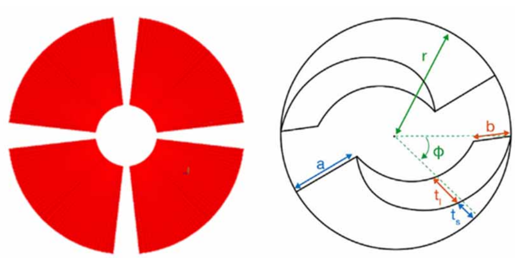

Figure 2: Typical range modulator wheel.

In addition to the range modulator wheel, another commonly used range modulator is the ridge filter. Ridge filters, also known as washboard filters, generally consist of continuous triangular pyramids. Each triangular pyramid section is generally not a rectilinear triangle in the strict sense, but a block of different thicknesses. The particle beam passes through the highest place with the lowest exit energy and the highest energy at the lowest, and the width of each block determines the distribution weight [5]. Generally, the size of the whole washboard is about 10 to 20 cm, and the mid-ridge filter is used to move laterally, and the particle beam skims over the surface of the ridge filter, and is broadened by energy-reducing materials of different thicknesses and widths.

Models and SOBP Simulation

Based on the theory of Thomas Bortfeld and simplified adaptation function method, four different range modulator models were designed and compared by using the FLUKA simulation codes. The four models were: uneven ridge filter, smooth ridge filter, uneven range modulator wheel, and smooth range modulator wheel.

Taking ridge filter modelling as an example, a single ridge tooth was modelled first, and the overall effect can be achieved by motion equivalence. From the size conversion, one single ridged tooth was divided into a PMMA cuboid combination with a thickness of 73 layers, and a 73-layer cuboid was constructed in the void area, with the Z coordinate of each layer set to the PMMA thickness, the Y coordinate set to the weight adaptation width, and the X coordinate is uniformly set to 2 cm to build a uniform "triangular pyramid", while a gap of 1e-6 cm inserted between each layer. The material used to fill these voids is vacuum, so there is no additional energy loss. The OR operation in the Boolean operation was used to combine the above spatial volumes into a whole, and the material was selected as PMMA to obtain a single ridged tooth structure of the ridge filter, see Fig. 3. The smoothing filter model was obtained by converting its edges into elliptic curves by quadratic term fitting. The range modulation wheel model construction methods were similar.

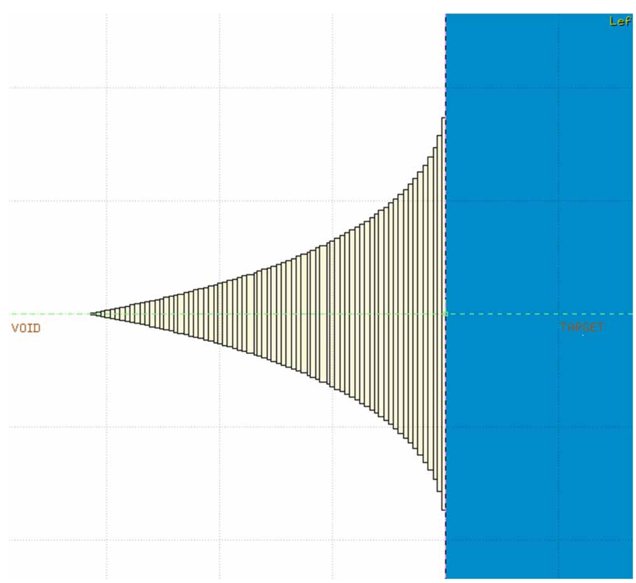

Figure 3: A single ridge filter tooth structure.

RESULTS

By adjusting the sensitivity coefficient k value in the adaptation function method, the proton Bragg peak broadening curve gradually changed from a downward trend to an uptrend, and the best broadening effect existed. According to the calculation of flatness and flat width, the best broadening effect was achieved for the ridge filter and the range modulation wheel under the corresponding weigh ratio

ISBN: 978-3-95450-212-7 ISSN: 2673-5482 doi:10.18429/JACoW-CYCLOTRONS2022-WEPO002

Table 1: SOBP Effects of the Four Models

Average Value of the Difference	Uneven Ridge Filter	Smooth Ridge Filter	Uneven Range Modulator Wheel	Smooth Range Modulator Wheel
100 MeV - 3 cm SOBP	0.99%	0.86%	0.92%	0.88%
100 MeV - 5 cm SOBP	1.18%	1.02%	1.10%	1.06%
230 MeV - 10 cm SOBP	1.21%	0.94%	1.24%	0.96%
230 MeV - 20 cm SOBP	1.62%	1.08%	1.52%	1.06%

when k = 0.7. At the 98% confidence level, the widening results of the uneven ridge filter were as follows: the SOBP ping area was [4.10, 7.42] cm, and the flatness of the corresponding flat area was 99.14%. The remaining results can be found in Table 1.

The results showed that in ideal motion condition, the four models all showed the ideal range modulation effect. The average value of the difference was less than 2%. The evenness of the smooth models is improved compared with the uneven models. The smooth ridge filter model performed best.

DISCUSSION

For a certain sensitivity coefficient k, the broadening results of the range modulator designed according to the corresponding weights had an upward slope trend compared with the multi-energy particle weight matching model, which indicates that the high-energy region weight of the physical model was higher than that of the theoretical model.

The possible reason is that the construction of the physical model increased the scattering effect of the particles [6-8]. Because in the theoretical model, through the user-defined program, single-energy proton beams of different intensities and different energies were shot vertically into the water model target area. And the area passed through before entering the target area was vacuum, and there was no side scattering phenomenon, and side scattering can exist only when entering the water model. In the physical model, the equivalent single-energy proton beams first passed through the PMMA shielding layer of different thicknesses and then entered the water, which increased the process of proton movement in the PMMA material. The protons in the scattering bifurcation part didn't pass through the expected length of the PMMA shield to attenuate enough energy, but kept the higher energy out of the material through the vacuum and hit the target, leading to the detector received additional high-energy proton signals. At the same time, the lower the energy, the coarser the trail, and the expected share of low-energy protons through the shielding layer was larger, and the share of lateral scattering was larger. The higher the energy, the finer the trail, the smaller the bifurcation, the thinner the shield that was expected to pass through, and the smaller the chance of lateral scattering. On the whole, the physical model had an extra share of side scatter, and it was expected that low-energy protons were more likely to be side-scattered to reduce energy attenuation, thereby increasing the share of high-energy regions.

In order to verify whether the weight ratio changed due to the dose contribution of secondary particles, the two physical models of k = 0.7 and k = 2.1 were divided into fine grids in the YZ direction to simulate the dose distribution. The upper result in Fig. 4 is the YZ direction dose distribution at k = 0.7, it can be seen that protons were uniformly deposited at this scale, basically no obvious deviation, although more energy is deposited in the range modulator, and the proton dose injected into the water mold was low overall, but it is relatively uniform and the broadening effect is the best. Another result is the YZ plane dose distribution while k = 2.1, showing an obvious discrete state. The energy deposition is concentrated around Y = 0 and Z = 0, and the thickness of the PMMA layer passed through by the proton beam near the Y = 0 straight line corresponded to the smaller the energy injected into the water mode, and the more shares of these protons were deposited in the modulator. And the proportion of protons after injection into water naturally decreased. However, the proton beam deviating from Y = 0 was less deposited in the modulator, and the proportion of injection into the water mold values from k = 0.7 and k = 2.1 can also be verified from naturally increased, so the effect of widening the flat area

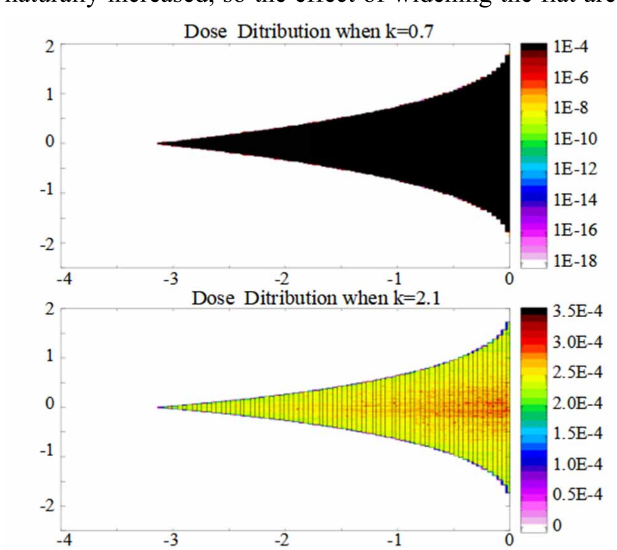

Figure 4: Dose distribution of two physical models of k = 0.7 (top) and k = 2.1 (bottom).

ISBN: 978-3-95450-212-7 ISSN: 2673-5482 doi:10.18429/JACoW-CYCLOTRONS2022-WEPO002

was tilted upward. The un-normalized water mode dose the side of the two models: the dose in the broadened ping area when k = 0.7 was 3.38E-5, while the dose in the k = 2.1 broadened flat area fluctuated from 3.3E-5 to 3.70E-5, which showed that there was a difference in dose deposition in the physical model of k = 2.1, and less dose was deposited compared with the k = 0.7 model.

POTENTIAL OPTIMIZATION

On the basis of smooth RF model, we tried to realize the movement of the SOBP region by adding a binary shielding layer. The results showed that the SOBP region can move in a small range at the expense of acceptable accuracy error.

CONCLUSION

The essence of proton range modulation is to weight protons of different energies. In this study, FLUKA was used for Monte Carlo calculation, and the broadening results of four different range modulator models were calculated and compared, and finally the optimal broadening model was obtained by screening. Based on the calculation results, the influence of secondary particle dose contribution in the range modulation process was discussed, and possible improvement schemes were explored to lay a foundation for subsequent research.

ACKNOWLEDGEMENTS

Valuable discussions and help from Dr. J. L. Wang of CIAE are acknowledged.

REFERENCES

[1] S. Michiels *et al.*, "Patient-specific bolus for range shifter air gap reduction in intensity-modulated proton therapy of head-and-neck cancer studied with Monte Carlo based plan optimization", *Radiotherapy and Oncology*, vol. 128, no. 1, pp. 161-166, 2018. doi:10.1016/j.radonc.2017.09.006

[2] H. Suit *et al.*, "Proton vs carbon ion beams in the definitive radiation treatment of cancer patients", *Radiotherapy and Oncology*, vol. 95, no. 1, pp. 3-22, 2010. doi:10.1016/j.radonc.2010.01.015

[3] C. H. Kim *et al.*, "Practical biological spread-out Bragg peak design for a carbon beam", *J. Korean Phys. Soc.*, vol. 67, pp. 1440-1443, 2015. doi:10.3938/jkps.67.1440

[4] S. B. Jia *et al.*, "Designing a range modulator wheel to spread-out the Bragg peak for a passive proton therapy facility", *Nucl. Instrum. Methods Phys. Res., Sect. A*, vol. 806, pp. 101-108, 2016. doi:10.1016/j.nima.2015.10.006

[5] M. H. Jung *et al.*, "Design of a ridge filter for spread-out Bragg-peak production in a pulsed 100-MeV proton beam", *J. Korean Phys. Soc.*, vol. 63, pp. 1441-1445, 2013. doi:10.3938/jkps.63.1441

[6] L. Rezaee, "Design of spread-out Bragg peaks in hadron therapy with oxygen ions", *Reports of Practical Oncology & Radiotherapy*, vol. 23, no. 5, pp. 433-441, 2018. doi:10.1016/j.rpor.2018.08.004

[7] I. Park, "A new approach to produce spread-out Bragg peak using the MINUIT fit", *Curr. Appl Phys.*, vol. 9, no. 4, pp. 852-855, 2009. doi:10.1016/j.cap.2008.07.022

[8] D. W. Kim *et al.*, "Prediction of output factor, range, and spread-out Bragg peak for proton therapy", *Med. Dosim.*, vol. 36, no. 2, pp. 145-152, 2011. doi:10.1016/j.meddos.2010.02.006

ISBN: 978-3-95450-212-7 ISSN: 2673-5482 doi:10.18429/JACoW-CYCLOTRONS2022-WEPO003

BEAM DYNAMICS IN A NEW 230 MeV CYCLOTRON

O. V. Karamyshev†, Joint Institute for Nuclear Research, Dubna, Russia

Abstract

A new cyclotron for proton therapy concept is a compact, but non-superconducting accelerator, that is simple, but cheap. Proposed concept uses 4 sectors with double spiral design and 4 RF cavities operating at harmonic 8, making the central region and extraction a challenging task that needs to be carefully simulated. High injection and extraction efficiency is presented.

INTRODUCTION

The cyclotron project for proton therapy using approach similar to [1] is presented. A detailed description of the proposed project is given in [2] this conference. Center region of the cyclotron is presented in [3] this conference.

Magnet sectors of the cyclotron consist of two parts:

- wide-aperture part with a vertical distance of 50 mm and low helicity,
- small-aperture part with a vertical distance of 25 mm and high helicity.

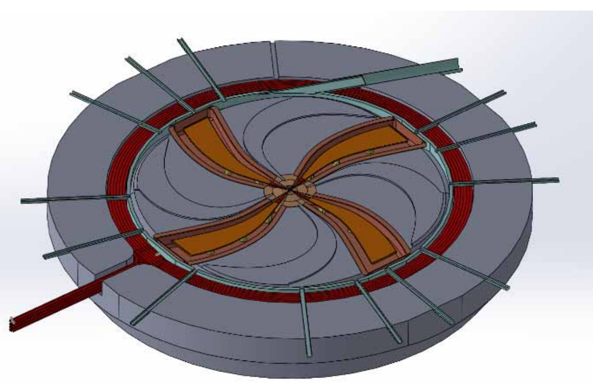

Figure 1: 3D computer model of the cyclotron.

Main parameters of the cyclotron are presented in Table 1.

Table 1: Cyclotron Parameters

Accelerated particles	protons
Final energy	232 MeV
Ion source	Internal, PIG
Extraction scheme	1 ESD, 2 correctors
Magnet Power Consumption	95 kW
RF power consumption	100 kW (wall losses)
Dimensions	(3850 x 3850 x 2000) mm^3
Beam current	Up to 100 µA

This structure makes it possible, firstly, to place the deflector between the sectors in the wide-aperture part, while retaining the valleys for placing the resonators, and, secondly, to ensure isochronous growth and vertical focusing due to the small-aperture part of the sector.

Computer model of the cyclotron (see Fig. 1) was built in CAD and simulated in CST studio.

CODE CORD

CORD code [4] was used for estimation of the field characteristics. CORD is providing particle dynamics analysis based on a combination of magnetic field map analysis with electric field map analysis. The first part of the code is searching for closed orbits (without acceleration) and calculating the focusing properties of the magnetic field. There are two types of closed orbits: orbits having the same N-fold symmetry as the cyclotron (no imperfections) and orbits obtained in a real field map with errors like low number harmonics.

In CORD we fix the radius r and match p_r and energy T. Initial values for each orbit are independent of other orbits, therefore parallel calculation is possible. A single iteration of the iterative scheme consists of the following 3 stages:

- Calculating the orbit's initial guess values $r(\theta_i)$, $pr(\theta_i)$, $T(r(\theta_i))$, θ_i is the initial angle and θ_f is the final angle.
- Finding $r(\theta_f)$, $pr(\theta_f)$, by solving ODE with MATLAB's ode45 solver, ODEs are simultaneously solved for a large set of radii (multiple orbits).
- New initial values for the next iteration:

$$p_r(\theta_i) \to p_r^{new}(\theta_i) = \frac{p_r(\theta_f)+p_r(\theta_i)}{2},$$

$$T \to T^{new} = T\frac{2r(\theta_i)}{r(\theta_i)+r(\theta_f)},$$

$$p^{new} = \sqrt{\frac{T^2}{c^2} + 2Tm}.$$

The number of iterations is constant and can be set to provide the necessary precision.

MAGNET FIELD ANALYSIS

Code CORD can present mean magnetic field and flutter (see Fig. 2), betatron frequencies in a tune operating diagram (see Fig. 3), calculates orbital frequency (see Fig. 4) and the difference between average magnetic field and isochronous one (see Fig. 5).

ISBN: 978-3-95450-212-7 ISSN: 2673-5482 doi:10.18429/JACoW-CYCLOTRONS2022-WEPO003

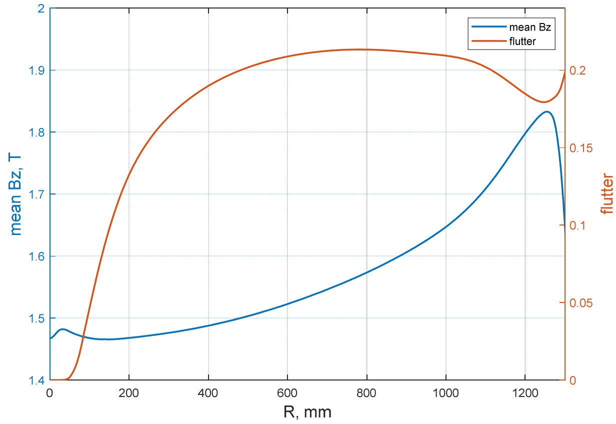

Figure 2: Average magnetic field and flutter along the radius.

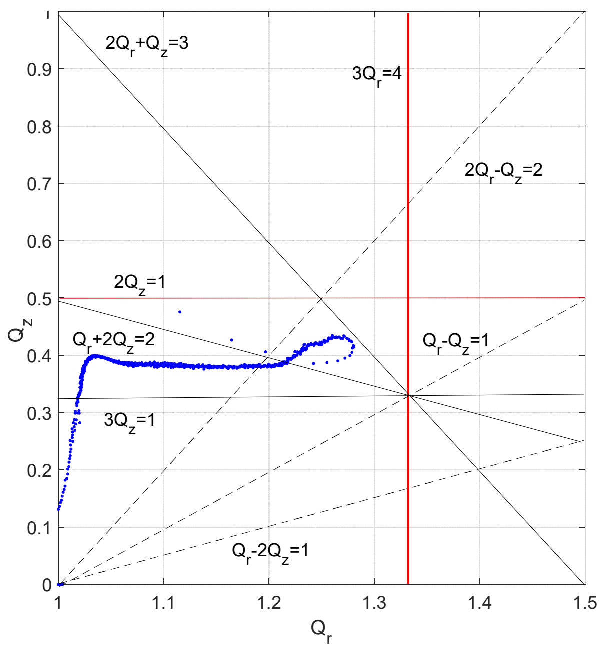

Figure 3: Tune diagram.

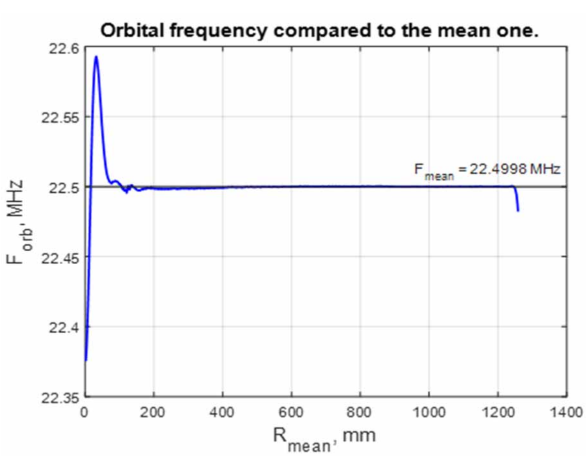

Figure 4: Orbital frequency against radius.

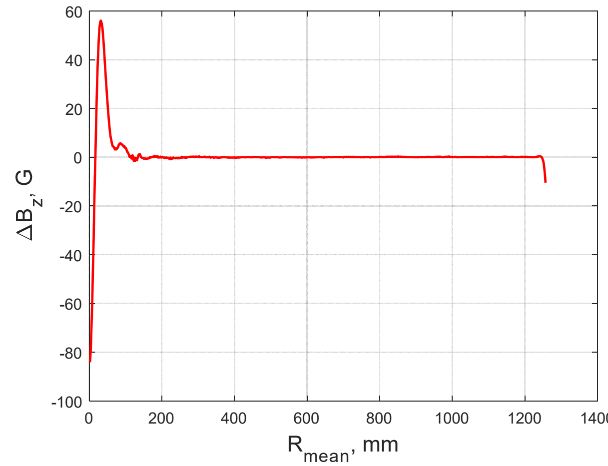

Figure 5: Difference between average magnetic field and isochronous one.

ACCELERATING FIELD ANALYSIS

We calculate effective azimuthal extent of the cavities (see Fig. 6), defined as the angular distance between the maxima of the electric field distribution in the median plane for the entire range of radii. Code CORD defines the voltage across the accelerating gaps as the integral of the electric field strength along the arc of a circle passing through the gap (see Fig. 7). The integral phase slip is presented in Fig. 8. Number of turns and orbit radial step against the radius (Fig. 9) were also calculated by CORD code. Table 2 shows the accelerating parameters of the accelerator.

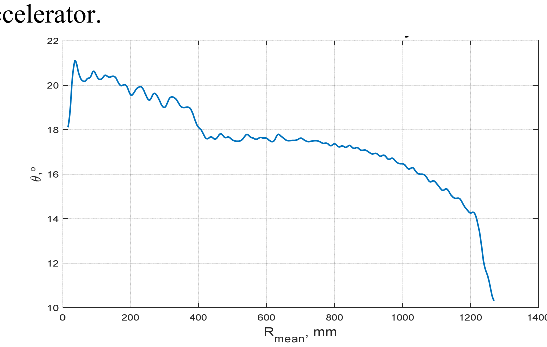

Figure 6: Azimuthal extent of the cavities against radius.

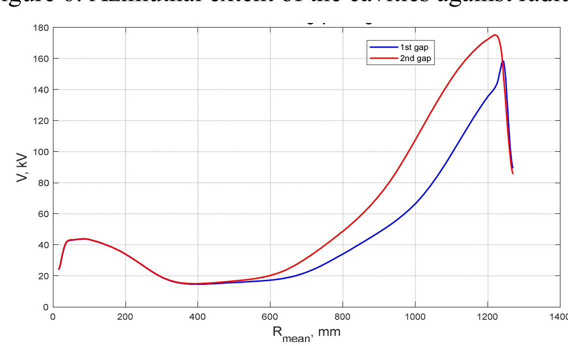

Figure 7: Voltage distribution along radius.

ISBN: 978-3-95450-212-7 ISSN: 2673-5482 doi:10.18429/JACoW-CYCLOTRONS2022-WEPO003

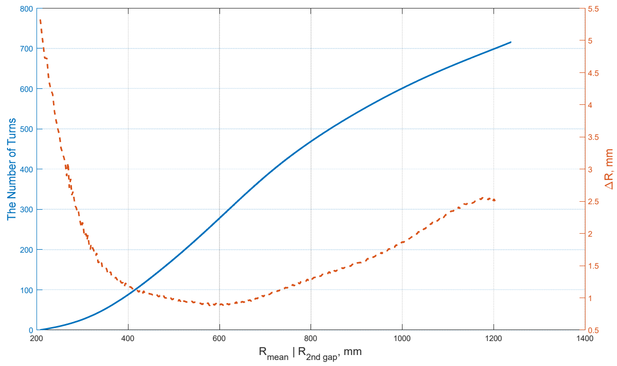

Figure 8: Number of turns (blue solid line) and orbit separation distance (red dash line) in the cyclotron along the radius.

Table 2: Accelerating System Parameters

Frequency [MHz]	180
Harmonic number	8
Q-factor	11000
Voltage center/extraction [kV]	30/160

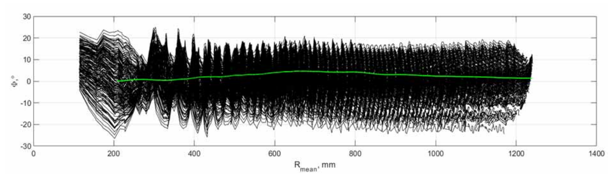

Figure 9: Integral phase slip along the radius. Positive phase corresponds to the lagging particle. Black lines – phase motion of the beam from particle tracking, green line – CORD.

EXTRACTION SYSTEM

The beam extraction for this machine can be carried out by means of 1 electrostatic deflector (ESD), located between the sectors, and 2 passive focusing magnetic channels (MC1 and MC2). We restricted electric field in deflector by the value of 90 kV/cm.

The beam, after being pulled with the deflector, passes through the accelerating RF-cavities and magnetic channels. Passive magnetic channels are located inside sector's gap.

MATLAB allows the import of 3D CAD models, which makes it possible to draw beam trajectories against the background of a full cyclotron model. The beam tracing, displayed on the Fig. 10, could be seen visually the beam passing inside the cyclotron structure which helps to control the process of acceleration and extraction.

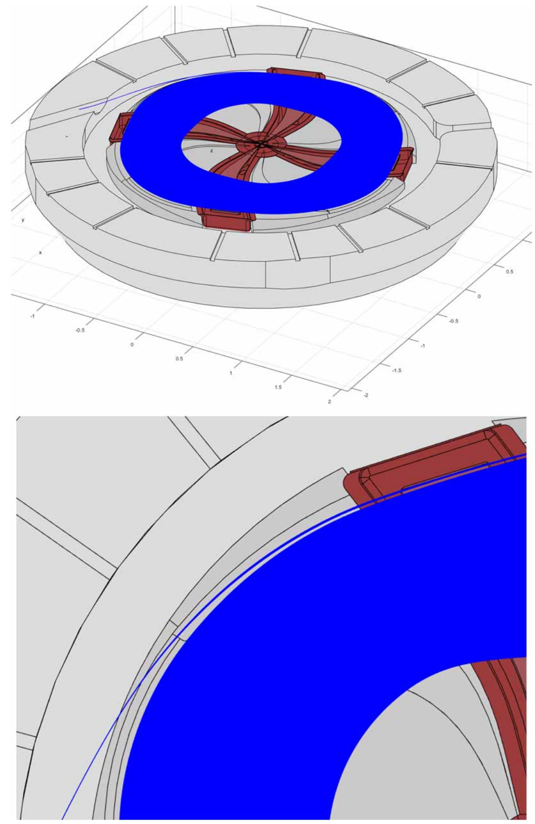

Figure 10: The beam tracing in the cyclotron structure.

CONCLUSION

The main feature of the proposed designs is the small number of A*turns of the coils. Together with the energy-efficient acceleration system, this determines low power consumption of the project. Such a coil has small dimensions, so the accelerator has acceptable dimensions, despite the large pole diameter. A small copper coil is economically attractive. Beam dynamics simulations revealed no problems with particle acceleration and extraction.

REFERENCES

[1] O. Karamyshev, "New Design of Cyclotron for Proton Therapy", in *Proc. IPAC'22*, Bangkok, Thailand, Jun. 2022, pp. 2973-2976. doi:10.18429/JACoW-IPAC2022-THPOMS015

[2] O. Karamyshev, "A new concept of cyclotrons for medical application", presented at Cyclotrons'22, Beijing, China, Dec. 2022, paper THBO01, this conference.

[3] O. Karamyshev, "High power central region with internal ion source", presented at Cyclotrons'22, Beijing, China, Dec. 2022, paper WEPO004, this conference.

[4] O. Karamyshev *et al.*, "Cord (Closed Orbit Dynamics): A New Field Map Evaluation Tool for Cyclotron Particle Dynamics" *Phys. Part. Nucl. Lett.*, vol. 18, no. 4, pp. 481–487, Aug. 2021. doi:10.1134/S1547477121040117

ISBN: 978-3-95450-212-7 ISSN: 2673-5482 doi:10.18429/JACoW-CYCLOTRONS2022-WEPO004

HIGH POWER CENTER REGION WITH INTERNAL ION SOURCE

O. V. Karamyshev†, Joint Institute for Nuclear Research, Dubna, Russia

Abstract

Cyclotrons for medical isotope production require high beam current. Author proposes the design of central region with internal ion source at 6.6 kV potential placed in the center of cyclotron and delivering the beam to every RF cavity symmetrically, thus significantly increasing the beam current.

INTRODUCTION

The line of cyclotrons from 15 to 230 MeV, that uses same magnet field level and RF frequency 145 MHz and utilises many identical solutions within the line-up to make it cheaper to produce and run was described in IPAC 2022 [1]. The author has developed and presented here a variant of the similar line-up for the accelerating frequency 180 MHz [2].

Of course, high frequency of RF system can potentially lead to poor capture of particles in the first accelerating gap. In fact, if ion source would be placed in front of RF puller with such high frequency the capture would be equal to 0. But this problem can be solved if in the first accelerating gap particles will arrive with some energy, thus travel through first gap much quicker.

Particles start from the PIG source, which is placed under 6600 V and accelerate to the “ninja star” housing, see Fig. 5 (zero potential) and arrive to the first gap with 6.6 keV energy. Also, the advantage of such central region is that one ion source placed in the middle can deliver beam in each gap simultaneously, due to the symmetry of such central region. A similar center for three sectors cyclotron was described in [3], here the author presents a variant for four sectors structure and frequency 180 MHz at harmonic 8.

VIRTUAL PROTOTYPING

The idea of a new engineering methodology Virtual Prototyping is to replace physical mock-ups by an integrated software prototypes that include all functional simulations based on CAD/CAE/CAM techniques.

Usually when designing a cyclotron some systems are developing separately. An integrated platform which encapsulates these distributed components and provides an inter-communication mechanism is extremely useful, as it will contribute to the creation of a more optimal cyclotron.

We have combined the development of the individual cyclotron systems through a framework in MATLAB (Fig. 1).

The shapes of sectors and cavities of the magnet are selected directly in MATLAB, then sent to CAD (Solidworks) to create parametrized model of the cyclotron, and then individual systems are sent to CST studio to simulate in the corresponding modules. The calculation results of the electromagnetic fields from CST are imported into MATLAB, where they are analyzed using code CORD [4] and beam tracking codes. Careful calculations of the beam dynamics are performed for the central region and the exit zone. Based on the results of the analysis, changes are made to the structure of the cyclotron systems. The iterative procedure is repeated until an acceptable result is achieved, namely, successful injection, acceleration and beam extraction.

In a compact cyclotron, all systems compete with each other for space (Fig. 2). An integrated approach to design is necessary to ensure that the decision on the privileges of a particular system is made objectively, taking into account the interests of each system.

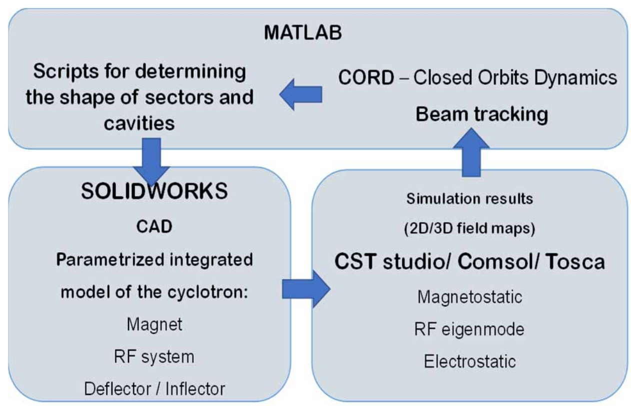

Figure 1: The framework of the cyclotron VP MATLAB integrated platform.

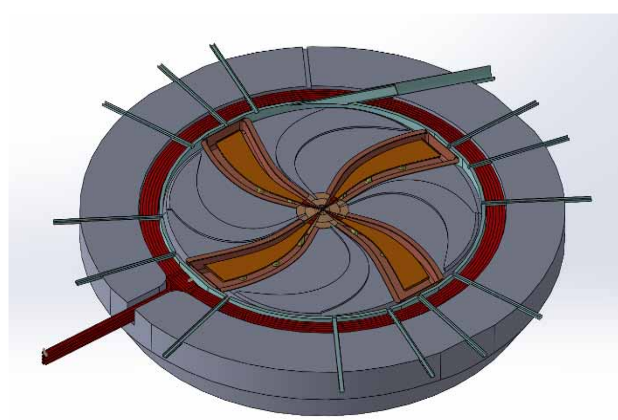

Figure 2: Parametrized model of the cyclotron.

BEAM DYNAMICS SIMULATION

When calculating particle, an electromagnetic field was specified in the form of a field maps obtained as a result of model calculations (3D field maps). We used 3D field maps received in CST RF eigenmode solver for accelerating field (Fig. 3) and magnetostatics solver for magnet simulation (Fig. 4).

† olegka@jinr.ru

ISBN: 978-3-95450-212-7 ISSN: 2673-5482 doi:10.18429/JACoW-CYCLOTRONS2022-WEPO004

The movement of particles begins from the PIG ion source that is placed under 6600 V, then particles are accelerating to a grounded "Ninja star" housing, and then by an accelerating system (see Figs. 6 and 7).

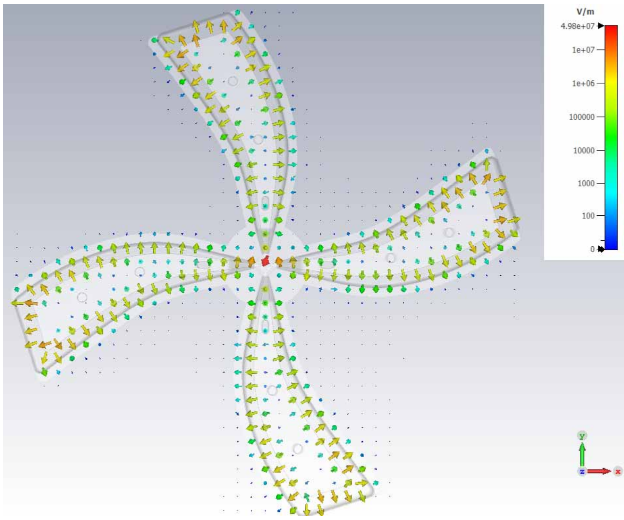

Figure 3: Electric field vector plot.

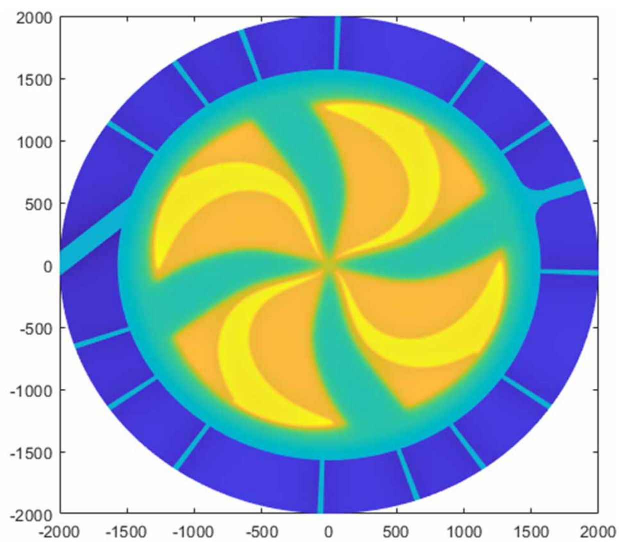

Figure 4: Magnetic field.

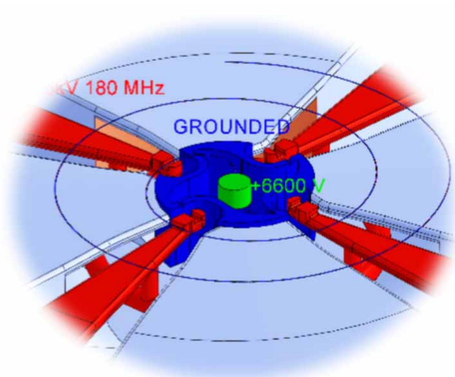

Figure 5: Center region view. Dark blue – "ninja star" housing, blue – anti-dees, red – dee tips, green- PIG ion source.

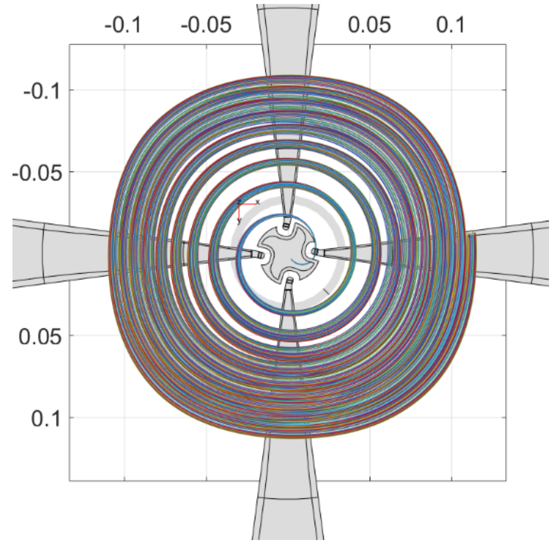

Figure 6: Beam trajectories from one gap.

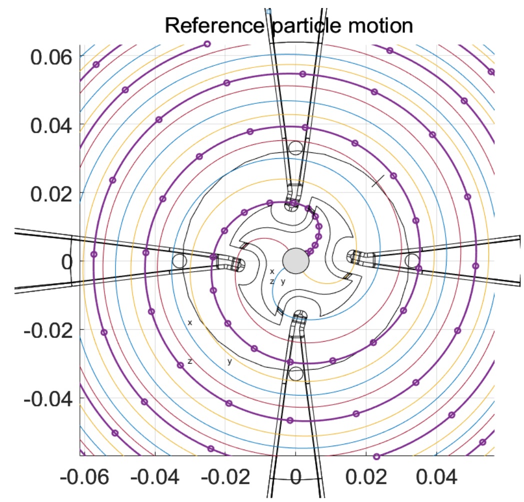

Figure 7: Four trajectories of reference particles are shown. Dots mark every 180 RF degrees.

Magnetic focusing caused by the decreasing field begins after a radius R = 35 mm (see Fig. 8). For a radius less than 35 mm (approximately one turn), an electric accelerating field provides vertical focusing of lagging particles (Fig. 9).

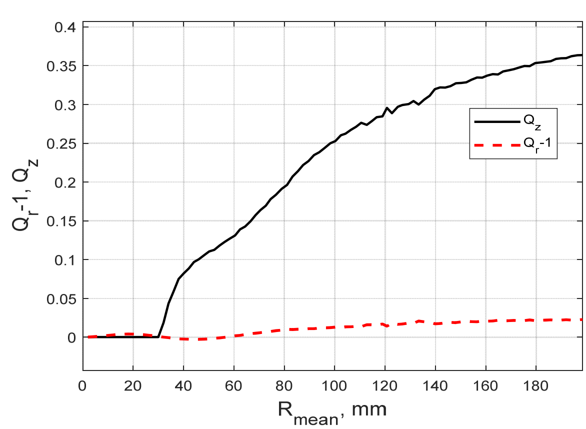

Figure 8: Betatron tunes in the center region.

ISBN: 978-3-95450-212-7 ISSN: 2673-5482 doi:10.18429/JACoW-CYCLOTRONS2022-WEPO004

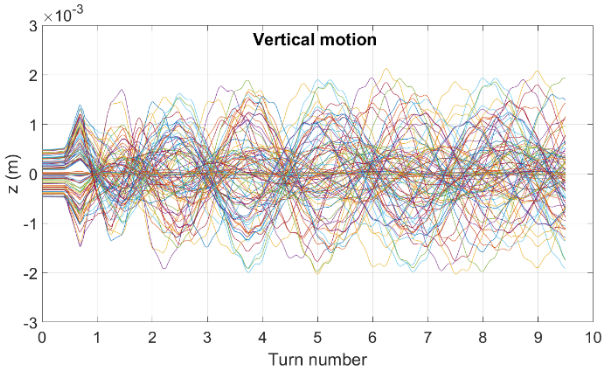

Figure 9: Vertical motion of the beam.

CONCLUSION

Advantages of the proposed scheme of central region:

- At least 4 times higher current, as 4 bunches captured at the same time
- Much higher capture in each 1st gap due to initial acceleration. In this case from 0 to 15 deg RF.
- Only protons arrive to the RF puller, less erosion of RF parts.
- Improved vacuum in the cyclotron, as ion source is separated from the rest of the chamber by "Ninja star" housing. Additional pump can be used to pump gas from ion source from the inside of the "Ninja star".

Of course, 8 harmonic acceleration is not an ideal option for truly high-power cyclotron, however such design of center region if used with 4th harmonic acceleration, especially with even higher voltage on the source can lead to 10 mA currents and higher.

REFERENCES

[1] O. Karamyshev, "New Design of Cyclotron for Proton Therapy", in *Proc. IPAC'22*, Bangkok, Thailand, Jun. 2022, pp. 2973-2976. doi:10.18429/JACoW-IPAC2022-THPOMS015

[2] O. Karamyshev, "A new concept of cyclotrons for medical application", presented at Cyclotrons'22, Beijing, China, Dec. 2022, paper THBO01, this conference

[3] O. Karamyshev, "A New Design of PET Cyclotron", in *Proc. IPAC'22*, Bangkok, Thailand, Jun. 2022, pp. 2977-2980. doi:10.18429/JACoW-IPAC2022-THPOMS016

[4] O. Karamyshev *et al.*, "Cord (Closed Orbit Dynamics): A New Field Map Evaluation Tool for Cyclotron Particle Dynamics," *Phys. Part. Nucl. Lett.*, vol. 18, no. 4, pp. 481–487, Jul. 2021. doi:10.1134/S1547477121040117

ISBN: 978-3-95450-212-7 ISSN: 2673-5482 doi:10.18429/JACoW-CYCLOTRONS2022-WEPO007

THE DESIGN OF A SUPERCONDUCTING DIPOLE MAGNET BASED ON TILTED SOLENOIDS

Liang Zhu[1], Junsong Shen[1,2], Zou Wu[2], Fang Fang[1]
[1]Hefei CAS Ion Medical and Technical Devices Co., Ltd, Hefei, China
[2]Institute of Plasma Physics, Chinese Academy of Sciences, Hefei, China

Abstract

As a core component of proton therapy equipment, the gantry can project the proton beam onto a tumor from different angles. The weight of the gantry with normal conducting magnets (mainly normal dipole magnets and quadrupole magnets) is usually more than 150 tons, which demands high requirements for the design, processing and fabrication. For the realization of light-weight gantry, this article puts forward a design of Canted-Cosine-Theta (CCT) superconducting magnet (to be used on superconducting gantry). Since the superconducting CCT magnet can produce higher magnetic field compared with normal magnets, for the proton beam with the same magnetic stiffness, the deflection radius of the magnet can be significantly reduced, thus reducing the radius and volume of the gantry.

In this article, the finite element analysis software and Biot-Savart principle were adopted to establish the method of magnetic field calculation for CCT superconducting magnet, and MATLAB was used to simulation and validation of particle path, which finally realize the design of CCT superconducting magnet applied on gantry.

INTRODUCTION

Table 1: Physical Requirements for the Deflecting CCT Magnet

Parameter	Value
Maximum proton energy	280 MeV
Deflecting Angle	58.5°
Deflecting Radius	0.9 m
Magnetic field intensity	2.8 T
Effective length	918.9 mm
Good field radius	30 mm
Magnetic field homogeneity	1×10^{-3}

CCT superconducting magnet has the following characteristics: high magnetic field strength, flexible multi-stage field combination, high uniformity of integral field and transverse field; and when it comes to structure, it has the characteristics of light weight, simple winding process, large range of good field (two-thirds of conductor coil radius), etc [1]. Both LBNL (USA) and CERN (Europe) have developed superconducting CCT dipole prototypes (linear CCT magnets) [2]. In order to optimize the rotating gantry, this paper specially studies the deflection CCT superconducting magnet used in the gantry, and determines its feasibility. According to beam optics requirements of the gantry, the physical requirements for the deflecting CCT superconducting magnet are shown in Table 1.

THEORETICAL MODEL OF DEFLECTING CCT SUPERCONDUCTING MAGNET

Deflecting CCT superconducting magnet trajectory equation can be established in two ways: one is in the cylindrical coordinates and another is in the toroidal coordinates [3-5].

The trajectory equation of the linear CCT superconducting magnet in the cartesian coordinates is as shown in Eq. (1), where the origin of coordinates is at the center of the cylindrical surface:

$$\begin{cases} x = r\cos\theta \\ y = r\sin\theta \\ z = \sum\left[\dfrac{r}{n\tan\alpha}\sin(n\theta) + \dfrac{\omega}{2\pi}\theta\right] \end{cases} \tag{1}$$

where: r is the radius of the cylindrical surface where the trajectory of the single-layer coil is located, unit mm; α is the tilt angle between single layered coil and horizontal plane, unit rad; θ is the azimutrical angle, the changing angle of trajectory in the cylindrical coordinate system, unit rad, with changing range of $[-N\pi, N\pi]$, N is the number of coil turns; ω is the distance between turns of single-layer coil, unit mm; n is the magnetic pole series (n = 1 for dipole, n = 2 for quadrupole, and so on).

It can be understood that the deflecting magnet, according to the definition, is like the linear magnet bends along the center trajectory with a radius of R, which is the deflecting radius of the deflecting magnet. Therefore, according to Eq. (1), the trajectory equation of deflecting CCT superconducting magnet can be shown as following in Eq. (2):

ISBN: 978-3-95450-212-7 ISSN: 2673-5482 doi:10.18429/JACoW-CYCLOTRONS2022-WEPO007

$$\begin{cases} x = (R + r\cos\theta)\cos\varphi \\ y = (R + r\cos\theta)\sin\varphi \\ z = r\sin\theta \\ \varphi = \sum\left[\dfrac{r}{n\tan\alpha}\sin(n\theta) + \dfrac{\omega}{2\pi}\theta\right] \times \dfrac{1}{R} \end{cases} \quad (2)$$

In the toroidal coordinates (η,ζ,ϕ), the parametric equation of deflecting CCT superconducting magnet is as shown in Eq. (3):

$$\begin{cases} \eta = \eta_0 \\ \zeta = \zeta \\ \phi(\zeta) = \sum\left[\dfrac{\cot\alpha}{n\sinh\eta_0}\sin(n\zeta) + \dfrac{\phi_0}{2\pi}\zeta\right] \end{cases} \quad (3)$$

where: α is the tilt angle between single layer coil and horizontal plane, unit rad; ζ is the torus angle, unit rad, with a changing range of $[-N\pi, N\pi]$, N is the number of coil turns; ϕ_0 is the angle between turns of single-layer coil, unit rad; n is the magnetic pole series (n = 1 for dipole, n = 2 for quadrupole, and so on).

Linear CCT is periodic in the axial direction, and the turns spacing ω of any two adjacent points is constant. The deflecting CCT has symmetry in the bending direction, and the angular distance ϕ_0 between any two adjacent points is constant. Considering that the trajectory equation established by Eq. (2) is not conducive to the inter-turn analysis, Eq. (3) is used for the analysis of deflecting CCT magnet.

STRUCTURAL MODEL OF DEFLECTING CCT SUPERCONDUCTING MAGNET

Solution of the Angular Distance ϕ_0

The distance between adjacent wiring turns in the deflecting CCT magnet and the tangent value of the tilt angle of the deflected CCT magnet are values that vary with the torus angle ζ, which can be obtained by establishing a local orthogonal coordinate system on the trajectory path. The solution is as follows:

$$\delta(\zeta) = \frac{a\phi_0}{\cosh\eta_0 - \cos\zeta}(\sinh^{-2}\eta_0 + \phi'(\zeta))^{-1/2} \quad (4)$$

$$\tan(\alpha) = \frac{1}{\sinh\eta_0\phi'(\zeta)} \quad (5)$$

where: a is the pole value of bipolar coordinates, unit mm. $\delta(\zeta)$ is the turn-to-turn distance, unit mm. Using Eq. (4) and Eq. (5), we can get:

$$\delta(\zeta) = a\phi_0\sin\alpha\frac{\sinh\eta_0}{\cosh\eta_0 - \cos\zeta} \quad (6)$$

The analysis shows that the turn-to-turn distance is the smallest at the inner side of the deflect CCT coil, where $\zeta = \pi$. Outside of the coil, where $\zeta = 0$, the turn–to-turn distance is the largest. The extreme value of turn-to-turn distance is shown as follows:

$$\begin{cases} \min(\delta)\big|_{\zeta=\pi} = a\phi_0\sin\alpha\tanh(\eta_0/2) \\ \max(\delta)\big|_{\zeta=0} = a\phi_0\sin\alpha\coth(\eta_0/2) \end{cases} \quad (7)$$

Let δ_0 be the minimum rib thickness of skeleton wire slot, and wd be the width of skeleton superconducting wire slot. According to the minimum turn-to-turn distance in Eq. (7), the angular distance ϕ_0 can be obtained as follows:

$$\phi_0 = \frac{\delta_0 + \mathrm{wd}}{a\sin\alpha\tanh(\eta_0/2)} \quad (8)$$

In the formula, the pole coordinates a and η_0 can be determined by the deflecting radius R and the cylinder radius r:

$$\begin{cases} a = \sqrt{R^2 - r^2} \\ \eta_0 = \dfrac{1}{2}\ln\dfrac{R+a}{R-a} \end{cases} \quad (9)$$

Model Analysis

According to the physical requirements in Table 1 and the above solution process, the structural parameters of the deflecting CCT superconducting magnets are determined as shown in Table 2.

Table 2: Parameters of Deflecting CCT Superconducting Magnets

Parameter	**Value**
Pore size at room temperature	40 mm
Number of coil layers	2 layer
Deflecting Radius	900 mm
Coil tilt Angle	30°
Number of coil turns	120 t
Inner coil radius	56 mm
Outer coil radius	66 mm
Minimum interturn rib thickness	0.4 mm
Maximum interturn rib thickness	3.9/4 mm
Inter-turn angular distance	0.0085 rad
Current of a single superconducting wire	< 1000 A

ISBN: 978-3-95450-212-7 ISSN: 2673-5482 doi:10.18429/JACoW-CYCLOTRONS2022-WEPO007

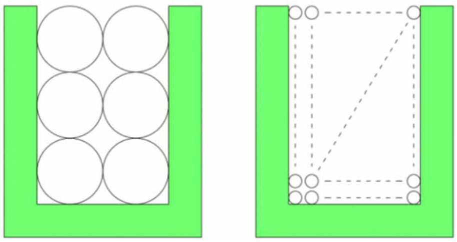

Figure 1: Schematic diagram of multi-step linear approximation.

The Opera-3D finite element analysis software and MATLAB mathematical tool were used to analyze and calculate the magnetic field simulation and optimization analysis of the deflecting CCT magnet, and the results was ensured by comparison and verification. In Opera-3D finite element simulation analysis, 8-node blocks in the software were used for splicing modelling, and the tangent direction of the node blocks was the same as that of the coil track, so as to ensure that the conductor height direction was always perpendicular to the surface of the cylindrical skeleton. When using Biot-Savart magnetic field integral law for analysis in MATLAB, in order to ensure the consistency between the analyzed conductor and the actual conductor and improve the accuracy of calculation, the conductor section is divided by multi-step linear approximation method, as shown in Fig. 1.

According to the parameter equation of Eq. (3) and the magnet parameters of Table 2, when n = 1, the deflecting dipole magnet model was established by node modelling in Opera-3D, as shown in Fig. 2. The center trajectory model is established in MATLAB, as shown in Fig. 3.

Figure 2: Opera-3D CCT model.

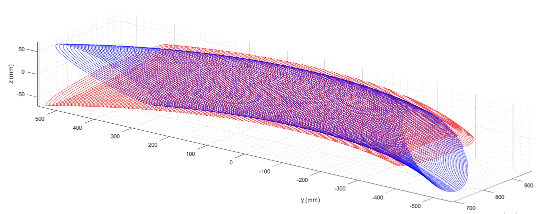

Figure 3: Center trajectory model.

Magnetic Field Optimization

According to the above analysis, when n = 1, the Biot-Savart law is used in MATLAB to calculate the transverse magnetic field and the magnetic field in the direction of the trajectory respectively, and the results are shown in Figs. 4 and 5, in which, By_inner and By_outer represent the contribution of the inner and outer coils to the magnetic field respectively. Through the analysis, it can be clearly seen that the transverse magnetic field uniformity is poor and there is a negative gradient, which is caused by the higher order components, especially the higher order components of the first and second order.

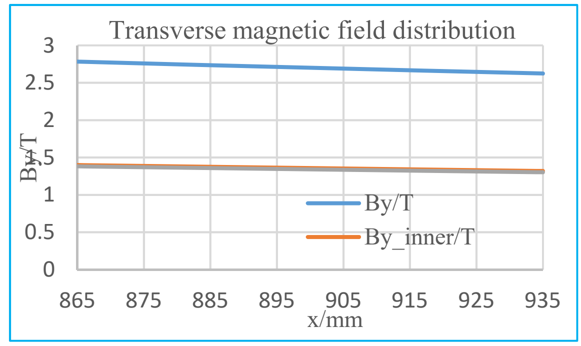

Figure 4: Transverse magnetic field by distribution (x = -35 ~ 35, y = 0, z = 0).

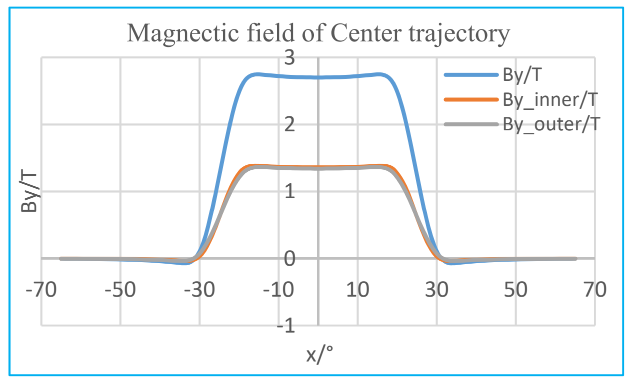

Figure 5: By distribution on the particle central trajectory(x = 0, y = 0, z = -65 ~ 65°).

In order to improve the uniformity of the magnetic field and reduce the harmonic wavelength, paths such as quadrupole (n = 2), six-level field (n = 3) and eight-level field (n = 4) can be added to the pure bipolar CCT path (n = 1), and the corresponding adjustment coefficients (k_1, k_2, k_3, k_4 and etc.) can be introduced for harmonic adjustment. The $\phi(\zeta)$ in Eq. (3) can be changed as shown in Eq. (10). In this way, the periodicity of each order component can be guaranteed, and the turn-to-turn angular distance can be equal.

$$\phi(\zeta)=\sum\left[k_n\frac{\cot\alpha}{n\sinh\eta_0}\sin(n\zeta)\right]+\frac{\phi_0}{2\pi}\zeta \tag{10}$$

where k_n is the adjustment coefficient (n = 1 is the first-order adjustment coefficient, n = 2 is the second-order adjustment coefficient, n = 3 is the third-order adjustment coefficient, etc.); therefore, when n = 1 and $k_1 = 1$, k_n / n (when $n \geq 2$) represents the proportion of each higher-order magnetic field in the main magnetic field. After several iterations, each higher-order harmonic component is shown in Table 3. The magnetic field distribution on the circumference of the cross section of the magnet and the magnetic field distribution inside the circumference are shown in Figs. 6 and 7 respectively.

ISBN: 978-3-95450-212-7 ISSN: 2673-5482 doi:10.18429/JACoW-CYCLOTRONS2022-WEPO007

Table 3: Harmonic Components

Item	Parameter	Value
Adjustment coefficient	K1	1
	K2	0.0548
	K3	0.003
Harmonic component	1	1.92E-04
	2	1.74E-04
	3	7.36E-05
	4	4.72E-06
	5	2.06E-07
	6	7.40E-09

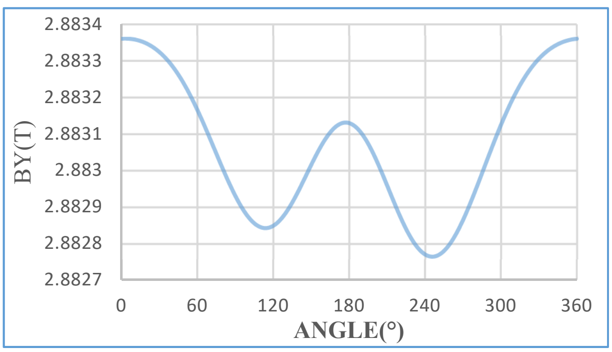

Figure 6: Magnetic field distribution on the cross-section circumference(r = 35mm).

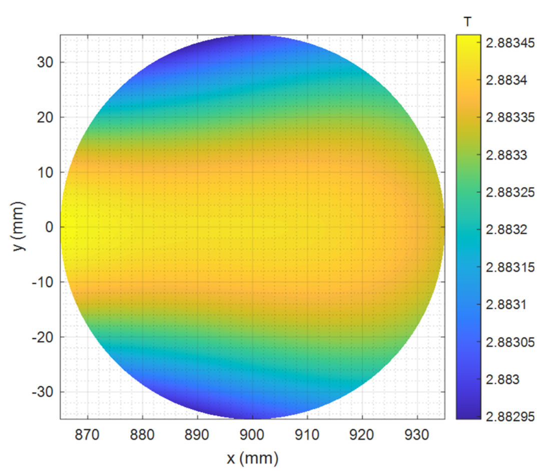

Figure 7: Magnetic field distribution in the circumferential section (r ≤ 35mm).

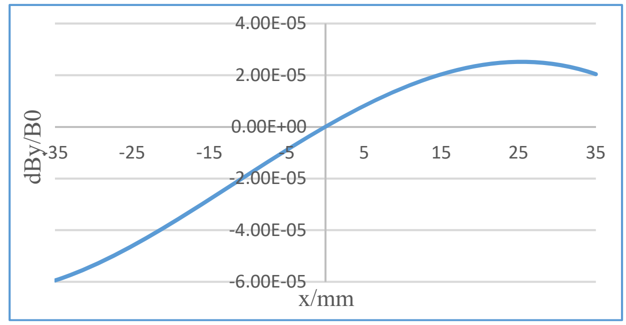

Figure 8: Transverse field uniformity(r = ±35 mm, y = 0, z = 0).

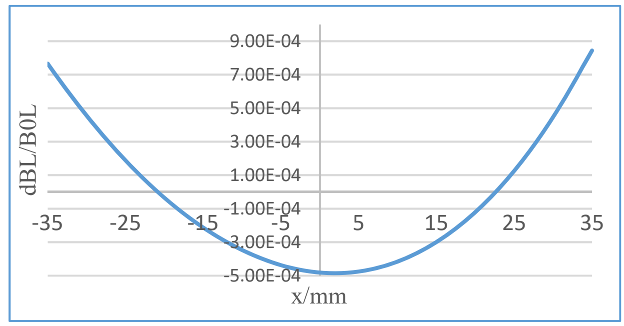

Figure 9: Integral field uniformity (r ≤ ±35 mm, y = 0).

After reducing the harmonics, the transverse field uniformity and the integral field uniformity of the magnet are improved, as shown in Figs. 8 and 9, which is in the range of ±1E-3 and meet the design requirements. The polar plane deflection angle is 4 degrees by calculation.

CONCLUSION

In this paper, the path equations of CCT magnets are established in cylindrical coordinate system and toroidal coordinate system, and the key parameters in the model are analyzed and calculated based on the circular coordinate system.

By setting the adjustment coefficient of high order harmonics, revising the parametric equation and iterative calculating, the high order harmonics component was reduced and the uniformity of magnetic field was improved after several iterations.

The analysis model is established by means of node modelling and coordinate transformation using Opera-3d finite element analysis software, and the magnetic field analysis is carried out. At the same time, the center trajectory path is established using MATLAB, and the multi-step linear approximation method is adopted to analyze the magnetic field by using Biot-Savart integral law. Comparing the two results and selecting the optimized design of CCT magnet that meets the physical requirements.

ISBN: 978-3-95450-212-7 ISSN: 2673-5482 doi:10.18429/JACoW-CYCLOTRONS2022-WEPO007

REFERENCES

[1] Y. Liang, "R&D of the Canted-Cosine-2eta Superconducting Magnets", Beijing, China: University of Chinese Academy of Sciences, 2018.

[2] A. Hafalia *et al.*, "The structural design for a 'Canted Cosine–Theta' superconducting dipole coil and magnet structure-CCT1", *IEEE Trans. Appl. Supercond.*, vol. 24, no. 3, p. 4001904, Jun. 2014. doi:10.1109/TASC.2013.2284429

[3] L. Brouwer, S. Caspi, and S. Prestemon, "Structural analysis of an 18 T hybrid Canted–Cosine–Theta superconducting dipole", *IEEE Trans. Appl. Supercond.*, vol. 25, no. 3, p. 4000404, Jun. 2015. doi:10.1109/TASC.2014.2361027

[4] G. Montenero *et al.*, "Mechanical structure for the PSI canted-cosine-theta (CCT) magnet program", *IEEE Trans. Appl. Supercond.*, vol. 28, no. 3, p. 4002805, Apr. 2018. doi:10.1109/TASC.2017.2787596

[5] L. N. Brouwer, "Canted-cosine-theta superconducting accelerator magnets for high energy physics and ion beam cancer therapy", Ph.D. thesis, University of California, Berkeley, CA, USA, 2015.

ISBN: 978-3-95450-212-7 ISSN: 2673-5482 doi:10.18429/JACoW-CYCLOTRONS2022-WEPO008

H^- INTRA-BEAM STRIPPING LOSS RATE IN ISOCHRONOUS CYCLOTRON*

Y.-N. Rao†, TRIUMF, Vancouver, Canada

Abstract

Binary collisions inside a H^- bunch result in H^- stripping and subsequent particle loss. This phenomenon, called intra-beam stripping, was observed in LEAR and SNS superconducting linac. We mimic the derivation made for the linac to derive the intra-beam stripping loss rate for an isochronous cyclotron. And then, we apply this theory to the TRIUMF 500 MeV H^- cyclotron to estimate the loss.

INTRODUCTION

Beam loss is one of the major concerns for high power proton (and H^-) accelerators. With the growing of beam power, the fractional beam loss permitted by the machine radioactivation issue becomes smaller and thus more challenging. For H^- accelerators, the primary beam loss mechanisms include halo formation through beam dynamics problems (e.g. coupling resonance crossing) [1], residual gas stripping [2], electromagnetic (Lorentz) stripping [3], and intra-beam stripping [4]. In the TRIUMF 500 MeV H^- cyclotron, the total beam loss outside the central region is $<$ 10% at present: ~1% by gas stripping (under 2×10^{-8} Torr residual pressure), ~3% by electromagnetic stripping (from 400 to 480 MeV), and ≤2% by vertical halo growth due to resonance crossings. It was queried how much loss is caused by the intra-beam stripping. The intra-beam stripping arises from binary collisions inside a H^- bunch that cause loosely-bound electrons to be stripped off, leaving neutral H^0 particles, which are subsequently lost due to lack of focusing, steering, and acceleration. This phenomenon was first observed in LEAR [4] and afterwards at SNS superconducting linac [5]. To address this issue for the TRIUMF cyclotron [6], we mimic the derivation made for the linac to derive the intra-beam stripping loss rate for an isochronous cyclotron. And then, we apply the theory to the TRIUMF cyclotron to estimate the loss.

DERIVATION OF LOSS RATE

The particle loss rate due to the intra-beam stripping can be calculated by considering a differential volume $d\vec{r} = dxdydz$ in which the incident particles with velocities between $\vec{v}_1$ and $\vec{v}_1 + d\vec{v}_1$ impinge on the target particles in the same bunch at the same location with velocities between $\vec{v}_2$ and $\vec{v}_2 + d\vec{v}_2$. The number of particles scattered into a solid angle $d\Omega$ over unit time from this collision is the product of number of incident particles, the differential cross section, and the number of target particles. In the beam frame, the loss rate is represented as:

$$\begin{aligned}\frac{dN}{dt} &= -\frac{1}{2}\iint d\vec{r}d\vec{v}_1 Nf(\vec{r},\vec{v}_1)\int d\vec{v}_2 Nf(\vec{r},\vec{v}_2)|\vec{u}|\frac{d\sigma}{d\Omega}d\Omega \\ &= -\frac{N^2}{2}\iint d\vec{r}d\vec{v}_1 f(\vec{r},\vec{v}_1)\int d\vec{v}_2 f(\vec{r},\vec{v}_2)|\vec{u}|\sigma(|\vec{u}|), \quad (1)\end{aligned}$$

where the distribution function $f(\vec{r},\vec{v})$ is normalized to 1 and $f(\vec{r},\vec{v})d\vec{r}d\vec{v}$ gives the fraction of particles with coordinates and velocities in the range $\vec{r}$ to $\vec{r}+d\vec{r}$, and $\vec{v}$ to $\vec{v}+d\vec{v}$. N is the number of particles in the bunch, $\vec{u} = \vec{v}_1 - \vec{v}_2$ is the relative velocity between colliding particles, $\sigma(|\vec{u}|)$ is the total cross section for single electron stripping. The factor $1/2$ in the front of the integral removes the double counting of each collision in the integral.

Equation (1) is a general expression. In an isochronous cyclotron, particles in a bunch have no collision longitudinally. This is because any fast moving particle cannot surpass the slow moving ones. Unlike the synchrotron where there exists periodical phase oscillation longitudinally, isochronous cyclotron has no phase oscillation; instead, particles of different energies have the same revolution period. In this case, the particle's longitudinal velocity does not matter to the loss rate, only the transverse velocities involve. So, $f(\vec{r},\vec{v})$ can be written as a product of independent probability density as follows:

$$f(\vec{r},\vec{v}) = f(x,v_x)\,f(y,v_y)\,f(z). \quad (2)$$

The density distribution is assumed to be gaussian. For the x-x' plane (similar for the y-y' plane), it is:

$$f(x,x') = \frac{1}{2\pi\sigma_x\sqrt{\epsilon_x/\beta_x}}\exp\left[-\frac{x^2}{2\sigma_x^2}-\frac{(x'+\alpha_x x/\beta_x)^2}{2\epsilon_x/\beta_x}\right], \quad (3)$$

where $\sigma_x = \sqrt{\beta_x\epsilon_x}$. This means that the velocity distribution at certain location x has a mean value $\bar{x'} = -\alpha_x x/\beta_x$ and a standard deviation $\sqrt{\epsilon_x/\beta_x}$. What matters to the intra-beam stripping is the local velocity (angular) spread $\sqrt{\epsilon_x/\beta_x}$ rather than the entire velocity (angular) spread $\sqrt{\gamma_x\epsilon_x}$. So, in the beam frame, $f(x,v_x)$ can be written as:

$$f(x,v_x) = \frac{1}{2\pi\sigma_x\sigma_{v_x}}\exp\left(-\frac{x^2}{2\sigma_x^2}-\frac{v_x^2}{2\sigma_{v_x}^2}\right), \quad (4)$$

similar for the $f(y,v_y)$, while $f(z)$ is expressed as:

$$f(z) = \frac{1}{\sqrt{2\pi}\sigma_z}\exp\left(-\frac{z^2}{2\sigma_z^2}\right). \quad (5)$$

Equation (1) is then represented as:

$$\frac{dN}{dt} = -\frac{N^2}{2}I_x I_y I_z|\vec{u}|\sigma(|\vec{u}|), \quad (6)$$

* TRIUMF receives funding via a contribution agreement through the National Research Council of Canada.
† raoyn@triumf.ca

where

$$I_x \equiv \iint f(x, v_{x_1}) dx dv_{x_1} \int f(x, v_{x_2}) dv_{x_2} = \frac{1}{\sqrt{4\pi}\sigma_x} \int f(v_{x_1}) dv_{x_1} \int f(v_{x_2}) dv_{x_2}, \quad (7)$$

where

$$f(v_{x_{1,2}}) = \frac{1}{\sqrt{2\pi}\sigma_{v_x}} \exp\left(-\frac{v_{x_{1,2}}^2}{2\sigma_{v_x}^2}\right). \quad (8)$$

Similarly, we have

$$I_y \equiv \frac{1}{\sqrt{4\pi}\sigma_y} \int f(v_{y_1}) dv_{y_1} \int f(v_{y_2}) dv_{y_2}, \quad (9)$$

and

$$f(v_{y_{1,2}}) = \frac{1}{\sqrt{2\pi}\sigma_{v_y}} \exp\left(-\frac{v_{y_{1,2}}^2}{2\sigma_{v_y}^2}\right), \quad (10)$$

while

$$I_z \equiv \int f^2(z) dz = \frac{1}{(\sqrt{2\pi}\sigma_z)^2} \int_{-\infty}^{+\infty} \exp\left(-\frac{z^2}{\sigma_z^2}\right) dz = \frac{1}{\sqrt{4\pi}\sigma_z}. \quad (11)$$

So Eq. (6) becomes:

$$\frac{1}{N}\frac{dN}{dt} = -\frac{N}{2(4\pi)^{3/2}\sigma_x\sigma_y\sigma_z} \int f(\vec{v}_1) d\vec{v}_1 \cdot \int f(\vec{v}_2) d\vec{v}_2 |\vec{u}| \sigma(|\vec{u}|), \quad (12)$$

where

$$f(\vec{v}_{1,2}) = \frac{1}{2\pi\sigma_{v_x}\sigma_{v_y}} \exp\left(-\frac{v_{x_{1,2}}^2}{2\sigma_{v_x}^2} - \frac{v_{y_{1,2}}^2}{2\sigma_{v_y}^2}\right),$$
$$d\vec{v}_{1,2} = dv_{x_{1,2}} dv_{y_{1,2}}. \quad (13)$$

In order to perform the Eq. (12) integration, we do variable transformations:

$$\vec{u} = \vec{v}_1 - \vec{v}_2, \quad \vec{w} = \vec{v}_1 + \vec{v}_2, \quad (14)$$

which are

$$u_x = v_{x_1} - v_{x_2}, \quad w_x = v_{x_1} + v_{x_2},$$
$$u_y = v_{y_1} - v_{y_2}, \quad w_y = v_{y_1} + v_{y_2}. \quad (15)$$

So we have

$$v_{x_1}^2 + v_{x_2}^2 = \frac{u_x^2 + w_x^2}{2}, \quad v_{y_1}^2 + v_{y_2}^2 = \frac{u_y^2 + w_y^2}{2}, \quad (16)$$

and

$$dv_{x_1} dv_{x_2} = \frac{1}{2} du_x dw_x, \quad dv_{y_1} dv_{y_2} = \frac{1}{2} du_y dw_y, \quad (17)$$

where $\frac{1}{2}$ is the Jacobian of transformation. Equation (12) thus becomes

$$\frac{1}{N}\frac{dN}{dt} = -\frac{N}{2(4\pi)^{3/2}\sigma_x\sigma_y\sigma_z} \frac{1}{2\pi\sigma_{v_x}\sigma_{v_y}} \frac{1}{2\pi\sigma_{v_x}\sigma_{v_y}} \frac{1}{4} \cdot \iint_{-\infty}^{+\infty} \exp\left(-\frac{w_x^2}{4\sigma_{v_x}^2} - \frac{w_y^2}{4\sigma_{v_y}^2}\right) dw_x dw_y \cdot \iint_{-\infty}^{+\infty} \exp\left(-\frac{u_x^2}{4\sigma_{v_x}^2} - \frac{u_y^2}{4\sigma_{v_y}^2}\right) |\vec{u}| \sigma(|\vec{u}|) du_x du_y. \quad (18)$$

Using the basic formula

$$\int_{-\infty}^{+\infty} e^{-ax^2} dx = \sqrt{\frac{\pi}{a}} \quad (a > 0), \quad (19)$$

we can easily work out the integration over $\vec{w}$:

$$\iint_{-\infty}^{+\infty} \exp\left(-\frac{w_x^2}{4\sigma_{v_x}^2} - \frac{w_y^2}{4\sigma_{v_y}^2}\right) dw_x dw_y = 4\pi\sigma_{v_x}\sigma_{v_y}. \quad (20)$$

So we arrive at

$$\frac{1}{N}\frac{dN}{dt} = -\frac{N}{64\pi^{5/2}\sigma_x\sigma_y\sigma_z\sigma_{v_x}\sigma_{v_y}} \iint_{-\infty}^{+\infty} \sigma(|\vec{u}|) \sqrt{u_x^2 + u_y^2} \cdot \exp\left(-\frac{u_x^2}{4\sigma_{v_x}^2} - \frac{u_y^2}{4\sigma_{v_y}^2}\right) du_x du_y. \quad (21)$$

When the relative velocity dependence of the stripping cross-section is neglected, or, for estimation purpose, we could insert a maximum value σ_{max} of the cross-section and pull it out of the integral. Next, we denote

$$X \equiv \frac{u_x}{2}, \quad Y \equiv \frac{u_y}{2}, \quad (22)$$

Eq. (21) then reads

$$\frac{1}{N}\frac{dN}{dt} = -\frac{N\sigma_{max}\sqrt{\sigma_{v_x}^2 + \sigma_{v_y}^2}}{8\pi^{5/2}\sigma_x\sigma_y\sigma_z} \iint_{-\infty}^{+\infty} \frac{\sqrt{X^2 + Y^2}}{\sqrt{\sigma_{v_x}^2 + \sigma_{v_y}^2}} \exp\left(-\frac{X^2}{\sigma_{v_x}^2} - \frac{Y^2}{\sigma_{v_y}^2}\right) \frac{dX dY}{\sigma_{v_x}\sigma_{v_y}}. \quad (23)$$

We finally obtain

$$\frac{1}{N}\frac{dN}{dt} = -\frac{N\sigma_{max}\sqrt{\sigma_{v_x}^2 + \sigma_{v_y}^2}}{8\pi^2\sigma_x\sigma_y\sigma_z} \cdot F(\sigma_{v_x}, \sigma_{v_y}), \quad (24)$$

where

$$F(a, b) = \frac{1}{\sqrt{\pi}} \iint_{-\infty}^{+\infty} \sqrt{\frac{X^2+Y^2}{a^2+b^2}} \exp\left(-\frac{X^2}{a^2} - \frac{Y^2}{b^2}\right) \frac{dX dY}{ab} \quad (25)$$

is a dimensionless form factor.

ISBN: 978-3-95450-212-7 ISSN: 2673-5482 doi:10.18429/JACoW-CYCLOTRONS2022-WEPO008

Should be noted that the above derivations are performed in the beam frame. Next, we have to do relativistic transformation from the beam frame to the lab frame:

$$dt \longrightarrow dt/\gamma, \quad \sigma_z \longrightarrow \gamma\sigma_s,$$

and

$$\sigma_{v_x} = \beta\gamma c\theta_x, \quad \sigma_{v_y} = \beta\gamma c\theta_y.$$

We end up getting the loss rate in the lab frame:

$$\frac{1}{N}\frac{dN}{dt} = -\frac{N\sigma_{max}\beta c\sqrt{\theta_x^2+\theta_y^2}}{8\pi^2\gamma\sigma_x\sigma_y\sigma_s}\cdot F(\theta_x,\theta_y), \tag{26}$$

where β and γ are the relativistic factors, $\sigma_{x,y} = \sqrt{\beta_{x,y}\epsilon_{x,y}}$ are the rms beam sizes in x and y, $\theta_{x,y} = \sqrt{\epsilon_{x,y}/\beta_{x,y}}$ are the rms angular spreads, σ_s is the rms bunch length. Clearly, the loss rate is proportional to the density of particles in the real space.

The reason why we write the form factor as $F(\theta_x,\theta_y)$ instead of $F(\beta c\gamma\theta_x, \beta c\gamma\theta_y)$ is because $F(a,b)$ does not depend on the absolute values of its parameters (a,b) but only on their ratio, that is,

$$F(a,b) = \frac{E\left(1-b^2/a^2\right)}{\sqrt{1+b^2/a^2}}, \tag{27}$$

where $E(k)$ denotes the complete elliptic integral of the second kind:

$$E(k) = \int_0^{\pi/2}\sqrt{1-k^2\sin^2\psi}\,d\psi, \quad |\arg(1-k)| < \pi, \tag{28}$$

where $\arg(1-k)$ denotes the phase angle of $(1-k)$ in the complex plane. When k is real and $(1-k) \geq 0$, then $\arg(1-k) = 0 < \pi$ and $E(k)$ is real. This implies a condition $b^2/a^2 \geq 0$, which is always true in our case here.

LOSS ESTIMATE FOR TRIUMF CYCLOTRON

Since the stripping cross-section depends on the velocity of particles, first of all we have to find out the relative velocity in the beam frame. We use smooth approximation for the cyclotron, so we have for the radial direction

$$\sigma_{v_x} = \beta\gamma c\theta_x = \beta\gamma c\sqrt{\frac{\epsilon_x}{\beta_x}} = c\sqrt{\beta\gamma\epsilon_{xn}\frac{Q_x}{\overline{R}}}, \tag{29}$$

and similarly for the vertical direction

$$\sigma_{v_y} = c\sqrt{\beta\gamma\epsilon_{yn}\frac{Q_y}{\overline{R}}}, \tag{30}$$

where ϵ_{xn} and ϵ_{yn} are the normalized emittances of circulating beam, Q_x and Q_y denote the radial and vertical tunes along an equilibrium orbit of average radius $\overline{R}$.

We've calculated the Q_x, Q_y and $\overline{R}$ values for 1563 static equilibrium orbits with energy from 0.3 MeV (injection) to 500.14 MeV (extraction) in a step of 0.32 MeV. The 0.32 MeV energy step accounts for a rf amplitude of 92 kV and rf phase excursion of 30° in average. Besides, we take $\epsilon_{xn} = \epsilon_{yn} = 1\pi$mm-mrad. These parameters are pessimistic estimates, so we are slightly exaggerating the accumulated loss. Figure 1 shows the resulting relative velocity over the entire energy range. It's seen that the total relative velocity is between 3×10^{-4} and 7×10^{-4}. This is almost falling on the plateau of the cross section curve [5], shown in Fig. 1, where the stripping cross section is ~4×10^{-15} cm^2.

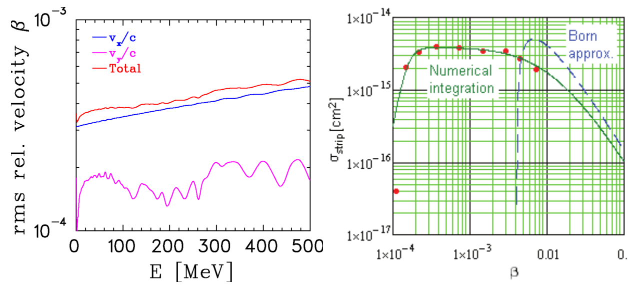

Figure 1: (Left) rms relative velocity of particles in the beam frame over the entire energy range of TRIUMF cyclotron. (Right) intra-beam stripping cross section vs. rms relative velocity.

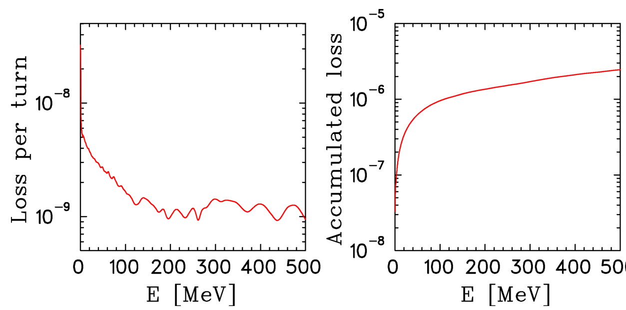

Figure 2: (Left) fractional loss per turn vs. energy. (Right) accumulated fractional loss vs. energy.

We assume a typical rf phase width of 40° for the bunch and a peak current of 300 µA. These, along with the nominal rf frequency of 23.055 MHz, give a bunch half length increasing from 1.8 cm to 55 cm, and particle density in the real space $(N/(\sigma_x\sigma_y\sigma_s))$ decreasing from 2.5×10^8/cm^3 to 1.2×10^7/cm^3. Figure 2 shows the resulting fractional loss per turn and the accumulated loss. The accumulated loss up to 500 MeV, in comparison with the electromagnetic stripping loss [7], is 3 to 4 order of magnitude lower. This is hardly measurable.

SUMMARY

The intra-beam stripping loss rate of H$^-$ in an isochronous cyclotron is derived. Estimate for the loss is then made for the TRIUMF 500 MeV cyclotron. The accumulated loss up to 500 MeV turns out to be 3 – 4 order of magnitude lower than the electromagnetic stripping loss. This is hardly measurable. Thus it is not a concern. Nevertheless, it's worthwhile to

ISBN: 978-3-95450-212-7 ISSN: 2673-5482 doi:10.18429/JACoW-CYCLOTRONS2022-WEPO008

mention that the intra-beam stripping theory is applicable to other hydrogen molecular ions like H_2^+ and H_3^+. When the particle density reaches the order of $>10^{11}/\mathrm{cm}^3$, the loss rate might become a concern, depending on the stripping or dissociation cross section.

ACKNOWLEDGMENTS

The author is grateful to R. Baartman and D. Kaltchev for useful discussions.

REFERENCES

[1] Y.-N. Rao and L. G. Zhang, "Coupling Resonance Correction and Avoidance for the TRIUMF 500 MeV Cyclotron", *J. Instrum.*, to be published.

[2] M. K. Craddock *et al.*, "Improvements to the Beam Properties of the TRIUMF Cyclotron", *IEEE Trans. Nucl. Sci.*, vol. 24, no. 3, pp. 1615–1617, June 1977. doi:10.1109/TNS.1977.4329028

[3] G. M. Stinson *et al.*, "Electric dissociation of H⁻ ions by magnetic fields", *Nucl. Instrum. Methods*, vol. 74, pp. 333–341, 1969. doi:10.1016/0029-554X(69)90359-0

[4] M. Channel *et al.*, "Measurements of H^- Intra-Beam Stripping Cross Section by Observing a Stored Beam in LEAR", *Phys. Lett. B*, vol. 192, no. 3,4, pp. 475–477, 1987. doi:10.1016/0370-2693(87)90141-9

[5] V. Lebedev, N. Solyak, and J.-F. Ostiguy, "Intrabeam Stripping in H^- Linacs", in *Proc. LINAC'10*, Tsukuba, Japan, 2010, paper THP080, pp. 929–931.

[6] Y.-N. Rao, "H^- Intra-Beam Stripping Loss In TRIUMF Cyclotron", TRIUMF Beam Physics Note, TRI-BN-12-03, Oct. 2012.

[7] R. Baartman *et al.*, "Beam Developments at TRIUMF", *IEEE Trans. Nucl. Sci.*, vol. 28, no. 3, pp. 2879–2881, June 1981. doi:10.1109/TNS.1981.4331945

ISBN: 978-3-95450-212-7 ISSN: 2673-5482 doi:10.18429/JACoW-CYCLOTRONS2022-WEPO009

STATUS REPORT AND FUTURE PLAN FOR MOLECULAR IMAGING CENTER (I-One) FACILITY

M. Alredhi, S. Milibari, R. Alsaif, M. Balkheir, M. Sharaf, S. Farhood, S. S. Lingawi
Molecular Imaging Center (I-One), King Abdul Aziz University, Jeddah, Saudi Arabia

Abstract

The radio-pharmaceuticals production and imaging facility is known as I-One at King Abdul-Aziz University in the western region of Saudi Arabia. Started the first production in 2018. We will discuss the facility features, considering the university's existence, where some basic research and training in different aspects of cyclotron operation and radio-pharmaceutical production.

INTRODUCTION

According to IAEA [1], the facility's layout should have planning to achieve the intended product quality and safety, and a manufacturing facility's design and layout must be adequate. Additionally, it is important to recognize that each facility will have its own unique characteristics depending on a variety of variables, such as any applicable national or international legislation and standards, the availability of resources, and the nature of the project. Aspects of facility architecture and layout also differ greatly between member states. For more details, the non-controlled area is the entrance to a facility with access restrictions, the offices, the cleaning facilities, the bathrooms, and the warehouses for materials while the controlled area that needs to be managed to guarantee GMP or radiation protection are included in the restricted area. Furthermore, cleanroom Production must take place in a controlled atmosphere to provide product quality control and conformity with GMP rules for pharmaceutical manufacturing, which may be accomplished in a suitably built cleanroom. Controlled access for both people and materials and the purity of the air inside the room are two aspects of the cleanroom's particular construction requirements. Layouts and air handling equipment that is appropriately constructed help to accomplish both qualities (HVAC). Other considerations, floors, walls and ceilings, doors and windows, benches, waste disposal sink, drainage pipes, ventilation and containment, and radioactive storage facilities these structural and auxiliary elements demand meticulous care.

Several studies used PETtrace™ 800 cyclotrons for medical applications [2–4]. The PETtrace™ 800 central component is a compact, well-proven negative ion cyclotron with a vertical mid-plane that includes both protons and deuterons for optimum versatility and reduced cost radioisotope synthesis [5]. Figure 1 shows a paper burn test with beam location and profile when it hits the target.

MOLECULAR IMAGING CENTER (I-One)

The I-One facility is the first cyclotron in the western region of Saudi Arabia. Building started in 2013 in King Abdul Aziz University. First Beam has been performed on Oct. 2017. In April 2019, I-One center started to distribution the radiotracer production under special consideration. Despite that the nearest cyclotron is more than 1000 km away in Riyadh city, I-One is the first and only center of its kind in the Kingdom of Saudi Arabia which specialized in both the production of radioactive isotopes and offers positron emission tomography scanning services. Moreover, I-One follows the highest standards of quality and good manufacturing for the building, quality management system, and productions that have been manufactured such as ^{18}F-FDG, ^{18}F-NaF, and ^{18}F-PSMA. The conducted of first bone examination in the western region using ^{18}F-NaF was performed in early 2022 besides the main and common radiotracer ^{18}F-FDG which is used for oncology, cardiology, and neurological examinations.

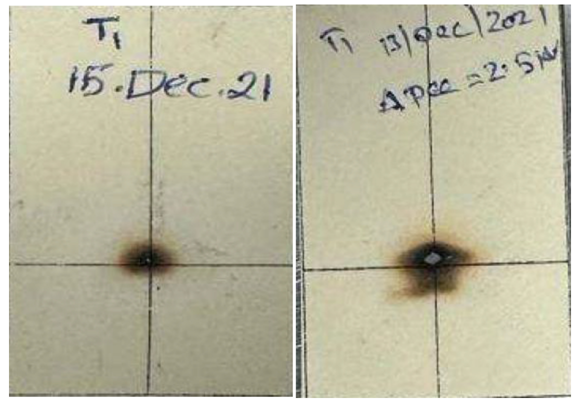

Figure 1: Here we see a paper burn test, which show the beam location and profile when it hits the target.

The I-One Facilities

The facility covers an area of 8000 m^2, where 1200 m^2 is for cyclotron and radio-pharmaceutical production (Fig. 2). The facility is near the university's gate 2 for easy access to radio-pharmaceutical distribution. The production department involves duplicated shielded rooms for any future investments. The radio-pharmaceuticals quality control room is substantial to accommodate more equipment in the future. The center facilities are following the highest standers and measurements. The controlled area includes:

Cyclotron Section The section contains four rooms which are the shielding vault housing of the cyclotron, the service room, the control room, and the power supply room. The cyclotron vault provides shields against ionizing radiation. Typically, strong steel is used to construct the vault. Also, an offer additional bunker to a self-shielded cyclotron is available.

ISBN: 978-3-95450-212-7 ISSN: 2673-5482 doi:10.18429/JACoW-CYCLOTRONS2022-WEPO009

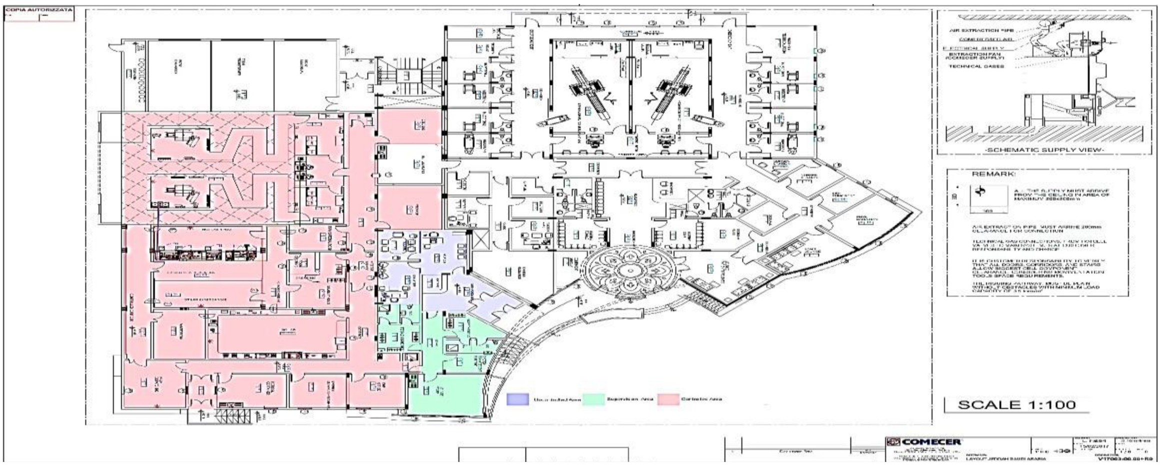

Figure 2: Diagram for I-One facility imaging facility.

Radio-pharmaceutical Production Section The area is divided into two sections. Section 1 includes the raw material warehouse and gowning room. However, section 2 includes the clean room where the radiolabeling synthesis takes place. For any future production plan, another empty room is available with its special features. The hot laboratory has advanced equipment for producing isotopes, including two dispenser modules Timotheo and Theodorico2. Timotheo can be dispensed manually for one vial by the manual arm, while Theodorico 2 can be dispensed robotically for more than 30 vials. Consequently, the ability to distribute to a wide variety of clients is present as shown in Table 1.

Table 1: the Production Parameters of ^{18}F

Item	Value
Number of installed targets	2
Max. current on each target	65 µA
Production time	2.0 hours
^{18}F transfer time	3:15 min
Synthesis time	23 min
Max current on the probe	0.8 mA
Max current on foil	75.6 µA
Current on collimator	4.5–5.7 µA
Collimator / Target current	8 %
Beam loss	<2.5 %

QC Laboratory The quality laboratory receives great attention and high monitoring to ensure that obtains a product that conforms to specifications and standards according to European Pharmacopeia by performing several tests. For example, HPIC determines the impurities in the final product. Besides that, GC is to measure residual solvents. Also, Gamma spectra, TLC, and endotoxin (PTS) are performed to ensure product's conforming to the standers. Moreover, sterility tests are performed after decay.

The colored area illustrated the production department, pink area is the controlled area where all production chain takes place, green illustrated the supervised area including the staff lounge, and purple illustrated the uncontrolled area.

FUTURE AIMS

- As an advanced center owned by King Abdulaziz University, I-One has the advantages of collaboration with university's research colleges for possible development of radio-pharmaceuticals production.
- Believing in the effective social role of community initiatives and contributions, I-One started a training program for both under graduated and graduated students.
- I-One center aims to provide consulting for different medical and pharmaceuticals facilities.

REFERENCES

[1] IAEA, "Cyclotron Produced Radionuclides: Guidance on Facility Design and Production of Fluorodeoxyglucose (FDG)", *Radioisot. Radiopharm. Ser.*, 2012. https://www.iaea.org/publications/8529/cyclotron-produced-radionuclides-guidance-on-facility-design-and-production-of-fluorodeoxyglucose-fdg

[2] A. Darafsheh *et al.*, "Feasibility of proton FLASH irradiation using a synchrocyclotron for preclinical studies", *Med. Phys.*, vol. 47, pp. 4348–4355, 2020. doi:10.1002/mp.14253

[3] D.O. Antuganov *et al.*, "Modification of Automatic Synthesis of [^{18}F]Fluoromisonidazole on a GE TracerLAB Fx F-N Synthesis Module", *Radiochemistry*, vol. 60, pp. 45–50, 2018. doi:10.1134/S1066362218010083

[4] K. Kushwaha *et al.*, "On the production of pharmaceutical grade indium-111-chloride in the medical cyclotron from natural cadmium target and its use in formulation of diagnostic patient dose of 111In-pentetreotide for imaging somatostatin receptor overexpression", *J. Radioanal. Nucl. Chem.*, vol. 328, pp. 835–846, 2021. doi:10.1007/s10967-021-07652-9

[5] General Electric, PETtrace™ 800 cyclotron series, 2018, https://www.gehealthcare.com/-/jssmedia/feature/gehc/products/cyclotrons/pt800-cyclotron-system-data-sheet-rev6.pdf

ISBN: 978-3-95450-212-7 ISSN: 2673-5482 doi:10.18429/JACoW-CYCLOTRONS2022-WEPO010

HIGH INTENSITY CYCLOTRON SYSTEM INTEGRATION AND COMMISSIONING FOR INDUSTRIALIZATION APPLICATION

Pengzhan Li†, Tianjue Zhang, Xianlu Jia, He Zhang, Jingfeng Wang, Shigang Hou, Hongru Cai, Guang Yang, Guofang Song, Gaofeng Pan
China Institute of Atomic Energy, Beijing, China

Abstract

Up to 430 μA beam intensity was obtained in 10 MeV CRM cyclotron (CYCIAE-CRM) at China Institute of Atomic Energy (CIAE) in 2010. Whereafter, CIAE built a series of 14 MeV high intensity external ion source cyclotrons for medical isotope application and its relevant research. Compared with research cyclotron facility, cyclotron for industrialization application requires higher level of safety, usability and stability. Therefore, mechanical and electrical system integration and optimum are applied in the cyclotron design and commissioning. Electrical devices of cyclotron, including power supply, RF amplifier and PLC controller, are integrated into four standard industrial shielding cabinets with electromagnetic compatibility (EMC) design to improve electromagnetic interference and operation stability. Besides, earthing system is rearranged in regular laboratory maintenance period to minimize electromagnetic coupling of different signal systems. Based on the previous compact system integration, communication system is integrated into each electrical device as well and could be operated in local and remote mode for the convenience of commissioning. Industrial Ethernet standard PROFINET is adopted as communication protocol to improve the efficiency of protocol interaction towards millisecond level. Regarding RF system, start-up sequence of LLRF is optimized to increase uptime and reliability. The commissioning is also presented in this paper.

INTRODUCTION

Cyclotron laboratory of China Institute of Atomic Energy is committed to the research and development of high intensity cyclotron. A 10 MeV CRM cyclotron (CYCIAE-CRM) was developed and 430 μA beam intensity was obtained in 2010 [1, 2]. This cyclotron is featured with external multi-cusp H- ion source, fundamental harmonic buncher [3], half-wave RF resonator [4] and vertically positioned extraction system. It's also the prototype and research platform of high intensity cyclotron CYCIAE-100. Then, CIAE develop a series of 14 MeV high intensity cyclotrons [5, 6] for medical isotope application (CYCIAE-14A) and its relevant research (CYCIAE-14B), based on the experience of CYCIAE-CRM.

In order to provide higher level of safety, usability and stability for industrialization application, system integration and other improvements have been carried out on the design and commissioning of research cyclotron, and thus CYCIAE-14A could achieve better performances.

SYSTEM INTEGRATION

CYCIAE-14A [6] could provide two kinds of injection line for various vaults: for type I, the injection line is installed on the top side of cyclotron, while for type II on the bottom. The latter one is optimized both in mechanical structure and electrical circuits, and then to be applicable for small vault with the advantage of compactness, economy and convenience.

Power Supply

Take the main magnet power supply for example, full bridge resonant soft switching inverter circuit is adopted to decrease switching noise (25 kHz) and its electromagnetic interference. One blocking capacitor is added into the primary circuit of the power transformer to improve the situation of core saturation, which is deduced by the unbalance of volt-second when the power IGBT is on and off. This topology also helps to reduce the volume of power supply.

Figure 1: Power supply integration comparison (Left: discrete power supply for CYCIAE - CRM , Right: integrated power supply for CYCIAE-14A).

Full digital control is used in main magnet power supply to realize the high precision regulation of PWM, and PID parameters could be adjusted locally and remotely. Current ramping rate adjustment is designed and applied for the convenience of field ramping commissioning. By the accurate control algorithm, the current instability of the main magnet power supply (180 A/110 V) is obtained as better than 0.01 % in long term operation (8 h) which meets the requirement of magnet system (Fig. 1).

† lipengzhan@ciae.ac.cn

ISBN: 978-3-95450-212-7 ISSN: 2673-5482 doi:10.18429/JACoW-CYCLOTRONS2022-WEPO010

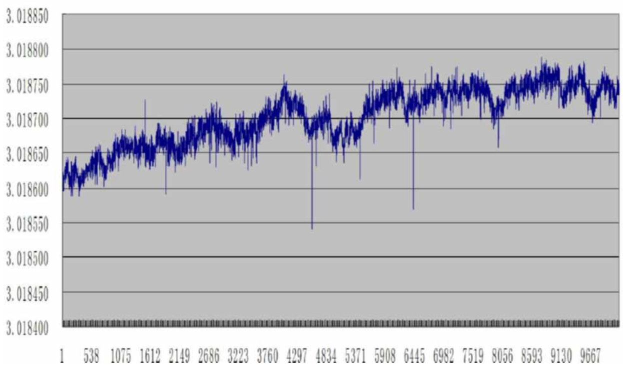

Figure 2: Current instability test of main magnet power supply in long term operation (8 h).

Control System

Main magnet power supply and other power supplies of injection line devices (two quadrupoles, two solenoids and one spiral inflector) are all integrated into one standard industrial shielding cabinet (L800 × W600 × H1800 mm, Fig. 2), and their local control and remote-control systems are integrated as well, which use uniform industrial Ethernet standard PROFINET as communication protocol. In this protocol, control command and state command are configured in the interactive process of communication to realize the functions of adjustment, enable/disable, reset and fault alarm. With the communication protocol integration and optimization, the efficiency of protocol interaction could reach millisecond level, which helps to improve real-time response and failure detection.

ELECTROMAGNETIC COMPATIBILITY DESIGN

Laboratory Earthing System

For the cyclotron laboratory, the earthing system is designed as TN-C-S earthing type (Fig. 3), in which the neutral and earth wires are combined within the supply cable. Due to the separation location of PE and N, the TN-C-S earthing system could provide more effective performances for electromagnetic compatibility (EMC) issues than TN-S earthing system, especially for common mode interference suppression. The TN-C-S earthing system is also featured with low earthing resistance of the PEN conductor. Therefore, the cyclotron could work with a solid reference earthing.

To achieve a much more accurate measurement for beam diagnosis and small signal processing and to minimize the electromagnetic coupling of different signal systems, an additional signal earthing system is applied when the cyclotron is shut down for regular maintenance. The earthing resistance of this signal earthing system is measured as 0.3 Ohms after some necessary improvements.

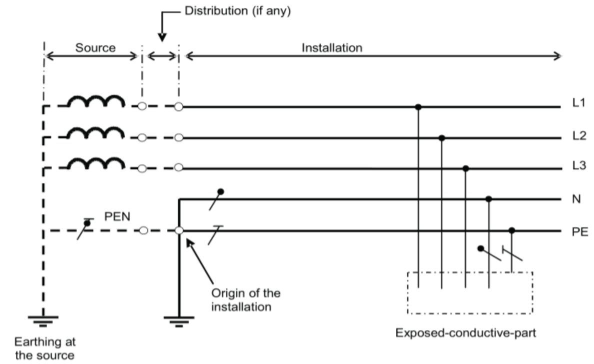

Figure 3: TN-C-S system 3-phase, 4-wire, where the PEN is separated into PE and N at the origin of the installation [7].

Power Supply EMC Design

The cyclotron power supply design complies with the EMC general requirements of IEC 61326-1:2005 applying for electrical equipment for measurement, control and laboratory use. For the immunity requirements, the industrial cabinets are well grounded and shielded to resist electrostatic discharge (ESD) and electromagnetic interference, and the power, signal and control ports are equipped with relevant devices to resist burst, surge and conducted RF interference. For example, the surge protective device (SPD), high-frequency ferrite, varistors and AC EMI filter are inserted in the supply cable in series or parallel between circuit breaker and regulation unit of the power supply. Filter capacitors for DC bus are designed with relatively higher value to compensate voltage dip.

While for the emission requirements, soft switching technology is adopted in the power supply design to reduce IGBT dissipation and electromagnetic emission, especially for the suppression of surge current and spike voltage. Other methods such as differential signalling, shielded cable, varistors, bypassing capacitors and filters are used to improve electromagnetic emission as well.

The EMC design and technology mentioned above have been applied and verified in the magnet power supply of 230 MeV superconducting cyclotron [8] for proton therapy and irradiation, which requires higher level EMC ability. And the power supply passed the internal EMC test referred to IEC 60601-1-2:2004 applying for medical electrical equipment, in which the requirements are much stricter than IEC 61326-1:2005.

The EMC design and integration of RF amplifier and PLC controller are carried out referring to the one of power supply. Thereby, all electrical devices are integrated into four standard industrial shielding cabinets with EMC design to improve electromagnetic interference and operation stability.

RF SYSTEM OPTIMUM

Regarding RF system [5, 9], some significant improvements have been performed to achieve higher reliability. One of the most important issues is concerned with the RF window. Due to heating and multi-pactoring effect, the silver brazing solder between ceramic plate and inner

ISBN: 978-3-95450-212-7 ISSN: 2673-5482 doi:10.18429/JACoW-CYCLOTRONS2022-WEPO010

conductor is excited and pulled out, and then the solder coated on the ceramic plate of RF window in the vacuum side after long term operation, shown in Fig. 4. Thereafter the leakage occurs and the RF window fails to work. To solve this problem, the RF window was removed 88 mm away from the magnet yoke with the magnet field decreasing from 160 Gauss to 70 Gauss. Air cooling by Teflon tube instead of water cooling is provided to the ceramic plate of the RF window. It's expected to decrease the deterioration possibility of multi-pactoring effect and its coating surrounding the silver brazing region in magnet field. After these modifications, the RF window has been running stably for more than two years.

Figure 4: RF window coated with silver brazing solder.

Meanwhile, the start-up sequence of LLRF is optimized to increase uptime and reliability. In the previous design, the state transition includes four modes: pulse mode (S1), DDS tuning mode (S2), capacitor tuning mode (S3) and DDS tracing mode (S4). In order to improve the start-up sequence efficiency, additional compensating capacitor is added into the cavity and then adjusted to reduce the frequency difference between S2 and S3. Thereafter, the frequency sweeping time of S1 will be decreased.

Due to the good performance of RF cavity cooling system of CYCIAE-14A type II, the DDS tracing mode is proved unnecessary anymore. In the new LLRF design, this mode is replaced by power ramping mode and labelled as S3. This new mode follows the DDS tuning mode (S2) and it is defined as a temporary mode. In this mode, the RF cavity is tuned by capacitor tuning loop, and the ramping rate of S3 is set as a relatively higher value, then the power ramping could be finished in less than five seconds. The original capacitor tuning mode follows the new S3 mode. It is redefined as final normal working mode and relabelled as S4. The only difference between new S3 and S4 lies in the operation power level.

Based on the previous operation experiences, the tuner position monitoring of RF cavity is reserved to detect the possible faults even if the original DDS tracing mode is cancelled. The fact is that the central region may be reinstalled in the period of cyclotron regular maintenance. If the reinstallation is not calibrated by network analyser, the RF cavity could work in the condition without enough tuning range. In other words, the frequency drift due to thermal effect would cause RF cavity tuning failure in long term operation if the tuning range is not covered appropriately. The insufficient RF cavity cooling will cause the similar problems mentioned above. Therefore, the function of tuner position monitoring in LLRF provides the additional method to indicate the possible problems for operators if failure occurs.

With the modifications and improvements, the state transition proceeds faster towards the final working mode, and the operation experience proves the effectiveness and reliability of these improvements.

SUMMARY

To promote 14 MeV high intensity proton cyclotron industrialization applications, system integration and other improvements have been carried out on the design and commissioning of research cyclotron, and thus CYCIAE-14A could achieve better performances. Electrical devices of cyclotron are integrated into four standard industrial shielding cabinets to improve EMC characteristics. Other EMC issues such as earthing system and electrical devices EMC design are presented and discussed. RF window and LLRF start-up sequence are optimized as well. These integrations and improvements help to enhance the stability and reliability of cyclotron for industrialization applications.

REFERENCES

[1] T. J. Zhang *et al.*, "Independent research and development, and innovative applications of high intensity proton cyclotrons towards serialization", Chinese Science Bulletin, to be published.

[2] Z. G. Li *et al.*, "Beam Test of 10 MeV High Intensity Cyclotron", *Atomic Ener. Sci. Technol.*, vol. 45, no 5, pp. 588-594, May 2011. doi:10.7538/yzk.2011.45.05.0588

[3] P. Z. Li *et al.*, "Development of Bunching System for High Intensity Cyclotron at CIAE", *J. Nucl. Sci. Technol.*, vol. 59, no. 11, pp. 1370-1374, Apr. 2022. doi:10.1080/00223131.2022.2058103

[4] P. Z. Li *et al.*, "Alternative Cavity Tuning Control for CRM Cyclotron", in *Proc. PAC'09*, Vancouver, Canada, May 2009, paper WE5PFP069, pp. 2165-2167.

[5] T. J. Zhang *et al.*, "Overall design of CYCIAE-14, a 14 MeV PET cyclotron", *Nucl. Instrum. Methods Phys. Res. B*, vol. 269, no. 24, pp. 2950-2954, Dec. 2011. doi:10.1016/j.nimb.2011.04.049

[6] X. L. Jia *et al.*, "14 MeV high intensity cyclotrons: Two projects in progress", *Nucl. Instrum. Methods Phys. Res. B*, vol. 466, pp. 42–46, Mar. 2020. doi:10.1016/j.nimb.2020.01.009

[7] IEC 60364-1:2005, Low-voltage electrical installations - Part 1: Fundamental principles, assessment of general characteristics, definitions, Nov. 2005.

[8] T. J. Zhang *et al.*, "Developments for 230 MeV Superconducting Cyclotrons for Proton Therapy and Proton Irradiation", *Nucl. Instrum. Methods Phys. Res. B*, vol. 406, pp. 244-249, Sep. 2017. doi:10.1016/j.nimb.2016. 11.010

[9] P. Z. Li *et al.*, "Development of a low-level RF control system for PET cyclotron CYCIAE-14", *Nucl. Instrum. Methods Phys. Res. A*, vol. 735, pp. 184-187, Jan. 2014. doi:10.1016/j.nima.2013.09.026

ISBN: 978-3-95450-212-7 ISSN: 2673-5482 doi:10.18429/JACoW-CYCLOTRONS2022-WEPO011

UPGRADING THE BEAM DIAGNOSTIC OF THE HZB-CYCLOTRON FROM AN ANALOGUE TO A NEW DIGITAL PLATFORM

J. Bundesmann†, A. Dittwald, T. Fanselow, G. Kourkafas, A. Denker[1]
Helmholtz-Zentrum Berlin GmbH für Materialen und Energie (HZB), Berlin, Germany
[1]also at Berliner Hochschule für Technik, Berlin, Germany

Abstract

The HZB-Cyclotron delivers since a long time reliable beam for experiments and Proton Therapy. Now the old analogue beam diagnostic is outdated and hard to maintain. We developed a digital replacement for the multiplexers for 30 Faraday cups and 12 beam profile monitors. Both use as hardware platform a single-board-controller with FPGA-technology with integrated analogue and digital signals in a client-server architecture. Here we present the new features after more than one year of operation.

MOTIVATION FOR THE NEW MULTIPLEXER DESIGN

A layout of the accelerator complex can be found in [1]. Two injectors serve the k=130 isochronous sector cyclotron. One high energy beam leads to the treatment room and one to the experimental station. Overall, 27 Faraday cups and 10 beam profile monitors (BPM) are installed. The beam diagnosis system dates to the eighties, when the accelerator complex was erected. As more and more Faraday cup channels in the analogue cup current system failed due to contact problems in the wire-wrap cabling, a replacement system had to be designed and constructed.

In order to keep the financial effort for the new system in the accelerator within limits, it was decided to use also in the future the excellent working existing current transformers (I/U converter with 5 ranges from 1 nA to 10 µA full scale) and cabling between measuring points and multiplexer. The converters had been developed in-house and can still be easily repaired. Furthermore, they are working very reliable

One of the challenges for the conversion from the old system to the new design was that it had to be done without impacting on the scheduled beam time, especially not interfering with the scheduled proton therapy blocks. Thus, the installation and commissioning of the new system had to be carried out in just one service period of two weeks. Hence, the new design was developed in a separated setup.

LAYOUT OF THE NEW FARADAY CUP MULTIPLEXER

The following features were described as minimum demands:

- at least 24 channels for Faraday cups and radial probes available
- an auto range feature switching to the active Faraday cup channel in the optimum range of the I/U-converter automatically.
- an auto range feature switching to the active Faraday cup channel in the optimum range of the I/U-converter automatically.
- the choice to select a fixed range of a selected Faraday-cup channel to display
- two simultaneously measured channels with all information, as both injectors are sometimes operated in parallel
- readout of the I/U-converters with a sampling rate of 10 kHz and processing these data to provide information about the mean value, minimum, maximum, and the standard deviation
- display of the processed values to the operator (Min-Max-Mean-Standard Deviation)

Figure 1 shows the data of a Faraday cup as displayed in the control room. The operator sees which Faraday Cup or radial probe is selected, the range of the I/U converter, the beam intensity of 0.36 µA, the minimum value of 0.32 µA, maximum value of 0.4 µA and a standard deviation of 3.8%. Beam tuning is now easier, especially when aiming for high beam stability, i.e., low standard deviation. Two graphs in the lower part provide the history of the past 100 s. The upper graph shows mean, maximum, and minimum beam intensity. The lower part shows the standard deviation. All these data are updated every 100 ms. The dip in the minimum beam intensity and the rise in the standard deviation shows the influence of a beam profile monitor to the beam: The rotating wires cut a small section of the beam, such influencing the standard deviation quite a lot, while the mean beam intensity is scarcely affected.

For the off-line development of the Multiplexer, 15 I/U converters with current sources were set up. Some of the current sources were connected to function generators to simulate beam instabilities. Thus, the programming of the FPGAs and LabVIEW could be done without using beam time.

The layout of the new system is shown in Fig. 2. The backbone of the system are two sbRIO9637 FPGA boards from NI which are connected via a new backplane interface to the existing I/U converters. All the analogue input signals are sampled simultaneously with a sampling rate of 10 kHz. Every 100 ms the 1000 values of each channel are streamed via TCP-IP to the server, where they are processed to provide the desired values: mean, minimum and maximum beam intensity, and standard deviation

The communication between the server and the display PC is done via EPICS communication. Thus, we use in LabVIEW the CA Lab interface [2], which converts Lab-

† bundesmann@helmholtz-berlin.de

ISBN: 978-3-95450-212-7 ISSN: 2673-5482 doi:10.18429/JACoW-CYCLOTRONS2022-WEPO011

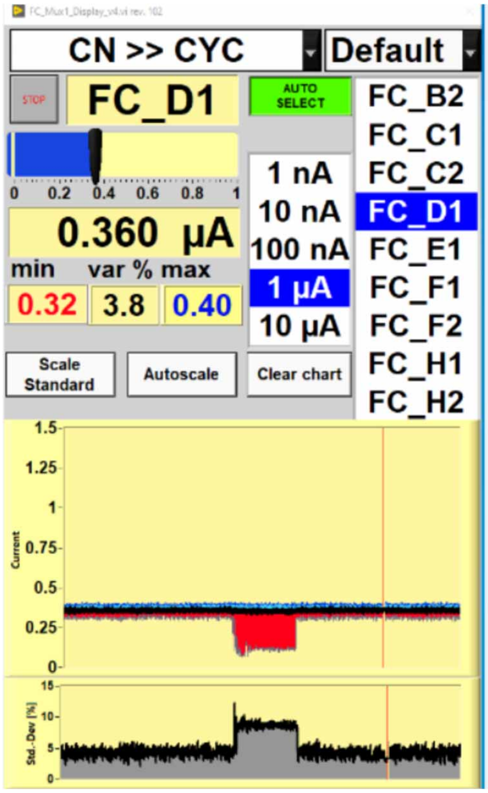

Figure 1: Display showing relevant data of the selected channel (name, range, value); the upper graph shows mean (black), maximum (blue), minimum value (red); the lower graph shows the standard deviation. The graphs show the history of the last 100 s and are updated every 100 ms.

VIEW data to EPICS variables and vice versa. Thus, the server and display-PC only have to be in the same VLAN to exchange data.

Three Multiplexer channels are available: One for the beam line from the Van-de-Graaff injector to the cyclotron, one for the beam line between the Tandetron injector and the cyclotron and one for the high energy beam line.
In addition to the required features, an oscilloscope display and alarm processing has been implemented. In the oscilloscope mode the raw values without processing are display, meaning that they are displayed with 10 kHz. For example, a 50 Hz periodic noise on the signal becomes visible. This helps when error tracking, e.g., hunting for a noisy power supply. The operator may now also set alarm thresholds for minimum and upper limit of the beam intensity. This is mainly used when the accelerator is in standby. When the beam drops below the threshold or surpasses the upper value an acoustic signal alerts the operator

LAYOUT OF THE NEW BEAM PROFILE MULTIPLEXER

After the successful implementation of the new Multiplexer system for the Faraday cups the idea was close to use the same hardware for the BPM multiplexer. It has only one new backplane interface and sbRIO9637. One further server processes the data and runs a softIOC to transfer the BPM-data as EPICS process variables.

Three out of 16 BPM´s can be displayed simultaneously. The distribution of the BPMs to the displays is chosen in such a way that the focussing in dedicated beam line sect-

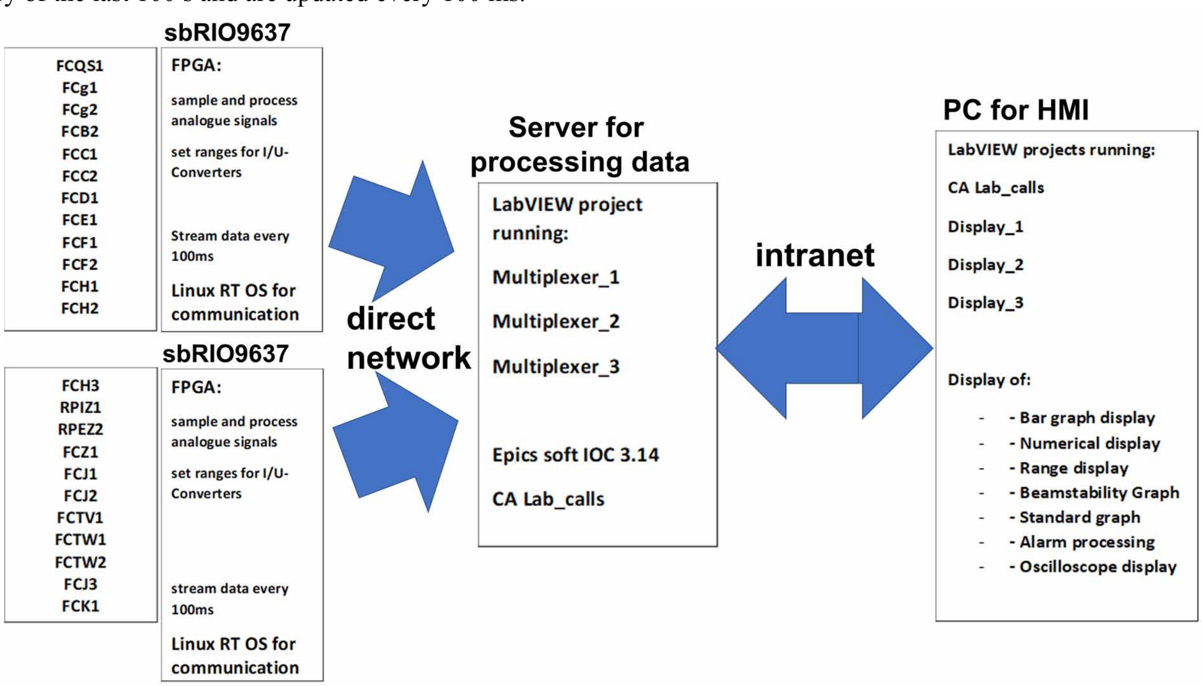

Figure 2: Layout of the new Faraday-cup Multiplexer. There are two FPGA-boards (sbRIO9637 from NI) with a new backplane interface to the I/U-converters. Continuously all analogue input channels from the FPGAs are sampled simultaneously with 10 kHz, after 1000 values each channel values is processed (calculating standard deviation, and mean value, searching for minimum and maximum). These values are streamed to the server via TCP-IP. There, in three separated LabVIEW-projects the streamed data are converted back to current values. Via digital outputs of the FPGAs the range setting is obtained. The processed data are sent to the PC in the control room as EPICS-variables.

23rd Int. Conf. Cyclotrons Appl. CYCLOTRONS2022, Beijing, China JACoW Publishing
ISBN: 978-3-95450-212-7 ISSN: 2673-5482 doi:10.18429/JACoW-CYCLOTRONS2022-WEPO011

ions is visible. They are updated with 25 Hz, each profile consists of 400 points.

One example is shown in Fig. 3, which displays the focusing after the Van-de-Graff. Beam line calculations requests focal points in the first and third BPM, while the beam is broader in the middle.

It is now possible to save the BPM images and reload them for comparison of the focussing. This reference signal from the same BPM can be overlayed to the live signal, allowing easy beam correction. This is especially important for the last BPM in front of the cyclotron: At this position, the fringe field of the main magnets influences the beam path. For this reason, the beam, especially when using light ions, is not on axis. The fringe field depends on ion species and energy. The ideal position for injection into the cyclotron varies with the above-mentioned parameters. In the past, it was the experience of the operators to identify a beam profile which allows good injection into the cyclotron. By reloading the beam profile of a beam with good injection transmission, the tuning becomes far easier.

CONCLUSION

The new multiplexers are running reliable since 2019. The overall investment was reasonable. The new functions for Faraday cups are very useful in fine tuning the beam stability in respect of focussing of the beam, adjusting phases and amplitudes of the RF-systems. The save-and-restore function of the BPMs is very helpful when comparing beam settings and is often employed. The use of nearly the same hardware set-up for both systems made the development easy and straightforward

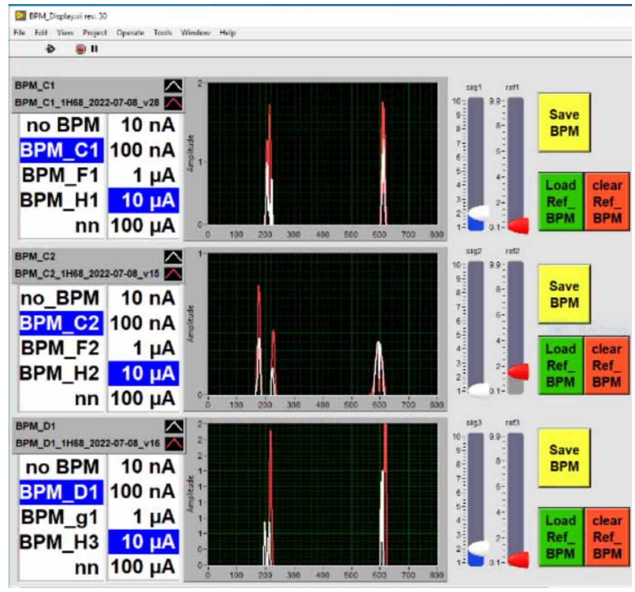

Figure 3: Display of the new BPM Multiplexer system. Up to three BPMs can be displayed simultaneously. Saved BPM images (red) can be overlaid to the actual profile (white). Each profile displays the cross-section of the beam in x- (left) and y-direction (right).

REFERENCES

[1] J. Bundesmann *et al.,* “Beam properties at the experimental target station of the Proton Therapy in Berlin”, in *Proc. 22nd Int. Conf. on Cyclotrons and their Applications (Cyclotrons’19)*, Cape Town, South Africa, Sep. 2019, pp. 199-201. doi:10.18429/JACoW-Cyclotrons2019-TUP020

[2] CA Lab, https://www.helmholtz-berlin.de/zentrum/locations/it/calab/

23rd Int. Conf. Cyclotrons Appl. CYCLOTRONS2022, Beijing, China JACoW Publishing
ISBN: 978-3-95450-212-7 ISSN: 2673-5482 doi:10.18429/JACoW-CYCLOTRONS2022-WEPO012

UPGRADE OF BEAM DIAGNOSTIC SYSTEMS OF JULIC CYCLOTRON

Yu. Valdau[1], P. Niedermayer[1], R. Gebel[1]
GSI Helmholtzzentrum für Schwerionenforschung GmbH, 64291, Darmstadt, Germany
O. Felden, Forschungszentrum Jülich, Institut für Kernphysik, IKP4, 52428, Jülich, Germany
U. Giessen, H. Soltner, R. Lohoff, Forschungszentrum Jülich, Zentralinstitut für Engineering und Technologies, ZEA-1, 52428, Jülich, Germany
N. O. Fröhlich, Deutsches Elektronen-Synchrotron DESY, 22607 Hamburg, Germany
[1]also at Forschungszentrum Jülich, Institut für Kernphysik, IKP4, 52428, Jülich, Germany

Abstract

The JULIC cyclotron is in operation since already more then 50 years. Many subsystems of the cyclotron have been upgraded since then, to meet a requirements of the users or simply to the state of the art. In this contribution status of upgrade of the cyclotron beam diagnostic and magnet field control system is presented. Besides that, an example of application of laser doppler vibrometer and proof-of-principle experiment for none-destructive low beam current and position measurement are described.

JULIC CYCLOTRON

The Institute für Kernphysik (IKP) of Forschungszentrum Jülich exploits JULIC cyclotron since already more than 50 years. The JULIC cyclotron is build as a classical isochronus cyclotron with axial injection from the external particle sources. It has a large normal conducting magnet, 100 kW power HF-system with three Dee's for the acceleration and electrostatic extraction system. Almost last 30 years JULIC is mainly used as injector for the accelerator and storage ring COoler-SYnchrotron Jülich (COSY-Jülich) [1]. This is why presently JULIC is only used for acceleration of light negative H - and D - ions for the stripping injection into the COSY ring, at the energies of 45 and 55 MeV, respectively.

Besides operation as COSY injector, JULIC is frequently used for the irradiation of the electronic components, new materials, and for the development of the new generation of the accelerator driven High Brilliance neutron Source (HBS) [2].

VIBRATION OF THE CYCLOTRON INTERNAL ELEMENTS

Since significant time JULIC users have been confronted with a 33 Hz noise ripple in the extraction pulse of the cyclotron. This strong intensity fluctuation disturb COSY operation and due to the injection scheme of the storage ring (20 ms injection pulse every two seconds) did not allow beam intensity optimisation in the machine. The ripple was sudden appearing and disappearing in the extraction pulse of the cyclotron in unpredictable manner, making search for the source of the noise extremely difficult.

To find a noise source, a special action to measure vibrations in the cyclotron bunker has been undertaken. Using commercial laser-doppler vibrometer [3] a presence of

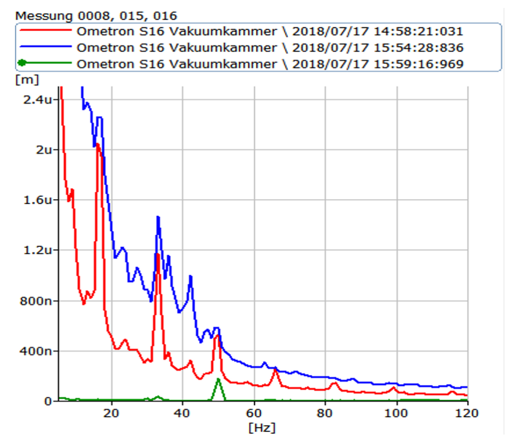

Figure 1: Vibration frequency spectra measured through the vacuum window at the HF-elements of the cyclotron using Omertron S16 vibrometer. The blue spectra is measured before any modification, red - after the first improvements, green - after all the dampers have been installed.

strong 33 Hz vibration at the internal parts of the cyclotron has been detected (see blue spectra in Fig. 1). With the help of the special microphone and frequency spectrum analysis software the source of the vibration in the cyclotron bunker has been identified and removed (red and green spectra in Fig. 1). The three scroll pumps in the cyclotron bunker, used only during regeneration of the main cyclotron cryo-pumps, have not been equipped with original vibration dampers and were producing strong vibrations at 33 Hz harmonic. After installation of standard and additional vibration dampers the level of the vibration at 33 Hz harmonic at the internal elements of the cyclotron even in case of simultaneous regeneration of all three cryo-pumps has been reduced to the insignificant level. As a result of this action, 33 Hz noise in the extraction pulse of the JULIC have completely disappeared and did not return.

UPGRADE OF THE JULIC MAGNET FIELD CONTROL SYSTEM

The JULIC cyclotron magnet field control system is used to keep field in the cyclotron constant to the 0.1 ppm using a high precision magnet field measurement, special coil, and precision power supply. In this upgrade program an NMR magnet field measurement system has been upgraded

ISBN: 978-3-95450-212-7 ISSN: 2673-5482 doi:10.18429/JACoW-CYCLOTRONS2022-WEPO012

using the newest Metrolab PT-2026 system [4]. Besides improvement in magnet field measurement resolution, the new system is capable to measure magnet field of the cyclotron magnet in a complete range of operation. However, this advantage only became available once the sensor with fluoride sample material has been specially produced for JULIC by the Metrolab. Detail of fluoride sample parameters are presented in the Table 1. Standard sensors with H2 and D2 samples was coupling to the cyclotron HF and was not usable for the normal cyclotron operation. The new Metrolab NMR system with fluoride as a sample material and new specially developed LabView based software are now in use in the magnet field control system of the JULIC cyclotron.

Table 1: Magnet field and Larmor frequencies of the atoms in fluoride sample in comparison to the standard JULIC parameters. Parameters of the cyclotron: main magnet field B [T] and acceleration frequency F [MHz] in three standard mode of operation are presented. Calculated Larmor frequency F_L [MHz] for the atoms in fluoride sample and critical field B_K, then Larmor frequency is equal to the acceleration frequency of the JULIC cyclotron are presented. The new fluoride sensor from Metrolab can be used for all the standard modes of the JULIC.

Mode	B [T]	F [MHz]	F_L [MHz]	B_K [T]
H-	0.345	29.94	13.78	0.740
D- (55 MeV)	0.555	23.66	22.21	0.589
D- (75 MeV)	0.650	27.37	26.03	0.683

UPGRADE OF THE JULIC BEAM CURRENT MEASUREMENT SYSTEMS

To meet growing requirements of the JULIC users for the more stable cyclotron operation and better beam transport significant investment in cyclotron beam current measurements system has been made. In total, there are more than 59 channels with different diagnostic signals distributed across the cyclotron and it beam lines. Old custom build analogue electronic has been upgraded using 24 bit four channels TetrAMM devices from CAENels [5], distributed across the facility. All the TetrAMM ADC are implemented into the common EPICS based data acquisition and control environment developed by the COSY controls team. The beam current pulse measured using TetrAMM and new software are presented in Fig. 2. Significant improvement in the handling of the diagnostic information using TetrAMM devices has been achieved. However, new electronics is relatively sensitive to the noise figure in the diagnostic lines and still require special measures to show the complete performance in a noisy cyclotron environment.

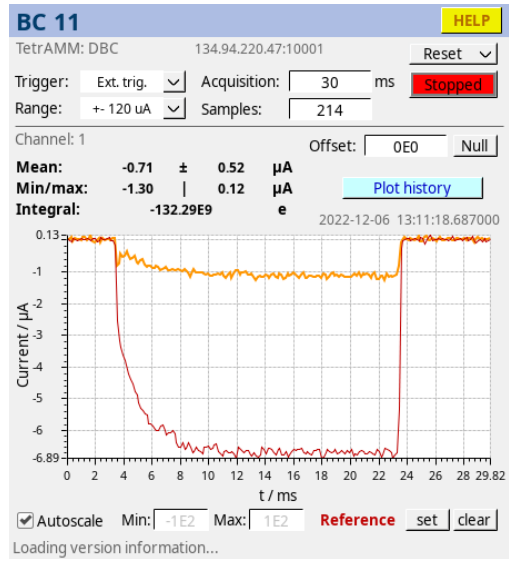

Figure 2: Beam current measurement with TetrAMM at one of the cyclotron cups. Standard readout TetrAMM parameters, measured spectra and reference curve are presented.

NON-DESTRUCTIVE LOW CYCLOTRON BEAM CURRENT DIAGNOSTIC

For the normal operation of the cyclotron usually destructive beam current measurements methods are used. However, for various reasons it is not always possible to readout current from the irradiated materials. In this case it is even more difficult to obtain information about the position of the cyclotron beam during irradiation without usage of the special apertures or collimator in front of the target.

The first experiments of the High Brilliance Source collaboration [2] has been made using maximal cyclotron proton beam current of 10 nA. Under this conditions in a single cyclotron bunch (30 MHz) there only about $\approx$ 2000 protons. Hence, none-destructive beam diagnostics of such a low intensity beams is a special challenge which can only be solved by a measurements in frequency domain.

To meet this challenging requirements of the HBS experiment a high resolution lock-in amplifier based data acquisition (DAQ) system, developed for the TRIC experiment at COSY [6], has been used. The Fast Current Transformer (FCT) and Integrating Current Transformer (ICT), developed by the Bergoz company, and standard COSY Beam Position Monitor (BPM) have been installed in the HBS beam line. The chain of custom build preamplifiers and commercially build amplifiers, presented in Fig. 3, connects none destructive beam sensors with DAQ. The DAQ was located as close as possible to the beam sensors but at the same time in location with moderate radiation conditions.

Noisy cyclotron environment does not allow any kind of significant diagnostic measurement using FCT, ICT or BPM in time domain. Furthermore, due to the presence of the strong signal from the cyclotron HF system in all the signals at the cyclotron, diagnostic measurements in the frequency

ISBN: 978-3-95450-212-7 ISSN: 2673-5482 doi:10.18429/JACoW-CYCLOTRONS2022-WEPO012

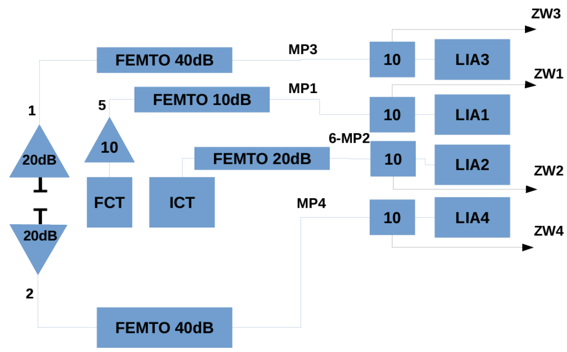

Figure 3: Non-destructive beam current and position measurement readout scheme during HBS experiment in 2018. The signals from the BPM, FCT, and ICT are amplified using custom build and FEMTO amplifiers before they are connected to the Lock-In Amplifiers SR844 from the Stanford Research. The Lock-In Amplifiers (LIA) are readout using DAQ running on a server PC.

domain are only possible starting from the second harmonic of the signal.

In the particular HBS experiment it was demonstrated that relative beam current and position can be measured using lock-in [7] based technique and DAQ discussed in Ref. [6] up to the DC beam currents of the 2 nA.

CONCLUSION

The diagnostic systems of the JULIC cyclotron has undertaken significant upgrade program. The beam diagnostic system has been upgraded using TetrAMM instruments. The newest NMR system from Metrolab is in use in the JULIC magnet field control system. Commercially available doppler vibrometer has been applied to find a source of disturbing 33 Hz vibrations in the cyclotron. Finally, during one of the HBS experiments a lock-in based high resolution DAQ has been successfully used for none-destructive beam current and position diagnostic up to the DC currents of 2 nA.

REFERENCES

[1] H.-P. May, M. Bai, O. Felden, and R. Gebel, "Status of the COSY/Jülich Injector Cyclotron JULIC", in *Proc. 21th Int. Conf. on Cyclotrons and their Applications (Cyclotrons'16)*, Zurich, Switzerland, Sep. 2016, pp. 310–312. doi:10.18429/JACoW-Cyclotrons2016-THP04

[2] O. Felden, V. Kamerdzhiev, R. Gebel, K. Grigoriev, and Y. Valdau "ULIC - driver accelerator for HBS", presented at the 23rd Int. Conf. on Cyclotrons and their Applications (Cyclotrons'22), paper THPO005, this conference.

[3] https://www.ometron.com/

[4] Metrolab "NMR Precision Teslameter PT2026", User Manual, ver. 2.1, 2017.

[5] CAENels, "4-Channel Fast Interface Bipolar Picoammeter with Integrated HV Bias Source", User Manual, Rev. 1.8, 2018.

[6] Y. Valdau, S. Mikirtytchiants, S. Trusov, L. Eltcov, and P. Wuestner, "Development of high Resolution beam current measurement system for COSY-Jülich", in *Proc. 5th Int. Beam Instrumentation Conf. (IBIC'16)*, Barcelona, Spain, Sep. 2016, pp. 434–437. doi:10.18429/JACoW-IBIC2016-TUPG41

[7] Stanford Research Systems, "Model SR844 RF Lock-In Amplifier", Rev. 2.9, 2016

ISBN: 978-3-95450-212-7 ISSN: 2673-5482 doi:10.18429/JACoW-CYCLOTRONS2022-WEPO016

A NEW 18 GHz ECR ION SOURCE FOR CYCLOTRON AT CIAE

B. Tang†, B. Q. Cui, L. Zhang, R. G. Ma, G. Guo, Y. F. Wang, H.N. Chen, Y. T. Li, Y. J. Ma, L. Sui
L.H. Chen, China Institute of Atomic Energy, Beijing 102413, China
C. Qian*, ‡, L. T. Sun, P. Zhang, W. Lu, L. B. Li, J. D. Ma, Z. H. Jia, X. Z. Zhang
Institute of Modern Physics, Chinese Academy of Sciences, Lanzhou 730000, China
Y. T. Li, College of Nuclear Science and Technology, Fundamental Science on Nuclear Safety and Simulation Technology Laboratory, Harbin Engineering University, Harbin 150001, China

Abstract

In order to meet the requirements of ion beam for the single event effect experiment, the ion source needs to supply ion beams of N, Ne, Si, Ar, Fe, Kr, Xe, and so on for the cyclotron. The most effective way to increase the energy of the cyclotron is to increase the charge state, and the Kr ion charge state reaches 22+ while the Xe ion charge state reaches 35+. A new room-temperature Electron Cyclotron Resonance (ECR) ion source operating at 18 GHz has been developed and assembled at China Institute of Atomic Energy (CIAE). This new ECR ion source is based on the Lanzhou Electron Cyclotron Resonance ion source No.5 (SESRI-LECR5) developed at Institute of Modern Physics (IMP). The magnetic confinement of the new ECR ion source is realized by the axial mirror field provided by two set of room temperature pancake coils while the radial hexapole field is supplied by a permanent magnet hexapole. A dual-sputter disk injection component was designed for the production of metallic cocktail ion beams. This paper will give the detailed design of this ion source, and some preliminary highly charge state ion beam production results will also be presented.

INTRODUCTION

A heavy ion cyclotron (K=120) [1] has been rebuilding at CIAE. The cyclotron is a versatile machine，
which is employed for the production of protons, deuterons, alpha-particles and heavy ions in the variable energy The energy of proton is variable at 10-72 MeV, the maximum current intensity is 200 eμA , the deuterium ion energy is variable at 10-65 MeV, the alpha ion energy is variable at 20-130 MeV, and the heavy ion energy is 120- MeV * Q^2/A (Q and A are the charge state and mass number of accelerated ions respectively). For heavy ions, the energy of the ion beam extracted by the accelerator is proportional to Q^2. It is very important to improve the charge state of the ion beam to improve the maximum beam energy accelerated by this accelerator. The original injector of the accelerator is a 10 GHz CAPRICE 1 Tesla ECR ion source was developed in 1992 [2]. The charge state that can be generated for heavy nuclide particles is low. For example, the charge state of Kr can only reach 18+, while the charge state of Xe can only reach 27+. Therefore, the development of a new ion source with the ability to produce higher charge state ion beam, is necessary to meet the requirements of the basic and application research of heavy ion, such as the research of low energy nuclear physics, single particle effect, ion radiation damage and so on.

THE LAYOUT OF THE INJECTOR

The original 10 GHz ion source injector was equipped below the cyclotron. The horizontal ion beam is injected into the vertical section through a 90-degree electrostatic deflector and enters the central hole of the magnetic pole under the cyclotron. Two sets of triple quadrupole lens matching beam envelope are set in the vertical section, and finally injected into the cyclotron through an electrostatic deflector (mirror) for acceleration.

The new 18 GHz high charge state ECR ion source injector is set directly below the original 10 GHz ion source injector, as shown in Figs. 1 and 2. According to the requirements of cyclotron, the maximum high voltage of the ion source is 20 kV, and the total ion beam is about 5 emA. Magnetic elements are used on the beam line to reduce the influence of space charge effect on the ion beam. A solenoid lens is set behind the ion source to match the change of ion beam angle under different extraction voltage conditions to meet the requirements of the optical envelope of the dipole magnet. The dipole is a dual-focusing magnet with a deflection radius of 500 mm and the deflection angle is 90 degrees, and the mass resolution is better than 60.

A set of triple quadrupole lens is set behind the dipole magnet, and the analyzed ion beam is matched into the electrostatic deflector and injected into the vertical beam line of the original injector. The large radius electrode plate of the electrostatic deflector is movable. When the beam is supplied by the new injector, the large radius electrode plate of the electrostatic deflector will be move out, and then the ion beam can pass through the electrostatic deflector. Two XY magnetic guides are also set on the beam line to correct the ion beam transmission direction.

ION SOURCE

A high performance room temperature ECR ion source was proposed for various ion beams injection. According to the scaling laws of an ECR ion source [3, 4]. Its design is based on SESRI-LECR5 [5] parameters and optimized for the magnetic field of the SECRAL operating at 18 GHz [6]. Compared with a superconducting ECR ion source, a room temperature 18 GHz ECR ion source has the advantages of more accessible construction, lower cost, and more convenient maintenance.

* contributed equally to this work
† tangb364@126.com
‡ qianc@impcas.ac.cn

ISBN: 978-3-95450-212-7 ISSN: 2673-5482 doi:10.18429/JACoW-CYCLOTRONS2022-WEPO016

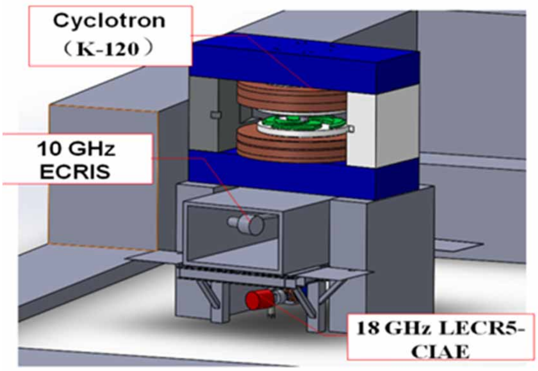

Figure 1: Layout of the cyclotron system.

Figure 2: The picture of the new injector.

As shown in Fig. 3. The axial magnetic field to achieve a mirror field uses two coils that injection and extraction coils. It is advantages to tuning on the electron temperature through the magnetic gradient at resonance. Besides, the magnetic field at the injection side is reinforced by a thick iron plug that obtains a high-B mode magnetic profile. The axial field of 2.6 T at the injection is achievable, as shown in Fig. 4. A hexapolar system gives the radial magnetic field. The optimum configuration for such a system is given by the so-called Halbach array composed of 36 block permanent magnets (88 mm inner diameter, 188 mm outer diameter, and 320 mm long). Using the higher remanence material N50M NdFeB (Br=1.407 T, Hc=-1043 kA/m) improves the radial magnetic field strength, and uses higher polarization coercivity material N48SH NdFeB (Br=1.386 T, Hc=-1011 kA/m) solves the self-demagnetization problem in the six critical magnetic segments. The radial magnetic field at a chamber wall of 1.2 T is achievable, and the large and long plasma chamber (80 mm in diameter and 340 mm long) allows a long lifetime for the ions to produce high charge states. Table 1 presents the parameters of the LECR5-CIAE ion source.

The gas inlet system of the ion source is equipped with four gas inlet pipes, each of which is independently adjustable by a needle valve, and can inject various gases into the ion source, simultaneously. At the same time, a dual-sputter disk injection component is designed for the production of metallic cocktail ion beams to meet the experimental requirements of single event effects research (Fig. 5).

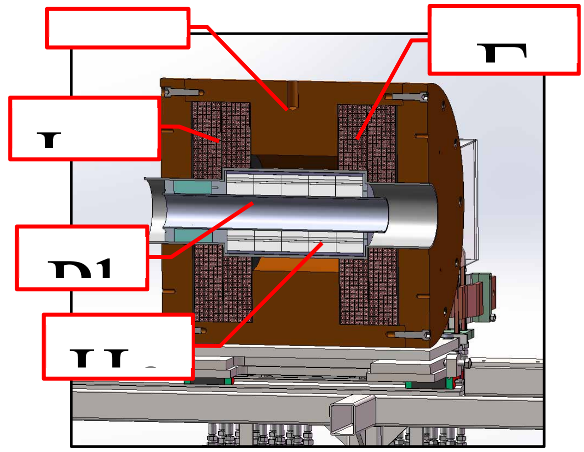

Figure 3: Layout of the LECR5-CIAE ion source.

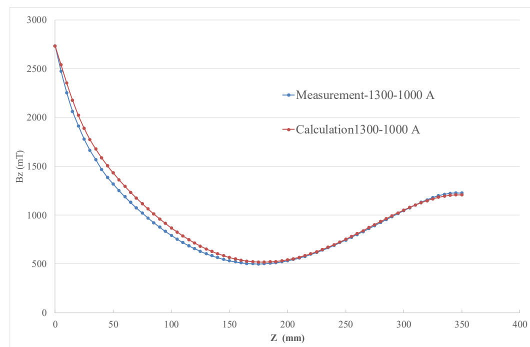

Figure 4: The calculated and measured magnetic field.

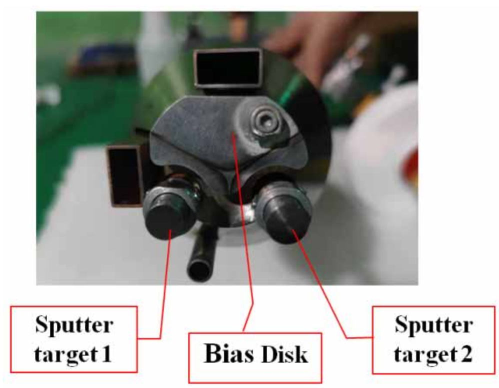

Figure 5: Injection component.

Table 1: The Parameter of the LECR5 Ion Source

Parameter	Value
Microwave frequency (GHz)	18
Maximum power(kW)	2.0
Binj (T)	2.6
Bext (T)	1.4
Brad (T)	1.2
Mirror Length (mm)	340
Plasma chamber D (mm)	80
Maximum HV(kV)	30

ISBN: 978-3-95450-212-7 ISSN: 2673-5482 doi:10.18429/JACoW-CYCLOTRONS2022-WEPO016

FIRST BEAM EXPERIMENT

A large number of experimental studies on ion beam generation have been carried out, and the ion beams of elements such as silicon, oxygen, nitrogen, neon, krypton, xenon, etc. have been produced. The high voltage of the ion source reaches 25 kV, which is better than the design value of 20 kV. The beam generation methods for different forms of elements are studied. For gaseous elements, such as oxygen, nitrogen, neon, etc., gas intake is used. For solid elements, silicon uses the gaseous compound of SiH_4, while iron, tantalum, etc., uses the sputtering method. The typical beam intensity is shown in Table 2, in which the Fe^{15+} ion beam reaches 6 eμA with sputter target. $^{84}Kr^{22+}$ ion beam reaches 6.8 eμA with nature Kr gas. $^{129}Xe^{35+}$ion beam reaches 1.1 eμA. All are better than the acceptance index. The mass spectrometry of the Kr ion beams and the mixture beams of Ne, N and Ar are shown in Figs. 6 and 7, respectively.

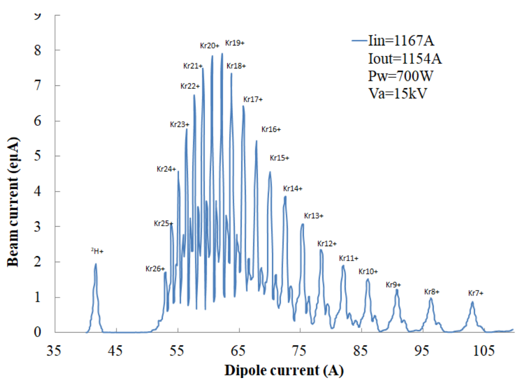

Figure 6: The ^{nat}Kr ion beam.

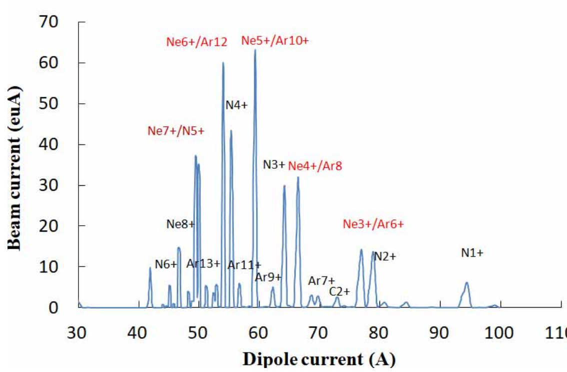

Figure 7: The mixture beams of Ne, N and Ar.

Table 2: Typical Beam Current

Beam	Beam Current (eμA)
$^{14}N^{4+}$	95
$^{20}Ne^{6+}$	75
$^{28}Si^{8+}$	15
$^{40}Ar^{12+}$	29
$^{56}Fe^{15+}$	6
$^{84}Kr^{22+}$	6.8
$^{129}Xe^{35+}$	1.1

CONLUSION

A new room-temperature ECR ion source operating at 18 GHz have been developed at CIAE. The preliminary tests show that the ion source has the ability to produce silicon, oxygen, nitrogen, neon, krypton, xenon single or mixed cocktail beams. In the later stage, further research will be carried out, and the experimental research on the acceleration and extraction of cocktail beam by the accelerator will be carried out in cooperation with the cyclotron.

REFERENCES

[1] G. Heidenreich and Th. Stammbach, "Some aspects of the 100 μA operation of the SIN injector cyclotron", in *Proc. 9th Int. Conf. on Cyclotrons and their Applications*, Caen, France, Sep. 1981, pp. 365-370.

[2] B. Jacquot *et al.*, "La source CAPRICE 10 GHz en mode harmonique $2(\omega_{HF}-\omega_{ce})=0$", *Nucl. Instrum. Methods* A, vol. 287, pp. 341-347, 1990. doi:10.1016/0168-9002(90)91545-M

[3] R. Geller, *Electron Cyclotron Resonance Ion Sources and ECR Plasma*, Philadelphia, PA, USA: Institute of Physics Publishing, 1996, pp. 394-398.

[4] D. Hitz, "Recent progress in high frequency electron cyclotron resonance ion sources", *Advances in Imaging and Electron Physics*, vol. 144, p. 047075, 2006. doi:10.1016/S1076-5670(06)44001-5

[5] C. Qian *et al.*, "A new room temperature LECR5 ion source for the SESRI project", *Rev. Sci. Instrum.*, vol. 91, p. 023313, 2020. doi:10.1063/1.5128514

[6] H. W. Zhao *et al.*, "Advanced superconducting electron cyclotron resonance ion source SECRAL: design, construction, and the first test result", *Rev. Sci. Instrum.*, vol.77, p. 03A333, Mar. 2006. doi:10.1063/1.2149307

ISBN: 978-3-95450-212-7 ISSN: 2673-5482 doi:10.18429/JACoW-CYCLOTRONS2022-WEPO017

A NEW DESIGN OF CYCIAE230 SUPERCONDUCTING CYCLOTRON RF-DRIVEN SYSTEM*

Zhiguo Yin†, Shilun Pei, Xiaoliang Fu[1], Xueer Mu, Tianjue Zhang
China Institute of Atomic Energy, Beijing, China
[1]also at TRIUMF Vancouver, Canada

Abstract

A superconducting cyclotron with a beam energy of 246.2 MeV has been developed and commissioned by the China Institute of Atomic Energy. The RF system of the first CYCIAE-230 cyclotron adopts two tetrode amplifiers to drive the cavities simultaneously. The driven power is 180 degrees out of phase, and each amplifier was designed to deliver 75 kW RF power to the resonators. In practice, it was found that the driven power is beyond necessary, and only 80 kW RF power is required for the beam. Hence, an upgrade of the existing RF-driven system to the stare-of-art of solid-state technology is put forward by the CIAE cyclotron team. Furthermore, this alternative design also includes an optimization of the coupling between amplifiers and the cavities since the old coupler shows nonidealities under long-term high-power operations. A driven schema utilizing multiple low-power capacitive couplers is designed to address this issue, taking advantage of the cavity as a power combiner. In this paper, a review of the existing RF-driven system will be given first. It will be followed by an analysis of the limitation of such a system in practice. A new design of the solid amplifier, the new driven method, and a capacitive window will also be reported.

INTRODUCTION

Proton cancer therapy has been increasingly adopted in China's domestic medical activities. To address cancer, a growing threat to Chinese public health, a superconducting cyclotron, namely CYCIAE-230, has been developed and commissioned by the China Institute of Atomic Energy in the last serval years [1] under the support of the program of proton therapy and space science launched by China National Nuclear Corporation (CNNC).

This superconducting cyclotron uses Ni-Ti alloy in liquid hilum temperature to generate about 3 Tesla magnet fields [2] to constrain the proton and uses second harmonics RF field to accelerate it from several electron voltages to 242.6 MeV. In total, before extraction, the particle is accelerated about 5,300 times, eight times per turn. The diameter of the magnet pole is ~890 mm, while the weight is about 90 tons.

The RF system of CYCIAE230 consists of a set of resonators, two independent 75 kW amplifiers, and one set of LLRF control [3]. The resonators are two capacitive coupled similar coaxial cavities.

Each cavity shares the same resonance parameters, such as identical capacitance, inductance, and shunt impedance. Two identically designed cavities are electromagnetically joined together by the distributed capacitance in the central region. The system resonance frequency can be determined as formula below.

$$\begin{cases} Y_{AB} = \dfrac{1}{R_1} + j\left(\omega C_{11} - \dfrac{1}{\omega C L_1}\right) + \dfrac{\omega^2 C_{12}^2}{\dfrac{1}{R_2} + j\left(\omega C_{22} - \dfrac{1}{\omega C L_2}\right)} \\ C_{11} = C_{12} + C_1 \\ C_{22} = C_{12} + C_2 \end{cases}$$

R_1, L_1, C_1, R_2, L_2, and C_2 are parallel impedance, distributed inductance, and capacitance of the two Dees, respectively. C_{12} is the coupling capacitance between the two groups. In an ideal condition, let the two cavities be the same, e.g., $R_1 = R_2$, $C_1 = C_2$, and $L_1 = L_2$; the resonators have the same resonance frequency, ω_0. And, let the coupling coefficient be defined as $K = \frac{C_{12}}{\sqrt{C_{11}C_{22}}}$ The resonant frequency can be solved as,

$$\omega^2 = \frac{(1 \pm K)}{(1+K)(1-K)}\omega_0^2$$

this gives two resonance frequencies:

$$\begin{cases} \omega_l = \dfrac{1}{\sqrt{1+K}}\omega_0 \\ \omega_u = \dfrac{1}{\sqrt{1-K}}\omega_0 \end{cases}$$

The π resonance mode, ω_l , is selected as the operation mode for beam acceleration for cyclotron CYCIAE230, which is the 2nd harmonic particle cyclotron frequency. A push-pull driven method is chosen to roll out the resonance at ω_u.

CHARACTER OF EXISTING RF SYSTEM

Two groups of resonators are involved in the π mode beam acceleration, each of which has an independent power coupler. These two couplers are used simultaneously and are driven by two separated 75 kW tetrode amplifiers in a push-pull configuration. By applying RF power with 180 degrees out-of-phase, the simulated mode of the cavities group can be simplified, as shown in Fig. 1.

The measurement setup is shown in Fig. 1a. The drive RF is taken from network analyzer port-1 and is divided using a push-pull power divider to drive through the identical-length rigid transmission to the two couplers. A cavity

† zhiguoyin@ciae.ac.cn

ISBN: 978-3-95450-212-7 ISSN: 2673-5482 doi:10.18429/JACoW-CYCLOTRONS2022-WEPO017

pickup is connected with network analyzer port 2. In this way, the cavities response is measured at low power; the result is shown in Fig. 1b. It can be easily found that no extra resonance mode can be stimulated with this driven method other than the π resonance mode. Compared to the single coupler/one amplifier-driven approach, parasitics [3] can be greatly limited.

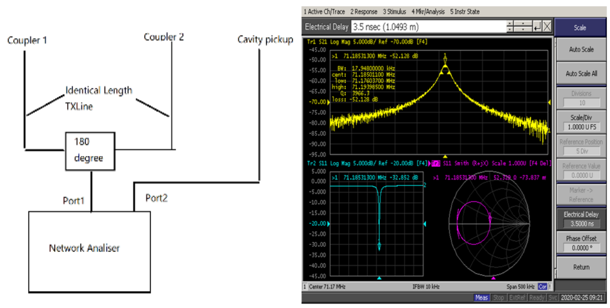

Figure 1: Resonator transfer function measurement, a) test setup, b) network analyser results.

The driven amplifiers in the beam tuning phase are two tetrode-based designed systems. It was designed to provide 150 kW RF-driven power to the cavities in total. However, in practice, the cavities only need 80 kW to establish the required acceleration voltage. The power reservation, in this case, is too much. The polarization and the typical runtime parameters of the final stage amplifier tube 4CW100,000E are tabulated in Table 1. It's easy to find out that, for the amplifier system, the drawback of this scenario is that the power efficiency is lower than expected. This is one reason to design a new RF-driven system for the RF of the CYCIAE230 cyclotron.

Table 1: Parameters of the Tetrode FPA

Item	Value	Unit
Anode Potential	13.5	kV
Screen Potential	900	V
Grid Potential	-280	V
Anode DC Current	5.5	A
Driven Power	1.5	kW
Output power	40	kW
Power efficiency	70	%
Anode dissipation	13	kW

The driven stage amplifier is a solid-state design capable of delivering 4 kW RF in CW mode. The RF window and the FPA transmission line are two 4’½ rigid lines about 30 m long. An amplitude and phase adjusting device is included at a low power level to drive the two amplifiers simultaneously. The FPA and the power supply are shown in Fig. 2.

The existing RF windows broke several times during the beam commissioning phase. The couplings of the two resonators are independent of two loops. Both of them are located at the bottom of magnet valley. The ceramic vacuum sealing is about 1/4 lambda away from the loop, outside the return yoke beneath the cyclotron. The stationary leaking magnet filed is in orders of several kilo gauss.

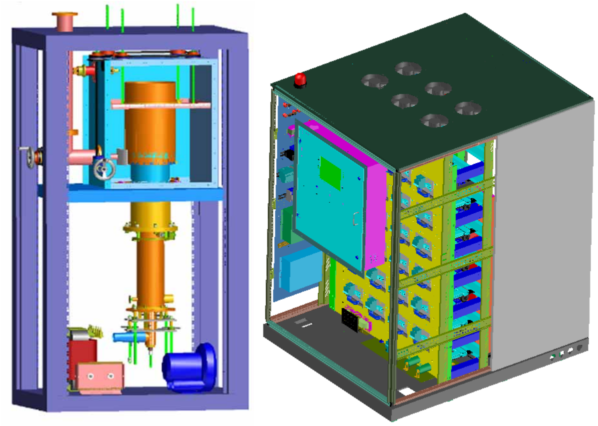

Figure 2: 75 kW Tetrode Amplifier, a) FPA, b) power supply.

In the beginning, the vacuum at the ceramic window is not ideal, which leads to a material sputtering on the ceramic. According to the analysis, the discharge on the ceramic is a two-stage process. In the beginning, it was the electron bombardment, the discoloring on the ceramic is gray. Without interference, it will develop into the second stage, the plasma discharge, which is fatal for the ceramic, as shown in Fig. 3a. The issue is solved by increasing the vacuum level around the ceramic and removing the outgassing item (when exposed to the electron cloud).

However, the ceramic window still breaks sometimes. This time, instead of sputtering copper on the ceramic, which creates a short circuit in the insulator, the vacuum seal fails, as shown in Figs. 3b and 3c. As analyzed previously, in stage one, the field-emitted electrons' trajectory is controlled by the RF e-field and the leaking magnet field. It is believed that is the reason for uneven burn marks on the ceramics. To address this issue, we added a magnetic field near the ceramic insulator to manipulate the movement of the electrons. Fig. 3b was an unsuccessful trial to modulate the geometry of the ceramic insulator. With the magnet field corrector, it still brokes. The TiN coating on the surface of this unsuccessful trial also indicates that the electrons are not initially from the ceramic itself.

With these improvements above, the mean time between coupling windows significantly increased. However, the ceramic still breaks from time to time occasionally. Most of them happen when there is significant sparking inside the cyclotron dee system, e.g., when finger contact of the rear part of the Dee is burned. It is believed that two issues can not be further improved with the current loop antenna design. One of them is that the loop cannot shield electrons from the dee plate, which traveled along the magnet line, from the Dee plate to heat the inner conductor. This will lead to secondary electrons moving along the leaking magnet field, eventually heating the ceramic insulator. The second is that the leaking magnet field greatly influences the ceramic outside the magnet field. The local magnet field line needs to be better defined. Based on these considerations, a new capacitive window is designed, as will be descript in the following section.

ISBN: 978-3-95450-212-7 ISSN: 2673-5482 doi:10.18429/JACoW-CYCLOTRONS2022-WEPO017

Figure 3: Ceramic insulator failure, a) material sputtering, b) geometry changed, c)without magnet field, with disk-type ceramic.

DESIGN OF NEW DRIVEN SYSTEM

As pretty standard in RF combiner design, the coupling coefficiency of each port to the combined port follows:

$$C_{1N} = 10 \log \frac{1}{|S_{21}|^2} = 10 \log N \cdots (N \neq 1)$$

where, N is the port number of the combiner. In the CYCIAE230 cavity case, each resonator is either capacitive coupled inside the cyclotron or is directly connected. Therefore, it can be easily seen that this coupling is acting like a port in the combiner's case. So, the coupling coefficiency of multiple coupling windows for the CYCIAE230 cavity is:

$$C_{1N} = 10 \log(2N) \cdots (N \neq 1)$$

where, N is the number of coupling windows. N is equal to two in the existing RF system of the CYCIAE230 cyclotron. Hence, if measured directly using a network analyzer, the S_{11} is -6 db. Later, if desired, four coupling windows are used in the new system. The S_{11} is expected to be -9 db.

A new solid-state RF amplifier was built to replace existing tetrode amplifiers with higher configuration flexibility. The configuration of the solid-state amplifier is four identical cabinets, each of which can provide 30 kW of RF driven with a 4'½ line output. This can be used directly in the case of four resonator couplers. If only two couplers exist, two power combiners will be added to adapt to the existing RF-driven method.

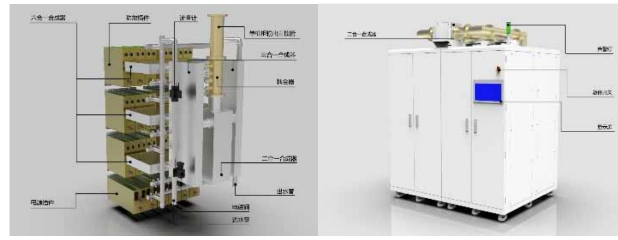

Figure 4: 60 kW Solid-state Amplifier Module, a) 30 kW SSA module, b) 60 kW SSA.

Each 60 kW solid-state amplifier consists of two 30 kW modules. The internal view of each 30 kW module is shown in Fig. 4a. And the output power is combined at the top of the cabinet, as shown in Fig. 4b. The amplification unit is made of Ampleon power LDMOS transistor ART2K0FE, and each unit can provide 1500 kW RF output and is protected with a 2 kW circulator module. The output RF power is combined using a 1 to 6 combiner, then combined with a 1 to 3 combiner, followed by a 1 to 2 combiner. Therefore, 36 modules are integrated to get 30 kW output with a comfortable redundancy.

Multiple new disc-type ceramic windows and capacitive couplers are planned to be manufactured in early 2023. These new couplers will be installed inside several valleys of the cyclotron, where well-defined magnetic lines are expected to constrain field-emitted electrons, preventing the spark from developing into the second stage. Since this installation location is near the main cyclotron chamber, a better vacuum level is expected too. One capacitive coupler, two capacitive couplers, or four capacitive couplers configurations will be tested with the new solid-state RF amplifiers to determine which is the best choice for the driven method of the CYCIAE230 cyclotron RF system. The stretch of the new coupler is shown in Fig. 5.

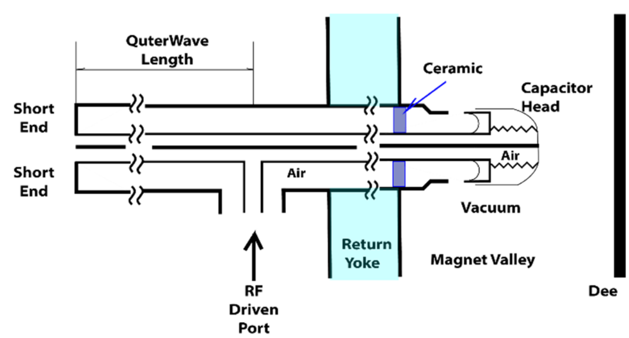

Figure 5: A sketch of the capacitive coupler with disk ceramic insulator.

CONCLUSION

An analysis toward improving the CYCIAE230 RF driven system has been put forward. The new amplifer as well as the new coupling window are planed to be build in year 2023. A test will be carried on to verify the new driven method of this cyclotron RF system.

ISBN: 978-3-95450-212-7 ISSN: 2673-5482 doi:10.18429/JACoW-CYCLOTRONS2022-WEPO017

REFERENCES

[1] T. J. Zhang *et. al.*, "Developments for 230 MeV superconducting cyclotrons for proton therapy and proton irradiation," *Nucl. Instrum. Methods Phys. Res. Sect. B*, vol. 406, part A, pp. 244-249, Sep. 2017. doi:10.1016.j-nimb.2016.11.010

[2] M. Li *et al.*, "Field Mapping System Design for the Superconducting Cyclotron CYCIAE-230," *IEEE Trans. Appl. Supercond.*, vol. 28, no. 3, pp. 1-4, April 2018. doi:10.1109/TASC.2018.2789447

[3] Z. G. Yin *et.al.*, "Design of RF system for CYCIAE-230 superconducting cyclotron," *Nucl. Instrum. Methods Phys. Res. Sect. A*, vol. 854, pp. 25-30, May 2017. doi:10.1016/j-nima.2017.02.051

23rd Int. Conf. Cyclotrons Appl. CYCLOTRONS2022, Beijing, China JACoW Publishing
ISBN: 978-3-95450-212-7 ISSN: 2673-5482 doi:10.18429/JACoW-CYCLOTRONS2022-WEPO018

PROGRESS IN THE DESIGN OF A NEW 150-MHz FLAT TOP CAVITY FOR THE PSI RING CYCLOTRON

J.-Y. Raguin*, M. Bopp, R. Fortunati, J. Grillenberger, T. G. Lucas, M. Pedrozzi, M. Schneider, M. Stoll, Paul Scherrer Institut, 5232 Villigen PSI, Switzerland
E. Solodko, Transmutex SA, 1214 Vernier, Switzerland

Abstract

Increasing PSI's 590-MeV main cyclotron beam current to 3 mA requires the replacement of the existing power-limited 150-MHz flat top cavity with a new cavity. This new cavity has been designed to withstand a 700-kV peak voltage and a 140-kW dissipated average power. Although very similar in its geometry to the original flat top cavity currently in operation, in the new design, special attention has been paid to the shaping of the four electrodes for maximizing the shunt impedance. Furthermore, the topology of the cooling water channels has been optimized to increase the power handling capabilities of the cavity. Finally, in order to mitigate multipacting observed in the current design, variations on the new cavity baseline geometry have started to be explored.

INTRODUCTION

The PSI High Intensity Proton Accelerator (HIPA) facility consists primarily of the 72-MeV injector cyclotron (Injector II) and the 590-MeV Ring cyclotron. The Injector II cyclotron is currently being upgraded through the installation of new 50-MHz aluminum cavities designed to withstand a peak voltage of 400 kV and an average dissipated power of 50 kW [1]. The Ring cyclotron has been progressively upgraded with four new copper 50-MHz cavities capable of generating a 1-MV peak voltage and able to dissipate an average power of 500 kW [2]. However, the 150-MHz flat top cavity is currently the limiting feature of the Ring cyclotron [3].

For a 3-mA beam current, each 50-MHz main cavity of the Ring cyclotron requires a peak accelerating voltage of 910 kV. The required peak voltage of the 150-MHz flat top cavity would then be 640 kV [4]. Adding some reserve, the new cavity is being designed for a maximum peak voltage of 700 kV.

RF DESIGN STUDIES

Since the existing mechanical constraints severely limit deviations from the current geometry, the new cavity RF studies performed with the 3D electromagnetic code ANSYS HFSS [5] mainly focused on optimizing the electrodes that protrude into the cavity. Several cavities without RF coupler were designed with electrodes thickness of 45 mm, 55 mm and 65 mm and with a horizontal gap between electrodes ranging from 140 mm to 250 mm, this later distance being considered as maximum to reduce field leakage. The virtual tuning to reach the design frequency of 151.8984 MHz in each of these cavities was done by adjusting the cavity height (along the Z-axis in Fig. 1). The inner maximum length, the inner width and the length of the four electrodes, which are 2700 mm, 200 mm and 2585 mm, respectively, have been kept the same as in the actual cavity. The minimum vertical distance between the electrodes is also the same and is 30 mm. Figure 1 shows one-half of the vacuum volume of the new cavity.

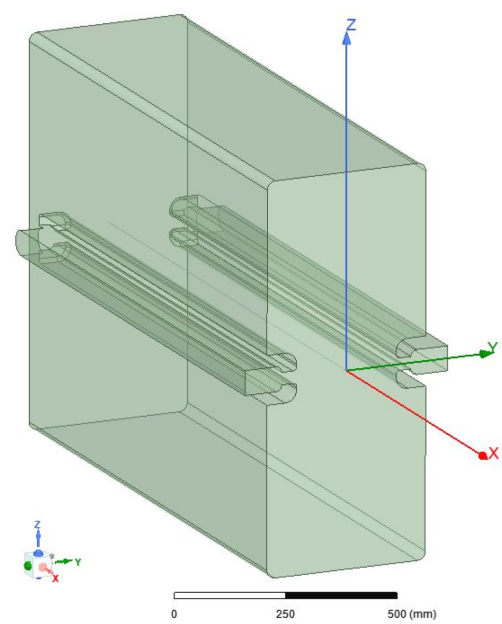

Figure 1: Vacuum volume of the new flat top cavity - One-half shown.

A substantial modification of the cavity consisted in shaping the electrodes to increase the peak shunt impedance R_{sh} ($R_{sh} = V_g^2/P_d$ where $V_g = \int | E_y(0, y, 0) | dy$ is the peak gap voltage and P_d is the power dissipated on the total inner surface). Whereas the tip of the electrodes in the actual cavity is characterized by the single radius 22.5 mm, leading to a maximum electrodes thickness of 45 mm, in the new cavity, the curvature radius closest to the beam plane (XY plane in Fig. 1) was decreased to 10 mm. Such a radius reduction leads to an increase of the shunt impedance. The maximum surface electric field also increases but still stays well below the Kilpatrick limit.

The results of the parametric studies done by varying the horizontal gap between electrodes and the electrode thickness Δz_{elec} are illustrated by Fig. 2. For an aluminum conductivity of 34 MS/m, a peak gap voltage maintained to 700 kV and a gap between electrodes increasing from

* jean-yves.raguin@psi.ch

ISBN: 978-3-95450-212-7 ISSN: 2673-5482 doi:10.18429/JACoW-CYCLOTRONS2022-WEPO018

140 mm to 250 mm, the total dissipated power decreases from about 220 kW to about 130 kW. Moreover, thickening the electrodes leads to an increase of the dissipated power, the effect being clearly more pronounced when the distance between electrodes decreases.

A similar trend is observed when computing the dissipated power per electrode (also Fig. 2). For the same variation of distance between electrodes, the dissipated power per electrode decreases from about 13 kW to about 4 kW, a clear consequence of the reduction of the electrodes' surfaces.

These considerations lead to the adoption of an inner volume baseline geometry where the horizontal inter-electrode distance is 250 mm and the thickness of the electrodes is 45 mm.

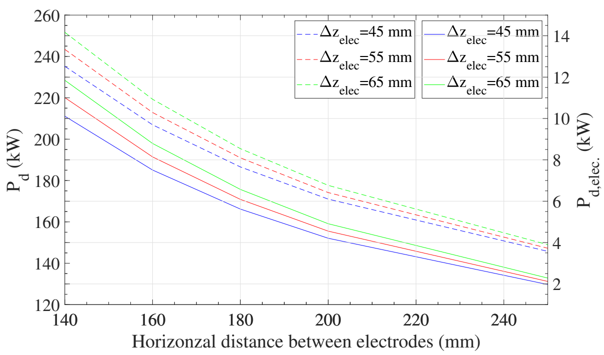

Figure 2: Cavity dissipated power P_d (——) and dissipated power per electrode $P_{d,elec.}$ (- - -) vs. horizontal distance between electrodes and electrode thickness Δz_{elec}.

MECHANICAL DESIGN

The goal of the mechanical design is to define a mechanical structure with a cooling channel system able to keep a relatively low and homogeneous temperature and, consequently, a reasonable deformation of the cavity body to minimize the required range of the tuning system. Within the ANSYS platform Workbench [6], a two-stage approach has to be used:

- One-way analysis defining the temperature distribution and the corresponding structural deformation (HFSS → Steady State Thermal → Static Structural).
- Feedback analysis to evaluate the impact of the deformation on the frequency using the results from the first stage as an input for another iteration of HFSS.

Due to the asymmetry of the mechanical structure of the cavity, the full internal volume (cavity and adjacent vacuum chamber) was simulated with HFSS.

In HFSS, the power dissipated on the outer surface of the vacuum volume has been retrieved. As it is the same surface as the internal surface of the cavity body, results could be imported as Heat Flux (W/m^2) in the ANSYS Steady State Thermal module. Figure 3 shows this imported heat flux map. Note that to simplify the simulations the region of the cavity where the coupler is located (middle of the cavity's top) has been closed by the same material than the rest of the body. A dedicated study with the RF coupler shall be done at a latter stage.

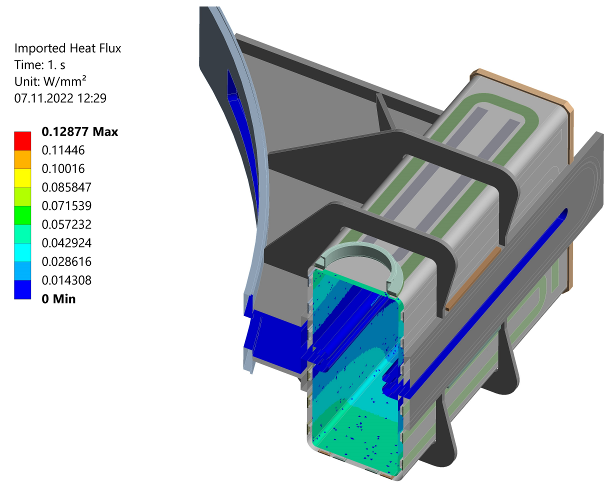

Figure 3: Imported heat flux on the new flat top cavity surface including the adjacent vacuum chamber.

The convection heat transfer coefficient for the forced convection derives from the Dittus-Boelter equation [7] and is 4986 W/(m^{2}K). The water velocity inside the cooling channels (10 mm × 40 mm) is set to 1.2 m/s. This value derived from considerations about possible cavitation and consequently corrosion problems. Higher values of velocity, up to 1.5 m/s, could be considered but do not significantly decrease the temperature. The ambient temperature value is 26 °C and is the temperature inside the HIPA bunker. Air convection coefficient is also considered in the setup and is 10 W/(m^{2}K). The calculated temperature distribution in the flat top cavity body, represented in Fig. 4, has a maximum temperature of 70 °C.

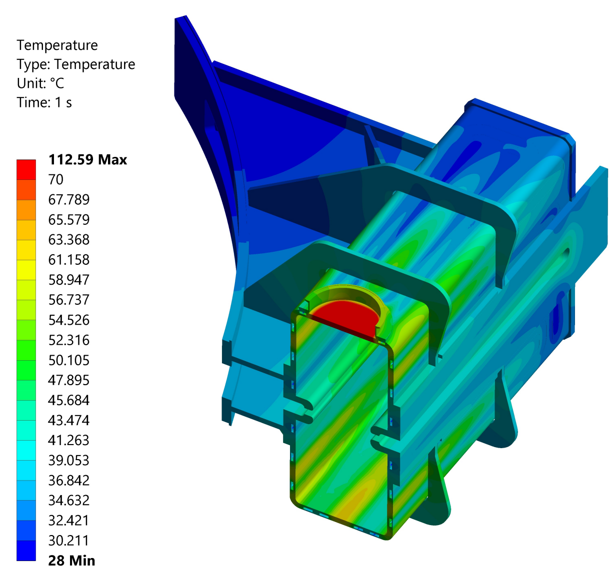

Figure 4: Temperature distribution in the body of the new flat top cavity.

ISBN: 978-3-95450-212-7 ISSN: 2673-5482 doi:10.18429/JACoW-CYCLOTRONS2022-WEPO018

The cooling water temperature varies from 28 °C to 39 °C which gives a temperature difference of 11 °C. These values are acceptable for the existing PSI cooling scheme.

The loads in the ANSYS Static Structural analysis are applied in three steps and represent the real sequence of the cavity setup cycle. They are: pumping out of air inside of the cavity (applying an external pressure of 1 bar), installation of the inflatable gasket from the flat side of the flange (applying a pressure of 1.7 bar) and heating up the cavity (importing the temperature distribution from the Steady State Thermal).

Figure 5 represents the results after the last step. The magnitude of the resulting deformation reaches a maximum of 1.29 mm. Currently in progress, the second step of the mechanical design where the feedback of the structural deformation is included should answer the question of the tuning range.

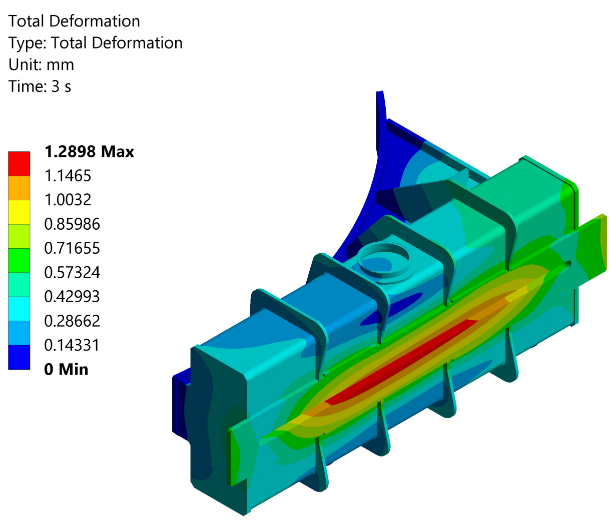

Figure 5: Total deformation of the new flat top cavity.

MULTIPACTING STUDIES

Probe measurements from the current flat top cavity have illustrated that there appears to be multipacting occuring on the original cavity back wall (see cavity back plane discoloration in Fig. 6). Using the Particle-in-Cell (PIC) solver from CST Studio's Suite [8], multipacting simulations were performed. It was possible to obtain similar crescent-shaped electron distributions when without the presence of the cyclotron static magnetic field maps (see Fig. 7). These simulations involve coupling the electromagnetic field maps generated by CST's eigenmode solver to the PIC solver. The cavity surfaces within the PIC solver settings were assigned a secondary emission yield curve of copper and aluminium, the values of which were taken from [9]. The source location of the electrons being unknown, an homogeneous electron distribution was assumed throughout a volume closed to the cavity back wall and comprising the electrodes' ends.

Applying identical settings, simulations were run for the new baseline geometry and for different electrode shapes. It was found that these crescent-shaped electron distributions were inherent to the cavity design even as the new cavity does not have the original cavity triangular-shaped reinforcements (see Fig. 6). Geometric changes of the back wall in the vicinity of the electrodes' ends and of horizontal middle cavity plane are being explored in order to remove the potential well which traps the particles between the four electrodes and the back wall.

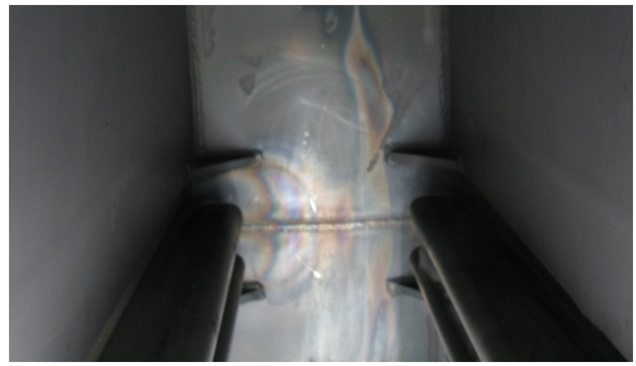

Figure 6: Back plane of the original cavity.

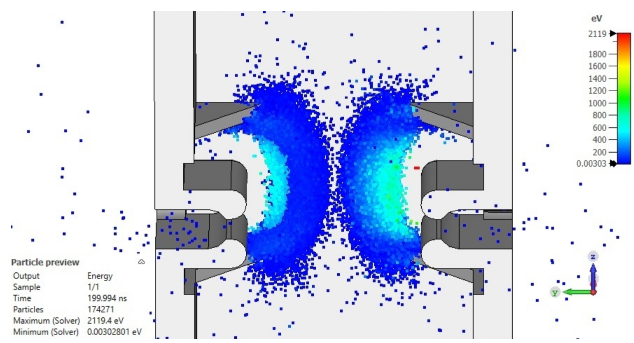

Figure 7: Multipacting simulations of the original cavity assuming copper material.

CONCLUSION

Designed to withstand a peak voltage of 700 kV and an average power of 140 kW, the RF design studies of the new 150-MHz flat top cavity show that adopting a horizontal distance between the electrodes of 250 mm and a maximum electrode thickness of 45 mm minimizes the required cavity dissipated power. Moreover, the modest dissipated power per electrode indicates that dedicated electrode cooling channels are not required. This new cooling channel system designed and simulated with ANSYS is such that the maximum cavity body does not exceed 70 °C. A one-way ANSYS Static Structural analysis of the cavity shows that the maximum structural deformation is less than 1.5 mm and self-consistent simulations are in progress. PIC CST Studio Suite multipacting studies have also been initiated by modifying the cavity back wall close to the electrodes' end.

ISBN: 978-3-95450-212-7 ISSN: 2673-5482 doi:10.18429/JACoW-CYCLOTRONS2022-WEPO018

REFERENCES

[1] L. Stingelin, M. Bopp, and H. Fitze, "Development of the new 50 MHz resonators for the PSI Injector II cyclotron", in *Proc. 18th Int. Conf. on Cyclotrons and their Applications (Cyclotrons'07)*, Giardini-Naxos, Italy, Oct. 2007, pp. 467-469.

[2] H. Fitze, M. Bopp, and H. Frei, "Development of a new high power cavity for the 590 MeV ring cyclotron at PSI", in *Proc. 1999 Particle Accelerator Conf. (PAC'99)*, New York, NY, USA, Mar.-Apr. 1999, paper MOP58, pp. 795-797.

[3] N. J. Pogue, L. Stingelin, and A. Adelmann, "Analysis and supression of RF radiation from the PSI 590 MeV cyclotron flat top cavity", *Nucl. Instrum. Methods Phys. Res. A*, vol. 828, pp. 156-162, 2016, doi:10.1016/j.nima.2016.05.026

[4] M. Bopp, H. Fitze, P. Sigg, and L. Stingelin, "Upgrade concepts of the PSI accelerator RF systems for a projected 3 mA operation", in *Proc. 16th Int. Conf. on Cyclotrons and their Applications (Cyclotrons'01)*, East Lansing, MI, USA, May 2001, paper P4-21, pp. 300-302.

[5] ANSYS HFSS, https://www.ansys.com/products/electronics/ansys-hfss

[6] ANSYS Workbench, https://www.ansys.com/products/ansys-workbench

[7] P. W. Dittus and L. M. Boelter, "Heat transfer in automobile radiators of the tubular type", *University of California Publications in Engineering*, vol. 2, no. 13, pp. 443-461, 1930. Reprinted in *Int. Comm. Heat Mass Transfer*, vol. 12, pp. 3-22, 1985.

[8] CST Studio Suite, https://www.3ds.com/products-services/simulia/products/cst-studio-suite

[9] V. Baglin *et al.*, "The secondary electron yield of technical materials and its variation with surface treatments", in *Proc. 7th European Particle Accelerator Conf. (EPAC'00)*, Vienna, Austria, Jun. 2000, paper THXF102, pp. 217-221.

ISBN: 978-3-95450-212-7 ISSN: 2673-5482 doi:10.18429/JACoW-CYCLOTRONS2022-THAI01

RECENT PROGRESS OF RESEARCH AND DEVELOPMENT FOR THE COST-EFFECTIVE, ENERGY-EFFICIENT PROTON ACCELERATOR CYCIAE-2000*

Tianjue Zhang†, Wei Fu, Chuan Wang, Shilun Pei, Zhiguo Yin, Hongji Zhou, Ziye Yin, Hao Le, Suping Zhang, Jingyuan Liu, Xiaofeng Zhu, Fei Wang, Yang Wang, Hongru Cai, Gaofeng Pan, Xianlu Jia, Zhaojun Jin, Xueer Mu, Jun Lin, Bohan Zhao, Aolai He, Zhichao Chu, Mingzhi Hu, Qiqi Song, and the Cyclotron Team at CIAE

China Institute of Atomic Energy, Beijing 102413, P R China

Abstract

The MW class proton accelerators are expected to play important roles in many fields, attracting institutions to continue research and tackle key problems. The continuous wave (CW) isochronous accelerator obtains a high-power beam with higher energy efficiency, which is very attractive to many applications. Scholars generally believe that the energy limitation of the isochronous cyclotron is ~1 GeV. Enhancing the beam focusing becomes the most crucial issue for the isochronous machine to get higher beam power.

Adjusting the radial gradient of the average magnetic field makes the field distribution match the isochronism. When we adjust the radial gradient of the peak field, the first-order gradient is equivalent to the quadrupole field, the second-order, the hexapole field, and so on. Just like the synchrotron, there are quadrupoles, hexapole magnets, and so on, along the orbits to get higher energy, as all we know.

If we adjust the radial gradient for the peak field of an FFA's FDF lattice and cooperate with the angular width (azimuth flutter) and spiral angle (edge focusing) of the traditional cyclotron pole, we can manipulate the working path in the tune diagram very flexibly. During enhancing the axial focusing, both the beam intensity and the energy of the isochronous accelerator are significantly increased. And a 2 GeV CW FFA with 3 mA of average beam intensity is designed. It is essentially an isochronous cyclotron, although we use 10 folders of FDF lattices. The key difficulty is that the magnetic field and each order of gradient should be accurately adjusted in a large radius range.

As a high-power proton accelerator with high energy efficiency, we adopt high-temperature superconducting (HTS) technology for the magnets. 15 RF cavities with a Q value of 90000 provide energy gain per turn of ~15 MeV to ensure the CW beam intensity reaches 3 mA. A 1:4 scale, 15-ton HTS magnet, and a 1:4 scale, 177 MHz cavity, have been completed. The results of such R&D will also be presented in this paper.

INTRODUCTION

High energy and high current proton accelerators are widely and importantly applied in frontier research fields such as nuclear physics and particle physics, national economic fields such as public health and advanced energy, and even national security [1, 2]. A Proton accelerator with an average beam power of 5-10 MW has been the world's dream machine for more than 30 years [3, 4]. LINAC is considered to be the most promising, and high-energy CW superconducting LINAC is still under development so far [5]. On the other hand, a serious limitation of CW cyclotrons is the maximum energy achievable, which for protons is about 1 GeV for isochronous operation, due to relativistic effects [6, 7]. A 2 GeV CW FFA (or it can be called an alternating gradient cyclotron) has been investigated since 2013 at CIAE, and more detailed R&D activities have been conducted in recent years. The design goal is to provide a 6 MW proton beam with higher energy efficiency than LINAC. It is expected to be up to 30% with overall energy efficiency and keep the cyclotron's advantages of being cost effective for construction and operation.

GENERAL CONSIDERATIONS IN THE OVERALL DESIGN OF 2 GEV CW FFA

Basic Description and Progress of Overall Design since 2019

The 2 GeV FFA facility, CYCIAE-2000, consists of three stages: a 100 MeV isochronous cyclotron as a pre-injector, an 800 MeV isochronous cyclotron as an injector, and the main machine of 2 GeV CW FFA, which are shown in Fig. 1. Compared with the design scheme published in 2019, the main progress is summarized as follows.

FDF field distribution In the previous study [8], the working path in the tune diagram which crosses the resonance of νr=3 asks to control the third harmonics B3 at about 1 Gs level. This is particularly challenging for magnet construction. Two more possible solutions to the working path were studied and will be described in the following sections of this paper. Instead of the tremendous amount of tentative numerical calculations by adjusting the magnetic field intensity, angular width, and spiral angle of the 10-fold F and D magnets, along the radius, the third-order peak field distribution of F and D magnets, was analysed into zero-order (dipole, traditional cyclotron sector field), first-order (quadrupole), second-order (hexapole), and third-order (octupole) radial gradients of the peak magnetic field. This method of accurately adjusting the radial gradients of the peak magnetic field, assisted by traditional

* This work was supported in part by the National Natural Science Foundation of China under Grant 12135020 and the basic research fund from the Ministry of Finance of China under Grant BRF201901.
† 13641305756@139.com

edge focusing means, makes it easier, more flexible, and more convenient to build the required working path in the tune diagram.

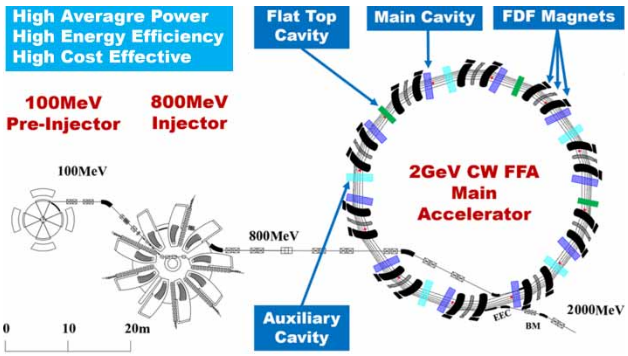

Figure 1: Layout of 2 GeV CW FFA accelerator complex.

Several issues of injection, extraction, current limitation and related RF in the overall design Compared with the 2019 design, the injection from the 800 MeV cyclotron into the 2 GeV main machine is also improved, as shown in Fig. 1. Based on the preliminarily matching by TRACE3D, except the longitudinal matching of the bunch and the buncher design. The extractions by various methods are also investigated. Considering that turn separation is the rigid demand for high current beam extraction, five RF cavities are added to the original design of 10 RF cavities so that the energy gain per turn is up to 15 MeV. Thereby, the turn separation is increased from 10 mm to 15 mm, and the turn separation can be further increased to about 30 mm by precession. This is also conducive to ensuring a high intensity of the circulating beam. From the PSI's experience, the beam intensity, dominated by the space charge, is proportional to the third power of the energy gain per turn [9]. The current limit of this 2 GeV machine can also be estimated by using the method proposed by Dr. Baartman in 2013 for separated turn cyclotrons [10]:

$$I_{max} = \frac{h}{2g_r\xi^3\beta^3\gamma\nu_x^4}\frac{V_{rf}^3}{V_m^2 Z_0} \approx 5.3\,\text{mA} \qquad (1)$$

The beam intensity of ~5 mA for 10 MeV and more than 10 mA for 15 MeV energy gain per turn. Such a high current limitation is also due to the big transverse acceptance of FFA. It is conservatively estimated to be 3 mA/6 MW for this overall design. It can be seen that the design will enable the 2 GeV FFA machine to have a potential to hit the ultimate aim of 10 MW average beam power.

In this configuration, we still have five valleys with enough space, one for injection/extraction and the rest for flattop cavities. The multi-particle simulation shows that the flattop cavities can effectively reduce the radial size of the bunch. In case of the worst case, the expectation of this high-power machine operation is assuming two RF systems fail. Our solution is to improve the Q value of each main RF cavity in the design stage. Then we should be able to increase the acceleration voltage of each RF cavity by 20% to maintain the 15 MeV energy gain per turn. At present, we have completed the 1:4 scale RF cavity test, and the test result of the Q value encourages this idea.

The vertical tune shift for space charge dominated beam is well-known [11] and can be derived into a more convenient form for isochronous cyclotrons [12]:

$$\Delta(\nu_{\square}^{2}) = -\frac{4}{\beta\gamma^3}\cdot\frac{I}{I_0}\cdot\frac{R_\infty}{b(a+b)} \qquad (2)$$

Taking into account the relativistic effects of the high energy beam, γ^3 has been added to the denominator. The tune shift results of the space charge effect for 3 mA and 6 mA CW beams, respectively, are shown in Fig. 2. It should be clarified that the vertical tune in Fig. 2 is different from the one we proposed in 2019 and the radial tune avoids the νr=3 resonance. For the 6 mA beam, we can find that the tune shift by space charge is 0.1 in 800 MeV and 0.025 near the extraction region specifically. It demonstrates again that the 3 mA/6 MW is a confident design.

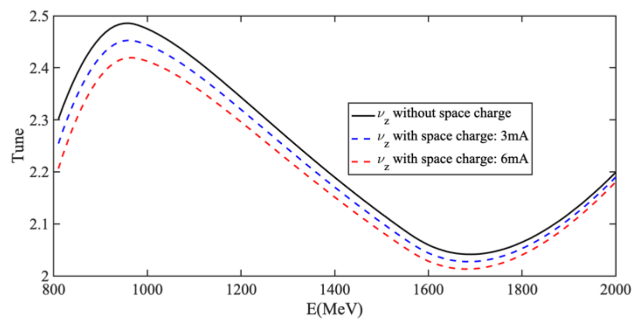

Figure 2: The vertical tune shift of 3 mA and 6 mA CW beams.

The Fermilab researcher reported the energy efficiencies of the three operational accelerators with the highest beam power in the world [13]. The energy efficiency of the PSI isochronous cyclotron is about 3 times of the other types. The isochronous accelerator is an excellent technical route to develop high average beam power, high power efficiency, and high cost-effective proton machine. It can be estimated optimistically that the energy efficiency of a 2 GeV CW FFA with 3 mA of average beam intensity can be increased from PSI's ~20% to 30% if a high-temperature superconducting magnet is used to replace the room temperature magnet at PSI, and an RF cavity with a Q value of 90000 to replace the 45000 cavities at PSI. 1:4 scale equipment: high-temperature superconducting magnet based on YBCO tape and high Q RF cavity have been processed and measured to verify the feasibility of the design, which will also be presented in this paper.

Realization Strong Focusing with Adjustment of Magnetic Field Gradients in Wide Radial Range

Synchrotrons work by rapidly and synchronously adjusting the RF frequency and the magnetic field to match the relativistic effect of the accelerated beam. In a synchrotron, the particle orbits are fixed within a small radial range, and the tune is easily controlled so that the energy can reach higher levels than in a cyclotron. It is comfortable to arrange quadrupole, hexapole, and octupole magnets along the orbit, obtain strong focusing, adjust the working path

ISBN: 978-3-95450-212-7 ISSN: 2673-5482 doi:10.18429/JACoW-CYCLOTRONS2022-THAI01

in the tune diagram flexibly, traverse various resonances, and get a high energy acceleration ultimately.

Besides the bending effect, the main magnets of CYCIAE-2000 provides an additional focusing effect by adjusting the radial gradient, which is equivalent to the quadrupole, hexapole, and octupole magnets particularly used in the synchrotron. Introducing the first-order, second-order, and third-order gradients of the peak magnetic field in a wide radial range provides strong focusing and an approach to realizing chromaticity compensation. Most importantly, modulating the magnetic field gradient in a wide radial range provides a means to modulate the tune diagram flexibly during acceleration. In CYCIAE-2000, the FDF lattice design was adopted. Each focusing and defocusing magnet has a third-order magnetic field gradient in the radial direction, which can achieve the effect of the dipole to octupole magnets, and thereby balance the isochronism and focusing. Based on this principle of adjusting gradient to provide strong focusing, we add higher-order nonlinear magnetic field components, e.g. quadrupole, hexapole, octupole, etc., at important resonance crossing, resulting in a "radial local achromatic" effect.

BEAM DYNAMICS

Resonance Study

As mentioned above, we have completed a scheme to avoid integer resonance using regulation of radial peak field, which is numbered as Scheme 2. The tune diagram which contains three possible working paths is illustrated in Fig. 3.

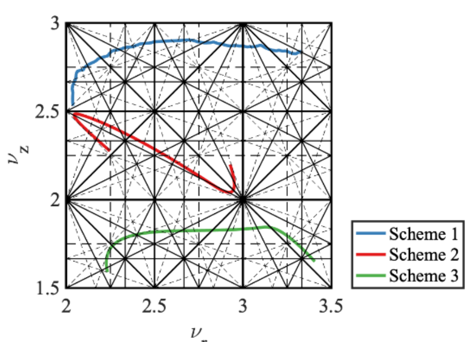

Figure 3: Tune diagram.

Resonance study is carried out especially for Scheme 2. We have summarized the crossed resonance lines for the three schemes in the Table I. This table shows that low-order resonances, such as integer resonances, are the main barriers for higher energy acceleration, especially for the CW FFA machine. Part of the numerical simulation results can be found in Ref [14]. It can be concluded that with the benefit of a strong focusing of the alternating radial gradient, the axial envelope is effectively controlled for the coupled resonances. In summary, also through the multi-particle simulation, the beam envelope does not significantly increase when considering the non-ideal magnetic field, except for the second harmonic field at some particular phases. These simulations show that the lattice structure design of Scheme 2 can tolerate a certain amount of non-ideal magnetic field components and is feasible in magnet construction.

Table 1: Summary of resonance study

Resonance	Driving term	Scheme 1 Energy	Scheme 2 Energy	Scheme 3 Energy
$\nu_r = 2$	B_2	800~850	800~900	/
$\nu_r = 3$	B_3	1640~1680	1850~2000	1690
$2\nu_r = 5$	dB_5/dr	1280	1280	1320
ν_r-ν_z=0	$d\bar{B}/dr$	1560	1120	/
ν_r+ν_z=5	dB_5/dr	1030	1640	1870
ν_r+2ν_z=7	d^2B_7/dr^2	/	1390	/
ν_r-2ν_z=-2	d^2B_2/dr^2	/	1250	/
2ν_r-ν_z =2	d^2B_2/dr^2	1230	1030	/
2ν_r+ν_z=8	d^2B_8/dr^2	/	1730	1790
3ν_r=7	d^2B_7/dr^2	1150	1160	1170
3ν_r=8	d^2B_8/dr^2	1400	1410	1420
3ν_r=10	d^2B_{10}/dr^2	2000	/	1960

To maintain the isochronism, the concept of Integer Resonance Suppressor (IRS) [15] is adopted in Scheme 3. The working path of Scheme 3 crosses the $\nu_r = 3$, and with the help of IRS, the radial beam envelope can be inhibited. In addition, Scheme 3 crosses Walkinshow resonance when the beam is almost extracted. Since energy gain per turn is relatively large, it can be verified by numerical simulation that the beam envelop grows only slightly when the amount of off-center is about 1 cm, and half envelop increases to 10 mm at the case of 3 cm off-center, which is shown in Fig. 4.

High order resonance $2\nu_r + 2\nu_z = 10$ is also under consideration. It is an inherent resonance in our machine, while the highest of magnetic field is 3rd, only small amount of driving term at extraction. A case of 0.5 Gs/m^3 is simulated, and the phase of the B_{10} field is random. Figure 4 shows that the beam envelope is growing a little due to this resonance.

Various Solutions for Extraction

The following two methods are under consideration to increase turn separation for a clean extraction. 1) Layout of long drift sections can add a large number of high-frequency cavities to maximize the energy gain; 2) Off-centering injection can produce precession at the extraction position, increasing the separation of the last turn, but integer resonance needs to be carefully considered.

Scheme 2 utilizes integer resonance for extraction, tunes the working path near the extraction area reasonably, and controls $\nu_r \approx 3$ resonance to drive radial oscillation. The isochronism is sacrificed, which leads to the stretch of beam phase width and energy dispersion increasing during extraction. The beam envelope grows during precession extraction, as shown in Fig. 5.

ISBN: 978-3-95450-212-7 ISSN: 2673-5482 doi:10.18429/JACoW-CYCLOTRONS2022-THAI01

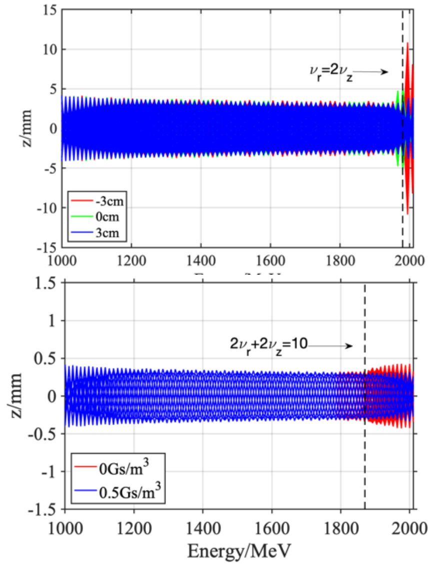

Figure 4: Vertical beam envelop of off-center beam, $\nu_r = 2\nu_z$ (up), $2\nu_r + 2\nu_z = 10$ (down).

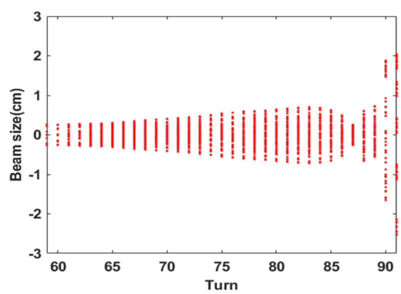

Figure 5: Radial beam envelope growth during precession extraction, scheme 2.

With the help of IRS and half-integer resonance extraction, the plan can be reconsidered in Scheme 3. Half-integer resonance extraction has a relatively mature solution in isochronous circular accelerators, and the turn separation is doubled to 25 mm, recording to Fig. 6.

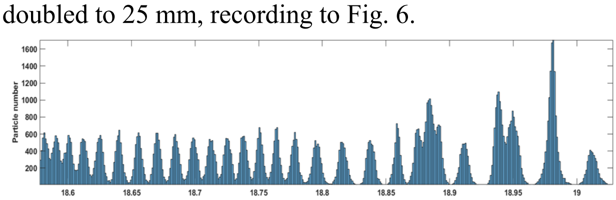

Figure 6: Particle distribution on radial probe.

Parallel Computing Results in the FFA machine

Some preliminary computation by OPAL-CYCL with AMR (adaptive mesh refinement) is undergoing in CIAE. Preliminary results with faster large-scale multi-particle simulation for Scheme 3 are presented below. The bunch's initial parameters for simulation are: transverse emittance is 2 π·mm·mrad; phase width is 3°; beam current is 3 mA/6 mA. Moreover, the transverse size of the bunch decreases to around ± 7 mm at the final turn, making it potentially appropriate for extraction. The followings are the compared results with and without the space charge effect in more detail. As compared in the first and second rows of Fig. 7, the beam quality is significantly better without a space charge, demonstrating that the space charge effect is primarily responsible for the vortex effect in the CW FFA. It is also indicated in the second row and the third row in Fig. 7 that higher beam current results in a more significant space charge effect, which increases the transverse size near ± 1 cm. Nevertheless, with higher energy gain provided by RF cavities and properly arranged extraction elements, turn separation is promisingly increased to 30 mm, which is suitable for extraction.

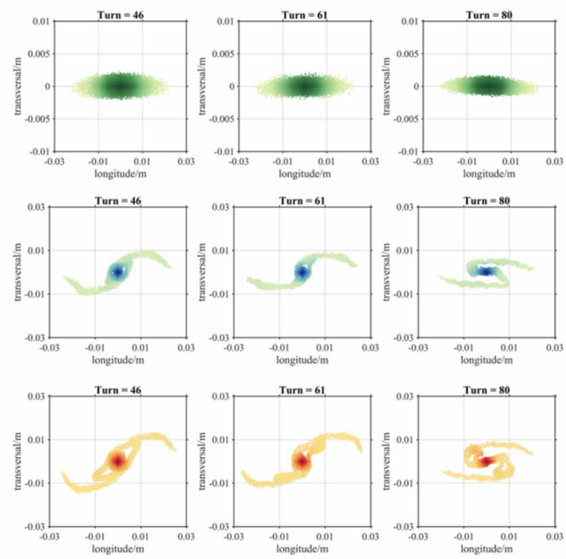

Figure 7: Longitudinal and transverse beam shape variation, from the 1st column to the 3rd column, 46, 61, 80 turns; from the 1st row to the 3rd row: 0 mA with space charge (green); 3 mA with space charge (blue-green); 6 mA with space charge (yellow).

RECENT PROGRESS IN KEY TECHNOLOGIES

Design and Verification of HTS Magnet System

Three different field maps are found for High-temperature superconducting (HTS), gap shaped magnet design. Full-scaled magnets are designed based on the FEM code. For the application of HTS in the 2 GeV FFA accelerator, third-order magnetic field matching, fringe field, and shielding current field are three major difficulties that need technological verification. An integral equation method has been developed to design gap-shaped magnets better. According to this method, final FEM models and magnetic field differences are shown in Fig. 8, which illustrates that the relative error of the mean-field can be adjusted to 2%.

Besides the theoretical analysis of full-scaled magnets, a scaled model of HTS magnets is also designed and fabricated at CIAE. The quarter scaled model is wound along the spiral angle of a full-scaled model to ensure the stress between turns is equals. Unlike LTS coils, this HTS magnet is spineless and challenging to fit the spiral angle exactly. A 3-dimensional winding machine has been developed for this type of concave coil. But in practice, we adopted f-clamps instead to avoid customization and for rapid manufacturing.

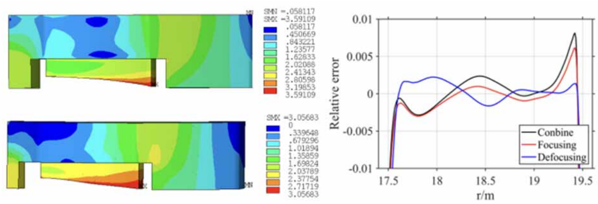

Figure 8: Magnetic field distribution map and relative deviation for the mean field.

The pancake coils and assembly are shown in Fig. 9. Since these HTS coils are no-insulated, each of the six double-pancakes will be tested in liquid nitrogen to check the insulative between turns after it has been wound. The time constant is calculated to ensure the consistency of these six double-pancakes. The HTS magnet assembly has completed the excitation test without an iron yoke. Field measurement results at 30 K show that the magnet can operate normally under the design's current value, which lays a solid foundation for the subsequent design of full-scale magnets.

As mentioned above, superconducting coils have been independently tested, and the experimental results of 6 sets of double-pancake coils show that they can work stably above 130 A. The combined coil assembly can be cooled to 25 K by cold helium gas and can run stably at the design current value of 270 A. At the same time, there is an adjustable range of 30 A. In other words, the coil assembly can be remapped to 300 A in 30 K, indicating that the winding technology of concave coils is successful and performable.

Moreover, the terminal voltage of HTS coils has been kept below 3 mV during the stability test in Fig. 10, which proves that this type of HTS magnet could be reliable in the future for FFA applications. In addition, we are planning to carry out radiative tests for this scaled magnet since the beam loss in the extraction region is inevitable, which will cause a quench of superconducting magnets.

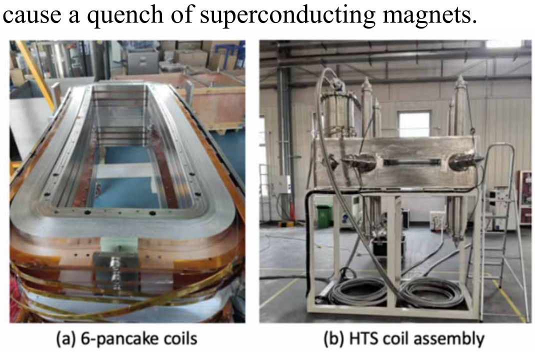

Figure 9: Schematic diagram of the installation process of the 1:4 scaled magnet and the assembly.

A 1:4 scaled gap shaped iron is also designed and fabricated, which weighs approximately 7 tons. The field distribution of the theoretical design determines the shape of the gap. A spacer is located at the head of the iron to control the shape of the deformation. Mechanical analysis indicates that the amount of deformation is about 0.07 mm, and the field deviation is at the Gs level. The field distribution is measured and compared with the analytical result. Recently, HTS coils have been assembled with gap-shaped iron magnets to prepare for excitation and field measurement, as shown in Fig. 11. Excitation is carried out for this HTS magnet assembly, and the magnet is successfully ramping to 243 A at 25 K.

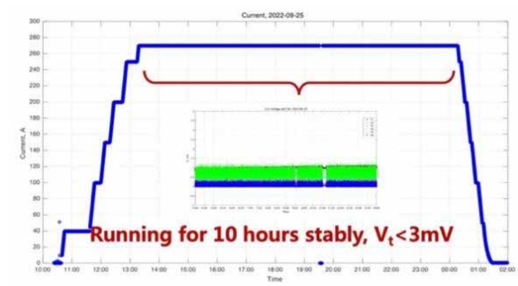

Figure 10: Terminal voltage of the whole HTS coil during stability test.

Figure 11: 1:4 scaled magnet assembly.

High Energy Efficiency RF system

For the 2 GeV FFA, N.C. (Normal Conducting) RF cavities will be applied to boost the proton beam energy from 800 MeV to 2 GeV. Due to the heavy beam loading, the development of the N.C. high-power waveguide type RF cavity with high-quality factor Q and high shunt impedance R is crucial. This would certainly be beneficial for the RF energy efficiency enhancement. Four geometries (i.e., the rectangular, the omega, the racetrack, and the boat ones) of the waveguide-type RF cavities were investigated extensively, and it is found that the boat shape RF cavity has the highest Q (~90000), and the highest R (11~20 MΩ along the radial beam aperture), and is the best candidate [16].

As the beam dynamics requirement, the high energy efficiency RF system of the 2 GeV FFA was designed to consist of 10/15 sets of identical sub-systems, as shown in Fig. 12.

ISBN: 978-3-95450-212-7 ISSN: 2673-5482 doi:10.18429/JACoW-CYCLOTRONS2022-THAI01

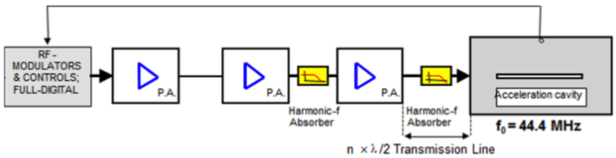

Figure 12: One typical sub-system of the high energy efficiency RF system

The final stage RF power amplifier was designed to provide RF input of up to 1.5 MW for each cavity. The 15 cavities are driven separately, thus, the RF amplitude is independently regulated while the phase of each cavity is locked with the master oscillator. Therefore, 15 MeV energy gain per turn can be obtained with an estimated consumption of about 1 MW power.

R&D studies on a 177.6 MHz 1:4 scale boat shape prototype cavity (L × W × H = 2.4 m × 1.4 m × 2.5 m for the copper cavity and the stainless-steel supports, while L × W × H = 2 m × 0.5 m × 0.8 m for the copper cavity only) were carried out, to investigate technical aspects of the RF cavity. The cavity's Q and R_{max} were calculated to be ~43500 and ~7.61 MΩ, respectively.

For the prototype cavity, ~100 kW designed RF power dissipated on the cavity walls is planned to be brought away by the cooling water, and a ~±170 kHz tuning range is demanded by deforming the RF cavity walls with the electric cylinders. With 35℃ cooling water, the maximum temperature rise is ~42℃ and is located at the left and right ends of the nose cones. To improve the mechanical design, a self-consistent multi-physics coupled simulation study (i.e., RF-thermal-structural-RF analysis) with ANSYS HFSS and Workbench [17] was carried out by using the mechanical model shown in Fig. 13, which includes ~280 body components. Figure 14 shows the ANSYS Project Schematic giving the data linkage between the Geometry, the HFSS Design, the Static-State Thermal, and the Static Structural.

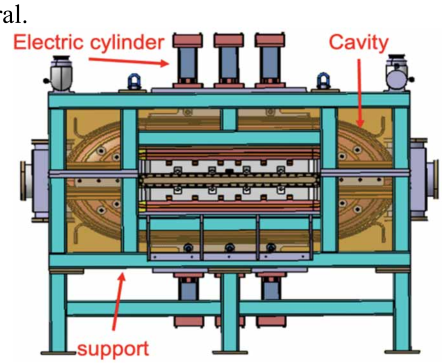

Figure 13: The mechanical model used in the multi-physics coupled simulation study.

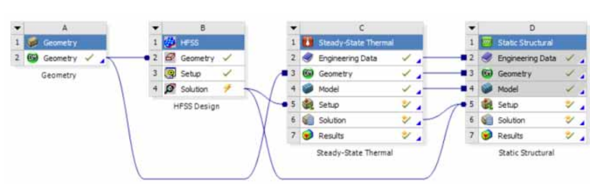

Figure 14: The ANSYS Project Schematic.

Considering the irregular shape of the boat-shaped RF cavity, it is very important to control the deformation during manufacturing and accurately determine the position during the welding. Special tooling and welding process were designed for manufacturing the cavity. Especially, Electron beam welding (EBW) technology was fully adopted to weld all the copper cavity walls together. Most of the parts of the copper cavity were formed by mold pressing. Due to the existence of the spring-back phenomena and the difficulty of finding an accurate reference for the wire-electrode cutting, additional CNC machining was applied. Finally, all the dimension errors were compensated by fine-finishing the nosecone according to the measurement during the cavity pre-assembling process. All of the water-cooling pipes were attached to the outer cavity wall by soldering. The Q and resonant frequencies were checked frequently to ensure the cavity's performance was consistent with the physical design.

Figure 15 shows one of the two half-cavities after the all-manual polishing and the surface roughness measurement, which is better than 0.1 µm. After the quarter-scale cavity assembly was connected with the vacuum pump, the measured resonant frequency is ~177.77 MHz at a vacuum level of ~1×10^{-5} Pa. With maximum deformations of ±2.5 mm at both the upper and lower sides of the cavity body, the measured frequency tuning range is about ±180 kHz. The measured unloaded Q is higher than 42300, which is ~97% of the calculated values of 43500. Figure 16 shows the onsite installation of the quarter-scale cavity at CIAE. The high-power test is being planned and will be conducted very soon.

Figure 15: One of the two half-cavities and the surface roughness measurement.

Figure 16: The onsite installation of the quarter-scale cavity at CIAE.

ISBN: 978-3-95450-212-7 ISSN: 2673-5482 doi:10.18429/JACoW-CYCLOTRONS2022-THAI01

CONCLUSION

Due to its diverse application, the high energy and high current isochronous proton accelerator are actively researched in the modern accelerator field. Based on the extensive experience of successful construction, commissioning, and operation of the high-power compact cyclotron CYCIAE-100, a CW FFA is proposed by CIAE to produce a 2 GeV/6 MW proton beam. Beam dynamics results show good isochronism towards 2 GeV and have a very large acceptance of the beam phase space. Resonance analysis shows the beam quality could be guaranteed because of the flexible modulating of the tune diagram by precisely adjusting the magnetic field gradient in a wide radial range. The turn separation can be increased to ~3 cm with 5 additional cavities and off-centered injection, which seems to be enough for 6 MW beam extraction. R&D Activities for key components, including the 1:4 HTS magnet and the high energy efficiency RF system, are finished for the 2 GeV high power CW FFA accelerator complex.

ACKNOWLEDGMENTS

We would like to extend our cordial gratitude to experts from TRIUMF, PSI, INFN-LNS, and the international cyclotron community for their long-term support and the recent email discussion with Dr. Baartman and Dr. Calabretta about the beam physics for the 2 GeV machine. The authors would also like to thank Dr. Jianjun Yang for the valuable discussion in person and Dr. Ming Li and Dr. Tianjian Bian for their previous research, which are cited in the reference list.

REFERENCES

[1] R. Garoby *et al.*, "Proton drivers for neutrino beams and other high intensity applications", *J. Phys. Conf. Ser.*, vol. 408, no. 1, Feb. 2013, pp. 012016. doi:10.1088/1742-6596/408/1/012016

[2] C. L. Morris *et. al.*, "New Developments in Proton Radiography at the Los Alamos Neutron Science Center (LANSCE)", *Exp. Mech.*, vol. 56, pp. 111-120, 2016. doi:10.1007/s11340-015-0077-2

[3] C. Rubbia *et al.*, "Conceptual design of a fast neutron operated a high power energy amplifier", CERN/AT/95-44 (ET).

[4] Th. Stammbach, "High Intensity Problems, Revisited or Cyclotron Operation Beyond Limits", in *Proc. Cyclotrons'98*, Caen, France, Jun 1998, paper E-01, pp 369-376.

[5] A. Jansson, "The Status of the ESS Project", in *Proc. IPAC'22*, Bangkok, Thailand, Jun. 2022, pp. 792-795. doi:10.18429/JACoW-IPAC2022-TUIYGD1

[6] Luciano Calabretta *et al.*, "Cyclotrons and FFAG Accelerators as Drivers for ADS", Internal Report, BNL-111770-2016-JA, 2016.

[7] Y. Ishi *et al.*, "Status report on KURNS FFAG Facility", FFAG-18 Workshop, Sep. 2018.

[8] T. J. Zhang *et al.*, "A New Solution for Cost Effective, High Average Power (2 GeV, 6 MW) Proton Accelerator and its R&D Activities", in *Proc. Cyclotrons'19*, Cape Town, South Africa, Sep. 2019, pp. 334-339. doi:10.18429/JACoW-CYCLOTRONS2019-FRA01

[9] M. Seidel *et al.*, "Production of a 1.3 MW Proton Beam at PSI", in *Proc. IPAC'10*, Kyoto, Japan, May 2010, paper TUYRA03, pp. 1309-1313.

[10] R. A. Baartman, "Space Charge Limit in Separated Turn Cyclotrons", in *Proc. Cyclotrons'13*, Vancouver, Canada, Sep. 2013, paper WE2PB01, pp. 305-309.

[11] L. Laslett *et al.*, "On intensity limitations imposed by transverse space-charge effects in circular particle accelerators", Summer Study on Storage Rings, BNL Report 7534, pp. 325-367, 1963.

[12] R. A. Baartman, "Intensity Limitations in Compact H^- Cyclotrons", in *Proc. Cyclotron'95*, Cape Town, South Africa, Oct. 1995, pp. 440-445.

[13] V. P. Yakovlev *et al.*, "The Energy Efficiency of High Intensity Proton Driver Concepts", in *Proc. IPAC'17*, Copenhagen, Denmark, May 2017, pp. 4842-4847. doi:10.18429/JACoW-IPAC2017-FRXCB1

[14] T. Zhang *et al.*, "Innovative research and development activities on high energy and high current isochronous proton accelerator", *ICFA Beam Dynamics Newsletter*, vol. 84, JINST_212P_1022, to be published.

[15] T. Bian *et al.*, "Possible solution for the integer resonance crossing problem of GeV-class isochronous fixed-field alternating gradient accelerators", *Nucl. Instrum. Methods*, vol. 1031, pp. 166594, May 2022. https://doi.org/10.1016/j.nima.2022.166594

[16] S. Pei *et al.*, "Design on High Quality Factor and High Shunt Impedance Waveguide-type RF Cavity for 2 GeV FFAG Proton Accelerator", *Atomic Energy Sci. Technol.*, vol. 54, no. 8, 2020, pp. 1519-1524. doi:10.7538/yzk.2019.youxian.0495

[17] ANSYS is a finite element code developed by ANSYS Inc. Canonsburg, PA, https://www.ansys.com/

ISBN: 978-3-95450-212-7 ISSN: 2673-5482 doi:10.18429/JACoW-CYCLOTRONS2022-THAI02

STRIPPING EXTRACTION AND LORENTZ DISSOCIATION

Hui Wen Koay, TRIUMF, Vancouver, B.C. Canada*

Abstract

Stripping extraction of hydrogen molecular ions has gained immense interest in the cyclotron industry due to its high extraction efficiency. However, the magnetic field could result in undesired Lorentz dissociation of the hydrogen anion/molecular ions during acceleration. This work summarizes and compares the Lorentz dissociation of several types of hydrogen ions, as well as other important aspects that are crucial when deciding the best candidate for stripping extraction in a cyclotron.

INTRODUCTION

This paper is a brief summary of a more extensive and in-depth discussion of Lorentz dissociation of hydrogen ions in [1]. Generally, stripping extraction involves the stripping of one or more electrons from the accelerated ions. Owing to the nature of the change in the charge-to-mass ratio, the stripped particles have different trajectories after stripping. This leads to the possibility of having a close to 100% extraction efficiency. This feature is appealing, as final turn separation is no longer mandatory for a clean extraction. However, there are other issues associated with this. Among all, one of the very critical one is the Lorentz dissociation of the accelerated ions under the effect of external magnetic field. The following will discuss briefly the effect of Lorentz dissociation on the potential candidates to produce a proton beam: H^-, H_2^+ and H_3^+.

LORENTZ DISSOCIATION OF HYDROGEN IONS

In general, Lorentz dissociation is a quantum mechanical effect where the bound electron or proton can tunnel out of its potential well because in its own reference frame, the magnetic field is an electric field that tilts the well. Dissociation occurs anywhere along ions' orbits and so they are lost, not extracted and eventually cause activation.

In the particle's rest frame, the electric field component perpendicular to the motion can be simplified as:

$$\mathcal{E} = \gamma\beta c B_z \cong (3\,\mathrm{MV/cm})\gamma\beta(B_z/1\,\mathrm{T}) , \qquad (1)$$

where $\mathcal{E}$ and B_z are the equivalent electric field and the perpendicular magnetic field respectively; β is the ratio of the particle's speed, v, to the speed of light, c and $\gamma = \frac{1}{\sqrt{1-\beta^2}}$.

H^-

The time constant, i.e. the probability of the ion to survive a time t is $e^{-t/\tau}$. It can be expressed by [2]:

$$\tau = \frac{A_1}{\mathcal{E}} \exp\frac{A_2}{\mathcal{E}} . \qquad (2)$$

The constants A_1 and A_2 are fitted constants from experimental results [3]. They are: $A_1 = 3.07 \times 10^{-6}$ V-s/m and $A_2 = 4.414 \times 10^9$ V/m respectively. Due to the popularity of stripping extraction of H^-, this effect is well studied and documented by many past researchers [3, 4]. Using Eq. (2) and assuming B is a constant, the integrated fractional loss F is shown in Fig. 1 (the energy gain per turn is taken as 0.48 MeV).

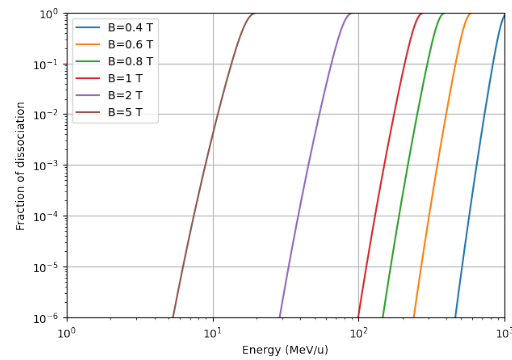

Figure 1: Integrated fractional dissociation of H^- as a function of energy for various B. Note that this calculation assumed a constant B and the energy gain per turn is 0.48 MeV. However since the loss as such a steep function of B, this can be taken as the peak B for cyclotrons with flutter.

From Fig. 1, F of H^- particles accelerated up to 1 GeV is 100% for any $B > 0.4$ T. Taking a maximum loss of 0.01%, the maximum permissible beam energy at a low B of 0.4 T is about 600 MeV; at a very large radius of $r = 10$ m. Hence, any acceleration at high energy is uneconomic, as the average magnetic field will be too low to achieve the desired beam loss, and the machine has to be extremely large to accommodate such a low magnetic field.

H_2^+

H_2^+ is a diatomic ion with an equilibrium bond distance of about 1.06 Å. The binding energy of H_2^+ is about 2.7 eV, which is 3.6 times larger than the binding energy of H^-. Unlike the H^- ion that has a well-studied time constant, there is a lack of experimental work to study Lorentz dissociation of H_2^+. To fill in the missing piece of information, some theoretical models are used here as the preliminary tools to estimate the Lorentz dissociation of H_2^+.

The ionic lifetime of each vibrational v state (rotational state $J = 0$) at different electric fields can be obtained from Hiskes' calculation [5]. The lifetimes of high v states are generally comparable to the revolution period of H_2^+ in a cyclotron (~10^{-8} s), i.e. the ions at high v states will dissociate completely within a turn of revolution. Therefore, instead of the lifetime, it is the state population that limits the fraction of dissociation. Unlike H^- that has only one bound state,

* hkoay@triumf.ca

ISBN: 978-3-95450-212-7 ISSN: 2673-5482 doi:10.18429/JACoW-CYCLOTRONS2022-THAI02

H_2^+ has many populated bound states that highly depend on the initial conditions of the source. Many studies had shown consistently that more than 90% of the population lie at $v < 12$ [6–9]. Among them, the most important work was done by Busch, as a comparison between calculation and experiment was made [7]. If we assume the state populations p_v are distributed as Busch and the lifetime prediction is as given by Hiskes, the integrated fractional loss F of H_2^+ at different B fields can be estimated. Similar to the calculation done for H^-, flutter is omitted and the energy gain per turn is taken as 0.48 MeV. This result is summarized in Fig. 2.

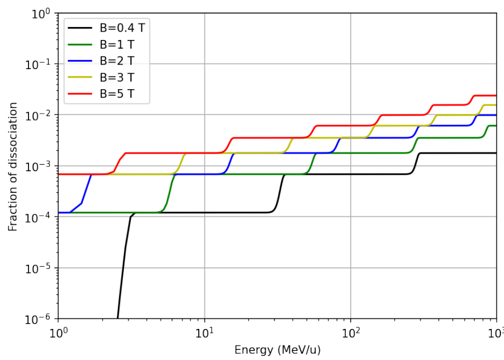

Figure 2: The total dissociated fraction of H_2^+ from all v states when $B = 0.4, 1, 2, 3$ and 5 T respectively. Each plateau indicates the maximum dissociated fraction at each v state. This corresponds to the population of states in [7]. For instance, the blue line is the summation of all vibrational states at $B = 2$ T. As B increases from 1 to 5 T, the total dissociated fraction also increases up to $\sim 2\%$.

At $B = 2$ T, the equivalent electric field for 100 MeV/u of H_2^+ is 2.8 MV/cm. At this $\mathcal{E}$, 0.35% of ions lying at $v \geq 15$ will dissociate. As the energy or magnetic field increases, $\mathcal{E}$ increases, and so does the number of populated v states that are prone to dissociation. For example, at energy of 1 GeV/u, ions lying at $v \geq 13$ and at $v \geq 11$ will dissociate when $B = 2$ T and 5 T respectively. This amounts to a total dissociated fraction of about 1% and 2% respectively. If we take the maximum permissible power loss of 1 W/m for hands-on-maintenance, the maximum current allowed at $B = 2$ T and 5 T for acceleration up to 1 GeV/u are merely 1.8 and 0.7 µA. If acceleration at a higher current (say 1 mA) is desired, the H_2^+ beam has to be cooled or state-selected so that more than 99.9% lie at $v \leq 11$ [10, 11].

H_3^+

The binding energy (dissociation energy) of H_3^+ is about 4.5 eV [12], which is about 2 times larger than H_2^+, and is thus the most stable among the hydrogen ions discussed in this work.

Despite of its better stability and higher abundance, only very few works studied directly the effect of external field on the dissociation of H_3^+ so far. This is mainly due to the complex dynamical structure of the non-linear tri-atomic molecule [13–15]. Reckzügel et al. are among the few who had looked into this for the case of a linear and triangular H_3^+ [14]. Figure 5 in [14] shows the change of the potential energy surface of a triangular H_3^+ as the external electric field increases. A higher electric field lowers the dissociation energy barrier, causing the ions to disintegrate more easily into a proton and a hydrogen molecule. The relationship between the dissociation energy (E_d) and $\mathcal{E}$ field (in MV/cm) is extracted from [14] with a fitted function given as follows:

$$E_d = (4.5\,\text{eV}) \exp\left[-\frac{\mathcal{E}}{128\,\text{MV/cm}}\right] \quad (3)$$

As with the H_2^+ case, it is excited states and their population that set the limit. In fact, there are over hundreds of bound excited states with non-zero quantum numbers [16]. The full population of all these states with transition time is not easy to determine. V.G. Anichich had computed a simpler estimation of the state populations of only the symmetric mode with a quantum number v forming from the ground-state H_2^+ and H_2 [17]. As there is no work done so far to determine the lifetime of v states at various $\mathcal{E}$, here we assume that it is short as compared to the acceleration period (as in the case of H_2^+). The maximum dissociation at a particular $\mathcal{E}$ can then be estimated by utilizing the state populations and Eq. (3). Figure 3 shows the state population as distributed in the one-harmonic model from [17].

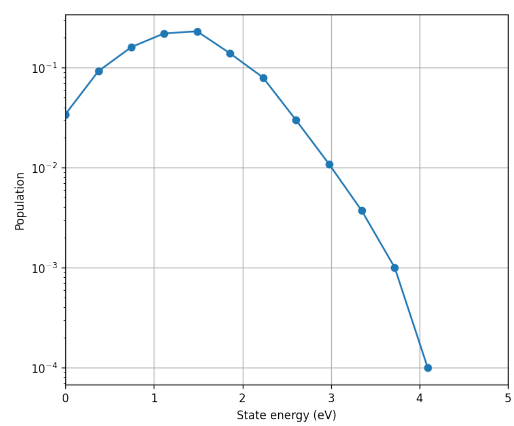

Figure 3: The population of state from the one-harmonic model in [17]. Each point corresponds to a bound v state from $v = 0$ at the left to $v = 11$ at the right.

Taking H_3^+ of energy 1 GeV/u under a constant B field of 3 T, the equivalent $\mathcal{E}$ is about 16.3 MV/cm. This corresponds to a dissociation energy of about 4.0 eV and a dissociation of only the highest state with a population of about 0.01% from Fig. 3. The result is similar even if the population of the more detailed two-anharmonic model from [17] were used. If we assume a maximum beam loss of 1 W/m, acceleration of 1 mA of H_3^+ at a high energy of 1 GeV/u is possible at low $B = 1.7$ T. Note that this is about two times the maximum energy per nucleon attainable by H^- at the same radius of 10 m and the same beam current of 1 mA. Therefore, if the state population of an actual H_3^+ beam can be controlled or cooled [18, 19] so that it is similar to the one adopted here

ISBN: 978-3-95450-212-7 ISSN: 2673-5482 doi:10.18429/JACoW-CYCLOTRONS2022-THAI02

(> 99.9% lying at states with dissociation energy >4.0 eV), we can infer that the effect of external Lorentz field on the beam loss of H_3^+ is very minimal at high-energy (>500 MeV) extraction.

CONCLUSIONS

To summarize, the order of stability goes from $H_3^+ > H_2^+ > H^-$ at energy greater than 100 MeV. Nevertheless, the estimations given in this work, especially for H_2^+ and H_3^+ are based on the information that we have gathered so far from the literature, i.e. many factors such as the higher excited states with $J \neq 0$ have been omitted. In real practice, the Lorentz dissociation of H_2^+ and H_3^+ are more complex and it could vary by more than a factor 10, as it highly depends on the initial beam condition [20, 21]. Therefore, experimental verification of Lorentz dissociation using real hydrogen ions shall be the next to be done before H_2^+ and H_3^+ ions can be fully implemented at a higher beam power.

REFERENCES

[1] H. W. Koay, "Lorentz dissociation of hydrogen ions in a cyclotron," *J. Instrum.*, vol. 18, no. 03, P03027, 2023. doi:10.1088/1748-0221/18/03/P03027

[2] G. Darewych and S. Neamtan, "On the mean life of H^- ions in accelerating devices," *Nucl. Instrum. Methods*, vol. 21, pp. 247–248, 1963. doi:10.1016/0029-554X(63)90123-X

[3] P. Keating *et al.*, "Electric-field-induced electron detachment of 800-MeV H^- ions," *Phys. Rev. A*, vol. 52, no. 6, p. 4547, 1995. doi:10.1103/physreva.52.4547

[4] G. M. Stinson, W. Olsen, W. McDonald, P. Ford, D. Axen, and E. Blackmore, "Electric dissociation of H^- ions by magnetic fields," *Nucl. Instrum. Methods*, vol. 74, no. 2, pp. 333–341, 1969. doi:10.1016/0029-554X(69)90359-0

[5] J. R. Hiskes, "Dissociation of molecular ions by electric and magnetic fields," *Phys. Rev.*, vol. 122, no. 4, pp. 1207–1217, May 1961. doi:10.1103/PhysRev.122.1207

[6] A. G. Brenton, P. G. Fournier, B. L. Govers, E. G. Richard, and J. H. Beynon, "The vibrational population distribution of $H_2^{+\cdot}$ formed from a series of different precursor molecules," *Proc. R. Soc. London. A. Math. Phys. Sci.*, vol. 395, no. 1808, pp. 111–125, 1984. doi:10.1098/rspa.1984.0092

[7] F. von Busch and G. H. Dunn, "Photodissociation of H_2^+ and D_2^+: Experiment," *Phys. Rev. A*, vol. 5, no. 4, pp. 1726–1743, Apr. 1972. doi:10.1103/PhysRevA.5.1726

[8] J. Ozenne, J. Durup, R. Odom, C. Pernot, A. Tabché-Fouhaillé, and M. Tadjeddine, "Laser photodissociation of the isotopic hydrogen molecular ions. comparison between experimental and ab initio computed fragment kinetic energy spectra," *Chem. Phys.*, vol. 16, no. 1, pp. 75–80, 1976. doi:10.1016/0301-0104(76)89024-6

[9] G. H. Dunn, "Franck—Condon Factors for the Ionization of H_2 and D_2," *J. Chem. Phys.*, vol. 44, no. 7, pp. 2592–2594, 1966. doi:10.1063/1.1727097

[10] A. Sen, J. W. M. Gowan, and J. B. A. Mitchell, "Production of low-vibrational-state H_2^+ for collision studies," *J. Phys. B: At. Mol. Phys.*, vol. 20, no. 7, pp. 1509–1515, 1987. doi:10.1088/0022-3700/20/7/018

[11] J. Schmidt *et al.*, "Trapping, Cooling, and Photodissociation Analysis of State-Selected H_2^+ Ions Produced by (3 + 1) Multiphoton Ionization," *Phys. Rev. Appl.*, vol. 14, no. 2, p. 024 053, Aug. 2020. doi:10.1103/PhysRevApplied.14.024053

[12] A. Carrington and R. A. Kennedy, "Infrared predissociation spectrum of the H_3^+ ion," *J. Chem. Phys.*, vol. 81, no. 1, pp. 91–112, 1984. doi:10.1063/1.447357

[13] G.R. Haste, J.L. Dunlap, H. Postma, and L.H. Reber, "Lorentz dissociation of H_3^+ in DCX-1," *Nucl. Fusion*, vol. 5, no. 2, Apr. 1965. doi:10.1088/0029-5515/5/2/010

[14] M. C. Reckzügel, W. Drachsel, and J. H. Block, "Structure of H_3^+ in high electric fields with implications for the structure of adsorbed H_3," *J. Chem. Phys.*, vol. 102, no. 19, pp. 7708–7713, 1995. doi:10.1063/1.469022

[15] H. Medel Cobaxin and A. Alijah, "Vibrating H_3^+ in a uniform magnetic field," *J. Phys. Chem. A*, vol. 117, no. 39, pp. 9871–9881, 2013. doi:10.1021/jp312856s

[16] J. J. Munro, J. Ramanlal, and J. Tennyson, "Asymptotic vibrational states of the H_3^+ molecular ion," *New J. Phys.*, vol. 7, pp. 196–196, Sep. 2005. doi:10.1088/1367-2630/7/1/196

[17] V. Anicich and J. Futrell, "A computer study of the formation of H_3^+ and its vibrational deactivation using a statistical model," *Int. J. Mass Spectrom. Ion Processes*, vol. 55, no. 2, pp. 189–215, 1984. doi:10.1016/0168-1176(84)85033-8

[18] A. Sen and J. B. A. Mitchell, "Production of H_3^+ ions with low internal energy for studies of dissociative recombination," *J. Phys. B: At. Mol. Phys.*, vol. 19, no. 16, p. L545, Aug. 1986. doi:10.1088/0022-3700/19/16doi.

[19] X. Urbain, A. Dochain, R. Marion, T. Launoy, and J. Loreau, "Photodissociation as a probe of the H_3^+ avoided crossing seam," *Phil. Trans. R. Soc. A*, vol. 377, p. 2154, 2019. doi:10.1098/rsta.2018.0399

[20] A.C. Riviere and D.R. Sweetman, "Dissociation of H_2^+ and He^- by electric fields," *Phys. Rev. Lett.*, vol. 5, no. 12, pp. 560–562, Dec. 1960. doi:10.1103/PhysRevLett.5.560

[21] H. Postma, G. R. Haste, and J. L. Dunlap, "Proton trapping in DCX-1 resulting from lorentz dissociation of H_2^+," *Nucl. Fusion*, vol. 3, no. 2, pp. 128–129, Jun. 1963. doi:10.1088/0029-5515/3/2/011

ISBN: 978-3-95450-212-7 ISSN: 2673-5482 doi:10.18429/JACoW-CYCLOTRONS2022-THAO01

ON THE ENERGY LIMIT OF COMPACT ISOCHRONOUS CYCLOTRONS

W. Kleeven
Ion Beam Applications (IBA), Louvain-La-Neuve, Belgium

Abstract

Existing analytical models for transverse beam dynamics in isochronous cyclotrons are often not valid or not precise for relativistic energies. The main difficulty in developing such models lies in the fact that cross-terms between derivatives of the average magnetic field and the azimuthally varying components cannot be neglected at higher energies. Taking such cross-terms rigorously into account results in an even larger number of terms that need to be included in the equations. In this paper, a method is developed which is relativistically correct and which provides results that are practical and easy to use. We derive new formulas, graphs, and tables for the radial and vertical tunes in terms of the flutter, its radial derivatives, the spiral angle and the relativistic gamma γ. Using this method, we study the $2\nu_r = N$ structural resonance (N is number of sectors) and provide formulas and graphs for its stopband. Combining those equations with the new equation for the vertical tune, we find the stability zone and the energy limit of compact isochronous cyclotrons for any value of N. We confront the new analytical method with closed orbit simulations of the IBA C400 cyclotron for hadron therapy.

INTRODUCTION

In this paper we derive the maximum energy that can be realized in compact isochronous cyclotrons. This limit is determined by two competing requirements namely the need for sufficient vertical focusing on the one hand and the need to avoid the stopband of the half-integer resonance $2\nu_r = N$ on the other hand (ν_r is the radial tune). With increasing energy, the isochronous field index increases rapidly and more and more azimuthal field variation f is needed to remain vertically stable; but with higher f, the stopband of the resonance broadens, and the energy limit associated with it rapidly reduces. The energy limit depends on N and on the spiral angle ξ of the sectors. We assume that the magnetic field is perfectly N-fold rotational and median plane symmetric and therefore do not consider other, than the half-integer linear resonance. We derive practical formulas which are useful especially in the cyclotron design phase. Our main assumption/approximation is that f is not too large. Results are derived up to $O(f^2)$ (equivalent to $O(F)$, where F is the flutter). For compact cyclotrons F is generally well below 1 and for these machines we expect our results to be precise. For separate sector cyclotrons, care should be taken, however. The special case of such cyclotrons with radial sectors (no spiraling) has been studied by Gordon [1], by assuming a hard-edge model where in the magnet sections the orbits are perfectly circular and in the empty straight sections the magnetic field is zero. In Gordon's model, there is no need to assume a small flutter, but on the other hand, his assumptions will probably not be valid for compact cyclotrons and maybe also less accurate for coil-dominated superconducting ring cyclotrons where the magnetic field has the tendency to spread out more smoothly and non-uniformly. For separate sector cyclotrons with a larger magnetic filling factor, the flutter drops quickly ($F \approx 0.25$ for a filling factor of 80%) and we expect our results to become more accurate. Another interesting derivation of the isochronous cyclotron energy limit has been made by Danilov *et al.* from the JINR [2]. In their analysis however, they consider only the first dominant Fourier component of the field and they further assume that its amplitude is independent on radius and its phase increases linearly with radius. Also, contributions due to higher order radial derivatives of the average magnetic field are ignored. A similar approach was used by King and Walkinshaw [3]. We closely follow the Hamiltonian approach that has been firstly introduced by Hagedoorn and Verster [4]; in this paper we wish to pay tribute to them. The derivation is too elaborate and complex to show in detail and therefore in this paper, we present a strongly compressed version. The full derivation and results can be found in reference [5].

METHOD OF DERIVATION

We study the static (non-accelerated) motion near a given constant radius r_0 defined by $P_0 = qr_0\bar{B}(r_0)$, where P_0 is the particle kinetic momentum. The reduced magnetic field $\mu(r,\theta) = B(r,\theta)/\bar{B}(r_0)$ is represented by a Fourier series with respect to the azimuth θ. The radial dependence of the average field $\bar{\mu}(r)$ and of the Fourier components $A_n(r), B_n(r)$ of the azimuthally varying field profile $f(r,\theta)$, are Taylor expanded relative to the same radius r_0. The magnitude of f is approximately equal to the magnitude of the dominant Fourier component $C_N = (A_N^2 + B_N^2)^{1/2}$ and the flutter F is approximately equal to $C_N^2/2$. In all our derivations we use a perturbation analysis where $|f|$ serves as the measure for precision. In general any quantity of interest $g(\theta)$ can be split in its average part $\bar{g} = \frac{1}{2\pi}\oint g(\theta)d\theta$ and its oscillating part $\mathrm{osc}(g) = g(\theta) - \bar{g}$. Oscillating parts of $O(f)$ can be moved to the next higher order by a properly constructed canonical transformation. In doing so, new average contributions of $O(f^2)$ are generated. Our goal is to derive results up to $O(f^2)$. The reason for this is that the first significant terms in the expressions for the isochronous magnetic field and the radial and vertical tunes are of $O(f^2)$. In line with the HV-paper [4], we keep the average part of any azimuthally varying term up to $O(f^2)$, but neglect oscillating terms $O(f^2)$ as they would generate new terms of $O(f^3)$ when transforming them to higher order. However, we make one important generalization/improvement as compared to the HV-paper. Hagedoorn and Verster assumed that radial derivatives of the average magnetic field $(\bar{\mu}', \bar{\mu}'', \bar{\mu}''', \ldots)$ are small quantities of $O(f^2)$ and therefore neglected cross-terms between those derivatives and

ISBN: 978-3-95450-212-7 ISSN: 2673-5482 doi:10.18429/JACoW-CYCLOTRONS2022-THAO01

the Fourier content in all expansions (note that we define the prime-operator for radial derivatives of a function $h(r)$as $h' = r\frac{dh}{dr}$, $h^{(n)} = r^n d^n h/dr^n$). This is valid at low but not at relativistic energies, as is shown in Fig. 1.

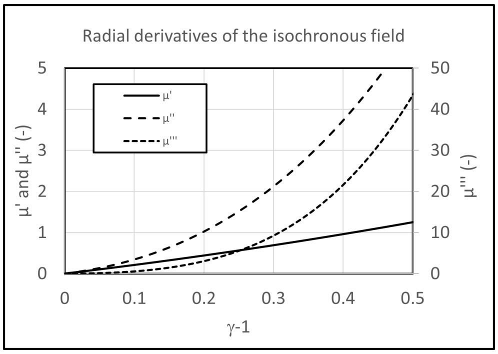

Figure 1: Derivatives of the isochronous magnetic field.

As we are interested in the cyclotron energy limits we must consider the derivatives $\bar{\mu}', \bar{\mu}'', \bar{\mu}''', \dots$ as terms of $O(f^0)$. This makes the derivation (and the final results) considerably more complex as many more terms need to be kept in the Hamiltonian expansion and certain canonical transformations used in the HV-paper, must be modified/generalized.

Our derivation starts from a general cyclotron Hamiltonian in polar coordinates. We introduce reduced canonical coordinates (by normalizing with respect to r_0), reduced canonical momenta (by normalizing with respect to P_0) and the reduced magnetic field (by normalizing with respect to $\bar{B}(r_0)$). The two transverse motions are decoupled by assuming that the horizontal motion is in the median plane and the projection of the vertical motion follows the Equilibrium Orbit (EO). This gives two separate Hamiltonians: H_x for the horizontal and H_z for the vertical motion. The EO is found by the requirement that it must be a periodic solution of H_x, and therefore can be expressed as a Fourier series. New canonical variables w.r.t. the EO are introduced and the Hamiltonian H_x is Taylor expanded with respect to these variables. Only terms up to second degree in the canonical variables need to be kept. This corresponds to linear motion and is sufficient as the half-integer resonance $2\nu_r = N$ is linear. By a second canonical transformation, H_x is brought to the normal form of the structure $H(p, x, \theta) = \frac{1}{2}p^2 + \frac{1}{2}(\nu_{x0}^2 + f_x(\theta))x^2$ (and similar for H_z). Here the parameters ν_{x0} and $f_x(\theta)$ depend only on the reduced magnetic field quantities. The term ν_{x0} is $O(f^0)$ and the term $f_x(\theta)$ is an oscillating term (zero average) of $O(f^1)$. We design a third linear canonical transformation, that moves the oscillating part $f_x(\theta)$ to new terms of the next higher order $O(f^2)$. Within our required level of approximation, we only need to keep the average of these new terms. This solves the motion ($O(f^2)$) as H becomes independent of θ. The betatron tune of the motion becomes $\nu_x^2 = \nu_{x0}^2 + \frac{1}{2}\sum \frac{c_n^2}{n^2 - 4\nu_{x0}^2}$. Here the c_n are the Fourier amplitudes of the function $f_x(\theta)$.

For derivation of the $2\nu_r = N$ resonance we first introduce action-angle variables in an horizontal phase space that rotates with frequency $N/2$ and then design a canonical transformation that moves the oscillating part of $O(f)$ to the next higher order $O(f^2)$. This gives us the following general expression for the lower and upper limits of the stopband:

$$\nu_{x0}(1,2) = \frac{N}{2} \mp \frac{c_N}{2N} - \frac{3}{8}\frac{c_N^2}{N^3} - \frac{1}{2N}\sum_{n>N}\frac{c_n^2}{n^2 - N^2} .$$

Here ν_{x0} and c_n must be expressed in terms of reduced magnetic field parameters $\bar{\mu}', \bar{\mu}'', \dots, C_n, C_n', \dots, \varphi_n'$.

The $O(f^2)$ contributions to the final results all have a similar structure of the following general form:

$$R^{(2)} = \sum_n \alpha_n(\bar{\mu}', \dots)C_n^2 + \beta_n(\bar{\mu}', \dots)C_n^2\varphi_n'^2 + \gamma_n(\bar{\mu}', \dots)C_nC_n' + \delta_n(\bar{\mu}', \dots)C_n'^2 ,$$

where the summation runs over all Fourier components n, the coefficients $\alpha_n, \dots$ depend on $\bar{\mu}', \bar{\mu}'', \bar{\mu}''', \dots$ and the variables C_n, φ_n are the amplitude and phase of harmonic n. To simplify this structure, we make a few approximations. Firstly, we assume a perfectly isochronous magnetic field. In this case the coefficients $\alpha_n, \dots$ will depend on γ only. Secondly, we assume that the phase-derivatives φ_n' do not depend on n. In practice this is accurately true for the first several (often up to 5) Fourier components. Since contributions of higher components rapidly drop with increasing n-value, this approximation will be accurate. In this way the variable $\varphi_n' = \varphi'$ can be taken out of the series summations (note that φ' is related to the frequently used spiral angle ξ as $\varphi' = \tan\xi$). Thirdly, we introduce a method where the higher Fourier harmonics ($n > N$) are expressed in terms of the dominant harmonic ($n = N$). For this we assume a symmetrical hard-edge profile of the azimuthally varying field with equal hill and valley angle. This approximation is reasonable because the optical quantities are dominantly determined by the principal harmonic; it allows us to approximate the higher harmonic content and therefore is expected to be more accurate than only considering the dominant harmonic. For such a profile we have:

$$F(r) = \frac{\langle B^2(\theta, r)\rangle - \langle B(\theta, r)\rangle^2}{\langle B(\theta, r)\rangle^2} ,$$

$$C_n^2 = \frac{N^2}{n^2}C_N^2 = \frac{16F}{\pi^2(2k+1)^2} , \qquad k = 1, 2, \dots .$$

The n-dependence of the harmonic amplitudes C_n can now be included in the coefficients $\alpha_n, \dots$ and the dominant component C_N can be expressed in terms F and taken outside of the summation. Finally, we sum the series analytically and express the results in elementary functions of γ and N. The $O(f^2)$ terms are thus transformed to the simpler form:

$$R^{(2)} \approx F\left(a_N(\gamma) + b_N(\gamma)\varphi'^2 + c_N(\gamma)\frac{F'}{F} + d_N(\gamma)(\frac{F'}{F})^2\right) .$$

ISBN: 978-3-95450-212-7 ISSN: 2673-5482 doi:10.18429/JACoW-CYCLOTRONS2022-THAO01

RESULTS: SOME EXAMPLES

Following the approach as outlined in the previous paragraph, we find the following expression for the radial tune:

$$\nu_x^2 = 1+\bar{\mu}'_{rel} + \frac{8N^2F}{\pi^2}\left[\tilde{a}_N + \tilde{b}_N\varphi'^2 + \tilde{c}_N\frac{F'}{F} + \tilde{d}_N\left(\frac{F'}{F}\right)^2\right] .$$

Here $1+\bar{\mu}'_{rel} = \gamma^2$ and the coefficient $\tilde{a}_N, \tilde{b}_N, \tilde{c}_N, \tilde{d}_N$ depend on γ as follows:

$$\tilde{a}_N(\gamma) = \tilde{q}_1 t_2 + \tilde{q}_2 t_1 + (\tilde{q}_3 + \tilde{q}_5 t_2)(1+t_2^2) + \tilde{q}_4 ,$$

$$\tilde{b}_N(\gamma) = \frac{\pi}{8\gamma N}(t_1 - 2t_2) ,$$

$$\tilde{d}_N(\gamma) = \frac{\pi}{128\gamma^3 N}\left(\frac{3\pi\gamma}{N} + t_1 - 8t_2\right) ,$$

$$\tilde{c}_N(\gamma) = \frac{\pi}{96\gamma^3 N}[(11-9\gamma^2)\frac{3\pi\gamma}{N} + 3(\gamma^2+1)t_1 + 24(2\gamma^2-3)t_2 - \frac{12\pi\gamma}{N}(\gamma^2-1)t_2^2] ,$$

where $t_1 = \tan(\pi\gamma/N)$, $t_2 = \tan(\pi\gamma/2N)$ and the coefficients $\tilde{q}_i$ are defined as:

$$\tilde{q}_0(\gamma) = \frac{1}{4\gamma^4}(4+(\gamma^2-1)(\gamma^2+10))(\gamma^2-1)^2 ,$$

$$\tilde{q}_1(\gamma) = \frac{-\pi}{8N\gamma^3}[6-\tilde{q}_6+15\tilde{q}_0] , \qquad \tilde{q}_2(\gamma) = \frac{+\pi}{32N\gamma^3}\tilde{q}_6 ,$$

$$\tilde{q}_3(\gamma) = \frac{\pi^2}{16N^2\gamma^2}[4-\tilde{q}_6+7\tilde{q}_0] , \qquad \tilde{q}_5(\gamma) = \frac{-\pi^3\tilde{q}_0}{16N^3\gamma} ,$$

$$\tilde{q}_4(\gamma) = \frac{+\pi^2}{32N^2\gamma^2}[4-\tilde{q}_6+16\tilde{q}_0] , \quad \tilde{q}_6(\gamma) = (\gamma^2+1)^2 .$$

Above equations are elaborate but not difficult as they depend on elementary mathematical functions only. We developed a cyclotron design template in excel in which the first three columns (radius r, flutter $F(r)$, magnetic sector center-azimuth $\varphi(r)$) must be pasted by the user and only three more constants (N, revolution frequency f_{rev} and the central field B_0) must be defined. The template then calculates all results derived in the paper such as the tunes, the resonance stopband limits, the isochronous field profile $B_{iso}(r)$ and the relation $\gamma = \gamma(r)$.

To validate the derivations, we compare our results with the C400 hadron therapy cyclotron [6–8]. This K=1600 machine is now in construction by the company Normandy Hadron Therapy (NHa) based in Caen, France, in collaboration with IBA. Figure 2 shows the Fourier properties and a histogram plot of the C400 magnetic field. The upper left shows the flutter F and the normalized amplitudes of the first five structural components and the lower left their spiral angles ξ_n. It is seen that the ξ_n are all closely the same and the flutter is roughly equal to $C_4^2/2$ as stated earlier.

The lower right figure shows different alternatives for the definition of the spiral angle. The first one uses the azimuth at which the magnetic field around a circle reaches its maximum. The second and third alternatives use the azimuth at

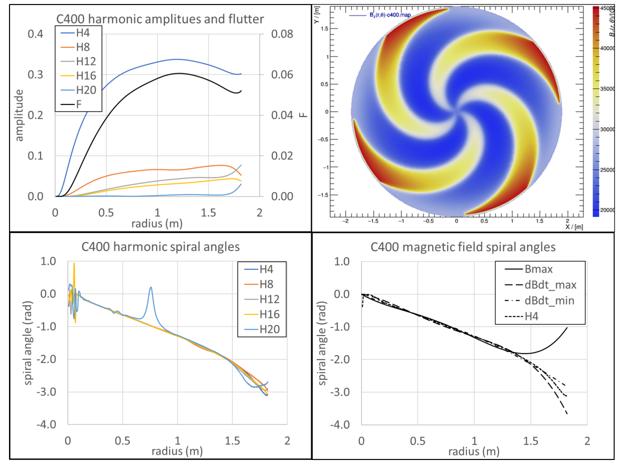

Figure 2: C400 harmonics and spiral angle comparison.

which the azimuthal derivative of the magnetic field reaches its maximum (at sector entrance) or minimum (at sector exit) respectively. The fourth alternative uses the azimuth at which the basic harmonic component C_4 reaches its maximum. The first alternative is not a good choice, because it deviates too much at high radii. For the radial tune and the $\nu_r = N/2$ stopband, the other three alternatives give closely the same results. However, as we will see later, for the vertical tune the average of the second and third alternatives give the best match with the C400 closed orbit simulations. This makes sense because it is at the sector edges where the strong vertical focusing takes place. We therefore use this definition in our paper. Figure 3 compares our analytical radial tune (black curve) with the numerical closed orbit tune (blue curve). In the left figure the relativistic contribution to the tune (=γ) is also shown separately (red curve). At extraction, this contribution accounts for almost 75% of the total. The right of Figure 3 shows the part of the radial tune that is due to the flutter only. Here there is good agreement between the analytical and the closed orbit results. There is a small difference because in the derivation of the tune, the approach towards the half-integer resonance was ignored (as this is treated separately). The dashed curve in the right of Figure 3 show the flutter contribution to the radial tune that is obtained if the energy-dependence of the tune-coefficients would have been ignored (simulated by evaluating the coefficients at the value $\gamma = 1$). This is equivalent to a derivation in which the cross-terms between the average field radial derivatives and the magnetic field Fourier terms are neglected (as was done in the HV-paper). This approximation becomes inaccurate at relativistic energies.

The derivation and final equations of the vertical tune are very similar to those of the radial tune. The vertical tune depends critically on the definition of the spiral angle. The reason for this is that ν_z^2 is obtained as a difference between two larger numbers (negative field index $\bar{\mu}'$ and positive flutter-terms), which to a large extent cancel each other.

This is illustrated (for the C400) in Figure 4. The numerical CO result is shown in blue. The red curve (Bmax) uses the spiral angle obtained from the azimuth where the

ISBN: 978-3-95450-212-7 ISSN: 2673-5482 doi:10.18429/JACoW-CYCLOTRONS2022-THAO01

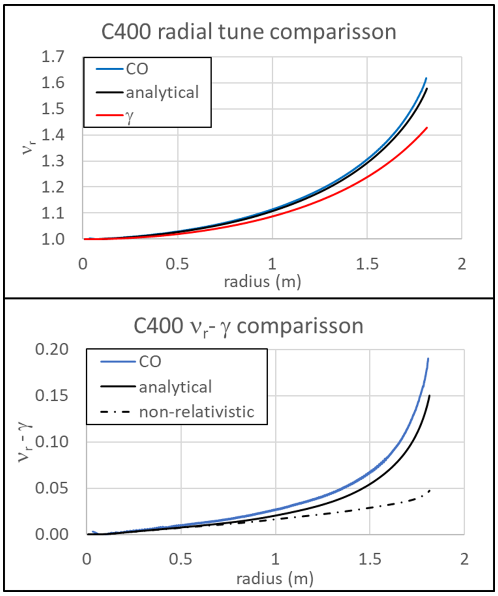

Figure 3: C400 radial tune comparison.

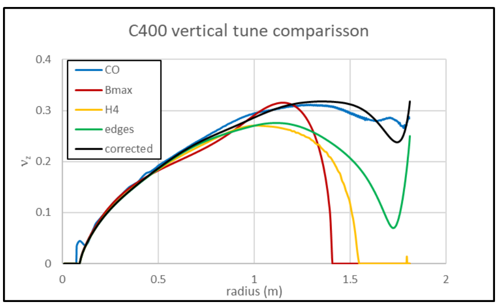

Figure 4: C400 vertical tune comparison.

magnetic field around a circle is maximum. This model fits well up to a radius of about 1.2 m (≈125 MeV/u), but beyond that immediately collapses. The orange curve (H4), based on the phase φ_4 of the basic harmonic, gives some improvement but is still not satisfactory. The green curve (edges), based on the average of the sector-in and sector-out azimuths, shows a further improvement but still deviates substantially from the numerical curve at higher energies. The black curve shows our best result. Here the spiral angle (from the previous case - edges) is corrected for the fact that the EO is not circular and therefore enters and exits from the sector with a non-zero radial momentum. We find the following formula for the correction [5]:

$$\varphi'_{corr} = \varphi' \left(1 + \frac{\pi^2 F}{4N^2}(1 + \varphi'^2)\right) + O(f^4) \,.$$

For the lower and upper limits $\gamma_{1,2}$ of the $2\nu_r = N$ resonance stopband we find the following equation:

$$\gamma_{1,2} = \frac{N}{2} \mp \frac{2\sqrt{F}}{\pi N}\sqrt{(1 + \frac{N^2}{4} + \frac{F'}{2F})^2 + N^2\varphi'^2}$$
$$- \frac{F}{\pi^2 N^3}\left(\bar{a}_N - \bar{b}_N\varphi'^2 - \bar{c}_N\frac{F'}{F} + \bar{d}_N(\frac{F'}{F})^2\right) \,.$$

Its right-hand-side consists of contributions of $O(f^0)$ (first term), $O(f^1)$ (second term) and $O(f^2)$ (third term).

Table 1 shows the values of the $O(f^2)$-term coefficients $\bar{a}_N, \bar{b}_N, \bar{c}_N, \bar{d}_N$ for a range of N-numbers.

Table 1: Stopband Coefficients

N	a_N	b_N	c_N	d_N
3	312.4	41.1	52.8	1.164
4	877.2	73.1	92.9	1.164
5	2043.8	114.2	144.4	1.164
6	4145.6	164.4	207.4	1.164
8	12856.6	292.2	367.6	1.164
10	31149.8	456.6	573.7	1.164
12	64346.3	657.6	825.6	1.164

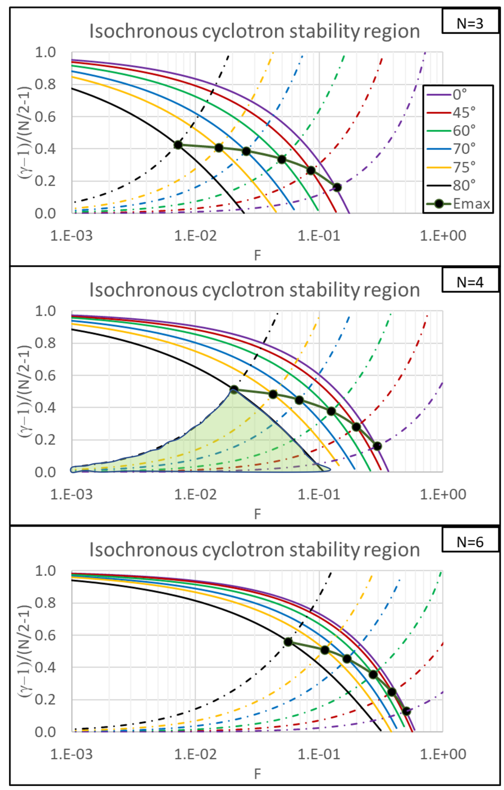

Figure 5: Stability diagram of the isochronous cyclotron.

Figure 5 shows in one plot the resonance limits (solid lines) and the vertical focusing limits (dashed lines) as function of the flutter F and for several spiral angles ξ. The focusing limit is determined by the condition $\nu_z = 0$. It increases monotonically with increasing F and ξ, whereas the normalized resonance limit $(\gamma - 1)/(\frac{N}{2} - 1)$ decreases monotonically with increasing F and ξ. To have a stable cyclotron, the operating point as defined by F, ξ and γ must be below the corresponding solid lines and the corresponding dashed lines (the green-colored zone in the middle figure). The lines itself represent extreme limits of stability and in practice sufficient distance must be taken. For the vertical tune one could require for example a minimum value $\nu_{min} > 0$. If γ_0 is the focusing limit found from Figure 5 then the dashed line in the plot will shift down by the amount $\Delta\gamma \approx -\nu_{min}^2/(2\gamma_0)$. At the intersect between solid and dashed lines the highest achievable energy is found for a given spiral angle. These points are shown as black dots. Table 2 shows these energy limits as a function of the design spiral ξ and several N-numbers. The table also shows the corresponding flutter values that are required to achieve these limits. The energy limits are the absolute limits for the isochronous cyclotron as dictated by the beam dynamics of these machines. In practice there are of course other limits determined by technology.

Table 2: Energy Limits of Isochronous Cyclotrons

	N=3		N=4		N=6	
ξ deg	F –	T MeV/u	F –	T MeV/u	F –	T MeV/u
0	0.1384	75.7	0.2934	151	0.5063	243
45	0.0858	125	0.1995	263	0.387	464
60	0.0495	157	0.1245	352	0.272	668
70	0.0257	180	0.0686	418	0.168	850
75	0.0153	190	0.0424	450	0.111	950
80	0.0072	198	0.0204	477	0.056	1045
	N=8		N=10		N=12	
0	0.6324	294	0.7135	326	0.7697	348
45	0.5180	587	0.6085	673	0.6741	732
60	0.3945	891	0.4880	1049	0.5607	1170
70	0.2653	1193	0.3510	1465	0.4250	1677
75	0.1852	1380	0.2571	1738	0.3231	2034
80	0.1000	1572	0.1488	2047	0.1975	2471

Figure 6 shows the tunes for a H_2^+ cyclotron with symmetry N=3, that has been studied at IBA. The upper figure shows the radial tune and vertical tune (2x) obtained from a numerical closed orbit code (black-solid and red solid respectively), and the radial tune (black-dashed) and vertical tune (2x, red-dashed) calculated analytically. In this example, the half-integer resonance hits at the radius of 48.2 cm, corresponding with an energy of 187.5 MeV/u and a vertical tune value of ν_z=0.27. The lower figure shows the flutter F and the spiral angle ξ of the magnetic field. At the resonance energy they are F=0.0074 and ξ=79.5° respectively. Table 2 shows an extreme energy for ξ=80° of 198 MeV/u. Correcting this value for the non-zero vertical tune (=0.27), we obtain the stopband energy at E=186.5 MeV/u. This is extremely close to the numerical result of 187.5 MeV/u. Our result for $N = 3$ agrees very well also with the result found by King and Walkinshaw [3] who report, in their study on the conversion of the Harwell synchrocyclotron, a proton energy limit of 190 MeV for a spiral angle of about 75°.

CONCLUSION

This work determines the minimum number of sectors that are needed for obtaining a given top energy with a compact isochronous cyclotron. It also provides the best trade off between spiral angle and flutter. The provided equations, graphs and tables may facilitate the conceptual and/or preliminary design of a new cyclotron.

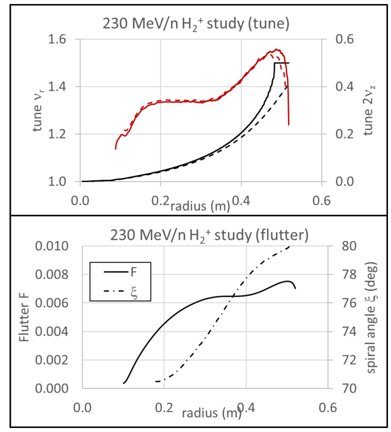

Figure 6: Example for a 230 MeV/u H_2^+ cyclotron.

ACKNOWLEDGMENT

The author wishes to express gratitude to Dr. Rick Baartman and Dr. Thomas Planche for many helpful discussions.

REFERENCES

[1] M. M. Gordon, "Orbit Properties of the Isochronous Cyclotron Ring with Radial Sectors", in *Ann. Phys.*, vol. 50, pp. 571-597, 1968. doi:10.1016/0003-4916(68)90132-2

[2] V. I. Danilov, Yu. N. Denisov, V. P. Dmitrievskij, V. P. Dzhelepov, A. A. Glazov, *et al.*, "Cyclotron With Space Variation Of The Magnetic Field", in *Proc. 2nd Int. Conf. High-Energy Accelerators and Instrumentation (HEACC'59)*, CERN, Geneva, Switzerland, Sept. 14-19, 1959, pp. 211-226.

[3] N. M. King and W. Walkinshaw, "Spiral Ridge Cyclotron Particle Dynamics Applied to Conversion of the Harwell Synchrocyclotron", in *Nucl. Instrum. Methods*, vol. 2, pp. 287-298, 1958. doi:10.1016/0369-643X(58)90115-4

[4] H. L. Hagedoorn and N. F. Verster, "Orbits in an AVF Cyclotron", in *Nucl. Instrum. Methods*, vol. 18,19, pp. 201-228, 1962. doi:10.1016/S0029-554X(62)80032-9

[5] W. Kleeven, in *On the Energy limit of compact isochronous cyclotrons*, Accepted for publication in the Journal of Instrumentation (JINST) as contribution to a special issue of the ICFA newsletter #84, on: *Dynamics of High Power and High Energy Cyclotrons*, Ed. Rick Baartman. Preprint: doi:10.48550/arXiv.2211.01029

[6] Y. Jongen *et al.*, "IBA-JINR 400 MeV/u Superconducting Cyclotron for Hadron Therapy", in *Proc. 19th Int. Conf. Cyclotrons and their Applications*, Lanzhou, China, 2010, pp. 404-409, paper FRM1CIO03.

[7] J. Mandrillon *et al.*, "Carbon Cyclotron for Particle Therapy", presented at CYCLOTRONS'22, Beijing, China, Dec. 2022, paper THBI01, this conference.

[8] V. Nuttens, J. Mandrillon, W. Kleeven, Q. Flandroy, Ph. Cailliau, and Ph. Velten, "Vacuum Model of the C400 Cyclotron for Hadrontherapy", presented at CYCLOTRONS'22, Beijing, China, Dec. 2022, paper THPO009, this conference.

ISBN: 978-3-95450-212-7 ISSN: 2673-5482 doi:10.18429/JACoW-CYCLOTRONS2022-THAO02

BEAM EXTRACTION SIMULATION AND MAGNETIC CHANNELS' DESIGN FOR MSC230 CYCLOTRON

D. Popov†, O. Karamyshev, V. Malinin, I. Lyapin, S. Shirkov
Joint Institute for Nuclear Research, Dubna, Russia

Abstract

MSC230 is a novate cyclotron for proton (FLASH included) therapy research, designed and developed by JINR. The extraction system of this machine includes only one electrostatic deflector followed by two magnetic correctors. These correctors were designed and included in global model to simulate beam extraction. The peculiarities of the design procedure and the outcome of the simulation is discussed in this paper.

INTRODUCTION

Joint Institute for Nuclear Research (JINR) is working on the design for the new cyclotron for proton therapy: MSC230 – Medical Super Conducting cyclotron of 230 MeV energy [1].

The main idea is to build very reliable and easy in production machine. This allows to maximize extracted beam current to be enough to FLASH therapy.

In order to do that, MSC230 combines advantages of two most successful accelerators in proton therapy – PROSCAN's Varian and IBA's C235. From C235 we took a low magnetic field and the fourth harmonic of acceleration, from Varian we took a superconducting coil, to reduce its weight to ~100 tones, and a constant gap between the sectors along the radius, wide enough to accommodate an electrostatic deflector, and as a result we have four free valleys for placing accelerating cavities connected in center.

JINR International Biomedical Research Center

The final goal of the project is to design and create an international biomedical innovation center at JINR, based on MSC230, for the next purposes:

1. Carrying out fundamental and applied research in the field of radiation biology and medicine, first of all, the FLASH method based on the methods of conformal irradiation from the medical beam of the Medical Technical Complex (MTC DLNP).
2. Training and improving qualifications of specialists in the field of radiation biology and medicine.
3. Creating necessary conditions for the introduction of the latest technologies in the field of proton therapy of oncological diseases into clinical practice.

ABOUT THE EXTRACTION SYSTEM

The extraction system of MSC230 is planned to be done by placing one electrostatic deflector (ESD) followed by two magnetic channels (MC1 and MC2), see Fig. 1. Every element is located under the sectors and surely must take into the account the dimension restriction caused the length of the sector's gap, normal to median plane, is being 50 mm. The azimuthal extent of every element is 40°.

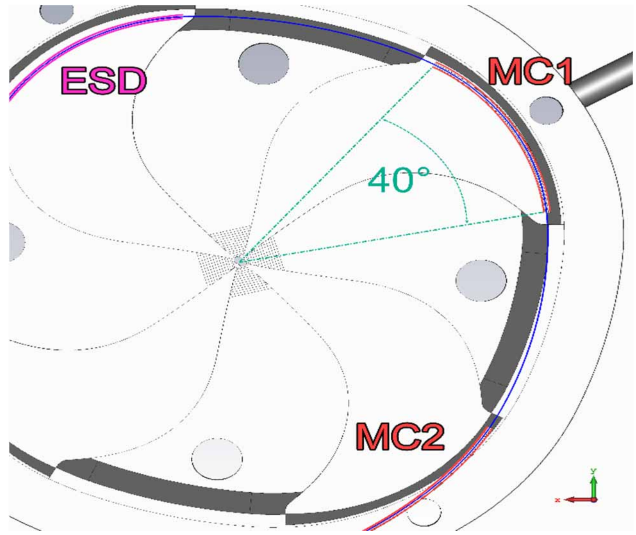

Figure 1: The location of the extraction system elements along beam extraction trajectory (blue curve).

ESD is placed with the idea to catch the beam right after it exits the second accelerating gap. The reliable design of the cyclotron allows to accelerate the beam only in 500 turns which provides the distance between equilibrium orbits of 1.5 mm at the deflector entry. Such design also decreases the requirements for voltage to be quite safe: the eclectic filed strength is only 100 kV/cm at maximum, i.e. the electrode voltage – 50 kV. Due to main beam losses mostly happen on the encounter face of the deflector's septum, septum thickness was chosen 0.1 mm. The aperture of the deflector is 5 mm

The beam, deflected by ESD, enters the first magnetic channel MC1 which continues extraction and decrease horizontal defocusing.

The sole purpose of MC2 is to suppress horizontal defocusing, for the beam to fit the required aperture.

MAGNETIC CHANNELS' REQUIREMENTS

The basic requirements for the channels are the following (see Table 1), which should be delivered along the intervals of the beam trajectory into the magnetic field shown in the Fig. 2.

Table 1: The Requirements for the Magnetic Channels

Channel	Aperture [mm]	Gradient [Gs/mm]	B_z shift [Gs]
MC1	10	100	-600
MC2	10	170	0

ISBN: 978-3-95450-212-7 ISSN: 2673-5482 doi:10.18429/JACoW-CYCLOTRONS2022-THAO02

We set the following tolerances for the requirements: one needs to meet gradient requirements within 12 mm aperture on median plane, keeping gradient deviation in 10%, for the external field of the average value (Fig. 2, grey lines). A channel, fitting these tolerances, is expected to be able to execute its function correctly.

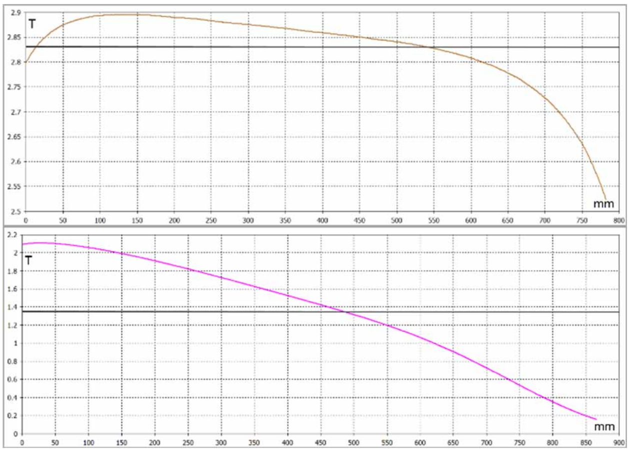

Figure 2: The vertical component of the magnetic field (B_z) along trajectory intervals for MC1 (top) and MC2 (bottom). Grey line is an averaged value.

Finally, the last pursue is to make channels more compact, that provides several benefits at once. Small mass reduces the effect of magnetic field distortions in the area of circulating beam, as well it reduces magnetic forces applied on the channel, reducing the size and complexity of the mount. And obviously, small dimensions of the channel make its displacement adjustment easier in several ways, also leaving room for other cyclotron devices.

DESIGN PROCEDURE PECULIARITIES

The design and simulation of magnetic channels were performed in CST studio suite.

Initial Design Stage

The initial design was done in the parametric model which simulates 2D cross section magnetic channels normal to the beam trajectory.

The major part of this search for the design is the variation of the form of the channel cross section in order to achieve the magnetic field alteration which is close to the requirements as much as possible. CST studio helps to automate this process and immensely reduce time spent on this procedure, due to the following two features. The first CST allows to parameterize the value of almost every initial variable of the model you build, in our case the dimensions (form) of the channel. The second – is easy way to process the results, in our case: to evaluate field on desired curve (or area), then to calculate the gradient on that curve, to give the integral deviation from required once (according to the chosen functional space metric), as the single scalar value outcome. This turns the model simulation into a scalar function from the parameters as arguments. The only thing is needed – is to enforce the convergence below desired tolerance by finding minimum of that function, which could be made manually, using Parametric Sweep dialog, or, in some cases, automatically by using Optimizer.

Full Magnet 3D Simulation

Once the initial design, that fits the requirements of 2D model, was found, the channels were inserted into 3D model of cyclotron magnet in order to perform the following actions. The first – is to check whether they fit the requirements all along the trajectory. If they failed to fit, then it could be corrected: 1) by going back and perform better initial design, 2) by varying parameters (e.g. thickness) or adding elements along trajectory. After that being done, one could conduct the extraction part of the beam dynamics simulation into full 3D magnetic field map to assess the quality of the channels.

THE RESULTS

Designed Channels' Overview

The initial design procedure was enough to create the following channels, using only 2D-like simulation. They have rather small dimensions and there for weight which makes them easy to place, easy to move, easy to hold. Nevertheless, the channels' aperture is relatively big, which results in good beam channeling and small collision beam losses.

The main idea is to get as close as possible to gradient requirements (Table 1) on the blue line, establishing B_z shift requirements in beam center, see Fig. 3. This resulted in the following channel profile design, enforcing required tolerance of 10% for MC1 and even twice less tolerance of 5% for MC2. MC1 and MC2 are made of steel 1010 and have a mass of 325 g and 525 g respectively.

The maximal error from required gradient in beam aperture zone for MC1 and MC2 is 40% and 23% respectively, which might seem big, but in fact, such deviation only occurs at the beam aperture border and affects very small portion of particles, where us for most of the particles the deviation is less than 15% and 10% respectively.

The magnetic field in MC2 almost comes down to a zero closer to the channel's end, as shown in bottom plot of Fig. 2. It was the reason for us to investigate and to mention here the possibility of the replacement of the last half of MC2 with a channel made of permendur vanadium, which provides better magnetic qualities keeping the same size [2, 3]. We will leave this procedure as additional adjustment option, since the beam dynamics simulation proved designed channels to be sufficient for the extraction.

ISBN: 978-3-95450-212-7 ISSN: 2673-5482 doi:10.18429/JACoW-CYCLOTRONS2022-THA002

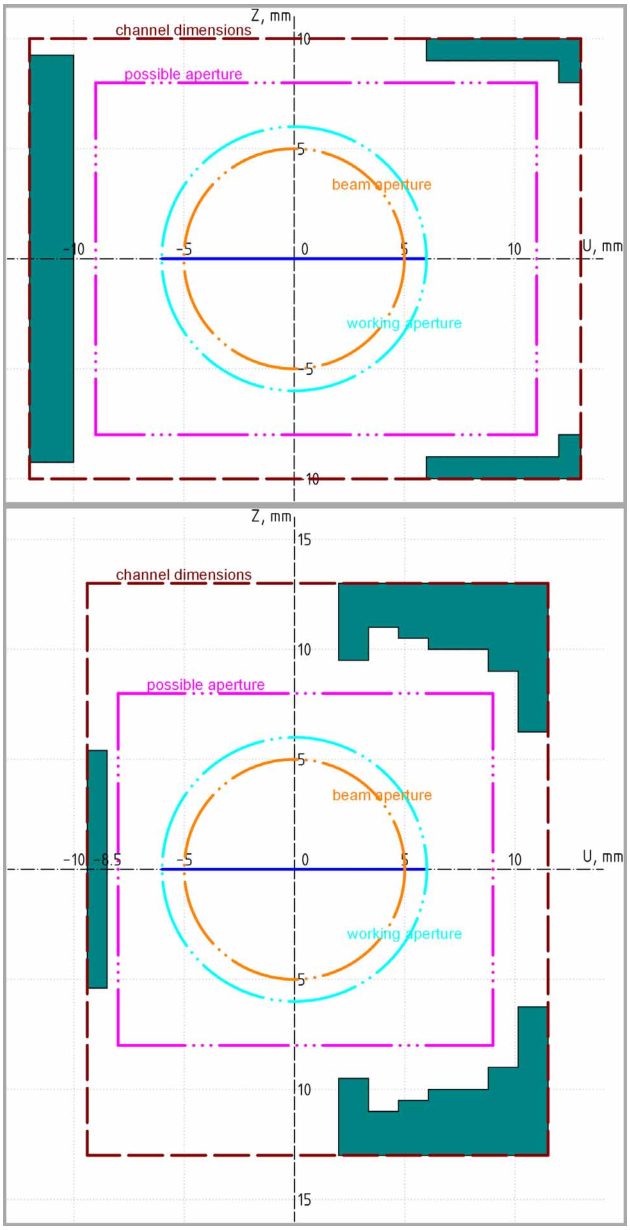

Figure 3: Axial cross section of MC1 (top) and MC2 (bottom), centered on the beam center. Blue line – the result line for 2D simulation.

Extraction Beam Dynamics

The tracing of beam though the extraction system was performed in 3D magnetic field maps which were calculated taking into account the magnetic channels and the compensating channels. The simulated computer model with correctors is shown in Fig. 4. The beam tracing, displayed on this figure, could be seen visually which helps to control the beam passing inside the cyclotron structure. The particle traces of the extracted beam are also presented in Fig. 5.

Beam dynamics provided pretty good results holding the beam within the aperture of 10 mm (Fig. 5). The calculated horizontal emittance at the accelerator's exit is about 8π mm·mrad, whereas the vertical one is about 2π mm·mrad.

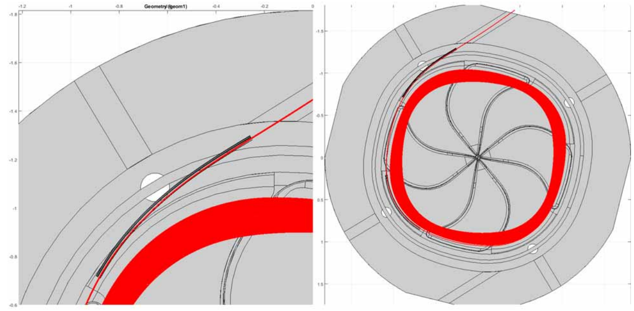
Figure 4: Beam dynamics simulation for the extraction interval conducted in full 3D field, above the cyclotron structure.

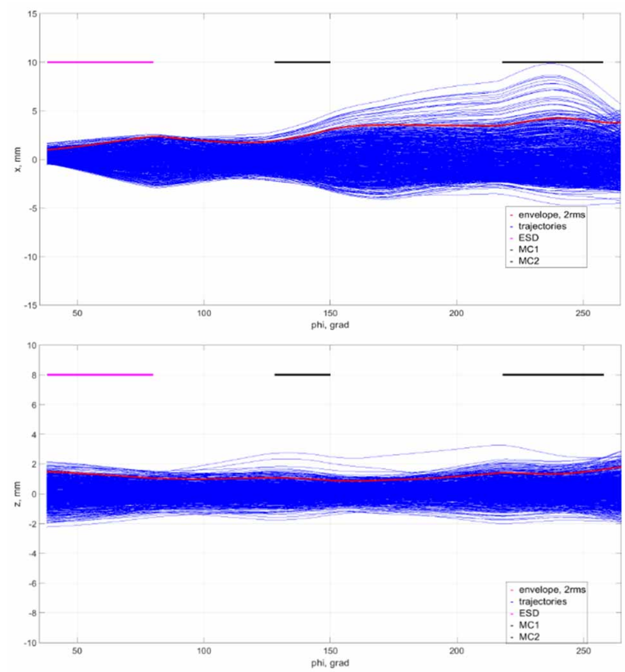

Figure 5: Radial motion (top) and vertical motion (bottom) of the particles through the extraction system.

FINAL WORDS

Created Channels

The MCs' design has been done within rather small tolerances for the requirements, during the initial 2D design stage. As the result, being inserted into full magnet 3D model, the channels immediately produced the magnetic field alteration that managed to perform the desired extraction through beam dynamics simulation. Also, the channels have rather small weight and dimensions which simplifies the mounting and the adjustment. Permendur vanadium option was taking into account in case of unforeseen complications.

CST Studio for Channel Design

The capabilities of CST EM Studio for magnetic channels design were thoroughly investigated. Despite the studio provides only 3D simulation for channels problem, in 3D we've managed to create parametric model for 2D channel axial cross section in external (main) magnetic

ISBN: 978-3-95450-212-7 ISSN: 2673-5482 doi:10.18429/JACoW-CYCLOTRONS2022-THAO02

field. The model was also supplied with Post Processing module that evaluates required values after every solver run. Special model geometry allows differentiate the field alteration with an error less than 0.5 Gs, consuming only 2 seconds. As se result, the search for the right channel profile has been done within dozens of minutes.

FUTURE PLANS

Developing Automation Application

The most important outcome for cyclotron design is that, during this job, there were automated several significant design steps. Combined with acquired experience, it is planned to create special application for magnetic channels design. For a start, we are planning to create CST module (macros most probably). When it's completed we will write MATLAB code to orchestrate the action of other modules of other simulation packages (COMSOL [4], Tosca, Maxwell, FEMM, etc...) which will be added in future. This code will join other MATLAB codes (e.g. CORD [5]) to become a part of integrated platform for cyclotron virtual prototyping.

REFERENCES

[1] O. V. Karamyshev *et al.*, "Research and Development of the SC230 Superconducting Cyclotron for Proton Therapy", *Phys. Part. Nucl. Lett.*, vol. 18, pp. 63-74, Feb. 2021. doi:10.1134/S1547477121010088

[2] L. Neri *et al.*, "New method to design magnetic channels with 2D optimization tools and using permendur vanadium", *J. Phys. Conf.: Ser.*, vol. 1401, pp. 012007, Lanzhou, China, Oct 2018. doi:10.1088/1742-6596/1401/1/012007

[3] L. Neri *et al.*, "3D Magnetic Optimization of the New Extraction Channel for the LNS Superconducting Cyclotron", in *Proc. Cyclotrons'19*, Cape Town, South Africa, Sep. 2019, pp. 54-57. doi:10.18429/JACoW-Cyclotrons2019-MOP014

[4] D. Popov *et al.*, "Continuous Beam Dynamics Simulation in COMSOL Multiphysics", in *Proc. IPAC'21*, Campinas, Brazil, May 2021, pp. 4153-4155. doi:10.18429/JACoW-IPAC2021-THPAB192

[5] O. Karamyshev *et al.*, "Cord (Closed Orbit Dynamics): A New Field Map Evaluation Tool for Cyclotron Particle Dynamics", *Phys. Part. Nucl. Lett.,* vol. 18, pp. 481-487, Feb. 2021. doi:10.1134/S1547477121040117

ISBN: 978-3-95450-212-7 ISSN: 2673-5482 doi:10.18429/JACoW-CYCLOTRONS2022-THBI01

STATUS ON NHa C400 CYCLOTRON FOR HADRONTHERAPY

J. Mandrillon†, M. Abs, Ph. Cailliau, S. Deprez, X. Donzel, G. Goose, Y. Jongen, W. Kleeven, L. Koffel, V. E. Nuttens, Y. Otu, Y. Paradis
Ion Beam Applications (IBA), Louvain-La-Neuve, Belgium
O. Cosson, L. Maunoury, Ph. Velten, Normandy Hadrontherapy (NHa), Caen, France

Abstract

The NHa C400 is an isochronous cyclotron for cancer therapy delivering high dose rates of alphas to carbons at 400 MeV/amu and protons at 260 MeV. NHa company, of which IBA is a major shareholder, designs, produces and markets the new multi-ions C400 based therapy system while IBA experts are deeply involved in all aspects of its conception. IBA and NHa have restarted studies in 2019 based on the conceptual report from the JINR and IBA collaboration, reviewed in 2009 by cyclotron community experts. Final designs of major subsystems are presented highlighting some specific aspects related to the complexity of this large cyclotron.

THE C400

Parameters in Table 1 have barely changed from the conceptual study [1], published in [2, 3]. IBA and NHa have launched an extra pass on the design of subsystems before releasing drawings for manufacturing.

Table 1: C400 Design Parameters

Parameter	Value
Accelerated ions	H_2^+;$^4He^{2+}$;($^6Li^{3+}$); ($^{10}B^{5+}$);$^{12}C^{6+}$
Injection energy	26 keV/Z
Final energy of ions,	400 MeV/amu
protons	265 MeV
Number of turns (ions)	~2100
Magnet system	
Iron weight	738 Tons
Outer diameter	7 m
Pole radius	1.87 m
Max field (Hill; Valley)	~4.5 T; 2.45 T
Stored energy	55 MJ
Superconducting material	NbTi
Conductor peak field	3.9 T
Current density	~31 A/mm²
RF system	
Frequencies ($^{12}C^{6+}$; H_2^+)	75 MHz; 75.6 MHz
Operation	4th harmonic
Number of dees	2
Voltage (centre; extraction)	60 kV;150 kV

The C400 has three independent ion sources (H_2^+;$^4He^{2+}$;$^{12}C^{6+}$) mounted on a platform on top of the cyclotron vault (Fig. 1). Protons are obtained via stripping of H_2^+ at 265 MeV/amu while ions are extracted via an electrostatic deflector followed by a magnetostatic channel. Magnet poles are 4-fold symmetry, hills and valleys are strongly spiralized, hills have an elliptical shaped vertical aperture for the beam (Figs. 2 and 3).

The cryostat houses two subsoils per coil (Fig.4) balancing currents between them allows magnetic field profile corrections, which is necessary to switch between isochronous fields of each particle.

The large size of the cyclotron is inherently challenging for many aspects of the project. Indeed, transport/handling/assembly on site, accessibility for maintenance, etc. all become critical requirements for any subsystem design. The multi-particle feature also provides its share of complexity, especially concerning the management of the specific beam tuning required for each extraction modes.

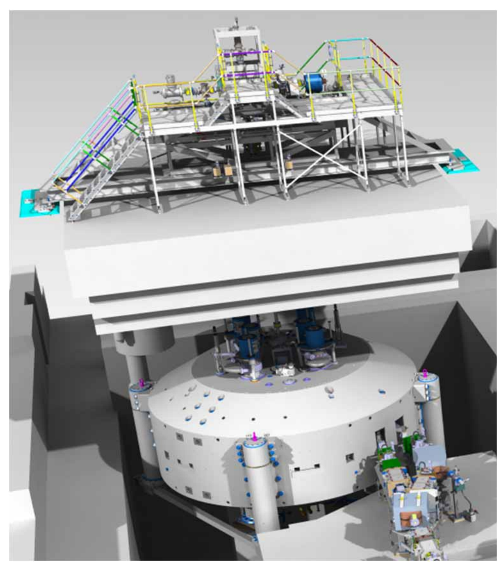

Figure 1: Layout of the C400 cyclotron and its injection system. A vertical transport line passing through the concrete floor connects the two systems.

Magnet Design

Few recent modifications had a large impact on the magnet detailed design. To reduce pumping time and to keep high transmission for molecular hydrogen acceleration, as described in [4], the holes in the valleys of the pole have been significantly enlarged since [1], this imposing a slight reduction of the azimuthal width of the hills.

ISBN: 978-3-95450-212-7 ISSN: 2673-5482 doi:10.18429/JACoW-CYCLOTRONS2022-THBI01

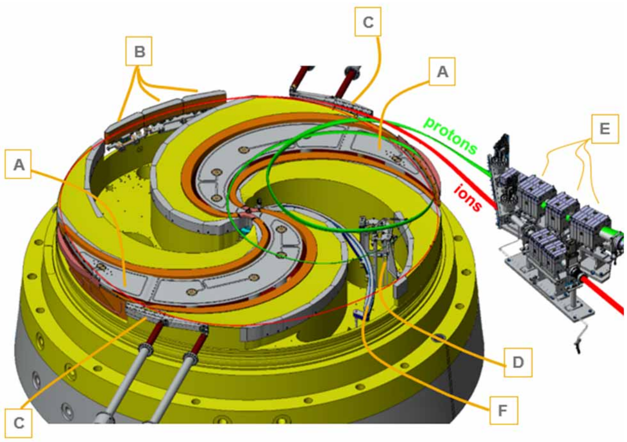

Figure 2: C400 inside view with its subsystems on bottom pole: (A) Dees; (B) Electrostatic deflector; (C) Magnetostatic Channel & symmetrical parts; (D) Stripper positioning system; (E) Extraction tables with permanent magnet quadrupole assemblies, (F) Radial probe.

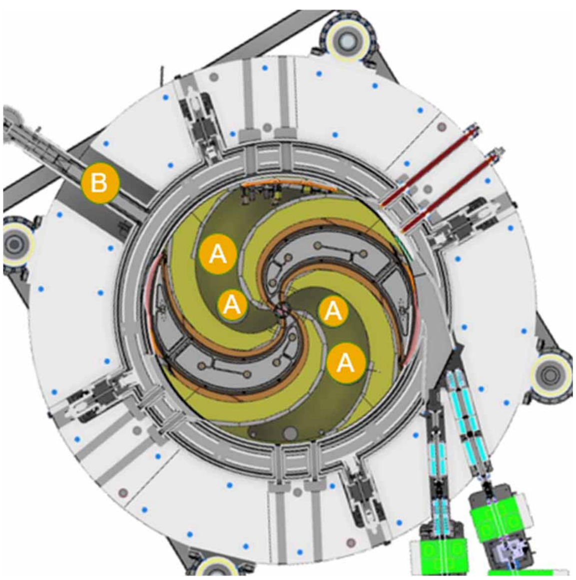

Figure 3: C400 yoke at median plane: (A) Enlarged pumping holes, (B) Umbilical of Helium vessel.

The resulting magnetic field drop is efficiently compensated by field increase produced by few extra centimetres on yoke diameter, while alternatively an increase of the nominal current would have result in an excessive hoop stress on the selected conductor.

Figure 3 shows the final arrangement of the different penetrations in the return yoke, cancelling harmonic #1 in the magnetic field under the poles.

Large and thin resistive coils with opposite currents will be installed on top and bottom of the cryostat (see Fig. 4), providing a mean to compensate possible median plane errors and to lower related asymmetrical vertical forces on cold mass at the same time.

As shown on Fig. 4, 360° iron rings have been designed on the maximum radius of the - single cast – poles (top and bottom) to compensate the magnetic field drop resulting from the insertion of these resistive coils in the upper and lower yokes.

Moreover, grooves are machined in these rings to house radial vacuum seals between poles and cryostat.

Following the 2009 design, the magnet assembly is divided into sub parts weighing up to 70 tons. All those building blocks have already been manufactured and will be assembled directly on site in the coming months (Fig. 5).

Superconducting coils and cryostat are designed and manufactured by SigmaPhi® company. Coils have been winded and placed in the helium vessel (Fig. 6).

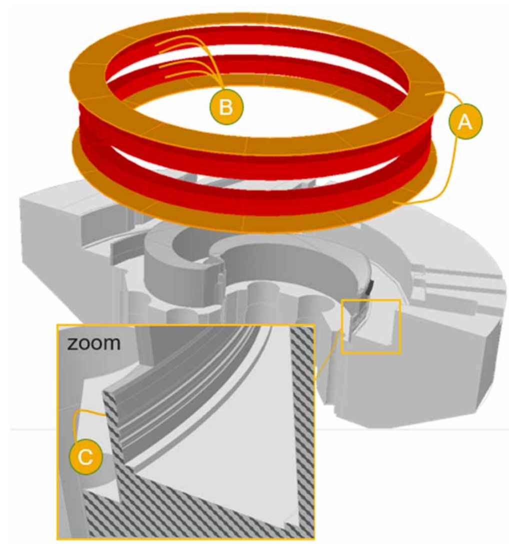

Figure 4: C400 coils and iron cut view through RF valleys: (A) The two resistive coils for median plane errors correction; (B) The 4 superconducting sub-coils; (C) 360° iron ring.

Figure 5: Manufactured part of C400 yoke.

Figure 6: C400 Helium vessel, welding completed.

23rd Int. Conf. Cyclotrons Appl. CYCLOTRONS2022, Beijing, China JACoW Publishing
ISBN: 978-3-95450-212-7 ISSN: 2673-5482 doi:10.18429/JACoW-CYCLOTRONS2022-THBI01

RF System

RF power consumption has been optimized mainly by shaping the stems and adjusting acceleration gaps width. For movable tuners, that can slide over 200 mm, are installed on cavities to switch to adequate frequency for each type of particle. Each of the two RF cavities will be powered by 128 kW - IBA designed - solid state amplifier, expecting 80 kW RF losses per cavity at nominal voltage.

Specific and adaptative geometries of the dee and liner enclosures at maximum radius have been designed to provide the protons enough space to loop at the back of the cavities before being extracted. The position of the protons loop can vary by few centimetres according to the stripper position (Fig. 7) and by few millimetres according to the shimming of the pole edges during the mapping process to isochronize the machine, with large impact on transmission and beam transversal emittances at cryostat exit.

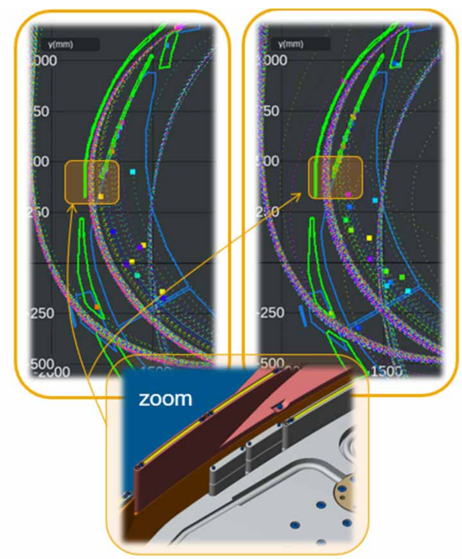

Figure 7: C400 RF geometry and protons internal loop; (zoom) adaptative length of the dee closure at pole maximum radius; (left and right) 2 potential positions of horizontal trajectories of protons for 2 different positions of the stripper foil.

The cavities are currently being manufactured following this process: sheet metal work, TIG welding and finally remachining of over-thicknesses (see Fig. 8).

Figure 8: Shop test assembly of a C400 liner.

Extraction Systems - Ions

The positions and orientations of the ElectroStatic Deflector (ESD) and MagnetoStatic Channel (MSC) are crucial during the beam commissioning. Therefore, actuators have been included by design to allow for a fine tuning of the transmission and transversal emittance of the extracted beam. Beam dynamics studies with AOC code [5] have validated the design of a single ESD in a non-RF valley to extract the ions from the C400 pole with ~160 kV/cm electric field between septum and high voltage blade.

The MSC has been enlarged to account for the potential need for steering the extracted beam to optimize extraction. It has also been shortened to clear out the protons extraction path from the close-by cryostat walls.

Extraction Systems - Protons

The stripping device must however be removed from median plane in the other ion modes to achieve acceleration up to 400 MeV/amu. Also, the stripping foil itself is a consumable that needs to be replaced periodically, ideally without breaking the cyclotron vacuum to avoid a >10h downtime following maintenance [4]. Following these requirements, a precise positioning system has been designed to fit in the hole of the adjacent non-RF valley. The adjustability range and repeatability precision that such a mechanical system needed to fulfilled was cross-checked with extensive beam dynamic studies. Figure 9 illustrates the motion range of the stripper holding arm.

Drawings have been released, the arm motion and the sequence of operations in the stripper air locker will be tested and validated in factory.

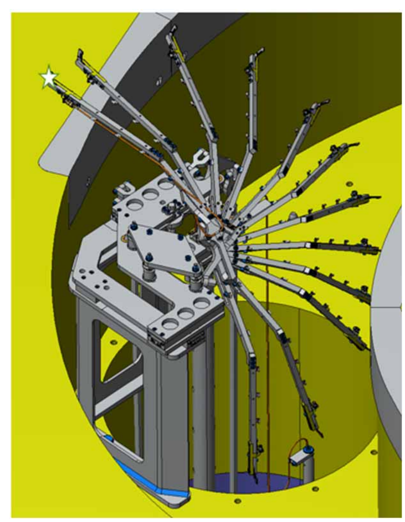

Figure 9: Stripper holder motion from stripping position (star) to air locker, combined rotation and translation.

Passive Extraction Tables

Beams extracted from the cryostat are transported to the beam lines located outside of the C400 magnetic field via permanent magnet quadrupoles assemblies providing longitudinal and transversal adjustment capabilities (Fig 10.)

23rd Int. Conf. Cyclotrons Appl. CYCLOTRONS2022, Beijing, China JACoW Publishing
ISBN: 978-3-95450-212-7 ISSN: 2673-5482 doi:10.18429/JACoW-CYCLOTRONS2022-THBI01

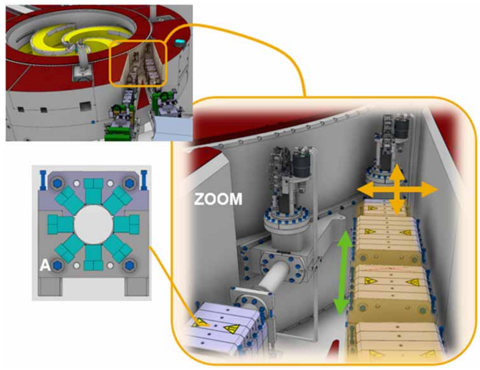

Figure 10: Extraction PMQ assemblies; On Zoom: (orange arrows) steering capabilities; (green arrow) focusing capabilities; (A) transversal view of permanent magnet quadrupole slice.

Fundamental Resonance Crossing

The conceptual physics design of this cyclotron imposes a $3\nu_r$=4 fundamental resonance crossing located at around 250 MeV/amu.Beam dynamics studies were conducted to identify and implement the most efficient means to reduce the beam losses induced by the vanishing of the horizontal stability that occurs during this crossing.

First action is to lower the number of turns in the instability region by introducing grooves and rods in harmonic #2 along pole profiles. It speeds up the increase of the horizontal tune parameter (Fig. 11) while balancing phase advance and phase delay before and after the resonance.

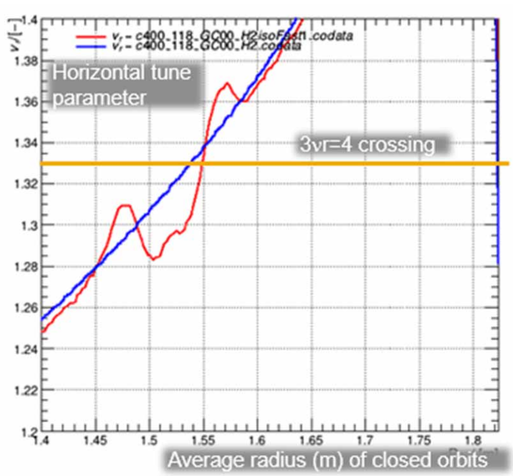

Figure 11: $3\nu_r$=4 crossing – Horizontal tune parameter as a function of closed orbits average radius; Red (resp. blue): With (resp. without) specific grooves and rods along the pole edges.

Nevertheless, as illustrated looking at the density of points on Fig. 12 (A), the more the particle is off-centre, the more the amplitude of its horizontal oscillation grows from turn to turn. Therefore, the major mitigation happens in central region: a pillar between the two first turns of acceleration intercepts off-centre part of beam at low energy to avoid activation of parts at resonance level (Fig. 13).

For the 400 MeV/amu beams, the complete tracking model with AOC code [5] from the vertical injection line to the exit flange of the cryostat has shown that 1 particle is lost in resonance for 5 particles reaching the exit. Considering additionnal losses over the extraction process, 50% of the high energy beam reaches cryostat exit flange in AOC simulations.

CONCLUSION

Starting on the solid basis of the 2009 conceptual report, an extra pass on all subsystems has been necessary before releasing drawings of the c400. Manufacturing of cryostat, magnet and RF cavities are being completed, NHa and IBA expect beam commissioning by end of 2025.

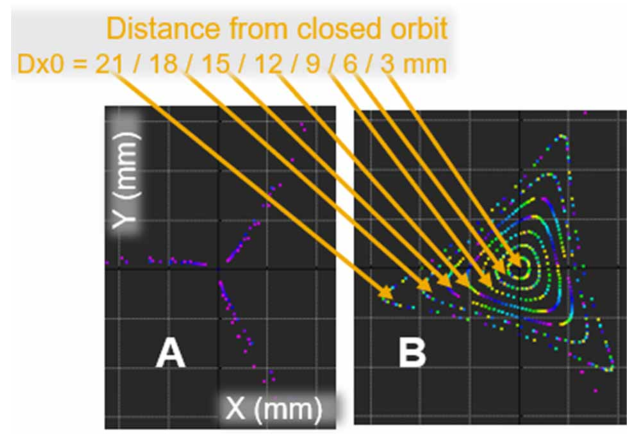

Figure 12: Centres of curvatures (averaged on each turn, plot once every turn) for 7 orbits oscillating around closed obit over 100 turns – no acceleration; (A) at resonance level – 250 MeV/amu; (B) outside resonance – 280 MeV/amu.

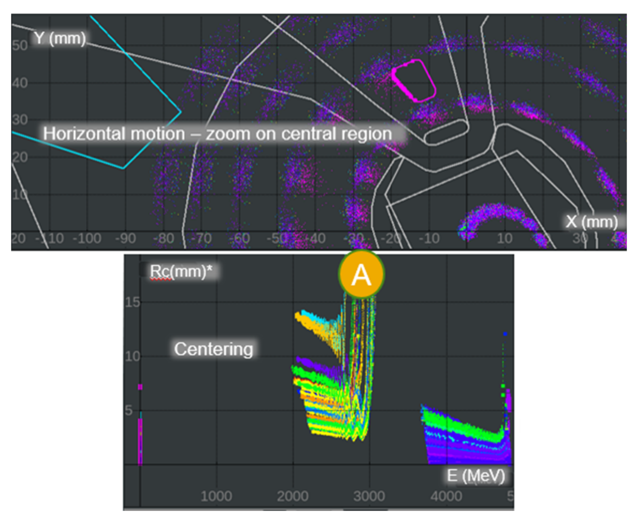

Figure 13: (top) Particles horizontal trajectories in central region with a pillar - in pink - to stop off-centre beam; (bottom) radius of centres of curvature (averaged on each turn) of the accelerated beam as a function of total energy for C^{6+}. (A) Residual beam losses at resonance crossing for the most off-centre particles.

ISBN: 978-3-95450-212-7 ISSN: 2673-5482 doi:10.18429/JACoW-CYCLOTRONS2022-THBI01

REFERENCES

[1] G. Karamysheva *et al.*, "Design Report of Superconducting Cyclotron C400 for Hadron Treatment", IBA internal report, 2009, unpublished.

[2] Y. Jongen *et al.*, "Current Status of the IBA C400 Cyclotron Project for Hadron Therapy", in *Proc. EPAC'08*, Genoa, Italy, Jun. 2008, paper TUPP120, pp. 1806-1808.

[3] Y. Jongen *et al.*, "Iba C400 Cyclotron Project for Hadron Therapy", in *Proc. Cyclotrons'07*, Giardini-Naxos, Italy, Oct. 2007, pp. 151-156.

[4] V.E. Nuttens *et al.*, "Vacuum model of the c400 cyclotron for hadrontherapy", in *Proc. Cyclotrons'22*, Beijing, China, Dec. 2022, paper THPO009, this conference.

[5] W. Kleeven *et al.*, "AOC, a beam dynamics design code for medical and industrial accelerators at IBA", in *Proc. IPAC'16*, Busan, Korea, May 2016, pp. 1902-1904. doi:10.18429/JACoW-IPAC2016-TUPOY002

ISBN: 978-3-95450-212-7 ISSN: 2673-5482 doi:10.18429/JACoW-CYCLOTRONS2022-THBI02

STATUS REPORT ON THE CYCLOTRON INJECTOR FOR HIMM*

G. L. Dou[1,2], B. Wang †,[1], X. Chen[1,2], Q. G. Yao[1], X. W. Wang[1], L. Yang[1], C. C. Li[1], L. T. Sun[1,2], H. W. Zhao[1,2]

[1]Institute of Modern Physics, Chinese Academy of Sciences, Lanzhou, China

[2]School of Nuclear Science and Technology, Univ. of Chinese Academy of Sciences, Beijing, China

Abstract

HIMM (Heavy Ion Medical Machine) is an accelerator complex designed by Institute of Modern Physics, CAS, which accelerates carbon ions to the energy 400 MeV/A for tumour therapy. The main accelerator of HIMM is a synchronous accelerator. As a special design, we use a cyclotron as the injector of the synchrotron. The cyclotron is a compact cyclotron to accelerate $^{12}C^{5+}$ ions to the energy 6.8 MeV/A, and the extracted beam intensity of the cyclotron is 10 eμA. For stability and simplicity operation, we use two identical permanent magnet ECR ion sources in the axial injection line, that the ion sources can interchange with each other rapidly with the same performance, and only one main exciting coil with no trim coils in the cyclotron magnet. Up to now, three cyclotrons have been accomplished, one of them was operated in Gansu Wuwei Tumour Hospital to treat more than six hundred cancer patients in the last two and a half years, the other one had been fully commissioned in Lanzhou Heavy Ion Hospital about two years ago. After a short introduction to the heavy ion cancer treatment facility development in China, this paper will present operation status of the cyclotrons for HIMM. Typical performance and on-line operation reliability will be discussed.

INTRODUCTION

HIMM (see Fig. 1) is an accelerator complex designed by Institute of Modern Physics, CAS, which can accelerate carbon ions to the energy 400 MeV/A for tumour therapy. The beam is generated from the ECR ion source and passes through the LEBT, the injector HIMM-IC (Injector cyclotron), the MEBT, the main accelerator HIMM-SYN (Synchrotron) and the HEBT to the treatment terminals.

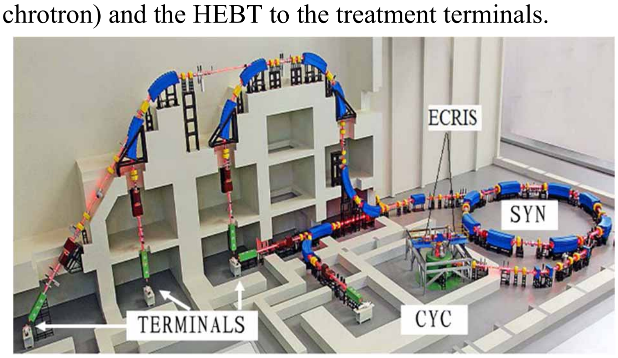

Figure 1: Layout of HIMM. ECRIS: ECR ion sources. CYC: Injector cyclotron. SYN: Synchrotron. TERMINALS: Treatment terminals.

*Work supported by Technology development programme 22ZY2QA003.
†email address: wangb@impcas.ac.cn

As a unique design, HIMM is the only medical cancer treatment facility in the world that uses a cyclotron as an injector. HIMM-IC (see Fig. 2) is a compact isochronous cyclotron [1, 2], which has a whole magnet without any trimming coils. It can accelerate $^{12}C^{5+}$ ions to the energy of 6.8 MeV/A at extraction, beam intensity no less than 10 eμA.

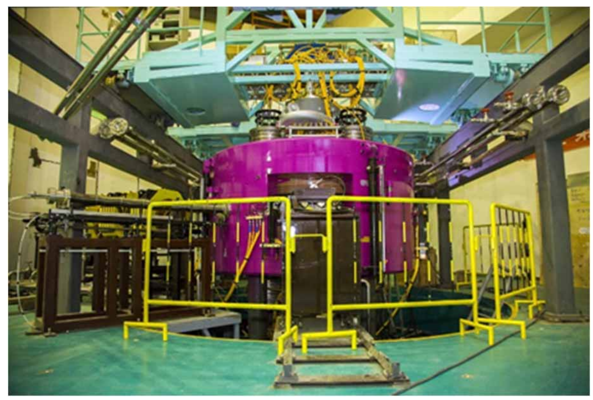

Figure 2: HIMM-IC installed on site.

Up to now, there are three HIMM facilities built and installed in China [3]. The HIMM in Gansu Wuwei Tumour Hospital (see Fig. 3) has treated more than six hundred cancer patients in the last two and a half years. The other two HIMMs in Lanzhou and Putian have also completed installation and are now being prepared and commissioned before clinical treatment.

Taking Wuwei's HIMM facility as an example, for routine operation of the HIMM-IC, an extraction of 5.5 μA (CW) ion beam has been made, which enables the acceleration of 2000 μA (pulsed) C^{5+} beam intensity (see Fig.3) with the main accelerator HIMMSYN, and the beam intensity delivered to the treatment terminals is typically 4×10^8 ppp. These indexes have well met the requirements of medical cancer treatment facilities.

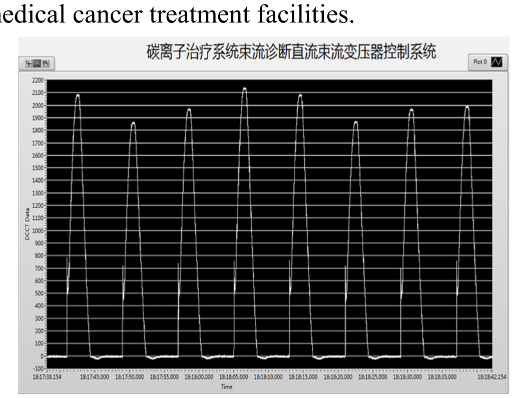

Figure 3: Beam intensity in the synchrotron.

23rd Int. Conf. Cyclotrons Appl. CYCLOTRONS2022, Beijing, China JACoW Publishing
ISBN: 978-3-95450-212-7 ISSN: 2673-5482 doi:10.18429/JACoW-CYCLOTRONS2022-THBI02

CHARACTERISTICS OF HIMM-IC

The HIMM-IC is a compact cyclotron without any trimming coils. Considering the conditions of application of medical facilities, we focused on the stability and simplicity of the cyclotron in design and manufacture phase. The main parameters of the cyclotron are shown in Table 1.

Table 1: HIMM-IC Main Parameters

Parameter	Value
Particle	$^{12}C^{5+}$
Energy	6.8 MeV/A
Intensity	10 eμA
Emittance	20-25 π•mm•mrad
Magnet Size	Φ2920mm×1520mm
Energy spread	±1%
Extraction radius	750 mm

Injection System

We use the external ion source combined with axial injection line [4] in order to obtain a high beam stability and beam intensity. The axial injection system of HIMM-IC is mainly composed of two permanent magnet ECR ion sources and axial injection line. The structure of axial injection system is shown in Fig. 4.

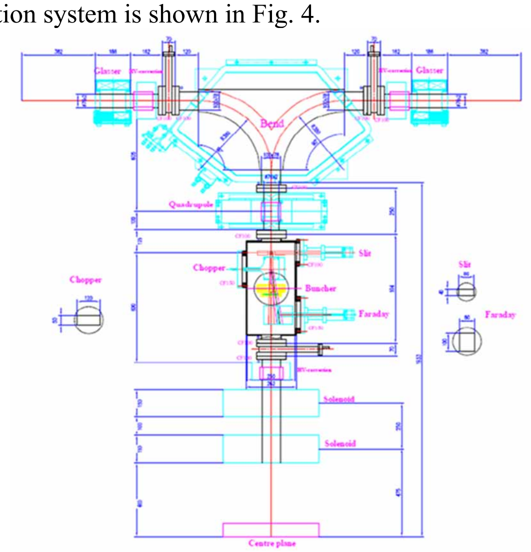

Figure 4: Layout of axial injection system.

The permanent magnet ECR ion source has the advantages of high stability and lower cost. We designed and installed two ECR ion sources for HIMM-IC, which can make continuous beam supply in case of breakdown of the operating ion source. The ion sources can provide maximum 150 eμA $^{12}C^{5+}$ beam at the extraction energy of 4.4 keV/A was used for long-term routine operation.

The axial injection system is composed of double direction dipole magnets, measurement chamber, solenoids and multi-harmonic buncher. It is very compact, and the whole length is only 3.5 meters. It can transport the beam from the exit of ECR ion source to the inflector at the cyclotron central region. The multi-harmonic buncher can improve the utilization of the DC beam deliverd by the ECR ion source, which enables the transmission efficiency to reach 59%.

Magnet

Considering the conditions and requirements of medical facility, the magnet [5] of HIMM-IC (see Fig. 5) is simple which is composed of a whole magnet without any trimming coils. So, we trim the sector edge and optimize the hill gap to achieve the requirement of the isochronism. The main parameters is shown in Table 2.

Table 2: Magnet Main Parameters

Parameter	Value
Central magnet field	1.212 T
Maximum magnet field	1.705 T
Magnet sectors	4
Sector angle	56°
Pole radius	84 cm
Hill gap	70-80 mm
Valley gap	360mm

The designed magnet can provide isochronous magnetic field with ±10 Gs error (see Fig.5) to the theoretical magnetic field. The results of the tune diagram satisfy the focusing in the acceleration region and avoid dangerous resonance before extraction (see Fig. 6).

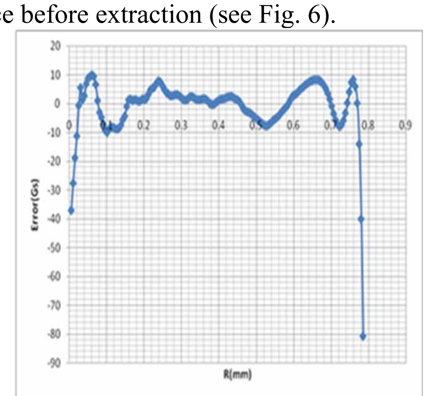

Figure 5: Magnet field error.

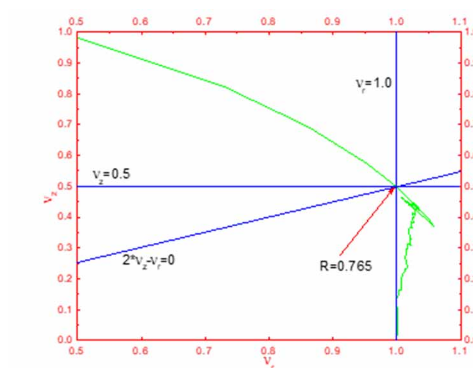

Figure 6: Tune diagram.

RF System

HIMM-IC has two independent RF cavities (see Fig. 7) and two 50 kW amplifiers to generate the acceleration electric field. The RF cavities were installed into the valleys of

ISBN: 978-3-95450-212-7 ISSN: 2673-5482 doi:10.18429/JACoW-CYCLOTRONS2022-THBI02

the magnet, two capacitance couplers near the outer radius of Dees imported rf power into cavities, two 50 kW rf amplifiers connected the couplers with coaxial transmission lines respectively. Near the short plane of cavities, we installed frequency tune device and rf sampling device to tune the cavities tinnily. To satisfy the stability of the accelerator operation, we demanded the higher stability of the cavity's amplitude, phase, and frequency. The detailed parameters of RF system are shown in Table 3.

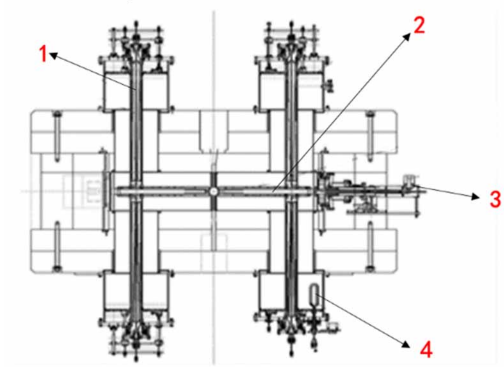

Figure 7: RF system.1-Inner steam, 2-Dee, 3-Coupling import, 4-Tuner.

Table 3: RF System Main Parameters

Parameter	Value
RF frequency	31.02 MHz
Dee voltage	70 kV
Dee angle	30°
Outer radius	750 mm
Inner radius	35 mm
Phase stability	±1°
Amplitude stability	$\pm5\times10^{-4}$/day
Frequency stability	$\pm1\times10^{-6}$/day
Q value	7800
Amplifier number	2
Amplifier power	50 kW

Extraction System

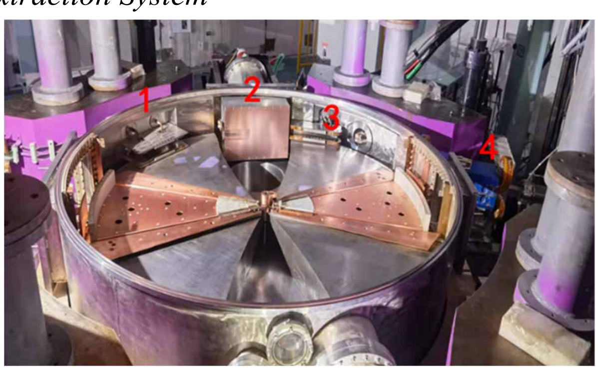

Figure 8: Layout of extraction system:1-BUMP, 2-ESD, 3-GCC, 4-MC.

The extraction system (see Fig. 8) was composed of a bump coil (BUMP), a electrostatic deflector (ESD), and a gradient corrector with compensation coil (GCC) and a magnetic deflector channel (MC) [6]. We could increase the turn separation to 10 mm using the bump field before the entrance of ESD. To improve the horizontal focus of MC and reduce its effect to sector's magnetic field in the outer radius, we optimized the MC's design to add a GCC ahead of it and make its yoke to be magnetic saturation. The detailed parameters are shown in Table 4.

Table 4: RF system main parameters

Parameter	Value
ESD E field	80-85 kV/cm
ESD gap	10 mm
BUMP B field	300 Gs
GCC G field	10 T/m
MC B field	1.1 T
Turn separation	10 mm

Beam Simulation

After the basic design, we simulate the beam transport from the ECR ion source to the match point of the MEBT (middle energy beam line). We used the cyclotron beam dynamics software-SNOP to complete the above simulation and obtained the end-to-end orbit (see Fig. 9) [2].

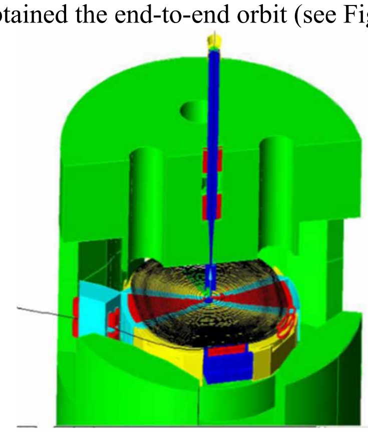

Figure 9: The end-to-end orbit.

We tracked the beam trajectory throughout the simulation and obtained the beam horizontal emittance of 60 π•mm•mrad and an axial emittance of 13 π•mm•mrad at the matching point of the MEBT, with a momentum dispersion of ≤±0.5% (see Figs. 10 and 11), which meet the requirements of the synchrotron. In addition, by tracking the number of macro-particles at different positions during the simulation, we obtained the beam transmission efficiencies as shown in Table 5.

Table 5: Beam Transmission Efficiency (Simulation)

Parameter	Value
Emittance of ECR	75 π•mm•mrad
ECR beam intensity	100 eμA
Efficiency of beam line	90%
Efficiency of injection	43%
Efficiency of extraction	47%
Total transmission efficiency	18%

ISBN: 978-3-95450-212-7 ISSN: 2673-5482 doi:10.18429/JACoW-CYCLOTRONS2022-THBI02

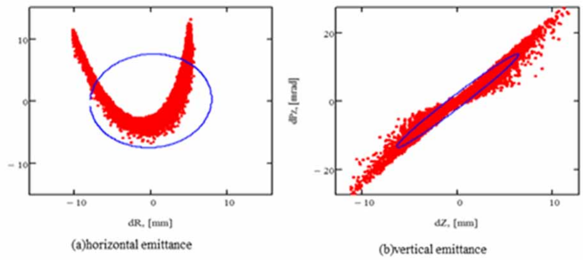

Figure 10: The phase space at the match point of the MEBT. Left: (x, x') plane. Right: (z, z') plane.

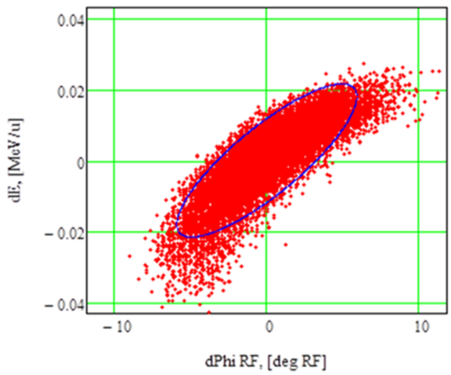

Figure 11: The longitudinal phase space at the match point of the MEBT.

MANUFACTURES AND OPERATIONS

Manufactures

HIMM-IC was designed from 2006 until its successful commissioning in 2014. The milestones are given below [3].

- The design phase: 2006-2014.
- The first cyclotron (see Fig.12) installed in IMP: 2014.08.
- The first commissioning of the cyclotron: 2014.08.15.
- The first extracted beam: 2014.08.16, 1 enA beam extracted.
- Extracted beam intensity reached 12 eμA: 2014.09.26.

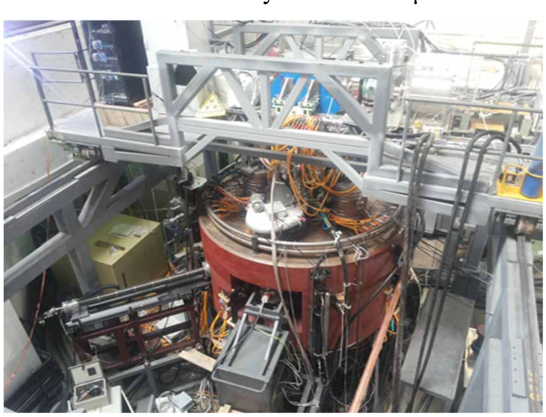

Figure 12: The first HIMM-IC in IMP.

Operations

The HMM-IC was relocated in Gansu Wuwei Tumor Hospital in 2015 and used for treating the patients since April 1st, 2020. Up to now, more than 600 patients have completed their treatment in the hospital. It shows a good operation status.

The operating efficiency of HIMM-IC in the last two years is shown in Table 6, which is well above 99%. And the maximum beam current can reach 11 eμA (see Fig. 13) when the ECR ion source provided 80 eμA. So, the overall transmission efficiency of HIMM-IC is about 13 percent.

Table 6: Operating Efficiency of HIMM-IC

Scheme	Operation time(h)	Failure time(h)	Operation rate
20200326-20210123	7296	31.62	99.57%
20210322-20220129	7536	66.05	99.12%
20220216-20220822	6936	54.15	99.22%

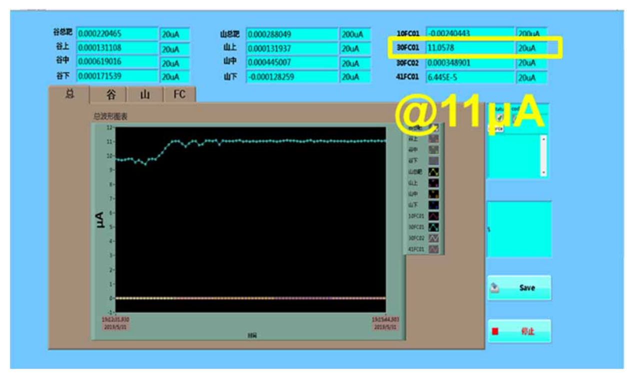

Figure 13: The extraction intensity in Cyclotron.

Considering the operating environment and condition of medical facility, we need to strictly control the beam radiation, stability of operation and other problems. We will stop the machine every two years for overhaul, and check and clean the inflector once a year. Consequently, long-term routine operation at the beam intensities (see Fig. 14) of HIMM-IC 5.5 eμA, and HIMM-SYN 2000 eμA is guaranteed that is essential for reliable clinical treatment operation. And the transmission efficiency is about 11% (see Table 7).

Table 7: Beam Transmission Efficiency (Measurement)

Parameter	Value
Exit of ECR	50 eμA
Central region	19.2 eμA
Extraction region	18.94 eμA
Match point of MEBT	5.5 eμA
Efficiency of injection	38.4%
Efficiency of extraction	29%
Total transmission efficiency	11%

The second HIMM-IC was installed in Lanzhou Heavy Ion Hospital, Lanzhou city, Gansu province, China, in 2017. And the third cyclotron was installed in Mazu Heavy Ion Hospital, Putian City, Fujian province, China, in 2020.

ISBN: 978-3-95450-212-7 ISSN: 2673-5482 doi:10.18429/JACoW-CYCLOTRONS2022-THBI02

HIMM-IC in Lanzhou has been used for clinical treat-ment trial operation in 2022, and HIMM-IC in Putian has been recently successfully commissioned with beam extraction.

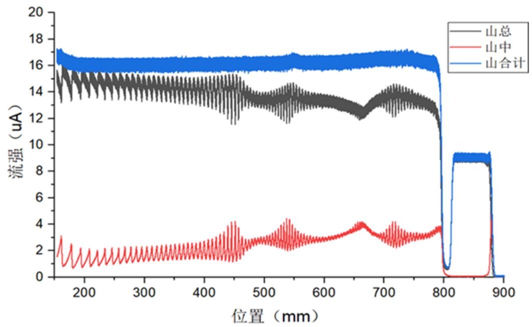

Figure 14: The beam intensity measured by radial probe. Red: Beam intensity measured by differential target. Black: Beam intensity measured by total target. Blue: Real beam intensity.

CONCLUSION AND OUTLOOK

According to the operation status of HIMM-IC, we think the cyclotron can be stably and reliably used as injector of synchrotron for heavy ion therapy. And the design of the cyclotron injector for HIMM is feasible.

As a continuous work of this study, we are not satisfied with the total transmission efficiency of the cyclotron injector and the extracted beam quality, and expect to improve it in the future to further boost the performance of the overall HIMM facility.

REFERENCES

[1] B. Wang *et al.*, “Design and construction progress of a 7 MeV/u cyclotron”, in *Proc. 19th Int. Conf. on Cyclotrons and their Applications (Cyclotrons’10)*, Lanzhou, China, Sep. 2010, paper TUA2CCO03, pp. 317-320.

[2] B. Wang *et al.,* “Computer design of a compact cyclotron”, *Phys. Part. Nucl. Lett.*, vol. 9, no. 3, pp. 288–298, 2012. doi:10.1134/S1547477112030053

[3] Lanzhou Ion Therapy Co., Ltd, “Operation of HIMM-IC in Wuwei”, unpublished.

[4] J.Q. Zhang *et al.*, “Axial injection beam line of a compact cyclotron”, in *Proc. 19th Int. Conf. on Cyclotrons and their Applications (Cyclotrons’10)*, Lanzhou, China, Sep.2010, paper MOPCP100, pp. 254-255.

[5] Q. G. Yao *et al*., "The magnetic field design of HITFiL cyclotron," in *IEEE Trans. Appl. Supercond.* vol. 22, no. 3, p. 4401004, Jun. 2012. doi:10.1109/TASC.2011.2175190

[6] H. F. Hao *et al.*, “Beam extraction system of compact cyclotron”, in *Proc. 19th Int. Conf. on Cyclotrons and their Applications (Cyclotrons’10)*, Lanzhou, China, Sep.2010, paper MOPCP101, pp. 256-257.

23rd Int. Conf. Cyclotrons Appl. CYCLOTRONS2022, Beijing, China JACoW Publishing
ISBN: 978-3-95450-212-7 ISSN: 2673-5482 doi:10.18429/JACoW-CYCLOTRONS2022-THB001

A NEW CONCEPT OF CYCLOTRONS FOR MEDICAL APPLICATIONS

O. V. Karamyshev†, Joint Institute for Nuclear Research, Dubna, Russia

Abstract

Demand for cyclotrons for medical applications is growing rapidly. Cyclotrons delivering proton beams from 15 MeV up to 230 MeV are being used for isotopes production and proton therapy. Author proposes a concept that allows to significantly reduce cost of cyclotrons by making them more compact and power efficient without using superconducting coil. In the proposed design ratio between azimuthal length of sectors and valleys is over 3 to 1, with RF system operating at high frequency and acceleration at harmonic mode of 2 times the number of sectors. Compact size is achieved not by increasing the magnet field level, but by reducing the coil and RF system dimension. Cyclotrons will have 4 sectors and 4 rf cavities operating at harmonic 8 with 1.55 T mean field and accelerating frequency 180 MHz.

MOTIVATION

The production of new cyclotrons for physics research has slowed down since the 1990s (see Fig. 1, the green triangles). At the same time, demand for cyclotrons intended for isotope production and proton therapy is growing. Cyclotrons have a limited lifetime due to irradiation, etc., which means there is a need to replace old cyclotrons with new ones. Cyclotrons are becoming better: more compact, cheaper, more reliable, power efficient.

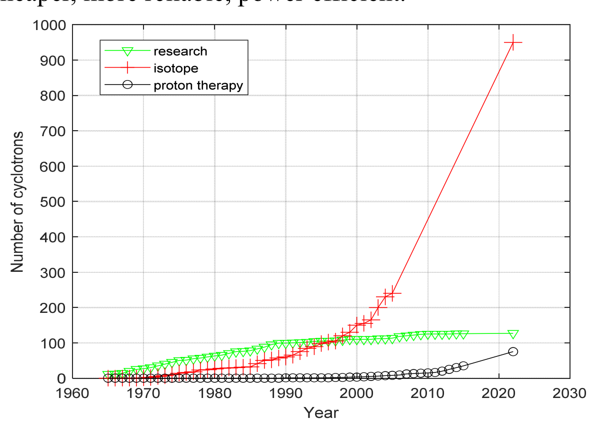

Figure 1: Number of cyclotrons versus years. The green triangles are cyclotrons in operation at research centers, the red crosses the cyclotron for medical radioisotopes production, and the black circles cyclotron for proton therapy [1]. Graphs are updated for year 2020 by data from [2, 3].

THE NEW CONCEPT

The main goal in creating a cyclotron is to make a light and compact design. In past years, the trend has been to increase the magnetic field, thereby decreasing the pole radius (see Fig. 2).

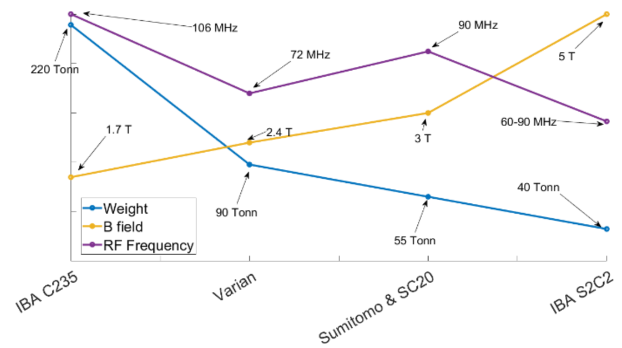

Figure 2: Weight, mean magnetic field and accelerating frequency of the proton therapy cyclotrons.

Superconducting coils is the only way to achieve high B field in cyclotron. Do cyclotrons with superconducting coils are more compact? Yes, the pole diameter is smaller, but cryogenics equipment around cyclotron is huge! Dry magnets with cryocoolers are more compact, but are there power efficient? Cryocoolers consume power 24x7 during operation and more during cooling down. So cyclotrons with superconducting coils have smaller pole diameter but they have the following disadvantages:

- Long time to turn on/off the magnet.
- Long time to cool down.
- Expensive.
- Requires servicing.

Moreover, superconducting cyclotrons do not exist! We only have cyclotrons with superconducting coils. Cyclotron is an accelerator and number one system of any accelerator is an accelerating system, magnet just keeps the beam focused and arrive in time! Superconducting RF systems do not yet work in cyclotrons.

I propose another way to reduce the size of the cyclotron, to make the accelerating RF system and coils more compact by increasing the frequency of the RF system, thereby reducing the valley depth. Reducing the valley depth will result in fewer A coils in the magnet, which will make the coil smaller, which in turn will result in a smaller yoke size. (Fig. 3).

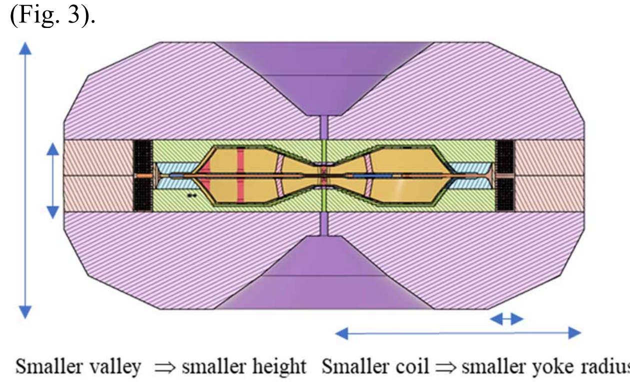

Figure 3: Dimensions of the cyclotron.

† olegka@jinr.ru

ISBN: 978-3-95450-212-7 ISSN: 2673-5482 doi:10.18429/JACoW-CYCLOTRONS2022-THBO01

So, in order to reduce the size of the cyclotron, the frequency of the accelerating system can be increased, but how much? If we look at frequency allocation chart [4] we will find out that the highest frequency in medical cyclotrons is 106.8 MHz, used by IBA C235 [5] is also the end of the lane dedicated for FM Radio, but between 108 and 136 MHz there are frequencies dedicated for aeronautical navigation, therefore it is not suitable for cyclotron. So the frequency for RF system in cyclotron can be 145 MHz, which is dedicated for amateur use or between 174 and 216 MHz.

VIRTUAL PROTOTYPING

A single parametrized model of the cyclotron, that integrates every major system of accelerator is developed in CAD (Solidworks). Individual systems are sent to CST studio to simulate in the corresponding modules. If changes are applied to one of the system, other system automatically adjusted and re simulated.

The "flagship" cyclotron accelerates protons to 230 MeV, magnet has 4 sectors, acceleration on 8^{th} harmonic, accelerating frequency is 180 MHz. Smaller energy models are going to be derived from the big cyclotron.

Main magnet parameters are presented in Table 1.

Table 1: Magnet Parameters

Magnet Type	**Compact, Copper Coils**
Number of sectors	4
Material of magnet	Steel 1010
Sector and Valley gap	20/50 mm, 320 mm
Weight of magnet	130 Ton
Coil type	2x4 double pancakes
Nominal current/ total A-turn	1224A / 57kA-turns
Conductor type	15x25mm^2
Cooling pressure, water speed	4 bar, 1.95 m/s
Power consumption	80 kW
Water temperature rise	15 degrees

Magnetic Field CST Simulation

In order to minimize the A-turns number the design of the magnet is following the rule: maximize the amount of steel inside the cyclotron. Another important feature applied in cyclotron magnet design – so called "double sector".

"Double sector" consists of two parts (see Fig. 4):

1. wide-aperture part with a vertical distance of 50 mm and low helicity.
2. small-aperture part with a vertical distance of 20 mm and high helicity.

This structure makes it possible, firstly, to place the deflector between the sectors in the wide-aperture part, while retaining all the valleys for placing the RF cavities, and, secondly, to ensure isochronous growth and vertical focusing mainly due to the small-aperture part of the sector.

An increase in the azimuthal width of the small aperture part of the sector with a radius increases the magnetic field flutter (see Figs. 5 and 6), and a large helicity angle of the small aperture part of the sector (see Fig. 7) provides the necessary vertical focusing.

To ensure the growth of the mean field in the extraction zone, we also set the shape of the chamfer of the sector edge not around a circle centered at the geometric center of the cyclotron, but along the shape of the trajectory of the accelerated particles, which differs from the circle the more, the higher the flutter of the magnetic field.

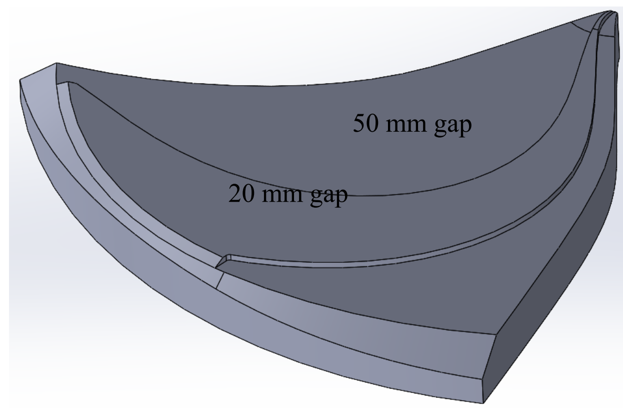

Figure 4: Double gap sector, double spiral, chamfered along beam trajectory.

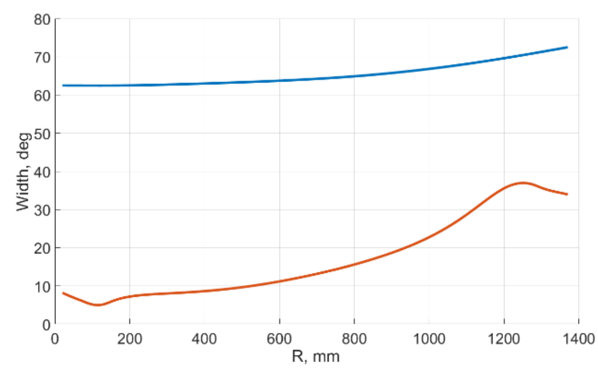

Figure 5: Azimuthal width sector.

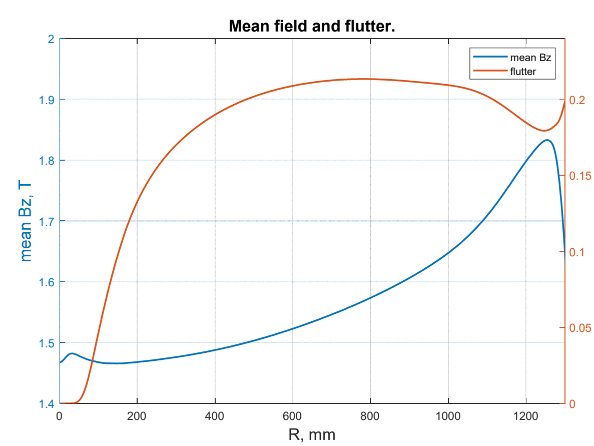

Figure 6: Mean field and flutter.

ISBN: 978-3-95450-212-7 ISSN: 2673-5482 doi:10.18429/JACoW-CYCLOTRONS2022-THB001

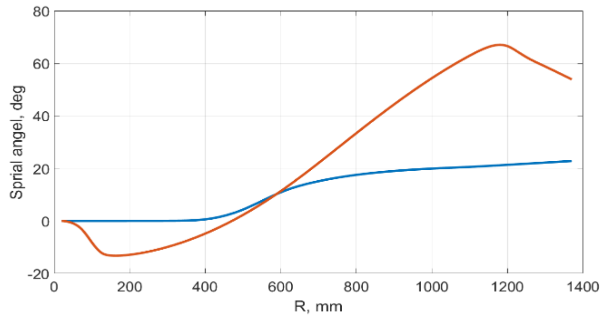

Figure 7: Spiral angle of the sector.

Accelerating System

To accelerate protons, it is planned to use 4 double gap delta RF cavities with 3 stems (see Table 2, Fig. 8) located in the valleys of the magnet (8th harmonic acceleration mode).

Table 2: Acceleration System Parameters

Parameter	Value
Frequency, MHz	180
Harmonic number	8
Q-factor	11000
Voltage center/extraction, kV	30/160
Power loss	30-50 kW total

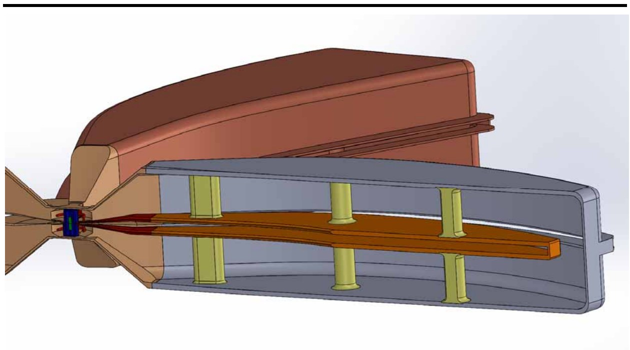
Figure 8: View of the accelerating system.

Accelerating voltage and azimuthal extension of the cavities along radius were calculated and presented in Ref. [6].

Particle Dynamics

The particle dynamics studies were carried out using magnetic and electric field maps obtained by simulating the corresponding systems in the CST studio. CORD code was used for estimation of the field characteristics. CORD is providing particle dynamics analysis based on a combination of magnetic field map analysis with electric field map analysis [6, 7].

Center Region

Capturing the beam from the ion source into the acceleration at high frequency of the accelerating field is an issue. If the particles from the ion source start with zero energy, only a few (or zero?) particles can be captured at 180 MHz, but even a small initial velocity of 5 keV allows the beam to be captured with a phase expansion up to 15 deg. External injection, of course, is the obvious solution for such a cyclotron, but there is an alternative to increase the capture efficiency from internal ion source. Efficient center region for this cyclotron is described in detail in Ref. [8].

Particles start from the PIG source, which is placed under 6600 V and accelerate to the "Ninja star" housing (zero potential) and arrive to the first gap at 6.6 keV energy.

Most challenging part of the central region design was to leave enough space for connection of all 4 dees, leave big enough hole for the ion source at 6600V and have B field with "bump" distribution to provide vertical focusing (Figs. 9 and 10).

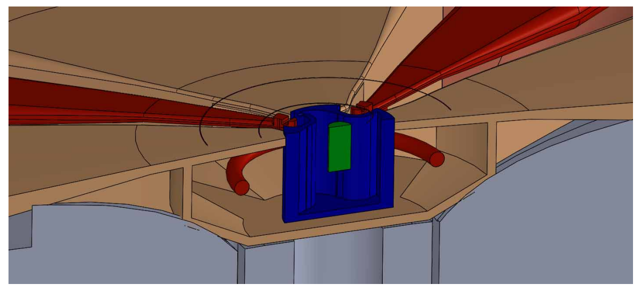
Figure 9: Center region design.

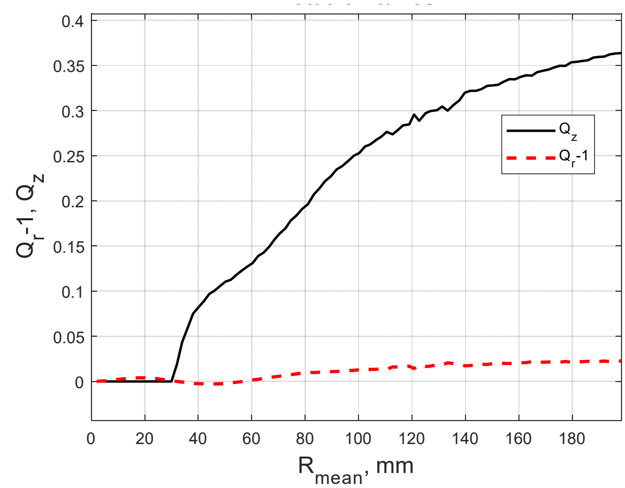

Figure 10: Betatron tunes in the center region.

Advantages of the proposed scheme of central region:

- At least 4 times higher current, as 4 bunches captured at the same time.
- Much higher capture in each 1st gap due to initial acceleration. In this case phase range increases from 0 to 15 deg RF.
- Only protons arrive to the RF puller, resulting in less erosion of RF parts.
- The ion source is separated from the rest of the chamber by a "Ninja star" housing, which provides an improved vacuum in the cyclotron. An additional pump can be used to pump gas from the inside of the "Ninja star".
- Only safe voltage is used. Smallest gap is 3.0 mm, voltage on RF puller is 25 kV, so electric field strength is just 83 kV/cm at frequency 180 MHz.

ISBN: 978-3-95450-212-7 ISSN: 2673-5482 doi:10.18429/JACoW-CYCLOTRONS2022-THBO01

Of course, 8th harmonic mode of acceleration is not an ideal option for truly high power cyclotron, however such design of the center region if used with 4th harmonic acceleration, especially with even higher voltage on the source can lead to 10 mA currents and higher.

Extraction

The beam extraction for this machine will be carried out by means of 1 electrostatic deflector (ESD), located between the sectors, and passive focusing magnetic channel (Fig. 11) [6]. The electric field strength in the deflector is 80 kV/cm.

This extraction scheme is presented as a proof-of-concept, author is currently analyzing alternative schemes.

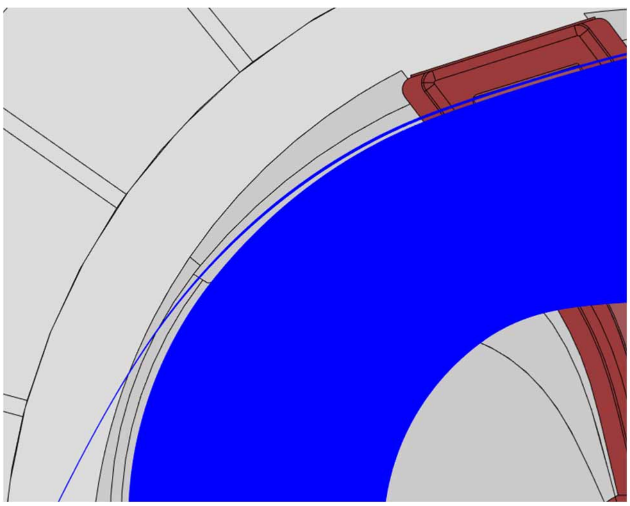

Figure 11: Beam extraction.

CONCLUSION

New concept of cyclotrons for medical application has been developed.

The advantages of the concept are:

- Compact but non-superconducting design, thus cheaper.
- All cyclotrons in the line from 15 to 230 MeV will share the same RF frequency, making many parts identical for different models.
- The design is simple and robust, no extreme solutions, moderate currents, power, voltages on deflector etc.

The new concept opens up the possibility of using HTS. HTS does not work well (requires low temperatures) in a magnetic field. In proposed design the magnetic field in the coil is low (about 1.5 T), which means it is possible to use high-temperature superconductor at temperatures >70 K, which will significantly reduce the power consumption and cost of cryogenic equipment.

Looking for partnership to advance from virtual prototyping to real prototypes!

REFERENCES

[1] L. Calabretta and M. Seidel, "50 years of cyclotron development", *IEEE Trans. Nucl. Sci.,* vol. 63, no. 2, pp. 965-999, 2016. doi:10.1109/TNS.2015.2499238

[2] P. Schaffer *et al.,* "Direct production of 99mTc via 100Mo(p,2n) on small medical cyclotrons", *Physics Procedia,* vol. 66, pp. 383–395, 2015. doi:10.1016/j.phpro.2015.05.048

[3] https://www.ptcog.ch/index.php/facilities-in-operation

[4] https://www.ntia.doc.gov/files/ntia/publications/2003-allochrt.pdf

[5] W. Kleeven *et al.*, "The IBA superconducting synchrocyclotron project S2C2", in *Proc. Cyclotrons'13*, Vancouver, BC, Canada, paper MO4PB02, pp.115-119.

[6] O. Karamyshev, "Beam dynamics in a new 230 MeV cyclotron", presented at Cyclotrons'22, Beijing, China, Dec. 22, paper WEPO003, this conference

[7] O. Karamyshev , T. Karamysheva, I. Lyapin, V. Malinin, and D. Popov, "Cord (Closed Orbit Dynamics): A New Field Map Evaluation Tool for Cyclotron Particle Dynamics", *Phys. Part. Nucl. Lett.,* vol. 18, no. 4, pp. 481–487, 2021. doi:10.1134/S1547477121040117

[8] O. Karamyshev, "High power center region with internal ion source", presented at Cyclotrons'22, Beijing, China, Dec. 22, paper WEPO004, this conference

ISBN: 978-3-95450-212-7 ISSN: 2673-5482 doi:10.18429/JACoW-CYCLOTRONS2022-THBO02

SAPT- A SYNCHROTRON BASED PROTON THERAPY

M. Z. Zhang †, Z. L. Chen, R. Li, M. Gu, L. R. Shen, Z. T. Zhao, Shanghai Advanced Research Institute, Chinese Academy of Sciences, Shanghai, China
D. M. Li, Shanghai Institute of Applied Physics, Chinese Academy of Sciences, Shanghai, China
X. B. Wu, Shanghai APACTRON Particle Equipment Co., Ltd., Shanghai, China

Abstract

SAPT is a synchrotron-based proton therapy which built in Shanghai, China. There are 4 treatment rooms and a main ring, a linac injector and the transport lines that between them. The main ring is a 24.6 m long and 8 dipoles synchrotron. The synchrotron employees multi-turn injection and 3rd order extraction. The treatment rooms are ocular beam line, fixed beam line, 180-degree gantry beam line and 360 gantry beam line. Now, the first unit (fixed beam line, 180-degree gantry beam line) has finished the 3rd party testing and clinical trial, will open to patient treatment soon. the accelerator and beam lines will be described in this paper.

INTRODUCTION

As the first proposal by Wilson at 1946 [1], proton deposits most energy at the end of its trace [2], well known as 'Bragg Peak'. In comparison with photons, the normal tissue that proton passed receive very low dose. The most important thing is proton can stop. And the vital organs are refrained from irradiation, because there is no energy deposited after the 'Bragg Peak'. These features, proton therapy is known as one of the best ways for cancer treatment. Since the and the first dedicated proton therapy in hospital in 1990s [3], the requirement and application of proton therapy grew rapidly, especially in the 2010s. The number of proton centers in operation increases to 98 and 31 centers under construction at 2022 [4].

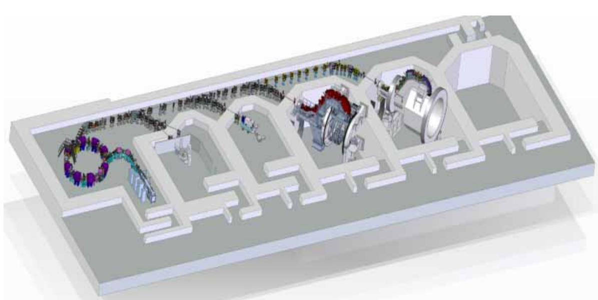

Figure 1: Layout of gantry beam lines.

Shanghai APACTRON proton therapy (SAPT) [5] is a synchrotron-based proton therapy that funded by Shanghai local government and science and technology department of China. There are 4 treatment rooms and 5 beam lines, including an ocular beam line, an experiment beam line, a fixed beam line, a half gantry beam line and a full gantry beam line, as shown in Fig. 1. The installation started at the end of 2016 and the commissioning of the accelerator started at the end of April 2017. The first unit (accelerator, fixed treatment room and half gantry room) has passed the 3rd party testing and clinical trial at 2021 and 2022, and will open to patient soon. The general specifications of this facility are shown in Table 1. The details of accelerator and treatment systems are described in the next sections.

Table 1: General Specifications

Parameters	Value
Energy Range	70~235 MeV
Energy Levels	94
Range in Water:	0~34.0 g/cm^2
Dose rate:	1 Gy/min/Liter
Extraction intensity per spill:	4~8×10^{10}
Accelerator:	FODO, 8 bends
Circumference:	24.6 m
Injection :	Multi turn painting
Extraction:	3rd resonance
Ramping time:	0.7 s
Repetition rate:	0.5~0.1 Hz(variable)
Field size:	30 cm ×40 cm
Beam Delivery Method:	Spot Scanning

ACCELERATOR

The accelerator includes a 7 MeV LINAC, a synchrotron, two different gantries, and transport lines between them. Synchrotron is the main part of the accelerator.

Synchrotron

The synchrotron of SAPT is a FODO-like structure of 4 cells and 2 super periods, totally 24.6 meters long ring. It consists of 8 dipoles and 12 quadrupoles to suppress the beta function to less than 5 meters at the vertical plane in dipole, as shown in Fig. 2. More smaller beta function will make more larger acceptance. The space charge effect [7], which leads to tune shift and limits the maximum beam current, will benefit from the large acceptance. There are 4 long straight section for injection and extraction, RF cavity. 8 short straight sections are used for the beam diagnostic and vacuum elements.

In order to reduce the beam loss at the electronic extraction septum, the Hardt condition that aligns the separatrices of different momentum [8] is satisfied on the lattice. The protons keep below transition energy, and in order to avoid head-tail instability, the chromaticity should be negative. That means the sign of dispersion and its derivative should

† zhangmz@sari.ac.cn

ISBN: 978-3-95450-212-7 ISSN: 2673-5482 doi:10.18429/JACoW-CYCLOTRONS2022-THB002

be different. Two sextupoles are used to correct the chromaticity. The phase advance of these two sextupoles are nearly 2π, thus they affect the resonance driven term very little if the strengths and signs of them are same.

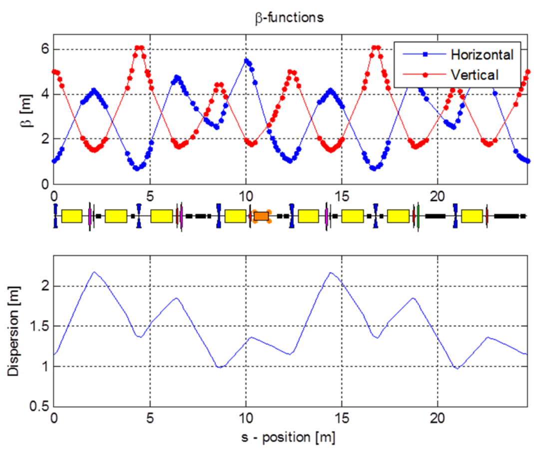

Figure 2: Twiss Function.

Injection

In order to reach the beam intensity requirement, a multi-turn injection scheme is employed for beam accumulation. The injection scheme employed a magnet septum, an electronic septum and two bumps. The beam intensity is limited by space charge effect. The space charge effect can be reduced by enlarge the beam emittance via phase space painting method. Horizontal phase space painting is performed by around 30 turns bump decrease. And the circulating beam current is about 10 times as large as the injection current from the Linac accelerator. Vertical phase space painting is realized by Twiss parameters and orbit mismatch. Figure 3 shows the horizontal phase space painting result.

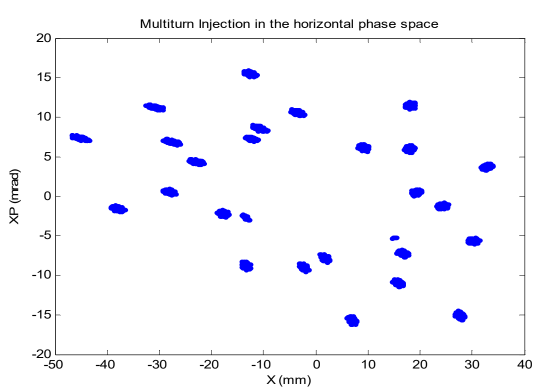

Figure 3: Painted beam in Horizontal phase space.

After injection, the proton beam is captured and accelerated to the required energy. After the eddy current correction by the power supplies [9], the maximum particle number after acceleration is 1.3×10^{11} with second and third harmonic RF voltage.

Extraction

The proton beam is extracted by a 3rd order resonance slow extraction. The horizontal tune should be closed to 2/3. The oscillation of beam is excited by RFKO and the tune is measured by oscilloscope. The current of QF and QD is changed to correct the tune. Two sextupoles are placed on opposite sides of the ring to produce resonance driven term. The strengths of these two sextupoles are opposite, so they will not affect the chromaticity. Figure 4 shows the phase space after sextupoles are turned on. The particles, that enter the unstable region and cross the septum filament, are kicked by the electronic field. Then they pass quadrupoles and dipoles. Finally, they are kicked by magnetic septum and are extracted to the high energy transport line.

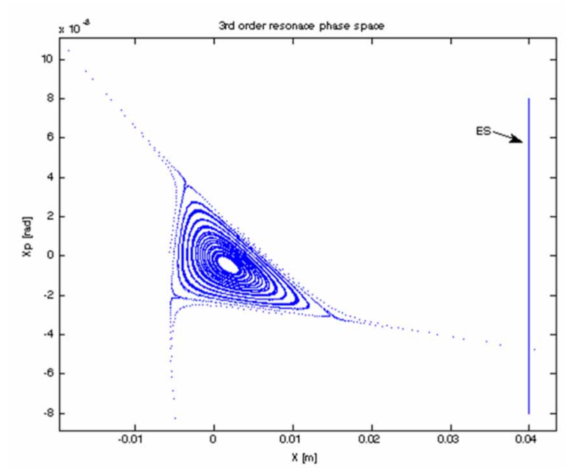

Figure 4: Extraction phase space.

The extraction current, which is decide by the rate of particles enter unstable region, is controlled by the amplitude modulation of RFKO (Radio Frequency Kick Out) system [5, 10, 11]. The extraction beam current is shown in Fig. 5.

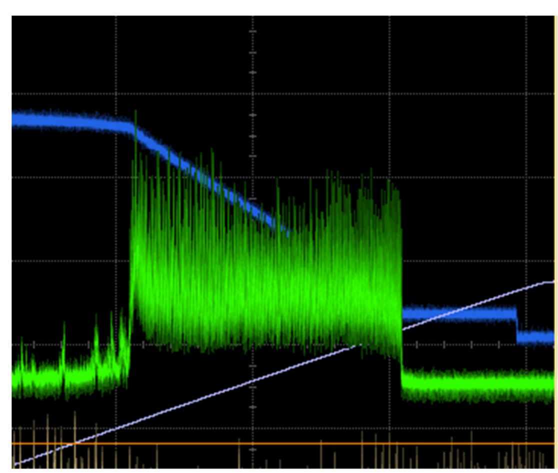

Figure 5: Extraction beam current.

Gantry

Rotating gantry is the most advantage of proton therapy compared to heavy ion therapy. It gives the medical physicist more choice to reduce the dose at normal tissue. Two

ISBN: 978-3-95450-212-7 ISSN: 2673-5482 doi:10.18429/JACoW-CYCLOTRONS2022-THB002

gantries based on round beam method is designed [12]. Figure 6 shows the structure of the half gantry. The magnets of this gantry form a telescope that makes the beam at the exit of this gantry is the same of the one at the entrance. The weight of rotated part is around 100 tons and whole weight is around 170 tons. In order to reduce the size and weight, short SAD and combine function dipoles are used in the full gantry. The measured accuracy at the ISO center is 0.2 mm when the gantry rotated.

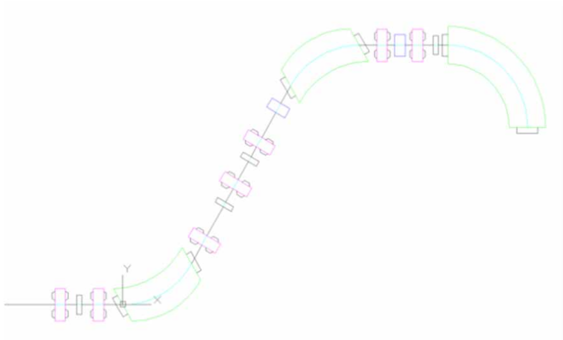

Figure 6: The lattice structure of the full gantry.

TREATMENT SYSTEM

The treatment system includes beam delivery system, positioning system, treatment control system and so on. We positioning the patients or QA equipment to the required place by using a robot couch, laser system and IGRT. The movement and rotation accuracy is 1 mm and 0.2 degree. The treatment control system receives treatment plans and image information from TPS, then send them to IGRT and beam delivery system, respectively. At last, receives and conforms the results after positioning or treatment.

Beam Delivery System

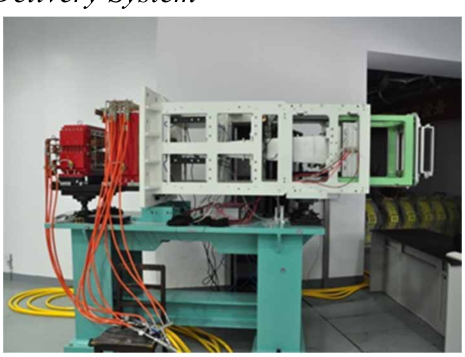

Figure 7: The structure of nozzle.

Pencil beam spot scanning is more and more widely used in the hadron therapies because of the excellent three-dimensional conformability. The beam delivery systems of fixed beam, two gantry beams are all this type. It includes 2 scanning magnets (Horizontal and vertical) in order to swap the beam to the required position. There are also 2 dose monitors and 1 position monitor and their electronics. The former ones are used to double check the passed proton number to control the dose. The later one is used to monitor the beam position They are all iron chambers. Figure 7 shows the structure of these parts, named nozzle. And the control system of the beam delivery system is outside the treatment room.

Beam Performances

The most important beam performances of a therapy facility are always measured in the treatment room. Table 2 shows several parameters of the facility.

Table 2: Beam Performances

Parameters	**Value**
Dose Linearity	<3%
Dose repeatability	<2%
Dose stability	<2%
Range stability	<0.3mm
Spot Dose accuracy(rms)	<30 counts
Dose rate	8-10 MU/s
Position accuracy	<1mm
Beam Size accuracy	<15%

Figure 8 shows the beam size of every energy, and Fig. 9 shows the beam position at center. All the beam performance passed the 3rd party testing and acceptance of the hospital. And the clinical trials that has finished shows very good curative effect.

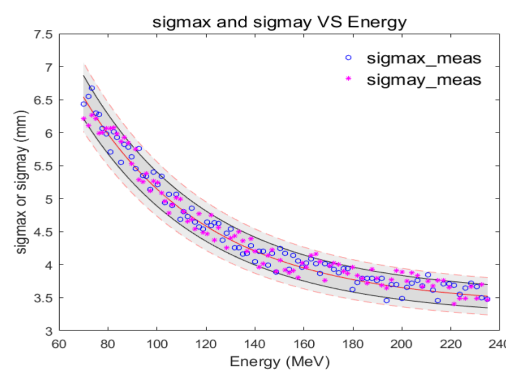

Figure 8: Beam size of every energy.

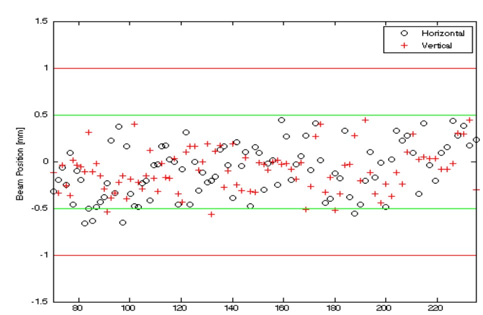

Figure 9: Beam position.

CONCLUSION

A dedicated synchrotron is designed, constructed and commissioned in Shanghai. The lattice, injection, acceleration, extraction, gantry and beam delivery system have been well studied and commissioned. The beam parameters reached the requirements and passed the 3rd party testing and clinical testing. The full gantry room and ocular beam line should take more time for the commissioning.

ACKNOWLEDGEMENTS

We would like to thank all the experts who help us for the design, construction and commissioning. They give us lots of advices and helps. And also we would like to thank our team members. Their hard work made this project come to ture.

REFERENCES

[1] R. R. Wilson, "Radiological use of fast protons", *Radiobiology*, vol. 47, no. 5, pp. 487-491, 1946. doi:10.1148/47.5.487

[2] M. G. Pullia, "Synchrotrons for hadron therapy", *Reviews of Accelerator Science and Technology*, vol. 2, pp. 157-178, 2009. doi:10.1142/S1793626809000284

[3] F. Cole, P. V. Livdahl, F. Mills, *et. al.*, "Design and application of a proton therapy accelerator", in *Proc. Accel. Conf.*, Washington DC., USA, 1987, pp. 1985-1987, doi:10.1111/jmi.12335

[4] Particle Therapy Co-Operative Group, http://www.ptcog.ch

[5] D. Shi, L. H. Ouyang, M. Gu, *et. al.*, "The RF-knockout slow-extraction for Shanghai proton therapy facility", *Nucl. Sci. Tech.*, vol. 35, no. 3, 231-235, 2012. doi:10.1007/s11783-011-0280-z

[6] M. Z. Zhang, D. M. Li, K. Wang, *et. al.*, "Commissioning of Shanghai Advance Proton Therapy", in *Proc. IPAC'18*, Vancouver, Canada, Apr.-May 2018, pp. 1151-1154. doi:10.18429/JACoW-IPAC2018-TUPAL059

[7] L. J. Laslett, "On Intensity limitations imposed by the transverse space charge effects in circular accelerators", *eConf.*, vol. C630610, p. 324, 1963.

[8] Accelerator Complex Study Group, Proton-ion medical machine study (PIMMS) Part I, CERN/PS 99-010, 1999.

[9] M. Z. Zhang, M. Zhang, X. C, Xie, *et. al.*, "Study of eddy current effects in a high field dipole", *Nucl. Sci. Tech.*, vol. 28, no. 12, p. 173, 2017. doi:10.1007/s41365-017-0325-5

[10] K. Noda, M. Kanazawa, A. Itano, *et. al.*, "Slow beam extraction by a transverse RF field with AM and FM", *Nucl. Instrum. Methods Phys. Res. Sect. A*, vol. 374, no. 2, pp. 269-277, May 1996. doi:10.1016/0168-9002(96)00096-4

[11] Y. H. Yang, M. Z. Zhang, D. M. Li, *et. al.*, "Simulation study of slow extraction for the Shanghai advance proton therapy", *Nucl. Sci. Tech.*, vol. 28, no. 9, p. 120, Aug. 2017. doi:10.1007/s41365-017-0273-0

[12] Z. X. Yang, D. M. Li, M. Z. Zhang, *et. al.*, "Optics design of beam for proton therapy gantry based on Geant4", *Nucl. Tech.*, vol. 36, no. 7, Jul. 2013. doi:10.11889/j.0253-3219.2013.hjs

ISBN: 978-3-95450-212-7 ISSN: 2673-5482 doi:10.18429/JACoW-CYCLOTRONS2022-THBO05

COMMISSIONING OF A 70 MeV PROTON CYCLOTRON SYSTEM OF IBS, KOREA*

J.W. Kim#, Y. H. Yeon, Institute for Basic Science, Daejeon, Korea

Abstract

A 70 MeV H- cyclotron system was installed at the Shindong campus of Institute for Basic Science from Nov. 2021. Installation was guided by precision survey so as to locate main components to their final positions. Electrical cables and utility lines were then connected and validation was followed for the control and safety systems. Internal beams were accelerated in May and utilized to isochronize the magnetic field by Smith-Garren method involving a series of magnetic shimming. A beam of 70 MeV was firstly extracted in July and two beam lines were commissioned for the beam energies of 40-70 MeV. Site acceptance tests were carried out with a temporary beam line installed to measure beam profiles at the location of ISOL target, Finally, a maximum beam power of 50 kW was successfully tested for six hours.

INTRODUCTION

Institute for Basics Science (IBS), Korea made a contract with IBA, Belgium for a 70 MeV cyclotron and two beam line systems in July, 2019 as part of Rare Isotope Science Project (RISP) [1, 2]. Table 1 lists main parameters of the cyclotron [3] to be used as a driver of ISOL system. The building was in fact already built prior to this contract, so that pre-survey could be carried out in the end of 2019.

Table 1: Main Cyclotron Parameters

Parameter	Value
Energy	30-70 MeV
I_{max}	750 μA
Number of sectors	2
Hill field B_{max}	1.6 T
Harmonic number	4
Rf frequency	61 MHz
Ion source I_{max}	10 mA
Weight	140 tons

When cyclotron yokes were transported to the Shindong site in Nov. 2021 we started to install entire system. A crane of 1200 tons was used to rig a half of cyclotron yoke weighing around 70 tons because of the need of a long arm. Components were located to their final positions guided by precision survey, which took about two weeks to complete for the cyclotron and main beam line components.

By the end of March 2022, most of utilities were connected to the cyclotron and beam line components. Then connections were verified by involving the control system. Furthermore, since IBS PLC system dedicated to personal safety overlooking building interlocks was already available, secure cables were simply connected to IBA PLC, which handles beam safety enabling beam on and off.

A temporary beam line was installed in a cave to measure beam properties using beam profile monitor at the position of ISOL target. At the end of the beam line, a beam dump was attached along with a collimator defining the beam size. A beam wobbler placed a few meters upstream was used to manipulate beam shapes at the profile monitor. High-power beam tests were then performed in the other cave. Beam tests for site acceptance were completed at the end of Oct.

INSTALLATION AND TESTS

The facility layout is shown in Fig. 1. Two caves are prepared for ISOL uses, but only one is equipped with modules in Cave A that can be remotely handled. Two beam lines were first installed up to the entrance of ISOL tunnels, ending with beam dumps capable of handling up to 50 kW of beam power. Beam line commissioning was performed using 40 and 70 MeV protons to check beam alignments while measuring beam properties.

Spare area shown in Fig. 1 is ready to be used for future expansion when a new beam line is constructed to 2nd extraction port, where switching magnet already exists to adjust beam trajectories of different energies.

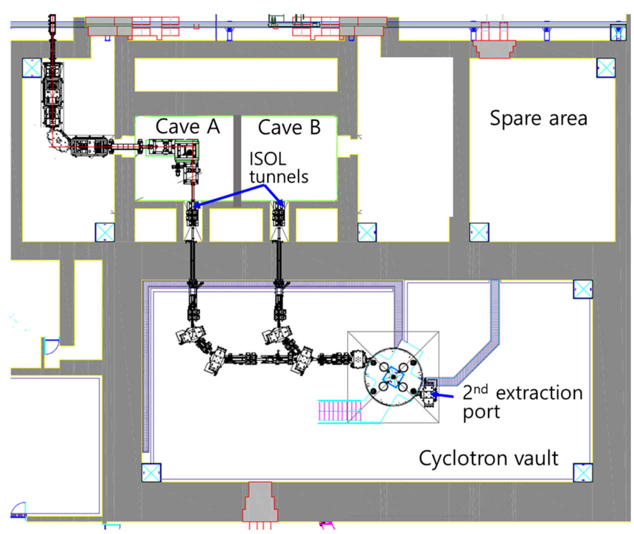

Figure 1: Layout of the cyclotron facility showing two caves and spare area.

Most of utilities such as electricity, compressed air and cooling water were connected by April, 2022. Since power supply room shared by control room is located in first floor

*Work supported through the National Research Foundation of Korea (NRF) funded by Ministry of Science, ICT and Future Planning (MSIP) under Contract 2013M7A1A1075764.
#jwkim@ibs.re.kr

while the cyclotron vault is located 10 m below ground, cable pulling through vertical penetration holes took a few weeks as new cable trays were also needed. Remaining penetration holes and empty holes were then filled with high-density silicon compounds for radiation shielding. Figure 2 shows a photo of cyclotron vault when installation was nearly completed.

Figure 2: Cyclotron and two beam line components installed in cyclotron vault.

The injection line was tested with a radial probe placed near cyclotron center to stop the beam. A multi-cusp ion source biased at 30 kV can provide a maximum current of 10 mA and its beam shape at the exit was checked with a paper burn. Considerable increase of injection efficiency was observed by turning on rf buncher in the injection line. The efficiency increased almost 10% for a beam current of tens of μA, but it reduced less than a few percent when the beam current is higher than a few hundreds of μA.

RF voltage at the center was checked by measuring beam profiles using a differential radial probe. The design voltage of 50 kV was confirmed by well-defined turn separation and radial gains per turn.

Magnetic shimming using thin steel plates was carried out based on Smith-Garren method, which takes iteration of beam current measurement versus main-coil current as a function of radius. A main-coil current margin of 0.2 A was achieved as shown in Fig. 3 so as to maintain isochronism against some changes of magnet temperature for instance.

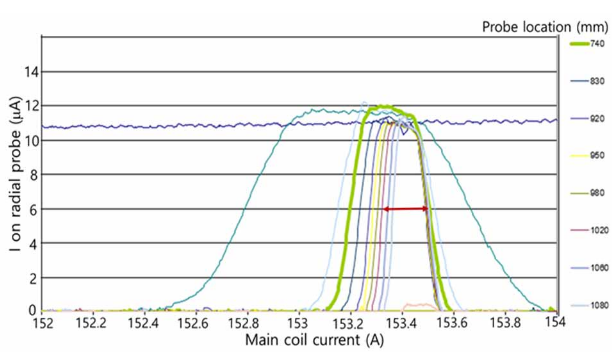

Figure 3: Beam current measurement versus main coil current at different radii known as Smith-Garren method.

BEAM MEASUREMENTS

A beam of 70 MeV was delivered to the beam dump in cave A in early Oct. 2022 for the first time. A temporary beam line was set-up as shown in Fig. 4. The beam line ends at the beam dump attached with a collimator (ϕ2 or 5 cm). Beam profile and position monitors were placed upstream to see the beam shapes and positions, respectively.

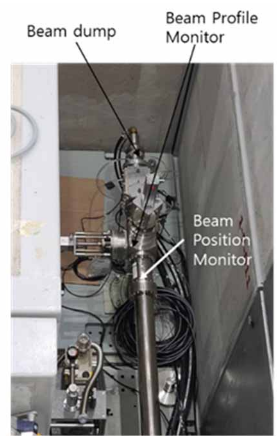

Figure 4: Temporary beam line set-up for beam measurement as site acceptance.

The beam position monitor (BPM), which was built in house, was calibrated using a precision wire system moving in steps of 0.1 mm at a detector lab of Pohang Light Source as shown in Fig. 5. A rf wave of 61 MHz was applied to the wire using waveform generator. For signal handling Libera Spark HL™, which is tuned for single pass hadron beam, was used.

Figure 5: Beam position monitor calibrated using a moving wire system at Pohang Light Source.

The control screen of BPM is displayed in Fig. 6 when a beam was turned on twice during the first beam delivery in Cave A, showing that Δx is around 1 mm and Δy less than 0.5 mm. Off-center of the beam in horizontal direction is apparent. The beam current read at the beam dump was around 10 μA, which allows calibration of beam current reading by BPM.

ISBN: 978-3-95450-212-7 ISSN: 2673-5482 doi:10.18429/JACoW-CYCLOTRONS2022-THBO05

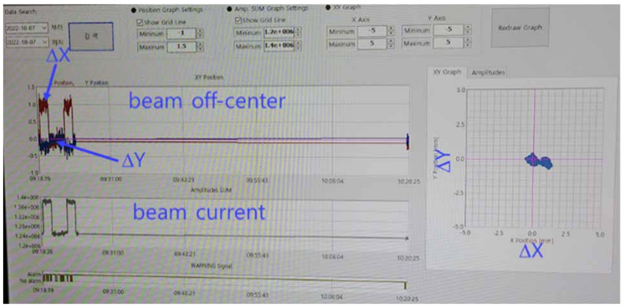

Figure 6: Display of beam position monitor's control screen showing beam off-centers in both transverse planes and also beam current. On the right-hand side dots of 2D beam positions accumulated are shown.

A beam profile measured at 70 MeV in Cave A without wobbling is shown in Fig. 7. One sigma can be varied by controlling focusing quadrupoles to a range of 1.5 ~ 6 mm for both transverse planes. This profile monitor uses two moving wires made of $\phi = 0.5$ mm thick tungsten and takes a few seconds to scan each plane.

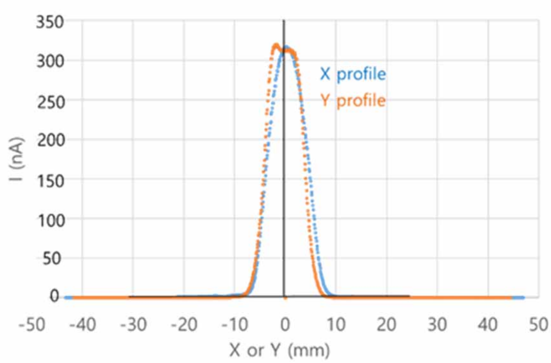

Figure 7: Beam profiles measured at a waist without beam wobbling applied.

Before wobbling, the beam shapes of both planes should be controlled as similar, so that the wobbled beam shape can be axially symmetric. Beam shapes formed by turning on the wobbler at two energies of 40 and 70 MeV are shown in Fig. 8. Two different beam profiles flat and hollow in the center are demonstrated with the controls of beam width. Wobbling frequency is 60 Hz.

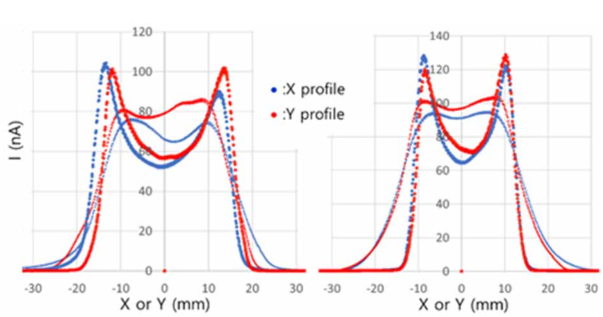

Figure 8: Two different beam profiles obtained by wobbling at two different energies of 40 MeV (left) and 70 MeV (right).

Tests of high-power beams were performed in Cave B using wobbling to reduce maximum power deposit on the vacuum window made of Ti. Transverse spread of the beam by wobbling was monitored by beam losses at the 4-jaw collimator. Before performing this high-power test for six hours, ISOL tunnel of Cave B was heavily shielded using concrete blocks around the beam dump to localize radio-activation. Screen display of beam currents measured at the dump and 4-jaw collimator is given in Fig. 9. During six-hour operation there were many rf voltage trips, but overall the system operated stably with quick recovers.

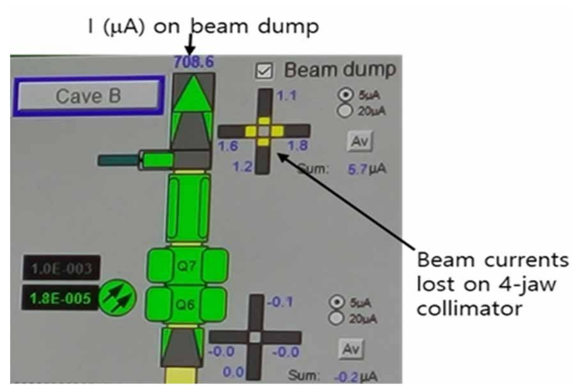

Figure 9: Screen display of beam currents measured at the beam dump and 4-jaw collimator.

CONCLUSIONS

A 70 MeV cyclotron system was installed at the Shindong campus of IBS from Nov. 2021. Beam tests started from May 2022 and ended in the end of Oct. It took about three years from contract to completion. The cyclotron and beam line in Cave A is now prepared to deliver a beam for ISOL operation. The wobbler will be used to shape beam profiles for ISOL target as tested for acceptance. Beam tests were carefully planned to minimize unnecessary facility activation and radiation exposure to workers. In Cave B the maximum beam power test was finished in the next day after the beam current extracted reached over 700 µA for the first time. Since 2nd extraction port is currently not used, future addition of a new beam line will allow a full operation of the cyclotron sending two beams at the same time for different applications.

REFERENCES

[1] J. W. Kim, Y. Choi, S. Hong, and J. H. Kim, "Plan of a 70 MeV H- Cyclotron System for the ISOL Driver in the Rare Isotope Science Project", in *Proc. Cyclotrons'13*, Vancouver, Canada, Sep. 2013, paper MOPPT015, pp. 64-66.

[2] J. W. Kim, J. Kang, J. H. Kim, and T. S. Shin, "Status of a 70 MeV Cyclotron System for ISOL Driver of Rare Isotope Science Project in Korea", in *Proc. Cyclotrons'19*, Cape Town, South Africa, Sep. 2019, pp. 205-207. doi:10.18429/JACoW-CYCLOTRONS2019-TUP022

[3] S. Zaremba *et al.*, "Design of the Cyclone®70p", in *Proc. Cyclotrons'16*, Zurich, Switzerland, Sep. 2016, pp. 175-177. doi:10.18429/JACoW-Cyclotrons2016-TUP06

ISBN: 978-3-95450-212-7 ISSN: 2673-5482 doi:10.18429/JACoW-CYCLOTRONS2022-THB006

THE DESIGN OF THE CENTER REGION OF MSC230 CYCLOTRON

V. Malinin†, D. Popov, O. Karamyshev. T. Karamysheva[1], I. Lyapin, A. Sinitsa
Joint Institute for Nuclear Research (JINR), Dubna, Russia
[1]also at Federal Research Center "Computer Science and Control" Russian Academy of Sciences, Moscow, Russia

Abstract

MSC230 is an innovative efficient medical superconducting cyclotron for the study and investigation of the conventional proton and FLASH therapy, developed by JINR for its new biomedical research center. The machine has an internal injection system provided by a PIG ion source and, for better efficiency, 4 RF dees connected in the center. Despite these restrictions, it is possible to create a center region design which allows initial acceleration with minimal losses sufficient for the FLASH therapy. The design and its features presented in this talk.

INTRODUCTION

MSC230 cyclotron's project is expected to be implemented in the next few years by the joint efforts of Joint Institute for Nuclear Research (JINR, Dubna, Russia) and Efremov Institute of Electrophysical Apparatus (NIIEFA, St. Petersburg, Russia) [1].

JINR has been developing such medical cyclotrons as C400 and C235 together with IBA. And the CS200 cyclotron, together with the Institute of Plasma Physics in China, which was successfully launched recently. The MSC230 accelerator should become a source of an intense proton beam. It is a part of a planned modernization of the equipment of the Medical-Technical Complex at JINR. It is required to increase the current for the possibility of FLASH therapy. An important advantage of using a cyclotron is a sufficiently high beam intensity for FLASH therapy. This is a promising method of therapy that can significantly reduce damage to healthy tissues. In addition, this allows to reduce the number of necessary procedures and work with types of cancer that are not treatable by conventional therapy. Compared to radiation therapy at a conventional dose rate (1–7 Gy/min), FLASH irradiation is performed at a dose rate ~ 100 Gy/s. In order to deliver 100 Gy/s, extracted beam current should be at least 10 μA [2].

When developing the MSC230, we focused on the closest analogues - C235 and Varian. The goal was to take the best from both projects. Such as low magnetic field in the center, constant gap between sectors, sufficient for ESD, superconducting winding, 4 resonators operating at the 4th harmonic. Therefore, the MSC230 design aims for the following features: low power consumption, high beam quality, reduced engineering effort and complexity, rather small size and weight of the accelerator.

Central Region of SC200

The successful launch of the SC200 cyclotron was mentioned in the introduction. The project of the SC200 center was proposed by JINR. In the recent experiments an internal beam of 350 nA was achieved. The internal beam current is in good accordance with calculations (400 nA internal current was predicted).

However, this design had problems, caused by the high magnetic field in the center (3 T): the bump design makes the field in the very center below isochronous, causing the lagging particles at the beginning to lag even more (the phase reached 60°), if the lag is too large, there is not enough acceleration. This was solved by varying the size of the gaps in the center to increase the efficiency of proton extraction from the source while at the same time trying to avoid breakdowns. The experience of designing SC200 was useful in designing the new MSC230 cyclotron.

CENTRAL REGION OF MSC230

The project was developed in such a way that the following tasks were solved:

- Ensuring the possibility of forming a well-centered beam (less than 1 mm offset at a radius of 100 mm), consistent with the acceptance of the accelerator. Phase acceptance ± 20° RF.
- By varying the position of the accelerating gaps, we have to ensure sufficient vertical focusing by the electric field in the first or second turn.
- Minimization of the possibilities of breakdowns.

Two different center region designs are offered (operating with the same RF system). The first is an axially symmetrical design of the central region (see Fig. 1), the second is an optimized central region design developed for reducing the variation in the kinetic energies of the particles (shown in Fig. 2).

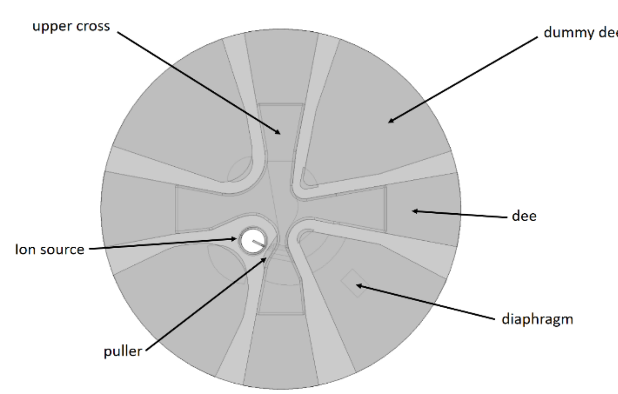

Figure 1: Structure of the central region: axially-symmetric version.

ISBN: 978-3-95450-212-7 ISSN: 2673-5482 doi:10.18429/JACoW-CYCLOTRONS2022-THBO06

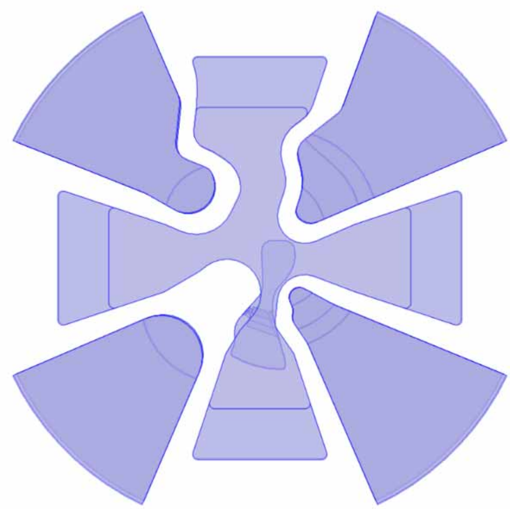

Figure 2: Structure of the central region: optimized version.

Improving Beam Parameters

The results of the phase acceptance calculation for the two versions are shown in Fig. 3. The total transmission through the central region turns out to be about 15% for optimized and 10% for symmetrical. That is, both options provide a sufficient beam quality.

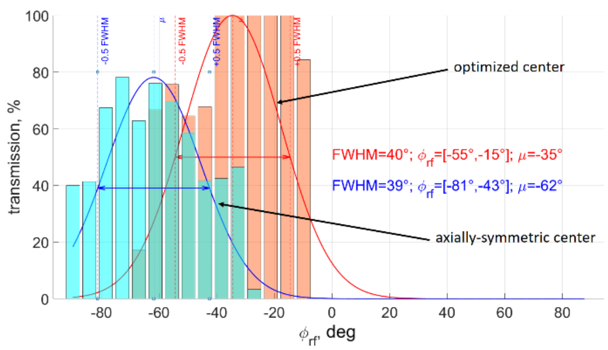

Figure 3: Phase acceptance of the central region– axially-symmetric (orange)/ cyan - optimized (cyan).

Figure 4 shows the dependence of the phase shift on the angle for the two versions of the central region. Positive phase corresponds to lagging particles.

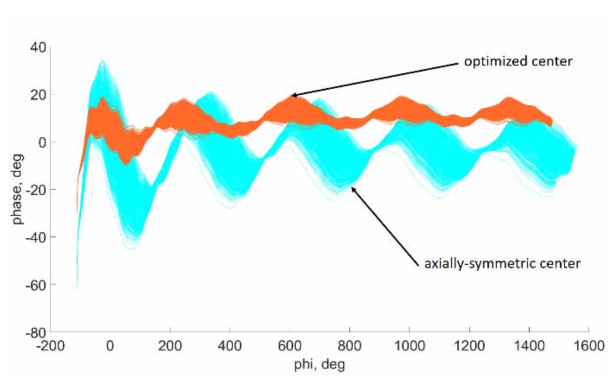

Figure 4: Phase shift in the central region– axially-symmetric (orange)/ cyan - optimized (cyan).

To provide vertical focusing, we create a bump (radial gradient) of the magnetic field (80-100 Gauss). Magnetic focusing caused by the decreasing magnetic field begins after a radius R = 30 mm, the average magnetic field along the radius is shown in Fig. 5 (top).

For R< 30 mm the accelerating electric field provides vertical focusing of lagging particles. The vertical motion of the particles is shown in Fig. 5 (bottom).

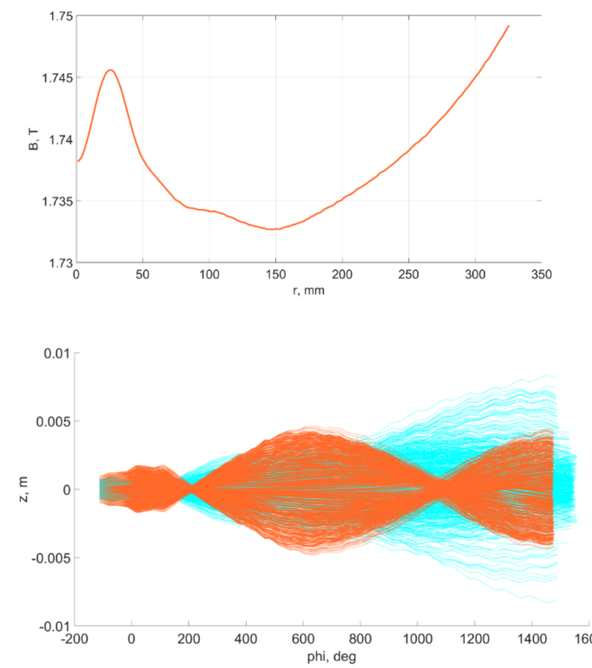

Figure 5: Average magnetic field along the radius (top) and vertical motion (bottom) of the particles in the central region (axially-symmetric (orange)/ optimized (cyan)).

Good vertical focusing and reduction of the variation in phase shifts helps to reduce the energy variation of the accelerated particles, therefore improving beam quality. Figure 6 shows the variation in the kinetic energies of the particles at R = 10 cm, for the two central region designs. The variation for the optimized version is significantly lower.

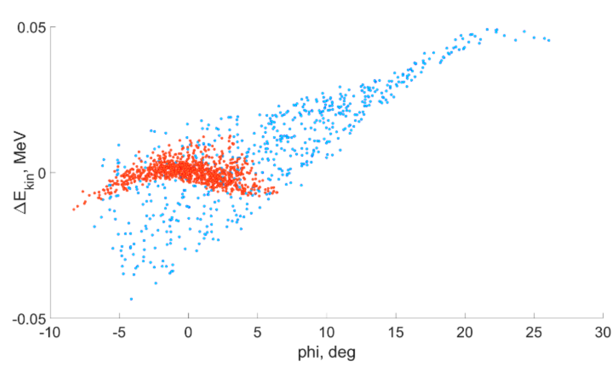

Figure 6: Variation in the kinetic energies of the particles at R = 10 cm. Axially-symmetric (orange)/ optimized (cyan).

ISBN: 978-3-95450-212-7 ISSN: 2673-5482 doi:10.18429/JACoW-CYCLOTRONS2022-THBO06

CONCLUSION

The design of the central region of the MSC230 was presented in this talk. Axially-symmetric and optimized designs we compared: optimized design has better beam properties (lower phase shift variation, lower energy gain variation). Axially-symmetric central region design can be used for RF tuning, optimized version works with the same RF system and has better beam properties. Simulation shows good phase acceptance, making it possible to reach beam intensity, required for FLASH therapy.

REFERENCES

[1] O. V. Karamyshev *et al.*, "Research and Development of the SC230 Superconducting Cyclotron for Proton Therapy", *Phys. Part. Nucl. Lett.,* vol. 18, pp. 63-74, Feb. 2021. doi:10.1134/S1547477121010088

[2] S. Jolly *et al.*, "Technical challenges for FLASH proton therapy" *Phys. Med.*, vol. *78*, pp. 71-82, Oct. 2020. doi:10.1016/j.ejmp.2020.08.005

23rd Int. Conf. Cyclotrons Appl. CYCLOTRONS2022, Beijing, China JACoW Publishing
ISBN: 978-3-95450-212-7 ISSN: 2673-5482 doi:10.18429/JACoW-CYCLOTRONS2022-THPO001

COLUMBUS - A SMALL CYCLOTRON FOR SCHOOL AND TEACHING PURPOSES

C. R. Wolf, M. Prechtl, University for Applied Sciences, 96450 Coburg, Germany

Abstract

In the early 2012 the project "COLUMBUS - a Small Cyclotron for School- and Teaching Purposes" started. Supported by the FZ Jülich and some German companies a small cyclotron was built at the University of Applied Sciences of Coburg, Germany. After the first beam was detected in 2014, the cyclotron was continuously improved and expanded. At the same time, an educational concept based on the studies and curricula in Germany was developed. Since then, workshops and internships, which are the two columns of the concept, have enjoyed increasing popularity among students and, fortunately, among female students as well. Furthermore, future improvements of the accelerator and the educational concept are presented.

INTRODUCTION

A cyclotron is, in theory at least, an easy-to-understand accelerator. It is therefore part of the standard repertoire in all physics books in secondary schools. In practice, however, it looks very different. This shows that a cyclotron is a complex structure made up of a wide variety of systems that must be precisely coordinated with one another. For this reason, hardly any student has had any practical experience with this accelerator. This is where the COLUMBUS project comes in, providing students with a functioning small cyclotron with which they can learn accelerator physics and carry out their own experiments.

TECHNICAL DEVELOPMENT

After the FZ Jülich provided a magnet, VACOM, a company for vacuum components, sponsored a suitable vacuum chamber and a pumping station was bought by the University of Applied Sciences of Coburg, the assembly of the cyclotron COLUMBUS began in 2012. The first results were presented at Cyclotrons'13 in Vancouver [1]. Figure 1 shows the setup of the cyclotron COLUMBUS at the end of 2013.

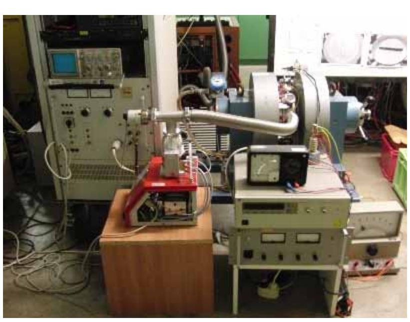

Figure 1: Cyclotron COLUMBUS 2013.

The first beam was registered in April 2014 (see Fig. 2), which was followed by the first workshop with students in autumn of the same year.

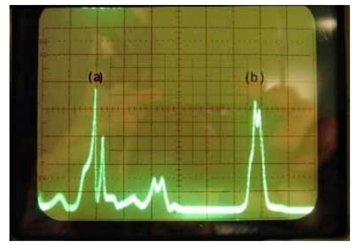

Figure 2: First Beam (a) H^+ (b) H_2^+.

The cyclotron was continuously improved and expanded with the involvement of pupils and students. A cooling system for the magnet, a linear translator for the detector and many other improvements complemented the accelerator.

A mechanical cyclotron, as shown in Fig. 3, and a simulation of the ion paths which was presented at Cyclotrons'16 in Zurich [2], improved the educational concept.

Figure 3: Mechanical Cyclotron.

Pupils and students are currently dealing with topics related to the accelerator in workshops and internships. For example, the first 3D-printed vacuum chamber was shown at Cyclotrons'19 in Cape Town [3].

The cyclotron available today (see Fig. 4) has a vacuum chamber with a diameter of 200 mm and a height of 75 mm. With an improved matchbox, two cyclotron frequencies of 2.82 MHz and 5.64 MHz are available. The technical data of the cyclotron are shown in Table 1.

Figure 4: Cyclotron COLUMBUS 2022.

Table 1: Technical Data of the Cyclotron

Description	Value
Diameter of the Dees	140 mm (5.5 in)
Flux density	185 mT (H^+) | 370 mT (H_2^+)
Vaccum in the chamber	10^{-6} mbar
dto with H_2	10^{-5} mbar
Cyclotron frequency	2.85 MHz | 5.64 MHz
Dee Voltage	0.5 – 3.0 kV
Final Energy	~ 4,1 keV (H^+) | 7,5 keV (H_2^+)

EDUCATIONAL CONCEPT

Parallel to the construction of the cyclotron, an educational concept was developed to bring the theory closer to the pupils and students. This concept rests on two pillars:

- Workshops.
- Internships.

While the workshops are aimed at pupils, the internships are primarily intended for students.

Workshops

The workshops are available in several formats:

- Two-day in-depth workshop.
- One-day workshop.
- Online workshop with three sessions and one face-to-face session in the lab.

A workshop takes place in groups with up to 6 participants. If more people register, up to 12 persons can be accepted, who will then be divided into two groups. Online workshops were added due to the pandemic situation, but were also used in a cross-border workshop.

The program of all workshops is primarily based on the valid curricula for physics in Germany, so that the participants can use the knowledge they have acquired directly at school.

All workshops have similar programs. In the first part, the participants receive an interactive presentation in which the development of the accelerators is shown. In particular, the difference between DC- and AC-accelerators is explained. A special focus lies on the discussion of the acceleration principle as the resonance of an alternating electric field with the circulation of the ions. A mechanical cyclotron is used to illustrate this. Finally, the formulas for the cyclotron frequency and the energy of the ions are derived.

The second part introduces the accelerator itself. The subsystems as shown in Fig. 5 (magnetic-, vacuum-, ion-, acceleration- and detector-system) are explained. The students are involved so that they can operate the accelerator themselves under supervision.

In the third part, an experiment is carried out in which the students analyse the ions occurring in the beam. To do this, the detector is set to a specific position and the magnetic field is continuously increased. With very specific magnetic fields, there are peaks in the beam current as evident in Fig 6. Using a computer interface, the beam current and magnetic field are caught, saved, and plotted. As

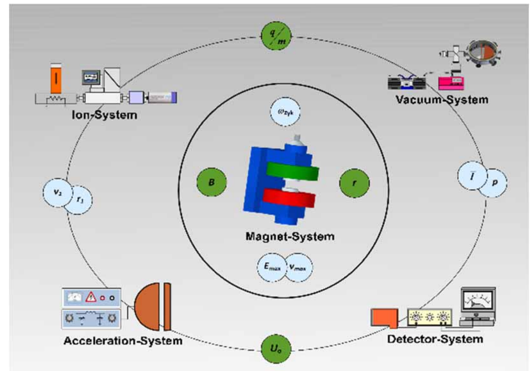

Figure 5: The Cyclotron and its Subsystems.

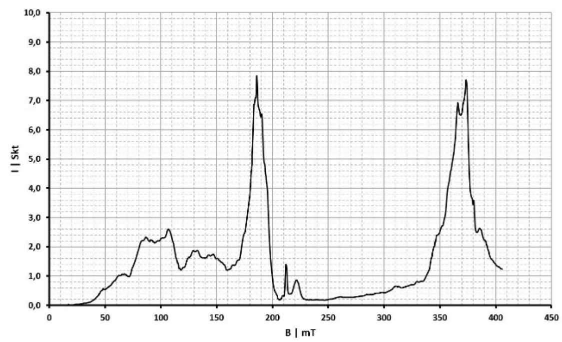

Figure 6: Beam Spectrum.

a result, the experiment is largely automated, so that several beam spectra can be recorded. The students change various parameters, such as acceleration voltage, gas flow or the heating current of the filament and observe the effects on the beam spectrum.

One of these spectra is evaluated as an example by assigning the corresponding ions to the individual peaks by calculating the specific charge. This is done dividing the known cyclotron frequency by the measured flux density.

Since the participants receive the measurement data of all experiments carried out, they can be used for further evaluations at home, at school or for seminar papers.

The one-day workshops focus on the two main peaks for H^+ and H_2^+ ions, while the two-day workshop can also analyse other peaks e.g., the peaks that correspond with the third or fifth of the nominal velocity.

During the two-day workshop, this program will be supplemented by additional elements such as simulations and specialist lectures, for example on the vacuum system or the RF system.

In recent years, these workshops have also been increasingly popular with girls. There have even been a few workshops where the number of girls exceeded that of the boys.

Internship

In addition to the workshops, internships are offered, especially for students. Here the participants carry out in-depth experiments such as spatially resolved measurement of the flux density of the magnet, develop parts that supplement the cyclotron, e.g., a linear translator with which the Faraday cup can be positioned, or investigate a Penning ion source with the aim of using it for the installation in the accelerator.

ISBN: 978-3-95450-212-7 ISSN: 2673-5482 doi:10.18429/JACoW-CYCLOTRONS2022-THPO001

Reports, papers, bachelor, or master theses then emerge from these activities. Publications in specialist journals were also the result of internships.

Pupils who take part in such internships mainly work on competition topics, e.g., for “Jugend forscht” or the “Innovation Award” by the Schaeffler company.

FUTURE PROJECTS

Finally, an outlook on future projects should be given.

In August last year, with the support of the IBA, Belgium, the constructing of an extraction system for the ions was started. The aim of this project is to deflect the ion beam and guide it through a Wien Filter to measure the speed and energy of the ions. These values can be compared with the calculated ones. A further advantage arises from the use of a Wien Filter. Like the cyclotron, this also belongs to the classic applications of electromagnetic fields and is - unfortunately only theoretically - known to the students from school. Thus, a Wien Filter represents a valuable practical addition to the school material.

But not only the accelerator itself should be improved and supplemented, an addition to the educational concept is also planned. This is a questionnaire about the material of the workshop. This should be filled in by the participants before and after the workshop. From the difference in the respective answers, you can see which parts of the workshop have been understood and how much the students have caught. In this way, targeted improvements can be made in the educational concept.

CONCLUSION

The COLUMBUS project, started in 2012, has developed very positively in the last 10 years. In addition to the technical development of the actual accelerator, an educational concept was created that has become increasingly popular with both male and female students. The additional online format of the workshop was not only able to adequately replace the face-to-face events during the pandemic, but also seems to prove itself in cross-border workshops.

In addition, the internships offered by this project give the students the opportunity to enlarge meaningfully their theoretical knowledge.

ACKNOWLEDGEMENTS

The authors thank Prof. Rudolph Maier and especially Dr. Ralf Gebel from the FZ Julich for their continous support and help during the whole period of development.

Furthermore, we thank the companies VACOM GmbH and Pfeiffer Vacuum GmbH for purchasing vacuum equipment.

A big thank also goes to the company IBA Group and here to Wiel Kleeven and Quentin Flandroy for the assistance in investigating an extraction system.

REFERENCES

[1] M. J. Frank, E. Held, and C. R. Wolf, “Columbus - A simple ion source”, in *Proc. Cyclotrons'13*, Vancouver, Canada, Sep. 2013, paper WEPPT021, pp. 364-365.

[2] C. R. Wolf, M. Prechtl, and R. Rueß, “Simulation and detection of the helical ion-paths in a small cyclotron”, in *Proc. Cyclotrons'16*, Zurich, Switzerland, Sep. 2016, pp. 21-23. doi:10.18429/JACoW-Cyclotrons2016-MOB02

[3] C. R. Wolf, F. B. Beck, L. Franz, and V. M. Neumaier, “3D printing for high vacuum applications”, in *Proc. Cyclotrons'19*, Cape Town, South Africa, Sep. 2019, pp. 317-320. doi:10.18429/JACoW-CYCLOTRONS2019-THC04

ISBN: 978-3-95450-212-7 ISSN: 2673-5482 doi:10.18429/JACoW-CYCLOTRONS2022-THPO002

STUDY ON PROTON RADIATION EFFECT AND SELF-REPAIR OF SiC-JBS DIODES

C. C. Liu†, G. Guo, Z. Zhang, F. Q. Zhang, Q. M. Chen, H. L. Shi
China Institute of Atomic Energy, Beijing, China

Abstract

In this study, the influence of proton irradiation experiments at 40 MeV and 2.2×10^{12} p/cm^2 on Silicon Carbide Junction Barrier Schottky (SiC-JBS) diodes with stripe cell and hexagonal cell was investigated, respectively. The experiment was implemented based on 100 MeV high intensity proton cyclotron of China Institute of Atomic Energy. The results show that the current voltage (IV) and capacitive voltage (CV) characteristics of the SiC-JBS diodes are obviously degraded by proton irradiation. After 168 h and 336 h room temperature annealing, the forward IV characteristics of the diodes are basically restored but the reverse leakage current is increased. And the CV characteristics are degraded of the two kinds of diodes permanently, which indicating that room temperature annealing cannot restore the proton radiation displacement damage defects. The analysis of structure of the diodes shows that the diodes with hexagonal cells are more resistant to proton irradiation and have stronger room temperature annealing self-repair ability than the diodes with stripe cells, even though its chip area is smaller. This means that the SiC-JBS diodes with hexagonal cells can be used preferentially in the radiation environment where there is a large amount of proton.

INTRODUCTION

The physical and electronic properties such as band gap width, thermal conductivity, electric field strength of SiC is attractive [1]. Also, the energy required to kick an atom out of the lattice position, i.e., the mean displacement energy, is higher than silicon (Si) [2]. Compared with other semiconductor materials, the performance advantages of SiC are shown in Fig. 1.

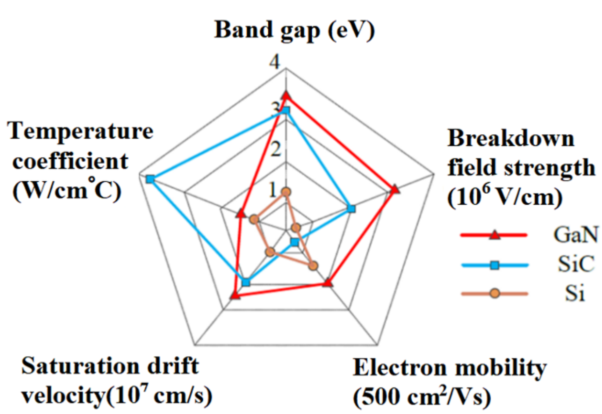

Figure 1: Performance advantages of SiC compared with other semiconductor materials.

As can be seen from Fig. 1, SiC is a promising semiconductor material for power device applications with additional advantages for harsh environments with high temperature and radiation [3]. At present, power systems for examples electric propulsion systems and photovoltaic inverter systems based SiC diodes, have further developed towards miniaturization, lightweight, high efficiency and low loss [4, 5]. And one of the most important points is radiation hardness, which makes SiC power devices the better choice than Si to complete space exploration tasks.

SiC junction barrier Schottky (JBS) diodes is a kind of SiC power device with simple structure and excellent performances. The previous researches show that after proton irradiation with a certain fluence, the breakdown voltage of SiC-JBS diodes will degrade, which is mainly related to the change of ionized charge at the SiO_2/4H-SiC interface in the device and the reduction of carrier concentration in the drift region [6]. And, the decrease of carrier concentration is attributed to the carrier removal phenomenon caused by radiation defects [7]. However, numerous degradation performances after proton or other high energy particles irradiation on SiC-JBS diodes without power supply are attributed to the displacement damage effect of irradiation defects, and there is little analysis on the impact of ionized charges [8, 9]. In order to study the influence of proton irradiation defects on the macro electrical performance of SiC-JBS diodes, and explore whether the diodes are also affected by ionization defects in the process of displacement damage, a proton irradiation experiment of SiC-JBS diodes under unbiased voltage was carried out, and the influence of ionized charges was investigated through room temperature annealing method.

PROTON IRRADIATION EXPERIMENT

Two kinds of 1200 V/40A SiC-JBS diodes with different cell designs were selected and named #a and #b respectively. The top surface and section structure of the diodes obtained by scanning electron microscope (SEM) analysis technology are shown in Fig. 2. Combined with the microstructure of these SiC-JBS diodes, the key performance parameters such as barrier height and carrier concentration can be calculated theoretically. It can be seen from Fig. 2 that the #a is with hexagonal cell designs, and its typical breakdown voltage (BV) is about 1230 V, the average Schottky barrier height (SBH) is about 1.15 eV, the average ideality factor (n) is about 1.02. The #b is with stripe cell design, and its typical BV is about 1450 V, the average SBH is about 1.13 eV, and the average n is about 1.06, respectively. Both diodes have extremely stable switching on voltages of about 0.4 V.

† sissiliu2020@163.com

ISBN: 978-3-95450-212-7 ISSN: 2673-5482 doi:10.18429/JACoW-CYCLOTRONS2022-THPO002

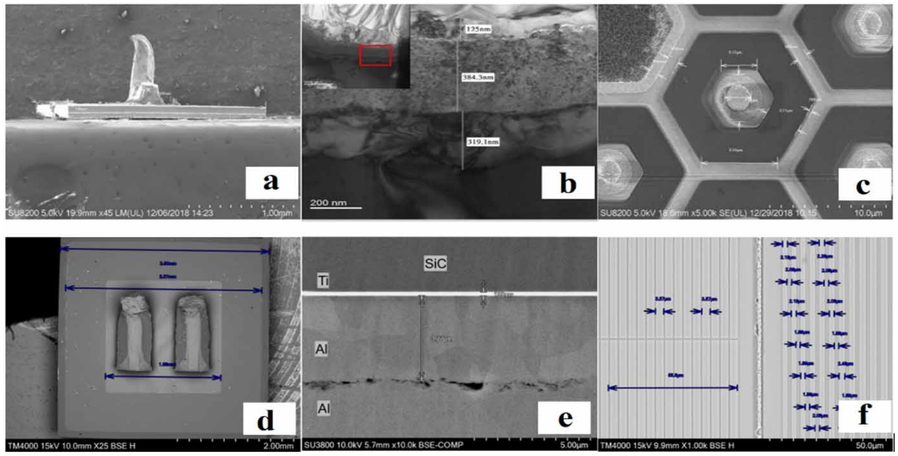

Figure 2: Microstructure images of the whole, section and top of #a (a)-(c) and #b (d)-(f) SiC-JBS diodes.

Realizing the reliable application of SiC power devices in today's typical aerospace orbit is an important step for SiC to help aerospace development. Considering that the proton energy on nowadays typical orbit is concentrated at 10 - 100 MeV [10], and the proton flux of 30 - 50 MeV is at the peak, the irradiation experiment of 40 MeV proton was carried out. The proton fluence accumulates to 2.2×10^{12} cm^{-2}. For SiC power devices, it can show the performance change coming from the accumulated displacement damage dose under the condition of geosynchronous orbit (GEO) operation for 20 years [11]. And the electrical characteristics of the diodes were measured using the Agilent B1505A power device analyzer.

RESULTS AND DISCUSSION

Forward IV

Before and after proton irradiation, the forward electrical properties of the SiC-JBS diodes were tested, and the self-repair of the diodes after room temperature annealing for 168 h and 336 h were analyzed. The forward IV characteristics of #a and #b at every condition are shown in Fig. 3. At lower forward voltages, there is an increase in current consistent with the introduction of recombination centers associated with proton-induced displacement damage [12]. At higher forward voltages, the current is decreased due to the defect energy level and interface state caused by irradiation. Figure 3 top shows the magnitude of the decrease of current measured at a forward voltage of 2 V. Note the percentage decrease in current is ~4% for #a and ~8% for #b separately after a fluence corresponding to more than 20 years in GEO. This decrease in the forward current and increase in the forward voltage drop after irradiation and annealing is attributed to the vacancies created by the impinging particles which in turn increase the resistance of the drift layer. However, after 168 h or 336 h annealing, we didn't observe the obvious self-repair of positive electrical characteristics, which shows that the room temperature annealing treatment has little effect on the self-repair of SiC-JBS diodes damaged by proton displacement damage defects.

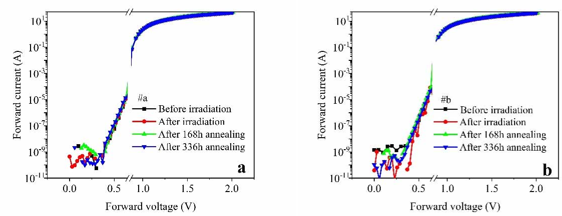

Figure 3: I_F-V_F of #a (a) and #b (b).

The SBH was extracted from the relationship [13]

$$J_F = A^*T^2 \exp\left(-\frac{qSBH}{nkT}\right)\left[\exp\left(\frac{qV}{nkT}\right)-1\right]. \quad (1)$$

where J_F is the forward current density at voltage V, A^* is effective Richardson's constant, which is about 146 $A\cdot cm^{-2}\cdot K^{-2}$ for 4H-SiC, T is the absolute measurement temperature, q is electronic charge, n is ideality factor, k is Boltzmann's constant, T is the absolute measurement temperature.

The forward voltage drop V_F for a SiC-JBS diodes, is related to the SBH and on-state resistance R_{on} from

$$V_F = \frac{nkT}{q}\ln\left(\frac{J_F}{A^*T^2}\right) + nSBH + R_{on}J_F. \quad (2)$$

where V_F is usually defined as the voltage at which J_F is 100 A/cm^2. The values of both diodes at every condition calculated according to the above equations is shown in Fig. 4, and both increase after irradiation and decrease after annealing.

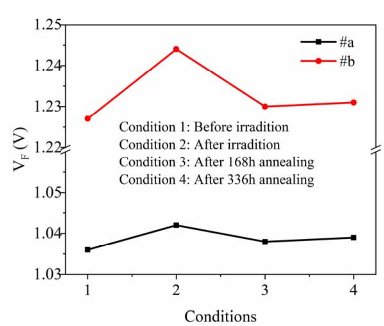

Figure 4: Forward voltage of SiC-JBS diodes.

ISBN: 978-3-95450-212-7 ISSN: 2673-5482 doi:10.18429/JACoW-CYCLOTRONS2022-THPO002

Reverse IV

The reverse electrical property of the SiC-JBS diode at each condition is tested, as shown in Fig. 5. The leakage current of # a has changed slightly, which is stable around 12 μA at 1200 V from before irradiation to 336 h annealing. But the leakage current of #b increases violently from 1 μA to 8 μA at 1200 V after 336 h annealing.

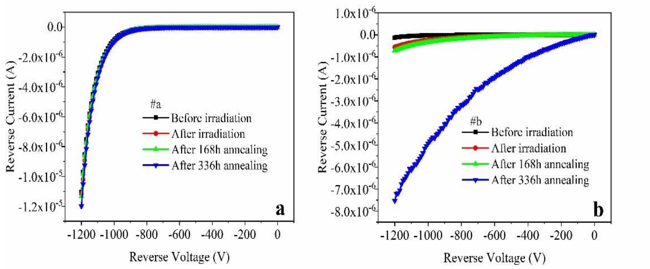

Figure 5: I_F-V_F of #a (a) and #b (b).

At the same time, Fig. 5(b) demonstrates the drain current of the #b after irradiation and annealing when the reverse voltage is applied. This is due to that irradiation defects will lead to the generation of interface state, and the damage of interface materials will lead to the formation of a leakage channel, which will enhance the tunneling current [14]. Therefore, this also means that damage introduced by proton irradiation is permanent and will not disappear completely through self-repair at room temperature.

Reverse CV

The relationships between capacitance C and voltage V after proton irradiation and annealing are shown in Fig. 6. The capacitance of #a is about 1480 pF at -1 V before irradiation, but is about 1380 pF after irradiation or annealing. The capacitance of #b is about 1650 pF at -1 V before irradiation, but the values are about 1300 pF, 1310 pF and 1390 pF respectively after irradiation, 168 h annealing and 336 h annealing. While the capacitance decreases significantly for #b, because the defects introduced by proton irradiation can form an interface state at the #b diode interface much easily than #a.

For SiC-JBS diodes, after numerical transformation, the CV relationship curve can be changed to a $1/C^2$ ~V relationship curve, which can be described by Eq. (3) [15]:

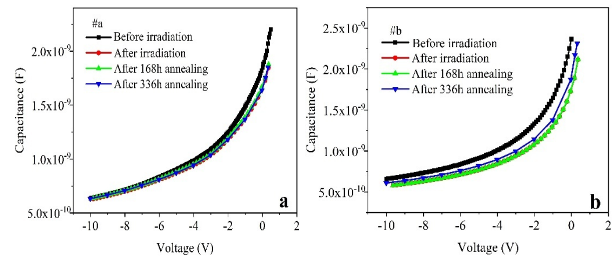

Figure 6: CV of #a (a) and #b (b).

$$\frac{1}{C^2}=\frac{2}{\varepsilon_s q A^2 N_{eff}}(V_{bi}+V) \qquad (3)$$

where A is the Schottky junction area, N_{eff} is the effective carrier concentration, V_{bi} is the value of built-in electric field, V is the external bias, ε_s is dielectric constant, which is about 9.7 F/m for SiC. And ε_s of the material is related to the polarization type, ambient temperature, electric field strength and other factors, its value affects the capacitance characteristics. Combining Eqs. (1) to (3) with the data in Figs. 4 and 6, the SBH, N_{eff}, R_{on} and n of the diodes were extracted. The results are shown in Fig. 7.

As we can see that the key electrical properties of the SiC-JBS diodes have changed significantly after proton irradiation and annealing. Proton irradiation leads to the increase of SBH and R_{on}, which leads to the decrease of forward current. In addition, proton irradiation introduces defects into the diode to form defect energy levels and trap levels, causing the increase in carrier removal or temporary trapping. The n represents the ratio of hot electron emission current. Some defects can form composite centres after irradiation by protons, which lead to an increase in the proportion of the composite current of the current. The interface defects also lead to the increase of tunneling current, so the ratio of hot electron emission current decreases and the value of increases after proton irradiation [16]. However, even after proton irradiation, then is still close to 1, indicating that the current of the diodes still dominated by thermionic emission current.

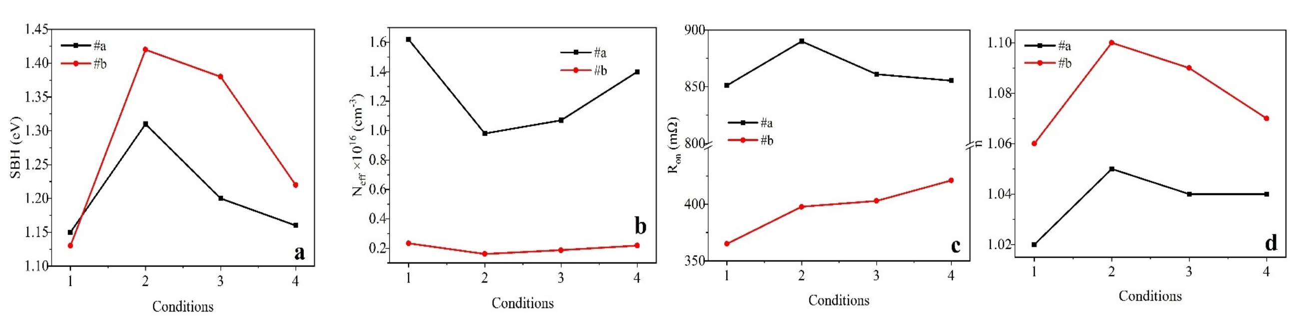

Figure 1: SBH (a), N_{eff} (b), R_{on} (c) and n (d) of SiC-JBS diodes.

ISBN: 978-3-95450-212-7 ISSN: 2673-5482 doi:10.18429/JACoW-CYCLOTRONS2022-THPO002

CONCLUSION

The proton irradiation experiments at 40 MeV and 2.2×10^{12} p/cm^2 were carried out using the 100 MeV high current proton cyclotron of the China institute of atomic energy. The displacement damage effect and room temperature self-repair phenomenon of SiC-JBS diodes were studied. The experimental results show that proton irradiation will introduce defects in the diodes, causing the potential barrier to rise and the carrier concentration to drop, resulting in changes in the electrical characteristics, especially the reverse leakage current will increase significantly under the impact of the operating bias voltage, and the capacitance characteristics of the diodes will also be significantly degraded due to the increase of interface states. The research on the self-repair phenomenon at room temperature shows that the defects caused by proton irradiation are difficult to be completely repaired. Even if the diodes show not degradation immediately after irradiation, potential damage has been formed inside the diodes, which seriously affects their service life and reliability. Comparing devices with different structures, it is found that the diodes with hexagonal cell have better radiation resistance and robustness. The principle of this phenomenon will be studied later, and suggestions for radiation resistance reinforcement will be put forward.

REFERENCES

[1] I. Capan *et al.*, "Influence of neutron radiation on majority and minority carrier traps in n-type 4H-SiC", *Nucl. Instrum. Methods Phys. Res. Sect. B*, vol. 478, pp. 224-228, 2020. doi:10.1016/j.nimb.2020.07.005

[2] H. Bencherif, L. Dehimi, N. Athamena, F. Pezzimenti, M. L. Megherbi and F. G. Della Corta, "Simulation study of carbon vacancy trapping effect on low power 4H-SiC MOSFET performance", *Silicon*, vol. 13, pp. 3629-3637, 2021. doi:10.1007/s12633-020-00920-5

[3] H. L. Heinisch, L. R. Greenwood, W. J. Weber, and R. E. Williford, "Displacement damage in silicon carbide irradiated in fission reactors", *J. Nucl. Mater.*, vol. 327, no. 2-3, pp. 175-181, 2004. doi:10.1016/j.jnucmat.2004.02.012

[4] X. Wang, Y. W. Zhong, H. B. Pu, J. C. Hu, X. F. Feng and G. Yang, "Investigation of lateral spreading current in the 4H-SiC Schottky barrier diode chip", *J. Semicond.*, vol. 42, no. 11, p. 112802, 2021. doi:10.1088/1674-4926/42/11/112802

[5] M. S. Tang *et al.*, "Method of field limiting rings spacing parameter for SiC JBS based on multiple linear regression and polynomial fitting", in *15th IEEE Conf. on Industrial Electronics and Applications (ICIEA'20)*, Kristiansand, Norway, Nov. 2020, pp. 1859-1863. doi:10.1109/ICIEA48937.2020.9248172

[6] Q. W. Song *et al.*, "Effects of proton radiation on field limiting ring edge terminations in 4H-SiC junction barrier Schottky diodes", *Sci. China Tech. Sci.*, vol. 62, no. 7, pp. 1210-1216, 2019. doi:10.1007/s11431-018-9394-8

[7] D. S. Chao *et al.*, "Influence of displacement damage induced by neutron irradiation on effective carrier density in 4H-SiC SBDs and MOSFETs", *Jpn. J. Appl. Phys*, vol. 58, no. SB, p. SBBD08, 2019. doi:10.7567/1347-4065/aafc9b

[8] A. Akturk, J. M. McGarrity, *et al.*, "Terrestrial neutron induced failures in Silicon carbide power MOSFETs and diodes", *IEEE Trans. Nucl. Sci.*, vol. 65, no. 6, pp. 1248-1254, 2018. doi:10.1109/TNS.2018.2833741

[9] R. D. Harris, A. J. Frasca and M. O. Patton, "Displacement Damage Effects on the Forward Bias Characteristics of SiC Schottky Barrier Power Diodes", *IEEE T. Nucl. Sci.*, vol. 52, no. 6, pp. 2408-2412, 2005. doi:10.1109/TNS.2005.860730

[10] C. Inguimbert and S. Messenger, "Equivalent displacement damage dose for on-orbit space applications", *IEEE Trans. Nucl. Sci.*, vol. 59, no. 6, pp. 3117-3125, 2013. doi:10.1109/TNS.2012.2221477

[11] M. A. Xapsos, E. A. Burke, F. F. Badavi, L. W. Townsend, J. W. Wilson, and I. Jun, "NIEL calculations for high-energy heavy ions", *IEEE Trans. Nucl. Sci.*, vol. 51, no. 6, pp. 3250-3254, 2005. doi:10.1109/TNS.2004.839136

[12] P. Hazdra and S. Popelka, "Displacement damage and total ionization dose effects on 4H-SiC Power Devices", *IET Power Electron.*, vol. 12, no. 2, pp. 1-9, 2019. doi:10.1049/iet-pel.2019.0049

[13] S. Nigam *et al.*, "High energy proton irradiation effects on SiC Schottky rectifiers", *Appl. Phys. Lett.*, vol. 81, no. 13, pp. 2385-2387, 2002. doi:10.1063/1.1509468

[14] B. Khorsandi, J. Kulisek, T. E. Blue, D. Miller, J. Baeslack, and S. Stone, "Analysis of displacement damage dose and low annealing temperatures on the I-V characteristics of SiC Schottky diodes using ANOVA method", *Nucl. Technol.*, vol. 172, no. 3, pp. 295-301, 2010. doi:10.13182/NT10-A10938

[15] Z. Luo *et al.*, "Proton radiation effects in 4H-SiC diodes and MOS capacitors", *IEEE Trans. Nucl. Sci.*, vol. 51, no. 6, pp. 3748-3752, 2004. doi:10.1109/TNS.2004.839254

[16] A. Siddiqui and M. Usman, "Radiation tolerance comparison of silicon and 4H–SiC Schottky diodes", *Mat. Sci. Semicon. Proc.*, vol. 135, p. 106085, 2021. doi:10.1016/j.mssp.2021.106085

ISBN: 978-3-95450-212-7 ISSN: 2673-5482 doi:10.18429/JACoW-CYCLOTRONS2022-THPO003

APPLICATIONS OF THE CYCIAE-100 CYCLOTRON IN NEUTRON-INDUCED SINGLE EVENT EFFECT

Q. M. Chen, J. Bao, G. Guo*, J. H. Han, X. Ma, S. Y. Zhao
China Institute of Atomic Energy, Beijing, China
National Innovation Center of Radiation Application, Beijing, China

Abstract

Neutron-induced single event effect is one of the significant factors affecting the reliability of semiconductor devices in avionics and ground facilities. The 100 MeV proton cyclotron in China Institute of Atomic Energy (CYCIAE-100) provides white neutron and quasi-monoenergetic neutron induced by proton and W/Li bombardment. Based on the white neutron beam of CYCIAE-100, the white neutron energy spectrum was measured by neutron time-of-flight method with double scintillator spectrometer, as well as the theoretical energy spectrum was calculated by the Monte Carlo method. The neutron irradiation test for ESA SEU monitor with different technology nodes were carried out, and the neutron single event upset sections are obtained simultaneously. In addition, based on the quasi-monoenergetic neutron beam line, the simulation of neutron energy spectrum was carried out. As a conclusion, the white neutron and quasi-monoenergetic neutron provided by CYCIAE-100 are well suitable applied to the study of neutron single event effects.

INTRODUCTION

Galactic cosmic rays and solar rays interact with nitrogen and oxygen in the earth's atmosphere to produce a large number of neutrons. Neutron incident semiconductor devices cause single event effects (SEEs), leading to logic inversion and functional failure, which seriously threaten the safety and reliability of aircraft electronic systems [1-3]. In addition, in the nuclear power stations and spent fuel reprocessing plants, neutron radiation produced by the nuclear reaction also reduce the reliability of electronic control systems and visual monitoring systems.

In order to measure the neutron-induced single event effects and to evaluate the risks of neutron radiation, accelerated tests based on the ground neutron sources were performed and progressively became the predominant approach, since the environmental atmospheric neutron test is time-consuming. Many neutron irradiation test equipment from white neutron source, quasi-monoenergetic neutron source and 14 MeV monoenergetic neutron source has been established, such as CHIPIR of ISIS [4], QMN of TSL [5], and so on. The white neutron source, which has an energy spectrum very close to the atmosphere neutron environment, are used to directly evaluate the atmospheric neutron effect. As a contrast, the monoenergetic and quasi-monoenergetic neutron sources are used to measure the cross-section curve of SEEs as a function of neutron energy, which is helpful in exploring the mechanism of the neutron SEEs.

* ggg@ciae.ac.cn.

In 2016, the first SEE experiment for electronic devices was carried out on the 100 MeV proton cyclotron (CYCIAE-100) in China Institute of Atomic energy (CIAE). This cyclotron provides a 70–100 MeV, 0.01-200 μA proton beam [6]. Meanwhile, with W and Li targets, both white neutron and quasi-monoenergetic neutron can be produced by proton and W/Li bombardment, which provides good neutron sources for experimental research of neutron SEEs.

In this paper, we first measured the white neutron energy spectrum by time-of-flight method with double scintillator, and then tested neutron SEE for ESA SEU monitor. The possibility and ability of irradiation test by quasi-monoenergetic neutron were also analysed.

WHITE NEUTRON EXPERIMENT

Prior to SEE testing, the neutron energy spectrum shall be accurately measured. Since the CYCIAE-100 induces a continuous proton beam, the withe neutron beam produced by proton bombards W targets is also a continuous beam. The conventional neutron measurement methods for pulsed neutron are not adequate. Therefore, the neutron time-of-flight (TOF) experiment with two scintillator detectors were performed. By measuring the neutron flight time at a certain distance, we obtain the flight speed of neutrons, and hence the energy of neutrons.

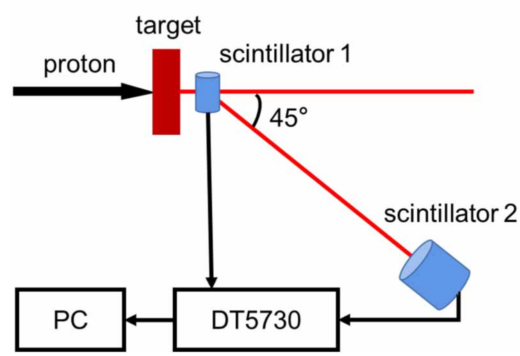

Figure 1: The measurement of white neutron spectrum.

The white neutron target is tungsten copper alloy WCu7, 93% of which is tungsten, 12 mm thickness and 75 mm diameter. After passing through 2 mm copper and 5 mm water, 100 MeV protons bombard the 12 mm thick WCu7 target and white neutron are produced.

As shown in Fig. 1, one liquid scintillator detector (scattering detector) is placed on the neutron beam behind the target, which is detect the start signal of flight neutron, and the other (main detector with high efficiency) is placed at a distance L (L=3 m) and 45° direction of the proton beam, which is detected the stop signal of flight neutron. The

ISBN: 978-3-95450-212-7 ISSN: 2673-5482 doi:10.18429/JACoW-CYCLOTRONS2022-THPO003

gamma signal was removed by pulse shape discrimination (PSD), and the time spectrum of flight neutron were acquired by a DT5730 digitizer in the coincidence mode, see Fig. 2.

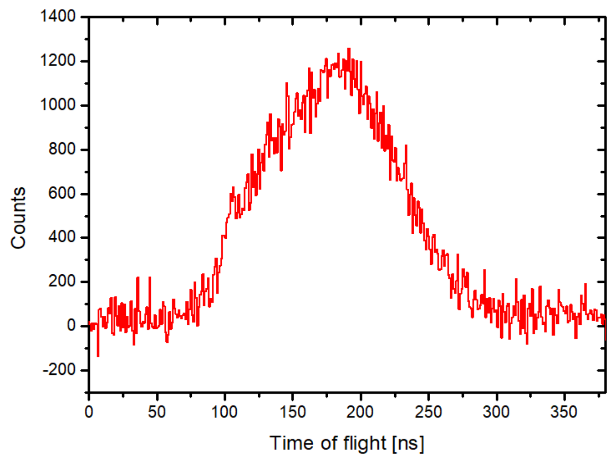

Figure 2: The TOF spectrum of white neutron spectrum.

With the detection efficiency correction for two liquid scintillators by Monte Carlo simulation, the neutronic energy spectrum can be obtained by converting the TOF spectrum with Eq. (1).

$$E = m_0c^2\left(\frac{1}{\sqrt{1-(\frac{L}{tc})^2}}-1\right) \tag{1}$$

where E is the energy of flight neutron, m_0 is the mass of neutron, L is the distance between two scintillator detectors, t is the flight time of neutron and c is the velocity of light.

Figure 3 shows the measured neutron energy spectrum and contrasts it with the theoretical spectrum simulated by Monte Carlo method. Limited by the need to discriminate against gamma rays, the lower limit energy of the neutron measured is only 3 MeV, the Fig. 3 showed that the measured energy spectrum almost completely coincided with the calculated one from 3 MeV to 100 MeV energy region.

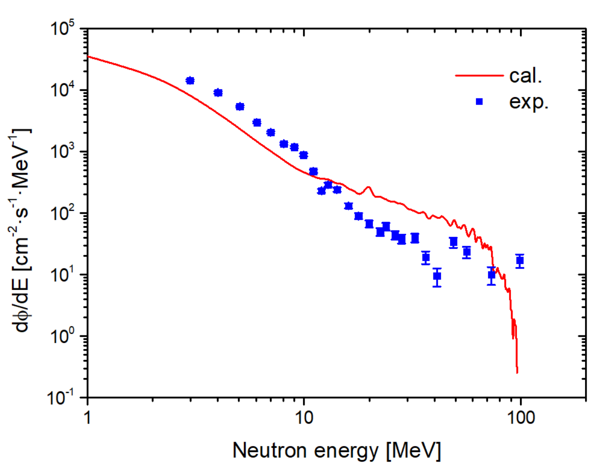

Figure 3: The measured energy spectrum, and compare to the theoretical spectrum by Monte Carlo simulation.

As a result, with 100 MeV/1 μA proton, 3.28×10^4 n/(cm^2·s) neutron from 3 MeV to 100 MeV were produced at the position 15 m away from the target in 0-degree direction, and neutrons above 10 MeV account for 12.4%.

Base on the white neutron spectrum, the Europe space agency single event upset monitor (ESA SEU Monitor) was applied to measure the cross section of neutron SEU.

The irradiation experimental results show that the neutron SEU cross section of the SEU Monitor (250 nm, 16 Mbit, 3.3 V) is 31.0 upsets/h with 3 μA proton, that is 5.47×10^{-15} upsets/(cm^2·bit). Usually, 10 MeV is considered as a threshold energy for high energy neutron SEE, but more and more evidences are provided to certify that less energy neutron can also lead to SEE in advanced electronic systems [7, 8]. The contribution of neutron below 10 MeV to SEE is critical too. Considering the energy above 10 MeV accounts for 12.4% of the white neutron source in CYCIAE-100, this neutron source is more suitable to test the neutron radiation effects for nuclear industry rather than for atmospheric environment.

QUASI-MONOENERGETIC NEUTRON SIMULATION

The monoenergetic neutron in the energy range of several MeV to 20 MeV are mainly produced by the two-body nuclear reaction induced by different light ions, such as the 14 MeV D-T neutron source. In the energy region above 20 MeV, ^{7}Li (p, n) ^{7}Be reactions are primary used.

The reaction energy of ^{7}Li (p, n)^{7}Be is -1.646 MeV and the threshold energy of neutron production is 1.881 MeV. At the incident proton energy of 1.9-2.4 MeV, the ^{7}Li (p, n)^{7}Be reaction produces only the ground state ^{7}Be, i. e., ^{7}Li (p, n_0)^{7}Be, and the produced neutrons are monoenergetic neutrons with a large cross section (300-500 mb). The proton energy exceeds 2.4 MeV and the produced ^{7}Be can be excited to its first excited state (0.43 MeV), i.e., ^{7}Li (p, n_0)^{7}Be and ^{7}Li (p, n_1)^{7}Be occur simultaneously. For SEE cross-sections, the energy dependence is not particularly sensitive, so both n_0 and n_1 are treated as single-energy peak neutrons. When the proton energy exceeds 3.68 MeV, the ^{7}Li (p, n^{3}He)^{4}He reaction channel is opened, which is a three-body reaction and produces neutrons as a continuum spectrum with energies below the monoenergetic peak. Higher proton energies even excite ^{7}Be to the second and third excited states as well as other multi-body breakup reaction. In summary, n_0 and n_1 from ^{7}Li (p, n_0)^{7}Be and ^{7}Li (p, n_1)^{7}Be constitute the monoenergetic peak neutron, while neutrons from other reaction channels constitute the continuous spectrum of neutrons with lower energy than the monoenergetic peaks.

Since the ^{7}Li (p, $n_{0,1}$)^{7}Be reaction has the largest cross section in the 0° emission direction, the neutron from 0° emission direction is chosen as the irradiation source. Figure 4 shows the cross sections of the ^{7}Li (p, $n_{0,1}$)^{7}Be reaction at different energy proton from 10 MeV to 800 MeV, and it can be seen that the cross sections are first increasing rapidly and then then tends to be flat (data source [9, 10]), as shown in Fig. 4.

ISBN: 978-3-95450-212-7 ISSN: 2673-5482 doi:10.18429/JACoW-CYCLOTRONS2022-THPO003

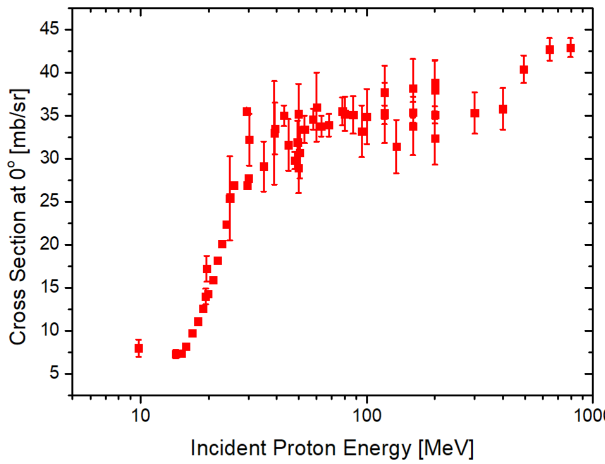

Figure 4: Nuclear reaction cross-section of ^{7}Li (p,$n_{0,1}$)^{7}Be.

The neutron flux of the monoenergetic peak emitted at the 0° direction can be calculated using the following equation

$$\Phi_{\theta=0}(n_{0,1}) = \sigma_{\theta=0}(n_{0,1}) \times \Phi_p \times \rho_{\,^7Li} \times d_{\,^7Li} \quad (2)$$

where $\sigma_{\theta=0}(n_{0,1})$ is the 0° direction ^{7}Li (p, $n_{0,1}$)^{7}Be reaction cross section, Φ_p is the incident proton intensity, $\rho_{\,^7Li}$ is the atomic density of the ^{7}Li target, and $d_{\,^7Li}$ is the ^{7}Li target thickness.

For 100 MeV/1 μA incident protons, the neutron flux calculated by Eq. (2) is 1.28×10^{4} n/(m^{2}·s) at a position 5 m away from the Li target.

In fact, the quasi-monoenergetic neutron target is natural Li, 6 mm thickness and 52 mm diameter. Figure 5 shows the theoretical spectrum by Monte Carlo simulation. With 100 MeV/1 μA proton, 2.92×10^{4} n/(cm^{2}·s) neutron from 0 MeV to 100 MeV were produced at the position 5 m away from the target in 0 degree direction, and monoenergetic peak neutrons account for 51.8%. Since 70, 80, 90, 100 MeV protons can be derived from the CYCIAE-100 directly, so four quasi-monoenergetic neutron sources are available for neutron radiation effects.

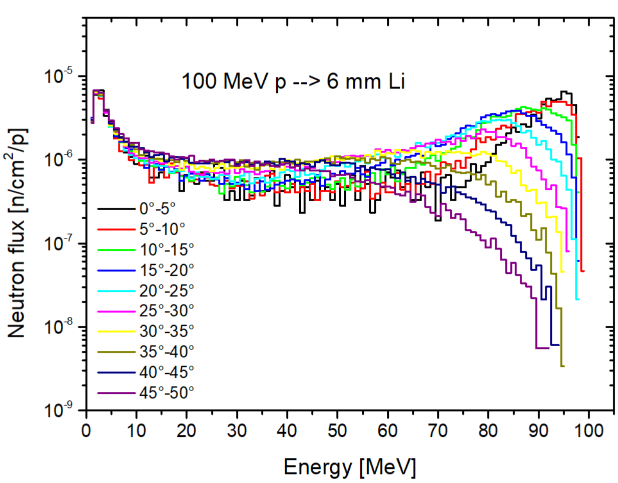

Figure 5: Neutron spectrum of 100 MeV proton bombards the 6 mm Li target.

As shown in Fig. 5, the neutron energy spectrum differs greatly in different emission directions, with the highest proportion of peak neutrons in the high-energy part of the 0-5 direction. The main reason is that the Li(p, n) reaction consists of direct nuclear reaction mechanism and compound nucleus reaction mechanism, the direct nuclear reaction is mainly the knockout reaction, which produces neutrons with foreshortening and high energy, while the compound nucleus reaction evaporation neutrons in all directions, which is homogeneity and is mainly low-energy neutrons. Therefore, the neutrons in the 0° emission direction have the best monochromaticity, which is used to carry out the irradiation text for neutron SEEs.

Because higher incident energy will lead to a multi-body breakup reaction, only quasi-monoenergetic neutrons can be obtained, thus their energy spectra contain not only monoenergetic peak fractions but also low-energy tail continuous fractions. These trailing neutrons can also trigger SEEs, which affect the accuracy of neutron SEEs cross section measurements. Nevertheless, since the quasi-monoenergetic neutron has a high proportion of monoenergetic peak neutrons, up to 40% or even higher, the SEEs due to low-energy neutrons can be corrected by the tail neutron correlation method and the accurate cross-section of neutron SEEs obtained.

CONCLUSION

The white neutron spectrum measurement and the first neutron single event effect test were performed based on the CYCIAE-100 cyclotron in CIAE. With 100 MeV/1 μA proton, 3.28×10^{4} n/(cm^{2}·s) neutron provided to irradiate the electronics device. Considering the neutrons above 10 MeV account for 12.4%, the white neutron source is more suitable to test the neutron radiation effects for nuclear industry rather than for atmospheric environment. The quasi-monoenergetic neutron spectrum simulated by Monte Carlo method, with 100 MeV/1 μA proton, 2.92×10^{4} n/(cm^{2}·s) neutron were provided to irradiate the electronics device. Since 70, 80, 90, 100 MeV protons can be derived from the CYCIAE-100 directly, so four quasi-monoenergetic neutron sources are available for neutron radiation effects.

ACKNOWLEDGEMENTS

Valuable discussions with Dr. W. W. Qu of Soochow university are acknowledged. We are grateful to the CYCIAE-100 cyclotron staff for the operation of the machine.

REFERENCES

[1] E. Normand, "Single-event effects in avionics", *IEEE Trans. Nucl. Sci.*, vol. 43, pp. 461-473, 1996. doi:10.1109/23.490893

[2] C. Dyer *et al.*, "Testing Across a Wide Range of Energies and Facilities and Implications for Standards", *IEEE Trans. Nucl. Sci.*, vol. 53, pp. 3596-3601, 2006. doi:10.1109/TNS.2006.886207

[3] P. Ramos *et al.*, "Evaluating the SEE sensitivity of a 45nm SOI multi-core processor due to 14 MeV neutrons", *IEEE*

ISBN: 978-3-95450-212-7 ISSN: 2673-5482 doi:10.18429/JACoW-CYCLOTRONS2022-THPO003

Trans. Nucl. Sci., vol. 63, pp. 2193-2200, 2016. doi:10.1109/TNS.2016.2537643

[4] C. Andreani *et al.*, "Facility for fast neutron irradiation tests of electronics at the ISIS spallation neutron source", *Appl. Phys. Lett.*, vol. 92, pp. 114101, 2008. doi:10.1063/1.28973

[5] V. Alexander *et al.*, "CUP–A New High-Flux Irradiation Position at the ANITA Neutron Facility at TSL", *IEEE Trans. Nucl. Sci.*, vol. 61, pp. 1929-1936, 2014. doi:10.1109/TNS.2014.2319098

[6] E. Ibe *et al.*, "An automatic phase matching technique of CYCIAE-100 cyclotron", *Nucl. Sci. Tech.*, vol. 28, pp. 1–6, 2017. doi:10.1007/s41365-017-0277-9

[7] J. L. Autran *et al.*, "Soft-error rate induced by thermal and low energy neutrons in 40 nm SRAMs", *IEEE Trans. Nucl. Sci.*, vol. 59, pp. 2658–2665, 2012. doi:10.1109/TNS.2012.2222438

[8] E. Ibe *et al.*, "Impact of scaling on neutron-induced soft error in SRAMs from a 250 nm to a 22 nm design rule", *IEEE Trans. Nucl. Sci.*, vol. 57, pp. 1527–1538, 2010. doi:10.1109/TED.2010.2047907

[9] H. Guo *et al.*, "Application of the continuum discretized coupled channels method to nucleon-induced Reactions on ^{6,7}Li for Energies up to 150 MeV", *Nucl. Data Sheets*, vol. 118, pp. 254–257, 2014. doi:10.1016/j.nds.2014.04.051

[10] Y. Iwamoto *et al.*, "Characterization of high-energy quasi-monoenergetic neutron energy spectra and ambient dose equivalents of 80-389 MeV ^{7}Li(p, n) reactions using a time-of-flight method", *Nucl. Instrum. Meth. Phys. Res. Sect. A*, vol. 804, pp. 50–58, 2015. doi:10.1016/j.nima.2015.09.045

ISBN: 978-3-95450-212-7 ISSN: 2673-5482 doi:10.18429/JACoW-CYCLOTRONS2022-THPO004

CSPT: A GPU-ACCELERATED LATTICE DESIGN TOOLKIT ESPECIALLY FOR CCT*

Y. C. Liao[1], R. X. Zhao[2], C. Y. Li[1], X. Liu[1], W. Wang[1], B. Qin[†,1]
[1]State Key Laboratory of Advanced Electromagnetic Engineering and Technology, School of Electrical and Electronic Engineering, Huazhong University of Science and Technology, Wuhan, China
[2]Shenzhen Institute of Computing Science, Shenzhen, China

Abstract

Canted-Cosine-Thera (CCT) superconducting magnet is a promising alternative for normal-conducting magnets in compact accelerator systems such as large hadron colliders or particle therapy facilities. For the convenience of lattice design with CCT, we develop the CCT Simulation and Particle Tracking (CSPT) toolkit. It's a program that can perform both simulations of the beam dynamic process within particle accelerators and basic electromagnetic harmonic analysis. The charged-particle tracking and electromagnetic calculation process can be accelerated by either CPU multicore or GPU parallel, with a maximum speed-up ratio of 457. The simulation result of the program is well consistent with Opera and COSY Infinity.

INTRODUCTION

In pursuit of high-field magnets, advanced superconducting technology is introduced into the accelerator area. Among the existing superconducting magnets, Canted-Cosine-Theta(CCT) has become quite popular with magnet designers due to it's superior field quality, outstanding mechanical properties and simple winding process [1]. The concept of CCT magnet is based on pairs of conductor wound and powered such that their transverse field components sum up and their axial (solenoidal) field components cancel [2]. As it possesses promising potential in collider, storage ring and particle therapy facility, many laboratories have carried out research on CCT magnets in recent years [3–6].

Thanks to the winding flexibility of CCT magnet, complex multipole field components can be generated. However, few optics and particle tracking software have embedded this type of magnet. Great efforts would be put forward for researchers to accurately simulate and control the beam dynamics in a lattice with CCT magnets. For the convenience of the CCT-related research, we present the CCT Simulation and Particle Tracking (CSPT) toolkit. In this report, the structure of the CSPT toolkit is discussed, and the calculation results are testified with finite element analysis software Opera and optics code COSY Infinity [7].

* Work supported by the National Natural Science Foundation of China under Grant No. 11975107, 12205111.
† bin.qin@mail.hust.edu.cn

SOFTWARE STRUCTURE

The CSPT toolkit, written in C++17 standard, is compatible with beam dynamic simulation and electromagnetic field analysis within CCT magnet. The structure of the toolkit is shown in Fig. 1.

Fundamental Classes

The gray block at the top of the structure contains the fundamental (low-level) classes of the toolkit that users are not supposed to call directly. The *P2/P3* class characterizes points or vectors in two or three dimensions. The *Coordinate System* class, composed of *P3* vectors, denotes the position of each element and particle.

In CSPT, lines in two dimensions are needed for every magnetic element, so that the position of a particle can be defined in the curvilinear coordinate system. The *Line2* class, which can generate lines in arbitrary curvature, is the base class of 2D lines. It's made up of *P2* points. The *Straight Line* and *Arc line* classes are the derived class of *Line2*. The ideal orbit of a lattice in the toolkit consists of several 2D lines with the vertical axis $y \equiv 0$. Each 2D line belongs to a magnetic element.

Magnetic Elements

At present, only magnetic elements are supported in CSPT toolkit. The *Uniform Magnet* and the *Multipole Magnet* generate ideal fields within the element regions (hard-edge). The *Multipole Magnet* can combine fields from dipole to octupole. To describe a complex field shape, the *Input Magnet Table* class shall be applied. And the class supports the Opera field format. The field calculation process of *CCT* is based on Biot-Savart Law. The field shape of the CCT magnet can be adjusted by modifying the path function of the windings. The CCT model in the CSPT can also be loaded to Opera as conductors. Besides, common harmonic analysis programs are provided for the magnetic classes so that users can check the field quality in the lattice space.

High-level Classes

Above all, the Particle classes and *Beamline* are the highest-level classes in the toolkit. They can be directly called by users. A type of particle with specific values of mass and charge can be defined in *Particle type* class. Then, the toolkit provides two methods to produce running particles. Users can generate a particle with position (x, y, z) and velocity (V_x, V_y, V_z) of a chosen type in *Particle Source*, or

ISBN: 978-3-95450-212-7 ISSN: 2673-5482 doi:10.18429/JACoW-CYCLOTRONS2022-THPO004

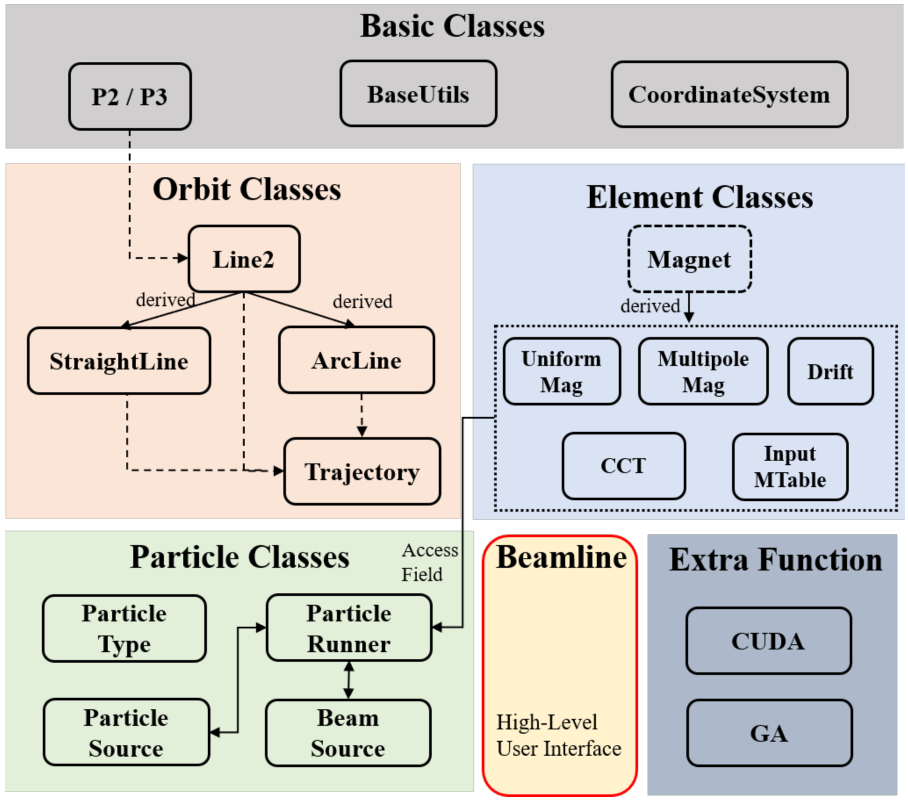

Figure 1: The structure of the CSPT toolkit. Each rectangle with round corners represents a C++ class in the toolkit.

define a beam of a specific number of particles with Gaussian or uniform distribution in *Beam Source*, which is a more useful way in a practicle simulation. The beam can be defined both in twiss or sigma parameters. The *Particle Runner* is responsible for calculating the Lorentz force and movement of each running particle in a small time step. Runge-Kutta45 is adopted for the particle tracking calculation.

To build a beam lattice easily, the *Beamline* class adopts MAD-style syntax. Users can simply define a magnetic element with several parameters, and the element would be directly jointed at the end of the present lattice. The program will calculate the position and direction of the element, and produce a *Line2* orbit for it automatically. What's more, the *Beamline* class offers several common particle tracking programs, so that users don't have to pay attention to the Particle classes.

To be noticed, the CSPT toolkit does not cover the calculation of particle-matter interactions. But the toolkit allows the user to input the particle information from Geant4 using the *Particle Factory* class. To accelerate the calculation speed of particle tracking and magnetic field (especially for CCT magnets), CPU multicore (OpenMP) and GPU parallel (CUDA) technology are applied. Besides, a Genetic Algorithm (GA) package is developed so that users can conduct lattice design and optimization just in the toolkit.

RESULTS

To prove the accuracy of CSPT results, we pick widely-used optics software COSY-Infinity as a reference for particle tracking results within ideal multipole elements, and finite element analysis software Opera as a reference for CCT magnetic field calculation results.

Validation of Beam Optics Calculation

A beamline lattice of HUST-PTF gantry [8] is generated in CSPT and COSY Infinity, respectively. And a particle is emitted at the start of the lattice and collected at the end. Phase space results of the particle in the programs are compared. We carried out 10 times of experiments. And for the first 5 experiments, the magnets parameters are changed randomly. For the last 5, the initial parameters of the particle are changed. Figure 2 shows the maximum error of the phase space results in the experiments. There is a well consistency of the CSPT toolkit with the optics software, with a maximum relative error of 0.92% and a maximum absolute error of 0.056 mm.

Validation of Field Analysis

A CCT magnet with 4 layers is generated in the CSPT toolkit. And the conductor model is then loaded to Opera. The multipole component distribution on the reference orbit is shown in Fig. 3. The dipole and quadrupole results show well consistency between the two programs. Differences on sextupole and octupole at the entrance and exit of the

ISBN: 978-3-95450-212-7 ISSN: 2673-5482 doi:10.18429/JACoW-CYCLOTRONS2022-THPO004

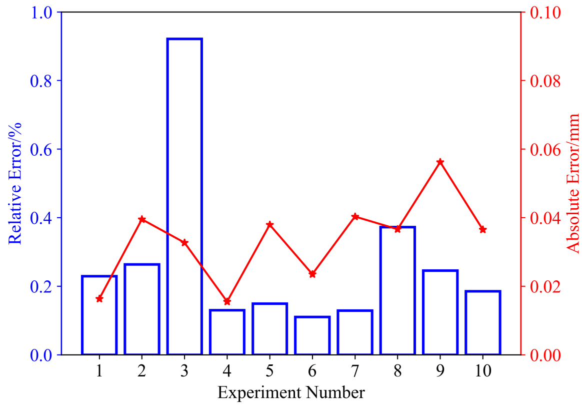

Figure 2: The error of the CSPT tracking results with respect to COSY Infinity.

magnet, which would lead to no significant divergence in the particle tracking results, are mainly due to the numerical error during the fast Fourier transform process. Figure 4 is the tracking result of an ideal particle in the CCT magnet in CSPT toolkit and Opera. The maximum difference between two programs, at the end of the lattice, is about 0.1 mm.

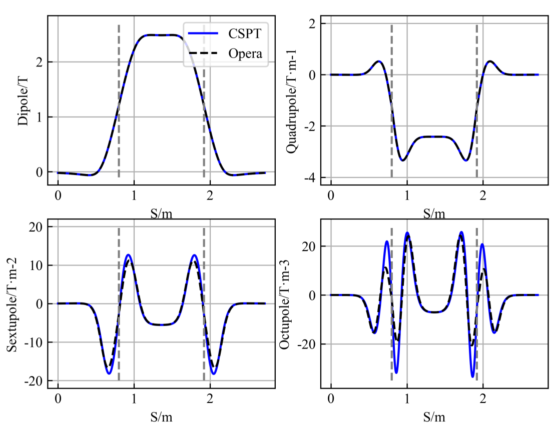

Figure 3: The field component of a 4 layers CCT magnet on the ideal orbit. The blue lines represent the results of CSPT toolkit, the black lines in dash are the Opera's results.

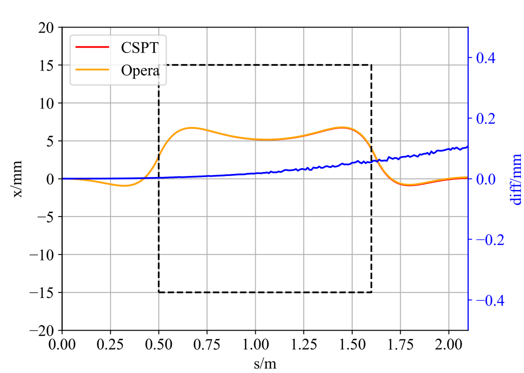

Figure 4: A particle tracking result of CSPT and Opera. The black box in dash line represents the CCT magnet.

Calculation Speed

The calculation speed of CCT magnetic field dominates the efficiency of lattice design and particle tracking, to a considerable extent. The field calculation with Biot-Savart Law is a very time-consuming process, because there are an enormous number of current units in a CCT manget. To alleviate the problem, CPU multicore and GPU parallel technology are applied in the toolkit. In Table. 1, the tracking time of 250 particles in a beamline with 2 CCT magnets is investigated. The GPU parallel enables the toolkit to calculate a maximum of 457 times faster than the single thread CPU version, exchanged with merely a 0.32% relative error increase.

Table 1: Calculation Time of 250 Particles in a Beamline under Different Settings

Method	Total time	Speed-up ratio
CPU (1 core)	77 298 sec	-
CPU (12 cores)	13 318 sec	5.8
CUDA (double)	531 sec	145.6
CUDA (float)	169 sec	457.0

CONCLUSION

CCT magnet, as a promising alternative for the next generation accelerator facilities, has drawn much attention over the world. But few optics software support accurate simulation of this kind of magnet. In this paper, we present a newly-developed program called the CCT Simulation and Particle Tracking toolkit (CSPT). It's capable of dealing with particle tracking and field analysis tasks. The experiment shows that the toolkit can produce accurate results with a relative error below 1.0% in a considerably short calculation time. Together with rich built-in functions, it's a simple and effective toolkit for lattice design with CCT magnet. Due to limited time, the Graphic User Interface(GUI) and lattice error analysis module are still ongoing.

REFERENCES

[1] S. Caspi *et al.*, "Design, Fabrication, and Test of a Superconducting Dipole Magnet Based on Tilted Solenoids", *IEEE Trans. Appl. Supercond.*, vol. 17, no. 2, p. 2266-2269, Jun. 2007. doi:10.1109/TASC.2007.899243

[2] L. B. Brouwer, "Canted-Cosine-Theta Superconducting Accelerator Magnets for High Energy Physics and Ion Beam Cancer Therapy", Ph.D. thesis, University of California, Berkeley, American, 2015.

[3] F. Bosi *et al.*, "Compact superconducting high gradient quadrupole magnets for the interaction regions of high luminosity colliders", *IEEE Trans. Appl. Supercond.*, vol. 23, no. 3, Art, no. 4001004, Jun. 2013. doi:10.1109/TASC.2012.2231716

[4] R. X. Zhao *et al.*, "Achieving a realistic design for a superconducting gantry with large momentum acceptance for proton therapy", *Nucl. Instr. Methods. Phys. Res. Sect. A*, vol. 1015, no. 1, p. 165773, Nov. 2021. doi:10.1016/j.nima.2021.165773

ISBN: 978-3-95450-212-7 ISSN: 2673-5482 doi:10.18429/JACoW-CYCLOTRONS2022-THPO004

[5] W. S. Wan *et al.*, “Alternating-gradient canted cosine theta superconducting magnets for future compact proton gantries”, *Phys. Rev. ST Accel. Beams*, vol. 18, no. 10, p. 103501, Oct. 2015. doi:10.1103/PhysRevSTAB.18.103501

[6] K. D. Wang *et al.*, “Achromatic beamline design for a laser-driven proton therapy accelerator”, *Phys. Rev. Accel. Beams*, vol. 23, no. 11, p. 111302, Nov. 2020. doi:10.1103/PhysRevAccelBeams.23.111302

[7] K. Makino *et al.*, “COSY INFINITY Version 9”, *Nucl. Instr. Methods. Phys. Res. Sect. A*, vol. 558, no. 1, p. 346-350, Mar. 2006. doi:10.1016/j.nima.2005.11.109

[8] B. Qin *et al.*, “Design and development of the beamline for a proton therapy system”, *Nucl. Sci. Tech.*, vol. 32, no. 138, 2021. doi:10.1007/s41365-021-00975-y

23rd Int. Conf. Cyclotrons Appl. CYCLOTRONS2022, Beijing, China JACoW Publishing
ISBN: 978-3-95450-212-7 ISSN: 2673-5482 doi:10.18429/JACoW-CYCLOTRONS2022-THPO005

JULIC – DRIVER ACCELERATOR FOR HBS

O. Felden, V. Kamerdzhiev, Forschungszentrum Jülich, IKP-4, Germany
R. Gebel, K. Grigoriev, Y. Valdau, GSI Helmholtzzentrum für Schwerionenforschung, Germany

Abstract

At the Forschungszentrum Jülich (FZJ) the energy variable cyclotron JULIC is used as injector of the Cooler Synchrotron (COSY) and for low to medium current irradiations of different types. Recently a new target-moderator-reflector-station (TMR) was set up and is mainly used for tests of new target materials, neutron target development and neutron yield investigations with high power proton or deuteron beam in perspective of a high brilliance accelerator based neutron source (HBS) with the Jülich Centre for Neutron Science (JCNS). Beside this, ToF-experiments are performed to investigate and optimize the pulsing structure for HBS. The TMR-station is installed inside an Experimental area close to the cyclotron bunker, offering space for complex detector and component setups for nuclear and neutron related experiments. It is used for other purposes like electronic or detector tests and irradiation as well. This report briefly summarizes the history of JULIC and the activities for its future perspectives.

INTRODUCTION

The Institute for Nuclear Physics (IKP) [1] is focusing on the tasks given by the Helmholtz Association (HGF). This comprises the design and preparations for the High Energy Storage Ring (HESR) of FAIR [2] with the PANDA experiment. The hadron physics program at the Cooler Synchrotron COSY exploits the internal experimental setups PAX, KOALA and the PANDA Cluster-Jet Target Development. The Jülich Electric Dipole Moment Investigation project (JEDI) [3] profits from the availability of polarized beams from the injector cyclotron and the unique capabilities and experiences at the COSY facility. The extracted beam is used for the PANDA experiment, detector tests and for high-energy irradiation in the area of the finished TOF experiment. The JESSICA and Big Karl-Experiment areas are also used with extracted beam for other FAIR related detector tests and developments like CBM e.g., Fig. 1 presents the layout of the COSY facility with the JULIC cyclotron and the experimental areas.

The COSY accelerator facility [4], operated by the Institute for Nuclear Physics at the Forschungszentrum Jülich, consists of the injector cyclotron JULIC and the Cooler Synchrotron COSY. Both accelerators are originally dedicated to fundamental research in the field of hadron, particle, and nuclear physics, to study the properties and behaviour of hadrons in an energy range that resides between the nuclear and the high energy regime. Operation of the cyclotron JULIC started 1968 and it provides mainly 45 MeV H^- respectively 76 MeV D^- with beam currents up to ~10 μA.

Within the framework of the High Brilliance neutron Source project [5], Jülich is developing a scalable pulsed

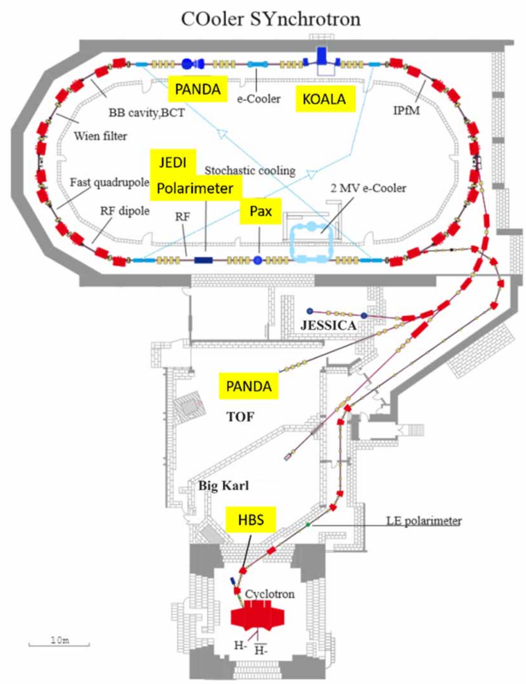

Figure 1: Layout of the COSY facility with the new beamline from the cyclotron into the Big Karl Experiment area.

accelerator-based neutron source capable of supporting thelarge scale facilities and providing an efficient network of small and medium neutron sources throughout Europa.

The HBS JULIC Neutron Platform is installed at the Big Karl experimental area aside the JULIC cyclotron providing experimental space for the development, testing and operation of components of pulsed accelerator-based neutron sources within the HBS project together with the Jülich Centre for Neutron Science.

Figure 2 shows the experimental setup in Big Karl-area with the Target-Moderator-Reflector-Setup (TMR) and possible experimental setups at different neutron beamlines like ToF-PGNAA or reflectometer, e.g., it further allows the design, construction and operation of basic scientific neutron scattering and neutron analytic instruments for development, training, education, and research in collaboration with university groups and industry.

CURRENT STATUS OF HBS ACTIVITIES

For experiments related to the HBS project, a dedicated beam line at the JULIC cyclotron at the COSY facility into the Big Karl area (Fig. 3) has been built in beginning of 2019.

At this beamline, experimental validations of cross section measurements and component tests for the HBS target development had been performed. With installation of the TMR the beamline was extended with additional kicker

ISBN: 978-3-95450-212-7 ISSN: 2673-5482 doi:10.18429/JACoW-CYCLOTRONS2022-THPO005

and dipole magnets and a dedicated three field permanent magnet [6] (Figs. 4 and 5) to connect the TMR directly to the cyclotron.

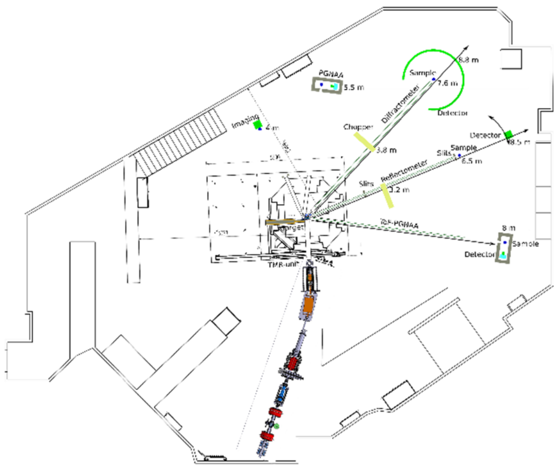

Figure 2: HBS-JULIC Neutron Platform in Big Karl area.

These additional magnets obtain the possibility to deflect the beam up to 40°, as foreseen in the proposed HBS-layout for driving three target stations.

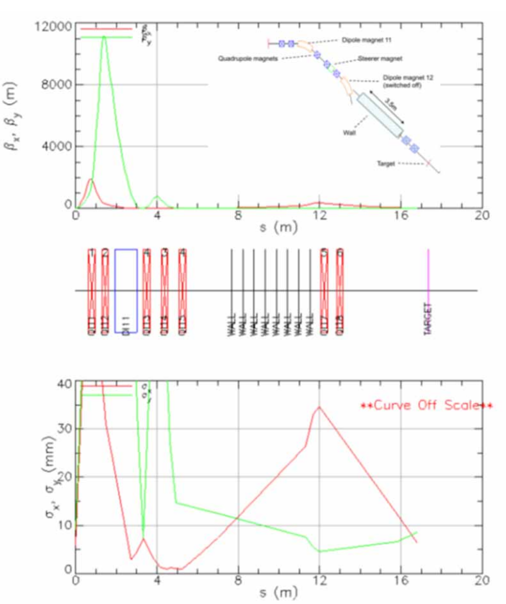

Figure 3: Beamline to Big Karl area. The figure shows the simulation results of transport calculations starting at the cyclotron, passing the shielding wall as well as the quadrupole setup.

The kicker magnet is used for testing the sophisticated timing scheme of HBS to run different target stations while the three-field permanent magnet obtains the possibility to bend the beam into three directions – straight, left- or right-handed [8]. For this purpose, the permanent magnet can be shifted using a stepper motor, so the beam enters the dedicated field region of the magnet.

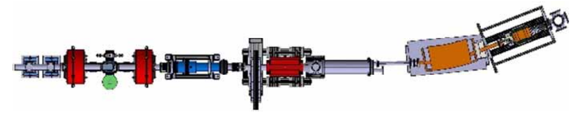

Figure 4: Beamline inside the Big Karl-Area with two quadrupoles, the Three-field, permanent magnet, fast Kicker and dipole-magnet to bend the beam into the TMR.

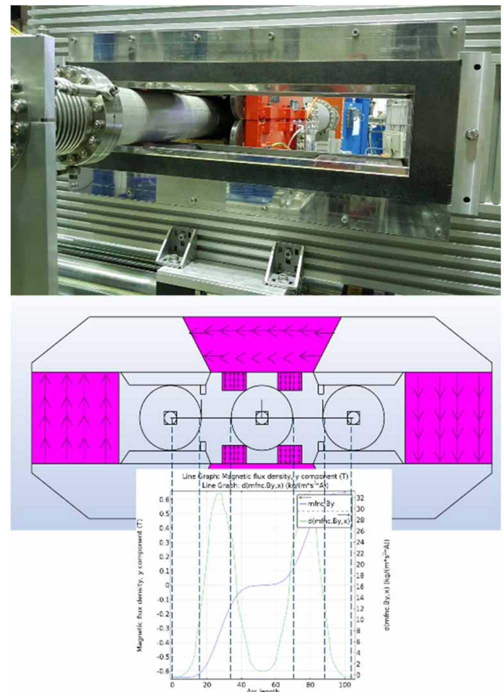

Figure 5: Three-field permanent magnet in position to bend the beam left-handed into the TMR. The lower sketch shows the dedicated field-regions and measured field-strength in the horizontal midplane.

For diagnostic purposes the beamline is equipped with current measurement as well as beam position and profile measurement tools.

Beam profile measurements (see Fig. 6) with a Multi Wire Proportional Chamber (MWPC) installed at the second exit window is used for optimizing the beam spot on target regarding to the experimental needs.

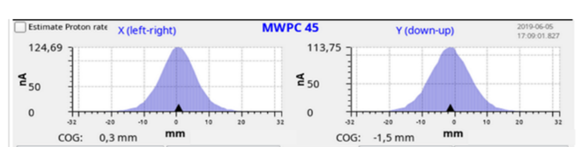

Figure 6: Beam profile at Big Karl target station. The beam size shown is ~15 mm FHWM.

Beam position is measured in both X and Y planes with a capacitive Beam Position Monitor System (BPM) [6, 7] (Fig. 7) utilizing four electrically isolated electrodes. Signal processing is done with preamplifiers FEMTO DHPVA-201 and lock-in-amplifiers Stanford Research SR844 [12] and data recorded via [13]. Newly developed graphical user interfaces based on [14] allow for display of measured beam orbit and currents.

ISBN: 978-3-95450-212-7 ISSN: 2673-5482 doi:10.18429/JACoW-CYCLOTRONS2022-THPO005

Beam current is measured with a Bergoz Fast Current Transformer (FCT) [10, 11] (Fig. 7) inside the Big Karl-area and on an isolated stainless steel foil separating target vacuum from cyclotron vacuum. At this foil H^- is stripped to H^+. A second, isolated stainless steel exit window and beam cup in the right-handed beam path gives another current measurement possibility. Data Acquisition is done with CAEN TetrAMMs [9], recorded via EPICS IOCs and visualized with Control System Studio (CSS).

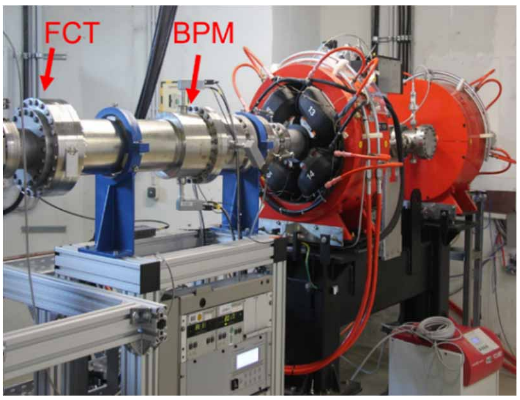

Figure 7: Beamline inside Big Karl area with Beam Position Monitor System (BPM) and Fast Current Transformer (FCT).

Additionally beam current is measured with different beam-cups which are installed along the beamline inside the cyclotron vault as well as inside the Big Karl-Area and the TMR (Fig. 8).

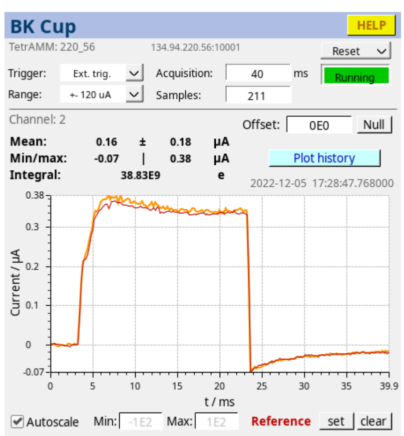

Figure 8: Beam current measurement at BigKarl Cup showing a pulsed beam of ~40nA.

The current permission for the radiation controlled area limits the operation to beam intensities of up to 10 nA. The area is going to be upgraded to the capabilities of the cyclotron.

Based on the routine parameters of the proton and deuteron beams offered by the JULIC the cyclotron can be used efficiently as part of a pulsed neutron source as in the concept for the NOVA ERA [15] or as existing accelerator based neutron facilities in Japan [16]. The pulsing scheme for proton beam of duration between 10 to 50 µsec has been realized.

Table 1: Parameters of the JULIC Neutron Platform

Description	Proton	Deuteron
Energy [MeV]	45	76
Current [µA]	10	10
Duty cycle [%]	4	4
Peak power [W]	450	760
Average power [W]	18	30

FUTURE ACTIVITIES

Based on the existing experimental station of the HBS project at the Big Karl area and the HBS target-moderator-reflector prototype (TMR) it is planned to further develop the compact neutron source concept with regards to targetry, neutron provision, moderator development and optimization of the TMR unit. Tests and developments of target handling, target cooling systems, biological shielding and any other development to improve neutron provision will be made possible. In addition, proton beam transport devices, beam control and dynamics, beam multiplexing or beam dump systems will be installed and tested at the platform. The multiplexer system, consisting of a fast kicker which deflects the beam up to 40° into a dedicated septa magnet, guiding the beam to three target stations will be tested and improved.

The new platform allows to design, construct and operate versatile neutron instruments for neutron scattering purposes as well as neutron analytics with competitive neutron flux. Shielding and Radiation protection calculations to run with 10 µA into the Big Karl-Area and permission process are in preparation.

Taking into account possible upgrades of the beam current of the JULIC cyclotron up to 10 µA beam power up to 30 W are achievable. This upgrade would promote the JULIC Neutron Platform in beam power and neutron flux an order of magnitude above current operated compact accelerator based neutron (CANS) facilities. It will allow for a full test of individual HBS structures including proof-of-principle experiments of components and performance tests of potential neutron scattering and analytic instruments an extension of the current installed experimental possibilities for HBS at the Big Karl area is in-tended. This extension will lead to a versatile platform for the operation and development of compact accelerator based neutron sources with dedicated neutron instrumentation used also by universities and industry for training, development and scientific service.

CONCLUSION

Using the JULIC cyclotron, it is possible to demonstrate a small accelerator-based neutron source with protons or deuterons in the energy range from 10 MeV to 45 MeV (76 MeV for deuterons) at COSY. This allows to test and develop critical components for the HBS project. In addition, it can provide access to neutron beam time for research and industry and with the expected performance of

ISBN: 978-3-95450-212-7 ISSN: 2673-5482 doi:10.18429/JACoW-CYCLOTRONS2022-THPO005

the neutron source at JULIC it is a unique option to strengthen the research with neutrons at the Forschungszentrum Jülich with the local universities, research institutions and industry.

REFERENCES

[1] Institute for Nuclear Physics, Forschungszentrum, Jülich, `http://www.fz-juelich.de/ikp/en`

[2] FAIR, GSI, `http://www.gsi.de/fair`

[3] `http://www.collaborations.fz-juelich.de/ikp/Jedi`

[4] R. Maier, "Cooler synchrotron COSY – performance and perspectives", *Nucl. Instrum. Methods Phys. Res. Sect. A*, vol. 390, no. 12, pp. 1-8, May 1997. . `doi:10.1016/S0168-9002(97)00324-0`

[5] U. Rücker *et al.*, "The Jülich high-brilliance neutron source project", *Eur. Phys. J.*, vol. 131, article no. 19, Jan. 2016. `doi:10.1140/epjp/i2016-16019-5`

[6] R. Maier *et al.*, "Non-beam disturbing diagnostics at COSYJülich", in *Proc. 2nd European Particle Accelerator Conf. (EPAC'90)*, Nice, France, Jun. 1990, pp. 800-802.

[7] J. Biri *et al.*, "Beam position monitor electronics at the cooler synchrotron COSY Jülich", *IEEE Trans. Nucl. Sci.*, vol. 41, no. 1, pp. 221-224, Feb. 1994. `doi:10.1109/23.281493`

[8] M.Rimmler – "Development of a Multiplexer System and Measurement of the Neutron Yield for a low-Energy Accelerator -Driven Neutron Source", volume 250 of Schriften des Forschungszentrums Jülich Reihe Schlüsseltechnologien/key Technologies, Forschungszentrum Jülich GmbH Zentralbibliothek, Verlag, Jülich, 2021

[9] CAEN ELS, User manual, "TetrAMM user's manual Rev. 2.6", Italy 2022

[10] Y. Valdau *et al.*, "Development of high resolution beam current measurement system for COSY-Jülich", *in Proc. 5th Int. Beam Instrumentation Conf. (IBIC'16)*, Barcelona, Spain, Sep. 2016, pp. 434437. `doi:10.18429/JACoW-IBIC2016-TUPG41`

[11] Bergoz Instrumentation, Fast Current Transformer, User's Manual, Rev. 3.1, 2015, devices 3272 and 3273 FCTCF10"-147.6-40-UHV-5.0-CAW.

[12] Agilent Technologies, User manual, "Agilent 33500 Series Waveform Generator", USA, 2012.

[13] Experimental Physics and Industrial Control System (EPICS), `http://www.aps.anl.gov/epics`

[14] Control System Studio Webpage, `http://controlsystemstudio.org`

[15] E. Mauerhofer *et al.*, "Conceptual design report - NOVA ERA (Neutrons obtained via accelerator for education and research activities) - A Jülich high brilliance neutron source project", volume 7 of Schriften des Forschungszentrums Jülich Reihe Allgemeines / General. Forschungszentrum Jülich GmbH Zentralbibliothek, Verlag, Jülich, 2017.

[16] Y. Kiyanagi, "JCANS network of compact neutron facilities in Japan", *Eur. Phys. J.*, vol. 131, article no. 132, May 2016. `doi:10.1140/epjp/i2016-16132-5`

ISBN: 978-3-95450-212-7 ISSN: 2673-5482 doi:10.18429/JACoW-CYCLOTRONS2022-THPO006

DESIGN AND IMPLEMENTATION OF ROBOT ADAPTER IN THERAPY CONTROL SYSTEM

Shangmeng Jiang[1,†], Zhiguo Yin[1], Yang Wang[1], Tianjue Zhang[1], Qiqi Song[1],
Qingzhen Zhu[2], Cheng Qi[3], Qiyong Ran[2]
[1]China Institute of Atomic Energy, Beijing, China
[2]Konica Minolta Zaiqi Medical Products (Shanghai) Co., Ltd., Shanghai, China
[3]Leoni Cable (China) Co., Ltd., Jiangsu, China

Abstract

The China Institute of Atomic Energy (CIAE) in Beijing has designed and established a proton therapy facility based on a superconducting cyclotron CYCIAE-230, which can provide proton beams with energy from 70 MeV to 230 MeV for cancer treatment. As the most critical and core part of the proton therapy system, therapy control system (TCS) consists of various components, each of which has corresponding processing services. Motion control of external hardware systems is one of the essential parts of TCS development, and adapters figure prominently in the interaction between services and these external hardware systems. One of the adapters, called robot adapter, is specially developed for the external robotic couch system, which is a vital equipment that directly contacts patients in the whole process of proton therapy. This adapter serves as the connection between TCS and robotic couch for communication and corresponding movement. In this paper, we introduced the communication protocols, design, and characteristics of robot adapter as well as the actual test contents and results with the robotic couch. The test results indicated that the robot adapter can satisfy the needs of couch motion control and status monitoring.

INTRODUCTION

Protons have been successfully utilized in the treatment of cancer in recent years, and proton therapy is superior to the conventional photon radiation therapy due to its physical properties, making it one of the world's preferred choice for cancer particle radiotherapy methods [1]. From 1954 to 2021, more than 324,000 patients worldwide underwent particle therapy, 86% of whom received proton therapy. According to Made in China 2025, high-performance medical equipment including proton heavy ion therapy system is explicitly listed as one of the top ten key industries [2]. CIAE has established a superconducting cyclotron that generates 230 MeV proton beam to promote the development of proton therapy in China [3].

Accelerator control system (ACS) is a complete automatic system for medical accelerator equipment, which realizes the automatic start-up, real-time monitoring, control, and protection of 230 MeV superconducting cyclotron related equipment. The system has complete status monitoring and fault diagnosis functions, including automation, operation status monitoring, equipment safety interlocking, automatic recording of operation data, etc. in each accelerator subsystem equipment.

† shangmeng99@foxmail.com

Beam control system (BCS) is a distributed control system with a standard control model structure. It uses an energy selection system that adjusts the energy of the extracted proton beam according to the different depths and thicknesses of the tumor. Energy degrader, the core component of the proton energy selection system, is mainly used to adjust the energy between 230 MeV and 70 MeV.

As the central system of proton radiotherapy, therapy control system (TCS) not only integrates all the execution systems involved in the treatment, but also is responsible for the management of the whole proton radiotherapy process. The treatment process includes patient setup, setup verification, equipment movement, dose delivery, treatment report, etc. It commands and controls the proton beam hardware in each link of the treatment process.

Scan dose diagnostic (SDD) is a software program of the Scan Dose system that enables a complete dose delivery nozzle by running maps and generating records, even though it is not designed for clinical dose administration. SDD can compute the threshold used and monitor the beam characteristics to ensure that the treatment is performed according to preset limits. In addition, SDD can record all parameters relevant to the treatment and provide room-centric and facility-centric interlock chains, so as to achieve fast beam shutdown.

In the whole proton therapy system, ACS can ensure the normal operation of the accelerator and the proton beam at 230 MeV. BCS can adjust the proton energy between 230 MeV and 70 MeV to meet the requirements of the clinical treatment regimen. It receives and processes the beam request of TCS, and arranges the beam supply to the designated treatment room. TCS uses the adapter to provide treatment prescription data to SDD. SDD distributes a predetermined dose of beam by controlling the extraction and monitoring the ionization chamber. If SDD is not directly connected to ACS, TCS can provide a channel between them.

ROBOT ADAPTER

Adapters support each specific subsystem independently. Each adapter is responsible for monitoring the status of its corresponding subsystem, and receiving and processing the operation information issued by services in TCS.

The robot adapter is designed for the external robotic couch system amid various adapters. Figure 1 shows the overview of the interaction between the robot adapter and the robotic couch and internal components in TCS.

ISBN: 978-3-95450-212-7 ISSN: 2673-5482 doi:10.18429/JACoW-CYCLOTRONS2022-THPO006

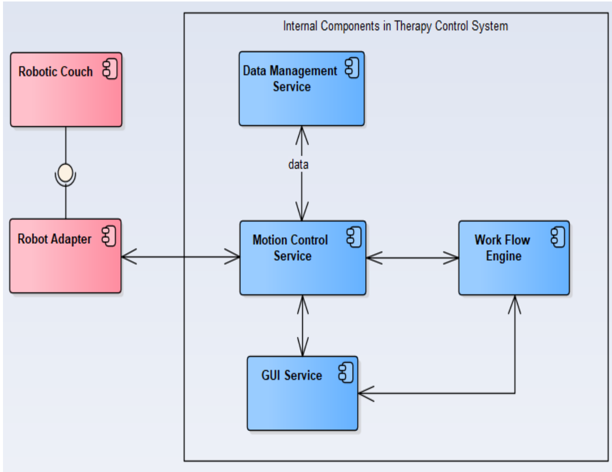

Figure 1: Interaction between the robot adapter and the robotic couch and internal components in TCS.

The motion control service in TCS is responsible for the motion control of the robotic couch, and feedback information such as couch status and coordinate position to the central workflow engine and TCS-GUI. The motion control service needs to send the motion requests of the robotic couch and modify the configuration parameters. Data management service stores patient setup information and verification results.

To invoke the interface of the robotic couch without altering the internal program of TCS, we extended TCS by developing a robot adapter. The interfaces implemented by the robotic couch are known as the provided interfaces, which denotes that the robotic couch offers robot adapter services. When the robot adapter requests services from the robotic couch, it should follow the required interfaces used by the robot adapter.

The robotic adapter controls and monitors the movement of the robotic couch system. It connects the data interaction between motion control service and robotic couch system. If there are specific requirements for the coordinate input of the robotic couch system, the robotic adapter is responsible for further converting the IEC coordinates transmitted by the motion control service.

Communication Protocols

TCS uses Data Distributed Service (DDS) to interact with the robot adapter to obtain high-performance real-time process data. DDS is a machine-to-machine middleware protocol and API standard of the Objective Management Group [4]. Interface Description Language (IDL) defines various data models (called topics in DDS terminology). By using DDS technology, TCS is completely decoupled from the external devices that need to be connected and controlled. The data flow interaction between TCS and robot adapter is only specified by the data model IDL.

The robot adapter uses Hyper Text Transfer Protocol (HTTP) to control the movement and status acquisition of the couch. The robotic couch can be remotely controlled on port 8081 by using HTTP/1.1 client.

Interface Information Summary

The robotic couch can be remotely controlled by using HTTP/1.1 client on port 8081. To use its API, JSON objects must be sent to the "/api" path on the ACU server. All commands should be HTTP POST. A method called "PromiseCommand" is compiled to implement requests for the robotic couch. Each request passes a command field, and the value is a specific operation instruction. The data structure requirements for command input parameters and response return values are shown in Tables 1 and 2, respectively.

Table 1: Command Input Parameters Type

Parameter	**Type**
command	string
param1_key	JSON
param2_key	JSON
…	
paramN_key	JSON

In Table 1, each command needs to enter a command name of string type. There can be multiple key-value pairs, and each value can be any JSON type.

Table 2: Response Return Value Type

Parameter	**Type**
command	string
returned_argument_1	JSON
returned_argument_2	JSON
…	
returned_argument_N	JSON
success	bool
error	string
masterId	string
result	object

In Table 2, a command is a confirmation of the received command name. It would be the same as the command parameters sent. There can be multiple return arguments, and each argument can also be any JSON type.

Success indicates whether the command is successfully received and executed. For motion commands, success means that the command is correctly interpreted and sent to the motion controller. If false, the "error" parameter should return the reason why this command failed. The command failure is described as the error if success is false. If there is no error, its value would be an empty string.

Functionalities

In the whole system, robot adapter act as a link between TCS and robotic couch. Therefore, the robot adapter should possess several principal functionalities as follows:

- Be able to establish a connection with the robotic couch and send commands to it in the format of HTTP POST.

ISBN: 978-3-95450-212-7 ISSN: 2673-5482 doi:10.18429/JACoW-CYCLOTRONS2022-THPO006

- Be able to get position information (IEC coordinate system) and joint position information from the robotic couch and send them to TCS.
- Be able to acquire the status of the robotic couch system at a regular interval and keep TCS informed of current status, including Ready, Moving, Error and Collision.
- Under the requirement of the motion of the robotic couch based on path or target position, the robot adapter can receive respective the corresponding parameters from TCS, and then instruct the robotic couch to move properly.

THE ROBOTIC COUCH REFERENCE

The robotic couch system has five states: CONFIG, READY, BUSY, UNHEALTHY, and COLLISION. The state transition of the system follows the state transition structure diagram (Fig. 2).

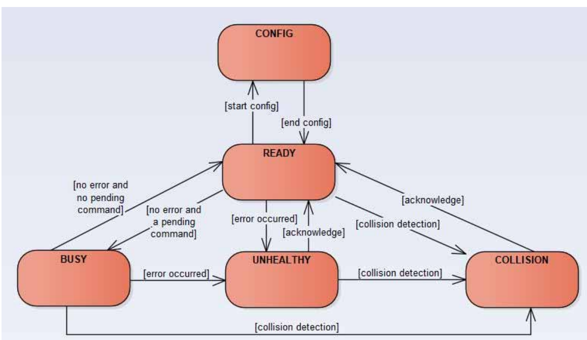

Figure 2: State transition structure diagram.

The robotic couch is involved in patient setup and setup verification, as shown in the following sequence diagrams (Figs. 3 and 4).

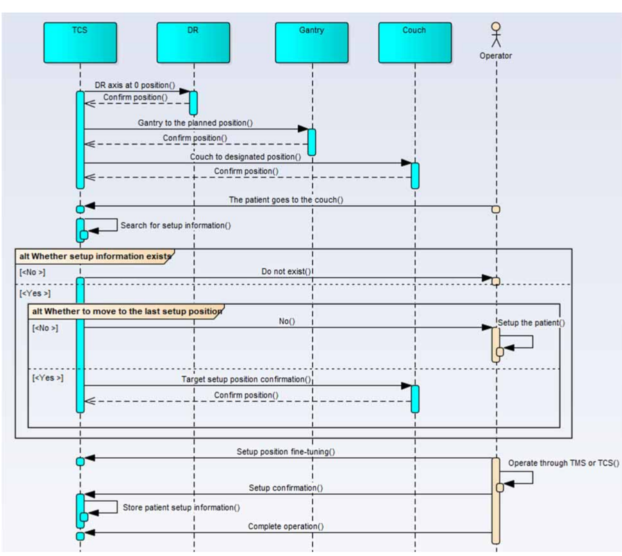

Figure 3: Setup sequence diagram.

Figure 3 shows the interaction during the patient setup process, which involves five objects: TCS, digital radiography (DR), gantry, couch, and operator. First, the DR axis is at position 0, and the gantry moves to the planned position. Then, the couch moves to the designated position, which facilitates the operator to help the patient move to the couch. Setup information can be searched using TCS in data management service. If the information does not exist or exists but the operator decides not to move to the last setup position, the manual setup will be performed. Otherwise, the couch will move to the target position. Afterward, the operator could fine-tune the setup position and confirm the position through TCS. Finally, the setup information of the patient can be stored in TCS.

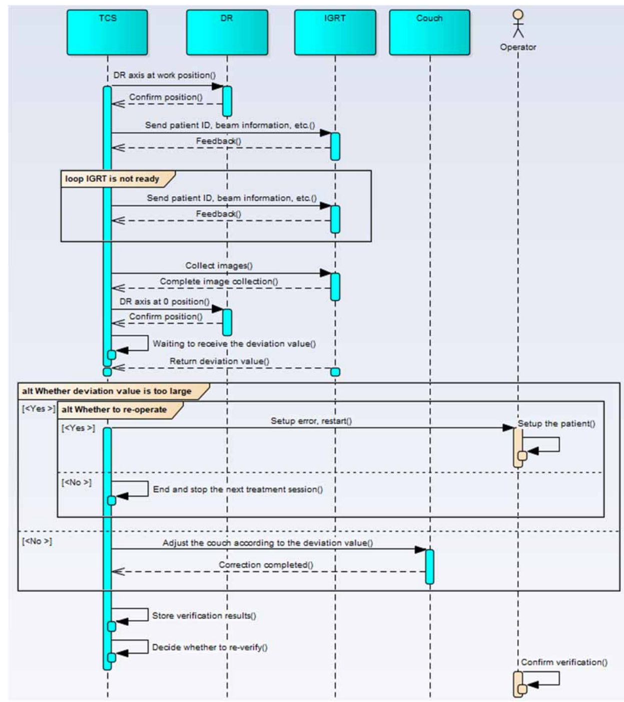

Figure 4: Setup verification sequence diagram.

Figure 4 shows the interaction during the setup verification process. This process involves five objects: TCS, DR, image-guided radiation therapy (IGRT), couch, and operator. First, the DR axis is at the work position, and TCS sends a message to IGRT. The sending operation will be repeated continuously if IGRT is not ready. Then, it is time for IGRT to collect images of the patient. The DR axis changes to position 0 and TCS waits to receive the deviation value computed by IGRT. If the deviation value is too large, the operator can decide to restart the patient setup process, or end and stop the next treatment session. If deviation value is not too large, the couch will be adjusted according to the deviation value. Then TCS stores the verification results and decides whether to verify again. Finally, the operator confirms the verification.

TEST WITH THE ROBOTIC COUCH

The network address was set to `http://192.168.0.2:8081` for testing. HTTP module of NodeJS was used to obtain the status of the robotic couch every 100 ms. In this way, the connection between robot adapter and robotic couch was established and maintained.

ISBN: 978-3-95450-212-7 ISSN: 2673-5482 doi:10.18429/JACoW-CYCLOTRONS2022-THPO006

Windows 10 64-bit Professional Edition was selected as the operating system and the unit test was performed using the robotic couch under the running environment of node 14.1.0 to verify the consistency between the functionality implemented in the interface and the interface design files.

With the help of the test tool, Postman, we simulated the following process: TCS sends requests to the robotic couch, the robotic couch receives and executes requests, then returns responses to TCS, and TCS receives the response.

Adding a new path needs the coordinates of several points. By moving the robotic couch to different locations and using the command `getStatus` at each location, the coordinates of a series of points will be obtained in the form of response, which can then be added to the new motion path as joints.

Adopting white box testing, unit test on relevant interface methods of the robotic couch is as follows (Table 3).

Table 3: Actual Tests

Interface	Description	Result
acquire-MasterSession	Control right gaining	Successfully gain control right in clinical mode
getStatus	Status acquisition of the robotic couch	Successfully get current position, moving speed, etc.
jogJoint	Single-axis motion	Successfully jog along a single axis
gotoCartesian	Multi-axis motion	Successfully move to a certain point at specified speed and acceleration
gotoPath	Movement based on the preset path	Successfully move along the path that has been saved in advance in the robotic couch system
creatOr-Modify-Path	Setting a new motion path for the robotic couch	Successfully add a new path with several points

CONCLUSION

In our design, the robot adapter connected TCS with the robotic couch. DDS was selected to interact with high-performance real-time process data in TCS, and HTTP was selected to communicate with the robotic couch. The robotic couch is involved in patient setup and setup verification. Unit test on relevant interface methods of the robotic couch has been conducted, and the results illustrated the functions of status monitoring, motion control, and path management.

REFERENCES

[1] B. Qin *et al.*, "Design study of a 250 MeV superconducting isochronous cyclotron for proton therapy", in *Proc. 12th Symposium on Accelerator Physics* (*SAP'14)*, Lanzhou, China, Aug. 2014, paper WEPMH3, pp. 23-25.

[2] K. Tian, Z. Peng, and X. Han. "Current situation and development trend of proton heavy ion hospital construction", *Chinese Hospital Architecture & Equipment*, vol. 23, no. 08, pp. 20-24, 2022.

[3] T. Zhang, C. Wang, *et al.*, "Developments for 230 MeV superconducting cyclotrons for proton therapy and proton irradiation", *Nucl. Instrum. Methods Phys. Res. Sect. B*, vol. 406, pp. 224-249, 2017. doi:10.1016/j.nimb.2016.11.010

[4] DDS, http://portals.omg.org/dds

ISBN: 978-3-95450-212-7 ISSN: 2673-5482 doi:10.18429/JACoW-CYCLOTRONS2022-THPO007

DIRECT SAMPLING DIGITAL LOW-LEVEL RF CONTROL FOR CIAE BNCT CYCLOTRON

Xueer Mu, Zhiguo Yin, Junyi Wei, CIAE, Beijing, China
Xiaoliang Fu†, TRIUMF, Vancouver, Canada

Abstract

Boron neutron capture therapy (BNCT) can be delivered using a high current cyclotron, resulting more compact and environmentally friendly design, yet the difficulties remain in the cyclotron part, particularly in RF systems. The high beam loading challenges the stability of the amplifiers, as well as the control loops. Especially in our case, the wall loss of each cavity is more than the beam-loading power of the CIAE BNCT cyclotron. To address the heavy beam loading coefficient, a higher-performance ADRC control algorithm is evaluated, together with the regular PID control. In the meantime, a direct sampling/synthesizing digital low-level RF control hardware design is put forward to have more flexibility in control implementation. Since this new design adopts Xilinx SOC as the main controller, it is convenient to combine real-time control algorithm with high-level control through Advanced Extensible Interface. In this LLRF design, the amplitude and phase control using PID control is implemented in the PS end, and the tuning control is taking advantage of the ADRC algorithm in the PL end. Using a symmetrical design, together with the buncher control, in total, regulation of three loops are achieved using two control boards. The software/hardware design as well as the commission result will be reported in this paper.

INTRODUCTION

The boron neutron capture therapy (BNCT) method can protect normal cells as much as possible while killing cancer cells. BNCT technology based on high current proton accelerators is gaining increasing attention in various countries due to the adjustable energy of the neutron beam of the accelerator and the fact that the accelerator also has safety advantages that reactors do not possess [1, 2].

The CYCIAE-14B cyclotron [3] for BNCT developed by the CIAE provides a 14 MeV, 1 mA proton beam for the production of neutrons for BNCT. The CYCIAE-14B cyclotron uses two 20 kW transmitters to drive two independent cavities respectively, and a 300 W amplifier to drive the buncher to increase the beam intensity. The low-level RF (LLRF) system requires amplitude and phase control of the three signals and tuning control of the two cavities [4]. Based on the characteristics of CYCIAE-14B high-frequency system, this paper proposes a design method of direct sampling/synthesis all digital low level control system, and completes the debugging task of this digital low level control system in CYCIAE-14B.

† xfu@triumf.ca

DESIGN OF BNCT LLRF SYSTEM

The design requirement of the digital LLRF system designed by the CIAE is to realize a set of broadband RF system to control the amplitude and phase of three channels of signals and the tuning of two cavities. The digital LLRF system is universal and can be applied to the RF control system of cyclotron in the CIAE. This paper mainly introduces the application of this system in CYCIAE-14B LLRF system. The LLRF system block diagram of CYCIAE-14B cyclotron is shown in Fig. 1.

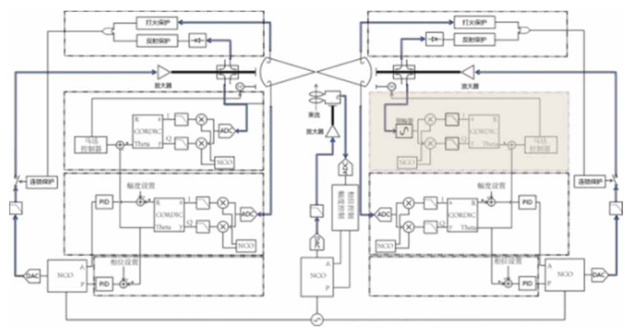

Figure 1: The LLRF system block diagram of CYCIAE-14B.

Hardware Design

The hardware architecture of the system is based on the ZYNQ series FPGA + dual ARM architecture. The FPGA is mainly used to modulate and demodulate the digital signal: After ADC sampling, the radio-frequency sampling signal and the sampling signal of the buncher form the IQ sequence. FPGA reads the IQ sequence, calculates the amplitude and phase information, and completes the demodulation operation. The function of the modulator is realized by DAC and NCO. The output amplitude of NCO is modulated by multiplying the output of NCO by hardware multiplier, and the modulation result is output by DAC to drive the amplifier. The dual ARM structure completes the control of the two RF auto-start processes [5], abnormal protection and online parameter modification, allowing the two RF systems to operate independently. The hardware system is designed with a 14-layer PCB and the physical diagram of the hardware system is shown in Fig. 2.

The LLRF system board will be installed in a LLRF chassis which will display the LLRF operation on the front panel. In order to visually display the running state of the LLRF system and provide driving for the stepping motor, a motherboard has been designed for the system and the core board can be plugged into the motherboard for use. A physical diagram of the motherboard is shown in Fig. 3. In the design of the motherboard, all input and output ports of

ISBN: 978-3-95450-212-7 ISSN: 2673-5482 doi:10.18429/JACoW-CYCLOTRONS2022-THP0007

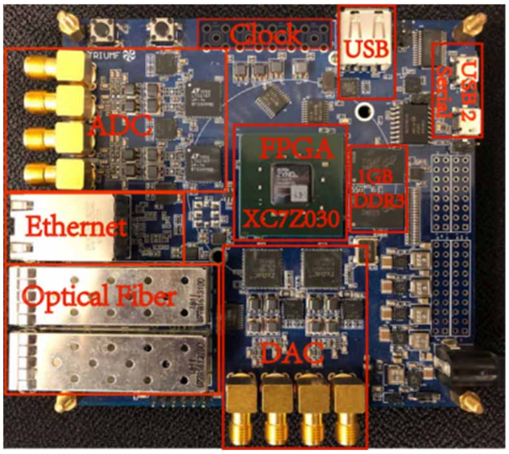

Figure 2: Digital LLRF platform for BNCT cyclotron.

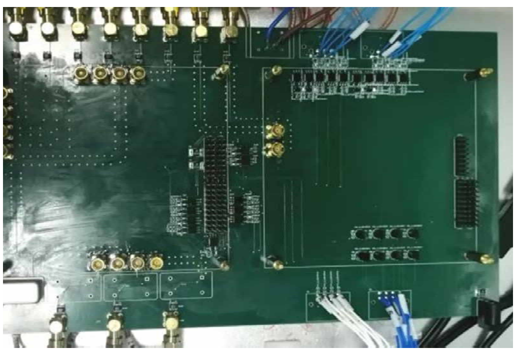
Figure 3: Motherboard for LLRF system board.

the daughter board are isolated in order to achieve complete electrical isolation of the inputs and outputs, increase the anti-interference capability and make the system work stably.

Core Algorithm

The core control algorithm of FPGA is realized by digital PID controller, and the realization expression of digital PID controller is:

$$u(k) = K_p \left\{ e(k) + \frac{T}{T_I} \sum_{k=0}^{n} e(k) + \frac{T_D}{T} [e(k) - e(k-1)] \right\} \quad (1)$$

The expression for an incremental PID controller can be obtained from the above equation as:

$$\begin{aligned} \Delta u(k) &= u(k) - u(k-1) \\ &= K_p[e(k) - e(k-1)] + K_I e(k) \\ &\quad + K_D[e(k) - 2e(k-1) + e(k-2)] \qquad (2) \end{aligned}$$

This expression is the basis for PID control using FPGAs. In practice, amplitude PID controller requires special handling of integral saturation and increased output limits. Unlike amplitude PID controllers, phase PID controller doesn't need to consider the case of integral saturation and do not need to add output limits.

In practical tests, in order to address the heavy beam loading coefficient, a higher performance ADRC control algorithm is proposed, which retains the characteristics of "error control by error" of PID technology, but also addresses the shortcomings of PID by introducing a non-linear Tracking Differentiator (TD), an Extended State Observer (ESO) and a Nonlinear State Error Feedback Control Law (NLSEF).The ADRC control algorithm using TD and ESO to process the reference input and system output respectively, and selecting the appropriate non-linear combination of state errors to obtain the NLSEF of the system, so as to obtain the output of the controller.

TEST RESULTS

The debugging block diagram of LLRF system is shown in Fig. 4.The power of the LLRF system output is increased after passing through the amplifier, and after the directional coupler, the reflection of the coupler is directly connected to the oscilloscope, and the forward signal is connected to the LLRF system through the attenuator; the pickup from the cavity is passed through the attenuator and power divider respectively and is connected one way to the oscilloscope and the other way to the LLRF system. At the same time the LLRF system output RF_OUT3 is used as the input to the buncher. With the wiring connected, the control of the LLRF system is implemented using the upper computer program. The control of the LLRF system is realised by computer program, which is used to set the closed loop point of the Dee voltage after the closed loop has been achieved in both cavities.

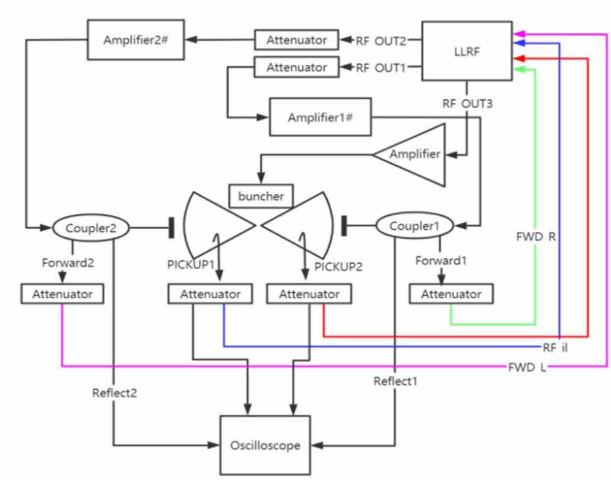

Figure 4: The debugging block diagram of LLRF system.

In the process of commissioning the accelerator with beam current, the resonant frequency of the RF cavity will shift due to beam loading [6] and heat loss causing the phase bias value calibrated when the beam was not added to be no longer accurate. Therefore, in the beam loading commissioning, the Dee voltage is set low, and after the system is closed loop, the phase set point is adjusted at a lower power level to minimise the reflected power, when the RF cavity is in resonance, the Dee voltage set point is then continuously increased to eventually achieve the power required for closed loop.

CONCLUSION

This set of digital LLRF system uses ZYNQ chip to make full use of on-chip resources, and completes the control function of LLRF system through a LLRF board card. During beam loading debugging, by increasing the LLRF system output, adjusting the output of the buncher and the phase difference between the two cavities, the problem that the beam intensity is not high enough under the condition of high beam loading is solved.

REFERENCES

[1] M. A. Dymova, S. Y. Taskaev, V. A. Richter, and E. V. Kuligina, "Boron neutron capture therapy: current status and future perspectives", *Cancer Commun.*, vol. 40, pp. 406-421, 2020. doi:10.1002/cac2.12089

[2] A. J. Kreiner, J. Bergueiro, D. Cartelli, *et al.*, "Present status of accelerator-based BNCT", *Rep. Practical Oncol. Radiother.,* vol. 21, pp. 95-101, 2016. doi:10.1016/j.rpor.2014.11.004

[3] T. Zhang, B. Cui, Y. Lv, "BRIF: From the first proton beam to RIB production", *Nucl. Instrum. Methods*, vol. 463, pp. 123-127, 2020. doi:10.1016/j.nimb.2019.06.045

[4] X. Fu, Z. Yin, K. Fong, *et al.*, "LLRF controller for high current cyclotron-based BNCT system", *IEEE Trans. Nucl. Sci.*, vol. 68, pp. 2452-2458, 2021. doi:10.1109/TNS.2021.3097702

[5] Z. Yin, X. Fu, B. Ji, *et al.*, "Digital control in LLRF system for CYCIAE-100 cyclotron", *Nucl. Instrum. Methods*, vol. 819, pp. 33-36, May. 2016 doi:10.1016/j.nima.2016.02.100

[6] X. Chengye, W. Zhijun, G. Zheng, H. Guirong, H. Ran, and M. Jinying, "Simulation and evaluation of beam loading feedforward Compensation for CiADS Linac", *Nucl. Phys. Rev.*, vol. 37, pp. 848-853, 2020. doi:10.11804/NuclPhysRev.37.2020023

ISBN: 978-3-95450-212-7 ISSN: 2673-5482 doi:10.18429/JACoW-CYCLOTRONS2022-THPO008

CONSIDERATION OF USING NON-DESTRUCTIVE DETECTORS IN THE BEAMLINE OF A PROTON THERAPY FACILITY*

Qushan Chen†, Aote Chen, Bin Qin
State Key Laboratory of Advanced Electromagnetic Engineering and Technology,
School of Electrical and Electronic Engineering,
Huazhong University of Science and Technology, Wuhan, China

Abstract

Ionization profile monitors (IPM) are a kind of nondestructive monitors mostly used in accelerators of high intensity pulsed beams. As for particle therapy accelerators, either based on cyclotrons or synchrotrons, the extracted beams are very weak, usually on the level of nano-Amperes. Up to date, the commonly used detectors in such low current machines are all destructive, such as fluorescent screens and gas ionization chambers. In this paper, we proposed for the first time to use a residual gas ionization monitor to measure the beam profiles in a proton therapy facility based on a superconducting cyclotron. The feasibility of such a scheme and some basic issues are discussed in this paper.

INTRODUCTION

There is a proton therapy facility based on a superconducting cyclotron under construction in the Huazhong University of Science and Technology (HUST-PTF) [1,2]. The HUST-PTF uses an energy degrader to modulate the beam energy from the cyclotron to match the clinical requirements [3]. The beam parameters from the superconducting cyclotron are summarized in Table 1. The layout of HUST-PTF is shown in Fig. 1.

Table 1: Beam parameters from the SC cyclotron.

Parameter	Value
Frequency	73 MHz (CW mode)
Energy	250 MeV
Energy spread	<0.5%
Intensity	60 ~ 500 nA

The proton beam extracted from the cyclotron has a fixed energy of 250 MeV and then is modulated to 70 ~ 230 MeV with an energy degrader, followed by three collimators to constrain the emittance and a momentum slit in the middle of the DBA section to restrict the energy spread [4]. Taking all the beam loss into consideration, the transmission rates of different beam energies vary dramatically, which is not acceptable in clinical treatment. So it is demanded that the cyclotron has the ability to output different intensity beams in accordance with the working energy points. According to our optimization result, the beam intensity from the cyclotron is divided into three levels (Fig. 2) and the final intensity for clinical treatment is shown in Fig. 3.

ANALYSIS OF THE IONIZATION PROFILE MONITOR

Nondestructive detection is always preferred in an accelerator. However, as the first attempt to build such a proton machine, the traditional fluorescent screen and strip ionization chamber are the two primary detectors used in the beamline [5]. Even so, the residual gas monitor, or ionization profile monitor (IPM), is considered as a potential candidate in the future upgrade. IPM is a kind of nondestructive detector, which collects the secondary particles produced from the interaction between the incoming high energy particles and the residual gas molecules [6–8]. The biggest challenging of using an IPM in our machine is the extremely low signal due to the nA-level beam current. In the following, some basic issues are discussed to investigate its performance.

Gain Analysis

Gain is the first issue that needs to be considered. The process of producing an ion-electron pair is evaluated with the Bethe-Bloch formula:

$$-\frac{d\mathrm{E}}{d\mathrm{x}} = (4\pi N_a r_e^2 m_e c^2)\rho \frac{Z}{A}\frac{z^2}{\beta^2}\left(\ln\frac{2m_e c^2\beta^2\gamma^2}{I} - \beta^2\right) \quad (1)$$

The gain is calculated from the energy of proton beams deposited in the residual gas and the ionization energy of the gas. The parameters used in our simulation is displayed in Table 2. As it is hard to tell the ingredient of the residual gas at the 10^{-4} Pa level, both the hydrogen and the nitrogen cases are calculated and the results are shown in Fig. 4.

Table 2: Simulation parameters for the gain of Hydrogen and Nitrogen.

Parameter	Value
Pressure	10^{-4}Pa
Temperature	298.15K
Detector length	10cm
Ionization energy	36eV of H_2, 36.4 of N_2

It is easy to conclude from the Bethe-Bloch formula and the simulation results that the hydrogen curve gives a lower gain, so it is reasonable to use the hydrogen curve to estimate the gain of the detector.

* Work supported by the National Natural Science Foundation of China (No. 12175077)
† chenqushan@hust.edu.cn

ISBN: 978-3-95450-212-7 ISSN: 2673-5482 doi:10.18429/JACoW-CYCLOTRONS2022-THPO008

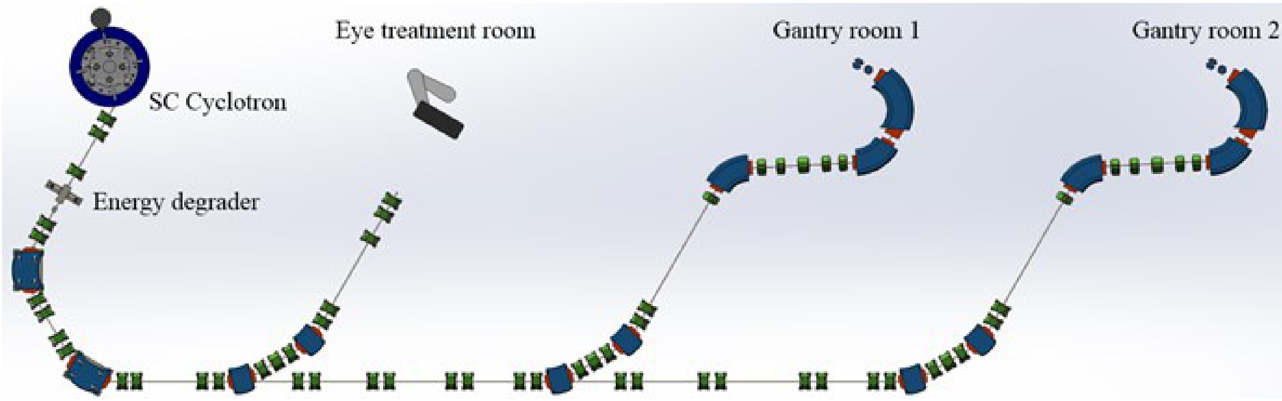

Figure 1: The beamline layout of the HUST-PTF.

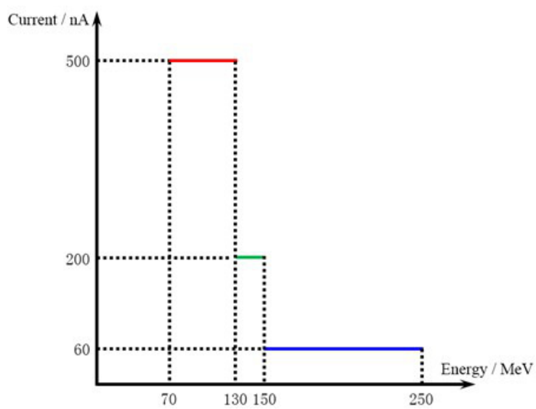

Figure 2: Beam intensity from the cyclotron under different working points.

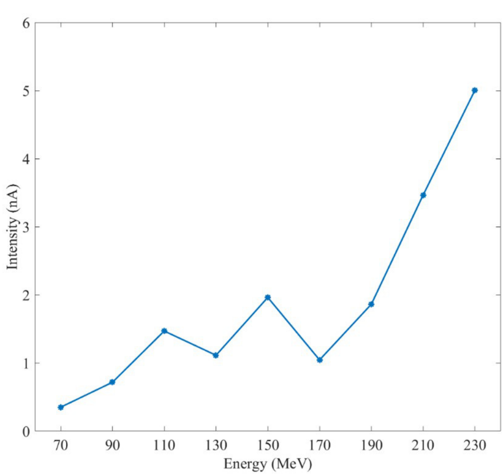

Figure 3: Beam intensity for clinical treatment under different working points.

Figure3 indicates the beam intensity increases with the beam energy while Fig. 4 indicates the gain decreases with the beam energy. Combining the results in Figs. 3 and 4, the lowest ionization signal occurs at the 70 MeV point, which corresponds to 1009 ion-electron pairs per second. It should be emphasized that the time resolution is not an important issue in the beam diagnostics of our machine and only the average parameters are concerned. With the help of a typical two-stage MCP with a gain of $10^6 \sim 10^7$, we feel confident in applying such an IPM detector in our machine.

Structure of the Detector

The main components of the IPM include the electrodes, MCP and readout electronics (Fig. 5). It includes the following key components. Electrodes: We are unable to make a choice on the collection particles, ions or electrons. Their difference and engineering challenges are not clear. As for the guiding B field that is necessary in many high intensity proton accelerators, I do not see its necessity in our case due to the ultralow incident beam current. MCP: A gain of 107 is not challenging for a commercial two-stage MCP, such as the Hamamatsu products. Readout: Compared with an anode scheme, a phosphor screen combined with a CCD camera is easier to obtain a better spatial resolution. The exposure time of the camera should be set to 1 s or larger.

Steering Effect

The transverse electrical field of the IPM may influence the transport of the proton beam. Take the 70 MeV proton beam for example. The kick angle imposed by the IPM is

$$\theta = \frac{\Delta p_x}{p_z} = \frac{qE_cL}{m_pc^2\gamma\beta^2} \tag{2}$$

where E_c is the cage E field of the IPM, L is the detector length. E_c = 5kV/cm, L = 10 cm. Then, the kick angle associated with the 70 MeV proton beam is 0.37 mrad. The steering effect is not a serious problem and can be compensated by the corrector magnets.

SUMMARY

Although the fluorescent screen and stripped ionization chamber are the primary detectors in the current configuration, we have been looking for appropriate nondestructive instruments. Cavity-BPM and IPM are the two candidates. The Cavity-BPM has advantage in spatial resolution, but its volume is relatively large. The IPM has a smaller insertion length compared to the Cavity-BPM, but there is

ISBN: 978-3-95450-212-7 ISSN: 2673-5482 doi:10.18429/JACoW-CYCLOTRONS2022-THPO008

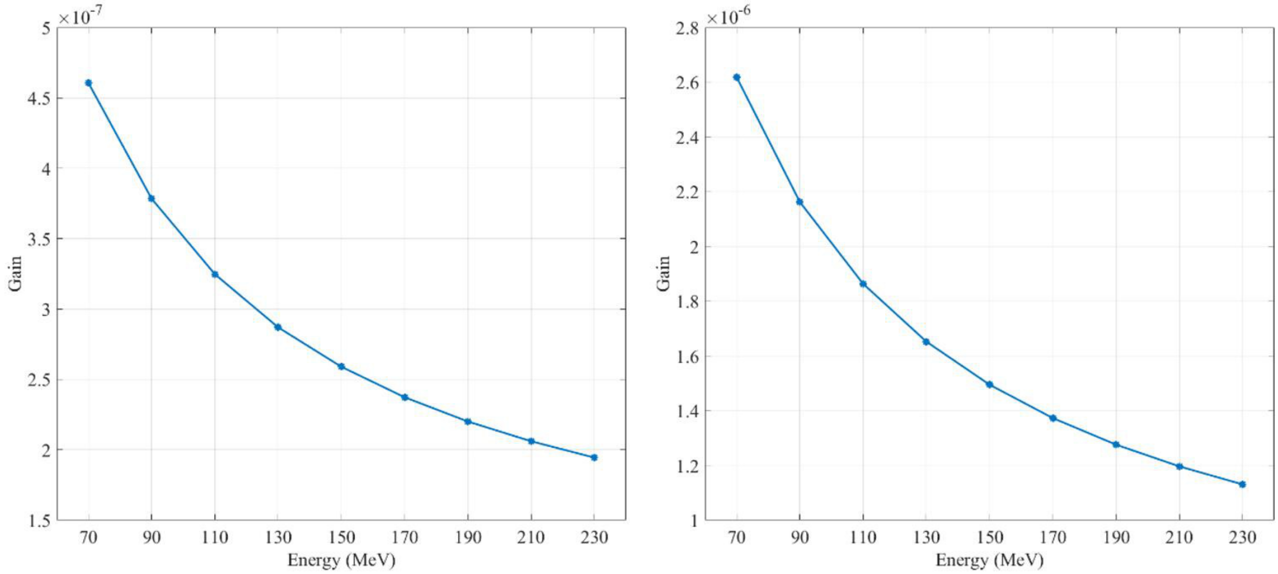

Figure 4: Gain curves of the hydrogen (Left) and the nitrogen (Right) at 10^{-4} Pa.

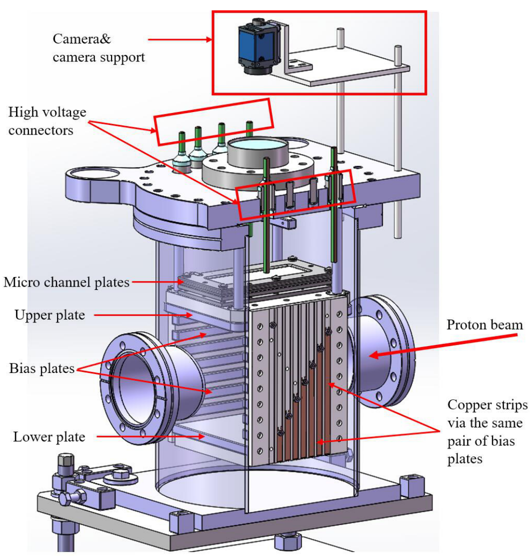

Figure 5: Schematic view of the IPM.

still much uncertainty in its output signal. Besides, the mechanical structure, high voltage supply, radiation protection of the CCD camera, signal distortion, etc. still need to be considered with more details.

REFERENCES

[1] Bin Qin *et al.*, "Design and development of the beamline for a proton therapy system", *Nucl. Sci. Tech.*, vol. 31, p. 138, 2021. doi:10.1007/s41365-021-00975-y

[2] S.Hu, K. Fan, L. Zhang, Z. Mei, Zhiyuan, X. Li, and Z. Zeng, "Beam loss issue study on the extraction system of a superconducting cyclotron at HUST", *Nucl. Instrum. Methods Phys. Res. Sect. A*, vol. 911, pp. 87–93, 2018. doi:10.1016/j.nima.2018.09.126

[3] Wei Chen *et al.*, "Transmission calculation and intensity suppresion for a proton therapy system", *Nucl. Instrum. Methods Phys. Res. Sect. A*, vol. 881, pp. 82–87, 2018. doi:10.1016/j.nima.2017.10.04

[4] Xu Liu *et al.*, X. Liu, W. Wang, Z. Liang, R. Zhao, K. Liu, and B. Qin, "Design of a light and fast energy degrader for a compact superconducting gantry with large momentum acceptance", *Physica Med.*, vol. 73, pp. 43–47, 2020. doi:10.1016/j.ejmp.2020.04.008

[5] Aote Chen *et al.*, "Prototype development of the beam diagnostic system of a proton therapy facility based on a superconducting cyclotron", *Nucl. Instrum. Methods Phys. Res. A*, vol. 998, p. 165208, 2021. doi:10.1016/j.nima.2021.165208

[6] C. D. Johnson and L. Thorndahl, "Non-destructive proton beam profile scanners for the CERN Proton Synchrotron, based on the ionization of residual gas in the beam vacuum chambers", in *Symposium on Beam Intensity Measurement*, Daresbury, Apr. 1968, pp. 227–237.

[7] H. Ishimaru, Z. Igarashi, K. Muto, and S. Shibata, "Beam profile measurements for KEK 12 GeV proton synchrotron", *IEEE Trans. Nucl. Sci.*, vol. 24, no. 3, pp. 1821–1823, 1977. doi:10.1109/TNS.1977.4329099

[8] T. Hardek, W. Kells, and H. Lai, "Very low intensity storage-ring prpofile monitor", *IEEE Trans. Nucl. Sci.*, vol. 28, no. 3, pp. 2219–2221, 1981. doi:10.1109/TNS.1981.4331642

ISBN: 978-3-95450-212-7 ISSN: 2673-5482 doi:10.18429/JACoW-CYCLOTRONS2022-THPO009

VACUUM MODEL OF THE C400 CYCLOTRON FOR HADRONTHERAPY

V. E. Nuttens†, J. Mandrillon, W. Kleeven, Q. Flandroy, Ph. Cailliau
Ion Beam Applications, Louvain-la-Neuve, Belgium
Ph. Velten††, Normandy Hadrontherapy, Caen, France

Abstract

Since 2020, NHa and IBA collaborate on the development of the C400 cyclotron dedicated to hadron therapy. This machine accelerates C^{6+} and He^{2+} up to 400 MeV/n and H_2^+ up to 260 MeV/n. The H_2^+ are extracted by stripping and the other particles by an electrostatic deflexion.

Vacuum management in the injection line and in the cyclotron are of prime importance to avoid large beam losses. Indeed, C^{6+} ions are subjected to charge exchange during collision with the residual gas. On the opposite, H_2^+ will suffer from molecular binding break up. According to cross section data, the constraints on the residual gas pressure is driven by C^{6+} in the injection line and by H_2^+ in the cyclotron. An electrical equivalent model of the vacuum system of the cyclotron, its injection and extraction lines has been developed in LTSpice® software to determine the pressure along the particle path. Contributions from outgassing surfaces, O-ring outgassing, and permeation are included, and vacuum pump requirement could be obtained. The expected beam transmission is then evaluated based on cross sections available from the literature.

INTRODUCTION

Detailed theoretical studies has been conducted to estimate the beam transmission expected in each sub-part of the C400 hadron therapy system. Electrical equivalent circuits are built using inputs as detailed as possible and coming from the IBA design office, including the complex geometries of the numerous components located inside the cyclotron accelerator chamber (RF parts, elements of the extraction systems, etc.). This enables to compute the pressure level expected in any point of the circuit which in turn drives the dimensioning and location of the vacuum pumps to achieve the required pressure level. Combining these outputs with the relevant cross-sections of the interaction of the ion beam with the residual gas, the transmission can be estimated with a reasonable level of confidence.

VACUUM MODEL IN LTSPICE®

Electrical Equivalent Circuit

Thanks to the similarity between the electrical equations and the molecular flow equations, it is possible to make use of modelling tools such as LTSpice® [1] to build simulated vacuum circuits providing the equivalencies shown in Table 1. Providing the vacuum system can be approximated by an ensemble of elements connected either in series or parallel and defined by their conductance and/or gas throughput, such a model can provide a relatively precise estimation of the pressure at any point in the circuit.

Table 1: Electricity/Vacuum Equivalencies

Electricity	Vacuum
Voltage / [V]	Pressure / [mbar]
Current / [A]	Gas throughput / [mbar.L/s]
Resistance / [Ω]	Conductance / $[L/s]^{-1}$

Conductance

The general conductance equation for a vacuum element is:

$$C = \frac{aAv}{4} \quad (1)$$

where a is the transmission probability ϵ [0,1];
A is the vacuum element transverse cross section in [m²];
$v = \sqrt{\frac{8RT}{\pi m}}$ is the average speed of the gas molecule of molar mass m in kg/mol at temperature T in K; $R = 8.3144621$ J/mol/K is the gas constant.

In the electrical equivalent circuit, the generic conductance is a simple resistor with resistance value equal to the inverse of the conductance.

The coefficient a is component dependent, in particular function of its geometry, see [2] for more detailed information of how the transmission probability is modelled using tabulated data for specific geometry taken from [3]. Moreover, parametric formula is directly implemented in LTSpice® to enable modelling of various geometries: tubes of different inner diameter, conduct having rectangular slit-like shapes, etc. The impact of the gas nature is modelled entirely into the gas speed through its molar mass. Therefore, to consider multiple gas effect, specific runs must be performed for each gas.

Gas Throughput

All gas throughput present in a vacuum system (outgassing surfaces, permeation, leaks) are modelled in the software by means of a source current. For example, an outgassing pipe will be represented by two resistors in series whose conductance value is computed as explained previously and with a source current connected between them. The total gas throughput is parameterized with the product of the inner pipe surface times the outgassing rate of the considered material.

† vincent.nuttens@iba-group.com
†† philippe.velten@normandy-hadrontherapy.com

ISBN: 978-3-95450-212-7 ISSN: 2673-5482 doi:10.18429/JACoW-CYCLOTRONS2022-THPO009

Contributions to the Residual Pressure

The following contributions were identified and modelled as precisely as possible within the model:

- Inner wall outgassing: The outgassing rate formula and values for different material used in this study are taken from [3], including time dependent formula to compute pumping speed, recovery after venting, etc.
- O-rings: Vacuum flange gaskets made of rubber like material provide contribution both from their permeation and outgassing of the material itself. In the C400 system, a mix of metal (no permeation), nitrile and Viton gaskets are used. The permeation rate values of water vapor for those materials are taken from [4].
- Outgassing and O-rings permeation calculations were performed with only water vapor as source of gas since it is the major contributions in those cases. But specific calculations were also performed using the neutral support gas coming out from the ion source (C_2H_2), since it is the major contributor in the first few meters downstream the extraction point of the ion source.
- Vacuum pumps are modelled as ideal diodes with a resistance in the passing current direction equal to the inverse of the pumping speed and infinite resistance in the blocking direction.

THE C400 VACUUM MODEL

Description of the Model

In the C400 system, the ions of interest are generated with dedicated ECR ion sources. The ion beams are extracted at 26 keV/Z, selected by a 90° switching magnet and transported down to the cyclotron through a ~10 m long vertical line. In the cyclotron, the Carbon and He beams are accelerated up to 400 MeV/u whereas H_2 are stripped to protons and extracted at about 260 MeV. Therefore, two extraction lines are present that are finally regrouped before reaching the degrader [5].

In the vacuum model, the system is divided into three sub parts: injection, cyclotron, and extraction. Each of them can be connected with each other to study their potential interdependencies and standalone run can be performed to investigate their specific dynamics. For brevity, only the cyclotron part is shown in Fig. 1. Representing the injection and extraction lines as equivalent electrical circuit is rather straightforward since their geometries naturally follow a linear layout. But for the geometry of the cyclotron, the inner volume needed to be ‘unfolded’ by approximating it as a succession of hills and valleys connected in series, as ‘seen’ by the accelerated particle trajectory. The

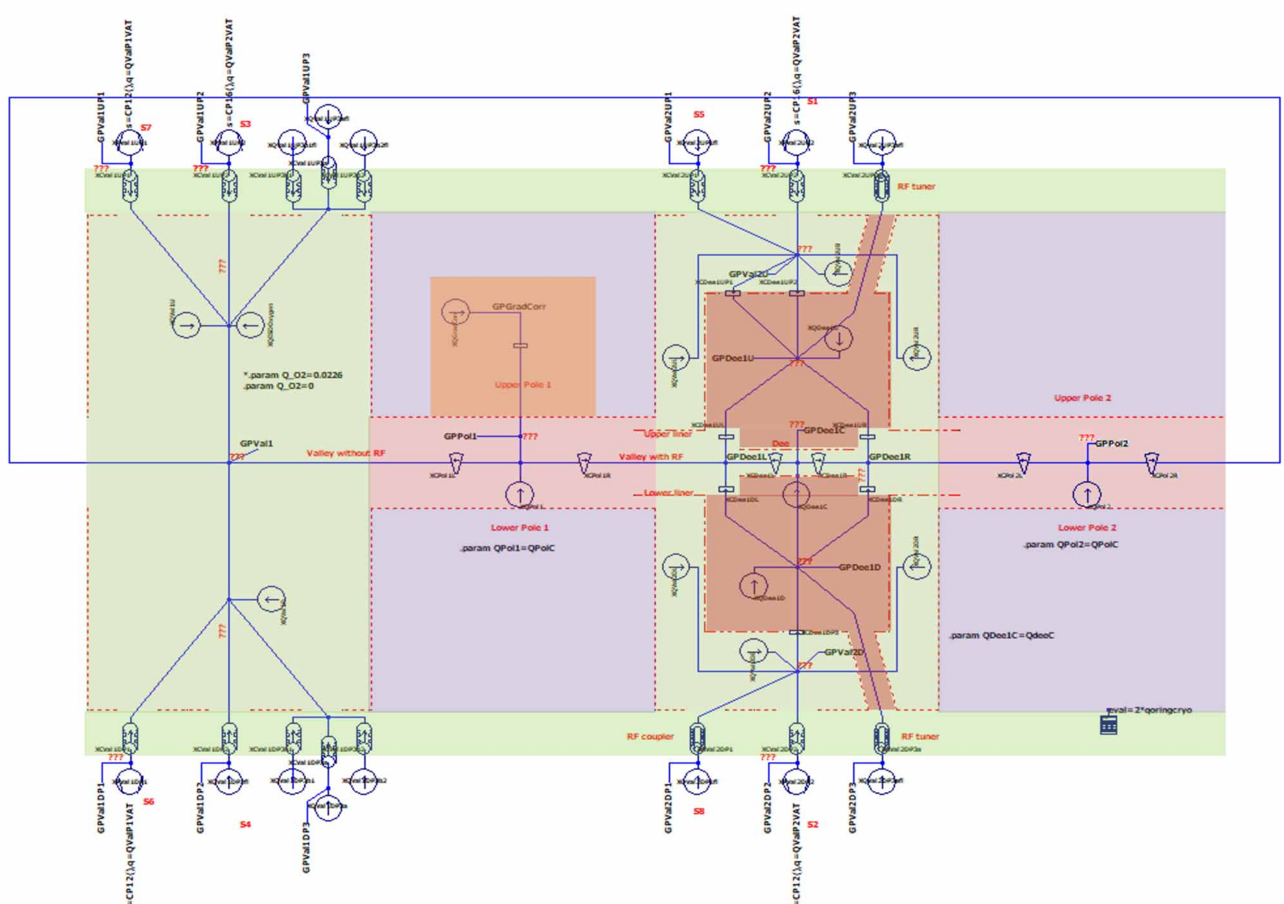

Figure 1: LTSpice® model of the C400 cyclotron.

ISBN: 978-3-95450-212-7 ISSN: 2673-5482 doi:10.18429/JACoW-CYCLOTRONS2022-THPO009

valleys themselves are considered as infinite conductance vacuum chambers but all elements present in those sectors and impacting the vacuum are included:

- the surfaces of all objects together with their materials, even from complex mechanical design like the Dees or the RF tuners and couplers,
- the pumping ports, including the flange diameter of the pumps to the estimate pumping efficiency,
- the O-rings of all sockets (pumps, valves, etc.).

The hills are represented by pie-slice shaped conducts whose conductance can be approximated by the integration of a bunch of variable thin, rectangular slit-like pipes connected in parallel [2].

Results and Discussions

Using these modelling tools, the conducted studies provided the following outputs:

- the dimension and performance of the cryopumps in the cyclotron have been increased to fulfil the required pressure level,
- the numerous O-rings in the cyclotron should not significantly compromise the pressure level, especially the two very large pairs of 3.65 m diameter O-ring between the yoke and the cryostat ensuring the vacuum of the accelerator cavity, with a separate differential pumping for the volume between the two O-rings of each pair.
- the pressure level in the extraction line whose requirement ($\sim 10^{-5}$ mbar) are lower than inside the cyclotron is not compromising the vacuum in the cyclotron either,
- the design of the injection line has been updated to stay as close as possible to the $\sim 10^{-6}$ mbar pressure level or below, especially in the first few meters downstream the ECR source extraction point. The critical point is to pump as efficiently as possible the neutral gas coming out of the source. A differential pumping system is foreseen to be located at this position (see Fig. 2).

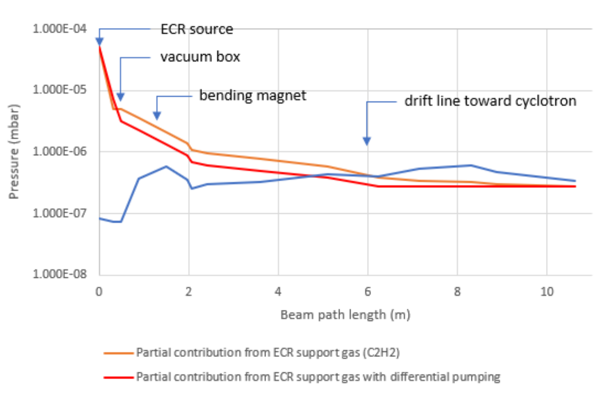

Figure 2: Pressure level coming from the contributions of the neutral ion source gas source gas and water vapor along the injection beam line.

TRANSMISSION CALCULATION

The general formula for transmission calculation with pressure and beam loss cross section is the following:

$$T = 1 - \frac{dN}{N} = 1 - \sigma(E)\frac{P}{k_B T}dl \qquad (2)$$

where N is the number of particles, σ the total gas stripping cross section, P the pressure, T the temperature and dl the elementary particle trajectory length. In the case of the transport beamlines, one must integrate only over the beam line length considering potential pressure variation, whereas the treatment is more complex inside the cyclotron. In the latter case, it is necessary to compute the closed orbit separated by the energy gain per turn and integrate over the energy range and length, also considering the variation of the cross-sections over the increasing energy.

In the injection line, beam losses are dominated by charge exchange cross-section of C^{6+} ions, whereas in the cyclotron, the pressure requirements are driven by the molecular break-up cross-section of H_2^+ ions [6].

H_2^+ Cross Sections

Literature has several references for the molecular hydrogen break-up cross section (Fig. 3). Olson has proposed a fit of the experimental data [7] that is being used here as the nominal case for the present study and for which σ goes from $\sim 2 \cdot 10^{-15}\ cm^2$ at low energy (<50 keV/u) down to $\sim 3 \cdot 10^{-18}\ cm^2$ at max energy (~200 MeV/u). Berkner-Gryzinski and Berkner-Born [8] cross section fits are used as maximum and minimum uncertainty limits.

Carbon Cross Section

The value of $\sigma \sim 6.8 \cdot 10^{-15}\ cm^2$ representing the electron capture by C^{6+} from H_2O already used in the C400 preliminary design report from 2009 [6] has been used in this study since no better input was found in the literature after cross-checks. The value $\sigma \sim 9.5 \cdot 10^{-15}\ cm^2$ is used for the electron capture by C^{6+} on the source support gas C_2H_2 at 26 keV/Z, following [9].

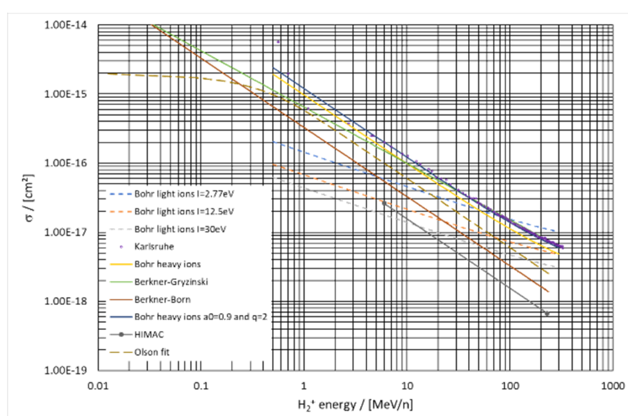

Figure 3: Molecular hydrogen break-up cross section from the literature as function of H_2^+ incident energy.

ISBN: 978-3-95450-212-7 ISSN: 2673-5482 doi:10.18429/JACoW-CYCLOTRONS2022-THPO009

Injection Line Results

Using the pressure output level from the electrical current model and the cross-section described before, it is found that a transmission between 80% and 95% should be achieved in the injection line and mainly depends on the pressure level at the extraction point driven by the support gas coming out from the source. The ECR source to generate the C^{6+} beam is still currently under development, but preliminary studies show that with such transmission level, the required carbon beam current of several μA should be easily achieved at the cyclotron injection level.

Cyclotron Results

Depending on the actual pressure achieved in the accelerator vacuum chamber, the beam transmission considering only the beam losses due to the interactions with the residual gas have been calculated and are shown on Fig. 4.

Outgassing of materials in vacuum depends not only on the material, but also on its surface state. In the case of an iron-dominated cyclotron, the surface of the poles therefore may play an important role. This is especially true for an accelerator dedicated to medical applications since the downtime following maintenance opening is one of its critical performance parameters. It was therefore studied whether pumping time could be significantly improved with the application of nickel-plating on the inner poles of the cyclotron. According to the simulation results (the different surface state cases are pointed out on Fig. 4), only a limited gain on transmission could be saved after a given pumping time. Therefore, since this procedure would not significantly impact the clinical functioning of the system and because of the risk presented by the manufacturing process (manual application of the nickel was mandatory due to the very large yoke size), it was decided not to proceed with the nickel plating of the poles.

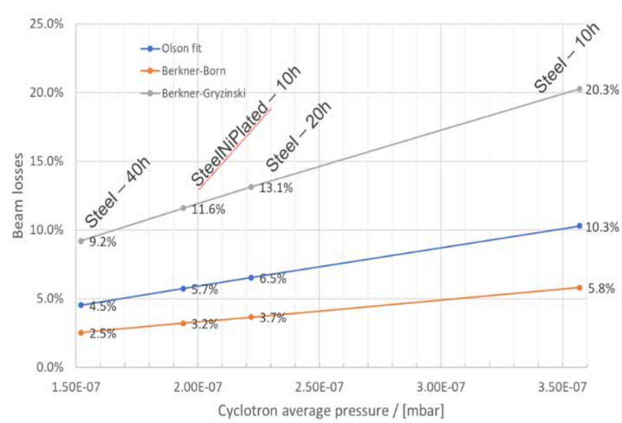

Figure 4: Beam loss versus cyclotron pressure after a given pumping time, with or without nickel plating, and according to different stripping cross section limits.

CONCLUSION

Models for the vacuum computation of the critical beam parts of the C400 system have been performed to help and orient various design steps. They confirmed that the pressure level was well under control to ensure a beam transmission matching the performance requirements. Those studies also permitted to optimize the vacuum, mechanical and manufacturing processes.

REFERENCES

[1] LTSpice®, `https://www.analog.com/en/design-center/design-tools-and-calculators/ltspice-simulator.html`

[2] V. Nuttens *et al.*, “Cyclotron Vacuum Model and H^- Gas Stripping Losses”, in *Proc. Cyclotrons'10*, Lanzhou, China, Sep. 2010, paper MOPCP075, pp. 200-202.

[3] J. F. O’Hanlon, “A User’s Guide to Vacuum Technology”, Wiley, 3rd Edition.

[4] Marco Rubber & plastics, "O-Ring Permeation Coefficient Chart of Common Materials," [Online]. Available: `https://www.marcorubber.com/o-ring-permeation.htm`

[5] J. Mandrillon *et al.*, “Carbon cyclotron for particle therapy”, presented at Cyclotrons’22, Beijing, China, Dec. 2022, paper THBI01, this conference.

[6] G. Karamysheva, "Beam losses due to interaction with the residual gas “, IBA internal report, 2009, unpublished.

[7] T. Tabata,H. Kubo, and M. Sataka, “Formulating analytic expressions for atomic collision cross sections”, Japan Atomic Energy Research Institute, JAERI-Research 2003-015, Aug. 2003 (23 pages).

[8] K. H. Berkner *et al.*, “Collisional breakup of high-energy H2+ ions”, *Phys. Rev.*, vol. 146, no. 1, p. 9, 1966. `doi:10.1103/PhysRev.146.9`

[9] J.B. Greenwood *et al.*, “Experimental investigation of the processes determining x-ray emission intensities from charge-exchange collisions”, *Phys. Rev. A,* vol. 63, no. 6. p. 062707, 2001. `doi:10.1103/PhysRevA.63.062707`

ISBN: 978-3-95450-212-7 ISSN: 2673-5482 doi:10.18429/JACoW-CYCLOTRONS2022-THPO010

AN AUTOMATED DOSE VERIFICATION TOOL FOR PROTON THERAPY PLANS USING GEANT4/TOPAS*

W. Wang[1], B. Qin[1], Z. Y. Yang[2], Y. C. Liao[1], P. L. Li[1], Y. Chen[1], X. Liu[1,†]
[1]State Key Laboratory of Advanced Electromagnetic Engineering and Technology,
School of Electrical and Electronic Engineering,
Huazhong University of Science and Technology, Wuhan, China
[2]Cancer Center, Union Hospital, Tongji Medical College,
Huazhong University of Science and Technology, Wuhan, China

Abstract

Proton therapy has become a significant treatment option for many tumors. In commercial treatment planning systems (TPS), the computationally efficient pencil-beam (PB) analytical algorithm is frequently utilized for dose calculation. Due to the PB algorithm's limited accuracy, a higher accuracy dose verification tool is a legal requirement for proton therapy. Therefore, we developed an automated treatment plan dose verification framework based on the Monte-Carlo (MC) algorithm.The MC beam model, including the phase space, energy spectrum, and the number of protons per MU, was derived from commissioning data and fed into our automated software. CT and treatment plan from TPS were input for the automated software. The developed tool was validated and compared with the PB algorithm of Pinnacle3 TPS for 85 prostate patients.The difference between the PB dose and the MC dose of our automated tool was evaluated using gamma analysis (3 mm/3%, and 2 mm/2% criteria) and mean absolute errors. Although the result shows good agreement and the passing rate was about 95%, the difference of all the indices was found to increase as the degree of tissue heterogeneity increased. The MC dose has a higher MAE in CTV, and femoral head compared to the PB dose.An automated framework can quickly calculate the MC dose with high accuracy among different cases. The automated software can facilitate patient plan verification in institutions and be useful for other clinical applications.

INTRODUCTION

Due to its Bragg peak characteristic, proton radiotherapy has increased clinical use in the last decade [1]. It has more homogeneous, conformal, and normal sparing than conventional photon radiotherapy. The actual dose distribution may differ from the planned dose because of the existence of uncertainties such as dose calculation uncertainties, anatomy changes, and so on [2]. Therefore, providing accurate dose calculation tools is essential for treatment planning and plan quality assurance.

Due to its high computation speed, the pencil beam (PB) analytic algorithm is widely used in commercial treatment planning systems (TPS). It uses the water-equivalent thickness longitudinally and assumes that the material on the central axis is laterally homogeneous [3]. Particularly in inhomogeneous tissues, the approximation of multiple Coulomb and nuclear reactions in the PB algorithm leads to dose discrepancy and range uncertainties [4]. The Monte-Carlo methods, regarded as the gold standard for dose calculation in radiotherapy, simulate physics interactions by many random sampling cross-sectional interactions [5]. Thus, developing the MC dose recalculation tool for post-planning dose verification is necessary for hospitals.

This study aims to build an automated MC dose recalculation framework for proton therapy treatment plans. Additionally, we compared it with the PB algorithm in prostate cancers. The dose discrepancy was evaluated using the gamma analysis method (3 mm/3% and 2 mm/2%). The mean absolute error between the MC dose and PB dose also was calculated to evaluate the dose discrepancy.

METHOD AND MATERIAL

An automated MC re-calculation framework was developed for dose checking of treatment plans. Figure 1. shows the workflow of the proposed tool. The Geant4-based TOPAS toolkit was used in our study [6]. The default physics list contains G4EMStandardPhysics_option4, HadronPhysics-QGSP_BIC_HIP, G4DecayPhysics, G4Ion-BinaryCascade Physics, G4HadronElasticPhyscisHP, and G4Stopping Physics. The IMPT plans were optimized in the Pinnacle3 TPS, v15.0 (Philips Healthcare, Fitchburg, WI, USA) and calculated by the PB algorithm. The DICOM data (CT, RS, and RN) were exported from TPS and then fed into our tool. After the simulation, the dose calculated by the MC tool was compared with that of the PB algorithm.

Beam Modeling

The beam data library (BDL), which contains beam parameters for various energies, is implemented in TOPAS as a look-up table. These parameters must be tuned to align the Monte-Carlo simulation with experimental measurement. The BDL includes three sections: energy spread, phase space, and the number of protons per MU.

- Energy spread: the energy distribution of proton beams is a Gaussian distribution with a mean and standard deviation.

* This work was supported by the National Key Research and Development Program of China (2016YFC0105305), the National Natural Science Foundation of China (12205111), and the Fundamental Research Funds for the Central Universities (HUST: 2022JYCXJJ010).
† lxhustliu@hust.edu.cn

ISBN: 978-3-95450-212-7 ISSN: 2673-5482 doi:10.18429/JACoW-CYCLOTRONS2022-THPO010

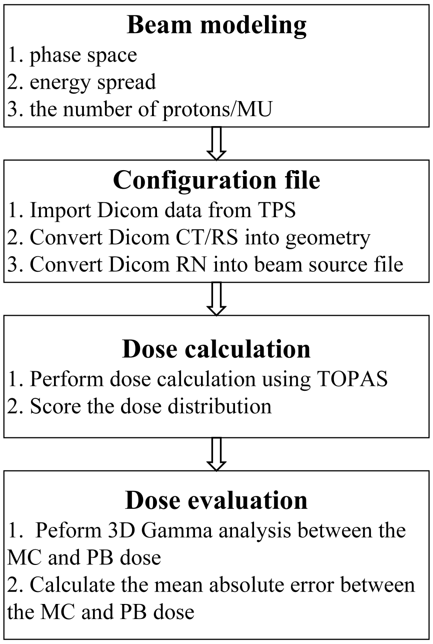

Figure 1: The workflow of our automated Monte-Carlo dose calculation tools.

- Phase space: phase space parameters are determined as a function of energy at the nozzle output, such as spot sizes and beam divergences
- The number of protons per MU For each nominal energy was calibrated.

Patient Data

In our study, 85 cases of prostate cancer were used. An institutional review board-approved protocol for retrospective data collecting included all patients. The beam angle was set at 90° and 270°, and all of the patient's plans were optimized using the multi-field optimization technique. The planning target volume (PTV), clinical target volume (CTV), bladder, rectum, left femoral head, and the right femoral head was contoured by radiation oncologists.

Dose Comparison

The 3D dose distribution calculated by the MC algorithm was compared to that of the PB algorithm. The difference was assessed using the mean absolute error between the PB dose and the MC dose. The 3D gamma index analysis (using 3%/3 mm and 2%/2mm criteria) was also used to evaluate the difference.

RESULT

Figure 2. shows the PB dose, MC dose distribution, their difference map, and DVH plots. While their DVH and dose distribution were comparable, there was a dose discrepancy in the high dose-gradient region. Additionally, the CTV, Bladder, and femoral head of the DVH in the Monte-Carlo method changed significantly from those in the PB algorithm.

The MAE between the MC dose and the PB dose was calculated and presented in Table 1. The MC dose had a higher MAE in CTV, and femoral head compared to the rectum and bladder. This also demonstrated that the PB dose has more calculation uncertainties in the complex tissue. Table 2 shows the gamma analysis result between the MC dose and the PB dose. Among the 85 prostate patients, the average gamma passing rate (2 mm/2% criteria) was about 96.7%.

Table 1: The mean absolute error relative to the maximum dose value between the MC dose and PB dose among 85 prostate cases, shown as mean ± standard deviation.

	MC dose – PB dose
CTV	3.74 % ±1.21 %
Bladder	1.01 % ±0.66 %
Rectum	0.84 % ±0.36 %
Left femoral head	1.38 % ±0.26 %
Right femoral head	1.31 % ±0.32 %

Table 2: The gamma passing rate (3 mm/3% and 2 mm/2% criteria) result between the MC dose and PB dose among 85 prostate cases, shown as mean ± standard deviation.

Criteria	**MC dose – PB dose**
3mm/3%	98.88 % ±0.92 %
2mm/2%	96.76 % ±1.95 %

DISCUSSION

In our study, the MC-based dose re-calculation tool was developed for dose checking in clinical. We compared the MC dose with the PB dose, showing a relatively significant difference in high-dose-gradient regions. Without an in-depth understanding of command line deployment, and function dependencies, clinical users can employ this tool and integrate it into commercial TPS. Excerpt for the physics dose, this tool also can calculate the dose-to-water, linear energy transfer, and dose deposited by another particle radiotherapy.

However, the huge calculation time is a significant problem for employing the tools in treatment plan optimization. It takes about 10 hours (compared to minutes for the analytical calculation within the TPS) to calculate a patient plan dose. Recent MC simulation studies have focused on improving MC calculation speed by simplifying the physics process and deploying parallel computing.

CONCLUSION

In summary, we developed an automated MC dose recalculation tool. It is a crucial tool for the dose verification and quality control of treatment plans. Additionally, the automated tool can easily be implemented in other institutions and be useful for other clinical applications.

ISBN: 978-3-95450-212-7 ISSN: 2673-5482 doi:10.18429/JACoW-CYCLOTRONS2022-THPO010

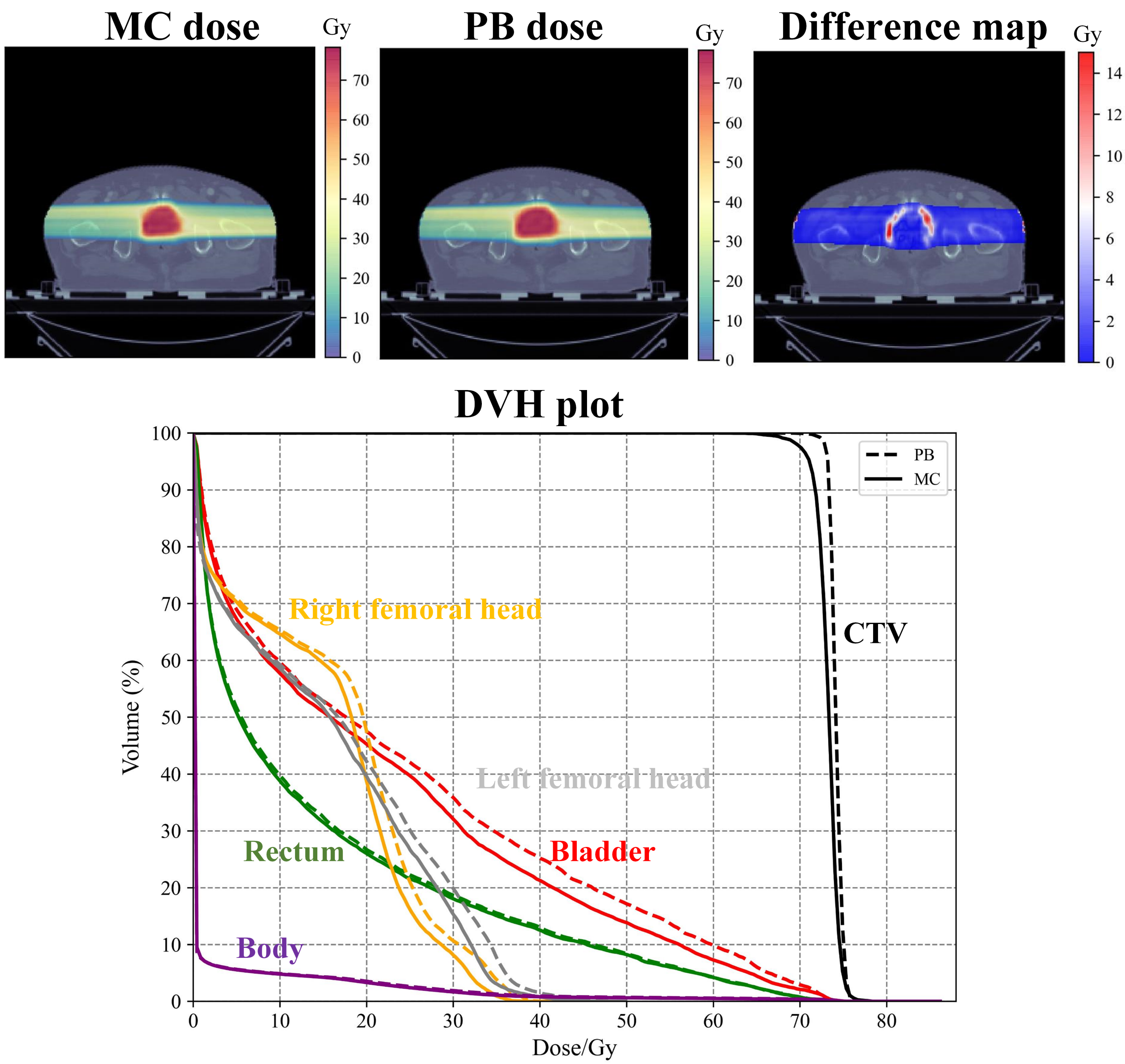

Figure 2: The dose result of the PB algorithm and MC algorithm, the dose difference map between the PB dose and the MC dose, and the DVH plots of the PB dose and MC dose.

REFERENCES

[1] R. R. Wilson, "Radiological use of fast protons," *Radiology*, vol. 47, no. 5, pp. 487–491, 1946.

[2] A. J. Lomax, "Intensity modulated proton therapy and its sensitivity to treatment uncertainties 1: the potential effects of calculational uncertainties," *Physics in Medicine & Biology*, vol. 53, p. 1027, jan 2008.

[3] L. Hong, M. Goitein, M. Bucciolini, R. Comiskey, B. Gottschalk, S. Rosenthal, C. Serago, and M. Urie, "A pencil beam algorithm for proton dose calculations," *Physics in Medicine & Biology*, vol. 41, p. 1305, Aug 1996.

[4] S. Huang, K. Souris, S. Li, M. Kang, A. M. Barragan Montero, G. Janssens, A. Lin, E. Garver, C. Ainsley, P. Taylor, Y. Xiao, and L. Lin, "Validation and application of a fast monte carlo algorithm for assessing the clinical impact of approximations in analytical dose calculations for pencil beam scanning proton therapy," *Medical Physics*, vol. 45, no. 12, pp. 5631–5642, 2018.

[5] X. Liang, Z. Li, D. Zheng, J. A. Bradley, M. Rutenberg, and N. Mendenhall, "A comprehensive dosimetric study of monte carlo and pencil-beam algorithms on intensity-modulated proton therapy for breast cancer," *Journal of Applied Clinical Medical Physics*, vol. 20, no. 1, pp. 128–136, 2019.

[6] J. Perl, J. Shin, J. Schümann, B. Faddegon, and H. Paganetti, "Topas: An innovative proton monte carlo platform for research and clinical applications," *Medical Physics*, vol. 39, no. 11, pp. 6818–6837, 2012.

ISBN: 978-3-95450-212-7 ISSN: 2673-5482 doi:10.18429/JACoW-CYCLOTRONS2022-THPO011

EFFECT OF 90 MeV PROTON IRRADIATION ON SPLEEN INJURY IN C57BL/6J MICE

Q. J. Wang, S. Li*, Q. Liu, Y. H. Gong, J. C. Liu, Y. Wang
China Institute of Atomic Energy, Beijing, China
National Innovation Center of Radiation Application, Beijing, China

Abstract

Proton therapy has become one of the most important physiotherapies for tumors in the world, which can greatly improve the cure rate of tumors that are ineffective by conventional treatments. In addition, proton is also the main source of radiation in space environment. Therefore, it is of great scientific significance to use accelerators to carry out basic research on proton radiotherapy and space radiobiology, which can provide technical support and basic data for the optimal design of proton therapy and risk assessment of personnel in space environment.

In this study, C57 mice were irradiated with 0, 0.2, 0.5 and 2Gy by 90 MeV protons from 100MeV cyclotron of China Institute of Atomic Energy. The mice were killed one day after irradiation. Body weight change and spleen organ coefficient were calculated. The expression of DNA damage-related protein γH2AX was detected by western blotting.

The results showed that compared with the control group, the body weight of mice in each irradiation group had no significant change, and the spleen organ coefficient decreased, indicating that the spleen atrophied after proton radiation, especially in 2Gy. The results of Western blotting showed that the expression of γ H2AX in spleen increased significantly on the 1 day after irradiation, especially in 0.5 and 2 Gy, indicating that the spleen DNA damage was the serious on the 1 day after proton radiation.

INTRODUCTION

With the development of China's aerospace industry, especially the advent of the space station era, the time spent by astronauts in space in the future will increase, and the impact of the space environment on the health of astronauts has also received more and more attention. Existing aerospace data show that medium and long-term space flight will affect multiple physiological systems of astronauts, such as genomic instability, cardiovascular function changes, bone loss, metabolic disorders, immune function changes and even the risk of carcinogenesis [1-3]. Space radiation is one of the important factors restricting manned spaceflight, protons are one of the main sources of space radiation, and its health effects on astronauts' health are particularly important [4].

The immune system is an important system for the body to perform immune responses and immune functions. It is composed of immune organs, immune cells and immune molecules. The immune system has the function of recognizing and eliminating antigenic foreign bodies, coordinating with other systems of the body, and jointly maintaining the stability of the environment and physiological balance in the body.

The spleen is the largest immune organ in the human body and the center of cellular and humoral immunity. Therefore, it is important to study the effect of proton radiation on the damage effect of the spleen.

In this study, 90 MeV medium energy protons generated by the 100 MeV proton cyclotron of the Chinese Institute of Atomic Energy were irradiated at different doses to mice, and the effect of 90 MeV proton irradiation on the spleen of C57 mice was studied. Spleen injury in C57 mice at different doses was obtained. In order to provide basic data and scientific basis for proton radiation protection.

MATERIALS AND METHODS

Animals and Experimental Design

Male C57BL/6J mice aged 6-8 weeks were obtained from SIPEIFU company, Beijing, China. The mice were acclimatized for a week under standard vivarium conditions. Next, we randomly divided the 24 animals into the experimental and control groups, including the control group of C57BL/6J(n=6), 0.2、0.5 and 2 Gy experimental group of C57BL/6J(n=6). At the end of the experiment, samples were collected on the first, third and seventh day.

Radiation Exposure

Proton irradiation was performed at the single-particle effect experimental terminal of CYCIAE-100 (Figs.1 and 2). Mice were exposed to 0.2、0.5 and 2 Gy of 90 MeV proton with 0.8 Gy/min. Control groups were subjected to a sham radiation procedure.

Figure1: The 100 MeV proton cyclotron.

Work supported by the Continuous Basic Scientific Research Project (No.WDJC-2019-11)
* lisui@ciae.ac.cn.

ISBN: 978-3-95450-212-7 ISSN: 2673-5482 doi:10.18429/JACoW-CYCLOTRONS2022-THPO011

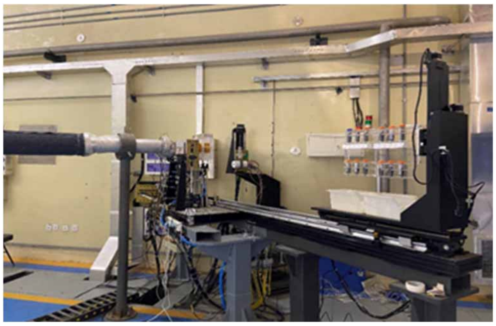

Figure2: The mice irradiation terminal diagram of cyclotron.

Weight and Organ Coefficients

All mice were weighed and recorded immediately after ear tags before irradiation, and weighed and recorded again before live killing, so as to obtain the weight changes of each group of mice before and after irradiation.

Remove the liver and place it on the filter paper, remove the residual water on the surface, weigh and record using an analytical balance, and the organ should correspond one-to-one with the mouse ear number. The organ coefficient is then calculated as follows:
Organ Coefficient (mg/g)= Organ Quality(mg)/ Weight(g).

Western Blot Experiment

Western blotting experiments were performed on mouse spleen 1 day after extraction. Tissue protein lysate was added to spleen and ground with a glass homogenizer. After centrifugation at 4℃, the supernatant was collected in EP tube and the protein concentration was measured by ultraviolet spectrophotometer. After protein denaturation-gel electrophoresis-film transfer-crosslinking-blocking, γ H2AX primary antibody was added and incubated at 4℃ (overnight), then incubated with corresponding secondary antibody at room temperature for 1 hour, and detected by chemiluminescence reagent kit. Finally, semi-quantitative analysis is carried out by Image J software.

RESULT AND DISCUSSION

The Results of Weight and Organ Index

The results showed that compared with the control group, the body weight of mice in each irradiation group had no significant change (Fig. 3). However, the spleen organ index of the irradiation group decreased significantly (p<0.05), indicating that after proton irradiation, the spleen atrophy of mice was most pronounced at 0.5 and 2 Gy (Fig. 4).

The Result of Western Blot

γ H2AX is a marker of DNA double-strand breaks. The results of western blotting showed that the expression of γ H2AX in the spleens of each irradiation group increased significantly 1 day after irradiation (p＜0.05), especially at 0.5 and 2 Gy (Fig.5), indicating that the DNA damage of the spleen was severe 1 day after proton irradiation.

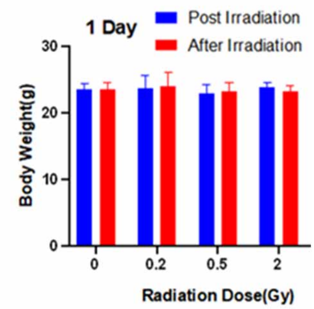

Figure 3: The effect of different doses of proton radiation on the weight change of mice.

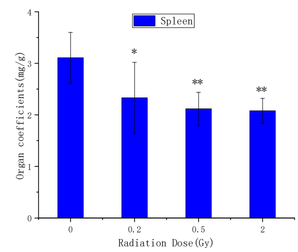

Figure 4: The effect of different doses of proton radiation on the changes in organ coefficients of spleen in C57BL/6J mice（vs 0 Gy,*p＜0.05，**p＜0.01).

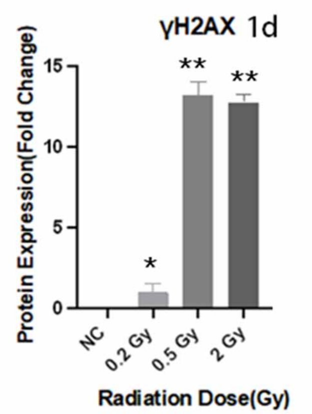

Figure 5: Semi-quantitative analysis results of γ-H2AX expression level in mice spleen tissue(vs 0 Gy,*p＜0.05，**p＜0.01).

Discussion

The organ coefficient, also known as the organ to body ratio, is generally a constant value, but when affected by external factors (such as ionizing radiation, drugs, etc.), some organs may be damaged, and their quality may change accordingly. Increased organ coefficient may be due to organ hyperemia, edema, or hyperplasia; Decreased organ factor may be due to organ atrophy or other degenerative changes. The results of this experiment showed that the spleen coefficient decreased significantly, indicating that the spleen is more sensitive to ionizing radiation, and proton radiation can cause spleen damage in the short term, destroy immune function, make the body in a state of susceptibility to infection, and is also an important cause of body death [5]. The organ coefficient is a very simple and

ISBN: 978-3-95450-212-7 ISSN: 2673-5482 doi:10.18429/JACoW-CYCLOTRONS2022-THPO011

clear indicator that can reflect the damage of proton radiation to the spleen of mice at the organ level.

In response to ionizing radiation-induced DNA DSB, H2AX is the earliest phosphorylated substrate, the most sensitive molecule in cells to sense DNA double-strand damage, can be used as a marker of DNA double-strand break damage, and the number of γH2AX foci and the number of DSBs are basically 1:1 in the number [6,7], which can achieve accurate quantification of DSB. In the results of western blot experiments on spleen DNA damage-related proteins at the molecular level, it is not difficult to find that protons can cause the expression level of DNA damage marker γ-H2AX to increase 1 day after irradiation, indicating that the more serious the DNA damage increases with the increase of proton irradiation dose.

CONCLUSION

In general, 90 MeV proton irradiation was used in C57 mice to study the effects of different doses of proton radiation on the spleen. The results showed that the spleen was highly sensitive to 90 MeV proton radiation, and atrophic degenerative changes began to occur at the 0.2 Gy dose. Further research on the DNA damage caused by proton radiation in spleen tissue found that 0.2 Gy proton radiation can induce spleen DNA double-strand breaks, and the DNA double-strand breaks become more severe with the increase of dose. It showed that proton radiation had a significant effect on spleen injury in mice, triggering the regulation of the immune system, thereby affecting the body's own damage repair.

ACKNOWLEDGEMENTS

We are grateful to the CYCIAE-100 cyclotron staff for the operation of the machine.

REFERENCES

[1] B. Comet *et al.*, "Medical survey of European astronauts during Mir missions", *Adv. Space Res.*, vol. 46, pp. 831-839, 2010. doi:10.1016/j.asr.2010.05.023

[2] B. Crucian *et al.*, "Immune system dysregulation during spaceflight: clinical risk for exploration-class missions", *J. Leukoc. Biol.*, vol. 86, pp. 1017–1018, 2009. doi:10.1189/jlb.0709500

[3] "Humans in space", *Chemical and Engineering News Archive* vol. 75, p. 5 1997. doi:10.1021/cen-v075n009.p005

[4] G. Sonnenfeld *et al.*, "Effects of the space flight environment on the immune system", *Rev. Environ. Health*, vol. 18, pp. 1-18, 2003. doi:10.1515/REVEH.2003.18.1.1

[5] Y. L. Wang *et al.*, "Role of the spleen in cyclophosphamide-induced hematosuppression and extramedullary hematopoiesis in mice", *Arch. Med. Res.*, pp. 249-255, 2009. doi:10.1016/j.arcmed.2009.04.003

[6] E. P. Rogakou *et al.*, "Megabase chromatin domains involved in DNA double-strand breaks in vivo", J. *Cell Biol.* pp. 905-915, 1999. doi:0.1083/jcb.146.5.905

[7] M. Löbrich *et al.*, "γH2AX foci analysis for monitoring DNA double-strand break repair: Strengths, limitations and optimization", *Cell Cycle*, pp. 662-669, 2010. doi:10.4161/cc.9.4.10764

ISBN: 978-3-95450-212-7 ISSN: 2673-5482 doi:10.18429/JACoW-CYCLOTRONS2022-THPO012

PROGRESS IN DESIGN OF MSC230 SUPERCONDUCTING CYCLOTRON FOR PROTON THERAPY

K. S. Bunyatov, V. A. Gerasimov, S. V. Gurskiy, O. V. Karamyshev†, G. A. Karamysheva, I. D. Lyapin, V. Malinin, M. S. Novikov, D. Nikiforov, D. Popov, V. M. Romanov, A. A. Sinitsa, G. V. Trubnikov, G. D. Shirkov, S. G. Shirkov, G. G. Hodshibagijan, S. L.Yakovenko
JINR, Dubna, Russia

Abstract

The current status of the MSC230 superconducting cyclotron designed for biomedical research is presented. MSC230 is an isochronous four-sector compact cyclotron with a magnetic field in the center of 1.7 T. Acceleration is performed at the fourth harmonic mode of the accelerating radio-frequency (RF) system consisting of four cavities located in the cyclotron valleys. The accelerator will use an internal Penning type source with a hot cathode. Particular attention is paid to extraction, as it must have a high extraction efficiency.

INTRODUCTION

Recent studies of a promising new method, called FLASH [1, 2], have shown that it has great potential for expanding the use of proton therapy on tumors that previously could not be treated with protons, at the same time significantly improving the quality of treatment. Compared to radiation therapy at a conventional dose rate (1–7 Gy/min), FLASH irradiation is performed at a dose rate over 50 Gy/s in less than 0.5 seconds. Healthy tissue is better able to withstand FLASH radiation, while the level of damage to the tumor is the same as with conventional treatment.

However, before proton FLASH therapy can be fully implemented in practice, it is necessary to solve several engineering and technical challenges. More particularly, there is a need in an accelerator that provides a high average beam current, which, according to various estimates, is 0.5-100 μA for the entire range of energies used in treatment.

The task of the FLASH research makes relevant the creation of a research and innovation center at JINR equipped with a modern proton accelerator, a beam delivery system and laboratory equipment for biomedical research.

An isochronous cyclotron cannot compete with synchrocyclotrons in dimensions and weight, but a cyclotron accelerates a quasi-continuous beam, therefore, it is the most promising accelerator for the application of a new method of radiation therapy - flash.

The MSC230 cyclotron [3] can produce a 230 MeV proton beam for therapy and biomedical research. Table 1 shows the main parameters of the MSC230 cyclotron. We plan to get about 10 μA of beam current in our cyclotron to study the efficiency of the flash method.

Figure 1 shows the interior of the magnetic and accelerating systems of the cyclotron.

Table 1: MSC230 Cyclotron Main Parameters

General properties	
Accelerated particles	Protons
Magnet type	SC coils, ‹‹warm›› yoke
Injection	Internal source
Number of turns	500
Beam Parameters	
Energy, MeV	230
The relative error of the proton beam energy, %	0.15
Extracted beam intensity (continuous mode), nA	2-1000
Extracted beam intensity (flash mode), nA	5000-10 000
Emittances of the extracted beam, π*mm*mrad, (2σ)	
Radial	8
Vertical	2
Magnetic system	
Average magnetic field (R_o/$R_{extr.}$), T	1,7/2,15
Dimensions (height × width), m	1,7 × 3,9
Magnet weight, tonne	~130
Hill/valley gap, mm	50(25)/700
Excitation current (1 coil), A*turns	270 000
Accelerating system	
Frequency, MHz	106.5
Harmonic number	4
Number of cavities	4
Power losses, kW (total)	60
Voltage center/extraction, kV	40/100
Extraction	
Extraction radius, m	1.08
Extraction system	ESD+2MC

Figure 1: View of the MSC230 cyclotron model.

ISBN: 978-3-95450-212-7 ISSN: 2673-5482 doi:10.18429/JACoW-CYCLOTRONS2022-THPO012

MAGNET SYSTEM

The MSC230 magnet is composed of a superconducting (SC) solenoid and an iron yoke. The technology with the use of a hollow composite SC cable, proposed at JINR and well-proven in the magnets of the Nuclotron synchrotron, was chosen as the basis for the manufacture of the solenoid. JINR has a base for the production of such a cable, which requires only the modernization of the existing equipment.

Work on the superconducting cyclotron system is currently being actively pursued. The MSC230 cyclotron cryogenic system is designed for creating a magnetic field in the cyclotron magnet yoke structure.

The simulation in CST studio of the MSC230 magnetic system (see working diagram in Fig. 2) was based on its main characteristics:

- Four-fold symmetry and spiral sectors
- Deep-valley concept with RF cavities placed in the valleys
- Pole radius = 118 cm
- Stray magnetic field in the 200 Gs range near the accelerator

The following mechanical model is proposed:

- The disk plate must have a hole for the vacuum o-ring with the cryostat;
- 2 lifting jacks for yoke opening;
- 4 numbers of feet;
- Technological holes.

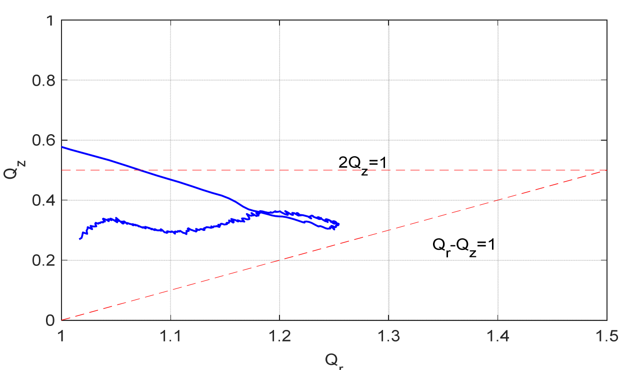

Figure 2: Working diagram.

The size of the vertical gap between the sectors is constant along the radius and is 50 mm, which is sufficient to accommodate the electrostatic deflector. To ensure the growth of the mean field in the extraction zone, we set the shape of the chamfer of the sector edge not around a circle centered at the geometric center of the cyclotron, but along the shape of the trajectory of the accelerated particles, which differs from the circle the more, the higher the flutter of the magnetic field. Another feature that serves this purpose is the "double sector" - part of the sector has a smaller vertical gap between the sectors, while maintaining enough space for the deflector (see Fig. 3).

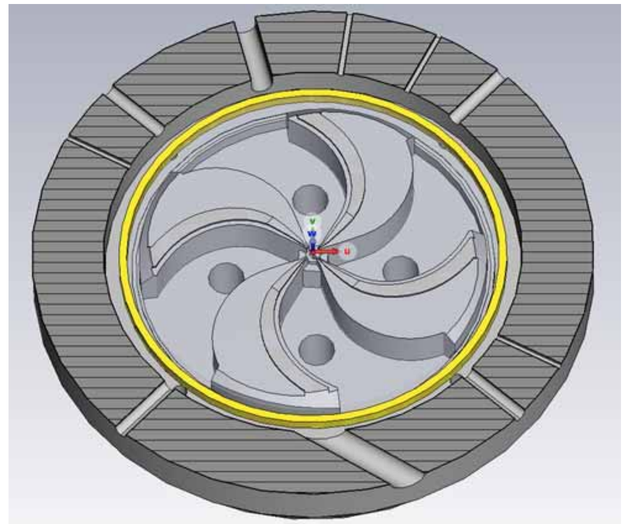

Figure 3: Magnet of the cyclotron MSC230.

ACCELERATING SYSTEM DESIGN

RF cavities are located at the valleys of the magnet, the geometry of the RF cavity is restricted by the size of spiral sectors. For proton acceleration, we are planning to use 4 accelerating RF cavities, operating on the 4th harmonic mode. The choice of 4th harmonic is a natural choice for a cyclotron with 4 sector and provides high acceleration rate. All four RF cavities will be connected in the centre and will be working on approximately 106.5 MHz frequency.

The characteristic parameters of the half-wavelength coaxial resonant cavity with two stems have been obtained from simulation in CST studio (see Fig. 4). Suitable accelerating frequency and voltage along radius were achieved.

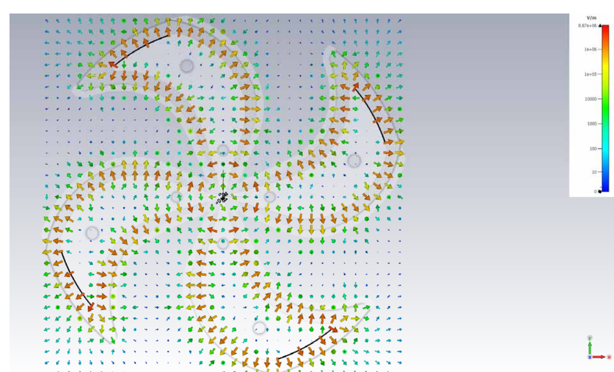

Figure 4: Electric field distribution.

CENTER REGION

To provide vertical focusing, we create a bump (radial gradient) of the magnetic field (80-100 Gauss). Magnetic focusing caused by the decreasing magnetic field begins after a radius R = 30 mm. For R< 30 mm: accelerating electric field provides vertical focusing of lagging particles. In the central region, a collimator should be placed, limiting the amplitude of vertical oscillations to 2-3 mm. Form of dee tips in the center region was optimized. Beam quality and transmission coefficient were improved (see Ref. [4]).

Comsol was used to simulate particle trajectories in the center (see Fig. 5). Comsol has the possibility to account for losses of accelerated particles on the accelerator walls. Blue circles show particles at the end of the tracking (it is assumed that when colliding with elements of the cyclotron structure the particles stop, which allows to see the place of loss of particles.

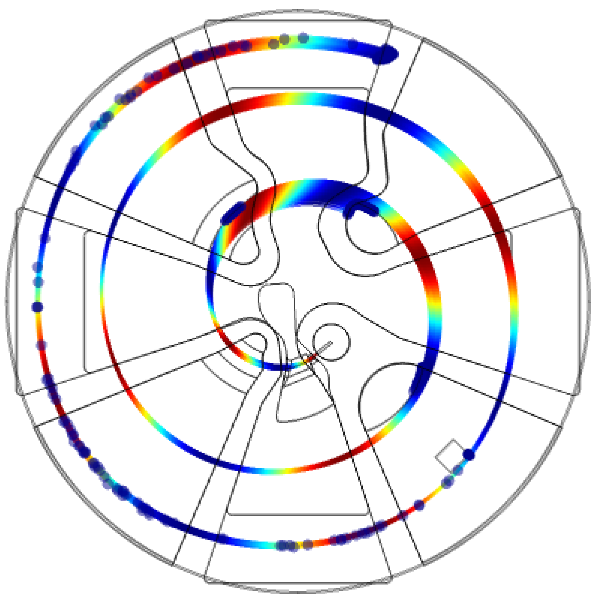

Figure 5: Beam trajectories in the optimized center (Comsol). Color indicates oscillation phase of the accelerating system.

EXTRACTION SYSTEM

The low magnetic field together with the high acceleration rate due to 4 resonators and the fourth harmonic mode will allow efficient extraction by means of an electrostatic deflector (ESD), located between the sectors, and 2 passive focusing magnetic channels (MC1 and MC2) [5]. We restricted electric field in deflector by the value of 100 kV/cm.

The beam, after being pulled with the deflector, passes through the accelerating RF-cavities and magnetic channels. Passive magnetic channels are located inside sector's gap, the first one decreases the average magnetic field for 600 Gs and provides gradient of 1000 Gs/cm, the second one only provides a gradient of 1700 Gs/cm.

The beam tracing though the extraction system was performed in 3D magnetic field maps which were calculated taking into account the magnetic channels and the compensating channels (Fig. 6).

The calculated horizontal emittance at the accelerator's exit is about 8π·mm·mrad, whereas the vertical one is about 2π·mm·mrad.

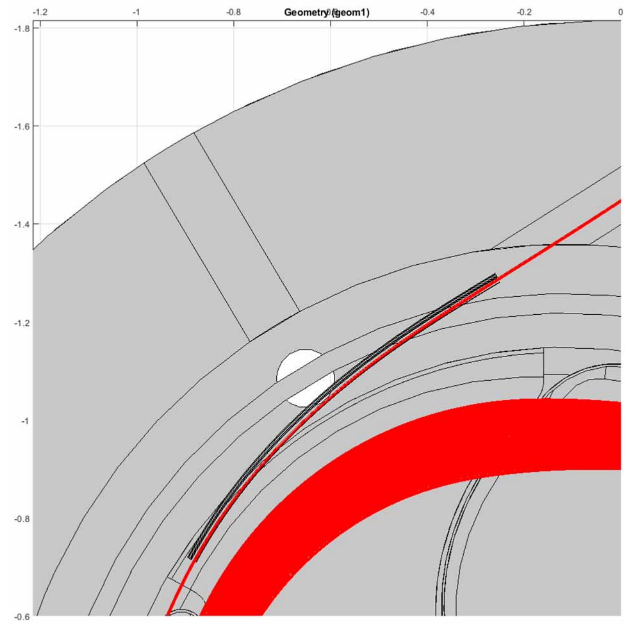

Figure 6: The beam tracing in the cyclotron structure.

CONCLUSION

The cyclotron design includes conservative and proven solutions that reduce risks and simplify engineering challenges. The MSC230 accelerator will be a source of an intense proton beam for the Medical Technical Complex of DLNP, JINR. On this basis, coupled with MTC's experience of treatment by the method of conformal therapy, opens up the possibility of equipment modernization. This is necessary for precise control and delivery of a high dose rate for studies of the FLASH therapy method.

The technical design and production of the main cyclotron systems began at Efremov Institute of Electrophysical Apparatus, St.-Petersburg.

REFERENCES

[1] A. A. Patriarca, L. De Marzi, V. Favaudon, and S. J. Meyroneinc, "FLASH radiation therapy: accelerator aspects", in *Proc. 11th Int. Particle Accelerator Conf. (IPAC'20)*, Caen, France, May 2020, p. 71. doi:10.18429/JACoW-IPAC2020-THVIR12

[2] S. Jolly, H. Owen, M. Schippers, and C, Welsch, "Technical challenges for FLASH proton therapy", *Physica Medica,* vol. 78, pp. 71-82, 2020. doi:10.1016/j.ejmp.2020.08.005

[3] O. Karamyshev *et al.*, "Research and development of the SC230 superconducting cyclotron for proton therapy", *Phys. Part. Nucl. Lett.,* vol. 18, no. 1, pp. 63-74, 2021. doi:10.1134/S1547477121010088

[4] V. Malinin, "The design of the center region of MSC230 cyclotron", presented at the 23rd Int. Conf. on Cyclotrons and their Applications (Cyclotrons'22), Beijing, China, Dec. 2022, paper THBO06, this conference.

[5] D. Popov "Beam extraction simulation and magnetic channels' design for MSC230 Cyclotron", presented at the 23rd Int. Conf. on Cyclotrons and their Applications (Cyclotrons'22), Beijing, China, Dec. 2022, paper THAO02, this conference.

ISBN: 978-3-95450-212-7 ISSN: 2673-5482 doi:10.18429/JACoW-CYCLOTRONS2022-THPO013

MAGNET DESIGN OF A COMPACT 16 MeV VARIABLE ENERGY CYCLOTRON FOR ISOTOPE PRODUCTION

S. W. Xu, W. W. Wang, Hefei CAS Ion Medical and Technical Devices Co., Ltd., Hefei, China
K. Z. Ding, J. Zhou, F. Jiang, Z. Wu
Institute of Plasma Physics, Chinese Academy of Sciences, Hefei, China

Abstract

A compact isochronous cyclotron, CIMV16, is under research and development at Hefei CAS Ion Medical and Technical Devices Co., Ltd, China (HFCIM). This cyclotron can accelerate negative hydrogen ion to variable energy in the range of 10~16 MeV for the stable production of widely-used medical isotopes in this energy range. It has a maximal diameter of only 1.8 m and adopts three radial-sector poles with the third harmonic acceleration. The design of magnet system and the analysis of final simulated static magnetic field were described in detail in this paper. Meanwhile, two suitable shimming methods were also proposed for later engineering optimization.

INTRODUCTION

To meet the explosive growth of domestic health needs, China is actively producing medical radioisotopes. Important among them are ^{11}C, ^{13}N, ^{15}O, ^{18}F, etc. for PET (Positron Emission Tomography) and ^{64}Cu, ^{67}Ga, ^{86}Y, ^{124}I, ^{225}Ac, etc. for other medical applications, all of which require proton energy in the range of 10~16 MeV to yield them through nuclear reactions [1]. Due to the advantages of producing isotopes with high specific activity and less radioactive waste, the cyclotron has gradually become a critical option for the production of short-lived radioisotopes [2].

A cyclotron with a single extraction energy could not be suitable for producing various isotopes efficiently, so a variable-energy cyclotron that can simultaneously produce several isotopes is more adopted to the market demand. Internationally, the existing variable-energy cyclotrons below 20 MeV are TR-19, BEST 35p, CYCLONE 30, CC-18/9M, and so on [2]. However, in China, only a few cyclotrons with single-energy are available, such as CYCIAE-14 from China institute of atomic energy (CIAE) [3]. For these reasons, HFCIM is developing a variable-energy cyclotron, CIMV16. To improve the extraction efficiency, it accelerates negative hydrogen (H^-) ion and extracts them by stripping foil, which can produce more than 100 μA protons with energies of 10~16 MeV, satisfying the production of the important isotopes described above.

The design of magnet system is the primacy of CIMV16. After the initial determine of magnet system parameters, the poles are further optimized according to the isochronous requirements. Then, the beam dynamics analysis is performed for a single particle, and the position of stripping foil is adjusted so that this particle can be extracted to a same focus point at different energies, which finally confirms that the magnet system meets our design requirements.

STRUCTURE DESIGN

The preliminary design of CIMV16 is based on the following assumptions:

- Primarily accelerates H^- ion.
- Isochronous cyclotron.
- Maximal extraction energy is 16 MeV.
- Isochronous field at $R = 0$ (B_0) is about 1.55 T.
- Axial betatron frequency (ν_z) is in the range of $0.10 < \nu_z < 0.25$ (beyond the central region).
- Radial-sector poles (spiral angle $\mu = 0$).
- Make enough space for RF system, and decrease RF voltage as much as possible.

Based on the above assumptions, The relativistic mass factor of H^- ion at maximal energy is expressed as $\gamma = (E_0 + E_k) / E_0 \approx 1.017$ (where E_0 is the rest energy 939.278 MeV and E_k is the maximal kinetic energy 16 MeV). Isochronism requires the maximal averaged field is calculated as $\langle B_e\rangle = \gamma B_0 \approx 1.58$ T. Therefore, the final orbit radius of particle (R_e) is estimated as 36.8 cm. Considering the magnetic field weakens so quickly in the pole-edge region and its distribution does not meet the requirements of radial focusing and isochronism, so the radius of pole is a little larger than R_e.

The next step is to evaluate the axial and radial focusing characteristics. Referring to the calculation by H. L. Hagedoorn and N. F. Verster [4], the 2nd order approximate expansion of radial and axial betatron frequency (ν_r and ν_z) can be written as Eq. (1) and (2):

$$\nu_r^2 \approx 1 + k + \frac{3N^2}{(N^2-1)(N^2-4)} F(1+\tan^2\mu), \quad (1)$$

$$\nu_z^2 \approx -k + \frac{N^2}{N^2-1} F(1+2\tan^2\mu), \quad (2)$$

where N is the number of poles, μ is the spiral angle of pole, F is the field flutter ($F = \langle B^2\rangle / \langle B\rangle^2 - 1$) and k is the positive field index ($k = R / \langle B\rangle \times \mathrm{d}\langle B\rangle / \mathrm{d}R$) for each radius R. k approaches to 0 at the radius of maximal averaged field. In order to make the ν_z here close to 0.20 without spiral angle ($\mu = 0$), the minimal field flutter 3.6% for 3 poles or 3.8% for 4 poles is required at this radius. For providing sufficient space for the RF system and other systems and ensuring the enough axial focusing, the three radial-sector poles with third harmonic acceleration is finally adopted in CIMV16.

The magnetic field in mid-plane is obtained by finite element analysis (FEA). After several iterations, this magnitude of magnetic field is provided by a combination of conventional coils, poles made of DT4 and yokes made of 10# steel. The preliminary selection of conventional coils and magnet parameters are listed in Table 1 respectively.

Table 1: Magnet System Preliminary Parameters

Parameter	Value
Cross section of coils	145 × 155 mm^2
Amperes × Turns	60000 A
Current density	266.96 A/cm^2
Number of poles	3
Max. radius of pole	420 mm
Height of pole	25 mm
Outer radius of yoke	900 mm
Hill gap / Valley gap	40 / 90 mm
Total height of magnet	900 mm
Central field	1.36 T
Max. averaged field	1.57 T

The 3D-model of magnet system is described in Fig. 1where the left is the external view and the right shows its lower part. The blue, red and yellow parts represent yokes, coils and poles respectively. Furthermore, the vertical cross-section of the half magnet is shown in Fig 2.

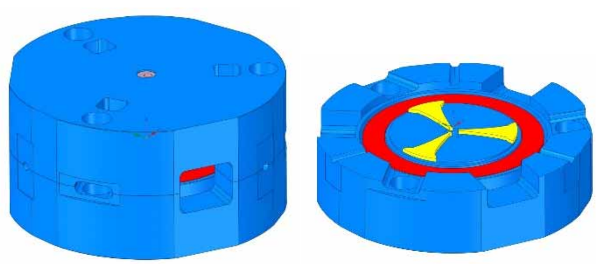

Figure 1: 3D-model of magnet system (left: external view; right: cross-section view).

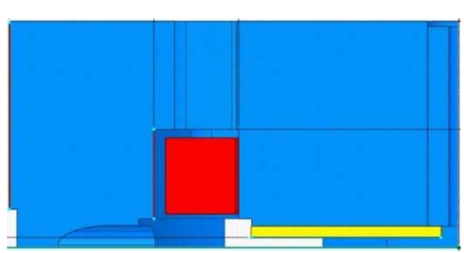

Figure 2: Vertical cross-section of magnet system.

ANALYSIS OF STATIC FIELD

After the initial parameters of the magnet system are determined, the average magnetic field in the mid-plane is gradually close to the isochronous one by optimizing the coil current, pole profile, and RF frequency according to isochronous requirements. A further model is obtained by considering both the magnetic field in the central region and the focusing properties in the extraction region, with the coil current eventually set to 60000 A and the RF frequency set as f_{RF} = 23.6 × 3 = 70.8 MHz. The static magnetic field simulated for this model is analysed below. Figure 3 depicts the comparison of averaged field (<B_z>) with isochronous one (B_{iso}). It can be seen that the <Bz> drops in the central and extraction region.

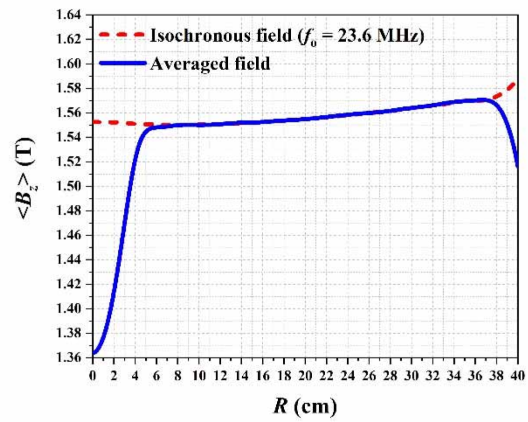

Figure 3: Comparison of averaged field (blue solid line) with isochronous field (red dash line).

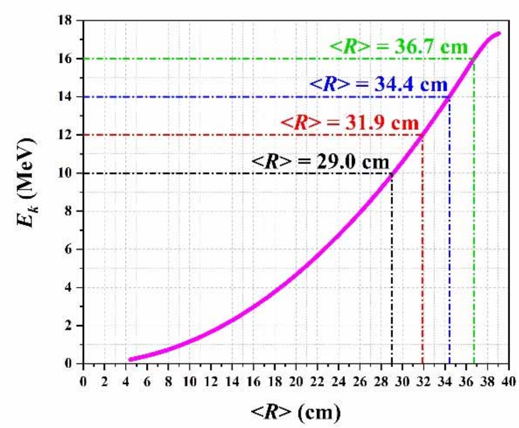

Figure 4: Relation between averaged radius and kinetic energy.

The relation between averaged radius (<R>) and kinetic energy (E_k) based on the static equilibrium orbit is shown in Fig. 4. Notably, 10, 12, 14, 16 extraction energy corresponds to 29.0, 31.9, 34.4, 36.7 cm averaged radius separately.

Figure 5 exhibits an important indicator of whether the isochronism is excellent: integral phase slip along the radius. The difference between averaged and isochronous field is also added in this figure. It is obvious that the difference between averaged and isochronous field has been controlled within ±10 G and integral phase slip has been controlled within ±10° less than 36.7 cm extraction averaged radius (16 MeV extraction energy).

The radial and axial betatron frequency (ν_r and ν_z) as shown in Fig. 6 can be also calculated from the static equilibrium orbit. As shown in this picture, sufficient axial focusing (0.10 < ν_z < 0.20) is provided in the radial range

ISBN: 978-3-95450-212-7 ISSN: 2673-5482 doi:10.18429/JACoW-CYCLOTRONS2022-THPO013

more than 6 cm. Aside from this, the Walkinshaw resonance (ν_r / 2 = ν_z) has been avoided before the particle is accelerated to 16 MeV (corresponding to 36.7 cm). From the Fig. 7 work diagram, the particle does not cross any dangerous resonance lines except for a fast crossing of $\nu_r = 1$ at the end of acceleration, 15.9 MeV. Thus, the focusing satisfies the demands.

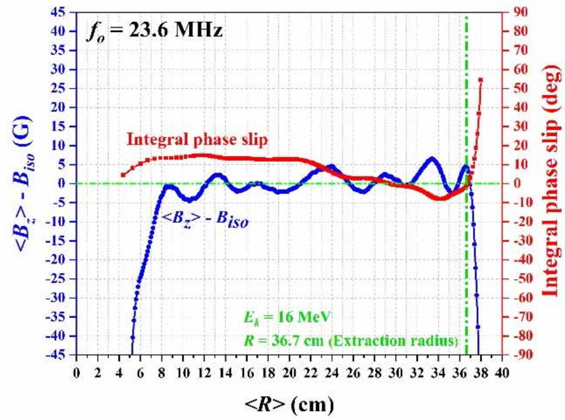

Figure 5: Difference between averaged and isochronous field (left axis); integral phase slip (right axis).

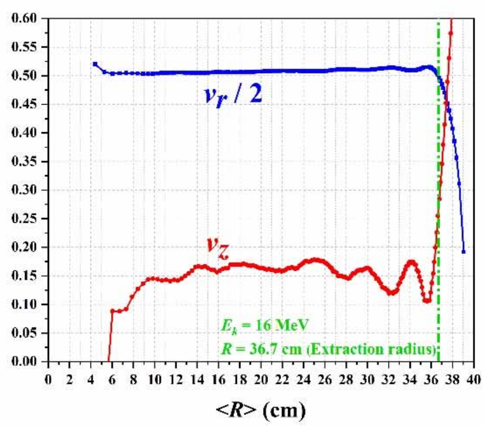

Figure 6: Radial and axial betatron frequency (ν_r and ν_z).

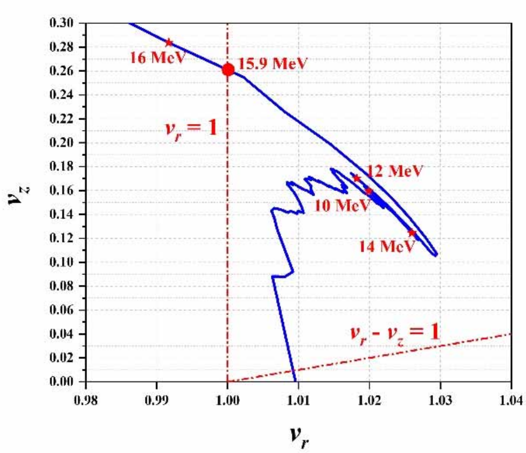

Figure 7: Work diagram.

DETERMINE OF EXTRACTION RADIUS

At last, to check whether the designed cyclotron can extract the beam at various energies successfully and to determine the location of extraction channels in the model of magnet system, the beam dynamics is performed for a single centre particle. Particle extraction energies of 10, 12, 14, 16 MeV are chosen and their beam trajectories are described in Fig. 8. H^- ion can be stripped out two electrons to become proton to be extracted by setting the stripping foils near the trajectories at the corresponding extraction energies. Via adjusting the radial and angular positions of the stripping foils (as summarized in Table 2), the protons with different energies can be extracted and intersect at the same point of around 110 cm. After this, the design of magnet system is completed.

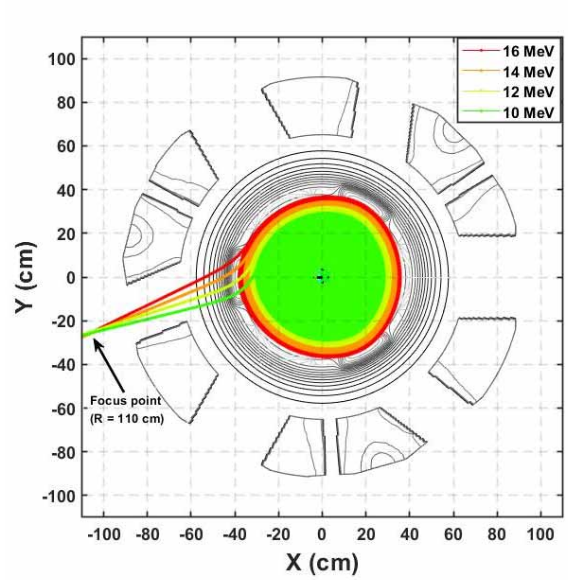

Figure 8: Trajectory of centre particle with different extraction energies.

Table 2: Parameters of magnet

Extraction Energy (MeV)	Stripping Foil Radius (cm)	Stripping Foil Angle (deg)
10	30.0	170
12	32.5	164
14	34.5	158
16	37.0	153

SHIMMING METHODS

Taking into account the poles shimming during the engineering phase, two methods are put forward as follows: The 1st is to fill the central groove (which is prepared in advance) at the surface of each pole; the 2nd is to cut the two laterals of poles. Their 3-D models are shown in Fig. 9.

For each method, a numerical algorithm expressed by J. Q. Zhong [5] can be used for calculating shimming value rapidly. For example, many shimming elements whose sizes are all 1 cm radius, 9 mm arc length, and 7 mm height are established along the radius for the 1st method, then

ISBN: 978-3-95450-212-7 ISSN: 2673-5482 doi:10.18429/JACoW-CYCLOTRONS2022-THPO013

their averaged field distributions along the radius are simulated by FEA, forming a matrix F. The result of them is depicted in Fig. 10. Assuming that the arc length of each element is expressed as a vector X, and vector D represents the required shimming field along the radius, then the X can be solved by least square method with the equation: $F \cdot X = D$. The same algorithm can be applied for the 2nd shimming method, where the size of each element is 1 cm radius, 3 mm arc length, and 25 mm height (the height of pole). Figure 11 shows the averaged field distributions along the radius of each element.

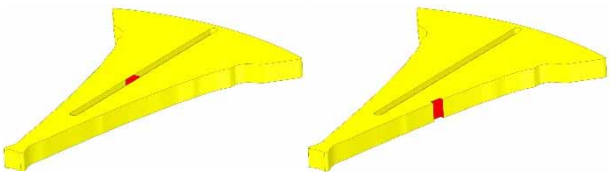

Figure 9: Two methods of poles shimming: to fill the central groove (left) and to cut the laterals (right). The red part is the shimming element.

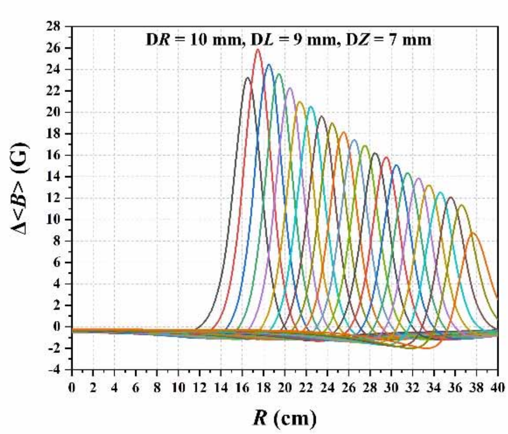

Figure 10: Averaged field distributions along the radius of each element for the 1st shimming method.

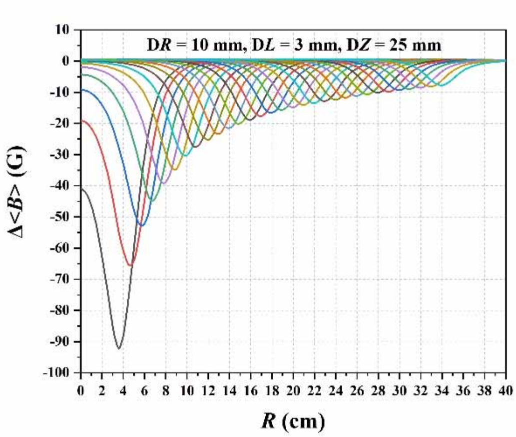

Figure 11: Averaged field distributions along the radius of each element for the 2nd shimming method.

CONCLUSION

This paper illustrates the process of designing the magnet system for a variable-energy cyclotron: CIM16V. Following the preliminary assumptions, it is confirmed that the three radial-sector poles with third harmonic acceleration is adopted for larger RF space. Also, the primary parameters of magnet system are determined. Then, about the final iterated model, analyses of the static magnetic field in mid-plane and the beam dynamics analyses of single particle result in the following conclusions:

- Difference between averaged and isochronous field has been controlled within ±10 G and integral phase slip has been controlled within ±10 deg.
- Sufficient axial focusing ($0.10 < \nu_z < 0.20$) is provided in the radial range more than 6 cm.
- The particle does not or does not slowly cross any dangerous resonance lines (rapidly cross $\nu_r = 1$)
- Realize the extraction of particle in the energy range of 10~16 MeV and make this particle with different energies intersect at a same focus point by the position adjustment of stripping foil.

After confirming that the design of magnet system is finished, two shimming methods of pole profile: to fill the central groove and to cut the laterals are proposed for the engineering optimization.

Currently, the design of other systems are in progress. HFCIM will finish the design and manufacture of this cyclotron as soon as possible to supply the isotopes for the domestic market, in particular the production of ^{18}F.

REFERENCES

[1] A. I. Papash and Yu. G. Alenitsky, “Commercial Cyclotrons. Part I Commercial Cyclotrons in the Energy Range 10-30 MeV for Isotope Production”, *Phys. Part. Nucl.*, vol. 39, no. 4, pp. 597–631, 2008. doi:10.1134/S1063779608040060

[2] P. Schmor, “Review of Cyclotrons for the Production of Radioactive”, *Rev. Accl. Sci. Tech.*, vol. 4, pp. 103–116, 2011. doi:10.1142/S1793626811000574

[3] T. J. Zhang *et al.*, “Overall design of CYCIAE-14, a 14 MeV PET cyclotron”, *Nucl. Instrum. Methods Phys. Res. Sect. B*, vol. 269, no. 24, pp. 2950-2954, Dec. 2011. doi:10.1016/j.nimb.2011.04.049

[4] H. L. Hagedoorn and N. F. Verster, “Orbits in an AVF Cyclotron”, *Nucl. Instrum. Methods*, vol. 18-19, pp. 201-228, 1962. doi:10.1016/S0029-554X(62)80032-9

[5] J. Q. Zhong *et al.*, “The physics design of magnet in 14 MeV cyclotron”, *Sci. Chin. Phys., Mech. Astron.*, vol. 54, no. S2, pp. 266–270, Dec. 2011. doi:10.1007/s11433-011-4551-2

ISBN: 978-3-95450-212-7 ISSN: 2673-5482 doi:10.18429/JACoW-CYCLOTRONS2022-THPO014

THE BEAM DYNAMICS SIMULATION OF A VARIABLE ENERGY CYCLOTRON FOR ISOTOPE PRODUCTION

W. W. Wang, S. W. Xu, Hefei CAS Ion Medical and Technical Devices Co., Ltd., Hefei, China
K. Z. Ding, J. Zhou, F. Jiang
Institute of Plasma Physics, Chinese Academy of Sciences, Hefei, China

Abstract

The isochronous cyclotron, CIMV16, has been designed by Hefei CAS Ion Medical and Technical Devices Co., Ltd, China (HFCIM) for widely used isotope production, which can extract proton with variable energy in range of 10~16 MeV. In this cyclotron, negative hydrogen ion will be accelerated to 10~16 MeV, and then stripped out two electrons to become proton to be extracted. We have performed beam tracking starting from the ion source to the extraction reference point, and optimized the position of the stripping target to make the beam of different energies converge at radius of 110 cm. The orbit centralization is optimized by the design of first harmonic, and the axial size of extraction beam is also optimized. All the results of beam dynamics simulations will be presented.

INTRODUCTION

Small cyclotrons for isotope production have developed greatly in past few years. According to the International Atomic Energy Agency (IEAE) official statistics, the energy distribution of low-level cyclotrons in China, the United States and Japan is mainly 10~18 MeV, and 75% of them are between 10~16 MeV. For cyclotrons with single energy extraction, it is difficult to meet the production of multiple isotopes at the same time. Therefore, if variable energy extraction can be realized in this energy range, it will certainly meet the demand of isotope production better. Based on this precondition, CIMV16 has been designed by HFCIM.

Referring to other medical isotope products of the same type, the CIMV16 adopts three Sector-shaped poles and use 3rd harmonic to accelerate. The parameters are shown in Table 1.

Table 1: Parameters of CIMV16

Parameter	Value
Accelerated particle	H^-
Central field	1.36 T
Max. averaged field	1.57 T
Outer radius of yoke	900 mm
RF frequency	70.8 MHz
Harmonic number	3
Energy	10~16 MeV
Beam Current	150 uA
Extraction mode	Stripping

SINGLE PARTICLE BEAM DYNAMICS SIMULATION

Based on the analysis of the equilibrium orbits, we finished the Single particle beam dynamics simulation. From the simulation results of single particles, we can see that particle can be accelerated to more than 16 MeV, and by adjusting the position of the stripping target, Proton with different energies in range of 10~16 MeV can be extracted, and we also make the beam converges at 110 cm after extracted by optimizing the position of the stripping target. The trajectories of different energy particle are shown in Fig. 1 and the positions of the stripping target corresponding to different energies are shown in Table 2.

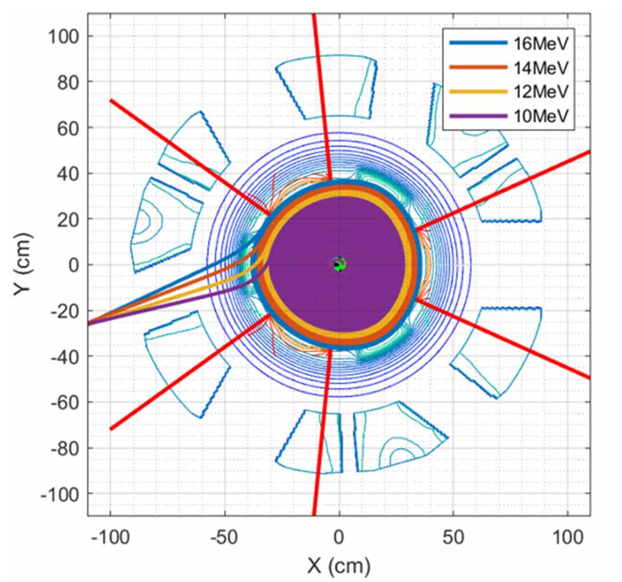

Figure 1: Trajectories of single particle with different energies.

Table 2: Position of Stripping Target

Energy (MeV)	Radius (cm)	Azimuth (deg)
16	30.0	170
14	34.5	164
12	32.5	158
10	37.0	153

ISBN: 978-3-95450-212-7 ISSN: 2673-5482 doi:10.18429/JACoW-CYCLOTRONS2022-THPO014

The integral phase motion of the 16 MeV extraction particle is shown in Fig. 2, we can see that the phase motion of the acceleration region is within plus or minus 10 degrees. The radius varies with the energy is shown in Fig. 3, we can see the radii of different energies from this figure. Through the above simulation results, we believe that the design of variable energy extraction in the energy range of 10~16 MeV and the isochronicity of magnetic fields have been achieved.

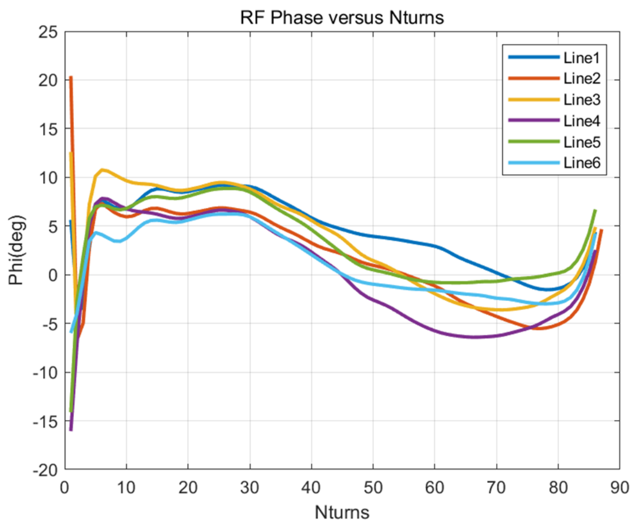

Figure 2: phase motion of the 16 MeV extraction particle.

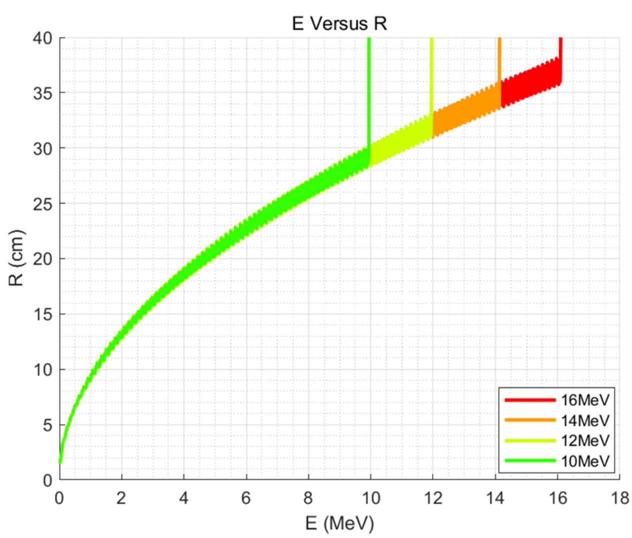

Figure 3: radius varies with the energy.

MULTI-PARTICLE BEAM DYNAMICS SIMULATION

Multi-particle beam dynamics have been down by the beam dynamics code cyclone and the self-develop code (CYCMOT). 5000 particles have been used. The parameters of initial particles are shown in Table 3.

Table 3: Initial Particles Parameters

Parameter		Value
radial	R	Rc±0.25 mm
	Pr	Prc ± 15°
axial	Z	0 ±2mm
	Pz	0 ± 5 °
Phase		-90°~0°

The particles with different initial phase have been marked to count the phase width that can be extracted. The radial and axial oscillations are also be calculated. To optimize the Ar of the beam, we design the first harmonic in the central region by magnetic poles.

The result of the phase width is shown in Fig. 4, and we can see that the phase width is about 70 deg.

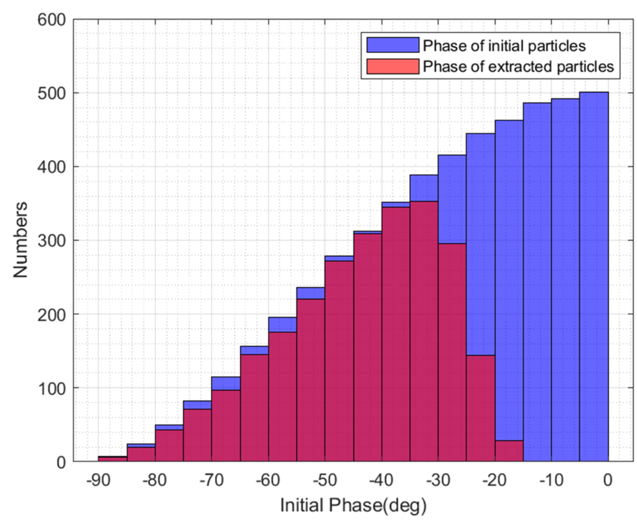

Figure 4: initial phase and extracted particles phase.

We have tried series first harmonic to optimize the radial oscillation and finally we choose the first harmonic with 100 Gs amplitude at radius of 2.5 cm, and the phase is about 110 deg. The distribution of first harmonic is shown in Fig. 5.

After we add this first harmonic the Ar of the beam is less than 3 mm and the Ac of the beam is less than 1 mm. the result is shown in Fig. 6.

We also optimized the axial size of the beam. In this optimization process, we use a brick in central region to block the particles with large axial oscillation, and after series simulations we found that the length of brick should larger than 8 mm along radius. In this way, we controlled the axial size of the beam in central region in range of -5~5 mm. The result is shown in Fig. 7.

23rd Int. Conf. Cyclotrons Appl. CYCLOTRONS2022, Beijing, China JACoW Publishing
ISBN: 978-3-95450-212-7 ISSN: 2673-5482 doi:10.18429/JACoW-CYCLOTRONS2022-THP0014

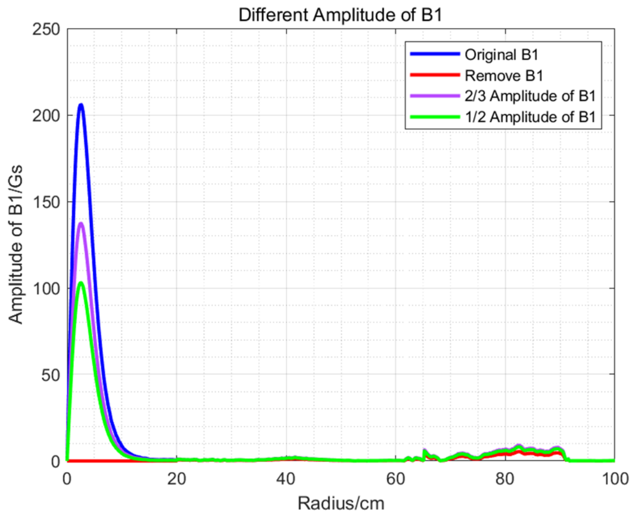

Figure 5: first harmonic distribution and optimization.

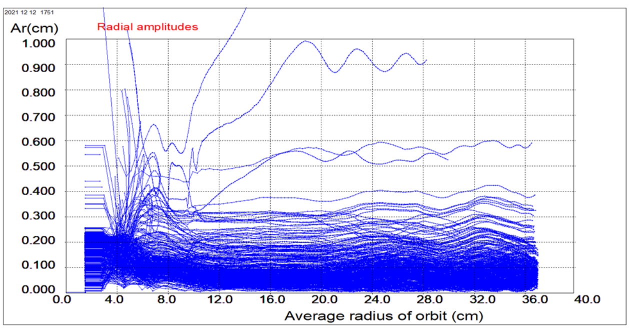

Figure 6: radial oscillations after optimization.

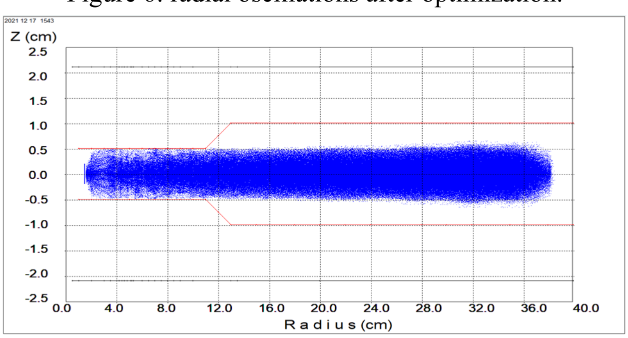

Figure 7: Axial oscillations after optimization.

There are 2525 particles from 5000 initial particles that can be accelerated to 16 MeV, it means that the transmission efficiency from ion source to stripping target is about 50.5%, a good transmission efficiency.

EXTRACTION

This cyclotron used stripping extraction method which can effectively increase the extraction efficiency. It should be noted that this method of extraction will cause the beam to have a large divergence due to the lack of focusing elements [1]. Based on this situation, we used axial brick to control the axial size of the beam, in addition, we also optimized the position of stripping target to make the beam of different energies converge at the same point which can make the further optimization easy.

The axial motion of beam after stripped before and after optimized are shown in Figs. 8 and 9.

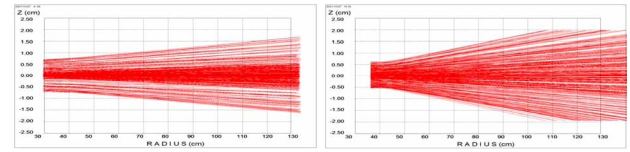
Figure 8: The axial motion of beam in energy of 10 MeV before optimized (left), and the axial motion of beam in energy of 16 MeV before optimized (right).

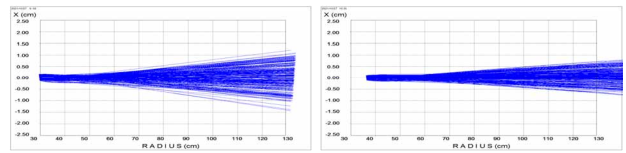
Figure 9: The axial motion of beam in energy of 10 MeV after optimized (left), and the axial motion of beam in energy of 16 MeV after optimized (right).

From the results, it can be seen that the axial size of the beam is controlled within 0.8 cm at reference point.

The extraction optimization result is shown in Fig. 10.

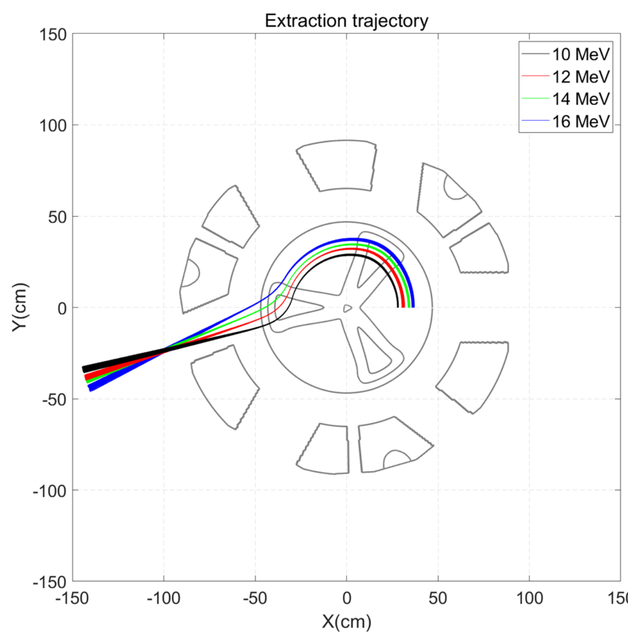

Figure 10: Extraction trajectories of different energies.

CONCLUSION

The beam dynamics analysis of the CIMV16 cyclotron have been finished from the ion source to exit of the cyclotron. The width of the phase is larger than 70 degrees and the beam transmission efficiency from the ion source to strip foil is larger than 50%. According to our simulations we can expect more than 45% beam transmission efficiency from the ion source to reference point [2].

The axial size of beam at reference point can be controlled smaller than 0.8 cm by using axial limit brick. The Ar can be controlled smaller than 3 mm by first harmonic in central region. And the different energy beam converges at reference point successfully.

ISBN: 978-3-95450-212-7 ISSN: 2673-5482 doi:10.18429/JACoW-CYCLOTRONS2022-THPO014

REFERENCES

[1] T. J. Zhang *et al.*, "Beam dynamics study for a small, high current 14 MeV PET cyclotron", *Nucl. Instrum. Methods Phys. Res. Sect. B*, vol. 269, pp. 2955–2958, 2011. doi:10.1016/j.nimb.2011.04.050

[2] G. Karamysheva and O. Karamyshev, "Beam dynamics simulations in the Dubna SC230 super conducting cyclotron for proton therapy", in *Proc. IPAC'19,* Melbourne, Australia, May 2019, pp. 2216-2219. doi:10.18429/JACoW-IPAC2019-TUPTS060

ISBN: 978-3-95450-212-7 ISSN: 2673-5482 doi:10.18429/JACoW-CYCLOTRONS2022-THPO015

R&D STUDIES ON A 177.6 MHz 1:4 SCALE BOAT SHAPE PROTOTYPE RF CAVITY FOR THE 2 GeV CW FFA*

S. Pei†, T. Zhang, Z. Yin, Y. Wang, J. Liu, S. Zhang, X. Zhu, L. Guan, F. Wang, M. Li, Z. Jin, G. Pan, G. Yang, Y. Jia, L. Wang, China Institute of Atomic Energy, Beijing, China
Y. Xing[1], B. Li, S. Xia, Institute of Plasma Physics, Chinese Academy of Sciences, China
[1]also at University of Science and Technology of China, China

Abstract

A proton circular accelerator complex composed of a 100 MeV separated radial sector cyclotron, an 800 MeV separated spiral sector cyclotron and a 2 GeV FFA was proposed and is being studied at CIAE. To satisfy the beam dynamics requirements of the FFA, NC RF cavity with high Q and R will be adopted. It is found that the boat shape cavity is the most promising candidate. Therefore, R&D on a 177.6 MHz 1:4 scale boat shape prototype cavity is being carried out to study all aspects of developing such a high-power cavity. In this scenario, self-consistent multi-physics coupled simulation study with ANSYS HFSS and Workbench was carried out. This paper describes the method to deal with a mechanical model including hundreds of bodies in the FEM analysis and shows the simulation results. In addition, the manufacturing technology and some testing results are also presented.

INTRODUCTION

CIAE has committed to the development of cyclotrons and constructed series of cyclotrons toward higher beam energy and intensity with a compact size. In recent years, the proton beam accelerator with ~GeV energy and ~MW power is being pursued, the purpose is to expand the application scopes of the proton accelerator in the fields of the fundamental physics, the nuclear industry, the home security, etc. In this situation, a proton circular accelerator complex was proposed and is being studied at CIAE [1]. The design goal is to extract a 2 GeV, 6 MW CW proton beam.

For the 2 GeV FFA, NC RF cavities will be applied to boost the proton beam energy from 800 MeV to 2 GeV. Due to the heavy beam loading, development of the NC high power waveguide type RF cavity with high Q and R is extremely important, which is unquestionably beneficial for the energy efficiency enhancement. Four geometries (i.e., rectangular, omega, racetrack, and boat) of the waveguide-type RF cavities were investigated extensively [2], it was found that the boat shape RF cavity has the highest Q and R, and is the most promising candidate.

In order to master the key technology of developing such a high-power RF cavity, R&D on a 177.6 MHz 1:4 scale boat shape prototype cavity is being carried out. For this cavity, ~100 kW RF power dissipated on the copper cavity walls needs to be brought away by the cooling water, ±170 kHz tuning range needs to be reached by deforming the RF cavity walls with the electrical cylinders. To make sure the mechanical design can meet the design demands, self-consistent multi-physics coupled simulation study (i.e., RF-thermal-structural-RF analysis) with ANSYS [3] was carried out, the optimized design results were obtained. Afterwards, the prototype cavity was fabricated by using technologies of the stamping forming, the vacuum EBW, etc. Cold test is being performed; hot test is being prepared and will be done in the very near future.

CAVITY AND COUPLER'S RF DESIGN

Figure 1 shows the RF design of the cavity and coupler. The calculated unloaded Q of the cavity is ~43500; the maximum and minimum shunt impedances along the midplane of the rectangular beam aperture (1 m × 0.03 m) are 7.61 MΩ and 3.79 MΩ, respectively. The accelerating gap length is 0.2 m. The scale of the cavity itself is 2 m×0.5 m×0.8 m. In the realistic cavity, two identical couplers are arranged; one is for RF power coupling, another is connected with a high-power RF load to simulate the beam loading. The calculated maximum β of the coupler is ~2.6.

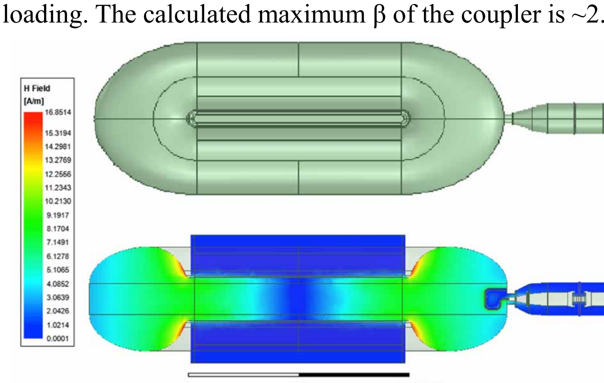

Figure 1: RF design of the cavity and coupler.

MULTI-PHYSICS ANALYSIS

Figure 2 shows the workflow and ANSYS Project Schematic giving the data linkage between the Geometry, the HFSS Design, the Static-State Thermal and the Static Structural. The bodies of the SolidWorks mechanical model imported into the Geometry can be divided into two types, namely the metal and the nonmetal ones. Each body should be named or numbered correctly in the Geometry to avoid unpredictable errors. In the HFSS Design, since only the nonmetal bodies and the metal bodies related to the RF fields are useful for the RF field calculation, all the other metal bodies can be set as Non Model to make the

* Work supported in part by the National Natural Science Foundation of China under Grant 12135020 and the basic research fund from the Ministry of Finance of China under Grant BRF201901.
† 39807556@qq.com.

ISBN: 978-3-95450-212-7 ISSN: 2673-5482 doi:10.18429/JACoW-CYCLOTRONS2022-THPO015

simulation executable and more efficient. To evaluate the structural deformation effect on the RF field, the Enable Stress Feedback option should be turned on and correct Model bodies must be selected. The calculated total power dissipation on the cavity walls should be scaled to the design value (e.g., ~100 kW) and is transferred to the Steady-State Thermal to serve as the heat flux. With the similar method described in [4], the thermal convection coefficient on the cooling water pipe's surface can be calculated by using the empirical formulae [5]. The calculated temperature distribution on the given model can be transferred to the Static Structural as one of the loads. In the Static Structural, by applying additionally the other loads (i.e., the earth gravity, the atmosphere pressure, the pushing or pulling forces of the cylinders, etc.) and the Degree of Freedom (DOF) constraints at the same time, the deformation and the Equivalent Stress distribution on the model can be simulated and fed back to the HFSS Design by turning Export After Solve on, then the RF performance of the cavity can be re-evaluated. By iterating the above process several times, a stable solution can be acquired, however for most cases one or two iterations is enough.

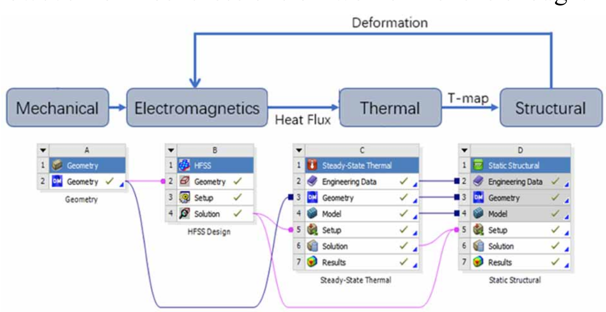

Figure 2: Workflow and ANSYS Project Schematic.

Figure 3 shows the SolidWorks [6] mechanical model of the cavity assembly with a scale of 2.4 m×1.4 m×2.5 m. In the multi-physics analysis, the electrical cylinders were excluded to facilitate the simulation. However, there are still ~280 bodies to be played.

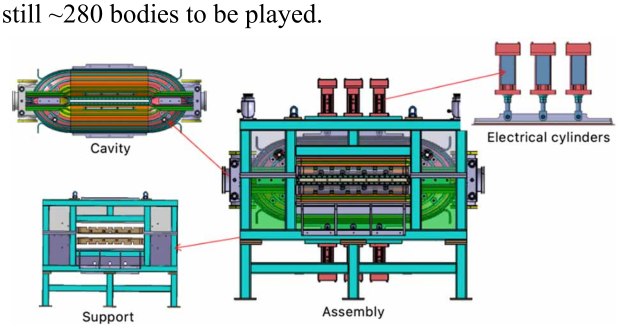

Figure 3: SolidWorks model of the cavity assembly.

The temperature distribution on the prototype cavity's copper walls is shown in Fig. 4. By applying 52 cooling pipes with 8 mm × 8 mm section size, the water temperature rise is 3.58°C at 2 m/s water velocity. With 35°C cooling water, the maximum temperature rise is ~42°C and locates at the left and right sides of the rectangular nose cones.

The simulated deformation and the equivalent stress distribution in the Static Structural with the earth gravity, the ~100 kW RF heating, the atmosphere pressure and the 14000 N pushing force (28000 N in total for both the upper and lower sides) applied are shown in Figs. 5 and 6, respectively. For this case, the cavity frequency is tuned by +176 kHz with a maximum deformation of 2.96 mm. Similar results can be obtained for the case of tuning the frequency by -164 kHz with 30000 N pulling force (60000 N in total) and a maximum deformation of 2.64 mm. The 16000 N force difference (32000 N in total) between the pushing and pulling cases is used to withstand the atmosphere pressure. The maximum secondary equivalent stress for both the pushing and pulling cases are ~187 MPa.

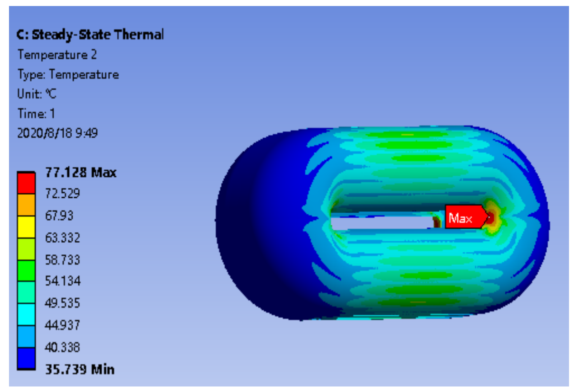

Figure 4: Temperature distribution on the cavity walls.

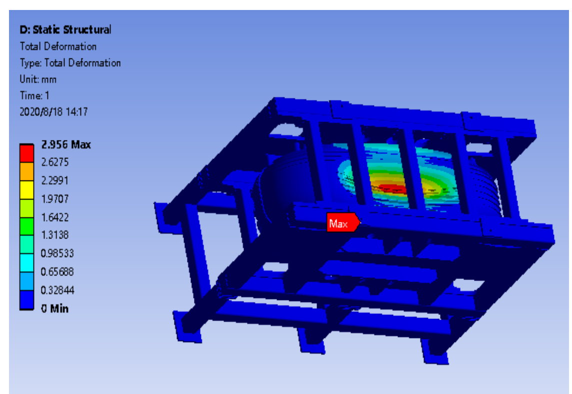

Figure 5: Deformation for +176 kHz frequency tuning.

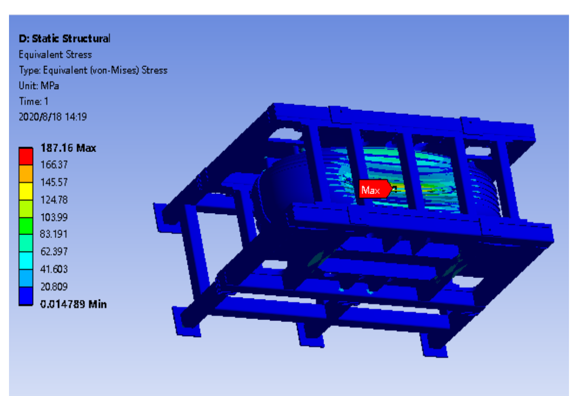

Figure 6: Stress for +176 kHz frequency tuning.

ISBN: 978-3-95450-212-7 ISSN: 2673-5482 doi:10.18429/JACoW-CYCLOTRONS2022-THPO015

CAVITY FABRICATION AND COLD TEST

By evaluating the maximum primary (<68 MPa at here) and the secondary stresses (~187 MPa at here) of the mechanical model with ANSYS and considering the application of the stamping forming technology in the cavity fabrication, half-hard (Y/2) 6 mm thick copper plate (~220 MPa tensile strength, ~103 MPa yield strength and ~65% extensibility) was selected as the cavity wall's raw material.

Due to the cavity's irregular shape, it is very important to control the distortion during the manufacturing and accurately determine the position during the welding. Special tooling and welding process were designed. Especially, EBW was fully adopted to weld all the copper cavity walls together. Figure 7 shows the detailed mechanical fabrication process. Most of the parts of the copper cavity were formed by the stamping forming. Due to the existence of the spring back phenomena and the difficulty to find an accurate reference for the wire-electrode cutting, additional CNC machining was applied. Finally, all the dimension errors were compensated by fine finishing the rectangular nosecone according to the measurement during the cavity pre-assembling process. All of the water-cooling pipes were attached to the outer cavity wall by soldering. The Q and resonant frequency were checked frequently to make sure the fabrication is going on the right way and the cavity's performance consistent with the RF design.

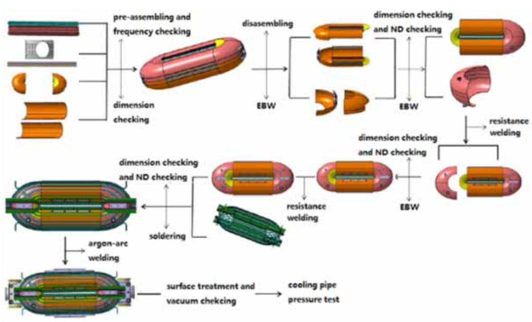

Figure 7: Cavity's mechanical fabrication process.

Figure 8: One of the two half-cavities and the surface roughness measurement.

Figure 8 shows one of the two half-cavities after the all-manual polishing and the measurement of the surface roughness, which is better than 0.1 µm. Mirror surface effect has been obtained. Figure 9 shows the cavity outside look after the soldering of all the cooling pipes. Figure 10 shows the cavity inside and the cavity assembly at the installation site of CIAE. Figure 11 shows the coupler and the Q measurement results. For the coupler, forced air cooling is used for the ceramic window, while water cooling for the coupling loop, the inner and outer conductors. For the Q measurement, two small loop probes with very small βs were used, indicates the unloaded Q is higher than 42314.3, which is ~97% of the design goal. The measured tuning range is ±180 kHz with maximum deformations of ±2.5 mm.

Figure 9: Cavity outside look after the soldering of all the cooling pipes.

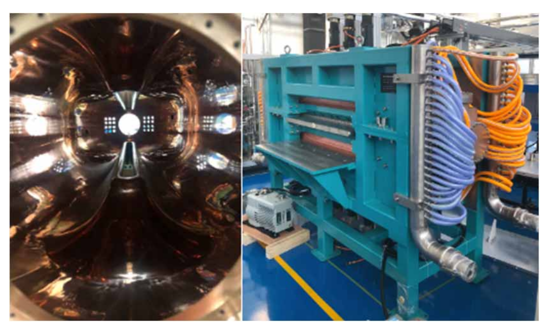

Figure 10: Cavity inside and the cavity assembly at the installation site of CIAE.

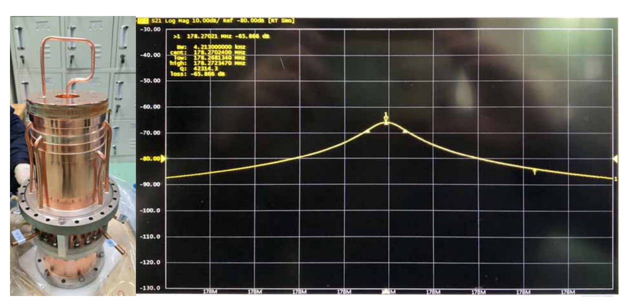

Figure 11: Cavity coupler and Q measurement.

ISBN: 978-3-95450-212-7 ISSN: 2673-5482 doi:10.18429/JACoW-CYCLOTRONS2022-THPO015

SUMMARY

A 177.6 MHz 1:4 scale boat shape prototype cavity has been fabricated with satisfied cold testing results. The hot test is being prepared recently and will be launched in the very near future.

REFERENCES

[1] T. Zhang *et al.*, “52 kW CW proton beam production by CYCIAE-100 and general design of high average power circular accelerator,” *Nucl. Instrum. Methods*, vol. 468, pp. 60-64, 2020. doi:10.1016/j.nimb.2020.02.025

[2] S. Pei, Z. Yin, T.;Zhang, and G. Yang, “Design on high quality factor and high shunt impedance waveguide-type RF cavity for 2 GeV FFAG protron accelerator,” *At. Energy. Sci. Tech.*, vol. 54, pp 1519-1524, 2020. doi:10.7538/yzk.2019.youxian.0495

[3] ANSYS, https://www.ansys.com/

[4] F. Shilun and S. Wang, “RF electro-magnetic field effects on the 571.2 MHz normal conducting sub-harmonic buncher,” *High Energy Phys. Nucl. Phys.*, vol. 29, no. 9, pp 912-917, 2005.

[5] Z. Xu, *Heat Transfer Theory*, China Machine Press, 1980.

[6] SolidWorks, https://www.solidworks.com/

ISBN: 978-3-95450-212-7 ISSN: 2673-5482 doi:10.18429/JACoW-CYCLOTRONS2022-THPO016

DESIGN AND ANALYSIS OF THE 230 MeV CYCLOTRON MAGNET FOR THE PROTON THERAPY SYSTEM

Xiaohu Zhang, Mengfei Chang, Qiang Gu, Chaochao Xing,
Jingjing Zhao, Xiaoping Zhang, Xiaowei Tian, He Dong
CGN Medical Technology (Mian Yang) Co., Ltd, Mian Yang, China

Abstract

This paper demonstrates the design and analysis of 230 MeV cyclotron magnet of the proton therapy system. The magnet is the core of the 230 MeV cyclotron, which can keep the beam orbit and limit beam divergence. The magnetic field calculation and modification are analyzed in detail, with the isochronous error of the magnetic field less than 0.2%. Meanwhile, the thermal analysis of the coil has been calculated by the empirical formula.

INTRODUCTION

The overall model of the C230 cyclotron and the structure of the accelerator is shown in Fig. 1.

The proton cyclotron magnet is mainly composed of magnetic pole, magnetic yoke and pad. In order to achieve the design goal of 230 MeV proton energy, a helical sector focusing structure, four blade poles and four harmonic accelerations are adopted (Fig. 1). To compensate for the increasing energy with radius and the increasing defocusing by the main field, the angle by which the hill-valley boundary is crossed increasing by making the hill-valley structure spirally shaped [1]. This kind of magnet structure is relatively simple and more compact. A replaceable tuning block is installed in the edge of the magnetic pole, and the isochronicity of the magnetic field can be adjusted by changing the tuning block size. In order to ensure isochronous acceleration conditions, the design goal is to limit isochronous error less than 0.2%.

The main magnet model of the accelerator was established in Opera3D, whose yoke material is low carbon steel. The magnetization curve was shown as the Fig. 2 below. The acceleration frequency and energy curves of the initial model are present respectively. Final particle energy can meet the design requirements, indicating that the profile is basically correct. However, the acceleration frequency fluctuation is large in the initial model, which does not full-fill the condition of iso-chronicity.

The change of the phase, stipulated by the change of the frequency of the accelerating voltage the electric intensity [2]. When the RF frequency is large, it indicates that the ideal reference particle is ahead of the acceleration voltage.

The cyclotron frequency of the particle will be reduced, through changing the magnetic field by adjusting the angle of the magnetic pole at the radius. Instead, it is necessary to increase the magnetic field, through increase the angle of the magnetic pole also. Finally, the particle energy can reach 232 MeV at the radius of 1060 mm, which meets the design requirements. The final optimized magnetic field has been shown in Fig. 3.

The custom oxygen-free copper wire with inner circle and outer square is selected, whose specification is 9.5 × 20.9 × 20.5 mm, further more total resistance of the coil is 298 mΩ. There are 352 turns of single coil totally, inner diameter of 2,360 mm, outer diameter of 3,340 mm, height of 350 mm.

Through the simulated resulting, the coil current density is 1.525 A/mm², and the ampere-turns 261,537.5 A. The coil current is about 743 A, and the power consumption is about 165 kW.

It is generally believed that the inlet temperature of coil cooling water is about 20 °C, and the outlet temperature is below 45 °C.

The total water flow $q = \frac{P}{c_p \cdot \rho \cdot \Delta T}$ is 94 L/min. The calculated pressure loss of cooling water in the coil is 1.149 MPa. The cooling system is set to cooling water pressure of 1.5 MPa, coil cooling flow of 99.2 L/min.

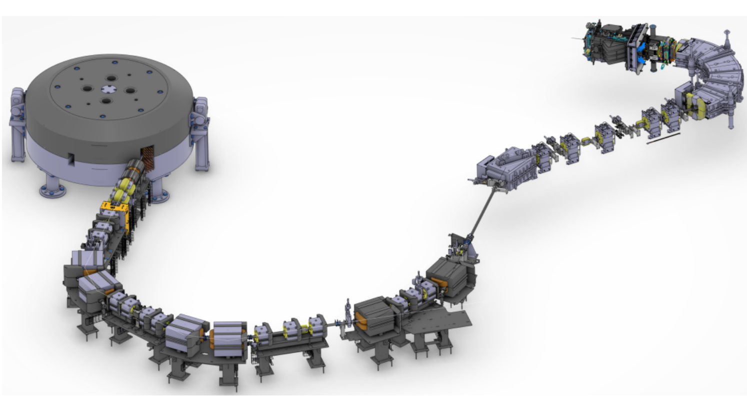
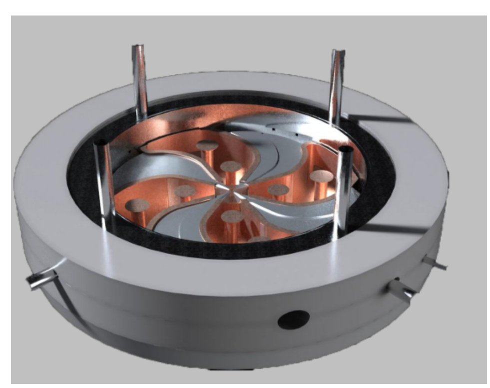

Figure 1: Overall model of C230 cyclotron and internal structure of the accelerator.

23rd Int. Conf. Cyclotrons Appl. CYCLOTRONS2022, Beijing, China JACoW Publishing
ISBN: 978-3-95450-212-7 ISSN: 2673-5482 doi:10.18429/JACoW-CYCLOTRONS2022-THPO016

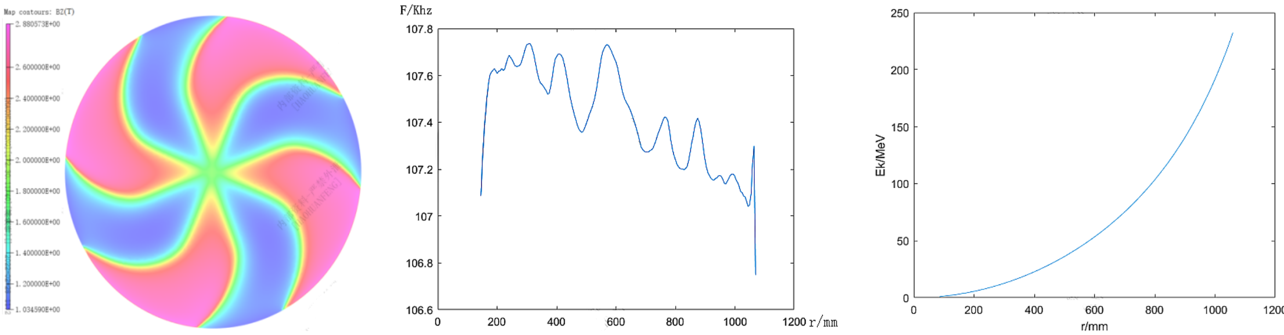

Figure 2: Initial iteration version cloud image of C230 magnetic field distribution, the acceleration frequency fluctuation is large in the initial model, particles of different radii accelerate in energy.

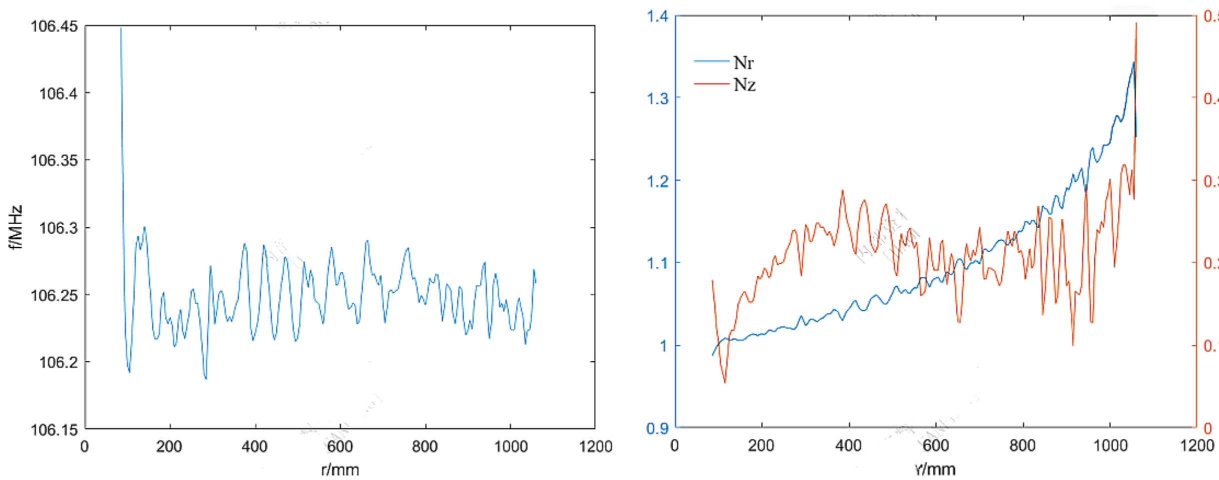

Figure 3: After model iteration, the acceleration frequencies of different radii tend to be stable.

By the formula:

$$\frac{1}{\sqrt{f}} = -2\lg\left[\frac{k_s}{3.7\cdot d} + \frac{2.51}{Re\cdot\sqrt{f}}\right], \tag{1}$$

$$\Delta P = 0.01\cdot f\cdot\frac{L\cdot v^2\cdot\rho}{2\cdot d} + \left[0.131 + 0.163\cdot\left(\frac{d}{R}\right)^{3.5}\right]\cdot 4\pi\cdot\frac{v^2\cdot\rho}{2\cdot 10^5}\cdot k, \tag{2}$$

The theoretical pressure loss of cooling water in the coil is 1.149 MPa. In order to preserve the margin and other factors, 1.5 MPa cooling water was selected and coil cooling single flow rate was 6.2 L/min, a total of 99.2 L/min.

CONCLUSION

In this paper, the electromagnetic field analysis software Opera3D is used for modeling and analysis of the cyclotron magnet, and by comparing with isochronous field, the magnetic model is modified accordingly.

Through the magnetic field calculation and modification, the isochronous error of particles is less than 0.2%. The magnetic field at a small radius has a negative gradient through adding a permanent magnet in the center area, which could provide an axial weak focusing force, so as to meet the axial stability condition. Finally, the ideal model of proton cyclotron magnet has been obtained. Meanwhile, the temperature rise and pressure drop of the coil have been calculated.

REFERENCES

[1] J. M. Schippers, “Cyclotrons for Particle Therapy”, Paul Scherrer Institut, Villigen PSI, Switzerland, 2015. doi:10.48550/arXiv.1804.08541 CERN Yellow Reports: School Proceedings, 2017. doi:10.23730/CYRSP-2017-001.165

[2] A. M. Voronin, J. Partyka, and A. Aldibekova, “Formation of Accelerated Particle Beam in Isochronous Cyclotron”, *Acta Phys. Pol. A*, vol. 125, pp. 1408-1411, 2013. doi:10.12693/APhysPolA.125.1408

ISBN: 978-3-95450-212-7 ISSN: 2673-5482 doi:10.18429/JACoW-CYCLOTRONS2022-THPO018

FFA ACTIVITY IN JAPAN AND FUTURE PROJECTS

Y. Ishi*, T. Uesugi and Y. Mori
Institute for Integrated Radiation and Nuclear Science, Kyoto University, Osaka, Japan

Abstract

An FFA facility at KURNS(Institute for Integrated Radiation and Nuclear Science, Kyoto University) has been operating for the experiment of various fields such as ADS(accelerator driven system), material science, medical physics and radiation damage of the memory chips since 2009. As ADS experiment which is original aim of this facility has been completed, we are planning several upgrade modifications of the ring aiming secondary particle production using the ERIT which stands for energy recovery internal target. In this presentation, two options of ERIT for the muon production facility and nuclear experiment of super heavy elements.

INTRODUCTION

At the Kyoto University Research Reactor Institute (KURRI), basic experimental studies on the ADS, which stands for accelerator driven system, have been started since 2009 using a one of research reactors Kyoto University Critical Assembly (KUCA) [1]. In these studies, the KUCA has been operated in the sub-critical mode and FFA accelerators has been used as a proton driver. In this report, an overview of the FFA accelerator complex, a current status of the usage of beams generated by the complex and discussion of possible upgrades of it will be presented.

It has been 12 years since the main ring started operation. In early 2009, we demonstrated the feasibility of ADS in the Uranium loaded sub-critical core under thermal system, hitting the tungsten target with proton beams of which energy is 100 MeV to generate the spallation neutron) [2]. In the next year, ADS experiments with Thorium loaded core were performed. For the next decade, experiments were conducted at this facility with a variety of core configurations. Finally, in 2019, phenomena of transmutations of MAs such as 237Np and 241Am in the ADS was confirmed using this facility [3]. As almost all the originally planned ADS experiments have been completed, reuse plans of the main ring of FFA facility at KURNS is now under consideration. In this report, we present two major options. One is modifying the main ring to a pion production ring aiming for producing decay muons for various purposes such as muon transmutations and muon-catalyzed fusion. The other modification is for producing super heavy elements of which mass is 119 or more. Both options are aimed at producing secondary particles using an ERIT mechanism [4].

CURRENT CONFIGURATION OF THE COMPLEX AT KURNS

The FFA accelerator complex at KURNS is shown in Fig. 1. It consists of an H^- ion source, a linac, an FFA synchrotron as a main ring and beam transport lines. The basic parameters of the KURNS FFA facility is shown in the Table 1. The output energy of the ion source is 30 keV

Table 1: Basic Parameters of KURNS FFA Accelerator Complex

LINAC	
Energy	11 MeV
Peak current	< 5 μA
Pulse length	< 100 μs (uniform)
Repetition rate	30 Hz
	200 Hz(max.)
MAIN RING	
Energy	11 - 100 (150) MeV
Field index k	7.5
Magnetic field	1.6 T (max.)
Revolution frequency	1.6 - 4.3 (5.0) MHz
Rf voltage	4 kV
Repetition rate	< 30 Hz

and the peak current is 2 mA with a duration of 100 μs. The linac is composed of 3 MeV RFQ, 7 MeV DTL and 11 MeV DTL. A charge stripping injection scheme is used in the main ring. The thickness of the stripping foil is 20 μg/cm^2 which is 2-fold of 10 μg/cm^2 thin carbon foil. It is located around the center of one of 12 main DFD triplet magnets to merge the injected beam to the circulating beam. Only one rf station is inserted in the straight section to accelerate the beam from 11 to 150 MeV with the peak rf voltage of 4 kV sweeping the frequency from 1.6 MHz to 6 MHz. As the turn separation in the FFA ring is much smaller than the beam size because of the high k value, the beam extraction needs kicker and septum magnets. The repetition rate is 30 Hz and the pulse length of the extracted beam is variable such as 10-100 ns using the bunch rotation scheme in the longitudinal phase space.

As the time structure of the beam from KURNS FFA synchrotron has very unique properties, it is very suitable for experiments such as nuclear data taking, flash radiotherapy, radiation damage on the memory chips and high energy physics detector development.

The H^- linac was built as an injector of the ERIT [1] ring which was a proof-of-principle ring of a neutron production ring with energy recovery internal target.The ERIT ring was

* ishi@rri.kyoto-u.ac.jp

[1] stands for Energy Recovery Internal Target

ISBN: 978-3-95450-212-7 ISSN: 2673-5482 doi:10.18429/JACoW-CYCLOTRONS2022-THPO018

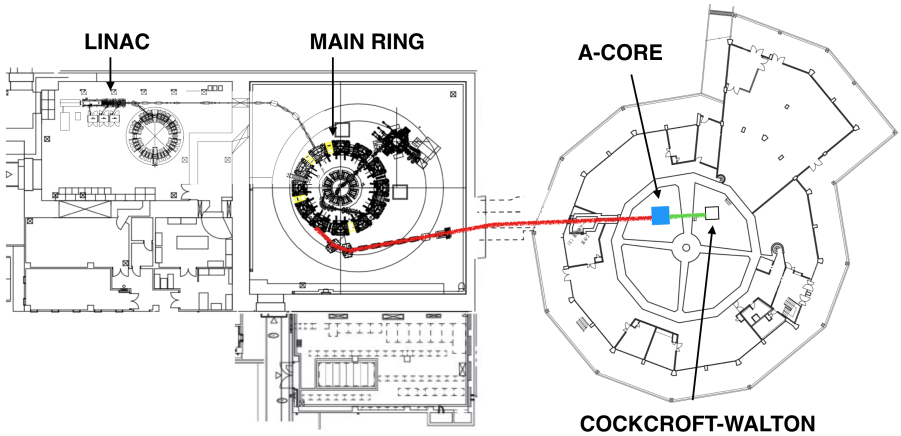

Figure 1: Layout of FFA accelerator complex and KUCA.

moved to Kyushu University in the spring of 2022 for use as a secondary particle production ring for nuclear physics experiments.

UPGRADE PLANS OF KURNS FFA SYNCHROTRON

The scaling FFA is the best ring to realize ERIT because of several unique characteristics as follows:

- A large acceptance in both horizontal and longitudinal directions.
- Zero chromaticity which guaranties constant tunes in both horizontal and vertical directions within wide range of momentum spread.

There are 2 major modification options of the FFA main ring at KURNS: a pion production ring to produce decay muons and a super heavy element production ring. Both use the ERIT mechanism.

Pion Production ERIT Ring

A basic design to convert the main ring at KURNS into a pion-producing ERIT ring (hereafter PiPER) is under consideration [5]. This plan is based on the assumption that the ring will be relocated to other facilities such as RIKEN, as it will require an injector capable of full energy injection of 300 MeV or higher.

The concepts and constraints are as follows:

- This ring is dedicated to pion production.
- It uses ERIT scheme that is no acceleration
- Injection beam is 330 MeV proton from the full energy injector e.g. AVF cyclotron at RIKEN
- It uses no reverse bending. That is, we use only F magnets with small k value for the horizontal focusing and the edge angle for vertical focusing.
- We aim for small tune variations and small CODs.

The structure of the magnets is shown in Fig. 2. It has thick return yoke only inside the ring in order to reduce the outer radius of the magnet. Using this structure, beam tracking simulations were performed with the 3-d magnetic field map obtained by using TOSCA. Finally, we got the sufficiently small tune variation and COD at most 1 mm as shown in Figs. 3 and 4, respectively.

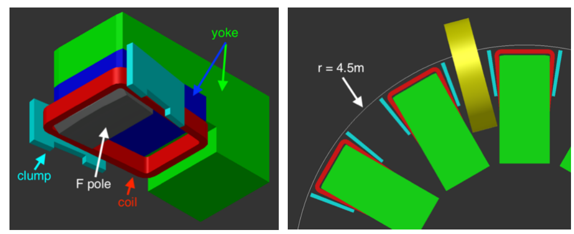

Figure 2: Remodeling of KURNS main ring to PiPER.

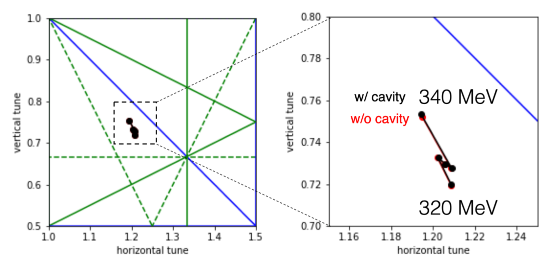

Figure 3: Tune variation in PiPER.

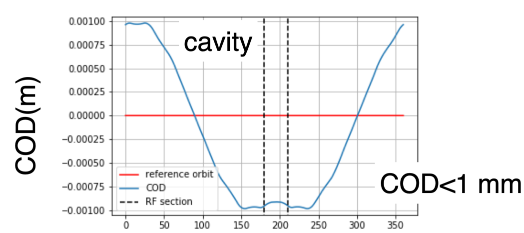

Figure 4: COD in PiPER with RF cavity as a COD source.

The main parameters of the PiPER are shown in Table 2.

Super Heavy Element Producing ERIT

Another option of reuse plan of the KURNS FFA main ring is modification into the ERIT ring aiming for producing super heavy elements of which mass number is 119 or more. Possible processes of producing super heavy elements are described by equations below.

$$ {}^{51}_{23}\mathrm{V} + {}^{248}_{96}\mathrm{Cm} \rightarrow {}_{119}\mathrm{Xx} \tag{1} $$

$$ {}^{54}_{24}\mathrm{Cr} + {}^{243}_{95}\mathrm{Am} \rightarrow {}_{119}\mathrm{Xx} \tag{2} $$

$$ {}^{54}_{24}\mathrm{Cr} + {}^{248}_{96}\mathrm{Cm} \rightarrow {}_{120}\mathrm{Xx} \tag{3} $$

$$ {}^{55}_{25}\mathrm{Mn} + {}^{243}_{95}\mathrm{Am} \rightarrow {}_{120}\mathrm{Xx} \tag{4} $$

ISBN: 978-3-95450-212-7 ISSN: 2673-5482 doi:10.18429/JACoW-CYCLOTRONS2022-THPO018

Table 2: Main Parameters of the PiPER

Beam species	proton
Beam energy	330 MeV
Radius of the central orbit	4.07 m
Tunes	(1.21,0.73)
$(\beta_x, \beta_y)_F$	(3.5 m,5.5 m
B at the central orbit	1.48 T
Beam current from the injector	1 pA
Target thickness	100 µm
Turns of survival	100
Pion production rate	200 π^-/s, 1000 π^+/s

Prior to these real super heavy element searches, it will be supposed to perform a test run such as

$$^{48}_{20}\mathrm{Ca} + {}^{238}_{92}\mathrm{U} \rightarrow {}^{286}_{112}\mathrm{Cn}. \tag{5}$$

For this process, we performed beam simulations to obtain over how many turns beam can survive (Fig. 5). We assume the production target is 200 µg/cm^2 thick UO_2 with the wedge factor $\eta > -0.5$. The wedge factor is defined as

$$\eta = \frac{D}{\rho}\frac{\partial \rho}{\partial R}, \tag{6}$$

where D is a dispersion function and ρ is the density of the target. The result of the growth of the horizontal emittance and the momentum spread are shown in Fig. 6. We expect over 100 turns can contribute to SHE producing process.

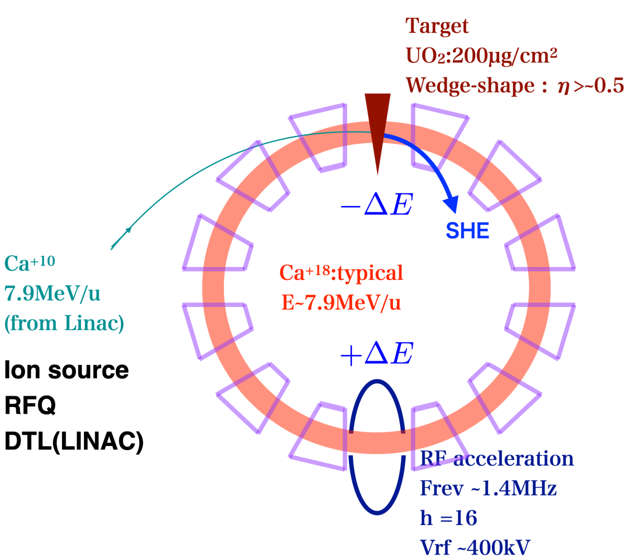

Figure 5: Schematic configuration of an ERIT system for producing super heavy elements.

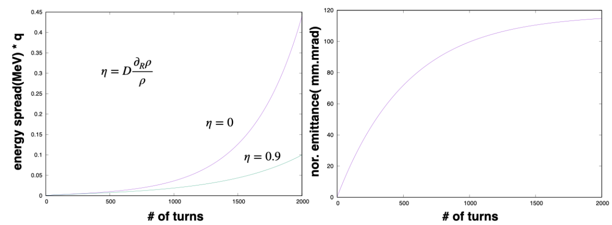

Figure 6: Beam simulation results of the growth of the horizontal emittance and the momentum spread.

SUMMARY

As almost all the originally planned ADS experiments have been completed, reuse plans of the main ring of FFA facility at KURNS is now under consideration. Two reuse options have been presented: modification of the main ring to a pion production ring aiming for producing decay muons for various purposes such as muon transmutations and muon-catalyzed fusion; and a super heavy element producing ring. Both options are aimed at producing secondary particles using an ERIT mechanism.

ACKNOWLEDGMENTS

This work was supported by MEXT(the Ministry of Education, Culture, Sports, Science and Technology) of Japan in the framework of a task entitled "Research and Development for an Accelerator-Driven Sub-critical System Using an FFA Accelerator".

REFERENCES

[1] Y. Ishi *et al.*, “Present Status and Future of FFAGs at KURRI and the First ADSR Experiment”, in *Proc. IPAC’10*, Kyoto, Japan, May 2010, paper TUOCRA03, p. 1327–1329.

[2] C. H. Pyeon *et al.*, “First Injection of Spallation Neutrons Generated by High-Energy Protons into the Kyoto University Critical Assembly”, *J. Nucl. Sci. Technol.*, vol. 46, no. 12, pp. 1091-1093, Aug. 2009. doi:10.1080/18811248.2009.9711620

[3] C. H. Pyeon *et al.*, “First nuclear transmutation of ^{237}Np and ^{241}Am by accelerator-driven system at Kyoto University Critical Assembly”, *J. Nucl. Sci. Technol.*, vol. 56, no. 8, pp. 684-689, May 2019. doi:10.1080/00223131.2019.1618406

[4] Y. Mori, “Development of FFAG accelerators and their applications for intense secondary particle production”, *Nucl. Inst. Meth. Phys. Res., A*, vol. 562, iss. 2, pp. 591-595, 2006. doi:10.1016/j.nima.2006.02.044

[5] K. Suga *et al.*, “Remodeling of 150 MeV FFAG Main Ring at KURNS TO Pion Production Ring”, in *Proc. IPAC’19*, Melbourne, Australia, May 2019, pp. 616–618. doi:10.18429/JACoW-IPAC2019-MOPRB021

ISBN: 978-3-95450-212-7 ISSN: 2673-5482 doi:10.18429/JACoW-CYCLOTRONS2022-THPO019

CONTROL OF A CYCLOTRON AND AN ECR ION SOURCE USING BAYESIAN OPTIMIZATION METHOD*

Yasuyuki Morita[1†], Mitsuhiro Fukuda[1], Hiroki Kanda[1], Tetsuhiko Yorita[1], Takashi Washio[2]
[1]Research Center for Nuclear Physics, Osaka University (RCNP), Japan
[2]The Institute of Scientific and Industrial Research, Osaka University (ISIR), Japan

Abstract

An enormous number of parameters are tuned during accelerator operation. The tuning is ultimately dependent on the operator's knowledge and experience. Therefore, there is a risk that tuning time and accuracy may vary depending on the operator. This tuning difficulty is an extremely important issue when implementing accelerometers in society, such as in medical applications. In this study, we developed an automatic tuning method using Bayesian optimization, one of the machine learning technique. The aim is to realize a tuning method that can supply beams in a short time with good reproducibility and comparable to manual tuning.

BAYESIAN OPTIMIZATION

Bayesian optimization [1] is a method that can efficiently utilize Gaussian process regression. The most important feature of Gaussian process regression is that it can calculate the expected value of the forecast (μ) and its variance (σ) from the obtained data. In general methods, the model is trained with a huge amount of data, and the next action is decided based only on the calculated predictions. Therefore, when the number of data is insufficient, the prediction may be inaccurate, and there is the problem of being trapped in local maxima. Bayesian optimization has the advantage that it can be used even with a small number of data because the model is less complex. Also, since the next action is determined from the mu and sigma calculated by Gaussian process regression, it actively adopts regions with a small number of data and is less likely to be trapped in local maxima. For example, in Lower Confidence Bound (LCB), the next action is determined from the acquisition function as shown in Eq. (1).

$$L_{LCB} = \mu + \alpha\sigma \tag{1}$$

where α is a constant. When this α is large, the error is more important and is less likely to be trapped in the local maxima. On the other hand, if the error is considered important, the number of searches increases, and the number of times required to find the optimal solution is likely to increase. Therefore, it is necessary to select a value that is somewhat appropriate for the problem. In this study, experiments were conducted with α = 4 fixed.

TUNING TEST FOR ECR ION SOURCE

Set Up

First, we developed an automatic tuning system using Bayesian optimization for tuning ion sources. In this experiment, a 10 GHz ECR ion source 'NANOGAN [2]' manufactured by Pantechnik was used as the ion source, and He ions were extracted at 50 kV acceleration. A schematic diagram of the test bench is shown in Fig. 1.

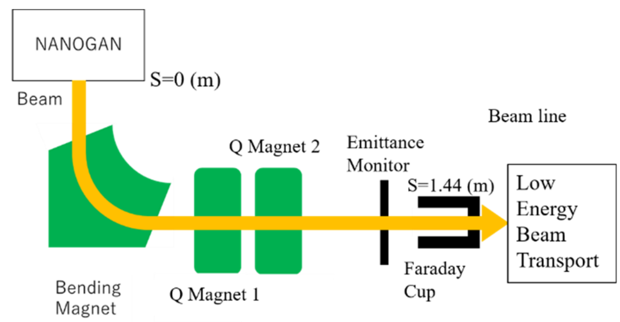

Figure 1: Schematic diagram of the test bench.

After extraction, the beam was bent 90° by a bending magnet to analyze the ion species, and then the beam emittance (ε) and beam intensity (I) were measured with a Pepper-pot emittance monitor (PPEM) [3] and Faraday cup (FC), respectively, using two quadrupole magnets. Beam brightness ($I/\varepsilon_{x-x'}\varepsilon_{y-y'}$) was calculated from the PPEM and FC measurements and adjusted to maximize brightness.

Tuning Experiments

In this experiment, four of the tuning parameters of the ion source were tuned: RF frequency, RF power, gas valve, and intermediate electrode voltage. The RF power was tuned by fixing the amplification factor of the Traveling Wave Tube Amplifier (TWTA) and varying the signal source power. The gas valve had a motor attached to the knob of the needle valve, and the amount of opening and closing was controlled by the amount of rotation [4]. The tuning range and minimum change for each tuning parameter are shown in Table 1. In this experiment, the number of parameter tuning was set to 108 times: 8 times for initial conditions and 100 times for tuning by Bayesian optimization. This is the number of tuning cycles that would take approximately 1.5 hours to complete.

† morita16@rcnp.osaka-u.ac.jp

ISBN: 978-3-95450-212-7 ISSN: 2673-5482 doi:10.18429/JACoW-CYCLOTRONS2022-THPO019

Table 1: The Tuning Range and Minimum Change for each Tuning Parameter

Parameter	Minimum value	Maximum value	Minimum change
RF Frequency	9.8 GHz	10.2 GHz	0.01 GHz
RF Power	-14.0 dBm	-10.0 dBm	0.1 dBm
Gas valve	11,500 steps	12,500 steps	100 steps
intermediate electrode	15.0 kV	25.0 kV	0.1 kV

Table 2: The Tuning Range and Minimum Change for each Tuning Parameter

Parameter	Experiment 1	Experiment 2
RF Frequency	10.0 GHz	10.0 GHz
RF Power	-13.7 dBm	-13.5 dBm
Gas valve	11,900 steps	12,100 steps
intermediate electrode	16.8 kV	15.5 kV
Beam Brightness	3.0×10^{-5} $\mathrm{mA/(mm \cdot mrad)^2}$	3.0×10^{-5} $\mathrm{mA/(mm \cdot mrad)^2}$

We performed the tuning experiment twice, changing only the first setting in this range. The results of these two experiments are shown in Table 2.

The results show that the beam can be extracted with good reproducibility. In addition, the experiment was conducted again with a wider tuning range for some parameters. The parameter ranges and tuning results for those parameters are shown in Tables 3 and 4. Figure 2 shows the maximum beam brightness and the number of parameter tuning cycles.

By expanding the tuning range, we were able to arrive at even better parameters. From these results, we believe that a wider tuning range is necessary to achieve higher intensity beam brightness, while considering the time required for tuning.

Table 3: The Tuning Range and Minimum Change for each Tuning Parameter

Parameter	Minimum value	Maximum value	Minimum change
RF Frequency	9.8 GHz	10.2 GHz	0.01 GHz
RF Power	-14.0 dBm	-8.0 dBm	0.1 dBm
Gas valve	11,500 steps	12,500 steps	100 steps
intermediate electrode	15.0 kV	39.0 kV	0.1 kV

Table 4: The Tuning Range and Minimum Change for each Tuning Parameter

Parameter	Experiment 1
RF Frequency	10.18 GHz
RF Power	-9.3 dBm
Gas valve	12,100 steps
intermediate electrode	15.1 kV
Beam Brightness	5.2×10^{-5} $\mathrm{mA/(mm \cdot mrad)^2}$

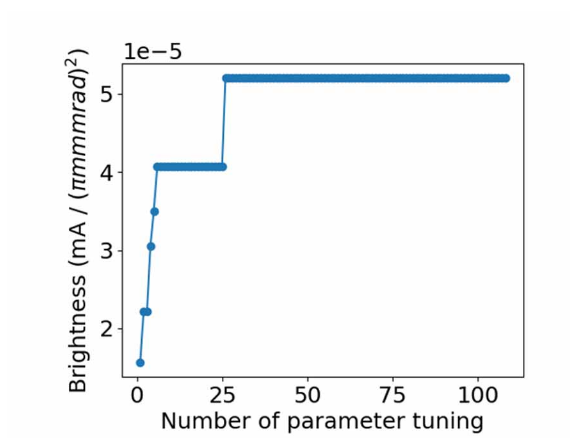

Figure 2: The maximum beam brightness and the number of parameter tuning cycles.

ISBN: 978-3-95450-212-7 ISSN: 2673-5482 doi:10.18429/JACoW-CYCLOTRONS2022-THPO019

TUNING TEST FOR LEBT

Set Up

Next, we experimented with fine-tuning the Low Energy Beam Transport (LEBT). In this experiment, we fine-tuned 14 electromagnets (two quadrupole magnets, four solenoid magnets, and eight steerer magnets) installed in the LEBT. Each electromagnet was set to a range of 10 steps of tuning based on the operator's prior tuning history. The settings for the AVF cyclotron, which is the trailing accelerator, were fixed, and a Bayesian optimization was constructed to maximize the beam intensity at the Faraday cup (F0) after acceleration. A schematic of the tuned LEBT is shown in Fig. 3.

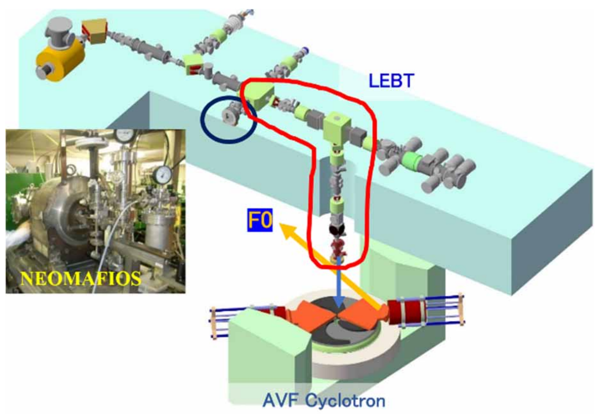

Figure 3: Schematic diagram of the LEBT, F0 is the Faraday cup that measures the beam intensity at the position after the accelerator.

The experiment involved the transport of $^{4}He^{2+}$ ions extracted from the ECR ion source 'NEOMAFIOS'. Two tuning experiments were conducted, one with the same amount of time as the operator and the other with less than half amount of the time as the operator, to verify the practicality and usefulness of the tuning by comparing the beam intensity with that of the operator's tuning.

Tuning Experiment

The number of tunings and measurement time after each tuning for the two experiments are shown in Table 5.

Table 5: The Number of Tunings and Measurement Time After each Tuning

	Initial data	Number of Tuning	Measurement time
Experiment 1	16	200	5 seconds
Experiment 2	16	600	2 seconds

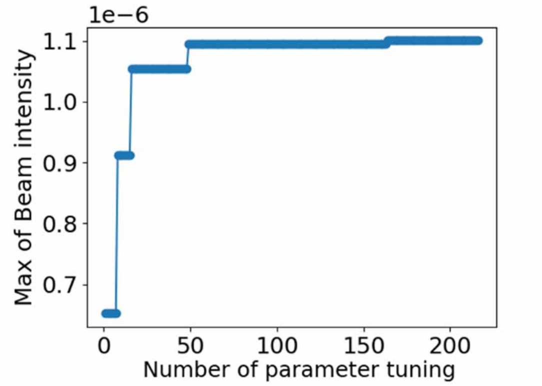

Figure 4: The number of tuning cycles and the maximum beam intensity for Experiment 1.

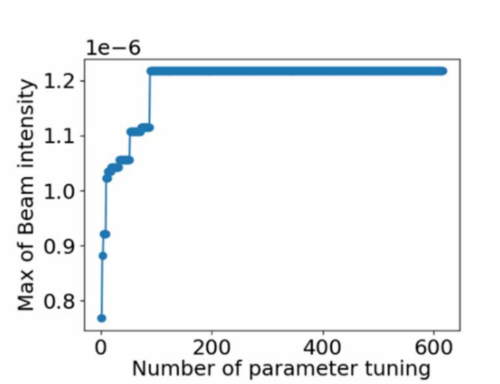

Figure 5: The number of tuning cycles and the maximum beam intensity for each experiment.

Figures 4 and 5 show the number of tuning cycles and the maximum beam intensity for each experiment. Although the maximum beam intensity values in the two experiments were different, both experiments showed a gradual finding of good points and improvement of the beam intensity.

The beam intensity at F0 after each experiment and when tuned by the operator before the experiment are shown in Table 6.

The results in Table 6 show that by using the same amount of time as the operator, the same beam intensity as the operator could be achieved. In addition, the beam intensity could be reached to more than 90% of the operator's beam intensity in one-third of the operator's time. The results show that the settings can be flexibly changed to meet the user's requirements during actual operation. For example, in medical accelerators, tuning time is important, and it is possible to set the required beam intensity and tune in a short time without pursuing the maximum beam intensity. On the other hand, in scientific experiments, it is possible to use as much time as is available and to request the beam intensity to be as close to the maximum as possible.

ISBN: 978-3-95450-212-7 ISSN: 2673-5482 doi:10.18429/JACoW-CYCLOTRONS2022-THPO019

Table 6: Comparison of Beam Intensity and Tuning Time After Tuning

	Beam Intensity	Tuning time
Experiment 1	1.1 μA	20 minutes
Experiment 2	1.2 μA	60 minutes
Operator tuning	1.2 μA	60 minutes

CONCLUSION

In this study, Bayesian optimization was used to automate the tuning of the ion source and LEBT.

In the tuning of the ion source, four parameters were tuned, and the tuning that maximized the beam brightness within the tuneable parameter range without prior information was achieved in about 1.5 hours.

In tuning the LEBT, 14 electromagnets were fine-tuned. By spending the same amount of time as the operators, we were able to provide the same beam intensity as the operators. It was also possible to provide nearly 90% of the beam intensity in one-third of the operator's time. These results show that the tuning time and beam intensity can be changed depending on whether the tuning time or beam intensity is more important for the application, and that a short tuning time is sufficient to provide a usable beam.

REFERENCES

[1] M Pelikan *et al.*, "BOA: The Bayesian Optimization Algorithm," in *Proc. 1st Conf. Genetic Evolutionary Computation (GECCO'99)*, Orlando, Florida, USA, vol. 1, Jul. 1999.

[2] `https://www.pantechnik.com/ecr-ion-sources/`

[3] Yasuyuki Morita *et al.*, "Developments of real time emittance monitors," *Rev. Sci. Instrum.*, vol. 91, no. 4, p. 043303, Ap. 2020. doi:10.1063/1.5128583

[4] Y. Morita *et al.*, "Developments of control system for ion source using machine learning," *J. Phys.: Conf. Ser.*, vol. 2244, p. 012105, 2022. doi:10.1088/1742-6596/2244/1/012105

ISBN: 978-3-95450-212-7 ISSN: 2673-5482 doi:10.18429/JACoW-CYCLOTRONS2022-FRAI01

DEVELOPMENTS AND PROSPECTS OF FFAS AT RAL

S. Machida†, STFC Rutherford Appleton Laboratory, Didcot, United Kingdom
on behalf of the FFA task team,

Abstract

A Fixed Field Alternating Gradient Accelerator (FFA) can offer several advantages for use as a proton driver for high power beam applications. In particular, control of the pulse structure can be easily done by RF gymnastics. A FFA is a sustainable (energy efficient) and reliable accelerator with the main magnets with DC operation. We will discuss the development of a FFA physics design for ISIS (spallation neutron and muon source) upgrade and its proto-type status.

INTRODUCTION

Studies are in progress to upgrade ISIS, the UK's spallation neutron and muon source, in a plan referred to as ISIS-II. The beam power of the proton driver is in the range 1.25 to 2.5 MW with a beam energy of 1.2 GeV. That level of beam power has already been achieved at PSI in Switzerland, SNS in the US and J-PARC in Japan and is therefore not seen as a major challenge. However, beam power is not the only figure of merit for future proton drivers. There are some other essential factors we must take into account.

The most important consideration is sustainability, a feature that becomes increasingly relevant of late. Without assuring a good measure of sustainability, we cannot operate the facility. At the present time a cyclotron is the most energy efficient accelerator. Another key factor is reliability of operation. Even if an accelerator has a state-of-the-arc design, users will hesitate to use it if it frequently breaks down. An accelerator like a cyclotron using DC magnets is robust and its robustness can be an important contributor to the reliability.

More specifically, in the spallation neutron community, accelerator-based facilities should have two features: capacity and capability. Capacity means that a facility can comfortably deal with the large number of experiments that is essential to meet or expand demand from the scientific community. Capability means that a facility can provide bespoke experiments. For example, it can provide flexible operation such as high peak current with low repetition or low peak current with high repetition depending on users' requests.

As a candidate for a future high power proton driver a cyclotron has many attractive features The only caveat is that it is not a pulsed machine, whereas neutron users need pulsed protons. A synchro-cyclotron is an option, or a Fixed Field Alternating Gradient Accelerator, FFA [1-3]. However, people are not easily convinced about the idea because no high power FFA exists. To show viability and convince the community that an FFA can provide the high power beams required, a project RAL has in mind to design and construct a small-scale demonstrator of an FFA-based high power machine [4]. Referred to as FETS-FFA, the ring will use the existing Front End Test Stand (FETS) as its injector. Since an FFA is a pulsed accelerator like a synchro-cyclotron, there are many challenges that are similar to those in a high intensity synchrotron. Table 1 shows the main parameters of FETS-FFA. The average current is about three orders of magnitude higher than any existing fixed-field accelerating ring.

Table 1: FETS-FFA Main Parameters

Parameter	Value
Beam energy	3 – 12 MeV
Average radius	4 – 4.2 m
Repetition rate	100 – 120 Hz
Number of protons per pulse	3×10^{11}
Average current	about 5 mA
Space charge tune shift	about -0.25

BEAM DYNAMICS ISSUES OF THE HIGH POWER BEAMS

This paper considers four topics that are of importance in the realisation of a high power FFA.

FD Doublet Spiral Lattice

We know that the operating tune should be close to the diagonal line in tune space. In other words, both horizontal and vertical tunes should be similar in a high power synchrotron. Radial sector FFAs use the field index *k* and the strength ratio of normal bend Bf and reverse bend Bd, which changes the flutter factor. However, the reverse bend makes the circumference larger. Spiral sector FFAs eliminate the reverse bend so that the circumference is smaller.

However, they do not provide full tune control because of the loss of flutter factor control. The idea of an FD spiral lattice was introduced a few years ago [5]. We keep the reverse bend for full control of tune, but make the strength of the reverse bend a minimum by having vertical focusing from the spiral angle as well.

In FETS-FFA, we choose the nominal tunes to be similar in both horizontal and vertical planes with values (3.41, 3.39). We have full control of tune at least as large as an integer to optimise high power operation by changing the field index *k* and Bd/Bf ratio. The directions of tune change under variations in each parameter are shown in Fig. 1.

We found that an FD doublet spiral lattice behaves like a triplet focusing with one focusing and one defocusing magnet. It is interesting to see that there is smooth transition from FD doublet radial sector optics (FD doublet) to spiral sector optics (DF doublet) through FD spiral optics (DFD triplet) as shown in Fig. 2.

† shinji.machida@stfc.ac.uk

ISBN: 978-3-95450-212-7 ISSN: 2673-5482 doi:10.18429/JACoW-CYCLOTRONS2022-FRAI01

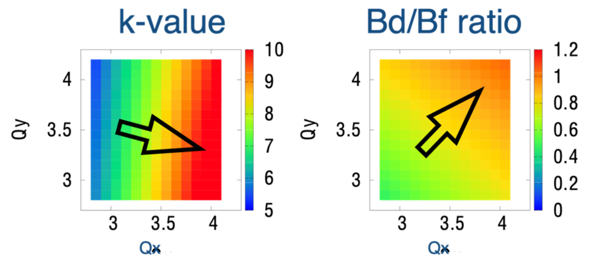

Figure 1: Direction of tune change when k increases (left) and of tune change when Bd/Bf ratio increases (right).

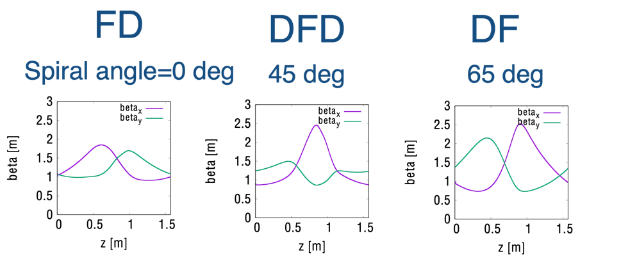

Figure 2: Radial sector optics (left), FD spiral sector optics (middle), and spiral sector optics with only Bf (right).

Lattice with Superperiod

One of the advantages of an FFA compared with a cyclotron is that we can make the magnets smaller by squeezing the orbit excursion from injection to extraction. Increasing the number of cells per ring increases the field index k, hence the orbit excursion becomes smaller. On the other hand, the same total circumference is made up of more straight sections and each of them becomes shorter. A long straight section is always preferred for handling high power beams at injection and extraction, and for RF cavities, collimation, etc. A compromise is to introduce a superperiod structure so that some straight sections become longer for some requirements.

We designed a lattice with 16-fold symmetry first. This gives a reasonably large field index k, making the orbit excursion less than half a metre. On the other hand, the straight section is less than a metre, which may be enough but it is better if we can create longer straight sections. Now we shorten some of the straight sections and lengthen others keeping the total circumference the same. Four FD doublet magnets are excited independently to minimise modulation of the lattice beta functions. Figure 3 (bottom) shows the lattice from such optimisation. We have 4 long straight sections that are over 50% longer than the original length. Some of the straights have to be shortened, but it should not be a problem.

Reducing the symmetry increases the number of systematic resonances. For example, if we make a 5-fold symmetric lattice out of a lattice with 15-fold symmetry, there will be a systematic 3rd order resonance within the possible operating tune region, that is 3.33 between 3.0 and 3.75. However, if we make a 4- or 8-fold symmetric lattice out of a lattice with 16-fold symmetry, systematic resonances up to 5th order will always be outside the operating tune region. Table 2 summarises the location of systematic resonances for lattices with different symmetries.

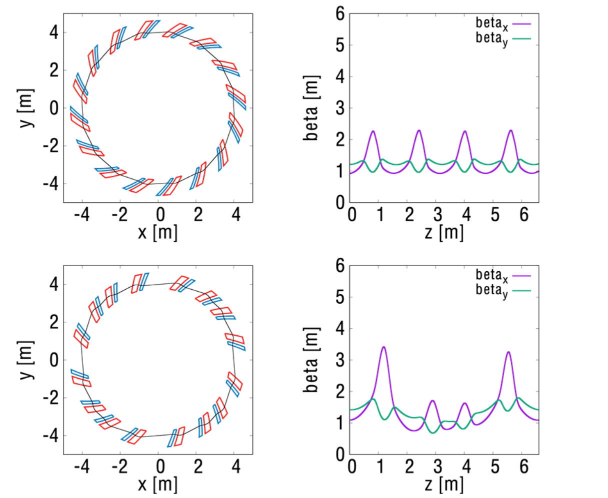

Figure 3: Top view and lattice functions of 16-fold symmetric lattice(top) and of 4-fold symmetric lattice (bottom).

Table 2: Location of systematic resonances for different symmetry lattice. $nQ = pk$, where n is the order of resonance, Q is tune, p is periodicity (p-fold symmetry), k is arbitrary positive integer.

	15-fold symmetry	5 (SP) x 3 (FD)	16-fold symmetry	8 (sp) x 2 (FD)	4 (sp) x 4 (FD)
Q range	3.0 - 3.75	3.0 - 3.75	3.2 - 4.0	3.2 - 4.0	3.2 - 4.0
n=2	7.5 k	2.5 k	8 k	4 k 4.0	2 k 4.0
3	5 k	1.67 k **3.33**	5.33 k	2.67 k	1.33 k 4.0
4	3.75 k 3.75	1.25 k 3.75	4 k 4.0	2 k 4.0	1 k 4.0
5	3 k 3.0	1 k 3.0	3.2 k 3.2	1.6 k 3.2	0.8 k 3.2, 4.0

Dynamic Aperture

One of the methods to mitigate against space charge effects is to enlarge the beam emittance. In SNS and J-PARC, the geometrical emittance is about 500 π mm mrad, which is created by injection painting. It is desirable to have a similar emittance and enough aperture in an FFA as well to reduce space charge effects. However, the FFA optics are highly nonlinear and dynamic aperture is a concern. Scanning dynamic aperture in tune space shows some resonance lines excited by nonlinearities as shown in Fig. 4.

Previous study shows dynamic aperture is mainly determined by amplitude dependent tune shift due to octupole components [6]. Tune approaches a nearby systematic resonance and a particle is lost. The primary location of octupole terms is in the fringe field region.

To see how the shape of fringe field extent affects dynamic aperture, two lattices are compared with different fringe field length. At the same time, multipole contents along the beam orbit are calculated. We found that reduction of octupole by increasing fringe field length more than doubles the dynamic aperture. A more systematic study using a map and normal form analysis is in progress [7].

In terms of dynamic aperture, we found that a strong dependence on the spiral angle, that is directly connected to

23rd Int. Conf. Cyclotrons Appl. CYCLOTRONS2022, Beijing, China JACoW Publishing
ISBN: 978-3-95450-212-7 ISSN: 2673-5482 doi:10.18429/JACoW-CYCLOTRONS2022-FRAI01

the fringe field extent. An interesting finding is that the FD double spiral lattice has the largest dynamic aperture compared with radial and spiral sector FFAs as shown in Fig. 5.

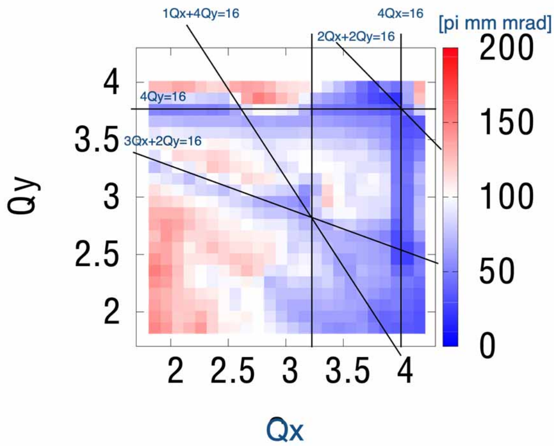

Figure 4: Dynamic aperture scan in tune space. Colour scale shows normalised dynamic apertures Qx and Qy in units of π mm mrad.

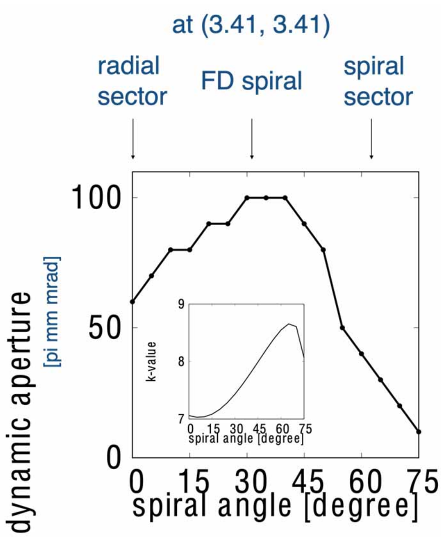

Figure 5: Dynamic aperture as a function of the spiral angle. The inset shows the k adjustment to keep the same tune.

Beam Stacking

From the accelerator point of view, it is always easier to increase repetition rate up to 50 to 100 Hz to obtain high average current. On the other hand, users, particularly neutron users, like to have a low repetition for their experiments, such as 10 to a maximum of about 30 Hz.

Beam stacking is one way to control the rate of the pulses provided to users while maintaining average beam power. It is worth noting that this can only be done by an accelerator with DC magnets like FFAs.

As shown in Fig. 6, a pulse from a linac is injected into an FFA and accelerated to top energy. Instead of extracting the beams every accelerator cycle, we keep the beams at top energy and repeat injection and acceleration N times until we have enough particles or until the number of particles reaches the space charge limit. After N cycles, all the beams are extracted together which gives a high peak intensity. Space charge effects decrease with momentum, hence more accumulation is possible at top energy rather than at injection energy. Figure 7 shows longitudinal phase space at top energy after 4th beam is accelerated and debunched. Since momentum spread increases linearly with the number of the stacked beams, the required RF capture voltage increases quadratically. Figure 7 also shows longitudinal phase space after adiabatically capturing the stacked beams. As an illustration, Fig. 8 shows the acceleration cycle and the beams seen by two targets. In this example, we assume that there are two target stations and the accelerator is running at 120 Hz. The figure shows that the target station 1 accepts the beams by stacking with 30 Hz repetition and the users see it every 33 ms. Target station 2 sees a beam pulse with 15 Hz.

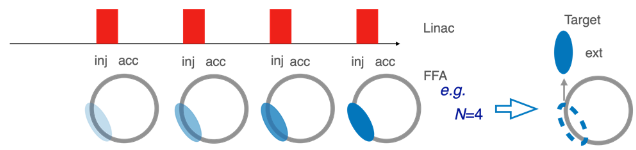

Figure 6: Beam stacking keeps N accelerated pulses at the top energy and extracts them all at once.

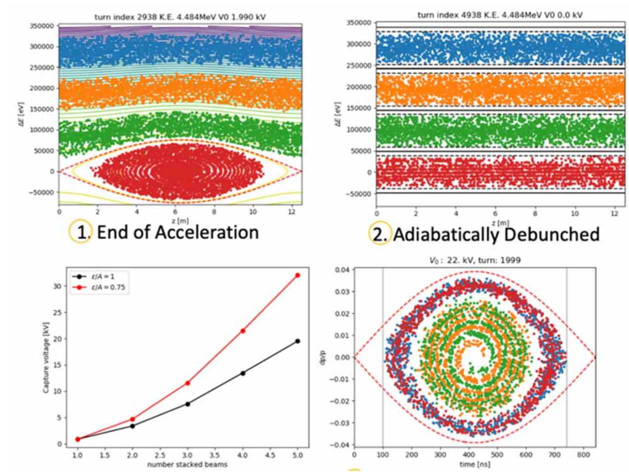

Figure 7: Longitudinal phase space at the end of acceleration of 4th beam (top, left), after debunching of 4th beam (top, right). Required RF voltage to capture the beams vs. the number of stacked beams (bottom, left). Longitudinal phase space after capture (bottom, right).

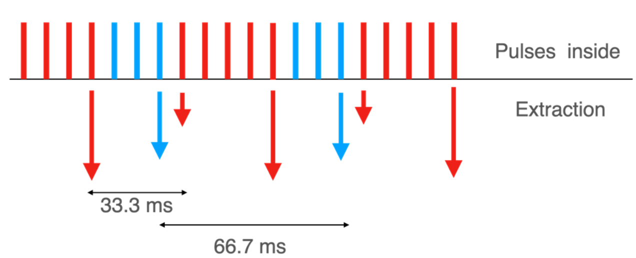

Figure 8: Accelerator runs at 120 Hz. Beam pulses for target station 1 (red) go every 33.3 ms (30 Hz) and beam pulses for target station 2 (blue) go every 66.7 ms (15 Hz).

ISBN: 978-3-95450-212-7 ISSN: 2673-5482 doi:10.18429/JACoW-CYCLOTRONS2022-FRAI01

HARDWARE DEVELOPMENTS

Magnets

Magnets are the most critical elements. The magnets for a high power FFA need to have the right field gradient which imposes high accuracy on the field index *k*. We have looked at several magnet designs to create the field gradient and control the field index over a large range from $k = 6$ to $k = 11$. We initially optimised the magnet with a 2D cross section (Fig. 9) and have now moved to 3D modelling (Fig. 10).

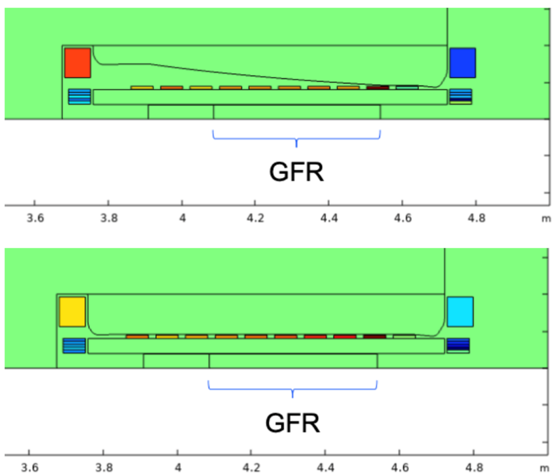

Figure 9: Field gradient is primarily determined by the gap shape. Trim coils along the gap adjust the field index *k*. (top) Field gradient is made by trim coils and the field index *k* is also adjusted by the same trim coils (bottom).

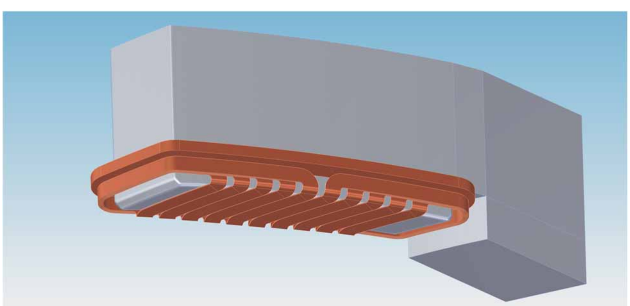

Figure 10: 3D modelling of spiral magnet with field gradient has started.

Diagnostics

Beam diagnostics are another crucial item. Unlike a cyclotron, we want to measure the beam position turn by turn for a wide range of orbits, such as 600 mm non-destructively. We have constructed a half-size Beam Position Monitor and tested it in the FFA at Kyoto University. We saw the beam moving as it is accelerated (Fig. 11). From small oscillations around the closed orbit, we can determine the tune both in horizontal and vertical planes.

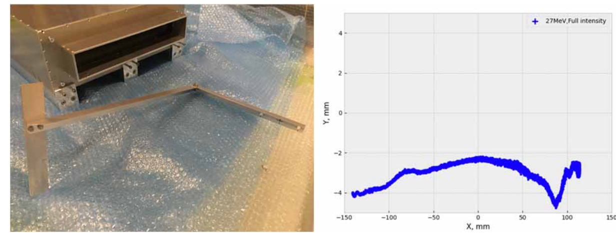

Figure 11: A half size model of Beam Position Monitor installed in the FFA at Kyoto University (left). Measured beam position signal (right).

RF Cavity

Magnetic Alloy is a possible candidate for the RF cavity core. We have started testing a sample core and measured the shunt impedance (Fig. 12).

Figure 12: Magnetic Alloy sample and setup for shunt impedance measurement (Courtesy: Gardner, see [8, 9]).

SUMMARY

Our goal is to demonstrate high power operation of a fixed-field alternating gradient accelerator (FFA). We chose a scaling FFA. From the physics design point of view, this paper discusses three subjects: a proper lattice structure ready for high intensity operation; a superperiodic lattice to give space for beam handling; and dynamic aperture to accommodate a large number of particles. From the operation point of view, we consider beam stacking to produce either high peak current with low repetition rate or low peak current with high repetition rate. We briefly mentioned the hardware design status. Prototyping of critical hardware elements has started.

REFERENCES

[1] T. Ohkawa, presented at the JPS Annual Meeting, 1953, unpublished.

[2] K. R. Symon, D. W. Kerst, L. W. Jones, L. J. Laslett, and K. M. Terwilliger, "Fixed-field alternating-gradient particle accelerators", *Phys. Rev.*, vol. 103, no. 6, pp. 1837-1859, Sep. 1956. doi:10.1103/physrev.103.1837

ISBN: 978-3-95450-212-7 ISSN: 2673-5482 doi:10.18429/JACoW-CYCLOTRONS2022-FRAI01

[3] A. A. Kolomensky and A. N. Levedev, *Theory of Cyclic Accelerators*. North-Holland, Amsterdam, Netherland: Publisher, 1966.

[4] J. Thomason, https://indico.stfc.ac.uk/event/487/contributions/3907/attachments/1311/2423/Thomason_ISIS.pptx

[5] S. Machida, "Scaling fixed-field alternating-gradient accelerators with reverse bend and spiral edge angle", *Phys. Rev. Lett.*, vol. 119, p. 064802, Aug. 2017. doi:10.1103/PhysRevLett.119.064802

[6] M. Aiba *et al.*, "Study of acceptance of FFAG accelerator", in *Proc. EPAC'02*, Paris, France, Jun. 2002, pp. 1226-1228.

[7] M. Topp-Mugglestone, https://indico.stfc.ac.uk/event/487/contributions/3913/attachments/1372/2424/20210929-ffa22slides-FINAL.pdf

[8] I. Gardner, https://indico.stfc.ac.uk/event/487/contributions/3584/attachments/1343/2378/ffa_school22_rf.mp4

[9] I. Gardner, https://indico.stfc.ac.uk/event/487/contributions/3584/attachments/1343/2374/RF-for-FFAs4.ppt

ISBN: 978-3-95450-212-7 ISSN: 2673-5482 doi:10.18429/JACoW-CYCLOTRONS2022-FRAI02

DESIGN OF A 2 GeV CYCLOTRON WITH CONSTANT RADIAL AND VERTICAL TUNES

Richard Baartman, Thomas Planche, TRIUMF, Vancouver, B.C. Canada

Abstract

We demonstrate that a cyclotron can be made to have precisely constant betatron tunes over wide energy ranges. In particular, we show that the horizontal tune can be made constant and does not have to follow the Lorentz factor γ, while still perfectly satisfying the isochronous condition. To make this demonstration we developed a technique based on the calculation of the betatron tunes entirely from the geometry of realistic non-hard-edge closed orbits. The technique is applied to the particular case of a 800 MeV to 2 GeV proton cyclotron to produce a design that is presented here.

INTRODUCTION

This paper is a brief summary of a more detailed article [1]. There we demonstrate that, in a cyclotron with mid-plane symmetry, the transverse tunes are entirely determined by the geometry of its closed orbits. Capitalizing on this property, we have established a method to calculate tunes and produce isochronous field maps by starting from the geometry of realistic non-hard-edge orbits. The main advantage of this method is that it produces realistic and perfectly isochronous field distributions, and the corresponding transverse tunes, in a split second. We take advantage of this speed to explore the range of possible isochronous fields, which leads us to find solutions with simultaneously constant vertical and horizontal tunes over wide energy ranges.

We have applied this technique and proposed designs for several sets of cyclotron parameters [1, 2]. In this paper, we focus our effort on the case of a high-energy cyclotron, choosing a set of parameters that resembles that of the recently proposed 2 GeV CIAE machine [3, 4].

THEORY: TUNES OF ISOCHRONOUS ORBITS

Let's consider a fixed-(magnetic-)field accelerator with mid-plane symmetry. In this circular accelerator, let's consider one closed orbit at one particular energy, to which is attached the Frenet-Serret coordinate system (x, y, s). It is interesting to note that, as a result of the application of Maxwell's equations, the infinitesimal transverse motion of particles is fully determined by the curvature $\rho(s)$ and the local field index $n(s) = -\frac{\rho}{B_0}\frac{\partial B}{\partial x}\Big|_{x=y=0}$ of the corresponding closed orbit [5, 6]. This implies that it is sufficient to know the functions $\rho(s)$ and $n(s)$ over one period of the accelerator to know the value of the transverse betatron tunes.

Now, instead of starting from a magnetic field distribution to compute the properties of the orbits, which is the common practice for designing a cyclotron, let's start from the geometry of the orbits represented by some arbitrary function:

$$\begin{aligned} r : \mathbb{R}^+ \times \mathbb{R} &\to \mathbb{R}^+ \\ (a, \theta) &\mapsto r(a, \theta) , \end{aligned} \tag{1}$$

where r is the radius of the closed orbit, a is the orbit's average radius, and θ is the azimuth. The periodicity of the closed orbits imposes that:

$$r(a, \theta) = r(a, \theta + 2\pi/N) \text{ with } N \in \mathbb{N}^* , \tag{2}$$

where N is the lattice periodicity, i.e. number of sectors. The question now becomes: can we calculate both $\rho(s)$ and $n(s)$ directly from $r(a, \theta)$?

Firstly, the relation between s and θ is, first of all, given by:

$$\frac{\mathrm{d}s}{\mathrm{d}\theta} = \sqrt{r^2 + \left(\frac{\partial r}{\partial \theta}\right)^2} , \tag{3}$$

secondly, ρ is immediately obtained from the standard formula for polar coordinates:

$$\frac{1}{\rho} = \frac{r^2 + 2\left(\frac{\partial r}{\partial \theta}\right)^2 - r\frac{\partial^2 r}{\partial \theta^2}}{\left(r^2 + \left(\frac{\partial r}{\partial \theta}\right)^2\right)^{3/2}} . \tag{4}$$

Finally, obtaining $n(s)$ requires a little more work. We start by remarking that, in a cyclotron, orbits are isochronous which imposes a relation between the particle velocity and the orbit circumference:

$$\beta(a) = \frac{\mathcal{R}(a)}{\mathcal{R}_\infty} , \tag{5}$$

where $\mathcal{R}_\infty$ is a constant, corresponding to the value of $\mathcal{R}$ in the limit that the particles' speed is light speed; and $\mathcal{R}$ is the orbit circumference divided by 2π:

$$\mathcal{R}(a) = \frac{1}{2\pi}\int_0^{2\pi} \frac{\mathrm{d}s}{\mathrm{d}\theta}\,\mathrm{d}\theta , \tag{6}$$

after imposing the isochronous condition, and applying the chain rule, we find an expression for n that depends only in $r(a, \theta)$ and its partial derivatives [1].

In conclusion, for any arbitrary continuum of closed orbits defined by the function $r(a, \theta)$, provided that r is smooth enough for the required partial derivatives to be defined, the transverse tunes of cyclotron depends on $r(a, \theta)$ and nothing else.

Corresponding Isochronous Field Map

So far we have needed only the knowledge of the shape $r(a, \theta)$ of the closed orbits to calculate tunes. The question

ISBN: 978-3-95450-212-7 ISSN: 2673-5482 doi:10.18429/JACoW-CYCLOTRONS2022-FRAI02

that comes to mind is: what magnetic field distribution produces these closed orbits? The answer will depend on the choice of the particle mass m and charge q, and the scale of the solution will depend on the value of $\mathcal{R}_\infty$. The magnetic field within the median plane is given by:

$$B(r,\theta) = \frac{\beta(a)}{\sqrt{1-\beta^2(a)}} \frac{m}{q\rho(a,\theta)}, \quad (7)$$

where $\rho(a,\theta)$ is given by Eq. (4), $\beta(a)$ is given by Eq. (5), and $a = a(r,\theta)$ is calculated from $r(a,\theta)$ using numerical root finding. The magnetic field off the median plan can be obtained from extrapolation using Maxwell's equations, see for instance Ref. [7].

In the examples presented below, the transverse tunes and orbital frequency are crosschecked using particle tracking in 2-dimensional polar field map with the reference code CYCLOPS [8]. The field maps provided to CYCLOPS are generated using Eq. (7).

HIGH-ENERGY RING CYCLOTRON EXAMPLE

Let's impose some constraints on $r(a,\theta)$ so that the orbits have long straight sections, as in a ring cyclotron with drift spaces between sectors. For this example we chose to use the same basic parameters – number of sectors = 10, $\mathcal{R}_\infty = 28$ m, etc. – of the proposed 0.8 to 2 GeV CIAE ring cyclotron [3, 4].

Smooth-Orbits With Straight Sections

We cover the area between 0.8 GeV and 2 GeV using again 5 different orbits. Each orbit is defined as a spline, with periodic boundary conditions. The splines are made to pass through a few points that are aligned, forcing each orbit to be straight over some minimum distance. Each spline is parametrized with 4 constraints: the angular width and tilt of the straight section, plus the angular position and radius of the center of the reversed bend. We also introduce for each orbit an angular shift with respect to the innermost one. This sums up to a total of $5 \times 4 + 4 = 24$ parameters. We then calculate the Fourier transform of each of the 5 orbits truncating at order $j = 9$. The values of each harmonics C_j and S_j are interpolated for intermediate values of a using cubic splines.

We let the optimizer adjust these 24 free parameters, with the objective to minimize the RMS tune variation of both horizontal and vertical tunes. We found a large number of solutions, and picked one with the tunes away from low-order betatron resonance lines, see Fig. 1. The corresponding orbit shapes and field distribution are presented in Figs. 2 and 3.

Constant-Tune 2 GeV Cyclotron

Both vertical and horizontal tunes are constant to within 0.01, and the field is isochronous to a very high precision, see Fig. 4. Particle tracking using the cyclotron code CYCLOPS[8], shown with solid lines on Fig. 4, confirms this result. The corresponding magnetic field presents ~9-degree wide low-field sections, see Figs. 2 and 3. The entire tune spread is barely visible on the tune diagram around the working point (2.78, 3.16), see Fig. 1.

CONCLUSION

We have demonstrated that there exists magnetic field distributions, that satisfy Maxwell's equations, that are precisely isochronous and produce a constant transverse focusing (constant betatron tunes) in both transverse directions over a wide energy region. This allows for the design of

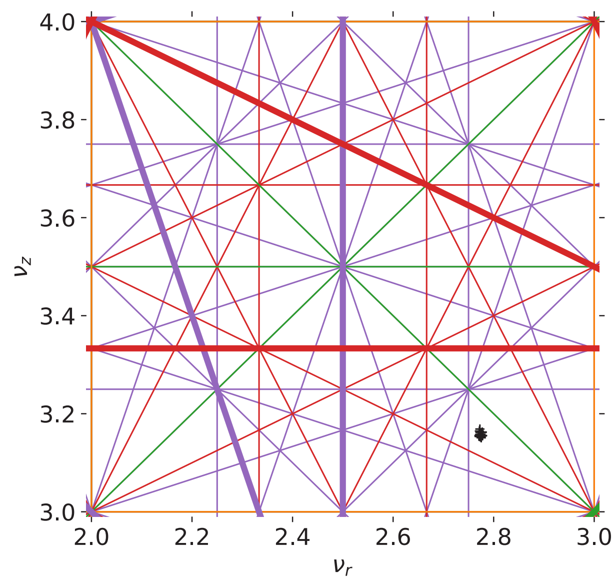

Figure 1: Tunes obtained using the field distribution shown in Fig. 2 are show in black, and appear as a small dot near the bottom right corner. Betatron resonance lines are shown up to 4th order, with the structural resonances shown with thick lines and non-structural with thin lines.

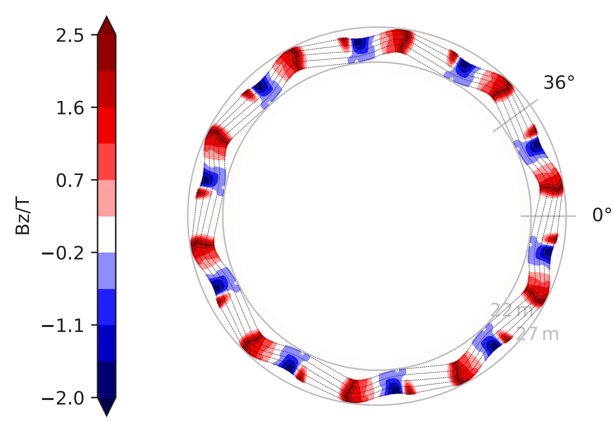

Figure 2: Magnetic field contours, with corresponding closed orbits, for a 10-sector 0.8 to 2 GeV proton cyclotron. Five closed obits are shown with thin dotted lines. The radii of the inner orbit and outer orbit are given for scale. Note the regions of low magnetic field are available for installation of rf cavities, injection and extraction systems, etc.

ISBN: 978-3-95450-212-7 ISSN: 2673-5482 doi:10.18429/JACoW-CYCLOTRONS2022-FRAI02

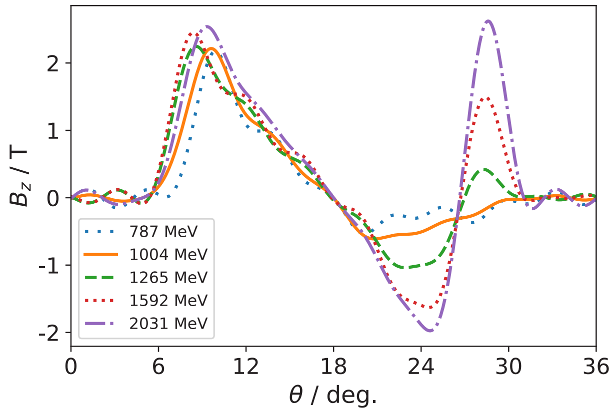

Figure 3: Magnetic field (B_z) along the 5 orbits shown in Fig. 2. The proton energy for each orbit is shown in the legend.

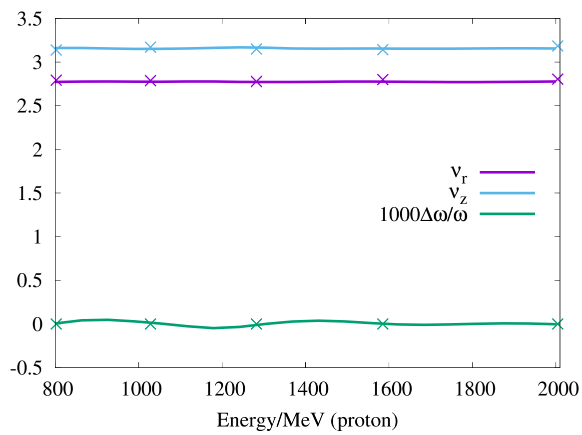

Figure 4: Transverse tunes, and relative variation of the orbital frequency, plotted as a function of the proton beam energy. Crosses show the results of calculation from `from_orbit`. Solid lines are results obtained after extracting a magnetic field map from `from_orbit`, and running it through the standard orbit code `CYCLOPS`.

high-energy cyclotrons that do not cross any betatron resonances, which could be a major advantage in the case of low-losses high-power machines.

The source code used to calculate tunes and generate fields maps for all the examples presented in this paper has been developed under a GPL-3 license and is available from: `https://gitlab.triumf.ca/tplanche/from-orbit`.

REFERENCES

[1] T. Planche, "Constant-tune cyclotrons," *J. Instrum.*, vol. 18, no. 03, p. P03019, Mar. 2023. doi:10.1088/1748-0221/18/03/P03019

[2] T. Planche, "Designing Cyclotrons and Fixed Field Accelerators From Their Orbits," in *Proc. Cyclotrons'19*, Cape Town, South Africa, Jun. 2020, pp. 353–357. doi:10.18429/JACoW-Cyclotrons2019-FRB01

[3] T. Zhang *et al.*, "A New Solution for Cost Effective, High Average Power (2 GeV 6 MW) Proton Accelerator and its R&D Activities," in *Proc. Cyclotrons'19*, Cape Town, South Africa, Sep. 2019, pp. 334–339. doi:10.18429/JACoW-CYCLOTRONS2019-FRA01

[4] T. Zhang *et al.*, "Innovative research and development activities on high energy and high current isochronous proton accelerator," *J. Instrum.*, vol. 18, no. 03, p. P03022, 2023. doi:10.1088/1748-0221/18/03/P03022

[5] E. Courant and H. Snyder, "Theory of the alternating-gradient synchrotron," *Ann. Phys.*, vol. 3, no. 1, pp. 1–48, 1958. doi:10.1016/0003-4916(58)90012-5

[6] R. Baartman, "Linearized Equations of Motion in Magnet with Median Plane Symmetry," TRIUMF, Tech. Rep. TRI-DN-05-06, 2005.

[7] L. Zhang and Y.-N. Rao, "Redundant field survey data of cyclotron with imperfect median plane," *J. Instrum.*, vol. 18, no. 03, p. P03021, 2023. doi:10.1088/1748-0221/18/03/P03021

[8] M. Gordon, "Computation of closed orbits and basic focusing properties for sector-focused cyclotrons and the design of CYCLOPS," *Part. Accel.*, vol. 16, pp. 39–62, 1984.

ISBN: 978-3-95450-212-7 ISSN: 2673-5482 doi:10.18429/JACoW-CYCLOTRONS2022-FRA002

FEASIBILITY STUDY ON 10 MW-CLASS ULTRA-HIGH POWER CYCLOTRON

Tianjian Bian†, Shizhong An, Fengping Guan, Luyu Ji, Sumin Wei
China Institute of Atomic Energy, Beijing, China

Abstract

10 MW-class ultra-high power cyclotron (UHPC) has great application prospects in cutting-edge sciences, neutron source, advanced energy and advanced material, etc. So far, Cyclotron with average beam power of 10 MW still have some bottleneck problems. Beam energy and current of a high-power cyclotron are typically less than 800 MeV and 3 mA. In this paper, bottleneck problems of UHPC are analysed, and then a preliminary design of UHPC-10 MW is presented.

INTRODUCTION

GeV-class proton beam with an average power of several megawatts has many important applications in particle physics towards the intensity frontier, as well as in the advanced energy and material science. There are three different types of constructed accelerators for high power proton beam production: The cyclotron, linear accelerator and rapid-cycling synchrotron. The highest beam power of these accelerators currently is 1.4 MW. Reference [1] reported the energy efficiency of the three operational accelerators with the highest beam power in the world, which showed that the energy efficiency of the PSI cyclotron is about 2 times of the other types, as shown in Table 1. W. Weng made a judgement that the beam/grid efficiency should be better than 30%, otherwise the Accelerator Driven subcritical-reactor System (ADS) becomes nonsense [2]. Studies have shown that the energy efficiency cyclotron is the highest which is expected to be 60%~65% in superconducting ring cyclotron [3]. As cyclotron is a good technical route to develop proton machines with high beam power and high-power efficiency, it shows good prospect in advanced energy.

The beam power of UHPC-10 MW aims at 10 MW, it composes of two stages. The first stage is a 150 MeV/amu injector and the second stage is a 1 GeV/amu ring cyclotron. If UHPC-10 MW is used to drive a spallation neutron source, the injector and the ring cyclotron can produce thermal neutron flux in the order of 10^{14} n/cm^2/s and 10^{15}n/cm^2/s, respectively. UHPC-10 MW based spallation neutron source will have higher thermal neutron flux than high-flux reactor based neutron source. Even the 150MeV/amu injector can produce high thermal neutron flux which comparable to middle flux reactor neutron source. Figure 1 shows the history of thermal neutron flux [4], and UHPC-10 MW based spallation neutron sources are marked with stars.

* This work was supported by the National Natural Science Foundation of China (Grant No. 12105370) and the Scientific Research Program for Young Talent Elite Project of China National Nuclear Corporation (Grant No. FY212406000404).
† biantianjian@foxmail.com

Table 1: Efficiency of different types of high-power accelerators.

Accel-eator	Type	Energy (MeV)	Power (MW)	Effi-ciency
SNS	Linac	1000	1.3	8.6%
JPARC	synchro-tron	3000	1.0	3%
SINQ	cyclotron	590	1.4	18%

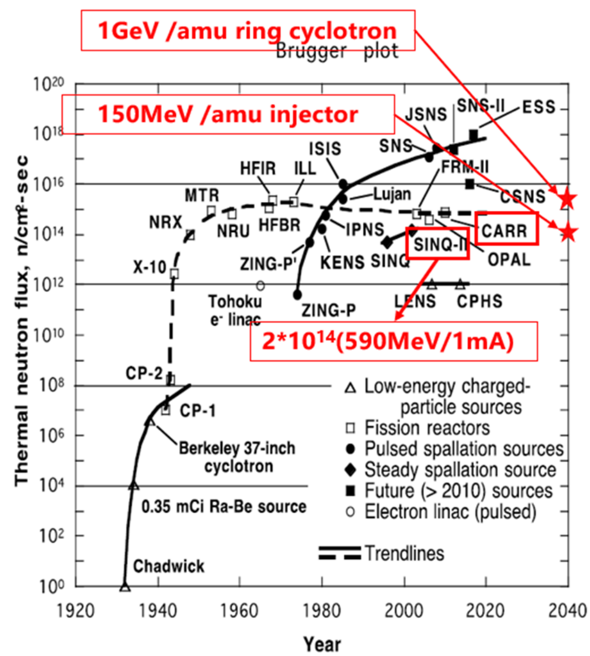

Figure 1: Thermal neutron flux history.

OVERALL DESIGN AND CONSIDERATION

Figure 2 shows the layout of UHPC-10MW. We choose a 1 MeV/amu RFQ as the pre-injector, and a separate sector cyclotron accelerate the beam from RFQ to 150 MeV/amu, finally the beam is injected to a 1 GeV/amu ring cyclotron.

Superconducting linac is the mainstream of high-power accelerator, due to relative higher technical maturity. So far, no well-approved design of 10 MW-class cyclotron is made due to some bottleneck problems. Radial tune is increasing linearly with beam energy in isochronous cyclotron, and thus the integer resonance crossing problem becomes an inevitable problem. Isochronous cyclotron is considered impossible to accelerate particles to a kinetic energy above its rest mass [5] typically 800 MeV/amu. Although cyclotron has continuous beam structure, the beam intensity is considered lower than 3 mA. The reason is enough clear region is need for beam extraction, otherwise the halo or tail particles will activate the deflector.

ISBN: 978-3-95450-212-7 ISSN: 2673-5482 doi:10.18429/JACoW-CYCLOTRONS2022-FRA002

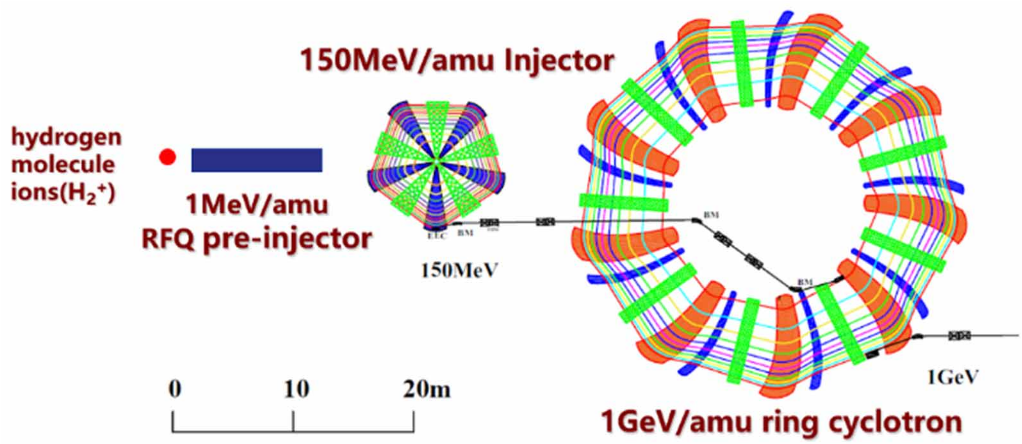

Figure 2: Layout of UHPC-10MW.

In the design phase of UHPC-10 MW, those problems need careful consideration and calculation. There are three bottleneck problems and their solutions:

(1) In low energy region, beam dynamics is dominated by space charge effect, so halo and tail particles are generated by space charge and non-adiabatic acceleration. In our design, we accelerate 5 mA of hydrogen molecule ions (H_2^+) instead of 10 mA of protons, which will mitigate the space charge effect [6].

(2) In high energy region, beam energy is limited by integer resonance. Beam integrates the harmonic field when passing through the integer resonance region, which drives large coherent oscillation. To solve those problems, an idea of integer resonance suppressor (IRS) was proposed [7]. IRS introduces the harmonic magnetic field intentionally to reduce the integration of driving harmonic field.

(3) In extraction region, single turn extraction with very low beam losses is also a very important issue of UHPC. The experience of PSI has shown that the upper limit of power deposition is 200 W. For 10 MW beam, relative losses should less than 2E-5. IRS can not only inhibit the radial oscillation and beam size blowup caused by integer resonance crossing but also contribute to a controllable coherent oscillation which is helpful to beam extraction with high efficiency [8]. With the help of IRS, turn separation can be enlarge to more than 30 mm.

150 MeV/amu INJECTOR

Parameters of 150 MeV/amu injector are listed in Table 2. 5 sectors scheme is adopted to avoid intrinsic resonance. Generous space between neighboring sectors can be used to install 5 powerful RF cavities. Beam is radially injected by a 1 MeV/amu RFQ pre-injector. Electrostatic deflector with a stripper foil placed upstream is used to high efficiency extraction.

To get the matched distribution, we track a coasting beam with 5 mA at 1 MeV/amu closed orbit until the equipartitioning process has resulted in a stationary distribution. Three cases with different phase width (9, 7, 6 rms degree) are simulated, as shown in Fig. 3. For those simulation, 10^4 particles and mesh of 32^3 grid points is used. In the coasting process, obvious longitudinal-radial coupling occurs and the gradually forms a round, compact distribution in 20 turns.

Table 2: Parameters of 150 MeV/amu Injector.

Parameter	Value
Accelerating particles	H2+
Extraction particles	H2+
Injection energy	1 MeV/amu
Extraction energy	150 MeV/amu
Extraction type	Electrostatic deflector
Turn separation at Extraction	~3 cm
Magnet sectors	5
Magnetic field of hill	3~3.7 T
Radius of pole	4.2 m
Cavity number	5
Harmonic number	7
Cavity frequency	~57 MHz
Cavity Voltage	~350 kV
Energy gain per turn	~3.4 MeV

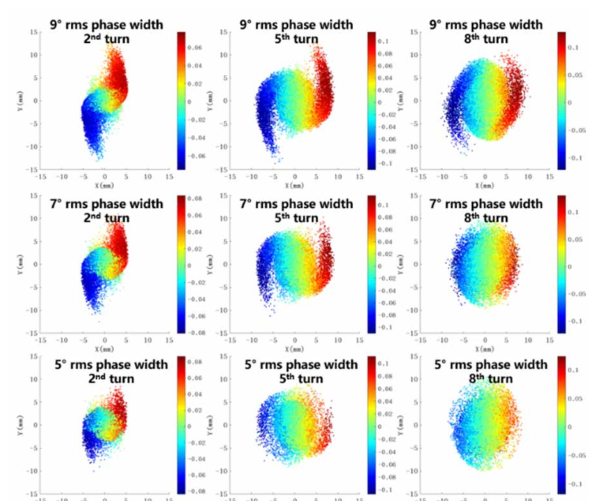

Figure 3: Longitudinal-radial coupling in the coasting process. Colour bars stand for energy deviation (MeV).

23rd Int. Conf. Cyclotrons Appl. CYCLOTRONS2022, Beijing, China JACoW Publishing
ISBN: 978-3-95450-212-7 ISSN: 2673-5482 doi:10.18429/JACoW-CYCLOTRONS2022-FRA002

Track the coasting beam for 50 turns and make statistics on beam parameters. Figure 4(a) and (b) show the relationship of beam parameters with phase width. We can find that both beam size and emittance are increasing with phase width. On the other hand, narrower phase width will develop into more compact distribution and wider phase width will lead to more halo particles, as shown in Fig. 4(c) and (d).

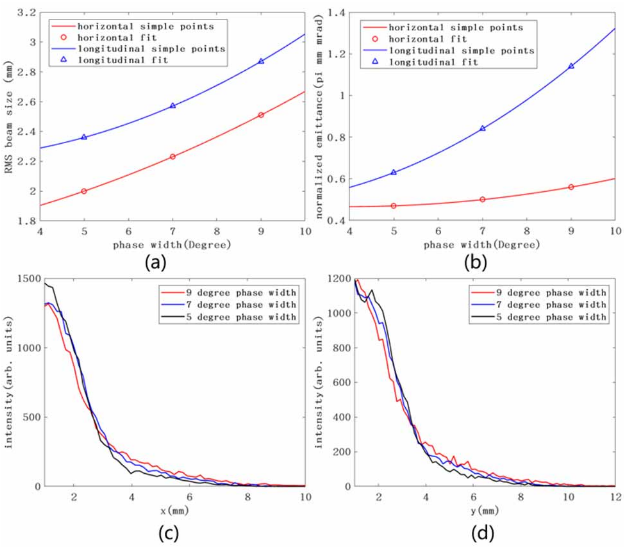

Figure 4: (a) Beam size as function of phase width. (b) Normalized emittance as function of phase width. (c) Distribution of matched beam in x direction. (d) Distribution of matched beam in y direction.

When acceleration is considered, beam halo will also increase due to nonadiabatic acceleration, especially in the low energy region. With contribution of acceleration and precession, turn separation is about 32 mm and the second and third to last turn overlap with each other. Beam is well controlled within ±6 mm in axial direction and septum is placed at the lowest intensity point, as shown in Fig. 5. If 0.5 mm is chosen as the septum thickness, the beam power at the deflector will be less than 30 W.

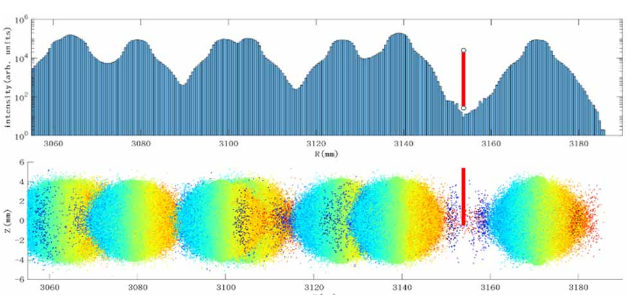

Figure 5: Beam intensity on radial probe.

1 GeV/amu RING CYCLOTRON

Parameters of 1 GeV/amu ring cyclotron are listed in Table 3. 9 high voltage RF cavities are installed in the space between neighboring sectors. Electrostatic deflector with a stripper foil placed upstream is used to high efficiency extraction.

Table 3: Parameters of 1 GeV/amu Injector

Parameter	Value
Accelerating particles	H2+
Extraction particles	H2+
Injection energy	150 MeV/amu
Extraction energy	1 GeV/amu
Extraction type	Electrostatic deflector
Turn separation at Extraction	~3cm
Cell number	9
Magnetic field of hill	2.7~4 T
Radius of pole	~11.2 m
Cavity number	9
Harmonic number	14
Cavity frequency	~57 MHz
Cavity Voltage	~1.3 MV
Energy gain per turn	~12 MeV
3rd harmonic Cavity number	3
Voltage of 3rd harmonic Cavity	10% of main cavity Voltage

In this ring cyclotron, beam is accelerated to beyond the integer resonance $v_r = 2$. In the extraction region, v_r extend to nearly 2.5 to enlarge the turn separation. Figure 6 shows the tune diagram.

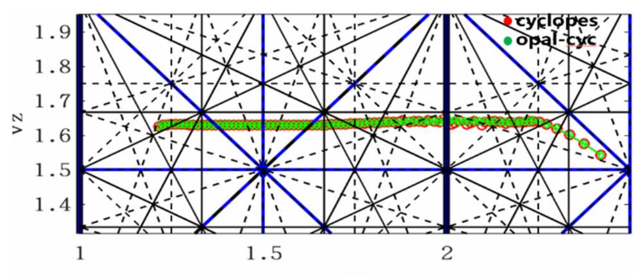

Figure 6: Tune diagram.

Beam integrates the harmonic field when passing through the integer resonance region, which drives large coherent oscillation. Second harmonic field B_2 of only 3Gs will drive coherent oscillation of 70 mm, which can be estimated with formula $\Delta A = \frac{\pi}{\sqrt{Q_\tau}} \frac{\bar{R}}{\bar{B}} \frac{B_2}{Q}$ [9]. Such large coherent oscillation is incompatible with the following resonance $4v_r = 9$ and the beam size is blown up. Figure 7(a) Shows that the radial beam size is increased about 2 times. One of the reasons is that intrinsic resonance $4vr = 9$ distorts the phase space, as shown in Fig. 7(b). IRS method is adopted to correct the large coherent motion before reaching the intrinsic resonance $4v_r = 9$. Figure 8 shows the structure and location of IRSs in the ring cyclotron. Coil current of IRSs marked by triangle and circle are oppositely directed. Coil current of IRSs marked by same colour have the same current value. Detailed structure and arrangement principle are explained in Ref. [7]. With the IRSs, radial oscillation is reduced to ±10 mm and the beam size is beam size will not be blown up, as shown in Fig. 9.

ISBN: 978-3-95450-212-7 ISSN: 2673-5482 doi:10.18429/JACoW-CYCLOTRONS2022-FRA002

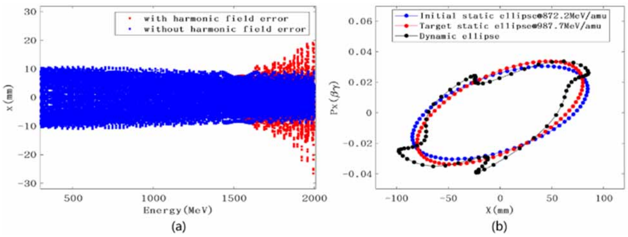

Figure 7: (a) Beam size evolution in the acceleration process. (b) Intrinsic resonance $4\nu r = 9$ distorts the phase space.

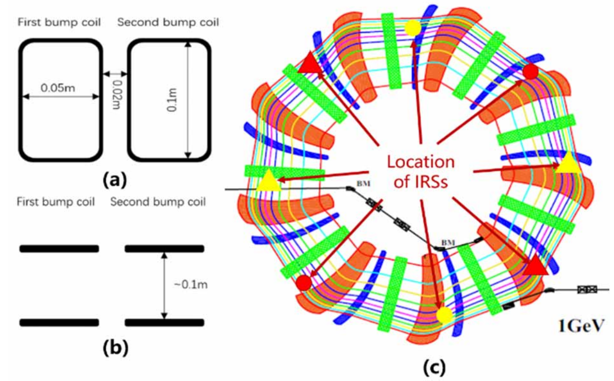

Figure 8: (a) Top view of an IRS. (b) Side view of an IRS. (c) Location of IRS in the ring cyclotron.

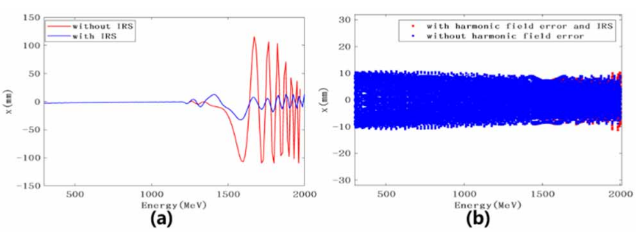

Figure 9: (a) Radial oscillation with and without IRS. (b) Beam size evolution with and without IRS.

With contribution of acceleration and precession, turn separation is about 35 mm. The space charge effect also has powerful influence on the beam dynamics. Figure 10 shows beam intensity on radial probe for different phase width. The emittance is 1 π mm rad and $25 \cdot 10^4$ macro particles and mesh of 32^3 grid points is used. For 2°rms phase width, space charge dominates the beam dynamics. A round, compact beam is developed due to vortex motion, but the beam will break up in the integer resonance crossing process. For 8°rms phase width, beam dynamics is dominated by emittance and the turn separation is much more clear. The case with 5°rms phase width is at the trans ition between the emittance-dominated and space- charge-dominated. For the optimized case, 7.5°rms phase width and 2.5 π mm rad is used and then a clear region is obtained at the extraction point. If 0.5 mm is chosen as the septum thickness, the beam power at the deflector will be less than 100 W.

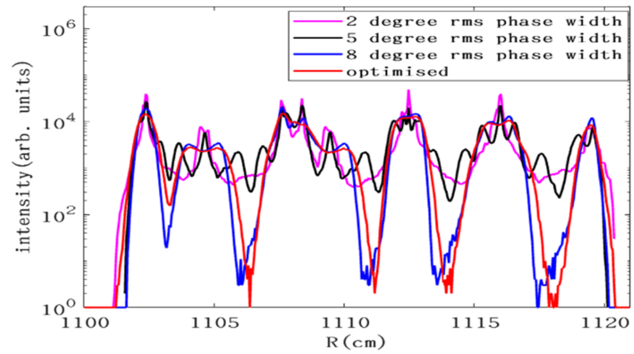

Figure 10: Beam intensity on radial probe for different phase width.

SUMMARY

This paper presents the preliminary design of UHPC-10 MW. Simulation results of beam power deposition on deflector show that the margin is sufficient. In particular, the 1 GeV/amu ring cyclotron accelerate the beam to beyond the integer resonance and IRS is used to control the oscillation. Simulations show that IRS can not only reduce the beam size growth rate to less than 5%, but also enlarge the turn separation to 35mm. That is to say, IRS not only acts as integer resonance suppressor, but also plays the role of separation optimizer between the last and second last turn. From our limited knowledge, we do not see any fundamental limits that prevent the construction of a 10MW-class cyclotron. OPAL [10] and Cyclops [11] are used in the beam dynamics simulation.

REFERENCE

[1] J. Grillenberger, M. Seidel, S.-H. Kim, M. Yoshii, and V. P. Yakovlev, "The energy efficiency of high intensity proton driver concepts", in *Proc. IPAC'17*, Copenhagen, Denmark, May 2017, pp. 4842-4847. doi:10.18429/JACoW-IPAC2017-FRXCB1

[2] W. Weng, "Developments of High Power Proton Accelerators", Brookhaven National Lab., Upton, NY, USA, 2018, unpublished

[3] L. Calabretta et al., "Cyclotrons and FFAG accelerators as drivers for ADS*", Rev. Accel. Sci. Technol.*, vol. 08, pp. 77-97, 2015.

[4] J. M. Carpenter, "Accelerator-based neutron sources: past, present, and future", Oct. 2018, unpublished, http://flnph.jinr.ru/images/content/Carpenter.pdf

[5] L. A. Sarkisyan, "Possibility of accelerating protons to energies above E0 in an isochronous cyclotron", Soviet Atomic Energy, vol. 30, pp. 584–586, 1971.

[6] J. Alonso *et al.*, "The IsoDAR High Intensity H2+ Transport and Injection Tests", *J. Instrum.*, vol. 10, p. T10003, 2015. doi:10.1088/1748-0221/10/10/T10003

[7] T. Bian *et al.,* "Possible solution for the integer resonance crossing problem of GeV-class isochronous Fixed-Field Alternating Gradient accelerators", *Nucl. Instrum. Methods Phys. Res. Sect. A*, vol. 1031, p. 166594, 2022. doi:10.1016/j.nima.2022.166594

ISBN: 978-3-95450-212-7 ISSN: 2673-5482 doi:10.18429/JACoW-CYCLOTRONS2022-FRA002

[8] T. Bian *et al.,* "Inhibition and Utilization of Integer Resonance in GeV/mA Class High Power Circular Accelerator", *Atomic Energy Science and Technology*, 2022, vol. 9, p. 056, 2022, in Chinese.

[9] R. Baartman, "Fast crossing of betatron resonances", presented at the FFAG Workshop, TRIUMF, Vancouver, BC, Canada, Apr. 2004, https://ffag2004.triumf.ca/

[10] M. M. Gordon, "Computation of closed orbits and basic focusing properties for sector-focused cyclotrons and the design of 'cyclops'", *Part. Accel.*, vol. 16, pp. 39-62,1984.

[11] Object Oriented Parallel Accelerator Library (OPAL), https://gitlab.psi.ch/OPAL/src/-/wikis/home

ISBN: 978-3-95450-212-7 ISSN: 2673-5482 doi:10.18429/JACoW-CYCLOTRONS2022-FRA003

ENGINEERING DESIGN AND FABRICATION TECHNOLOGY FOR SUPERCONDUCTING MAGNETS IN CYCLOTRON

X. L. Guo†, H. M. Tang, Bama Superconductive Technology Co. Ltd, Suzhou, China

Abstract

Magnets play an import role in cyclotrons. Application of superconducting magnets can make the cyclotron more compact, magnet field higher, and operation cost lower. In recent years superconducting cyclotrons is increasing number in heavy iron therapy application, and they are an easy and cheap way to get ion beams. As a superconducting magnet besides the electromagnetic design to meet the beam transport requirement, there are many special engineering design points, including mechanical, cooling, stability, safety, measurement and so on. To fabricate the superconducting magnets, especially those with specially winding shape and configuration, need to study the process including winding, resin vacuum pressure impregnation, superconductor welding, assembling and so on. This report describes the trends of superconducting magnet in cyclotron. Some projects and products developed in Bama Superconductive Tech Co. Ltd are also presented in this report,

INTRODUCTION

The applications of cyclotron accelerators have covered a number of research areas, such as for medical or industrial applications. One typical application of cyclotron as particle therapy system is shown in Fig 1. The basic modular of a particle therapy system include beam production system, beam transport system and beam delivery system. Magnets play import roles in each modular. In beam production system magnets are used in the cyclotron to accelerate the beam to designed energy level. In beam transport system magnet are used to guide the beam. In delivery system magnets are used to deliver the beam to the exact location of focal lesions.

Application of superconducting magnets can make the cyclotron more compact, magnet field higher, and operation cost lower. From 1982 the first external beam was extracted from the K500 cyclotron at MSU, cyclotrons based on superconducting magnets became a popular research field in science, research, medicine and so on. Especially in recent years superconducting cyclotrons is increasing number in heavy iron therapy application, and they are an easy and cheap way to get ion beams.

With the development of superconductive materials and superconducting magnet technology, many new design and fabricating technology are proposed. As a superconducting magnet besides the electromagnetic design to meet the beam transport requirement, there are many special engineering design points, including mechanical, cooling, stability, safety, measurement and so on. To fabricate the superconducting magnet, especially those with specially winding shape and configuration, need to study the process including winding, resin vacuum pressure impregnation, super-conductor welding, assembling and so on. This report describes the trends of superconducting magnet in cyclotron. Some projects and products developed in Bama Superconductive Tech Co. Ltd are also presented in this report.

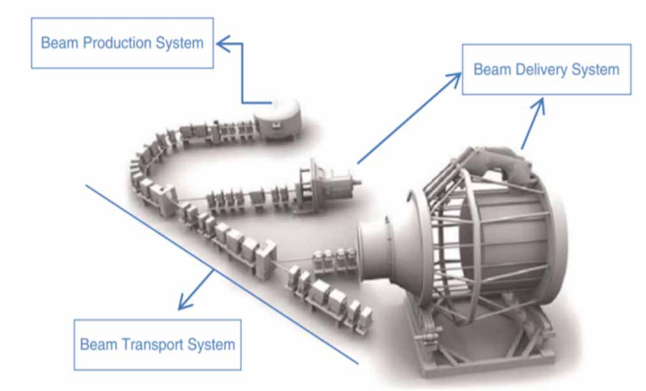

Figure 1: Basic modular design of particle therapy systems [1].

TRENDS OF SUPERCONDUCITNG MAGNETS IN CYCLOTRON

With the development of superconducting magnets technology and the requirement of particle therapy systems. Some new trends appeared in recent years.

Cryogen-free Superconducting Magnet

A superconducting azimuthally varying field (AVF) cyclotron, SC230, was developed for proton therapy by Sumitomo Heavy Industries, Ltd. in 2021. This isochronous cyclotron is compact owing to the high magnetic field generated by NbTi superconducting coils. The average magnetic field is 3.9 T at the outer region, and the extraction radius is 0.6 m. Because iron magnetization brings a limitation to iron-yoke isochronous cyclotrons, this SC230 SHI designed is probably at the lower limit in terms of weight and size. The coils are cryogen-free and cooled by conduction cooling using four 4 K-GM cryocoolers. The system is highly safe and easy to maintain, which reduces the effects of unstable helium supply. The heat inputs to the coils during beam operation are larger owing to the leakage radio frequency (RF) and beam loss are considered in detailed. The magnet is designed to have a sufficient temperature margin for stable operation. The coil temperature during the RF excitation is about 4.5 K. It was confirmed that the coil cools sufficiently at the critical temperature [2-3]. The schematic of the AVF cyclotron SC230 are shown in Fig. 2.

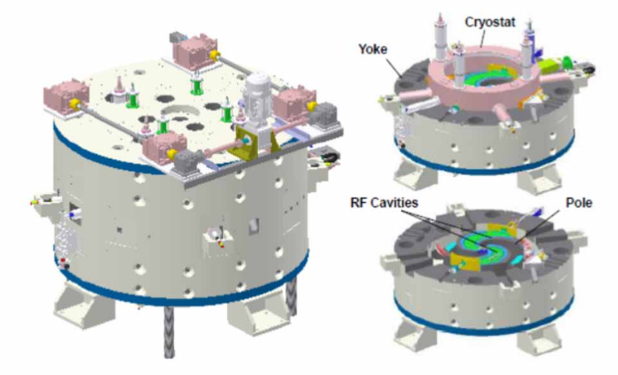

Figure 2: Schematic of the AVF cyclotron SC230 [3].

Ironless Cyclotron Superconducting Magnet

A concept of ironless superconducting magnet was proposed for further weight reduction of the cyclotron by Massachusetts Institute of Technology [4-5]. Their work demonstrates how multiple sets of superconducting coils can be used to replace the iron return yoke and pole pieces of a conventional cyclotron. Coil number, location, and current are used as optimization parameters for the required field profile and active shielding requirements of the machine. In comparison to the commercial Mevion Monarch 250 synchrocyclotron for proton therapy, the weight of the cyclotron magnet system is reduced by a factor of 6 by using the superconducting ironless design. Iron-free designs may also offer increased tuning ease during mass production, in the fashion of magnetic resonance magnets, and increased access to the midplane. Figure 3 shows the schematic of the ironless cyclotron superconducting magnet [4-5].

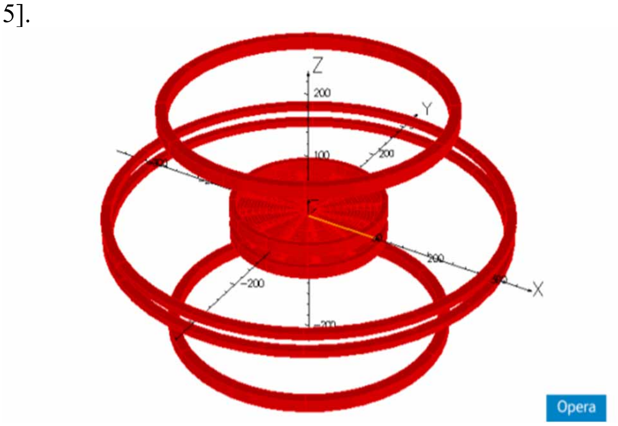

Figure 3: Schematic of the Ironless Cyclotron Superconducting Magnet [4].

High Temperature Superconducting Magnet

A study of high-temperature superconducting (HTS) magnets in cyclotron for particle therapy was carried out by the Research Centre for Nuclear Physics in Osaka, Japan [6]. This concept applies the quality improvements seen in HTS tapes over recent years to coils for the use in medical accelerators. The aim is also a yoke-free, ultra-compact, efficient, and high-energy AVF cyclotron with much reduced power consumption. Bean-shaped coils above and below the beam chamber are implemented in order to create a suitable AVF magnetic field structure needed for beam stability. The concept is still in early stages of development, and the technical difficulties of realizing any iron-free cyclotron requiring rapid energy variations for clinical treatment are not trivial. Figure 4 shows schematic of the HTS magnets in cyclotron [6].

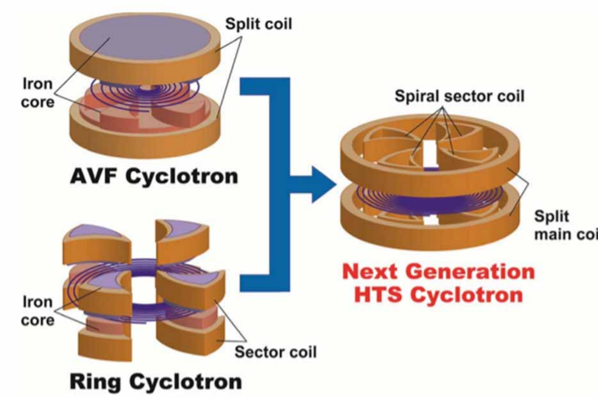

Figure 4: Schematic of the HTS magnets in cyclotron [6].

A study of HTS magnet for the 2 GeV FFAG accelerator lattice scheme was carried out by China Institute of Atomic Energy (CIAE) from 2019. In order to demonstrate the feasibility of manufacturing a spiral-shaped HTS magnet with concave edges based on ReBCO tapes, a 1:4 scaled HTS model magnet has been developed in CIAE. The whole assembled HTS magnet was cooled down to 23 K using helium gas pipeline contact cooling and operated on 300 A for over 24 hours. The central magnetic field reached 719.5 mT, without iron [7-8]. Figure 5 shows the Schematic of the HTS magnet for the 2 GeV FFAG accelerator in CIAE.

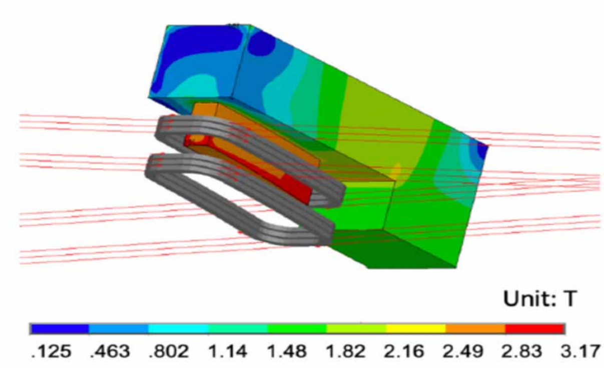

Figure 5: Schematic of the HTS magnet for the 2 GeV FFAG accelerator in CIAE [8].

Alternating-Gradient Canted Cosine Theta Superconducting Magnet

The concept of alternating-gradient canted cosine theta (AG-CCT) superconducting magnets for application in a gantry for proton therapy are proposed by Weishi Wan et al. [9]. The AG-CCT magnet allows a large momentum acceptance. A very big advantage is that all this can be done

ISBN: 978-3-95450-212-7 ISSN: 2673-5482 doi:10.18429/JACoW-CYCLOTRONS2022-FRA003

while keeping the AG-CCT fields fixed. This reduces the need for fast field ramping of the superconducting magnets between the successive beam energies used for the scanning in depth and it is important for medical application since this reduces the technical risk (e.g., a quench) associated with fast field changes in superconducting magnets. For proton gantries the corresponding superconducting magnet system holds promise of dramatic reduction in weight. For heavier ion gantries there may furthermore be a significant reduction in size. A systematic design procedure for an AG-CCT superconducting gantry is study in Huazhong University of Science and Technology in China, and Figure 6 shows the Schematic of the AG-CCT superconducting gantry [10].

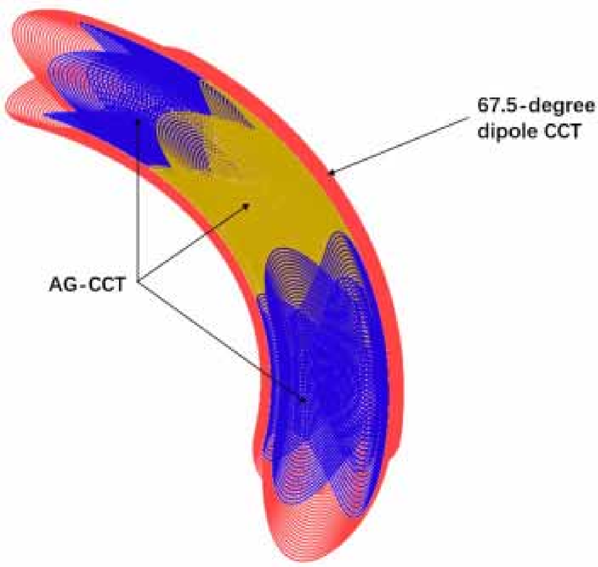

Figure 6: Schematic of the AG-CCT superconducting gantry in Huazhong University of Science and Technology [10].

TYPICAL SUPERCONDUCTING MAGNETS TECHNOLOG CASES IN BAMA SUPERCONDUCTIVE TECH CO.

Bama Superconductive Tech Co. Ltd was found in 2018 in China. It focuses on technology and equipment for ultimate environment creation including high magnetic, cryogenics and vacuum, especially on superconducting magnets.

Superconducting Magnet Technology

Bama has designed various superconducting magnets for big science projects, research instruments, industry and medical fields. The design technology including electromagnetism optimal design, cooling system design, mechanical design, power and quench protection system design for superconducting magnets.

Key components fabrication technology in superconducting magnets has been studied in Bama, including superconductor wire welding, vacuum pressure impregnation for superconducting magnets, high temperature current leads, high thermal conductive strips et al.

Customized and standard series NbTi magnets have been designed and fabricated by Bama. Figure 7 shows a equipment for HTS tape properties measurement using warm bore of a 5T superconducting magnet by Bama. Figure 8 shows the ReBCO defocusing magnet of 2 GeV FFAG accelerator in CIAE by Bama.

Figure 7: Schematic of an equipment for HTS tape properties measurement using warm bore of a 5T superconducting magnet by Bama .

Figure 8: Schematic of the ReBCO defocusing magnet of 2 GeV FFAG accelerator in CIAE by Bama.

GM Cryocoolers Technology

GM Cryocooler is the key components for cooking superconducting magnets. Bama has development series GM cryocoolers and helium compressors, including 4 K series for lower temperature superconducting magnets, 10 K series for cryo-vacuum pumps and 70 K single stage cryocoolers for thermal shields, high temperature superconducting magnets et al. These GM cryocoolers have been applied in many superconducting products of Bama, and are suppled in the market. Figure 9 shows the model of GM Cryocoolers by Bama.

CONCLUSION

Magnets play an import role in cyclotrons. Application of superconducting magnets can make the cyclotron more compact, magnet field higher, and operation cost lower. Many new trends of superconducting magnets in cyclotrons appeared in recent years including conduction cooling magnets, ironless magnets, HTS magnet and alternating-gradient canted cosine theta superconducting magnet.

ISBN: 978-3-95450-212-7 ISSN: 2673-5482 doi:10.18429/JACoW-CYCLOTRONS2022-FRA003

Figure 9: Model of GM Cryocoolers by Bama.

Bama Superconductive Tech Co. Ltd focuses on technology and equipment for ultimate environment creation including high magnetic, cryogenics and vacuum, especially on superconducting magnets. Bama has developed various Customized and standard series NbTi magnets and HTS magnet. GM Cryocooler as a key component for cooling superconducting magnets has also been developed and supplied in the market by Bama.

REFERENCES

[1] E. Pearson *et al.*, "Development of Cyclotrons for Proton and Particle Therapy", in *Particle Radiotherapy*, A. Rath, N. Sahoo, Eds. Springer, New Delhi, India, 2016, pp. 21-35. doi:10.1007/978-81-322-2622-2

[2] H. Tsutsui, A. Hashimoto, Y. Mikami, *et al.*, "Design study f a superconducting AVF cyclotron for proton therapy", in *Proc. Cyclotrons'13*, Vancouver, BC, Canada, Sep. 2013, paper MO3PB02, pp. 102-104.

[3] Y. Ebara *et al.*, "Performance of Cryogen-free Superconducting Magnet in Isochronous Cyclotron for Proton Therapy", in *IEEE Trans. Appl. Supercond.*, pp. 1-5, Feb. 2023. doi:10.1109/TASC.2023.3245563

[4] A. Radovinsky, J. V. Minervini, C. E. Miller, L. Bromberg, P. C. Michael, and M. Maggiore, "Superconducting Magnets for Ultra Light and Magnetically Shielded, Compact Cyclotrons for Medical, Scientific, and Security Applications", in *IEEE Trans. Appl. Supercond.*, vol. 24, no. 3, pp. 1-5, p 4402505, June 2014. doi:10.1109/TASC.2013.2287853

[5] A.L. Radovinsky, J.V. Minervini, P.C. Michael, L. Bromberg, and C.E. Miller, "Variable Energy Acceleration in a Single Iron-Free Synchrocyclotron", Sep. 2013, PSFC/RR-13. http://www1.psfc.mit.edu/library1/catalog/reports/2010/13rr/13rr009/13rr009_full.pdf

[6] H. Ueda *et al.*, "Conceptual Design of Next Generation HTS Cyclotron", in *IEEE Trans. Appl. Supercond*, vol. 23, no. 3, p. 4100205, June 2013. doi:10.1109/TASC.2012.2232955

[7] C. Wang *et al.*, "Preliminary Study of the High Temperature Superconducting Solution for 2 GeV CW FFAG Magnet", in *IEEE Trans. Appl. Supercond*, vol. 30, p. 4101804, Jun. 2020. doi:10.1109/TASC.2020.2981298

[8] W. Fu *et al.*, "Fabrication and Test of a 1:4 Scaled HTS Coil for the Defocusing Magnet of 2 GeV FFAG Accelerator", in *IEEE Trans. Appl. Supercond*, vol. 32, p. 4005404, Sep. 2022. doi:10.1109/TASC.2022.3159297

[9] W. Wan, L. Brouwer, S. Caspi, *et al.,* "Alternating-gradient canted cosine theta superconducting magnets for future compact proton gantries", *Phys. Rev. ST Accel. Beams*, vol. 18, p. 103501, 2015. doi:10.1103/PhysRevSTAB.18.103501

[10] R. Zhao, B. Qin, Y. Liao, X. Liu, *et al.*, "Achieving a realistic design for a superconducting gantry with large momentum acceptance for proton therapy", *Nucl. Instrum. Methods Phys. Res., Sect. A*, vol. 1015, p. 165773, 2021. doi:10.1016/j.nima.2021.165773

ISBN: 978-3-95450-212-7 ISSN: 2673-5482 doi:10.18429/JACoW-CYCLOTRONS2022-FRBI01

DIFFERENT METHODS TO INCREASE THE TRANSMISSION IN CYCLOTRON-BASED PROTON THERAPY FACILITIES*

V. Maradia[†1], D. Meer, D. C. Weber[2], A. J. Lomax[1], J. M. Schippers, S. Psoroulas,
Paul Scherrer Institute, Villigen PSI, Switzerland
[1]also at ETH Zurich, Zurich, Switzerland
[2]also at University Hospital Zurich and University Hospital Bern, University of Bern, Switzerland

Abstract

In proton therapy (PT), high dose rates could allow efficient utilization of motion mitigation techniques for moving targets, and potentially enhance normal tissue sparing due to the FLASH effect. Cyclotrons are currently the most common accelerator for PT, accounting for two-thirds of the total installations. However, for cyclotron-based facilities, high dose rates are difficult to reach for low-energy beams, which are generated by passing a high-energy beam through an energy degrader and an energy selection system (ESS); due to scattering and range straggling in the degrader, the emittance and energy/momentum spread increase significantly, incurring large losses from the cyclotron to the patient position. To solve these problems, we propose different options to transport the maximum acceptable emittance in both transverse planes (using new gantry beam optics, asymmetric collimators and/or scattering foil). We demonstrate in simulation that low-energy beam transmission can be increased up to a factor of 6 using these approaches compared to the currently used beamline and ESS. This concept is key to enhance the potential of PT by increasing the possibilities to treat new indications in current and future PT facilities while reducing the cost.

INTRODUCTION

The most advanced, and nowadays the most used method to deliver the dose is spot scanning or pencil beam scanning (PBS) [1]. Treatment delivery time with PBS PT depends both on the beam-on time and the dead time (the time required to change energy layers and/or lateral position) between pencil beams [2,3]. As such, PBS irradiation with high-intensity beams will reduce beam-on time and thus shorten total delivery times, making motion mitigation techniques such as breath-hold or gating more efficient and patient-friendly [4].

Most of the PT facilities use a cyclotron, which extracts proton beams at fixed energy (at PSI, we extract 250 MeV beam). However, to spread the dose over the depth of the tumor, different beam energies are needed for the treatment (70-230 MeV). In a cyclotron-based facility, the energy is lowered by passing the beam through energy-degrading material(s) (so-called energy degraders). However, due to scattering in the degrader, for low energy beams, the emittance after the degrader is in the range of a few hundred of π*mm*mrad. Additionally, due to range straggling in the degrader, the momentum spread of the beam will also increase. Therefore, to minimize beam losses in the beamline, it is necessary to use beam emittance selection collimators after the degrader and momentum selection slits in the energy selection system (ESS) to restrict the emittance and momentum spread to the requirement of the following beamline or gantry. Currently, all cyclotron-based PT facilities transport a maximum emittance of 30 π*mm*mrad through the beamline, which limits the transmission of low-energy beams. For example, for the lower energies transported by the Gantry 2 at our institute (70-100 MeV), transmission from the cyclotron to the isocenter is of the order of only 0.1% [5,6,7,8].

Therefore, to limit the losses in the beamline, in this paper, we are providing a summary of different ways to efficiently transport higher emittance through the beamline.

First, we propose the use of a large beam size and low divergence beam at the coupling point (CP) along with an imaging factor of 0.5 (2:1) in a new design of gantry beam optics to transport higher emittance through gantry while achieving higher transmission and thus increase beam intensity at the isocenter. Secondly, we propose the use of scattering foil to achieve the same emittance in both planes at the entrance of the gantry while transporting maximum acceptable emittance in both planes from the degrader, thus ensuring gantry angle-independent beam shape at the isocenter. In the end, to maximize the emittance transport through both transverse planes, we propose to use a collimation system, asymmetric in both beam size and divergence, resulting in symmetric emittance in both beam transverse planes as required for a gantry system.

This study was performed as a collaborative doctoral project between the center for proton therapy and a large accelerator facility group at PSI and published in [5,6,7,9,10,11]. In the following, all beam sizes, divergences, and emittances are expressed as 2-sigma values.

TRANSMISSION OPTIMIZATION THROUGH GANTRY

Conventional beam optics of cyclotron-based proton gantries were designed to provide point-to-point focusing in both planes, with an imaging factor of between 1 to 2 from

* THIS WORK IS SUPPORTED BY A PSI INTER-DEPARTMENTAL FUNDING INITIATIVE (CROSS)
† vivek.maradia@psi.ch

ISBN: 978-3-95450-212-7 ISSN: 2673-5482 doi:10.18429/JACoW-CYCLOTRONS2022-FRBI01

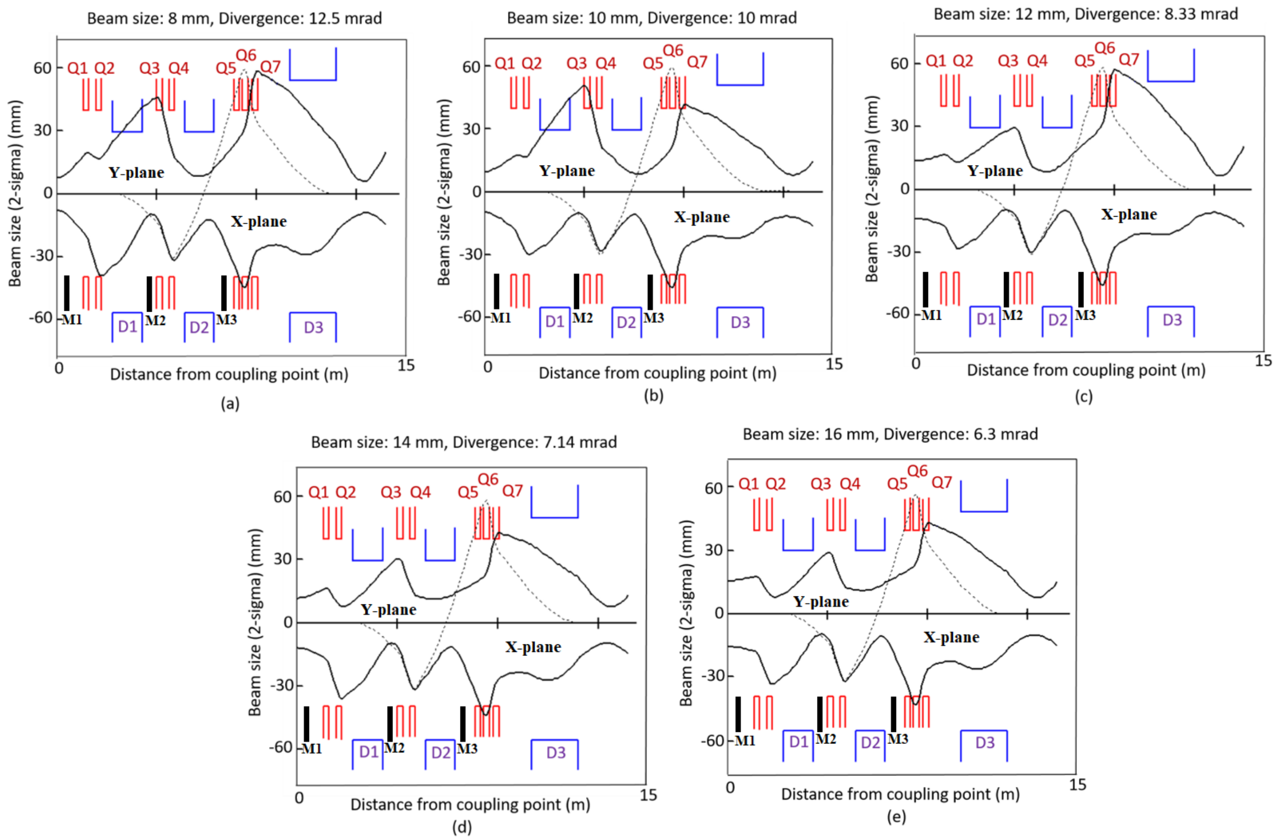

Figure 1: Gantry beam optics to transport 100 π*mm*mrad with different beam phase space at the CP. The beam envelopes show the beam size in 2-sigma values and the dispersion (dashed line) along PSI's Gantry 2 beamline (The lower half of each figure shows the beam envelope in the X-plane (bending plane) and the upper half shows the envelope in Y-plane). Figure (a), (b), (c), (d), and (e) represents 1:1, 1.25:1, 1.5:1, 1.75:1, and 2:1 imaging respectively. Elements D = dipole magnets and elements Q = quadrupole magnets. The dispersion only occurs in the bending plane (in our case, X-plane) [9].

the CP to the isocenter [6,7]. These increase the possibility of beam losses along the gantry as the beam envelope approaches the beam pipe. For instance, for PSI's Gantry 2, by transporting 30 π*mm*mrad emittance (3 mm beam size and 10 mrad divergence at the CP) with 1:1 imaging, the transmission of 57 % is achieved for lower energies (70-100 MeV). However, to achieve higher intensity for lower energy beams, it is desirable to transport a higher emittance through both the beamline and gantry. Here, we report on a new beam optics approach, which transports higher emittances through the gantry.

To study the effect of beam phase space at CP on gantry transmission, we chose five different phase space orientations of which each had the same 100 π*mm*mrad emittance. The gantry beam optics were then modified for all five cases to transport this same emittance through the gantry. In order to achieve the same beam size at the isocenter, however, beam optics with different magnification factors, depending on the beam size at CP, were designed. Figure 1 shows the selected beam size and divergence at CP, together with the resulting imaging factor for five different beam widths and their beam envelopes through the gantry.

A ±1% momentum spread (Δ p/p) was assumed for all cases. Due to the large dispersion, some beam is inevitably lost in the quadrupole triplet in all cases [9].

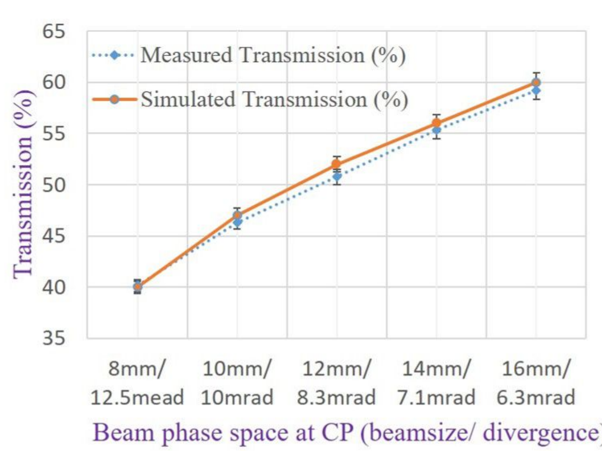

Figure 2: Beam transmission through gantry (simulation and measured) for transporting 100 π*mm*mrad through gantry with different beam parameters at the CP [9].

ISBN: 978-3-95450-212-7 ISSN: 2673-5482 doi:10.18429/JACoW-CYCLOTRONS2022-FRBI01

When transporting beams with 100 π*mm*mrad emittance through the gantry, we get a minimum transmission of about 40% for a beam size of 8 mm and large divergence (12.5 mrad) (Figure 2 (a)). By increasing the beam size and decreasing the divergence, however, one can see a gradual increase in transmission through the gantry, reaching a maximum transmission of about 60%, for the largest beam size at CP (16 mm), corresponding to the smallest divergence. This matches expectations as can be observed in Figure 1 and Figure 2. This improvement in transmission results from substantially less beam loss in the first two quadrupole and dipole magnets as the beam envelopes are now far from the apertures of these magnets for cases (d) and (e) compared to cases (a), (b) and (c). As such, and combined with 2:1 imaging, we get a maximum transmission through the gantry. Nevertheless, due to the maximal effect of the dispersion in the quadrupole triplet, it is still unavoidable to have some beam losses due to the 1% momentum spread [9].

TRANSMISSION OPTIMIZATION THROUGH FIXED BEAMLINE

As demonstrated in the previous section, the use of large beam sizes and low divergence at the CP allows the transport of larger emittances through the gantry while achieving reasonable transmission (>50%) through the gantry. Therefore, in this section, the aim is to find a way to transport about 100 π*mm*mrad or more emittance from the degrader exit to the gantry entrance (CP).

Use of scattering foil

The resulting proton beam from the energy degrader has a symmetric, but large phase space distribution in both transverse planes. This symmetry however is not fully compatible with an optimal transport through the first quadrupole magnet, which is either horizontally or vertically focusing. By modifying the emittance after the degrader such that it is asymmetric, transmission through the subsequent beam line can be substantially improved. For instance, after focusing the beam in the Y-plane using the first quadrupole after the degrader, the vertical beam size behind the second quadrupole is small enough to pass the following bending magnet of the ESS, thus allowing to select higher divergence acceptance in the Y-plane compared to the X-plane. Such an optimized beamline at our facility transports a maximum of 65 π*mm*mrad in X-plane (using beam size selection collimator radius of 6.5 mm and beam divergence collimator of 14.4 mm) and 139 π*mm*mrad in Y-plane (using beam size selection collimator radius of 6.5 mm and beam divergence collimator of 33.3 mm), but at the cost of an elliptical beam shape at the gantry entrance, leading to gantry angle dependent beam shapes at the isocenter [10,11].

However, in order to simplify beam commissioning and quality assurance, it is desirable to have gantry angle-independent beam optics and beam sizes at the isocenter. To achieve gantry angle independence, it is ideally required to have the same emittance in both planes by the time the beam gets to the gantry entrance.

Here, we report on the use of a thin scattering foil (made of tantalum (Ta) with a thickness of 30 μm and density of 16.69 g/cm^3), placed in the beamline between the ESS and gantry CP ((Figure 3(a)), to achieve equal emittances in both planes, whilst maintaining a high transmission through the beamline and gantry.

To achieve a similar emittance in both planes after the scattering foil, the beam optics from the degrader exit to the scattering foil (Figure 3(a)) have been redesigned, while still transporting the maximum emittances accepted by the beamline in both planes: 67 π*mm*mrad in X-plane and 139 π*mm*mrad in Y-plane. This results in almost equal emittances after the scattering foil of 148 π*mm*mrad in the X-plane and 145 π*mm*mrad in the Y-plane. With the use of the scattering foil, we measured an overall transmission of 0.4% from the cyclotron to the isocenter, which can be compared to only 0.13% transmission for the reference beam optics (clinically used beam optics at PSI). This comes at the cost of increased beam size. For the reference beam optics , the beam size at the isocenter is (11.2±0.6) mm whereas, with the high transmission and scattering foil beam optics, this increases to (20.2±0.8) mm, representing an 80% increase in beam size.

Table 1: Measured transmission using reference beam optics and new beam optics with scattering foil (measured) and asymmetric collimators (simulation). Transmission values are from the cyclotron to different locations along the beamline [5,10,11].

	coupling point (%)	isocenter (%)
Reference optics	0.22 ± 0.007	0.13 ± 0.004
New optics with scattering foil	0.93 ± 0.03	0.40 ± 0.012
New optics with asymmetric collimator	1.2 ± 0.036	0.72 ± 0.036

Use of asymmetric collimator

In this subsection, the main aim is to find an alternative solution to transport higher emittance through the fixed beamline without increasing the emittance.

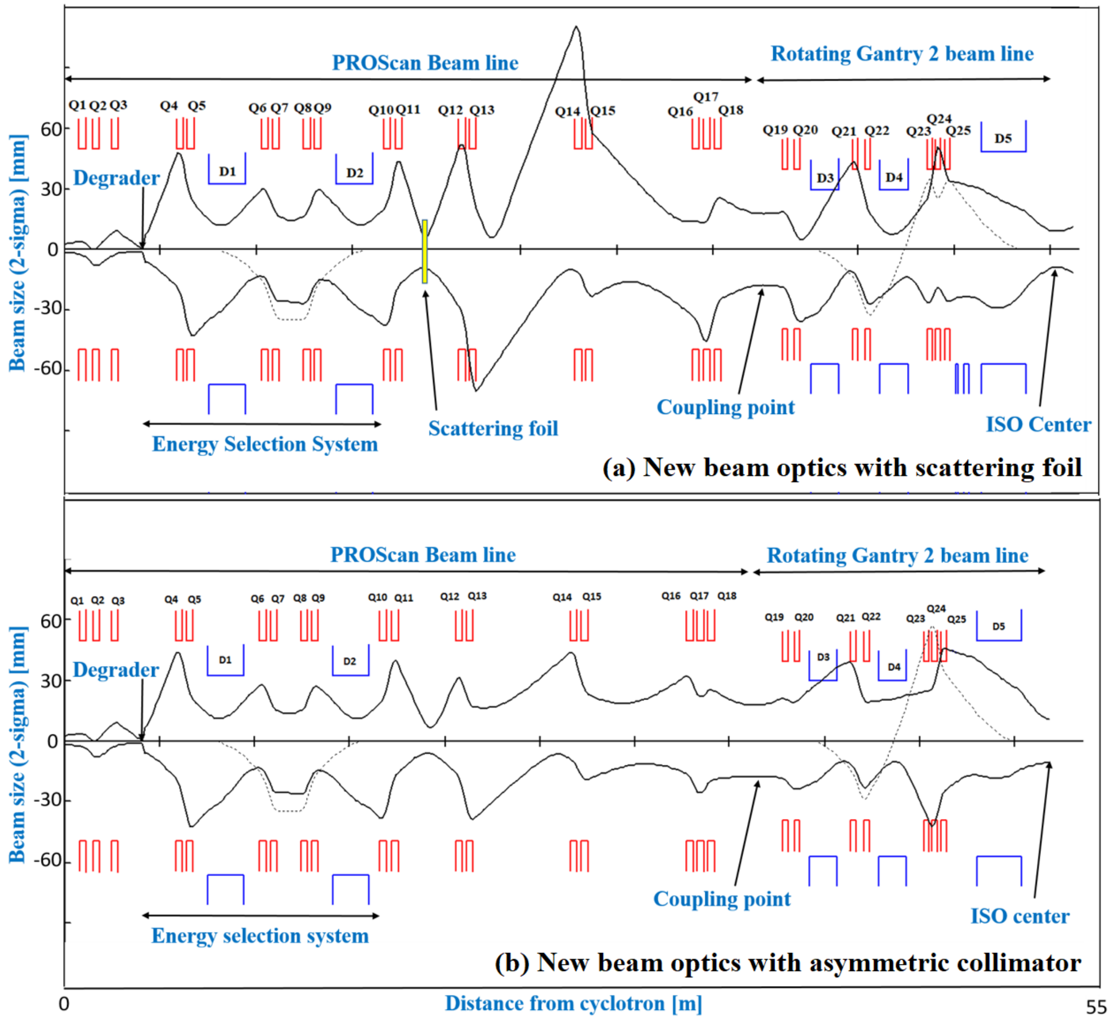

Figure 3: (a) shows the new beam optics with scattering foil transporting 67 *mm*mrad in X-plane and 139 π*mm*mrad in Y-plane up to scattering foil location and transporting almost 145 π*mm*mrad (in both planes) from scattering foil to isocenter. (b) shows the new beam optics with two asymmetric phase space selection collimators transporting 100 π*mm*mrad in both planes. [5,10]

As mentioned before, for proton beam delivery with a gantry, it is required to have the same beam properties at the isocenter for all gantry angles. The most straightforward method to achieve this is to have the same emittance (same beam size and divergence) in both planes at the entrance of the gantry. In general, in most cyclotron-based gantry facilities, two round-shaped collimators, positioned after the degrader, are used which then provide the same beam size and divergence in both planes, which is then symmetrically imaged to the gantry entrance point. Due to the alternating focusing signs of quadrupole lenses and bending magnets, the requirements for beam size and beam divergence at the start of the beam transport after the degrader can be quite different for obtaining a maximum transmission and symmetric emittance. A round-shaped collimator limits the emittance in both planes in the same way, to achieve the symmetric emittance requirement, but at the same time, it limits the emittance in one plane more than necessary.

As the PSI Gantry 2 can transport 100 π*mm*mrad emittance, we have designed the collimator system C1–C2 to select 100 π*mm*mrad in both planes too. We, therefore, selected the beam divergence selection collimator (C2) aperture such, to have the maximum acceptable divergences in both planes, being 10 mrad and 27 mrad in the X and Y-plane, respectively. To also obtain equal emittance in both planes, the beam size in the Y-plane must be three times smaller than the beam size in the X-plane. For this, we design collimator C1 such that it selects a 10 mm beam size in the X-plane, and a 3.7 mm beam size in the Y-plane.

Figure 3(b) shows the beam optics using elliptically shaped asymmetric collimators transporting 100 π*mm*mrad. Although this new beam optics was designed with TRANSPORT [12], BDSIM [13] has been used to estimate the transmission along the beamline. With an asymmetric collimation system, we thus predict an overall transmission from the cyclotron to the isocenter for 70 MeV beam of 0.72%, compared to 0.13% in the reference beam optics, corresponding to an increase of almost a factor of 6 in beam current reaching the patient.

However, this comes at a cost on beam size with the simulated beam size in the air for the reference optics at isocenter being 11.2 ± 0.6 mm, whereas for the asymmetric beam optics, beam size at isocenter is 17.2 ± 0.7 mm, representing an increase of about 50%. With the new system, we could achieve a maximum of 6 nA beam current at the isocenter for 70 MeV beam compared to 1 nA with the reference beam optics [5].

CONCLUSION

In summary, we have shown that for a fixed emittance value, it is possible to maximize proton beam transmission through a gantry by using a small divergence value and large beam size at the CP, together with de-magnifying beam optics imaging from CP to the isocenter. Additionally, we have shown that the use of scattering foil or asymmetric collimator allows transporting 100 π*mm*mrad emittance through fixed beamline while achieving an overall transmission gain of factor 3 or factor 6 respectively. We expect that our proposals for transmission improvement will be applicable in other cyclotron-based facilities to increase the transmission for low-energy beams. However, the magnitude of the transmission increase will be facility dependent due to differences in distances, apertures, materials, and cyclotron energies.

ACKNOWLEDGEMENTS

We thank Dr. Rudolf Doelling for his support in the measurements. We acknowledge the help of the PSI cyclotron operation group, PSI vacuum group, and PSI radiation protection group. This work is funded by PSI's CROSS funding scheme.

REFERENCES

[1] *E. Pedroni at al.*, "The 200-Mev proton therapy project at the Paul Scherrer Institute: conceptual design and practical realization", Med Phys. 1995;22(1):37-53 https://doi.org/10.1118/1.597522.

[2] *A. C. Giovannelli at al.*, "Beam properties within the momentum acceptance of a clinical gantry beamline for proton therapy", Medical Physics, 49(3):1417–1431, 2022. DOI: https://doi.org/10.1002/mp.15449.

[3] *V. Maradia at al.*, Universal and dynamic ridge filter for pencil beam scanning particle therapy: a novel concept for ultra-fast treatment delivery. Physics in Medicine Biology, 67(22):225005, nov 2022. DOI: https://doi.org/10.1088/1361-6560/ac9d1f.

[4] *V. Maradia at al.*, "Ultra-fast pencil beam scanning proton therapy for locally advanced non-smallcell lung cancers: field delivery within a single breath-hold", Radiotherapy and Oncology, jul 2022. DOI: https://doi.org/10.1016/j.radonc.2022.06.018.

[5] *V. Maradia at al.*, "A new emittance selection system to maximize beam transmission for low-energy beams in cyclotron-based proton therapy facilities with gantry", Medical Physics, 48(12):7613–7622, 2021. DOI: https://doi.org/10.1002/mp.15278.

[6] *V. Maradia at al.*, "New gantry beam optics solution for minimizing treatment time in cyclotron-based proton therapy facilities. In: PTCOG 2021 Conference", Particle Therapy Co-Operative Group; 2021. https://doi.org/10.3929/ethz-b-000497120.

[7] *V. Maradia at al.*, "A Novel Beam Optics Concept to Maximize the Transmission Through Cyclotron-based Proton Therapy Gantries", in Proc. IPAC'21, Campinas, SP, Brazil, May 2021, pp. 2477-2479. DOI: https://doi.org/10.18429/JACoW-IPAC2021-TUPAB407.

[8] *V. Maradia at al.*, "A Novel Intensity Compensation Method to Achieve Energy Independent Beam Intensity at the Patient Location for Cyclotron Based Proton Therapy Facilities", in Proc. IPAC'22, Bangkok, Thailand, Jun. 2022, pp. 3004-3006. DOI: 10.18429/JACoW-IPAC2022-THPOMS024

[9] *V. Maradia at al.*, "Increase of the transmission and emittance acceptance through a cyclotron-based proton therapy gantry", Medical Physics, 49(4):2183–2192, 2022. DOI: https://doi.org/10.1002/mp.15505.

[10] *V. Maradia at al.*, "Application of a scattering foil to increase beam transmission for cyclotron-based proton therapy facilities. Frontiers in Physics, 10, 2022. DOI: https://doi.org/10.3389/fphy.2022.919787.

[11] *V. Maradia at al.*, "A Novel Method of Emittance Matching to Increase Beam Transmission for Cyclotron Based Proton Therapy Facilities: Simulation Study", in Proc. IPAC'22, Bangkok, Thailand, Jun. 2022, pp. 3007-3010. DOI: 10.18429/JACoW-IPAC2022-THPOMS025.

[12] *K. L. Brown at al.*, "A Computer Program for Designing Charged Particle Beam Transport Systems", CERN; 1980 DOI: http://dx.doi.org/10.5170/CERN-1980-004

[13] *L. J. Navay at al.*, "BDSIM: an accelerator tracking code with particle–matter interactions. Comput Phys Commun. 2020; 252:107200. DOI: https://doi.org/10.1016/j.cpc.2020.107200

ISBN: 978-3-95450-212-7 ISSN: 2673-5482 doi:10.18429/JACoW-CYCLOTRONS2022-FRBI02

DESIGN OF A SPIRAL INFLECTOR AT iTHEMBA LABS FOR INJECTING THE BEAM INTO A CYCLOTRON

A. H. Barnard†, iThemba Laboratory for Accelerator Based Sciences, Cape Town, South Africa

Abstract

Using a Belmont-Pabot spiral inflector for axial beam injection presents difficulties when matching the beam emittance to the cyclotron acceptance. For an electrostatic inflector one of the potential solutions to this problem is to use transverse electric field gradients to influence and optimise the optics. Here we extend this approach to magnetic spiral inflectors. It is demonstrated that the gradient of the magnetic field along the central trajectory can be controlled by an appropriate permanent magnet inflector design, and that these gradients have a large influence on the optics. The transverse gradients are numerically optimised and the performance compared to an optimised electrostatic spiral inflector. A faster numerical method for accurately determining the electric field of an electrostatic inflector is also presented.

INTRODUCTION

Traditional Belmont-Pabot spiral inflectors suffer from a large vertical divergence, and in addition to this the transverse-longitudinal coupling results in a de-bunching longitudinal spread [1]. Both of these issues decrease the transmission of the cyclotron. Recent attempts at addressing these problems at several cyclotron facilities have made use of transverse electric field gradients along the central path to attempt to influence the optics and focus the beam [2-5]. In previous work [1] we have shown that in the most general case the electric potential can be described, to second order in the transverse displacements, by:

$$\phi = -u_r E_0 - Q_1 E_0 \frac{u_r^2 - h_r^2}{2} - Q_2 E_0 h_r u_r - \frac{u_r^2}{2} \hat{s}' \cdot \boldsymbol{E}_0$$

Where $Q_1(s)$ and $Q_2(s)$ are quadrupole parameters, and may be freely selected by an inflector designer. The coordinates $(u_r, h_r s)$ are the standard rotated coordinates used in spiral inflector design, where the electric field points in the $\hat{u}_r$ direction. The corresponding electric fields are then:

$$E_{u_r} = E_0 + u_r(Q_1 E_0 + \hat{s}' \cdot \boldsymbol{E}_0) + h_r Q_2 E_0 \quad \text{(1a)}$$

$$E_{h_r} = u_r Q_2 E_0 - h_r Q_1 E_0 \quad \text{(1b)}$$

$$E_s = u_r E_0' - h_r \kappa_s E_0 \quad \text{(1c)}$$

By numerically optimising the two free quadrupole parameters $Q_1(s), Q_2(s)$ an inflector design was obtained that showed good vertical and longitudinal performance. This device was constructed and experimentally shown to improve the transmission through the Solid Pole Cyclotron 2 (SPC2) at iThemba LABS by 60%.

In this article the application of a similar optimisation process to a permanent magnet spiral inflector is presented.

†hbarnard@tlabs.ac.za

FASTER NUMERICAL METHOD

Optimisation of an electrostatic inflector design involves repeated numerical computations of the electric field, for a great number of proposed inflectors. This was previously done using TOSCA, which required about an hour per inflector. To speed this up in the past a method was used to estimate the electric field, by combining the results from a number of pre-calculated TOSCA simulations and linearly extrapolating [5]. This method could compute the transfer matrix of a new inflector within about 5 seconds, but lacked accuracy.

A new numerical method was therefore developed that is able to accurately compute the inflector transfer matrix in a short time (about 4 seconds). It is based on calculating the surface charge density on the inflector electrodes, by minimising the potential energy.

Suppose that the inflector surface has been divided into approximate squares, of side length L_i and containing a charge q_i per square. Such a meshing of the electrodes is shown in Fig. 1.

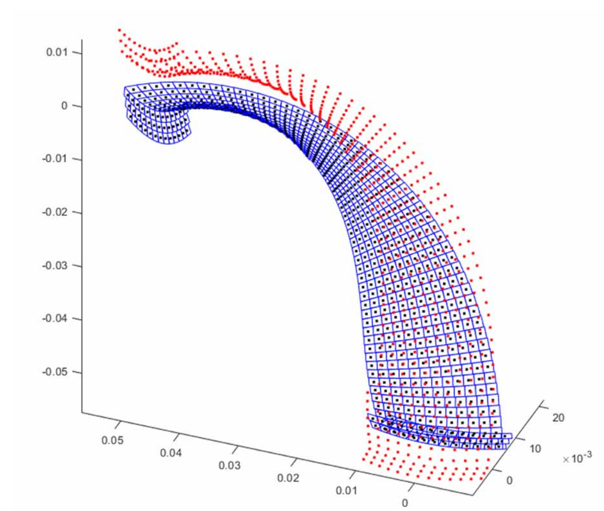

Figure 1: Square meshing of the negative electrode, also showing the centroids of the squares on both electrodes.

The total potential energy can be expressed as:

$$U = \frac{1}{2} \boldsymbol{q} \cdot \boldsymbol{V}_q + \boldsymbol{q} \cdot \boldsymbol{V}_E$$

Where $\boldsymbol{V}_q$ is the voltage due to the surface charges and $\boldsymbol{V}_E$ is an externally applied voltage. We write the voltage as $\boldsymbol{V}_q = D\boldsymbol{q}$ where:

$$D_{ij} = \frac{f_{ij}}{4\pi\epsilon_0 |\boldsymbol{r}_i - \boldsymbol{r}_j|}$$

23rd Int. Conf. Cyclotrons Appl. CYCLOTRONS2022, Beijing, China JACoW Publishing
ISBN: 978-3-95450-212-7 ISSN: 2673-5482 doi:10.18429/JACoW-CYCLOTRONS2022-FRBI02

Here $\boldsymbol{r}$ is the location of the centre of the square, and f_{ij} is a geometric factor to account for the finite size and relative orientation of the squares. As the squares become smaller we can set $f_{ij} = 1$. This is done for all squares, except where $i = j$, in which case the self-energy of a square results in:

$$D_{ii} = \frac{2}{4\,\pi\epsilon_0 q_i^2} \int\int \frac{1}{|\boldsymbol{r}_1 - \boldsymbol{r}_2|} dq_1 dq_2 \approx 2\frac{1.4865}{4\pi\epsilon_0 L_i}$$

The total charge on electrode n is fixed to be Q_n, and this constraint is enforced using the Lagrange multiplier λ_n. To help with this we introduce the electrode indicator c_i^n which is 1 if square i is in electrode n, and zero otherwise. The optimisation problem becomes:

$$\min \frac{1}{2}\boldsymbol{q}\cdot D\boldsymbol{q} + \boldsymbol{q}\cdot\boldsymbol{V}_E + \lambda_1 \boldsymbol{q}\cdot\boldsymbol{c}^1 + \cdots + \lambda_N \boldsymbol{q}\cdot\boldsymbol{c}^N$$

The solution is:

$$D\boldsymbol{q} + \boldsymbol{V}_E + (\lambda_1\boldsymbol{c}^1 + \cdots + \lambda_N\boldsymbol{c}^N) = 0$$

But note that $D\boldsymbol{q} + \boldsymbol{V}_E$ is in fact the total voltage $\boldsymbol{V}$, so the Lagrange multiplier is just negative of the voltage on an electrode $\lambda_n = -V^n$, and the surface charge per square is obtained from:

$$\boldsymbol{q} = \mathrm{D}^{-1}(\mathbf{V} - \mathbf{V}_{\mathrm{E}})$$

These surface charges $\boldsymbol{q}$ are computed first, and then stored. During run-time, when tracing the path of a particle through the inflector, the electric field at $\boldsymbol{x}$ is computed as:

$$\boldsymbol{E}(\boldsymbol{x}) = \frac{1}{4\,\pi\epsilon_0}\sum_i q_i \frac{\boldsymbol{x} - \boldsymbol{r}_i}{|\boldsymbol{x} - \boldsymbol{r}_i|^3}$$

With the caveat that the distance to the closest surface charge should not be too small. In practice this limit is found to be about twice the largest value of L_i.

This surface charge method was tested in several simple cases with known analytical solutions. For a parallel plate capacitor, the error in the electric field between the plates was 0.5%. The induced surface charge on a flat earthed plate due to the presence of an external test charge was computed to within 1%. A comparison of this method with TOSCA is provided in Fig. 2, where they correspond quite well.

MAGNETIC SPIRAL INFLECTOR

The use of permanent magnets to construct a magnetic spiral inflector has been proposed in the past [6]. An advantage of such a magnetic inflector is that higher injection energies can be achieved than with an electric inflector, which will reduce the impact of space-charge in the inflector. Here we investigate a magnetic inflector (in the absence of space charge for now), to see if it can be optimised in a similar way to the electric inflector, by creating quadrupole fields along the central path.

The magnetic field is selected so that the force on the central path due to the permanent magnets is the same as the electric force in an electric inflector:

$$\boldsymbol{E} = E_0\hat{u}_r \rightarrow \boldsymbol{B} = -\frac{E_0}{v}\hat{h}_r$$

The magnetic field is produced by a number of modified Halbach rings, which are known to create a strong internal magnetic field and a much weaker external field. Figure 3 shows such an inflector and Fig. 4 shows the numerically measured field on the central path.

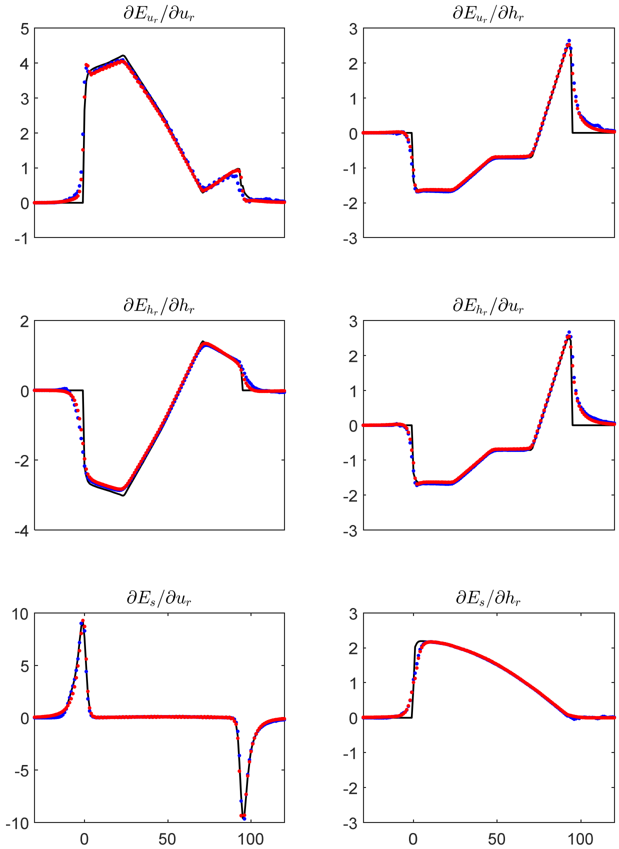

Figure 2: The field gradients of an inflector as computed using: TOSCA (blue dots), the surface charge method presented here (red dots), and the analytical approximation via Eq. (1) (black solid line).

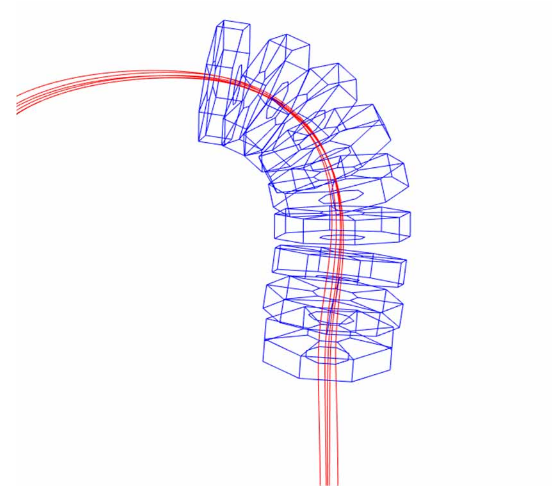

Figure 3: The magnetic inflector made of 8-sided Halbach rings.

ISBN: 978-3-95450-212-7 ISSN: 2673-5482 doi:10.18429/JACoW-CYCLOTRONS2022-FRBI02

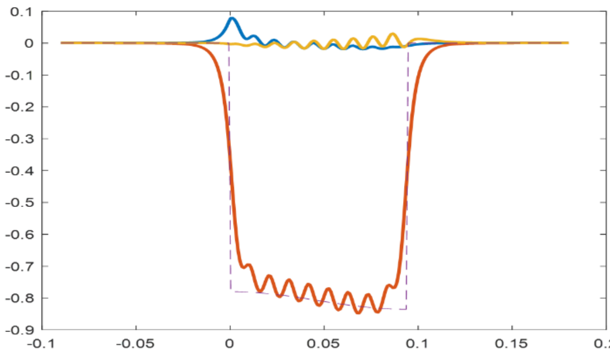

Figure 4: The magnetic field (T) along the central path (m). B_{u_r} is blue, B_{h_r} is red and B_s is yellow. The oscillations are due to the discrete number of rings.

The internal field of the Halbach ring is a function of the magnetisation of the ring segments. By using 8-sided rings, it is possible to create quadrupoles along the central path, as shown in Fig. 5. The radial and azimuthal components of the magnetisation of the ring can then be expressed as:

$$M_r = M_0(\sin\theta - K_1\cos 2\theta - K_2\sin 2\theta)$$
$$M_\theta = M_0(-\cos\theta - K_1\sin 2\theta + K_2\cos 2\theta)$$

Where θ refers to the azimuthal angle of the centre of each of the 8 segments, and K_1 and K_2 are quadrupole parameters.

The magnetic field due to the inflector only can be computed from the gradient of the scalar potential ψ. This is similar to the electric case, and by analogy this can be expressed as:

$$\psi = h_r B_0 - Q_1 B_0 \frac{u_r^2 - h_r^2}{2} - Q_2 B_0 u_r h_r - \frac{u_r^2}{2}\,\hat{s}'\cdot\boldsymbol{B}_0$$

Giving the fields to first order in the displacements u_r, h_r:

$$B_{u_r} = u_r(Q_1 B_0 + \hat{s}'\cdot\boldsymbol{B}_0) + h_r Q_2 B_0 \qquad (2a)$$
$$B_{h_r} = -B_0 + u_r Q_2 B_0 - h_r Q_1 B_0 \qquad (2b)$$
$$B_s = -h_r B_0' + u_r \kappa_s B_0 \qquad (2c)$$

These expressions were confirmed by numerically evaluating the fields, as shown in Fig. 6. Note that Q_1, Q_2 which describe the quadrupole nature of the magnetic fields, are almost proportional to K_1, K_2 which describe the magnetisation of the Halbach rings, but the exact relationship depends on the size of the rings and their placement along the central path.

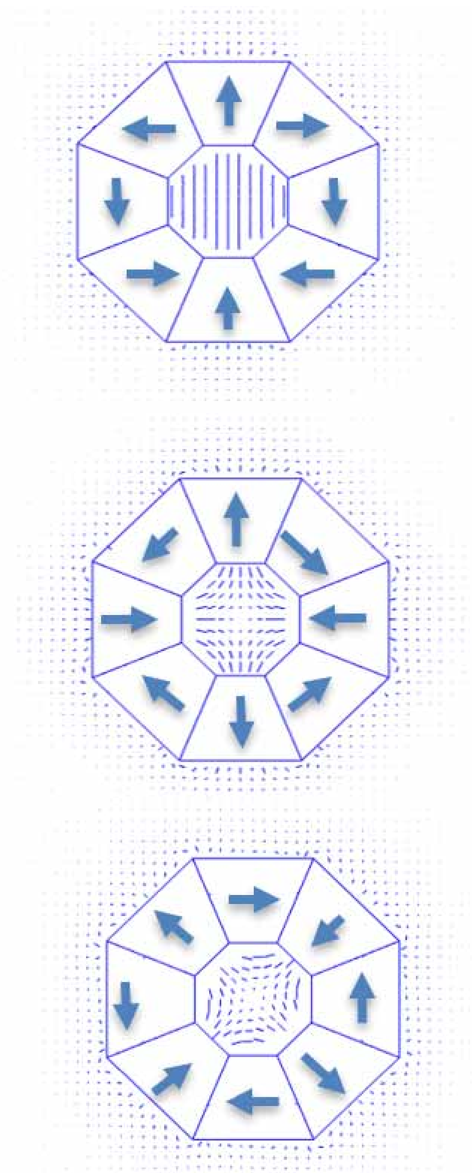

Figure 5: Magnetisation of the rings to produce a dipole field (top) and normal and skew quadrupole fields (middle and bottom).

ISBN: 978-3-95450-212-7 ISSN: 2673-5482 doi:10.18429/JACoW-CYCLOTRONS2022-FRBI02

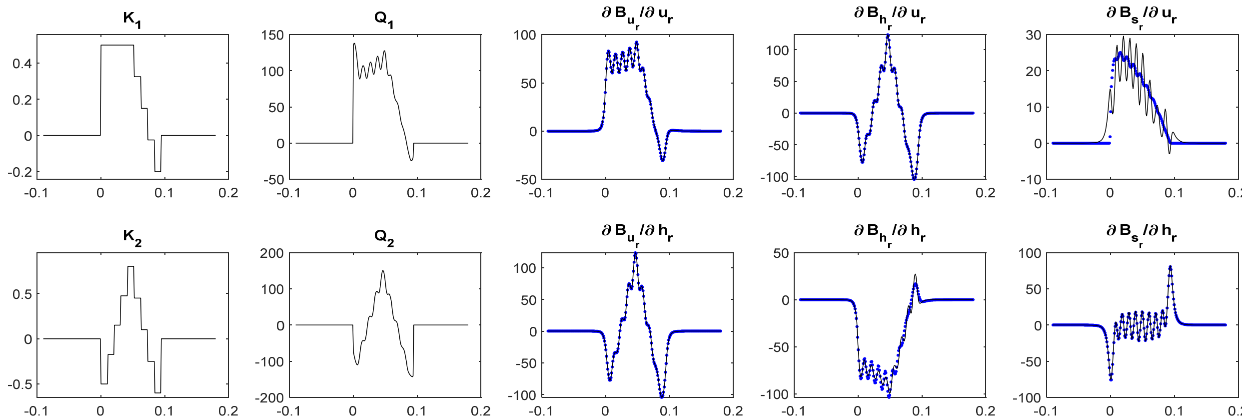

Figure 6: Numerical verification of Eq. (2), showing various properties plotted against the inflector path length (m). From left to right: 1) The K values use to design the Halbach rings. 2) The resulting Q values describing the quadrupole fields. 3) Gradients of B_{u_r}, with numerical values in blue and Eq. (2) in black. 4) Gradients of B_{h_r}. 5) Gradients of B_s.

OPTIMISATION

The aim was to optimise the transmission of the beam through the SPC2 cyclotron at iThemba LABS. In the past the acceptance of the cyclotron was not known, and hence the optimisation only aimed to limit the vertical and longitudinal emittance and spread [1, 5]. For this reason, a new numerical model of the SPC2 was created to evaluate its acceptance.

The magnetic fields were partly obtained from a full 3D TOSCA simulation of the cyclotron [7]. The electric field was based on a numerical solution of the electric field in the acceleration gap. Trim coils, based on TOSCA simulations, were added to obtain isochronism. The central trajectory was found by injecting a particle backwards from extraction, along an accelerated equilibrium orbit, and this trajectory corresponded well to the original central path calculated by the designers of SPC2. The main losses were radially on the slits in the central region and vertically on the slits and the dees.

It was found that an ellipse poorly represented the complex acceptance shape in phase space. A better representation of the acceptance was to select and number ($\sim 10^4$) of random points inside the acceptance and to replace each point with a ball of constant radius in phase space. The volume occupied by these balls was then a better representation of the acceptance, and testing if a new point lay inside the acceptance is very quick.

The inflector simulation started in the axial hole in the yoke where the magnetic field is zero, and ends in the region between the inflector exit and the first acceleration gap, where the electric field is almost zero.

The injected beam is focussed at the inflector entrance, and a first harmonic buncher is used. The voltage of the buncher is set so it focusses at the first acceleration gap, which requires accounting for the optical length of the inflector (R_{56}).

To compute the transmission of the beam through SPC2 when using a specific inflector, the procedure was:

1. Compute the linear transfer matrix of the inflector R
2. Select a random particle in the DC beam upstream of the buncher
3. Propagate to the start of the inflector calculation (not linear in time due to sinusoid in buncher)
4. Transfer the particle through the inflector using its linear transfer matrix R
5. Check if the particle is in the cyclotron acceptance
6. Go back to 2 and repeat for ~1e5 particles

RESULTS

The optimisation space for the electric inflector was the two functions $Q_1(s)$ and $Q_2(s)$. For the magnetic inflector it was the $K_1(n), K_2(n)$ parameters that had to be selected for each ring n. The optimal designs are shown in Fig. 7-8. Table 1 shows the transmission through SPC2 before and after optimisation, where the non-optimised inflector refers to the K = 0 case for magnetic inflectors, and the Q = 0 case for electric inflectors.

Table 1: Transmission through the Cyclotron

	Electric	**Magnetic**
Non-optimised	26%	33%
Optimised	43%	45%
Relative Improvement	65%	36%

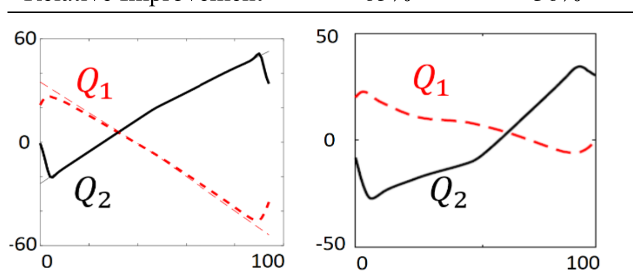

Figure 7: Quadrupole parameters (m^{-1}) vs path length (mm). The optimal design for the electric inflector in this work (left) and a comparison with previous work in [1] (right).

ISBN: 978-3-95450-212-7 ISSN: 2673-5482 doi:10.18429/JACoW-CYCLOTRONS2022-FRBI02

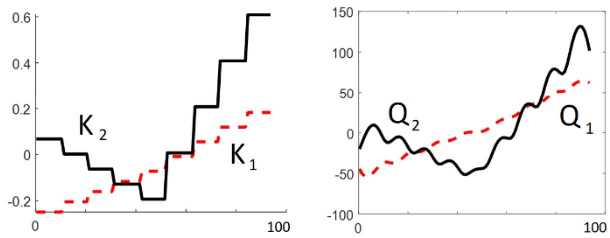

Figure 8: The optimal design of the magnetic inflector vs the path length (mm). Left: the ring magnetisation K values (unitless). Right: Q values (m^{-1}) of the resultant quadrupole fields.

DISCUSSION

In both the magnetic and electric case there is a substantial improvement when optimising the design. The final transmission of the electric and magnetic inflectors is similar. Note that the actual transmission through the SPC2 cyclotron is typically 5%, which is much less than these calculated values. This is partly because we have not accounted for losses at extraction yet (known to be a factor of about 3) and the emittance of the injected beam is also uncertain. This is to be investigated in further work in the future.

CONCLUSION

The magnetic inflector can be optimised in a similar way to the electric inflector, by creating quadrupole fields in the transverse plane.

REFERENCES

[1] A.H. Barnard *et al.*, “Longitudinal and vertical focusing with a field gradient spiral inflector,” *Phys. Rev. Accel. Beams*, vol. 24, Feb. 2021, pp. 023501. doi:10.1103/PhysRevAccelBeams.24.023501

[2] I. A. Ivanenko, “The Methods of Compensation of the Beam Vertical Divergence at the Exit of Spiral Inflector in Cyclotrons,” in *Proc. Cyclotrons'16*, Zurich, Switzerland, Sep. 2016, pp. 221-223. doi:10.18429/JACoW-Cyclotrons2016-TUP25

[3] V. L. Smirnov, “Central Region Design in a Compact Cyclotron.” *Phys. Part. Nucl. Lett.*, vol 16, Apr. 2019, pp. 34-45. doi:10.1134/S1547477119010114

[4] H. Tsutsui, “Accelerator and Cyclotron,” European Patent Office EP2391190A2, JP 2010120716, May 2010.

[5] A. H. Barnard *et al.*, “Vertical Focussing with a Field Gradient Spiral Inflector,” in *Proc. Cyclotrons'19*, Cape Town, South Africa, Sep. 2019, pp. 58-61. doi:10.18429/JACoW-CYCLOTRONS2019-MOP016

[6] L. Calabretta *et al.*, “Review of High-Power Cyclotrons and Their Applications,” in *Proc. Cyclotrons'19*, Cape Town, South Africa, Sep. 2019, pp. 289-293. doi:10.18429/JACoW-CYCLOTRONS2019-THB01

[7] J. G. De Villiers *et al.*, “Numerical Orbit Tracking in 3D Through the Injector Cyclotron for Heavy Ions at iThemba LABS,” in *Proc. Cyclotrons'16*, Zurich, Switzerland, Sep. 2016, pp. 71-74. doi:10.18429/JACoW-Cyclotrons2016-MOP10

ISBN: 978-3-95450-212-7 ISSN: 2673-5482 doi:10.18429/JACoW-CYCLOTRONS2022-FRB003

THE STUDY OF THE ISOCHRONOUS MAGNETIC FIELD AND THE EQUILIBRIUM ORBIT OF CS-30 CYCLOTRON

B. Fan[1], L. Chen[1], K. Li[1], J. Y. Peng[1], Z. H. Li[2,*]
[1] College of Physics Science and Technology, Sichuan University, Chengdu, China
[2] Key Laboratory of Radiation Physics and Technology of the Ministry of Education, Institute of Nuclear Science and Technology, Sichuan University, Chengdu, China

Abstract

The CS-30 accelerator of the Institute of Nuclear Science and Technology of Sichuan University is a three-fan accelerator with constant angular width (45 degrees) at small radius and blade thickness increasing with radius at larger radius. In this paper, the magnetic field is analyzed, and the static equilibrium orbit, revolution frequency, oscillation frequencies and other data are calculated. These functions can be integrated to guide the accurate magnet numerical model setup of the existing CS-30 accelerator, which can be used in de education demonstration and experimental phenomena analysis. The optimization algorithm is innovatively introduced in the static equilibrium orbit calculation, which reduces the dependence of the results on the initial value and significantly improves the calculation speed. The calculation method presented in this paper is suitable for all cyclotron.

INTRODUCTION

CS-30 is produced by TCC Company in the United States and introduced by the State Science and Technology Commission in February 1984. It is the first cyclotron with compact structure introduced from abroad in China. In 2003, the cyclotron was moved from Beijing to the Institute of Nuclear Science and Technology of Sichuan University. After one year of installation and tuning, proton beams and α ions were accelerated to the internal target. After then it was routinely in operation and provide beams for experimental more than 100 hours per year. Now, it's mainly be used to produce isotopes, study irradiation effect of materials, and teaching demonstration device. Its application was limited by the absence of the external target system. The extraction elements are works well, what we need to extract the beam out of the cyclotron are just the beam line and the target station. Recently a beam line will be built and an external He^{2+} radiation target station will be built, which can significantly expend the application of the cyclotron. Since we never extract beam out before and lack of the data of the extraction elements settings, we need to study the beam dynamics properties to guide us in finding them. In order to do this, we need setup the numerical model of the cyclotron, so that we can get the detailed magnetic field distribution, which can be used in beam dynamics analysis. At the same time, the numerical model can also be used in the education.

* lizhihui@scu.edu.cn

METHODS AND MODEL

The 3D model of CS-30 magnet is shown in Fig. 1. The only thing we are not sure is the height of the steps on the fan, which are used to get the final isochronous magnetic field. In order to find the right number of the steps height, we need to analysis the magnetic field calculated from the model. If it is the isochronous, then the model is right; if it is not, we need to change the steps height until the isochronous field is obtained.

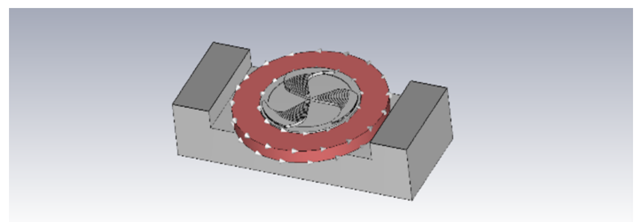

Figure 1: 3D model of the cyclotron magnet.

The magnetic induction intensity of CS-30 is shown in Fig. 2. To analyze the magnetic field. The most important thing is to calculate the equilibrium orbits. There are two main methods to calculate the equilibrium orbit. The first is the analytical method, which makes Fourier expansion of the magnetic field along the azimuth angle, and obtains the analytical solution under the first order approximation; the second is the numerical method, which is solved by the integral formula.

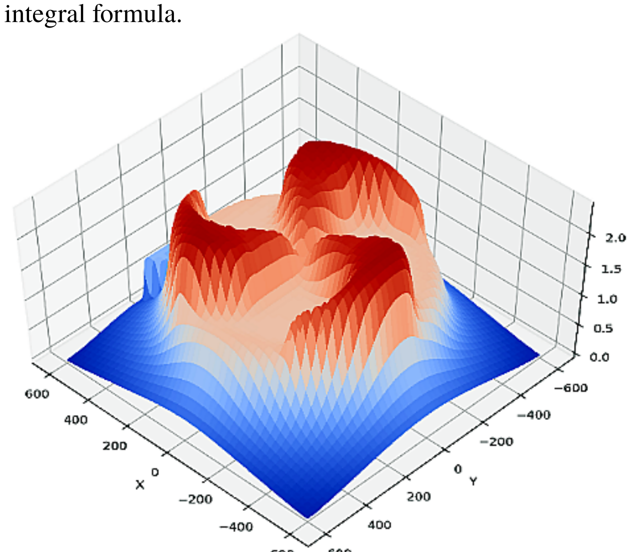

Figure 2: Magnetic induction intensity.

ISBN: 978-3-95450-212-7 ISSN: 2673-5482 doi:10.18429/JACoW-CYCLOTRONS2022-FRB003

Equilibrium Orbit

Analytical methods In the central plane of the synchrotron, the magnetic field distribution can be expressed as Eq. (1) [1]:

$$B(r,\theta) = \overline{B}(r)\,[1 + F(r,\theta)] \tag{1}$$

$F(r,\theta)$ is the magnetic field flutter function, which can be expanded by Fourier series:

$$F(r,\theta) = \sum_n A_n(r)\cos n\theta + B_n(r)\sin n\theta. \tag{2}$$

The motion of the central plane of the accelerator is:

$$\begin{aligned} \frac{dr}{d\theta} &= \frac{rp_r}{q}, \\ \frac{dp_r}{d\theta} &= q - \frac{ZerB_z}{p}, \\ \frac{dp_r}{d\theta} &= \sqrt{1 - p_r^2}. \end{aligned} \tag{3}$$

We could set the momentum $p = Zer_0\overline{B}(r_0)$ of static equilibrium orbits of particles are as follows:

$$r_e = r_0(1 + x_e). \tag{4}$$

where r_0 is the radius of the orbit corresponding to the momentum, similar to what we did with the magnetic field, Fourier expansion:

$$x_e = \gamma + \sum_n \alpha_n \cos n\theta + \beta_n \sin n\theta \tag{5}$$

$$\begin{aligned} \gamma = &-\sum_n \frac{3n^2-2}{4(n^2-1)^2}(A_n^2 + B_n^2) \\ &+ \frac{1}{2(n^2-1)^2}(A_n A_n' + B_n B_n') \end{aligned} \tag{6}$$

$$r_e = r_0\left(1 + \gamma + \sum_n \frac{A_n}{n^2+1}\cos n\theta + \frac{B_n}{n^2+1}\sin n\theta\right) \tag{7}$$

The equilibrium orbital in different radius are shown in Fig. 3.

Numerical methods From Eq. (3), the motion of a particle in a periodic field can be expressed as a matrix

$$Y(\theta) = MY(\theta_0) \tag{8}$$

$$Y(s) = \begin{pmatrix} y(\theta) \\ y'(\theta) \end{pmatrix}, \quad M = \begin{pmatrix} m_{11} & m_{12} \\ m_{21} & m_{22} \end{pmatrix} \tag{9}$$

For a given energy E, we can find the corresponding reference circle radius r_0 by the circular orbit approximation, set

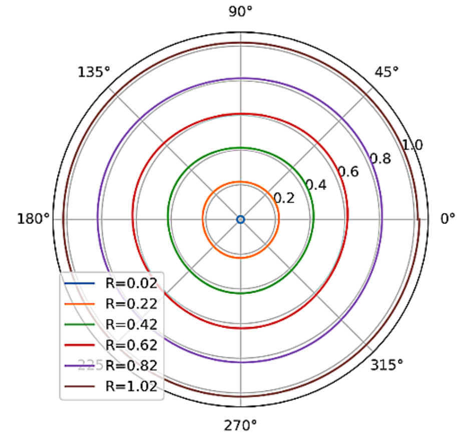

Figure 3: The equilibrium orbital computed analytically.

the initial position as (r_0, θ_0), there are three particles in the vicinity of (r_0, θ_0), their initial conditions are respectively

$$\begin{aligned} r = r_0 \quad p_r &= p_0, \\ r = r_0 + \delta r \; p_r &= p_0, \\ r = r_0 \quad p_r &= p_0 + \delta p, \end{aligned} \tag{10}$$

δr, δp are optional small quantities. Plug them into the equation of motion, integrate them and you get one cycle or one cycle. The latter solutions are respectively

$$\begin{aligned} r = r_{0f} \quad p_r &= p_{0f}, \\ r = r_{1f} \quad p_r &= p_{1f}, \\ r = r_{2f} \quad p_r &= p_{2f}, \end{aligned} \tag{11}$$

if (r_e, p_e) is the equilibrium orbit parameter at θ_0, then

$$y = r - r_e \quad y' = p - p_e \tag{12}$$

$$\begin{cases} m_{11}(r_0 - r_e) + m_{12}(p_0 - p_e) = r_{0f} - r_e \\ m_{21}(r_0 - r_e) + m_{22}(p_0 - p_e) = p_{0f} - p_e \\ m_{11}(r_0 + \delta r - r_e) + m_{12}(p_0 - p_e) = r_{1f} - r_e \\ m_{21}(r_0 + \delta r - r_e) + m_{22}(p_0 - p_e) = p_{1f} - p_e \\ m_{11}(r_0 - r_e) + m_{12}(p_0 + \delta p - p_e) = r_{2f} - r_e \\ m_{21}(r_0 - r_e) + m_{22}(p_0 + \delta p - p_e) = p_{2f} - p_e \end{cases} \tag{13}$$

Solve the equations above:

$$\begin{cases} m_{11} = \frac{r_{1f} - r_{0f}}{\delta r} \\ m_{12} = \frac{r_{2f} - r_{0f}}{\delta p} \\ m_{21} = \frac{p_{1f} - p_{0f}}{\delta r} \\ m_{22} = \frac{p_{2f} - p_{0f}}{\delta p} \end{cases} \tag{14}$$

Define:

$$\begin{aligned} m_{11}' &= m_{11} - 1 \\ m_{22}' &= m_{22} - 1, \\ A &= m_{11}' m_{22} - m_{12} m_{21}. \end{aligned} \tag{15}$$

ISBN: 978-3-95450-212-7 ISSN: 2673-5482 doi:10.18429/JACoW-CYCLOTRONS2022-FRB003

An approximation of (r_e, p_e) is obtained:

$$\begin{cases} r_e = r_0 + \frac{m_{22}'}{A}(r_0 - r_{0f}) - \frac{m_{12}}{A}(p_0 - p_{0f}) \\ p_e = p_0 + \frac{m_{11}'}{A}(p_0 - p_{0f}) - \frac{m_{21}}{A}(r_0 - r_{0f}) \end{cases} \tag{16}$$

By redoing the above calculation with (r_0, θ_0) instead of (r_0, θ_0), the exact value of (r_e, p_e) can be obtained after several iterations.

But this method relies heavily on the initial value, and it is easy to iterate over the answer because the initial value is not accurate enough.

This paper come up with a new method, which we call it optimization method. First, we set a particle with $[r_0, p_0]$. Put it in the equation of motion for 1/3 circle, then we could have $[r_e, p_e]$. Use sequential least squares to minimize D ($D = (r_e - r_0)^2 + (p_e - p_0)^2$) we can get pretty good equilibrium orbit.

There's a reason why this article uses 1/3 turn, because the magnetic field is triple symmetric, if you let the particles go all the way around. The particle will appear as shown in Fig. 4.

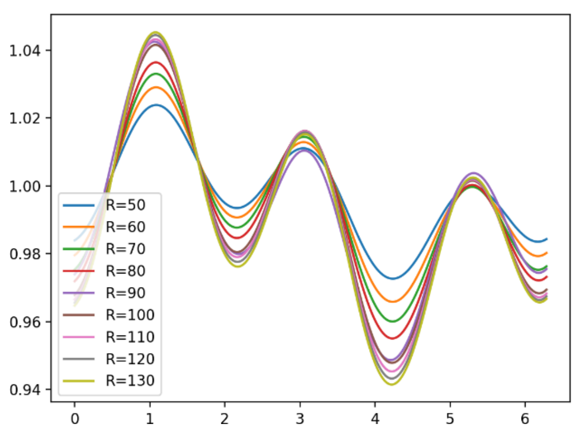

Figure 4: After one rotation.

Only if you set it to 1/3 turn can you get a triple symmetric equilibrium orbit (shown in Fig. 5).

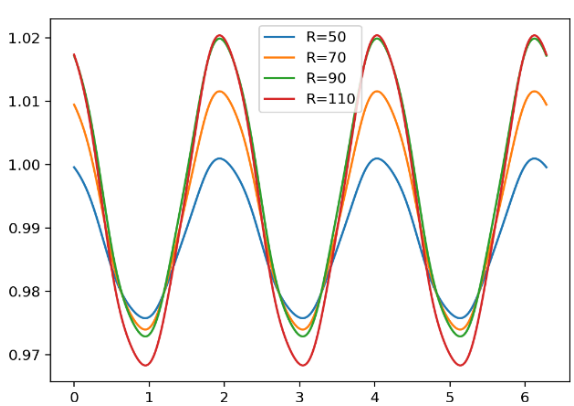

Figure 5: After one rotation.

Isochronous and Stable Evaluation

The oscillation frequency is shown in Fig. 6.

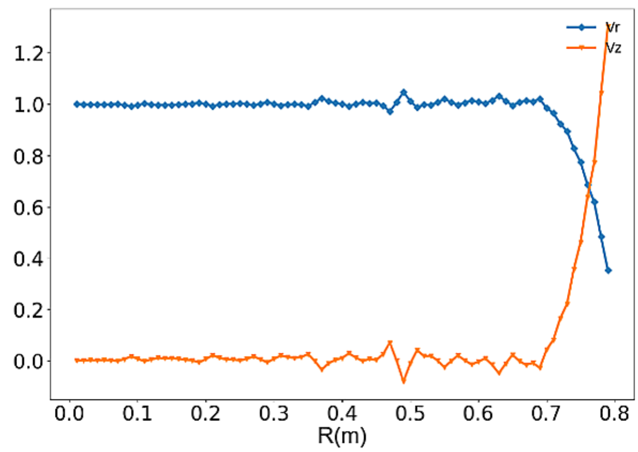

Figure 6: ν_r is the radial frequency, ν_z is the vertical frequency.

The period is shown is Fig. 7.

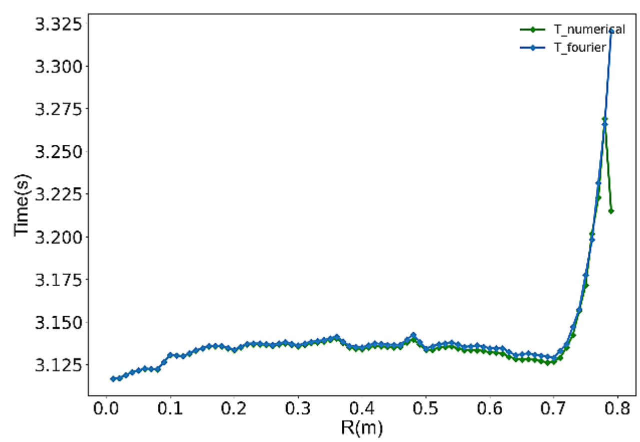

Figure 7: Period calculated by Numerical method and Analytical method.

CONCLUSION

The analysis of the magnetic field of the CS-30 is complete. A new method is adopted to calculate the equilibrium orbits. The magnetic field data is not accurate at large radius, which is speculated to be due to 1: inaccurate modelling, 2: The material of the yoke is unclear. I will solve these problems in my later work.

REFERENCES

[1] H. L. Hagedoorn and N. F. Verster, "Orbits in an AVF cyclotron", *Nucl. Instrum. Methods*, vol. 18–19, pp. 201-228, 1962. doi:10.1016/S0029-554X(62)80032-9

ISBN: 978-3-95450-212-7 ISSN: 2673-5482 doi:10.18429/JACoW-CYCLOTRONS2022-FRB004

ERROR MAGNETIC FIELD DUE TO THE MEDIAN PLANE ASYMMETRY AND ITS APPLICATIONS IN THE CYCLOTRON

Lige Zhang*, Yi-Nong Rao, Rick Baartman, Yuri Bylinskii, Thomas Planche
TRIUMF, Vancouver, B.C., Canada

Abstract

Cyclotrons have a median plane symmetric structure. But the pole's geometric error and the unevenly magnetized soft iron give rise to non-zero asymmetrical fields in the geometric median plane. The asymmetric field can shift the vertical position of the beam. Moreover, The error of the tilted median plane can be the driving force when the tunes pass through coupling resonances. In this paper, we take the TRIUMF 500 MeV cyclotron as an example to study the asymmetric field resulting from imperfect median plane symmetry. An approach due to M. Gordon, and a highly accurate compact finite differentiation method are used to investigate the historical field survey data, which reveals redundancy in the survey data. The redundancy was used in this study to correct the error in the measurement data. Further, the median plane asymmetry field could be manipulated using trim coils or harmonic coils with top and bottom coil currents in opposite directions ('Br-mode'). Using the created asymmetric field, we improved the vertical tune measurement method to investigate the linear coupling resonance in TRIUMF 500 MeV cyclotron. Eventually, the coupling resonance is corrected and avoided using the available harmonic coils and trim coils.

INTRODUCTION

The median plane asymmetric field in a small gap cyclotron or cyclotron with a high magnetic field is usually negligible, and in that case, the surveyed or calculated axial field B_z in the median plane is usually sufficient for the beam dynamics study. But for a large gap magnet with low magnetic field, such as the TRIUMF 500 MeV cyclotron, the asymmetric field can significantly shift the vertical position of the beam. Moreover, the error of the tilted median plane can be the driving force when the tunes pass through coupling resonances [1]. To study the effect of the asymmetric field on the beam dynamics, only the field survey data can be used while the finite element analysis calculation can not reveal the pole machining errors and the variations of material properties of the steel. Using Gordon's field expansion technique [2], we have discovered self-consistency errors in these field data. However, these are easily and convincingly corrected, as will be shown. After correcting the errors in the measurement data, we recalculated the properties of static equilibrium orbits. Further, we have optimized the trim coils' settings to achieve a better beam vertical centering.

* lzhang@triumf.ca

FIELD EXPANSION OUT OF MEDIAN PLANE: GORDON'S APPROACH

The magnetic field map must satisfy Maxwell's equations to sufficient order. In a cyclotron, a typical way is to expand the field relative to the median plane. Gordon's approach is one of these; it is derived from the scalar potential Ψ that satisfies Laplace's equation. By solving the 3D Laplace equation using an operator trick, we get the potential Ψ expanded in powers of axial position z as follows [2]

$$\begin{aligned}
\Psi &= \Psi_o + \Psi_e, \\
\Psi_o &= zB - \frac{z^3}{3!}\nabla_2^2 B + \frac{z^5}{5!}\nabla_2^4 B - \ldots, \\
\Psi_e &= C - \frac{z^2}{2!}\nabla_2^2 C + \frac{z^4}{4!}\nabla_2^4 C - \ldots,
\end{aligned} \tag{1}$$

where $B = B(r, \theta)$ and $C = C(r, \theta)$, and where ∇_2^2 is the 2-dimensional Laplace operator

$$\nabla_2^2 \Psi = \frac{1}{r}\frac{\partial}{\partial r}\left(r\frac{\partial \Psi}{\partial r}\right) + \frac{1}{r^2}\frac{\partial^2 \Psi}{\partial \theta^2}. \tag{2}$$

Thus, for example, $\nabla^2 \Psi = \frac{\partial^2 \Psi}{\partial z^2} + \nabla_2^2 \Psi = 0$.

The odd term Ψ_o produces a field with median plane symmetry, while the even term Ψ_e spoils this symmetry. The magnetic field is given by $\vec{B} = -\nabla\Psi$, that is

$$\begin{aligned}
B_z &= -B + z\nabla_2^2 C + \frac{z^2}{2!}\nabla_2^2 B - \frac{z^3}{3!}\nabla_2^4 C - \frac{z^4}{4!}\nabla_2^4 B + \ldots, \\
B_r &= -\frac{\partial C}{\partial r} - z\frac{\partial B}{\partial r} + \frac{z^2}{2!}\frac{\partial \nabla_2^2 C}{\partial r} + \frac{z^3}{3!}\frac{\partial \nabla_2^2 B}{\partial r} - \ldots, \\
rB_\theta &= -\frac{\partial C}{\partial \theta} - z\frac{\partial B}{\partial \theta} + \frac{z^2}{2!}\frac{\partial \nabla_2^2 C}{\partial \theta} + \frac{z^3}{3!}\frac{\partial \nabla_2^2 B}{\partial \theta} - \ldots.
\end{aligned} \tag{3}$$

In most orbit programs, C is ignored and only the zero-order B_z value and the first-order B_r and B_θ values are used. This is acceptable only for z very small compared with the magnet gap since it violates $\nabla \cdot \vec{B} = 0$ and can therefore lead to non-physical results for finite z values. This can be remedied by including the z^2 term in B_z. In general, when B_r and B_θ are given to order z^n, then B_z should be given to order z^{n+1}.

Ignoring C is appropriate in the initial design stage of a cyclotron, but not for finding tolerances for manufacturing errors, nor for detailed investigations of orbit excursions and resonance crossings in an as-built cyclotron. In the TRIUMF cyclotron, the vertical closed orbit excursion is as large as ±1.3 cm even after correction, as shown below. In a synchrotron, the closed orbit distortion is corrected with

ISBN: 978-3-95450-212-7 ISSN: 2673-5482 doi:10.18429/JACoW-CYCLOTRONS2022-FRB004

separate small dipole magnets. But in cyclotrons, where the radial extent of the beam gap is orders of magnitude larger than that gap, this is not possible; instead, orbits are corrected vertically using trim coils that are placed above and below the median plane. Powered in opposition to each other, they create radial field components that can correct the beam vertical position.

REDUNDANCY IN THE ERROR FIELD SURVEY DATA

The symmetrical part of the cyclotron field is directly given by the measured axial field in the median plane, while the axial derivative of this field and the transverse components in the median plane all are derived from the function $C(r,\theta)$. We use this fact to correct errors in the measured asymmetric field components.

By substituting $z = 0$ in Eq. (3), the magnetic field in the median plane is written as

$$\begin{aligned} B_r &= -\frac{\partial C}{\partial r}, \\ rB_\theta &= -\frac{\partial C}{\partial \theta}, \\ B_z &= -B. \end{aligned} \tag{4}$$

when the median plane symmetry is broken, the axial derivative of the axial field dB_z/dz in the median plane is non-zero and is expressed as

$$\frac{dB_z}{dz} = \nabla_2^2 C = \frac{\partial^2 C}{\partial r^2} + \frac{1}{r}\frac{\partial C}{\partial r} + \frac{1}{r^2}\frac{\partial^2 C}{\partial \theta^2}. \tag{5}$$

The asymmetric components B_r, B_θ and dB_z/dz were measured at $z = 0$ on a polar grid with 1° intervals in azimuth and 3 inch intervals in radius, but the final data are given as Fourier series in azimuth, up to 29 harmonics. Since different harmonics are orthogonal, every harmonic individually satisfies the Eqs. (4) and (5). The n^{th} harmonic of the map B_{rn}, $B_{\theta n}$ and dB_{zn}/dz satisfies

$$\begin{aligned} B_{rn} &= -\frac{\partial C_n}{\partial r}, \\ rB_{\theta n} &= -\frac{\partial C_n}{\partial \theta}, \\ \frac{dB_{zn}}{dz} &= \frac{\partial^2 C_n}{\partial r^2} + \frac{1}{r}\frac{\partial C_n}{\partial r} + \frac{1}{r^2}\frac{\partial^2 C_n}{\partial \theta^2}, \end{aligned} \tag{6}$$

where C_n is the n^{th} harmonic of the scalar potential of the asymmetric field. Writing the harmonic in complex form, Eqs. (6) are simplified to ordinary differential equations (ODE) which have only the radius r as variable

$$\begin{aligned} B_{rn} &= -\frac{dC_n}{dr}, \\ B_{\theta n} &= -jn\frac{C_n}{r}, \\ \frac{dB_{zn}}{dz} &= \frac{d^2 C_n}{dr^2} + \frac{1}{r}\frac{dC_n}{dr} - n^2\frac{C_n}{r^2}. \end{aligned} \tag{7}$$

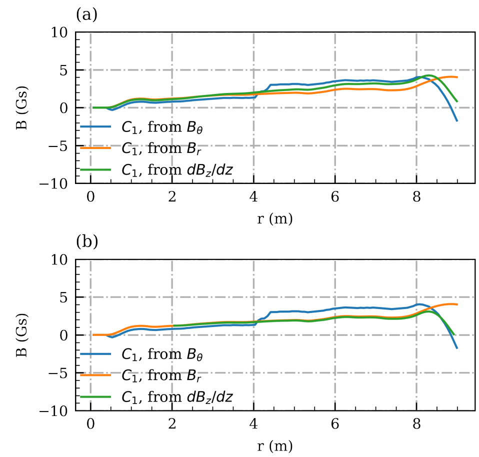

Figure 1: First harmonic of the asymmetric field potential map C_1. (a) Calculated using Eq. (7) starting from the center of the cyclotron, where the field is homogeneous and thus the ODE's initial conditions are $C_1(0) = -jB_\theta(0) = 0$ and $C_1'(0) = -B_r(0) = 0$. (b) Calculated using Eq. (7) starting from the radius of 2 m in the third ODE.

In the complex form of the n^{th} harmonic, n could be either sign. So Eq. (7) should be solved from -29^{th} to 29^{th} harmonics. By solving Eq. (7) numerically, we get three versions of the C map, from the survey data of B_r, B_θ and dB_z/dz respectively. As an example, Fig. 1 compares the obtained first harmonic of the C map. From B_θ, there are two regions of first derivative discontinuities, occurring at ~0.5 and 4 m respectively. This suggests the existence of some systematic error in the measurement data of B_θ. The difference between the C_1 as calculated from B_r and dB_z/dz grows with the radius, but this is easily corrected by changing the initial condition within uncertainty. As a result of the finite size of the flip coils, the survey data has a relatively larger error at a smaller radius. Thus, if integrating from a larger radius with a relatively constant slope in the field, the difference becomes smaller, as shown in Fig. 1(b).

APPLICATION I: CORRECTING THE ERROR IN THE FIELD SURVEY DATA

The redundancy in the survey data makes it possible to correct the error in the measurement data. Using Eq. (7), we can generate a full map from a single potential map C. To reduce numerical errors due to the interpolation while solving Eq. (7), we directly use the CFD method [3] to calculate the new maps. The equations used for the correction are obtained by substituting C_n with $jrB_{\theta n}/n$ in Eq. (7)

$$\begin{aligned} jnB_{rn} &= \frac{d(rB_{\theta n})}{dr}, \\ jn\frac{dB_{zn}}{dz} &= -\frac{d^2(rB_{\theta n})}{dr^2} - \frac{1}{r}\frac{d(rB_{\theta n})}{dr} + n^2\frac{rB_{\theta n}}{r^2}. \end{aligned} \tag{8}$$

The resulting first harmonic field is compared in Fig. 2. The B_θ survey data seems to be shifted upward at radii before 4 m and thereafter shifted downward, in comparison with

ISBN: 978-3-95450-212-7 ISSN: 2673-5482 doi:10.18429/JACoW-CYCLOTRONS2022-FRB004

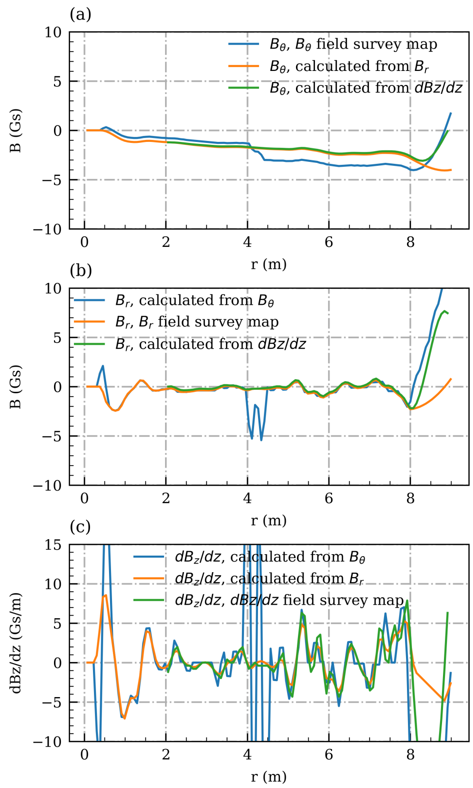

Figure 2: Comparison of the first harmonic of the asymmetric field components B_θ (a), B_r (b) and dB_z/dz (c), constructed with different survey data.

those calculated from the other two survey maps. The B_r survey map agrees with the calculated ones except for the spike at ~4 m occurring in the one calculated from B_θ (see Fig. 2 (b)). B_θ is too noisy to give a usable dB_z/dz map, while the calculated dB_z/dz from B_r agrees with the survey result (see Fig. 2 (c)) and is even smoother than the survey data because high-frequency components are filtered out.

Since the magnet gap is so large at ~0.5 m, it is inconceivable that the radial field can step discontinuously on a scale of the flip coil separation (< 0.08 m). We, therefore, choose the radial field B_r survey data to correct the error of the azimuthal field B_θ; this is also because the reconstruction is less sensitive to the initial conditions than using dB_z/dz as shown in Fig. 1. Figure 3 compares the corrected B_θ map with the survey result.

APPLICATION II: MEASURING VERTICAL TUNE

TRIUMF cyclotron is equipped with 54 pairs of trim coils, each consisting of two circular loops, one above and one below the mid-plane, and spaced at 15 cm intervals radially. They could be used with top and bottom coils in opposite currents (referred to as B_r-mode), to create a radial field and thereby move the beam vertically.

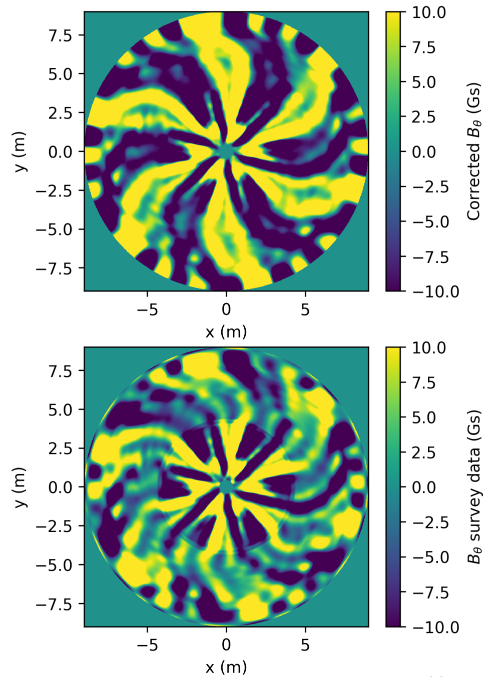

Figure 3: Azimuthal field map in the median plane. The survey map (lower) displays an obvious discontinuity at radius of ~4 m, and thereafter a blurred edge of the sector structure. The corrected map (upper) shows a sharper image of the sector edges of the main magnet.

The relation between the vertical displacement of the orbit Δz and the radial field is given in smooth approximation by

$$\Delta z = \frac{\overline{R}}{\overline{B}_z}\frac{\Delta\overline{B_r}}{\nu_z^2}, \tag{9}$$

where $\overline{B}_z = m\gamma\omega/q$, $\overline{R} = \beta c/\omega$ for isochronism, m is particle mass and ω is orbital frequency. Thus, the vertical tune can be found in the vertical displacement produced by creating a radial field using the B_r-mode of trim coil(s).

A detailed study of the tune measurement and adjustment is presented in our previous study [4]. Figure 4 shows the result. The measured results from different trim coil pairs agree well in the field overlap regions, meaning that both the trim coil field and the probe's radial position are consistently calibrated with the orbital average radius. The measured results reproduce several bumps of the CYC581 data, which is calculated from field survey data, but differ significantly in some areas. This could be because the trim coils were powered in a different pattern during the field survey than they are now, but this information has been lost over time.

APPLICATION III: CORRECTING THE LINEAR COUPLING RESONANCE

In the TRIUMF 500 MeV H$^-$ cyclotron, the linear coupling resonance $\nu_r - \nu_z = 1$ is crossed multiple times as shown by the CYC581 tune diagram in Fig. 5. This is calculated from the historical magnetic field survey data of 1974. It suggests that this resonance is crossed first around

ISBN: 978-3-95450-212-7 ISSN: 2673-5482 doi:10.18429/JACoW-CYCLOTRONS2022-FRB004

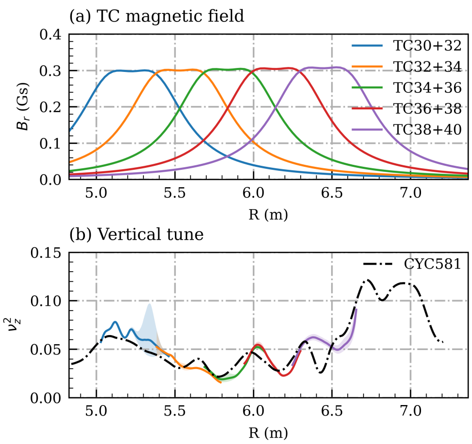

Figure 4: (a) The radial field profiles of indicated trim coil pairs, and (b) (with the same colour code) the measured vertical tune using these pairs, along with the CYC581 data.

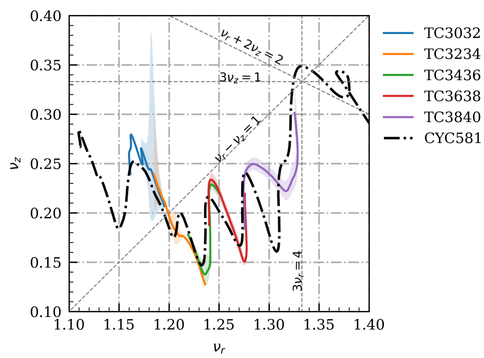

Figure 5: Tune diagram (coloured) experimentally measured using the indicated trim coil pairs, and (dot-dashed) obtained from the CYC581.

166 MeV and then again twice near 291 MeV. This resonance induces the exchange of betatron oscillation amplitudes between the radial and vertical directions. The usual technique would be to correct the resonance by applying a compensating radial first harmonic magnetic field of appropriate phase and amplitude. The TRIUMF cyclotron is equipped with 13 such ‘harmonic coils’. These each has radial widths of 60 cm and consist of six sectors, 60° wide, on top and bottom of the vacuum tank. Powered in opposite directions, and following a 6-part segmented sine wave, they create a first harmonic radial field in the geometric median plane. A detailed resonance correction is studied by Yi-Nong [5], we present part of the results in this paper (Figs. 6 and 7).

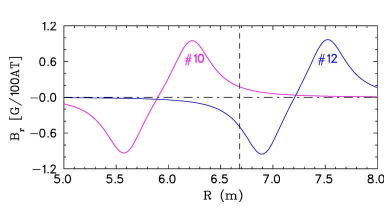

Figure 6: The B_r amplitude measured in the geometrical median plane due to harmonic correction coils HC10 and HC12 separately.

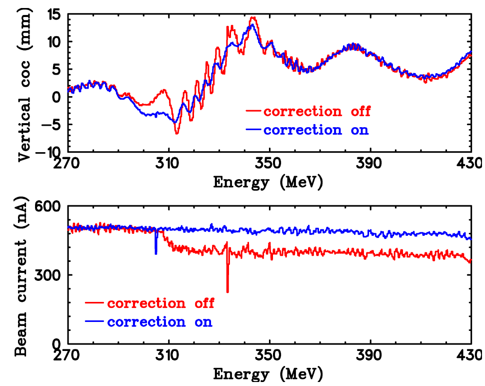

Figure 7: Radial probe measured vertical centre of charge (upper) and transmission (lower) vs. energy, before and after correction of the resonance. Here a coherent radial centring error of the beam orbit was intentionally introduced by detuning the HC2 B_z first harmonic amplitude.

CONCLUSION

By using Gordon’s approach, the redundancy in the field survey maps B_θ, B_r and dB_z/dz, resulting from the magnetic median plane tilt error, is revealed. Using the redundancy, we crosschecked the field survey data of TRIUMF cyclotron. A systematic error in the B_θ survey data was found and has been corrected. The median plane error field could also be used to measure the vertical tune and correct the coupling resonance. We discussed the examples of these applications in the TRIUMF cyclotron.

ACKNOWLEDGEMENTS

This work was funded by TRIUMF which receives federal funding via a contribution agreement with the National Research Council of Canada.

REFERENCES

[1] M. Gordon and W. Hudec, “Effects of field imperfections on radial stability in a three-sector cyclotron,” *Nucl. Instrum. Methods*, vol. 18, pp. 243–267, 1962. doi:10.1016/S0029-554X(62)80034-2

[2] R. Baartman and T. Planche, *Cyclotrons: Beam Dynamics and Design*. U.S. Particle Accelerator School, 2021.

[3] D.-O. Jeon, “Compact finite difference method for calculating magnetic field components of cyclotrons,” *J. Comput. Phys.*, vol. 132, no. 2, pp. 167–174, 1997. doi:10.1006/jcph.1996.5635

[4] L. G. Zhang, Y.-N. Rao, R. Baartman, Y. Bylinskii, and T. Planche, “Vertical Tune Measurement and Correction for the 500 MeV Cyclotron,” *TRIUMF Beam Physics Note TRI-BN-21-24*, 2021.

[5] Y.-N. Rao and L. G. Zhang, “Cyclotron Beam Development Shifts Summary on Measurements of Linear Coupling Resonance Correction and its Benefits,” *TRIUMF Beam Physics Note TRI-BN-21-23*, 2021.

ISBN: 978-3-95450-212-7 ISSN: 2673-5482 doi:10.18429/JACoW-CYCLOTRONS2022

List of Authors

Bold papercodes indicate primary authors; ~~strike through/black~~ papercodes indicate **no submission received**

ISBN: 978-3-95450-212-7 ISSN: 2673-5482 doi:10.18429/JACoW-CYCLOTRONS2022

ISBN: 978-3-95450-212-7 ISSN: 2673-5482 doi:10.18429/JACoW-CYCLOTRONS2022

ISBN: 978-3-95450-212-7 ISSN: 2673-5482 doi:10.18429/JACoW-CYCLOTRONS2022

ISBN: 978-3-95450-212-7 ISSN: 2673-5482 doi:10.18429/JACoW-CYCLOTRONS2022

ISBN: 978-3-95450-212-7 ISSN: 2673-5482 doi:10.18429/JACoW-CYCLOTRONS2022

ISBN: 978-3-95450-212-7 ISSN: 2673-5482 doi:10.18429/JACoW-CYCLOTRONS2022

Institutes List

AEC
Bern, Switzerland
- Braccini, S.
- Casolaro, P.
- Dellepiane, G.
- Gottstein, A.
- Mateu, I.
- Scampoli, P.

Agilent Technologies Italia SpA
Leini, Italy
- Audi, M.A.

Amity University, Amity School of Applied Sciences
Gurugram, India
- Kumar, A.
- Sharma, J.

ASIPP
Hefei, People's Republic of China
- Ding, K.Z.
- Jiang, F.
- Li, B.
- Shen, J.S.
- Wu, Z.
- Xia, S.B.
- Xing, Y.
- Zhou, J.

CCME
Beijing, People's Republic of China
- Liu, Liu,Z.

CGN
Mianyang City, People's Republic of China
- Zhang, X.H.

Charite
Berlin, Germany
- Cordini, D.
- Heufelder, J.
- Seidel, S.
- Stark, R.
- Weber, A.

Chuba
Aichi, Japan
- Watabe, T.

CIAE
Beijing, People's Republic of China
- An, S.
- Bao, J.
- Bian, T.J.
- Cai, H.R.
- Cao, L.C.
- Chen, L.H.
- Chen, Q.
- Chu, Z.C.
- Cui, B.Q.
- Ding, A.X.
- Fu, W.F.
- Fu, X.L.
- Gong, Y.H.
- Guan, F.P.
- Guan, L.L.
- Guo, G.
- Guo, Q.K.
- Han, J.H.
- He, A.L.
- Hou, S.G.
- Hu, M.Z.
- Huang, P.
- Ji, B.
- Ji, L.Y.
- Jia, X.L.
- Jia, Y.
- Jiang, S.M.
- Jiang, T.Y.
- Jiao, T.Y.
- Jin, Z.J.
- Le, H.
- Li, L.W.
- Li, M.
- Li, P.Z.
- Lin, J.
- Liu, C.C.
- Liu, J.C.
- Liu, J.Y.
- Liu, J.
- Liu, P.
- Liu, Q.
- Liu, Z.W.
- Ma, R.
- Ma, X.
- Ma, Y.J.
- Mu, X.
- Nong, Z.J.
- Pan, G.F.
- Pei, S.
- Shi, H.L.
- Song, G.F.
- Song, Q.Q.
- Sui, L.
- Tang, B.
- Wang, C.
- Wang, F.
- Wang, J.F.
- Wang, L.
- Wang, Q.J.
- Wang, Y.F.
- Wang, Y.
- Wei, J.Y.
- Wei, S.M.
- Wen, L.P.
- Xie, H.D.
- Xing, J.S.
- Yang, F.D.
- Yang, G.

ISBN: 978-3-95450-212-7 ISSN: 2673-5482 doi:10.18429/JACoW-CYCLOTRONS2022

- Yin, Z.G.
- Yin, Z.Y.
- Zhang, D.Z.
- Zhang, F.Q.
- Zhang, H.
- Zhang, L.
- Zhang, S.P.
- Zhang, T.J.
- Zhang, z.
- Zhao, B.H.
- Zhao, H.Y.
- Zheng, X.
- Zhou, H.
- Zhu, P.F.
- Zhu, X.F.

DELTECH
New Delhi, India
- -, A.
- Sharma, S.C.

DESY
Hamburg, Germany
- Fröhlich, N.-O.

ETH
Zurich, Switzerland
- Kirch, K.
- Maradia, V.

Federal Research Center "Computer Science and Control", Russian Academy of Sciences
Moscow, Russia
- Karamysheva, T.V.

FZJ
Jülich, Germany
- Felden, O.
- Gebel, R.
- Giesen, U.G.
- Kamerdzhiev, V.
- Lohoff, R.L.
- Soltner, H.
- Valdau, Y.

GANIL
Caen, France
- Kamalou, O.
- Savalle, A.

GSI
Darmstadt, Germany
- Gebel, R.
- Grigoryev, K.
- Niedermayer, P.J.
- Valdau, Y.

Gunma University, Heavy-Ion Medical Research Center
Maebashi-Gunma, Japan
- Nakao, M.

HeFei CAS Ion Medical and Technical Devices
Hefei, Anhui, China, People's Republic of China
- Zhu, L.

HFCIM
HeFei, People's Republic of China
- Shen, J.S.
- Xu, S.

HISKP
Bonn, Germany
- Beck, R.
- Eversheim, P.D.
- Sauerland, D.

Hokkaido University
Sapporo, Japan
- Noguchi, S.

HS Coburg
Coburg, Germany
- Prechtl, M.
- Wolf, C.R.

HUST
Wuhan, People's Republic of China
- Chen, A.T.
- Chen, Q.S.
- Chen, Y.
- Li, C.Y.
- Li, P.L.
- Liao, Y.C.
- Liu, X.
- Qin, B.
- Wang, W.
- Yang, Z.Y.

HZB
Berlin, Germany
- Bundesmann, J.
- Damerow, T.
- Denker, A.
- Dillenardt, S.
- Dittwald, A.
- Fanselow, T.
- Hildebrand, D.
- Hiller, U.
- Kourkafas, G.
- Ozierenski, S.
- Röhrich, J.
- Rössink, D.

IBA
Louvain-la-Neuve, Belgium
- Abs, M.
- Cailliau, P.
- Caulier, J.
- D'Agostino, G.
- Deprez, S.
- Donzel, X.
- Flandroy, Q.
- Geets, J.-M.
- Goosse, G.
- Jongen, Y.
- Kleeven, W.J.G.M.
- Koffel, L.C.L.
- Kral, E.K.

ISBN: 978-3-95450-212-7 ISSN: 2673-5482 doi:10.18429/JACoW-CYCLOTRONS2022

- Mandrillon, J.
- Michaux, O.
- Mine, N.A.R.
- Nuttens, V.
- Otu, Y.
- Paradis, Y.
- van der Kraaij, E.
- Verbruggen, P.

IBS
Daejeon, Republic of Korea
- Kim, J.-W.
- Yeon, Y.H.

IIT Delhi
New Delhi, India
- Dhawan, R.

IMP/CAS
Lanzhou, People's Republic of China
- Chen, X.
- Dou, G.L.
- Jia, Z.H.
- Li, C.C.
- Li, L.B.
- Li, Q.
- Li, Y.T.
- Lu, W.
- Ma, J.D.
- Ma, L.Z.
- Peng, P.
- Qian, C.
- Shi, J.
- Su, X.M.
- Sun, L.T.
- Wang, B.
- Wang, X.W.
- Xia, J.W.
- Xiao, G.Q.
- Xu, Z.
- Yang, J.C.
- Yang, L.
- Yao, Q.G.
- Yuan, Y.J.
- Zhan, W.-L.
- Zhang, P.
- Zhang, R.
- Zhang, X.Z.
- Zhao, H.W.

INFN/LNL
Legnaro (PD), Italy
- Antonini, P.
- Maggiore, M.
- Pranovi, L.
- Ruzzon, A.

INFN/LNS
Catania, Italy
- Calabretta, L.
- D'Agostino, G.

ISIR
Osaka, Japan
- Washio, T.

iThemba LABS
Somerset West, South Africa
- Barnard, A.H.
- Strydom, I.L.

JINR
Dubna, Moscow Region, Russia
- Bunyatov, K.
- Gurskiy, S.
- Hodshibagijan, G.G.
- Karamyshev, O.
- Karamysheva, G.A.
- Karamysheva, T.V.
- Nikiforov, D.
- Novikov, M.S.
- Popov, D.
- Romanov, V.M.
- Shirkov, G.
- Shirkov, S.G.
- Sinitsa, A.A.
- Trubnikov, G.V.
- Yakovenko, S.

JINR/DLNP
Dubna, Moscow region, Russia
- Gerasimov, V.A.
- Karamyshev, O.
- Lyapin, I.D.
- Malinin, V.
- Popov, D.

KEK
Tsukuba, Japan
- Otani, M.

King Abdul-Aziz University, I-one
Jeddah, Kingdom of Saudi Arabia
- Alredhi, M.
- Alsaif, R.N.
- Balkheir, M.A.
- Farhood, S.Y.
- Lingawi, S.S.
- Sharaf, M.A.

King Faisal Specialist Hospital and Research Centre
Riyadh 11211, Kingdom of Saudi Arabia
- Miliebari, S.M.

Konica Minolta Zaiqi Medical Products (Shanghai) Co., LTD.
Shanghai, People's Republic of China
- Ran, Q.

KRO
Bern, Switzerland
- Weber, D.C.

Kyoto University, Research Reactor Institute
Osaka, Japan
- Ishi, Y.
- Mori, Y.
- Uesugi, T.

ISBN: 978-3-95450-212-7 ISSN: 2673-5482 doi:10.18429/JACoW-CYCLOTRONS2022

Mevionchina
Kunshan, People's Republic of China
- Li, G.H.
- Lu, M.W.
- Tian, Y.

MIT
Cambridge, Massachusetts, USA
- Alonso, J.R.
- Conrad, J.M.
- Waites, L.H.
- Winklehner, D.

Naples University Federico II
Napoli, Italy
- Scampoli, P.

NHa
Caen, France
- Cosson, O.
- Maunoury, L.
- Velten, Ph.

Niigata University
Niigata, Japan
- Fukui, S.

Okayama University
Okayama, Japan
- Ueda, H.

OMPU
Takatsukishi, Japan
- Aihara, T.
- Hu, N.H.

PARTREC
Groningen, The Netherlands
- Both, S.
- Brandenburg, S.
- de Koster, R.J.C.
- Gerbershagen, A.
- Goethem, M.J.
- Schippers, J.M.
- Xiao, M.

PSI
Villigen PSI, Switzerland
- Adelmann, A.
- Baumgarten, C.
- Besana, M.I.
- Bopp, M.
- Colizzi, I.
- Eichler, R.
- Fortunati, R.F.
- Frey, P.
- Gabard, A.L.
- Grillenberger, J.
- Haj Tahar, M.
- Hartmann, M.
- Hohmann, E.
- Kan, R.
- Kirch, K.
- Kiselev, D.C.
- Knecht, A.
- Koschik, A.
- Kostezer, M.
- Künzi, R.
- Laube, D.
- Lomax, A.L.
- Lucas, T.G.
- Maradia, V.
- Meer, D.
- Mülhaupt, A.
- Pedrozzi, M.
- Psoroulas, S.
- Raguin, J.-Y.
- Rauber, T.
- Reggiani, D.
- Sapinski, M.
- Schibli, R.
- Schippers, J.M.
- Schmidt, A.
- Schneider, M.
- Snuverink, J.
- Stoll, M.
- van der Meulen, N.P.
- Weber, D.C.
- Wellenkamp, U.
- Werthmüller, D.
- Zhang, H.

PUMCH
Beijing, People's Republic of China
- Huo, L.H.

QST/Takasaki
Takasaki, Japan
- Ishioka, N.S.
- Kashiwagi, H.
- Kurashima, S.
- Miyawaki, N.
- Watanabe, S.

RCNP
Osaka, Japan
- Chong, T.H.
- Fukuda, M.
- Hara, T.
- Hatanaka, K.
- Imajo, S.
- Kanda, H.
- Kittaka, M.
- Matsui, S.
- Morinobu, S.
- Morita, Y.
- Nagayama, K.
- Saito, T.
- Shima, T.
- Takeda, K.
- Tamura, H.
- Tomono, D.
- Yasuda, Y.
- Yorita, T.
- Yoshida, H.
- Zhao, H.

ISBN: 978-3-95450-212-7 ISSN: 2673-5482 doi:10.18429/JACoW-CYCLOTRONS2022

RIKEN
Saitama, Japan
- Nagatomo, T.

RIKEN Nishina Center
Wako, Japan
- Fukunishi, N.
- Higurashi, Y.
- Komiyama, M.
- Kumagai, K.
- Ohnishi, J.
- Okuno, H.
- Uchiyama, A.
- Yamada, K.

RIKEN, Center for Advanced Photonics
Wako, Japan
- Takanashi, T.T.

RIKEN/RARF/CC
Saitama, Japan
- Nakagawa, T.

SARI-CAS
Pudong, Shanghai, People's Republic of China
- Chen, Z.L.
- Li, R.
- Zhao, Z.T.

SCU
Chengdu, People's Republic of China
- Fan, B.F.
- Li, Z.

Shenzhen Institute of Computing Science
Shenzhen, People's Republic of China
- Zhao, R.X.

SHI
Kanagawa, Japan
- Ebara, Y.
- Hirayama, T.
- Kumata, Y.
- Matsubara, Y.
- Mikami, Y.
- Miyashita, T.
- Nakajima, Nakajima,S.
- Takahashi, T.
- Tsurudome, T.
- Tsutsui, H.
- Yoshida, J.

SiLab
Bonn, Germany
- Dingfelder, J.
- Wolf, P.

SINAP
Shanghai, People's Republic of China
- Li, D.M.
- Zhang, M.Z.

SSRF
Shanghai, People's Republic of China
- Gu, M.
- Shen, L.R.

STFC/RAL/ISIS
Chilton, Didcot, Oxon, United Kingdom
- Machida, S.

Suzhou Bama Superconductor Tech. Co.,Ltd.
Zhangpu Town, People's Republic of China
- Guo, Z.XY.

Transmutex SA
Vernier, Switzerland
- Solodko, E.

TRIUMF
Vancouver, Canada
- Au, T.
- Baartman, R.A.
- Bylinskii, Y.
- Fong, K.
- Fu, X.L.
- Ilagan, M.
- Jung, P.M.
- Koay, H.W.
- Law, O.
- Laxdal, R.E.
- Leewe, R.
- Marchetto, M.
- Planche, T.
- Rao, Y.-N.
- Saminathan, S.
- Zhang, L.G.
- Zheng, Q.
- Zvyagintsev, V.

UCT Physics
Cape Town, South Africa
- Buffler, A.
- Hutton, T.
- Jarvie, E.
- Leadbeater, T.W.
- Maibane, K.
- Ndabeni, N.B.
- van Heerden, M.

University of Zurich, University Hospital
Zurich, Switzerland
- Weber, D.C.

VECC
Kolkata, India
- Bandyopadhyay, A.
- Bhattacharya, S.
- Chaddha, N.
- Debnath, J.
- Dey, M.K.
- Goswami, A.
- Nandi, C.
- Nandy, P.P.
- Pal, S.

ISBN: 978-3-95450-212-7 ISSN: 2673-5482 doi:10.18429/JACoW-CYCLOTRONS2022

- Pradhan, J.
- Pratihast, S.V.
- Roy, A.
- Sahoo, S.

Wang
Hefei, People's Republic of China
- Wang, W.

Waseda University
Tokyo, Japan
- Ishiyama, A.

ISBN: 978-3-95450-212-7 ISSN: 2673-5482 doi:10.18429/JACoW-CYCLOTRONS2022

The organisers of CYC2022 gratefully acknowledge the sponsors and exhibitors

ISBN: 978-3-95450-212-7 ISSN: 2673-5482 doi:10.18429/JACoW-CYCLOTRONS2022

KAITENG SIFANG

DOUBLE

bergoz
INSTRUMENTATION

ACF®
The Arizona Carbon Foil Co.